ANL/NSE-22/29

Neutron Source Facility of the National Science Center "Kharkiv Institute of Physics and Technology" at Kharkiv, Ukraine

Nuclear Science and Engineering Division
Argonne National Laboratory

ANL/NSE-22/29

Neutron Source Facility of the National Science Center "Kharkiv Institute of Physics and Technology" at Kharkiv, Ukraine

Prepared by:

Yousry Gohar, Laural L. Briggs, Yan Cao, Richard Fischer, Roger L. Kellogg, Adam Kraus, Elia Merzari, Alberto Talamo, Zhaopeng Zhong

Nuclear Science and Engineering Division
Argonne National Laboratory

Oct 3, 2022

(This page left intentionally blank)

Neutron Source Facility of the National Science Center "Kharkiv Institute of Physics and Technology" at Kharkiv, Ukraine

Table of Contents

Neutron Source Facility of the National Science Center "Kharkiv Institute of Physics and Technology" at Kharkiv, Ukraine

List of Figures

Neutron Source Facility of the National Science Center "Kharkiv Institute of Physics and Technology" at Kharkiv, Ukraine

List of Tables

Neutron Source Facility of the National Science Center "Kharkiv Institute of Physics and Technology" at Kharkiv, Ukraine

ABSTRACT

Argonne National Laboratory developed, designed, and supported the construction of a state-of-the-art Neutron Source Facility (NSF) at the Kharkov Institute of Physics and Technology (KIPT) in Kharkov Ukraine, under the U.S. DOE NNSA Russian Research Reactor Fuel Return (RRRFR) program. Ukraine approved the return of all highly enriched uranium in the country to Russia prior to the 2012 Nuclear Security Summit in return for the RRRFR program to fund the development, the design, and the construction of the NSF. The facility is designed to produce medical isotopes, train nuclear professionals, support the Ukrainian nuclear industry, and provide experimental capabilities for performing reactor physics, materials, and basic science research. The NSF was successfully started and operated in August 2021.

The NSF is the first facility of this type in the world, and it will be used to understand the physics of driven systems for energy production and the disposal of spent nuclear fuels. The NSF consists of a subcritical assembly using low enriched uranium (LEU) fuel driven with an electron accelerator. The NSF target design utilizes tungsten or natural uranium for producing neutrons through photonuclear reactions using 100-MeV electrons. The accelerator power is 100 KW, which produces $3x10^{14}$ neutrons per second from the uranium target. The subcritical assembly is designed to obtain the highest possible neutron flux intensity with an effective neutron multiplication factor of less than 0.98. Passive safety, reliability, and environmental considerations were included in the NSF design. The NSF utilization study shows that this neutron source has the capability of producing different medical isotopes. Several horizontal neutron channels are incorporated for performing applied and basic research. The NSF is configured to accommodate future design upgrades and new missions.

The facility design was approved by the Ukraine Academy of Sciences before starting the NSF construction. The construction, the equipment installation, and the operation of the different systems of the NSF were completed and approved by the Ukrainian regulators. In July 2020, the State Nuclear Regulatory Inspectorate of Ukraine (SNRIU) issued a license for the physical start-up of the NSF. The construction of facility was completed in early 2021.

Neutron Source Facility of the National Science Center "Kharkiv Institute of Physics and Technology" at Kharkiv, Ukraine

I Introduction

Argonne National Laboratory developed, designed, and supported the construction of a state-of-the-art Neutron Source Facility (NSF) at the Kharkov Institute of Physics and Technology (KIPT) in Kharkov Ukraine, under the U.S. DOE NNSA Russian Research Reactor Fuel Return (RRRFR) program. Ukraine approved the return of all highly enriched uranium in the country to Russia prior to the 2012 Nuclear Security Summit in return for the RRRFR program to fund the development, the design, and the construction of the NSF. The facility is designed to produce medical isotopes, train nuclear professionals, support the Ukrainian nuclear industry, and provide experimental capabilities for performing reactor physics, materials, and basic science research. The NSF was successfully started and operated in August 2021.

The NSF consists of a subcritical assembly using low enriched uranium (LEU) fuel driven with an electron accelerator. The NSF target design utilizes tungsten or natural uranium for producing neutrons through photonuclear reactions using 100 MeV electrons. The accelerator power is 100 KW, which produces $3x10^{14}$ neutron per second using the uranium target. The neutron source intensity, spectrum, and spatial distribution of the NSF have been studied as function of the electron beam parameters to maximize the neutron yield and to satisfy different engineering requirements. The subcritical assembly is designed to obtain the highest possible neutron flux intensity with an effective neutron multiplication factor of less than 0.98. Passive safety, reliability, and environmental considerations were included in the NSF design. The subcritical assembly is surrounded by a biological shield that keeps the radiation exposure of the facility workers in the subcritical assembly hall below the regulatory level. A pool to store spent fuel assemblies and spent targets is in the same hall as the subcritical assembly.

The NSF utilization study shows that this neutron source has the capability for producing different medical isotopes. Several horizontal neutron channels are incorporated for performing applied and basic research. The facility design was approved by the Ukraine Academy of Sciences before starting the NSF construction. The construction, the equipment installation, and the operation of the different systems of the NSF were completed and approved by the Ukrainian regulators. In July 2020, the State Nuclear Regulatory Inspectorate of Ukraine (SNRIU) issued a license for the physical start-up of the NSF. The construction of facility was completed in early 2021. The NSF is configured to accommodate future design upgrades and new missions.

The physical start-up of the NSF was completed, and the operating performance parameters of the different systems were measured. KIPT is increasing the NSF operating power in steps to achieve the maximum neutron flux of 2.5×10^{13} neutron per cm^2 per second with the uranium target for starting the NSF utilization. The NSF is the first facility of this type in the world, which will be used to understand the physics of driven systems for energy production and dispose of spent nuclear fuels. This report discusses the physics, the thermal-hydraulics analyses, and the structural analyses of the main facility components; and its capability for producing different medical isotopes. In addition, the required components and the procedures for loading and unloading the target, the fuel assemblies, the sample irradiation cassettes, the beryllium reflector elements, and the neutron absorber elements are discussed and analyzed.

II Target Designs for Generating Neutrons

II.1 Introduction

Two target designs are examined based on the use of tungsten or natural uranium material. Physics, thermal hydraulics, structural, and mechanical design analyses are presented in this section. The neutron yield of the tungsten target is about half of the uranium target, but the tungsten target has a longer operating lifetime. Therefore, both materials are considered for the target design of the NSF.

Several physics studies have been carried out to investigate the main target design choices and the system parameters for a satisfactory operating performance. These analyses are described in Section II.2. The principal focus is to maximize the neutron production for the available electron beam power. Target designs have been developed based on these studies and the engineering aspects including heat transfer, thermal hydraulics, structure, and material requirements.

As part of the design effort, high-fidelity computational fluid dynamics analyses of various target options have been performed using a realistic three-dimensional representation of each design. Section II.3 summarizes the results of the target design optimization for a tungsten target and a uranium target. It also addresses the safety performance of these target options.

The designs for these targets were subjected to a structural analysis by the finite element method, using the ANSYS R13.0 finite element program. This analysis is discussed in Section II.4. Finite element models were constructed and subjected to pressure, clamping, hydrostatic, and gravity loads. Results were compared to basic material properties and commonly accepted engineering principles were applied to determine the design safety factors.

Two target designs have been developed for use in the KIPT experimental neutron source facility. The first target design uses seven tungsten plates, and the second target design uses eleven uranium plates. The details of the mechanical design of each target type are presented in Section II.5.

The heat generated within the target is removed by the forced circulation of demineralized water through the target assembly and heat exchanger. The target cooling system provides coolant flow, heat removal, filtration, de-aeration, chemistry control, and system monitoring functions. The system is explained in detail in Section II.6. The key parameters of the target system are summarized in Section II.7.

II.2 Physics Analysis and Design

Tungsten and natural uranium were selected as target materials for generating neutrons from the electron interactions. The electron beam has a uniform spatial distribution with a square profile. The electron beam power is 100 KW using 100 MeV electrons. The neutron yield per electron for both target materials has been studied to determine the

optimal target length. The neutron yield was calculated by MCNPX [II.2.1], using ENDF/B-VII nuclear data libraries, as a function of target thickness, as shown in Figs. II.2.1 and II.2.2. The statistical error is included in these figures as an error bar. For these calculations, the electron beam is assumed to have evenly distribution over a 64 mm x 64 mm square, centered on a square target area that has outside dimensions of 66 mm x 66 mm. This target cross section is large enough to accommodate the 1% spread of the beam distribution outside the projection area and keep the beam electrons entirely within the target material.

First, a simplified, conservative target model without cladding and coolant channels is used in this study, with various target thicknesses. The neutron yield is calculated based on tallying the net neutron current on the six outer surfaces of the target.

The neutron yield per electron saturates as the target material length increases as shown in Fig. II.2.1. The saturation length is reached at ~70 and ~60 mm for natural uranium and tungsten materials, respectively. The uranium saturation yield of 0.0620 neutrons per electron is ~twice the tungsten saturation yield of 0.0317 neutrons per electron because the uranium fission events generate more neutrons. However, the tungsten target is expected to have a longer operational life than the uranium target. The fission gases from the uranium material cause swelling, which can reduce the coolant flow rate of the target design and increases the stress level in the clad material. These effects can shorten the target operational life and cause failure due to high thermal stresses or clad failure. Both materials are used for the KIPT neutron source facility.

The target design consists of stacked tungsten or uranium plates separated by water cooling channels. The plate surfaces is surrounded by cooling channels that remove the heat deposited by the electron beam. The uranium target plates have aluminum alloy clad to avoid water coolant contamination with fission products. The tungsten target plates are coated with tantalum to enhance the corrosion/erosion resistance of the tungsten target material. A schematic of this target geometry is shown in Fig. II.2.2. Heat transfer, thermal-hydraulics, and thermal stress parametric studies have been performed to define the target geometrical configuration, the size of the water coolant channels, and the temperature distribution in the target materials. Section II.3 shows the detailed discussion of these analyses. The water coolant channels between the target plates have a uniform thickness of 1.75 mm. Each target plate is cooled from both sides to minimize thermal deformation.

Square target plates are utilized, to match the square electron beam profile. The outside dimensions of the target plates are 66 mm × 66 mm. The uranium plates have a cross section of 64.6 mm × 64.6 mm with an additional 0.7 mm of aluminum alloy cladding on all sides of the uranium. The thin uranium plates (2.5 mm thick) have extra clad thickness as shown in Table II.2.1. The tungsten target dimensions are 65.5 mm × 65.5 mm, and the tantalum coating thickness is 0.25 mm on all sides. The plate thicknesses of the tungsten and the uranium targets are shown in Table II.2.1. The thicknesses of the coolant channels and the clad materials are also shown in Table II.2.1.

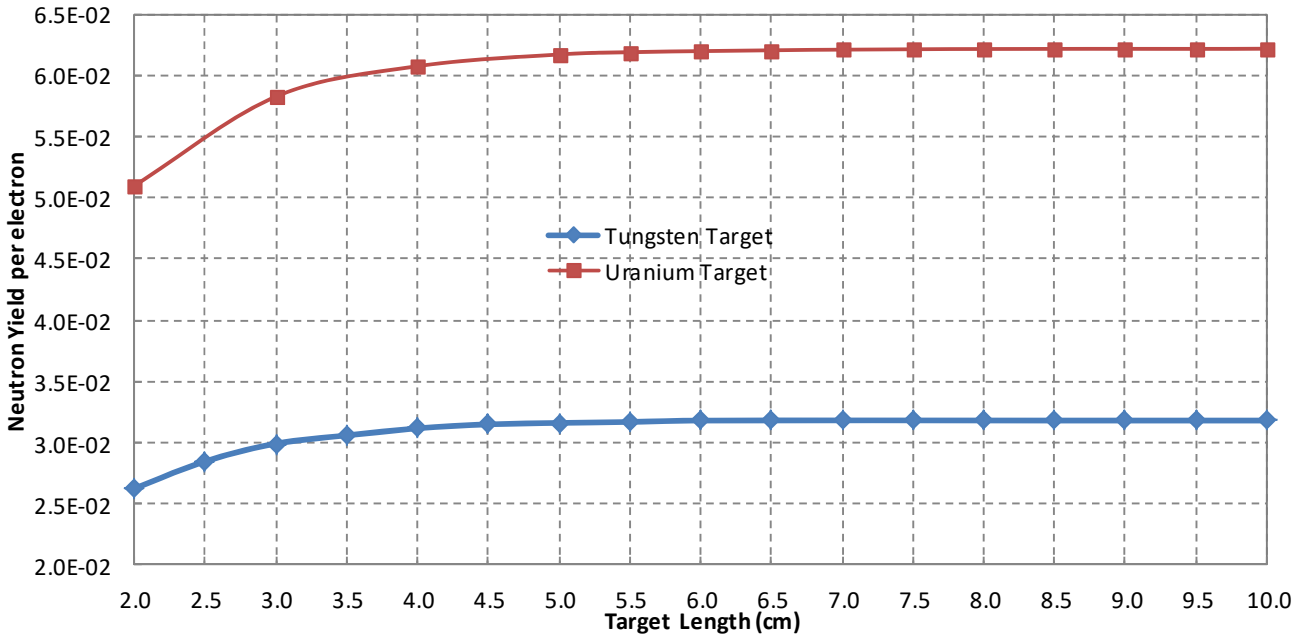

Figure II.2.1. Neutron yield per 100 MeV electron for tungsten and natural uranium as a function of the target length

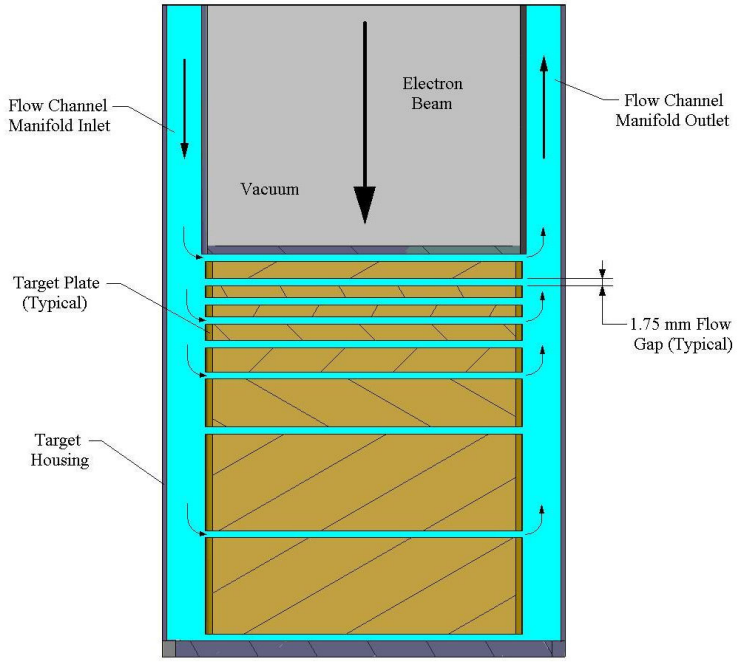

Figure II.2.2. Schematic of the stacked tungsten or uranium plates for generating neutrons from electron interactions

Table II.2.1. Thicknesses of the tungsten and the uranium target plates

Channel number	Tungsten Target		Uranium Target		
	Water channel thickness, mm	Target plate thickness*, mm	Water channel thickness, mm	Target plate thickness, mm	Clad thickness, mm
0	1.0		1.0		
1	1.75	3.0	1.75	3.0	0.7 × 2
2	1.75	3.0	1.75	2.5	0.95 × 2
3	1.75	3.0	1.75	2.5	0.95 × 2
4	1.75	4.0	1.75	2.5	0.95 × 2
5	1.75	4.0	1.75	3.0	0.7 × 2
6	1.75	6.0	1.75	3.0	0.7 × 2
7	1.0	10.0	1.75	4.0	0.7 × 2
8			1.75	5.0	0.7 × 2
9			1.75	7.0	0.7 × 2
10			1.75	10.0	0.7 × 2
11			1.00	14.0	0.7 × 2
Total	12.5	33.0	19.5	56.5	16.9**

*Including the tantalum coating

**The total clad thickness on top and bottom of all the plate

The uranium target consists of eleven plates, with a total uranium thickness of 56.5 mm, which is very close to the neutron yield saturation length. The tungsten target consists of seven plates with a total tungsten thickness (including the tantalum coating) of 33.0 mm. This thickness is less than the neutron yield saturation length. A tungsten thickness of 33.0 mm was selected because tungsten has a large absorption cross section for thermal neutrons. If extra tungsten thickness is used, the number of absorbed neutrons in the tungsten exceeds the number of the additional generated neutrons.

The effect of the tungsten target thickness on the neutron flux level has been evaluated by adding an eighth tungsten plate to the bottom of the target. MCNPX was used to determine the energy deposited inside the target, the neutron flux in the subcritical assembly, and k_{eff}, as a function of the thickness of this eighth plate. Parametric studies were performed by varying the thickness of the bottom plate while keeping the upper seven plates unchanged, as shown in Fig. II.2.3. For each target configuration, the number of fuel assemblies loaded was selected to keep k_{eff} close to, but less than, 0.98. Three configurations were considered, corresponding to each target configuration shown in Fig. II.2.3 and the MCNPX results are given in Table II.2.2. The addition of an eighth tungsten plate increases the number of fuel assemblies required to achieve a k_{eff} just below 0.98. Omitting the eighth tungsten plate reduces the number of the fuel assemblies, without reducing the neutron flux level. Therefore, the seven-plate tungsten target design with a total tungsten thickness of 33 mm was selected.

As discussed in Section III.3, the actual number of fuel assemblies in the subcritical assembly when a tungsten target is used has been set at 38, not the 42 listed in Table II.2.2. To ensure that k_{eff} will not exceed 0.98 under any circumstances, including the removal of the tungsten target from the subcritical assembly. See Section III.3 for a more detailed explanation. The energy deposition profiles in the targets have been calculated by using the mesh tally capability of MCNPX and they are plotted in Figs. II.2.4 and II.2.5. These profiles are used as input to the STAR-CCM+ thermal-hydraulic analysis presented in Section II.3 for both target options.

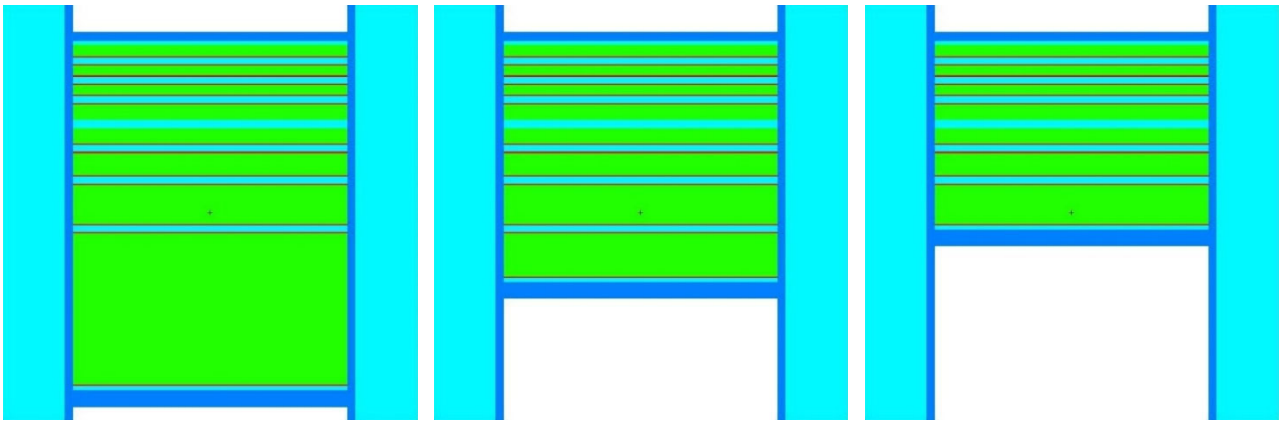

Total tungsten thickness 70 mm, and the 8th plate thickness 37 mm

Total tungsten thickness 44 mm, and the 8th plate thickness 11 mm

Total tungsten thickness 33 mm, only 7 plates included

Figure II.2.3. Tungsten target configuration with different thicknesses

Table II.2.2. Comparison of key parameters of the tungsten target and the subcritical assembly as a function of the tungsten target length

Number of target plates	Total tungsten thickness (cm)	Number of fuel assemblies	k_{eff}	Energy deposited in target (kW)	Average axial neutron flux (n/cm^2.s)
8	7	44	0.97665 ±0.00012	88.680 ±0.01%	1.038e+13 ±0.0033
	4.4	43	0.97881 ±0.00012	87.077 ± 0.01%	1.152e+13 ±0.0036
7	3.3	42	0.97855 ±0.00012	84.194 ± 0.01%	1.162e+13 ±0.0036

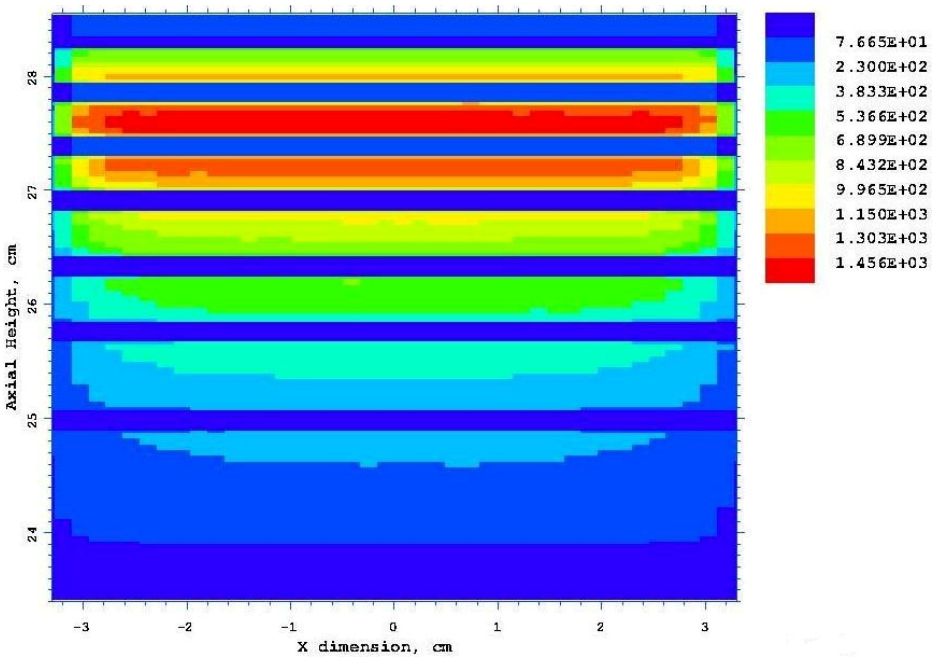

Figure II.2.4. Energy deposition profile inside the tungsten target, in w/cm^3, obtained by 100 kW/100 MeV electron beam, with 38 fuel assemblies

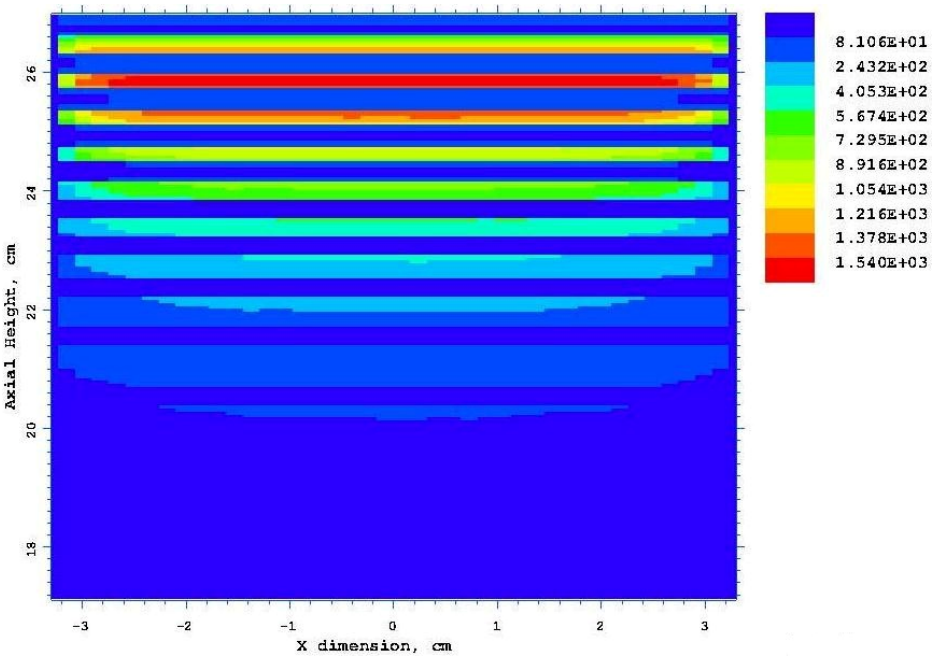

Figure II.2.5. Energy deposition profile inside the uranium target, in w/cm^3, Obtained by 100 kW/100 MeV electron beam, with 37 fuel assemblies

Reference

II.2.1 Denise B. Pelowitz, editor, “MCNPXTM USER’S MANUAL”, Los Alamos Report, LA-CP-05-0369, April 2005.

II.3 Thermal Hydraulics Analysis and Design

This section describes the modeling, the analyses and the optimization of the thermal hydraulics studies performed for the two target designs. In addition, it provides the detailed analyses for the selected tungsten and uranium target designs.

II.3.1 Introduction and Design Considerations

As a part of the development and the design optimizations, high-fidelity analyses of various target design options have been performed using a three-dimensional representation [Ref. II.3.1]. This report summarizes the optimization results for the tungsten and the uranium target designs. It also addresses the related safety analyses of both designs.

The optimization studies of the target design were initially performed via sequential neutronics, thermal-hydraulics, and structural analyses. The goal of the optimization is to maximize the neutron yield, streamline the flow field to avoid hotspots, and minimize the thermal stresses to increase the durability through an optimal configuration (number and size) of the target plates. In all considered cases, the target plate size is 64 x 64 mm in the plane normal to the electron beam direction. The axial length of each plate and the number of plates are the variable parameters in the optimization analyses.

A more extensive survey of design options was conducted previously in Sofu et al. [Ref. II.3.1]. This section focuses on the thermal-hydraulics simulations carried out as part of the optimization analyses and the safety assessment of the tungsten and the uranium targets. The codes used to perform such simulations are the CFD commercial codes STAR-CD 4.08 [Ref. II.3.2] and STAR-CCM+ 5.06 [Ref. II.3.3].

The chosen thermal-hydraulic guidelines for the optimization analyses are:

- a sufficient margin from the melting point of the materials used in the target assembly; and
- the coolant does not reach sub cooled boiling during operation and maintain low temperature as much as possible.

In addition, the temperature gradient needs to be sufficiently low to minimize the thermal stresses. However, this is a minor concern for tungsten. For uranium this constitutes an additional constraint.

Initially Sofu et al. looked at a relatively simple target design, with water flow descending through two channels, passing horizontally through the water channels between the target plates, and ascending again through two channels on the opposite side of the target, Fig. II.3.1.1. Details of the scoping analyses used to optimize the tungsten and the uranium target, the target casing, and the target coolant system design can be found in

Sofu et al [Ref. II.3.1]. The uranium target results show that, to have a sufficient margin for boiling and sufficiently low thermal stresses, over 4.1 kg/s water flow is required. Unfortunately, such water flow rate requires 7.5 m/s water velocity in the inlet channels. Such high velocity implies a higher coolant pressure through the target casing, which causes high stresses in the target casing.

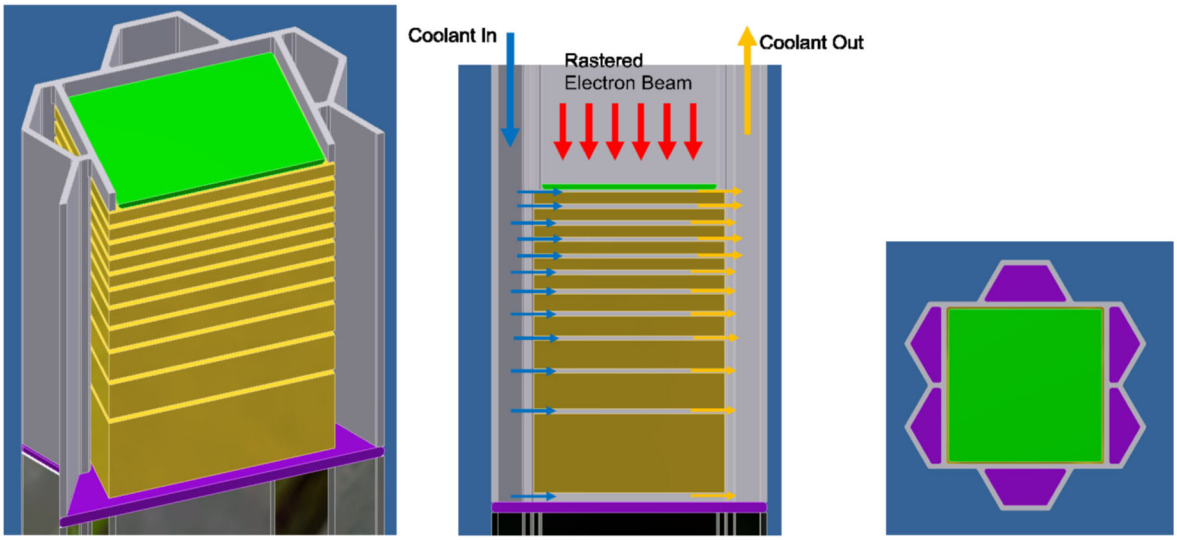

Figure II.3.1.1 Conceptual drawings of a simple target design

The stress analysis shows that that the allowable average water velocity in the inlet channel is 5 m/s based on the water pressure. Thus, an innovative flow path was developed to satisfy this design constraint. The inlet flow is divided to two streams following two separate paths. The target has six water channels around the target plates because of the hexagonal arrangement of the fuel assemblies. Three channels are used for inlet flow and the other three for the outlet flow. Two inlet channels are used to remove the heat from top set of the target plates. The third inlet channel is used to remove the heat from the bottom set of the target plates. To do such arrangement, the coolant in the third channel must flow directly to the bottom below all the target plates, then it flows upward and between the plates of the bottom set of the target plates, in the same direction as the flow through the top set of the target plates. Then the coolant flows down to the bottom to leave the target assembly in the outlet channel. The inlet flow for the three channels comes from a single coolant tube as well as the outlet for the three channels connect to a single coolant tube. So, the three inlet channels have the same pressure as well as the three outlet channels. Figure II.3.1.2 shows the target geometrical configuration, the target plates arrangement, and the coolant flow direction.

This flow configuration reduces the average velocity and the total pressure drop to acceptable levels. Conceptual figures are shown in Figs. II.3.1.2 and II.3.1.3. In Fig. II.3.1.3, red labels refer to the secondary line, while black labels refer to the main

line. The green region on the bottom of the left figure represents the lower manifold, or inversion manifold, where the flow is transferred from the bottom of the secondary line to the bottom of the primary line and vice-versa. Additional figures and discussion of the flow through the target are shown in Section II.5.

The discussion below uses the following terminology:

1. Primary and secondary lines refer to the two separate water flow paths for the top and bottom target plate sets,
2. Target channels refer to the channels of fluid separating the target plates, and
3. Ducts (six ducts) refer to the large trapezoidal and pentagonal flow regions bringing the water coolant into and out of the target plates.

Preliminary STAR-CCM+5.06 CFD calculations shows that if the primary and the secondary lines are allowed to merge as shown in Fig. II.3.1.3, flow instability occurs at the merger area of the two flows. This problem was addressed by introducing two flow separators to avoid the merger of the primary and the secondary lines as shown in Fig. II.3.1.2. The location of the separator was determined by performing a series of thermal-hydraulic calculations with the constraint of reducing the peak temperature in the target plates to a minimum value. This constituted a second stage of optimization.

Both the first and second stages of optimization were only conducted to analyze the flow in the target region, assuming a constant inlet velocity at both the primary line and secondary line. This choice was motivated primarily by the desire to be consistent with previous work. Moreover, it allowed examining the problem with a higher resolution, since it limits the region of interest to the 5.65 cm length of the target. A consequence of this choice is that the second stage optimization was performed considering the splitting ratio between the two flow streams as a parameter. This could have, in principle, had an impact on the optimization results. However, in Section II.3.2 a more general analysis considering the water flow through the whole target casing was simulated and presented. Using STAR-CCM+ 5.06, it was demonstrated that the ratio between the mass flows through the primary and the secondary lines has a weak dependency on the position of the flow separators.

II.3.2 Simulation of the Whole Domain

The simulation of the flow through the whole target casing was examined using STAR-CCM+5.06. An inlet-outlet hydraulic analysis was performed for different inlet mass flow rates and flow separator positions. The CFD model has the fluid region, as shown in Fig. II.3.2.1. Both primary and secondary lines are simulated. The target casing length above the window plate is assumed to be 2 meters long. The two lines are joined through simple inlet and outlet manifolds.

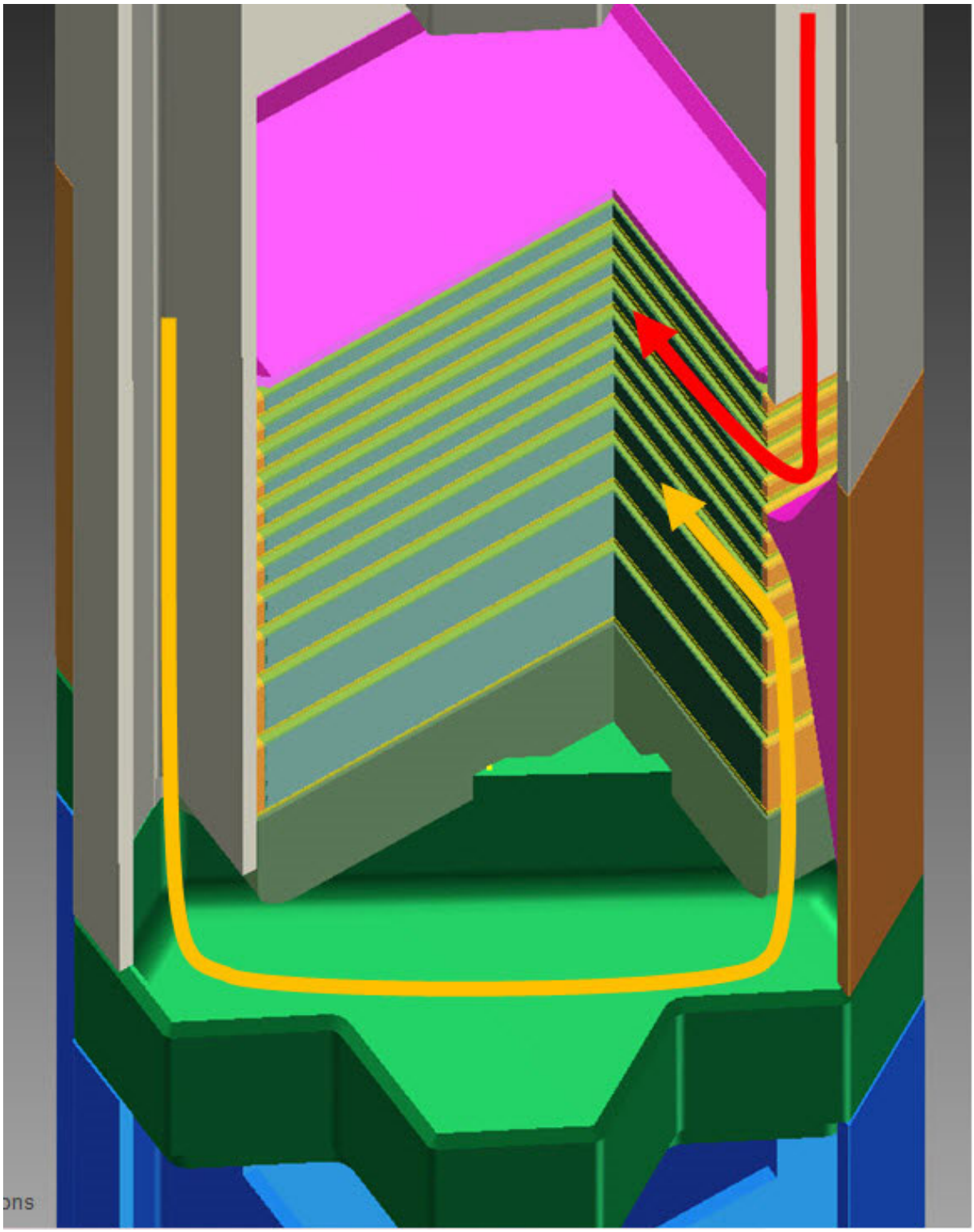

Figure II.3.1.2. Section view through the target assembly shows the coolant flow paths. The coolant in the two five-sided end channels passes through the top set of target plates (red line). The coolant in the trapezoidal side channel passes under target plates and then back up to flow through the bottom set of the target plates (yellow line).

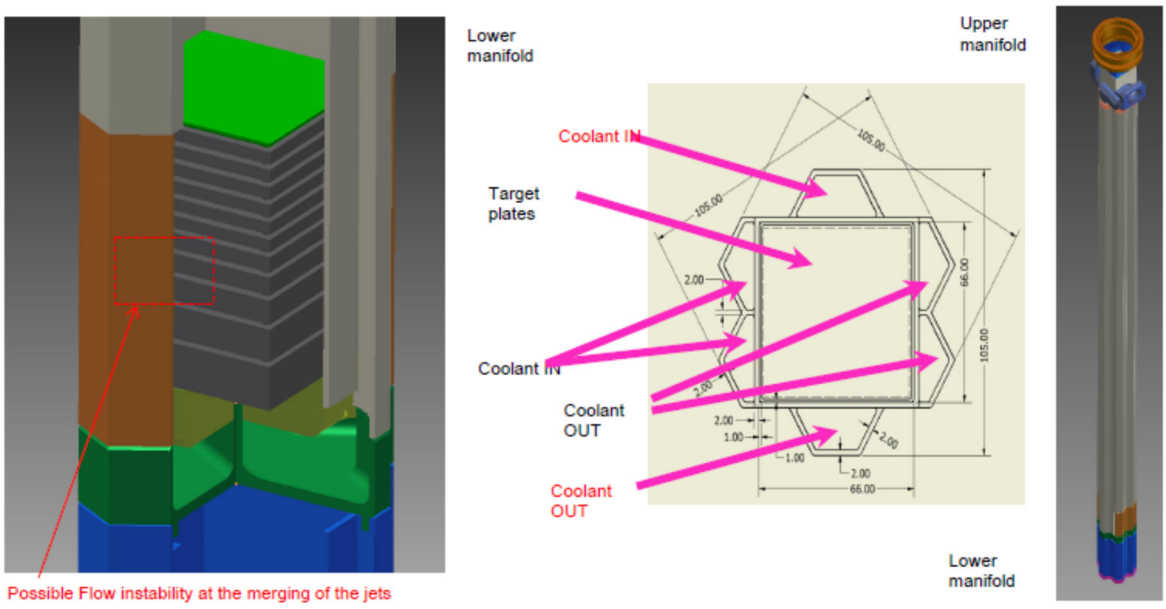

Figure II.3.1.3 Innovative design, from left to right: lower manifold, top view of the ducts feeding the primary and the secondary lines, overall view of the target

A grid was built with ~7 million polyhedral meshes and 14 thin mesh layers in the target channels for the STAR-CCM+ analysis as shown in Fig. II.3.2.2. A prism layer was introduced near the wall. The All-y+ wall treatment was used in conjunction with the k-ε turbulence model. A segregated flow solver was used, and convergence was achieved within 3,000 iterations for the continuity equation. The results show that the mesh is converged.

The main objective of this calculation was to determine the flow split between the two lines. For the 11 uranium target plates, coolant channel divisions of 6-6, 5-7, 3-9 and 2-10, the two numbers represent the number of channels fed by the primary and secondary lines, respectively, were examined. For the 7 tungsten target plates, divisions of 3-5, 4-4, and 5-3 were examined.

Given a set of N_T plates, there will be $N=N_T+1$ coolant channels. The first few coolant channels serve the plates that are closest to the electron beam window where most of the beam power is deposited. Therefore, these channels need most of the flow for removing the deposited power, the first coolant channel cools the beam window. If n is the number of channels fed by the primary line, then channel n+1 receives the least amount of flow because of its location at the end of the secondary line. The main line receives more flow because its flow cross section area is larger relative to the secondary line. In addition, the pressure drop in the coolant channels is relatively small relative to the primary and secondary lines.

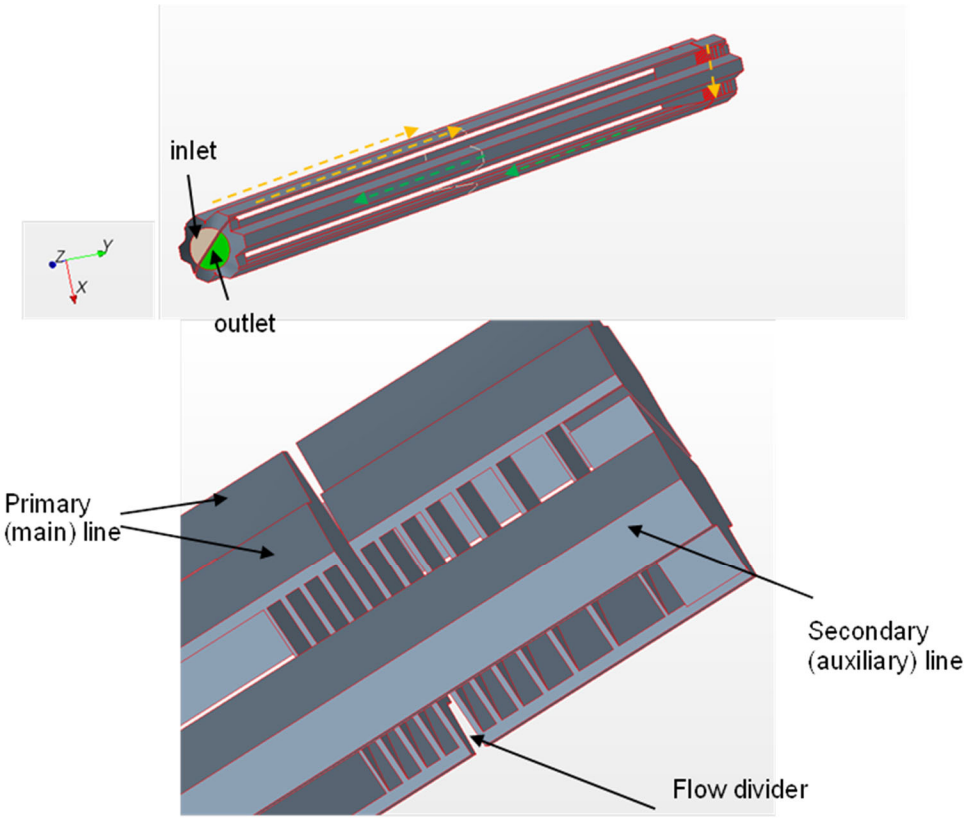

Figure II.3.2.1 CFD hydraulics computational model

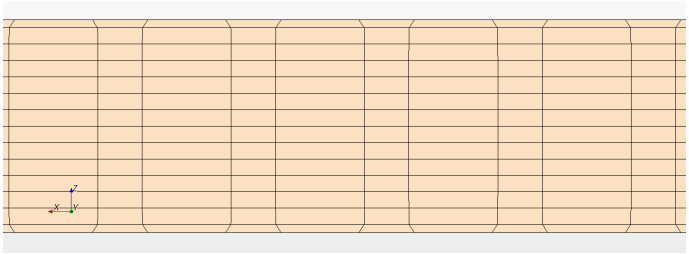

Figure II.3.2.2. Detail of the mesh in one of the coolant channels.

Figure II.3.2.3 shows the velocity distribution within the target casing from the simulation results using the CFD hydraulics computational model shown in Fig. II.3.2.1. In all the simulated cases, the mass flow fraction in the primary line is in the range of 0.56 to 0.58. Therefore, in the optimization process, the flow fraction in the primary lines is assumed equal to 0.58. Sections II.3.3 and II.3.4 describe the optimization process that resulted in selecting a 5-7 flow division for the uranium target and a 4-4 flow division for the tungsten target. The calculated pressure drop for the 4.79 kg/s mas flow rate is:

- 108 kPa in the uranium target (5-7 flow division for the 11 target plates),
- 117 kPa in the tungsten target (4-4 flow division for the 7 target plates).

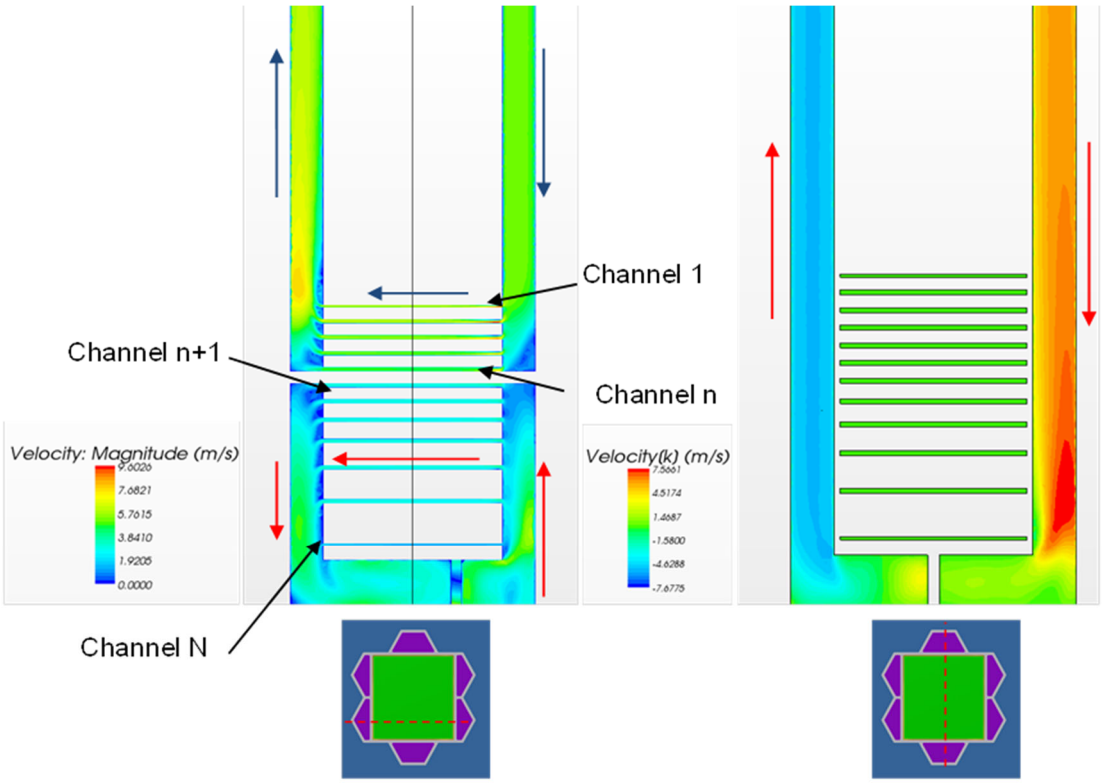

Figure II.3.2.3. Whole target casing simulation results display a section of the main line and its velocity magnitude on the left and a section of the secondary line and its velocity in the axial direction on the right. The red arrows represent the flow direction for the secondary line, while the blue arrows represent the flow direction for the primary line.

II.3.3 Optimization and characterization of the tungsten target cooling loop design

In this section, a sample of the tungsten target optimization studies is described. A full characterization of the optimized tungsten target is also presented.

II.3.3.1 Previous work on the tungsten target

In the previous examined configurations, no tantalum cladding was used and a single coolant feeding line was used. An example of the CFD models developed for the optimization studies is shown in Fig. II.3.3.1.1. Inlet and outlet boundary conditions are specified for the manifold flow boundaries.

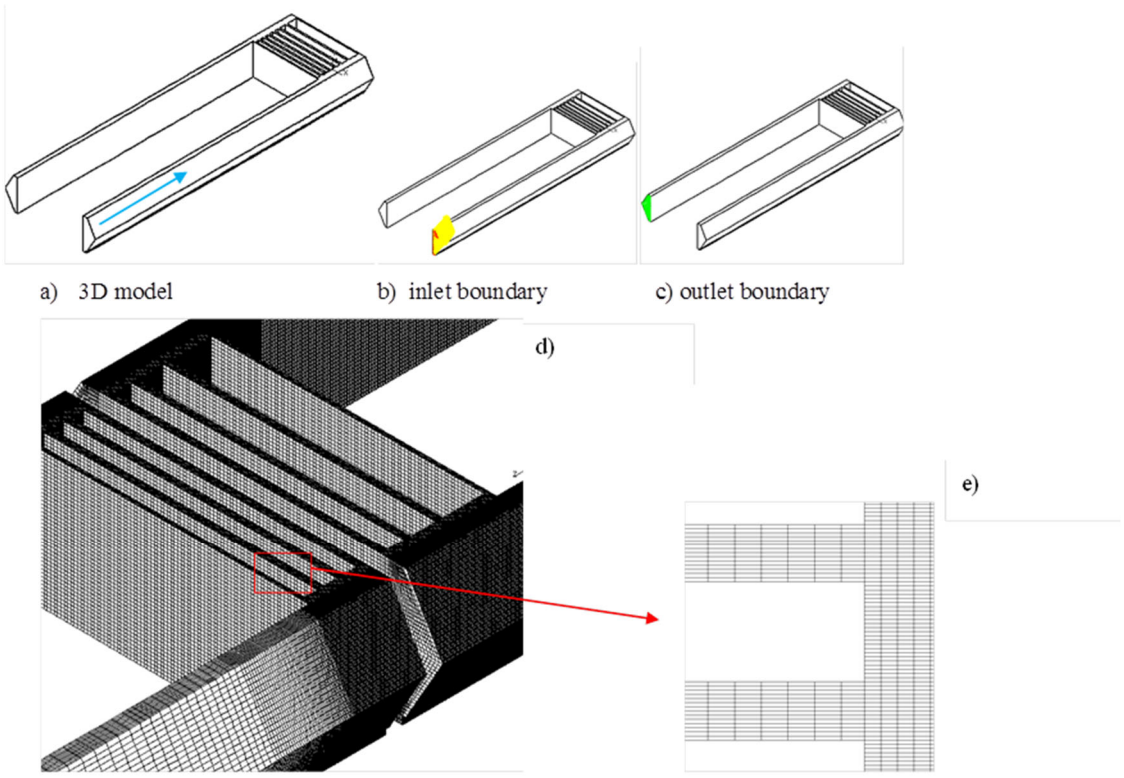

Figure II.3.3.1.1 CFD - fluid model shows the boundary conditions (a-c) and the used mesh (d-e).

The inlet boundary condition assumes a constant velocity equal to 5 m/s, and lower mass flow rates are also considered to evaluate the effects of abnormal operating conditions. The choice of 5 m/s is driven by the mass flow rate needed for the uranium target design since the same loop is used for both targets. The outlet boundary condition is a flow split boundary [Ref. II.3.2]. This boundary type assumes a von-Neumann boundary condition on the velocity and temperature.

In the simulations, the inlet temperature is 293 K (20 °C), and an adiabatic boundary condition is assumed for the outside walls of the aluminum casing. In all simulations, only half of the target is modeled to take advantage of the symmetrical condition to reduce the computational cost. In each coolant channel, five mesh points have been used to describe the flow field. The overall number of mesh elements is approximately 1.3 million. Further refinement did not have a significant change in the temperature distributions. High-Reynolds number wall treatment [Ref. II.3.2] was applied at the walls and the standard k-ε turbulence model was used [Ref. II.3.2]. A laminar case was also examined but it did not converge. Turbulence might be locally suppressed in the target channels, but it is significant in the manifold region, where the Reynolds number is consistently higher than 10^5. The discretization schemes used are upwind first-order scheme for the momentum equation and the MARS scheme, a blended second-order scheme [Ref. II.3.2]. The discretization practices are consistent with Ref. II.3.1.

In the optimization studies, the detailed power distribution was calculated for each configuration with MCNPX, see Section II.2 for a detailed discussion. The three-dimensional power distribution is mapped onto the CFD model using user subroutines. This was done for each material in the target plate within the electron beam profile of 64 x 64 mm. The power generated outside this domain is not included in the calculation, but a correction was applied to the coolant outlet temperature. This power fraction deposited out the electron beam profile is very small relative to the power deposited in the target plates. The temperature distribution was evaluated to define the number and thicknesses of the tungsten target plates. The adiabatic boundary condition for the outer walls of the aluminum casing is very conservative assumption because the subcritical assembly water coolant will remove some of the target power. The solver for the calculations is the traditional steady-state SIMPLE algorithm [Ref. II.3.2].

Several target configurations were examined. Three configurations are compared in Table II.3.3.1.1, two configurations with eight plates and one configuration with seven plates. In the final design, the eighth plate was removed because the neutron yield is almost identical for configuration B and configuration C. In addition, decreasing the target tungsten mass reduces the reactivity change in the subcritical assembly when the target is removed.

In all configurations, the channel separating the target window from the first plate and the last plate from the aluminum casing is 1 mm thick. All other channels are 1.75 mm thick. The temperature and the power distributions in the target plates of the three configurations are shown in Fig. II.3.3.1.2.

Table II.3.3.1.1 Tungsten target configurations

Plate Number	Configuration plate thickness, mm		
	A	B	C
1	3	3	3
2	3	3	3
3	3	3	3
4	3	4	4
5	4	4	4
6	8	6	6
7	13	10	10
8	33	37	

For all the cases, the peak temperature is 142 °C or less in the three configurations, which is well below the 3422 °C, and 600° C, the melting point temperature of tungsten and aluminum, respectively. In configuration C, the second coolant channel has the maximum temperature. where the surface temperature reaches 127 °C and the temperature of the closest layer of cells reaches 38.53 °C as shown in Fig. II.3.3.1.3.

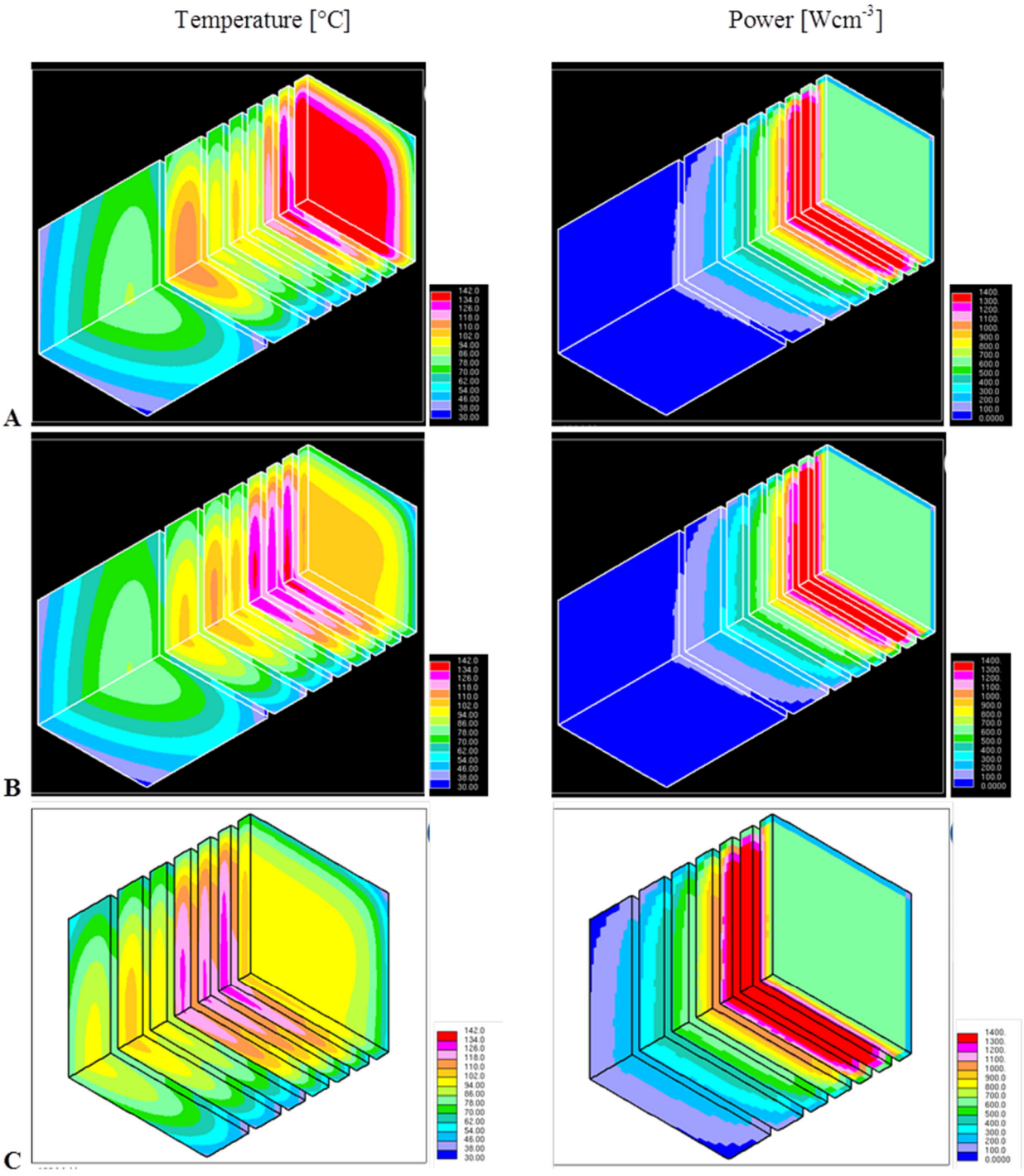

Figure II.3.3.1.2 Temperature and the power distributions for the three tungsten target cases presented in Table II.3.3.1.2.

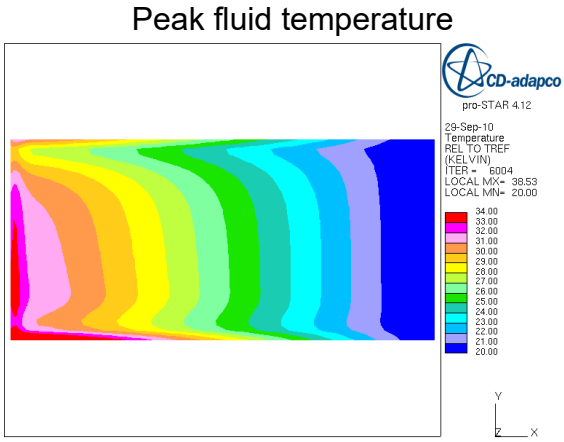

Figure II.3.3.1.3 Temperature distribution in the hottest channel (channel 2)

The average pressure in the target region is 1.84 bar considering the gravitational head and the pressure drop and the corresponding boiling temperature is 119 °C. Therefore, the present configuration has no margin to the boiling point for the surface temperature, but the first fluid layer has a temperature 80 ºC lower than the boiling point in the first fluid layer. This suggests that the present configuration has a sufficient margin to subcooled boiling. To verify this, the Berglers-Rosenhow correlation [II.3.4] that determines the superheating necessary, for a given heat flux, to have bubble stability and therefore subcooled boiling was applied. The correlation is given by:

$$T_{scb} = T_{sat} + (A\ddot{q}p^{-b})^{1/c} \quad (1)$$

where $\ddot{q}$ is the local heat flux, p is the pressure and A, b and c are coefficients dependent on the units used. The coefficients are listed in Table II.3.3.1.2. T_{scb}, or the temperature at which the onset to boiling is 134 °C for the present case. The pressure has been estimated conservatively by considering the loop preceding the target, the total pressure drops through the target and the piezometric head. Higher mass flow rates would bring an advantage in terms of margin to subcooled boiling (estimated using the Berglers-Rosenhow correlation), as can be seen in Table II.3.3.1.3.

Table II.3.3.1.3 Parameters of the Berglers-Rosenhow correlation, temperatures are assumed in [ºF], pressure in [psi] and heat flux in [BTU/hr/ft^2].

a	b	c	d
15.6	2.3	1.156	-0.0234

In case of depressurization, the margin to boiling would be reduced, which would probably lead to localized subcooled boiling if the accelerator beam were not stopped. However, the much lower fluid temperature makes widespread occurrence of subcooled boiling highly unlikely. Moreover, bubbles are not likely to propagate and survive long. Lower

mass flow rates lead invariably to lower margins to boiling, so it is recommended to maintain the present inlet velocity and the recommended mass flow rate.

Table II.3.3.1.4. Margins to subcooled boiling as function of the inlet velocity

Velocity in the inlet manifold	Pressure in the target region	T_{sat}	T_{wall} Temperature at the wall	Margin to Nucleate Boiling	Margin to Subcooled Boiling
5 m/s	1.84 bar	119 °C	127 °C	-	7 °C
5.5 m/s	2.22 bar	124 °C	119 °C	5 °C	19 °C
6 m/s	2.6 bar	129 °C	112 °C	17°C	30°C

II.3.3.2 Final Optimization of the Tungsten Target

The optimization process described in the previous section was conducted without tantalum cladding. After the optimization was performed, a 0.25 mm coating was used on all surfaces of each target plate, to protect the tungsten from interaction with the water coolant.

In the computational model, there are two inlet and two outlet channels. Only the upper half of the target assembly must be modeled due to the use of symmetry boundary conditions. The numerical practices (numerical schemes and meshing strategies), as well as the turbulence modeling, are identical to what is described in the previous section.

As mentioned in Section II.3.3.1, the inlet temperature assumed in the tungsten target optimization calculations is 19.85 °C (293 K). For an inlet temperature of 25 °C instead, 5.15 °C must be added to the simulation results to give accurate temperature predictions, and an additional 0.1 °C (obtained by dividing the additional power by the heat capacity and mass flow rate of water) should be added to all temperatures to account for the effect of side wall heating (the heat generated on the side channels), which is not included in the calculations. A different inlet temperature does not invalidate the calculations since the 5 °C temperature increase has negligible effect on the water properties. The calculation procedure (numerical schemes and meshing strategies), as well as the turbulence modeling, are identical to what is described in the previous section.

Figure II.3.3.2.1 shows a comparison between a 3-5 split and a 4-4 split. The peak temperature in the case of a 3-5 split is significantly higher. Thus, it was determined that the optimal configuration corresponds to a 4-4 split. The total mass flow rate considered is 4.79 kg/s. The mass flow rate fraction in the primary line is 0.58, as discussed in Section II.3.2.

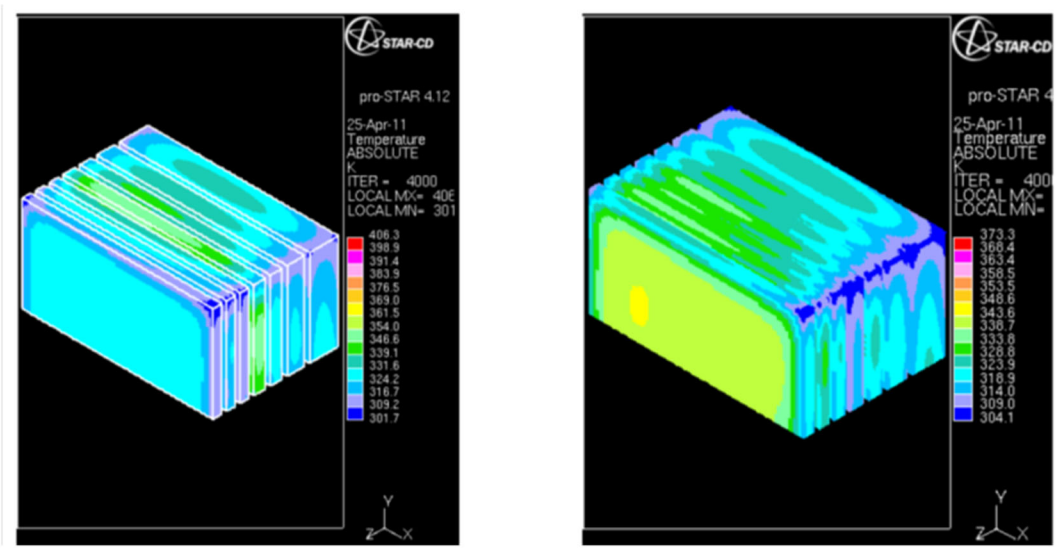

Split 3 -5

Peak 406.3 K

Split 4 -4

Peak 373.3 K

Figure II.3.3.2.1. Temperature distribution in the tungsten plates for the flow split of 3-5 and 4-4

A complete characterization of the target flow field and the temperature distribution is presented for the tungsten target design with 4-4 flow split. In the computational model there are two inlet and two outlet ducts (primary and secondary line) as shown in Fig. II.3.3.2.2. Only one-half of the target assembly is modeled because of the target symmetry. Outlet and inlet temperatures are within ±0.01 °C, and the peak temperature of the tantalum and tungsten are given within ±1 °C. The main parameters of the tungsten target are:

- The average flow velocity in the primary line feeding the upper four target coolant channels is 5.075 m/s.
- The average flow velocity in the secondary line feeding the bottom four target coolant channels is 3.675 m/s.
- The total mass flow rate is 4.79 kg/s with a total pressure drop across the whole target configuration of ~117.14 kPa. The pressure in the target region is 2.2 bar (2.69 inlet pressure, -0.69 bar pressure loss, and +0.2 bar gravity head).
- The saturation temperature is 123 °C at the target plates.
- In the initial calculations, the inlet fluid temperature is 293 K (19.85°C). The outlet fluid temperature in the primary line predicted from these calculations is 297.6 K, and the outlet fluid temperature in the secondary line is 296.54 K. The average temperature of the outlet is 297.16 K. Including the corrections described above to account for an inlet temperature of 25 °C (298.15 K) and 0.1 °C due to side wall heating give an outlet temperature of 29.3 °C.
- The peak cladding temperature is 98 °C. Accounting for the corrections previously described changes, this temperature is 104 °C.

- The peak tungsten temperature is 104 °C. Accounting for the corrections previously described changes this temperature to 109 °C.
- Application of the Berglers-Rosenhow correlation (Eq. 1 above) indicates that subcooled boiling would not occur at less than a 21 °C super-heating at this heat flux and pressure. With a saturation temperature of 123 °C, subcooled boiling would therefore not occur below a wall temperature of 123 °C + 21 °C = 144 °C. Since the peak wall temperature (the peak cladding temperature) is 104 °C, the total margin to subcooled boiling is estimated at 144 °C – 104 °C = 40 °C.
- The total power used in the CFD model is 85.7 kW and it is more than the integrated physics power value by less than 1%.

Figures II.3.3.2.3 through II.3.3.2.5 show the power and the temperature distributions within the target plates. Figure II.3.3.2.6 provides detailed distribution of the velocity and the temperature within the coolant channels and the tungsten plates in a cross section perpendicular to the electron beam direction. It is possible to observe the following:

- In the coolant channels fed from the primary line, the peak velocity occurs between the first and the second target plates.
- In the coolant channels fed from the secondary line, the peak velocity occurs between the sixth and the seventh target plates.
- The lowest velocities are encountered in the coolant channels furthest away from the inlet of the respective feeding lines, the first coolant channel, and the coolant channel between the fourth and the fifth target plates.
- Cladding temperature peaks are located near the symmetry line, with a bias toward the outlet.

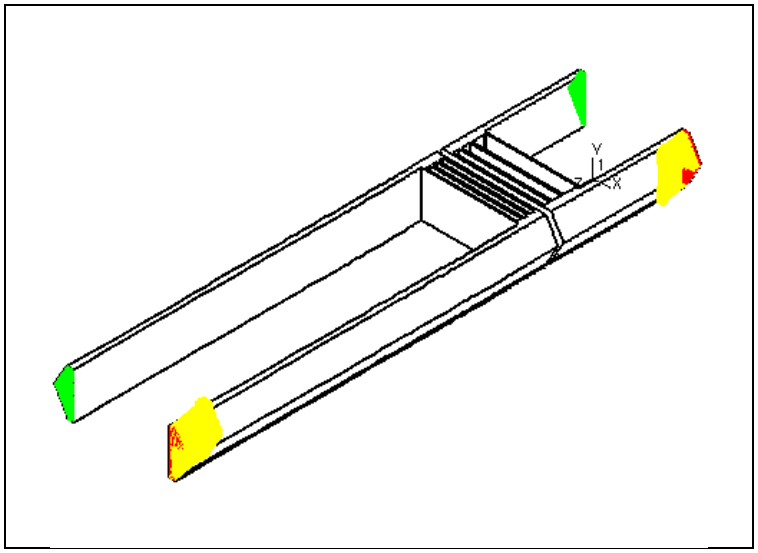

Figure II.3.3.2.2. CFD model for flow split of 4-4

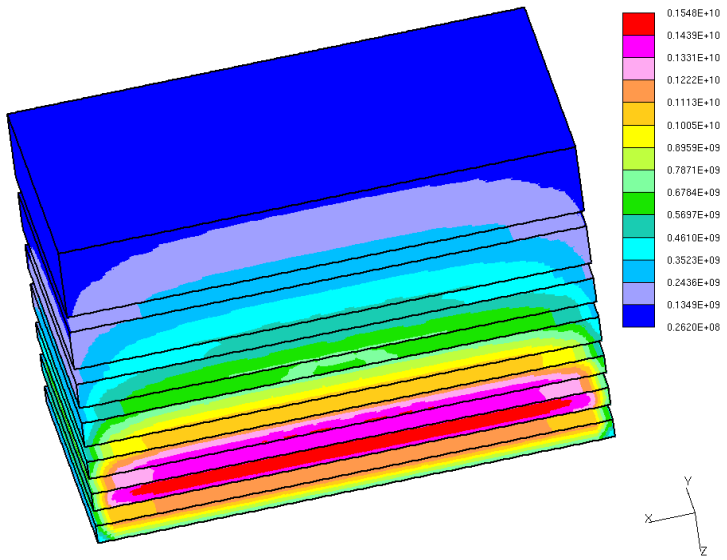

Figure II.3.3.2.3. Power distribution in the tungsten target plates [W/m^3]

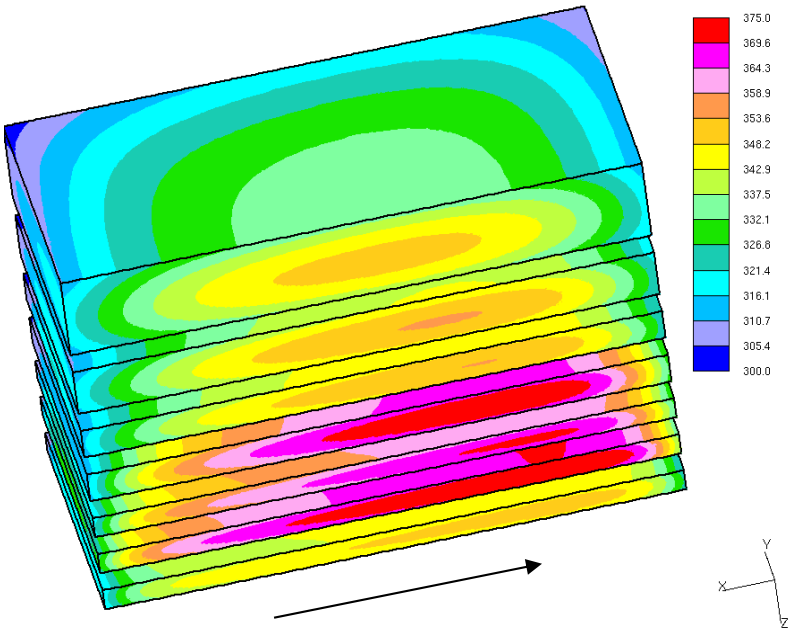

Figure II.3.3.2.4. Temperature distribution in the tungsten material [K], the arrow represents the flow direction.

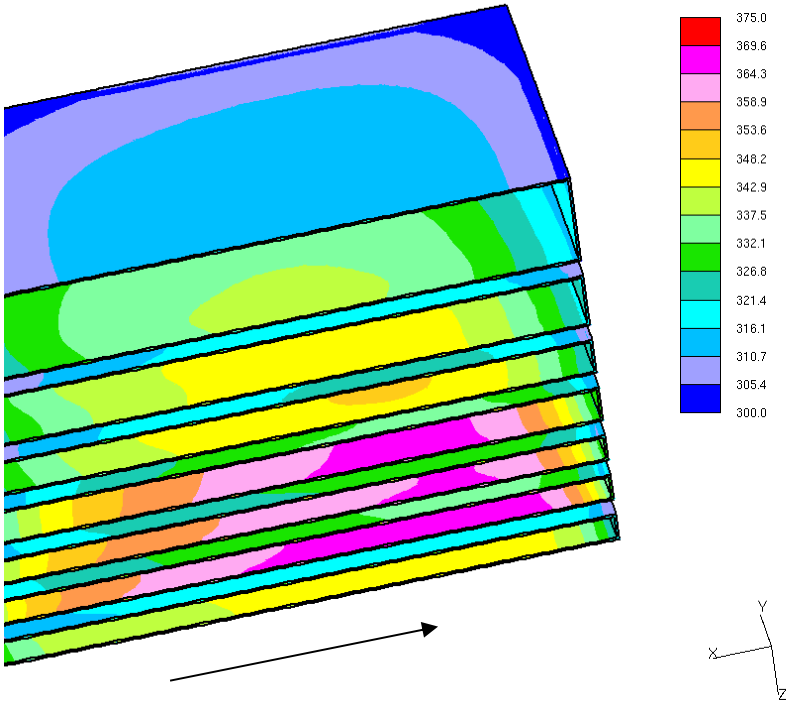

Figure II.3.3.2.5. Temperature distribution in the tantalum material [K], the arrow represents the flow direction.

Velocity magnitude in the coolant channel mid-section

First coolant channel

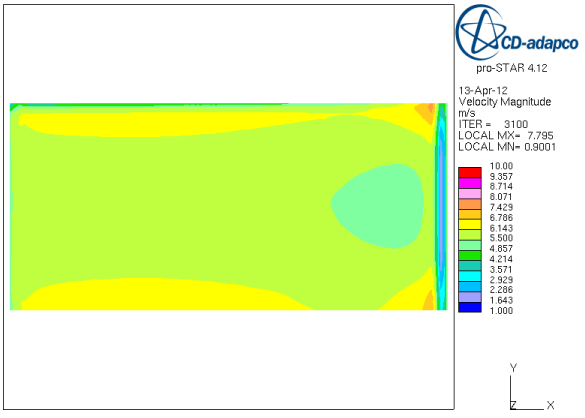

Second coolant channel

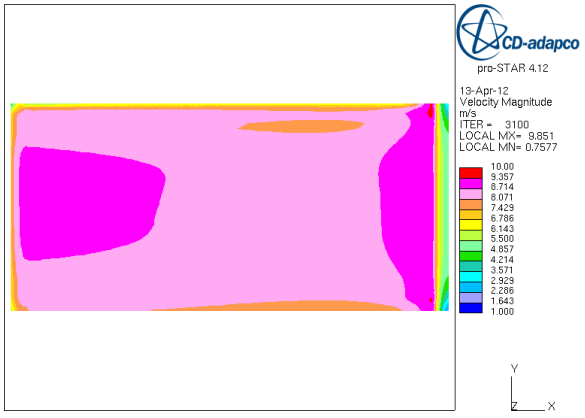

Third coolant channel

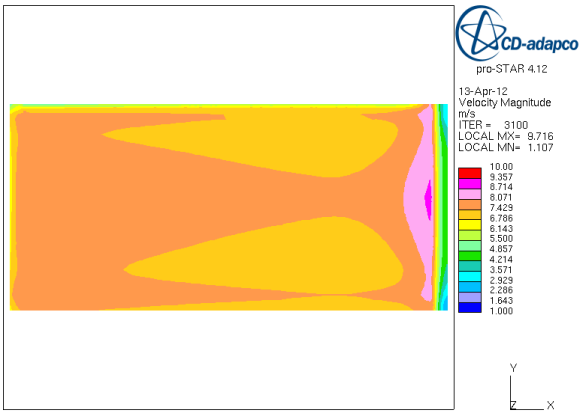

Fourth coolant channel

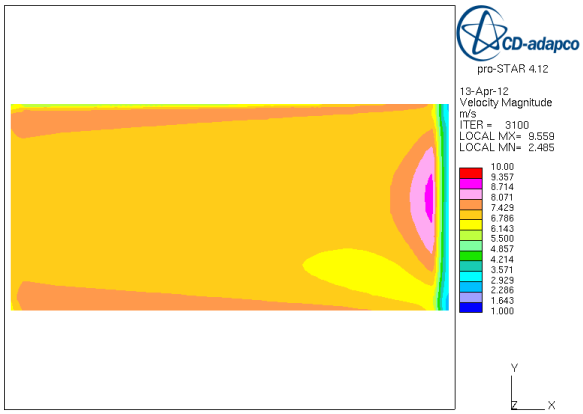

Fifth coolant channel

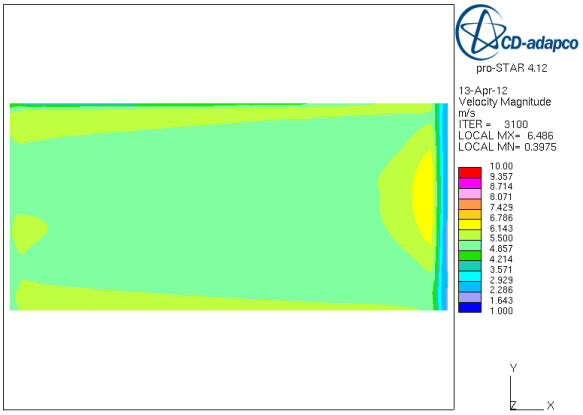

Sixth coolant channel

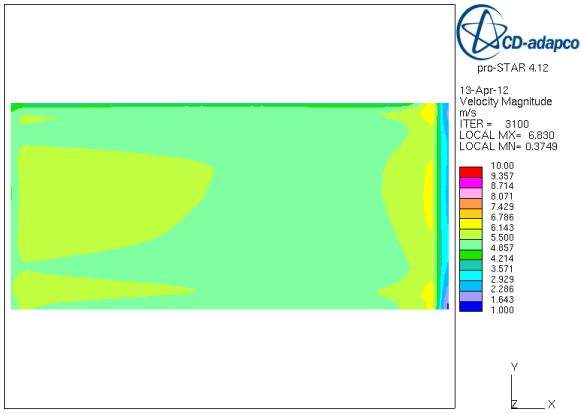

Seventh coolant channel

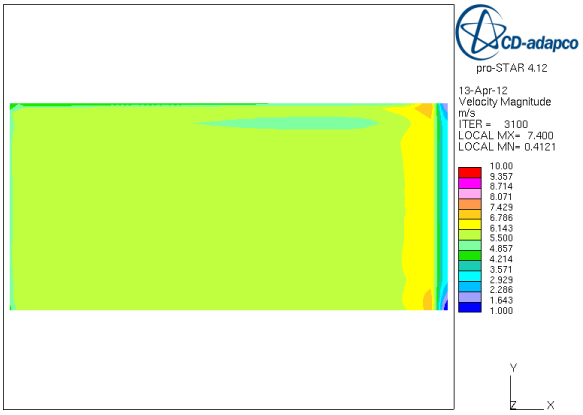

Eighth coolant channel

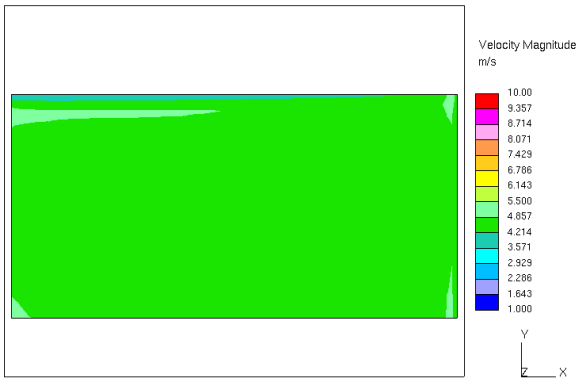

Temperature distribution in the coolant channel mid-section

First coolant channel

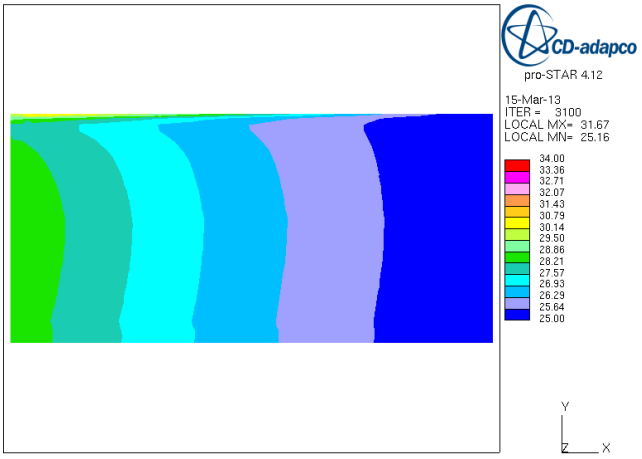

Second coolant channel

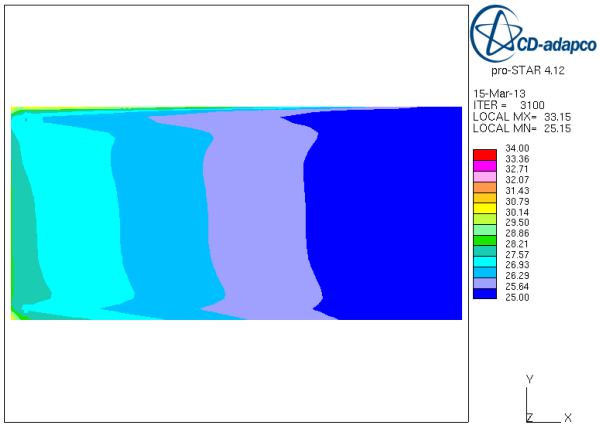

Third coolant channel

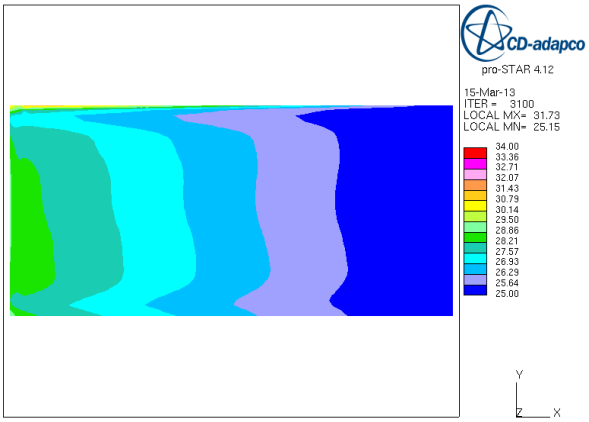

Fourth coolant channel

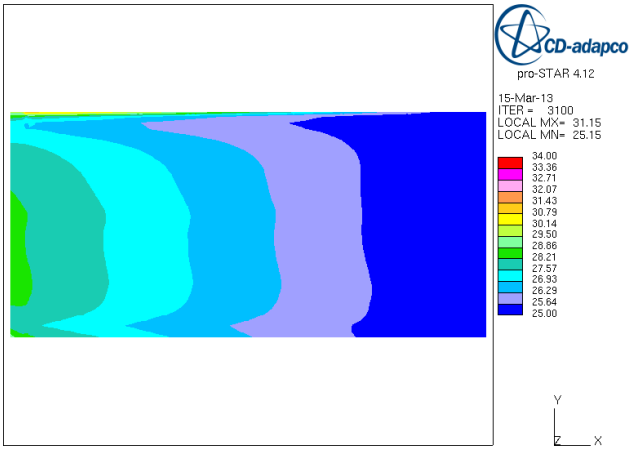

Fifth coolant channel

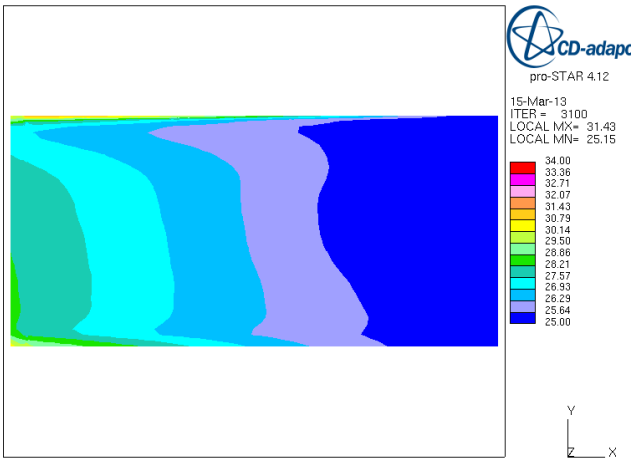

Sixth coolant channel

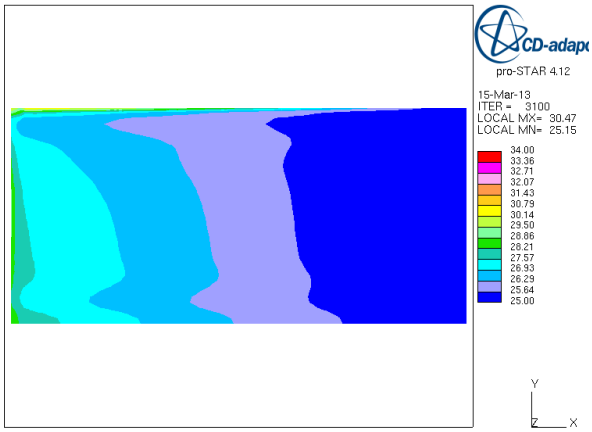

Seventh coolant channel

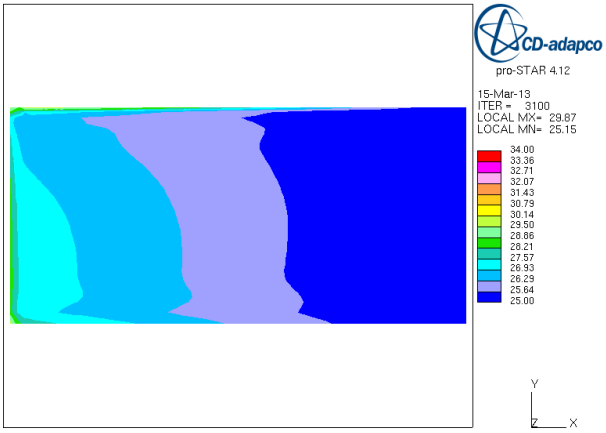

Eighth coolant channel

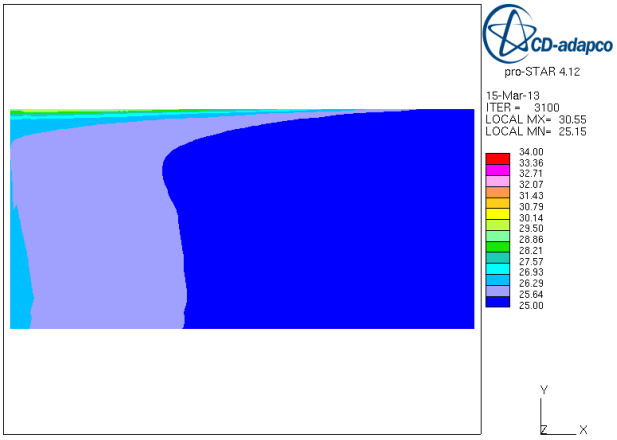

The tantalum surface temperature distribution for all plates

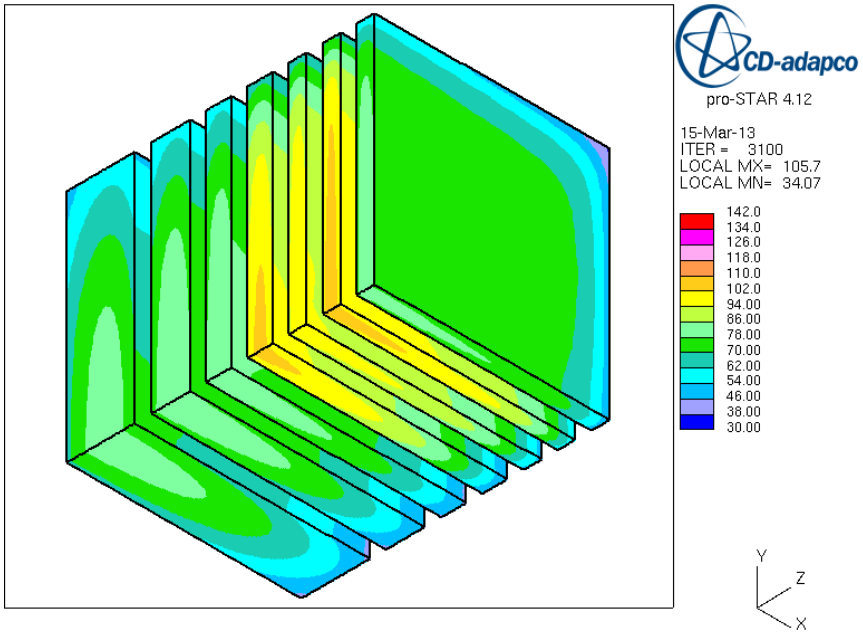

Front surface of the first target plate

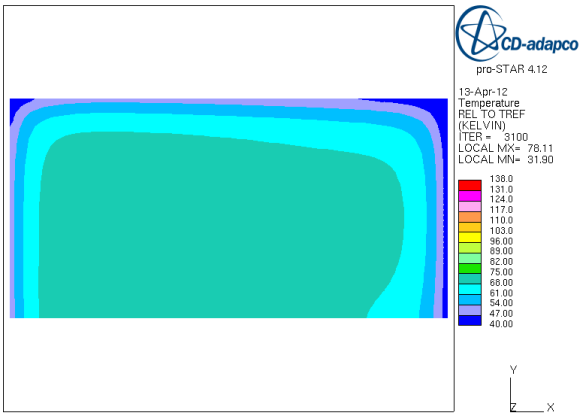

Back surface of the first target plate

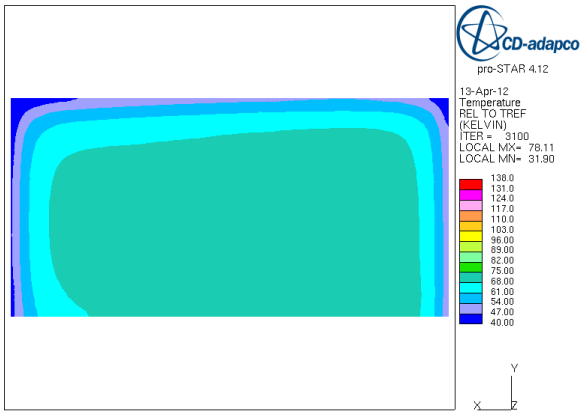

Front surface of the second target plate

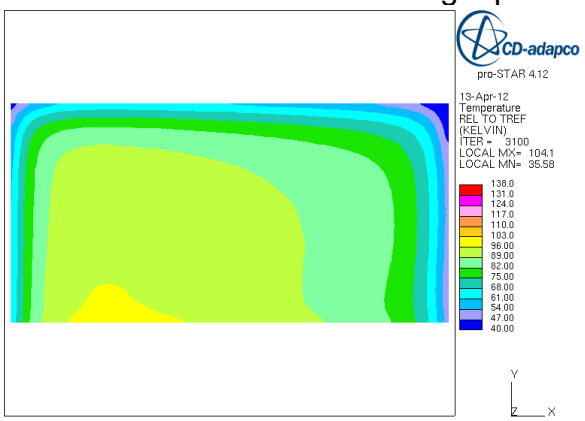

Back surface of the second target plate

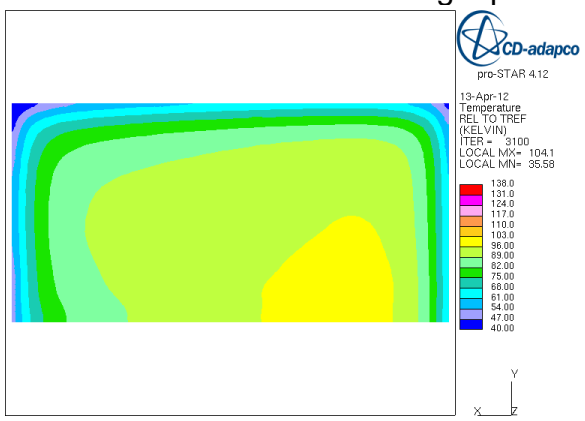

Front surface of the third target plate

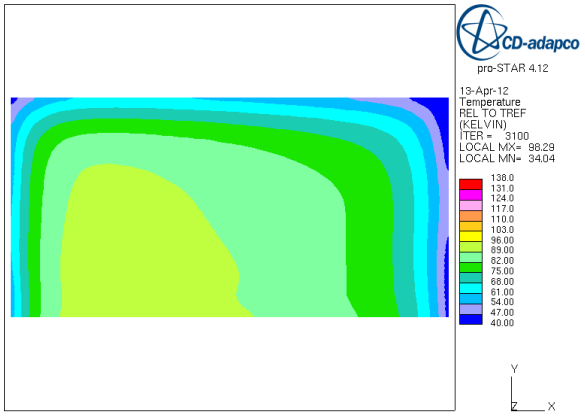

Back surface of the third target plate

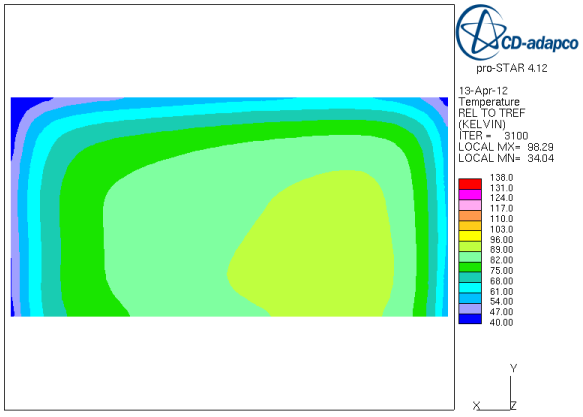

Front surface of the fourth target plate

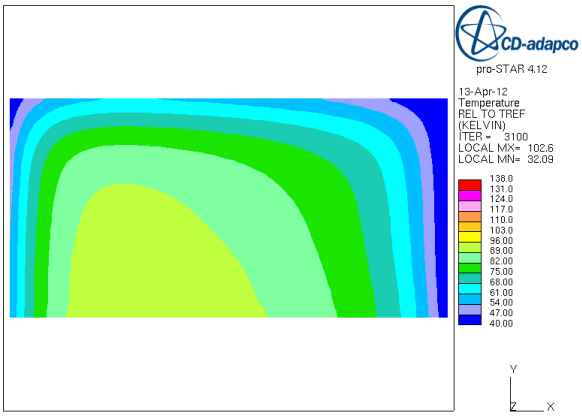

Back surface of the fourth target plate

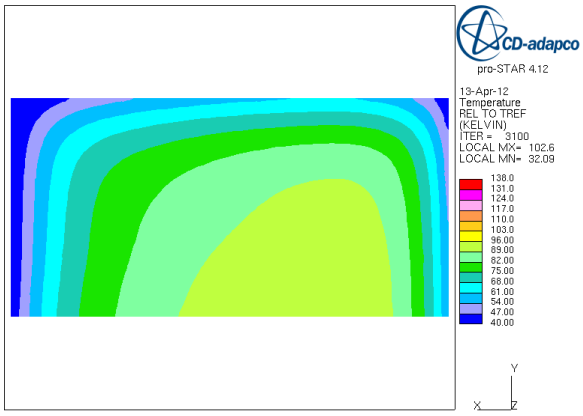

Front surface of the fifth target plate

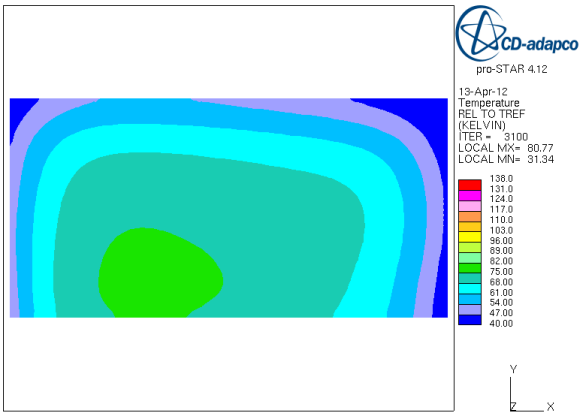

Back surface of the fifth target plate

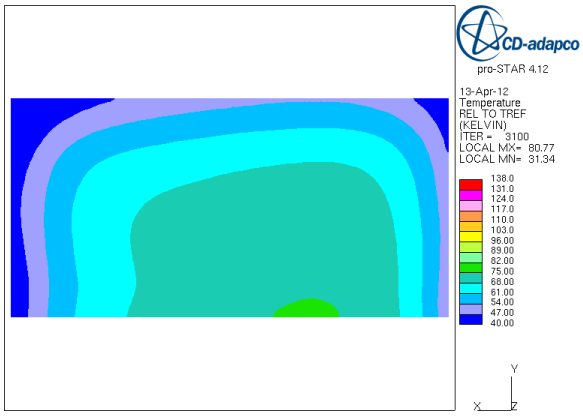

Front surface of the sixth target plate

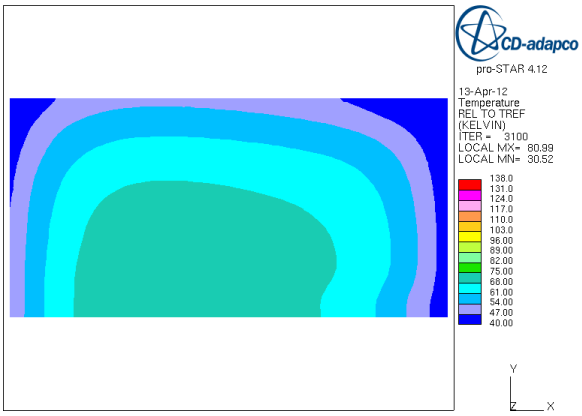

Back surface of the sixth target plate

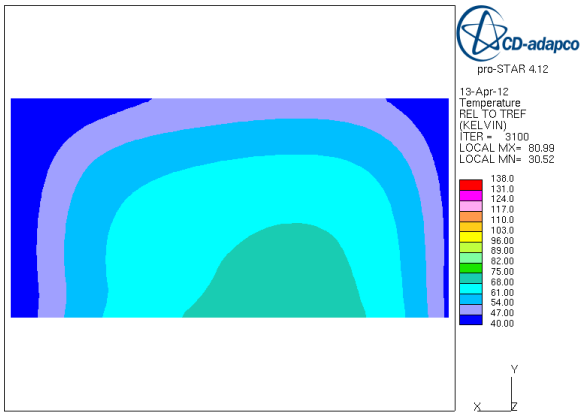

Front surface of the seventh target plate

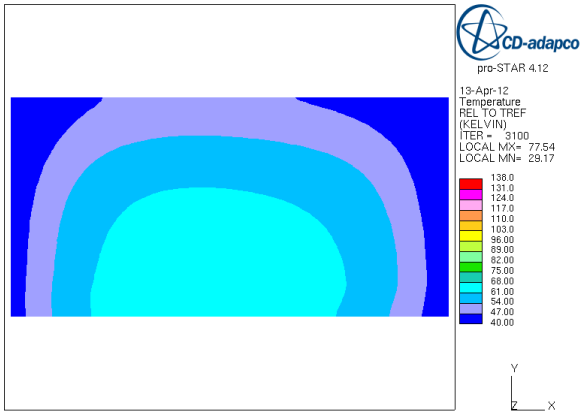

Back surface of the seventh target plate

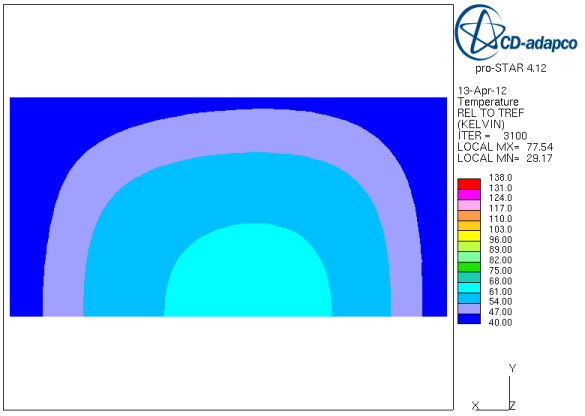

The temperature distribution of the plate mid-plan

First target plate

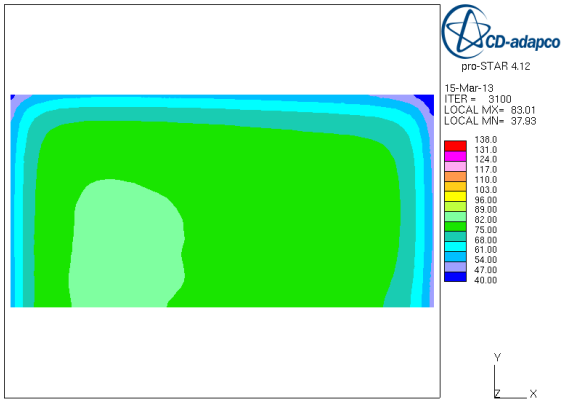

Second target plate

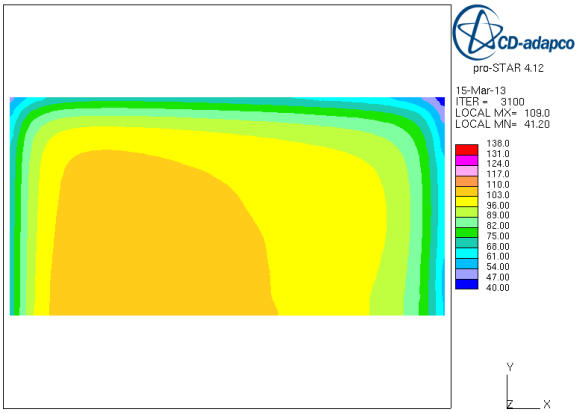

Third target plate

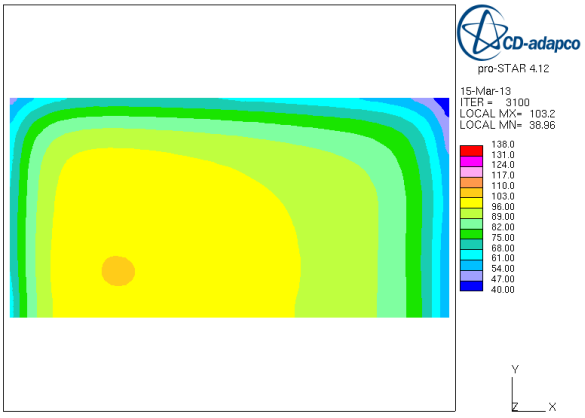

Fourth target plate

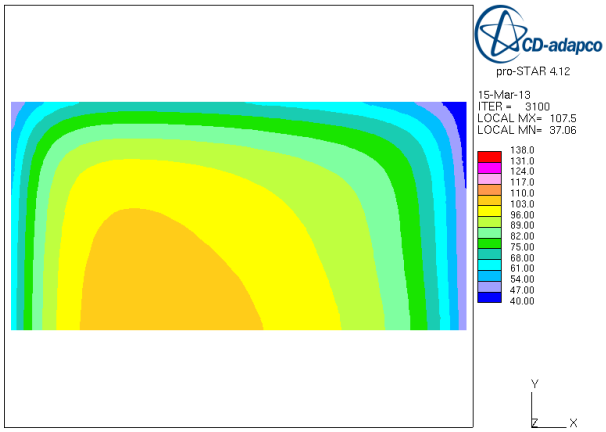

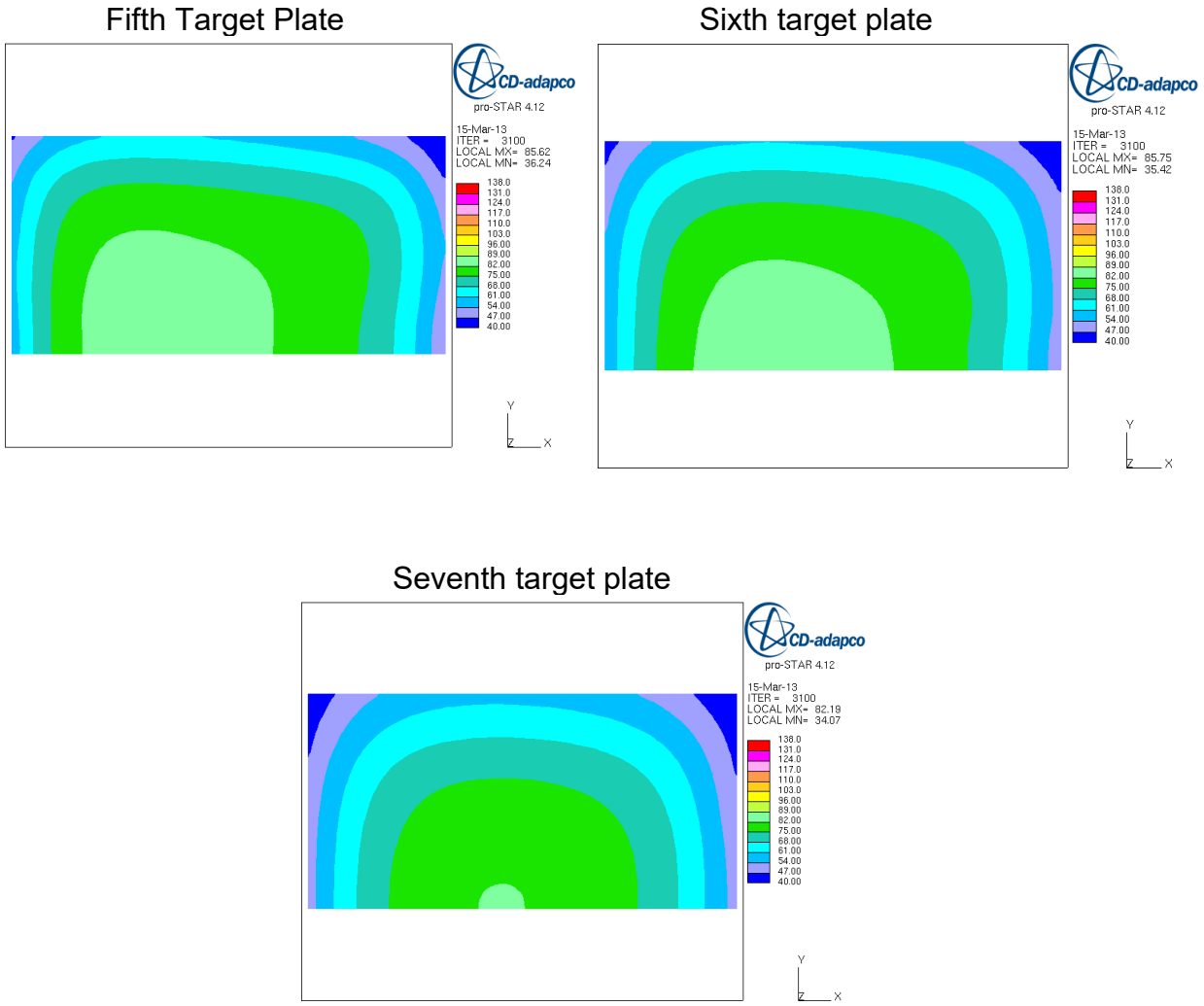

Figure II.3.3.2.6. Detailed distributions of velocity and temperature in the reference tungsten target

II.3.4 Optimization and Characterization of the Uranium Target

The optimization of the uranium target is described in the following section. A full characterization of the optimized uranium target is provided. The numerical practices (numerical schemes and meshing strategies), as well as the turbulence modeling, are identical to what was described in Sec. II.3.3 for the tungsten target analysis.

II.3.4.1 Preliminary Uranium Target Optimization

A full target optimization was performed in a manner like what was described in Section II.3.3.1 as part of the work of Sofu et al [Ref. II.3.1]. It was found that the optimum condition was achieved for an inlet velocity of 7.5 m/s with 12 plates. The target configuration and the temperature distribution in the target plates are shown in Fig. II.3.4.1.1. The axial thermal expansion of the uranium plates calculated at the plate

center is listed in Table II.3.4.1.1 for each plate. Then the last plate was removed since it has negligible effect on the neutron yield per electron as discussed before in Section II.2. The individual plate thicknesses are listed in Table II.3.4.1.2.

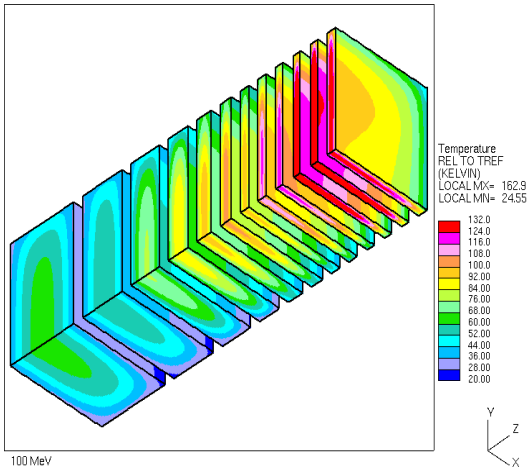

Figure II.3.4.1.1. Temperature distribution of the uranium 12 target plates with average inlet coolant velocity of 7.5 m/s

Table II.3.4.1.1. Peak thermal expansion of the uranium target plates

Plate Number	Thermal Expansion calculated at the target centerline [mm]
1	0.022480
2	0.020007
3	0.019712
4	0.018504
5	0.021818
6	0.020798
7	0.028172
8	0.034526
9	0.027672
10	0.065068
11	0.086632
12	0.140459

Table II.3.4.1.2. Uranium target configuration with 11 plates

Plate Number	Coolant Channel Width, mm	Plate Thickness, mm
	1.00	
1	1.75	3.0
2	1.75	2.5
3	1.75	2.5
4	1.75	2.5
5	1.75	3.0
6	1.75	3.0
7	1.75	4.0
8	1.75	5.0
9	1.75	7.0
10	1.75	10.0
11	1.00	14.0

II.3.4.2 Final Uranium Target Optimization

An additional study was conducted to reduce the average inlet manifold water coolant velocity of the uranium target like the tungsten target as discussed in Section II.3.3.2. A series of calculations with specified inlet and outlet boundary conditions was performed using the hydraulics model shown in Fig. II.3.4.2.1. Three splitting configurations were examined 4-8, 5-7, and 6-6 and the results are shown in Fig. II.3.4.2.2. The optimal flow splitting is 5-7 for the 11-plate configuration and the temperature and the power distributions are shown in detail in Fig.II.3.4.2.3. The thickness of the plates is listed in Table II.3.4.1.2.

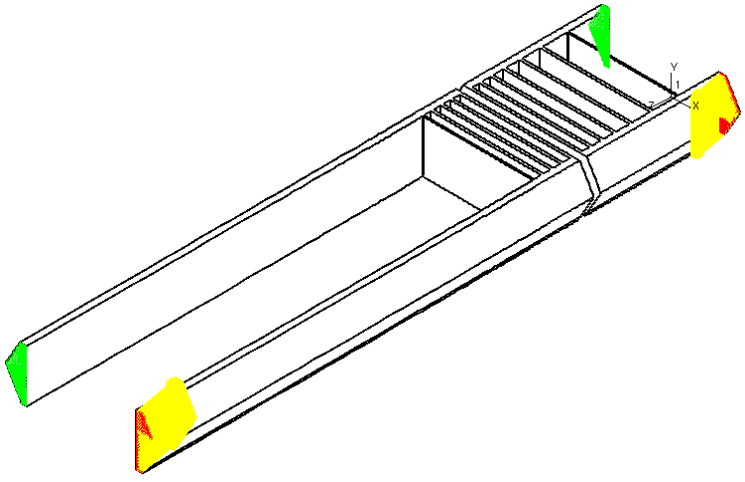

Figure II.3.4.2.1 CFD hydraulics Computational Model for 5-7 split

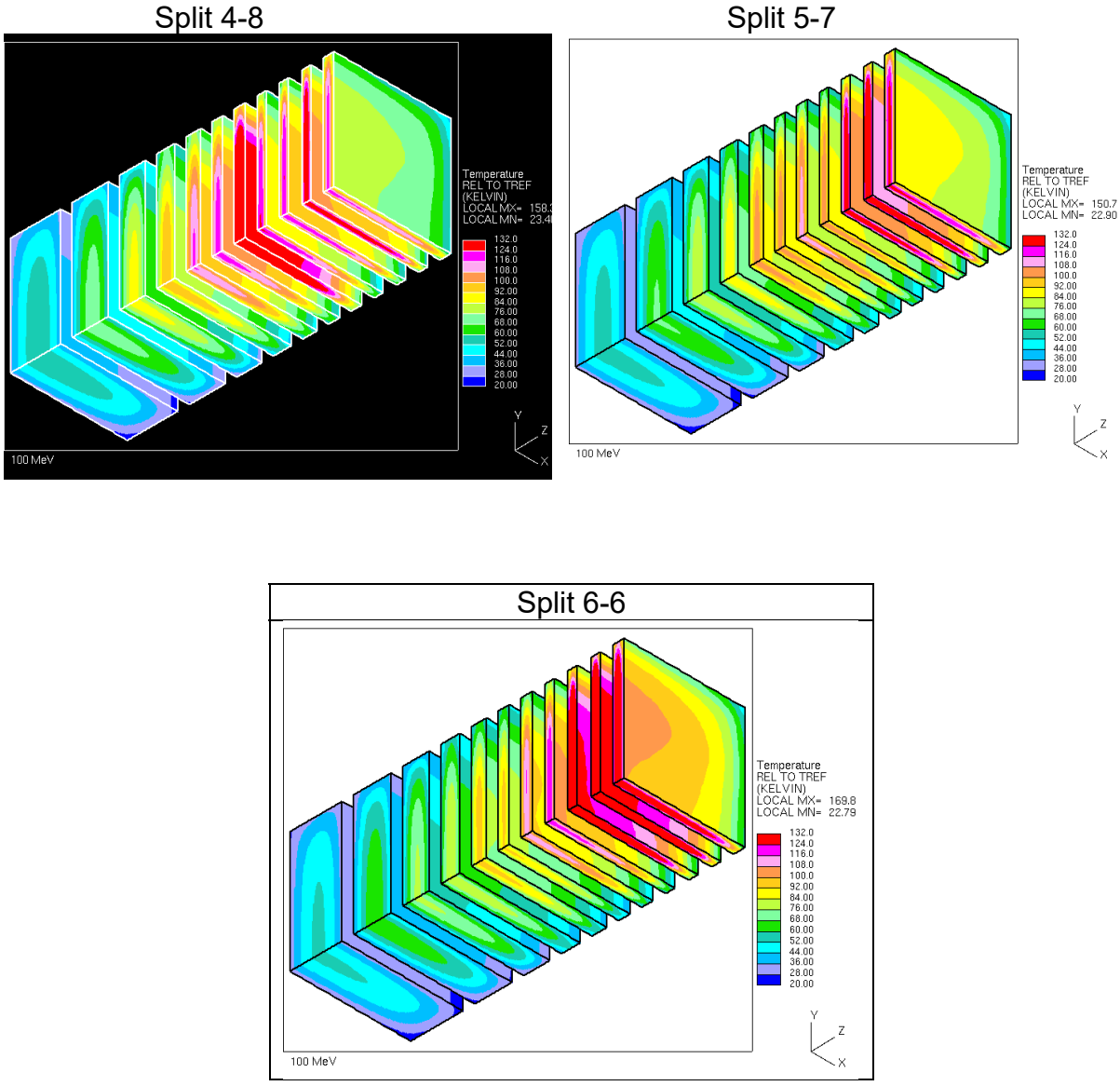

Figure II.3.4.2.2. Temperature distribution in the uranium plates for flow split of 4-8, 5-7, and 6-6.

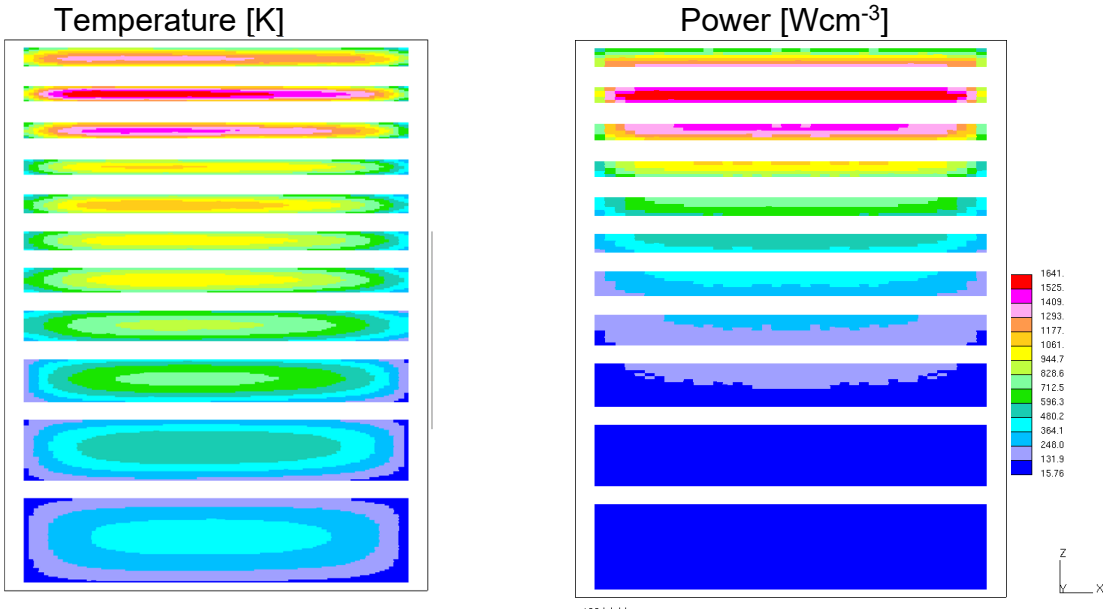

Figure II.3.4.2.3. Temperature and the power distribution of the 11-uranium target configuration with 5-7 flow split

The detailed results for the optimized configuration are shown in Fig. II.3.4.2.4. The outlet and the inlet temperatures are calculated with 0.01 °C accuracy and the peak temperatures of the tantalum and the uranium materials are given within ±1 °C. The main parameters of the uranium target are:

- The average flow velocity in the primary line feeding the upper four target coolant channels is 5.075 m/s.
- The average flow velocity in the secondary line feeding the bottom four target coolant channels is 3.675 m/s.
- The total mass flow rate is 4.79 kg/s with a total pressure drop across the whole target configuration of ~108.18 kPa. The pressure in the target region is 2.3 bar.
- In the initial calculations, the inlet fluid temperature is 293 K (19.85°C). The outlet fluid temperature of the primary line predicted by these calculations is 298.2 K, and the outlet fluid temperature of the secondary line is 296.06 K. The average temperature in the outlet is 297.3 K. Including the corrections described before for the tungsten target analyses to account for an inlet temperature of 25 ^{o}C (298.15 K) and the side heating, the average outlet temperature is 302.7 K (29.5^{o}C).
- The peak cladding temperature is 110 °C. Accounting for the corrections previously described changes this temperature is 115 °C.
- The saturation temperature is 123 °C at the target plates so the total margin to subcooled boiling is 29.25 °C using the same methodology of the tungsten target calculation.
- The total power in the target assembly is 90.5 kW

Velocity magnitude in the coolant channel mid-section

First coolant channel

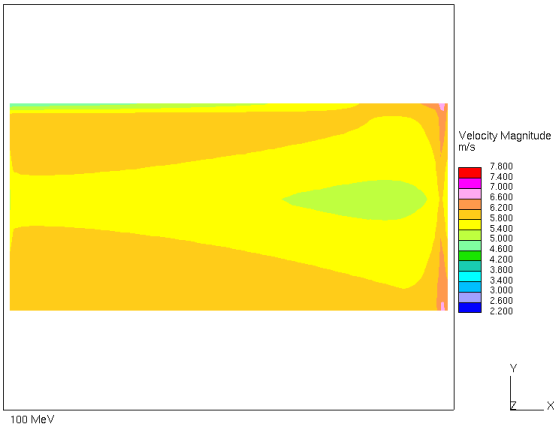

Second coolant channel

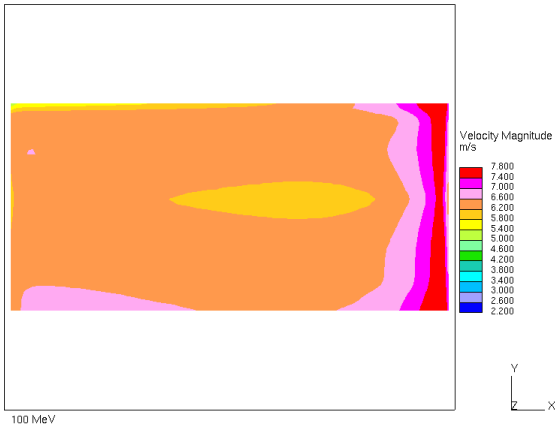

Third coolant channel

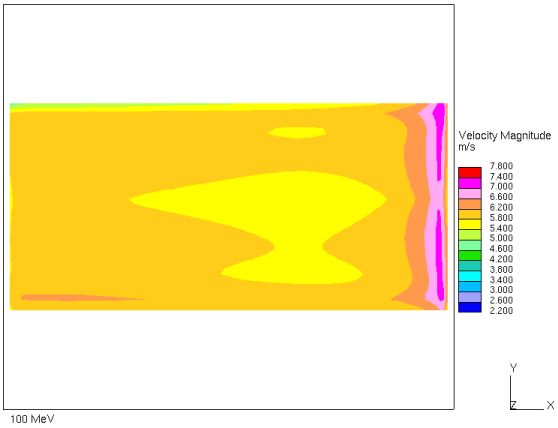

Fourth coolant channel

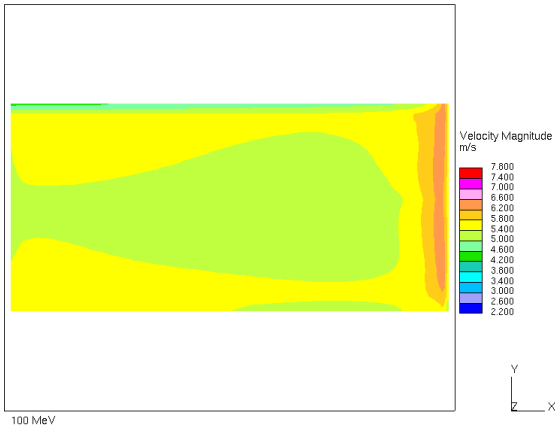

Fifth coolant channel

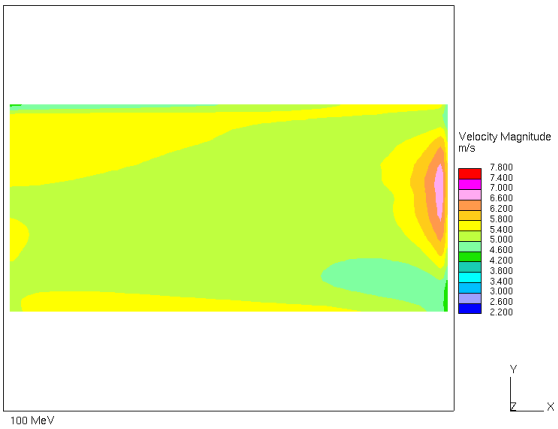

Sixth coolant channel

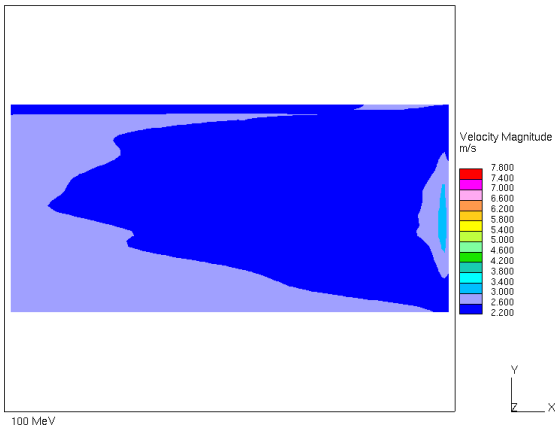

Seventh coolant channel

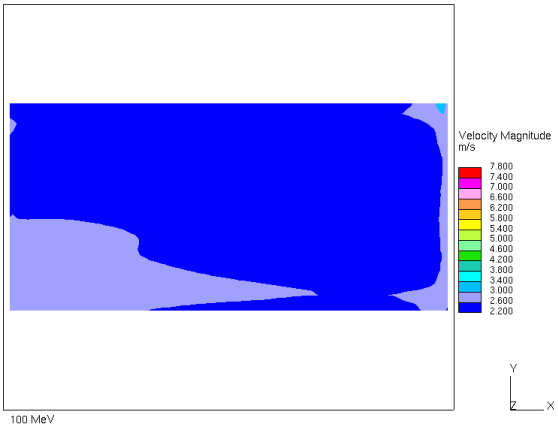

Eighth coolant channel

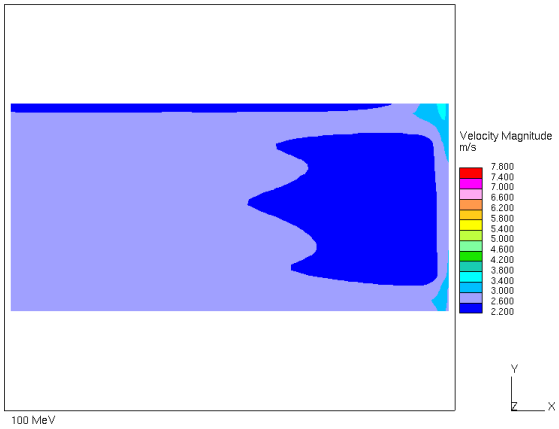

Ninth coolant channel

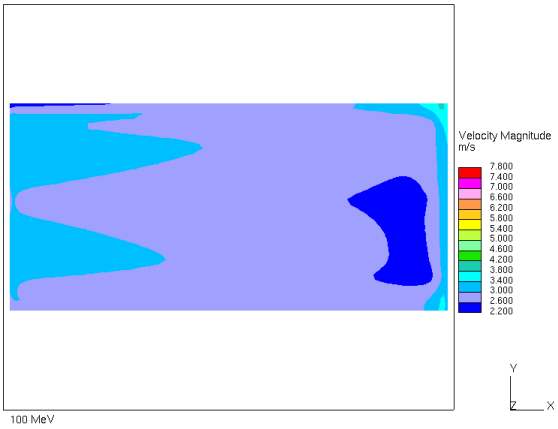

Tenth coolant channel

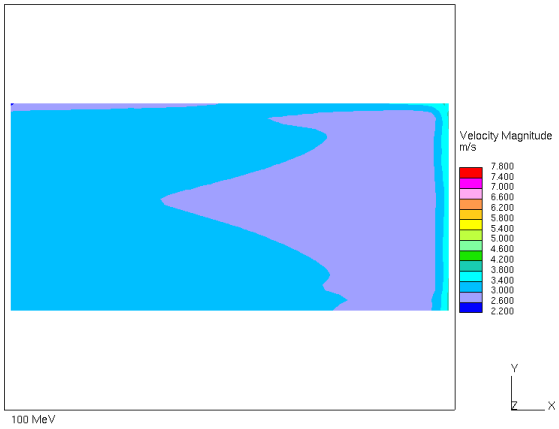

Eleventh coolant channel

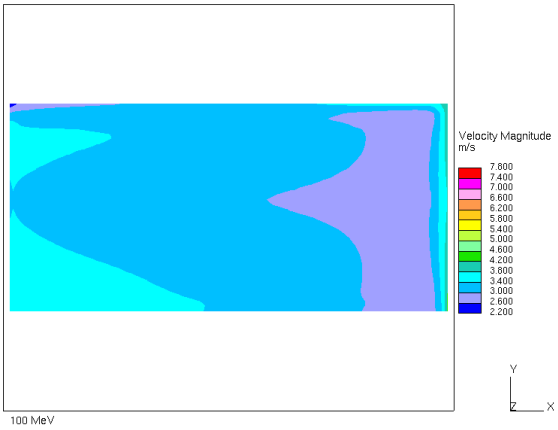

Twelfth coolant channel

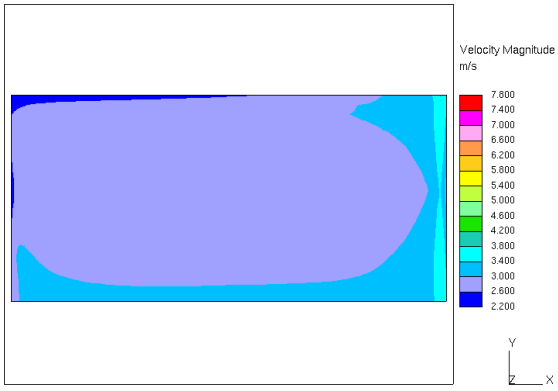

Temperature distribution in the coolant channel mid-section

First coolant channel

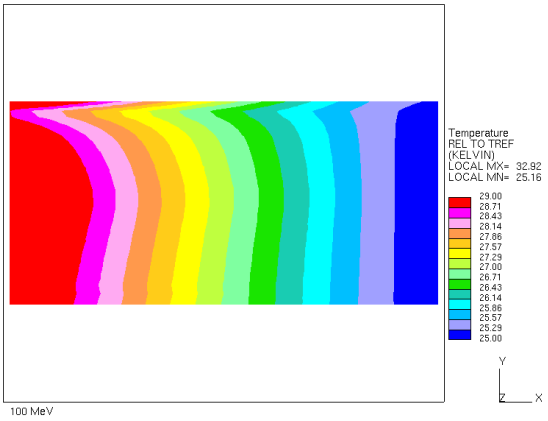

Second coolant channel

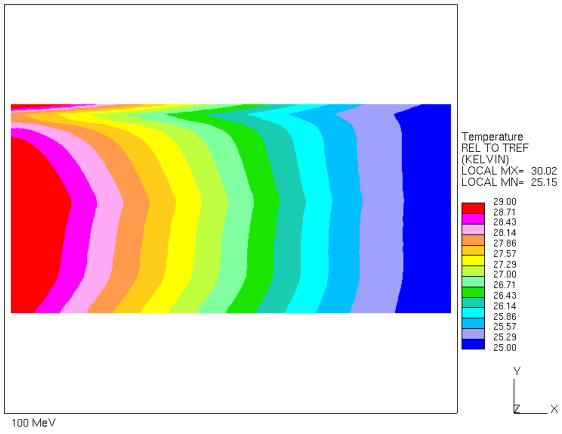

Third coolant channel

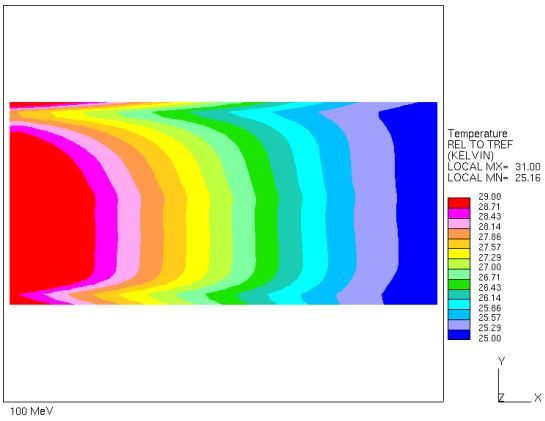

Fourth coolant channel

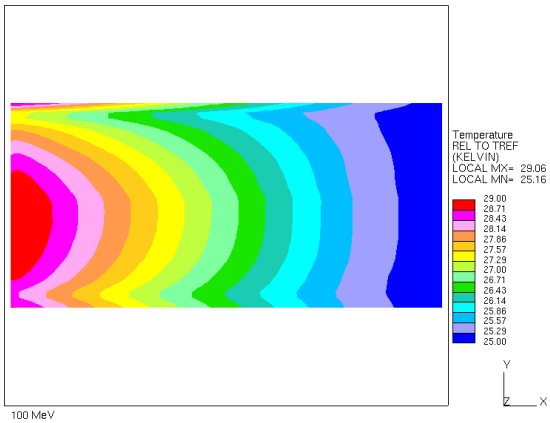

Fifth coolant channel

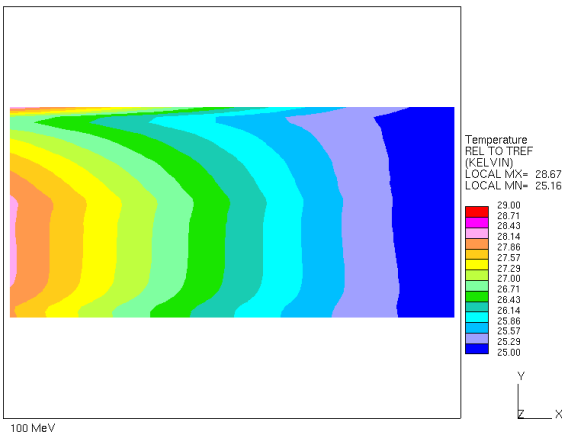

Sixth coolant channel

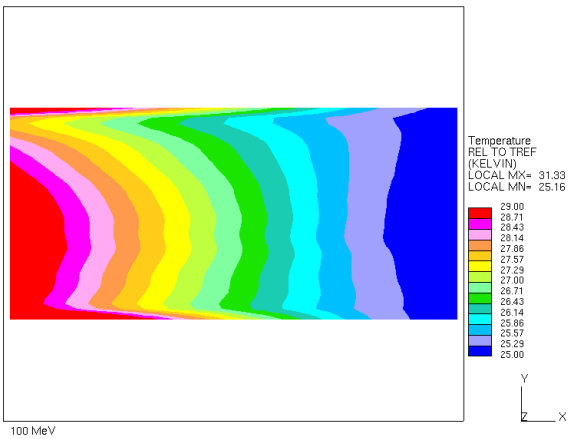

Seventh coolant channel

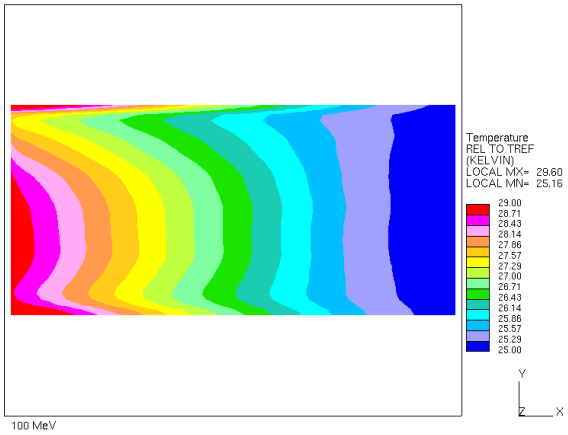

Eighth coolant channel

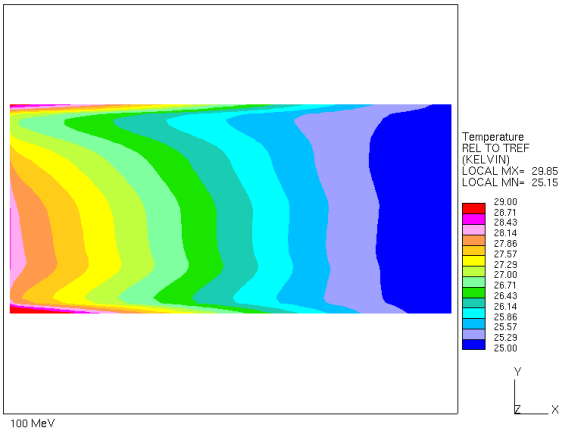

Ninth coolant channel

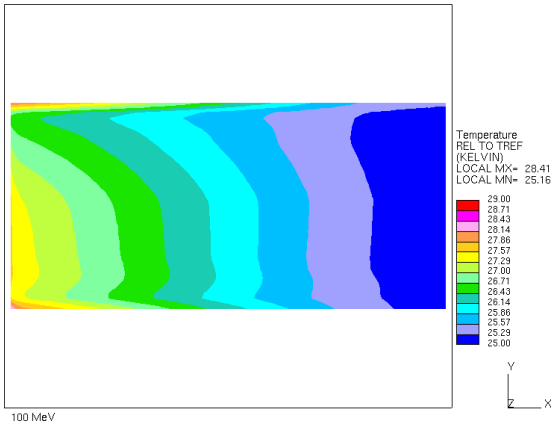

Tenth coolant channel

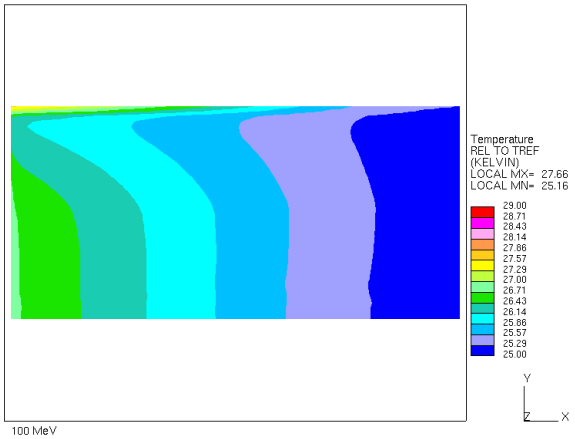

Eleventh coolant channel

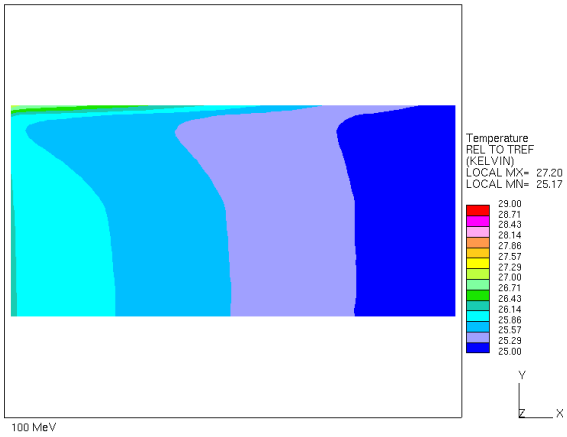

Aluminum surface temperature distribution of all plates

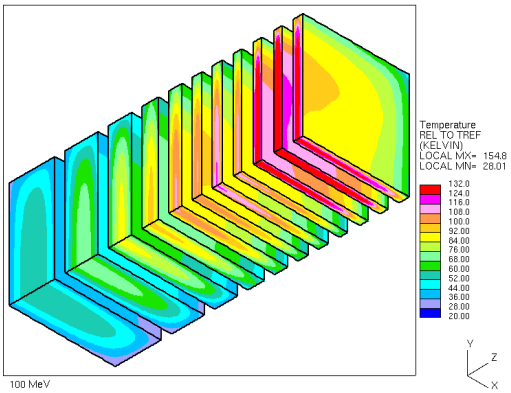

First Plate

Front Surface

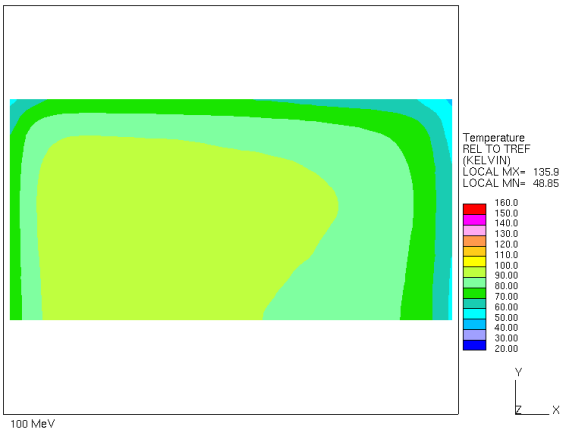

Back Surface

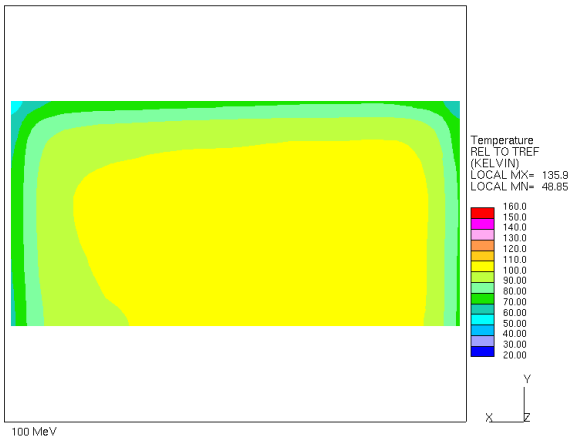

Second Plate

Front Surface

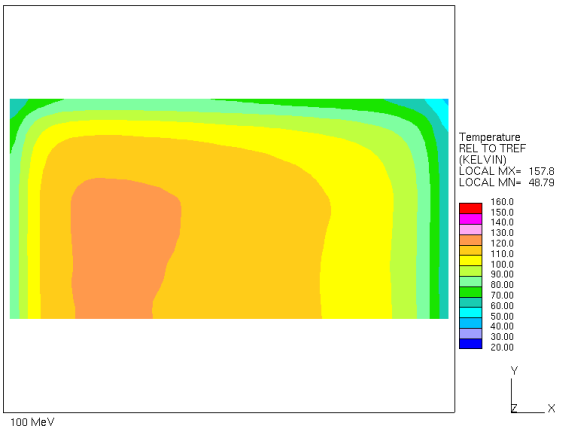

Back Surface

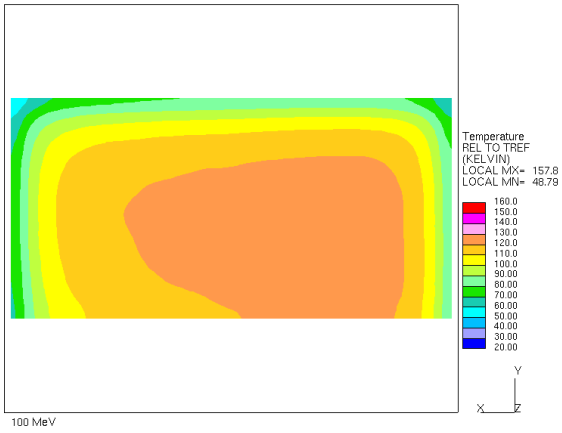

Third Plate

Front Surface

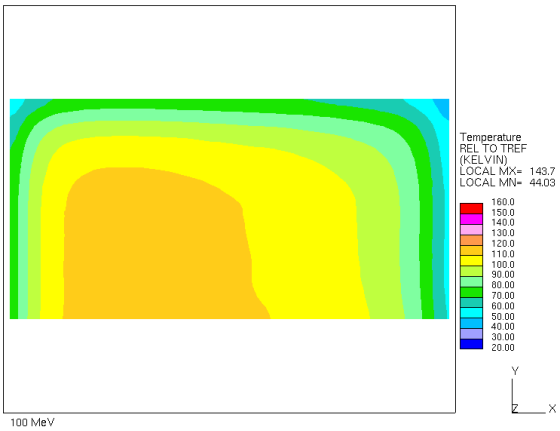

Back Surface

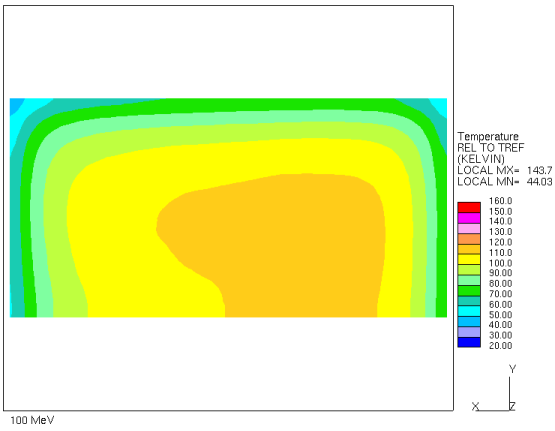

Fourth Plate

Front Surface

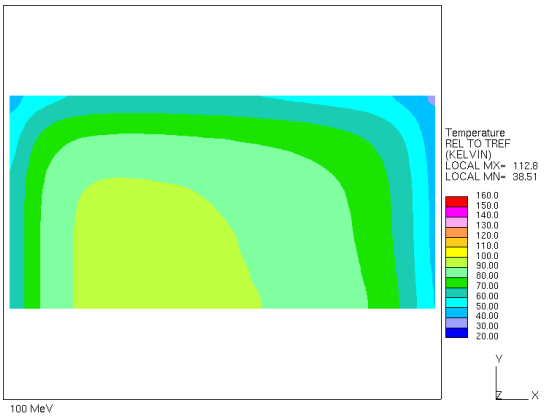

Back Surface

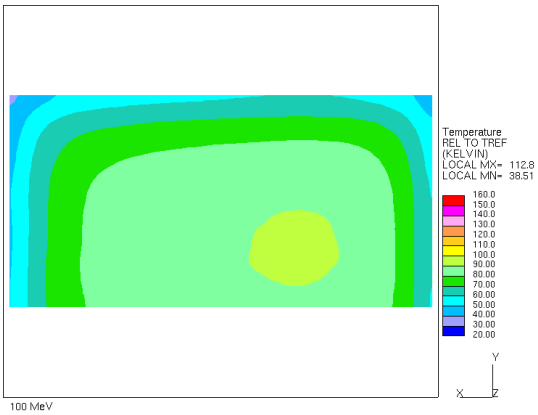

Fifth Plate

Front Surface

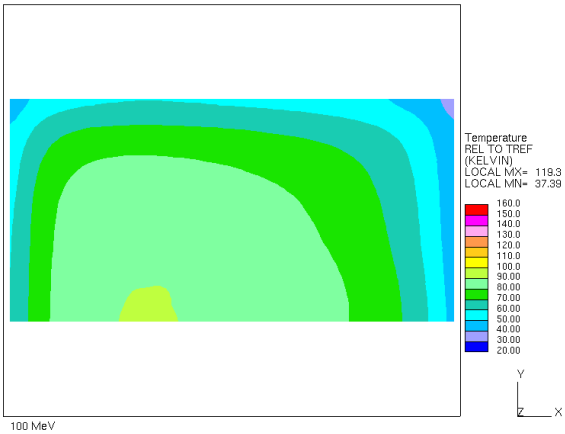

Back Surface

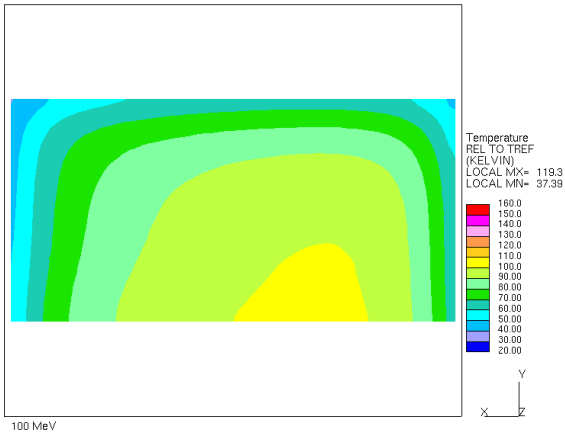

Sixth Plate

Front Surface

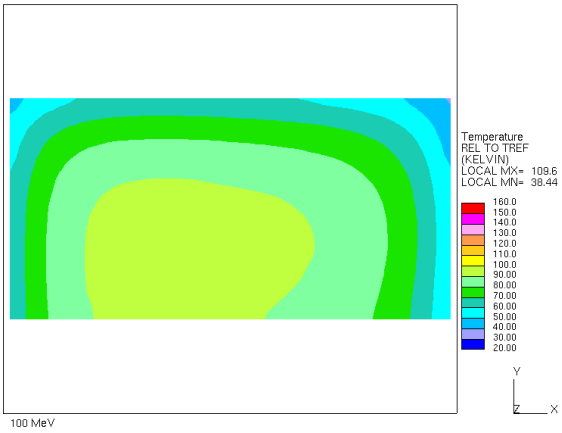

Back Surface

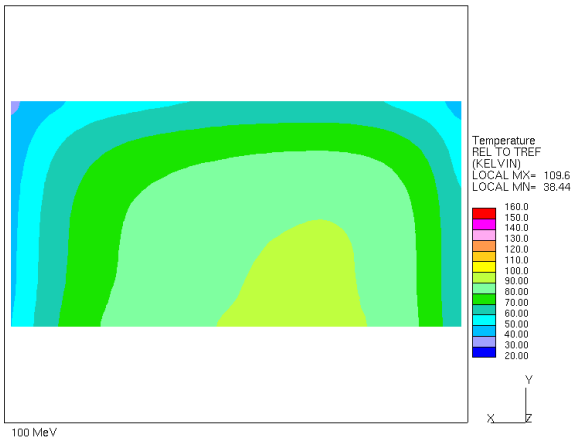

Seventh Plate

Front Surface

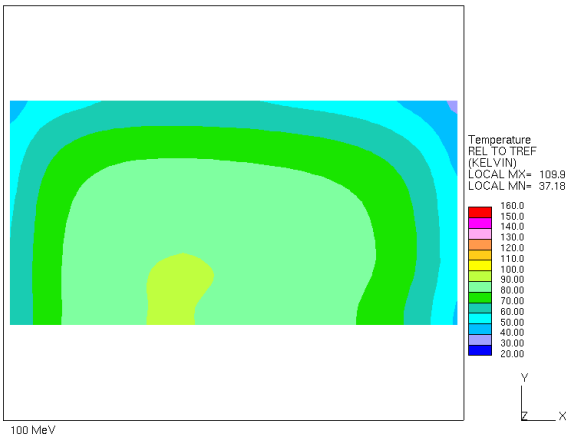

Back Surface

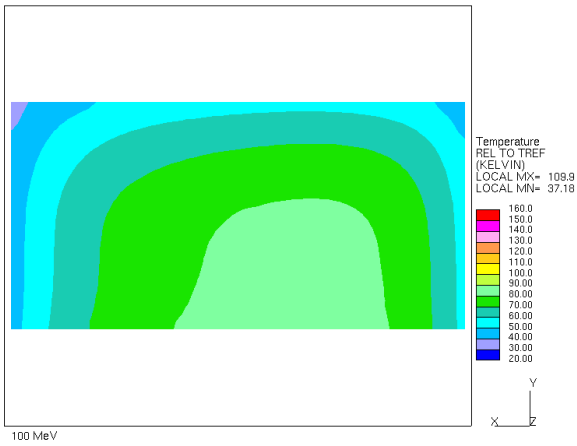

Eighth Plate

Front Surface

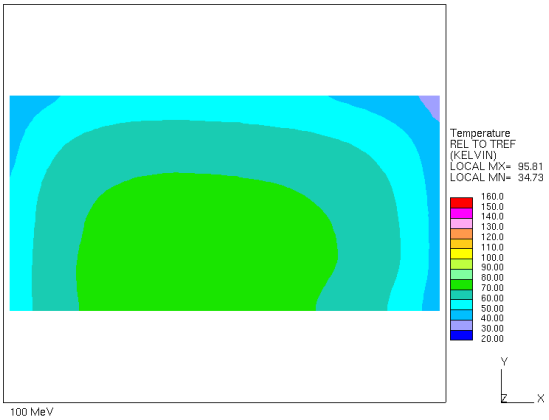

Back Surface

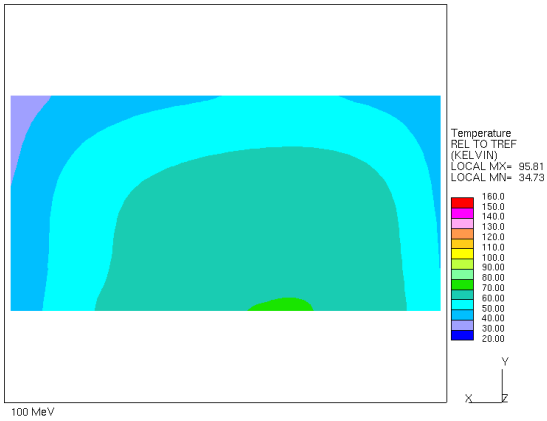

Ninth Plate

Front Surface

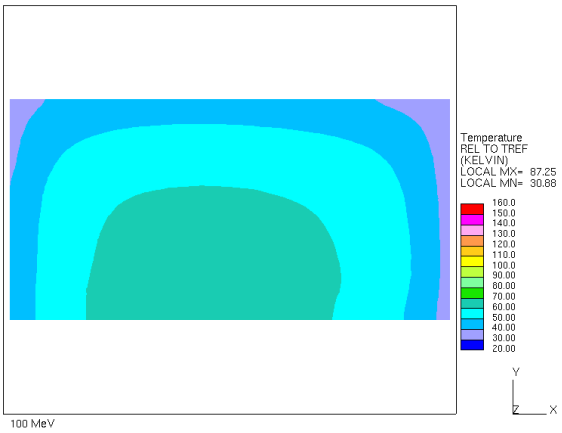

Back Surface

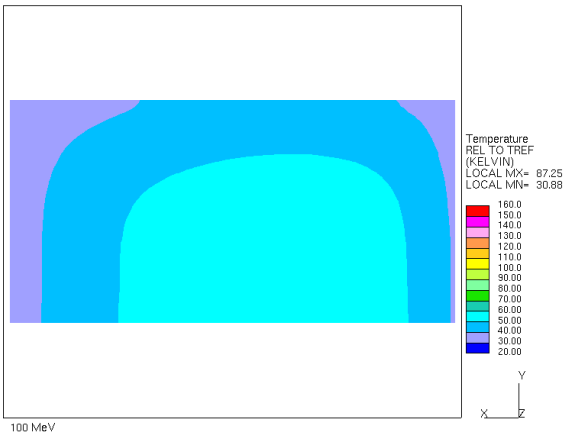

Tenth Plate

Front Surface

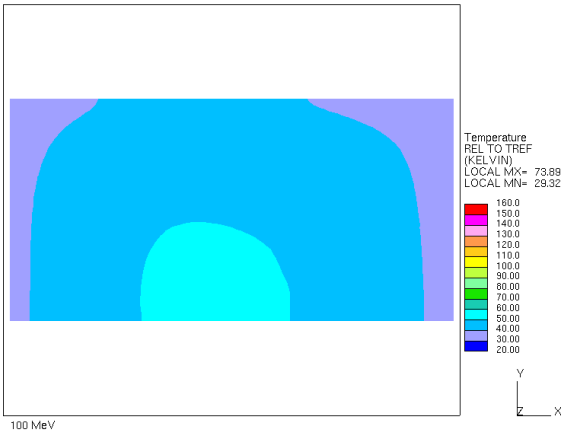

Back Surface

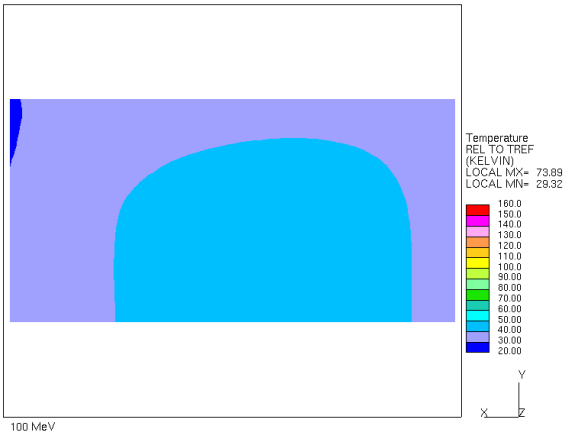

Eleventh Plate

Front Surface

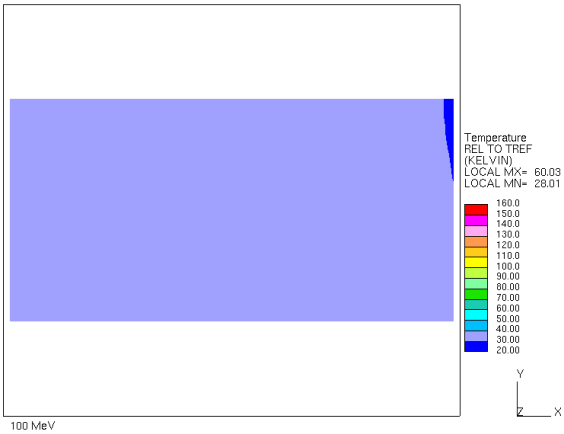

Back Surface

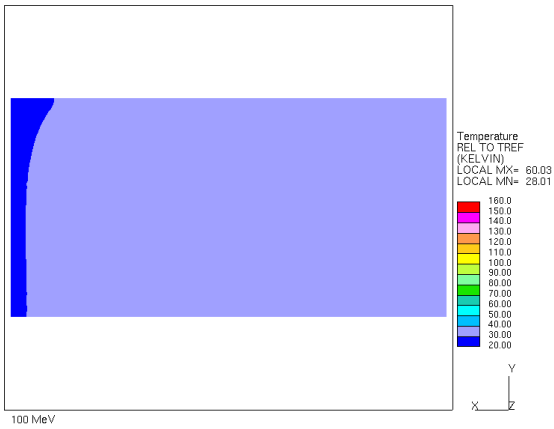

Temperature distribution of the plate mid-plan

First Target Plat

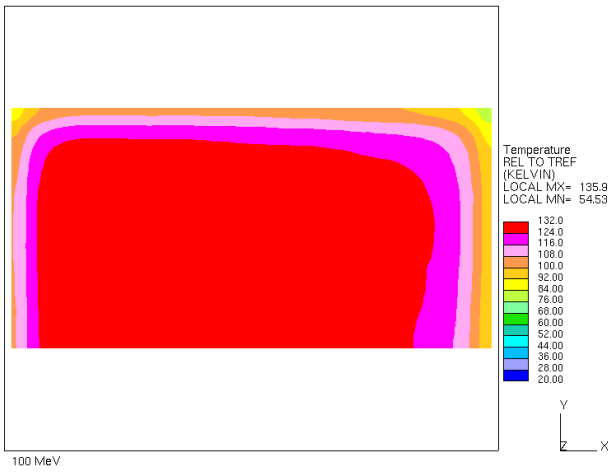

Second Target Plate

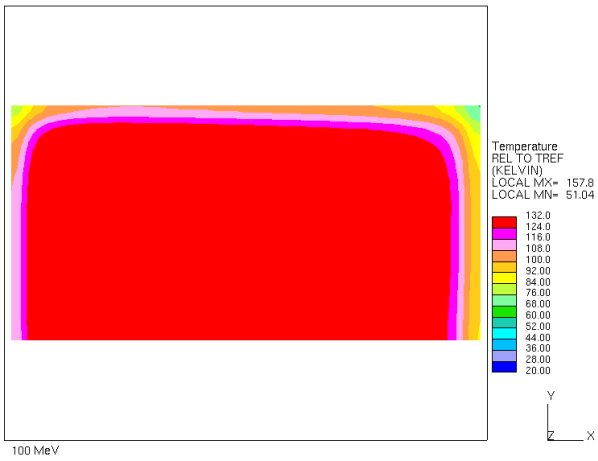

Third Target Plat

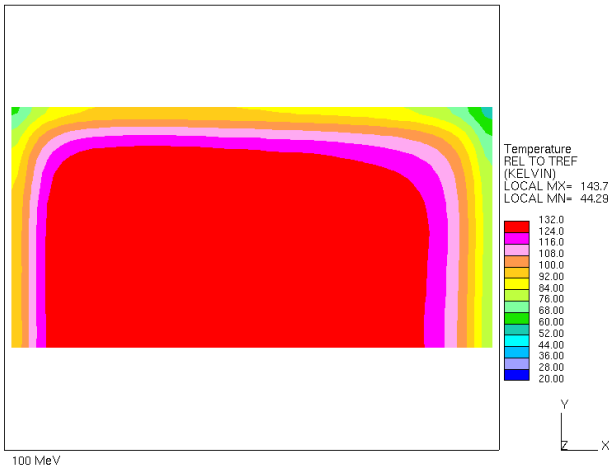

Fourth Target Plat

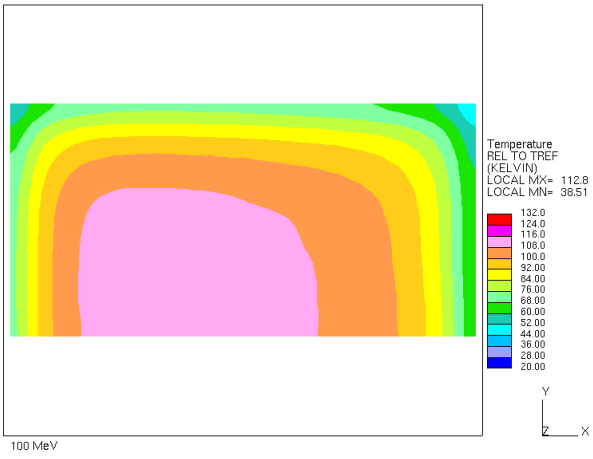

Fifth Target Plat

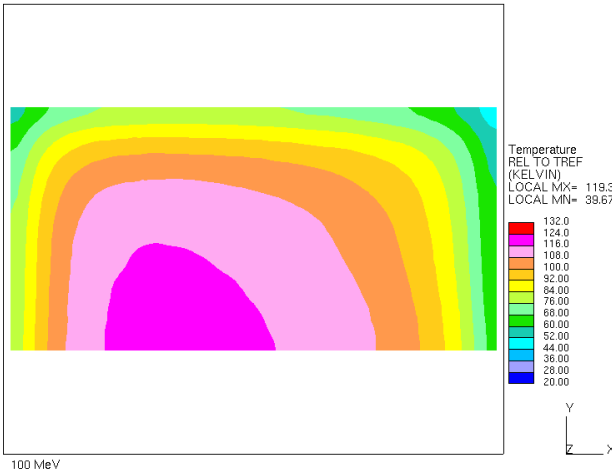

Sixth Target Plat

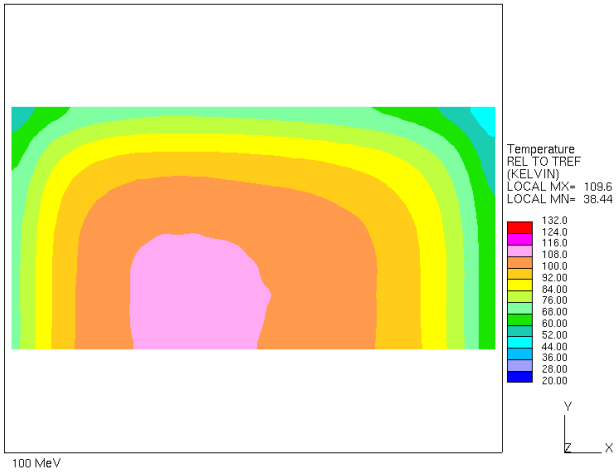

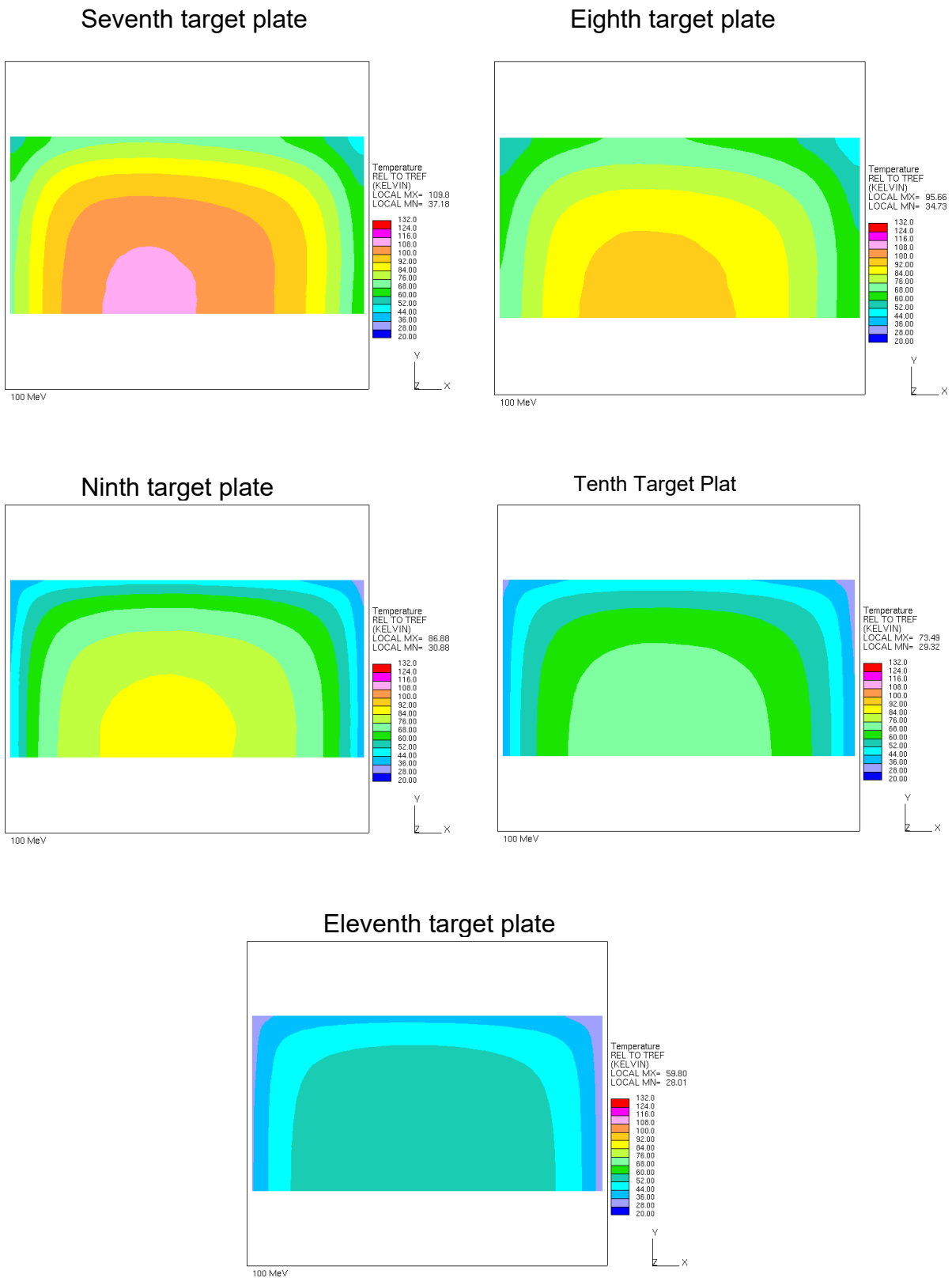

Figure II.3.4.2.4. Detailed distributions of velocity and temperature in the reference uranium target

II.3.5 Conclusions of the Thermal Hydraulics and the Design Analysis

Numerical simulations were performed to optimize the tungsten and the uranium target configurations with the commercial CFD code STAR-CCM+ 5.06. For an inlet water flow rate of 4.79 kg/s, the results show that subcooled boiling is not predicted to occur at the rated pressure with a margin of 30 ^{o}C to 40 ^{o}C. Moreover, the first layer of fluid cells has much lower temperature suggesting that any bubble departing from the wall would be short-lived. In conclusion, boiling should not be a concern at the rated pressure for the present target configurations.

II.3.6 Thermal Hydraulics Analysis of the Reference Design Options

CFD simulations were performed for the final planned target design. This geometry closely resembles that presented in Section II.3.4, with flow split between primary and secondary lines to cool the target plates. In these simulations, it was attempted to model the geometry as close to the actual fabricated geometry as much as possible.

The simulations feature the actual manifold geometry at the inlet/outlet, side, and lower regions. These are shown explicitly in Fig. II.3.6.1. These areas were not finalized and were simplified in prior calculations. Another addition is the corner parts used to support the target plates. These four-sided parts lie at the corners of each plate, as shown in Fig. II.3.6.2. They are constructed from the same materials as the cladding, i.e., tantalum for the tungsten target and aluminum for the uranium target. These differences change the flow within the coolant channels and allow for conduction between the plates through the cladding material. The base of the target window at the top of the channels was widened slightly to have it sit correctly on the corner parts.

II.3.6.1 Simulation Methods

All simulations were performed using the commercial CFD code STAR-CCM+ 7.06 of November 2012. Turbulence modeling was the same as in Section II.3.4, second-order upwind schemes were used for convection, and a SIMPLE-type solver was employed. Another difference between this and prior simulations is that the entire domain was simulated, hence no symmetry boundaries were used, and conjugate heat transfer was evaluated for all regions between the inlet manifold and the lower manifold. Conformal meshes were generated at the interfaces of these regions to correctly model the heat transfer.

Outer walls of the aluminum casing and the boundaries of the window were assumed adiabatic, which can be regarded as the most conservative case. A mass flow rate of 4.79 kg/s and an inlet temperature of 25°C were used for all cases. The velocity inlet and the flow-split outlet boundary conditions were used as before in section II.3.4. Constant physical properties were employed due to the relatively small temperature change throughout the domain.

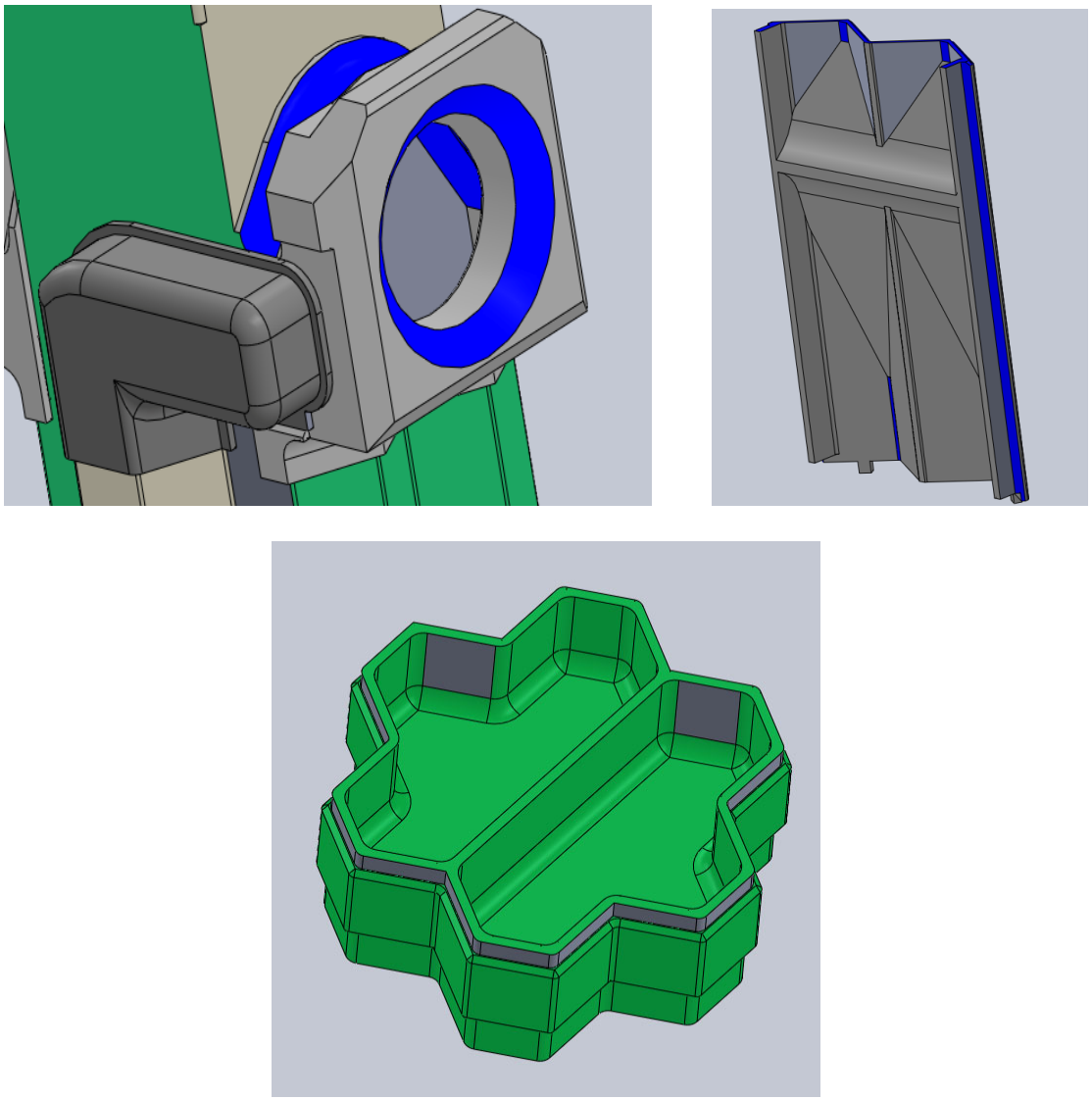

Figure II.3.6.1. Clockwise from top left: the inlet manifold, the side flow separation between the top and bottom plates, and the lower manifold.

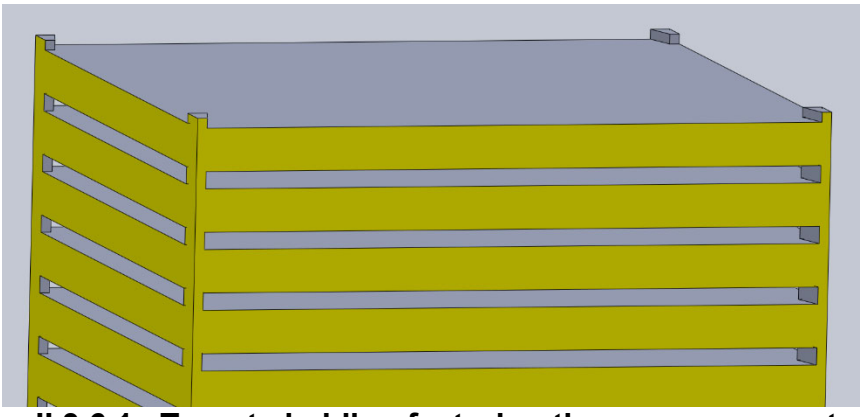

Figure II.3.6.1. Target cladding featuring the corner support parts.

The power distribution was the same as in previous analyses, obtained from MCNPX simulations. The profiles were mapped with FORTRAN subroutines adapted from those of the previous analyses. Due to the difference between the predominantly polyhedral mesh in STAR-CCM+ and the hexahedral mesh from MCNPX, there is overlapping of cells and the integrated power does not exactly match. Moreover, the heating in the target window and manifold sides was not included in the mapping. Because of this, the power in STAR-CCM+ was scaled by a constant factor so that the total power does match. For tungsten, this total power is 85.7 kW; for uranium, it is 90.5 kW. This method provides conservative estimates for peak cladding and tungsten/uranium temperatures since it overestimates local heating in the plate area.

Steady-state simulations were performed for both targets, but residuals did not decrease to a typically acceptable level. Various meshing and geometric changes were made that did not affect the obtained residuals. Unsteady simulations were then performed, which consistently reached steady-state behavior and had more acceptable residuals. Figure II.3.6.1.1 shows the variance in the velocity for the tungsten case given many samples in time. Higher variance indicates more “unsteadiness”, or a more significant time-dependence of the solution. The final lower manifold design exhibits unsteady behavior that was not present with simplified designs. Thus, unsteady simulations were performed to establish accurate flow and temperature results.

An attempt was made to reduce the flow instability by slightly changing the manifold geometry. The “step” shown in Fig. II.3.6.1.2 where the side and lower manifolds meet was smoothed out from the aluminum casing. This type of geometry is known to cause instability at high velocities. This change did reduce but did not adequately eliminate the instability, so the original geometry was used for all subsequent simulations for higher fidelity.

Time averaging was performed over the oscillatory results of the unsteady simulation. Mean and variance calculations were performed within STAR-CCM+ for velocity and temperature at various monitoring points in the domain. As these approached constant values, the simulations were regarded as exhibiting converged steady behavior. The mean and variance were calculated starting at different times and using different numbers of samples to ensure convergence.

II.3.6.2 Tungsten Target Results

The flow field and the temperature distribution throughout the target area were calculated with STAR-CCM+. The boundary conditions and the flow parameters were as described above. Since there have been many design iterations, the manifold and the duct velocities were not compared with prior analyses. Since the mass flow rate is the same, and these changes were small, velocities should be largely the same as previously shown in these areas.

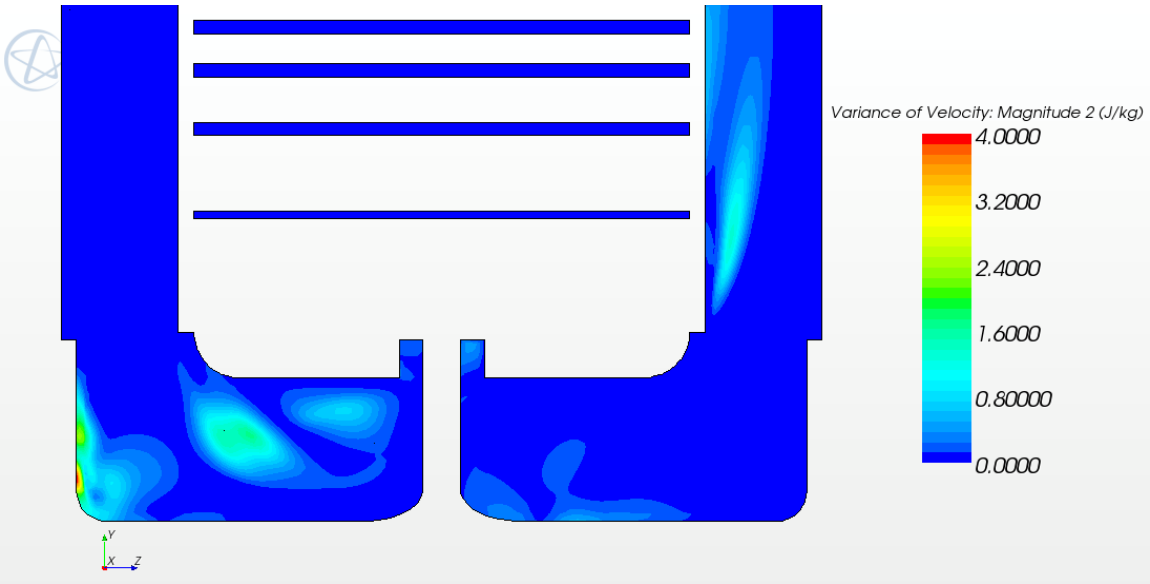

Figure II.3.6.1.1. Variance in the velocity magnitude in the lower manifold area.

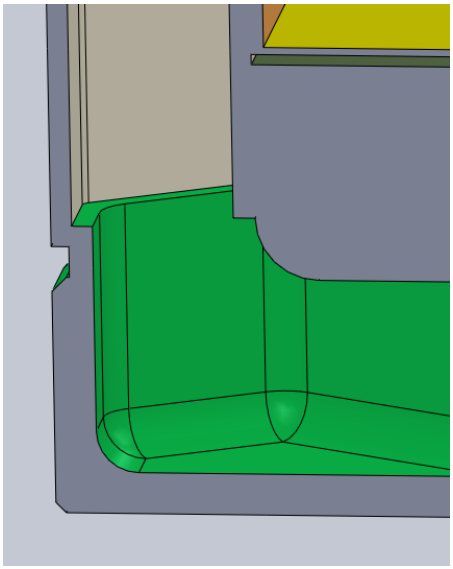

Figure II.3.6.1.2. "Step" region that commonly causes instability. For this case, the relatively high velocity and the complex flow bend are anticipated.

There are some notable differences between these results and the previous work. These are due to the differences in geometrical model fidelity, whole-domain simulation, and so forth. Generally, the results are similar.

- The flow split was confirmed at 57.1%, within range of that used in the optimization.
- The total mass flow rate was confirmed at 4.79 kg/s. The total pressure drop across the entire target system is 161.51 kPa, which is 44.37 kPa higher than previously. This is due to the inclusion of the form losses from multiple flow bends at the manifolds, the instability in the lower manifold, and the accurate representation of the geometrical details. Subtracting this loss from the inlet pressure and accounting for gravity head yields a new

estimate of 2.08 bar (2.69 bar at inlet - 0.81 bar loss + 0.2 bar gravity head) for the target region pressure. The corresponding saturation temperature is 121 °C.

- The water fluid inlet temperature is 25 °C and outlet temperature is 29.32°C.
- The peak cladding temperature is 101 °C, which is 3 °C lower than previously calculated.
- The peak tungsten temperature is 113 °C, which is 7 °C higher than previously calculated.
- Both peak temperatures are well below the melting point for tungsten (3422 °C), tantalum (3017 °C), and even aluminum (600 °C).
- The Bergles-Rohsenow correlation yielded a superheat of 22 °C for subcooled boiling to occur for this configuration. With T_{sat} of 121 °C, a wall temperature of 143 °C would be needed. Since peak wall temperature is 101 °C, the total margin to subcooled boiling is 143 °C - 101 °C = 42 °C. There is also a margin to nucleate boiling of 121 °C - 101°C = 20 °C.

Figure II.3.6.2.1 shows the power distribution throughout the domain and Figs. II.3.6.2.2 and II.3.6.2.3 present the temperature in the plates and cladding, respectively. Figures II.3.6.2.4 and II.3.6.2.5 show the complexity of the flow field in the lower manifold area. Figure II.3.6.2.6 provides the detailed distributions of the velocity and the temperature at the channel center planes, clad top and bottom surfaces, and plate center planes. These are all perpendicular to the electron beam. Note that in all figures, the +X-direction (red arrow) is the main direction of flow through the target channels. Plate 1 is closest to the electron beam, plate 2 is the next furthest, etc. Some conclusions are obtained from these results:

- Every channel has a different velocity distribution. Velocity is lowest in the channels furthest from the feeding line (channel before plate 1 for primary-fed and channel between plates 4 and 5 for secondary-fed). The channel before plate 1 has a different distribution due to the presence of the beam window.
- Velocity distributions for the primary-fed channels are roughly symmetric, as expected from the geometry. Velocity peaks at the centerlines emerging from each of the two ducts.
- The secondary-fed channels have more asymmetric velocity distributions due to the complex bending of the flow in the lower manifold region, which does not have sufficient distance to develop a symmetric profile before it reaches the channels.
- The peak temperatures of the tungsten plate and the tantalum coating are biased toward the channel outlet and are located near the symmetry line.
- The peak temperature is now located in plate 4. While plate 2 has a higher power density, it is cooled on both sides by the higher-velocity water from the primary line. Plate 4 has relatively high-power distribution, evident from Fig. II.3.6.2.1, but is cooled on one side by the lower-velocity secondary line.
- The fluid temperature in the first layer of cells from the wall is like that in the previous simulations, notably it is significantly lower than the wall temperature. While there are some local spots of higher fluid temperature, in large part due to relatively stagnant flow areas near the support parts, these occur at the sides and corners of the plates where the cladding surface is cooler. Thus, for the spots on the cladding surface where boiling would be most likely to occur, there is still a very large difference between wall and first-layer fluid temperature. This suggests that any bubbles departing from the wall would condense quickly.

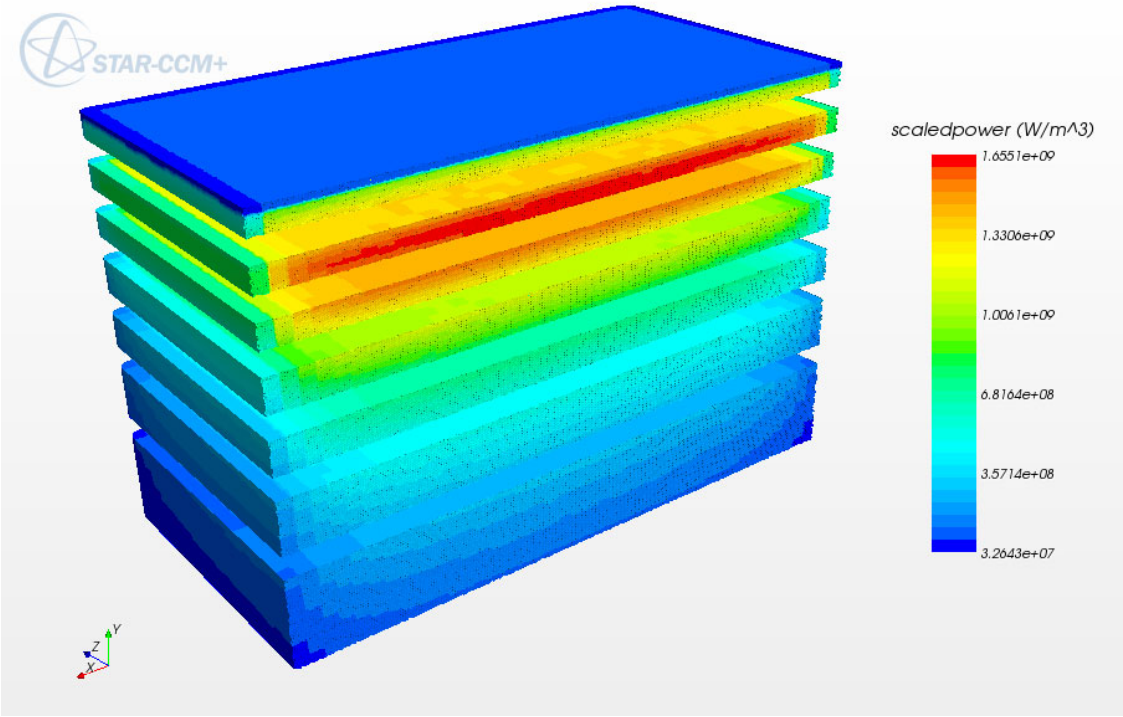

Figure II.3.6.2.1. Power distribution in tungsten plates (W/m^3). The Power mapping also extends to heating in cladding and water channels from neutrons within 64x64 mm clearance of beam center.

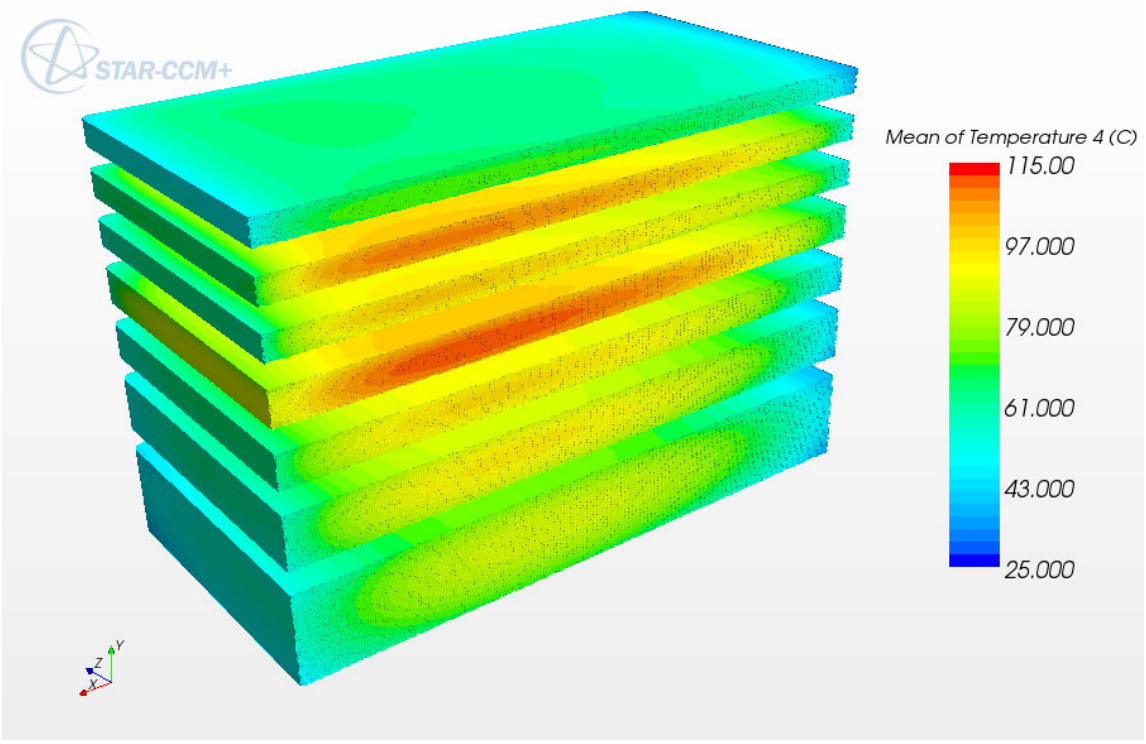

Figure II.3.6.2.2. Temperature distribution (°C) in the tungsten plates.

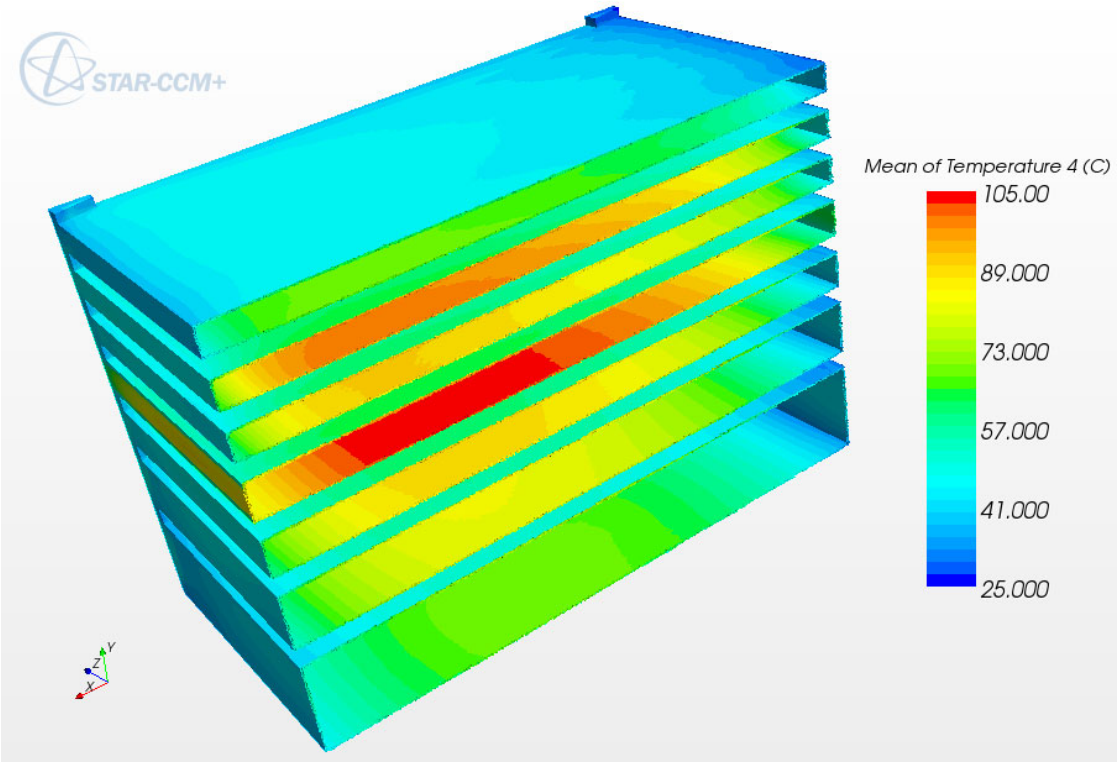

Figure II.3.6.2.3. Temperature distribution (°C) in the tantalum coating.

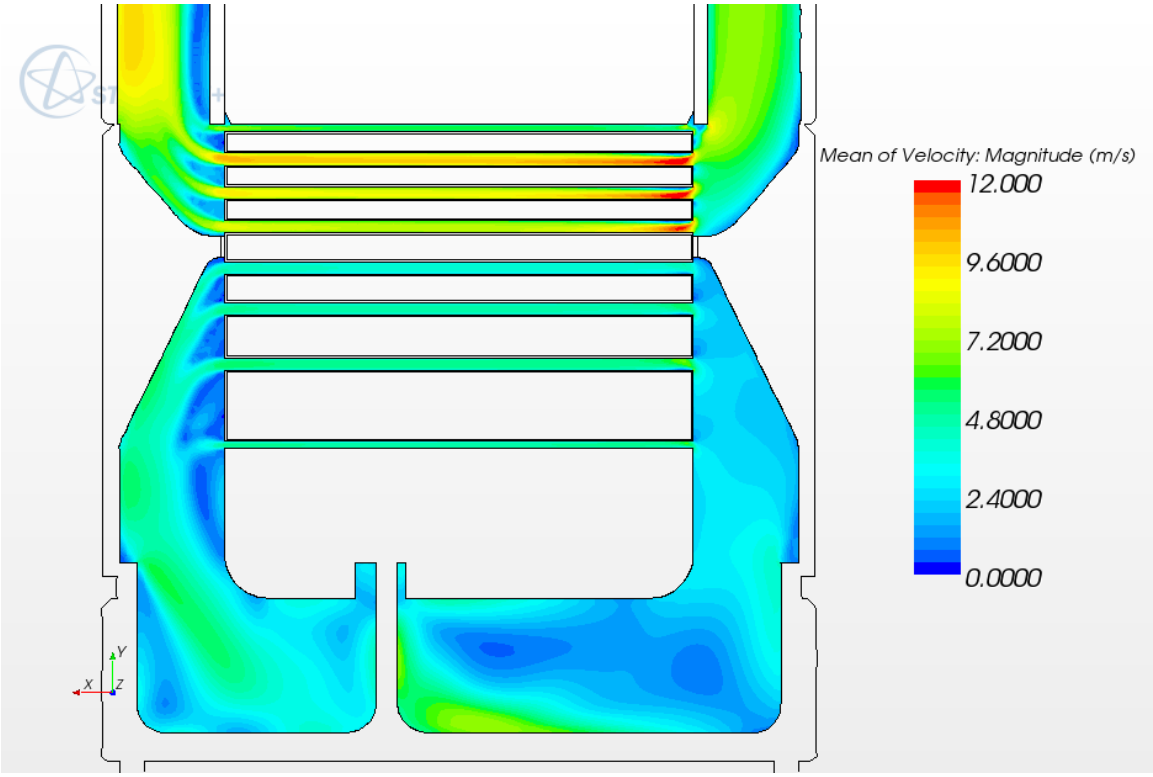

Figure II.3.6.2.4. Velocity magnitude (m/s) at plate centerline, parallel to channel flow.

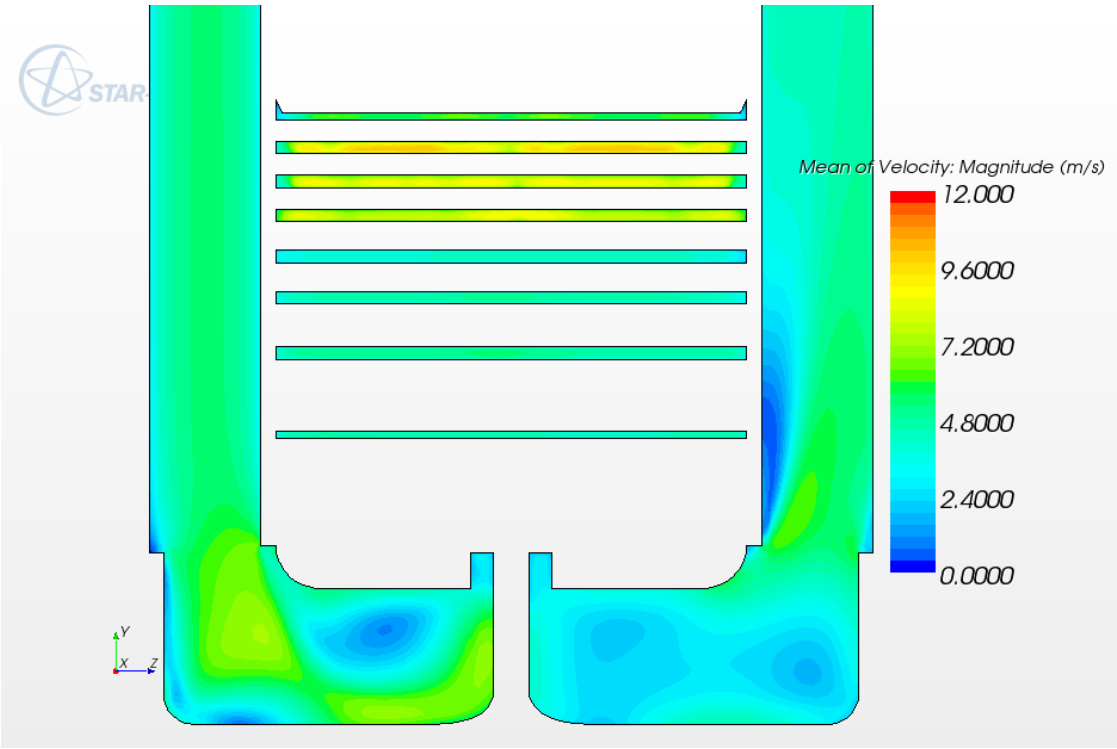

Figure II.3.6.2.5. Velocity magnitude (m/s) at the plate centerline, normal to the channel flow.

Velocity magnitude in the channel mid-section

Channel before Plate 1

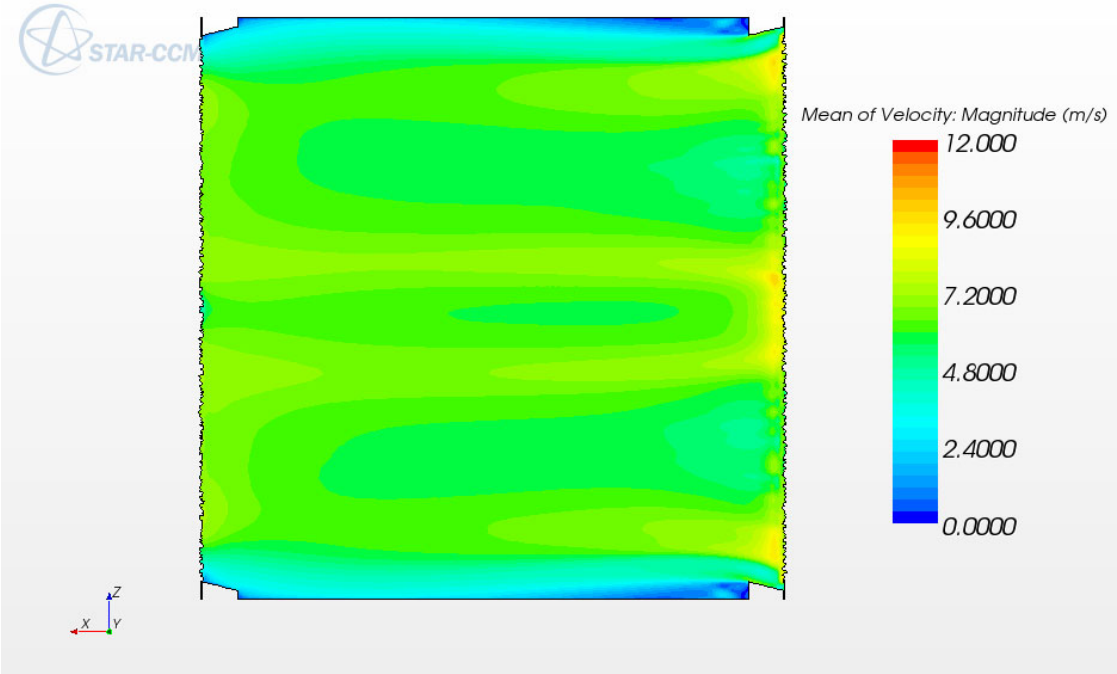

Channel between Plate 1 and Plate 2

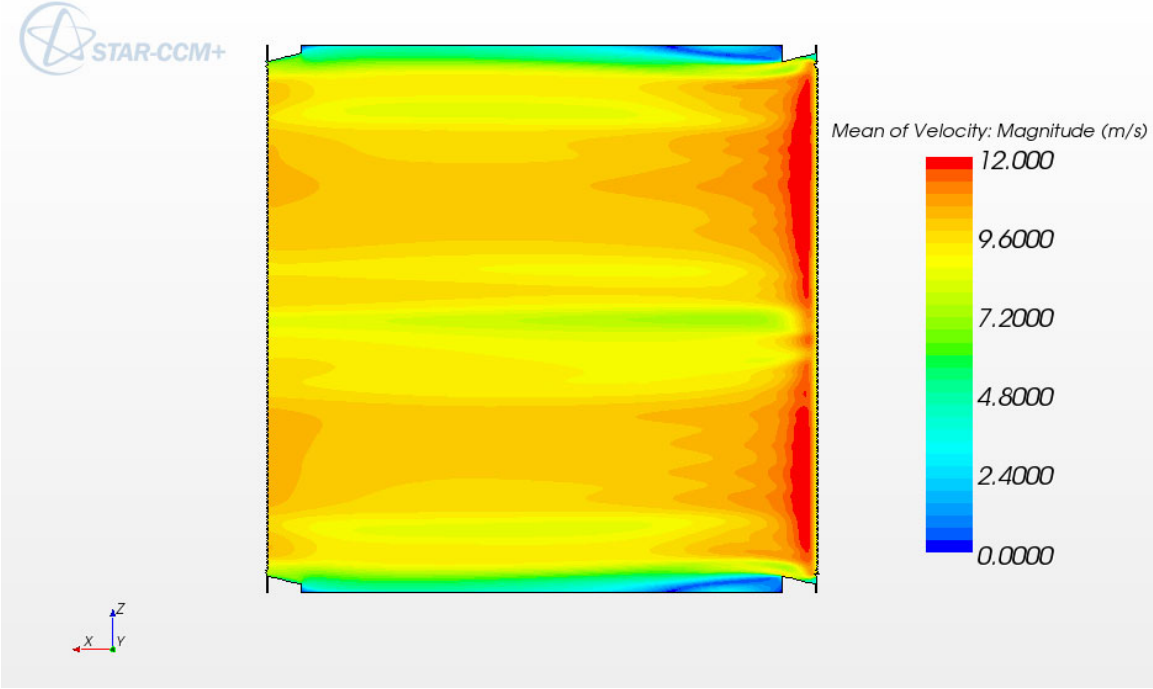

Channel between Plate 2 and Plate 3

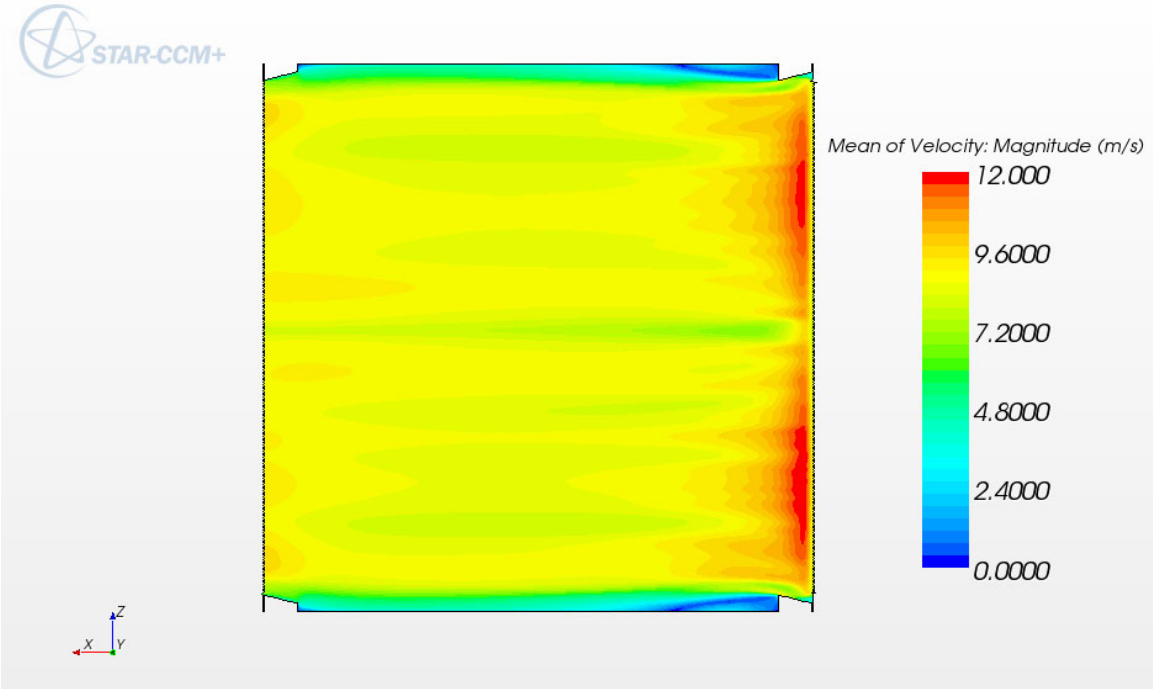

Channel between Plate 3 and Plate 4

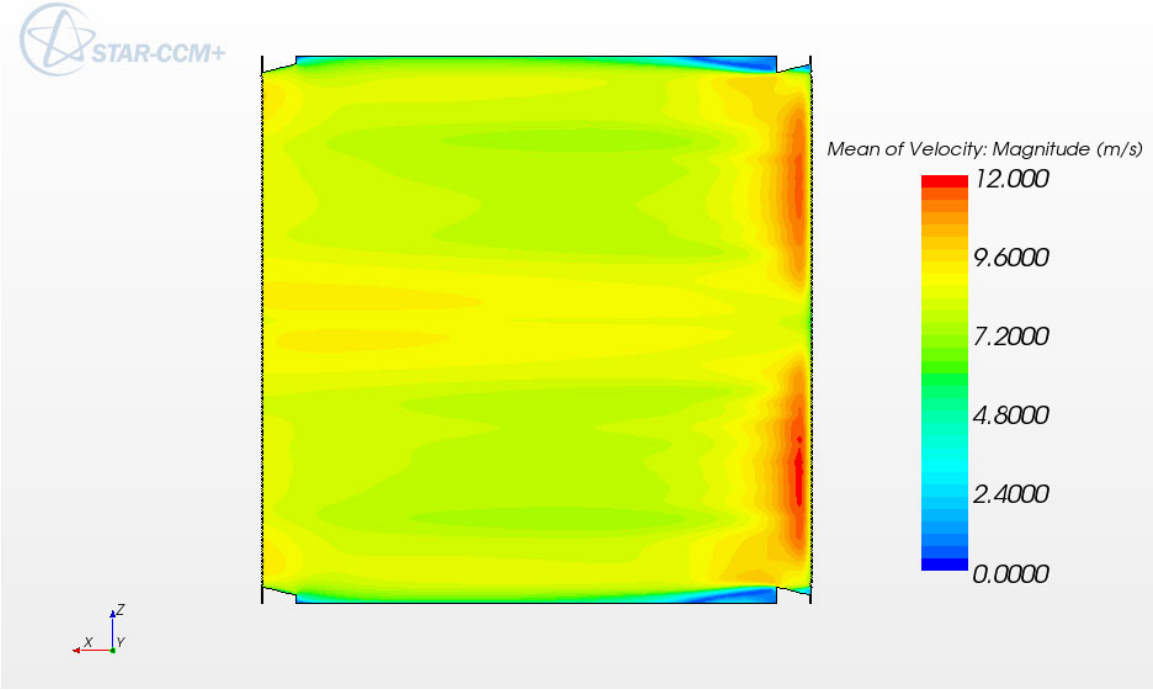

Channel between Plate 4 and Plate 5

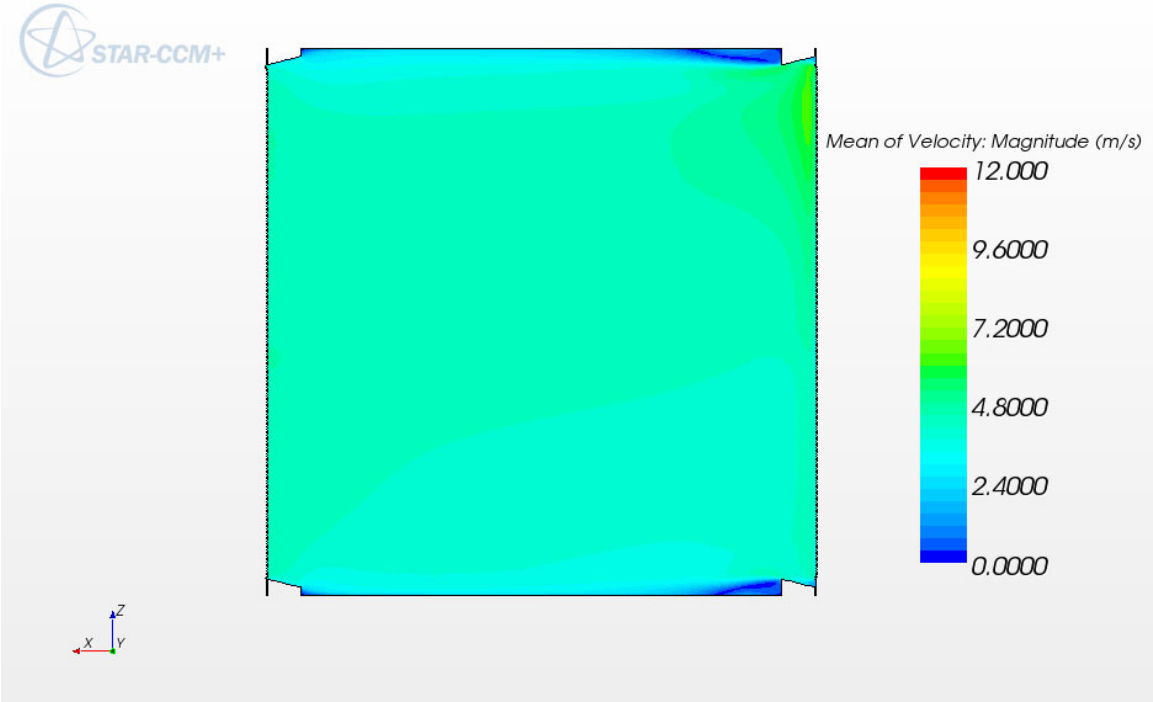

Channel between Plate 5 and Plate 6

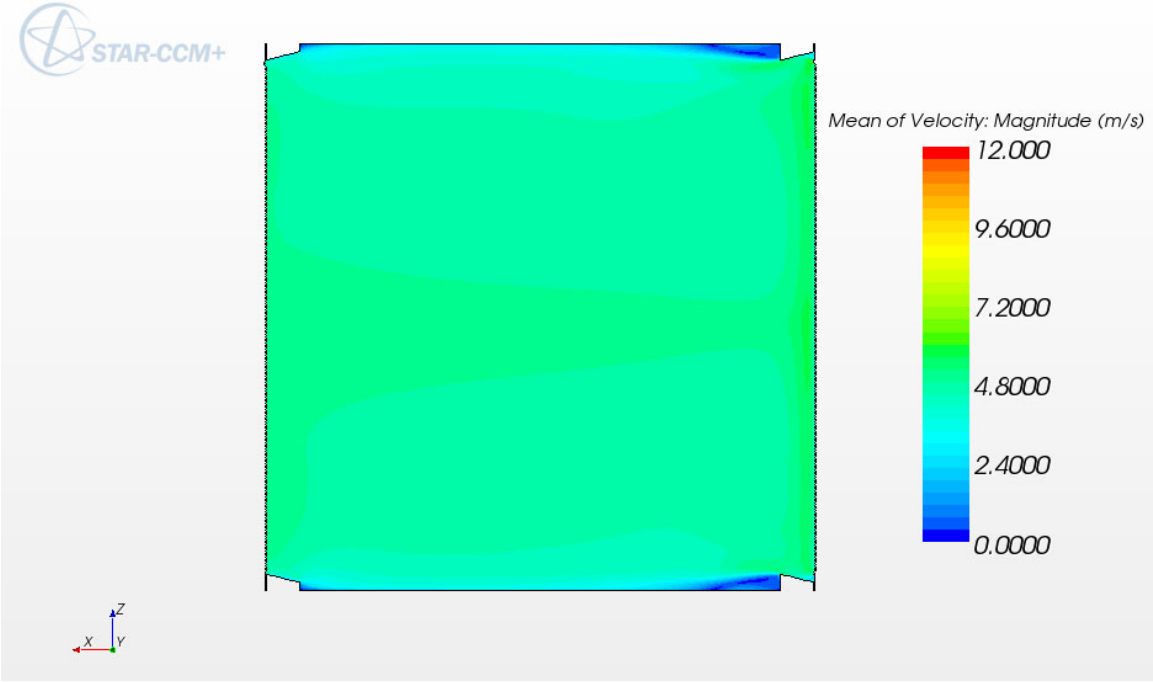

Channel between Plate 6 and Plate 7

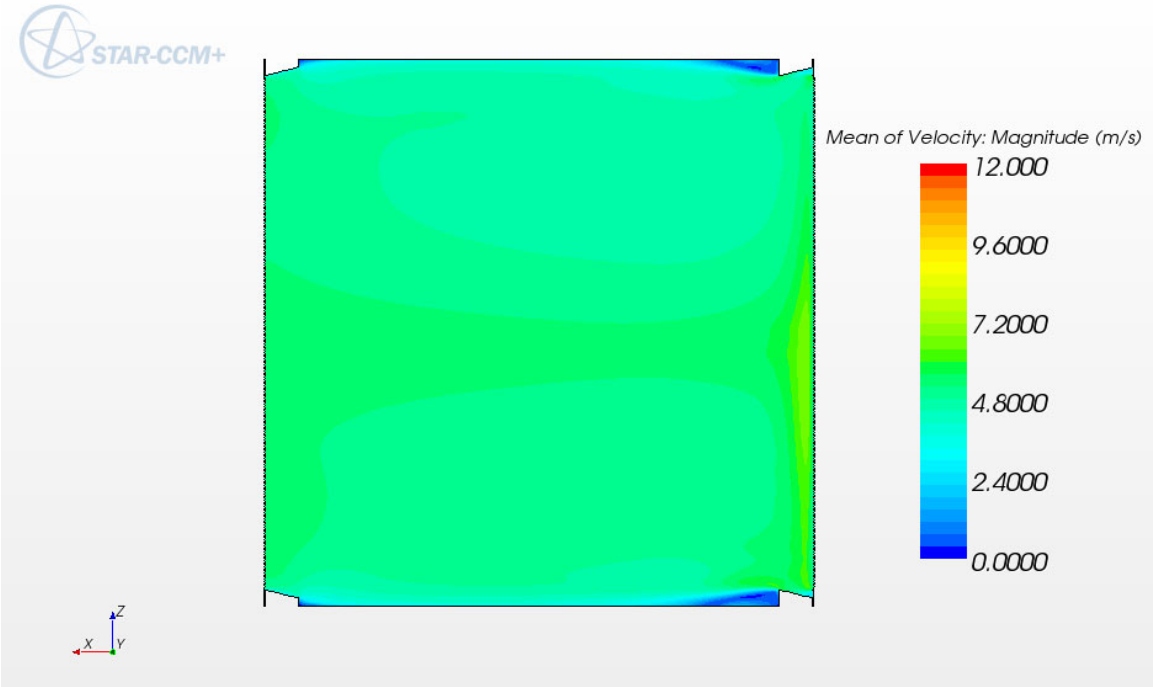

Channel after Plate 7

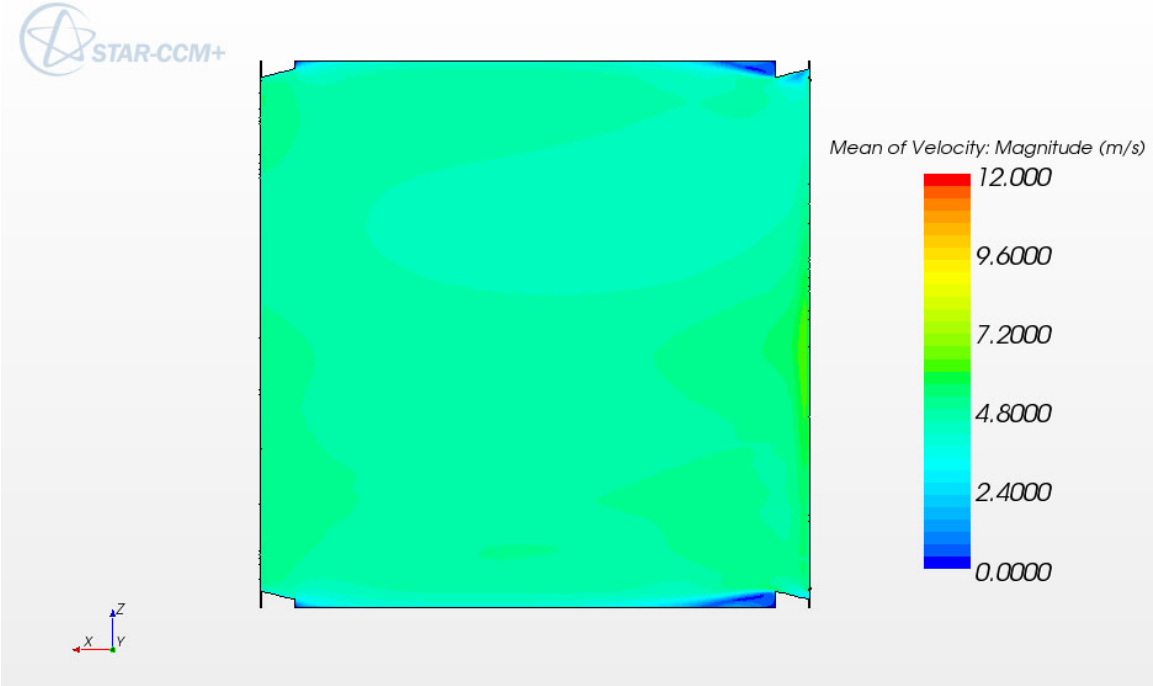

The temperature distribution in the channel mid-section

Channel before Plate 1

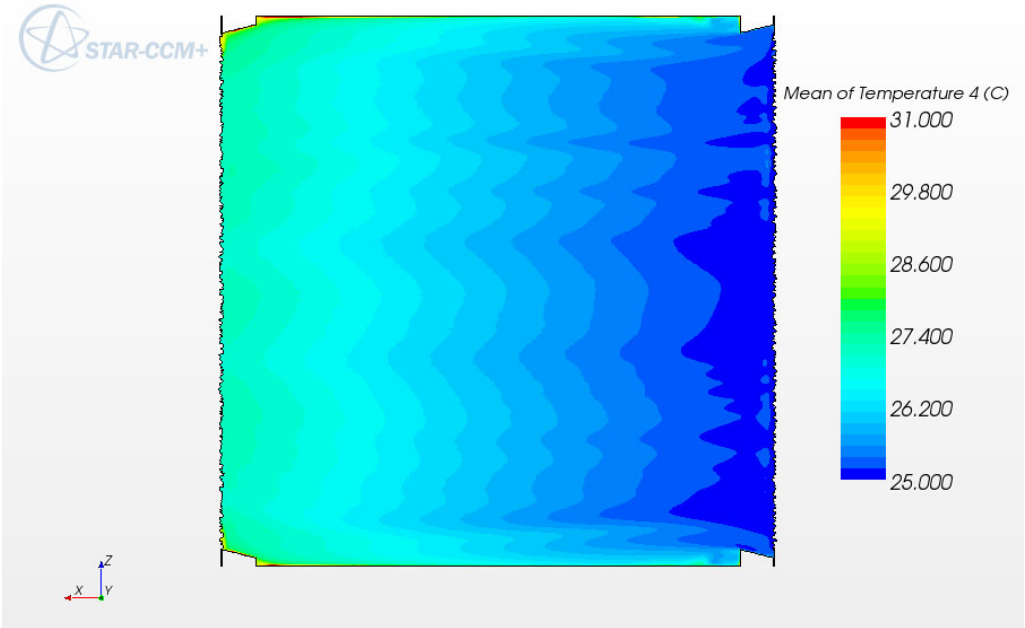

Channel between Plate 1 and Plate 2

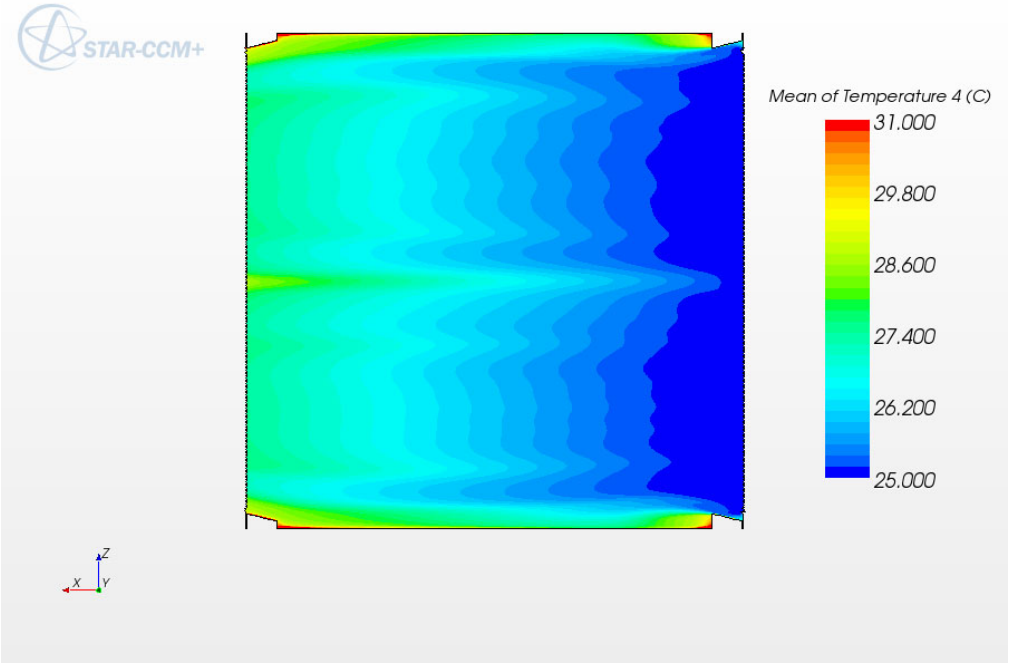

Channel between Plate 2 and Plate 3

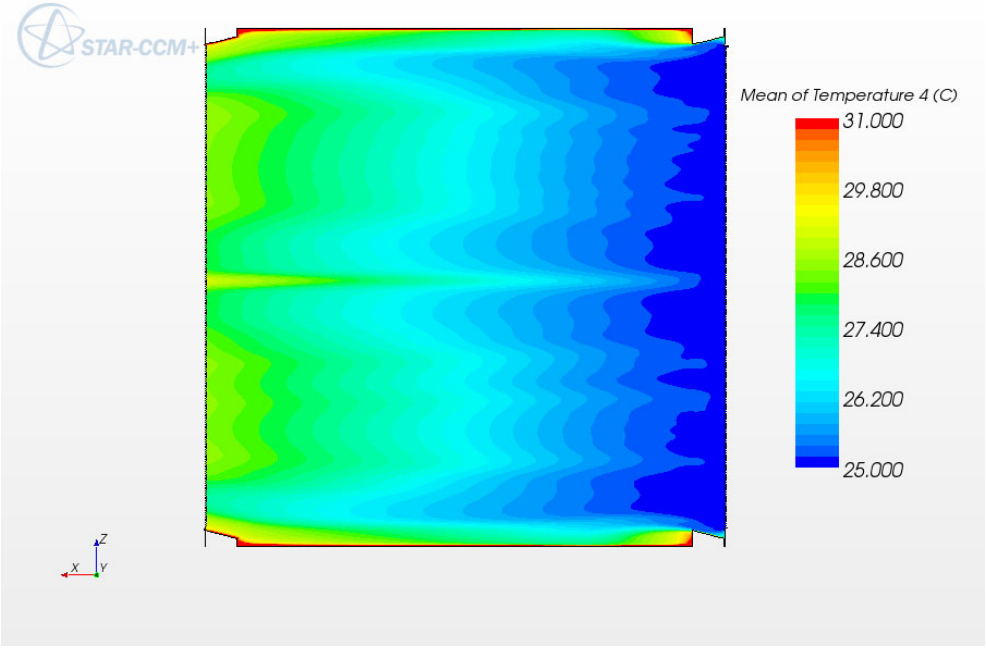

Channel between Plate 3 and Plate 4

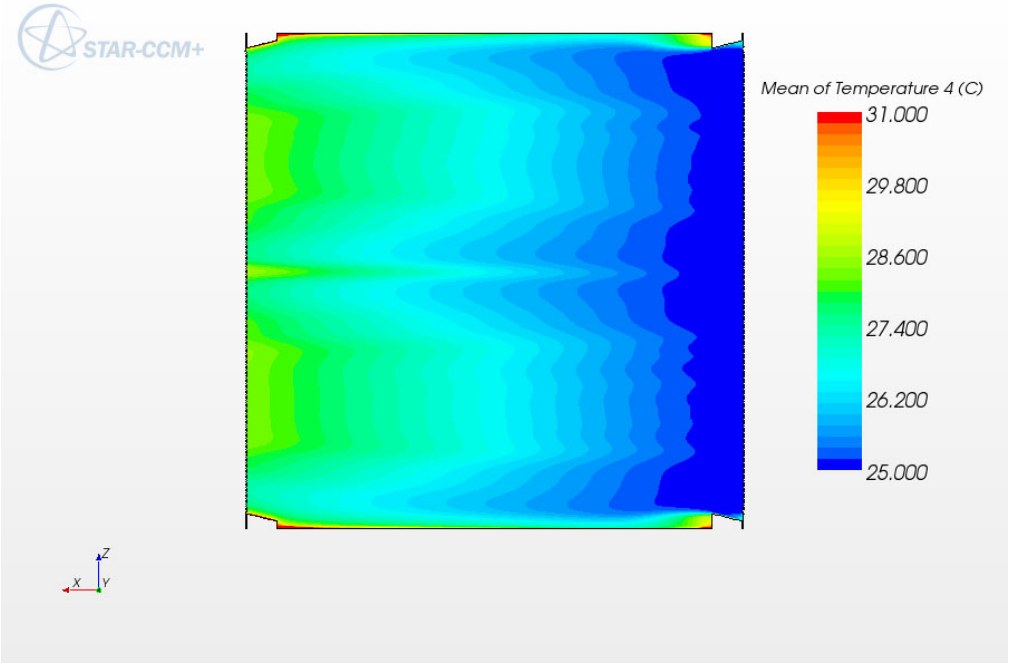

Channel between Plate 4 and Plate 5

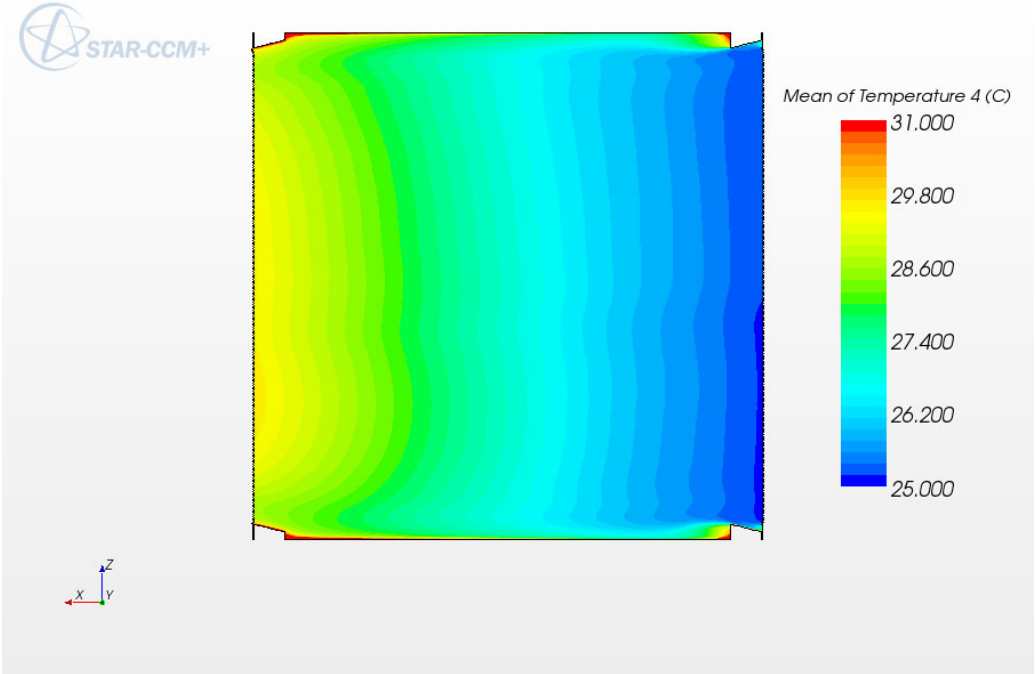

Channel between Plate 5 and Plate 6

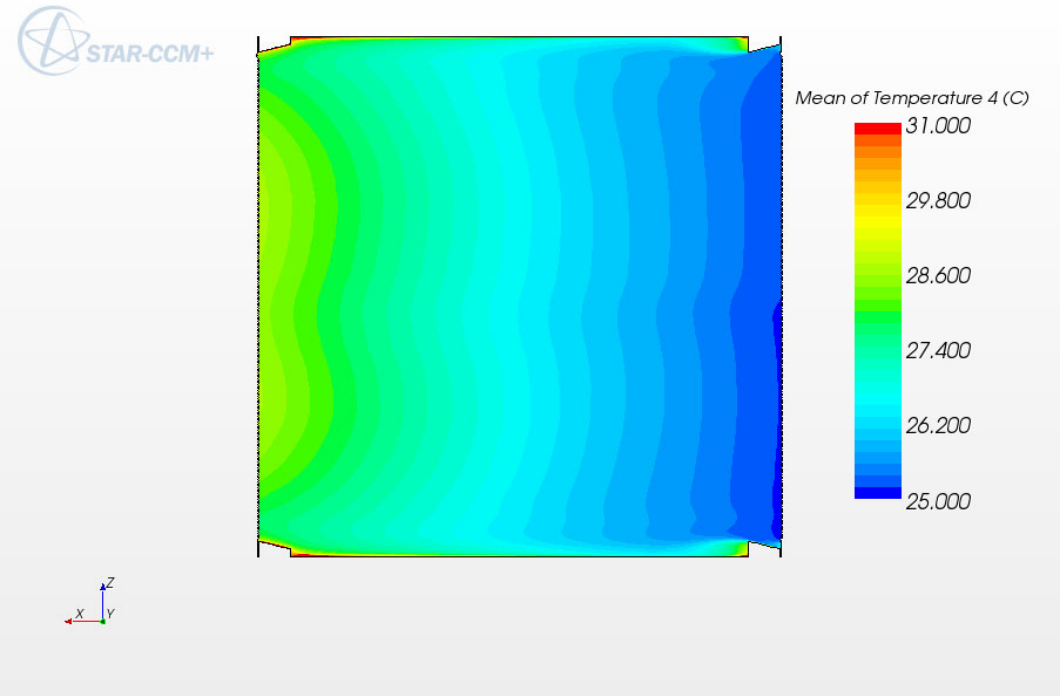

Channel between Plate 6 and Plate 7

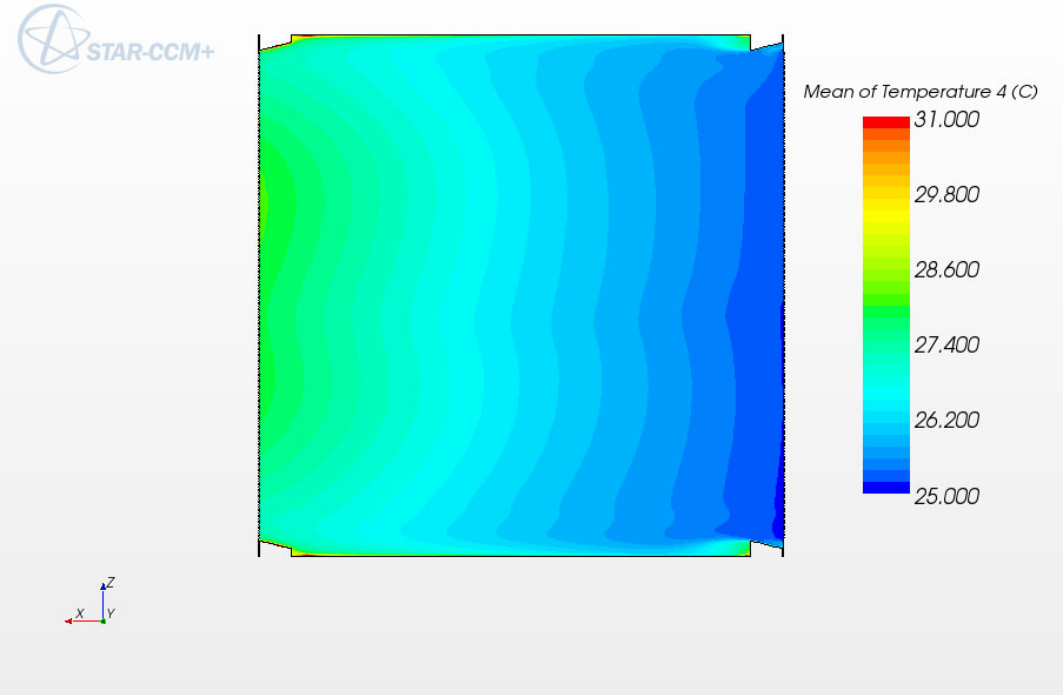

Channel after Plate 7

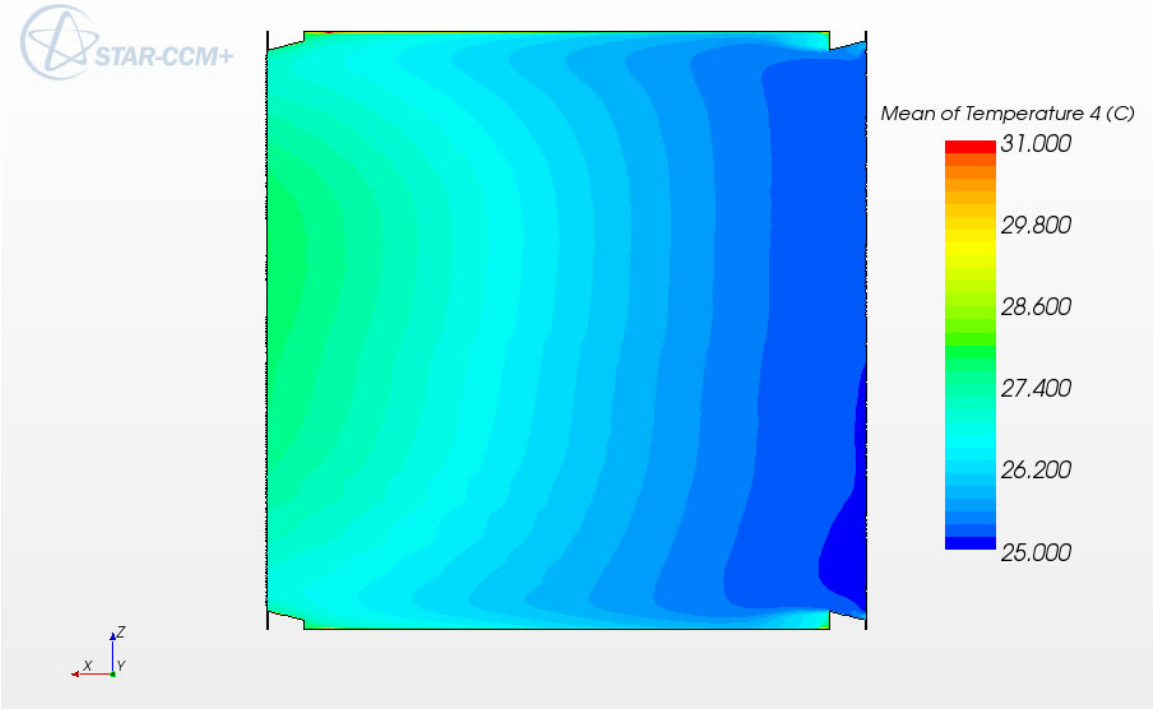

Temperature distribution on cladding surface

Plate 1 top

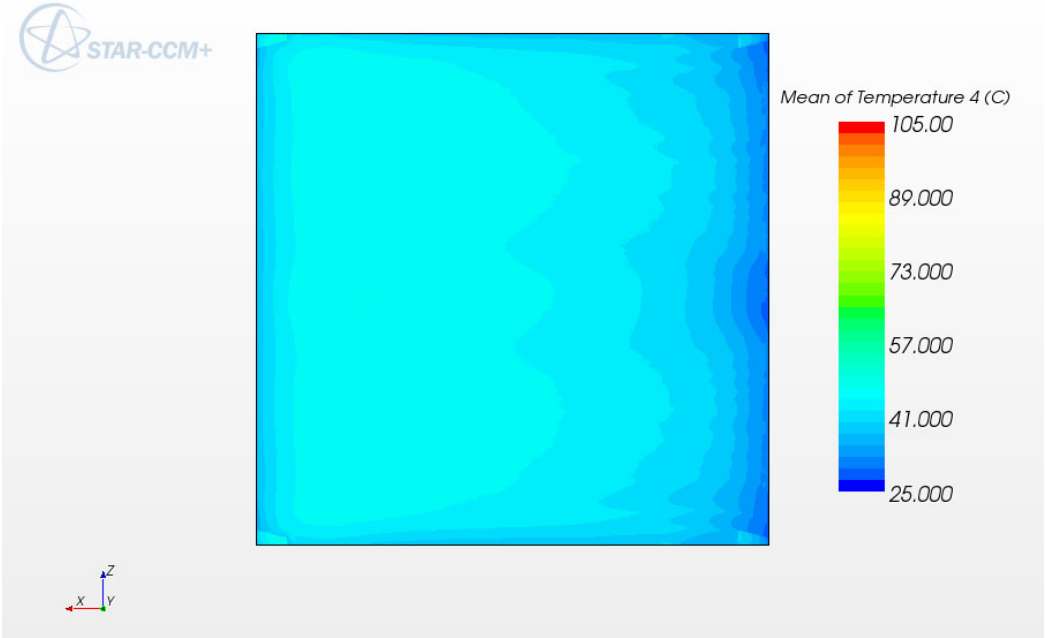

Plate 1 bottom

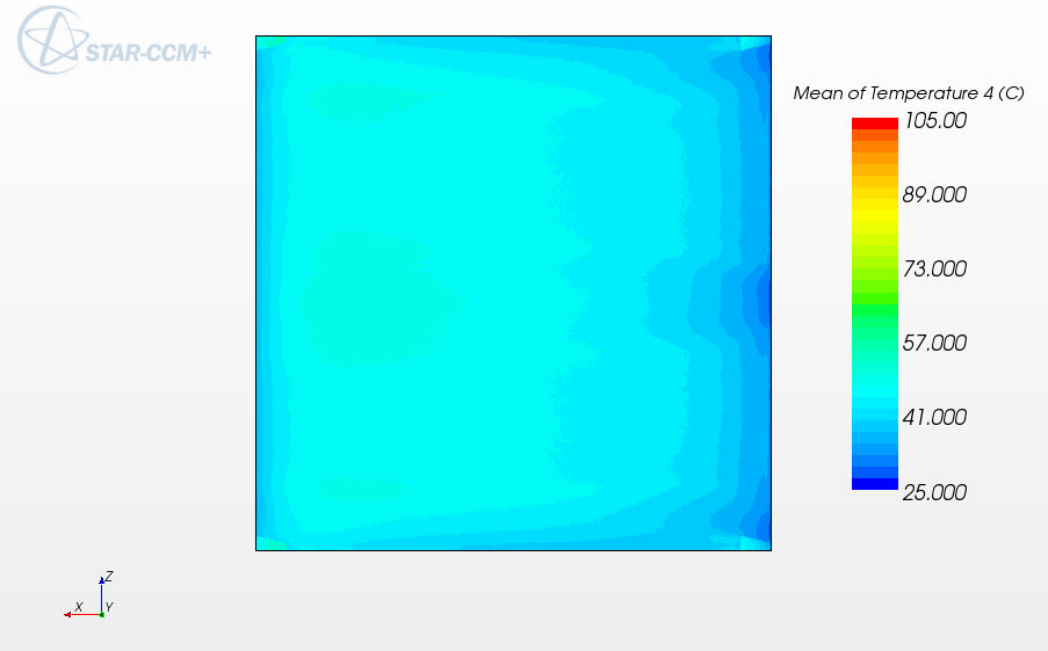

Plate 2 top

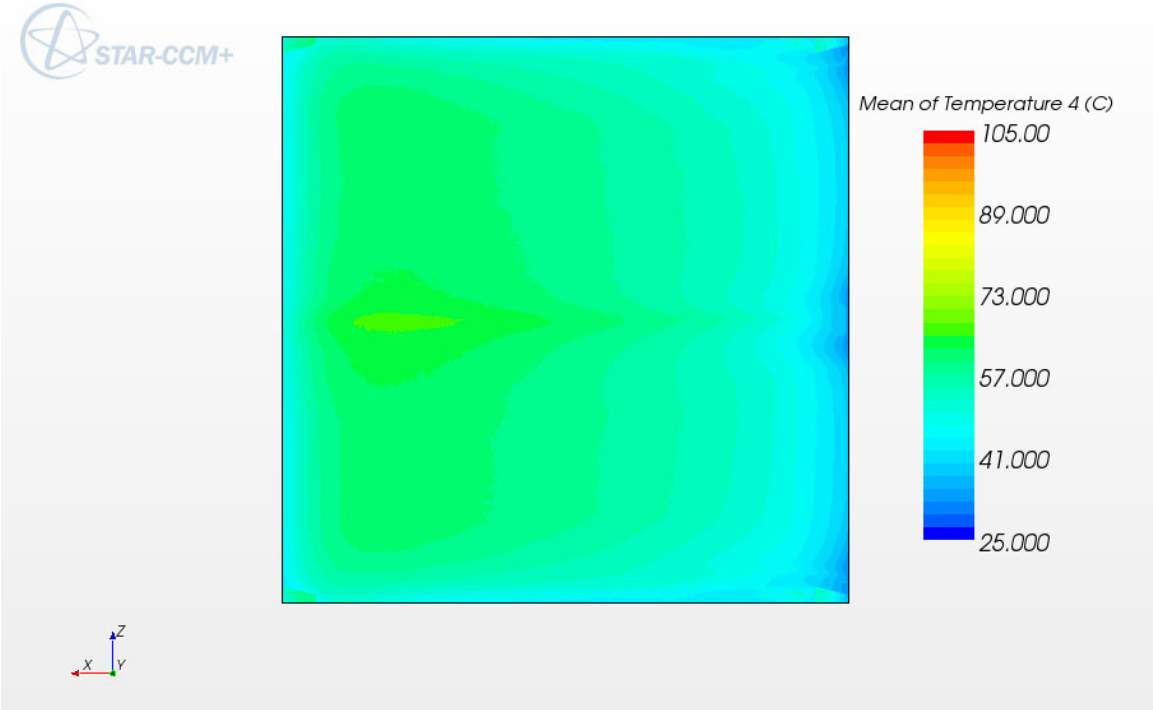

Plate 2 bottom

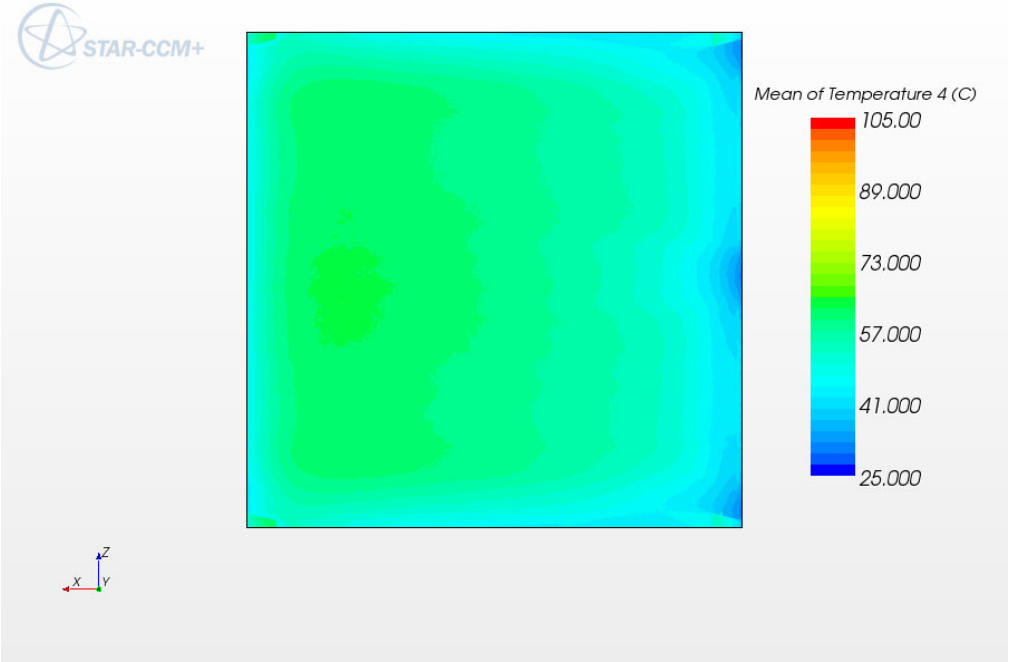

Plate 3 top

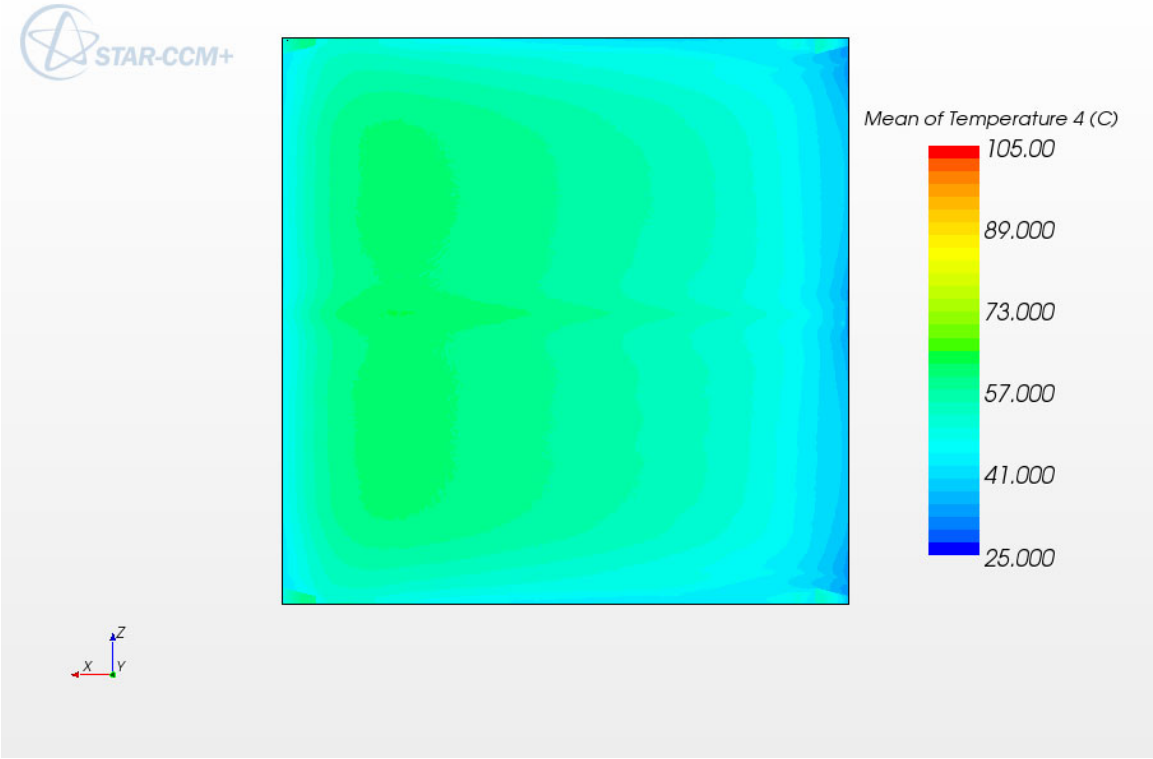

Plate 3 bottom

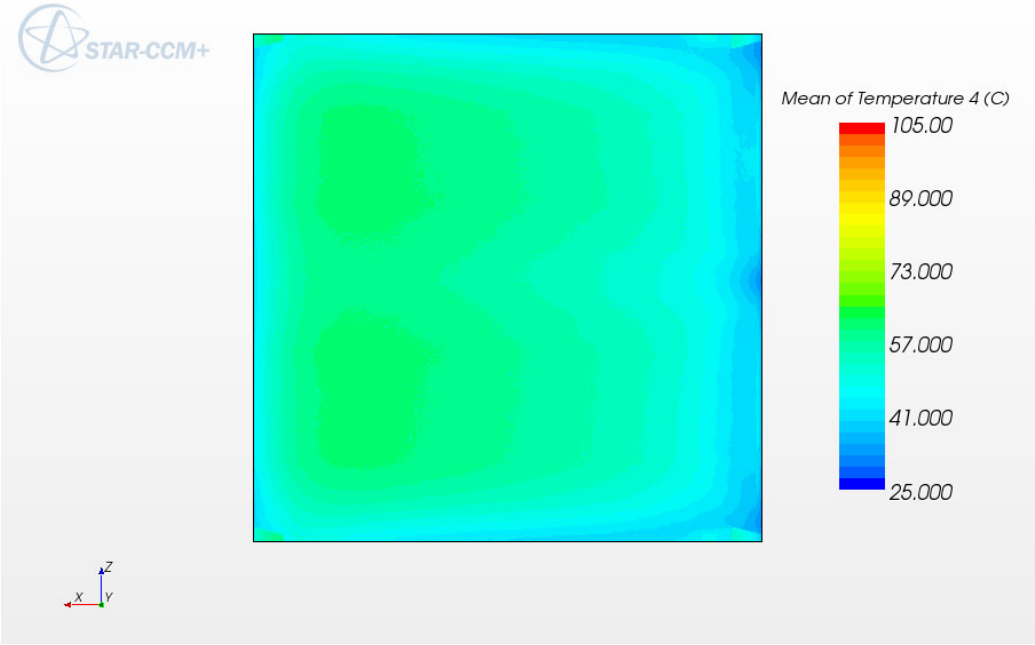

Plate 4 top

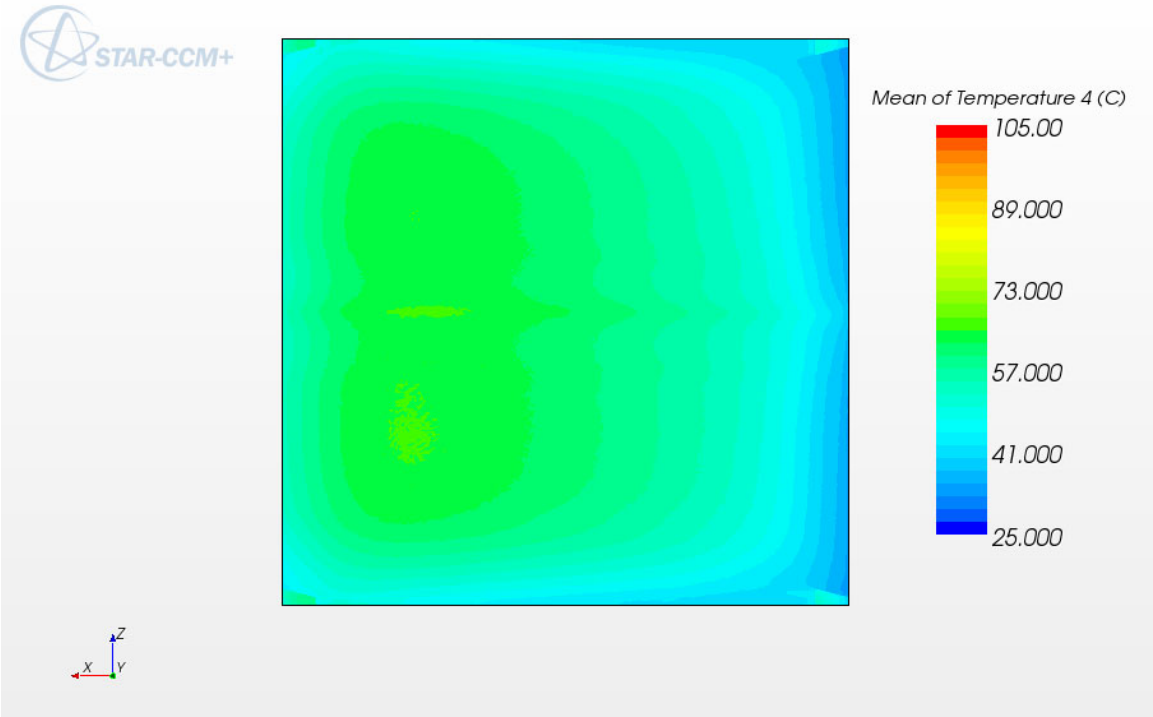

Plate 4 bottom

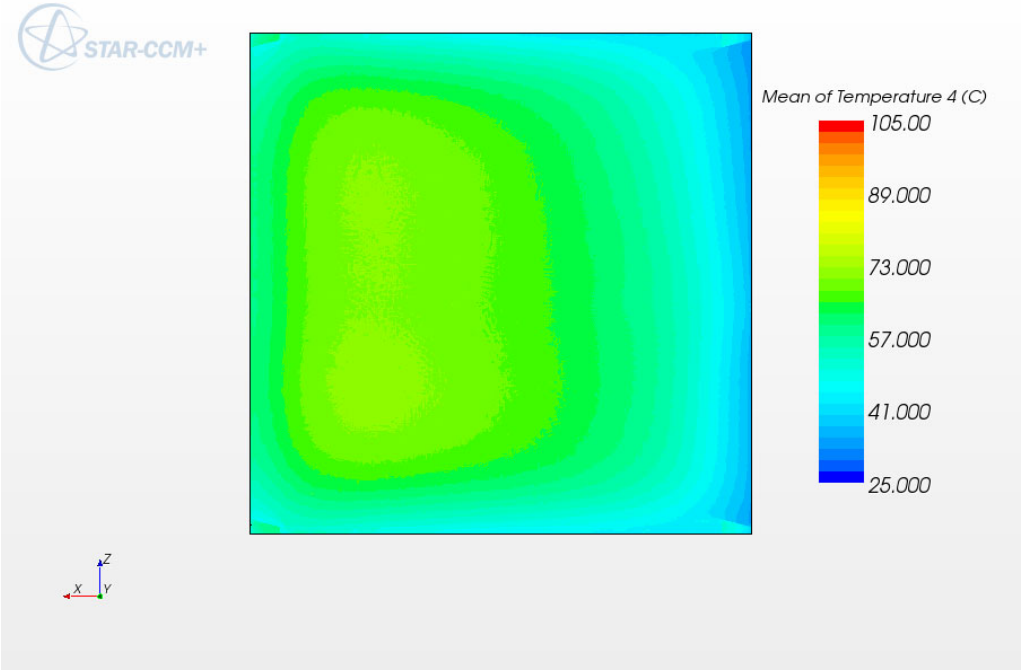

Plate 5 top

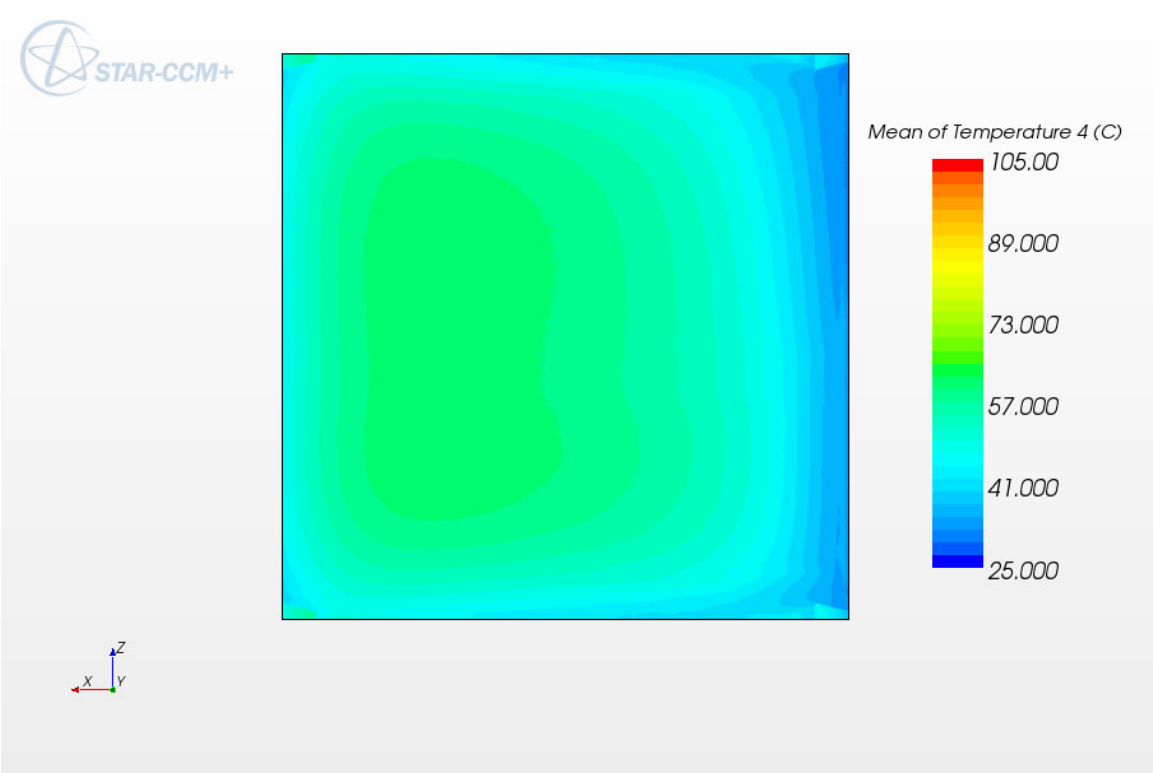

Plate 5 bottom

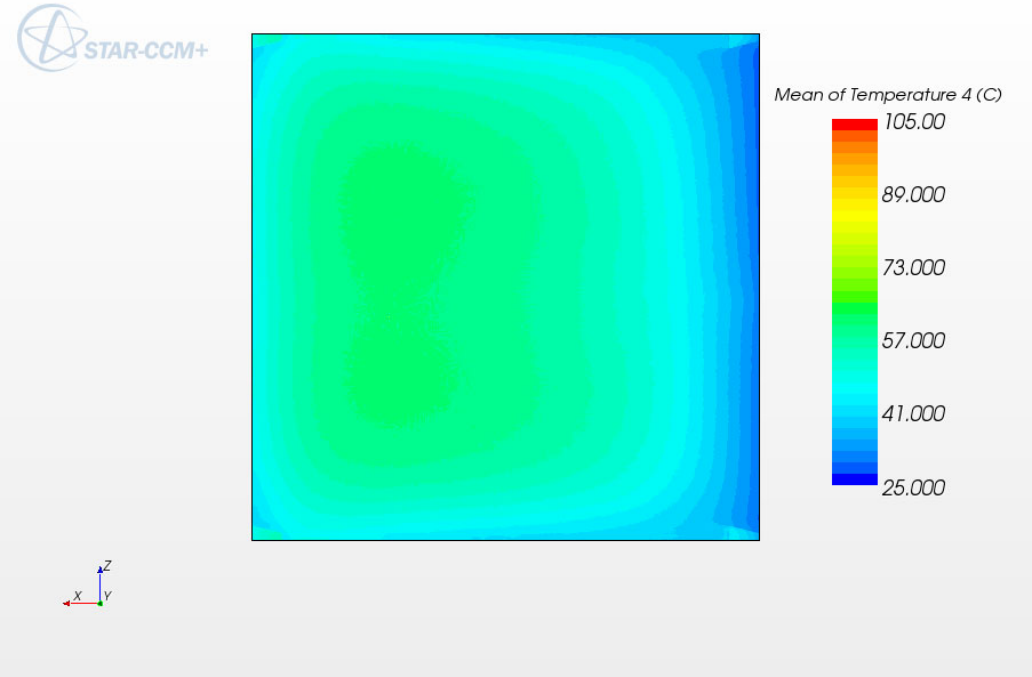

Plate 6 top

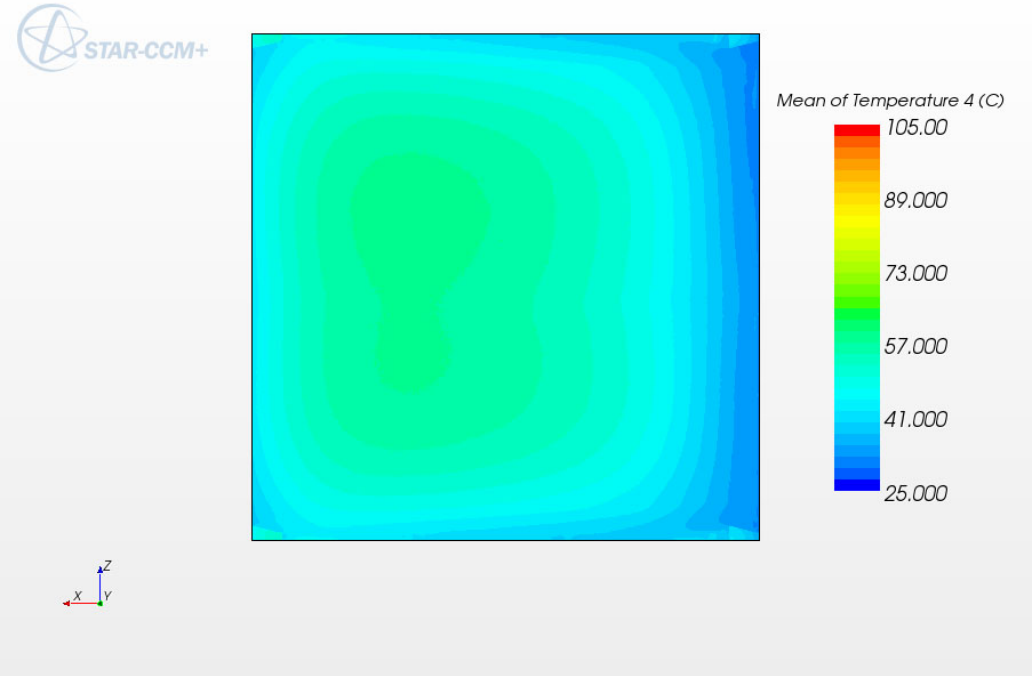

Plate 6 bottom

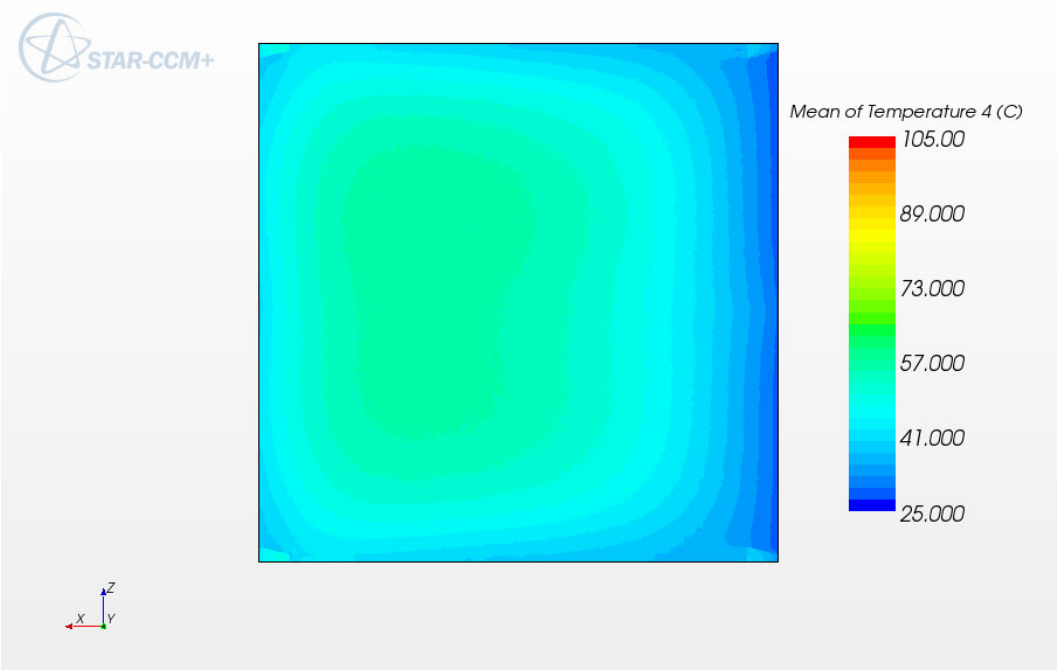

Plate 7 top

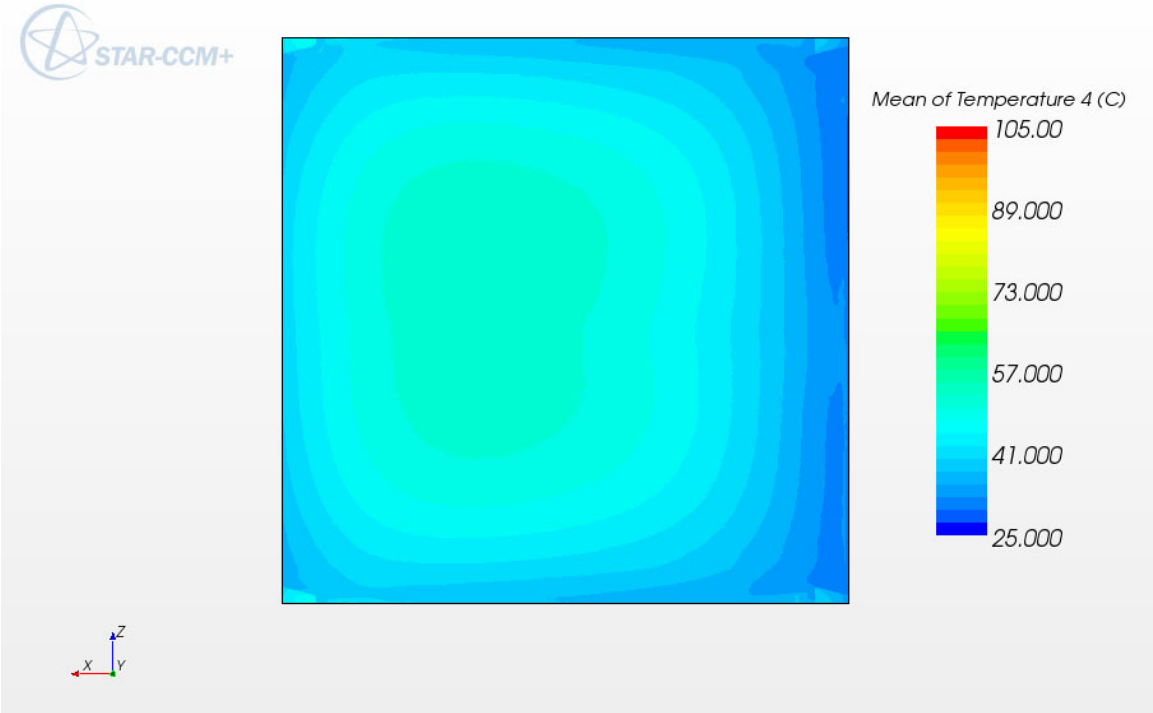

Plate 7 bottom

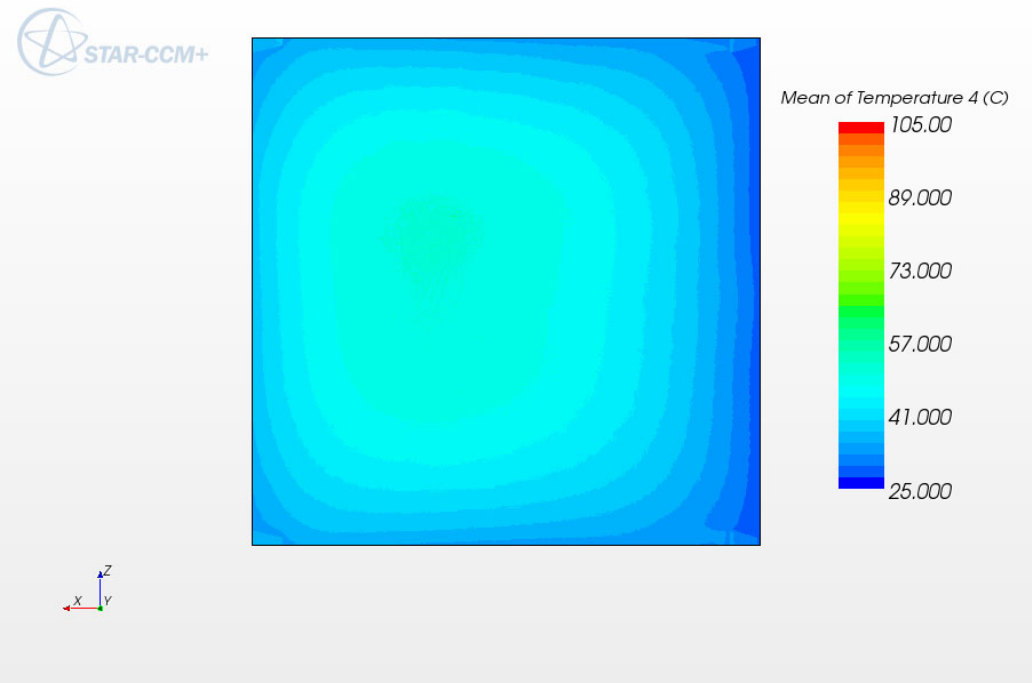

Temperature distribution at tungsten plate centerline

Plate 1

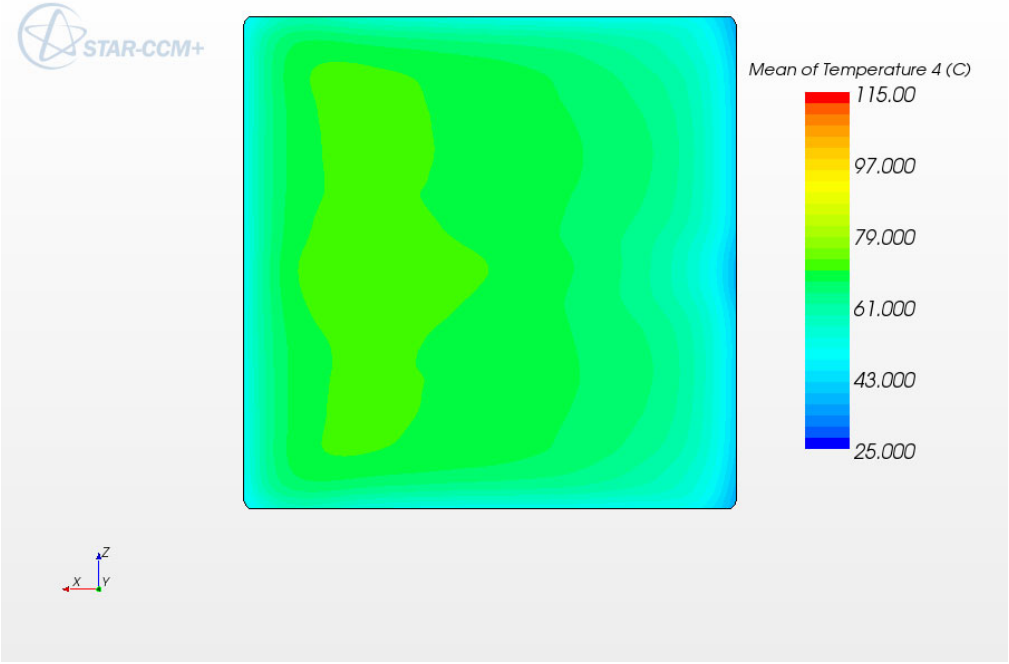

Plate 2

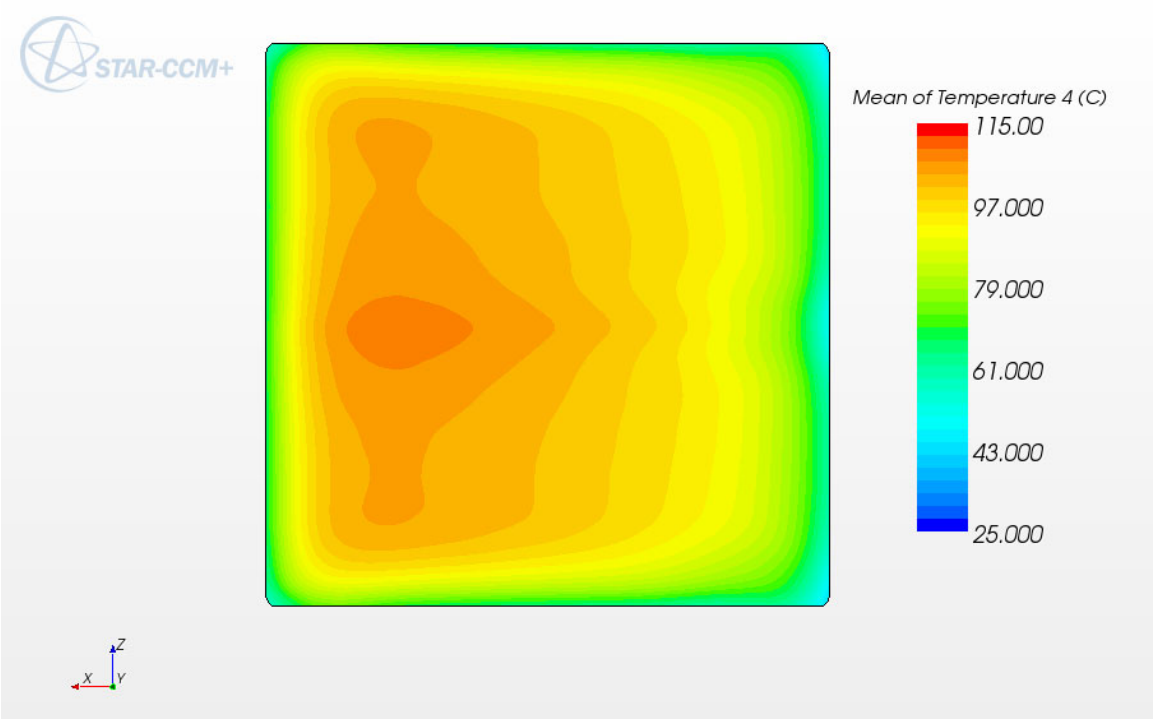

Plate 3

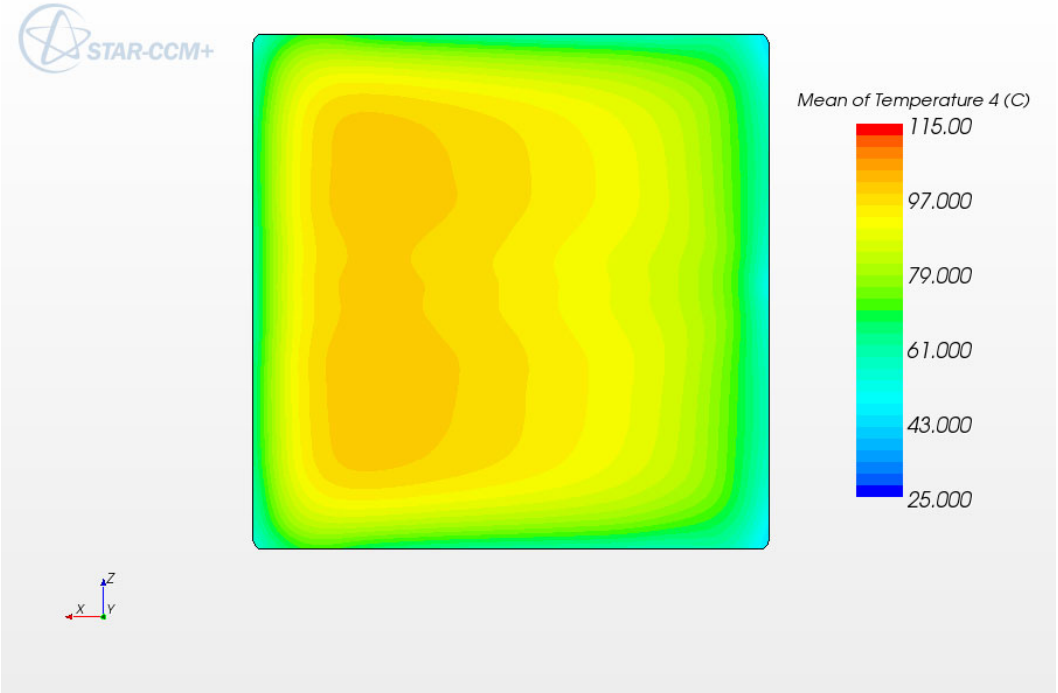

Plate 4

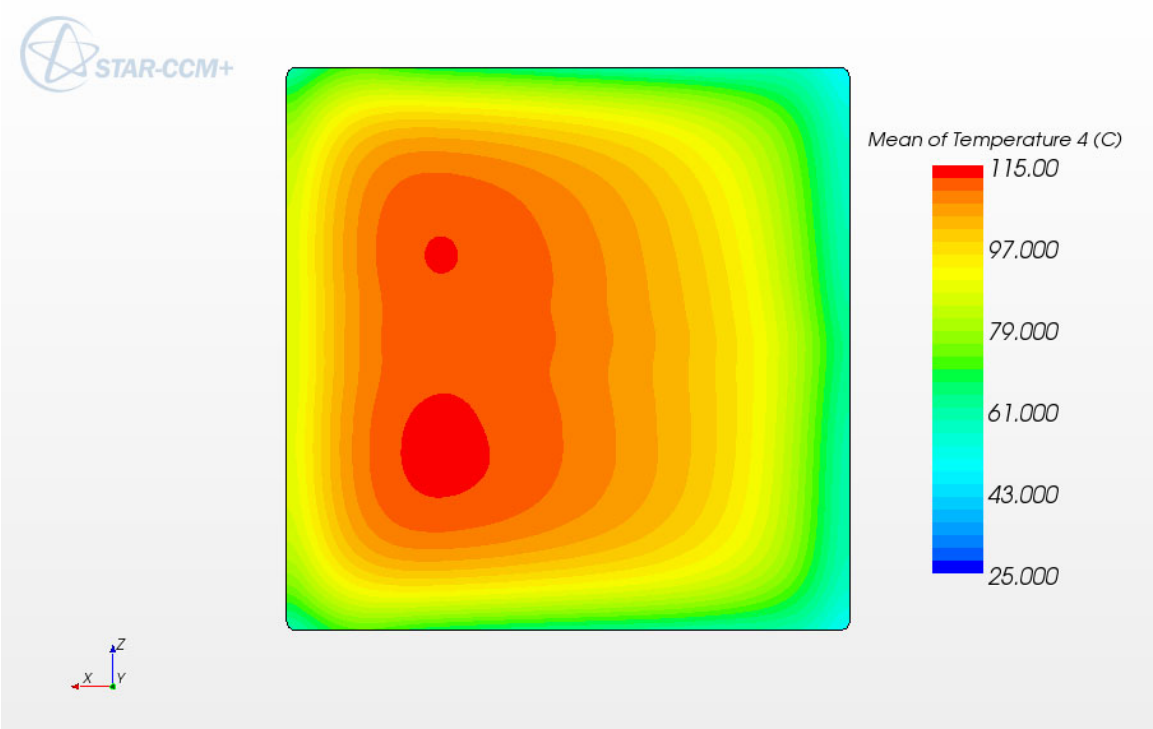

Plate 5

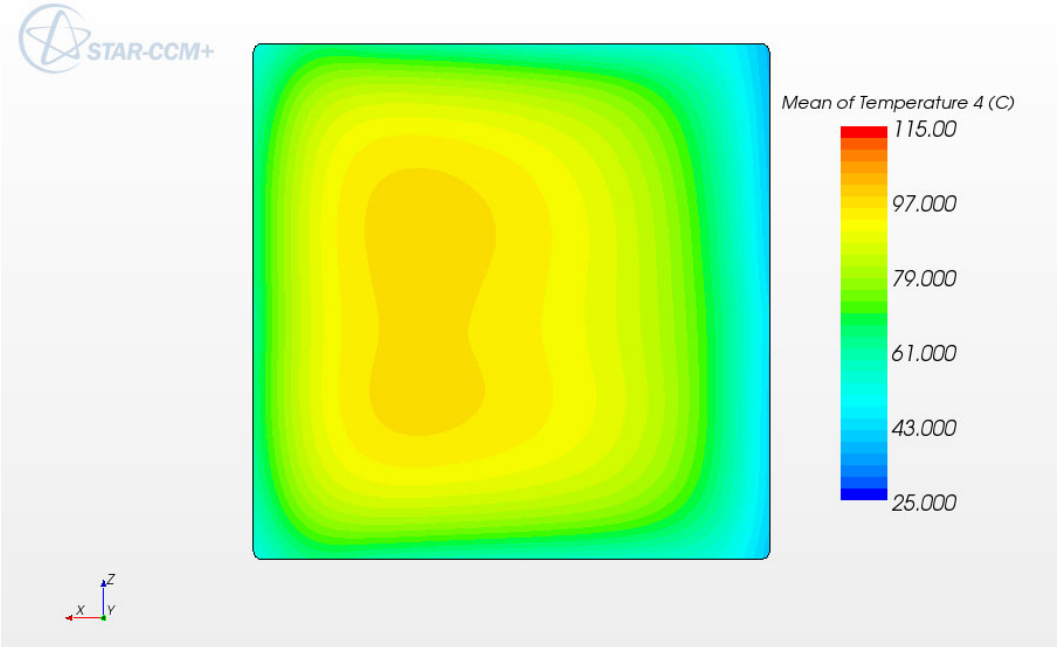

Plate 6

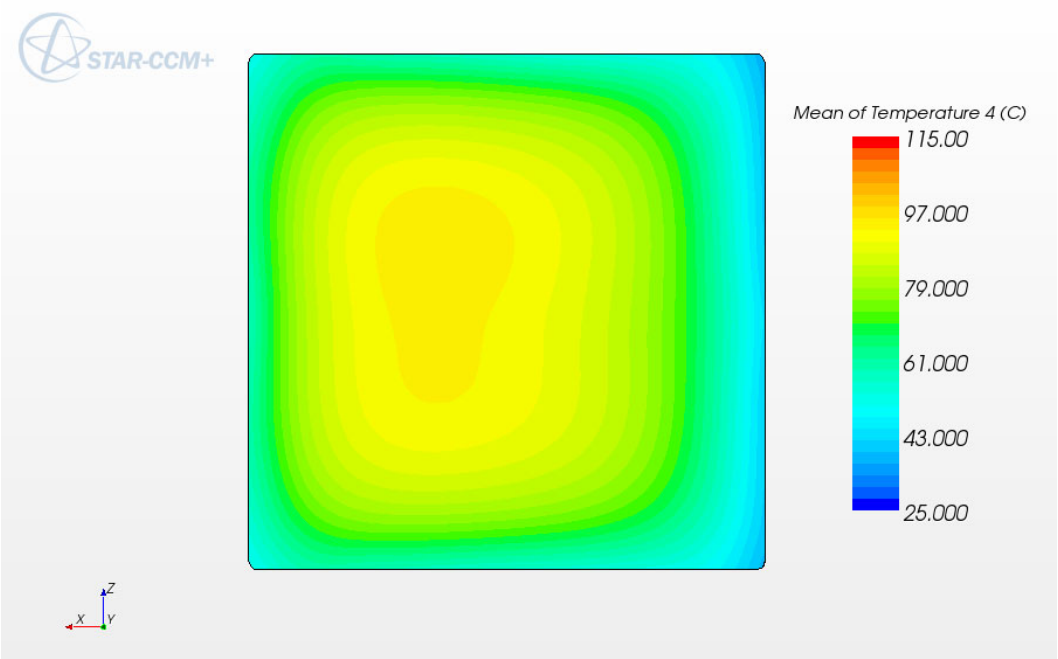

Plate 7

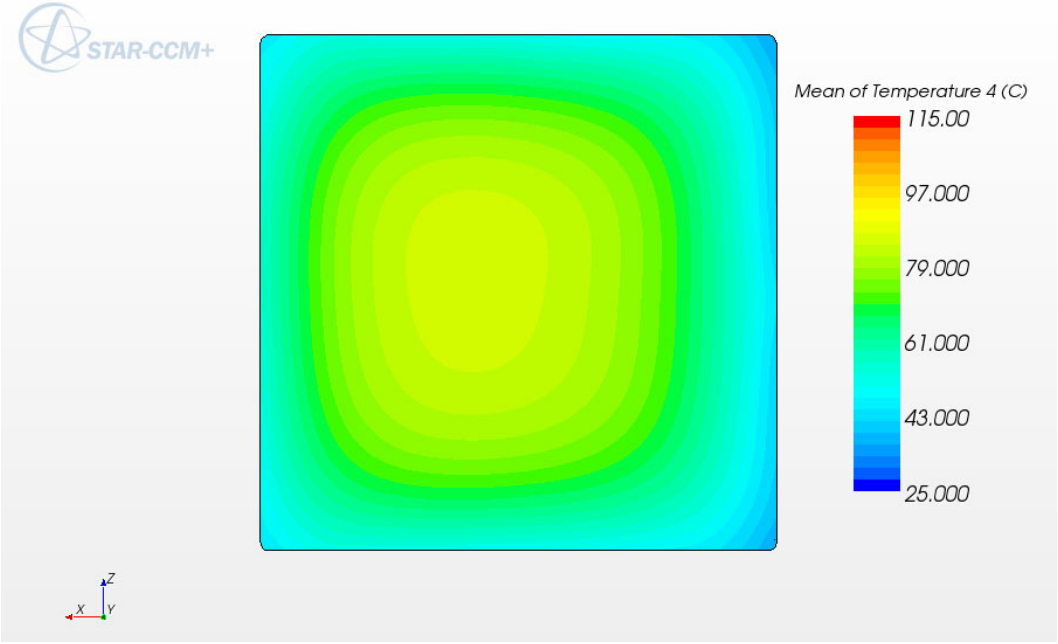

Figure II.3.6.2.6. Detailed distribution of the velocity magnitude and the temperature in the reference tungsten target.

II.3.6.3 Uranium Results

Similar methods and approaches were used for the uranium target. Again, results were largely like those from prior simulations. Many areas of the velocity field were like the tungsten case, as the only major structural difference is the larger target length needed to accommodate more plates.

Figure II.3.6.3.1 shows the power distribution throughout the domain and Fig. II.3.6.3.2 demonstrates the temperature in the plates. Figure 3.6.3.3 provides the detailed distributions of the velocity and the temperature at the channel center planes, the top and the bottom clad surfaces, and the plate center planes. These are all perpendicular to the electron beam direction. Note that in all figures, the +X-direction is the primary direction of flow through the target channels. Some conclusions can be drawn from these results:

- The velocity and the temperature distributions are generally similar in shape to those of the tungsten target. The peak temperatures of the plate and the fluid are higher throughout, while the velocity magnitudes in the channels are lower (same mass flow rate, more power to remove, more water channels than the tungsten target).
- The second plate with the peak power has the peak temperature. The power deposition of the plate cooled by the primary and secondary streams, plate 6 as shown in Fig. II.3.6.3.1, is much lower than corresponding plate of the tungsten target, plate 4 in Fig. II.3.6.2.1.
- The flow split was confirmed at 57.1%, within the range of that used in the optimization analyses.
- The total mass flow rate was confirmed at 4.79 kg/s. The total pressure drop across the entire target apparatus is 137.68 kPa. Subtracting this from the inlet pressure and accounting for gravity head yields a new estimate of 2.20 bar for the target region pressure. The corresponding saturation temperature is 123 °C.
- The water inlet temperature is 25 °C and the outlet temperature is 29.54 °C.
- The peak clad temperature is 112 °C, which is roughly 3 °C lower than previously calculated.
- The peak uranium temperature is 166 °C, which is roughly 13 °C higher than previously calculated.
- Both peak temperatures are well below the melting point for uranium (1132 °C) and even aluminum (600 °C).
- The Bergles-Rohsenow correlation yielded a necessary superheat of 21 °C to occur for this configuration. With T_{sat} of 123 °C, a wall temperature of 144 °C would be needed for subcooled boiling. Since peak wall temperature is 112 °C, the total margin to subcooled boiling is 144 °C - 112 °C = 32 °C. There is also a margin to nucleate boiling of 123 °C - 112 °C = 11 °C.

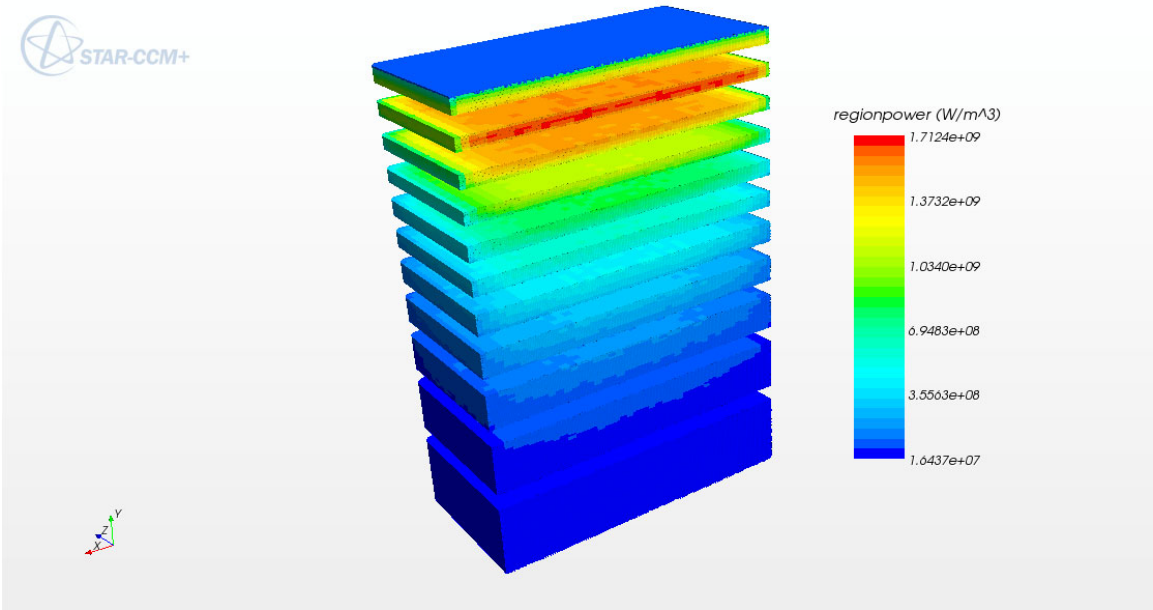

Figure II.3.6.3.1. Power distribution in the uranium plates (W/m^3).

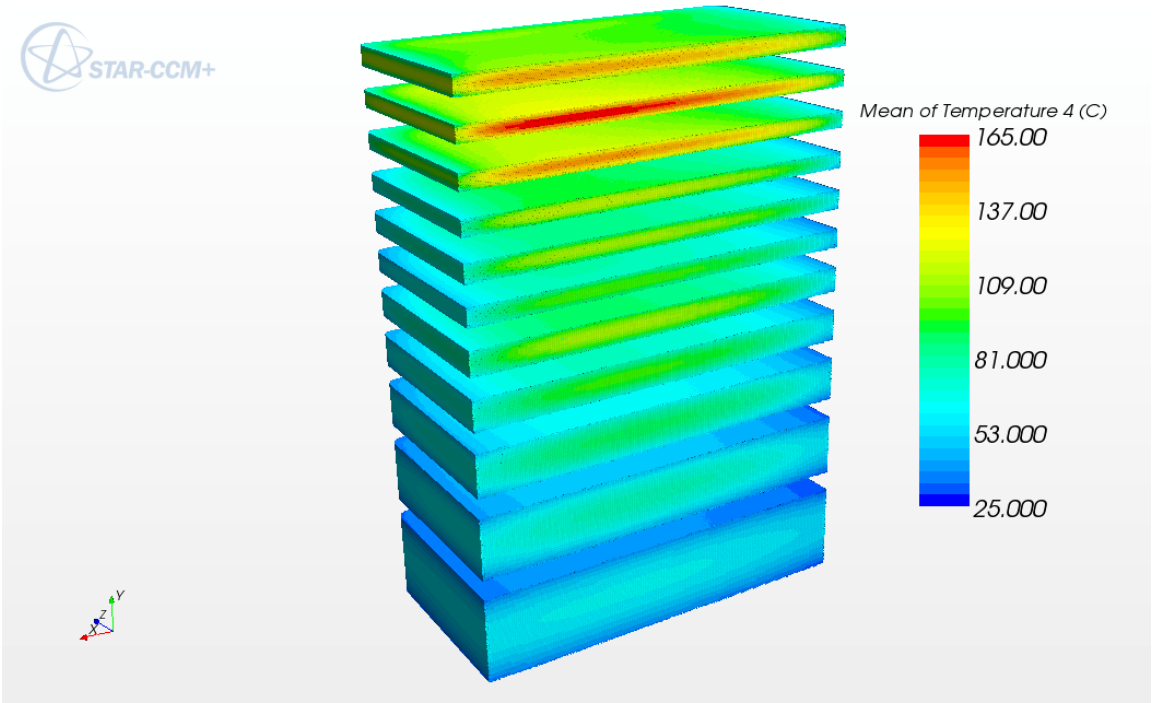

Figure II.3.6.3.2. Temperature distribution in the uranium plates (°C).

Velocity magnitude in the channel mid-section

Channel before Plate 1

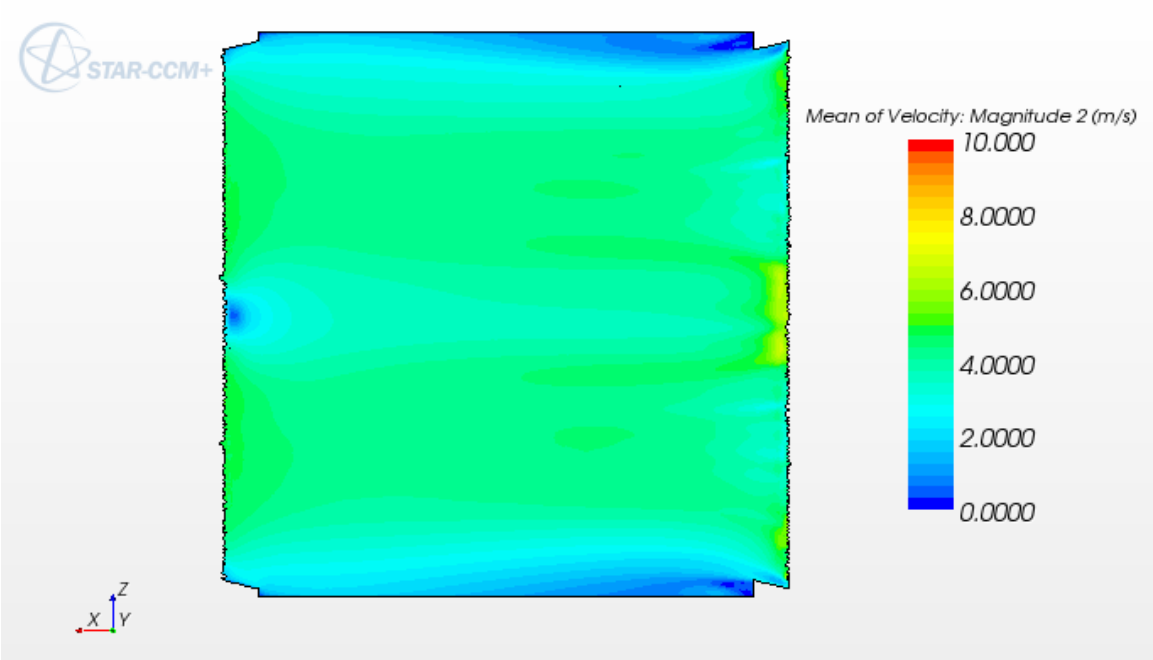

Channel between Plate 1 and Plate 2

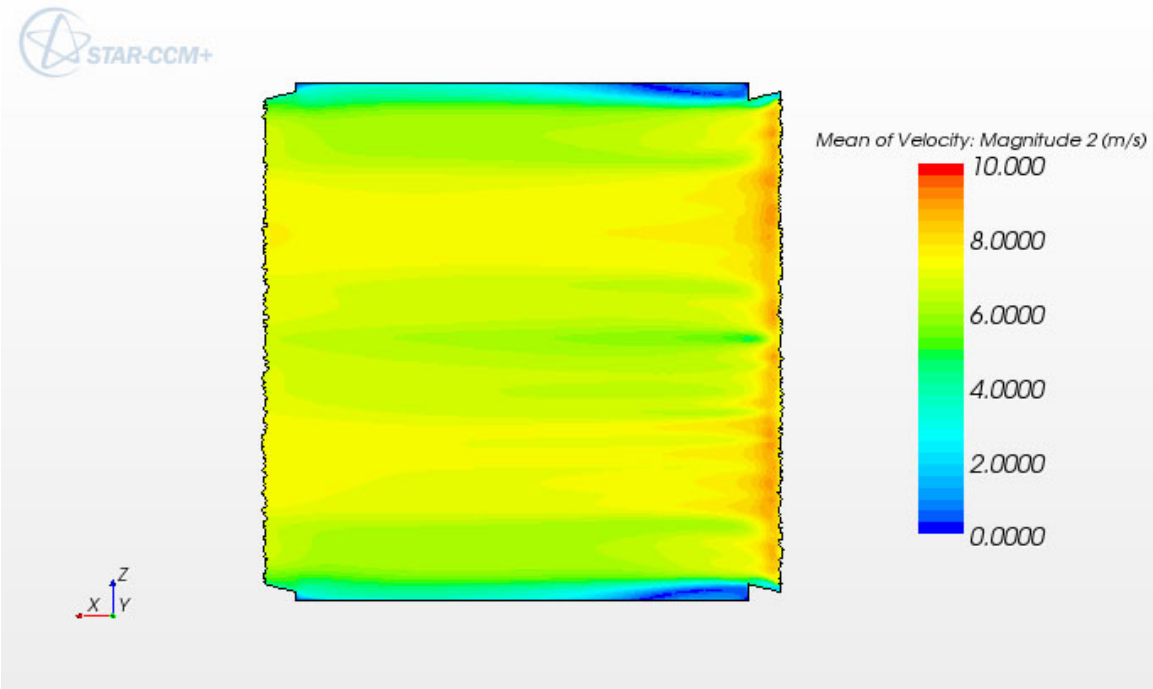

Channel between Plate 2 and Plate 3

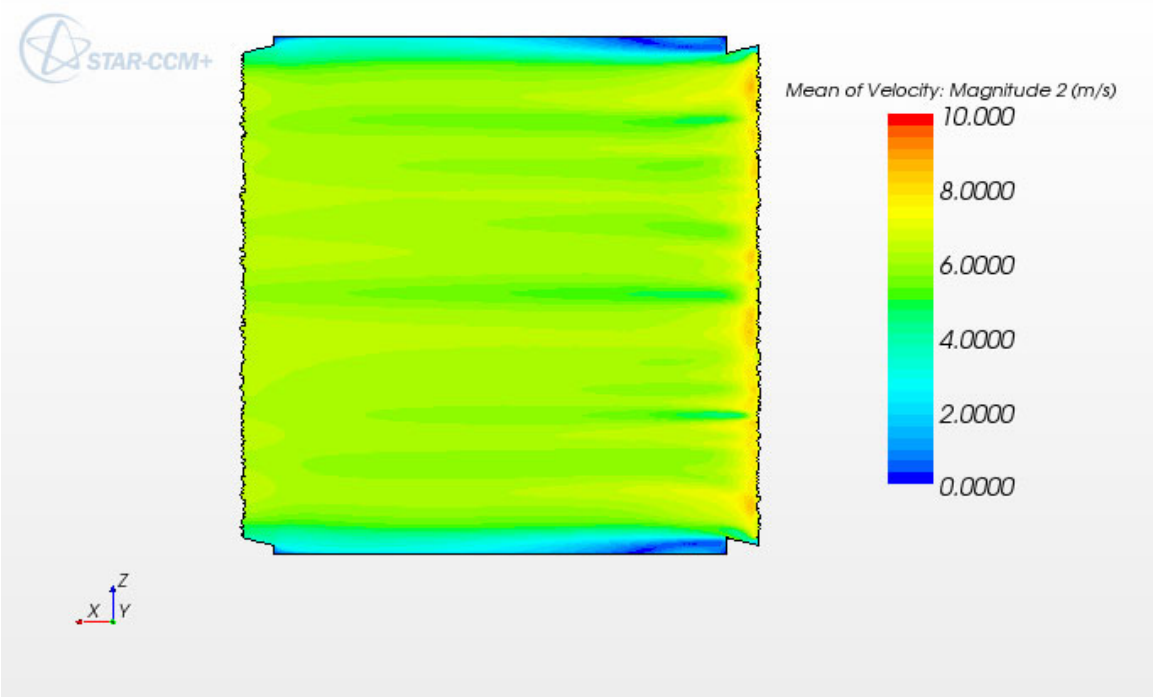

Channel between Plate 3 and Plate 4

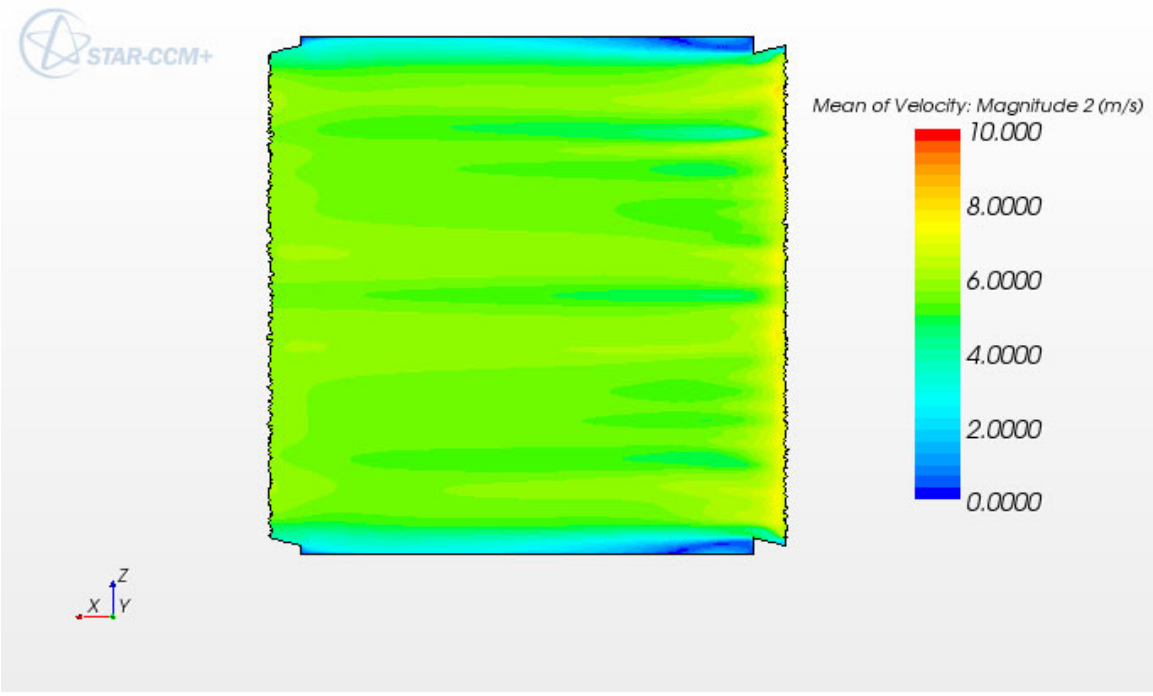

Channel between Plate 4 and Plate 5

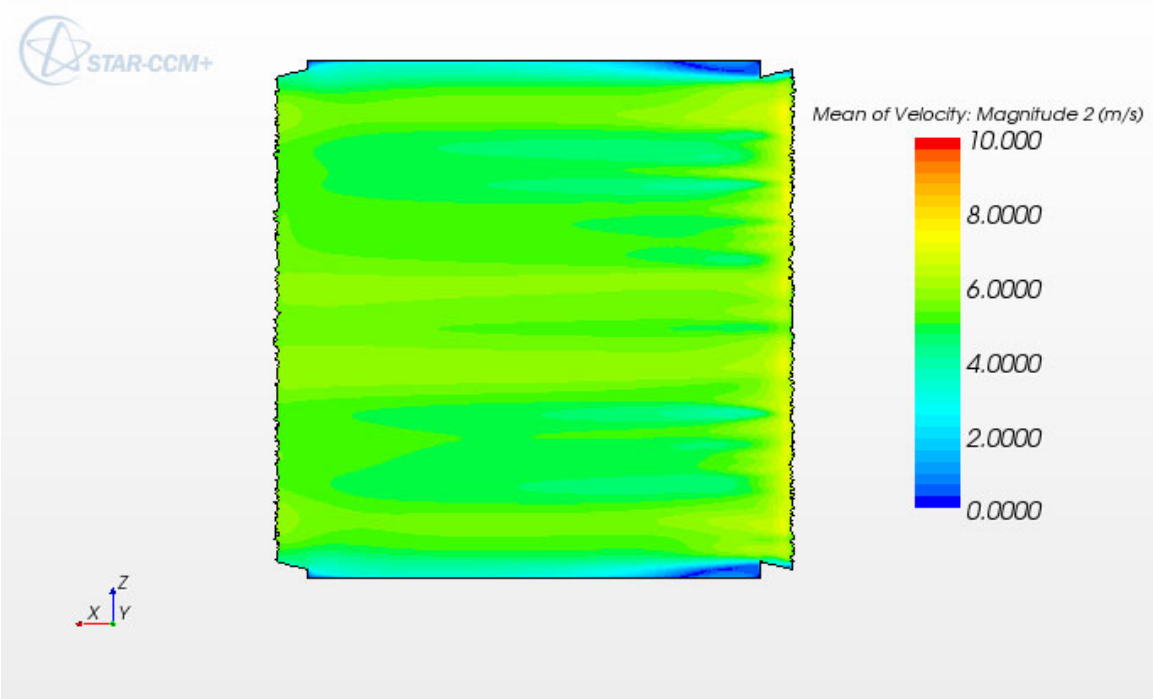

Channel between Plate 5 and Plate 6

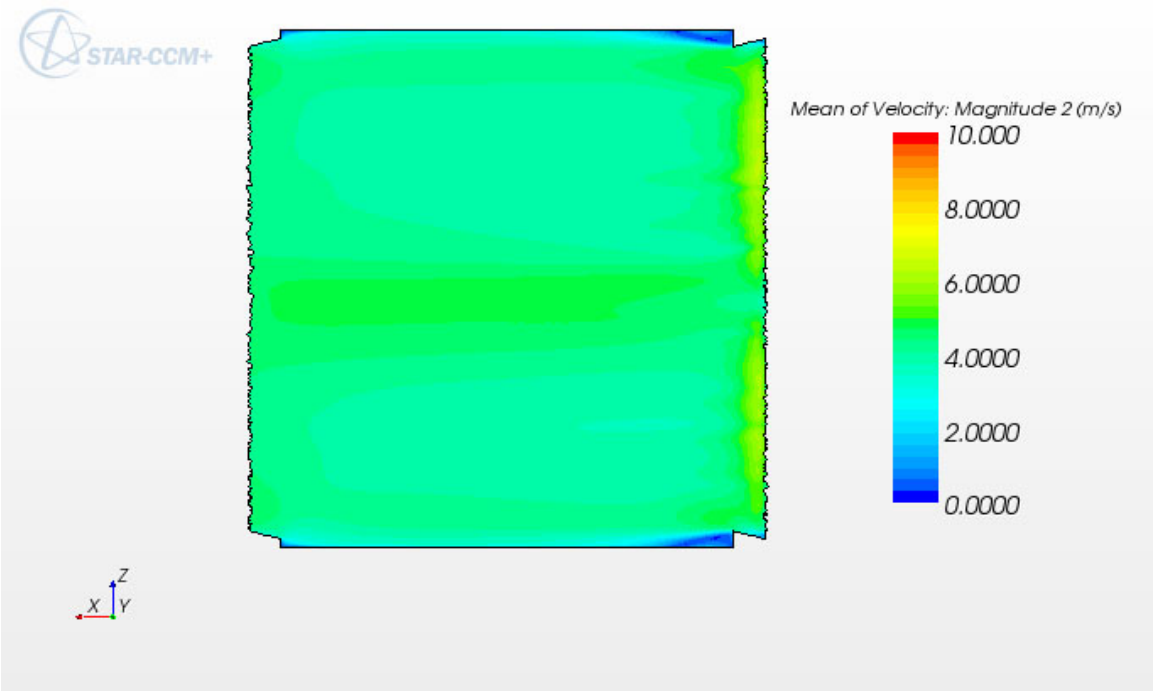

Channel between Plate 6 and Plate 7

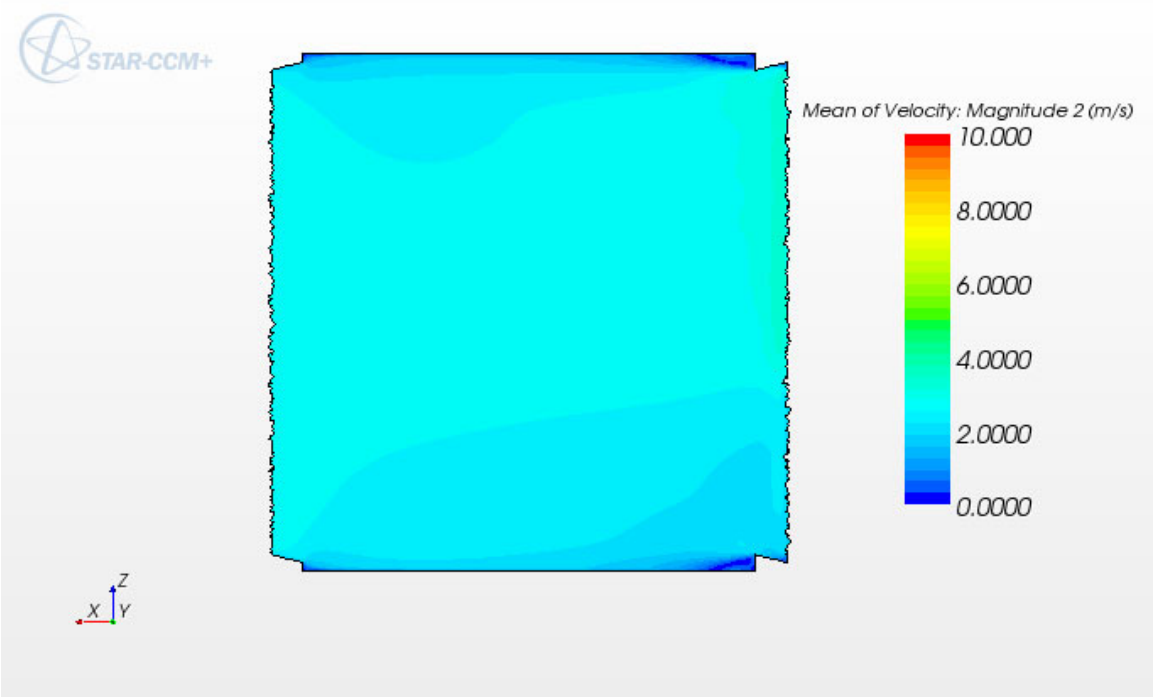

Channel between Plate 7 and Plate 8

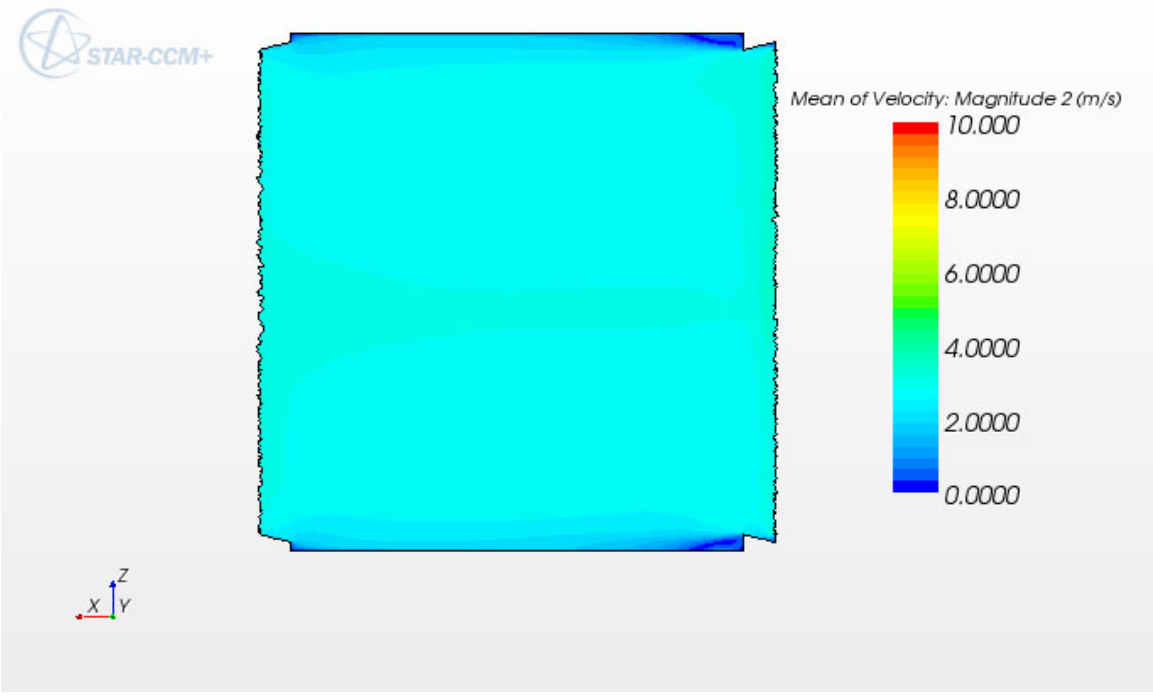

Channel between Plate 8 and Plate 9

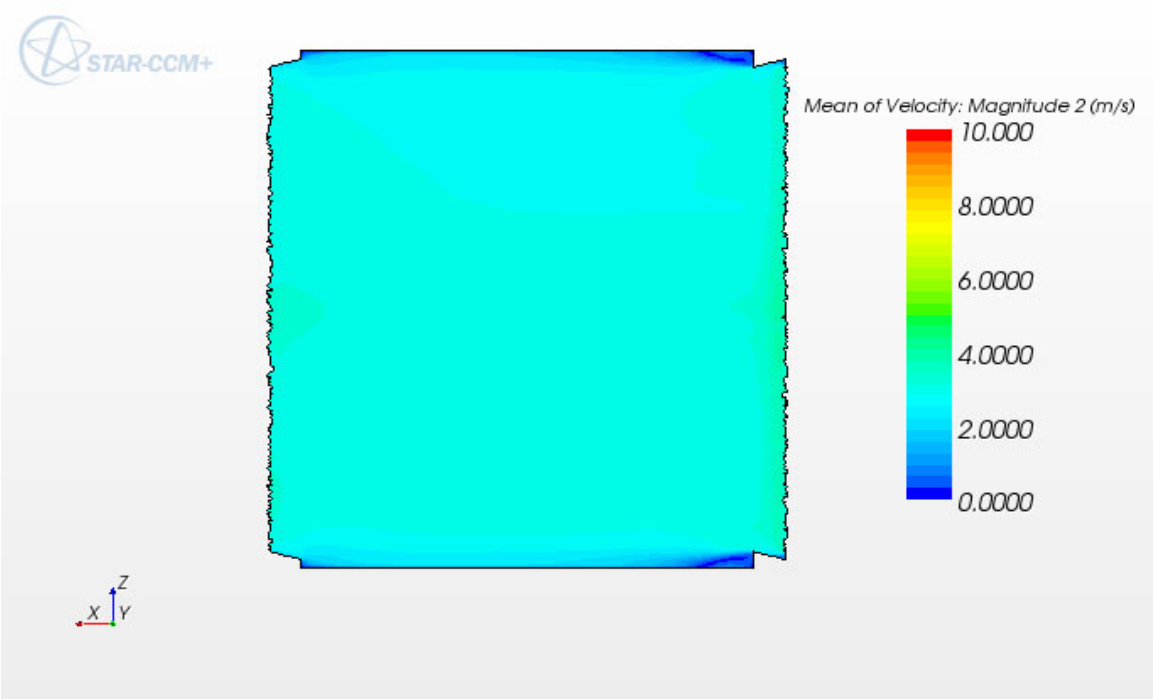

Channel between Plate 9 and Plate 10

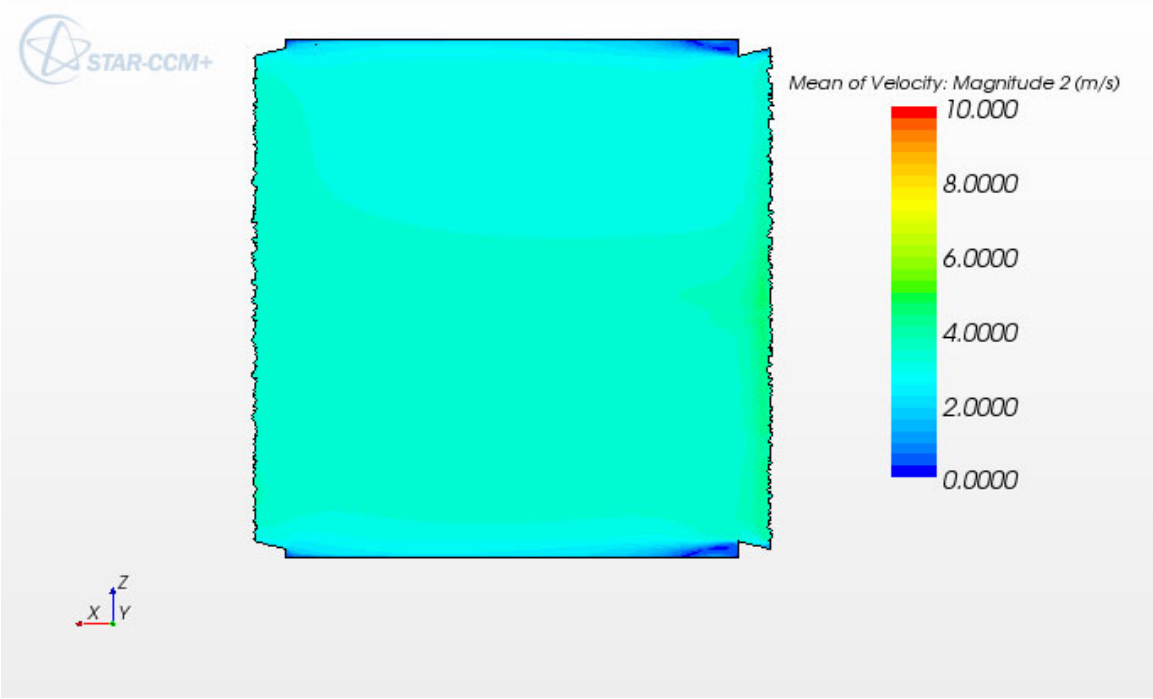

Channel between Plate 10 and Plate 11

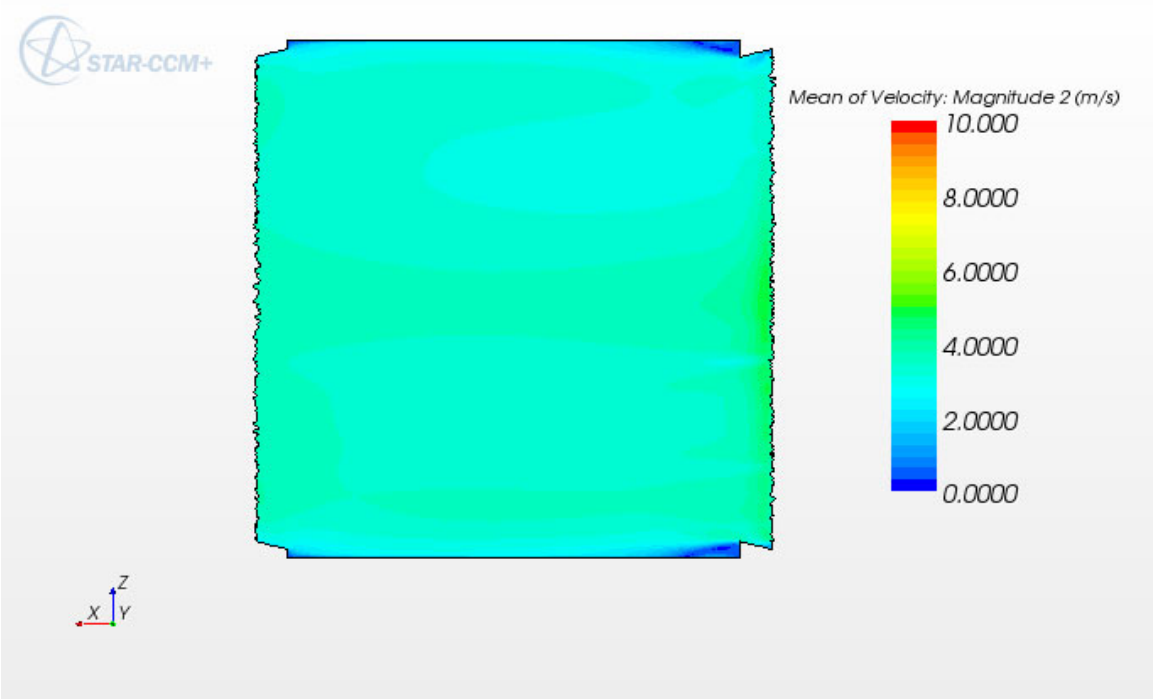

Channel after Plate 11

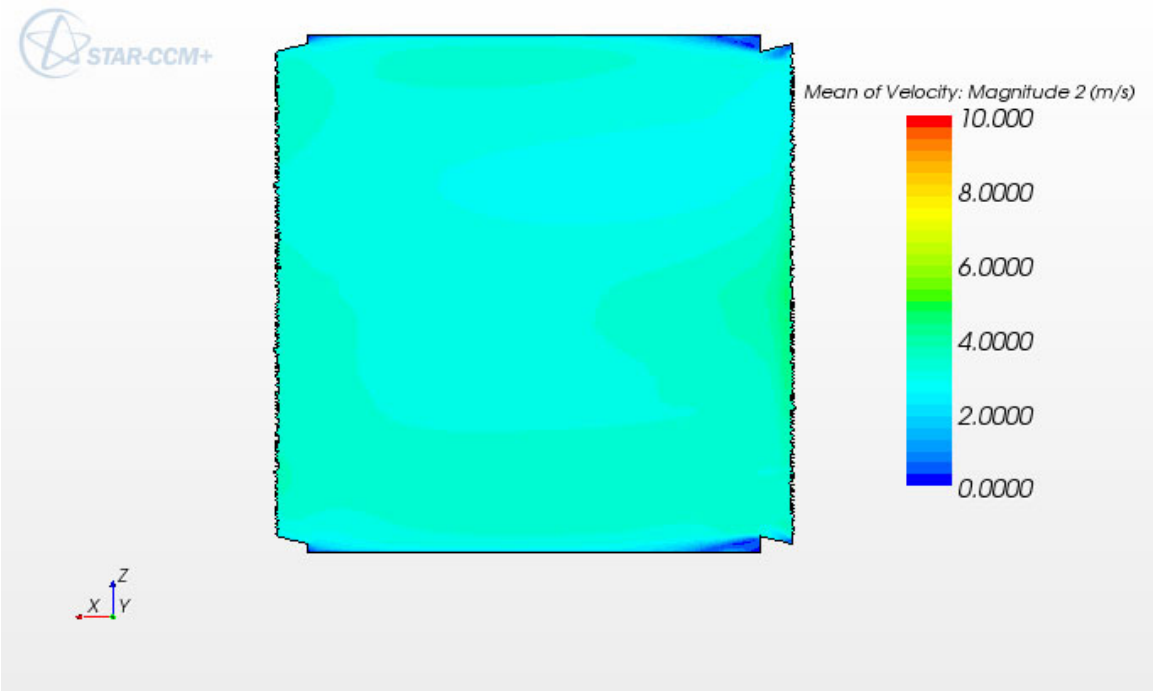

Temperature distribution in channel mid-section

Channel before Plate 1

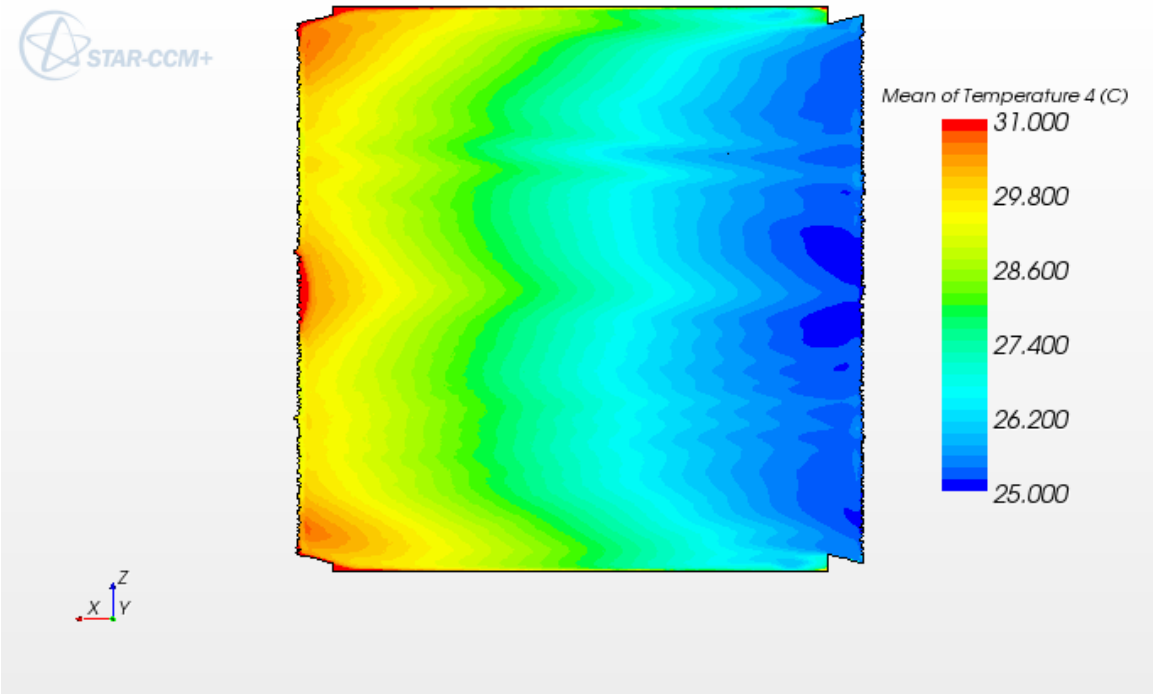

Channel between Plate 1 and Plate 2

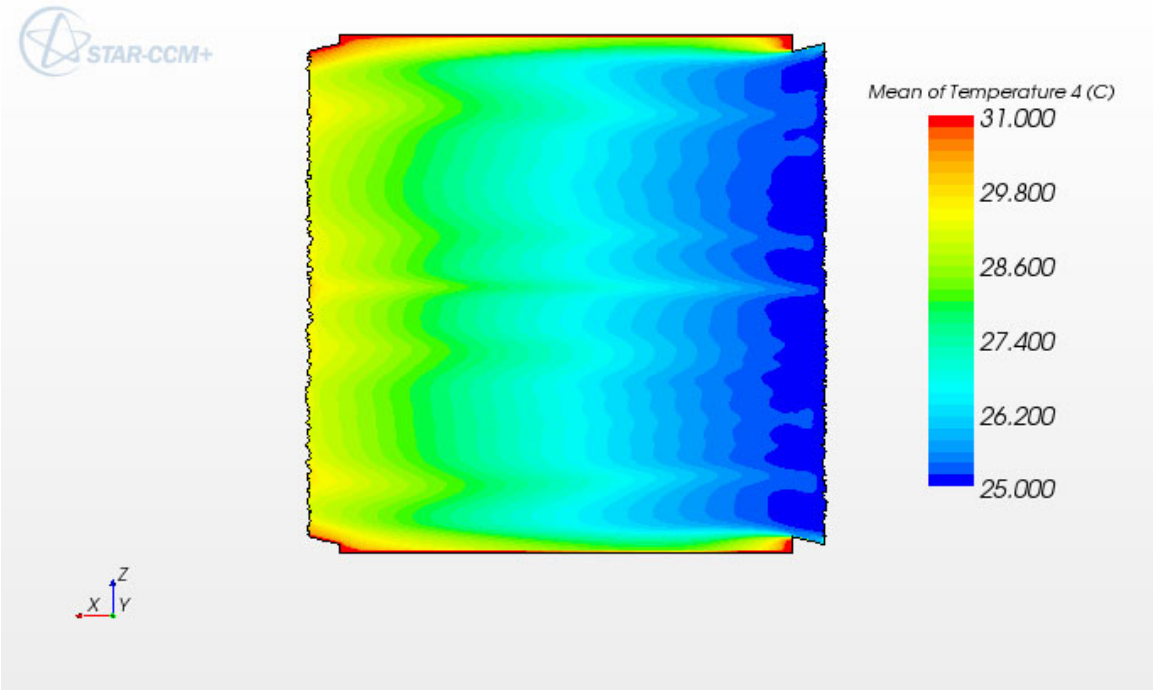

Channel between Plate 2 and Plate 3

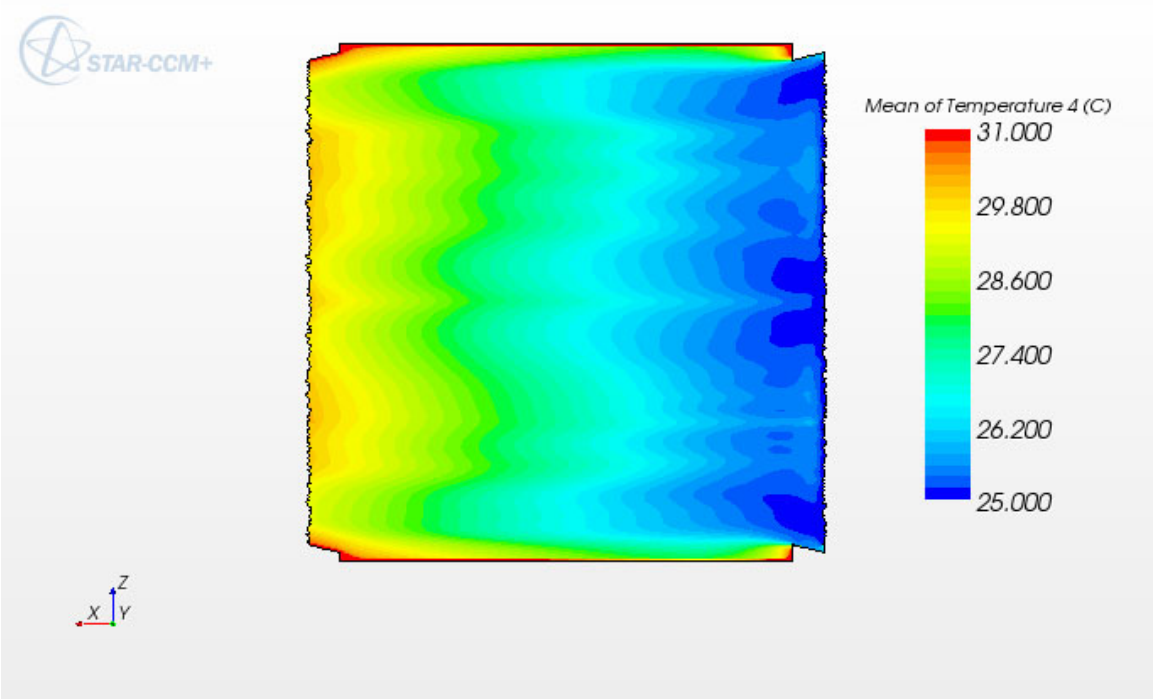

Channel between Plate 3 and Plate 4

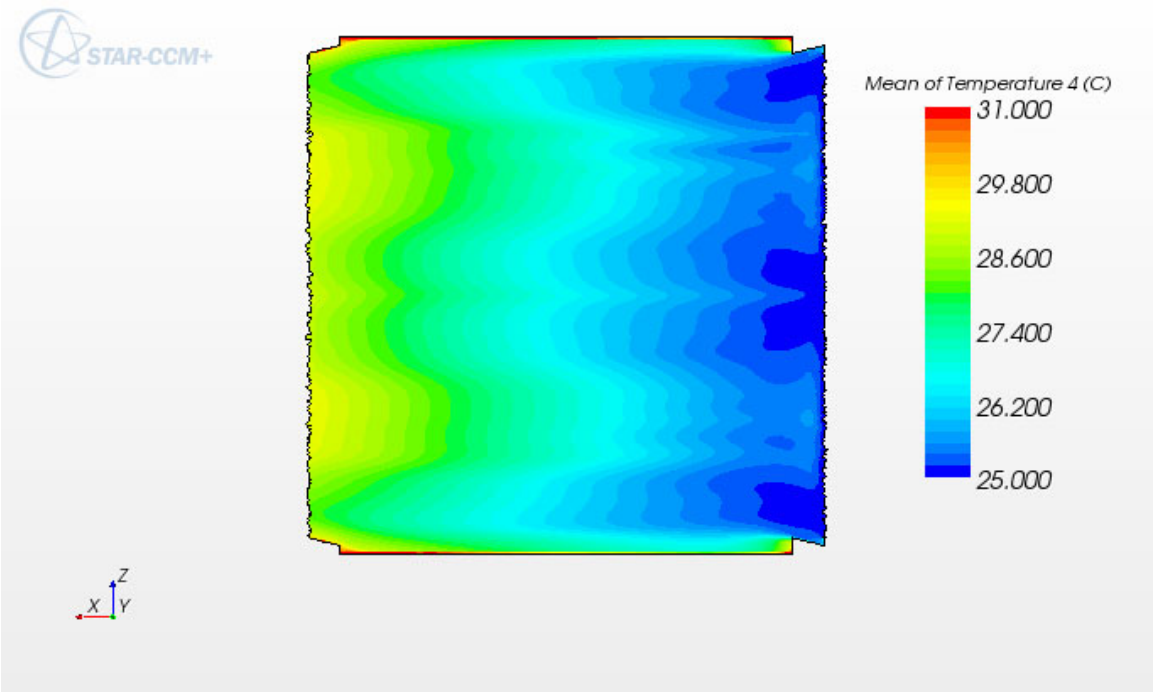

Channel between Plate 4 and Plate 5

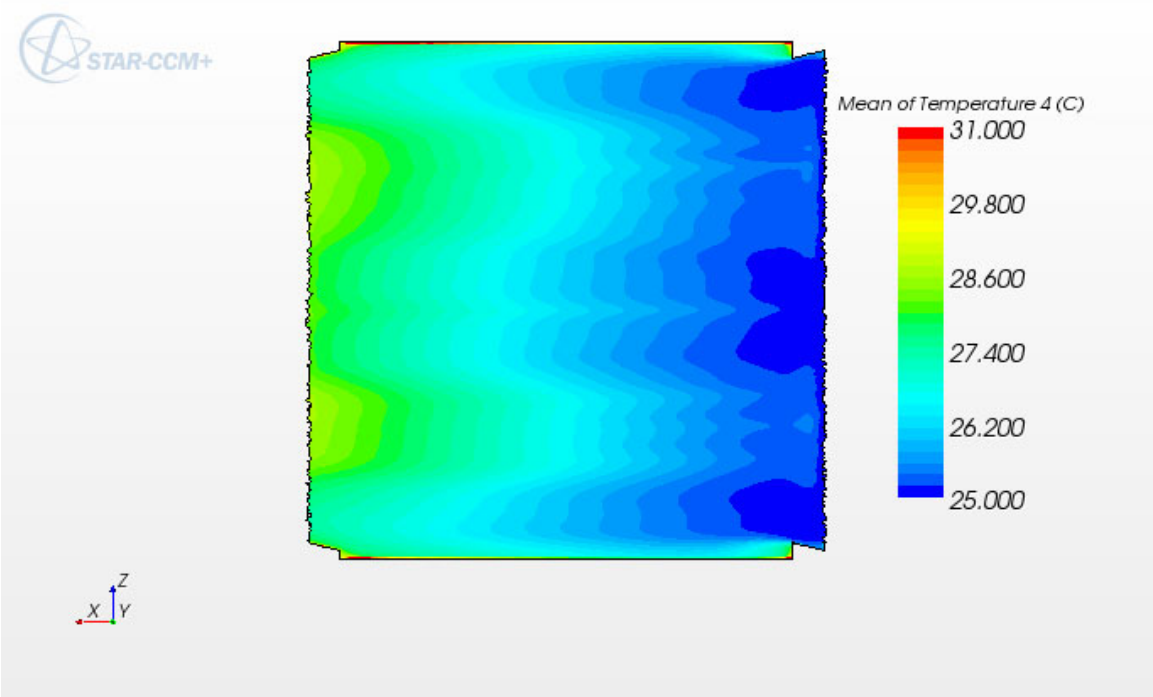

Channel between Plate 5 and Plate 6

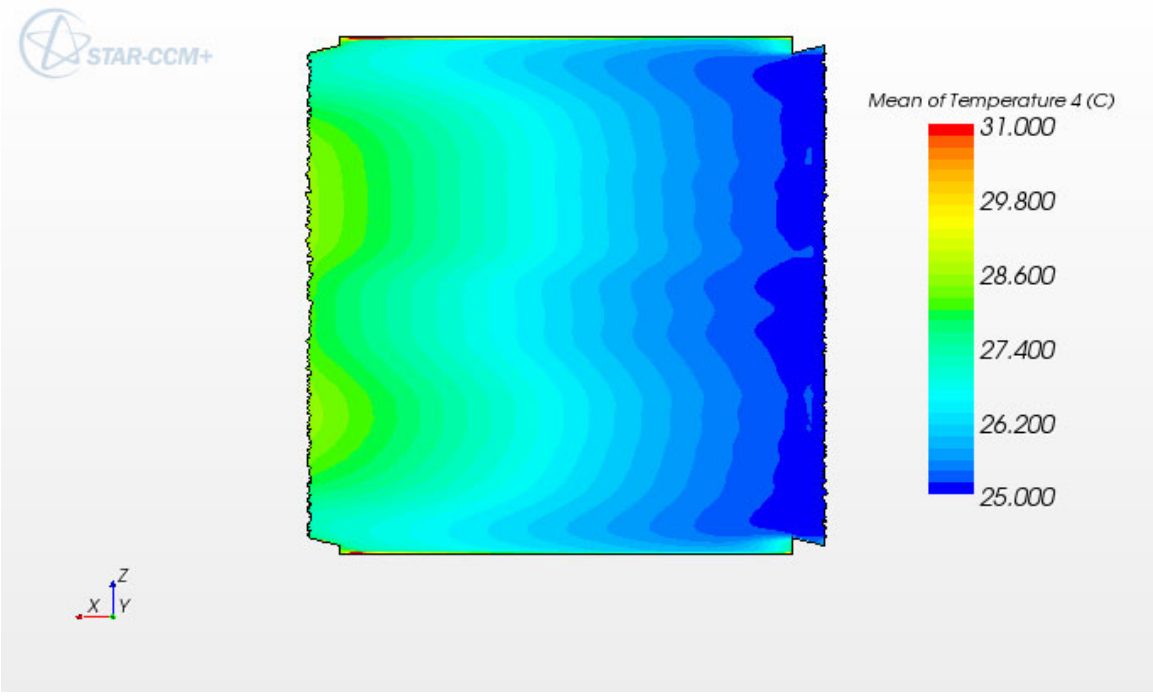

Channel between Plate 6 and Plate 7

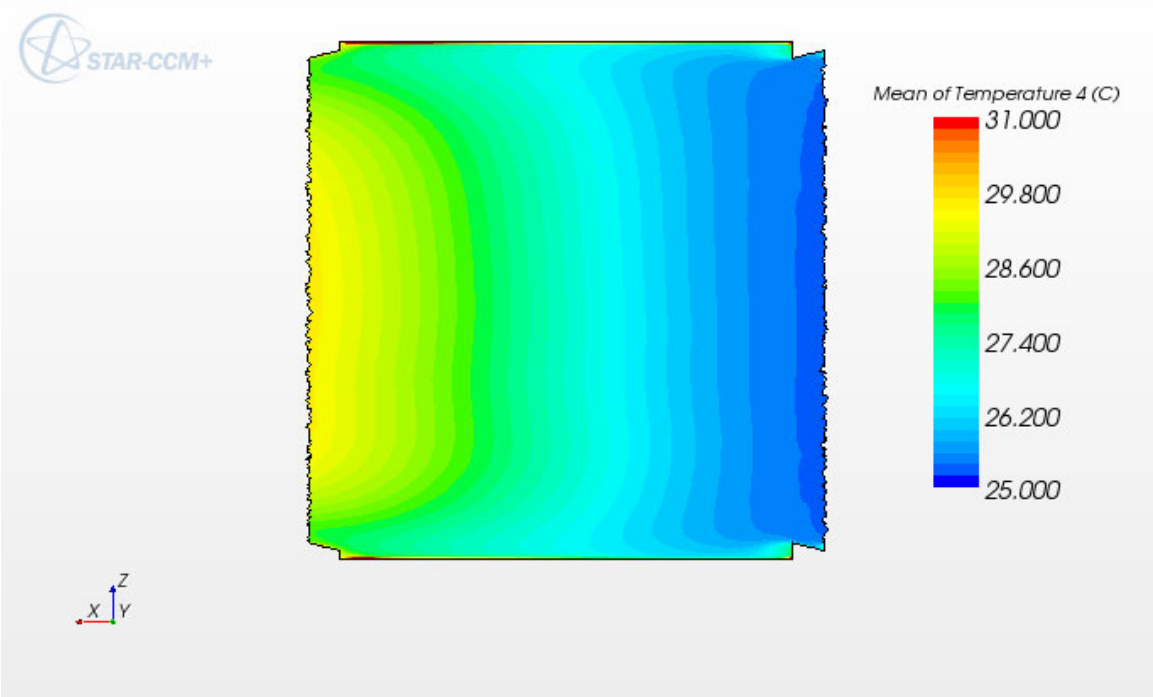

Channel between Plate 7 and Plate 8

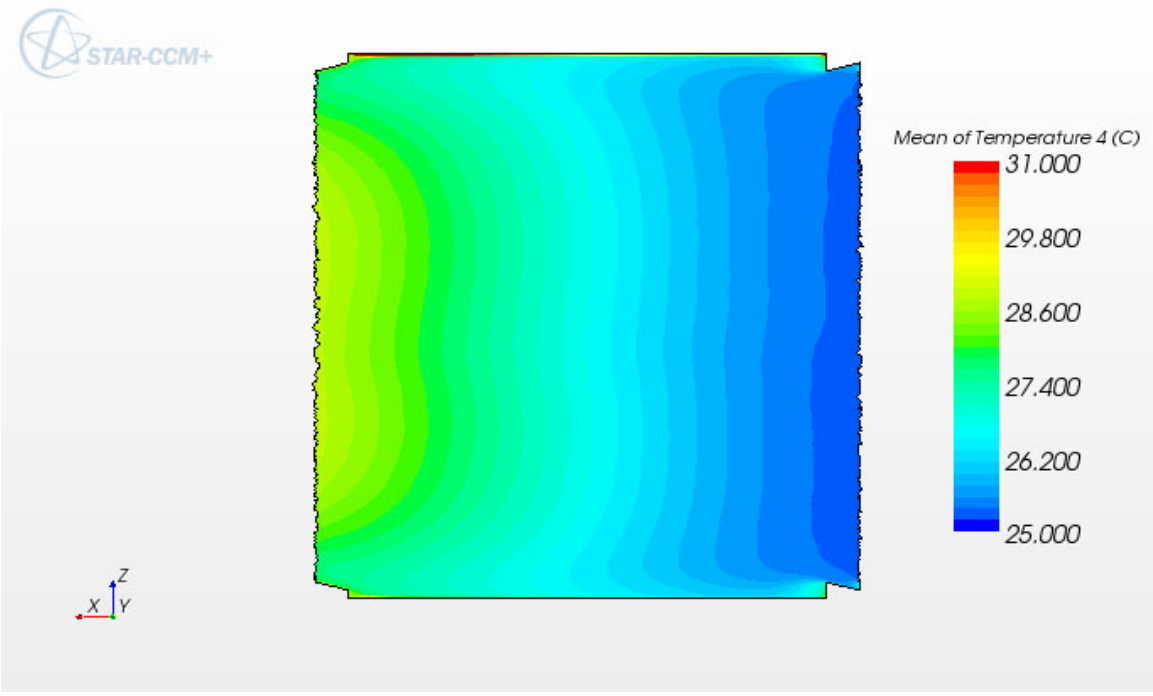

Channel between Plate 8 and Plate 9

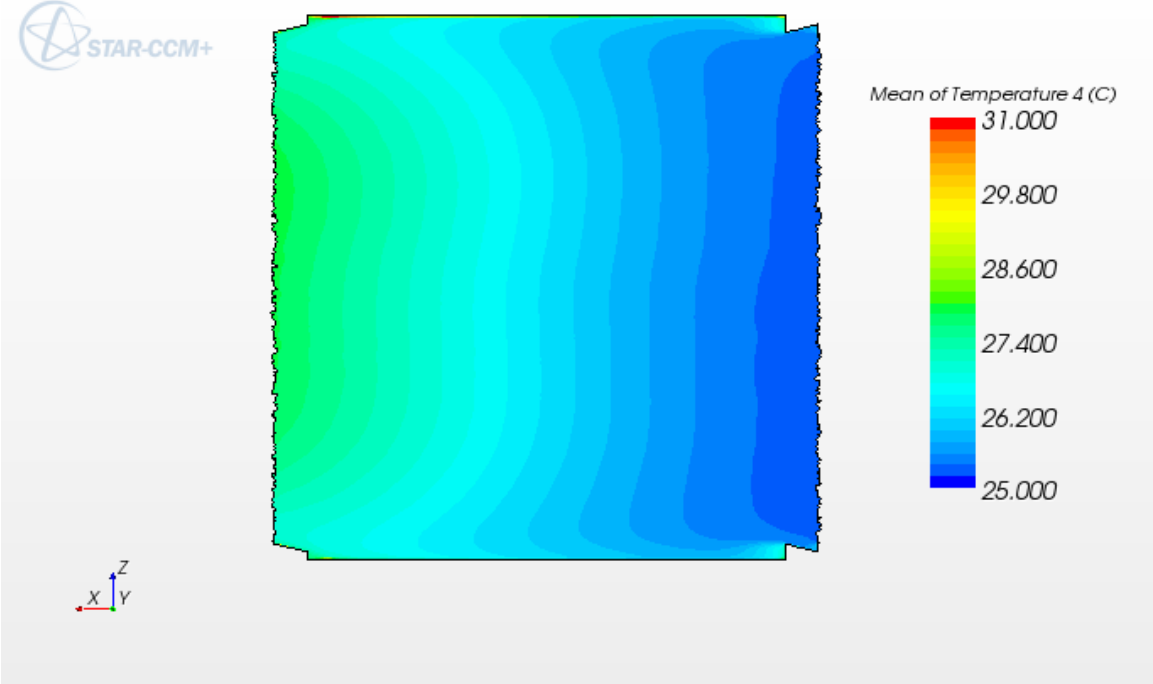

Channel between Plate 9 and Plate 10

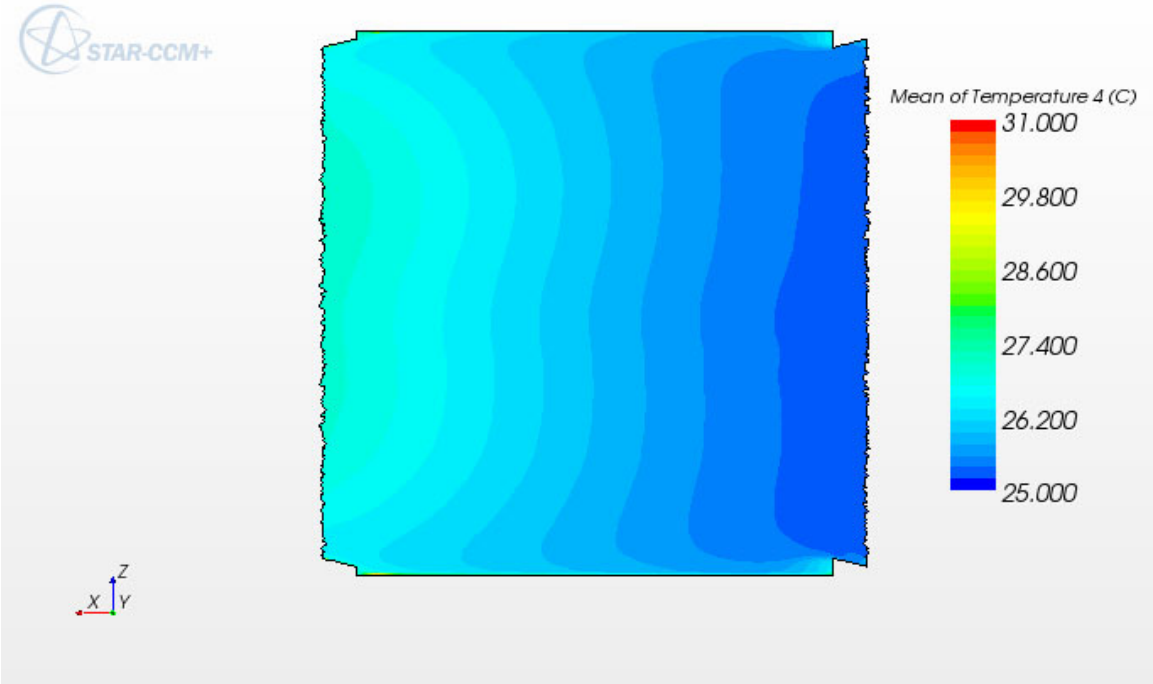

Channel between Plate 10 and Plate 11

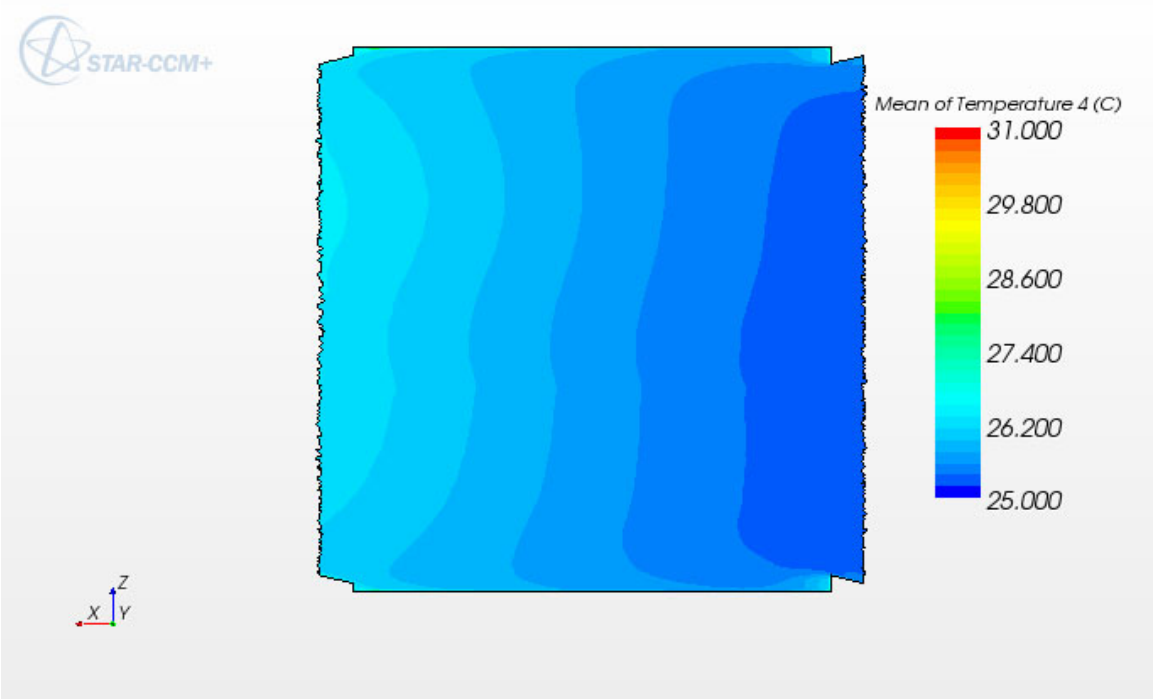

Channel after Plate 11

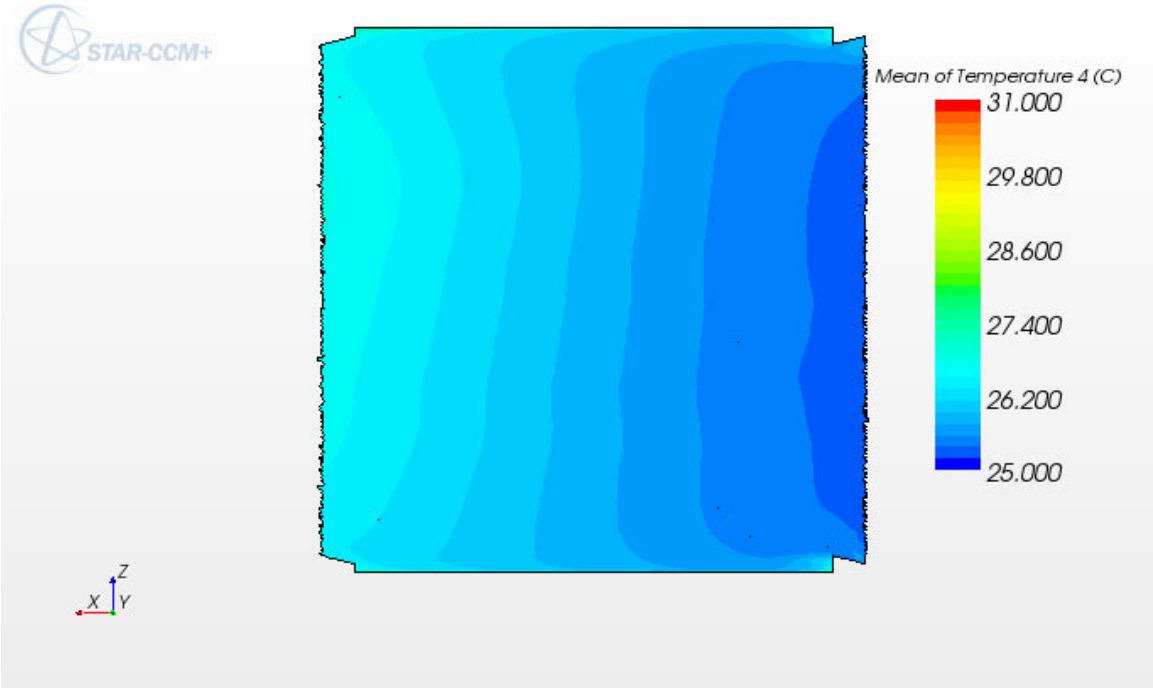

Temperature distribution on the cladding surface

Plate 1 top

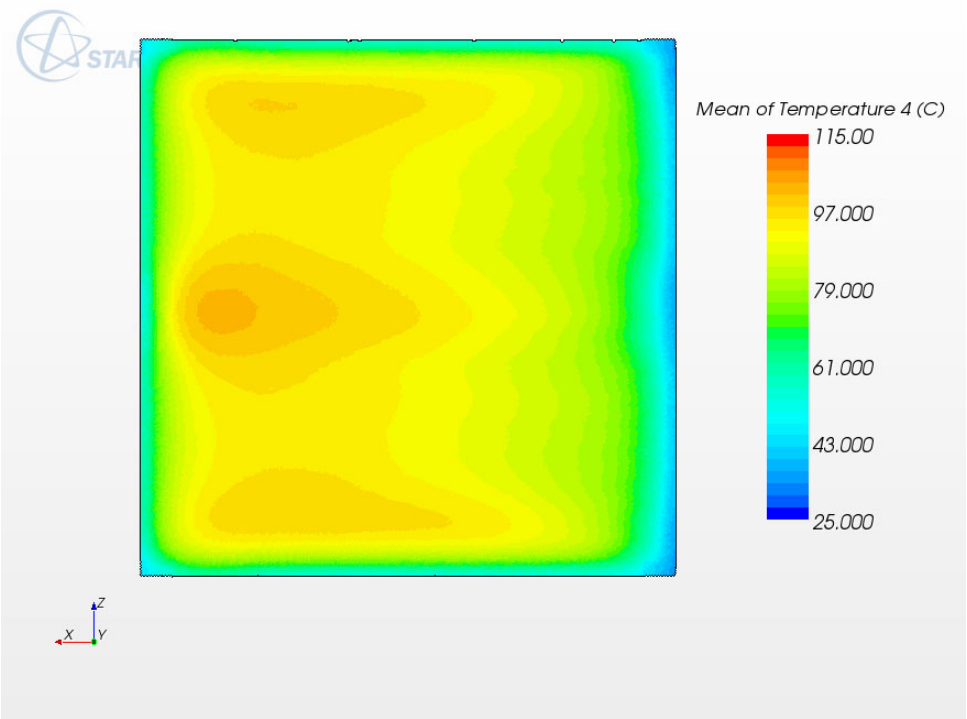

Plate 1 bottom

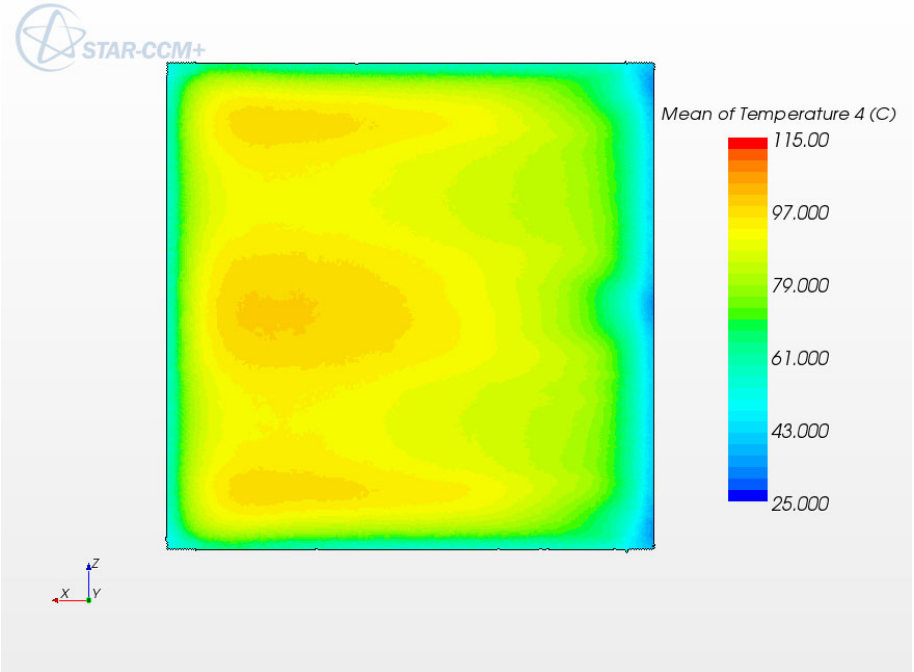

Plate 2 top

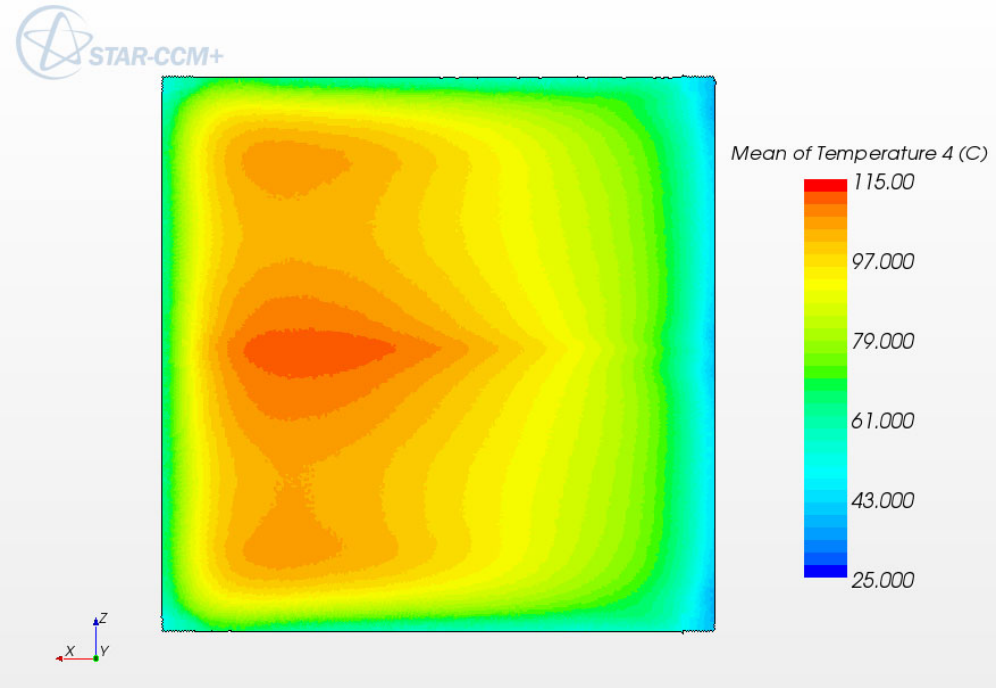

Plate 2 bottom

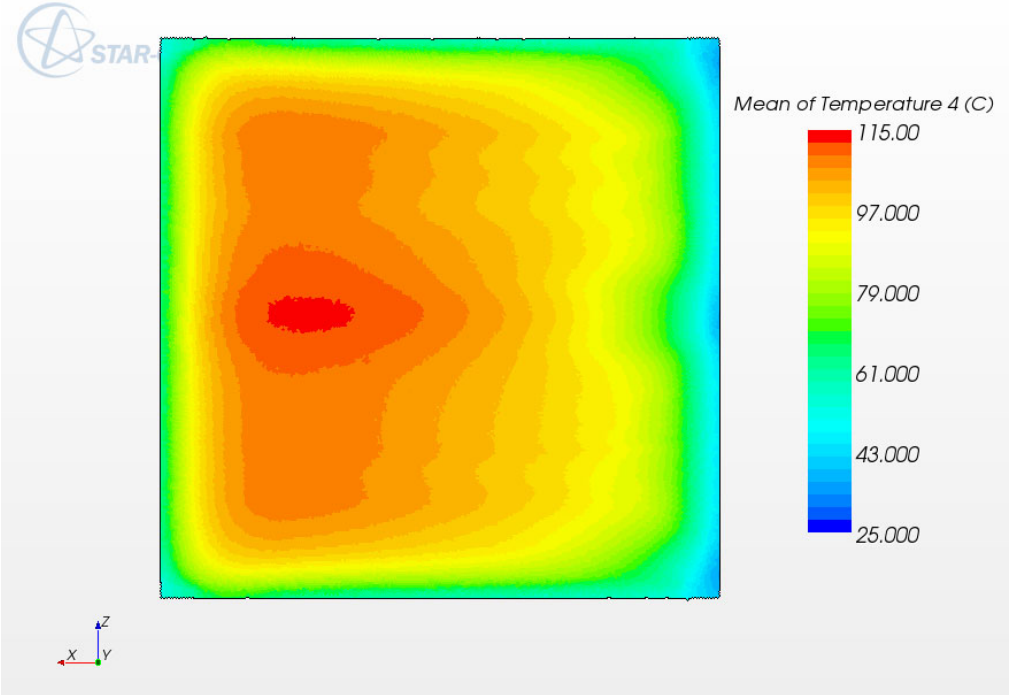

Plate 3 top

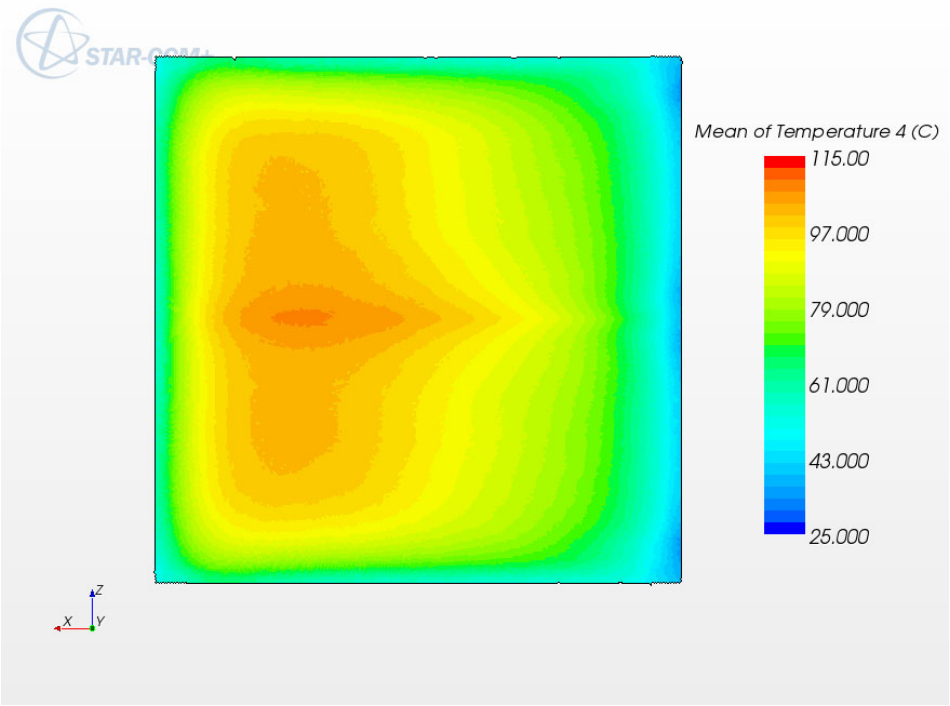

Plate 3 bottom

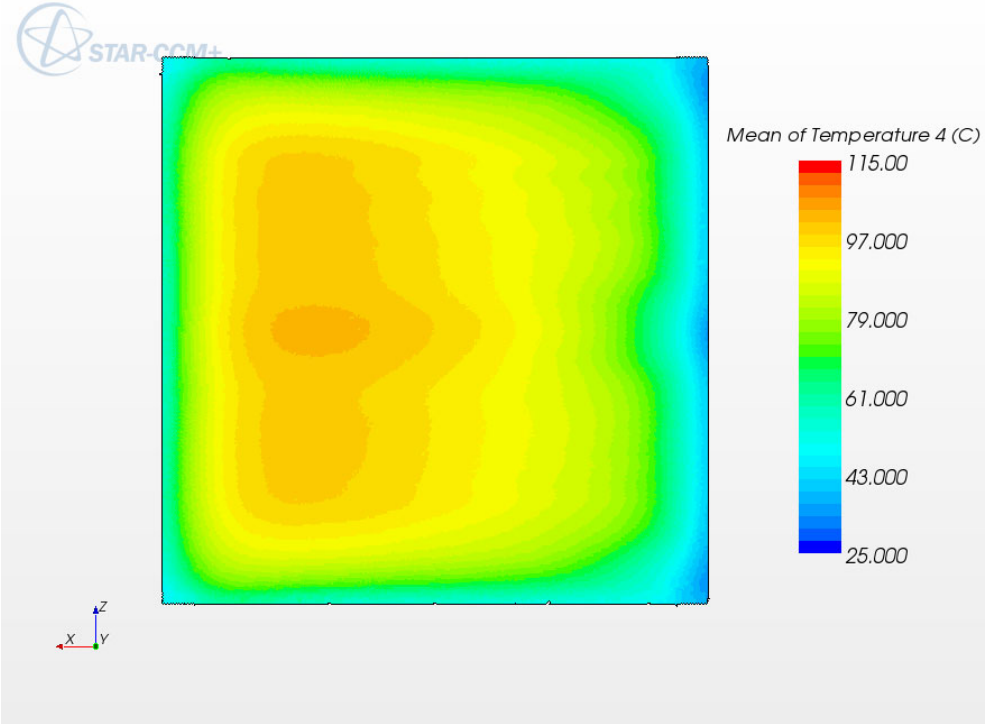

Plate 4 top

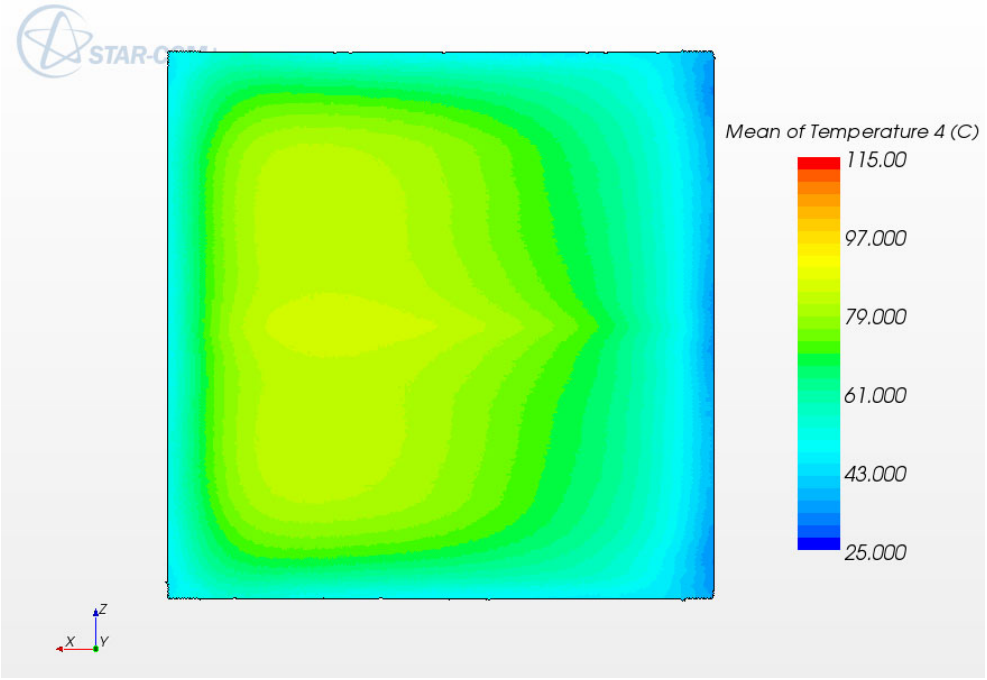

Plate 4 bottom

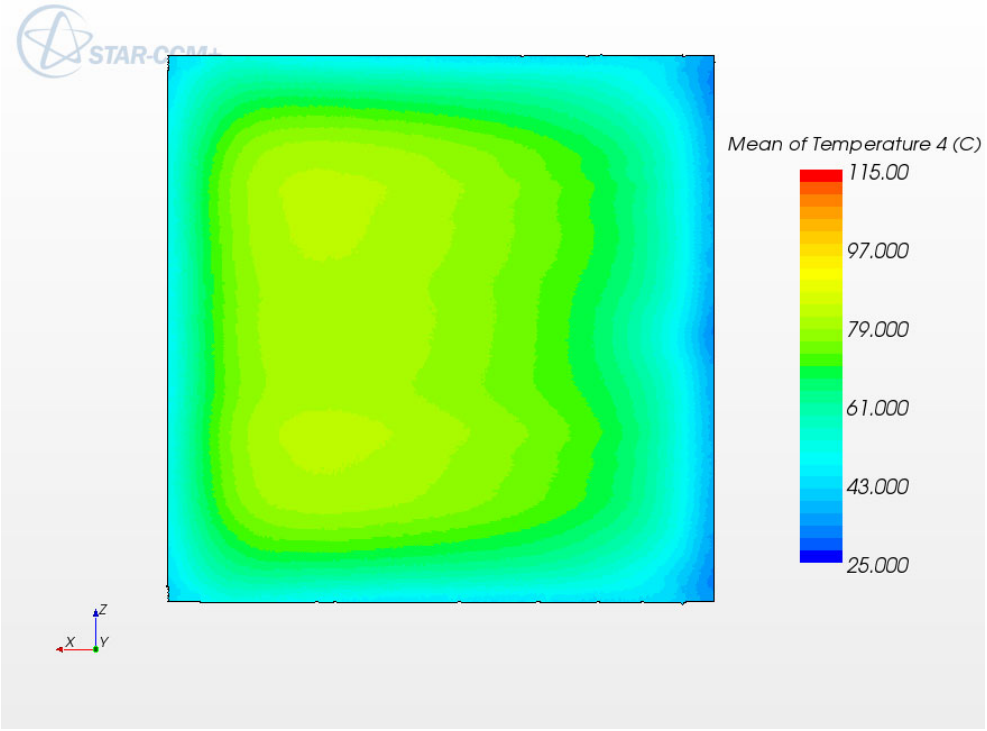

Plate 5 top

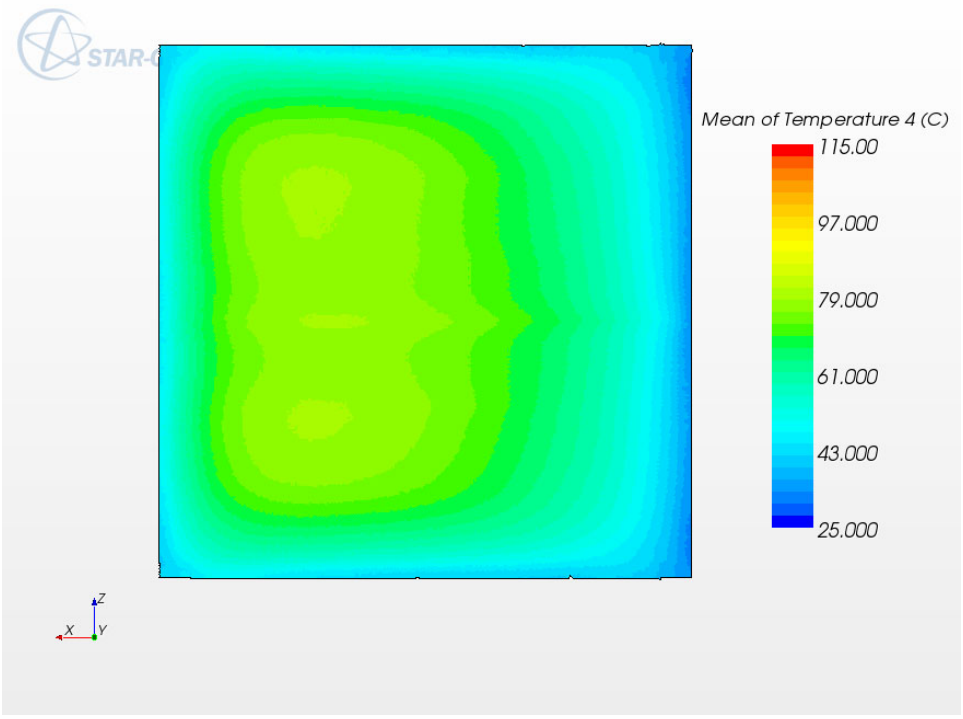

Plate 5 bottom

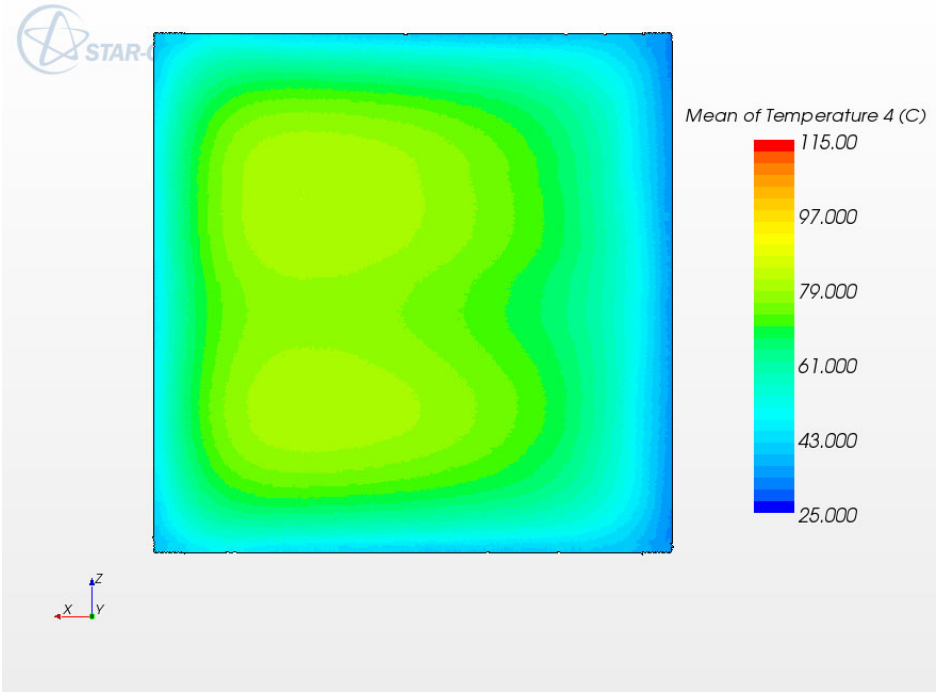

Plate 6 top

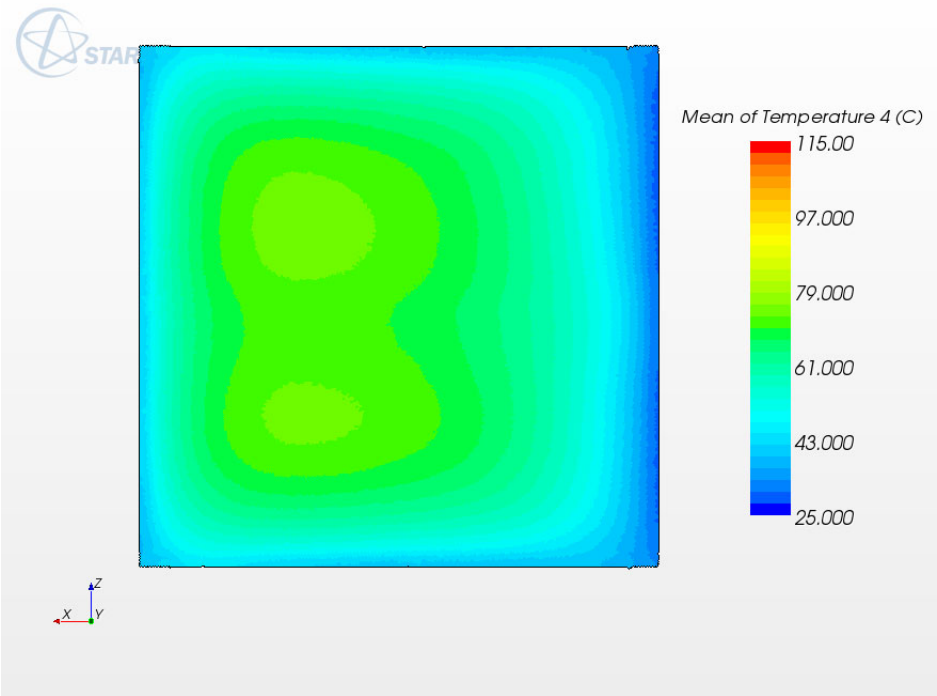

Plate 6 bottom

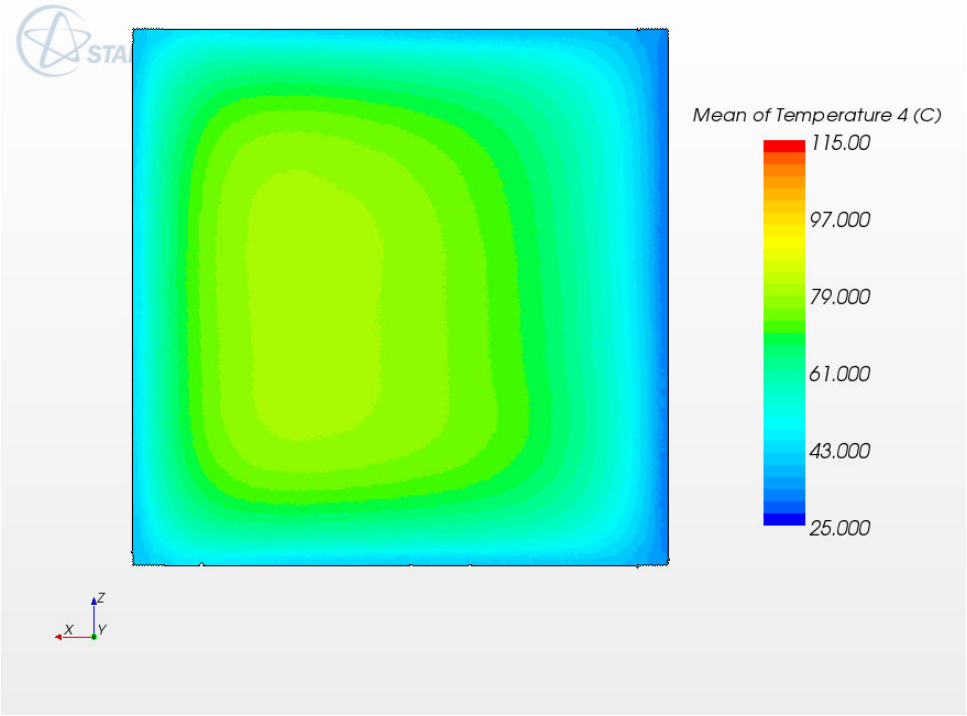

Plate 7 top

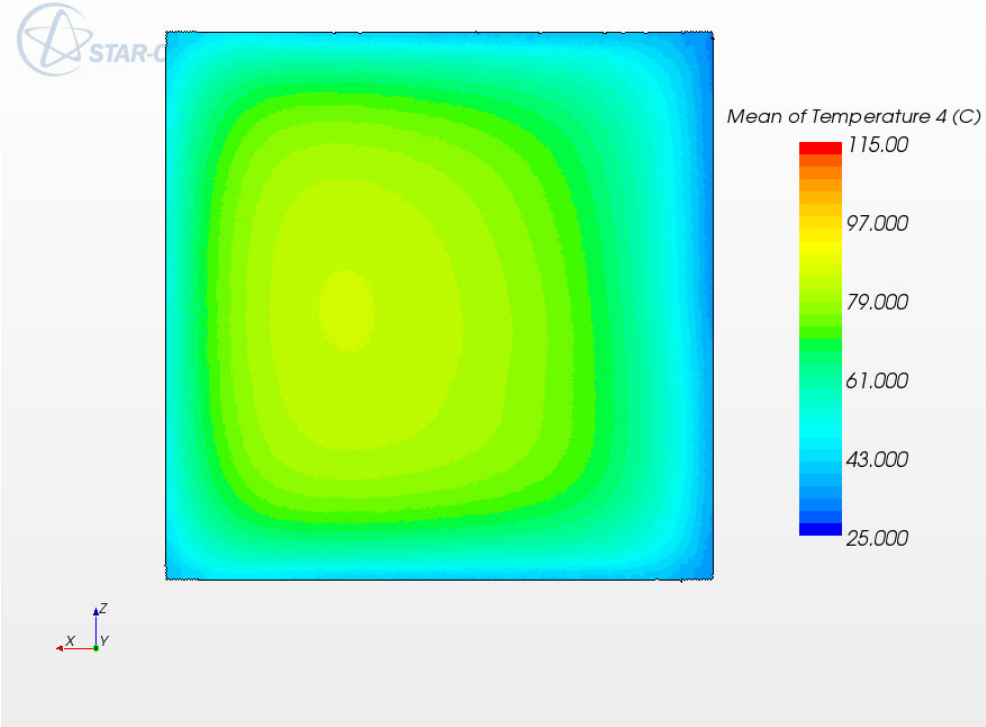

Plate 7 bottom

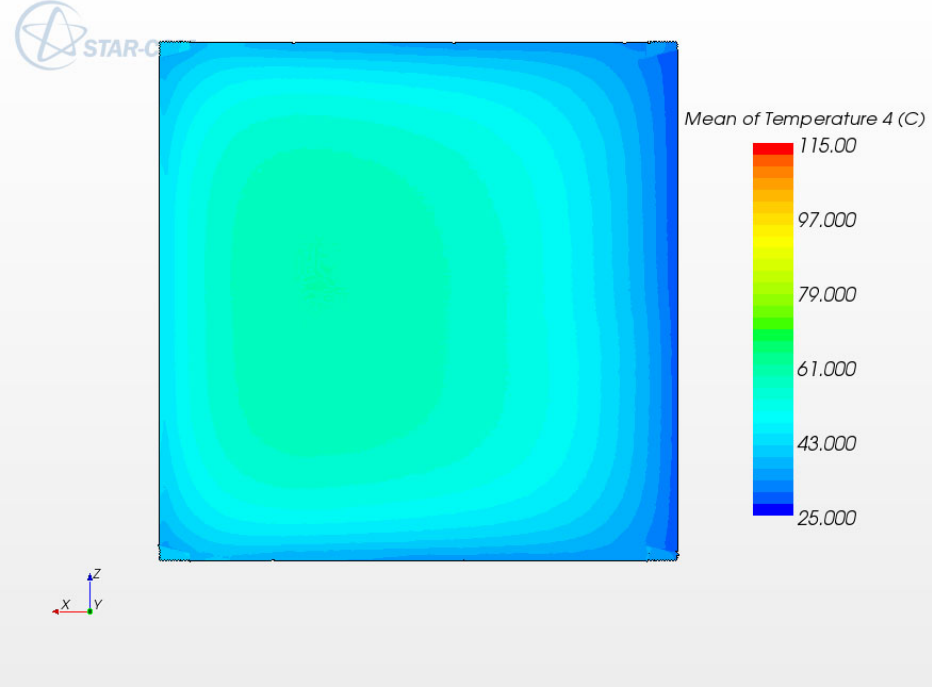

Plate 8 top

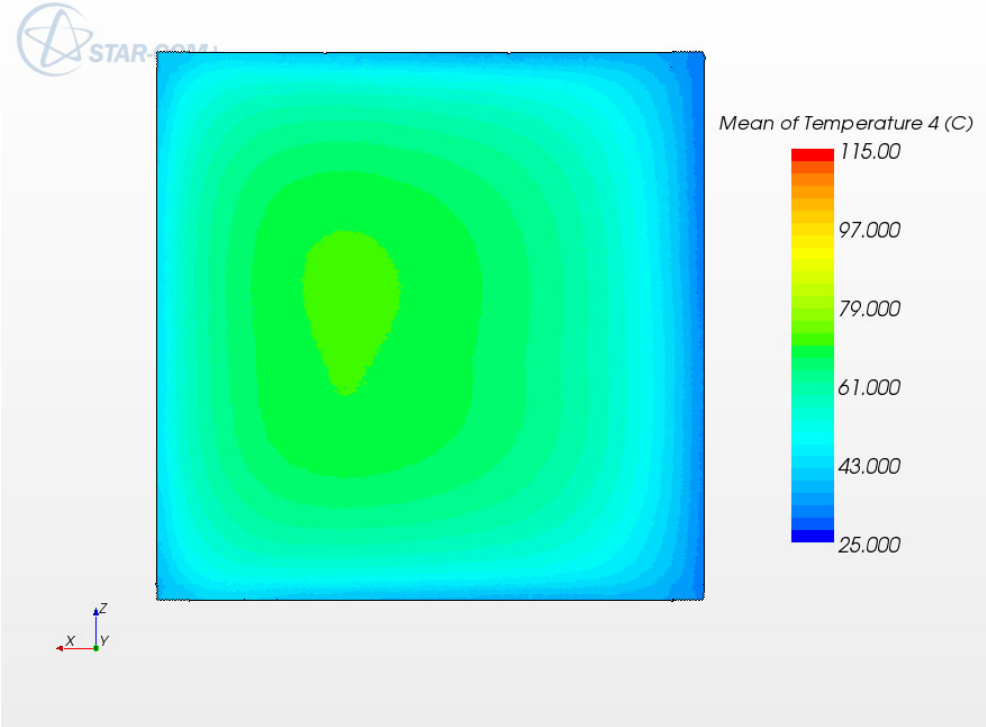

Plate 8 bottom

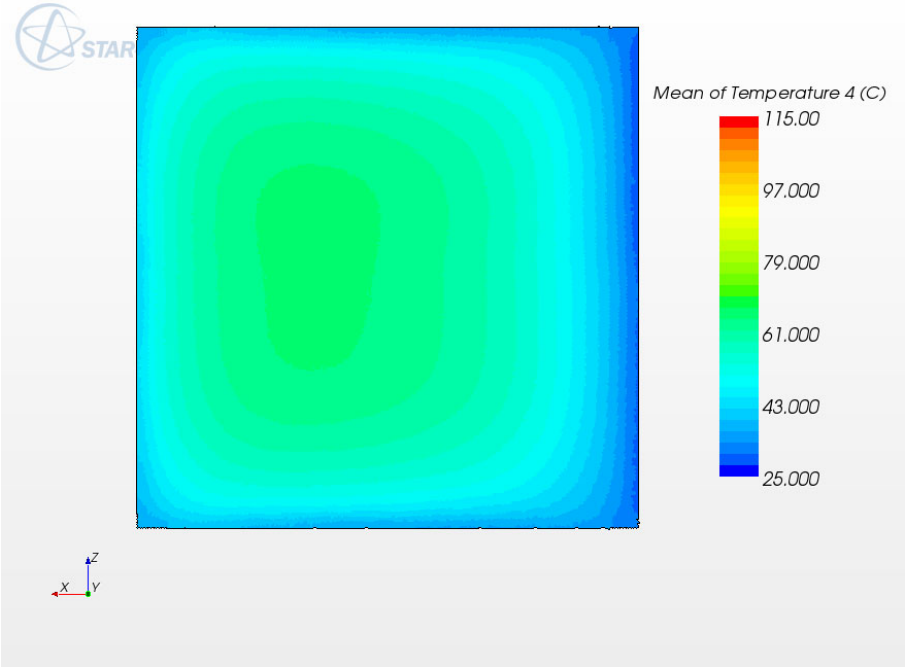

Plate 9 top

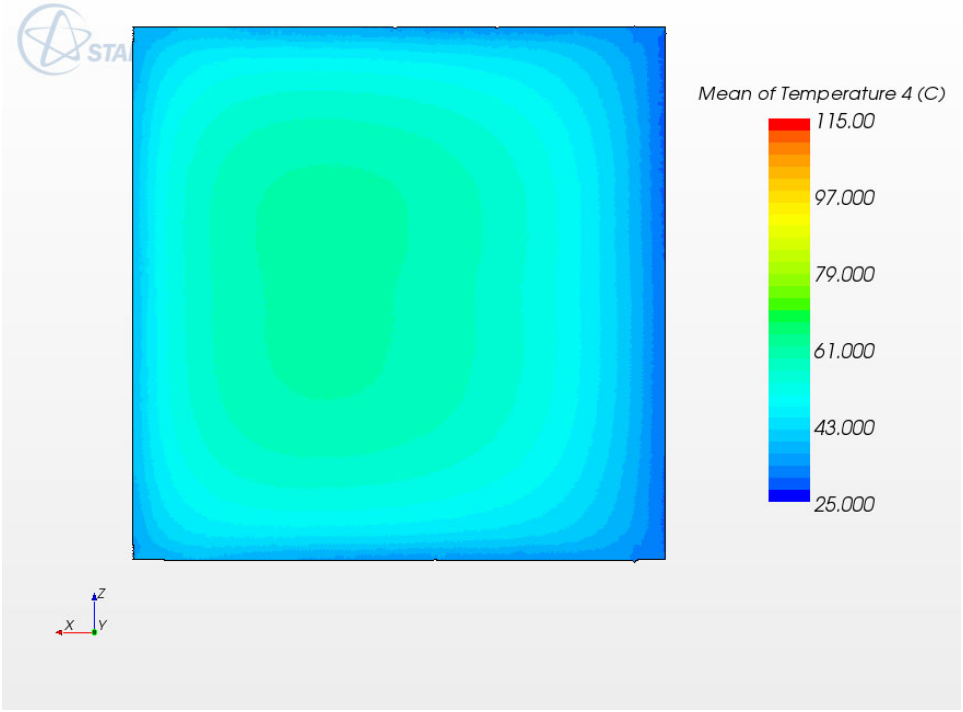

Plate 9 bottom

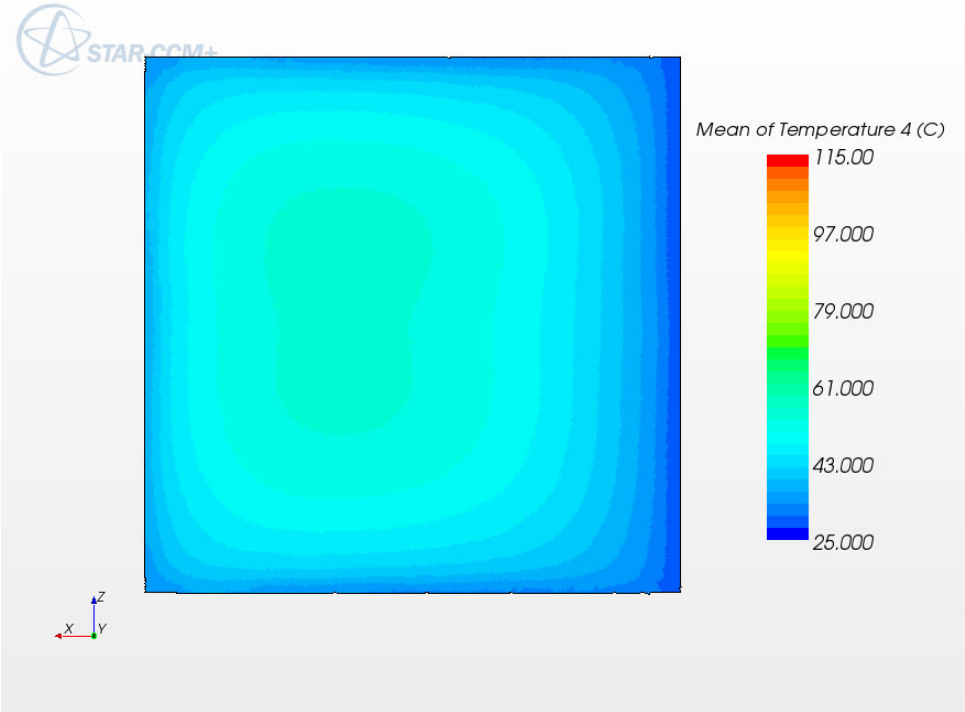

Plate 10 top

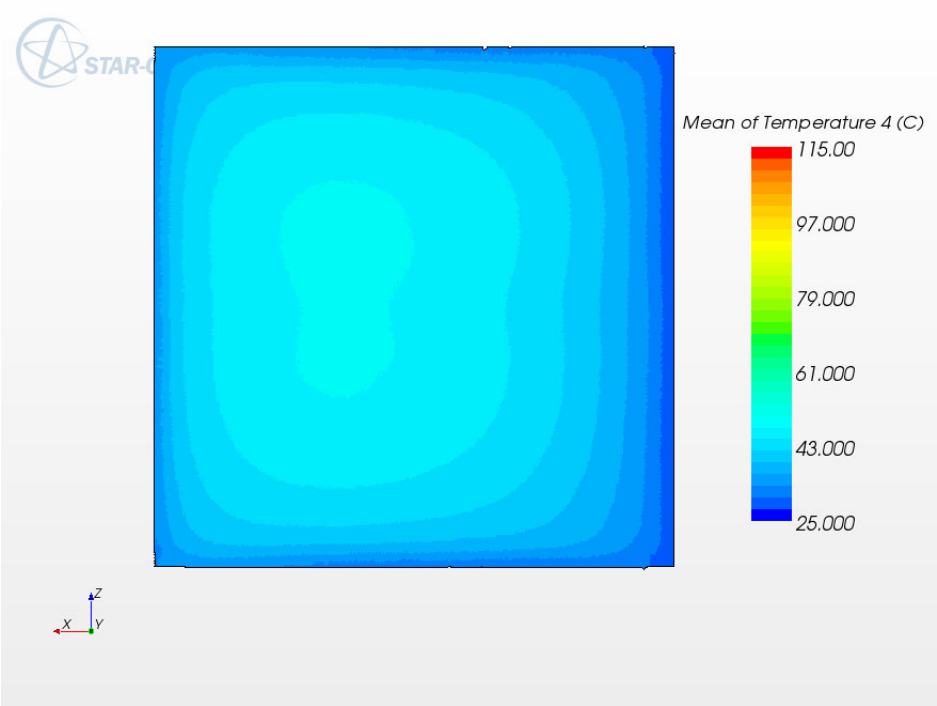

Plate 10 bottom

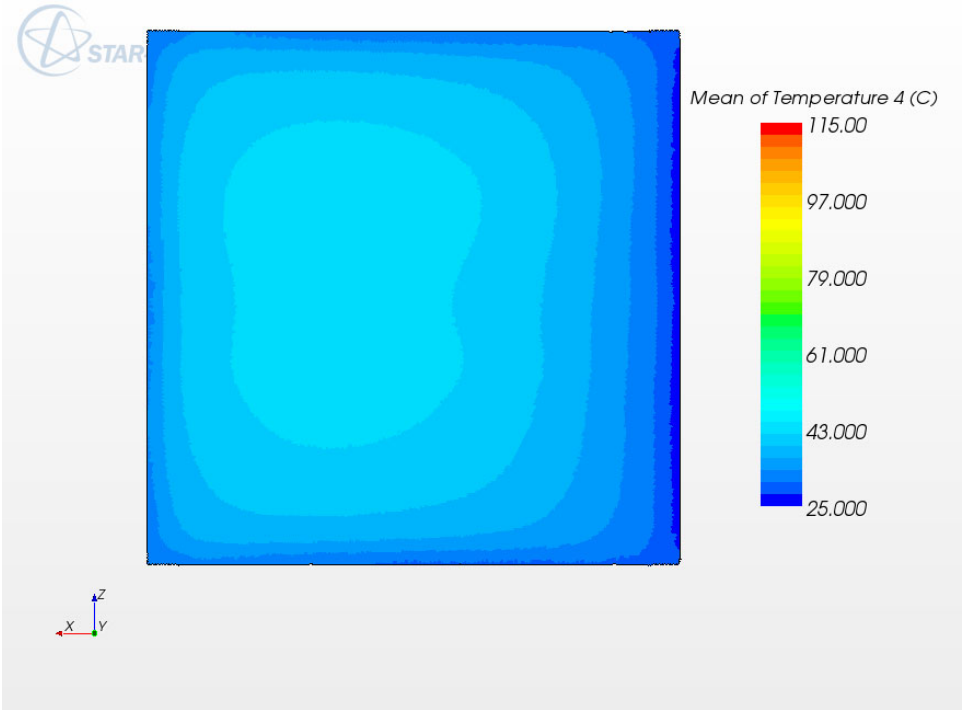

Plate 11 top

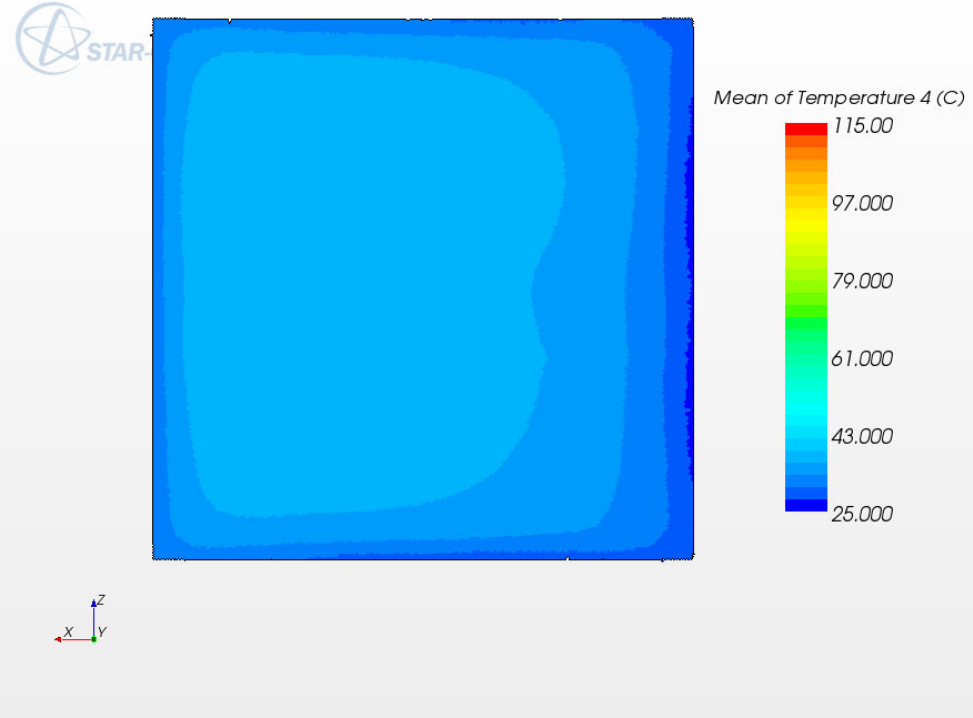

Plate 11 bottom

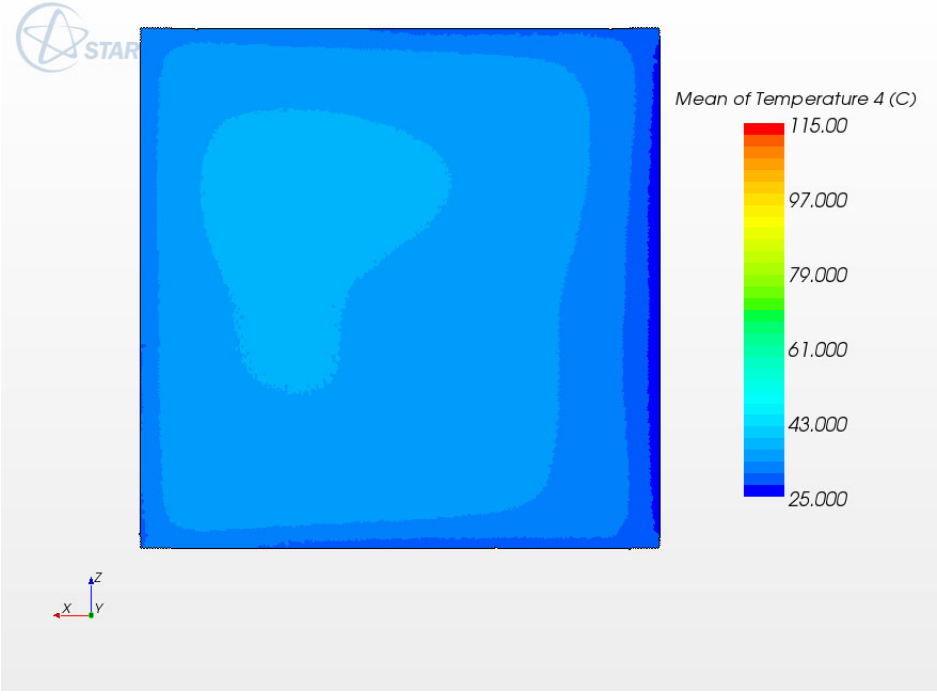

Temperature distribution at uranium plate mid-section

Plate 1

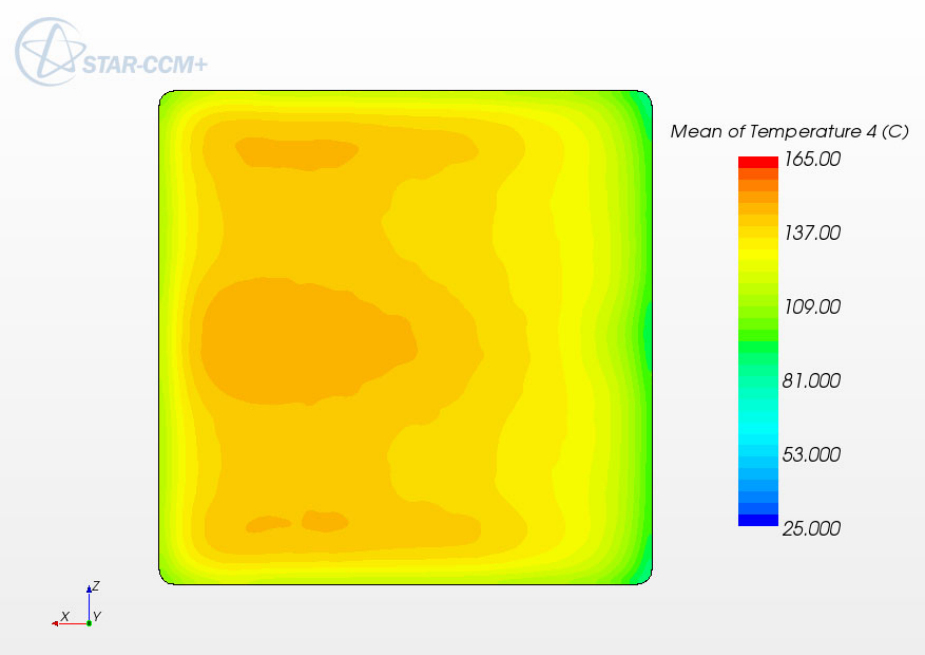

Plate 2

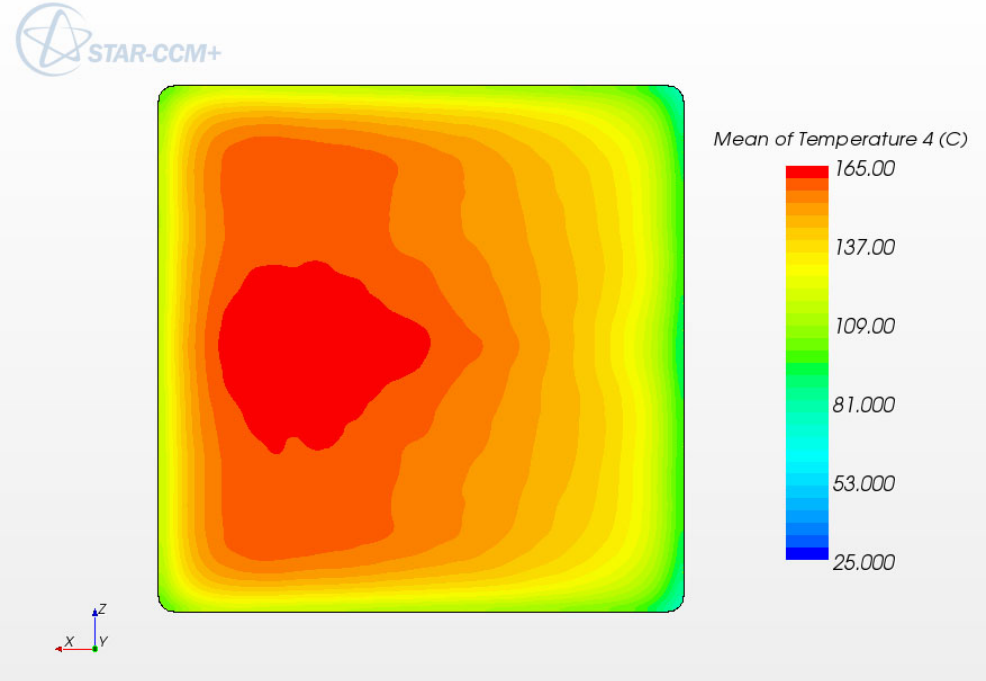

Plate 3

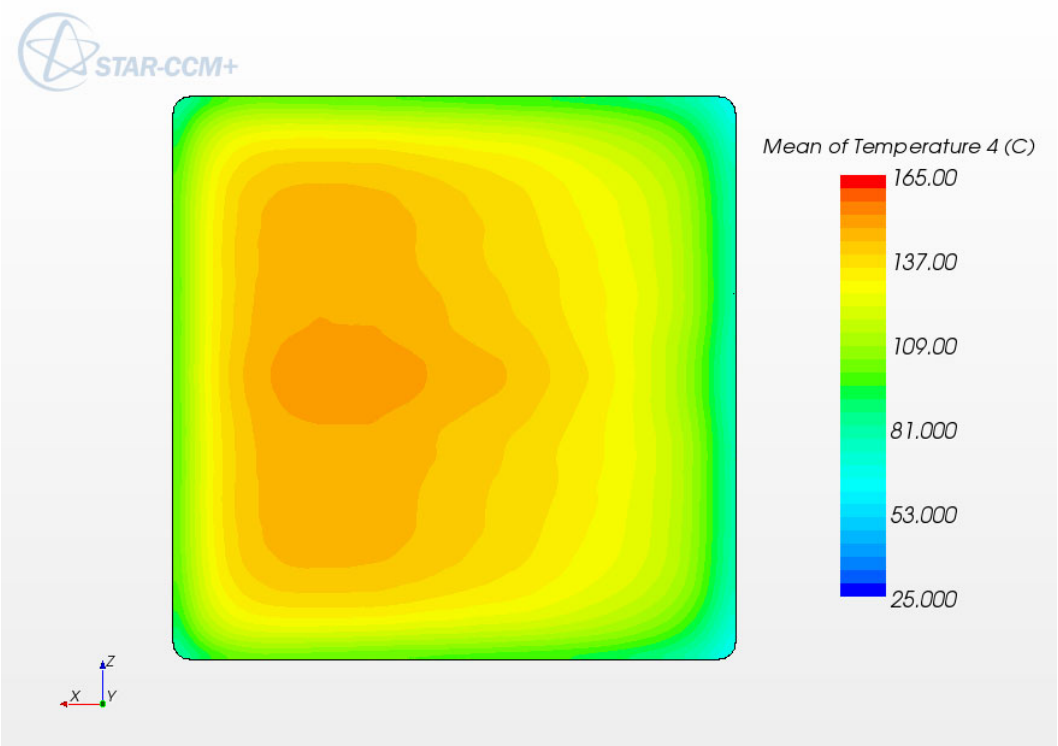

Plate 4

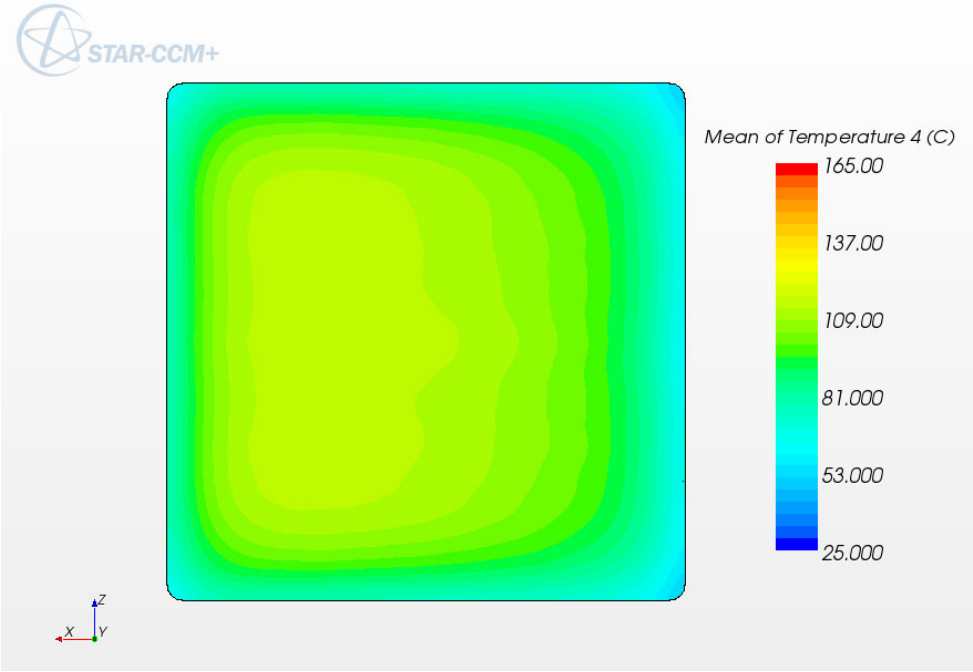

Plate 5

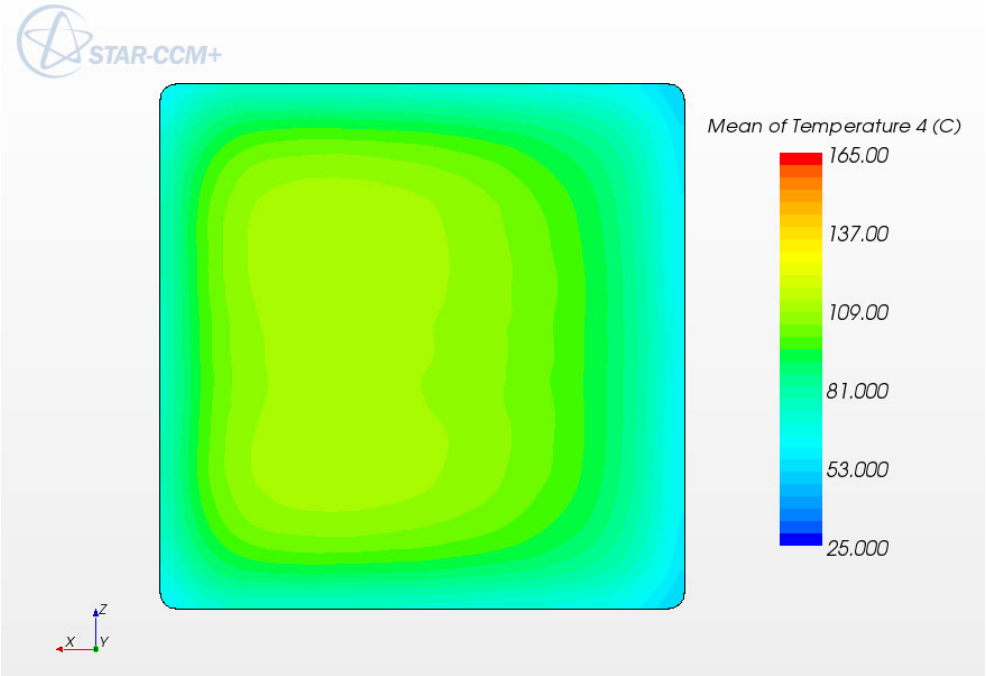

Plate 6

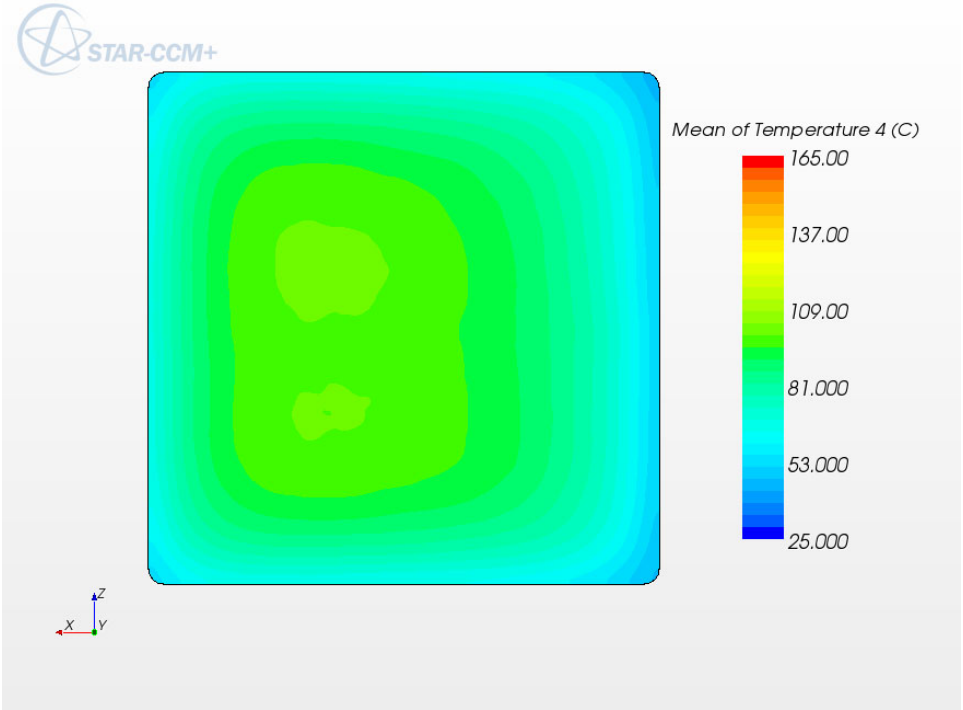

Plate 7

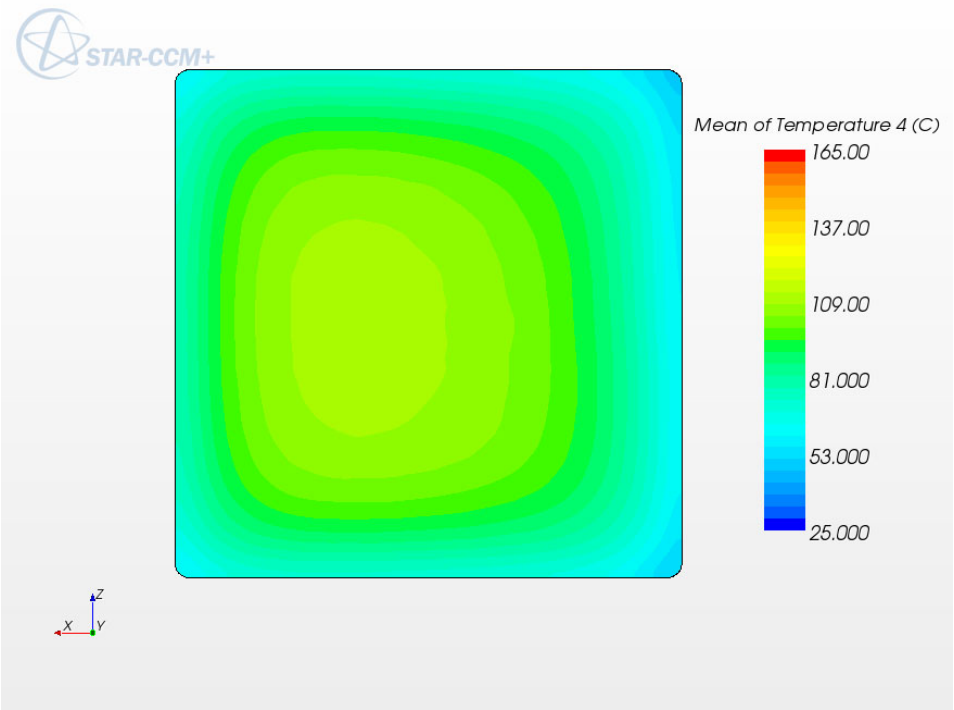

Plate 8

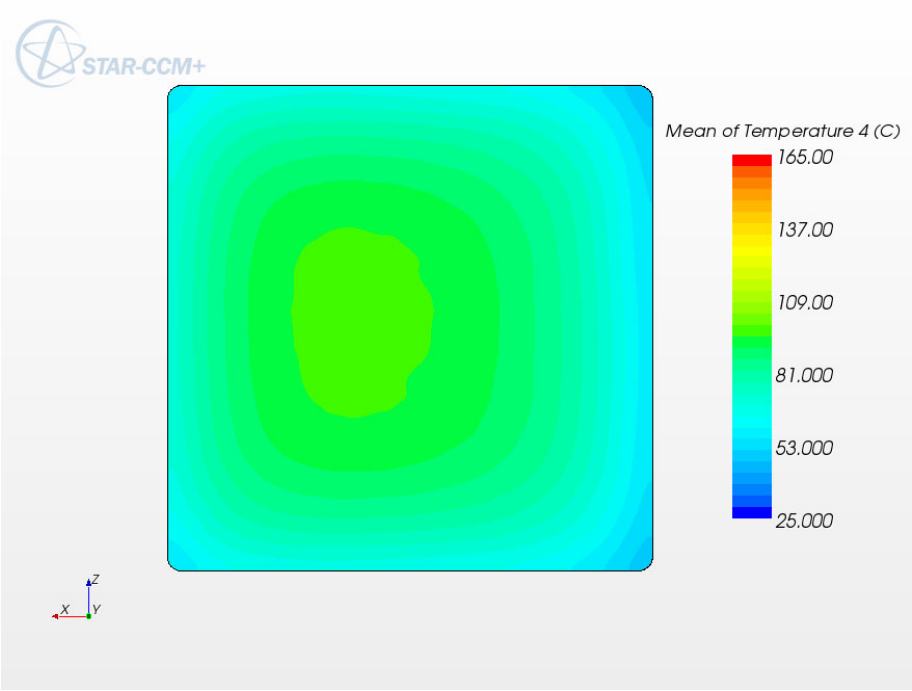

Plate 9

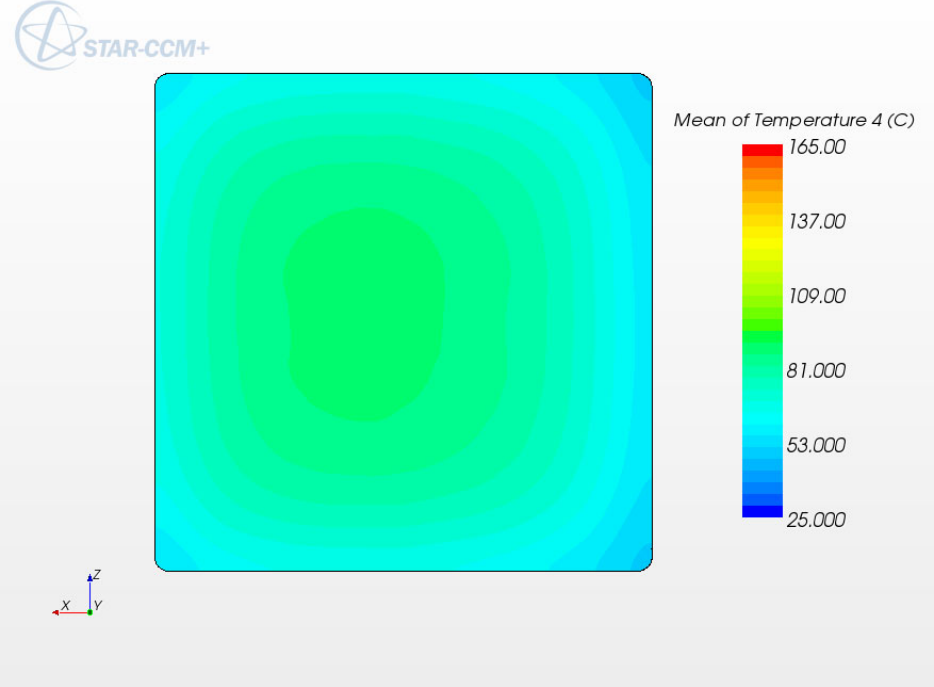

Plate 10

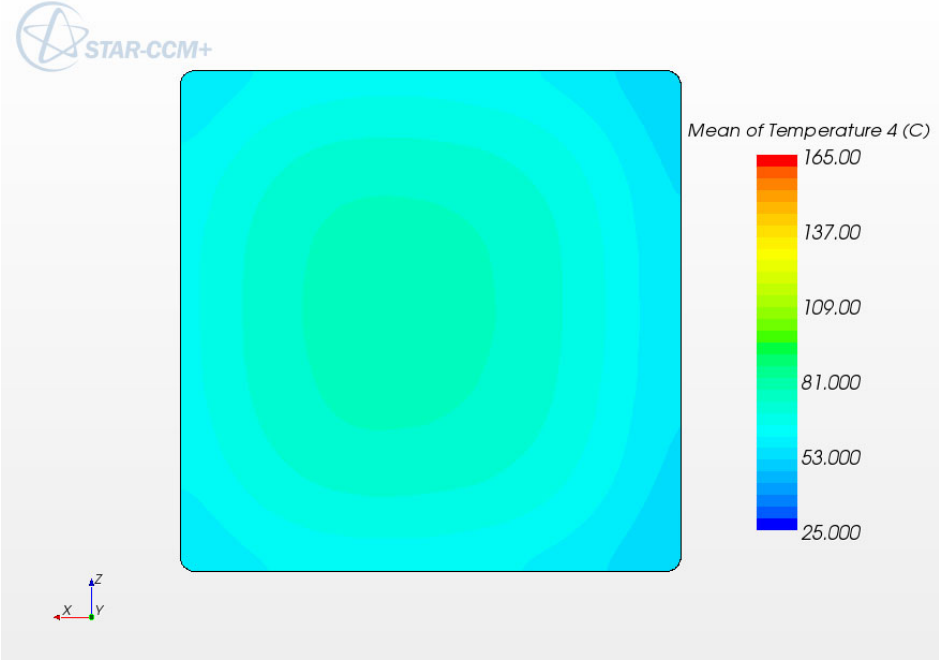

Plate 11

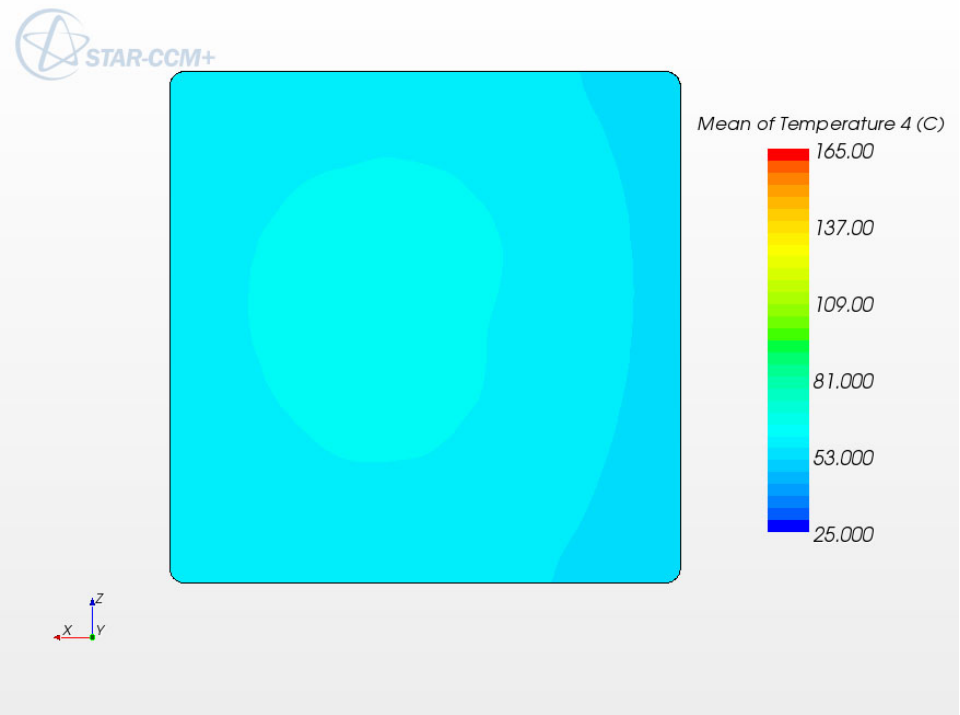

Figure II.3.6.3.3. Detailed distributions of velocity magnitude and temperature in the reference uranium target.

II.3.7 Conclusions of the Thermal Hydraulics Analysis of the Reference Design Options

Numerical simulations were performed to optimize the tungsten and the uranium target configurations with the commercial CFD code STAR-CCM+ 5.06. For an inlet water flow rate of 4.79 kg/s, the results show that subcooled boiling is not predicted to occur at the rated pressure with a margin of 30 ºC to 40 ºC. Moreover, the first layer of fluid cells has much lower temperature suggesting that any bubble departing from the wall would be short-lived. In conclusion, boiling should not be a concern at the rated pressure for the present target configurations.

Thermo-fluid simulations have been performed using STAR-CCM+ 7.06 for the reference target designs. The unsteady flow due to the lower manifold design does not strongly impact the flow distribution between the plates. It was shown that the results from these simulations do not impact the peak temperatures.

The calculations demonstrated that the temperatures in all materials are well below melting point during normal operation. For an inlet mass flow rate of 4.79 kg/s and inlet pressure of 2.69 bar, subcooled boiling is not predicted to occur. Margins of greater than 30 °C for subcooled boiling and 10 °C for nucleate boiling are predicted. The near-wall fluid cells have a significantly lower temperature than the cladding surface. Thus, boiling is not expected to be a concern for these target configurations.

References

II.3.1 Sofu T. et al., “Target Design Optimization for a Subcritical System Driven by an Electron Accelerator with Circular and Square Beam Profiles”, Argonne National Laboratory report number ANL-NE-08/25, October 30, 2008 (http://www.ipd.anl.gov/anlpubs/2008/10/62554.pdf).
II.3.2 “User Guide, STAR-CD 4.08”, CD-adapco, 2009, Mellville, NY, USA.
II.3.3 “User Guide, STAR-CCM+ 5.06”, CD-adapco, 2010, Mellville, NY, USA.
II.3.4 Berglers, A. E and Rohsenow, W. M. “The determination of forced convection surface boiling heat transfer”, J. Heat Transfer, 86, p. 363 (1964).

II.4 Target Structural Analysis and Design

II.4.1 Objective

The objective of this analysis was to perform static structural analyses of the uranium and the tungsten targets of the subcritical assembly of the KIPT ADS experimental neutron source facility.

II.4.2 Methodology

This analysis was carried out with the finite element method using the Ansys R13.0 finite element program [II.4.1]. Finite element models were constructed and subjected to estimated loads developed for the study. Results were compared to basic material properties and commonly accepted engineering principles.

II.4.3 Analysis Overview

Each target subassembly consists of an upper and a lower section, which are connected by an aluminum extrusion. The upper sections are the same for both target materials, while the internals of the lower section vary in length to accommodate different target plate configurations depending on the target material. Each section was evaluated separately, with multiple load cases. The upper section was analyzed by applying static clamping, water pressure and weight loads in the load cases summarized in Table II.4.3.1. The evaluations and the load cases for the lower sections are summarized in Table II.4.3.2.

The extrusion part was not evaluated by itself. Loads on the extrusion consist of reactions at the connection to the upper section that result from static pressure and clamping loads on the upper section, and reactions at the connection to the lower section due to static and hydrostatic pressures. Maximum stresses occur at these interfaces. A small section of the extrusion was included in each finite element model, and this served to capture these stresses for evaluation.

Table II.4.3.1. Summary of upper section load cases

No.	Load Case Description	Inlet Pressure (KPaa)	Outlet Pressure (KPaa)	Clamp Load	Hydrostatic Pressure
1	Base Pressure Only	269	152	0	0
2	Base Pressure, Clamp Load	269	152	17,103	0

Table II.4.3.2. Summary of lower section load cases

No.	Load Case Description
3	Base Pressure + Hydrostatic Pressure
4	Base Pressure + 1 atm Hydrostatic Pressure
5	Base Pressure + 2 atm Hydrostatic Pressure
6	Weld Analysis

II.4.4 Assumptions

This analysis is based on the following assumptions:

1. The material responses are linear elastic.
2. The material responses are constant with time (no effects of aging, creep, etc.).
3. The materials are isotropic and homogeneous.
4. The material response is consistent with small strain and small displacement.
5. The effects of neutron flux on the material properties are not included.
6. The residual stresses are not included.
7. The targets operate at room temperature.
8. The loads are applied slowly and do not vary with time.

II.4.5 Geometry

The finite element model for the upper section was based on the solid modeling geometry. The target assembly geometry was imported into Ansys Design Modeler, where a solid geometry model was created as shown in Fig. II.4.5.1. This model was taken into the Workbench module, where a mesh with 1,034,876 quadratic tetrahedral elements was created. This model is shown in Fig. II.4.5.2.

The finite element model for the 7-plate tungsten target lower section was generated using the same approach as for the upper section. The geometry model is shown in Fig. II.4.5.3, and the finite element model containing 936,707 quadratic tetrahedral elements is shown in Fig. II.4.5.4.

The finite element model for the 11-plate uranium target lower section was generated using the same approach. The geometry model and the finite element model, containing 936,707 quadratic tetrahedral elements, are similar to the tungsten target lower section. The components were connected with bonded contact elements. Initial attempts to create a multi-body part were unsuccessful because many of the components did not mate precisely with each other. This is often the case with weldments. This resulted in meshing errors at thin slivers and cracks in the solid geometry, etc.

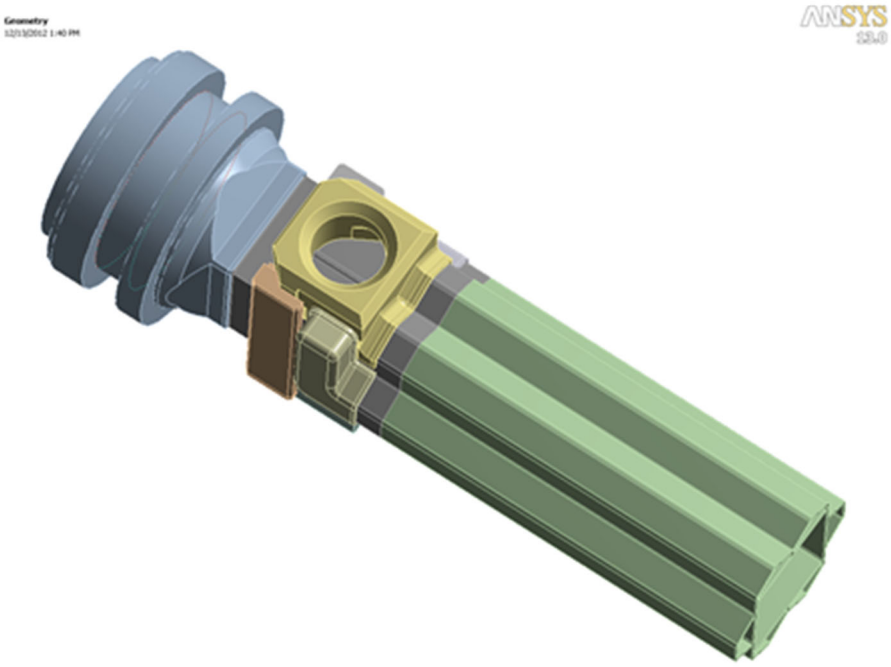

Figure II.4.5.1. Solid model of the upper section

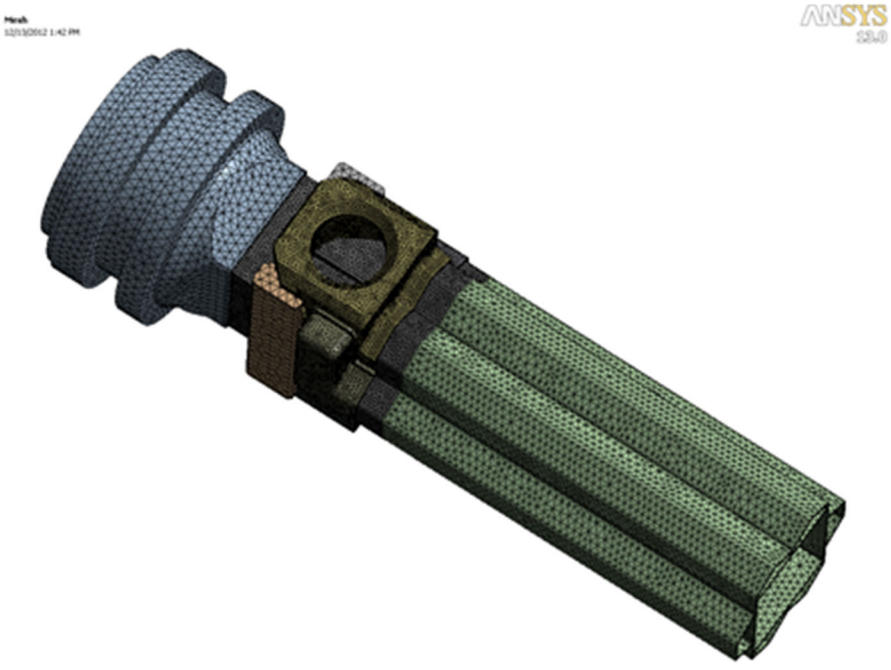

Figure II.4.5.2. Finite element model of the upper section

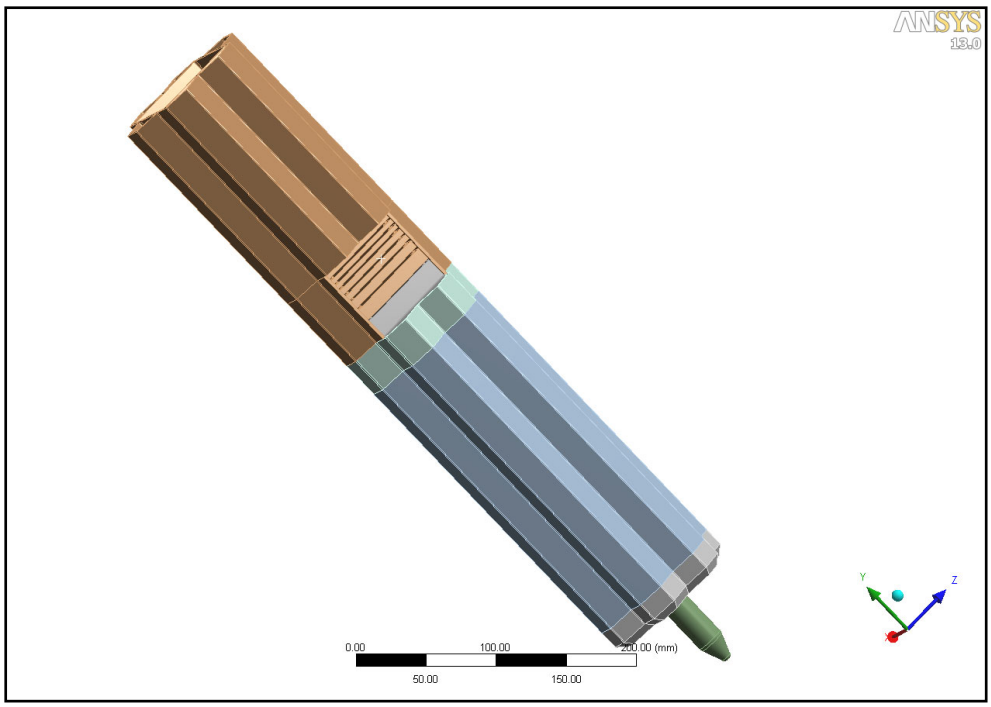

Figure II.4.5.3. Solid model of the tungsten target lower section

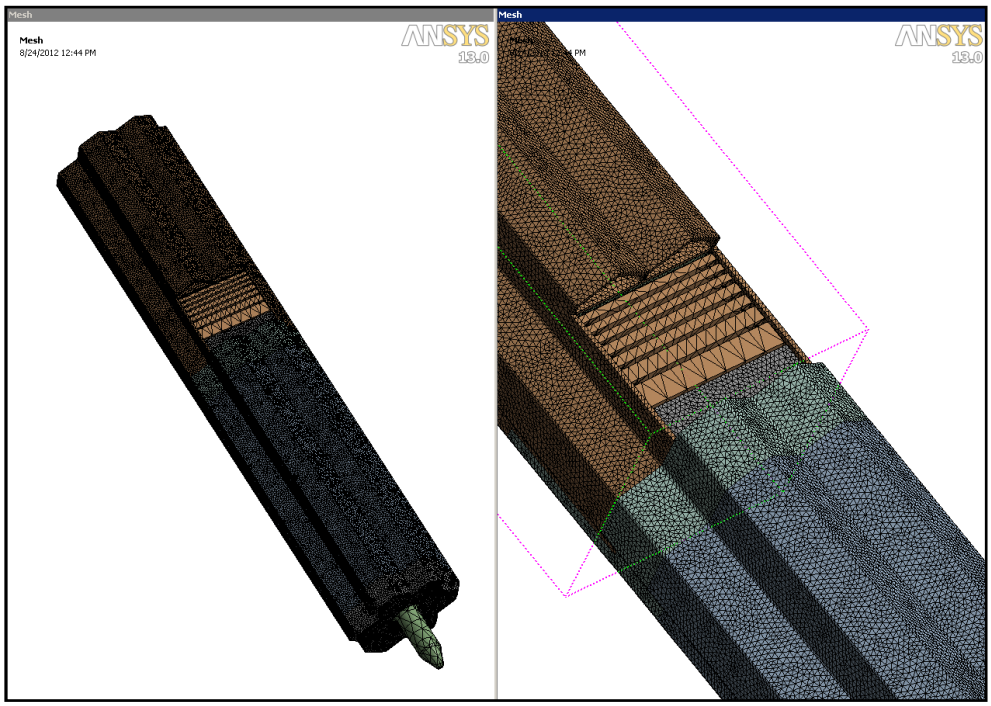

Figure II.4.5.4. Finite element model of the tungsten target lower section

II.4.6 Materials

The mechanical properties of SAV-1 used for this analysis are shown in Table II.4.6.1.

Strength values are based on “tempered and naturally aged” heat treatment of pressed sections. The material properties for SAV-1 were not readily available, so common values for similar grades were used when necessary.

Table II.4.6.1. SAV-1 Material properties

Property	Parent Material	Heat Affected Zone (HAZ)	Source
Elastic Modulus (MPa)	71,000	71,000	Common value
Ultimate Tensile Strength (MPa)	226	150	SAV-1 Alloy Data
Yield Strength (MPa)	157	90	SAV-1 Alloy Data
Elongation (%)	22	25	SAV-1 Alloy Data
Poisson’s Ration	0.33	0.33	Common value
Density (kg/m^3)	2,770	2,770	Common value

II.4.7 Loads and Boundary Conditions

The loads and the boundary conditions used for load cases 1 and 2 are shown in Figs. II.4.7.1 through II.4.7.4; those for load cases 3 to 6 are shown in Figs. II.4.7.5 through II.4.7.7. The magnitudes of the loads for load cases 1 and 2 are shown in Table II.4.7.1; those for load cases 3 to 6 are presented in Table II.4.7.2.

Table II.4.7.1. Summary of cases 1 and 2 loads

No.	Load Case Description	Inlet Pressure (KPa)	Outlet Pressure (KPa)	Clamp Load (N)	Weight (N)
1	Base Pressure Only	168	51	0	109
2	Base Pressure, Clamp Load	168	51	17,103	109

Table II.4.7.2. Summary of cases 3 through 6 loads

No.	Load Case Description	Inlet Pressure (KPa)	Outlet Pressure (KPa)	Hydrostatic Pressure (KPa)
3	Base Pressure + Hydrostatic Pressure	137	129	12.9
4	Base Pressure + 1 atm., Hydrostatic Pressure	238	230	12.9
5	Base Pressure + 2 atm., Hydrostatic Pressure	309	301	12.9
6	Weld Analysis	137	129	12.9

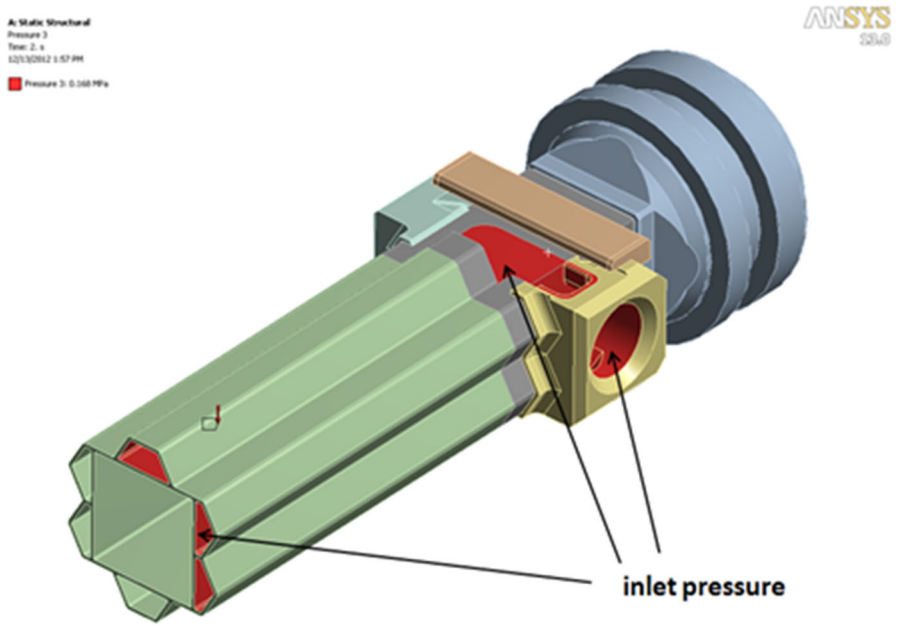

Figure II.4.7.1. Boundary conditions for load cases 1 and 2-A

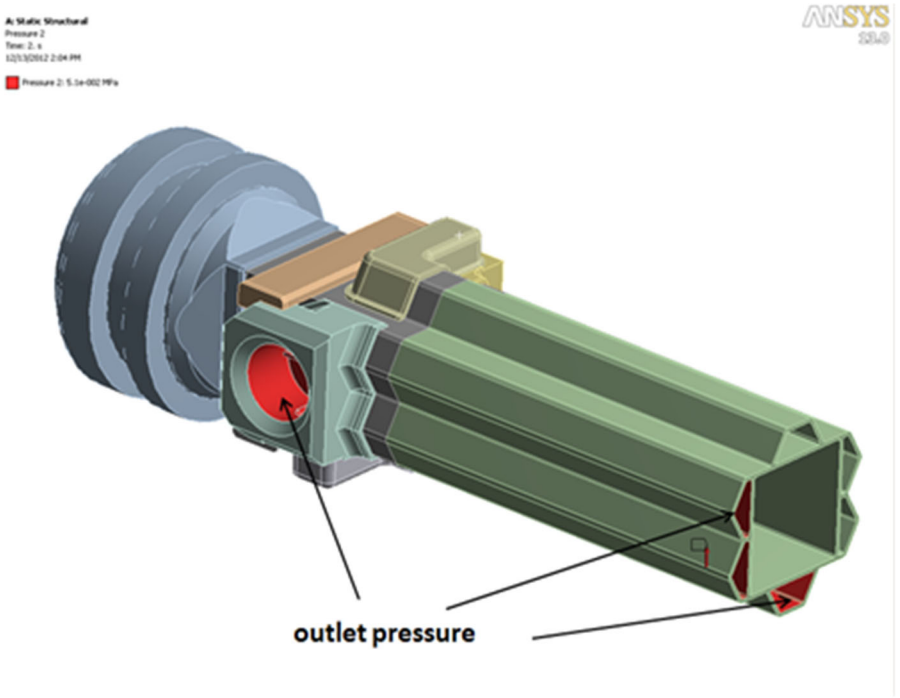

Figure II.4.7.2. Boundary conditions for load cases 1 and 2-B

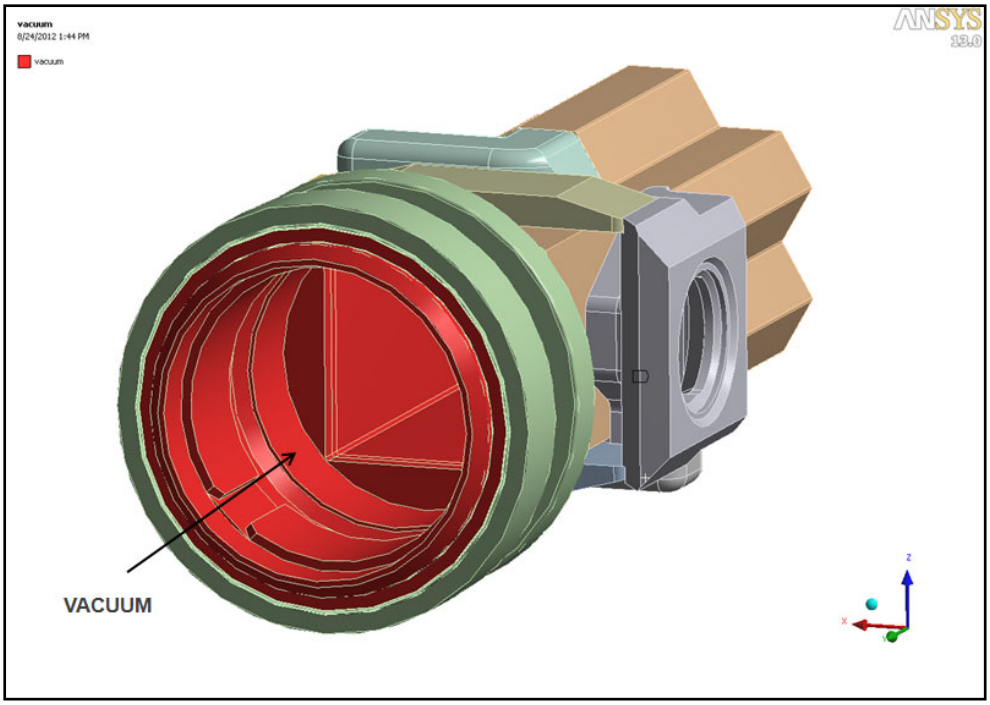

Figure II.4.7.3. Boundary conditions for load cases 1 and 2-C

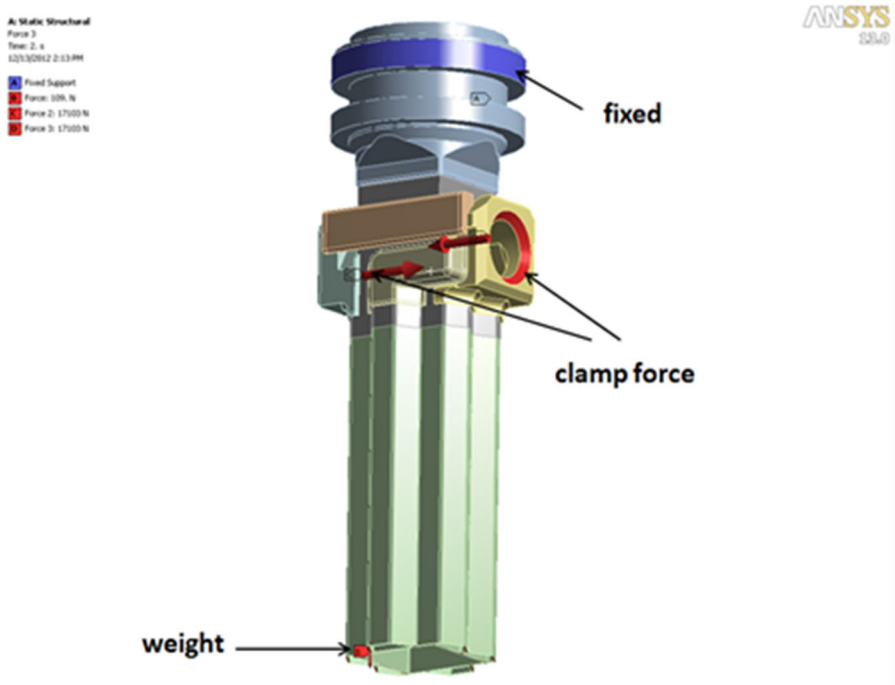

Figure II.4.7.4. Boundary conditions for load cases 1 and 2-D

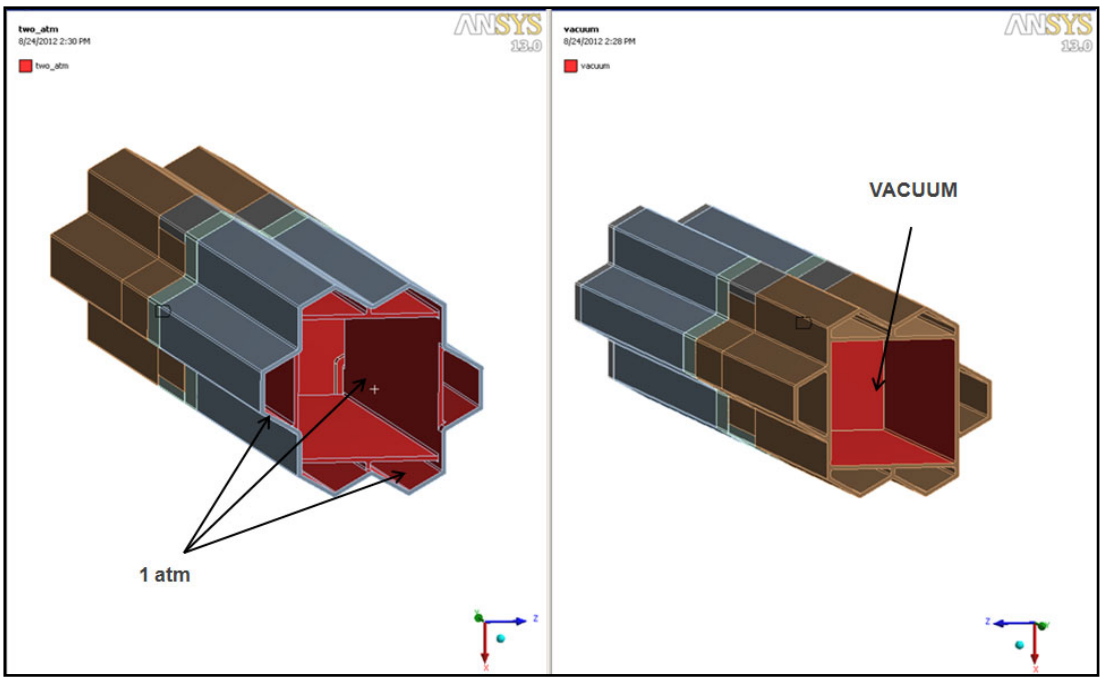

Figure II.4.7.5. Boundary conditions for load cases 3 through 6-A

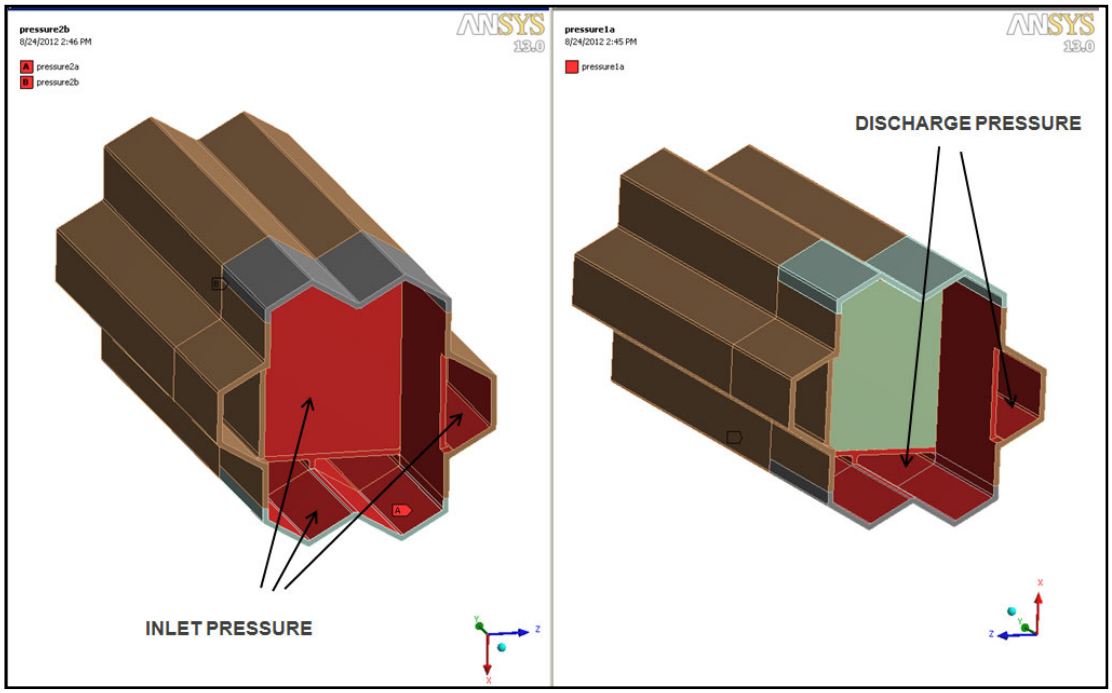

Figure II.4.7.6. Boundary conditions for load cases 3 through 6-B

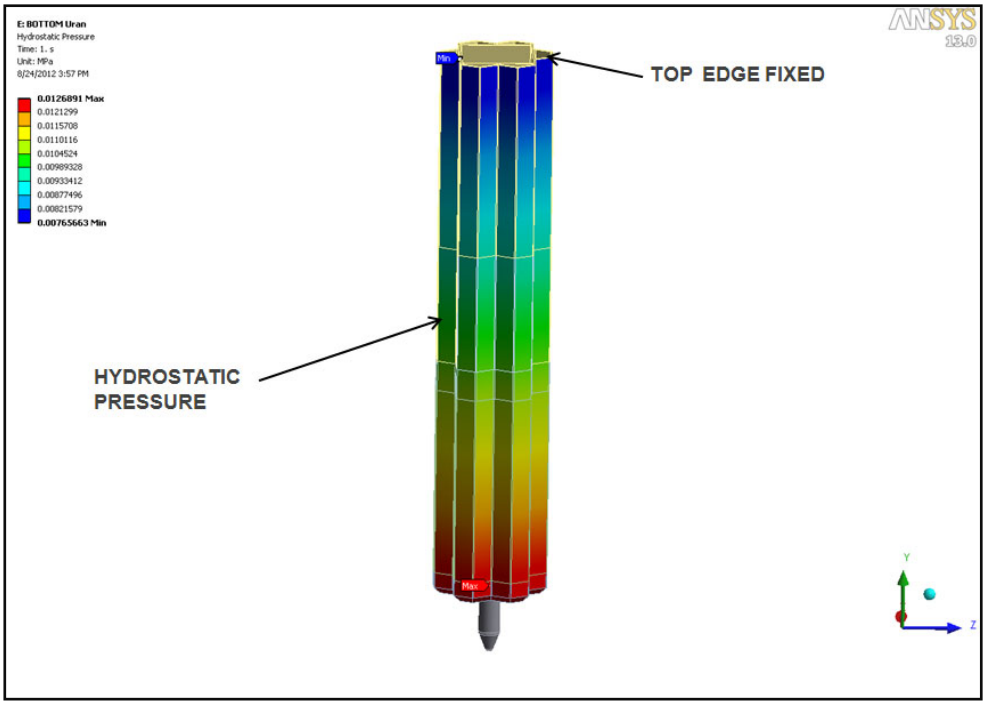

Figure II.4.7.7. Boundary conditions for load cases 3 through 6-C

II.4.8 Results

This assembly consists of several components connected in a way that results in abrupt changes in stiffness along the load path. This can result in localized high stresses, which are due in part to the use of a linear elastic material model. When these stresses are localized, Glinka's method (Ref. II.4.2) can be used to correct the strain and determine if yield has taken place. This was worked backwards to create a strain-corrected yield strength that can be compared directly to stress values.

The individual components were assembled with bonded contact. Contact was applied on surface patches immediately adjacent to welds, to capture the proper assembly stiffness. The use of bonded contact at welds sometimes results in high localized stresses that are an artifact of the bonded contact, and these stresses can be ignored.

II.4.8.1 Upper Section

II.4.8.1.1 Load Case 1

Plots of von Mises stress for load case 1 are shown in Figs. II.4.8.1.1.1 through II.4.8.1.1.7. The maximum stress of 347 MPa occurs in a port block, as shown in Fig. II.4.8.1.1.2. This is at a sharp ear that occurs when the block is machined to fit a blend on the extrusion. In practice this ear is supported by the extrusion. Since this feature is not welded, no bonded contact was used here, and there is no support in the finite element model. This results in the high stress value. It is a modeling artifact and can be ignored. There are some localized high stresses shown in Fig. II.4.8.1.1.3 caused

by the contact elements used to simulate the welds. Again, these are modeling artifacts that can be ignored. The highest real stresses in the port blocks are 229 MPa and 129 MPa, and both occur in a sharp corner at the base of a weld flange. This sharp corner is a stress concentrator, and a blend should be added here to reduce these stresses. Sharp corners result in a stress singularity which makes evaluating stresses difficult, so a 2 mm radius blend was added, and the analysis was rerun. Results for this revised port block are shown in Fig. II.4.8.1.1.4. The maximum real stress is 198 MPa, is localized, and it is below the strain corrected value of 264 MPa as shown in Fig. II.4.8.1.2.8. Figure II.4.8.1.1.5 shows stresses in the extrusion. The highest stress is 153.5 MPa and occurs at a sharp external corner. This is a modeling artifact and can be ignored. The highest real stress is 143 MPa, and it is located inside the extrusion near a corner. This is under a weld and is therefore in the heat effected zone (HAZ), and it is localized. This value is below the strain corrected value in the HAZ of 183 MPa as shown in Fig. II.4.8.1.2.9. Stresses in the L-shaped duct are shown in Fig. II.4.8.1.1.6. The maximum stress is 169 MPa and occurs at a virtual gap in support caused by the lack of bonding of the sharp ear in the port block. This is a modeling artifact and can be ignored. The highest real stress is 91.3 MPa, for a safety factor of 1.72. Stresses in the port block support are shown in Fig. II.4.8.1.1.7. There are some localized high stresses on either end caused by the bonded contact used to simulate welds. These are modeling artifacts and can be ignored. The real maximum stress is 55.6 MPa, for a safety factor of 2.82.

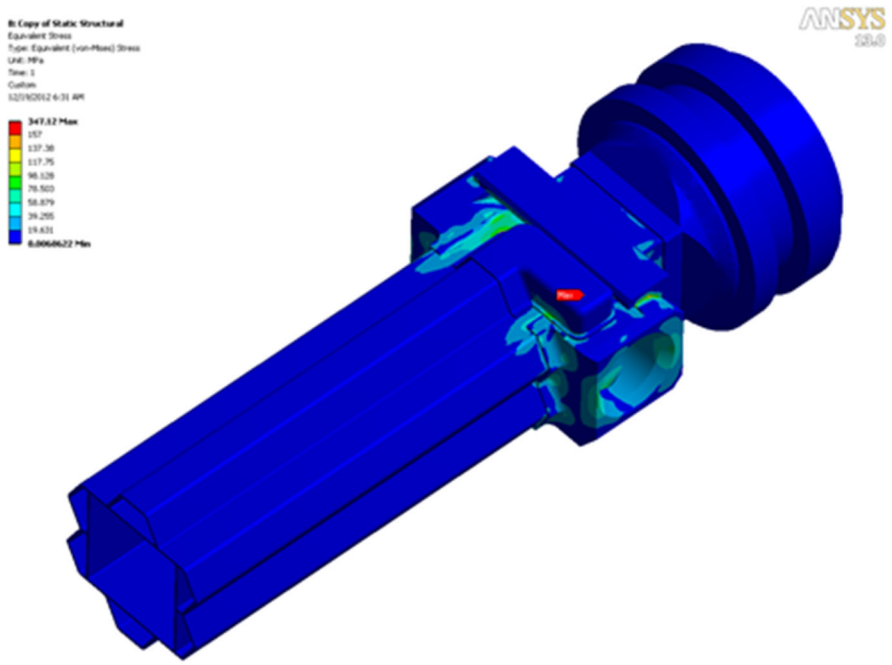

Figure II.4.8.1.1.1. Von Mises stress, load case 1

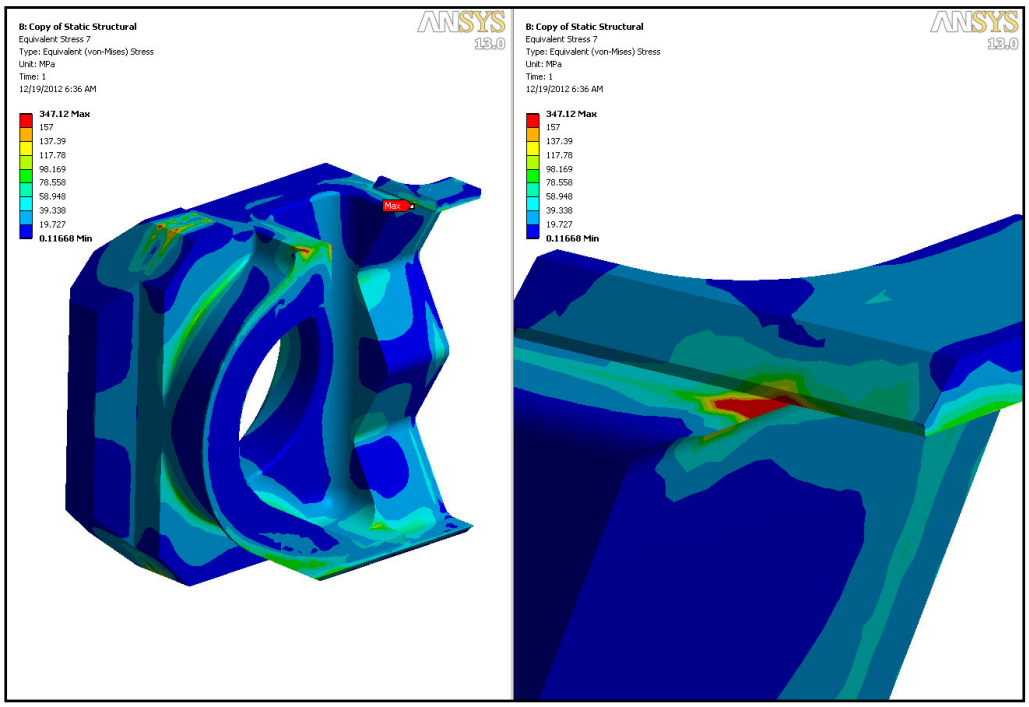

Figure II.4.8.1.1.2. Von Mises stress, port block, load case 1

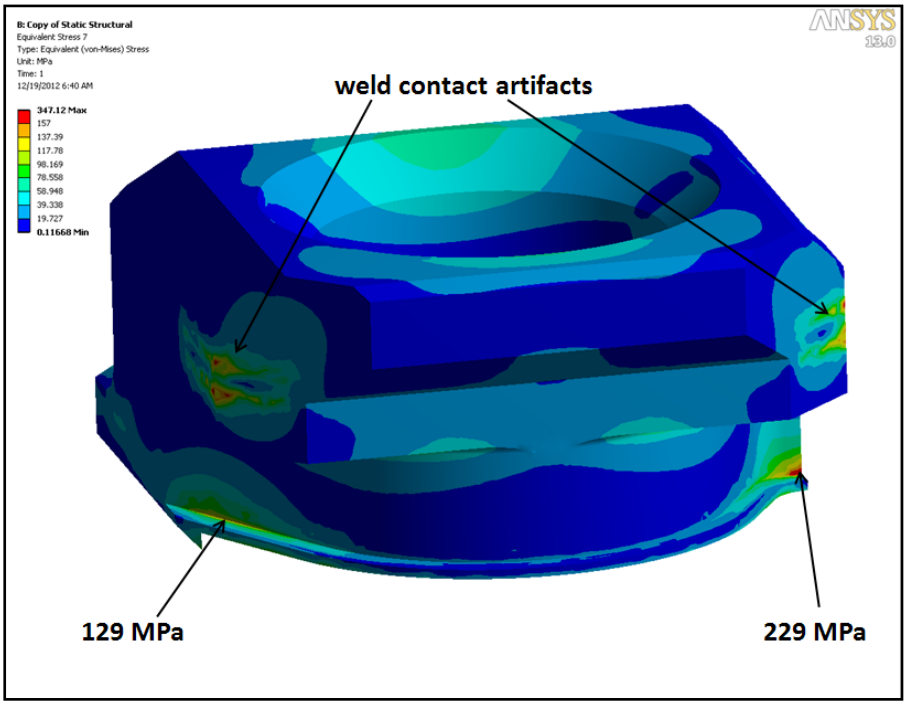

Figure II.4.8.1.1.3. Von Mises stress, port block, load case 1

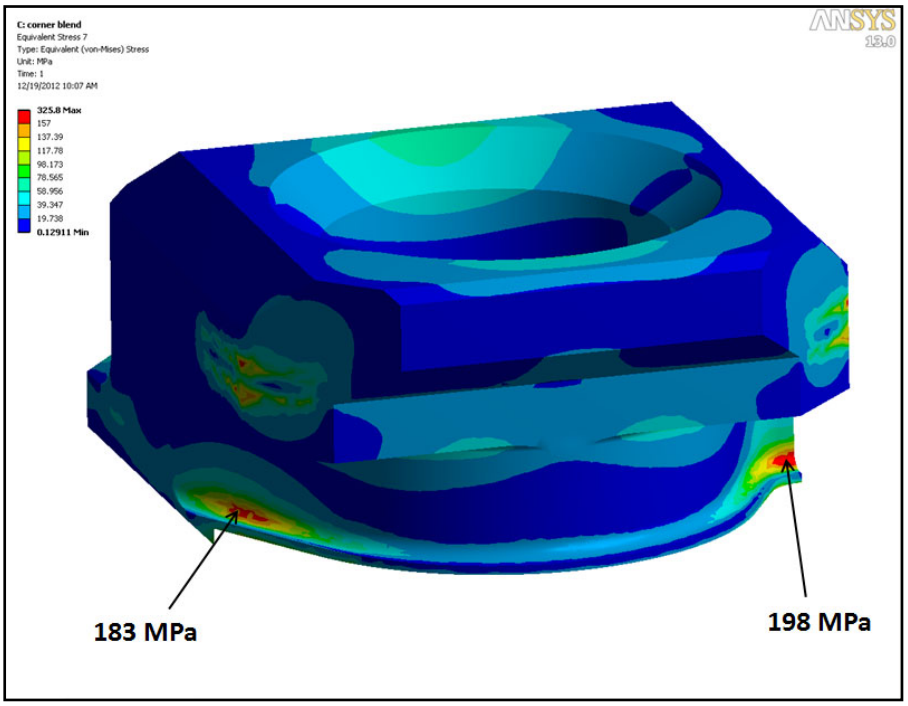

Figure II.4.8.1.1.4. Von Mises stress, revised port block, load case 1

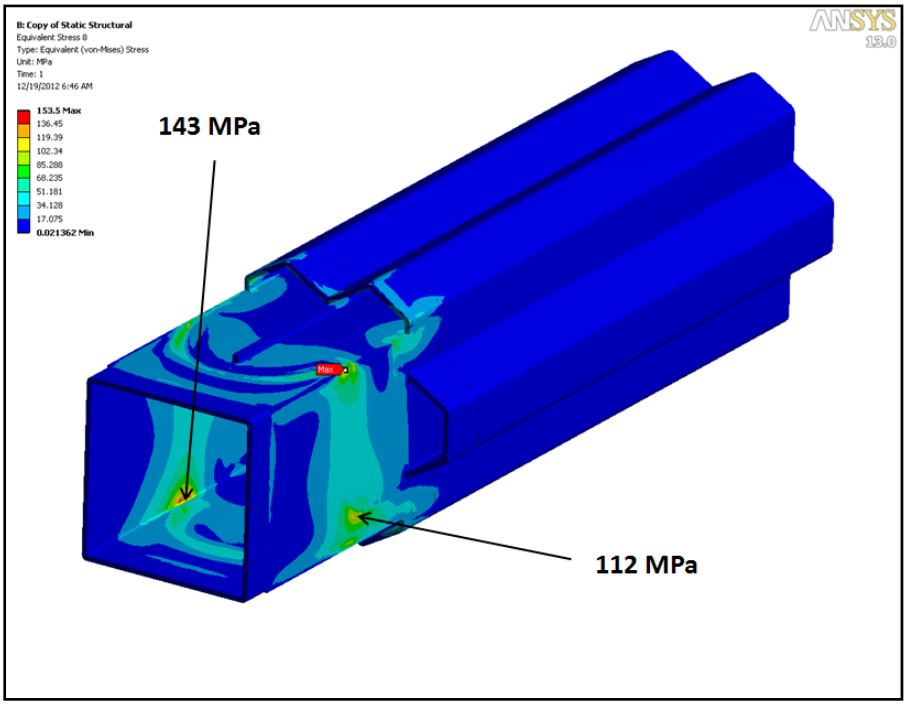

Figure II.4.8.1.1.5. Von Mises stress, extrusion, load case 1

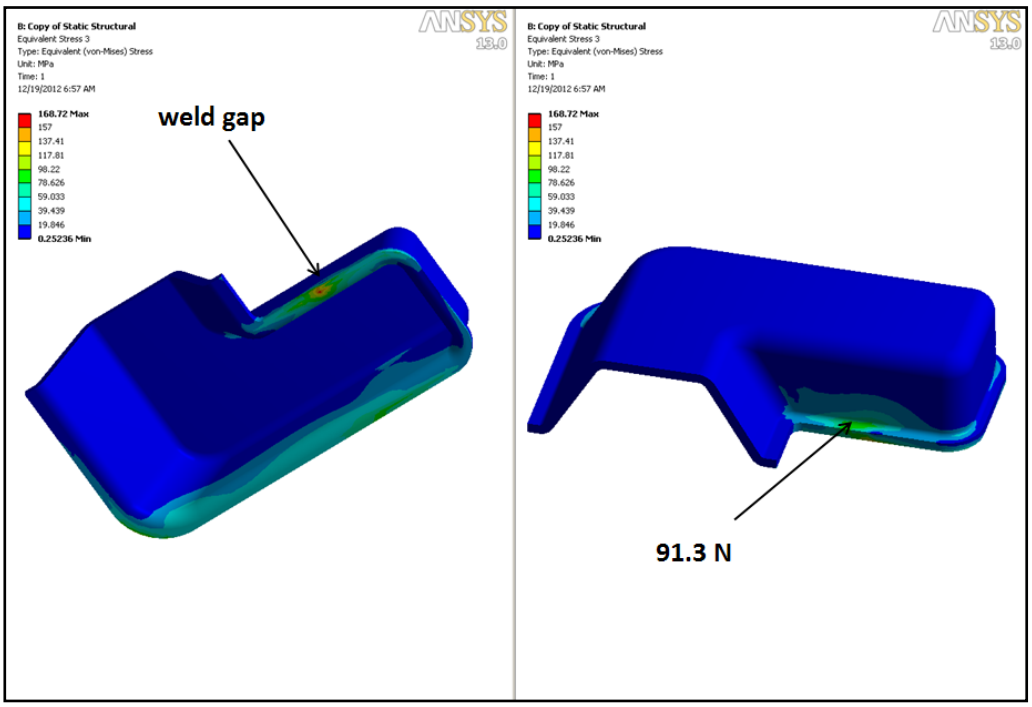

Figure II.4.8.1.1.6. Von Mises stress, L-shaped duct, load case 1

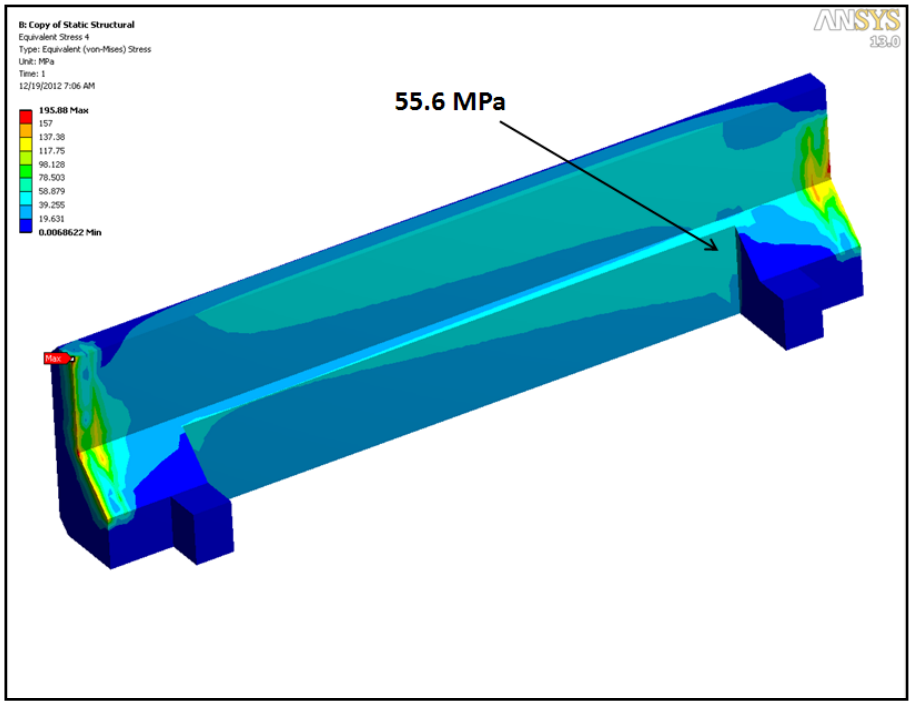

Figure II.4.8.1.1.7. Von Mises stress, port block support, load Case 1

II.4.8.1.2 Load Case 2

Plots of von Mises stress for load case 2 are shown in Figs. II.4.8.1.2.1 through II.4.8.1.2.7. Results are little changed compared to load case 1. The maximum stress of 362 MPa again occurs in the sharp ear of the port block (Fig. II.4.8.1.2.2), and again is a modeling artifact and can be ignored. As before there are some localized high stresses shown in Fig. II.4.8.1.2.3 caused by the contact elements used to simulate the welds, and again these are modeling artifacts that can be ignored. The highest real stresses in the port blocks are 226 MPa and 128 MPa, at the sharp corner at the base of a weld flange. After the 2 mm radius blend is added (Fig. II.4.8.1.2.4) the maximum real stress is 200 MPa. Figure II.4.8.1.2.5 shows stresses in the extrusion. The highest stress is 158.2 MPa and is located inside the extrusion near a corner. This is under a weld and is therefore in the HAZ, and it is fairly localized. Stresses in the L-shaped duct are shown in Fig. II.4.8.1.2.6. The maximum stress is 178 MPa and as before occurs at a modeling artifact and can be ignored. The highest real stress is 98 MPa, for a safety factor of 1.60. Stresses in the port block support are shown in Fig. II.4.8.1.2.7. The localized high stresses on either end are caused by the bonded contact used to simulate welds, and it can be ignored. The real maximum stress is 55.9 MPa, for a safety factor of 2.82.

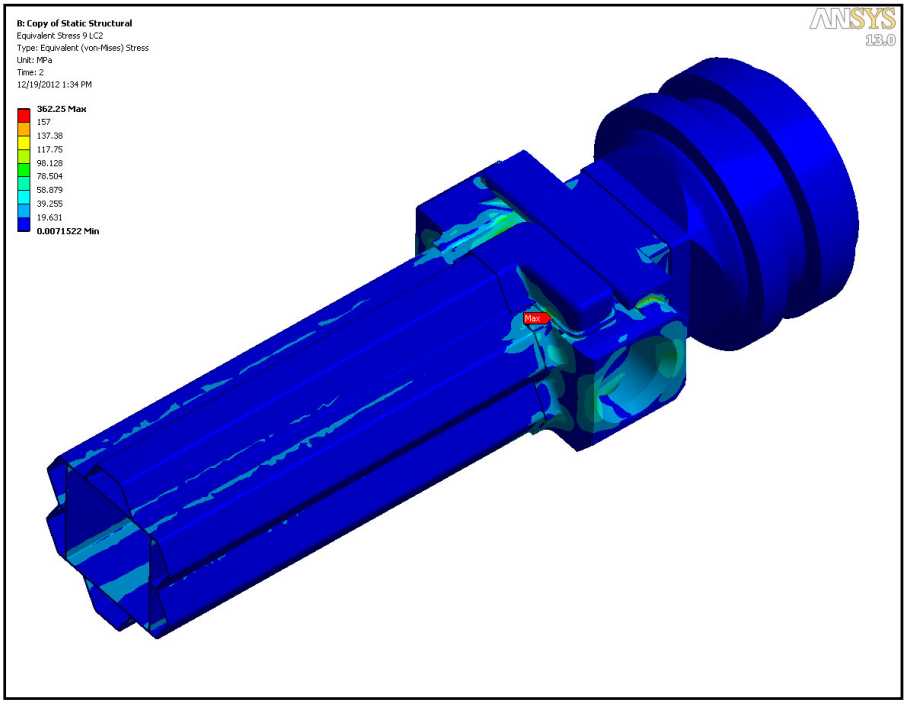

Figure II.4.8.1.2.1. Von Mises stress, load case 2

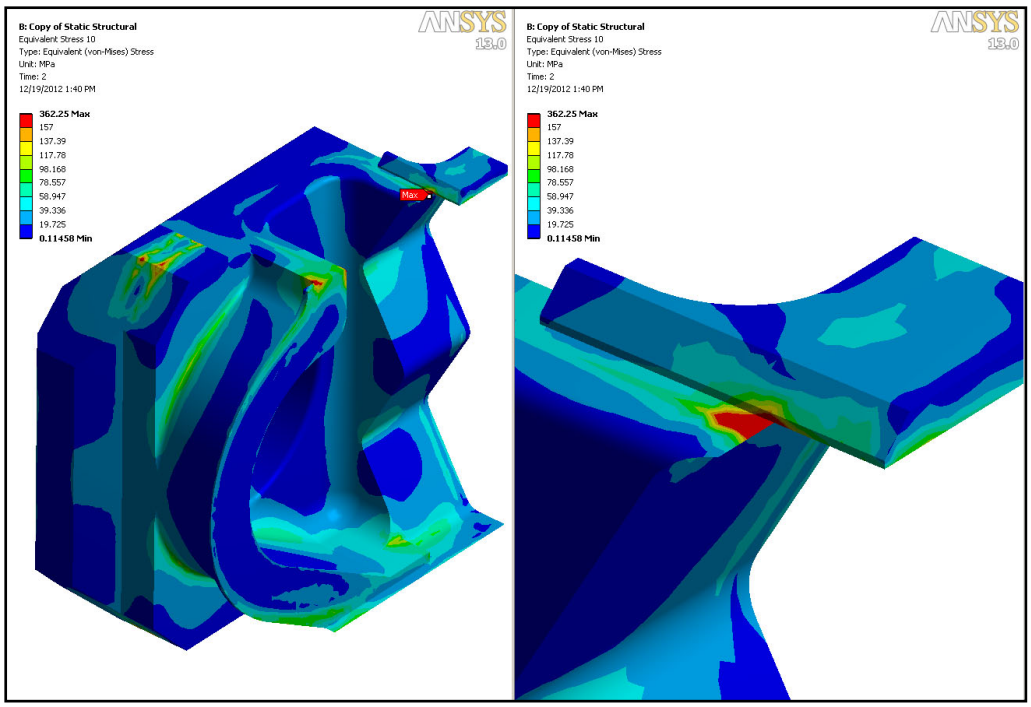

Figure II.4.8.1.2.2. Von Mises stress, port block, load case 2

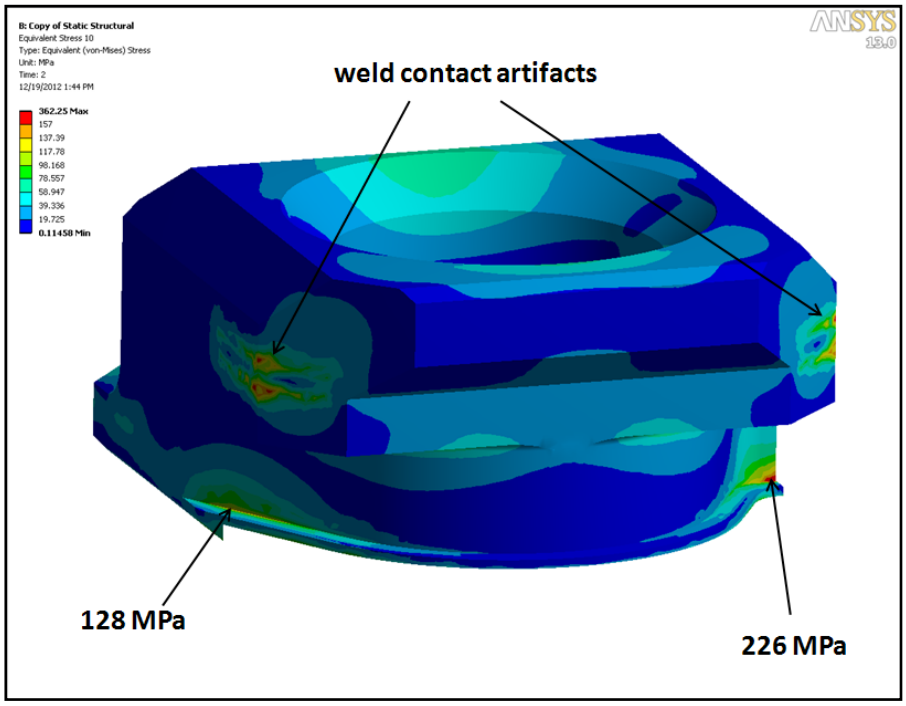

Figure II.4.8.1.2.3. Von Mises stress, port block, load case 2

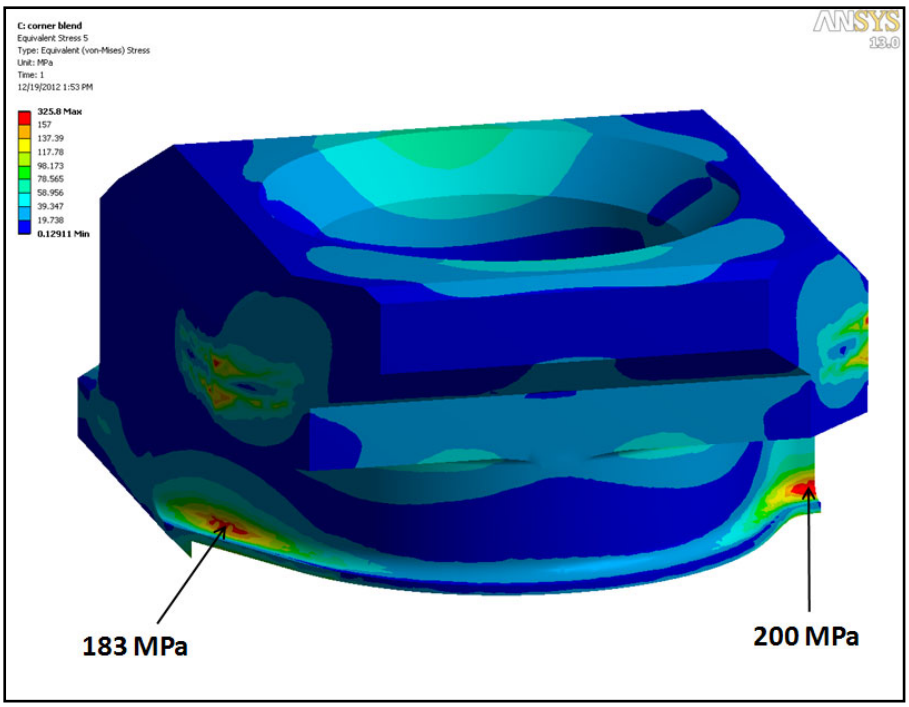

Figure II.4.8.1.2.4. Von Mises stress, revised port block, load case 2

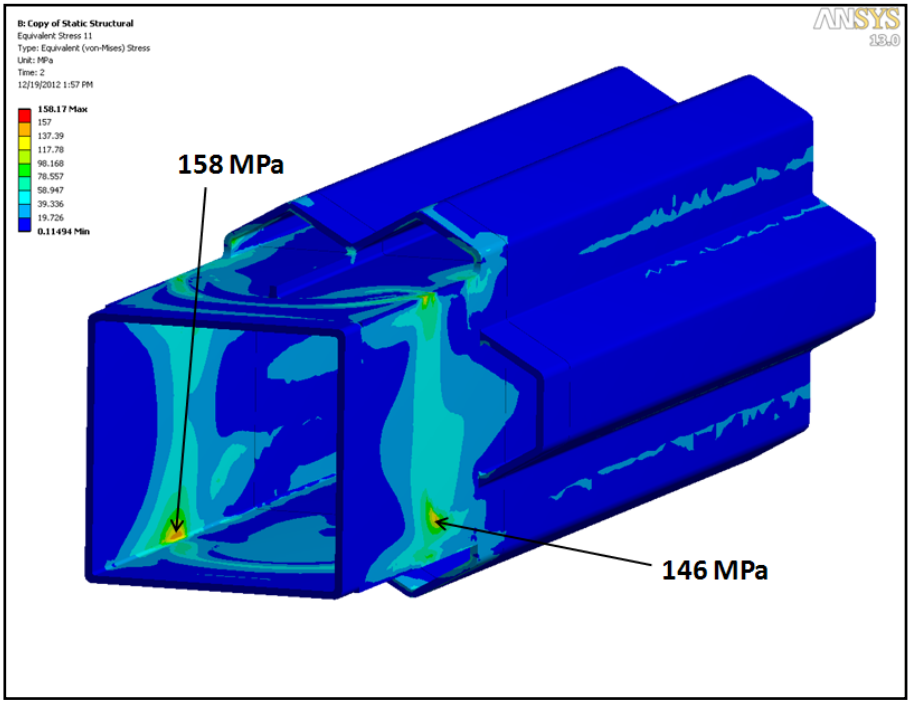

Figure II.4.8.1.2.5. Von Mises stress, extrusion, load case 2

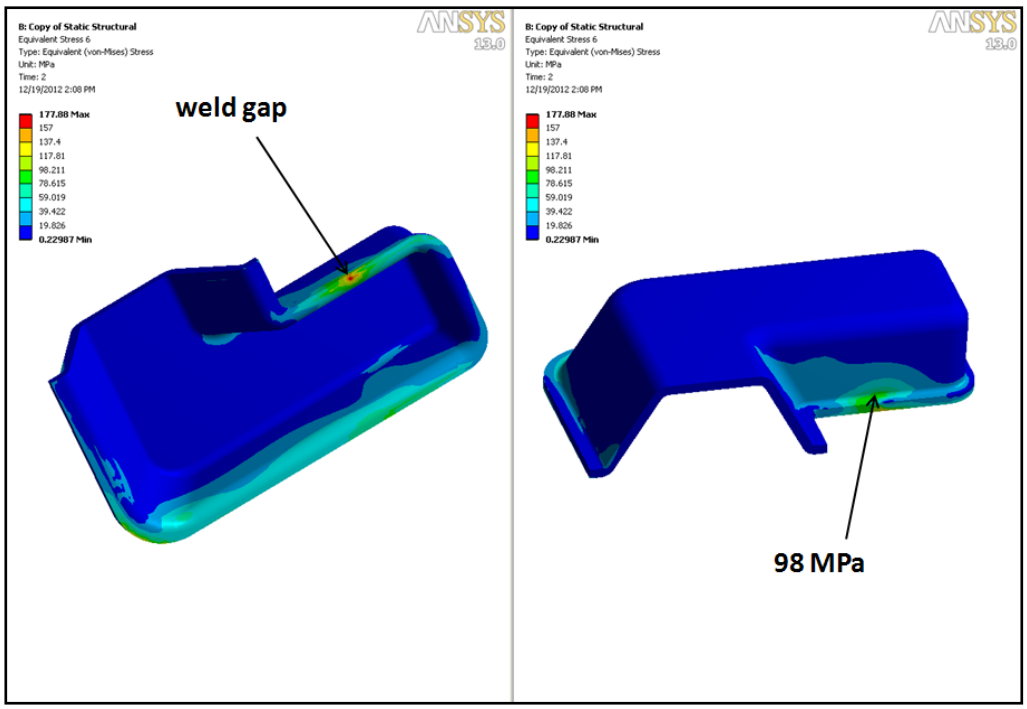

Figure II.4.8.1.2.6. Von Mises stress, L-shaped duct, load case 2

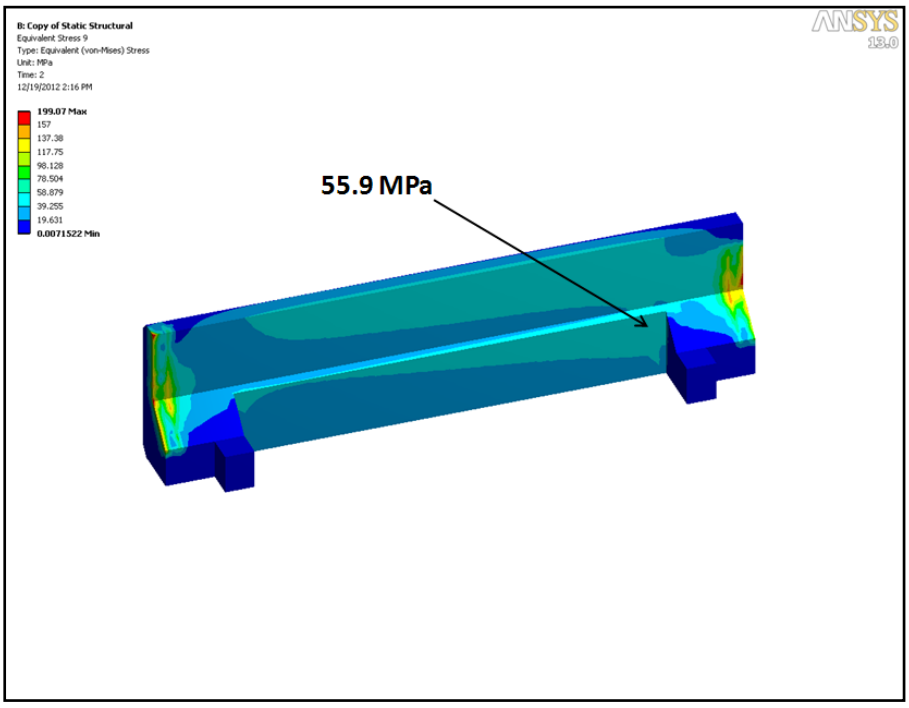

Figure II.4.8.1.2.7. Von Mises stress, port block support, load case 2

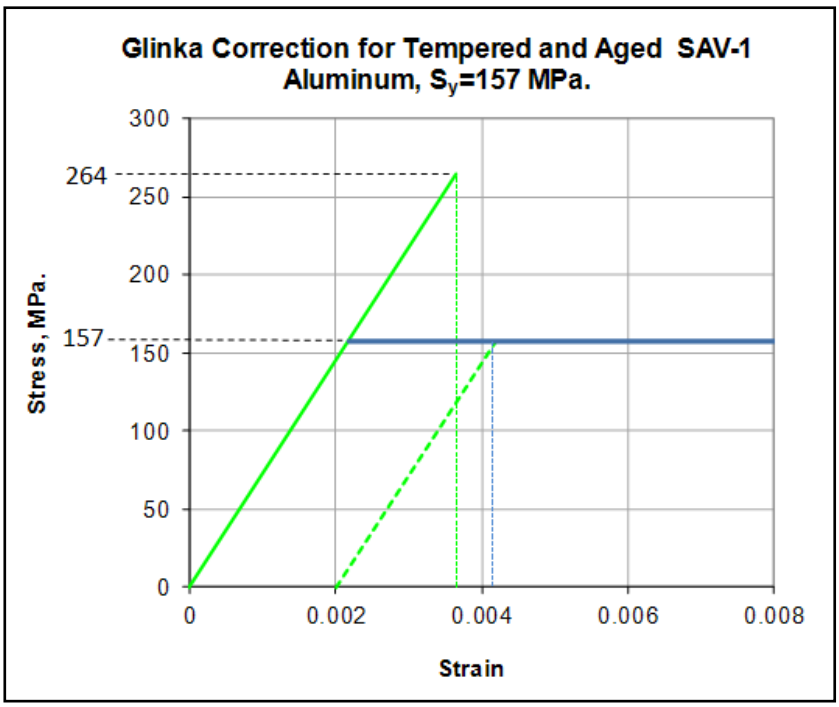

Figure II.4.8.1.2.8. Strain Corrected Yield Strength, SAV-1 Parent Material

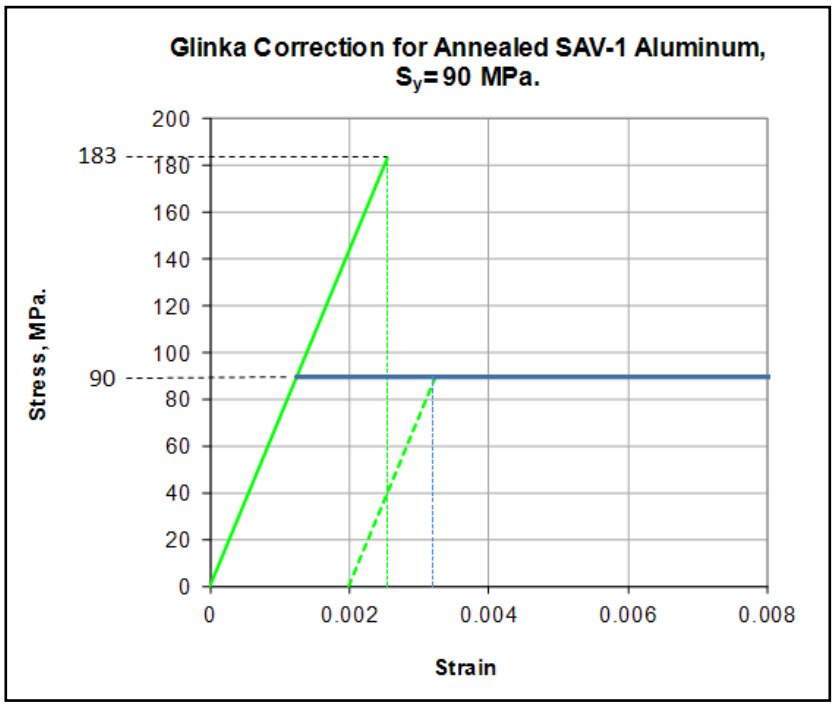

Figure II.4.8.1.2.9. Strain-corrected Yield Strength, SAV-1 Parent Mate

II.4.8.2 Lower Section, Tungsten Target Subassembly

Plots of von Mises stress for load case 3 are shown in Figs. II.4.8.2.1 through II.4.8.2.4.

The maximum stress of 79.8 MPa occurs in the HAZ in the window (Fig. II.4.8.2.2), for a safety factor of 1.13. This value is likely an artifact of the contact elements used to model the weld. The stress one element away from this location is 55.7, for a safety factor of 1.61. The next highest stress is in the main extrusion (Fig. II.4.8.2.3) and it is 62.5 MPa, for a safety factor of 1.44. The next highest stress is in the extrusion below the target (Fig. II.4.8.2.4) and it is 27.2 MPa, for a safety factor of 3.31.

Plots of von Mises stress for load case 4 are shown in Figs. II.4.8.2.5 through II.4.8.2.11. The maximum stress of 162.3 MPa occurs in the HAZ in the main extrusion. This value is likely an artifact of the contact elements used to model the weld. The stress one element away from this location is 127.3 MPa, which is below the strain-corrected value of 183 MPa. The next highest stress is in the window at a weld and is 120.9 MPa (Fig. II.4.8.2.7), which is again below the strain-corrected value. The next highest stress is in the transition piece below the target (Fig. II.4.8.2.8), and is 39.3 MPa, for a safety factor of 3.99. The next highest stress is in the extrusion below the target at a weld (Fig. II.4.8.2.9), and is 30.2 MPa, for a safety factor of 2.98.

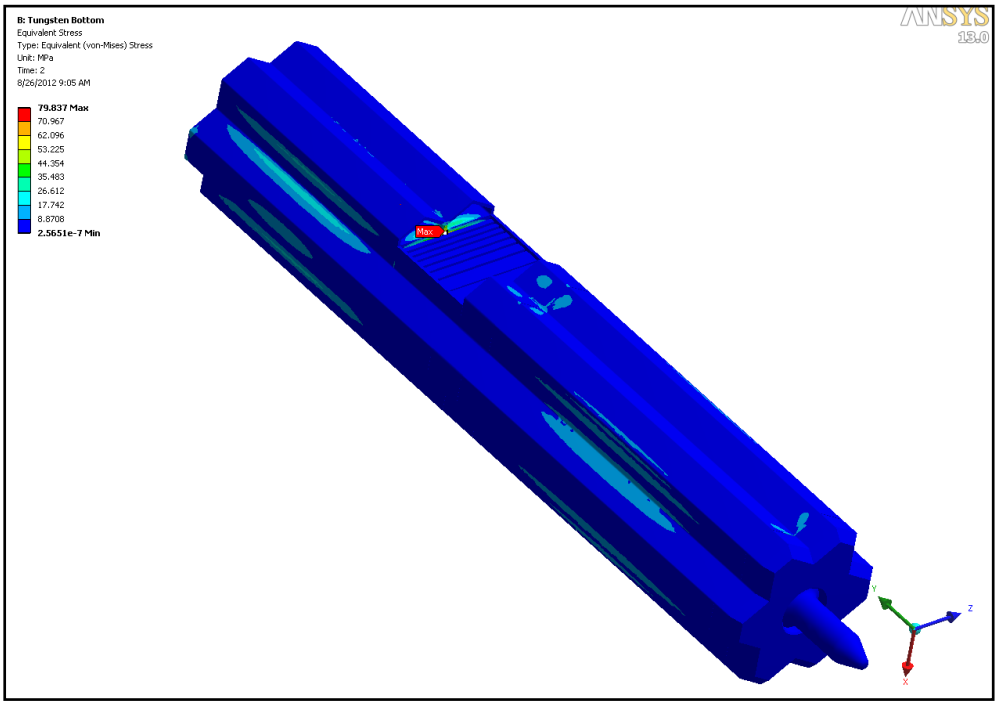

Figure II.4.8.2.1. Von Mises stress, lower section, tungsten target, load case 3

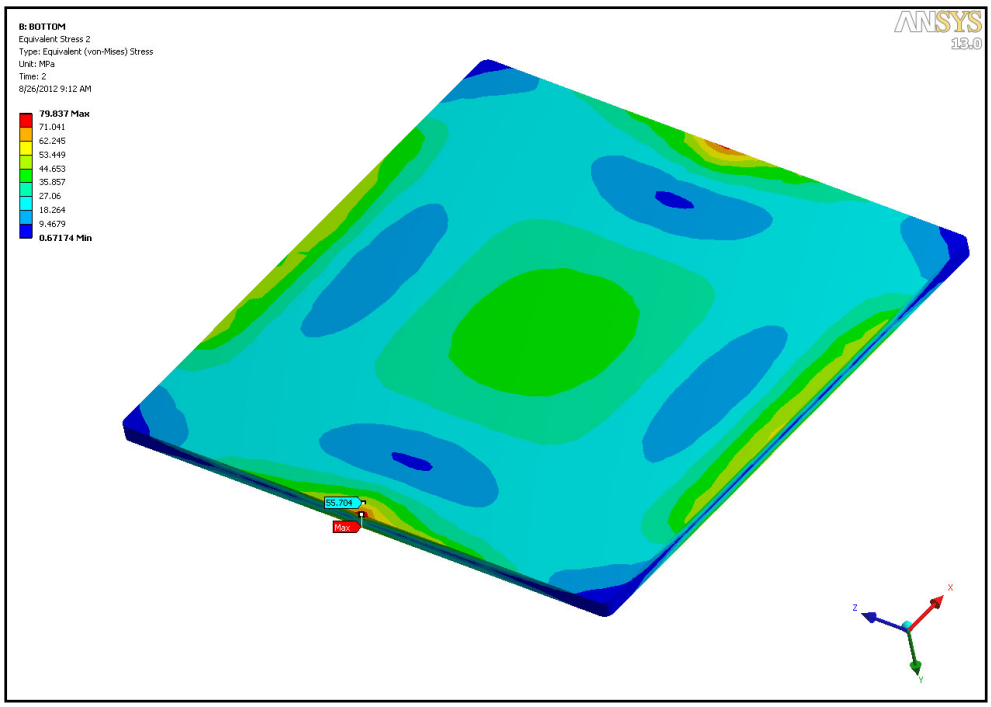

Figure II.4.8.2.2. Von Mises stress, lower section, tungsten target, load case 3

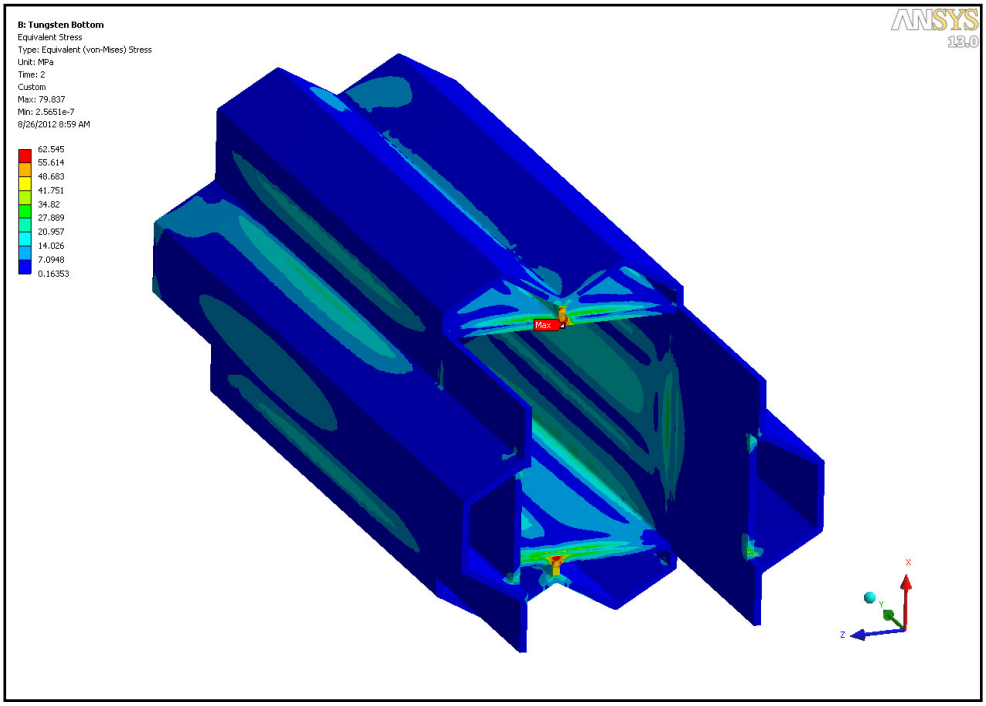

Figure II.4.8.2.3. Von Mises stress, lower section, tungsten target, load case 3

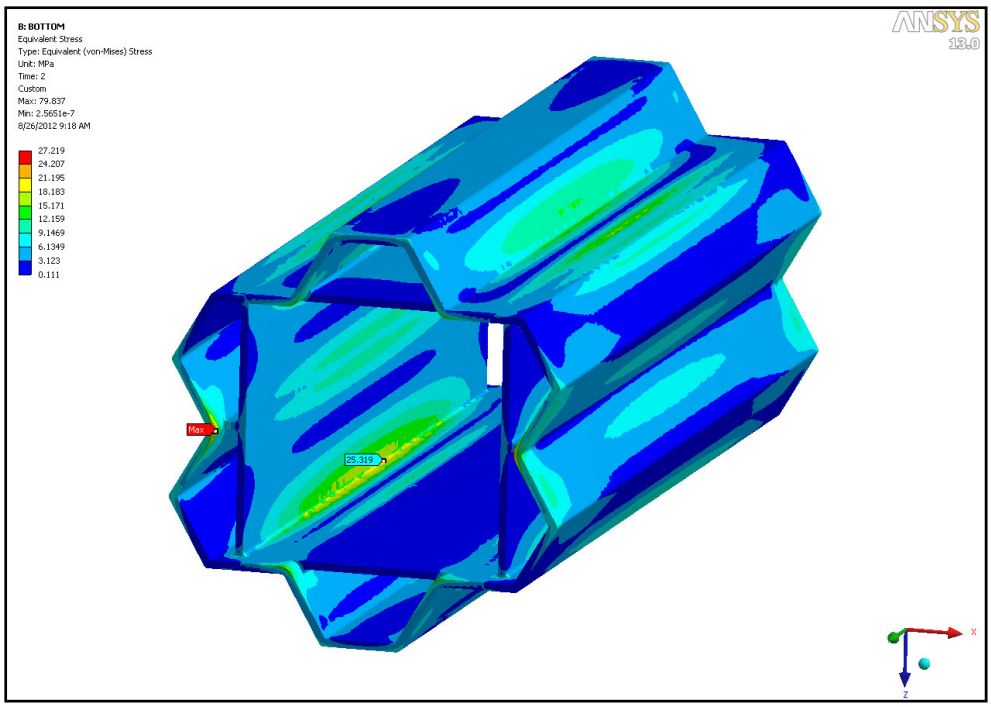

Figure II.4.8.2.4. Von Mises stress, lower section, tungsten target, load case 3

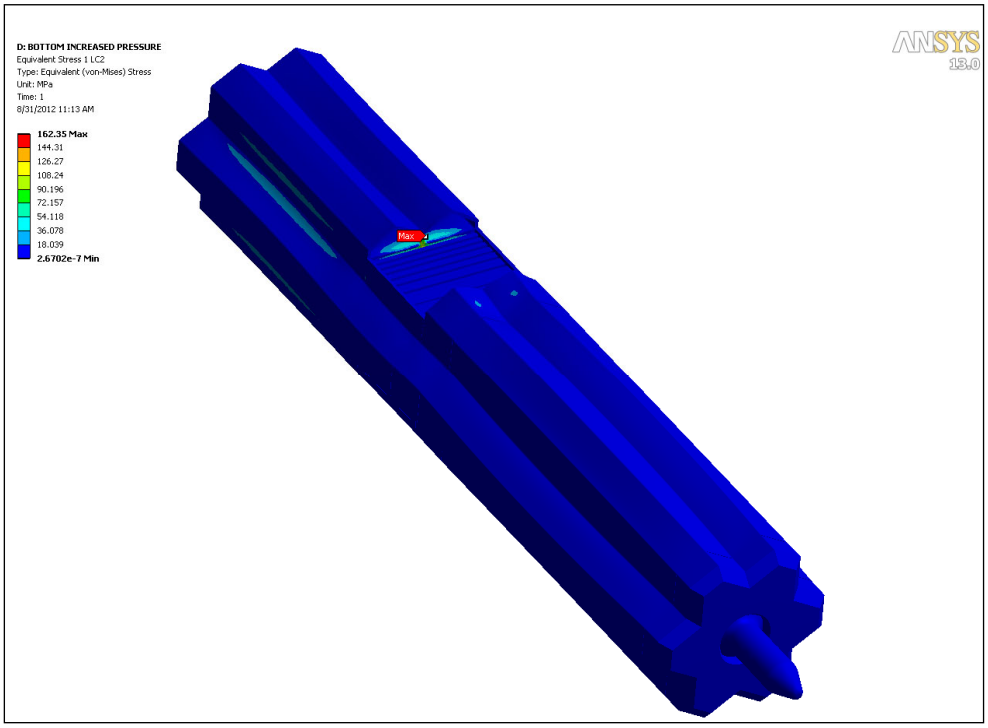

Figure II.4.8.2.5. Von Mises stress, lower section, tungsten target, load case 4

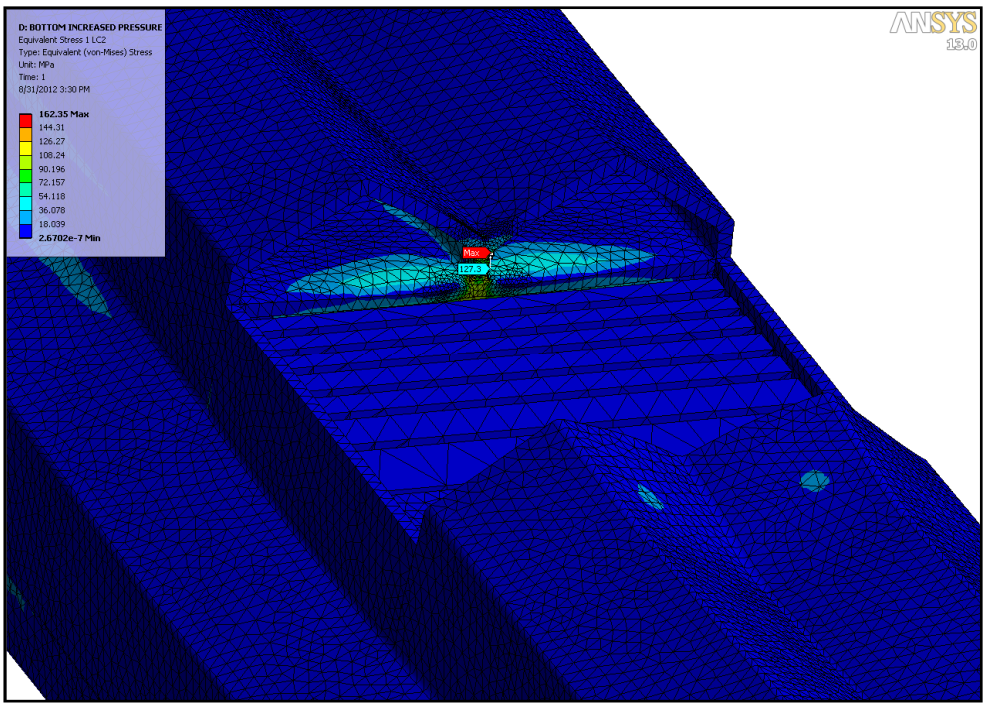

Figure II.4.8.2.6. Von Mises stress, lower section, tungsten target, load case 4

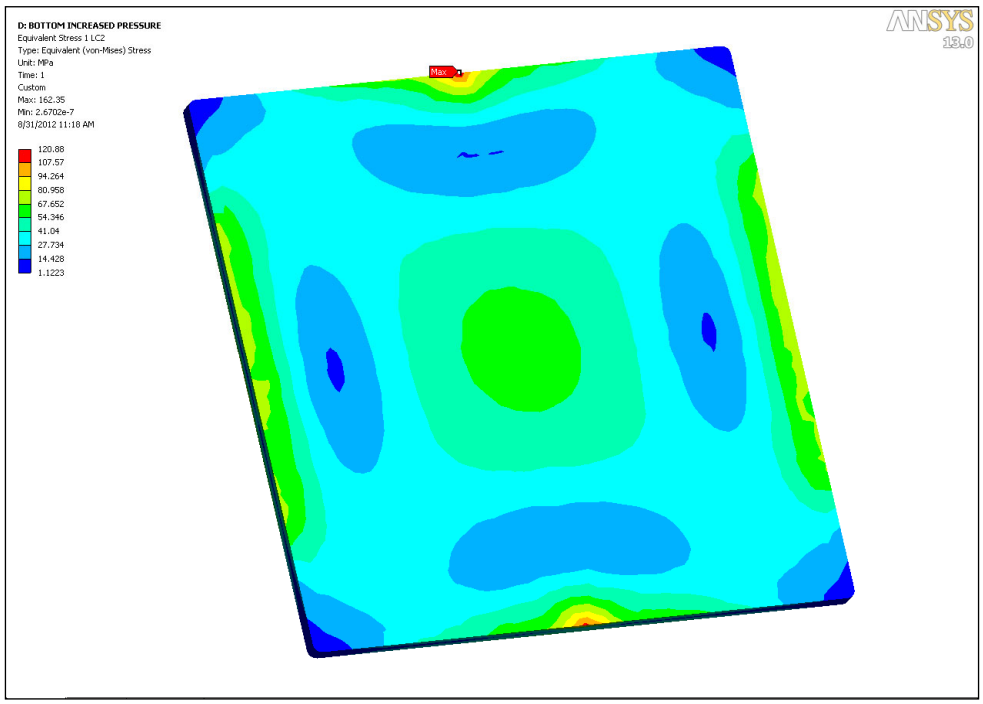

Figure II.4.8.2.7. Von Mises stress, lower section, tungsten target, load case 4

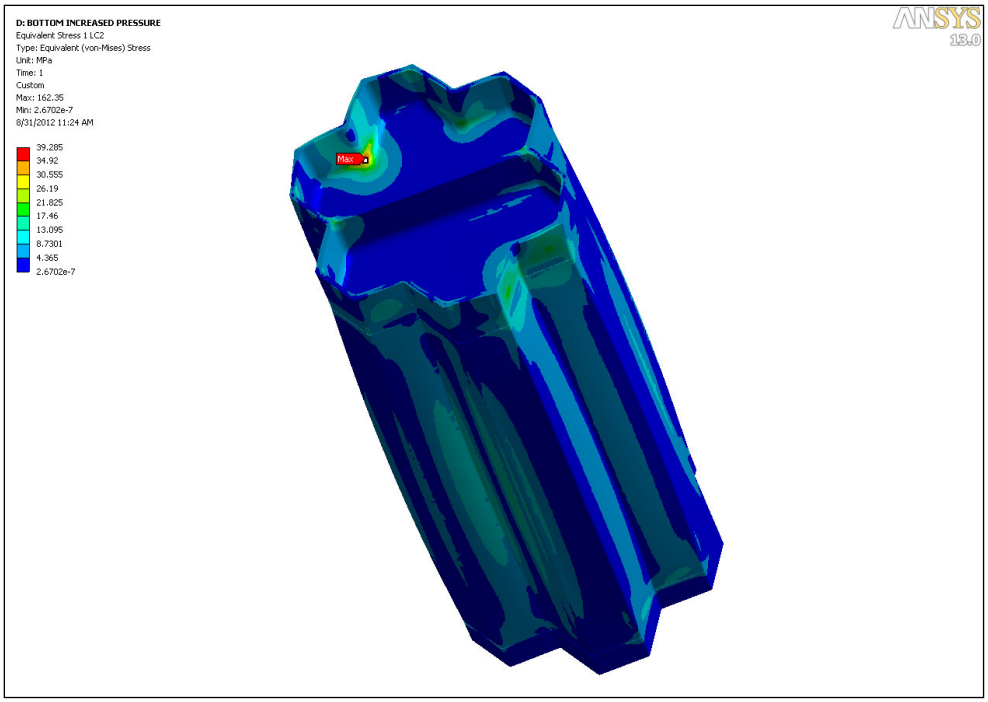

Figure II.4.8.2.8. Von Mises stress, lower section, tungsten target, load case 4

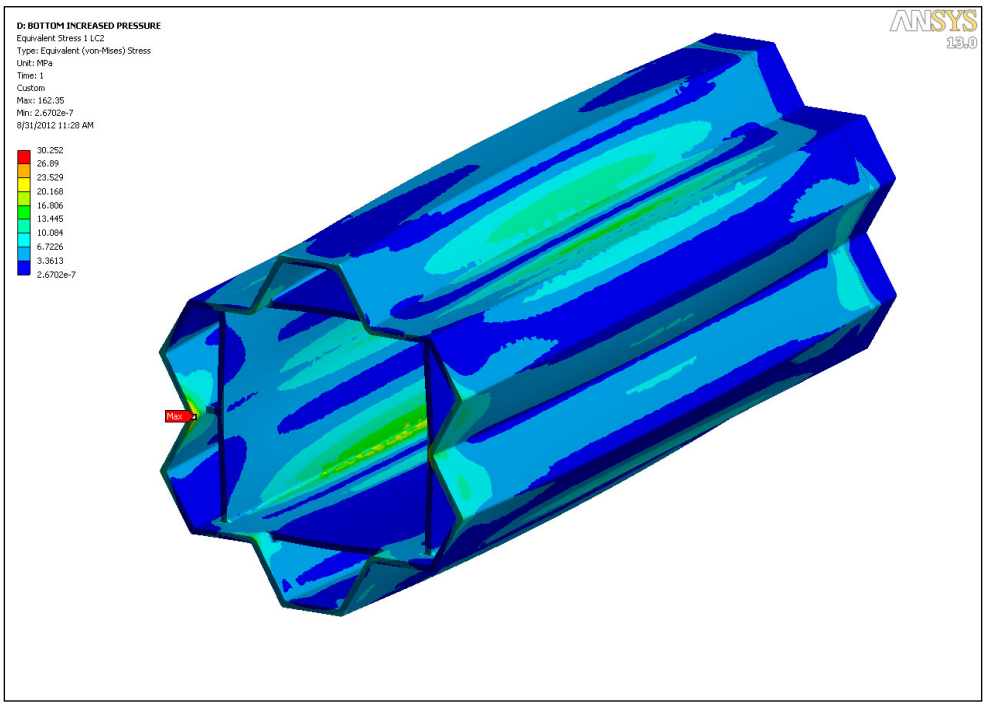

Figure II.4.8.2.9. Von Mises stress, lower section, tungsten target, load case 4

Load Case 5 was added to determine the linearity of any stress increase due to increases in pressure above Load Case 4. Table II.4.8.2.1 shows stress values at the highest stress

locations for load cases 3, 4, and 5, and Fig. II.4.8.2.10 shows these stresses plotted as a function of pressure.

Table II.4.8.2.1 Von Mises stress at selected locations, tungsten target, load cases 3, 4, and 5

Location	Description	Stress by load case (MPa)		
		3	4	5
1	Extrusion Web	62.5	162.3	245.6
2	Edge of Window	79.8	120.9	162.8
Pressure		Base	Base + 1 atm.	Base + 2 atm.

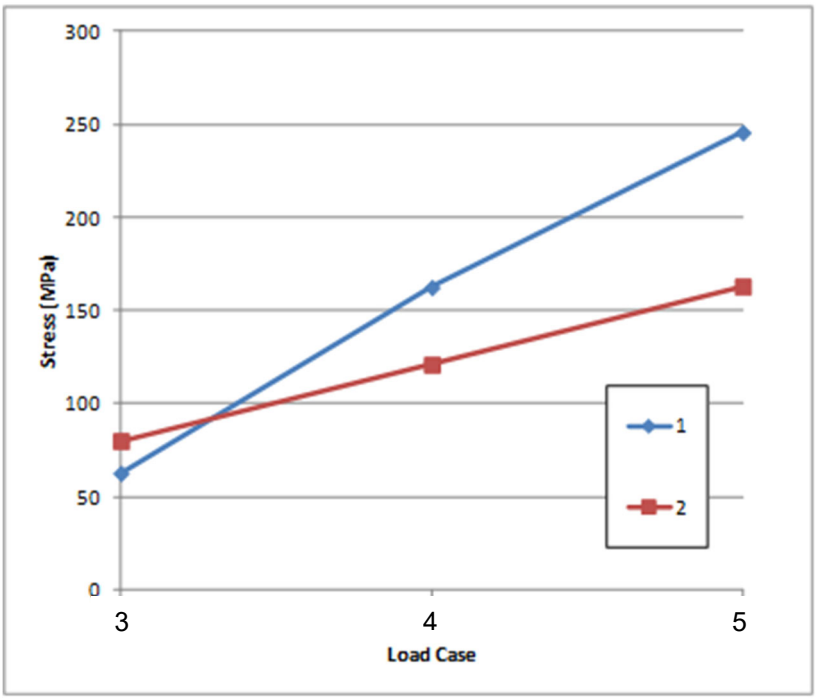

Figure II.4.8.2.10. Von Mises stress at selected locations vs. pressure, tungsten target, for load cases 3, 4 and 5 for locations 1 and 2

II.4.8.3 Lower Section, Uranium Target Subassembly

Plots of von Mises stress for the uranium target assembly for load case 3 are shown in Figs. II.4.8.3.1 through II.4.8.3.4. The maximum stress of 90.3 MPa occurs in the HAZ in the window (Fig. II.4.8.3.3). This value is likely an artifact of the contact elements used to model the weld. The stress one element away from this location is 59.9, for a safety factor of 1.50. The next highest stress is in the main extrusion (Fig. II.4.8.3.2) and it is 62.7 MPa, for a safety factor of 1.44. The next highest stress is in the extrusion below the target (Fig. II.4.8.3.4) and it is 27.2 MPa, for a safety factor of 3.31.

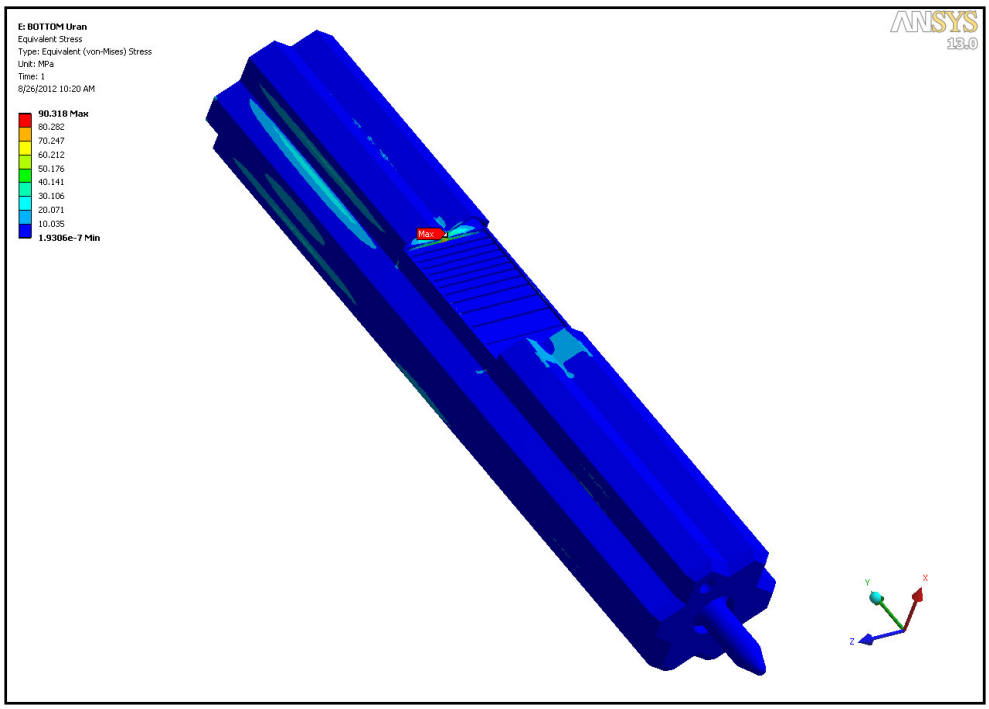

Figure II.4.8.3.1. Von Mises stress, lower section, uranium target, load case 3

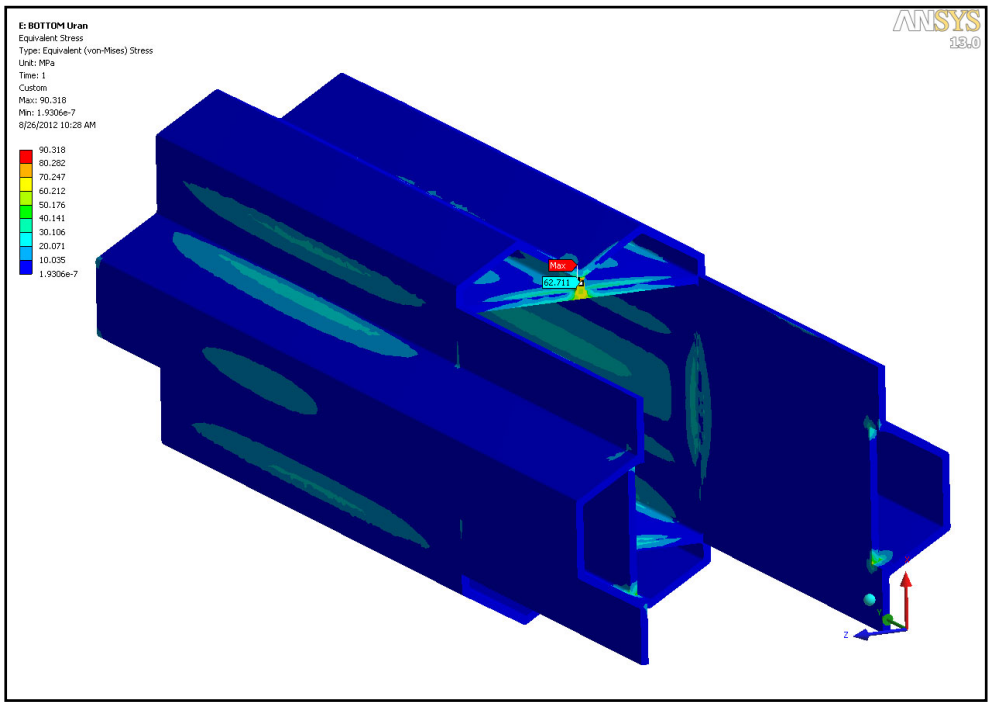

Figure II.4.8.3.2. Von Mises stress, lower section, uranium target, load case 3

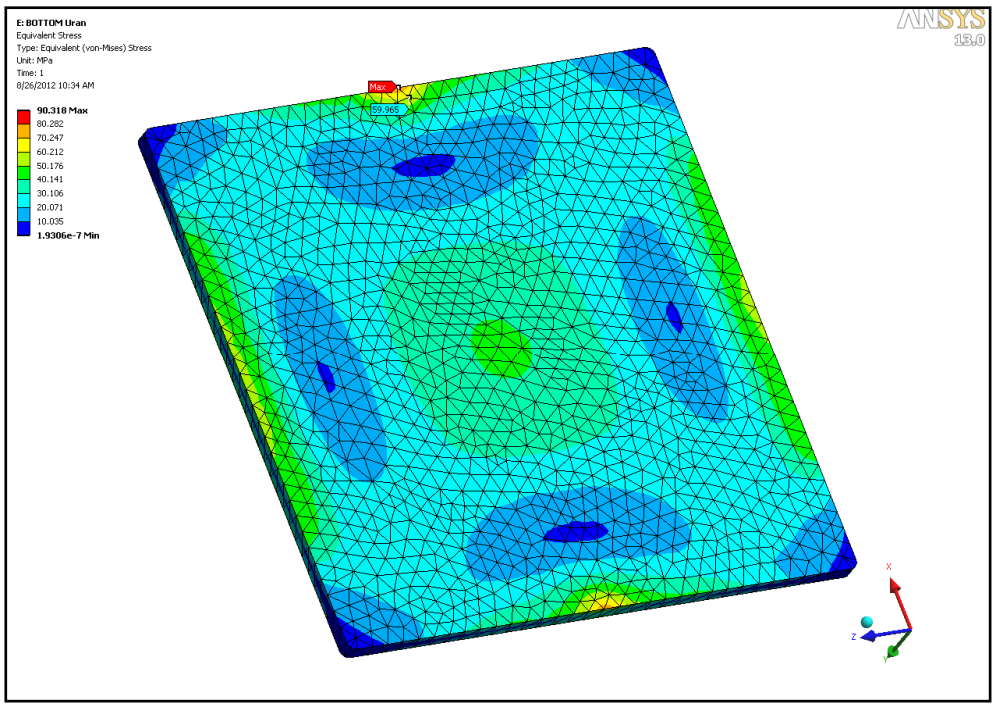

Figure II.4.8.3.3. Von Mises stress, lower section, uranium target, load case 3

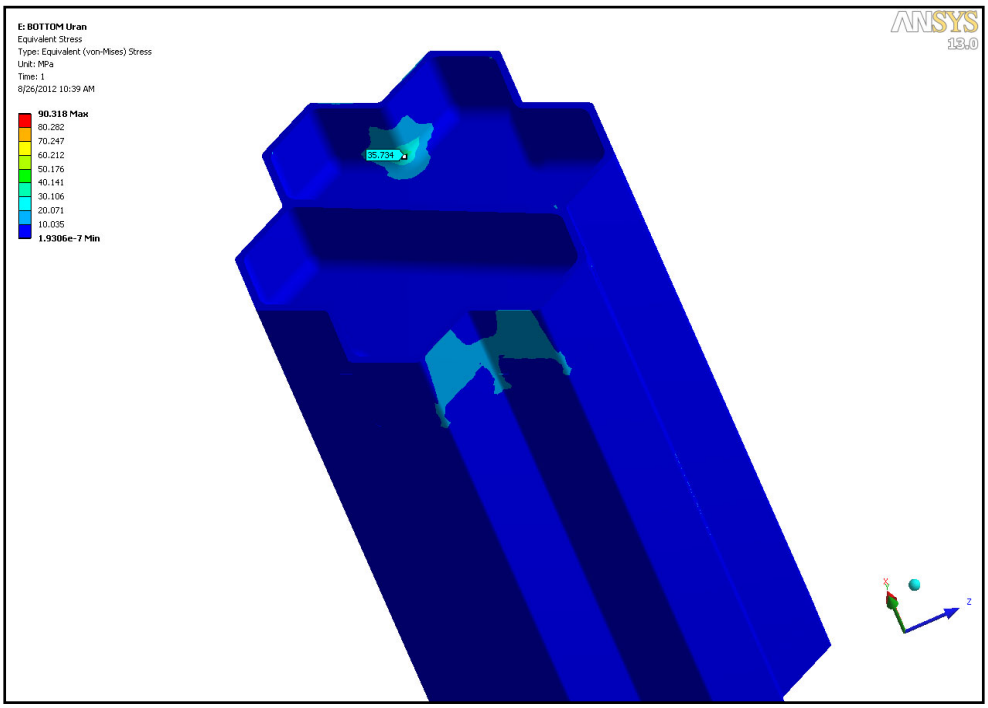

Figure II.4.8.3.4. Von Mises stress, lower section, uranium target, load case 3

Plots of von Mises stress for uranium target for load case 4 are shown in Figs. II.4.8.3.5 through II.4.8.3.9. The maximum stress of 231.6 MPa occurs in the HAZ in the main

extrusion (Fig. II.4.8.3.6). This value is likely an artifact of the contact elements used to model the weld. The stress one element away from this location is 192.2 MPa. The next highest stress is in the window at a weld, and it is about 94 MPa (Fig. II.4.8.3.8). The next highest stress is in the transition piece below the target (Fig. II.4.8.3.10), and it is 63.7 MPa, for a safety factor of 1.41. The next highest stress is in the extrusion below the target at a weld (II.4.8.3.11), and it is 40.2 MPa, for a safety factor of 2.24.

As before, load case 5 was added to determine the linearity of any stress increase due to increases in pressure above load case 4. Table II.4.8.3.1 shows stress values at the highest stress locations for load cases 3, 4, and 5, and Fig. II.4.8.3.10 shows these stresses plotted as a function of pressure.

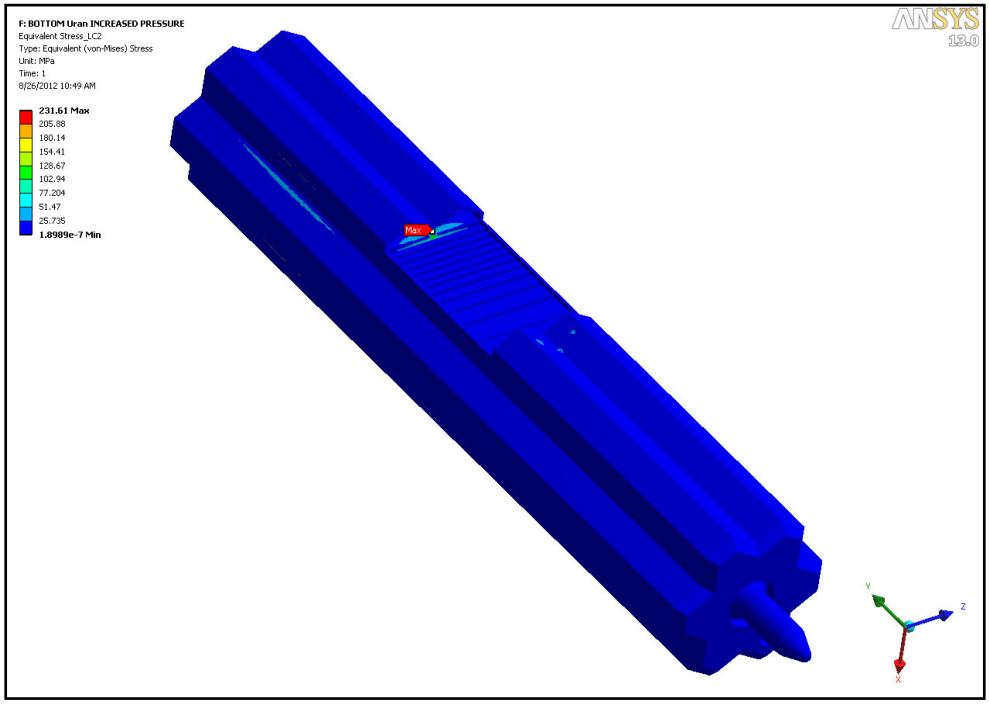

Figure II.4.8.3.5. Von Mises stress, lower section, uranium target, load case 4

Table II.4.8.3.1. Von Mises stress at selected locations, uranium target, load cases 3, 4, and 5

Location	Description	Stress by load case (MPa)		
		3	4	5
1	Extrusion Web	62.7	231.6	349
2	Edge of Window	90.3	118	160
Pressure		Base	Base + 1 atm.	Base + 2 atm.

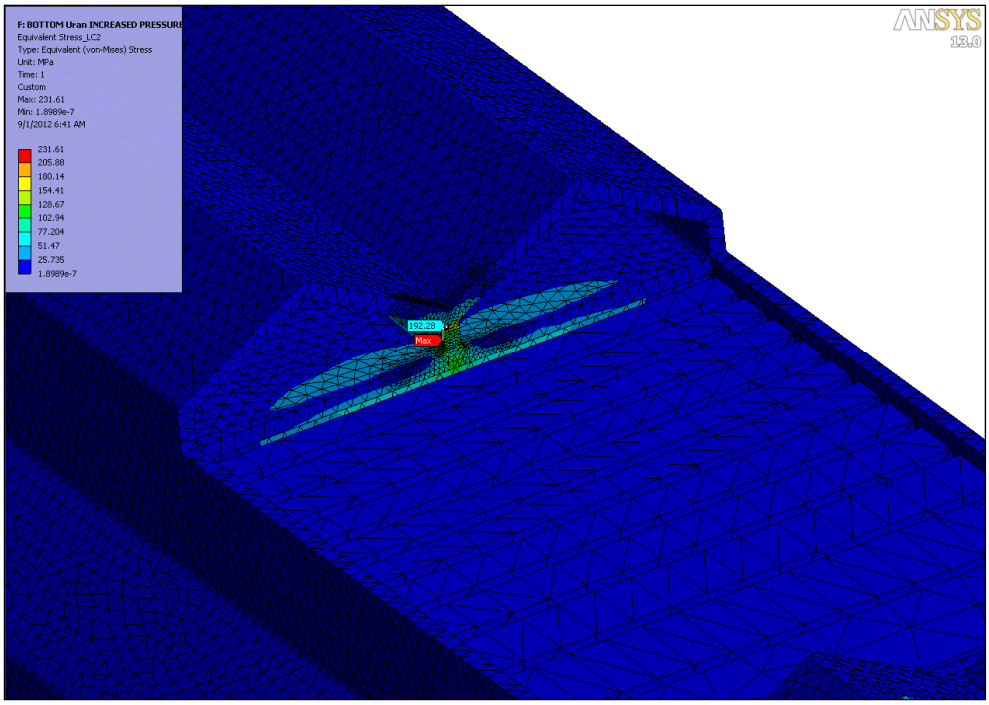

Figure II.4.8.3.6. Von Mises stress, lower section, uranium target, load case 4

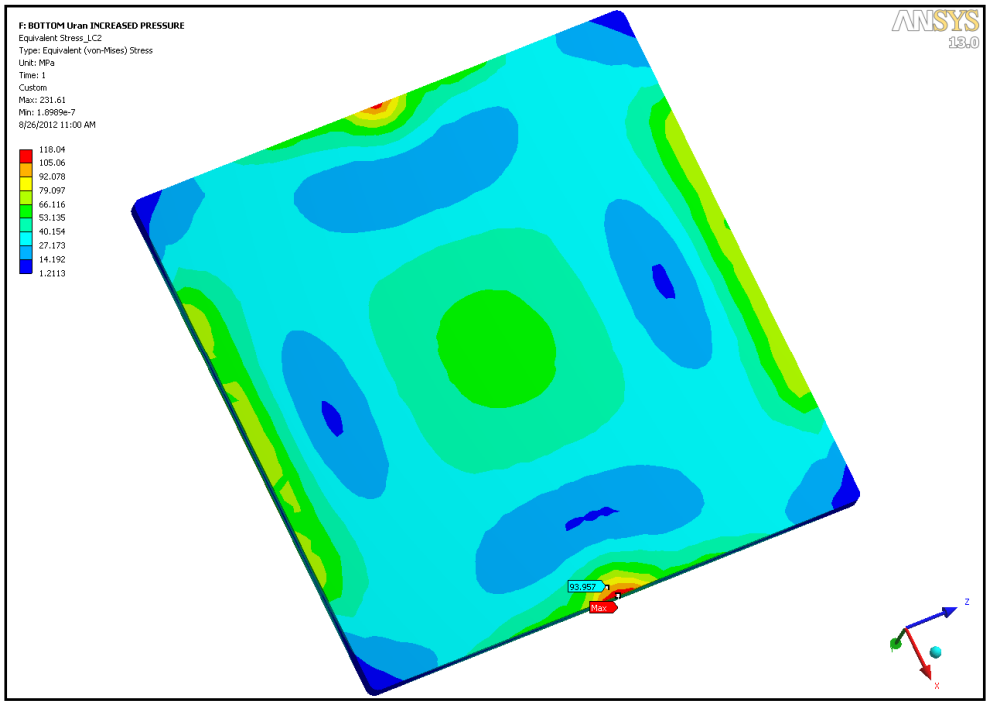

Figure II.4.8.3.7. Von Mises stress, lower section, uranium target, load case 4

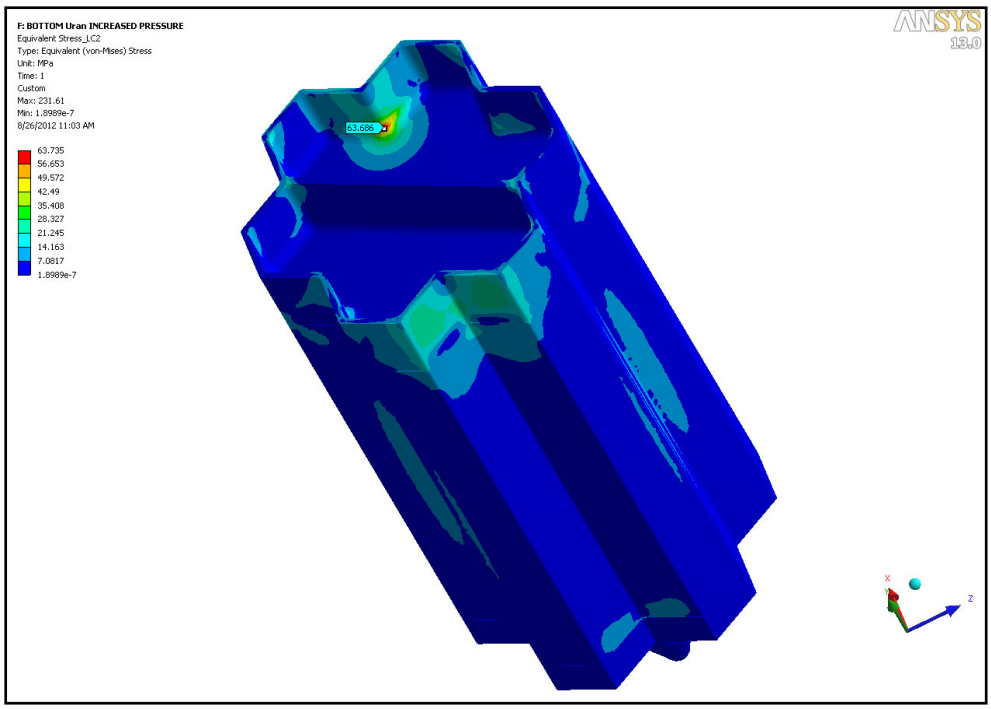

Figure II.4.8.3.8. Von Mises stress, lower section, uranium target, load case 4

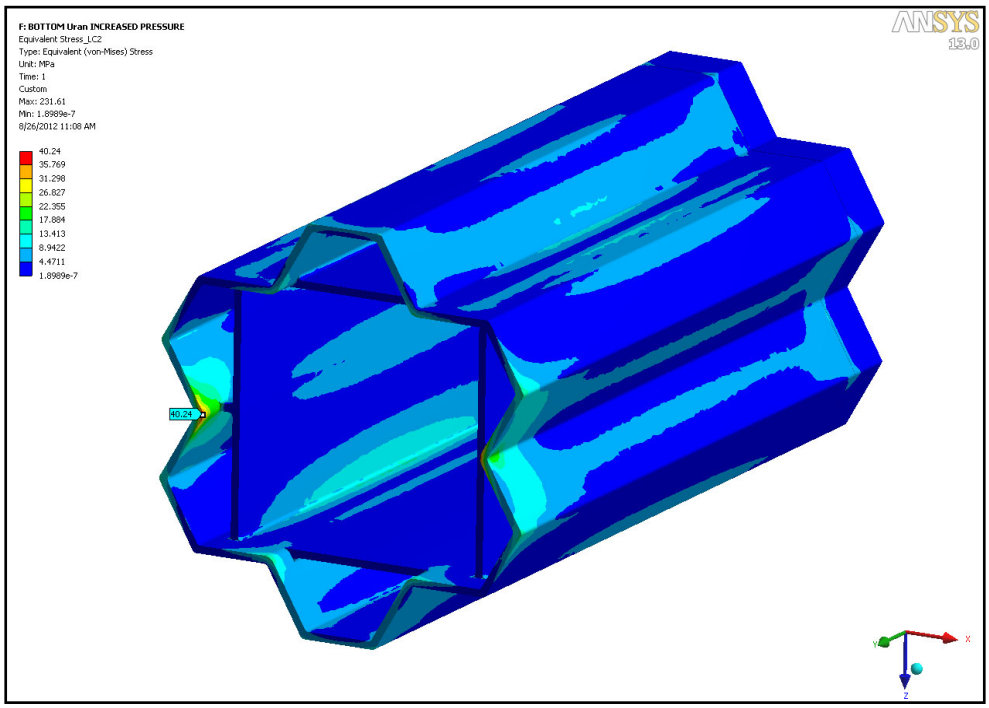

Figure II.4.8.3.9. Von Mises stress, lower section, uranium target, load case 4

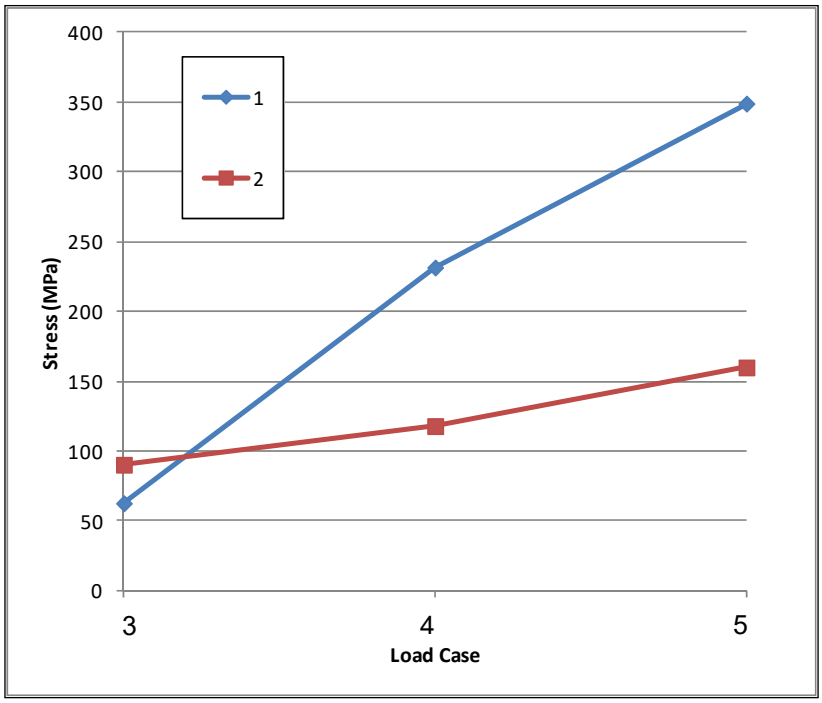

Figure II.4.8.3.10. Von Mises stress at selected locations vs. pressure, uranium target, for load cases 3, 4, and 5 at locations 1 and 2

II.4.8.4 Window Weld Analysis, Load Case 6

A weld analysis was performed on the continuous single-sided fillet weld that attaches the beam window to the main extrusion. This was done because this weld is crucial to proper target function. The CAD geometry here allowed a multi-body part to be created, which avoids the use of bonded contact and gives accurate weld reaction forces. A simplified model was created of the target and subjected to the pressure loads used in load case 3. Nodal reaction loads at the weld were extracted from the results with a macro and were used to determine weld stresses using the method described in Shigley [II.4.3]. The allowable weld stress and weld quality and efficiency values were taken from the ASME Boiler and Pressure Vessel Code (BPVC) [Ref II.4.4]. The weld was assumed to be continuous, un-machined, and uninspected. The basic weld size was assumed to be equal to the 2.0 mm window thickness. The von Mises stress is plotted in Fig. II.4.8.4.1, and the calculation is summarized in Table II.4.8.4.1, which shows a safety factor for this weld of 9.24

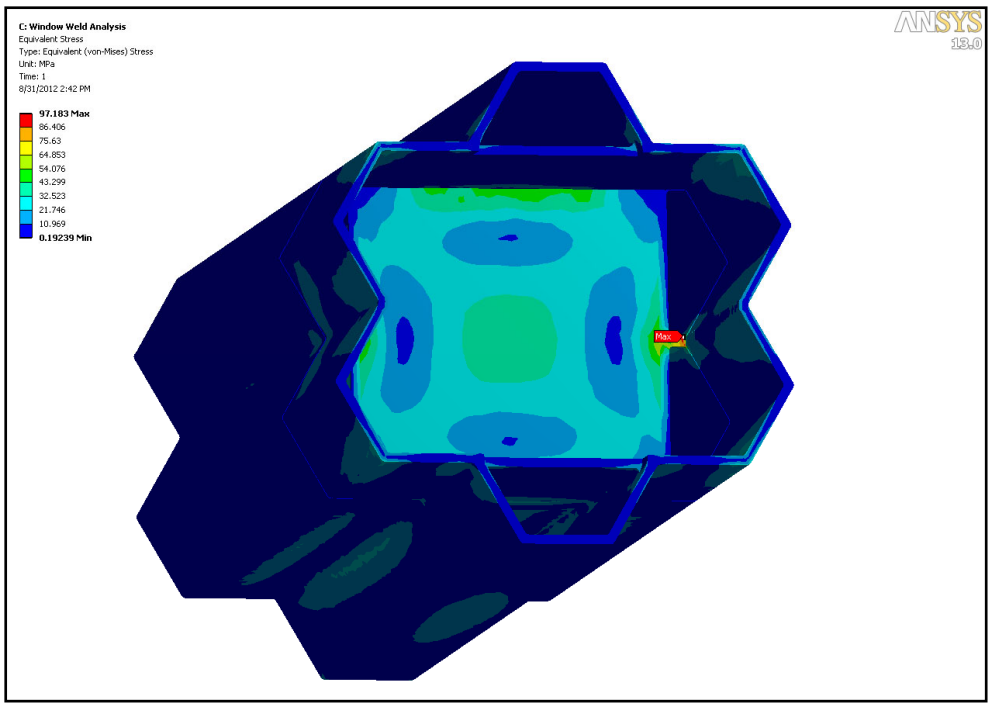

Figure II.4.8.4.1. Von Mises stress in weld analysis model

Table II.4.8.4.1. Summary of weld analysis calculations

F_{sy} = 90 MPa Weld Efficiency 0.50

F_s = 60.00 MPa Weld Quality 0.85

Weld	Leg Length (d)	Basic Weld Size	Throat Area (A)	Shear (FX)	Shear (FY)	Normal (FZ)	F_{shear_fx}	F_{shear_fy}	F_{normal_fz}	F_{weld}	$F_{allowable}$	FoS
	mm	mm	mm^2	Newton	Newton	Newton	Mpa	Mpa	Mpa	Mpa	Mpa	
1	64.000	2.000	90.496	219	-13	-120	2.42	0.15	1.33	2.76	26	9.24

II.4.9 Discussion

This analysis was carried out using the design concept, the mentioned assumptions, and the assumed weld configuration. Load cases did not include piping stresses, fluid swirling, temperature loading, etc. Some material properties are approximate. Accepted engineering principles were used for the analyses. Yielding was evaluated by comparing the von Mises stress as defined by the maximum distortion energy failure theory directly to the yield strength of the material. No knockdown factors for boundary condition uncertainty, material variability, surface finish, construction variations, etc. were applied. In general, stresses are low. The exceptions are localized stresses at two corners, and

at welds. The material used to construct the target assembly is ductile, and these localized stresses would be blunted by localized plastic response. These high stresses are in some cases due to the bonded contact used to join components at the welds. Stresses calculated with the finite element method at welds are generally not accurate because the actual weld geometry is not modeled.

It is recommended that the two-millimeter blend be added to the port block as detailed above in Sec. II.4.8.1.1. The stresses reported at the corner are likely low because of nodal averaging effects near the stress singularity in the corner. This is indicated by an increase in stress on the left side of Figs. II.4.8.1.1.4 and II.4.8.1.2.4. The stress values in these plots accurately represent the stress state in this part of the port block.

The analysis assumptions are reasonable and prudent for the design concept analysis. Von Mises stresses are generally low, so the use of a linear elastic isotropic homogeneous material model is justified. Where localized stresses are above yield, a suitable adjustment has been made. Deflections are small, so small deflection theory is appropriate. The other assumptions generally fit within the context of this analysis. Within the limits of these assumptions, it is believed that this analysis accurately represents the performance of this design for the intended use.

Conclusions

Based on the results of this analysis, and subject to the listed assumptions, it is concluded that the tungsten and uranium target subassemblies are structurally feasible designs.

References

II.4.1. Ansys Mechanical, Version 13.0, Build date 11/2/2009, Ansys Inc, Pittsburg, PA
II.4.2. Glinka, G, Energy Density Approach to Calculation on Inelastic Strain-Stress Near Notches and Cracks, *Engineering Fracture Mechanics*, Vol,22, No. 3, 1985.
II.4.3. Shigley, J. E. and Mitchell, L. D. *Mechanical Engineering Design, Fourth Edition*, McGraw Hill, New York, 1983, Chapter 7.
II.4.4. *ASME Boiler and Pressure Vessel Code, Section VIII, Division 1*, American Society of Mechanical Engineers, New York, NY 2010.

II.5 Target Mechanical Design

At the center of the KIPT subcritical assembly is a heavy metal target assembly. This target generates neutrons from the interaction of the high-energy electron beam from the linear electron accelerator with the target material. These neutrons drive the subcritical assembly, which utilizes low-enriched uranium fuel assemblies. The target assembly has a finite service life, and it is replaced as a unit at the end of its productive life. The target assembly is not intended to be reused.
Two target designs have been developed for use in the KIPT experimental neutron source facility. The first target design uses seven tungsten plates (the 7W target), and the second target design uses eleven uranium plates (the 11U target). The thickness of the plates

varies within the target stack as the energy deposition (and therefore heat load) varies with distance along the electron beam line. The two target assembly designs are physically interchangeable but have slightly different operational performance. Both target assemblies are shown in Fig. II.5.1.

The target material within the target assembly is made of tungsten or uranium plates, separated by small gaps for the water coolant flow. The coolant is forced through the gaps to remove the energy deposited in the target assembly by the electron beam and to maintain acceptable temperatures within the target assembly materials. Figures II.5.2 and II.5.3 identify the location of the target assembly position within the subcritical assembly. The target coolant is separated from the vacuum of the electron beam tube by the electron beam window, as shown in Figs. II.5.4 and II.5.6. Individual target plates are either cladded with aluminum alloy, in the case of the uranium target, or coated with a thin layer of tantalum. The tantalum coating prevents the coolant from contacting the tungsten material, which prevents the target erosion/corrosion by the water coolant.

The target assembly is a welded aluminum structure (SAV-1 aluminum alloy) containing the target plates. The body of the target assembly is an aluminum extrusion approximately 2.6 meters long. A cross section of the target body extrusion is shown in Figure II.5.5. The aluminum extrusion provides six channels for target coolant flow, and one central square channel for the electron beam to reach the target plates. The target assembly has a flange at the top to connect with the electron beam tube and two ports to connect the target primary coolant system. To allow service replacement of the target assembly during the operational life of the KIPT facility, the coolant and electron beam (vacuum) connections are located at the top of the target assembly, where they are relatively accessible. A detailed view of the ports for these connections is shown in Fig. II.5.7. The coolant and electron beam connections are clamped by specialized mechanisms that allow operation with simple long-handled tools to minimize radiation exposure to workers during the target assembly exchange. Figures II.5.10 and II.5.11 show the configuration of the vacuum clamp and the coolant clamp assemblies.

The lower end of the target assembly has a pin that engages a hole in the grid plate of the subcritical assembly, providing two degrees of positional control as shown in Figs. II.5.3 and II.5.4. The target assembly top flange is clamped to the flange of the electron beam tube, providing three additional degrees of positional control. The sixth degree of position control is determined by the hexagonal elements in the grid plate and held by the vacuum clamp. The target assembly is free to change length in response to temperature changes during operation.

Coolant enters the target assembly at the manifold at the top of the assembly. Coolant travels down to the target plates through two of the pentagonal end channels and one of the trapezoidal side channels, as shown in Fig. II.5.8. The coolant of the two end channels flows through the top half of the target plates and then travels to the opposite two end channels. The coolant of the side channel passes under the target plates, then back up to pass through the bottom half of the target plates, as shown in Fig.II.5.9. This coolant then travels back down and under the target plates before travelling upward

through the opposite side channel. Both the U11 and W7 target assemblies use this flow strategy.

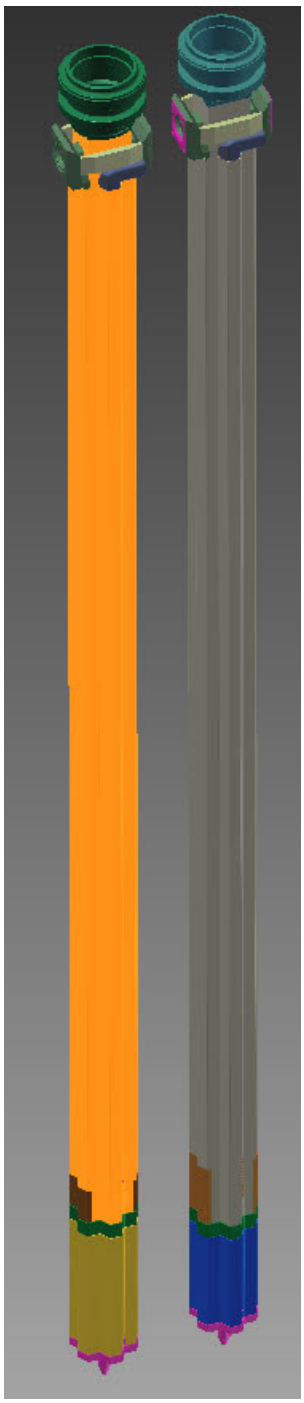

Figure II.5.1. The tungsten target assembly (left) and the uranium target assembly (right) are shown side by side. These two target assemblies are physically interchangeable but offer different performance.

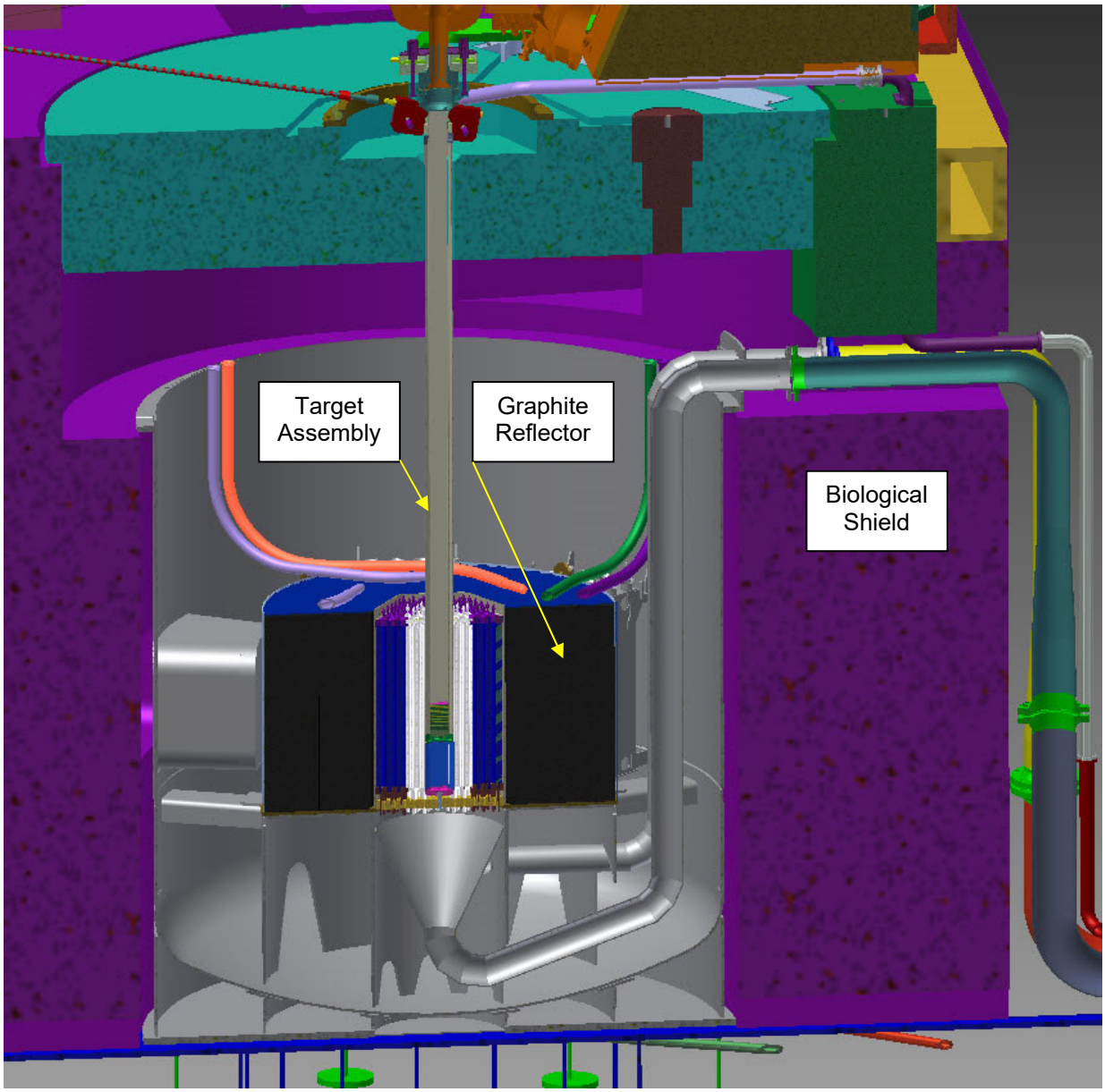

Figure II.5.2. Section view through the subcritical assembly shows the target assembly in the center, graphite reflector, tank, and biological shielding; vacuum clamp and coolant clamp are visible at top.

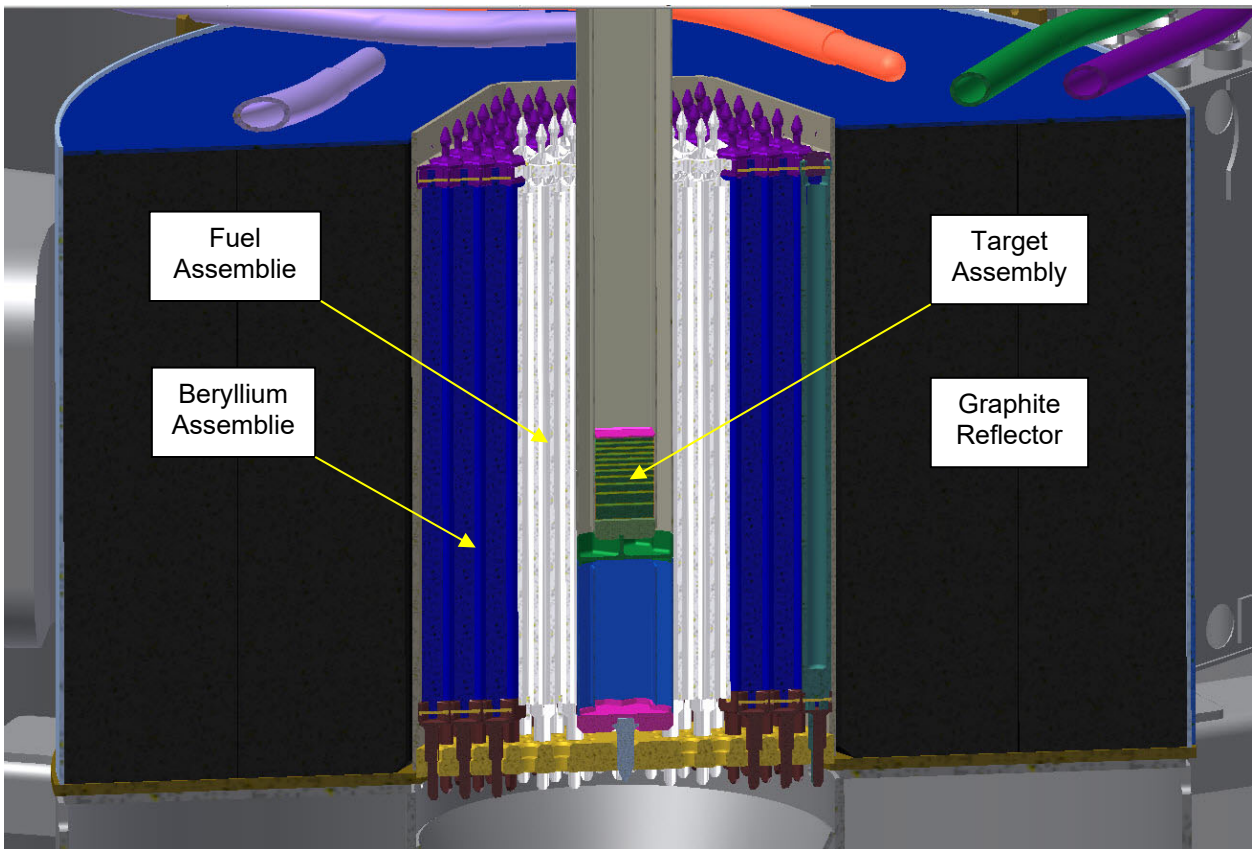

Figure II.5.3. Section view through the subcritical assembly shows the arrangement of target assembly, fuel assemblies, beryllium reflector assemblies, graphite reflector, and grid plate; the target plates are shown in the center.

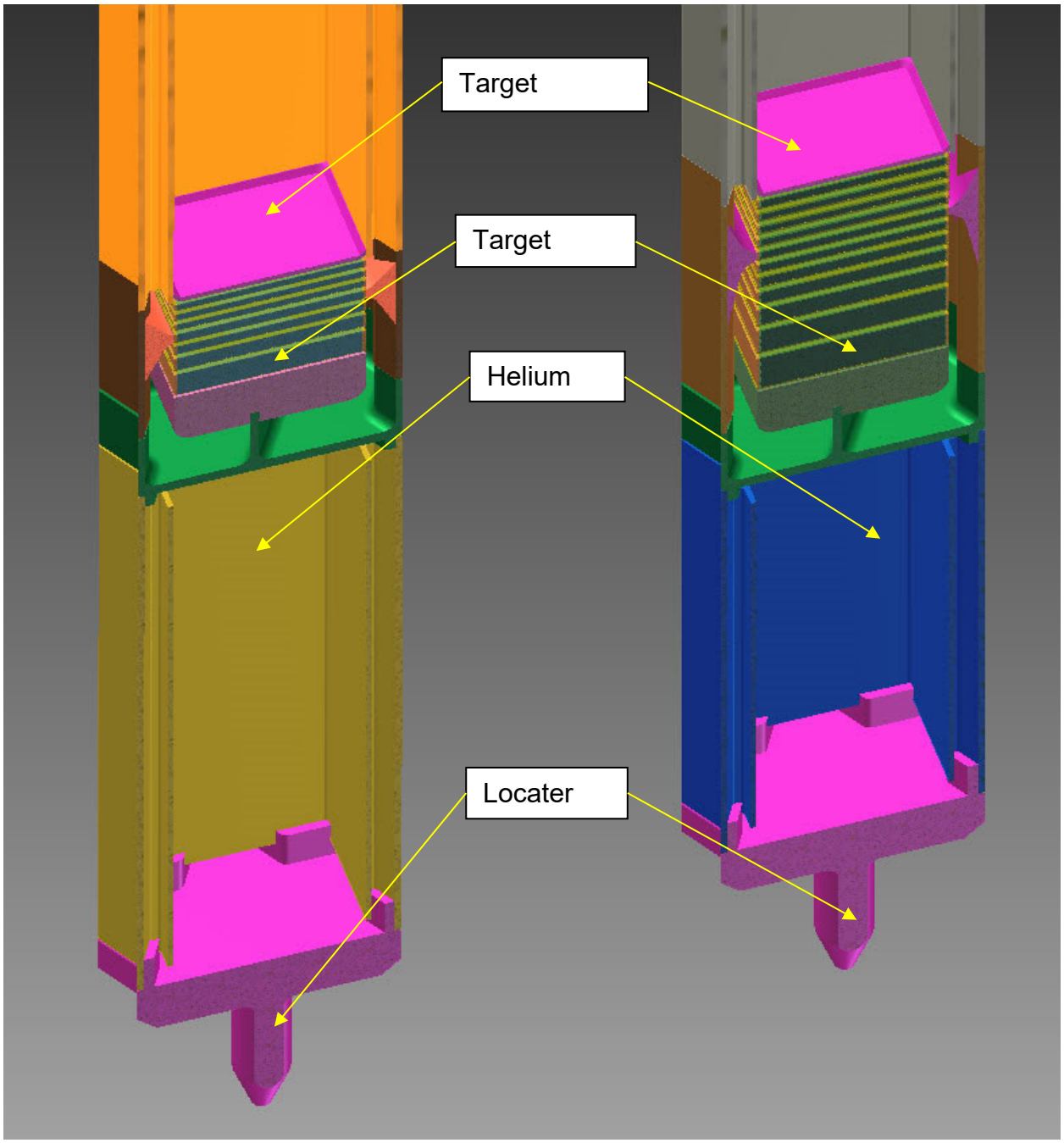

Figure II.5.4. The tungsten target assembly (left) and the uranium target assembly (right) are shown side by side in this offset section view. The effective center of both target plates is at the same height within the subcritical assembly. Bottom locator pin, helium chamber, lower manifold, target plates, and electron beam windows are visible.

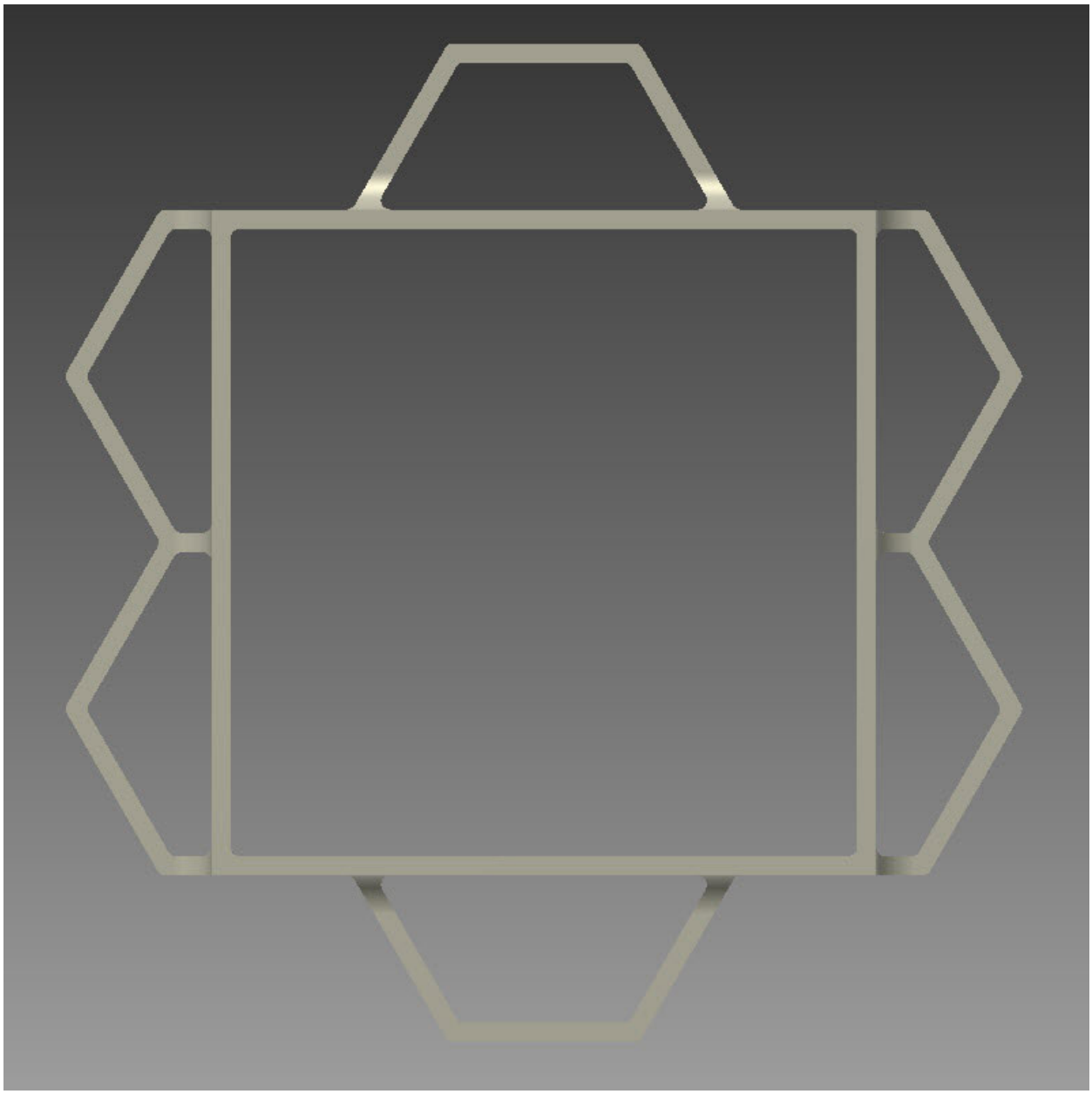

Figure II.5.5. Cross section shows the target assembly body. Square central space is the electron beam channel. The two trapezoidal and four pentagonal channels are for the target coolant flow. Exterior profile interfaces with 35 mm hexagon spacing of fuel element grid plate. Target plates fit within the central square region.

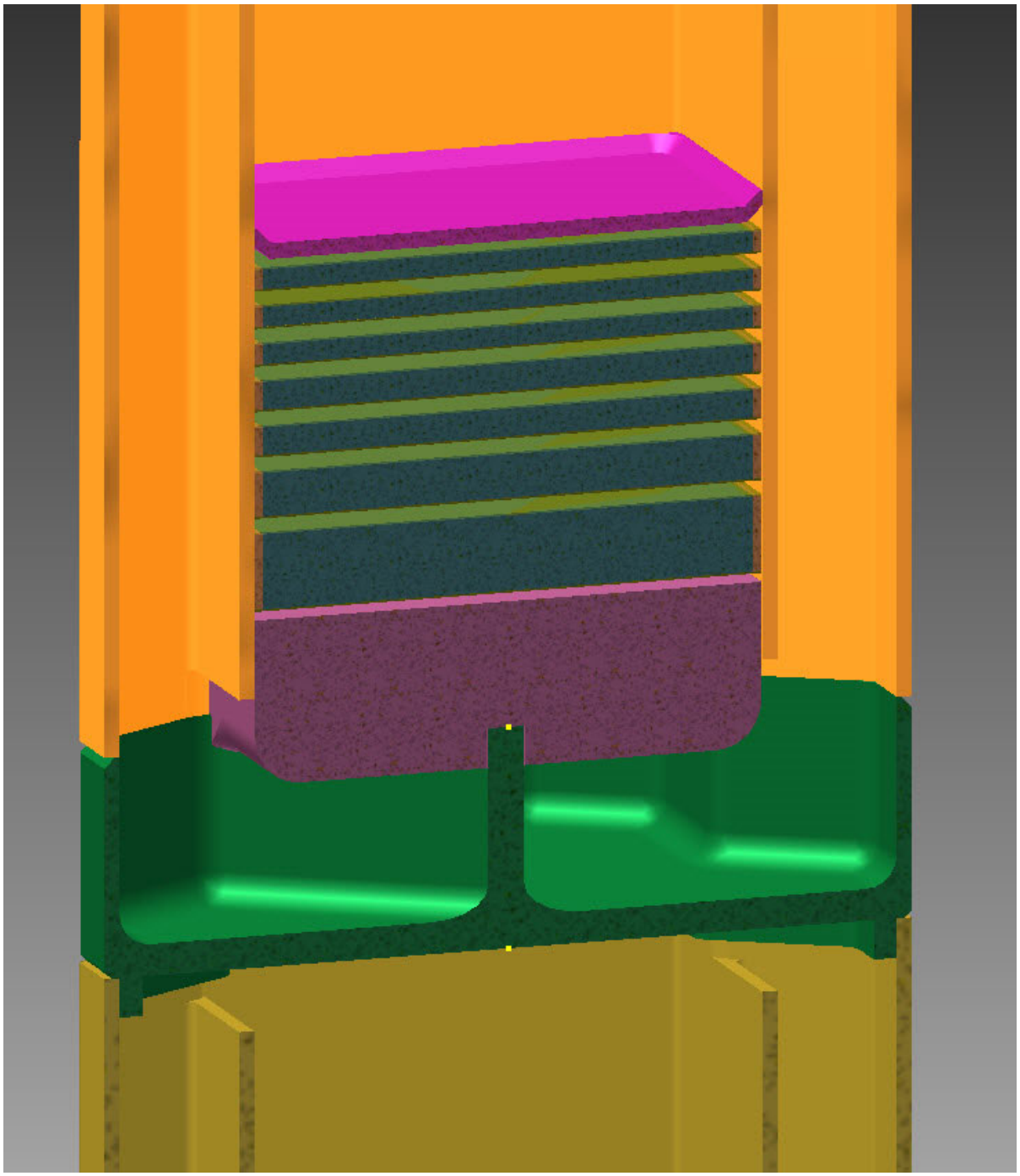

Figure II.5.6. Section view through the tungsten target shows the electron beam window, seven plate tungsten target plates, lower manifold, and helium chamber.

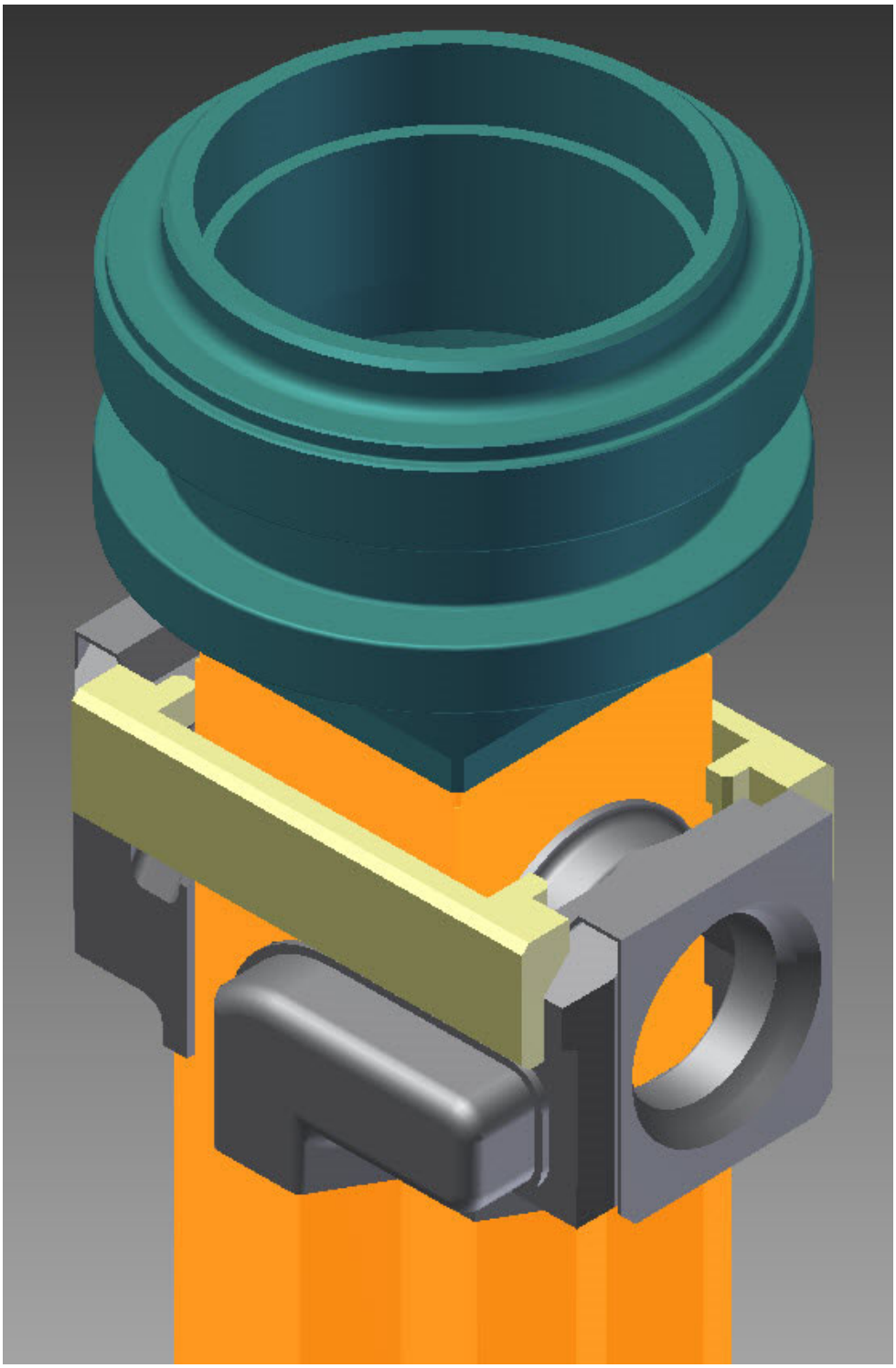

Figure II.5.7. Top end of target assembly shows the vacuum flange and the ports for target coolant connections.

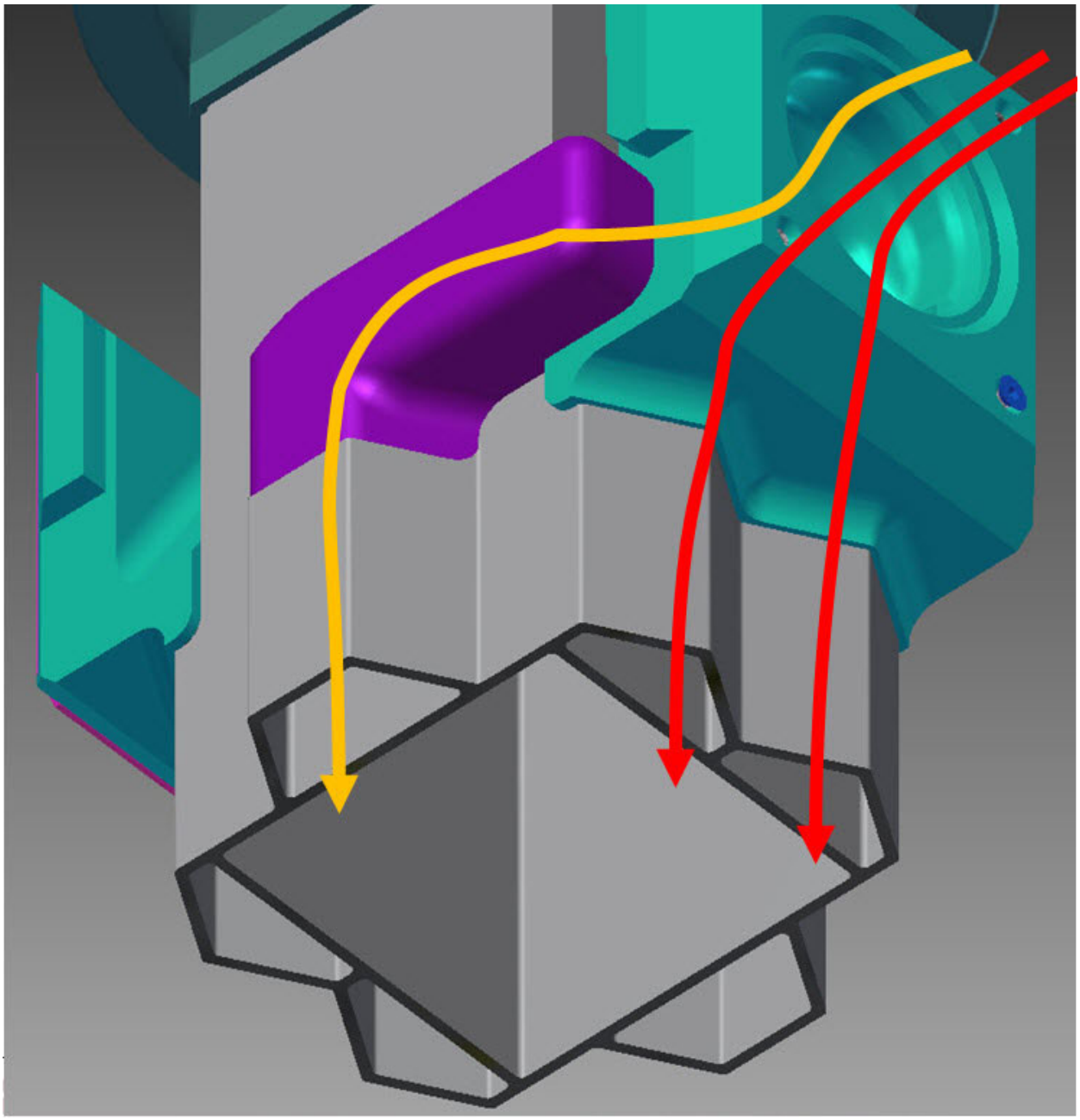

Figure II.5.8. Target manifold illustrates the coolant flow paths. Three channels carry coolant down to the target pack, and the other three channels carry coolant up from the target plates. Coolant in the two five-sided end channels flows through the top half of the target plates (red lines). Coolant in trapezoidal side channel flows through lower half of target plates (yellow line).

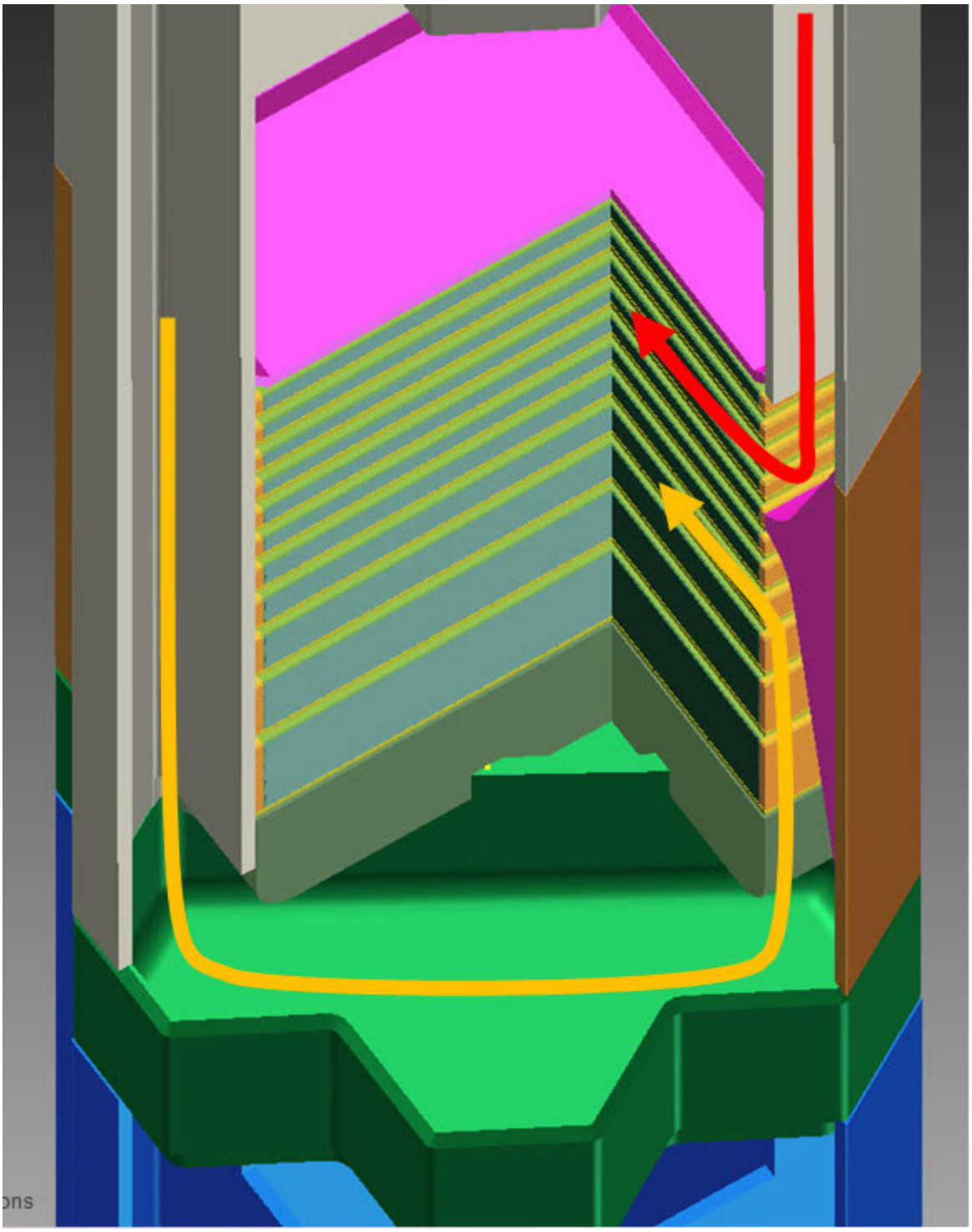

Figure II.5.9. Section view through target pack shows the coolant flow paths. Coolant in the two five-sided end channels passes through the top half of the target plates (red line). Coolant in the trapezoidal side channel passes under target plates and then back up to flow through the lower half of the target plates (yellow line).

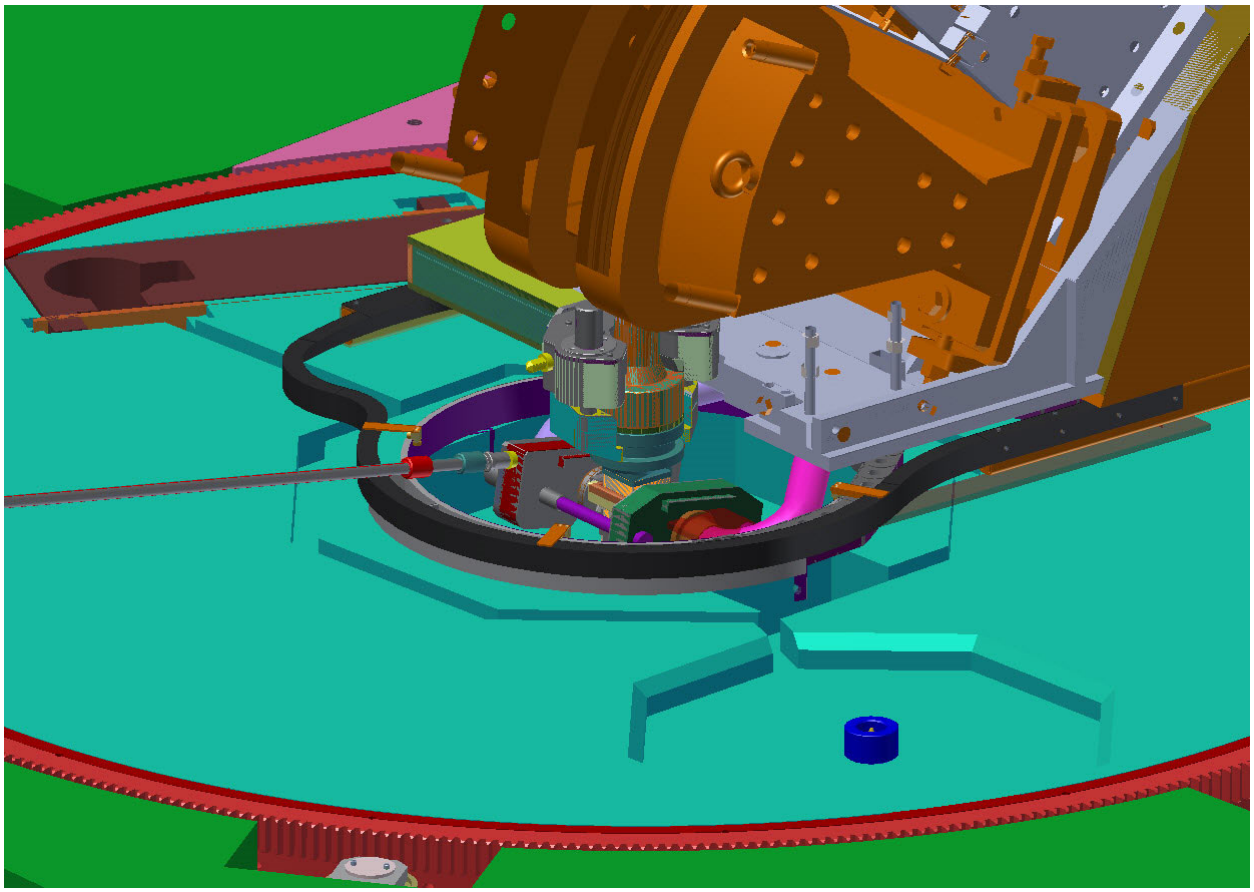

Figure II.5.10. Top of the target assembly as installed in SCA shows the arrangement of vacuum clamp and coolant clamp assemblies.

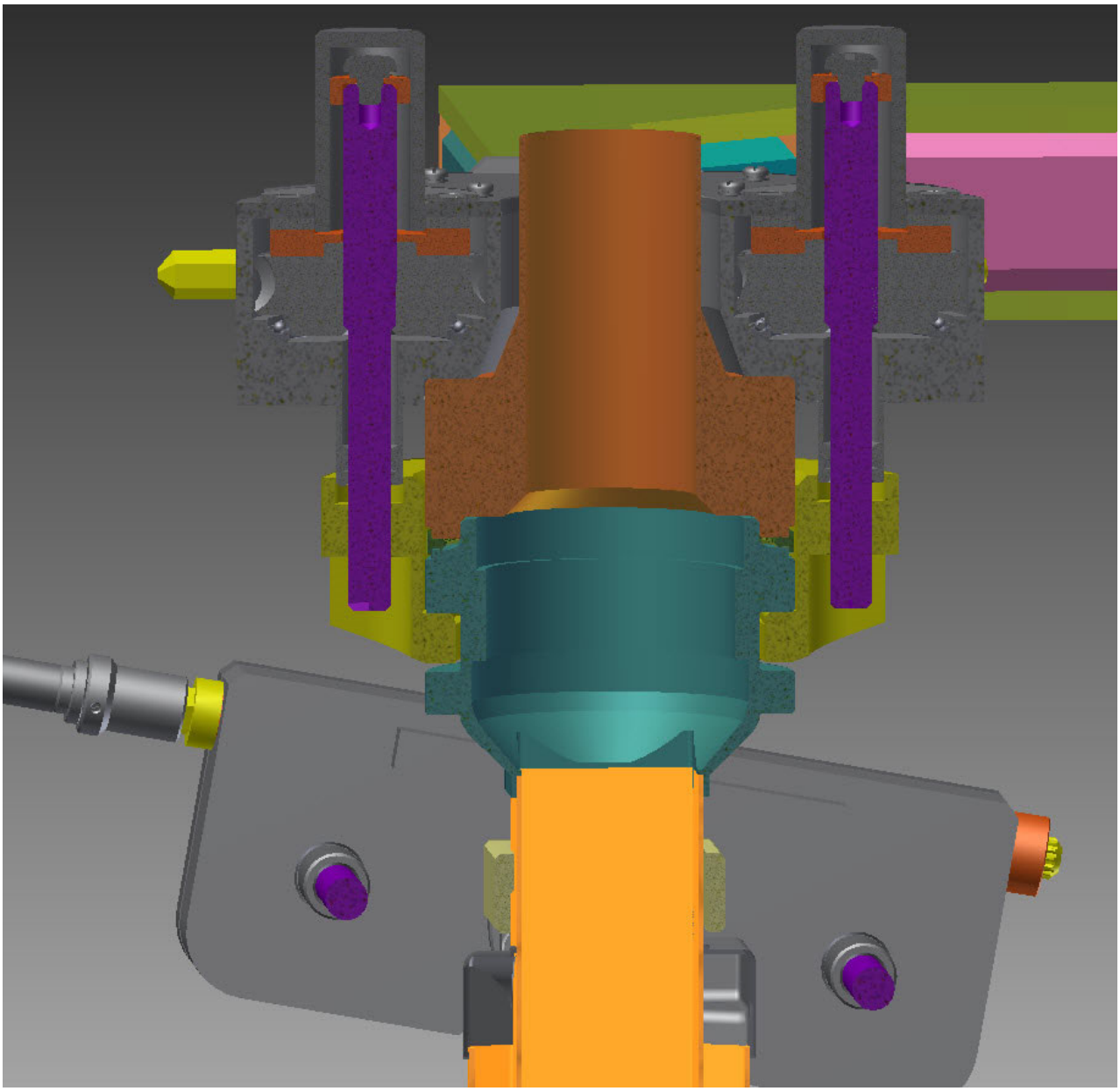

Figure II.5.11. Section is taken through the top of the target assembly and the vacuum clamp assembly.

II.6 Target Cooling System

II.6.1 Introduction

At the center of the KIPT subcritical assembly is a heavy metal target assembly. This target is bombarded by a high-energy electron beam to create a shower of neutrons. These neutrons drive the subcritical assembly, which is using low-enriched uranium fuel. The heat generated within the target assembly is carried away by the forced flow of water

through gaps between the target plates, keeping the target plates at a temperature that maximizes their useful life. The target cooling system provides fluid flow, heat removal, filtration, de-aeration, chemistry control, and system monitoring functions. The target cooling system is completely separate from and shares no components with the subcritical assembly cooling system. Section III.8 discusses the subcritical assembly cooling system.

II.6.2 Cooling System Overview

The target cooling system uses forced circulation of demineralized light water coolant for heat removal. While the target cooling system is isolated from the SCA cooling system, the two systems do both interface with three facility systems: 1) both systems use the same chilled water system as a secondary heat sink, 2) both systems use an inert gas system for coolant purge and leak testing, and 3) both systems use the same special ventilation system. The two cooling systems use separate water quality monitoring stations, to prevent cross-contamination between the systems. Figure II.6.2.1 is a simplified schematic diagram of the target cooling system.

II.6.3 Target Cooling System Design

The target cooling system is comprised of two overlapping loops. The heat removal loop provides coolant flow through the target assembly and heat exchanger. The filtration loop removes contamination from the coolant and provides a means for monitoring and controlling the quality of the coolant. The two-loop cooling system permits more accurate control of the pressure within the target assembly and allows the filtration loop to operate without the heat removal loop running. Approximately 100 kW of heat removed from the target assembly during operation.

II.6.3.1 Target Cooling System Heat Removal Loop

A centrifugal pump provides coolant flow through the target assembly. After the coolant leaves the target assembly, it passes through a heat exchanger to remove heat from the coolant. Facility chilled water is used as the secondary fluid in the heat exchanger. The coolant then returns to the surge tank.

II.6.3.2 Target Cooling System Filtration Loop

The filtration loop pump draws coolant from the surge tank and circulates it through a filter and a demineralizer before returning the coolant to the surge tank. The filter removes particulates from the water. The demineralizer removes dissolved minerals from the water. The demineralizer will accumulate activated particles during operation and is enclosed in a radiological shield. The water quality sampling station is attached to the filtration loop and measures pH, particle content, conductivity (resistivity), activation level, and cesium content.

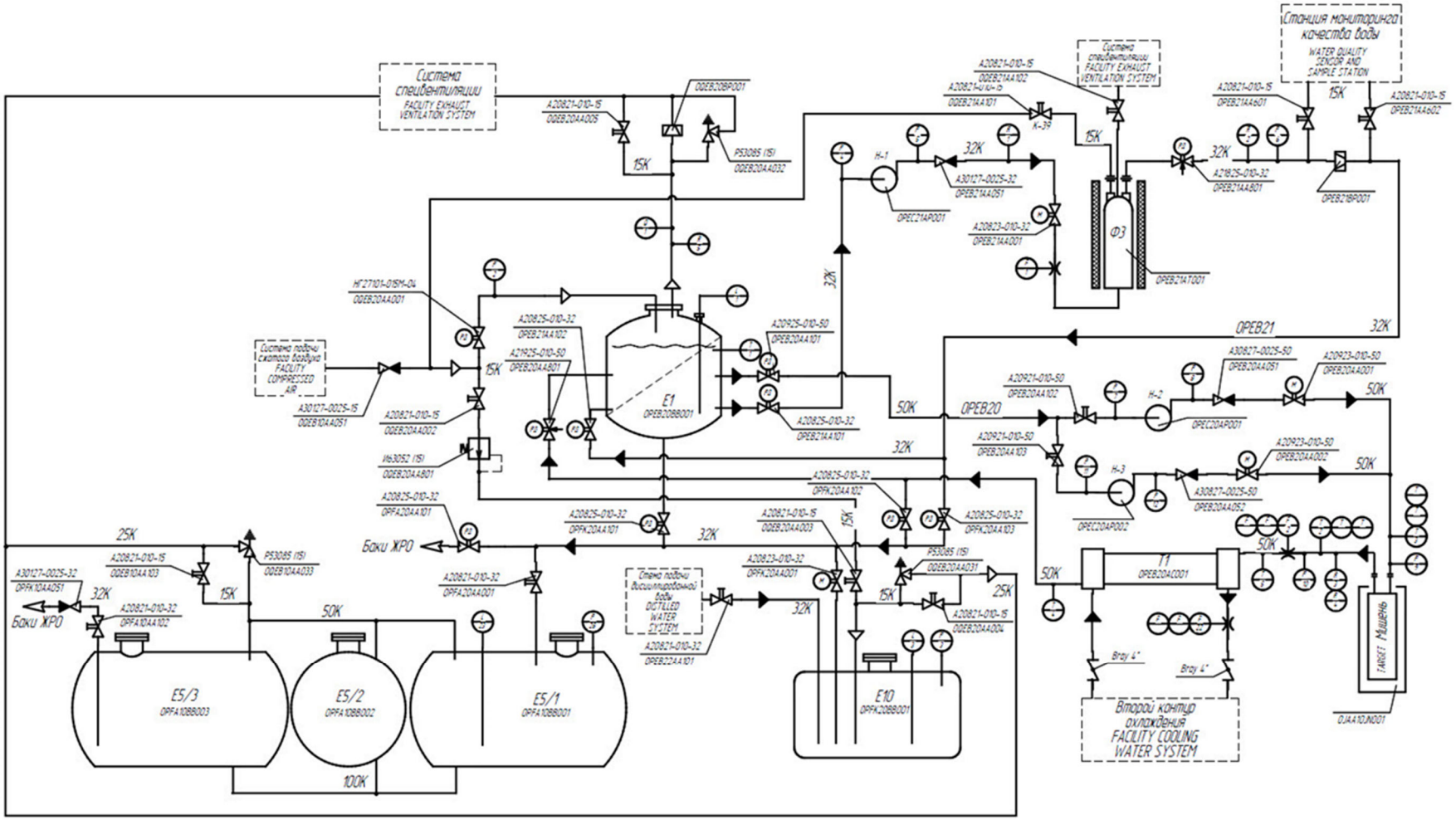

Figure II.6.2.1. Schematic of the Target Cooling System

II.6.3.3 Target Cooling System Surge Tank

The surge tank accommodates expansion of fluid within the system. The surge tank allows the fluid velocity to be reduced so that entrained gas can be separated. The surge tank also allows mixing of fluid between the heat removal loop and the filtration loop.

II.6.3.4 Target Cooling System Drain Tank

A drain tank provides short-term storage of coolant that has been drained from part of the system for component service and target assembly exchange. The secondary pump is used to pump the coolant that is in the drain tank through the filter and demineralizer, then back to the surge tank.

II.6.3.5 Target Cooling System Compressed Air System

A compressed air system is used to pressurize the water coolant. Controlling the chemistry of the compressed air prevents corrosion within the system. A small, constant flow of air is provided to prevent the accumulation of gases that may be generated within the target coolant system. The compressed air system provides a controlled pressure within the surge tank, which determines the suction side pressure at the pumps. The compressed air system is used to remove coolant from the target, pumps, heat exchanger, filter, and demineralizer prior to component exchange to minimize the amount of coolant lost. The compressed air system also provides a means of checking the system for leaks after component service or replacement without the mess of coolant loss.

II.6.4 Operational Limits – Target Cooling System

II.6.4.1 Surge Tank Coolant Level

During target cooling system operation, the level of the coolant in the surge tank is monitored via an electronic level sensor. A decrease in the coolant level may indicate a loss of coolant. Loss of coolant creating a fluid level deviation exceeding 40mm during operation will trigger an accelerator shutdown. An increase in the level of the coolant within the surge tank indicates a vapor void within the system, perhaps because of boiling within the target. An increase in coolant level exceeding 20 mm during operation will trigger an accelerator shutdown. Distilled water can be added to the system to make up for lost coolant. The amount of make-up water added is monitored over time to identify trends and spot possible leak conditions.

II.6.4.2 Operating Pressures

Pressures are measured at several key points of the target cooling system. This data is used to calculate flow rates and make inferences about the operational health of various components during operation. Pressure sensors are calibrated at startup when system pressures are assumed to be static head pressure. The nominal target inlet pressure is 269 kPa abs. The upper limit of this pressure is 296 kPa abs. Lower limits are calculated based on the corresponding fluid flow rate. Operational pressure limits are, in some cases, based on derived differential pressures. The pressure differential across the filter

and demineralizer are monitored as a predictive tool for management of service of these components. Monitoring the differential pressure across the target assembly can infer the condition of the target assembly and identify any impending coolant channel plugging issues.

II.6.4.3 Operating Temperatures

The target cooling system operates at nearly room temperature. In general, temperature information available in the target cooling system is used as a secondary tool to monitor the performance of various components. Temperatures within the target assembly are critical, and the differential temperature across the target assembly is a key operational parameter to monitor.

II.6.4.4 Synthesized Data

Measuring the differential pressure and the differential temperature across the target assembly can provide insight into conditions within the target itself. The pressure information is used to protect the target assembly from structural damage, and temperature information is used to protect the target assembly from thermal damage. If the coolant temperatures are rising, increasing the flow will reduce them but will also increase the pressures and resultant stresses within the target assembly. Efficient operation requires monitoring several pressure and temperature parameters simultaneously and making operating decisions based on the measured data.

II.7 Target Main Parameters

Table II.7.1. Thicknesses of the tungsten and uranium target plates and water-cooling channels

Channel number	Tungsten Target		Uranium Target		
	Water channel thickness, mm	Target thickness*, mm	Water channel thickness, mm	Target meat thickness, mm	Aluminum alloy cladding thickness, mm
0	1.0		1.0		
1	1.75	3.0	1.75	3.0	0.7 ×2
2	1.75	3.0	1.75	2.5	0.95 ×2
3	1.75	3.0	1.75	2.5	0.95 ×2
4	1.75	4.0	1.75	2.5	0.95 ×2
5	1.75	4.0	1.75	3.0	0.7 ×2
6	1.75	6.0	1.75	3.0	0.7 ×2
7	1.0	10.0	1.75	4.0	0.7 ×2
8			1.75	5.0	0.7 ×2
9			1.75	7.0	0.7 ×2
10			1.75	10.0	0.7 ×2
11			1.0	14.0	0.7 ×2
Total	12.5	33.0	19.5	56.5	16.9**

* Including the tantalum coating

**The total clad thickness on both sides

Table II.7.2. Thermal-hydraulic parameters for the two target configurations

Parameter	Tungsten Target	Uranium Target
Mass flow rate	4.79 kg/s	4.79 kg/s
Friction pressure drop (manifold to manifold)	162 kPa	138 kPa
Inlet temperature	25 °C	25 °C
Outlet temperature (with correction for side coolant heating)	29.3 °C	29.5 °C
Total power (with correction for side coolant heating)	85.7 kW	90.5 kW
Peak cladding temperature	101 °C	112 °C
Peak fuel temperature	113 °C	166 °C
Margin to boiling	42 °C	32 °C

Table II.7.3. Target Assembly Dimensions

Length	~2.6 m.
Electron beam cross-section dimensions	66 mm x 66 mm
Target plate cross-section dimensions	68 mm x 68 mm

III Subcortical Assembly

III.1 Introduction

The subcritical assembly (SCA) consists of uranium fuel assemblies that surround a uranium or tungsten target. Beryllium reflector assemblies surround the fuel assemblies, with a ring of graphite reflector blocks around the reflector assemblies. These components are all located within an aluminum tank that is filled with water. This water is used for both neutron moderation and heat removal. The tank is surrounded by a concrete biological shield. Six neutron channels have access to the subcritical assembly in the form of cans that pass through the biological shield and the tank. Five of these channels are used for neutron instruments, while the sixth provides a location where a cryogenically cooled moderator system could be added. Such a system would be used to slow neutrons down to meV energy range.

The WWR-M2 fuel assembly design used in Kiev Research Reactor was selected for the KIPT subcritical assembly. The fuel assembly characteristics are described in Sec. III.2. The arrangement of the fuel assemblies and the reflector blocks have been analyzed, with the objective of getting k_{eff} just less than 0.98. The subcritical assembly designs selected are comprised of 38 fuel assemblies for the initial loading when the tungsten target is used and 37 assemblies when the uranium target is used. The total thermal power of the facility is ~160 kW for the tungsten target case and ~300 kW for the uranium target case. The total fission power for the initial fresh fuel loading is ~70 kW when the tungsten target is used, and it is ~208 kW when the uranium target is used. The neutron flux and power profiles for the initial fresh fuel loading have been calculated, analyzed, and discussed in Sec. III.3. Fuel management and burnup analyses were performed, and the results are described in Sec. III.4. The fuel assemblies shuffling scheme was developed to preserve the reactivity during the operation, with the option of introducing fresh fuel assemblies to allow longer operation/depletion time.

The subcritical assembly is located within a water tank, where the water flowing down for heat removal. The water then passes through a heat exchanger, and it is recirculated back to the tank. A computational fluid dynamics analysis of the tank was performed to define the nominal thermal-hydraulic parameters of the subcritical assembly. This analysis is described in detail in Sec. III.5.

The subcritical assembly tank includes a grid plate at the bottom that supports uranium or tungsten target. The grid plate and tank were subjected to a structural analysis by the finite element method. Finite element models were constructed and subjected to static loads, and results were compared to the basic material properties. Commonly accepted engineering principles were applied to determine factors of safety. These analyses are presented in Sec. III.6.

The tank contains not only the subcritical assembly, target, and grid plate, but also number of other components essential to the operation of the facility. Flux detectors are used to monitor the system reactivity as fuel is being loaded; these detectors reside in tubes placed at several locations on the periphery of the graphite reflector. Fuel storage racks

are located between the graphite reflector and the tank wall; these racks are used to store spent fuel when it is removed from the subcritical assembly, before it is transferred to the spent fuel pool. There is also a fuel transfer station within the tank that positions the fuel assembly that has been removed from the hexagonal grid plate so that it can be inserted into the fuel transfer cask. Finally, there is a fuel orientation device that orients a fuel element correctly for placement in the grid plate. The mechanical design of the tank and these various components is covered in Sec. III.7.

The heat generated within the subcritical assembly is carried away by the forced flow of water through the tank. The SCA cooling system provides coolant flow, heat removal, filtration, and chemistry control functions. The cooling system is explained in Sec. III.8.

III.2 Fuel Characteristics

The WWR-M2 hexagonal fuel assembly design of the Kiev Research Reactor [III.2.1] with water coolant is utilized for the KIPT neutron source facility. It has a hexagonal geometry with 3.5 cm pitch. The coolant gap thickness between any two fuel assemblies is 0.3 cm. The fuel material is uranium oxide dispersed in an aluminum matrix and cladded with aluminum alloy, with active length of 50 cm. Based on the manufacturer's data, the U^{235} enrichment is 19.7%, the average U^{235} mass per assembly is 41.7 g [III.2.2], the average fuel meat (UO_2 + Al) density is ~4.603 g/cm^3, and the average uranium density in the fuel meat is ~2.226 g/cm^3.

The configuration of the WWR-M2 hexagonal fuel assembly is shown in Fig. III.2.1. It has a concentrically three-ring structure, with the inner two rings circular and the outer ring hexagonal. The fuel meat nominal thickness is 1.0 mm, cladded with 0.75 mm of aluminum alloy on each side. The parameters of each fuel ring are shown in Table III.2.1. The total length of a fuel assembly is 75 cm. The weight-bearing element of the fuel assembly is the outer hexagonal structure, which is connected with the top and bottom nozzles by molding and welding. The fuel assembly can be picked up and positioned by gripping the top nozzle, as shown in Fig. III.2.1. The bottom nozzle, shown in Figs. III.2.1 and III.2.2, is to be inserted and adjusted into the supporting grid plate.

Table III.2.1. Dimensions of the three rings for the WWR-M2 fuel assembly

Fuel Ring	Inner Clad		Fuel meat		Outer Clad	
	Inner radius (mm)	Outer radius (mm)	Inner radius (mm)	Outer radius (mm)	Inner radius (mm)	Outer radius (mm)
Ring 1 (inner)	3.0	3.75	3.75	4.75	4.75	5.5
Ring 2 (middle)	8.5	9.25	9.25	10.25	10.25	11.0
Ring 3* (outer)	13.5	14.25	14.25	15.25	15.25	16.0

*Hexagonal

Reference

III.2.1. R. B. Pond, et al., “Neutronic performance of the WWR-M research reactor in Ukraine”, *Proceedings of the 24th International Meeting on Reduced Enrichment for Research and Test Reactors*, San Carlos de Bariloche, Argentina, 3-8 November 2002.

III.2.2. VVR-M2 Fuel Assembles, Catalogue Description, 0001.04.00.000, 2006

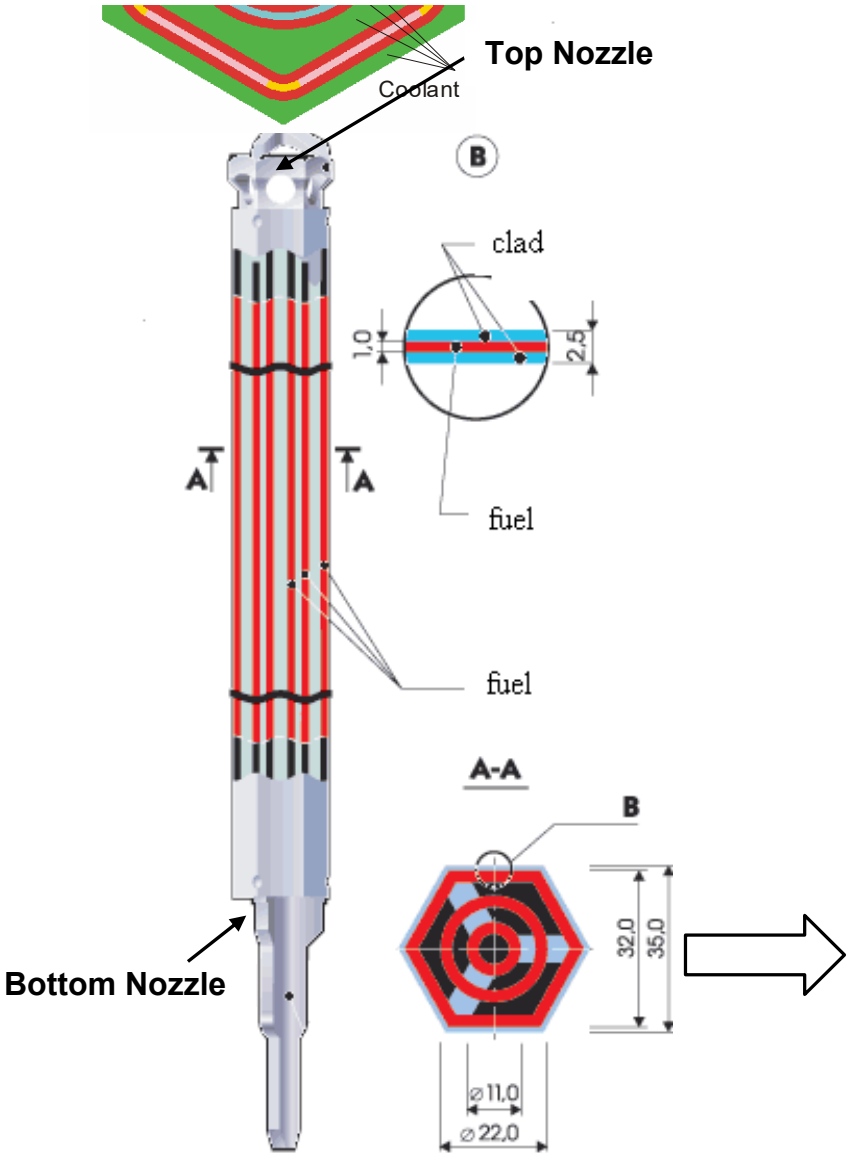

Figure III.2.1. WWR-M2 fuel assembly

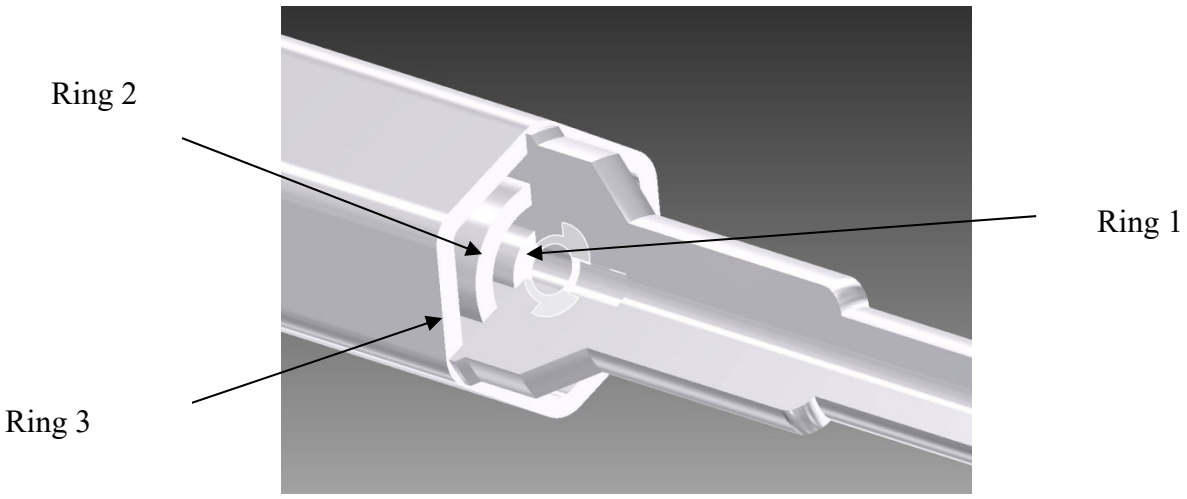

Figure III.2.2. Bottom part of the fuel assembly.

III.3 Subcritical Assembly Physics Analysis and Design

The subcritical assembly is composed of WWR-M2 fuel assemblies, which are assembled around the target assembly. The fuel assemblies are surrounded by reflector materials to reduce the neutron leakage. The reflector is divided radially into two parts: an inner region filled with beryllium blocks, and an outer region filled with a continuous graphite block. Any beryllium reflector block can be replaced by a fuel assembly or an irradiation cassette. The inner beryllium reflector region has a power density, which requires a heat removal. Therefore, the beryllium blocks have same size as the fuel assemblies, which is 3.2-cm flat to flat. The 0.3-cm gaps between the beryllium blocks and the fuel assemblies are used for heat removal. The outer graphite reflector block has a low power density, which does not require an internal coolant. The graphite ring is cladded with SAV-1 aluminum alloy, and it is immersed in the subcritical assembly water tank. The deposited heat in the graphite ring can be removed the by the water coolant of the subcritical assembly. The radial and axial configurations of the subcritical assembly plus the two reflector regions are shown in Figs. III.3.1 and III.3.2.

If graphite is used for the inner reflector region assemblies, these assemblies would need SAV-1 aluminum alloy clad to protect against any interaction with the water coolant. However, the fabrication of cladded graphite assemblies is expensive and difficult. Graphite is cheaper than beryllium, the alternative reflector material. However, the cladding process of small graphite blocks, 3.2-cm flat to flat, significantly increases the total cost of the graphite reflector blocks. Beryllium does not react chemically with the water coolant; and it form a stable beryllium oxide coating. Therefore, beryllium reflector blocks do not need an aluminum clad. In addition, the inner reflector blocks need to be replaced with fuel assemblies during the operation. This requires fabricating a mechanical feature for extracting the graphite blocks from the subcritical assembly. Such mechanical feature is difficult to implement because of the mechanical properties of the graphite material. In addition, if it is implemented, it will add to the fabrication cost. Thus, it was decided to use beryllium assemblies in the inner reflector region, while using a continuous

graphite block in the outer reflector region. The beryllium density in the reflector assemblies is 1.855 g/cm^3.

With this beryllium-graphite reflector design, an analysis performed using MCNPX concluded that a maximum of 42 fuel assemblies could be used with the tungsten target and a maximum of 37 fuel assemblies with the uranium target if k_{eff} is limited to less than 0.98. The calculated k_{eff} values are shown in Table III.3.1. The top surface of the first tungsten target plate is 32.50 mm above the centerline of the active fuel length, and the top surface of the first uranium target plate is 16.95 mm above the centerline of the active fuel length.

However, based on the results shown in Table III.3.1, removal of the tungsten target introduces a positive reactivity feedback, ~ 2000 pcm if the subcritical assembly is loaded with fresh fuel assemblies, due to the large neutron absorption cross section of tungsten, which could result in k_{eff} exceeding 0.98 if 42 fuel assemblies are used for the subcritical assembly. Therefore, another subcritical assembly configuration was developed for use with the tungsten target. It uses 38 fuel assemblies, which keeps k_{eff} below 0.98 when the tungsten target is removed. The subcritical assembly with 38 fresh fuel assemblies is selected for the design when the tungsten target is used.

The arrangements of fuel assemblies for the subcritical assembly used with the tungsten and uranium targets are shown in Fig. III.3.3. The neutron flux and energy deposition for these two targets, calculated by MCNPX, are shown in Table III.3.2. The neutron flux for each target case is averaged over the target coolant channels, the active fuel length, and along the target length. For the option of the tungsten target with 38 fuel assemblies, the total thermal power is ~160 kW and the subcritical power is ~75 kW. For the option using the uranium target with 37 fuel assemblies loaded, the total thermal power is ~299 kW and the subcritical power is ~208 kW.

For the subcritical configurations with the tungsten and uranium targets, the energy deposition profiles within the subcritical assembly have been calculated using the MCNPX mesh tally capability and plotted in Figs. III.3.4 through III.3.7 with different mesh schemes (R-Z or X-Y meshes). The neutron flux profiles within the subcritical assembly have also been calculated, and the fast (E > 100 keV), epi-thermal (1 eV < E < 100 keV), and thermal (E < 1 eV) neutron fluxes are tallied and plotted in Figs. III.3.8 through III.3.23.

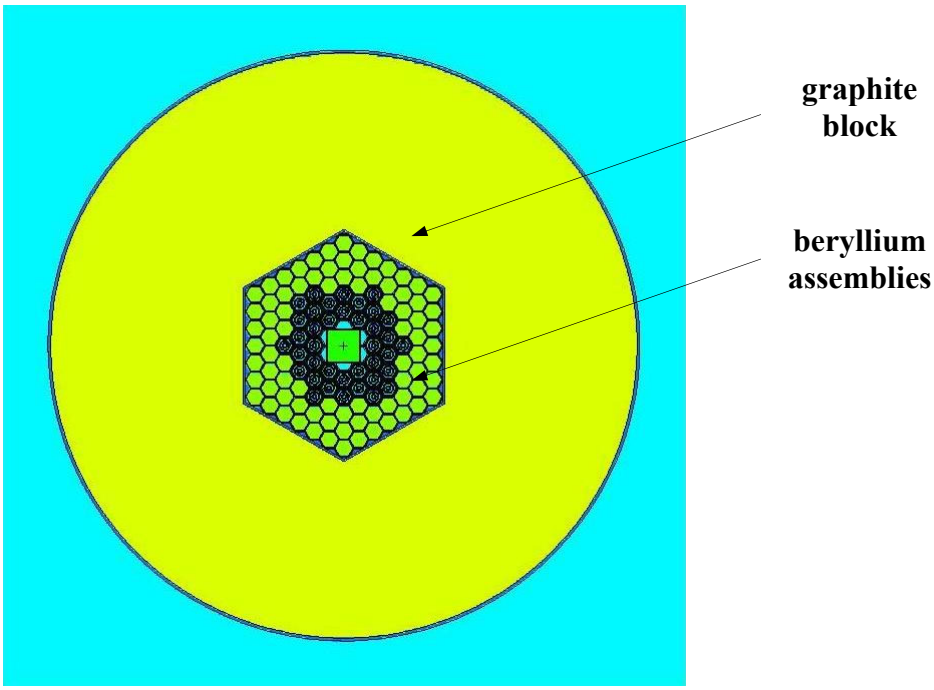

Figure III.3.1. Radial configuration of beryllium-graphite mixed reflector

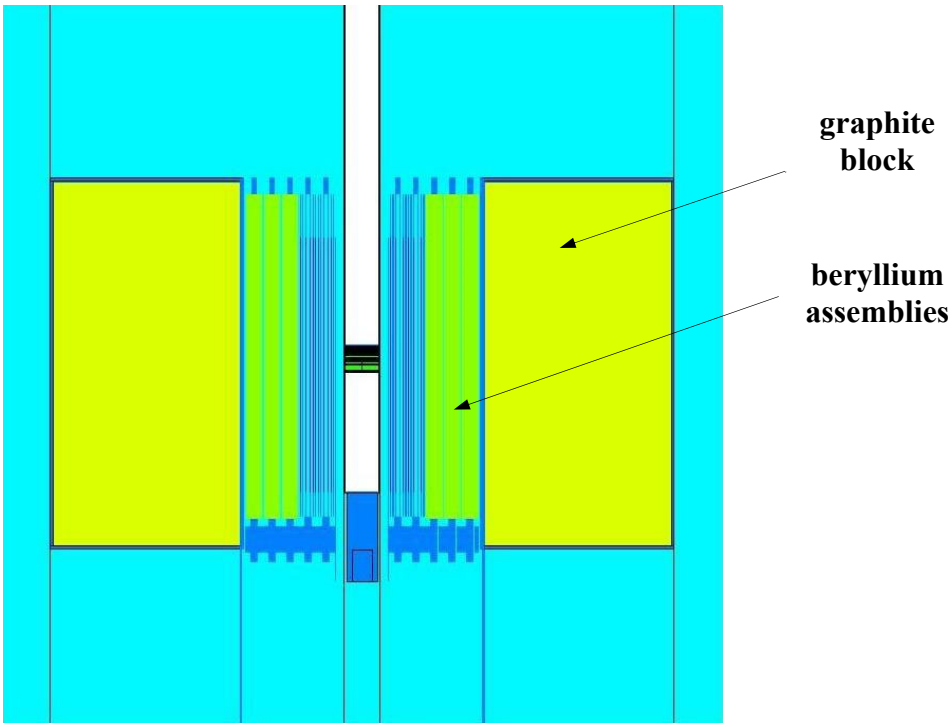

Figure III.3.2. Axial configuration of beryllium-graphite mixed reflector

Table III.3.1. k_{eff}, calculated by MCNPX for the different configurations with and without a target assembly

Target material	Number of fuel assemblies	k_{eff}	
		With target	Without target
tungsten	42	0.97855±0.00012	0.99623±0.00011
	38	0.95686±0.00013	0.97739±0.00011
uranium	37	0.97547±0.00012	0.97268±0.00012

Table III.3.2. Average neutron flux and energy deposition values using beryllium-graphite, reflector, uranium, or tungsten target, and 100 kW/100 MeV electron beam

Target	# of FAs	k-eff	Flux along the subcritical assembly (n/cm^2·s)	Flux along the target (n/cm^2·s)	Energy deposited in the target (kW)	Energy deposited in the subcritical assembly (kW)	Energy deposited in the reflector (kW)	Total energy deposition (kW)
W	38	0.95686 ±0.00013	6.281e+12 ±0.26 %	7.873e+12 ±0.23 %	85.70 ±0.01 %	69.19 ±0.24 %	5.84 ±0.13 %	160.73
U	37	0.97547 ±0.00012	1.965+13 ±0.26 %	2.470e+13 ±0.25 %	90.57 ±0.01 %	196.89 ±0.35 %	11.57 ±0.19 %	299.04

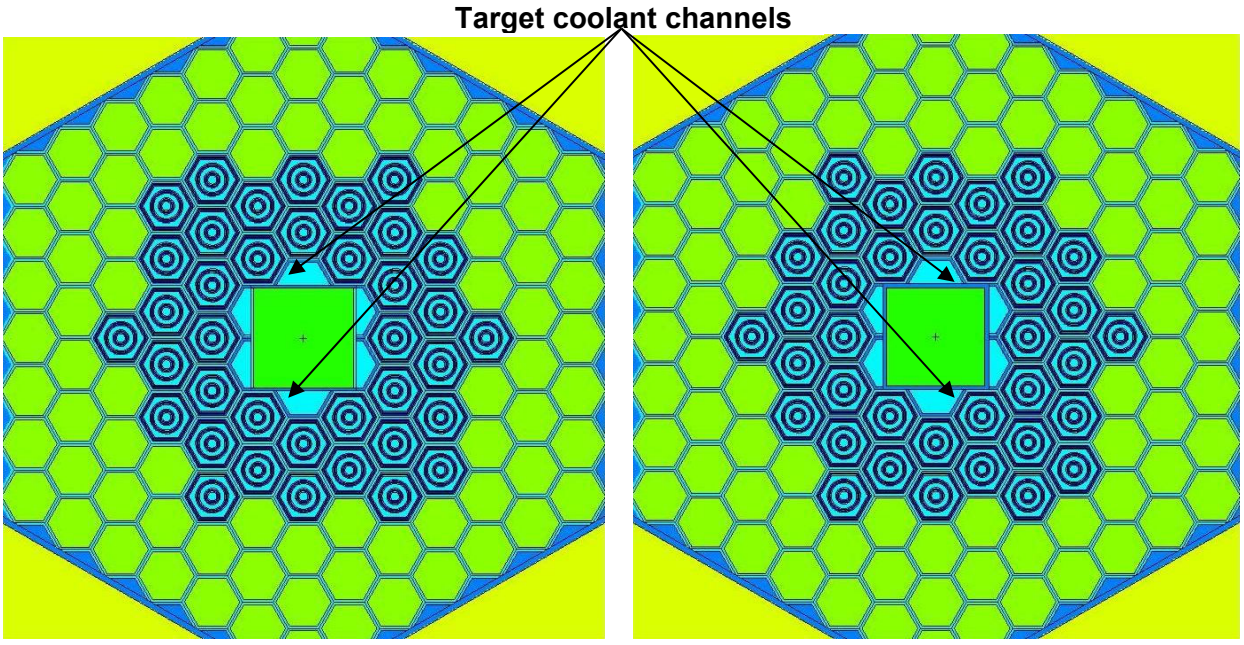

Tungsten target, with 38 fuel assemblies loaded

Uranium target, with 37 fuel assemblies loaded

Figure III.3.3. Fuel assembly arrangement of the subcritical assembly with beryllium-graphite reflector

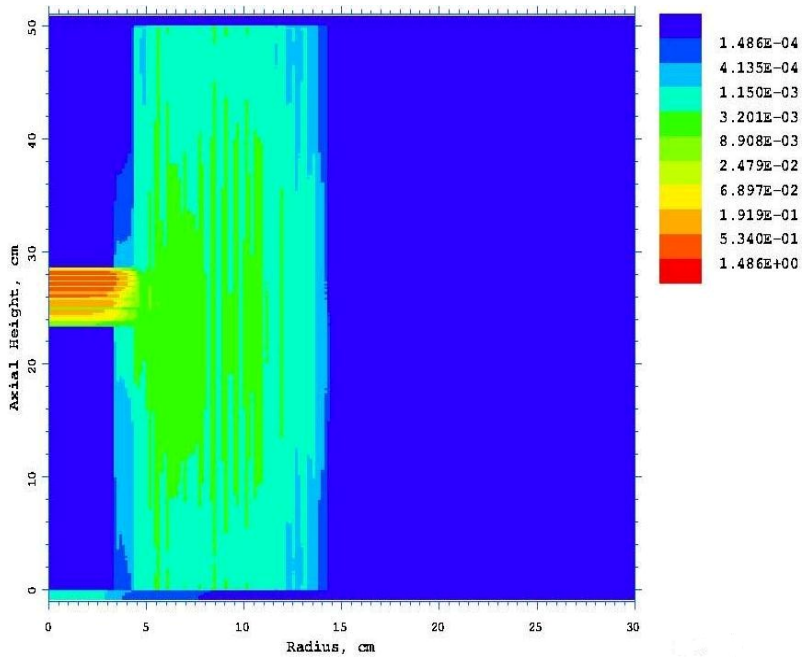

Figure III.3.4. R-Z view of the energy deposition in the subcritical assembly (kw/cm^3) with the tungsten target, 100 kW/100 MeV electron beam, and 38 fuel assemblies

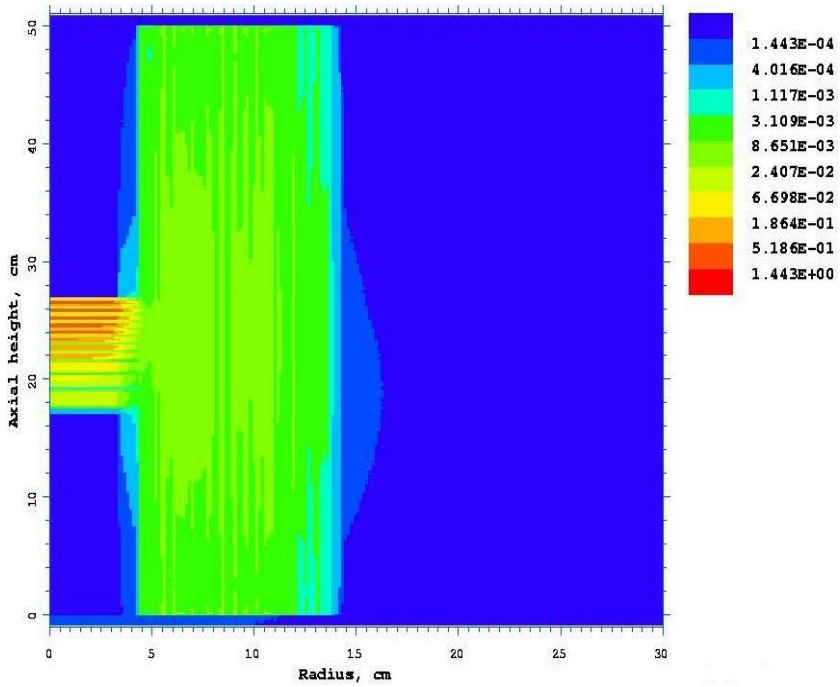

Figure III.3.5. R-Z view of the energy deposition in the subcritical assembly (kw/cm^3) with the uranium target, 100 kW/100 MeV electron beam, and 37 fuel assemblies

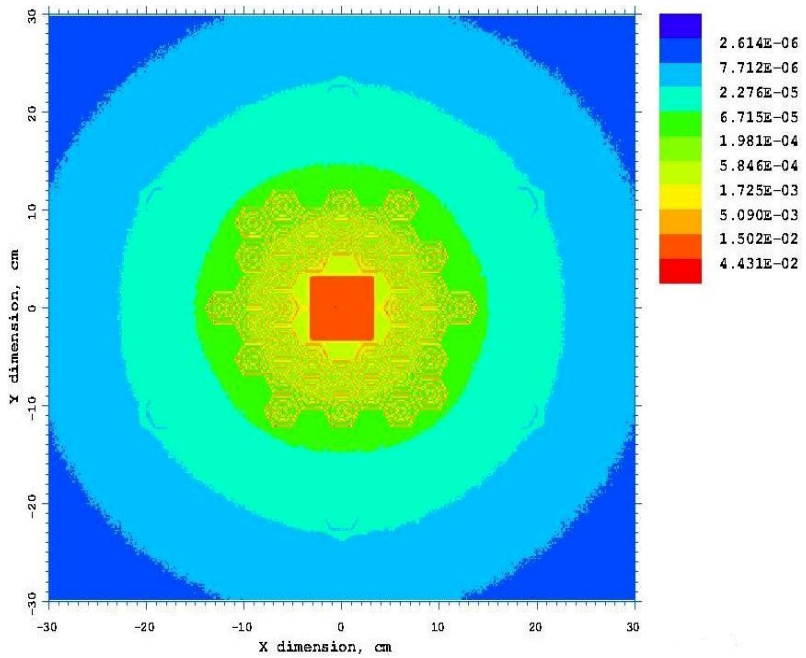

Figure III.3.6. X-Y view of the energy deposition in the subcritical assembly (kw/cm^3) with the tungsten target, 100 kW/100 MeV electron beam, and 38 fuel assemblies

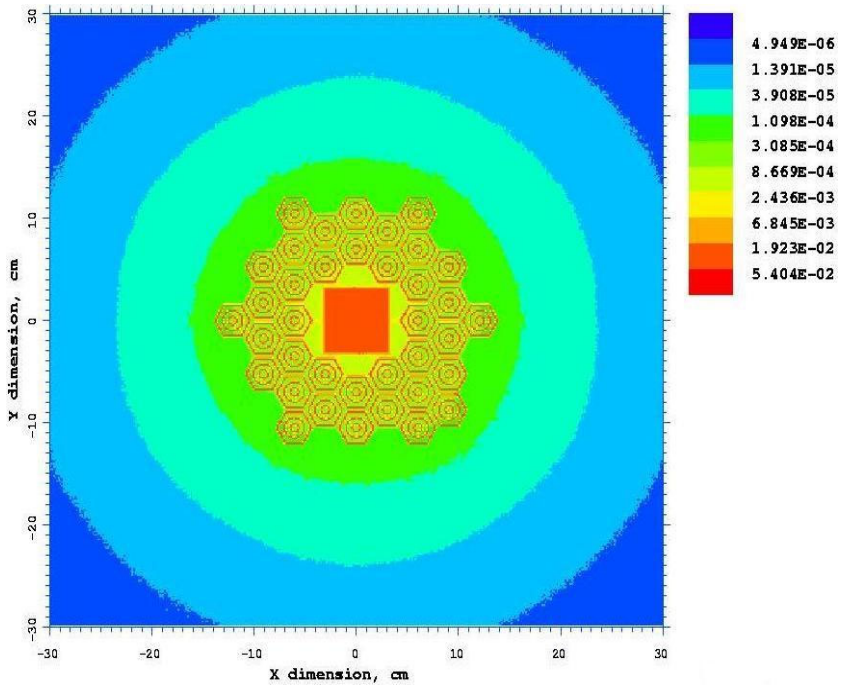

Figure III.3.7. X-Y view of the energy deposition in the subcritical assembly (kw/cm3) with the uranium target, 100 kW/100 MeV electron beam, and 37 fuel assemblies

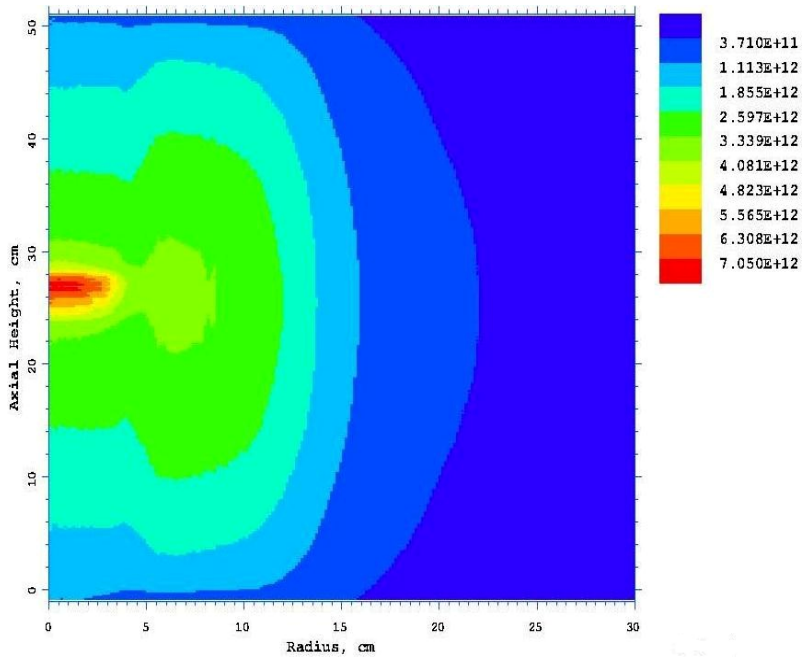

Figure III.3.8. R-Z view of the fast neutron flux (*E* > 100 keV) in the subcritical assembly (n/cm^2.s) with the tungsten target, 100 kW/100 MeV electron beam, and 38 fuel assemblies

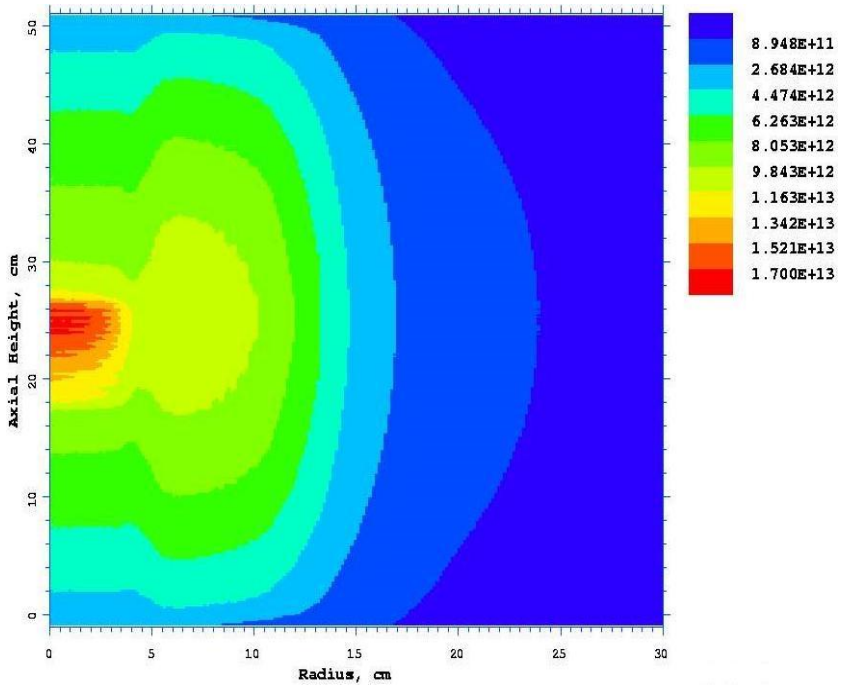

Figure III.3.9. R-Z view of the fast neutron flux (*E* > 100 keV) in the subcritical assembly (n/cm^2.s) with the uranium target, 100 kW/100 MeV electron beam, and 37 fuel assemblies

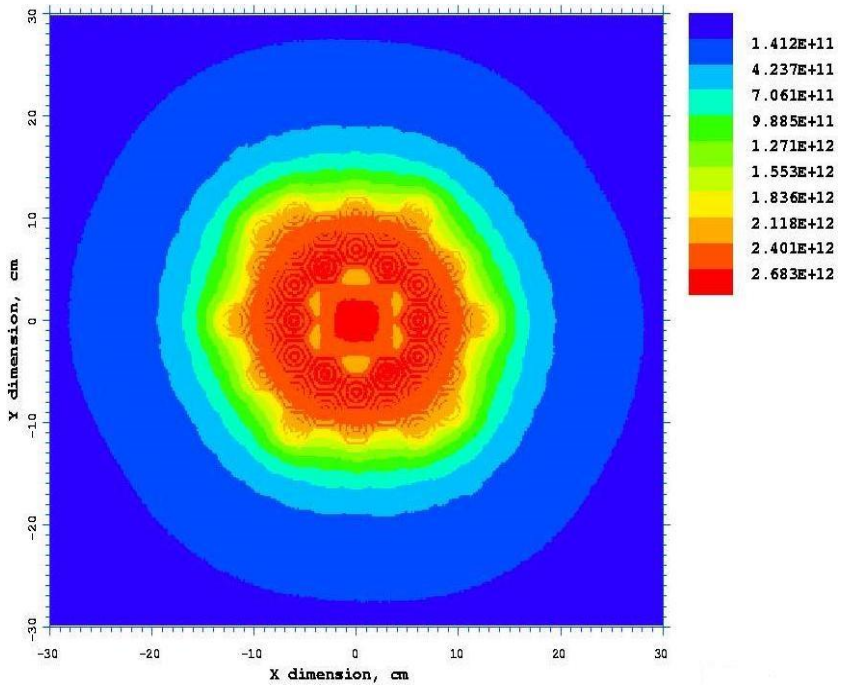

Figure III.3.10. X-Y view of the fast neutron flux (*E* > 100 keV) in the subcritical assembly (n/cm^2.s) with the tungsten target, 100 kW/100 MeV electron beam, and 38 fuel assemblies

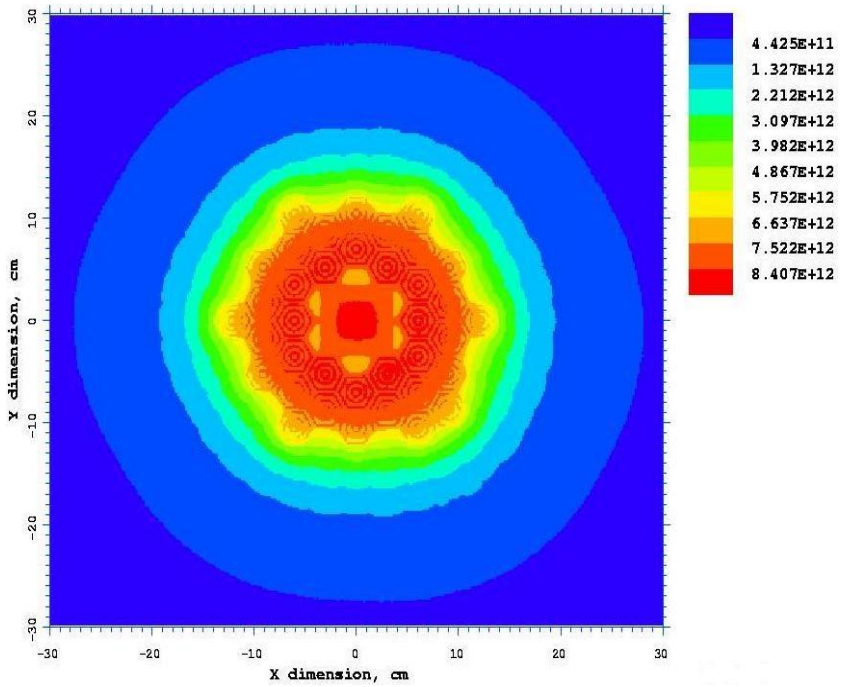

Figure III.3.11. X-Y view of the fast neutron flux (*E* > 100 keV) in the subcritical assembly (n/cm^2.s) with the uranium target, 100 kW/100 MeV electron beam, and 37 fuel assemblies

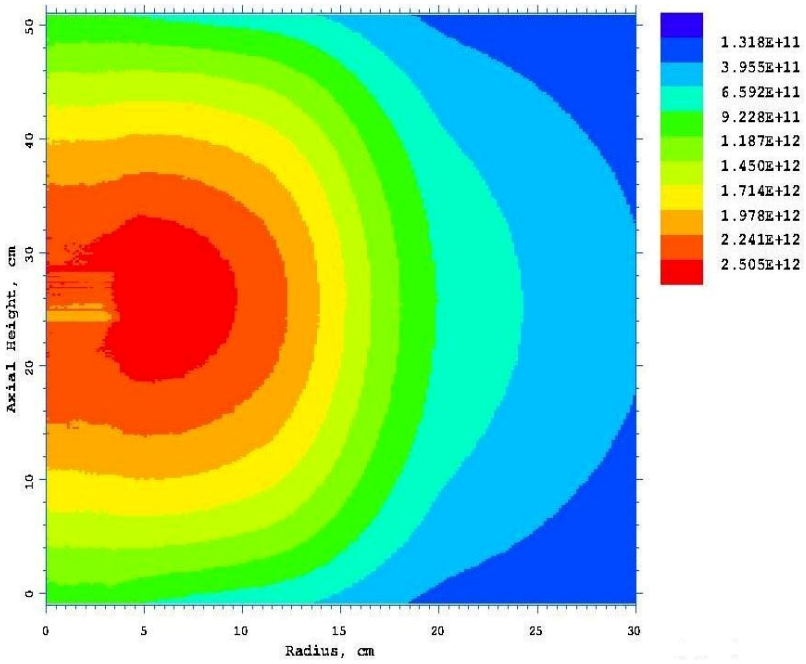

Figure III.3.12. R-Z view of the epi-thermal neutron flux (1 eV < *E* < 100 keV) in the subcritical assembly (n/cm^2.s) with the tungsten target, 100 kW/100 MeV electron beam, and 38 fuel assemblies

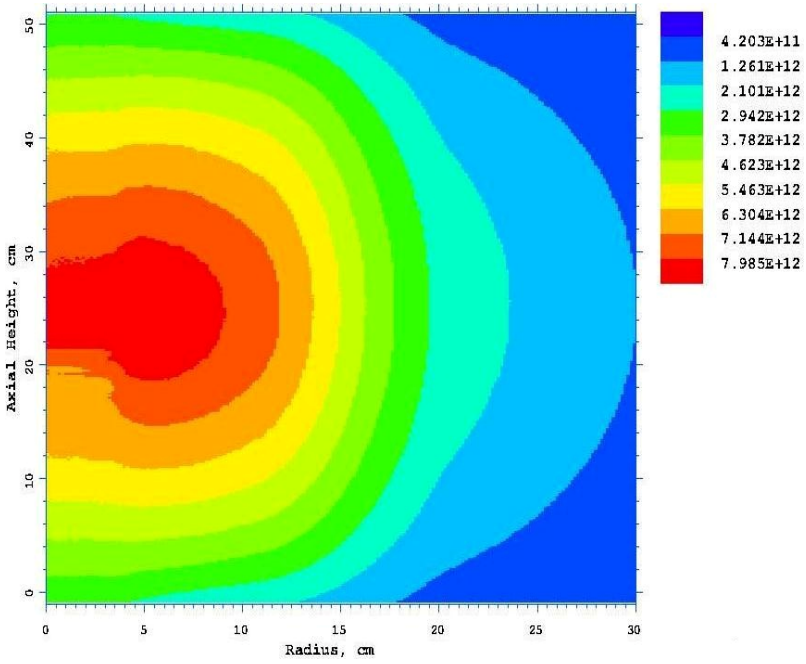

Figure III.3.13. R-Z view of the epi-thermal neutron flux (1 eV < *E* < 100 keV) in the subcritical assembly (n/cm^2.s) with the uranium target, 100 kW/100 MeV electron beam, and 37 fuel assemblies

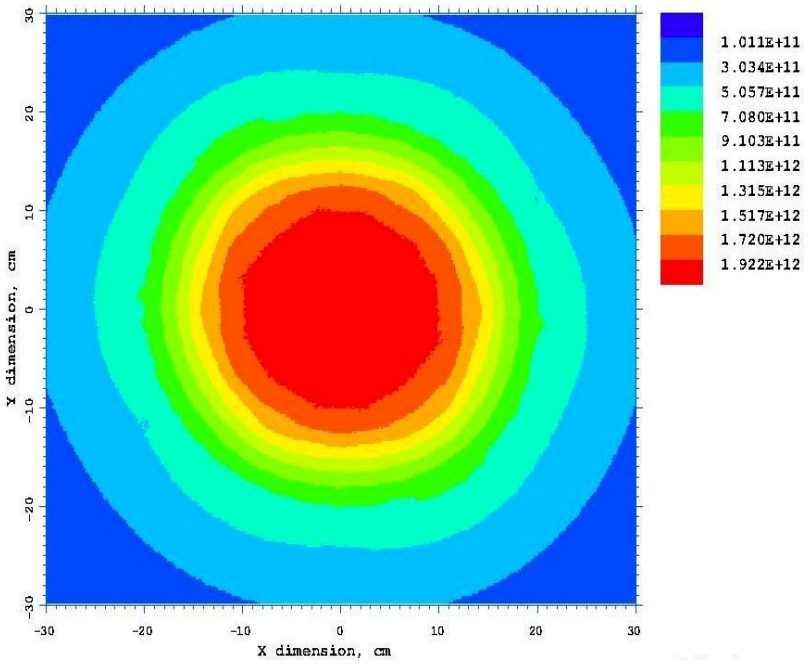

Figure III.3.14. X-Y view of the epi-thermal neutron flux (1 eV < *E* < 100 keV) in the subcritical assembly (n/cm^2.s) with the tungsten target, 100 kW/100 MeV electron beam, and 38 fuel assemblies

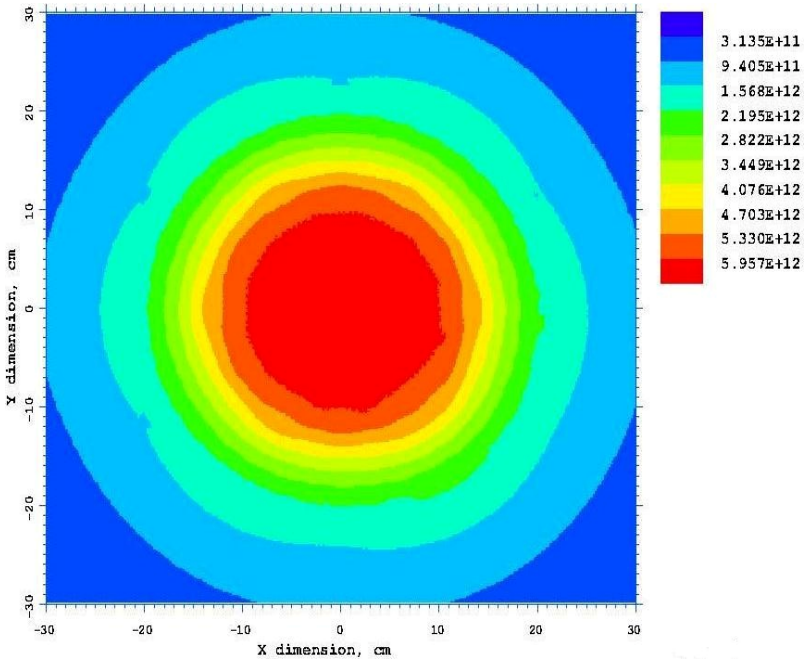

Figure III.3.15. X-Y view of the epi-thermal neutron flux (1 eV < *E* < 100 keV) in the subcritical assembly (n/cm^2.s) with the uranium target, 100 kW/100 MeV electron beam, and 37 fuel assemblies

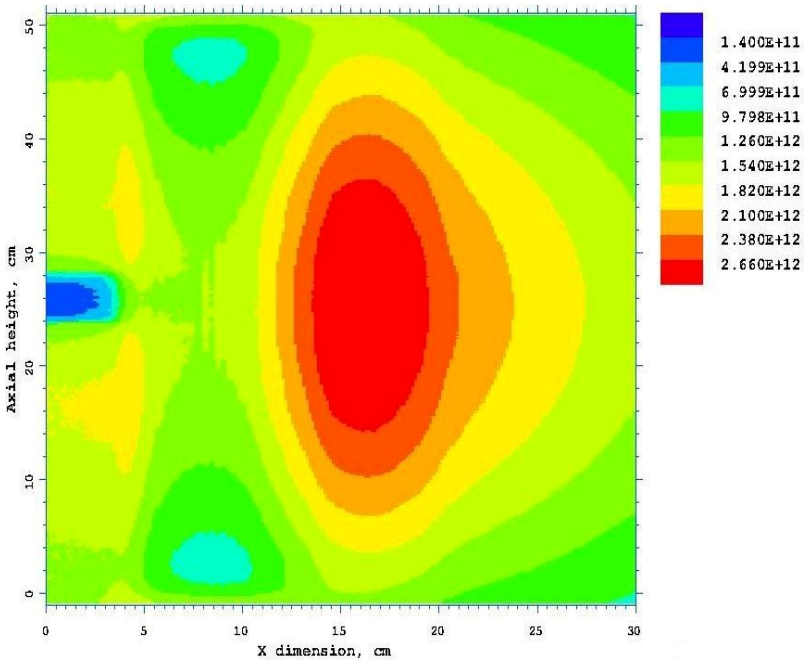

Figure III.3.16. R-Z view of the thermal neutron flux (*E* < 1 eV) in the subcritical assembly (n/cm^2.s) with the tungsten target, 100 kW/100 MeV electron beam, and 38 fuel assemblies

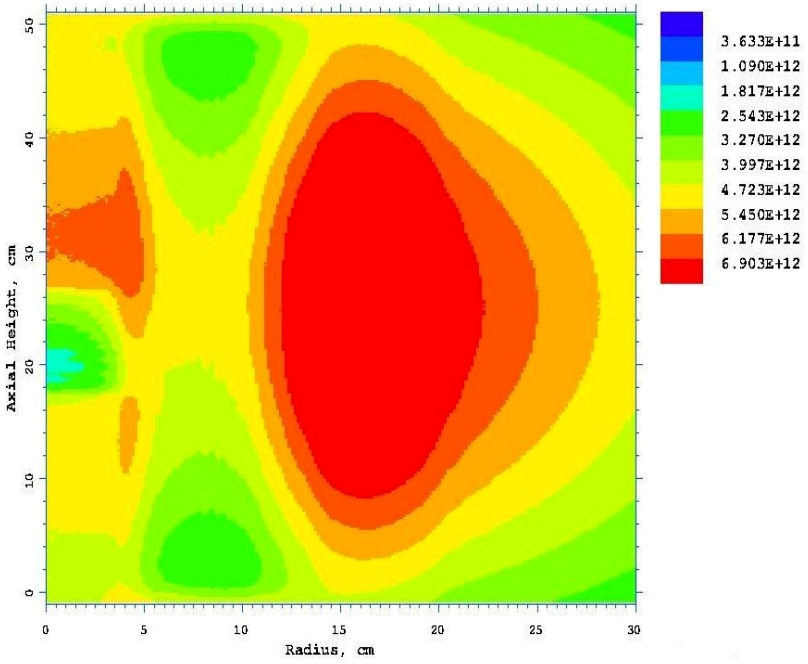

Figure III.3.17. R-Z view of the thermal neutron flux (*E* < 1 eV) in the subcritical assembly (n/cm^2.s) with the uranium target, 100 kW/100 MeV electron beam, and 37 fuel assemblies

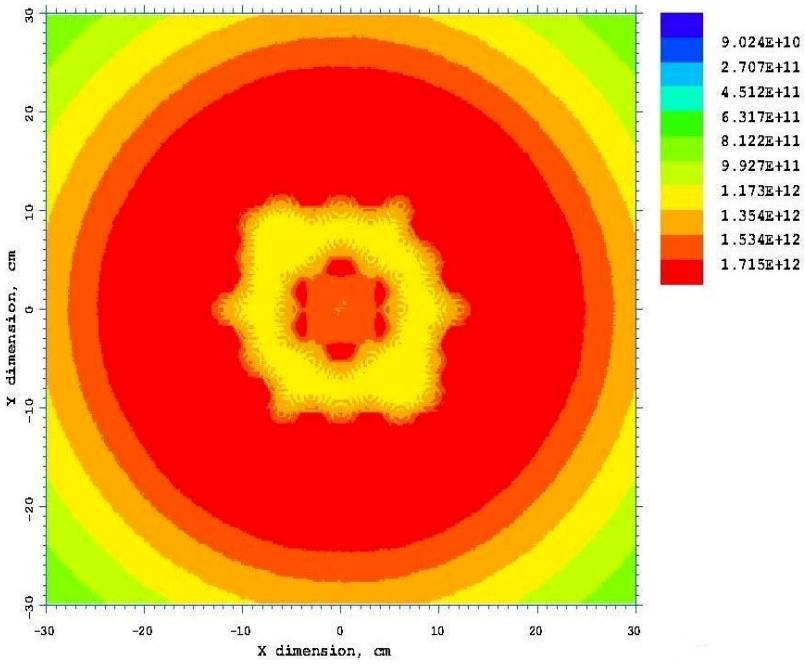

Figure III.3.18. X-Y view of the thermal neutron flux (*E* < 1 eV) in the subcritical assembly (n/cm^2.s) with the tungsten target, 100 kW/100 MeV electron beam, and 38 fuel assemblies

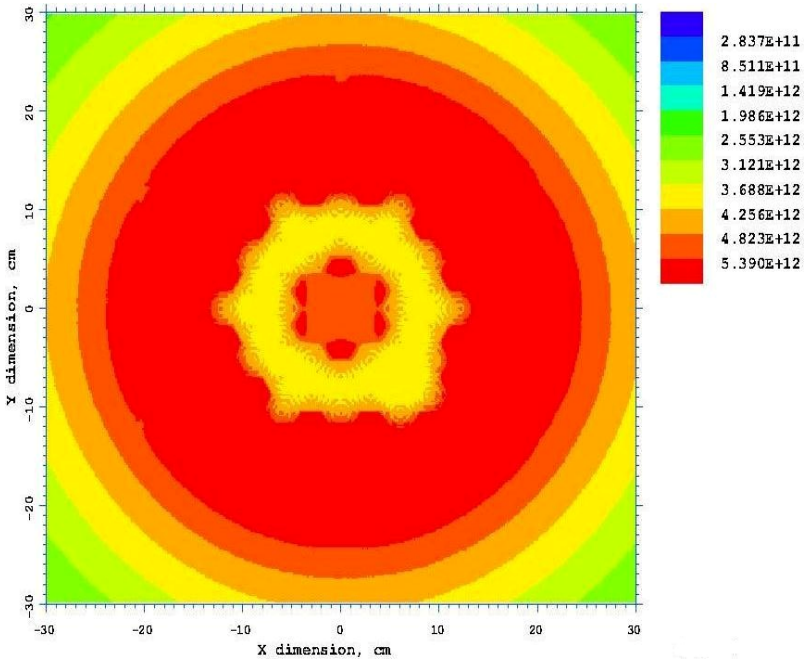

Figure III.3.19. X-Y view of the thermal neutron flux (*E* < 1 eV) in the subcritical assembly (n/cm^2.s) with the uranium target, 100 kW/100 MeV electron beam, and 37 fuel assemblies

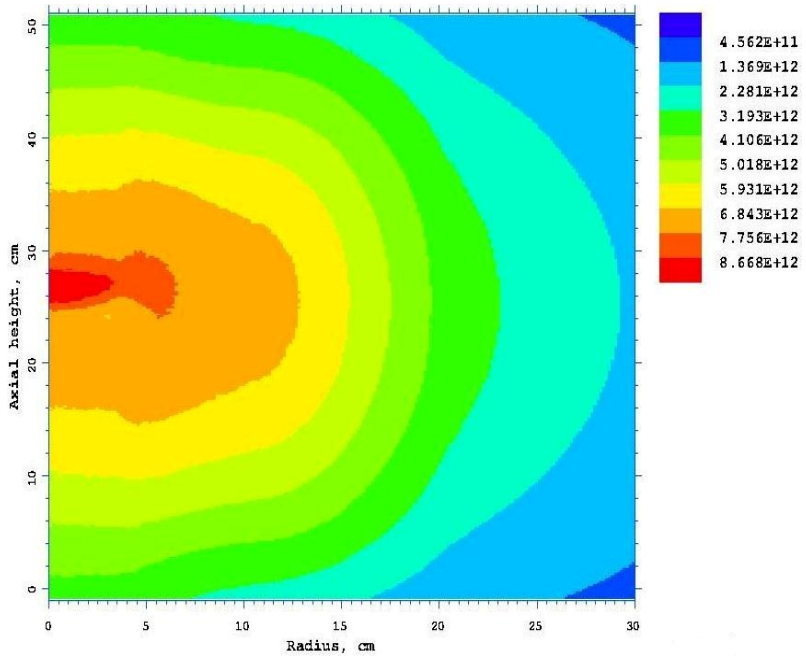

Figure III.3.20. R-Z view of the total neutron flux in the subcritical assembly (n/cm^2.s) with the tungsten target, 100 kW/100 MeV electron beam, and 38 fuel assemblies

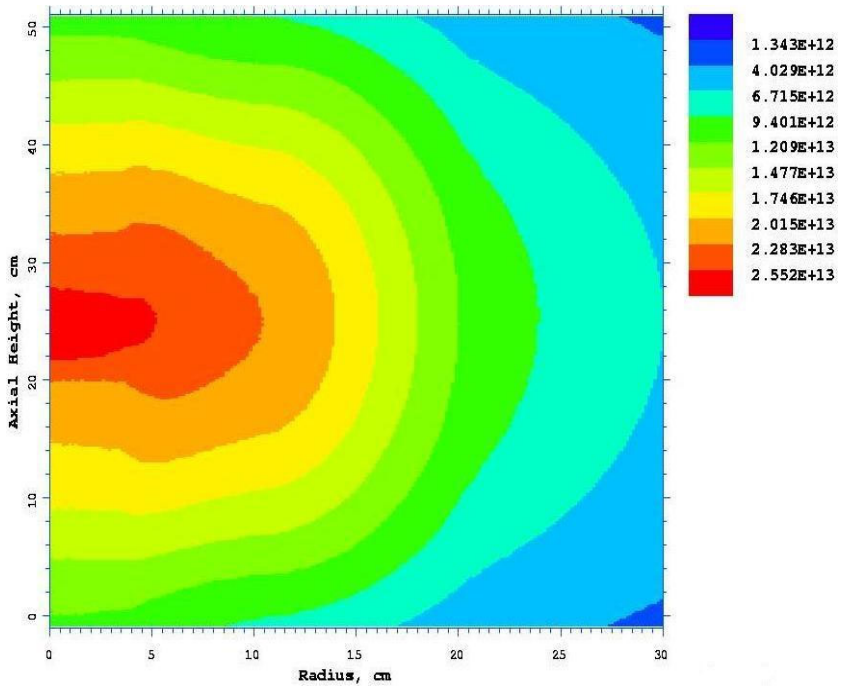

Figure III.3.21. R-Z view of the total neutron flux in the subcritical assembly (n/cm^2.s) with the uranium target, 100 kW/100 MeV electron beam, and 37 fuel assemblies

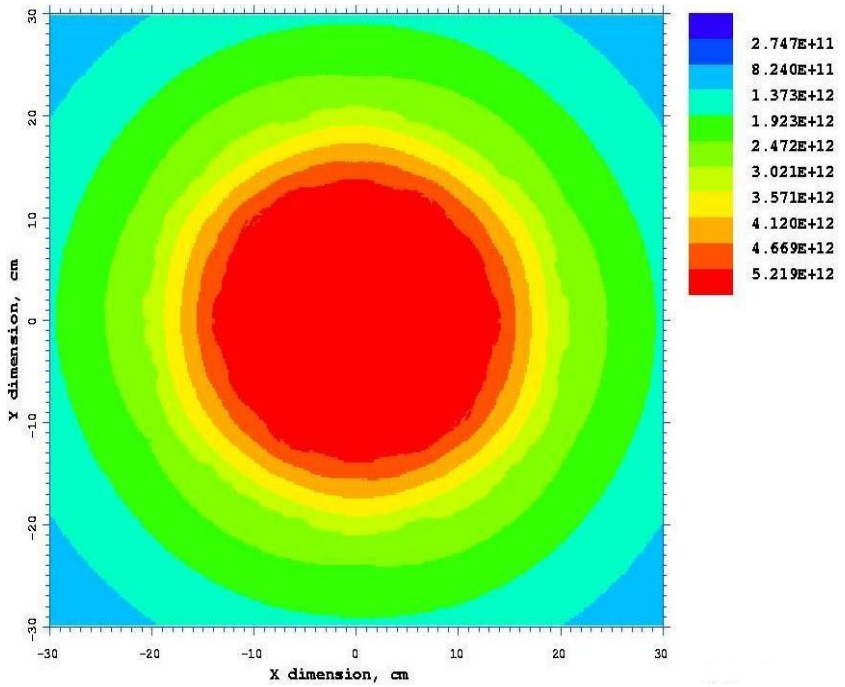

Figure III.3.22. X-Y view of the total neutron flux in the subcritical assembly (n/cm^2.s) with the tungsten target, 100 kW/100 MeV electron beam, and 38 fuel assemblies

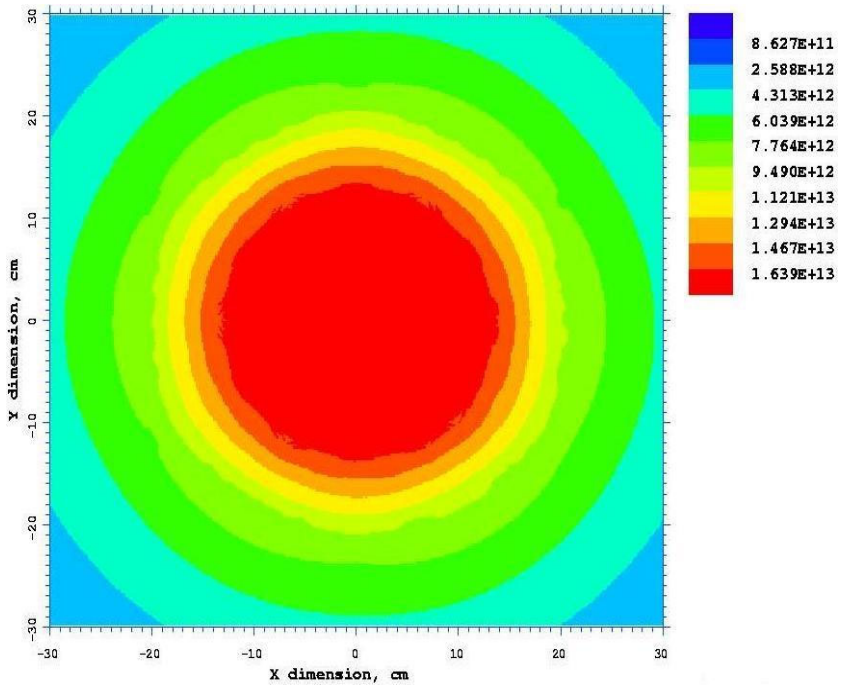

Figure III.3.23. X-Y view of the total neutron flux in the subcritical assembly (n/cm^2.s) with the uranium target, 100 kW/100 MeV electron beam, and 37 fuel assemblies

III.4 Burnup Analysis

III.4.1 Burnup Cycles

During operation, fissile material consumption and fission products buildup in the subcritical assembly fuel decrease the reactivity level and the subcritical assembly neutron flux level. Unlike critical reactors, the ADS facility does not have control rods or burnable poison materials to control its reactivity. Therefore, to maintain the neutron flux level, fuel assemblies will be shuffled in steps during each burn cycle to compensate for the reactivity loss. At the end of each burn cycle, additional fuel assemblies will be added to the subcritical assembly or few fuel assemblies with the lowest U-235 enrichment will be replaced. During all the time, the neutron multiplication factor, k_{eff}, of the subcritical assembly will not exceed the initial value with the fresh fuel assemblies.

Monte Carlo analyses can accurately determine the reactivity of the subcritical assembly. In addition, computer capabilities have been improved significantly, and parallel calculations using a large number of computer processors are now possible for scientific applications. Such capabilities provide the ability to perform three-dimensional burnup simulations using detailed geometry and a continuous energy description of the nuclear data [III.4.1]. The Monte Carlo computer codes MCNPX [III.4.2] and MCB [III.4.3] are examples of these capabilities.

At present, neither MCNPX nor MCB can alone simulate burnup in an accelerator-driven subcritical system. MCNPX can transport electrons, neutrons, and photons to simulate electron-driven subcritical assembly but does not have the capability to model depletion/burnup of this system. MCB can perform neutron transport and burnup calculations however, it cannot transport electrons for generating the neutron source. This difficulty is resolved by using a coupling procedure between MCNPX and MCB so that the two codes are used together to perform electron transport and burnup analysis of the KIPT neutron source facility. First, an MCNPX calculation is performed starting with 100 MeV electrons, with the neutron fission events turned off, to generate a volume neutron source file. This file includes the position, the energy, the direction vector, and the weight of each neutron generated inside the target material from the photonuclear reactions caused by the electrons. The file generation utilizes the user-defined subroutine TALLYX of MCNPX. Then the neutron source file is used by MCB through the user-defined subroutine SOURCE to drive the subcritical assembly. With this procedure, the neutron yield from electrons is simulated correctly in the MCB calculation, although no electron transport is modeled in the MCB calculations. The neutron source is normalized to the 100-kW electron beam power. The neutron source intensity calculated by MCNPX and used in the MCB calculation is 1.88×10^{14} neutrons per second for the tungsten target and 3.01×10^{14} neutrons per second for the uranium target, and the neutron source intensity is assumed to be constant during the entire burnup period.

In the MCB calculation, the fuel assemblies are divided into three burnup batches, based on their radial positions relative to the target center, as shown in Figs. III.4.1.1 and III.4.1.2, where each batch has a different color. Each batch is divided into five equally spaced axial zones, each zone is 10 cm in length, generating 15 zones altogether. When the

uranium target is used, each of the 11 target plates is also treated as a separate zone. Therefore, the total number of burnup zones in the MCB model is 15 when the tungsten target is used and 26 when the uranium target is used.

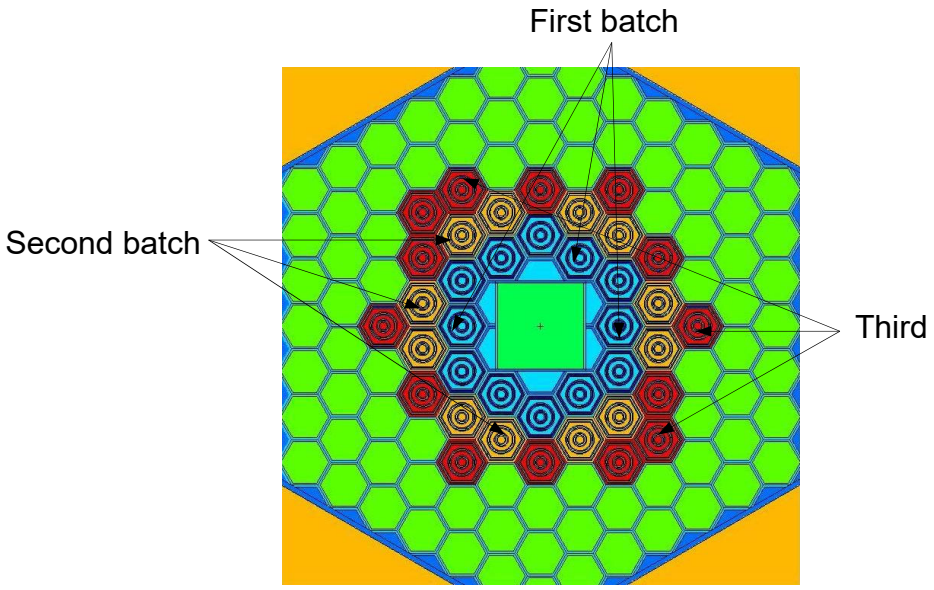

Figure III.4.1.1. Radial burnup zones of the subcritical assembly with tungsten target and 38 fuel assemblies

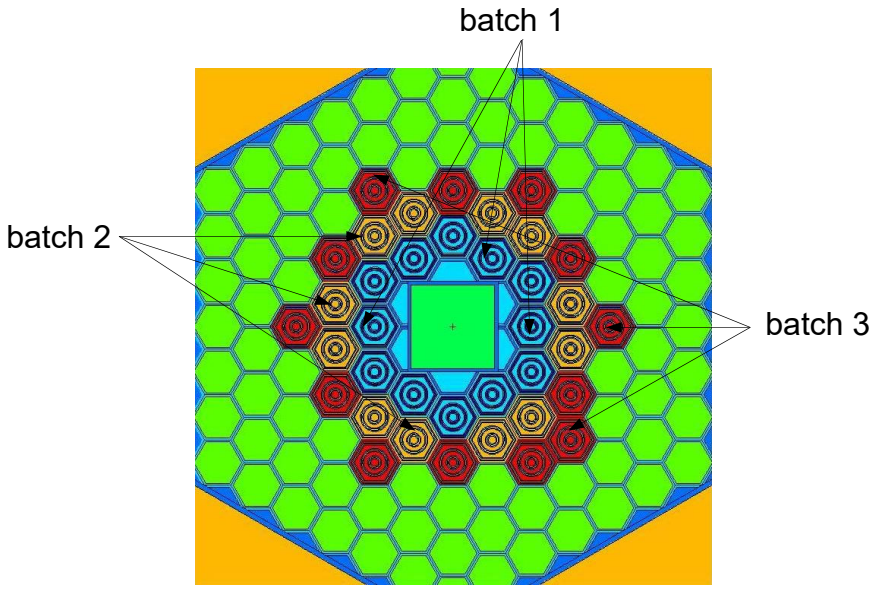

Figure III.4.1.2. Radial burnup zones of the subcritical assembly with uranium target and 37 fuel assemblies

As mentioned above, each burnup cycle is divided into multiple stages and fuel assemblies are shuffled after each stage within the subcritical assembly to compensate

for the reactivity loss due to the burnup of the fissile material and the buildup of the fission products. To minimize the neutron flux variation during operation, the reactivity loss of each burnup cycle stage is limited to 200 to 300 pcm range. The analyses have shown that adding fresh fuel assembly into the subcritical assembly increases reactivity by ~ 500 to 800 pcm depending on its position relative to the other fuel assemblies, which overcompensates the reactivity loss during the burnup stage. The analyses show that moving one peripheral fuel assembly radially in the beryllium reflector zone results in 200 - 300 pcm additional reactivity. Therefore, one fuel assembly is moved outward at the end of each burnup stage to compensate for lost reactivity. After all the fuel assemblies have been moved outward and reached the inner boundary of the graphite reflector, the fuel assemblies are moved back around the target assembly and new fuel assemblies are added to the subcritical assembly or old fuel assemblies are replaced with fresh or used fuel assemblies.

Thus, the burn cycle has many stages, and the end of each stage one fuel assembly is moved radially inside the beryllium reflector. The fuel cycle ends when the fuel assemblies reach the inner graphite boundary. Then the fuel assemblies are moved radially around the target assembly and fresh fuel assemblies are added to the subcritical assembly or old fuel assemblies are replaced.

III.4.2 Reactivity Limits During Operation

At the beginning of operation, fission products, including Xe^{135}, will begin to build up. With a short half-life of 9.14 hours for Xe^{135}, this isotope will accumulate in the system quickly. Due to the large thermal absorption cross-section of Xe^{135}, buildup of this isotope is the primary reason for a significant reactivity drop during the first two days following the startup of the subcritical assembly, even though the change in the U-235 enrichment is very small during these two days. The drop in k_{eff} is about 900 pcm when the uranium target with an initial subcritical assembly loading of 37 fresh fuel assemblies is used, as shown in Fig. III.4.2.1. The drop is significantly less for the tungsten target case with an initial subcritical assembly loading of 38 fresh fuel assemblies, about 400 pcm as shown in Fig. III.4.2.2, due to the lower neutron flux when the tungsten target configuration is used. The lower neutron flux and lower power of the tungsten target configuration result in a lower production of xenon and therefore a smaller reactivity drop. The results presented in Figs. III.4.2.1 and III.4.2.2 were generated by the MCB simulations.

After the shutdown, Xe^{135} decays quickly and the lost reactivity is recovered in a few days. Since the KIPT ADS uses a passive approach to control the neutron multiplication, k_{eff} must be always kept below 0.98, including the period during shutdown. For the uranium target option, this means that k_{eff} during operation will be ≤ 0.971.

For the tungsten target configuration, the tungsten material works as a neutron absorber, so its removal increases k_{eff} of the subcritical assembly. The tungsten target removal increases k_{eff} by ~2000 pcm, therefore k_{eff} of the fresh assembly must be ≤ 0.96. During operation, the k_{eff} value will be lowered by additional 400 pcm because of the Xe^{135} buildup.

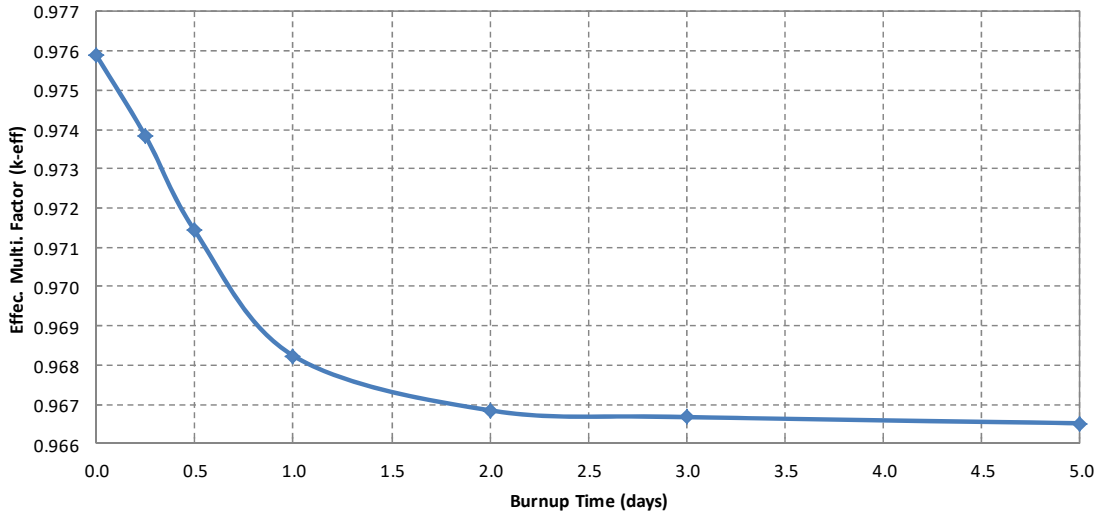

Figure III.4.2.1. The effective neutron multiplication changes during operation of the uranium target configuration with 37 fresh fuel assemblies.

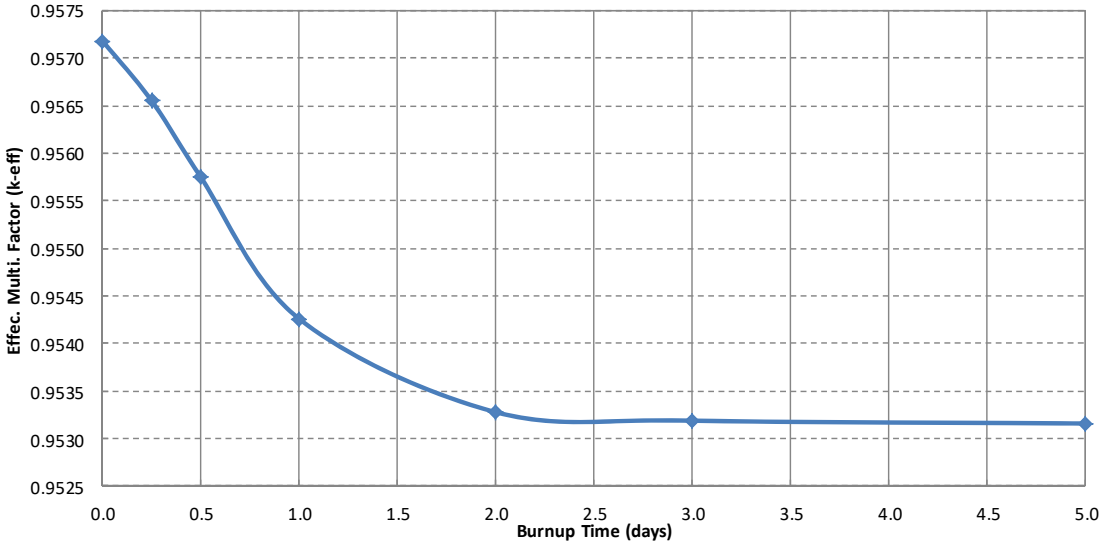

Figure III.4.2.2. The effective neutron multiplication changes during operation of the tungsten target configuration with 38 fresh fuel assemblies

III.4.3 Fuel Management During the First Burnup Cycle

The subcritical assembly configurations and the operation time of each depletion stage of the first burnup cycle are shown in Figs. III.4.3.1 and III.4.3.2 for the tungsten and uranium target configurations, respectively. The corresponding k_{eff} history calculated by MCB is shown in Figs. III.4.3.3 and III.4.3.4 for the tungsten and uranium target configurations, respectively. After two days of operation, one fuel assembly is radially moved in the reflector zone to compensate for the reactivity loss caused by Xe^{135} accumulation and other fission products. In succeeding stages, more fuel assemblies are moved radially outward to introduce more reactivity in a stepwise fashion.

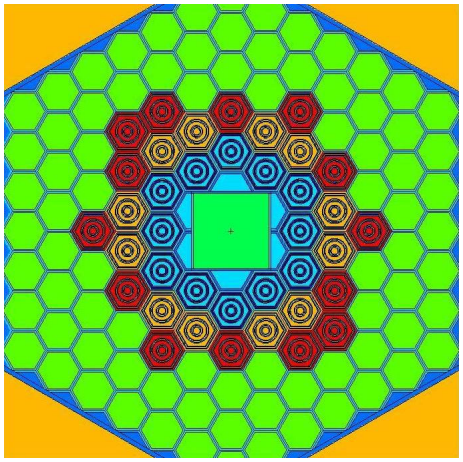

Stage 1, 0 ~ 2 days

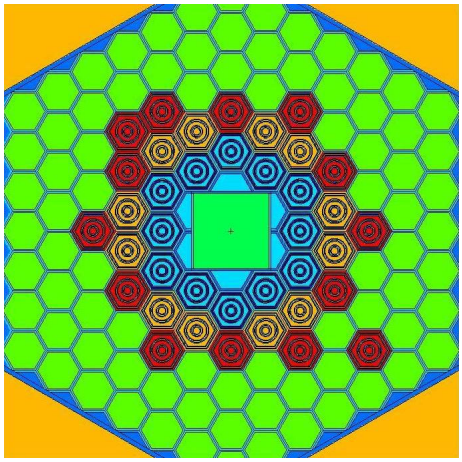

Stage 2, 3 ~ 52 days

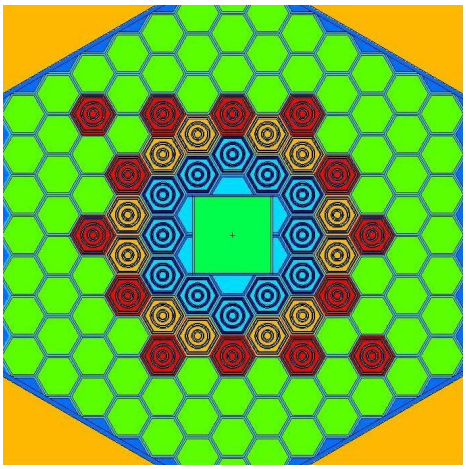

Stage 3, 53 ~ 147 days

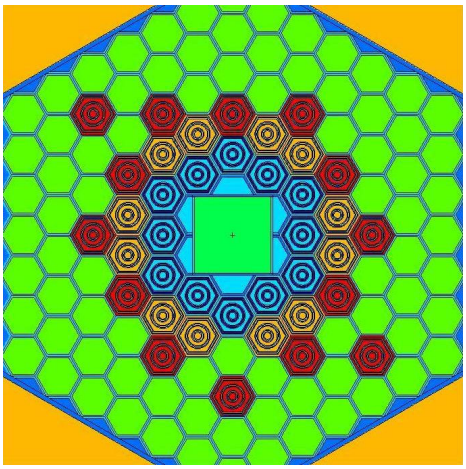

Stage 4, 148 ~ 272 days

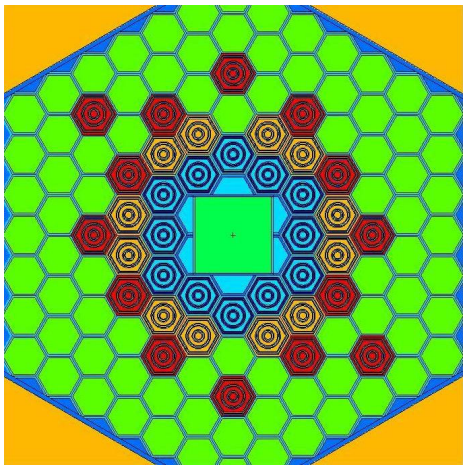

Stage 5, 273 ~ 397 days

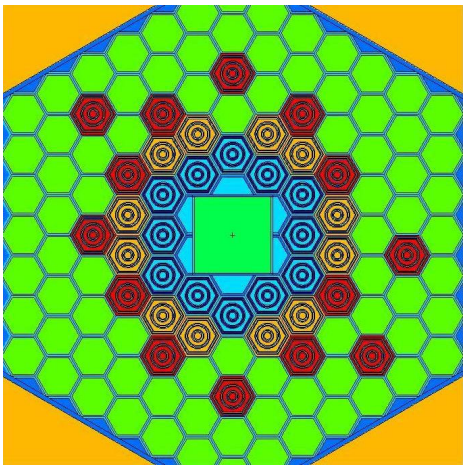

Stage 6, 398 ~ 507 days

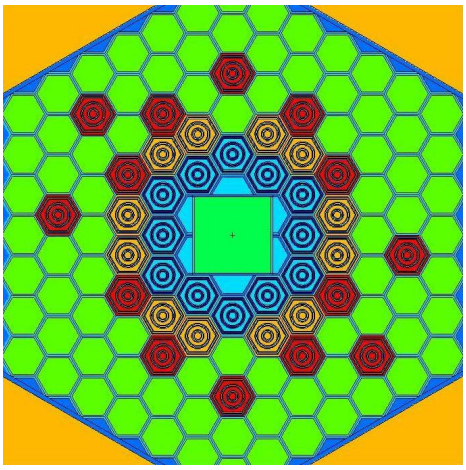

Stage 7, 508 ~ 647 days

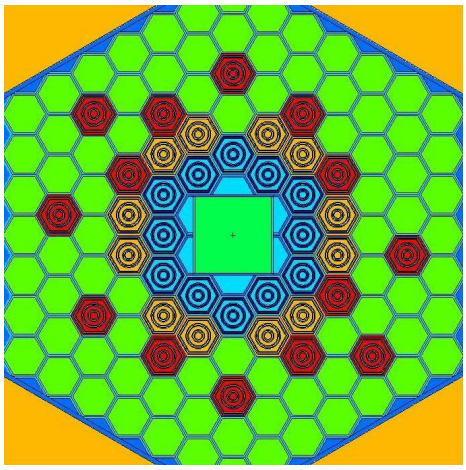

Stage 8, 648 ~ 827 days

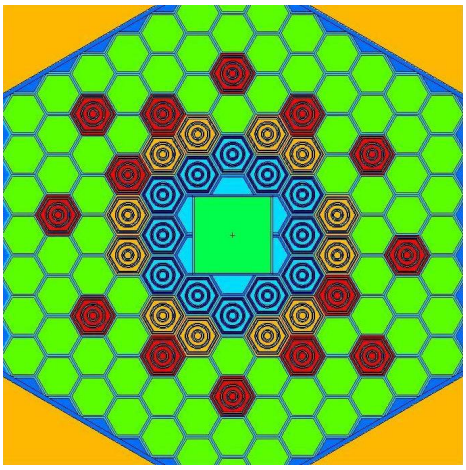

Stage 9, 828 ~ 967 days

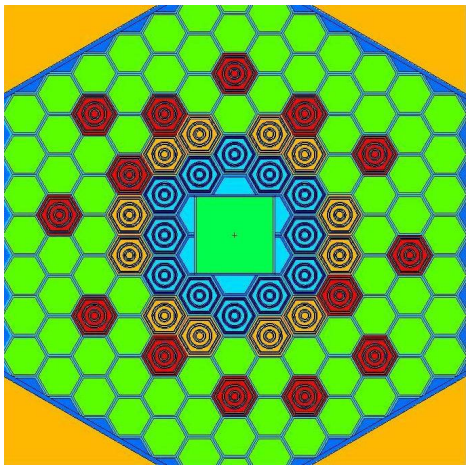

Stage 10, 968 ~ 1107 days

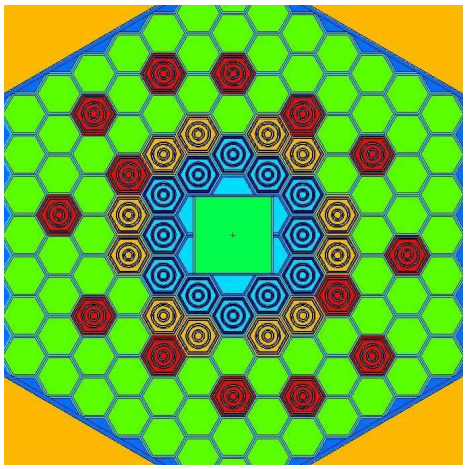

Stage 11, 1108 ~ 1227 days

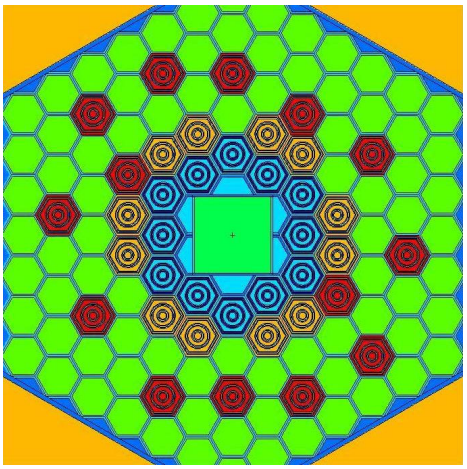

Stage 12, 1228 ~ 1327 days

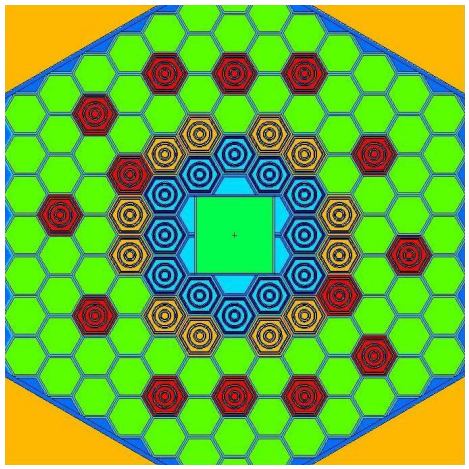

Stage 13, 1328 ~ 1427 days

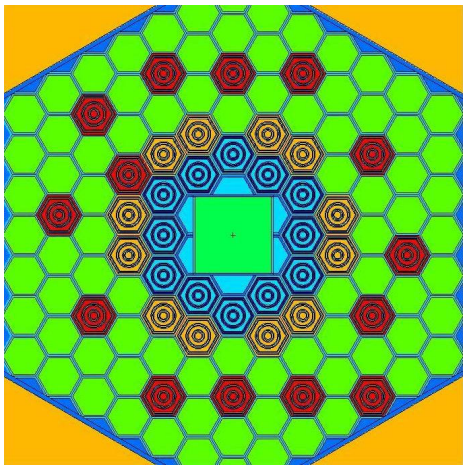

Stage 14, 1428 ~ 1527 days

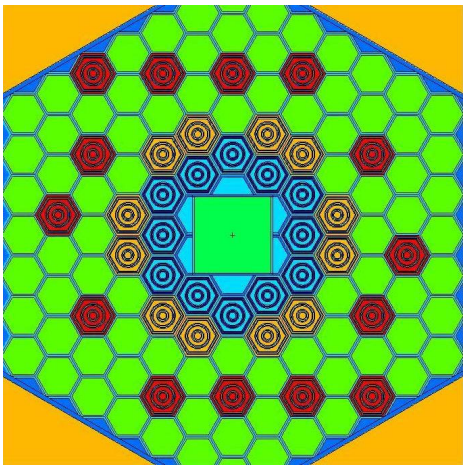

Stage 15, 1528 ~ 1627 days

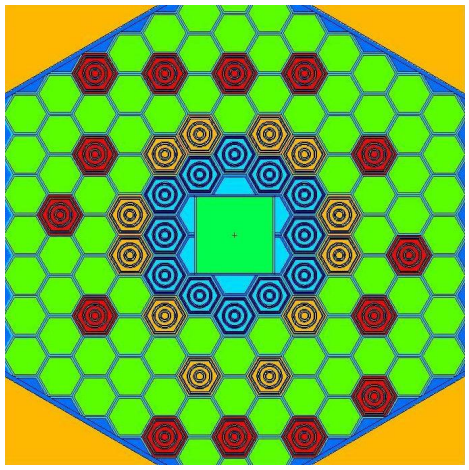

Stage 16, 1628 ~ 1727 days

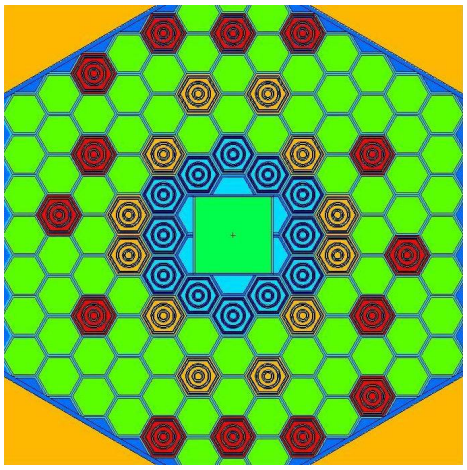

Stage 17, 1728 ~ 1827 days

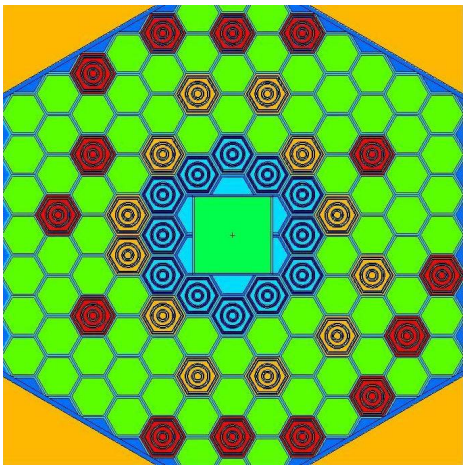

Stage 18, 1828 ~ 1907 days

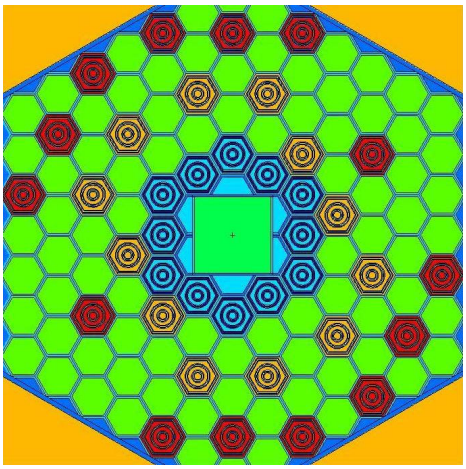

Stage 19, 1908 ~ 2007 days

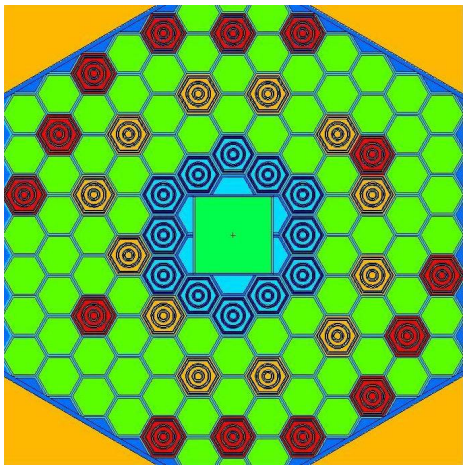

Stage 20, 2008 ~ 2107 days

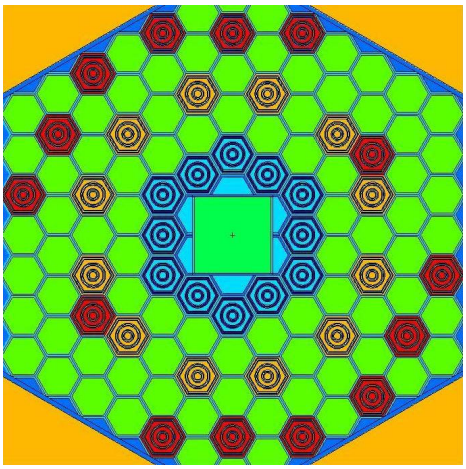

Stage 21, 2108 ~ 2207 days

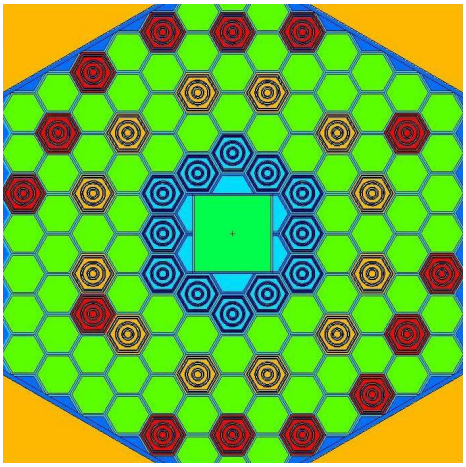

Stage 22, 2208 ~ 2267 days

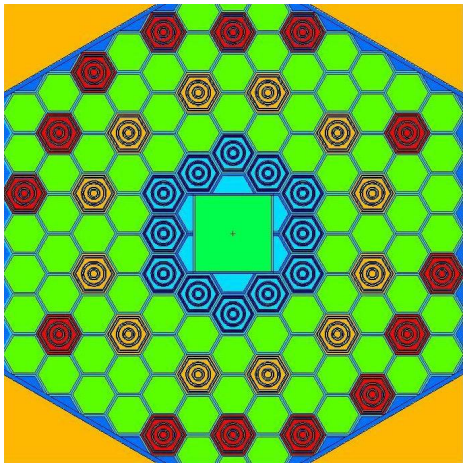

Stage 23, 2268 ~ 2347 days

Figure III.4.3.1. Subcritical assembly configurations for each burnup stage of the first burnup cycle using tungsten target and 38 fuel assemblies

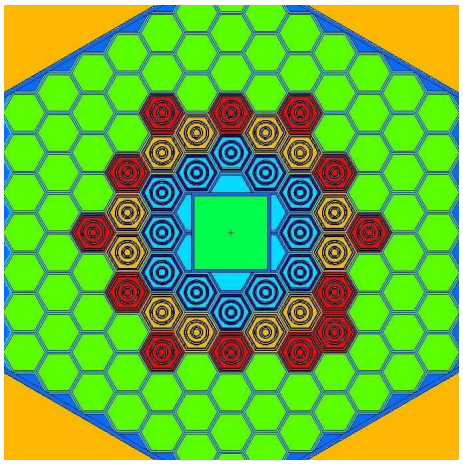

Stage 1, 0 ~ 2 days

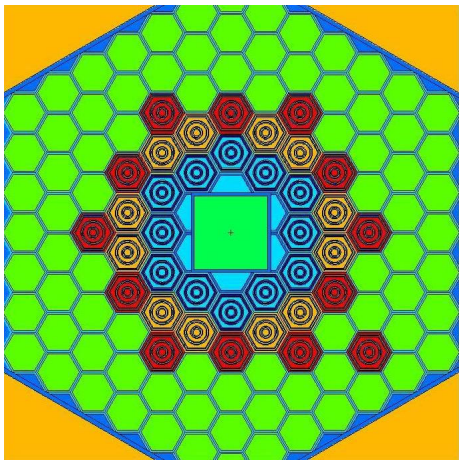

Stage 2, 3 ~ 32 days

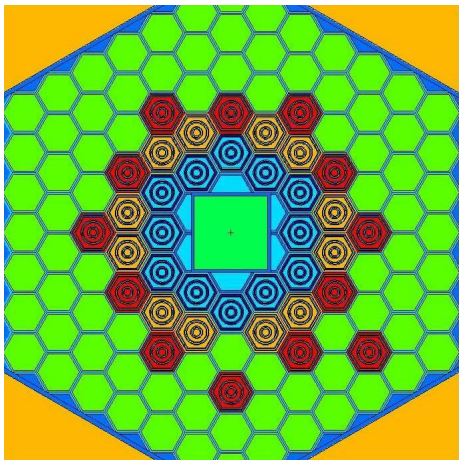

Stage 3, 33 ~ 72 days

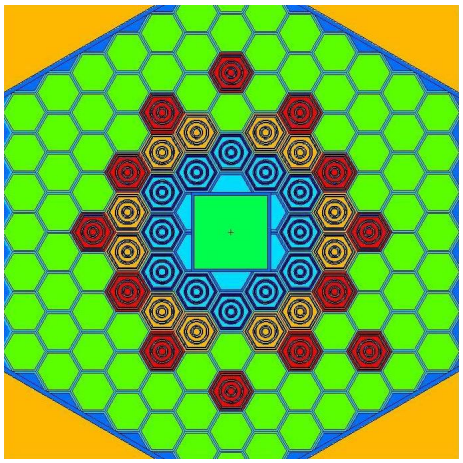

Stage 4, 73 ~ 112 days

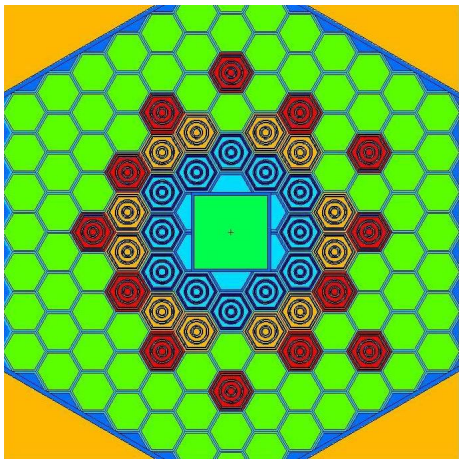

Stage 5, 113 ~ 162 days

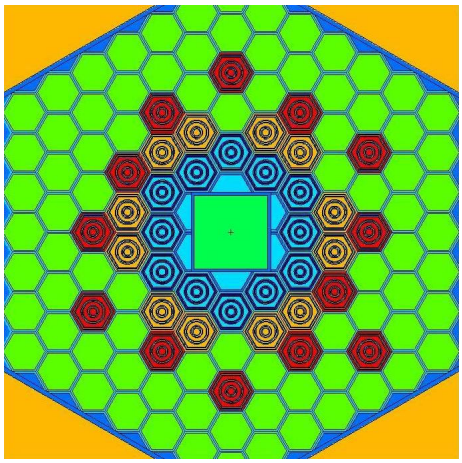

Stage 6, 163 ~ 222 days

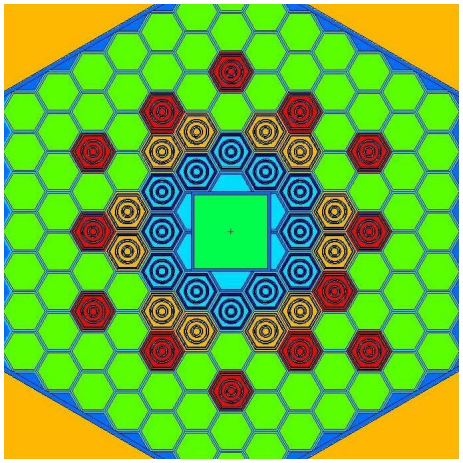

Stage 7, 223 ~ 282 days

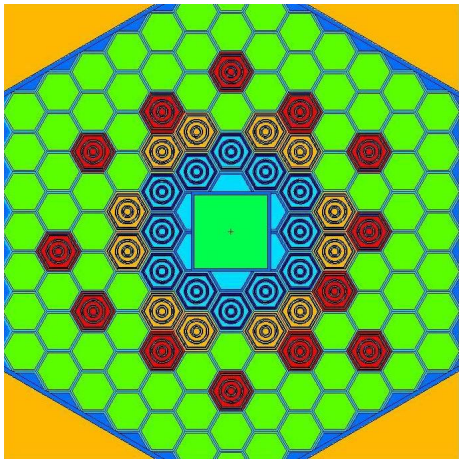

Stage 8, 283 ~ 342 days

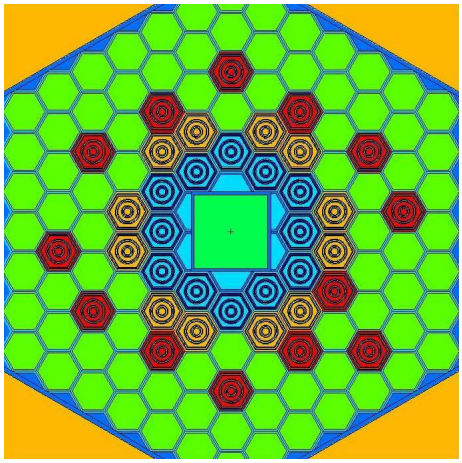

Stage 9, 343 ~ 402 days

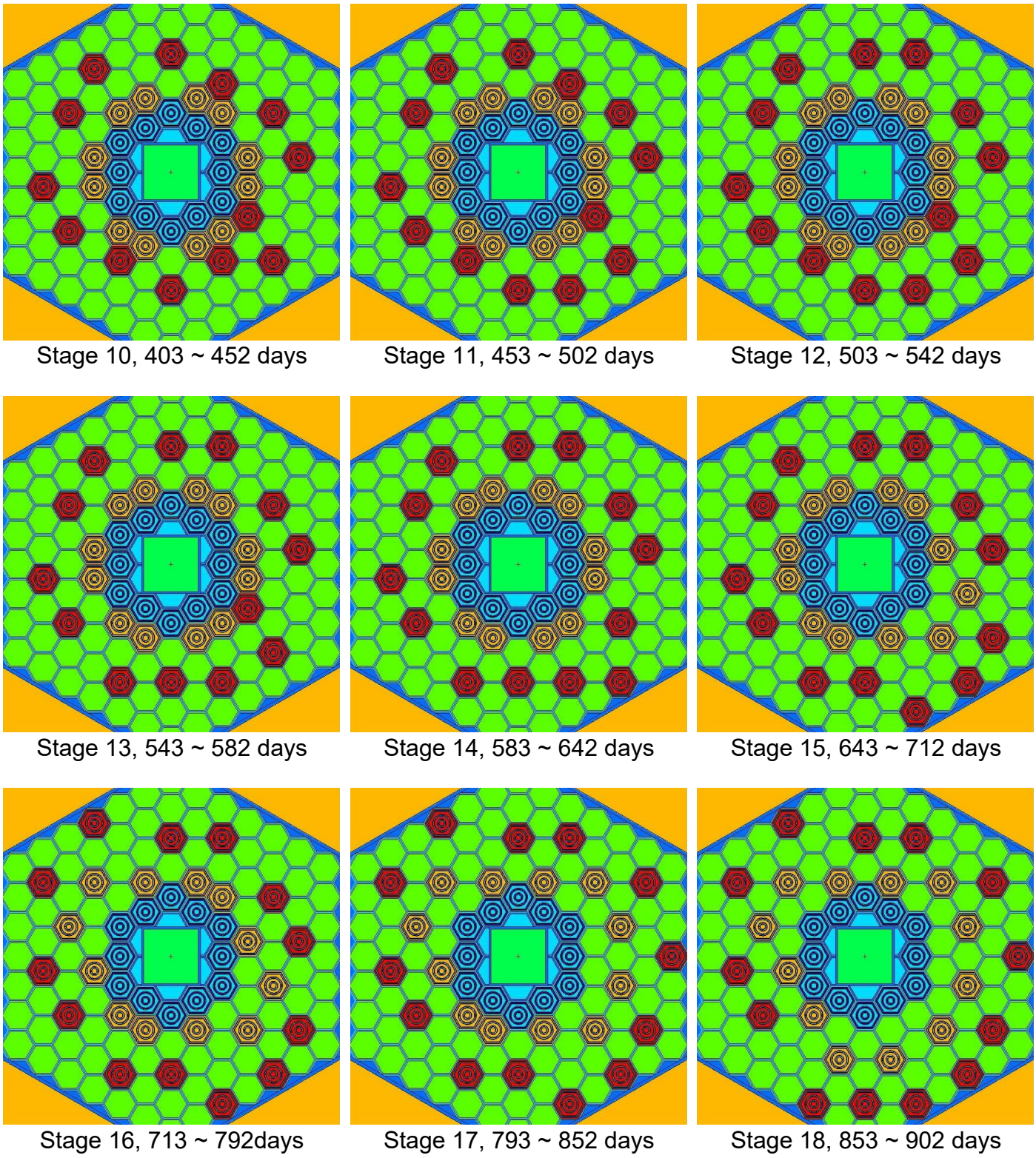

Figure III.4.3.2. Subcritical assembly configurations for each burnup stage of the first burnup cycle using uranium target and 37 fuel assemblies

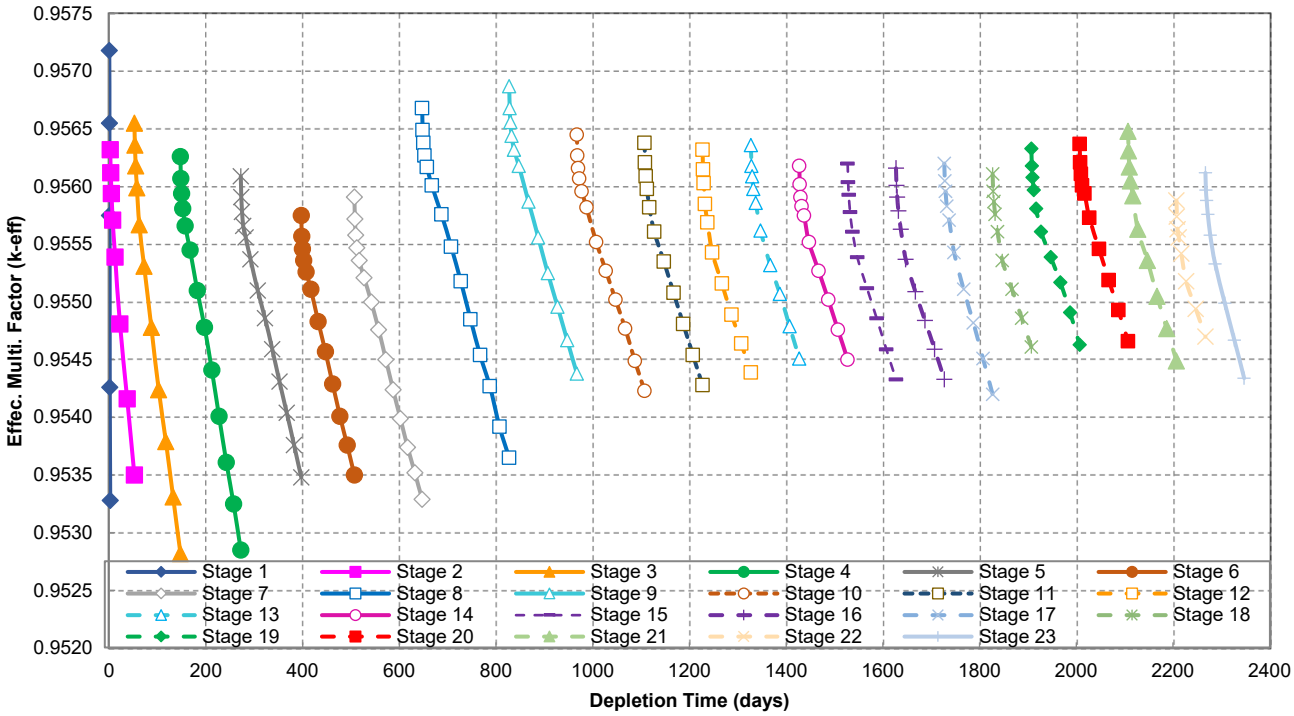

Figure III.4.3.3. k_{eff} values during the first burnup cycle for the subcritical assembly with the tungsten target and 38 fuel assemblies

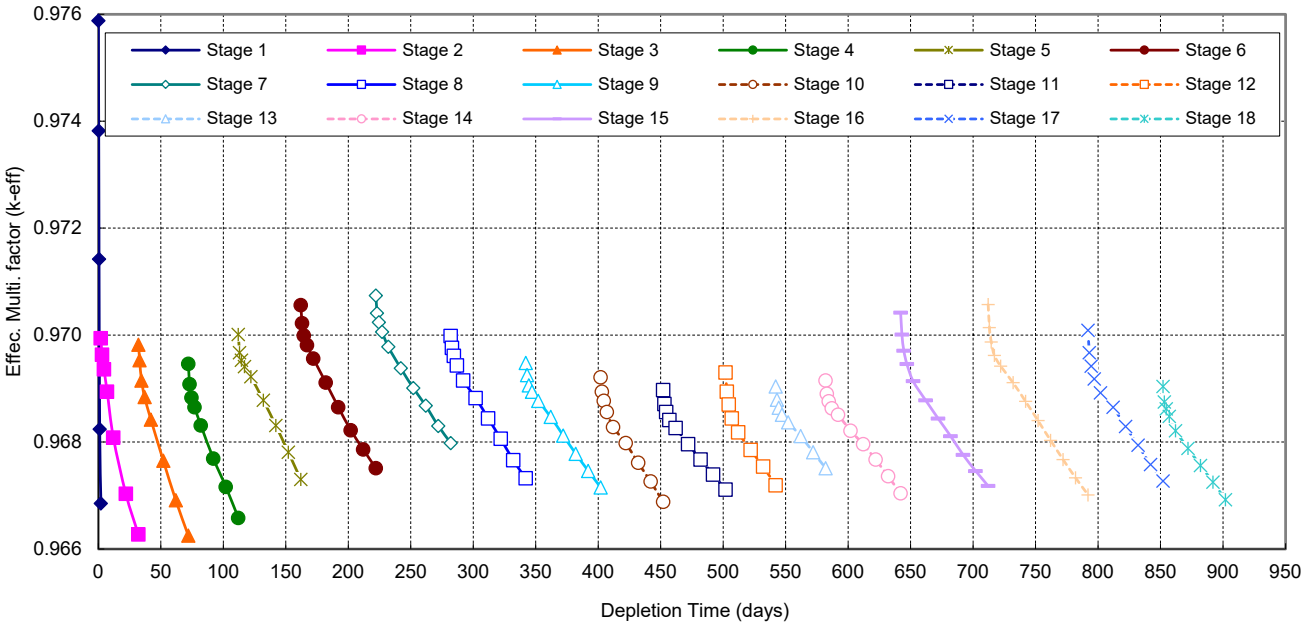

Figure III.4.3.4. k_{eff} values during the first burnup cycle for the subcritical assembly with the uranium target and 37 fuel assemblies

The average neutron flux values in the target coolant channels along the 50-cm active fuel length and along the target materials length (5.15 cm for the tungsten target and 9.19 cm for the uranium target) have been calculated by MCB at the beginning and the end of each burnup stage, and the results are shown in Tables III.4.1 and III.4.2 for the tungsten and uranium targets. Using the fuel shuffling scheme, k_{eff} is kept in the range of 0.953 to 0.956 for the tungsten target configuration and 0.967 to 0.971 for the uranium target configuration. The neutron flux level is relatively constant during operation, as shown in Tables III.4.3.1 and III.4.3.2.

The average burnup values of the three fuel batches at the end of each burnup stage during the first burnup cycle are listed in Tables III.4.3.3 and III.4.3.4 for the tungsten and uranium targets, respectively. These values show that the first and the third batch has the lowest and the highest burnup at the end of the cycle. The beryllium reflector increases the thermal neutron flux at the boundary of the fuel zone, which increases the burnup values. The same effect occurs when the fuel assembly is moved in the reflector zones to increase the reactivity of the subcritical assembly.

The average U^{235} enrichment of each fuel batch at the end of the first burnup cycle is shown in Table III.4.3.5. At the end of the first burnup cycle, when the fuel assemblies of the second and third fuel batches are distributed within the beryllium reflector zone, it is not possible to further increase the reactivity of the subcritical assembly by shuffling the fuel assemblies. However, the enrichment of the fuel assemblies is > 17.5%, so these fuel assemblies can still be utilized in the next fuel cycles. So, it is necessary to add some new fuel assemblies to the subcritical assembly.

Table III.4.3.1. k_{eff} and neutron flux at the beginning and end of each stage of the first burnup cycle of the subcritical assembly with tungsten target and 38 fuel assemblies during

Stages	Beginning of the burnup stage				End of the burnup stage			
	k_{eff}	Neutron flux along the fuel length	Neutron flux along the target length	Total fission heat in the fuel (kW)	k_{eff}	Neutron flux along the fuel length	Neutron flux along the target length	Total fission heat in the fuel (kW)
1	0.95718 ±12 pcm	6.340e+12 ±0.42%	7.992e+12 ±0.36%	64.28 ±0.44%	0.95328 ±12 pcm	5.771e+12 ±0.40%	7.394e+12 ±0.34%	58.06 ±0.42%
2	0.95632 ±12 pcm	6.133e+12 ±0.41%	7.765e+12 ±0.36%	62.48 ±0.44%	0.95350 ±13 pcm	5.781e+12 ±0.40%	7.390e+12 ±0.34%	58.56 ±0.42%
3	0.95655 ±12 pcm	6.134e+12 ±0.41%	7.765e+12 ±0.36%	62.93 ±0.43%	0.95282 ±12 pcm	5.701e+12 ±0.40%	7.299e+12 ±0.34%	58.02 ±0.42%
4	0.95626 ±12 pcm	6.115e+12 ±0.41%	7.727e+12 ±0.36%	63.04 ±0.43%	0.95285 ±11 pcm	5.610e+12 ±0.39%	7.198e+12 ±0.34%	57.33 ±0.42%
5	0.95609 ±12 pcm	6.044e+12 ±0.41%	7.653e+12 ±0.35%	62.55 ±0.43%	0.95348 ±12 pcm	5.734e+12 ±0.40%	7.337e+12 ±0.34%	58.95 ±0.42%
6	0.95575 ±12 pcm	5.959e+12 ±0.41%	7.582e+12 ±0.35%	61.84 ±0.43%	0.95350 ±12 pcm	5.727e+12 ±0.40%	7.325e+12 ±0.34%	59.13 ±0.42%
7	0.95591 ±12 pcm	6.016e+12 ±0.41%	7.624e+12 ±0.35%	62.73 ±0.43%	0.95329 ±13 pcm	5.714e+12 ±0.40%	7.301e+12 ±0.34%	59.24 ±0.42%
8	0.95668 ±12 pcm	6.142e+12 ±0.41%	7.753e+12 ±0.36%	64.45 ±0.44%	0.95365 ±13 pcm	5.740e+12 ±0.40%	7.325e+12 ±0.34%	59.75 ±0.42%
9	0.95687 ±11 pcm	6.153e+12 ±0.41%	7.762e+12 ±0.36%	64.88 ±0.44%	0.95438 ±11 pcm	5.795e+12 ±0.40%	7.378e+12 ±0.34%	60.69 ±0.42%
10	0.95645 ±11 pcm	6.004e+12 ±0.41%	7.603e+12 ±0.35%	63.38 ±0.44%	0.95423 ±11 pcm	5.735e+12 ±0.40%	7.305e+12 ±0.34%	60.22 ±0.42%
11	0.95638 ±11 pcm	6.016e+12 ±0.41%	7.606e+12 ±0.35%	63.70 ±0.43%	0.95428 ±12 pcm	5.742e+12 ±0.40%	7.3+12 ±0.34 %	60.46 ±0.42%
12	0.95632 ±12 pcm	5.941e+12 ±0.41%	7.525e+12 ±0.35%	63.12 ±0.43%	0.95439 ±11 pcm	5.760e+12 ±0.40%	7.335e+12 ±0.34%	60.90 ±0.42%
13	0.95636 ±12 pcm	5.985e+12 ±0.41%	7.577e+12 ±0.35%	63.84 ±0.43%	0.95451 ±12 pcm	5.776e+12 ±0.40%	7.355e+12 ±0.34%	61.34 ±0.43%
14	0.95618 ±12 pcm	6.001e+12 ±0.41%	7.580e+12 ±0.35%	64.25 ±0.43%	0.95450 ±12 pcm	5.801e+12 ±0.40%	7.361e+12 ±0.34%	61.79 ±0.42%
15	0.95620 ±11 pcm	5.929e+12 ±0.41%	7.511e+12 ±0.35%	63.69 ±0.43%	0.95433 ±12 pcm	5.747e+12 ±0.40%	7.306e+12 ±0.34%	61.42 ±0.42%
16	0.95616 ±11 pcm	5.988e+12 ±0.41%	7.547e+12 ±0.35%	64.88 ±0.43%	0.95433 ±11 pcm	5.754e+12 ±0.40%	7.306e+12 ±0.34%	62.06 ±0.42%
17	0.95620 ±12 pcm	5.912e+12 ±0.41%	7.469e+12 ±0.35%	64.62 ±0.43%	0.95420 ±11 pcm	5.688e+12 ±0.40%	7.224e+12 ±0.34%	61.77 ±0.42%
18	0.95611 ±11 pcm	5.924e+12 ±0.41%	7.474e+12 ±0.35%	65.20 ±0.43%	0.95461 ±12 pcm	5.739e+12 ±0.40%	7.276e+12 ±0.34%	62.86 ±0.42%
19	0.95633 ±12 pcm	5.854e+12 ±0.40%	7.379e+12 ±0.35%	64.87 ±0.43%	0.95463 ±12 pcm	5.680e+12 ±0.39%	7.202e+12 ±0.34%	62.62 ±0.42%
20	0.95637 ±12 pcm	5.917e+12 ±0.40%	7.450e+12 ±0.34%	65.78 ±0.43%	0.95466 ±11 pcm	5.687e+12 ±0.40%	7.201e+12 ±0.34%	62.94 ±0.42%
21	0.95648 ±12 pcm	5.919e+12 ±0.40%	7.443e+12 ±0.35%	66.05 ±0.43%	0.95449 ±11 pcm	5.653e+12 ±0.40%	7.156e+12 ±0.34%	62.72 ±0.43%
22	0.95588 ±12 pcm	5.823e+12 ±0.40%	7.341e+12 ±0.35%	65.14 ±0.43%	0.95470 ±12 pcm	5.676e+12 ±0.39%	7.186e+12 ±0.34%	63.26 ±0.42%
23	0.95612 ±11 pcm	5.803e+12 ±0.40%	7.322e+12 ±0.34%	65.20 ±0.43%	0.95434 ±12 pcm	5.655e+12 ±0.39%	7.155e+12 ±0.34%	63.18 ±0.43%

Table III.4.3.2 k_{eff} and neutron flux at the beginning and end of each stage of the first burnup cycle of the subcritical assembly with uranium target and 37 fuel assemblies during

Stage	Beginning of the burnup stage				End of the burnup stage			
	k_{eff}	Neutron flux along the fuel length	Neutron flux along the target length	Total fission heat in the fuel (kW)	k_{eff}	Neutron flux along the fuel length	Neutron flux along the target length	Total fission heat in the fuel (kW)
1	0.97588 ±12 pcm	1.968e+13 ±0.56%	2.475e+13 ±0.53%	194.74 ±0.57%	0.96685 ±11 pcm	1.441e+13 ±0.47%	1.854e+13 ±0.44%	140.16 ±0.48%
2	0.96994 ±12 pcm	1.568e+13 ±0.49%	2.002e+13 ±0.46%	154.50 ±0.50%	0.96627 ±12 pcm	1.399e+13 ±0.46%	1.802e+13 ±0.43%	136.86 ±0.47%
3	0.96982 ±11 pcm	1.554e+13 ±0.49%	1.983e+13 ±0.46%	153.92 ±0.51%	0.96625 ±12 pcm	1.400e+13 ±0.46%	1.801e+13 ±0.43%	137.68 ±0.48%
4	0.96946 ±12 pcm	1.554e+13 ±0.49%	1.984e+13 ±0.46%	154.65 ±0.51%	0.96658 ±12 pcm	1.414e+13 ±0.46%	1.819e+13 ±0.43%	139.84 ±0.48%
5	0.97001 ±12 pcm	1.566e+13 ±0.50%	1.997e+13 ±0.46%	156.82 ±0.51%	0.96730 ±12 pcm	1.432e+13 ±0.47%	1.840e+13 ±0.44%	142.41 ±0.48%
6	0.97056 ±12 pcm	1.598e+13 ±0.49%	2.032e+13 ±0.46%	160.92 ±0.51%	0.96751 ±11 pcm	1.442e+13 ±0.47%	1.850e+13 ±0.44%	144.02 ±0.49%
7	0.97074 ±12 pcm	1.604e+13 ±0.50%	2.036e+13 ±0.47%	162.22 ±0.52%	0.96798 ±12 pcm	1.478e+13 ±0.47%	1.891e+13 ±0.44%	148.44 ±0.49%
8	0.96998 ±12 pcm	1.557e+13 ±0.48%	1.983e+13 ±0.45%	157.83 ±0.50%	0.96732 ±12 pcm	1.447e+13 ±0.47%	1.853e+13 ±0.44%	145.67 ±0.49%
9	0.96948 ±12 pcm	1.530e+13 ±0.48%	1.949e+13 ±0.45%	155.38 ±0.50%	0.96715 ±12 pcm	1.437e+13 ±0.47%	1.842e+13 ±0.44%	145.08 ±0.49%
10	0.96921 ±12 pcm	1.494e+13 ±0.48%	1.909e+13 ±0.45%	152.04 ±0.50%	0.96688 ±12 pcm	1.411e+13 ±0.46%	1.811e+13 ±0.43%	142.84 ±0.48%
11	0.96897 ±12 pcm	1.501e+13 ±0.48%	1.915e+13 ±0.45%	153.32 ±0.50%	0.96711 ±12 pcm	1.423e+13 ±0.47%	1.825e+13 ±0.44%	144.53 ±0.49%
12	0.96930 ±12 pcm	1.508e+13 ±0.48%	1.924e+13 ±0.45%	154.54 ±0.50%	0.96719 ±12 pcm	1.416e+13 ±0.47%	1.814e+13 ±0.43%	144.35 ±0.48%
13	0.96904 ±12 pcm	1.495e+13 ±0.48%	1.906e+13 ±0.45%	153.67 ±0.49%	0.96751 ±12 pcm	1.426e+13 ±0.47%	1.826e+13 ±0.43%	145.94 ±0.48%
14	0.96915 ±11 pcm	1.517e+13 ±0.48%	1.933e+13 ±0.45%	156.75 ±0.50%	0.96704 ±11 pcm	1.423e+13 ±0.47%	1.826e+13 ±0.43%	146.03 ±0.49%
15	0.97042 ±12 pcm	1.571e+13 ±0.49%	1.995e+13 ±0.46%	164.00 ±0.52%	0.96718 ±11 pcm	1.416e+13 ±0.46%	1.813e+13 ±0.43%	146.54 ±0.48%
16	0.97057 ±12 pcm	1.582e+13 ±0.49%	2.004e+13 ±0.46%	166.43 ±0.51%	0.96701 ±12 pcm	1.409e+13 ±0.46%	1.806e+13 ±0.43%	146.83 ±0.48%
17	0.97009 ±12 pcm	1.547e+13 ±0.48%	1.962e+13 ±0.45%	163.77 ±0.50%	0.96727 ±11 pcm	1.405e+13 ±0.46%	1.798e+13 ±0.43%	147.51 ±0.48%
18	0.96904 ±11 pcm	1.499e+13 ±0.48%	1.906e+13 ±0.44%	159.27 ±0.49%	0.96692 ±12 pcm	1.402e+13 ±0.46%	1.793e+13 ±0.43%	148.02 ±0.48%

Table III.4.3.3. Average burnup per batch at the end of each burnup stage of the first fuel cycle for the subcritical assembly with tungsten target and 38 fuel assemblies

Stage	Length of stage days	Total burnup time days	Burnup kWD/kgU		
			Batch 1	Batch 2	Batch 3
1	2	2	13.90	13.71	16.20
2	50	52	356.62	354.23	419.16
3	95	147	1003.46	1000.03	1190.90
4	125	272	1843.04	1838.97	2192.96
5	125	397	2695.88	2691.35	3208.14
6	110	507	3440.94	3443.39	4096.12
7	140	647	4384.04	4406.47	5221.36
8	180	827	5616.24	5664.79	6688.76
9	140	967	6605.88	6676.13	7864.02
10	140	1107	7579.06	7679.89	9020.50
11	120	1227	8409.32	8543.59	10007.02
12	100	1327	9100.40	9270.77	10827.84
13	100	1427	9799.98	10012.83	11654.48
14	100	1527	10496.10	10753.05	12469.98
15	100	1627	11193.32	11497.05	13280.62
16	100	1727	11910.70	12269.97	14068.56
17	100	1827	12645.42	13068.57	14831.70
18	80	1907	13248.72	13721.31	15425.70
19	100	2007	14019.98	14553.45	16148.72
20	100	2107	14806.14	15383.15	16853.98
21	100	2207	15609.72	16213.33	17551.92
22	60	2267	16093.18	16716.25	17969.98
23	80	2347	16736.96	17391.99	18526.22

Table III.4.3.4. Average burnup per batch at the end of each burnup stage of the first fuel cycle for the subcritical assembly with uranium target and 37 fuel assemblies

Stage	Length of stage days	Total burnup time days	Burnup kWD/kgU		
			First batch	Second Batch	Third batch
1	2	2	37.31	36.85	43.78
2	30	32	548.99	544.45	650.92
3	40	72	1228.73	1220.03	1458.90
4	40	112	1909.75	1896.81	2266.52
5	50	162	2774.59	2758.09	3293.74
6	60	222	3833.85	3813.67	4551.18
7	60	282	4908.87	4888.25	5826.58
8	60	342	5969.85	5958.17	7080.50
9	60	402	7010.93	7018.75	8309.68
10	50	452	7866.03	7899.05	9317.72
11	50	502	8716.21	8789.93	10255.86
12	40	542	9403.27	9511.31	11065.16
13	40	582	10096.79	10245.71	11880.76
14	60	642	11136.35	11349.89	13092.86
15	70	712	12389.75	12690.89	14476.26
16	80	792	13849.55	14261.89	16030.06
17	60	852	14969.13	15462.11	17166.66
18	50	902	16093.51	16660.35	18246.70

Table III.4.3.5. Average U^{235} enrichment of each fuel batch at the end of the first burnup cycle

Target Material	Total burnup time days	U^{235} enrichment		
		First batch	Second Batch	Third batch
tungsten	2347	17.68 %	17.61 %	17.47%
uranium	902	17.78%	17.72 %	17.52%

Although the fuel shuffling scheme minimizes the reactivity and the neutron flux changes during operation, the decay of fission products primarily Xe^{135} increase the reactivity after shutting down, as discussed before. Therefore, it is important to check the possible maximum reactivity of the subcritical assembly due to shutdown at any time during the fuel cycle.

For the subcritical assembly with the uranium target, the highest k_{eff} value during the first burnup cycle occurs at the beginning of stage 7 as shown in Fig. III.4.3.4 and Table III.4.3.2. The fuel and the target compositions from the burnup calculations at the beginning of stage 7 were used for new MCB calculation without external neutron source. In this calculation, the decay of the fission products was observed and the change in the K_{eff} value was calculated as a function of the decay time after shutdown. The K_{eff} is plotted in Fig. III.4.3.5 as a function of the time after shutdown. The k_{eff} increases and saturates in about four days after shutdown. The increase in the k_{eff} value is ~800 pcm but k_{eff} values is less than 0.980.

For the subcritical assembly with the tungsten target, the maximum k_{eff} value occurs at the beginning of stage 9 as shown in Fig. III.4.3.3 and Table III.4.3.1. A similar MCB calculation was performed as it was done for the subcritical assembly with the uranium target. The results show that value saturates at ~0.961 as shown in Fig. III.4.3.6. Then k_{eff} is calculated without the tungsten target to check the multiplication factor of the subcritical assembly. The obtained k_{eff} value calculated with MCB is 0.978, which is below the 0.98 value. In addition, k_{eff} value was calculated at several other time points in the first burnup cycle as shown in Table III.4.3.6. The increase in the K_{eff} value due to the target removal decreases during the fuel cycle as the burnup time increases.

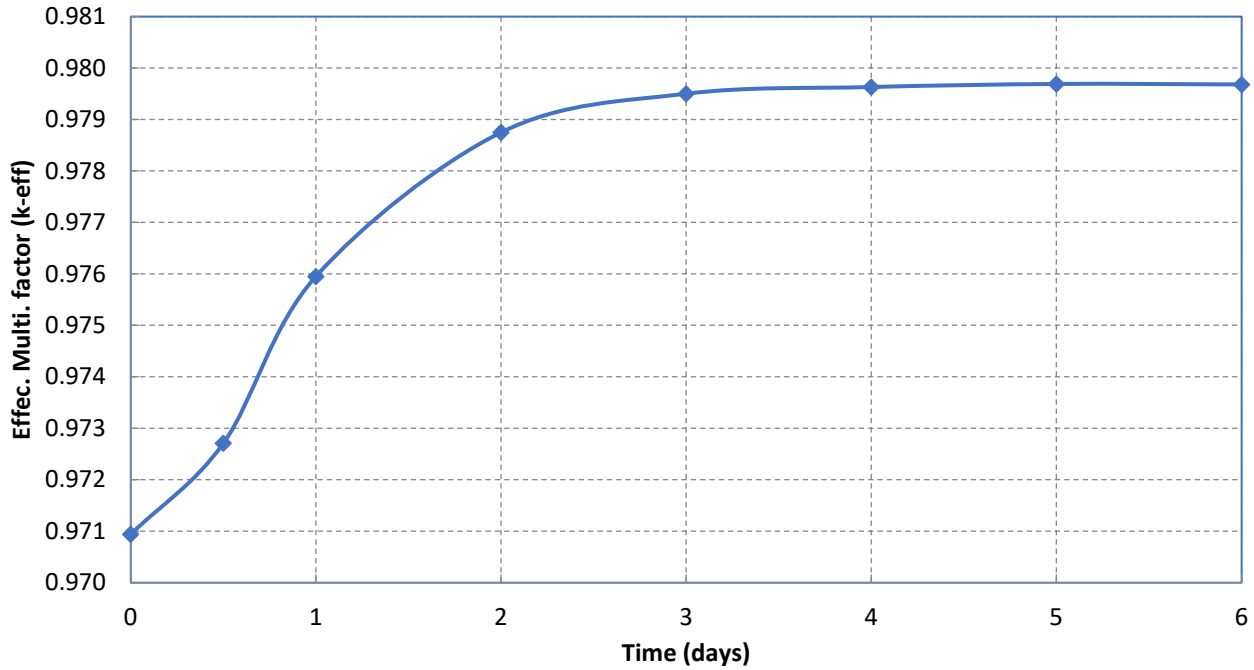

Figure III.4.3.5. k_{eff} value as a function of the time after shutdown at the beginning of stage 7 of the subcritical assembly with the uranium target

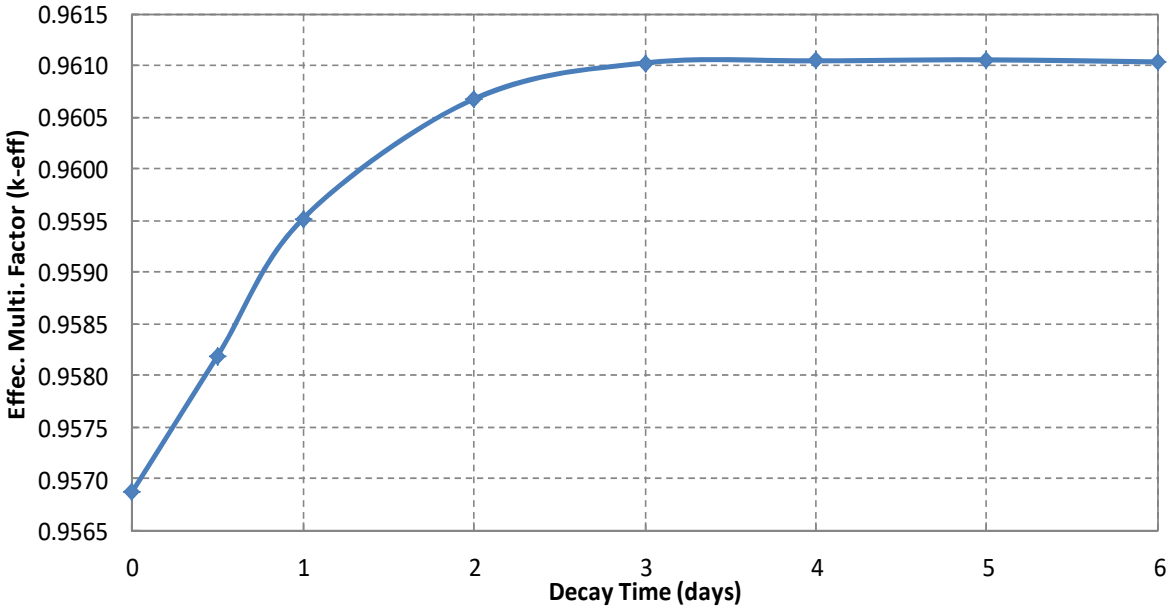

Figure III.4.3.6. k_{eff} value as a function of the time after shutdown at the beginning of stage 7 of the subcritical assembly with the tungsten target

Table III.4.3.6. Keff values of the subcritical assembly with and without the tungsten target at different time points in the first burnup cycle

Time Point	Burnup time days	k_{eff}		Δ Keff from target removal
		with target	without target	
Beginning of Stage 1	0	0.95712 ±0.00013	0.97739 ±0.00012	0.02027
Beginning of Stage 4	147	0.95626 ±0.00012	0.97548 ±0.00012	0.01922
Beginning of Stage 6	397	0.95575 ±0.00012	0.97401 ±0.00012	0.01826
Beginning of Stage 9*	827	0.96104 ±0.00012	0.97821 ±0.00011	0.01717

*After 6 shutdown days

III.4.4 Fuel Management During the Second Burnup Cycle

At the start of the second burnup cycle, the fuel assemblies are moved back into a compact configuration around the target and fresh fuel assemblies are added. Several MCNPX calculations were performed to determine the required number of the fresh fuel assemblies, which maintains k_{eff} <0.98 under all conditions. The results show that no more than six fresh fuel assemblies can be added into the subcritical assembly, for either the tungsten or the uranium target configurations. The added fresh fuel assemblies (batch 4) are as shown in Fig. III.4.41. The fuel assemblies of batches 1, 2, and 3 rearranged into a compact configuration to start the second burnup cycle. However, batch 3 is placed

around the target assembly and batch 1 is the outermost ring before the beryllium assemblies as shown in Fig. III.4.41. The second burnup cycle repeats the fuel shuffling scheme used for the first fuel cycle. At the beginning of the second burnup cycle, the subcritical assembly with the tungsten target has 44 fuel assemblies and the subcritical assembly with uranium target has 43 fuel assemblies.

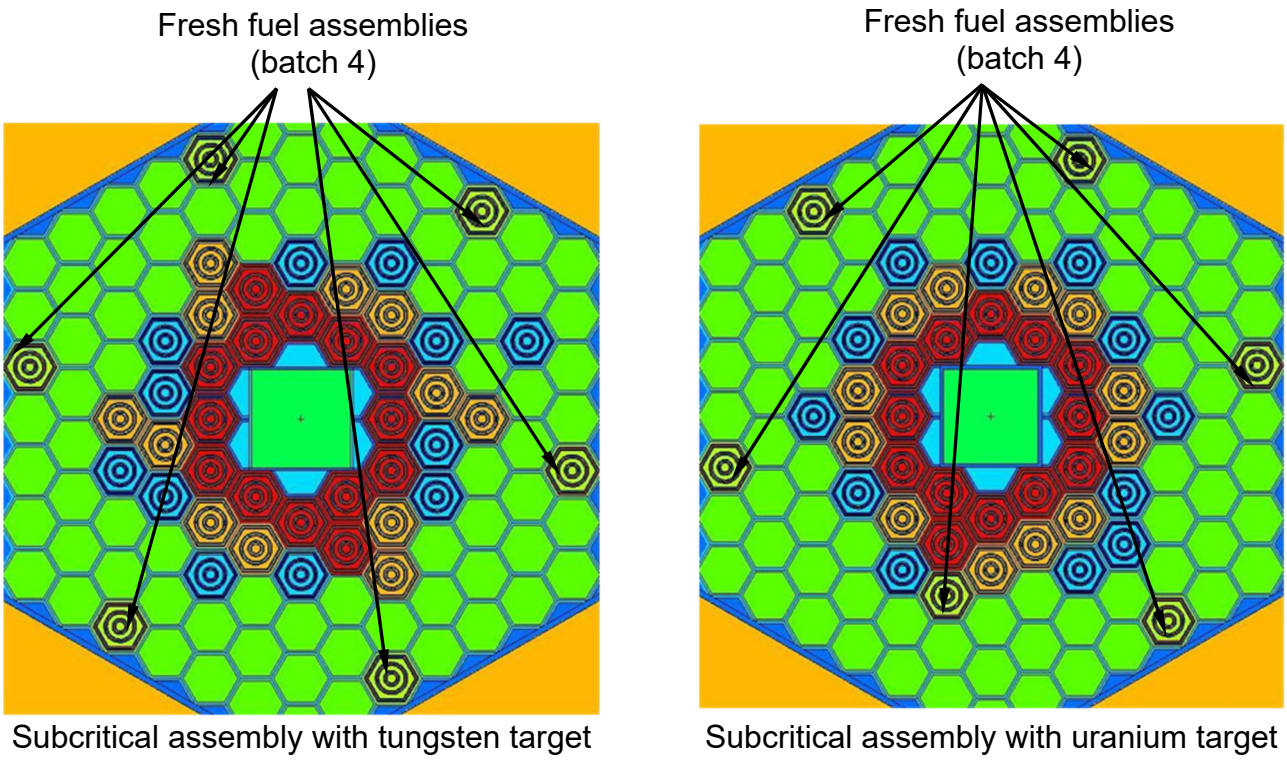

Figure III.4.4.1. Subcritical assembly configurations at the beginning of the second burnup cycle

As shown in Tables III.4.3.3 and III.4.3.4, the average burnup differs among the original three fuel batches at the end of the first burnup cycle. Batch 3 was originally loaded at the boundary next to the beryllium reflector and it has the highest burnup. As discussed in Sec. III.4.3, this is due to the thermal neutron flux peaking at the fuel-reflector boundary, caused by the neutron reflection from the beryllium reflector. While batch 1 was originally loaded next to the target and it has the lowest burnup. To even out the burnup during the second burnup cycle, the fuel batches 1 and 3 are switched where fuel batch 3 moved around the target and fuel batch 1 moved at the fuel-reflector boundary. For comparison purposes at the beginning of the second burnup cycle, k_{eff} values were calculated for the subcritical assembly configurations with the fuel batches 1 and 3 in their original positions of the first fuel cycle as shown in Fig. III.4.4.2 and the new positions as explained above. The k_{eff} values for each configuration were calculated by MCB and the results are shown in Table III.4.4.1. Switching these two fuel batches has very little impact on k_{eff}, as shown in Table III.4.4.1. The difference in K_{eff} value is ~22 pcm for the tungsten target case and ~46 pcm for the uranium target case.

Table III.4.4.1. Impact of the fuel patches 1 and 3 switching positions on k_{eff} at the beginning of the second fuel cycle with six added fresh fuel assemblies for the tungsten and the uranium targets

Target Material	Number of fuel assemblies (Old and fresh)	k_{eff}	
		Fuel patches 1 and 3 switched position	Fuel patches 1 and 3 in their original positions
tungsten	44	0.96052 ± 0.00011	0.96030 ± 0.00012
uranium	43	0.96998 ± 0.00012	0.96952 ± 0.00012

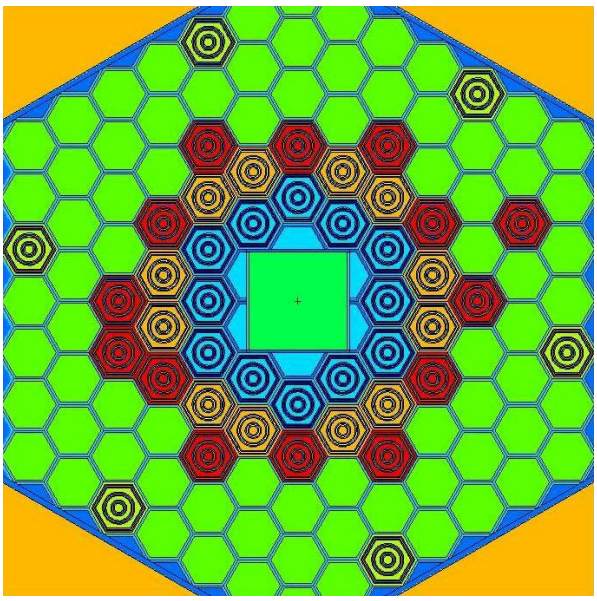

Tungsten configuration with 6 new fuel assemblies

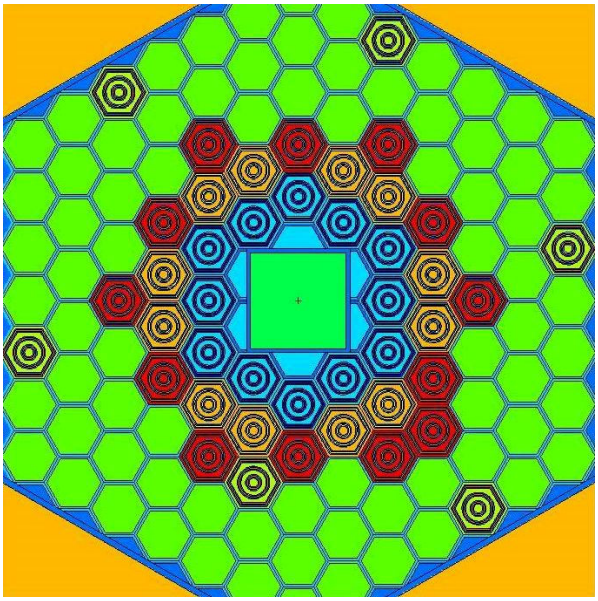

Uranium configuration with 6 new fuel assemblies target

Figure III.4.4.2. Subcritical assembly configurations at the beginning of the second burnup cycle with fuel batch 1 and 3 in their original positions.

For the uranium target configuration, k_{eff} is in the range of 0.967 - 0.971 during the second burnup cycle. In the second burnup cycle, the tungsten target removal increases k_{eff} by ~1400 pcm at the beginning of the cycle, so k_{eff} can be increased by about ~400 pcm relative to the first fuel cycle. Therefore, k_{eff} kept in the range 0.957 - 0.961.

For the second burnup cycle, the subcritical assembly configuration and the operation time for each burnup stage are shown in Fig. III.4.4.3 for the tungsten target configuration and in Fig. III.4.4.4 for the uranium target configuration. The k_{eff} history of the second burnup cycle has been calculated by MCB and is shown in Figs. III.4.4.5 and III.4.4.6 for the tungsten and the uranium target configurations, respectively.

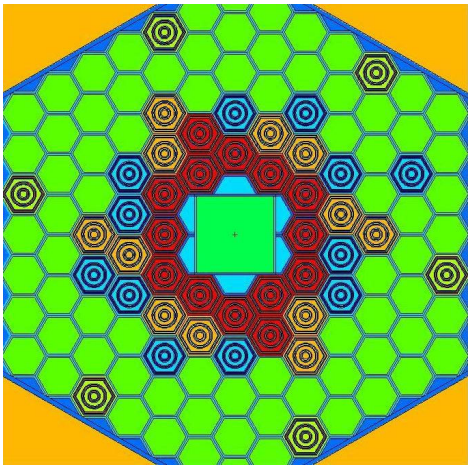

Stage 1, 0 ~ 120 days

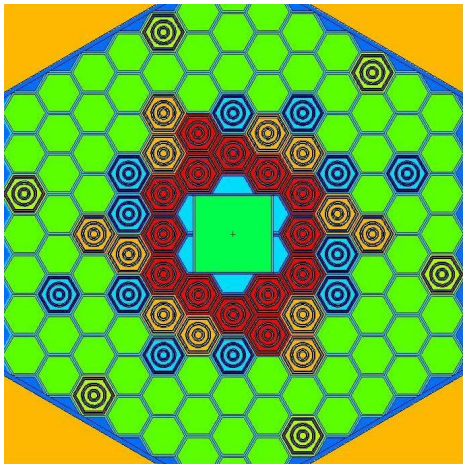

Stage 2, 120 ~ 220 days

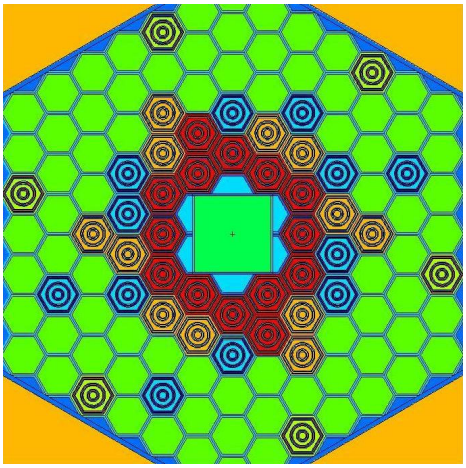

Stage 3, 220 ~ 320 days

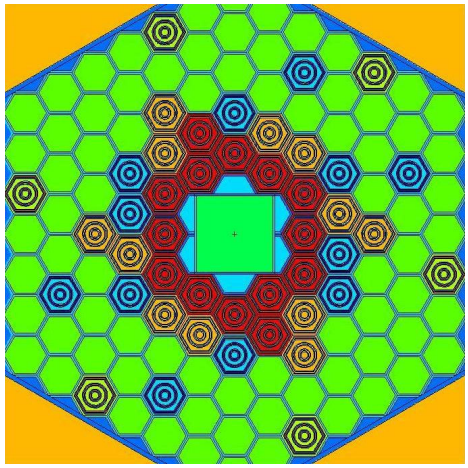

Stage 4, 320 ~ 420 days

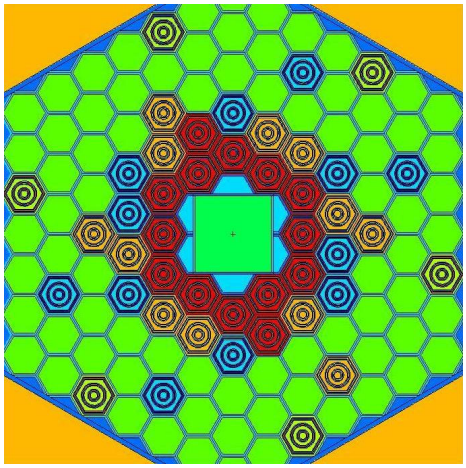

Stage 5, 420 ~ 520 days

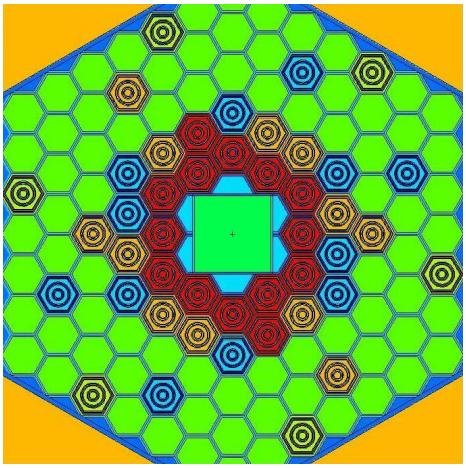

Stage 6, 520 ~ 640 days

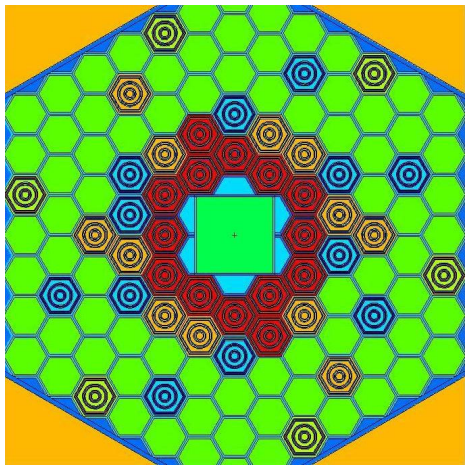

Stage 7, 640 ~ 760 days

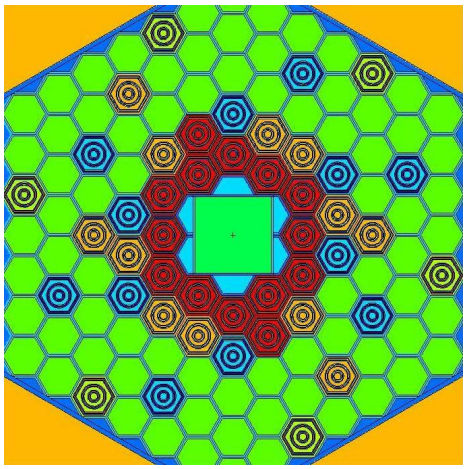

Stage 8, 760 ~ 880 days

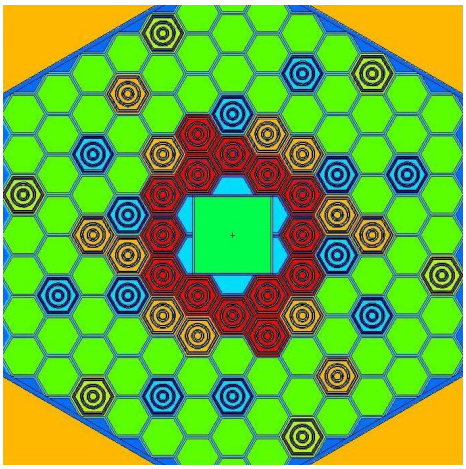

Stage 9, 880 ~ 1020 days

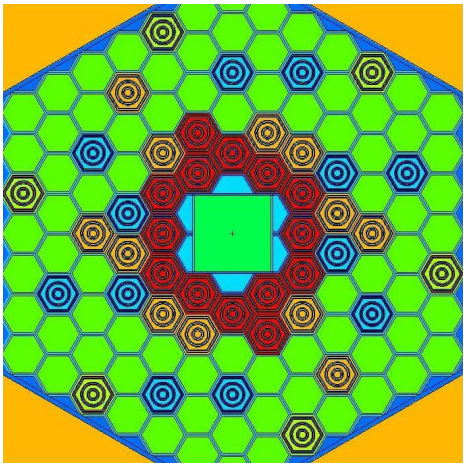

Stage 10, 1020 ~ 1140 days

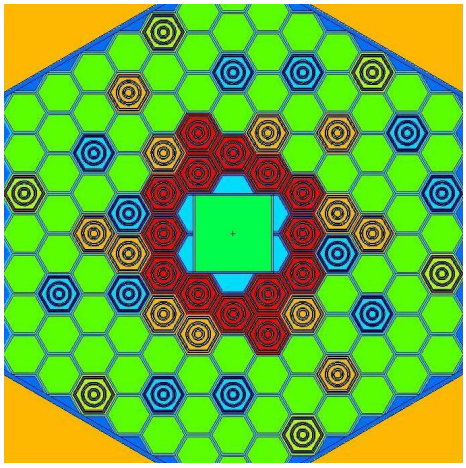

Stage 11, 1140 ~ 1260 days

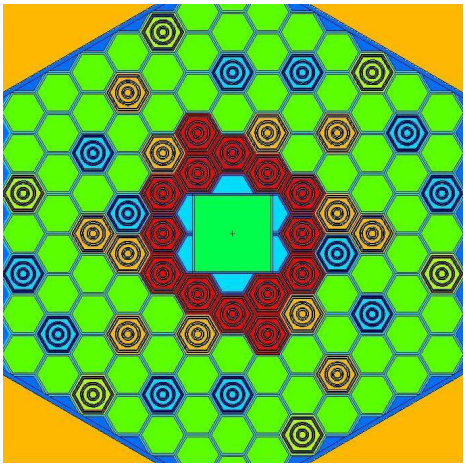

Stage 12, 1260 ~ 1400 days

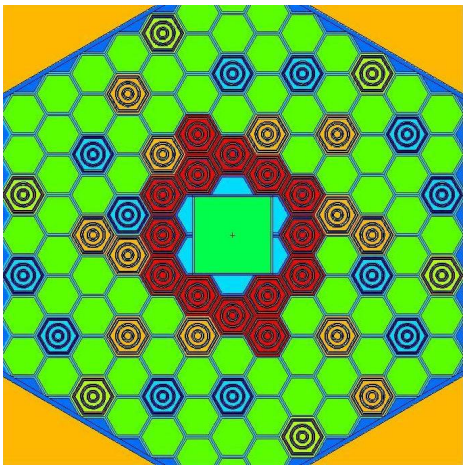

Stage 13, 1400 ~ 1520 days

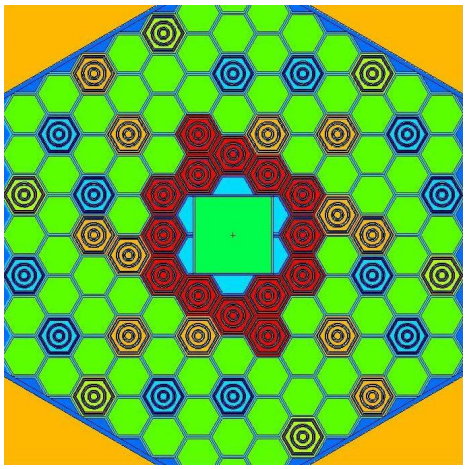

Stage 14, 1520 ~ 1600 days

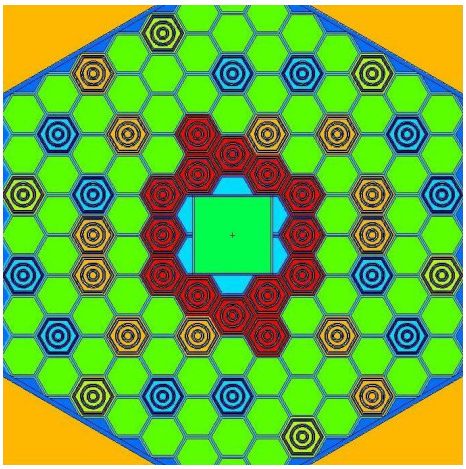

Stage 15, 1600 ~ 1680 days

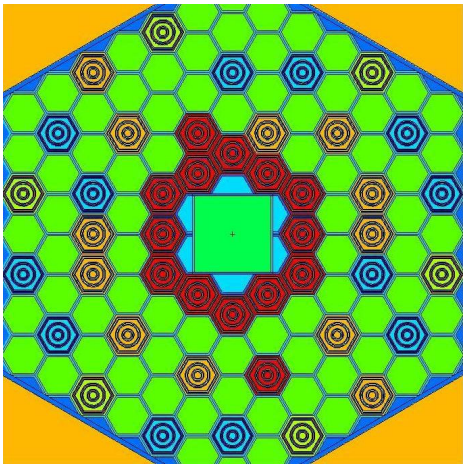

Stage 16, 1680 ~ 1760 days

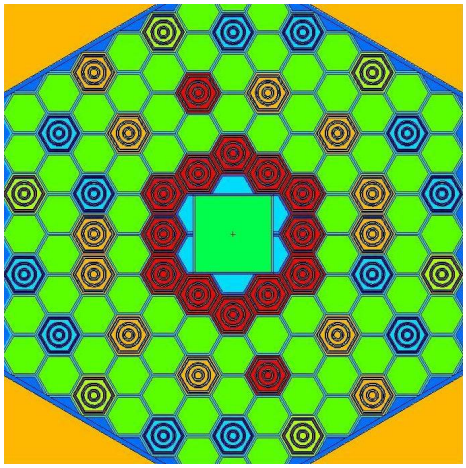

Stage 17, 1760 ~ 1820 days

Figure III.4.4.3. Subcritical assembly configurations for each burnup stage of the second burnup cycle using tungsten target and 44 fuel assemblies loaded

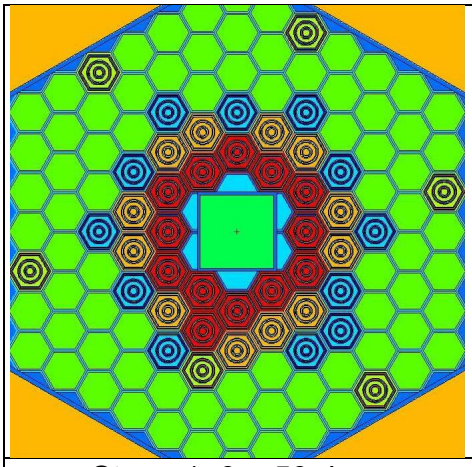

Stage 1, 0 ~ 50 days

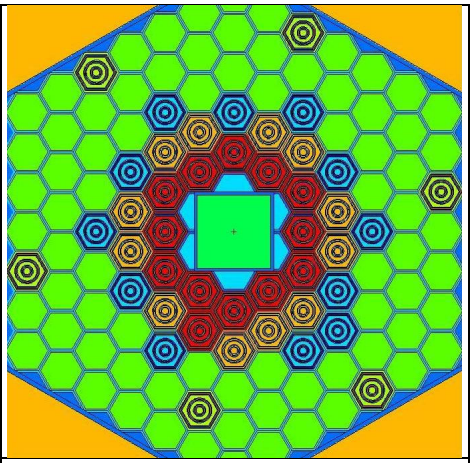

Stage 2, 50 ~ 120 days

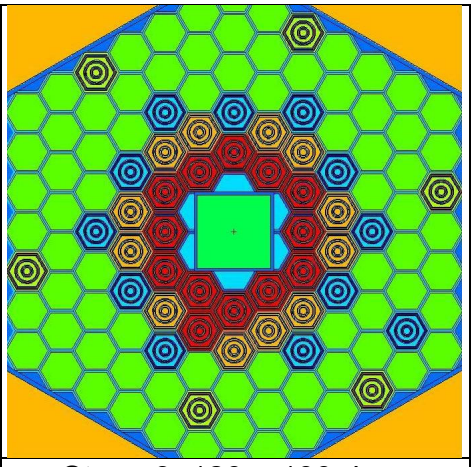

Stage 3, 120 ~ 190 days

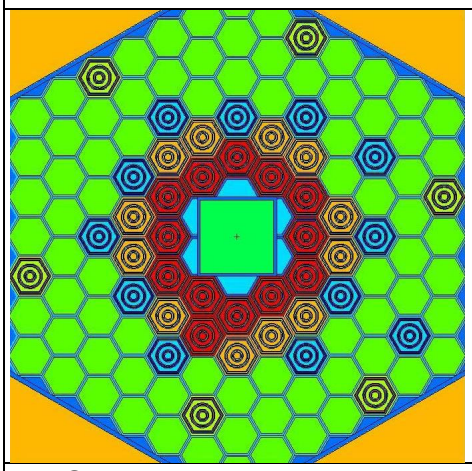

Stage 4, 190 ~ 260 days

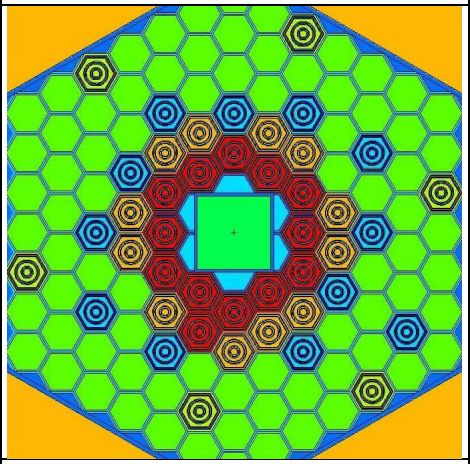

Stage 5, 260 ~ 330 days

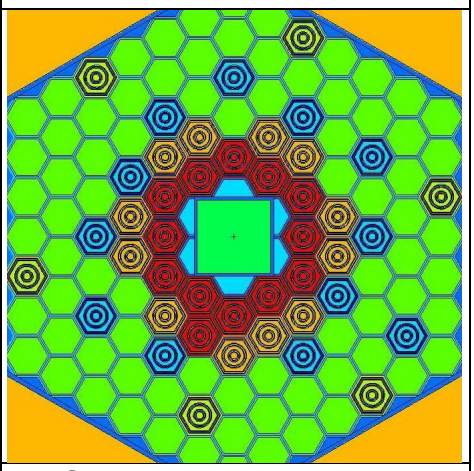

Stage 6, 330 ~ 400 days

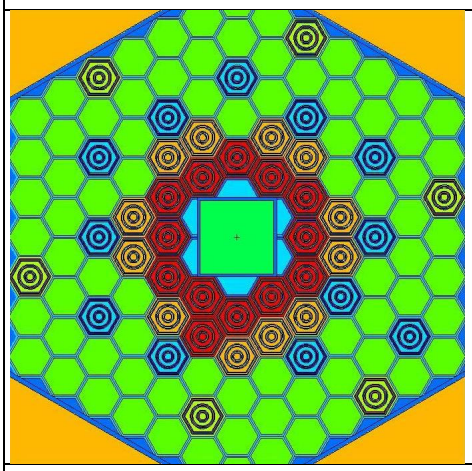

Stage 7, 400 ~ 440 days

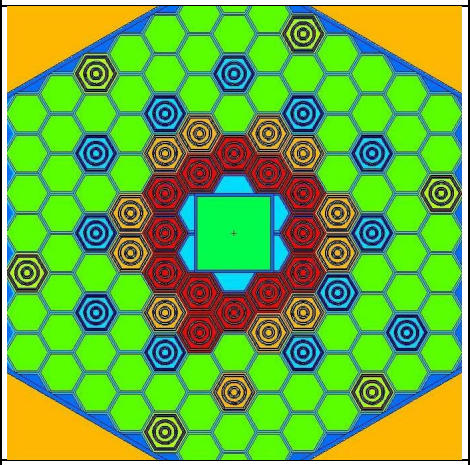

Stage 8, 440 ~ 510 days

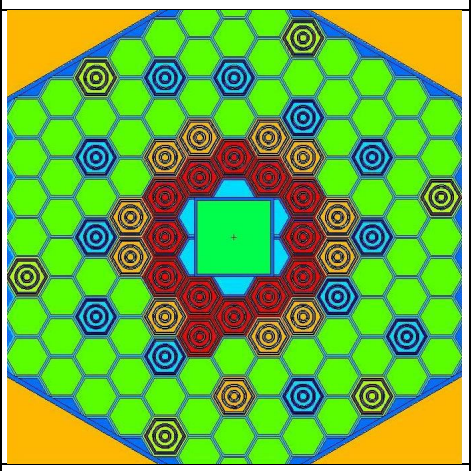

Stage 9, 510 ~ 580 days

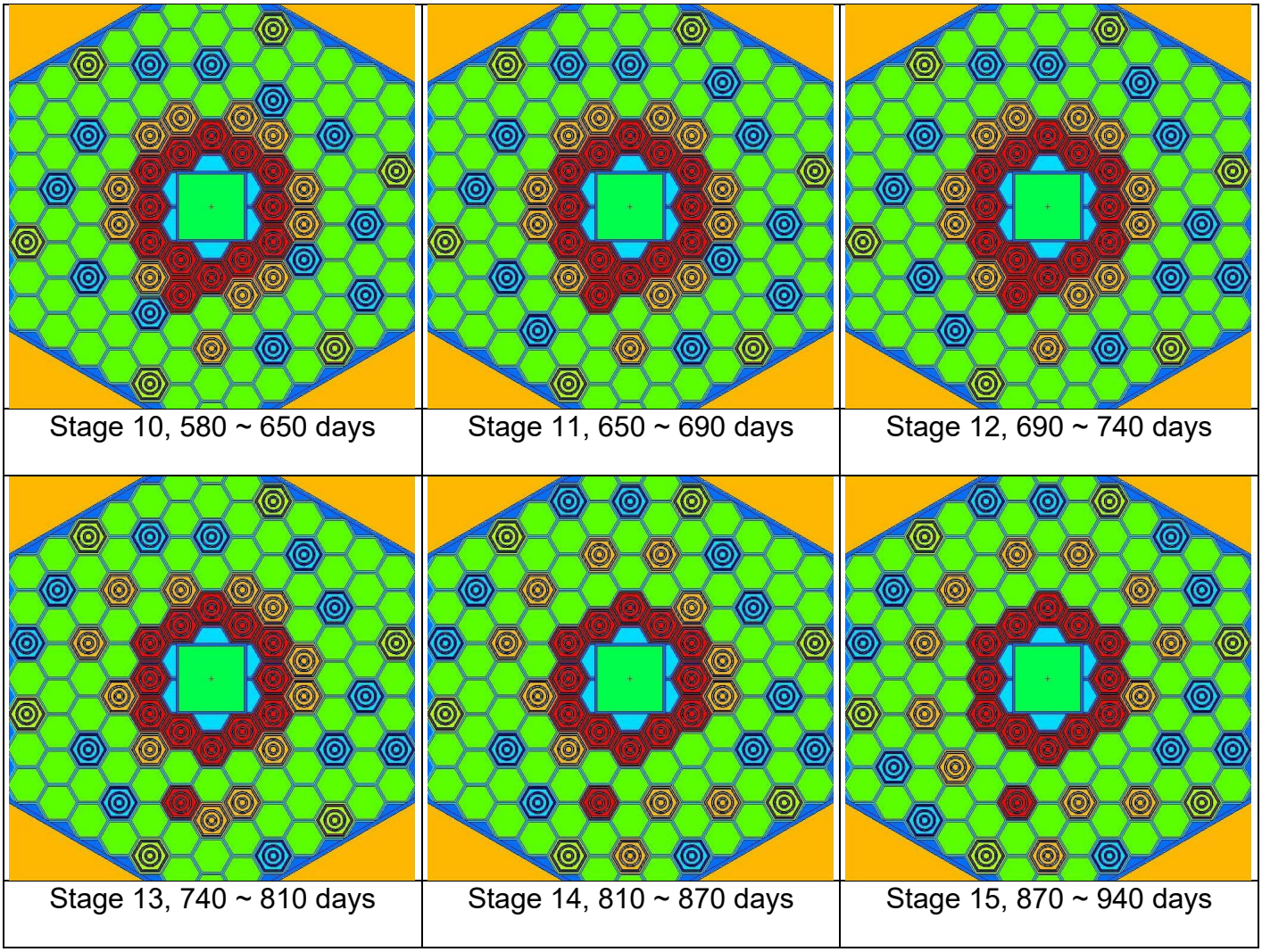

Figure III.4.4.4. Subcritical assembly configurations for each burnup stage of the second burnup cycle, using uranium target and 43 fuel assemblies loaded

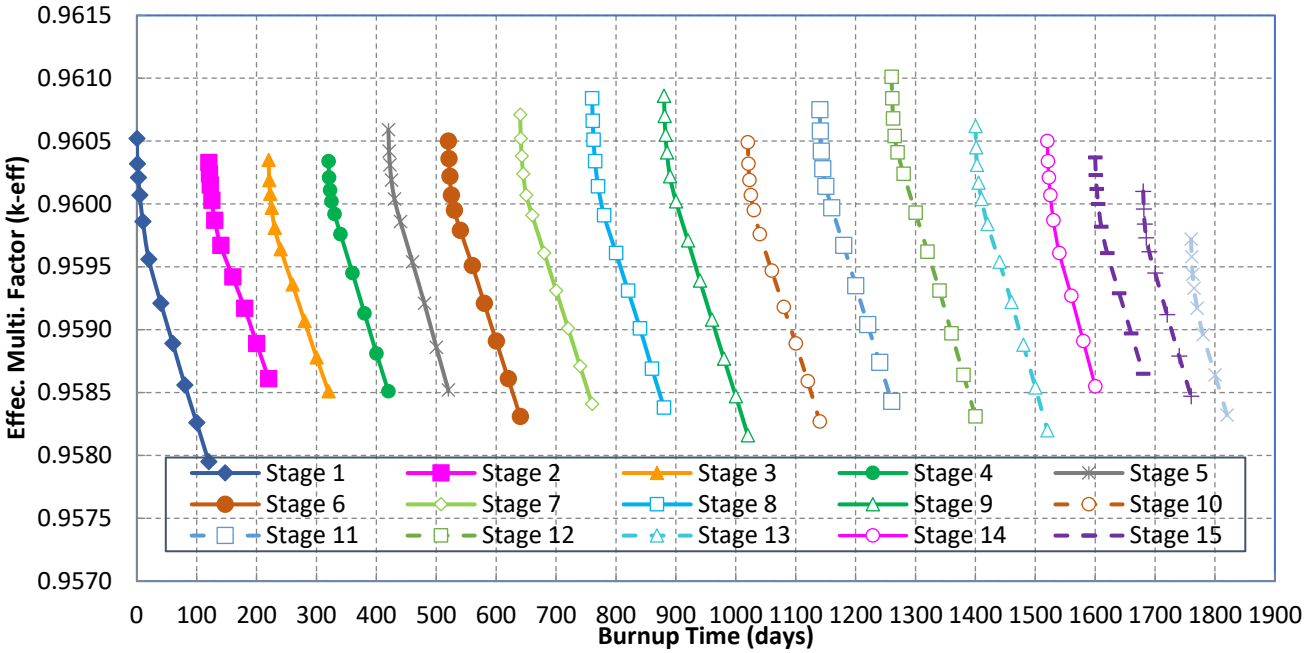

Figure III.4.4.5. k_{eff} values during the second burnup cycle for the subcritical assembly with the tungsten target and 44 fuel assemblies

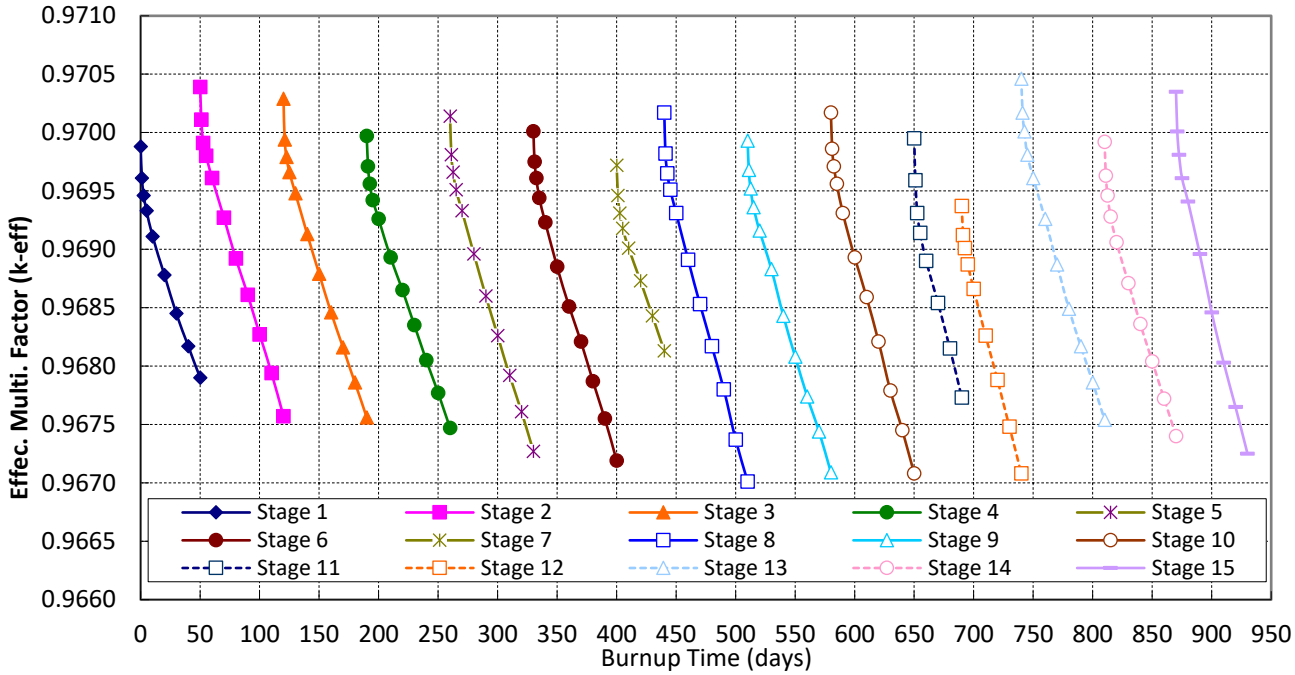

Figure III.4.4.6. k_{eff} values during the second burnup cycle for the subcritical assembly with the uranium target and 43 fuel assemblies

The average neutron flux values in the target coolant channels along the 50-cm active fuel length and along the target materials length (5.15 cm for the tungsten target and 9.19 cm for the uranium target) have been calculated by MCB at the beginning and the end of

each burnup stage, and the results are shown in Tables III.4.4.2 and III.4.4.3 for the tungsten and uranium targets.

Table III.4.4.2. k_{eff} and neutron flux at the beginning and end of each stage, with tungsten target and 44 fuel assemblies loaded in the second burnup cycle

Stage	At the beginning of the stage				At the end of the stage			
	k_{eff}	Neutron flux along the fuel length	Neutron flux along the target length	Total fission heat in the fuel (kW)	k_{eff}	Neutron flux along the fuel length	Neutron flux along the target length	Total fission heat in the fuel (kW)
1	0.96052 ±11 pcm	6.181e+12 ±0.43%	7.756e+12 ±0.37%	71.35 ±0.46%	0.95795 ±11 pcm	5.844e+12 ±0.42%	7.395e+12 ±0.36%	66.91 ±0.4%
2	0.96033 ±11 pcm	6.157e+12 ±0.43%	7.724e+12 ±0.37%	71.25 ±0.45%	0.95861 ±12 pcm	5.903e+12 ±0.42%	7.459e+12 ±0.36%	67.93 ±0.44%
3	0.96035 ±11 pcm	6.153e+12 ±0.43%	7.716e+12 ±0.37%	71.38 ±0.45%	0.95851 ±12 pcm	5.920e+12 ±0.42%	7.470e+12 ±0.36%	68.38 ±0.44%
4	0.96034 ±11 pcm	6.172e+12 ±0.43%	7.732e+12 ±0.37%	71.91 ±0.45%	0.95851 ±12 pcm	5.937e+12 ±0.42%	7.490e+12 ±0.36%	68.73 ±0.44%
5	0.96059 ±12 pcm	6.203e+12 ±0.43%	7.766e+12 ±0.37%	72.47 ±0.45%	0.95852 ±12 pcm	5.891e+12 ±0.42%	7.439e+12 ±0.36%	68.44 ±0.44%
6	0.96050 ±11 pcm	6.136e+12 ±0.43%	7.686e+12 ±0.37%	71.82 ±0.45%	0.95831 ±11 pcm	5.875e+12 ±0.42%	7.416e+12 ±0.36%	68.30 ±0.44%
7	0.96071 ±12 pcm	6.167e+12 ±0.43%	7.716e+12 ±0.37%	72.36 ±0.45%	0.95841 ±11 pcm	5.821e+12 ±0.41%	7.358e+12 ±0.36%	67.76 ±0.44%
8	0.96084 ±12 pcm	6.151e+12 ±0.43%	7.695e+12 ±0.37%	72.29 ±0.45%	0.95838 ±12 pcm	5.906e+12 ±0.42%	7.449e+12 ±0.36%	67.99 ±0.44%
9	0.96086 ±12 pcm	6.166e+12 ±0.43%	7.716e+12 ±0.37%	72.61 ±0.45%	0.95816 ±11 pcm	5.769e+12 ±0.42%	7.296e+12 ±0.36%	67.46 ±0.44%
10	0.96049 ±11 pcm	6.089e+12 ±0.43%	7.619e+12 ±0.37%	71.74 ±0.45%	0.95827 ±12 pcm	5.734e+12 ±0.41%	7.264e+12 ±0.35%	67.08 ±0.44%
11	0.96075 ±12 pcm	6.139e+12 ±0.43%	7.668e+12 ±0.37%	72.87 ±0.46%	0.95843 ±11 pcm	5.780e+12 ±0.42%	7.300e+12 ±0.35%	68.08 ±0.44%
12	0.96101 ±11 pcm	6.105e+12 ±0.43%	7.631e+12 ±0.37%	72.84 ±0.46%	0.95831 ±11 pcm	5.807e+12 ±0.42%	7.311e+12 ±0.36%	68.75 ±0.44%
13	0.96062 ±11 pcm	6.099e+12 ±0.42%	7.604e+12 ±0.36%	73.16 ±0.46%	0.95820 ±11 pcm	5.783e+12 ±0.42%	7.280e+12 ±0.36%	68.88 ±0.44%
14	0.96050 ±12 pcm	6.018e+12 ±0.42%	7.510e+12 ±0.36%	72.46 ±0.45%	0.95855 ±11 pcm	5.783e+12 ±0.41%	7.272e+12 ±0.35%	69.21 ±0.44%
15	0.96037 ±11 pcm	5.999e+12 ±0.42%	7.489e+12 ±0.36%	72.30 ±0.45%	0.95865 ±11 pcm	5.769e+12 ±0.41%	7.250e+12 ±0.35%	69.16 ±0.44%
16	0.96010 ±11 pcm	5.894e+12 ±0.42%	7.359e+12 ±0.36%	71.35 ±0.45%	0.95847 ±11 pcm	5.659e+12 ±0.41%	7.130e+12 ±0.35%	68.19 ±0.44%
17	0.95972 ±12 pcm	5.836e+12 ±0.42%	7.299e+12 ±0.36%	71.01 ±0.45%	0.95832 ±11 pcm	5.663e+12 ±0.41%	7.129e+12 ±0.35%	68.59 ±0.44%

The average burnup for each fuel batch at the end of each burnup stage of the second burnup cycle is shown in Tables III.4.4.4 and III.4.4.5 for the tungsten and the uranium targets, respectively. Switching the position of fuel batches 1 and 3 at the beginning of the second burnup cycle results in a more even burnup rates at the end of the second burnup cycle.

The average U^{235} enrichment of each fuel batch at the end of the second burnup cycle is listed in Table III.4.4.6. At the end of the second burnup cycle, batches 1-3 have been utilized for a total of 4167 days for the tungsten target configuration and 1832 days for the uranium target configuration. The average U^{235} enrichment for these three batches is ~16.0 and ~15.8% for the tungsten and uranium target configurations, respectively.

Table III.4.4.3 k_{eff} and neutron flux at the beginning and end of each stage, with uranium target and 43 fuel assemblies loaded in the second burnup cycle

Stage	At the begin of the stage				At the end of the stage			
	k_{eff}	Neutron flux along the fuel length	Neutron flux along the target length	Total fission heat in the fuel (kW)	k_{eff}	Neutron flux along the fuel length	Neutron flux along the target length	Total fission heat in the fuel (kW)
1	0.96988 ±12 pcm	1.445e+13 ±0.49%	1.846e+13 ±0.45%	158.48 ±0.51%	0.96790 ±12 pcm	1.350e+13 ±0.47%	1.734e+13 ±0.44%	146.94 ±0.49%
2	0.97039 ±11 pcm	1.472e+13 ±0.49%	1.875e+13 ±0.46%	162.19 ±0.51%	0.96757 ±11 pcm	1.347e+13 ±0.47%	1.730e+13 ±0.44%	147.13 ±0.49%
3	0.97029 ±12 pcm	1.459e+13 ±0.48%	1.859e+13 ±0.45%	161.46 ±0.51%	0.96756 ±12 pcm	1.343e+13 ±0.47%	1.724e+13 ±0.44%	147.42 ±0.49%
4	0.96997 ±12 pcm	1.456e+13 ±0.49%	1.856e+13 ±0.46%	161.50 ±0.51%	0.96747 ±11 pcm	1.342e+13 ±0.47%	1.722e+13 ±0.44%	147.77 ±0.48%
5	0.97014 ±12 pcm	1.445e+13 ±0.49%	1.840e+13 ±0.46%	160.45 ±0.51%	0.96727 ±11 pcm	1.336e+13 ±0.47%	1.715e+13 ±0.43%	147.22 ±0.49%
6	0.97001 ±11 pcm	1.449e+13 ±0.49%	1.847e+13 ±0.46%	161.39 ±0.51%	0.96719 ±12 pcm	1.317e+13 ±0.46%	1.691e+13 ±0.43%	145.37 ±0.48%
7	0.96972 ±12 pcm	1.423e+13 ±0.48%	1.813e+13 ±0.44%	158.64 ±0.50%	0.96813 ±11 pcm	1.362e+13 ±0.47%	1.743e+13 ±0.44%	151.15 ±0.49%
8	0.97017 ±12 pcm	1.456e+13 ±0.49%	1.851e+13 ±0.46%	163.07 ±0.51%	0.96701 ±11 pcm	1.318e+13 ±0.46%	1.692e+13 ±0.43%	146.28 ±0.48%
9	0.96993 ±11 pcm	1.458e+13 ±0.48%	1.853e+13 ±0.45%	164.04 ±0.51%	0.96709 ±11 pcm	1.311e+13 ±0.46%	1.682e+13 ±0.43%	146.16 ±0.48%
10	0.97017 ±10 pcm	1.434e+13 ±0.48%	1.823e+13 ±0.45%	161.84 ±0.50%	0.96708 ±11 pcm	1.317e+13 ±0.46%	1.687e+13 ±0.43%	147.62 ±0.48%
11	0.96995 ±11 pcm	1.425e+13 ±0.48%	1.814e+13 ±0.45%	161.69 ±0.50%	0.96773 ±11 pcm	1.344e+13 ±0.47%	1.719e+13 ±0.43%	151.62 ±0.49%
12	0.96937 ±11 pcm	1.384e+13 ±0.47%	1.765e+13 ±0.44%	157.02 ±0.50%	0.96708 ±11 pcm	1.319e+13 ±0.46%	1.688e+13 ±0.43%	148.75 ±0.48%
13	0.97046 ±11 pcm	1.452e+13 ±0.49%	1.841e+13 ±0.46%	166.42 ±0.52%	0.96754 ±11 pcm	1.326e+13 ±0.46%	1.695e+13 ±0.42%	150.55 ±0.48%
14	0.96992 ±11 pcm	1.431e+13 ±0.48%	1.814e+13 ±0.45%	165.33 ±0.50%	0.96740 ±11 pcm	1.314e+13 ±0.46%	1.679e+13 ±0.43%	150.50 ±0.48%
15	0.97035 ±11 pcm	1.425e+13 ±0.47%	1.810e+13 ±0.44%	166.59 ±0.50%	0.96725 ±11 pcm	1.309e+13 ±0.45%	1.673e+13 ±0.42%	151.53 ±0.48%

Table III.4.4.4. Batch-averaged burnup at the end of each stage, with tungsten target and 44 fuel assemblies loaded in the second burnup cycle

Stages	Length of cycle days	Total Burnup time days	Burnup kWD/kgU			
			Batch 1	Batch 2	Batch 3	Batch 4
1	120	120	17636.16	18224.49	19310.92	983.32
2	100	220	18401.70	18932.53	19973.18	1806.26
3	100	320	19171.70	19649.27	20637.64	2626.80
4	100	420	19939.60	20368.39	21298.92	3435.54
5	100	520	20709.78	21094.87	21966.62	4242.48
6	120	640	21622.52	21962.95	22768.64	5171.88
7	120	760	22552.36	22838.77	23578.56	6127.48
8	120	880	23480.08	23704.51	24382.80	7067.56
9	140	1020	24565.52	24716.31	25330.30	8157.30
10	120	1140	25493.18	25582.37	26146.26	9081.90
11	120	1260	26412.00	26473.55	26977.84	9996.54
12	140	1400	27468.84	27537.93	27962.44	11047.66
13	120	1520	28359.28	28440.47	28816.96	11931.44
14	80	1600	28948.96	29040.23	29398.98	12514.52
15	80	1680	29526.40	29632.39	29984.80	13089.18
16	80	1760	30077.84	30218.63	30574.90	13648.60
17	60	1820	30480.10	30662.83	31029.44	14063.86

Similar to, the first fuel burn cycle, the k_{eff} value of the subcritical assembly was examined to confirm that the value is always less than 0.98 under any condition during the second fuel burn cycle. The maximum value occurs if the operation is stopped at the beginning of the burn stage with the maximum k_{eff}. For the uranium target configuration, stage 13 has the largest K_{eff} as shown in Table III.4.4.3 and Fig III.4.4.6. During shutdown, k_{eff} increases because of the decay of the fission products as shown in Fig. III.4.4.7. The increase is about 800 pcm but the k_{eff} value stays less than 0.98.

For the tungsten target, the peak k_{eff} value during the second burnup cycle occurs at the beginning of stage 12, as shown in Table III.4.4.2 and Fig. III.4.4.5. The decay behavior was therefore analyzed at the beginning of stage 12 and the results plotted in Fig. III.4.4.8. If the facility shut down at the beginning of stage 12 unexpectedly, Fig. III.4.4.8 shows that k_{eff} would increase to nearly 0.966 after several days due to the decay of fission products. At the beginning of stage 12, the tungsten target removal increases k_{eff} by ~1000 pcm as calculated with MCB. Therefore, even if the tungsten target had to be removed after shutting down at the start of stage 12, k_{eff} would remain below 0.980 during the cooling period.

Table III.4.4.5. Batch average burnup at the end of each stage for the uranium target configuration with 43 fuel assemblies in the second burnup cycle

Stage	Cycle length (days)	Total burnup time (days)	Burnup kWD/kgU			
			Batch 1	Batch 2	Batch 3	Batch 4
1	50	50	16962.51	17410.81	18987.12	1103.28
2	70	120	18197.13	18481.59	20044.98	2422.48
3	70	190	19443.45	19555.21	21098.12	3728.08
4	70	260	20686.87	20627.93	22148.26	5014.28
5	70	330	21929.11	21702.81	23199.46	6282.48
6	70	400	23161.89	22771.75	24244.22	7527.28
7	40	440	23867.81	23385.67	24842.90	8233.32
8	70	510	25112.21	24488.83	25913.30	9453.64
9	70	580	26344.59	25599.11	26973.24	10648.22
10	70	650	27575.49	26730.97	28034.94	11832.30
11	40	690	28465.01	27562.87	28810.38	12680.38
12	50	740	29161.91	28227.45	29426.82	13350.06
13	70	810	30345.35	29430.01	30559.78	14518.22
14	60	870	31310.73	30467.31	31559.62	15477.38
15	60	930	32234.89	31548.51	32621.38	16432.04

Table III.4.4.6. U^{235} enrichment of each batch at the end of the second burnup cycle

Target	**Total burnup time days**	**U^{235} enrichment**			
		Batch 1	**Batch 2**	**Batch 3**	**Batch 4**
tungsten	2347				18.01 %
	4167	16.00 %	15.98 %	15.93%	
uranium	902				17.75 %
	1832	15.81%	15.90 %	15.75%	

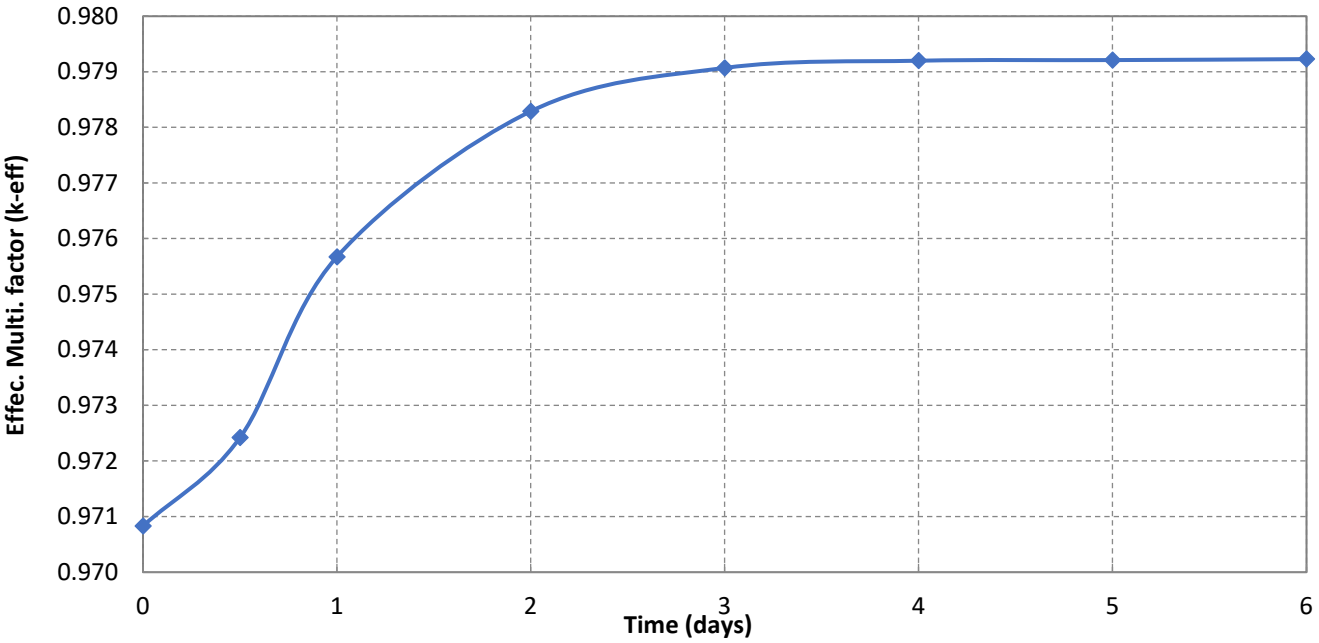

Figure III.4.4.7. k_{eff} value as a function of the time after shutdown at the beginning of stage 13 of the second burn cycle for the subcritical assembly with the uranium target

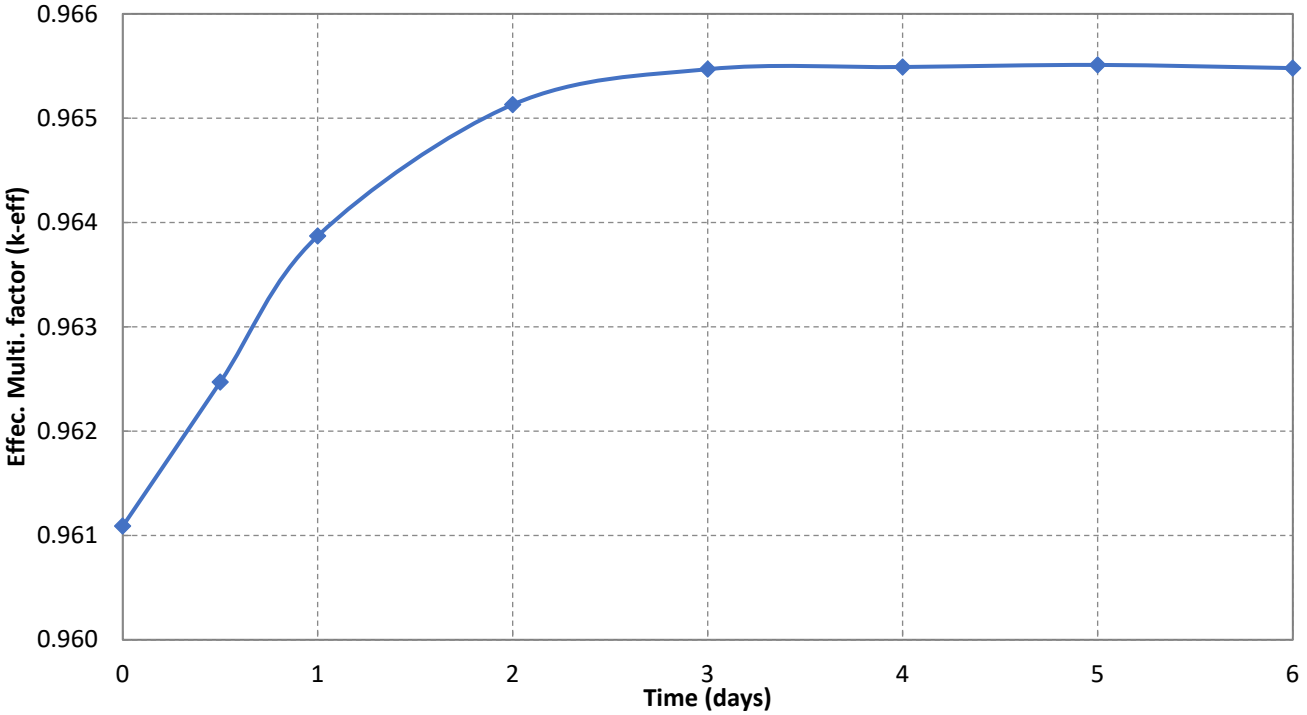

Figure III.4.4.8. k_{eff} value as a function of the time after shutdown at the beginning of stage 12 of the second burn cycle for the subcritical assembly with the tungsten target

Reference

III.4.1 Z. Zhong, Y. Gohar, A. Talamo, "Analysis of Fuel Management in the KIPT Neutron Source Facility", *Annals of Nuclear Energy*, Vol. 38, No. 5 2011 pp. 1014 -1022.
III.4.2 Denise B. Pelowitz, editor, "MCNPX^{TM} USER'S MANUAL", Los Alamos Report, LA-CP-05-0369, April 2005.
III.4.3 Cetnar, J., Gudowski, W., Wallenius, J., "User Manual for Monte Carlo Continuous Energy Burnup MCB Code", Version 1C, NEA-1643/01, August 2002.

III.5 Subcritical Assembly Thermal-Hydraulics Analysis

III.5.1 Introduction

The subcritical assembly is within a large water tank as shown in Figs. III.5.1.1.and III.5.1.2. The flow through the subcritical assembly is downward. The inlet and the outlet are both below the subcritical assembly. The lower tank presents a complex flow structure due to intricate passages through support structures and loaded assemblies. The outer region of the tank is characterized by an upward flow. The flow in the region between the water free surface and the assembly top surface is characterized by low velocities and low turbulence intensities. A suction pump is used to pump the coolant out of the subcritical assembly to the heat exchangers. All the thermal hydraulics analyses used the uranium target configuration. This configuration has the highest power, and it is more challenging configuration from the heat removal point of view.

The subcritical assembly with the uranium target configuration has 37 fuel assemblies at the startup of the first fuel burnup cycle and 43 fuel at the start of the second fuel burnup cycle surrounded by beryllium reflector assemblies as sown in Fig. III.5.1.1. As discussed in Sec. III.4, the configuration will change over time. A graphite ring is positioned around the subcritical assembly. Nuclear heating in the graphite is very low.

Actual pictures and CAD model of the fuel assembly geometry is shown in Fig. III.5.1.3. Each fuel assembly has three concentric rings, two cylinders and an outer hexagonal. The UO_2 fuel material is dispersed in an aluminum matrix. The cladding is aluminum on both sides and the dimensions of the fuel layers are listed in Table III.5.1.1

Due to the high thermal conductivity and the low power density, fuel and clad materials are homogenized in the present analysis with a constant thermal conductivity. The equivalent thermal conductivity of the uranium-aluminum matrix is 180 W/m-K. The power is localized within the uranium fuel region.

Two sets of analyses were performed:

a. Steady state analysis of the flow in the assembly through preliminary calculations and CFD simulation (Sec. III.5.2), and
b. Simplified analysis of the flow in the tank (CFD simulation, Sec. III.5.3).

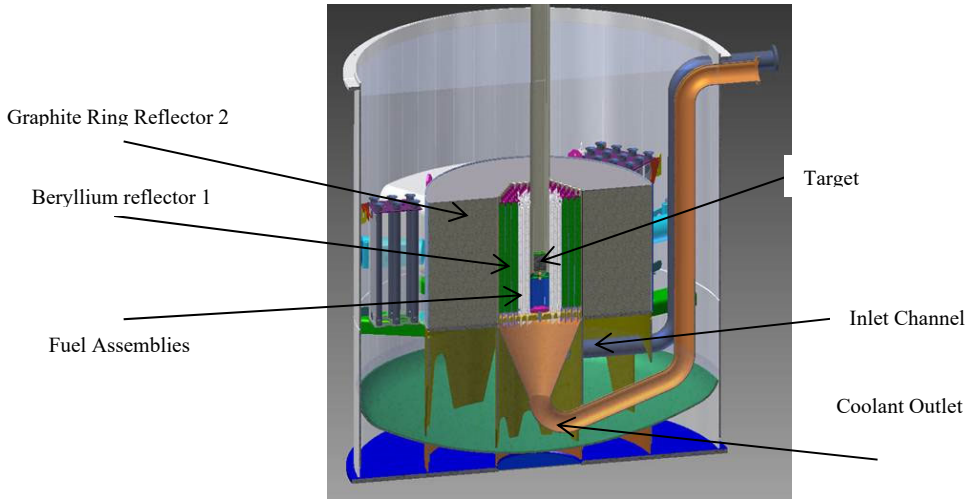

Figure III.5.1.1. Main components of the subcritical assembly

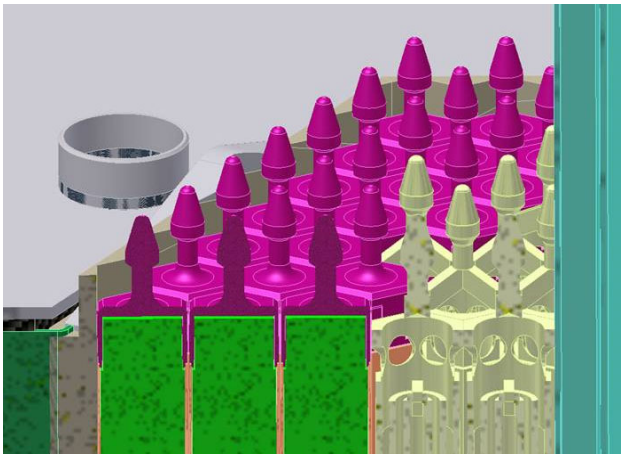

Figure III.5.1.2. Isometric view shows the details of the fuel and beryllium assemblies

Table III.5.1.1. Fuel assembly material dimension

Ring	Inner dimension (mm)	Outer dimension (mm)	Fuel material thickness (mm)
1	3.0	5.5	1.0
2	8.5	11.0	1.0
3	13.5	16.0	1.0

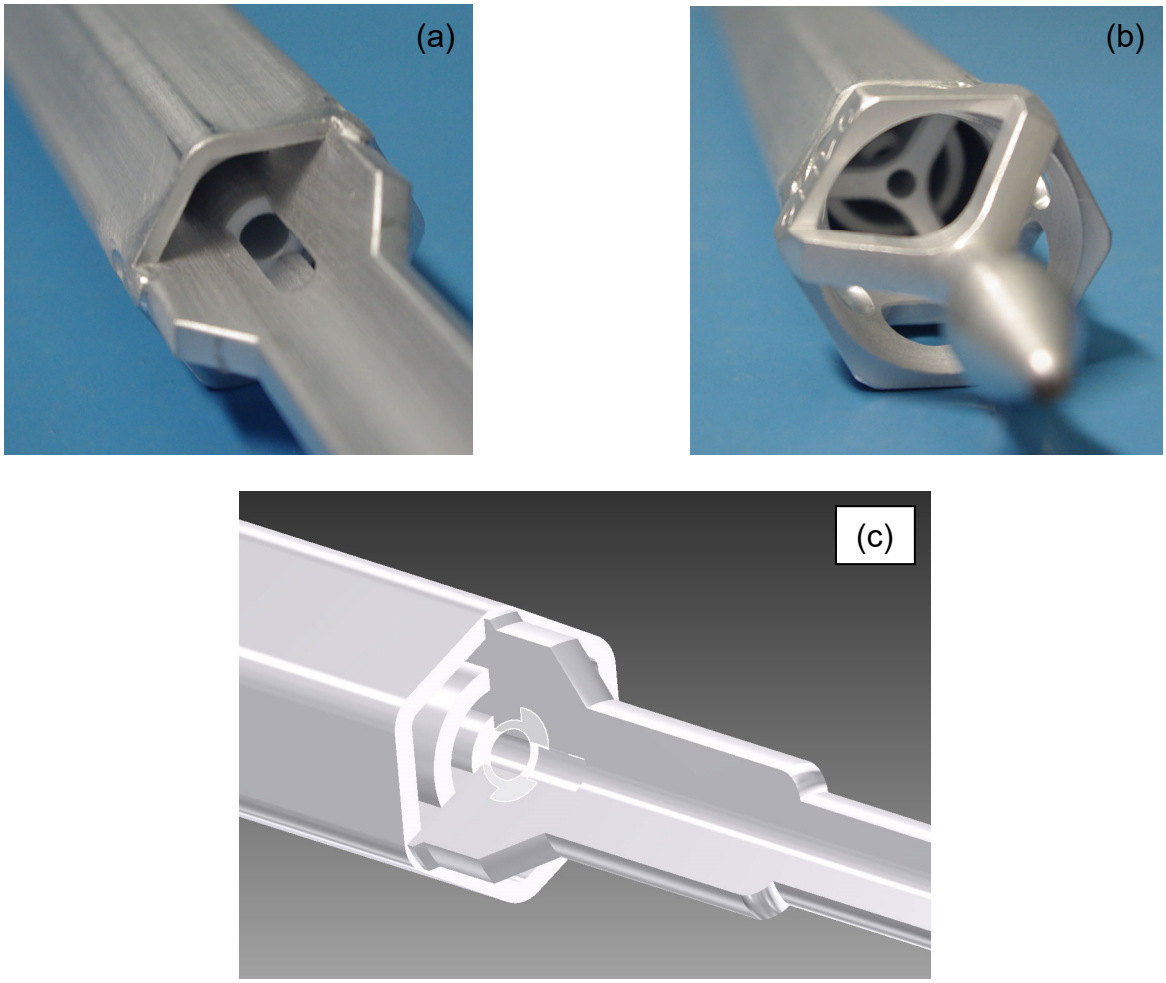

Figure III.5.1.3. Inlet (b) and Outlet (a and c) Nozzles of the fuel assembly

III.5.2 Steady-state flow analysis of the subcritical assembly

III.5.2.1 Global pressure drop

To evaluate the parameters of the subcritical assembly and the necessary margins, it is important to evaluate the ratio between flow in a single channel and total mass flow rate. The total mass flow rate in the hottest channel is related to the total mass flow rate by a simple analytical relationship, provided that the pressure drop in the assembly can be considered the major driver. This analysis does not include the effect of the support plate. Such an effect is not important since the plate distributes the pressure drop uniformly across the whole subcritical assembly.

From the Darcy law, the pressure drops due to friction in a channel is:

$$\Delta p = \rho f \frac{L}{D_h} \frac{v^2}{2} \quad (1)$$

where ρ is the density, L is the length of the channel, D_h is the hydraulic diameter, v is the velocity, and f is the Darcy friction factor. It is assumed that the pressure drop in two parallel channels is the same, since the pressure at the upper plenum and lower plenum can be considered uniform (both plena are large water pools). It then becomes apparent that the ratio r between the average velocity in the reflector region (g) and the fuel region (f)is given by:

$$r = \frac{v_g}{v_f} = \sqrt{\frac{f_f}{f_g}\frac{D_f}{D_g}} \tag{2}$$

Since the average velocity in the fuel region can be considered constant, the total mass flow rate $\dot{m_{tot}}$ can be expressed as a function of the mass flow rate in the hottest subassembly, $\dot{m}_f$:

$$\dot{m_{tot}} = \left(r\frac{A_g}{A_f}N_g + N_f\right)\dot{m}_f \tag{3}$$

where $\frac{A_g}{A_f}$ is the ratio between cross-sectional areas in the beryllium region and the fuel region. N_g is the number of beryllium assemblies and N_f is the number of fuel assemblies.

Cross-sectional areas details are in Table III.5.2.1.1. The beryllium assemblies contain only one channel (channel 4). Due to the very similar value of hydraulic diameter between the channels, the ratio r is very close to unity.

Table III.5.2.1.1. Fuel channels hydraulic characteristics

Item	Channel Number			
	1	2	3	4
flow area, m^2	2.8274E-05	1.3195E-04	2.5015E-04	1.8003E-04
hydraulic diameter, m	6.0000E-03	6.0000E-03	6.1964E-03	6.6631E-03
wetted perimeter, m	1.8850E-02	8.7965E-02	1.6148E-01	1.0808E-01
heated perimeter, m	1.8850E-02	8.7965E-02	1.6148E-01	1.0808E-01

The mass flow ratio is approximately the same as the area ratio. For the present case, this ratio has been evaluated as being between 62 and 65. The value in the subcritical assembly will be somewhat different due to uncertainty related to:

1. Entrance effects in the subcritical assembly,
2. Exit effects in the subcritical assembly, and
3. Effect of the support plate.

Due to the low flow rate above and below the assembly, it is likely that such effects will be small. To allow margin for these effects, a safety coefficient of 10% is applied to the median ratio of 63.5, leading approximately to:

$$\frac{\dot{m_{tot}}}{\dot{m}_f} \approx 70 \tag{4}$$

Once the lowest satisfactory $\dot{m}_f$ has been determined, the total mass flow rate will be determined using Eq. 4. The overall temperature difference across the assembly is then determined according to:

$$\Delta T = \frac{P}{c_p \dot{m_{tot}}} \tag{5}$$

P is the total power and c_p is the heat capacity. The inlet temperature and the material properties are evaluated at the inlet temperature of 25 °C (298.15 K).

III.5.2.2 Single channel model

Initially, simplified flow models of the hottest channel were examined using standard correlations while assuming a constant power. One of the major challenges is the heat transfer coefficient of the low flow conditions of the facility with Re<10,000, which is subject to considerable uncertainty [III.5.1]. The correlation usually employed [III.5.1, III.5.2] is the Gnielinski correlation, which is considered valid only above Re=3,000. Moreover, while the temperature in the tank is relatively constant, it may vary due to environmental conditions. This influences the Reynolds number and the peak temperature.

The analysis presented below compares peak temperatures obtained using the Gnielinski correlation (G), the Dittus-Boelter correlation (D) and the laminar result (L). All calculations are performed assuming atmospheric pressure and single-phase flow.

Figures III.5.2.2.1 to III.5.2.2.3 show that laminar flow can introduce water boiling. The fuel assembly is not designed for such conditions so laminar flow should be avoided. Since there is great uncertainty in the heat transfer coefficient with Re number below 3,000 [III.5.1], the subcritical assembly must operate with Re greater than 3,000 and the Reynolds number must be evaluated with the inlet temperature of 20°C. At this temperature for the mass flow rates of interest, a strong laminarization effect starts to take place as shown in Fig. III.5.2.2.4.

Moreover, for Reynolds numbers below 3,000, the ratio between friction forces and buoyancy forces:

$$r \cong \frac{f_D \rho \frac{L_{heat} V^2}{D \quad 2}}{L_{tot} \rho g \beta (T_{peak} - T_{inlet})} \cong f_D \frac{V^2}{D g \beta (T_{peak} - T_{inlet})} \tag{6}$$

tends to be below the minimum value of 10 (Fig.III.5.2.2.5) that was identified as a point at which the buoyancy forces are negligible compared to the friction forces for avoiding circulation. In Eq. 6, β is the thermal expansion coefficient, f_D is the Darcy friction factor, g is the gravity acceleration, ρ is the density, $D$is the hydraulic diameter, V is the bulk velocity, and $\left(T_{peak} - T_{inlet}\right)$ is the difference between the peak coolant temperature and the inlet temperature.

From these results, a value of 0.32 kg/s was selected as an appropriate value for the mass flow rate for each fuel assembly. The value was determined using water properties at 20°C and 10% margin to insure a minimum Reynolds number value of 3,000 inside the channels of the fuel assembly.

To verify the peak temperature value with the 0.32 kg/s mass flow rate, a three-dimensional CFD calculation was performed for the fuel assembly. A CAD file was used to create a three-dimensional representation of the flow and temperature field. Because of the geometrical symmetry, a computational model based on the CAD file using one-sixth of one fuel assembly was used to reduce computational time. The computational model includes the grid plate. Therefore, the model includes flow constrain at the outlet nozzle, which accelerates the flow in this area. The peak temperatures of the cladding and the fuel were defined as a function of the mass flow rate in the hottest fuel assembly.

The commercial CFD computer code STAR-CCM+ 5.06 [III.5.3] was used to perform the analysis. The mesh was created through a combination of prism layers, thin meshes, and polyhedral cells. Both fluid and solid (fuel plus cladding and structural materials) have been simulated. This analysis is a classic conjugate heat transfer problem. Second-order schemes have been used for the convection term. k-ε model has been used to model turbulence. A thick prism layer is used to achieve convergence.

In the design evaluation stage, buoyancy effects have been neglected, since the pressure difference induced by the temperature rise is negligible compared to the friction loss. The boundary conditions are shown in Fig. III.5.2.2.6.

An example of the employed mesh types is shown in Fig. III.5.2.2.7. The total number of meshes of this model is approximately 8 million. No significant difference in the results were observed when different mesh types were used.

The power distribution is obtained from neutronic calculations, as discussed in Sec. III.3. An appropriate axial distribution is imposed in each ring and the power within each ring is assumed constant over the cross section. The total power of the hottest fuel assembly is 6.8 kW. In the calculation, water properties are evaluated at the inlet temperature of 300 K, since the overall temperature variation within the water coolant is insiginficant.

The ratio between the average velocities in the four channels of the fuel assembly is as follows:

- Channel 1 is 1.099 of the bulk velocity;
- Channel 2 is 1.06 of the bulk velocity;
- Channel 3 is 1.085 of the bulk velocity; and
- Channel 4 is 0.89 of the bulk velocity.

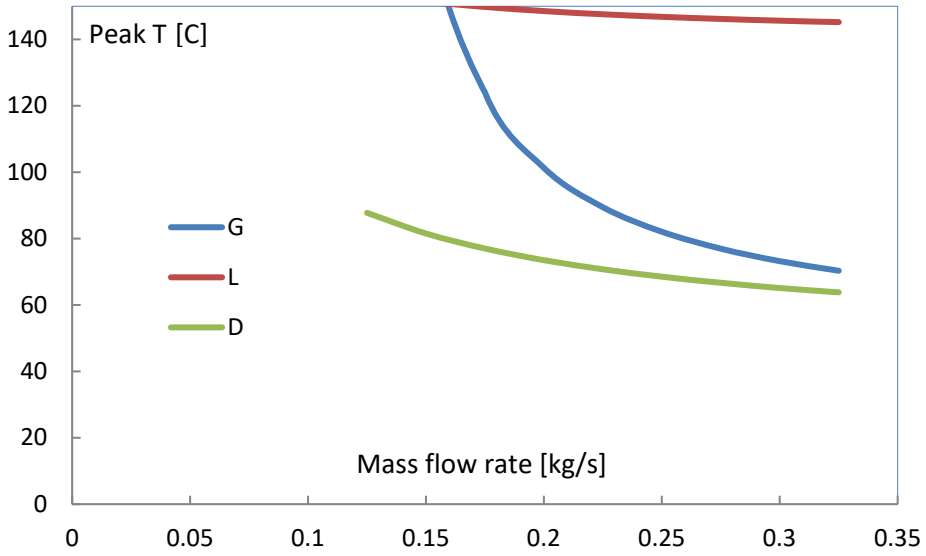

Figure III.5.2.2.1. Peak coolant temperature with water inlet temperature and properties at 10°C, no correlation is valid in this case (at 0.32 kg/s Re<3,000)

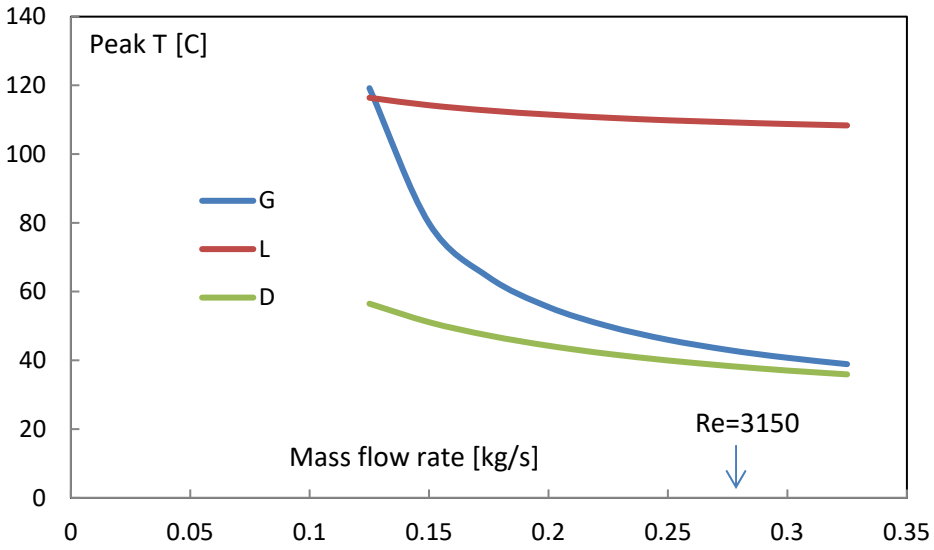

Figure III.5.2.2.2. Peak coolant temperature with water inlet temperature and properties at 20°C, no correlation is valid in this case (at 0.32 kg/s Re<3,000), only the Gnielinski correlation is valid in this case, but only above 0.3 kg/s

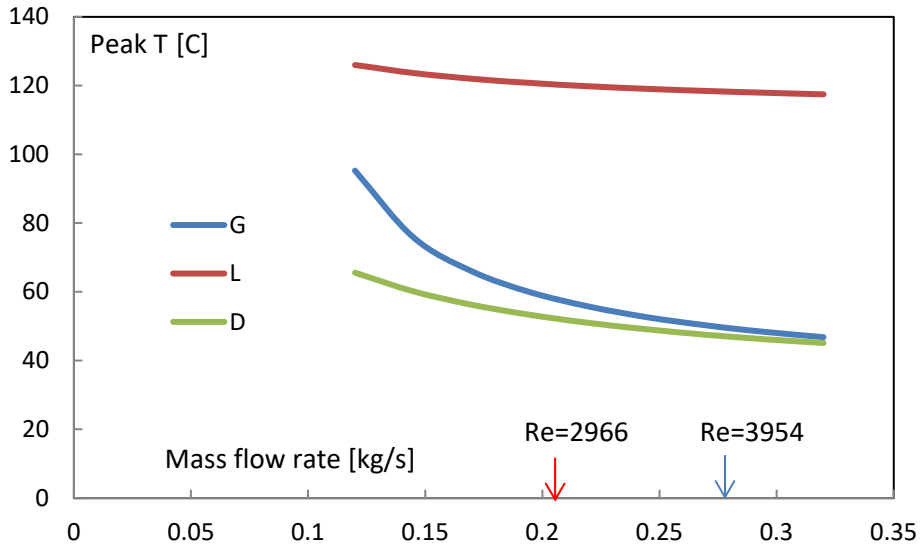

Figure III.5.2.2.3. Peak coolant temperature with water inlet temperature and properties at 30°C, only the Gnielinski correlation is valid in this case, but above 0.225 kg/s (red arrow)

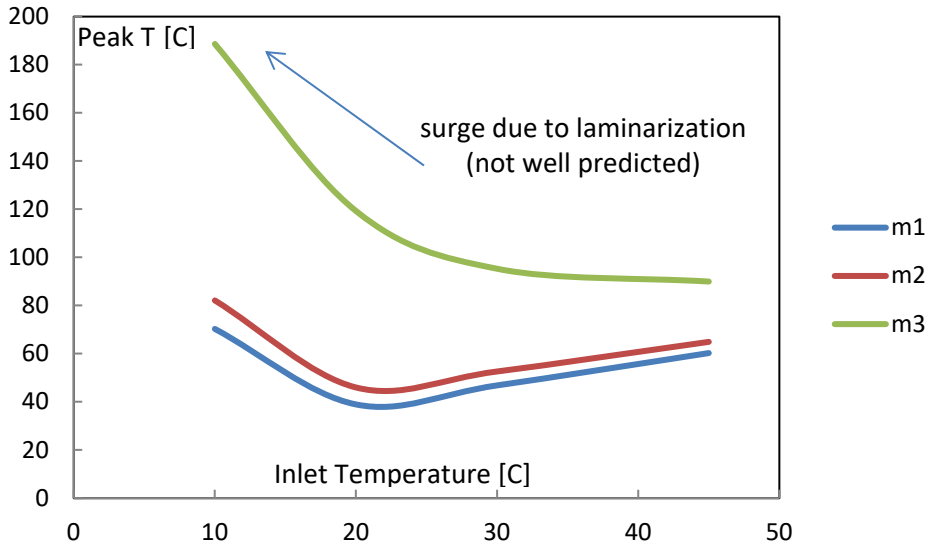

Figure III.5.2.2.4. Comparison of peak temperatures for the three mass flow rates using the Gnielinski correlation with water properties at the inlet temperature, m1 = 0.32 kg/s, m2 = 0.25 kg/s, and m3 = 0.125 kg/s

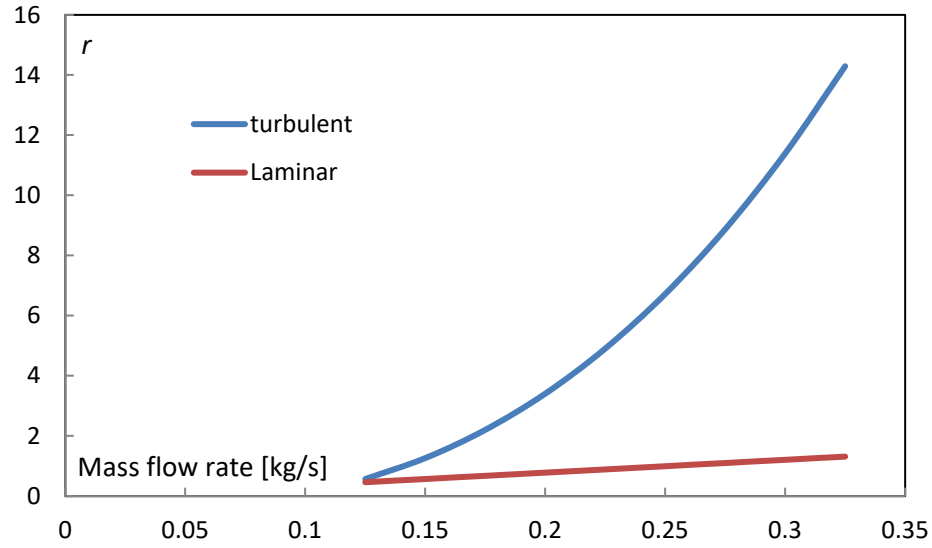

Figure III.5.2.2.5. Ratio (r) between turbulent (calculated using the Gnielinski correlation) and laminar flow for an inlet temperature of 20ºC.

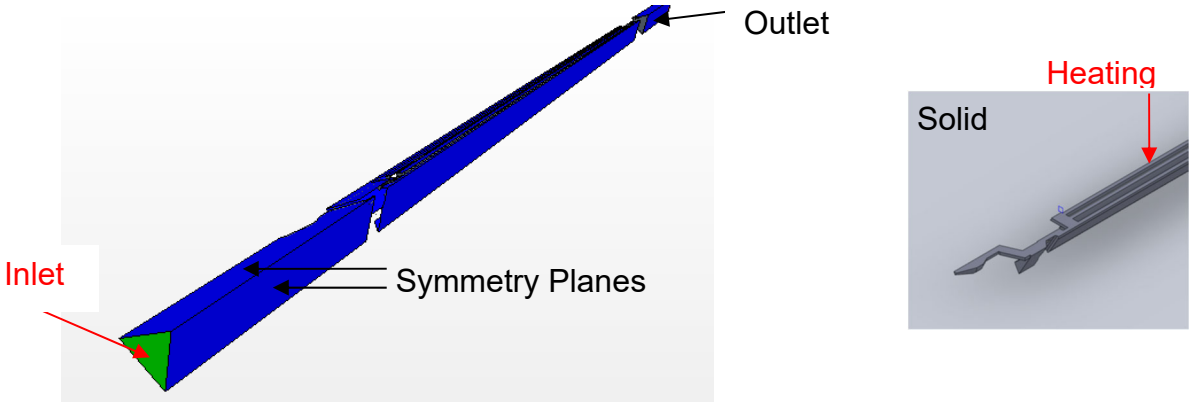

Figure III.5.2.2.6. Boundary conditions

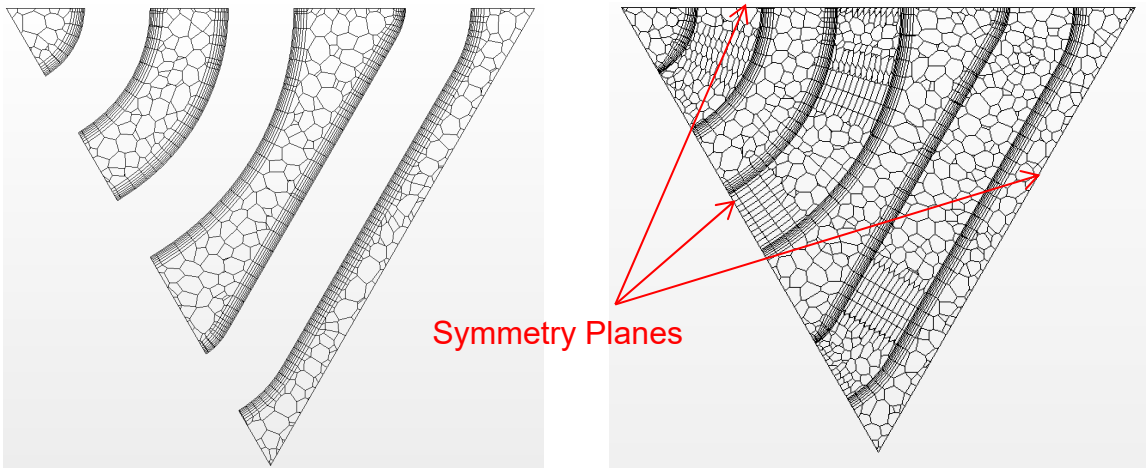

Figure III.5.2.2.7. Fluid mesh and fluid & solid mesh

This represents qualitative agreement with the values reported by the fuel manufacturer at higher Reynolds numbers where channel 1 experiences the highest velocity, followed by channel 3, then channel 2, and the lowest velocity in channel 4.

For a mass flow rate of 0.32 kg/s, the velocity distribution is shown in Fig. III.5.2.2.8 in the outlet nozzle region and the flow acceleration due to the presence of the grid plate is noticeable. Figures III.5.2.2.9 to III.5.2.2.11 show the development of the flow field in the four channels from the upper nozzle (inlet) to the lower nozzle (outlet). The inlet nozzle induces irregularities in the flow distribution that is balanced later downstream.

The temperature distribution within the fuel material is shown in Figs. III.5.2.2.12 to III.5.2.2.15. The maximum temperature within the fuel material is 314.8 K. The peak surface temperature is 314.6 K. Within the fluid the difference $T_{peak} - T_{inlet}$ is 14.6 K. The peak water temperature for 25 °C inlet water temperature is 39.6 °C. This value is close to the values predicted by the preliminary analysis using the Gnielinski correlation of Figs. III.5.2.2.1 to III.5.2.2.3. The fact that the peak temperature is lower due to the axial conduction within the fuel element.

Figures III.5.2.2.16 to III.5.2.2.20 show the temperature distribution in the water coolant and the fuel material regions at different position along the fuel assembly axis, z direction. The temperature gradient within the fuel material is small. Most of the temperature gradient is observed within the water coolant. Figures III.5.2.2.16, III.5.2.2.20, and III.5.2.2.21 show that axial conduction is significant since the temperature in the solid is significantly higher than the surrounding fluid.

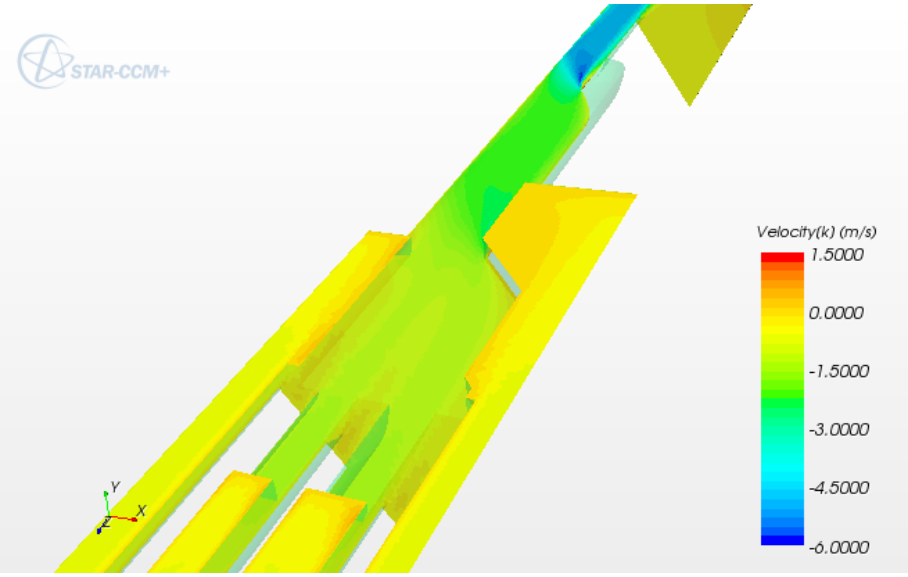

Figure III.5.2.2.8. Water velocity in the outlet nozzle

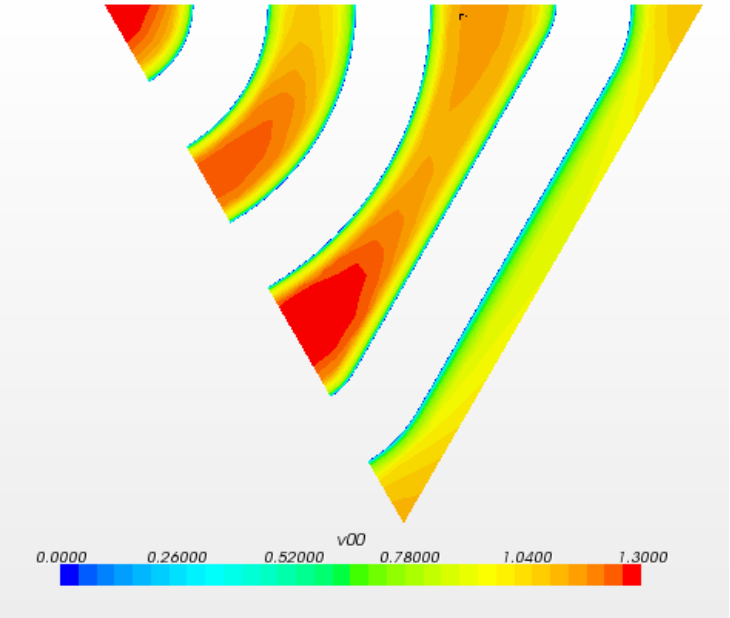

Figure III.5.2.2.9. Downward water coolant velocity at 0.4 m from the bottom of the fuel assembly

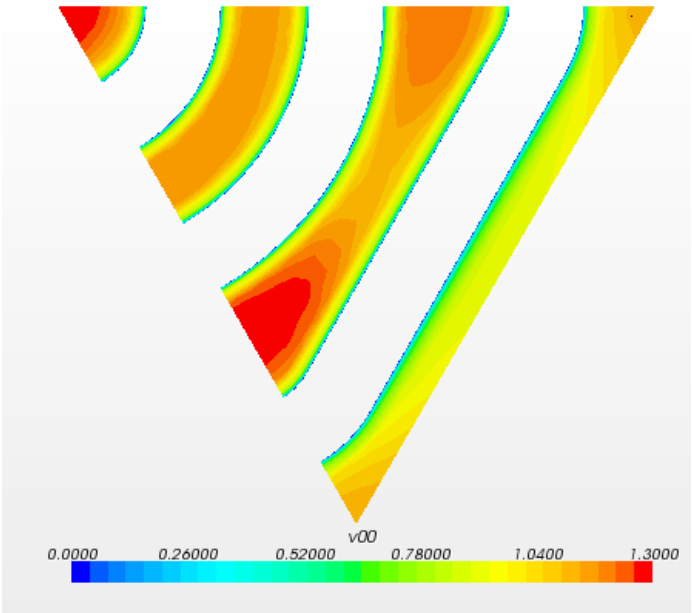

Figure III.5.2.2.10. Downward water coolant velocity at 0.25 m from the bottom of the fuel assembly

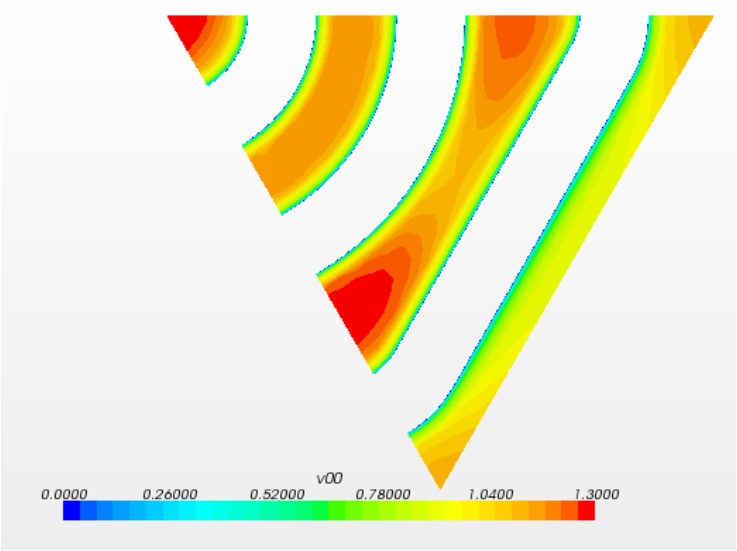

Figure III.5.2.2.11. Downward water coolant velocity at 0.15 m from the bottom of the fuel assembly

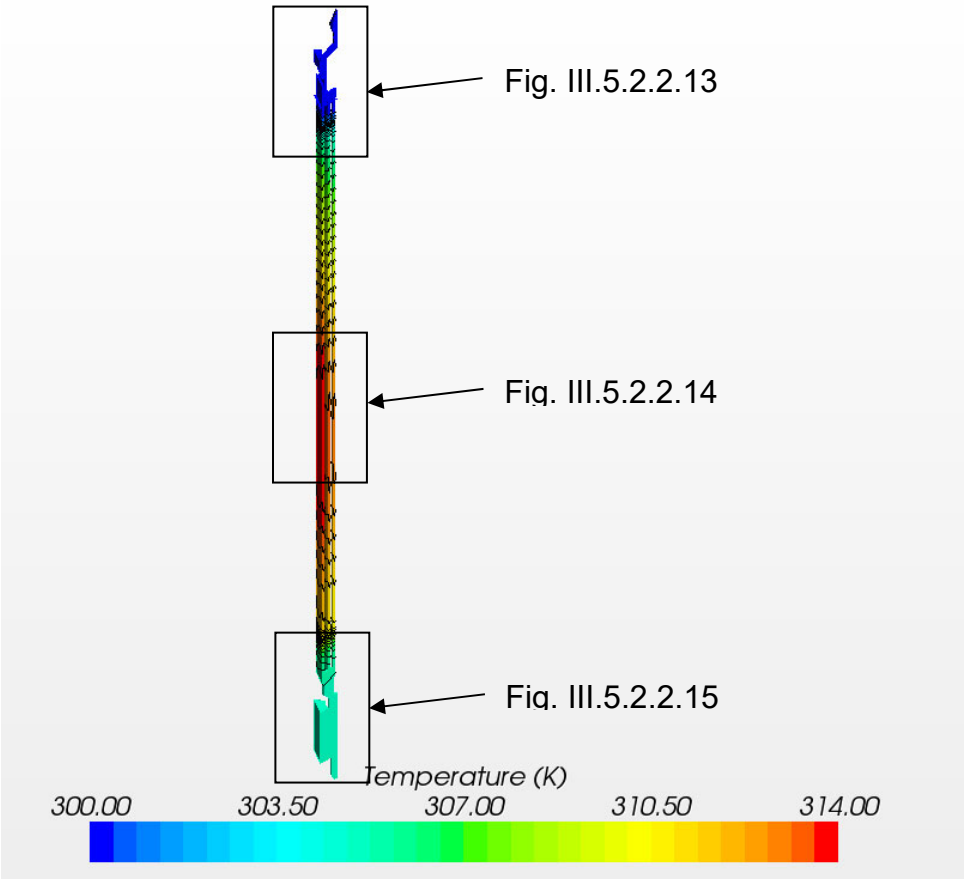

Figure III.5.2.2.12. Temperature distribution in the fuel assembly [K]

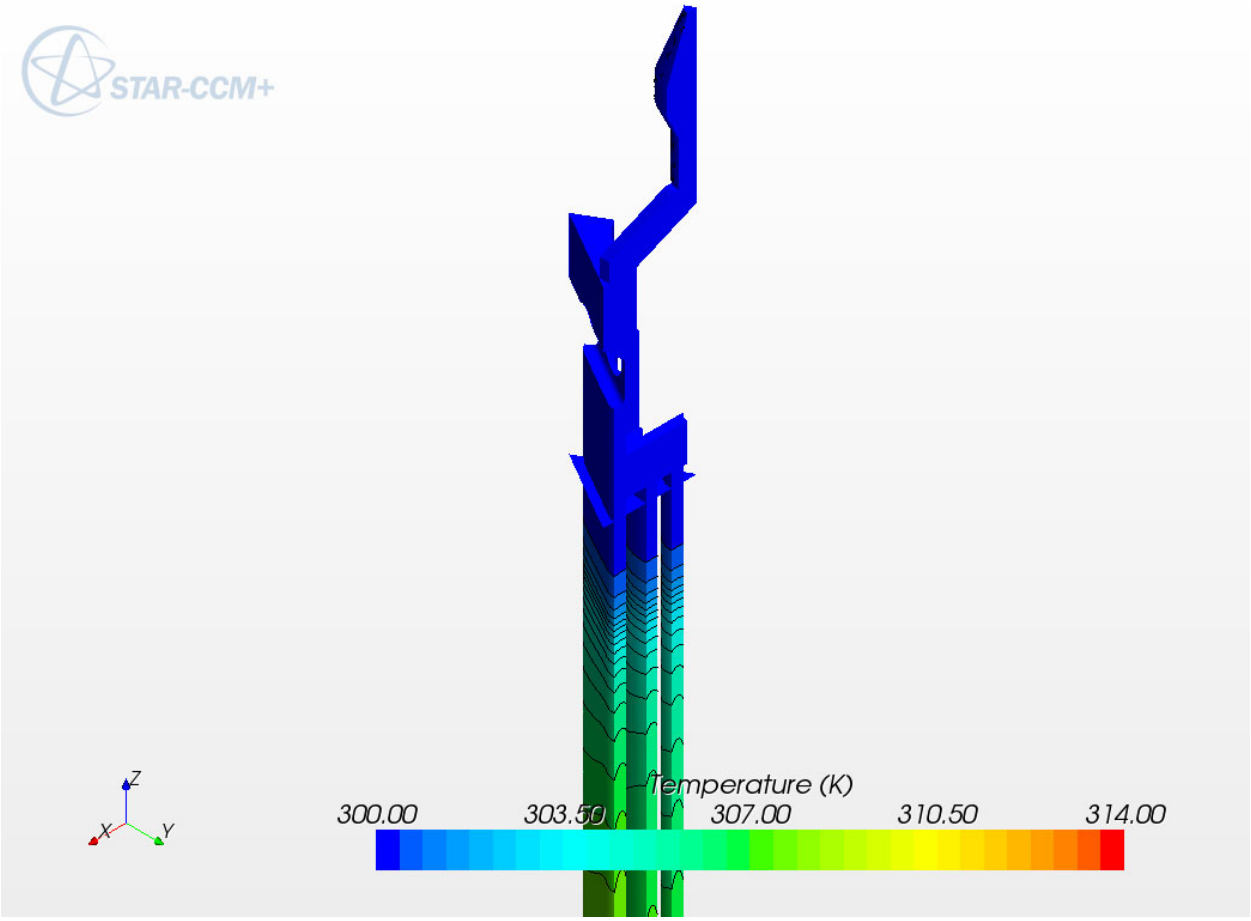

Figure III.5.2.2.13. Temperature distribution in the upper section of the fuel assembly [K]

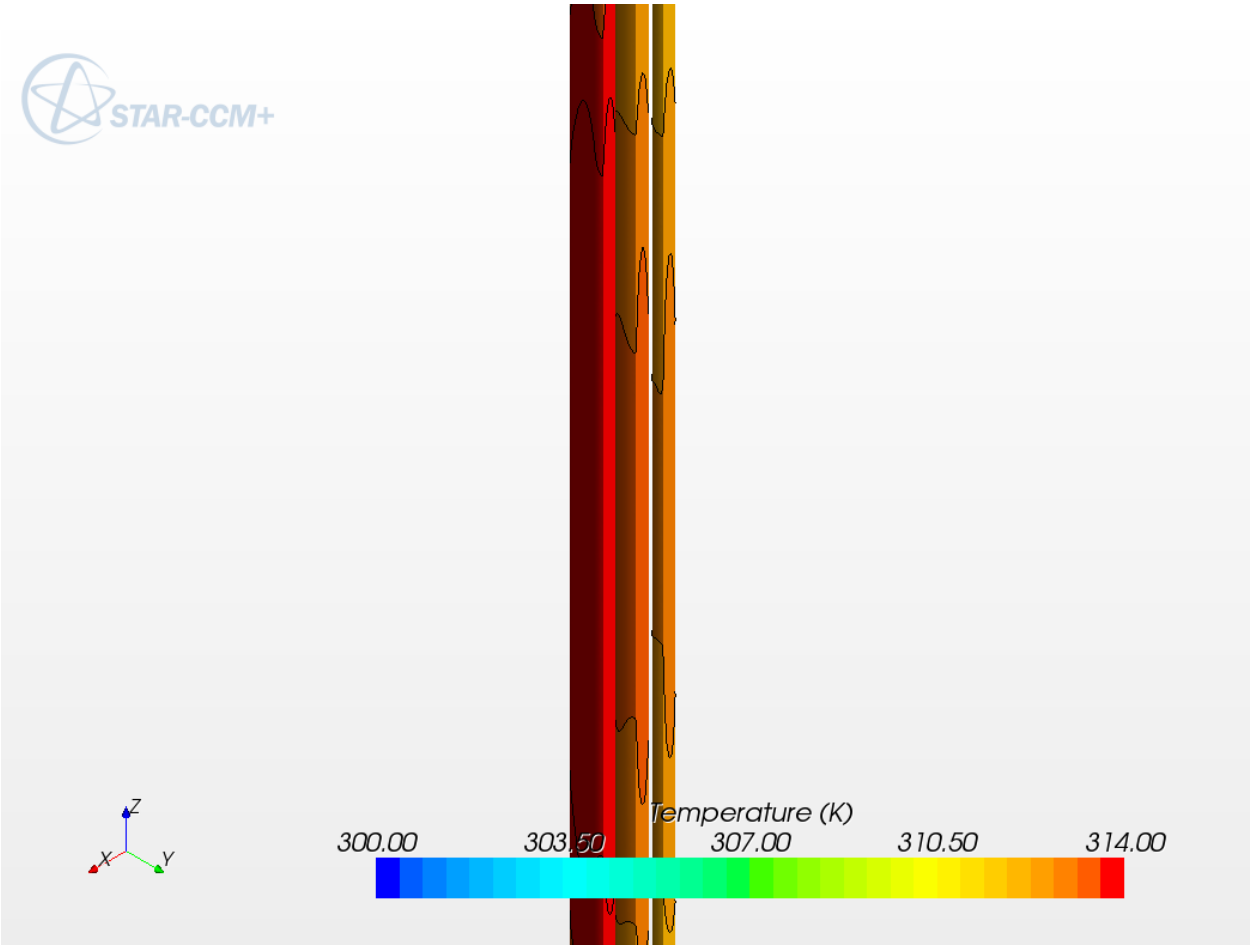

Figure III.5.2.2.14. Temperature distribution in the middle section of the fuel assembly [K]

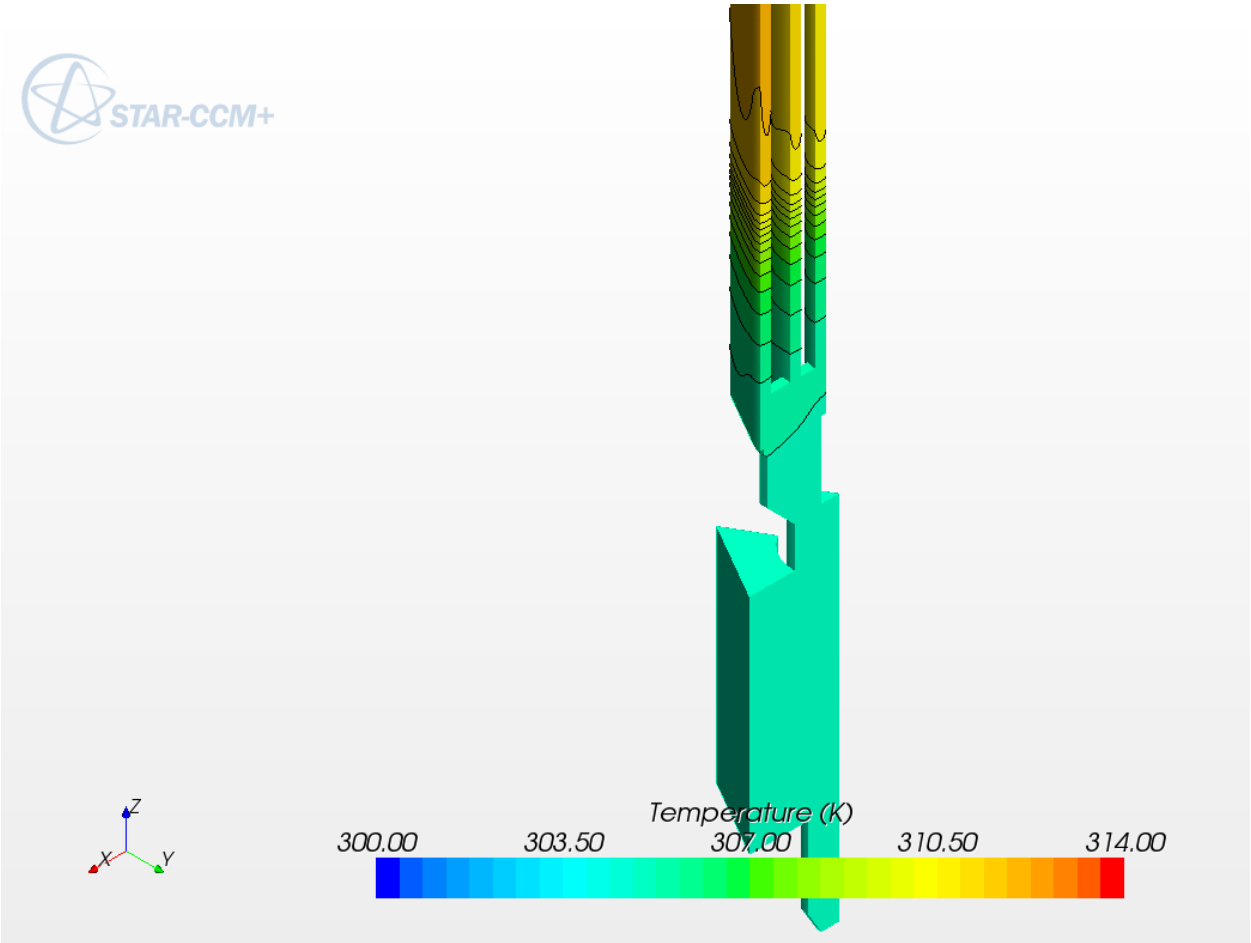

Figure III.5.2.2.15. Temperature distribution in the lower section of the fuel assembly [K]

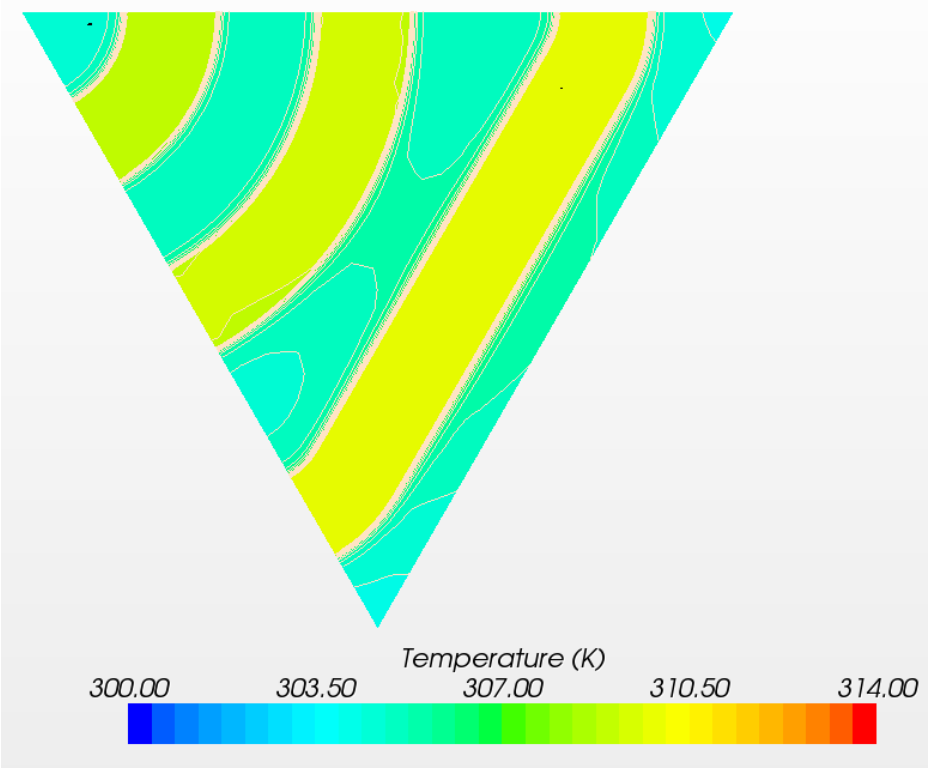

Figure III.5.2.2.16. Temperature distribution in the fuel assembly cross section at z=0.05 m, below the uranium region

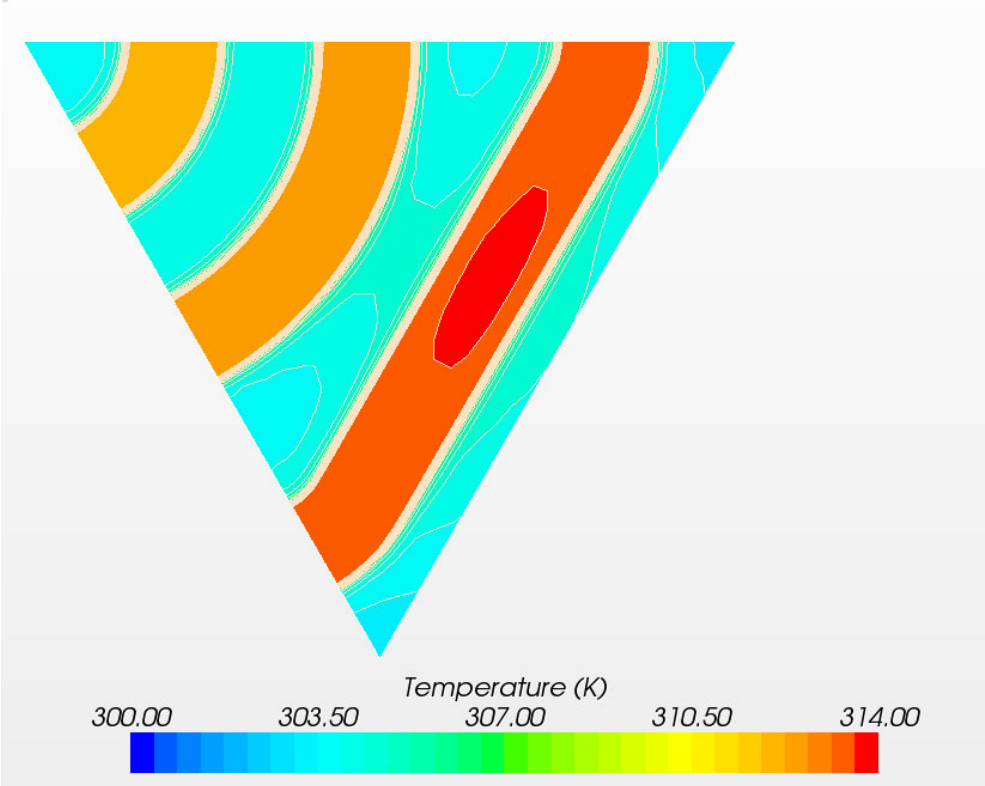

Figure III.5.2.2.17. Temperature distribution in the fuel assembly cross section at z=0.2 m

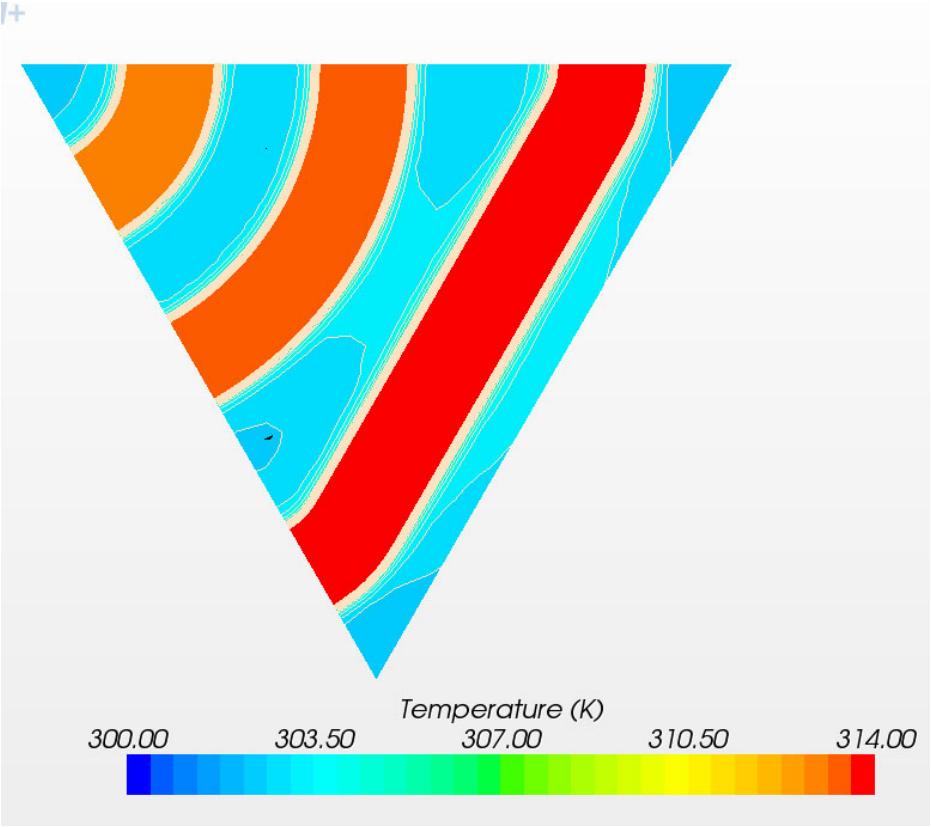

Figure III.5.2.2.18. Temperature distribution in the cross-section z=0.3 m.

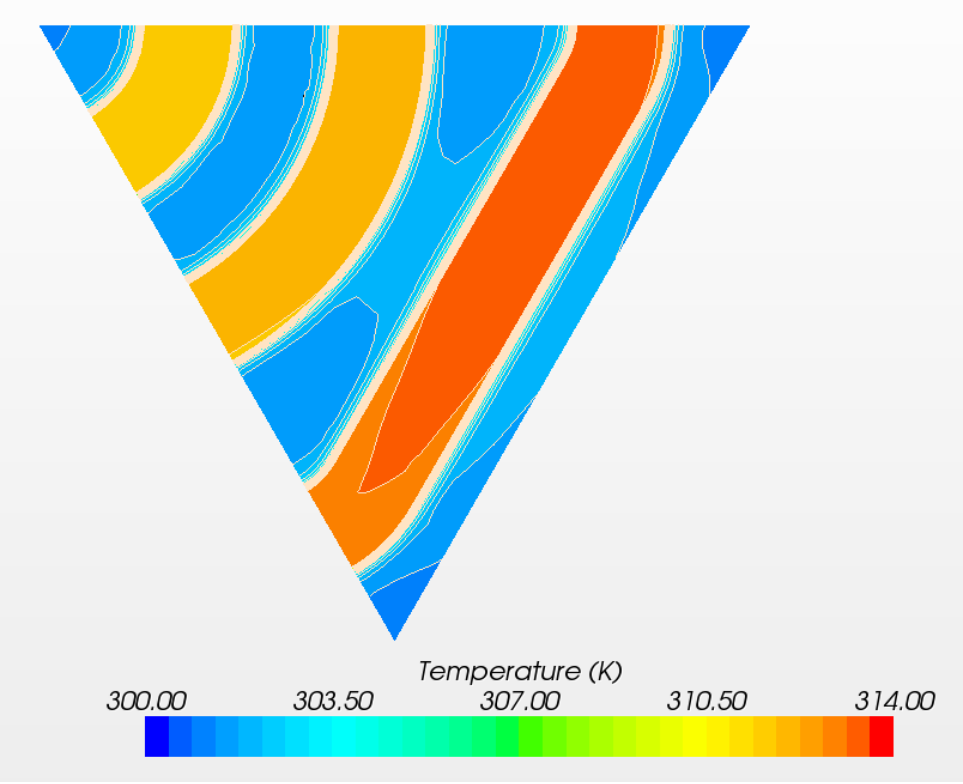

Figure III.5.2.2.19. Temperature distribution in the cross-section z=0.4 m.

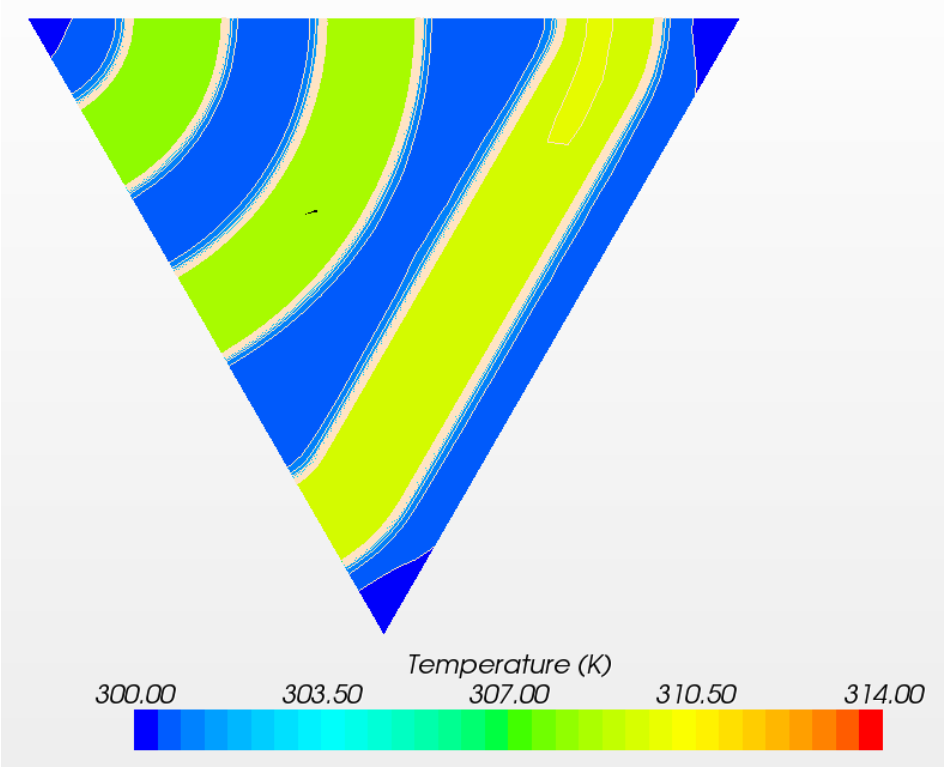

Figure III.5.2.2.20. Temperature distribution in the fuel assembly cross section at z=0.55 m, above the uranium region

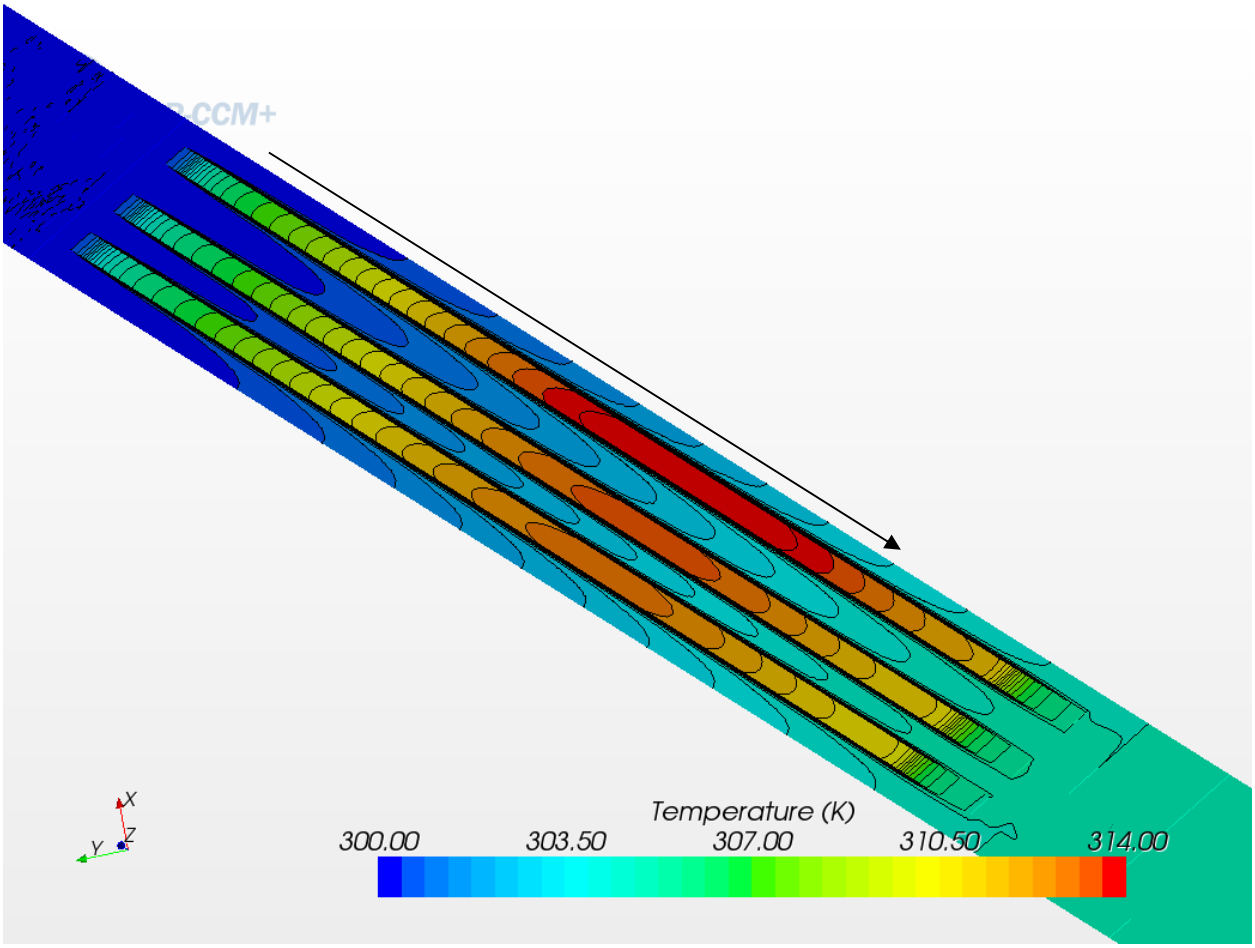

Figure III.5.2.2.21. Temperature distribution in the fuel assembly symmetry plane and the arrow represents the flow direction

III.5.2.3 Parameters

The total mass flow rate is 22.6 kg/s, which is corresponding to 0.32 kg/s per fuel assembly. The outlet temperature is 27.2 °C for an inlet temperature of 25 °C. The peak fuel temperature is 39 °C. The pressure drop through the fuel assembly and the grid plate is evaluated at 13.7 kPa.

III.5.3 Steady-state flow analysis of the subcritical assembly tank

A CAD file of the subcritical assembly tank was used to create a three-dimensional representation of the flow field. One of the analysis objectives is to quantify an upper bound for the residual velocity near the tank surface. A high velocity near the free surface could increase the probably of air entrainment. A computational model from the CAD file was created as shown in Figs. III.5.3.1 and III.5.3.2. The removal of the complex structures, such as the temporary storage units, increases the residual lateral velocity. Therefore, the present model overestimates the cross velocity, and the results will represent an upper bound.

The commercial CFD computer code STAR-CCM+ 5.06 [III.5.3] was used to perform the analysis. The mesh was created with a combination of prism layers and polyhedral cells as shown in Fig. III.5.3.3. The fuel region and the reflector have been simulated as porous media. Second-order schemes have been used for the convection term. The k-ω SST model has been used to model the turbulence because it is suitable for flows with partial swirl,

Because of the complex geometry and the model asymmetry, the flow appears to be unstable in the lower plenum. The steady-state solver failed to converge, while the unsteady solver reaches low residuals in a consistent manner. After an initial transient of approximately 10 s, the flow in the upper plenum stabilizes and the changes are insignificant. To confirm the convergence of the flow, a time average was performed and compared with instantaneous values.

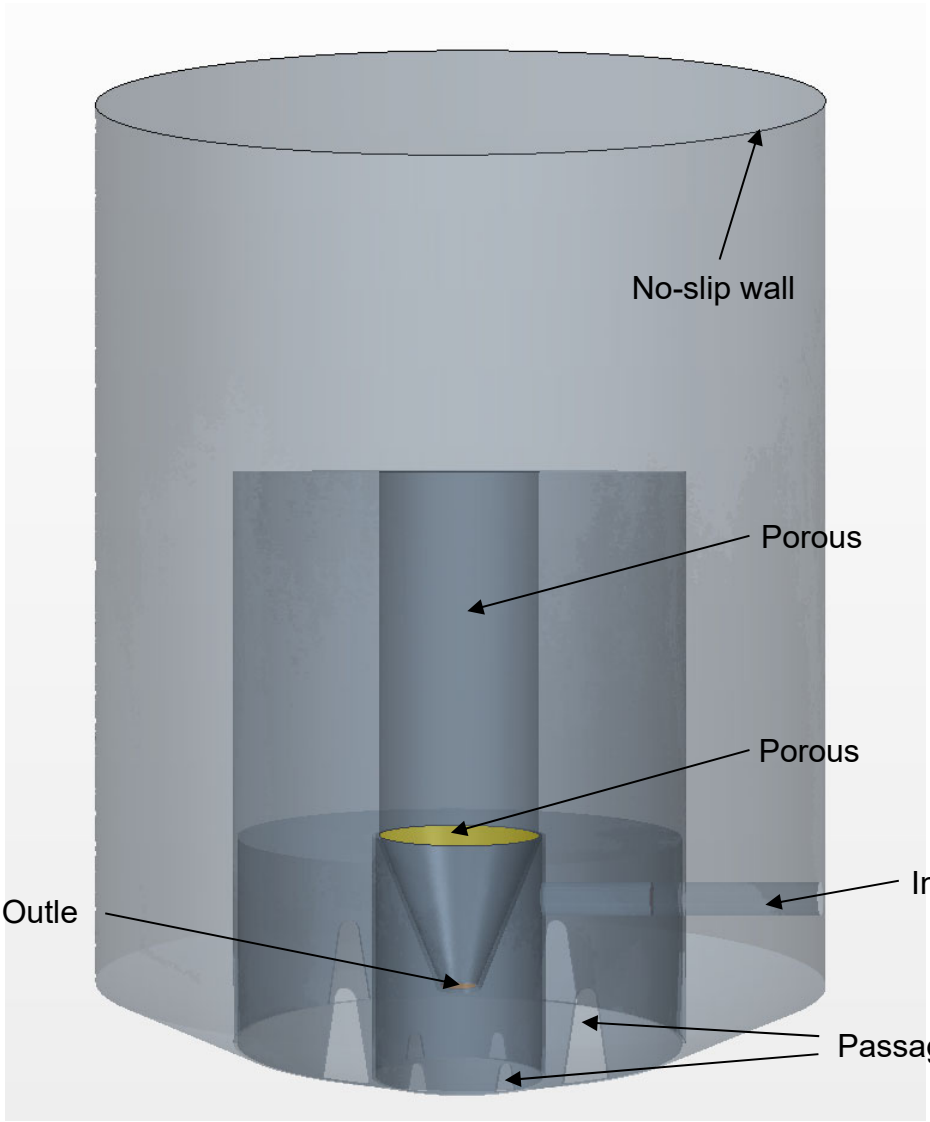

Figure III.5.3.1. Computational model of the subcritical assembly tank – side view

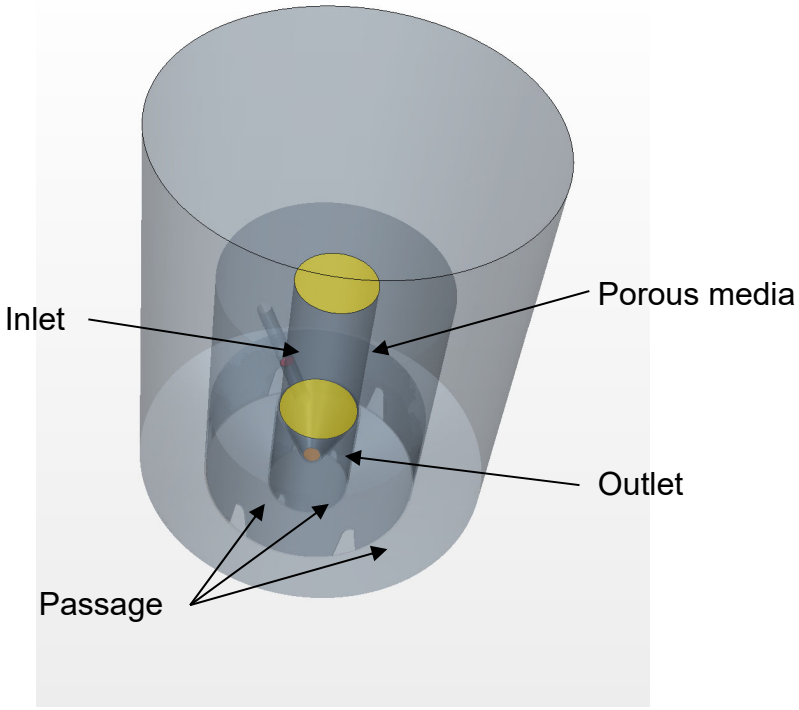

Figure III.5.3.2. Computational model of the subcritical assembly tank – top view.

Figures III.5.3.4 and III.5.3.5 show the average cross velocity $\sqrt{\frac{1}{\Delta T}\int_{T}^{T+\Delta T}\left(v_x^2+v_y^2\right)dt}$ in the domain for 10 s interval. At the upper surface the velocity has peaks around 1 cm/s both for the average velocity and the instantaneous cross velocity as shown in Fig. III.5.3.6. Such values are at least one order of magnitude lower than what would be needed to cause air entrainment.

The velocity iso-surfaces in the y direction are shown in Fig. III.5.3.7. The values of the lateral velocity at the bottom of the subcritical assembly tank do not reach the upper water surface in any significant way.

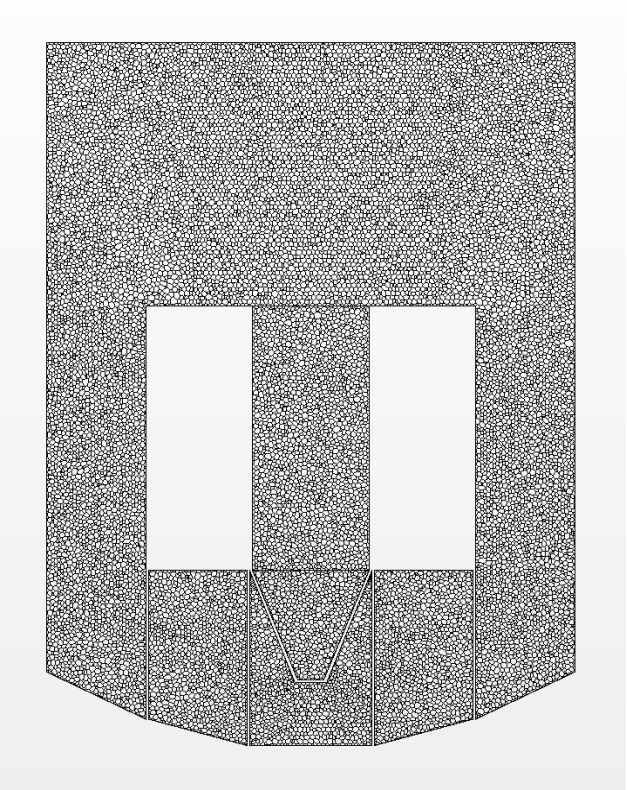

Figure III.5.3.3. The mesh of the subcritical assembly tank model

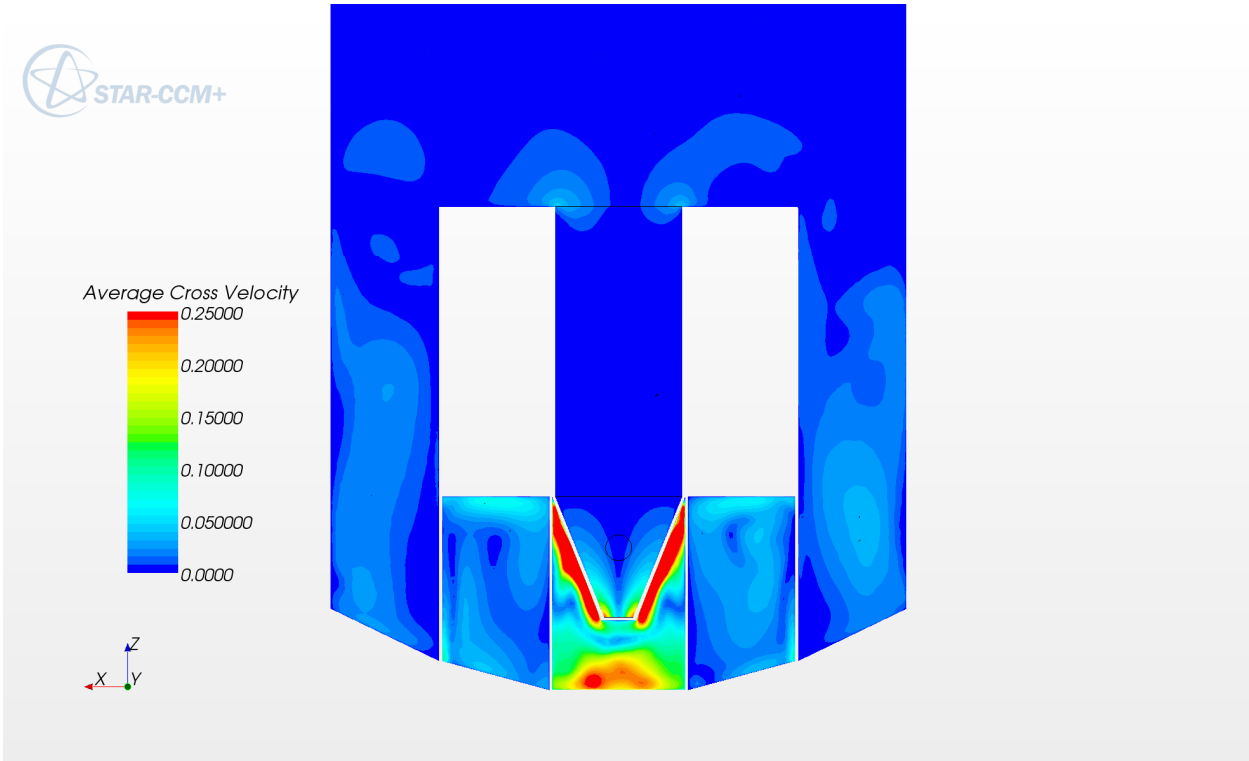

Figure III.5.3.4. Average cross velocity (m/s) at y=0 plane

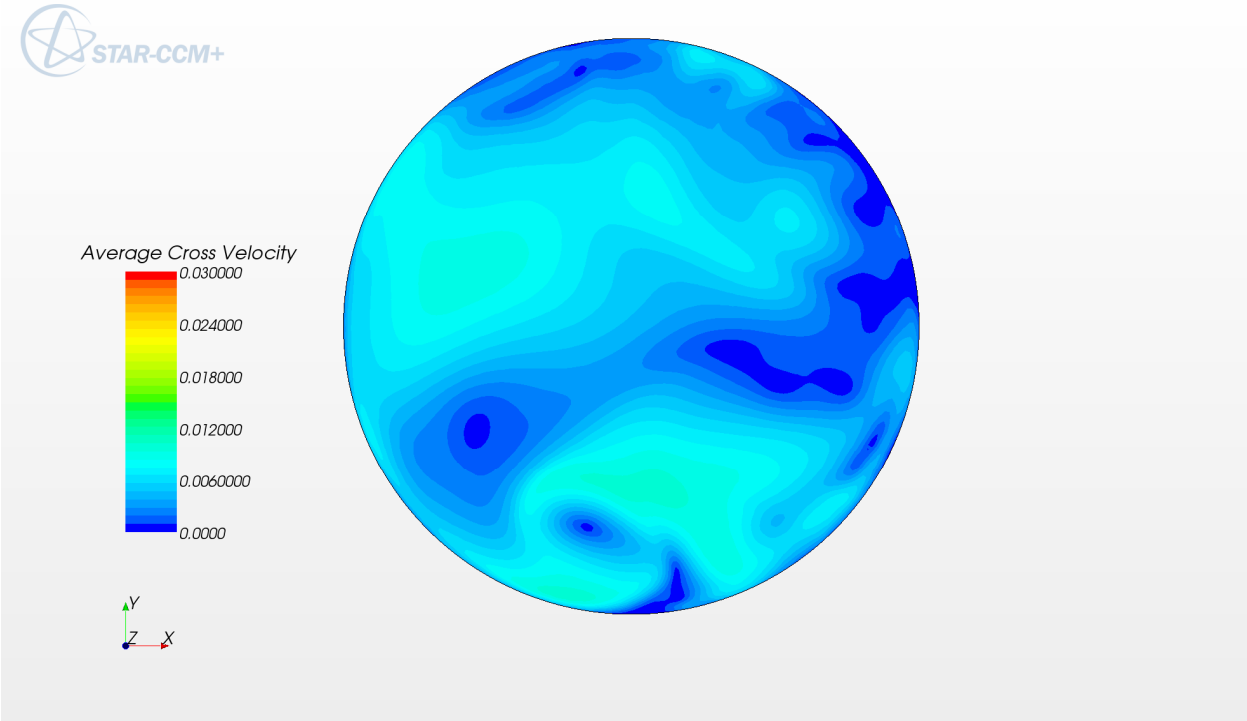

Figure III.5.3.5. Average cross velocity (m/s) at the water surface

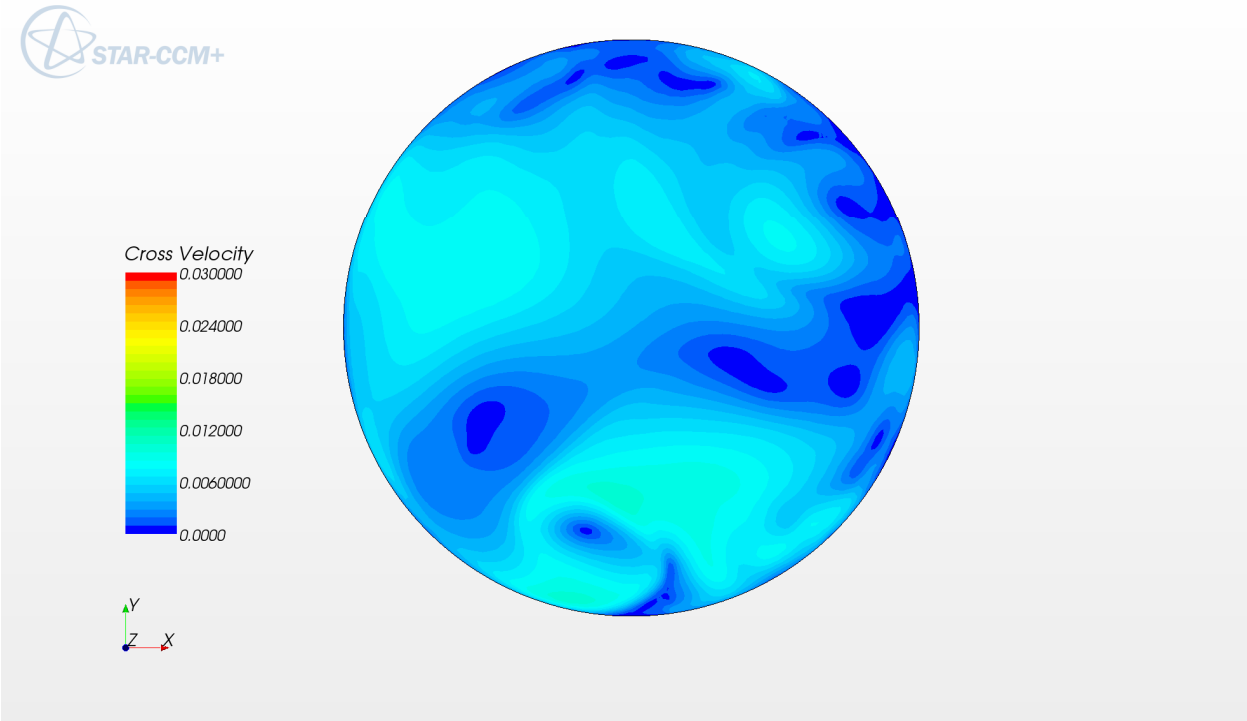

Figure III.5.3.6. Instantaneous cross velocity (m/s) at the water surface

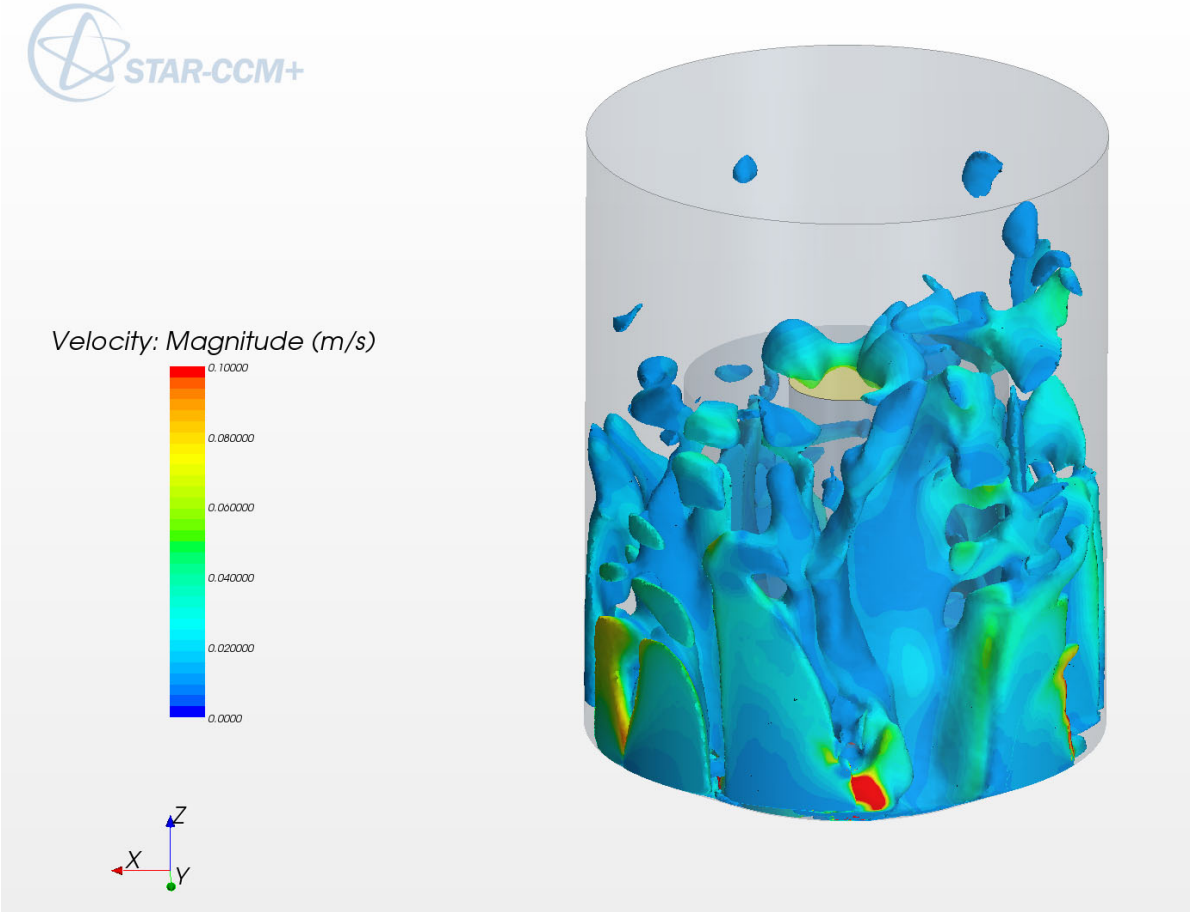

Figure III.5.3.7. Y-velocity iso-surfaces colored by velocity magnitude.

References

III.5.1 Incropera F.P., De Witt D.P. "Fundamentals of Heat and Mass Transfer", Wiley (2007)

III.5.2 Abraham J.P., Sparrow E. M. and Minkowycz W. J. "Internal-Flow Nusselt Numbers for the Low-Reynolds-Number End of the Laminar-to-Turbulent Transition Regime", University of Minnesota Report (2010)

III.5.3 "STAR-CCM+ 5.06 User's Guide", CD-adapco, Mellville, NY, USA.

III.5.4 Todreas N., Kazimi M., "Nuclear Energy Systems Volume I: Thermal Hydraulic Fundamentals," Third Edition Milton: Taylor & Francis Group, 2021.

III.6 Subcritical Assembly Structural Analysis and Design

III.6.1 Subcritical Assembly Tank

III.6.1.1 Objective

The objective of this analysis was to perform a structural feasibility study for the design concept of the subcritical assembly tank of the KIPT neutron source facility.

III.6.1.2 Scope

This analysis simulates the static, the fatigue and the seismic loadings on the subcritical assembly tank that contains: 1) the subcritical assembly, 2) a uranium or tungsten target for generating neutrons, and 3) water as a coolant and a neutron moderator.

III.6.1.3 Methodology

This analysis was carried out with the finite element method, using the ANSYS R13.0 finite element program [III.6.1]. A finite element model was constructed and subjected to estimated loads developed during the design phase. Results were compared to basic material properties, and commonly accepted engineering principles were applied to determine a safety factor.

III.6.1.4 Overview of Analysis

Four load cases were run that bound all loading situations of the tank. The four cases are summarized in Table III.6.1.4.1. These load cases were used to perform four evaluations, as summarized in Table III.6.1.4.2.

III.6.1.5 Assumptions

This analysis is based on the following assumptions:

1. The material response is linear elastic.
2. The material response is constant with time (no effects of aging, creep, etc).
3. The materials are isotropic and homogeneous.
4. The material response is consistent with small strain and small displacement.
5. The effects of neutron flux on material properties are not included.
6. Residual stresses are not included.
7. The tank operates at room temperature.
8. Butt welds are assumed to be continuous, full penetration and uninspected.
9. Fillet welds are assumed to be continuous, un-machined, and uninspected.

III.6.1.6 Geometry

The finite element model was based on solid modeling geometry. The model described in section III.7 has the specifications of this geometry, and it was imported into ANSYS Design Modeler. A midplane surface model, shown in Fig. III.6.1.6.1, was created. This model was taken into the Workbench module of ANSYS R13.0, where a quad dominant

mesh with quadratic quad and tri shell elements were created. This model is shown in Figure III.6.1.6.2.

Table III.6.1.4.1. Summary of load cases

Load Case	Description	Loads		
		Weight of Subcritical Assembly	Weight of Water	Weight of Tank
1	Empty Tank, in Place	yes	no	no
2	Full Tank, in Place	yes	yes	no
3	Full Tank, in Place, Seismic Loading	yes	yes	no
4	Full Tank, Lifting	no	no	yes

Table III.6.1.4.2. Summary of evaluations

Evaluation	Description	Load Cases
A	Empty Tank, in Place	2
B	Full Tank, in Place, Seismic Loading	3
C	Full Tank, Lifting	4
D	Fatigue Loading due to Repeated Filling, in Place	1, 2

III.6.1.7 Materials

Mechanical properties for SAV-1 used for this analysis are shown in Table III.6.1.7.1. Strength values are based on “tempered and naturally aged” heat treatment of rolled plate. Material properties for SAV-1 were not completely available, so common values for similar grades were used when necessary.

Fatigue data was not available for SAV-1, so Al 6061 alloy data were used based on the chemical composition similarity between the two alloys. An S/N curve for Al 6061-T6 was taken from Ref. III.6.2 and used for the bulk material, Figure III.6.1.7.1. Curves were taken from several sources, and the data shown in Figure III.6.1.7.1 was the most conservative. The data points for a fully reversed stress ratio (R=-1) were taken from Ref. III.6.2, converted to metric units, and fitted to a curve, Figure III.6.1.7.2. The heat affected zone (HAZ) was assumed to be annealed, and the only readily available data for AL 6061 was for 6061-O and was an endurance limit of 62.1 MPa at 5.0×10^8 cycles, Ref. III.6.3. This was used to estimate a fatigue curve, using the method presented in Ref. III.6.4. This estimated curve is shown in Figure III.6.1.7.3.

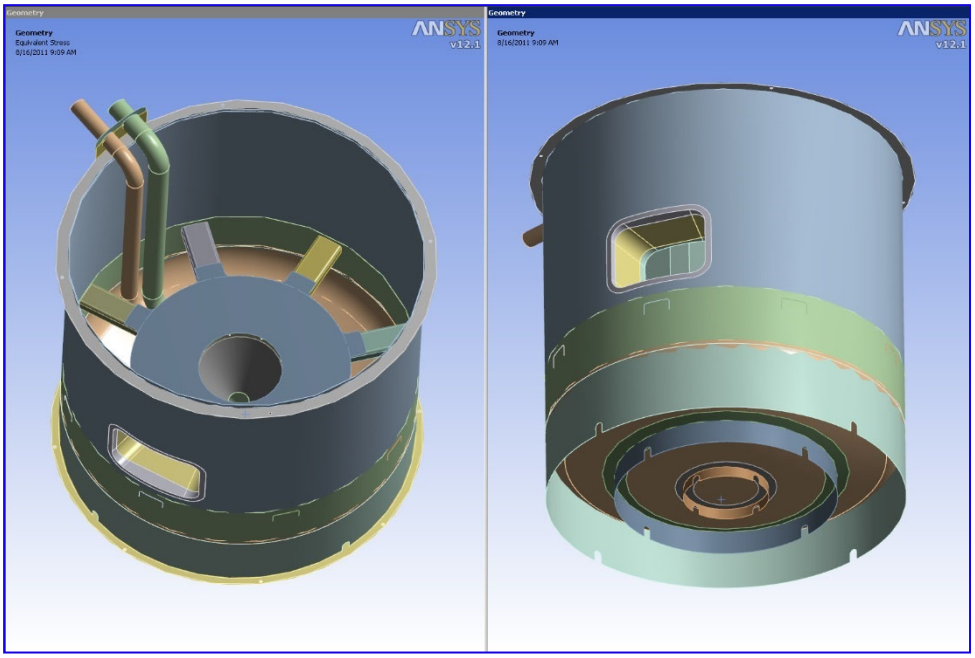

Figure III.6.1.6.1. Midplane surface model

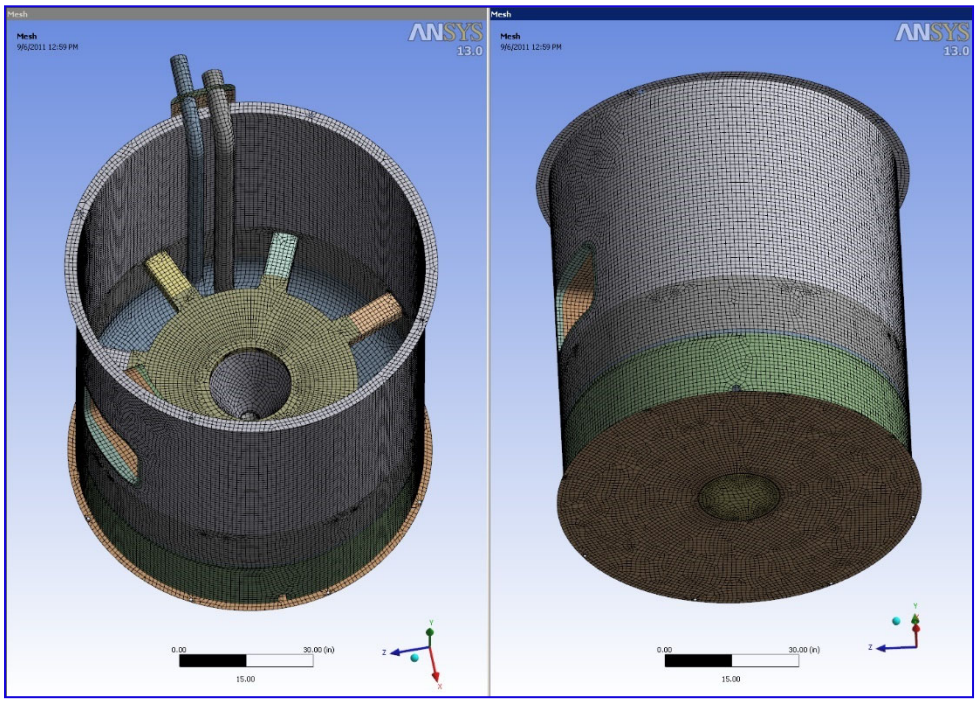

Figure III.6.1.6.2. Finite element model

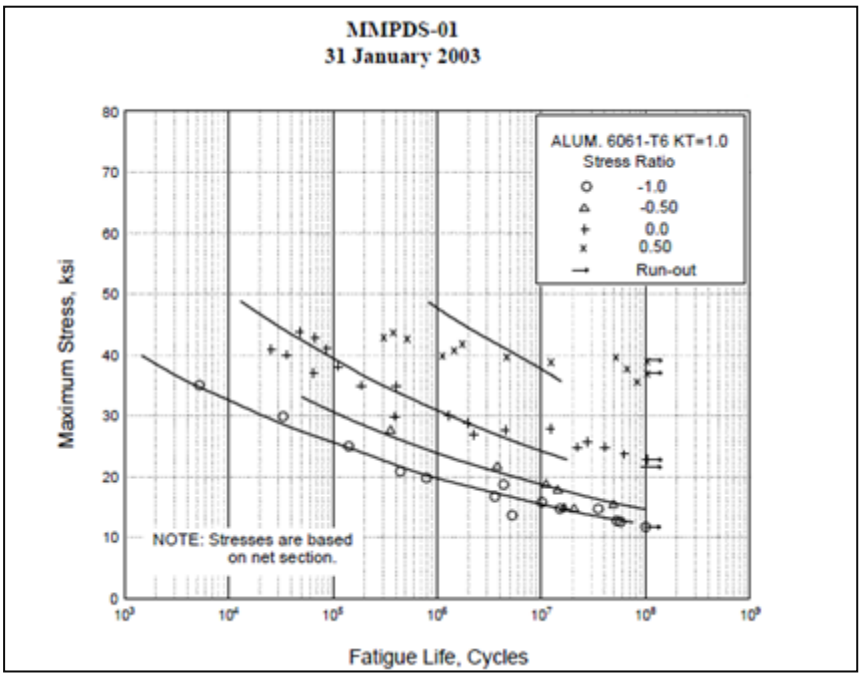

Figure III.6.1.7.1. Fatigue data for 6061-T6 from Ref. III.6.2

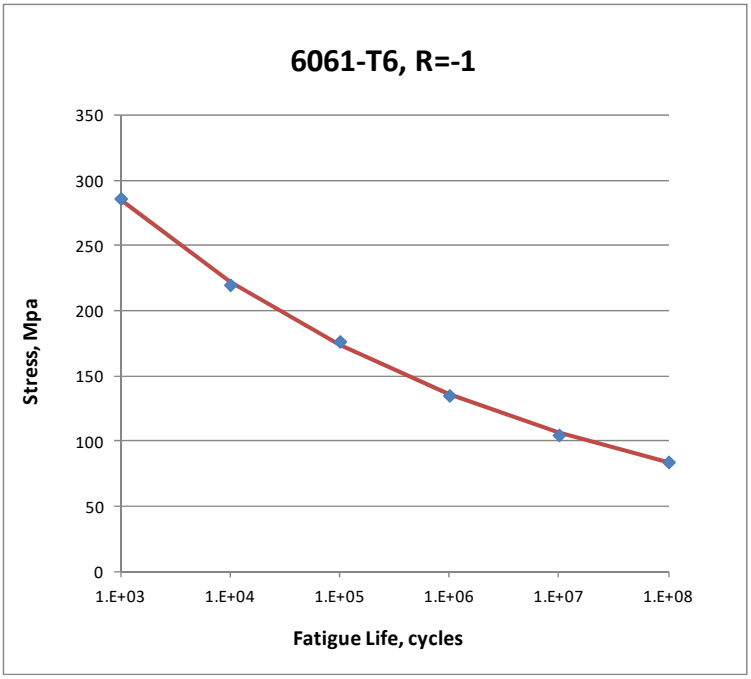

Figure III.6.1.7.2. S-N curve for 6061-T6

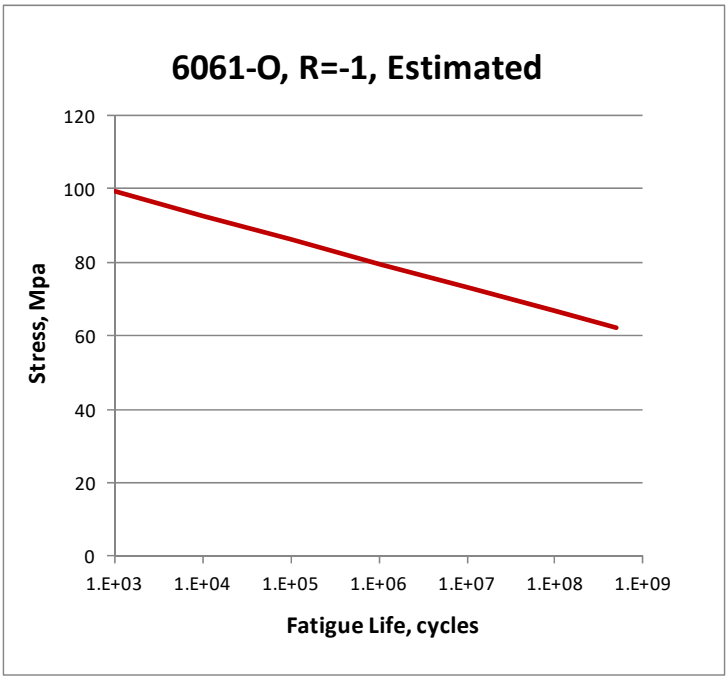

Figure III.6.1.7.3. S-N curve for 6061-O.

Table III.6.1.7.1. Material properties used for SAV-1

Property	Value	Source
Elastic Modulus (MPa)	71,000	Common value
Ultimate Tensile Strength (MPa)	216	Ref. III.6.2
Yield Strength (MPa)	118	Ref. III.6.2
Poisson's Ratio	0.33	Common value
Density (kg/m^3)	2,770	Common value

III.6.1.8 Loads and Boundary Conditions

The loads and boundary conditions used for the load cases 1 and 2 are shown in Fig. III.6.1.8.1. The tank is positioned by fixing the edges of the four mounting holes in the tank bottom, the current design uses eight mounting holes. The bottom of the tank is further fixed in the vertical direction (UY=0), which represents contact between the tank and its mounting slab. The estimated weight of the subcritical assembly of 11,074 N is distributed on the mounting plate. A hydrostatic pressure is used to account for the weight and the pressure of a full tank for the load case 2.

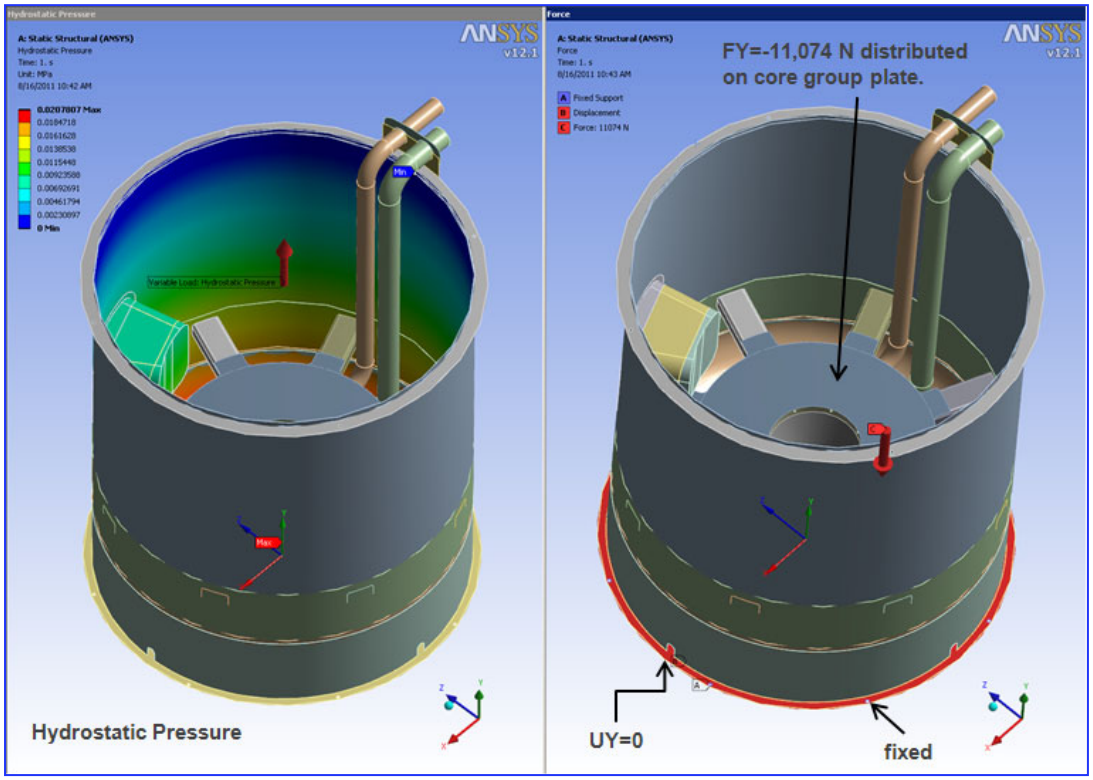

Figure III.6.1.8.1. Boundary conditions for the load Cases 1 and 2, static loading.

The load case 3 is the same as load case 2 with the addition of seismic loading. The seismic load specified for this evaluation was ax=az=0.1g, and ay=0.07g. To apply this, the following changes were made. First, a point mass was placed at the approximate center of the tank and assigned a mass value of 2460 kg, which is equal to the mass of the water when the tank is full. This point mass was tied to the inside surfaces of the tank. Next, the weight of the subcritical assembly was increased by 7% to 12,679 N, representing the vertical seismic acceleration component due to the subcritical assembly. Then, lateral loads equal to 10% of the subcritical assembly weight, or 554 N, were applied in both the X and Z directions to the subcritical assembly locating pin holes in the subcritical assembly plate, representing the lateral seismic acceleration component due to the subcritical assembly. Last, the seismic accelerations given above were applied to all bodies in the model. These loads are shown in Fig. III.6.1.8.2.

The loading for load case 4 is shown in Fig. III.6.1.8.3. The tank is positioned by fixing the X, Y and Z displacements at the inside diameter of the tank bottom. Loads are then applied at each of four lifting holes in the flange at the top edge of the tank. These loads are angled 30° from the vertical and intersect the tank centerline. They represent the reactions to four lifting cables. The vertical component of each load is 2303 N, 1/4 the total tank weight, and the horizontal component is 1330 N.

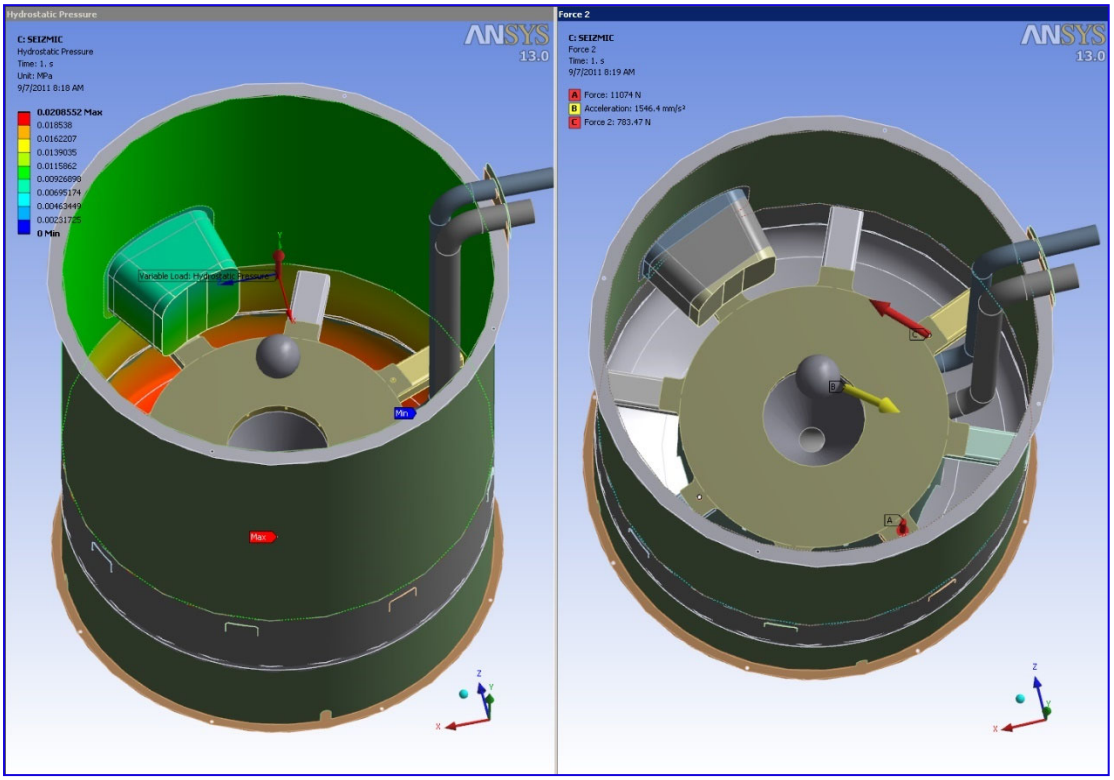

Figure III.6.1.8.2. Boundary conditions for load Case 3, seismic loading

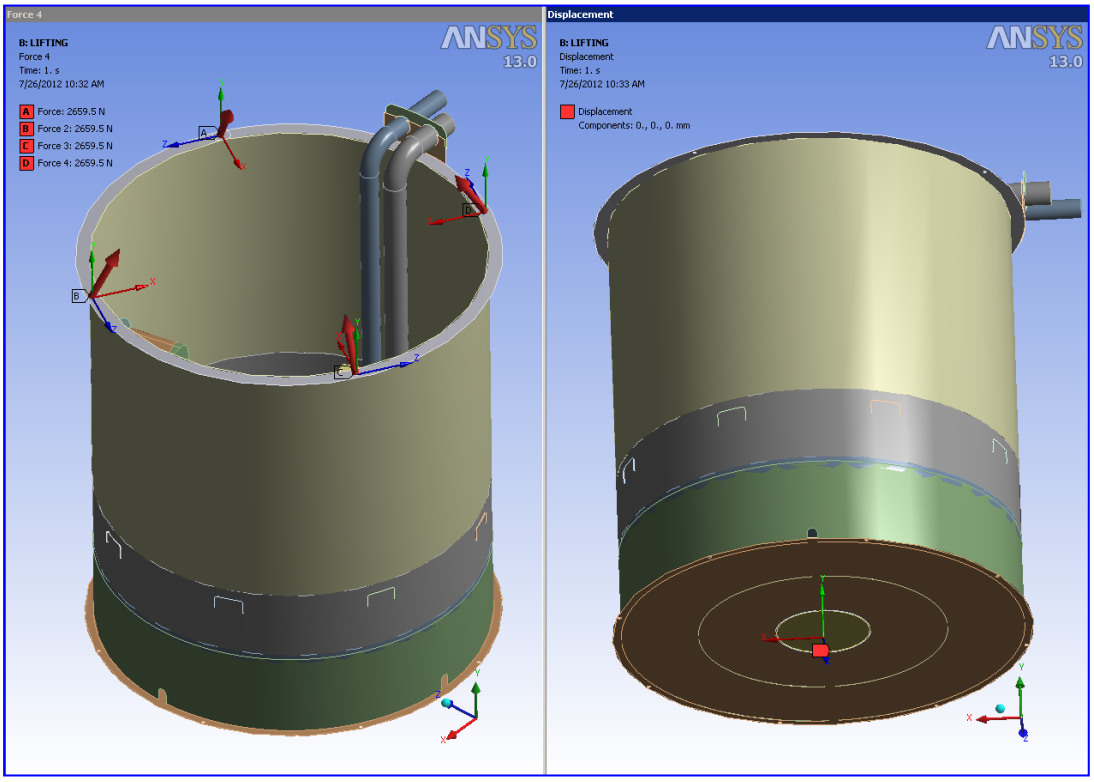

Figure III.6.1.8.3. Boundary conditions for load Case 4, lifting.

III.6.1.9 Results

III.6.1.9.1 Full Tank in Place, Static Loading

Load case 2 was used to evaluate a filled tank in place subject to static loading. Results for this evaluation are given in Figs. III.6.1.9.1.1 through III.6.1.9.1.9. Figures III.6.1.9.1.1 through III.6.1.9.1.4 show plots of equivalent, von Mises, stress at the surface of the shell elements. The maximum value is 10.24 MPa and it occurs at a small hole in the center support under the subcritical assembly plate. The safety factor with respect to the yield strength of 118 MPa is 11.52.

The tank is fabricated with full penetration butt welds and single-sided fillet welds, and these welds were evaluated per the ASME Boiler and the Pressure Vessel Code, BPVC Ref. III.6.6. Full penetration butt welds are evaluated by applying a suitable weld efficiency factor to the membrane stress at the weld. This weld efficiency factor varies from 1.00 for fully inspected double-sided butt welds to 0.60 for uninspected single-sided butt welds with no backing strip. Figures III.6.1.9.1.5 and III.6.1.9.1.6 show contour plots of equivalent shell membrane stress. The maximum value is 5.61 MPa and it occurs in a machined flange at the attachment of a fabricated pocket in the tank side. These stresses are very low. Taking the peak membrane stress of 5.61 MPa, the lowest weld efficiency of 0.6, and assuming the allowable stress to be 2/3 of the yield strength of 118 MPa, the minimum factor of safety is 8.41. This stress is not even at a weld, so it is reasonable to assume that the safety factor for all butt welds is above this value.

Selected fillet welds were evaluated by taking the peak equivalent membrane stress in the shell element at the weld, correcting it for the reduced area in the weld throat, applying the BPVC weld efficiency of 0.5, and comparing to the stress allowable. These welds are identified in Fig. III.6.1.9.1.7 and are summarized in Table III.6.1.9.1.1. All shell thicknesses are 10 mm, and all welds are assumed to be continuous single sided ¼” (6/35 mm) fillet welds. Again, the membrane stresses are very low, resulting in high safety factors.

Figures III.6.1.9.1.8 and III.6.1.9.1.9 show total and X-direction deflection plots. Deflection scale is 1X.

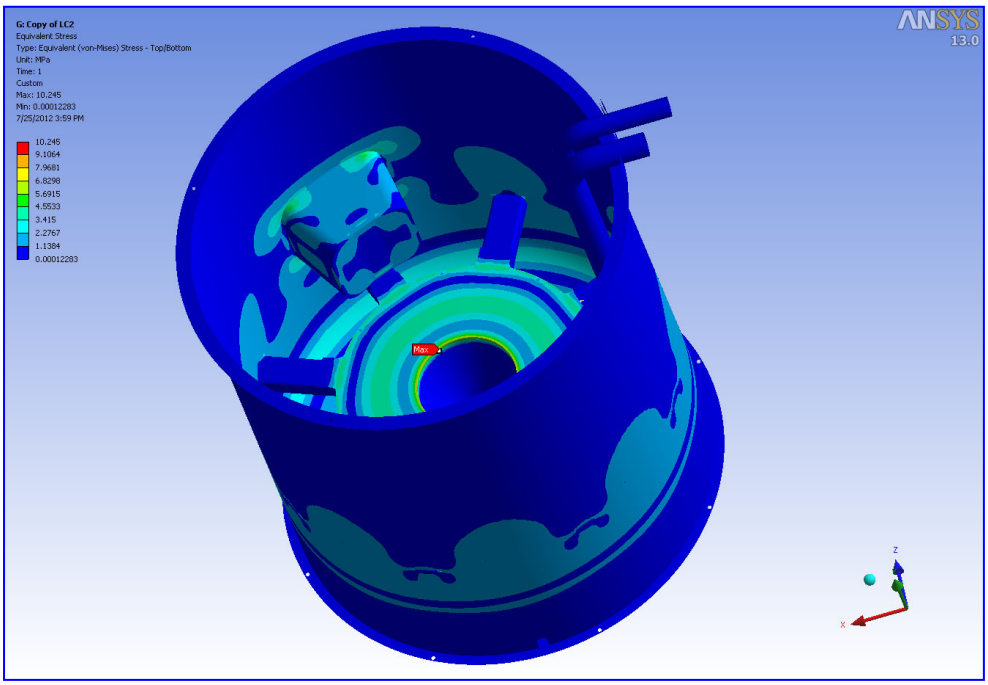

Figure III.6.1.9.1.1. Von Mises stress, full tank, static loading

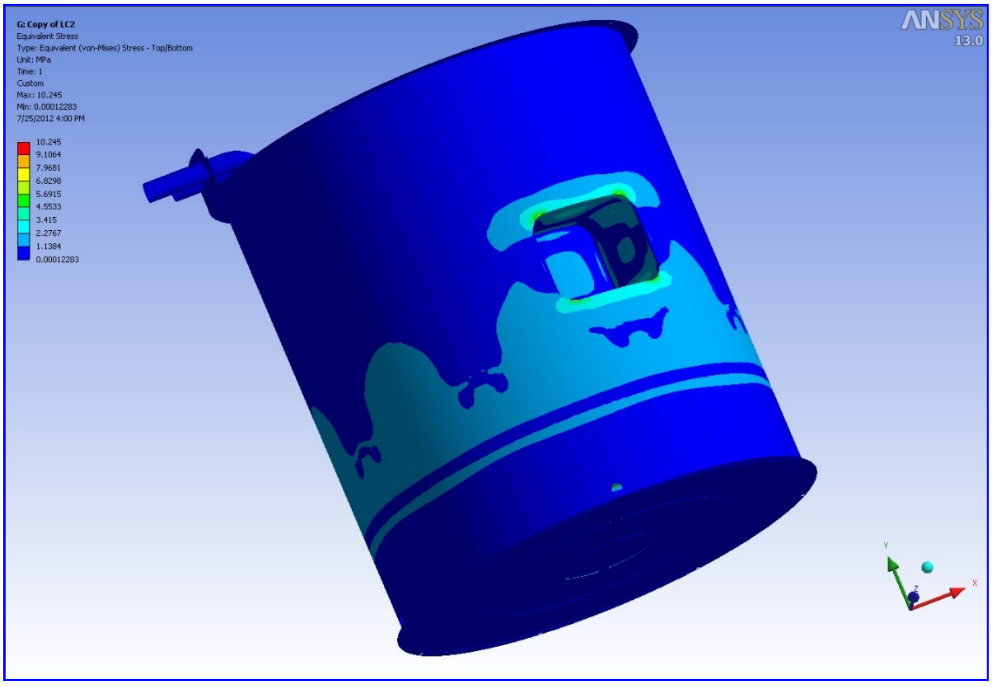

Figure III.6.1.9.1.2. Von Mises stress, full tank, static loading

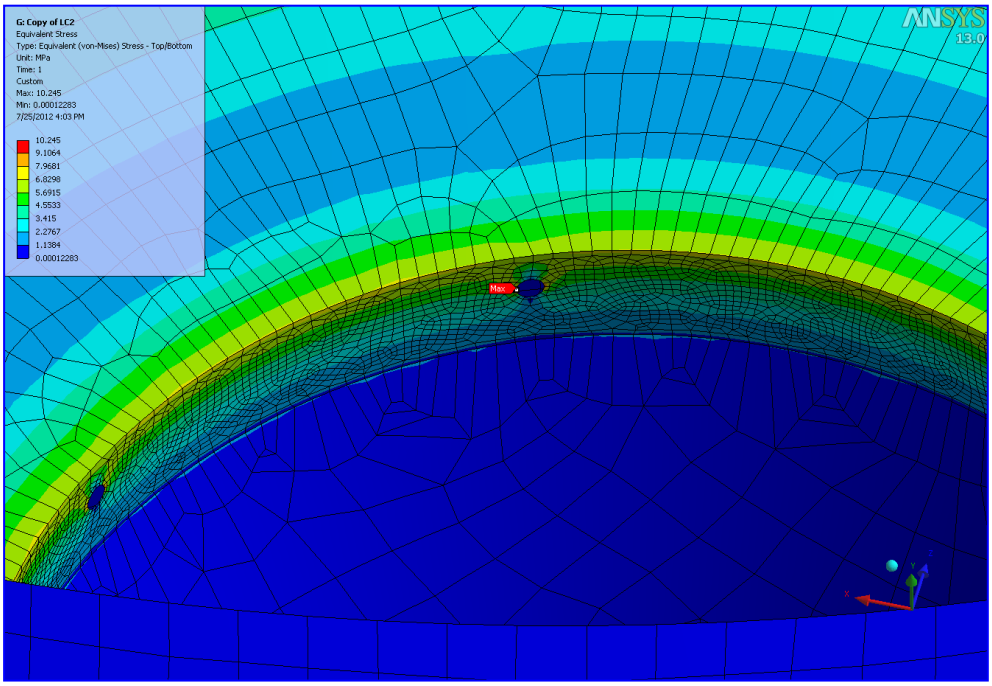

Figure III.6.1.9.1.3. Detail of maximum von Mises stress, full tank, static loading

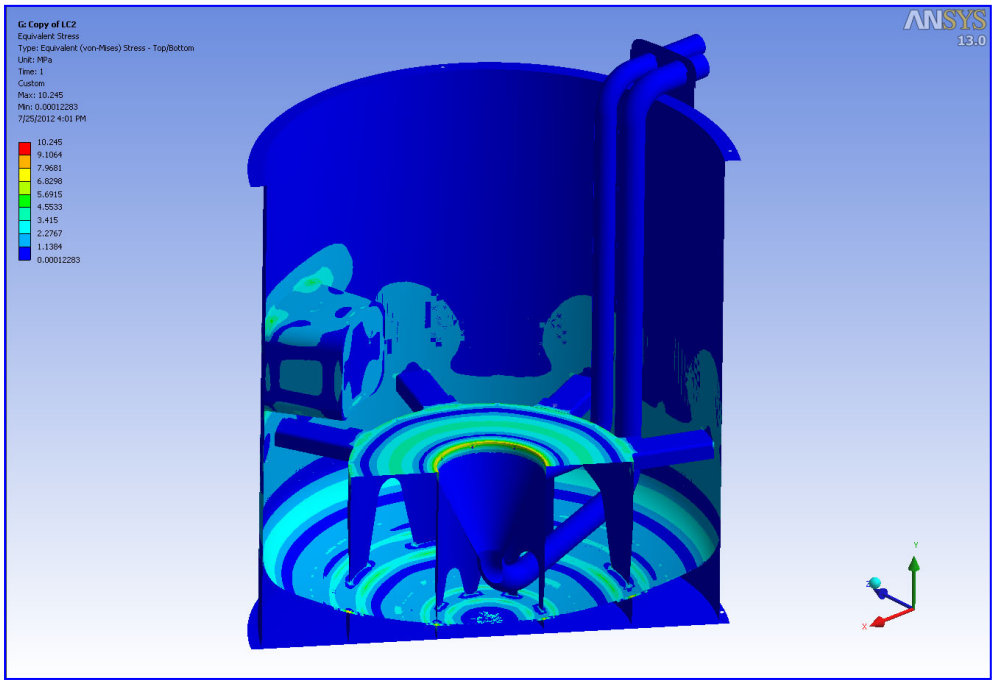

Figure III.6.1.9.1.4. Von Mises stress, full tank, static loading

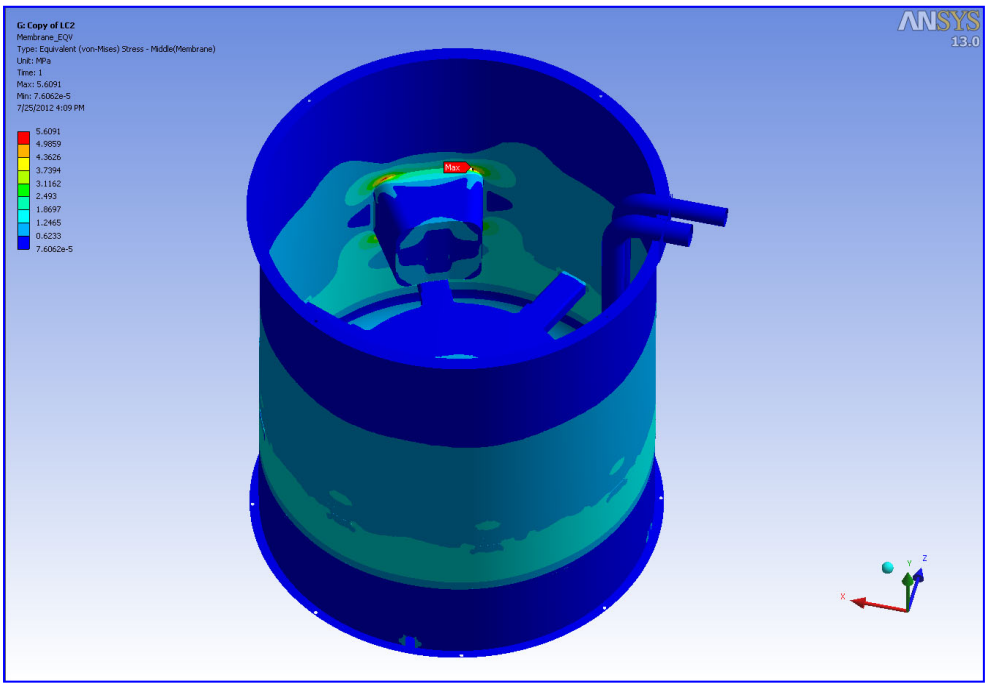

Figure III.6.1.9.1.5. Equivalent membrane stress, full tank, static loading

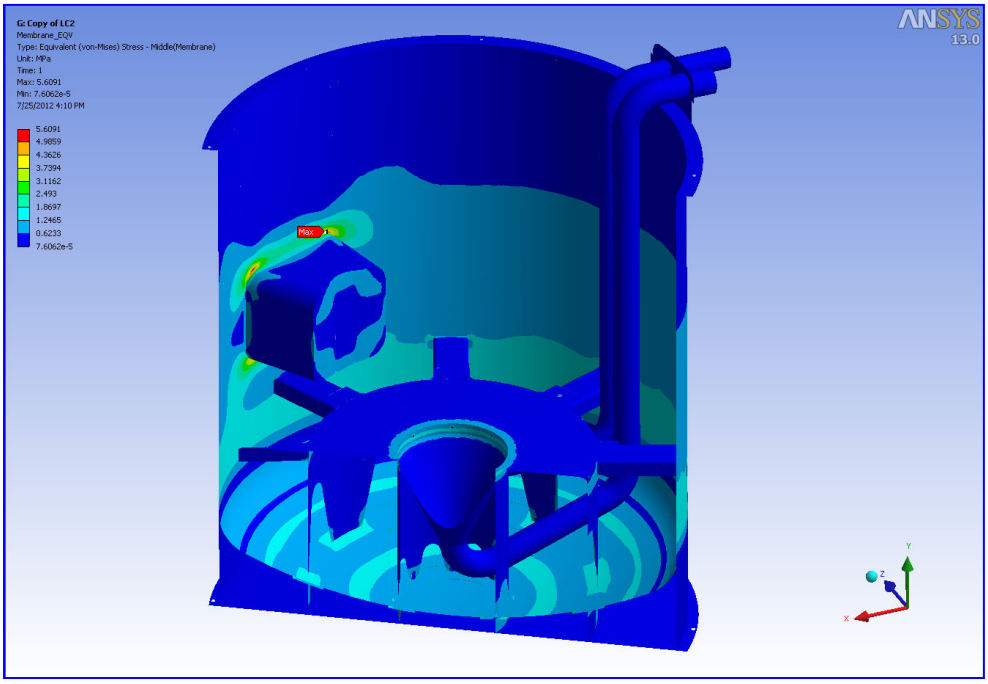

Figure III.6.1.9.1.6. Equivalent membrane stress, full tank, static loading.

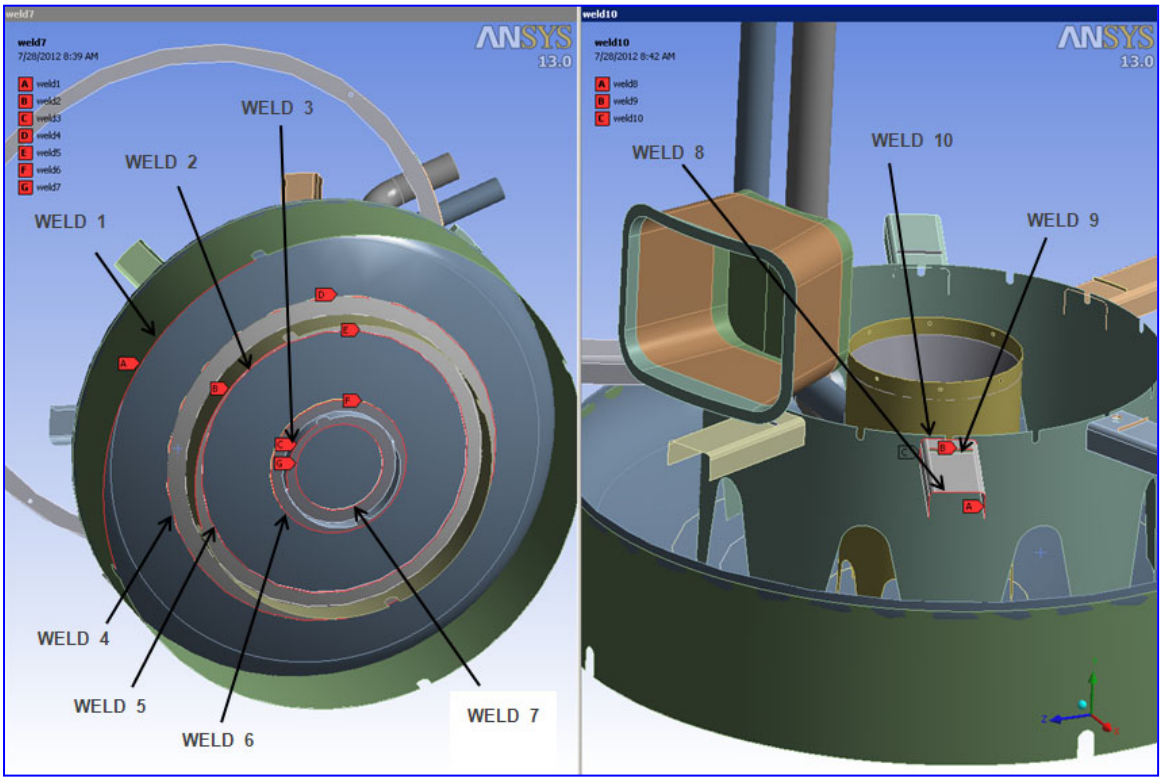

Figure III.6.1.9.1.7. Fillet welds

Table III.6.1.9.1.1 Summary of weld analysis, full tank, static loading

WELD	σ_{max} (MPa)	t (mm)	weld size (mm)	throat (mm)	S (MPa)	Weld Efficiency	FS
1	0.82	10	6.35	4.48945	79	0.5	21.63
2	1.236	10	6.35	4.48945	79	0.5	14.35
3	1.823	10	6.35	4.48945	79	0.5	9.73
4	1.36	10	6.35	4.48945	79	0.5	13.04
5	1.31	10	6.35	4.48945	79	0.5	13.54
6	1.45	10	6.35	4.48945	79	0.5	12.23
7	1.13	10	6.35	4.48945	79	0.5	15.69
8	1.738	10	6.35	4.48945	79	0.5	10.20
9	0.46	10	6.35	4.48945	79	0.5	38.55
10	2.372	10	6.35	4.48945	79	0.5	7.48

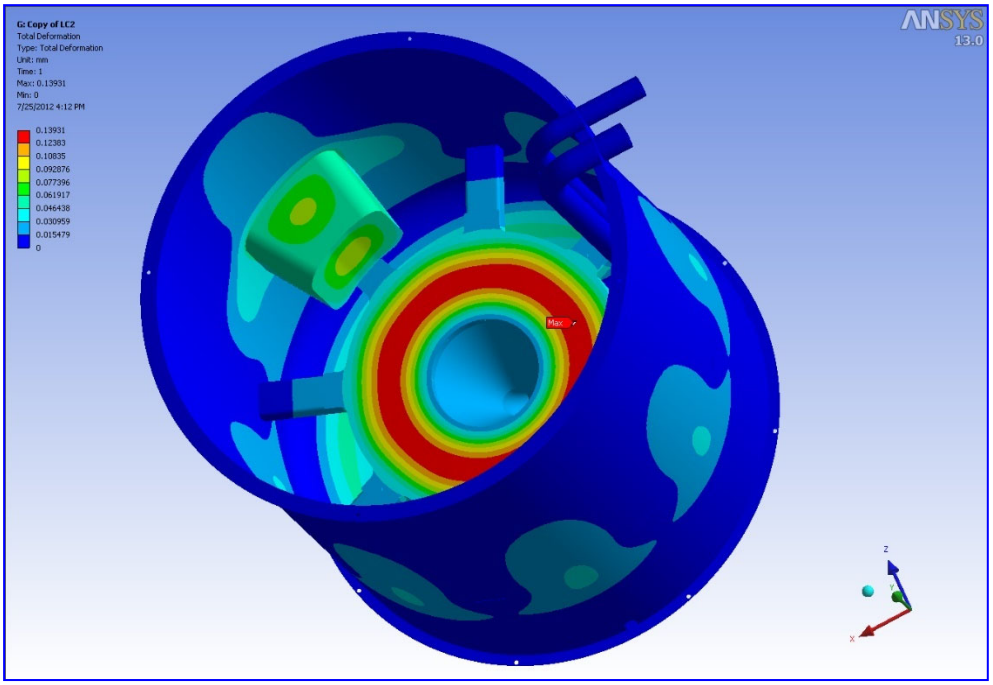

Figure III.6.1.9.1.8. Summed deformation

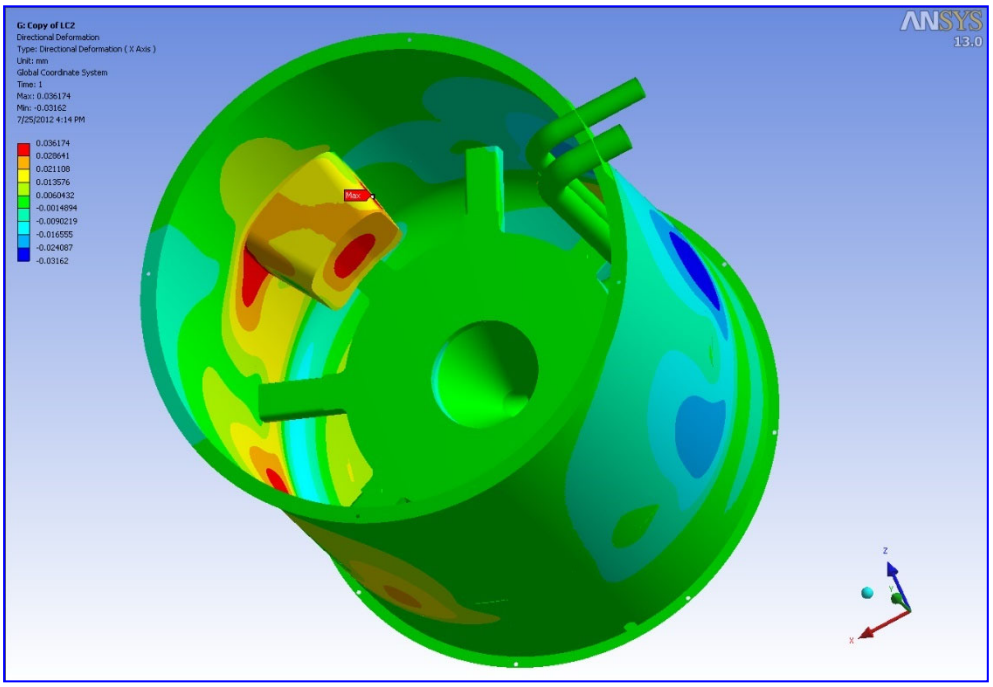

Figure III.6.1.9.1.9. X-direction deformation

III.6.1.9.2 Full Tank in Place, Seismic Loading

Load case 3 was used to evaluate the filled tank in place subject to seismic loading. Results for this evaluation are given in Figs. III.6.1.9.2.1 through III.6.1.9.2.7.

The additional seismic load is a small increase over the static load, so stresses increase only slightly. The maximum value is 11.93 MPa and it occurs at a fillet weld in a doubler, Fig. III.6.1.9.2.1. Fillet welds are evaluated separately, and this stress can be ignored for now. Figures III.6.1.9.2.2 through III.6.1.9.2.5 show von Mises stresses with the fillet welds suppressed. The highest stress is now 11.82 MPa and is again located at a small hole in the center support under the subcritical assembly plate. The factor of safety with respect to yield is 9.98.

Figures III.6.1.9.2.6 and III.6.1.9.2.7 show equivalent shell membrane stress, with a maximum value of 6.15 MPa. As before, full penetration butt welds are evaluated by combining the maximum membrane stress, the minimum weld efficiency, and the weld allowable to get a minimum factor of safety of 7.67. Again, the membrane stress at all butt welds is below the maximum value, resulting in higher safety factors in the butt welds. The fillet welds evaluated in Part A were reevaluated for seismic loading, and these results are shown in Table III.6.1.9.2.1.

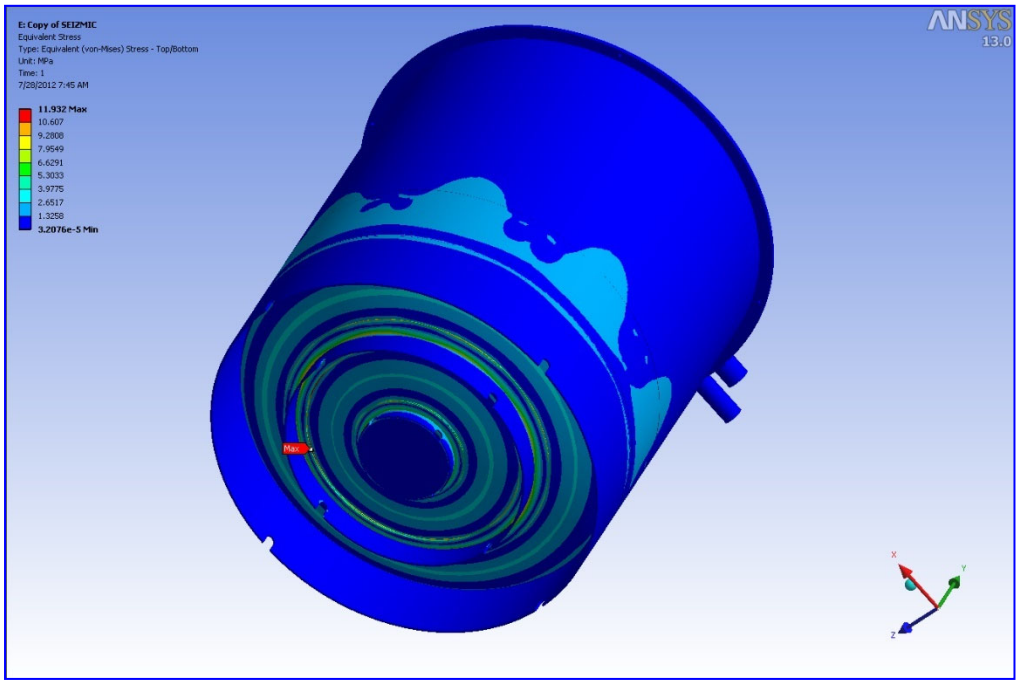

Figure III.6.1.9.2.1. Von Mises stress, full tank, seismic loading

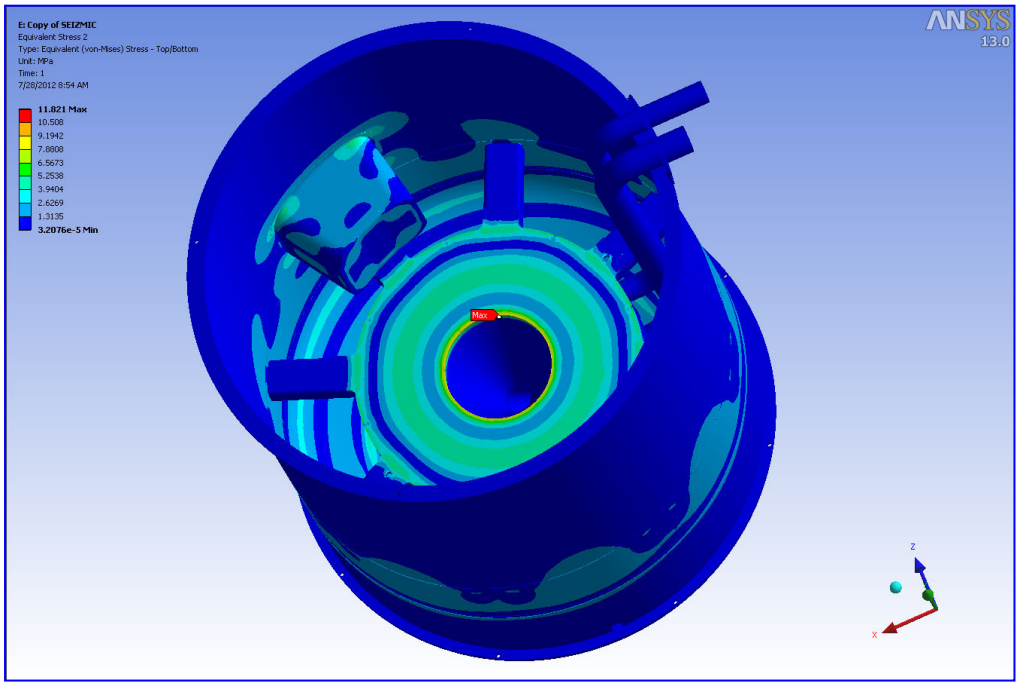

Figure III.6.1.9.2.2. Von Mises stress, full tank, seismic loading

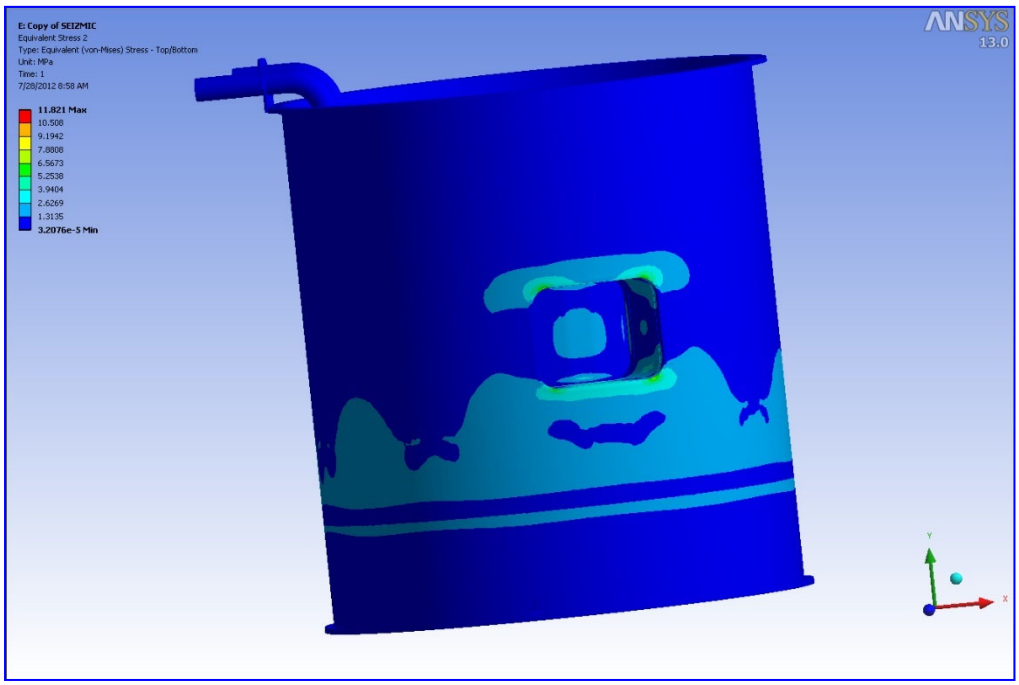

Figure III.6.1.9.2.3. Von Mises stress, full tank, seismic loading

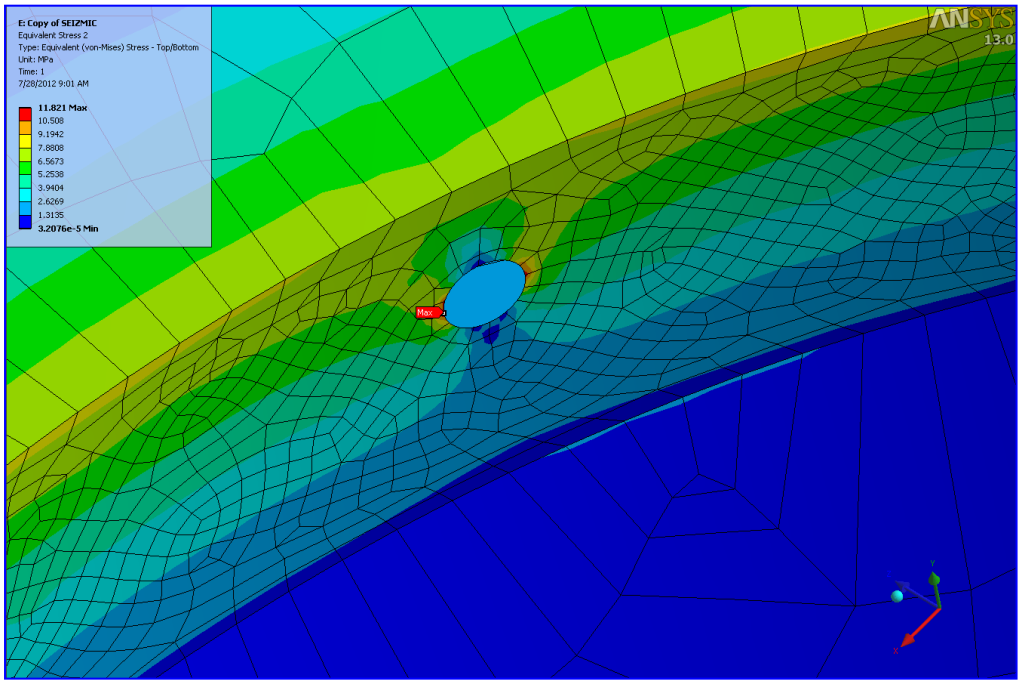

Figure III.6.1.9.2.4. Detail of maximum von Mises stress, full tank, seismic loading

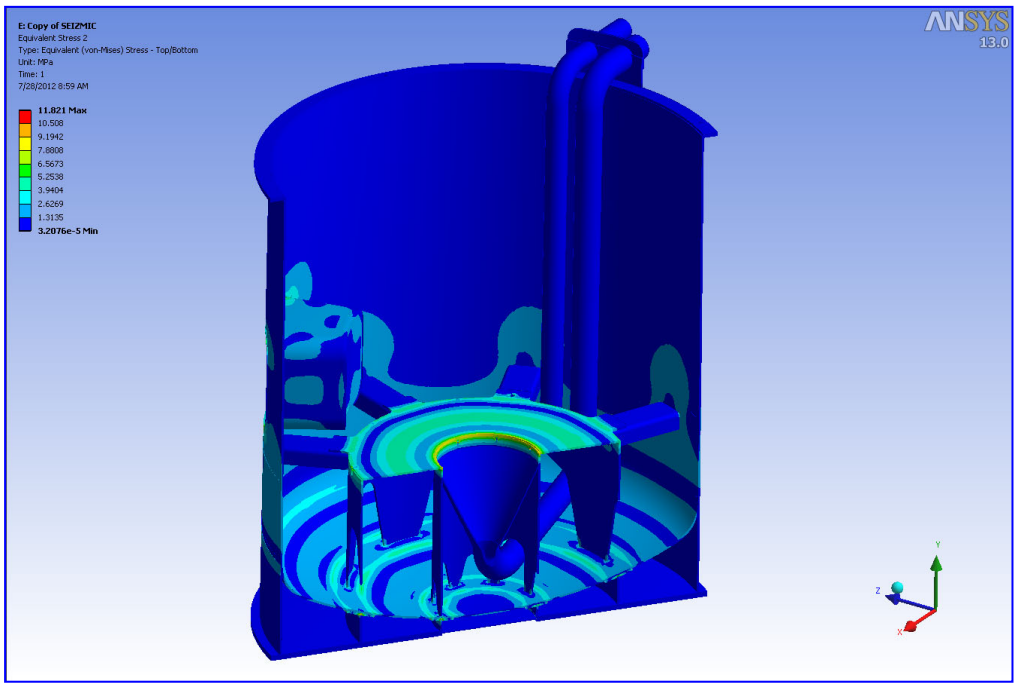

Figure III.6.1.9.2.5. Von Mises stress, full tank, seismic loading

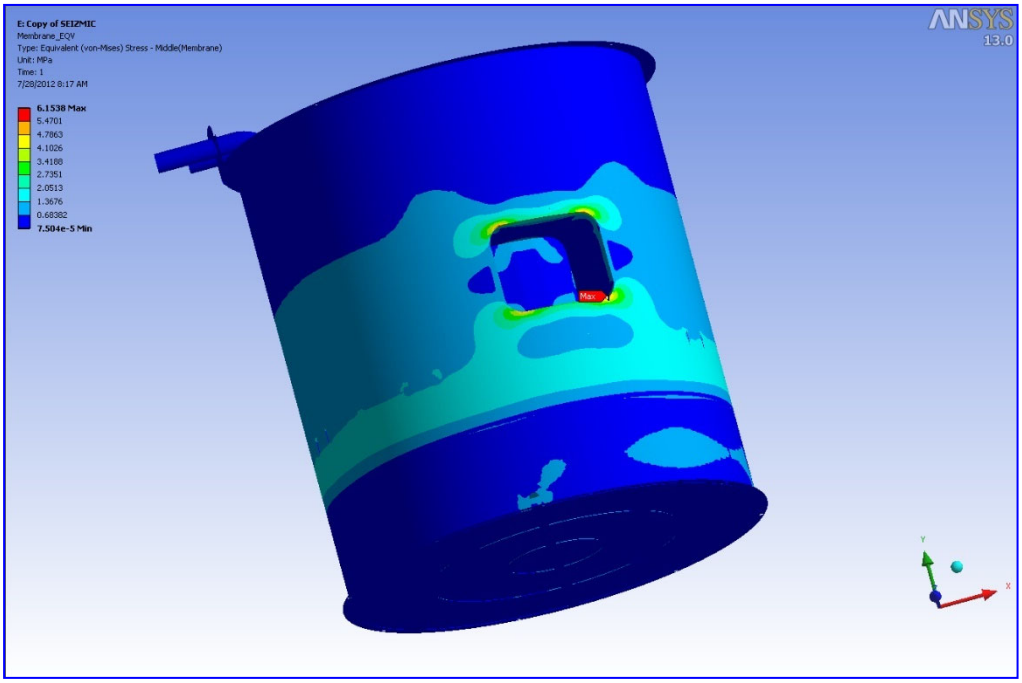

Figure III.6.1.9.2.6. Equivalent membrane stress, full tank, seismic loading

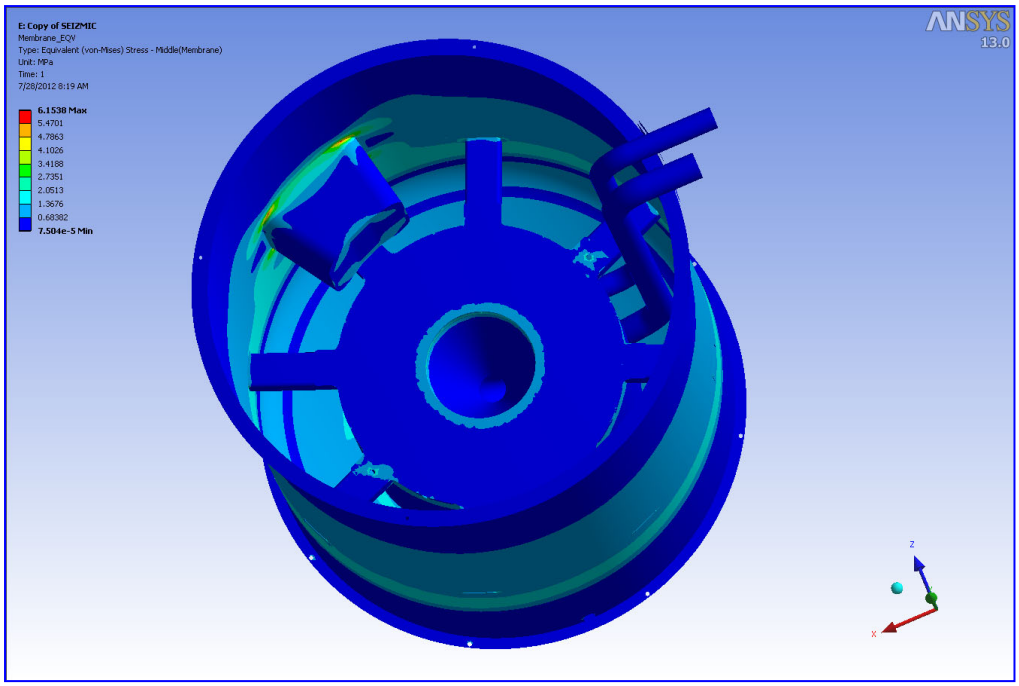

Figure III.6.1.9.2.7. Equivalent membrane stress, full tank, seismic loading

Table III.6.1.9.2.1. Summary of weld analysis, full tank, seismic loading

WELD	σ_{max} (MPa)	t (mm)	weld size (mm)	throat (mm)	S (MPa)	Weld Efficiency	FS
1	1.32	10	6.35	4.48945	79	0.5	13.43
2	1.71	10	6.35	4.48945	79	0.5	10.37
3	2.32	10	6.35	4.48945	79	0.5	7.64
4	1.49	10	6.35	4.48945	79	0.5	11.90
5	1.45	10	6.35	4.48945	79	0.5	12.23
6	1.62	10	6.35	4.48945	79	0.5	10.95
7	1.32	10	6.35	4.48945	79	0.5	13.43
8	1.9	10	6.35	4.48945	79	0.5	9.33
9	0.99	10	6.35	4.48945	79	0.5	17.91
10	3.14	10	6.35	4.48945	79	0.5	5.65

III.6.1.9.3 Empty Tank Lifting, Static Loading

Load case 4 was used to evaluate an empty tank as it is lifted during assembly. The tank is empty, with no water or subcritical assembly present. Plots of von Mises stress are shown in Figs. III.6.1.9.3.1 through III.6.1.9.3.3. The maximum stress is 32.06 MPa, and it is located at one of the lifting holes. Assuming a 118 MPa yield strength, the factor of safety is 3.68. This stress is likely higher than would be seen in practice. The force is applied at the inside edge of the hole, which produces something of a singularity. Also, the hole itself is a stress concentrator. In real practice, there would be an eyebolt, washers, etc., that would tend to locally stiffen the flange and distribute the load. Reference III.6.5 predicts a stress concentration factor of about 2.40, which would result in a real stress away from the hole of only 14 MPa. Compare this to the probed value of 17 MPa at the edge of the flange. This method of analysis was used to provide an upper limit on the stress during lifting, regardless of the exact configuration of the lifting tackle.

Stress levels at all four lifting holes are similar, with small variations due to the slightly non-symmetric configuration of the tank. Stress levels elsewhere in the tank are very low, typically under 3.5 MPa.

Figure III.6.1.9.3.4 shows total deflection plots for deflection scales of 1X and 430X.

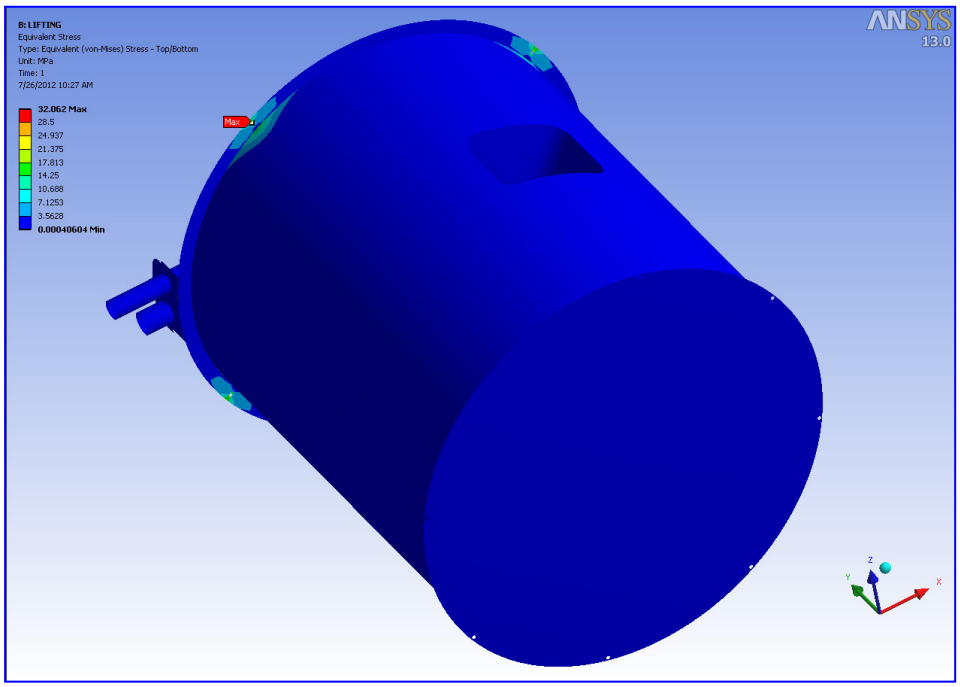

Figure III.6.1.9.3.1. Von Mises stress, empty tank, lifting loads

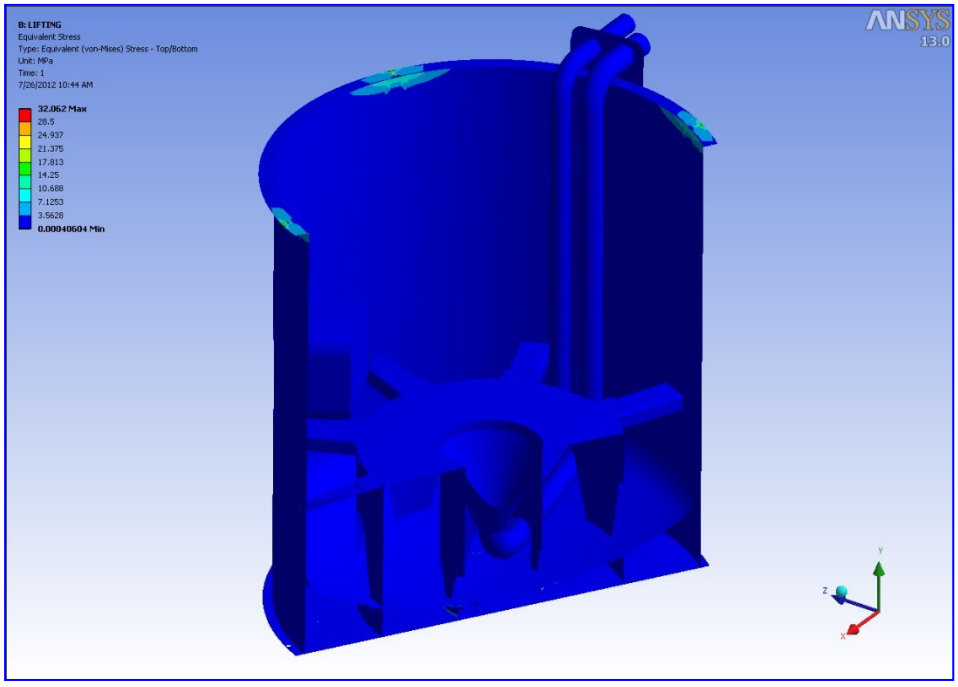

Figure III.6.1.9.3.2. Von Mises stress, empty tank, lifting loads

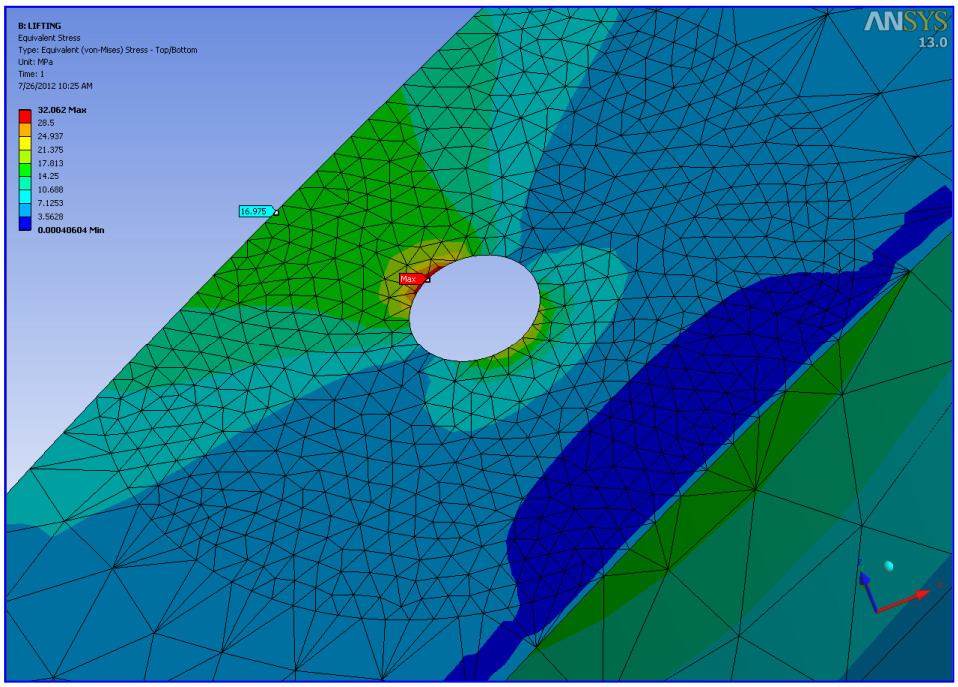

Figure III.6.1.9.3.3. Maximum von Mises stress at lifting hole

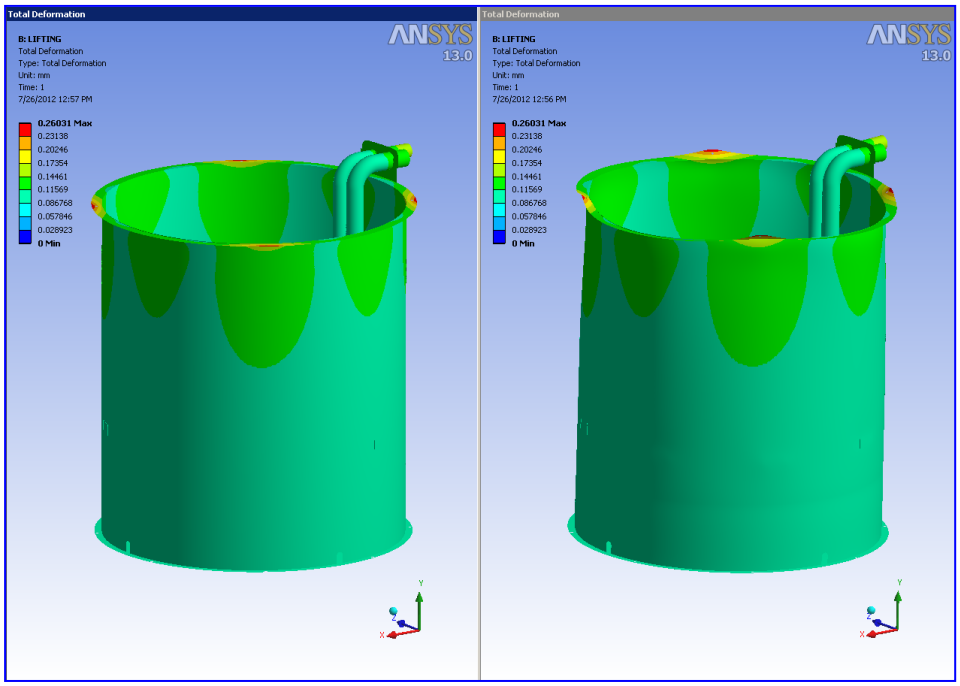

Figure III.6.1.9.3.4. Total deformation, 1X left, 430X right, empty tank, lifting loads.

III.6.1.9.4 Fatigue Loading

Fatigue evaluation was performed using the method found in the BPVC Section VIII, Division 2, Part 5, paragraph 5.5.3, Fatigue Assessment-Elastic Stress Analysis and Equivalent Stresses. It is based on computing an alternating effective stress from the nodal principal stresses. This alternating stress is then used to compute component life from an S-N curve. Principal stresses are read at the surface for each node, and used to calculate the effective alternating equivalent stress $DS_{P,k}$. This value is then modified with the appropriate prescribed penalty factors to get the effective alternating equivalent stress amplitude $S_{alt,k}$, and this value is taken to the S-N curve to get the fatigue life. A macro was written that reads the principal stresses, calculates the life at every location and creates a contour plot. These plots are shown in Figs. III.6.1.9.4.1 and III.6.1.9.4.2. This process was performed for both the bulk material and the heat affected zone (HAZ). The bulk material plot is based on the AL 6061-T6 S-N curve of Fig. III.6.1.7.2 and a fatigue strength reduction factor 1, which represents tempered material and no discontinuities. The plot for the HAZ was based on the AL 6061-O S-N curve of Fig. III.6.1.7.3 and a fatigue strength reduction factor of 4, which represents annealed material and an uninspected weld.

Small stresses result in very long-life predictions, which can distort the contour plots, so any calculated life greater than 1.0 x 10^7 cycles is reset to 1.0 x 10^7. As can be seen, both plots show a single contour value of 1.0 x 10^7, indicating that the calculated life is greater than 10 million cycles everywhere in the tank. Examination of the von Mises stress plots for load case 1 and load case 2, Figs. III.6.1.9.4.3 and III.6.1.9.4.4, show low stress levels and a small change between the two load cases. This suggests low mean and alternating stress values and high resistance to fatigue.

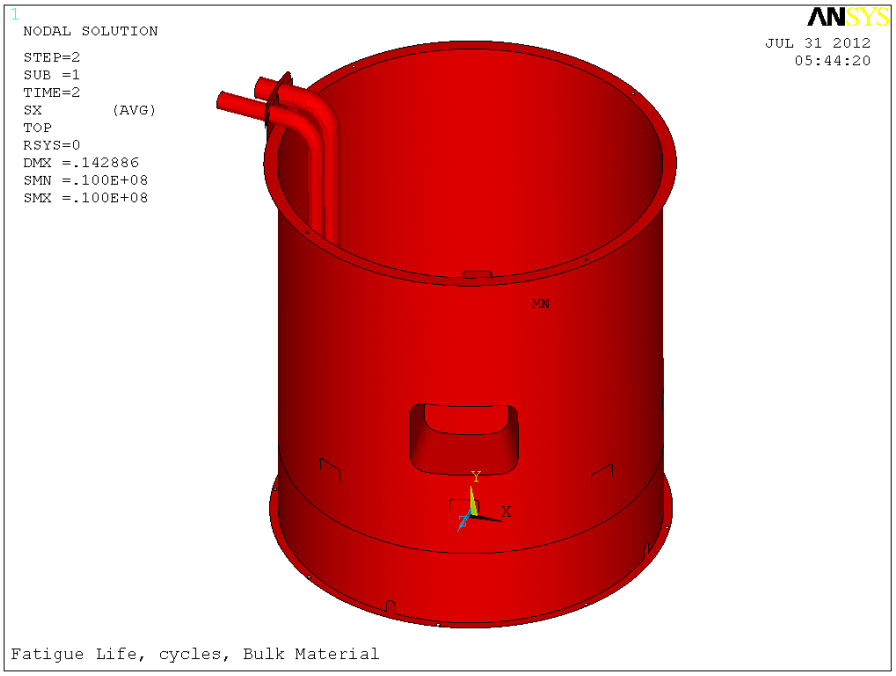

Figure III.6.1.9.4.1. Fatigue life, bulk material, full tank, static load

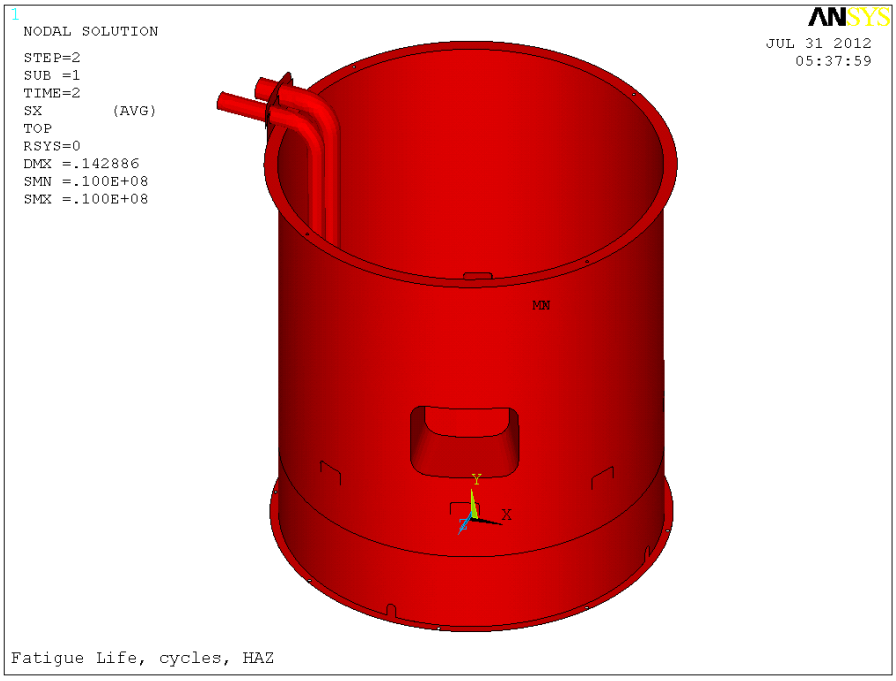

Figure III.6.1.9.4.2. Fatigue life, heat affected zone (HAZ), full tank, static load

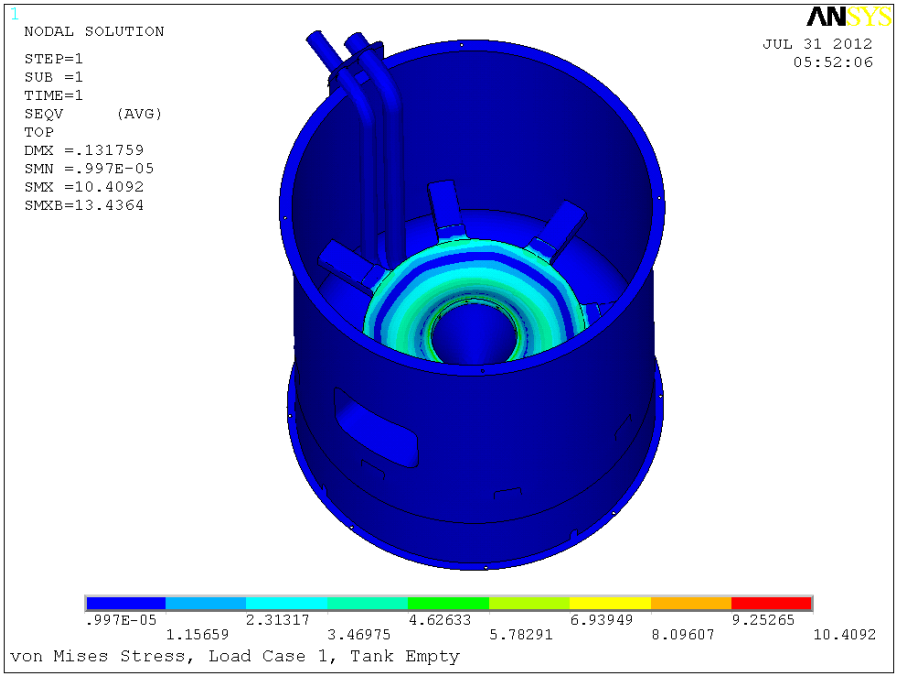

Figure III.6.1.9.4.3. Von Mises Stress, empty tank, static load

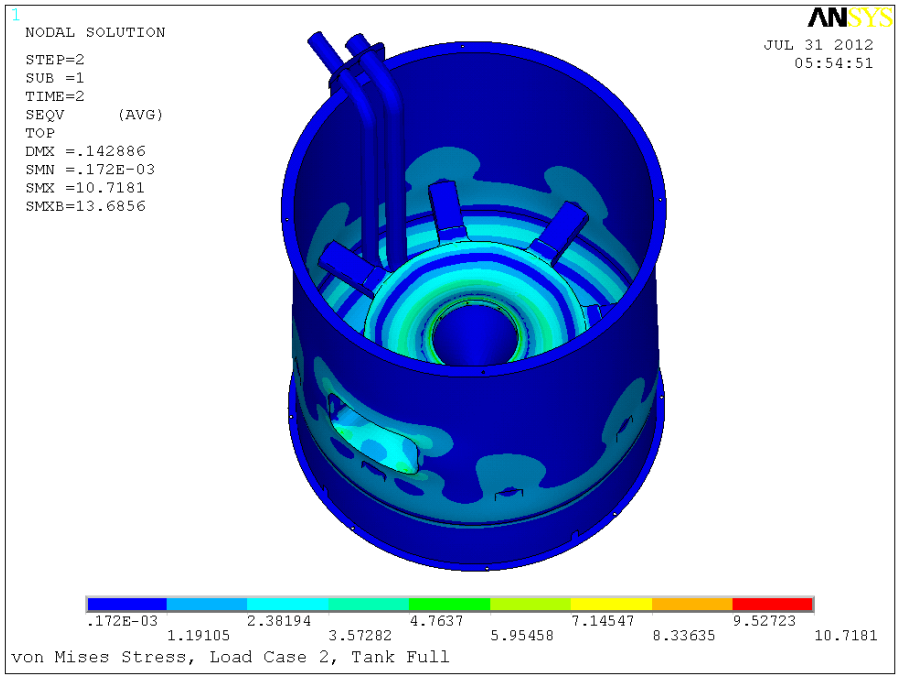

Figure III.6.1.9.4.4. Von Mises Stress, full tank, static load

III.6.1.10 Discussion

This analysis was carried out using the design concept and the discussed load cases. Piping stresses, fluid swirling, and thermal stress are not included in the analyzed load cases. However, the design concept has room temperature water coolant and low water coolant velocity in the tank, which do not result in a significant stress to the tank. The main coolant piping is included in the model.

Generally accepted engineering principles and the procedures contained in the BPVC were used. Yielding was evaluated by comparing the von Mises stress as defined by the maximum distortion energy failure theory directly to the yield strength of the material. No knockdown factors for boundary condition uncertainty, material variability, surface finish, construction variations, etc. were applied.

The BPVC was used for static weld analysis. It is based on the use of average membrane stress at a weld. In this analysis, the peak stress was used because it was provided directly with a path operation, and this result in conservative values. The BPVC was also used for the fatigue analysis. This was based on approximate stress allowables and fatigue data for a material not covered by the BPVC.

The assumptions listed above are reasonable and prudent for the design. Von Mises stresses are low, so the use of a linear elastic isotropic homogeneous material model is justified. Deflections are small, so small deflection theory is appropriate. It was assumed that continuous butt welds would be used on a liquid-tight vessel. The use of continuous fillet welds in non-sealing locations represents an upper bound that can be used as a basis

for developing detailed weld schedules. The other assumptions generally fit within the context of the analysis. Within the limits of these assumptions, it is believed that this analysis accurately represents the performance of this design for the intended use.

In general, stresses are very low, generally less than 10% of the yield strength. These stress levels result in high safety factors, indicating that this design will perform properly in its intended use. The exception is the lifting evaluation, where the safety factor at the lifting hole is only 3.68. A doubler could be added here if a higher safety factor is desired.

III.6.1.11 Conclusions

Based on the results of this analysis, and subject to the listed assumptions, it is concluded that the subcritical assembly tank is a structurally feasible design.

III.6.2 Subcritical Assembly Grid Plate

III.6.2.1 Objective

The objective of this analysis was to perform a structural feasibility study on the design concept of the subcritical assembly grid plate for the KIPT ADS experimental neutron source facility.

III.6.2.2 Scope

This analysis simulates the static loading on the subcritical assembly grid plate.

III.6.2.3 Methodology

This analysis was carried out with the finite element method, using the ANSYS R13.0 finite element program (Ref. III.6.1). A finite element model was constructed and subjected to the estimated loads developed during the design phase. The results were compared to basic material properties and commonly accepted engineering principles were applied to determine a safety factor.

III.6.2.4 Overview of Analysis

The analysis was carried out by applying the weight of the target, the fuel assembly, and the reflectors to the grid plate. A pressure loading, representing the pressure drop of cooling water that flows through the grid plate, was also applied.

III.6.2.5 Assumptions

This analysis is based on the following assumptions:

1. The material response is linear elastic.
2. The material response is constant with time (no effects of aging, creep, etc.).
3. The materials are isotropic and homogeneous.
4. The material response is consistent with small strain and small displacement.

5. The effects of neutron flux on material properties are not included.
6. The residual stresses are not included.
7. The grid plate operates at room temperature.

III.6.2.6 Geometry

The finite element model was based on solid modeling geometry imported into ANSYS Design Modeler, where a 1/6 symmetric solid model of the grid plate was created as shown in Fig. III.6.2.6.1. This solid model was then taken into the Workbench module and meshed with 1,293,966 10-node tetrahedral elements. The finite element model is shown in Fig. III.6.2.6.2.

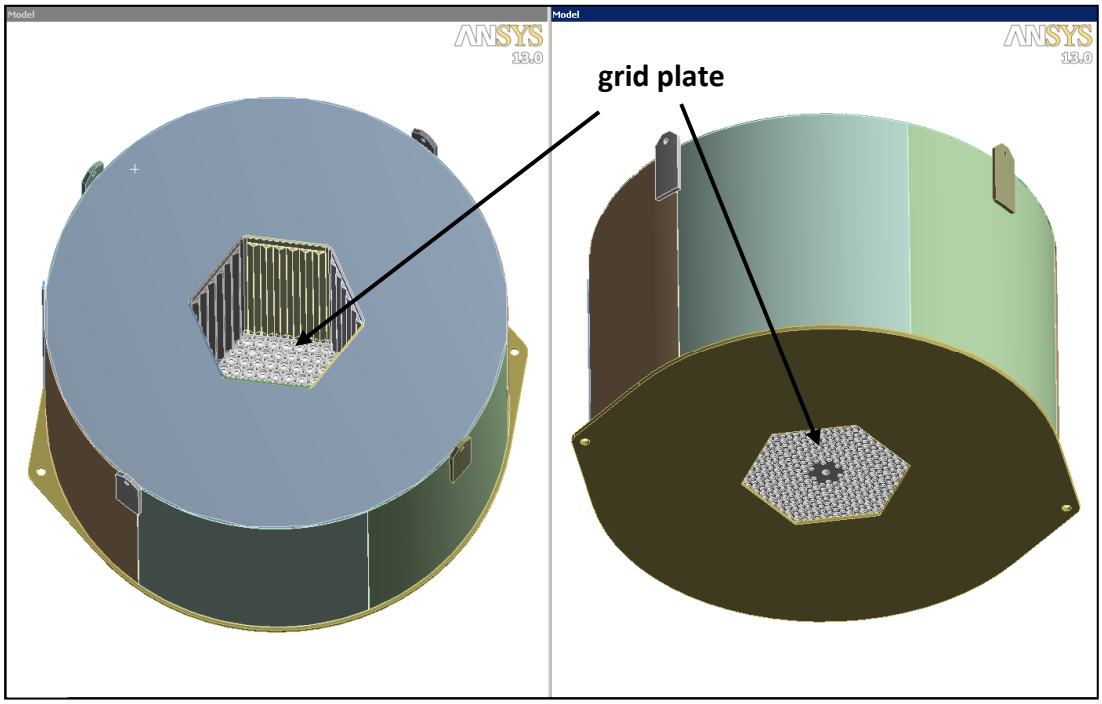

Figure III.6.2.6.1. Solid model of subcritical assembly

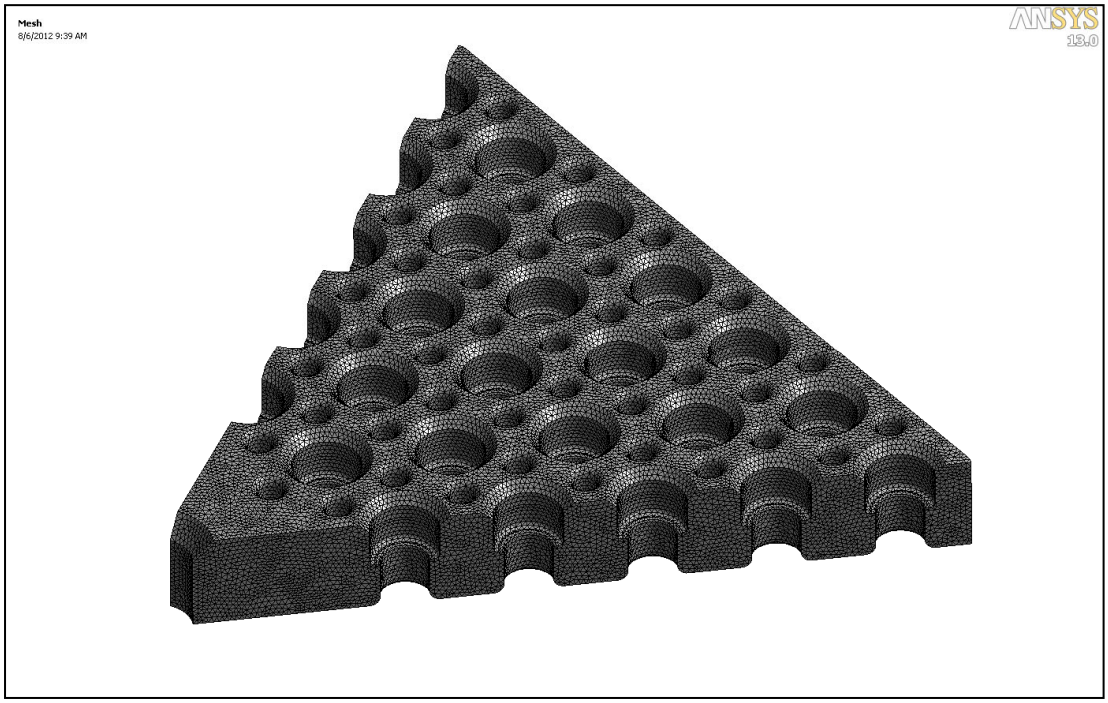

Figure III.6.2.6.2. Finite element model

III.6.2.7 Materials

Mechanical properties for AL 6061-T6 as used for this analysis are shown in Table III.6.2.7.1. Strength values are from Ref. III.6.2.

Table III.6.2.7.1 Material Properties for 6061-T6

Property	Value	Source
Elastic Modulus (MPa)	71,000	Common value
Ultimate Tensile Strength (MPa)	290	Ref. III.6.2
Yield Strength (MPa)	241	Ref. III.6.2
Poisson's Ratio	0.33	Common value
Density (kg/m^3)	2,770	Common value

III.6.2.8 Loads and Boundary Conditions

The boundary conditions used for Load Cases 1 and 2 are shown in Fig. III.6.2.8.1. The tank is positioned by placing symmetric boundary conditions on the symmetry planes and fixing the outer bottom edge in the Y direction.

Grid plate loads are shown in Fig. III.6.2.8.2. The loads shown for the total component, and actual loads applied to the model were reduced at the symmetry planes. The weights of the fuel rod and the graphite reflector assemblies were determined using the appropriate densities and summing component weights. The weight of the target came from the tungsten target using the appropriate densities and summing the component weights.

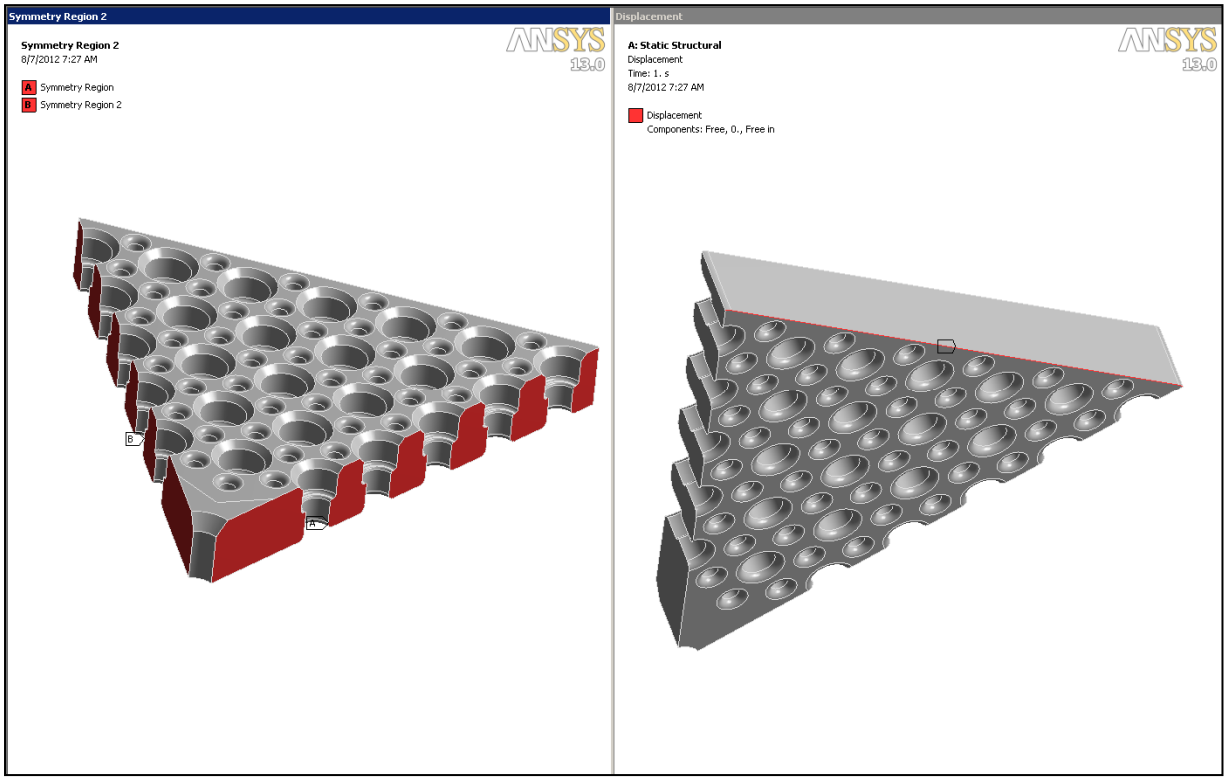

Figure III.6.2.8.1 Boundary conditions.

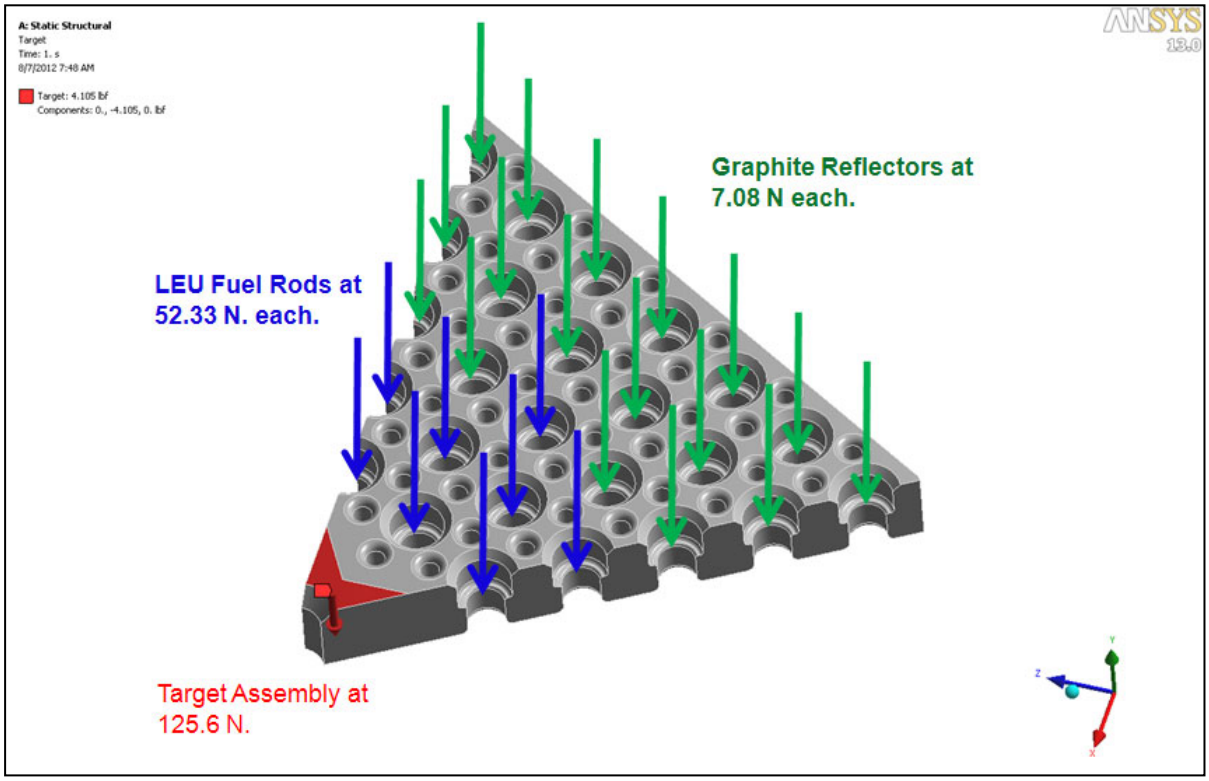

Figure III.6.2.8.2. Grid plate loads

III.6.2.9 Results

Plots of von Mises stress are shown in Figs. III.6.2.9.1 and III.6.2.9.2. The stresses are very low. The maximum stress in the grid plate is 18.03 MPa and occurs at the outer bottom edge. The factor of safety with respect to yield is 13.4. This stress occurs at a boundary condition applied at a corner and it is higher than what would be expected in practice. A more exact model would likely result in a lower stress. The highest stress away from this corner is 4.09 MPa and is located at a coolant hole near the center of the grid plate. The factor of safety with respect to yield is 58.9.

A plot of vertical deflection is shown in Fig. III.6.2.9.3. The maximum deflection is 0.023 mm downwards.

No knockdown factors for boundary condition uncertainty, material variability, surface finish, construction variations, etc. were applied.

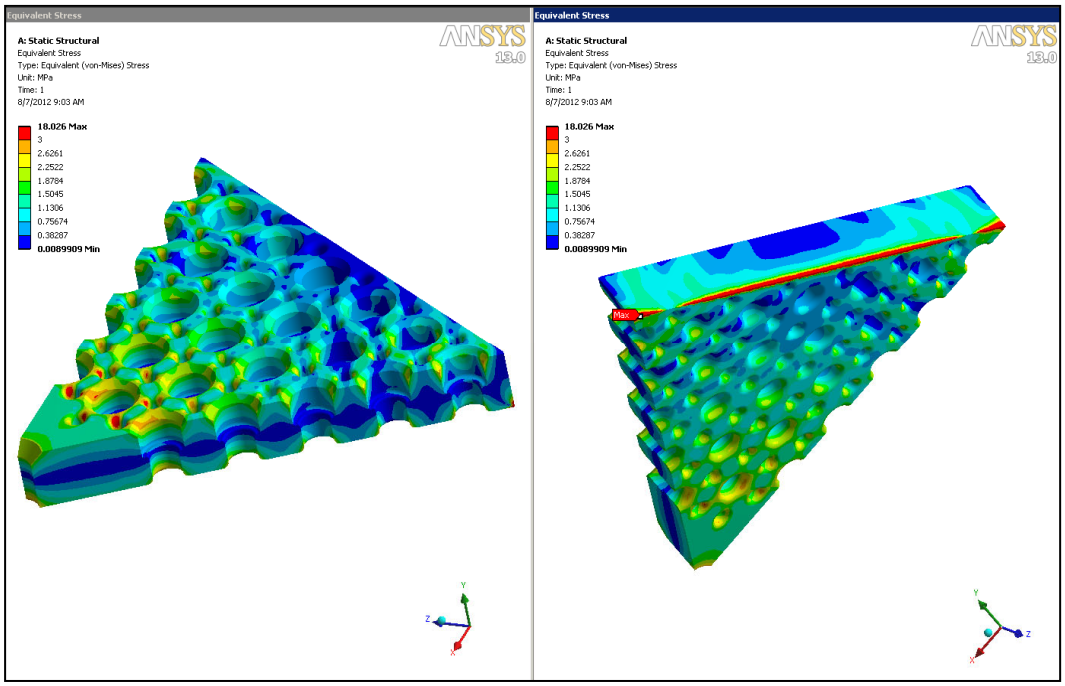

Figure III.6.2.9.1. Von Mises stresses in the grid plate (MPa)

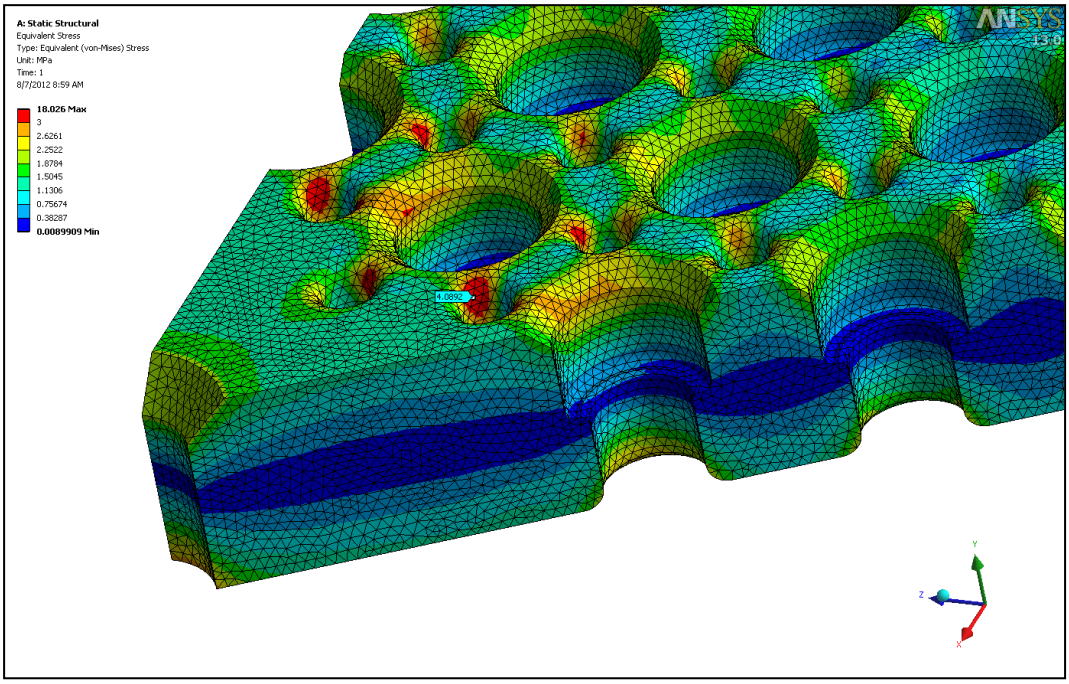

Figure III.6.2.9.2. Von Mises stresses in the grid plate (MPa)

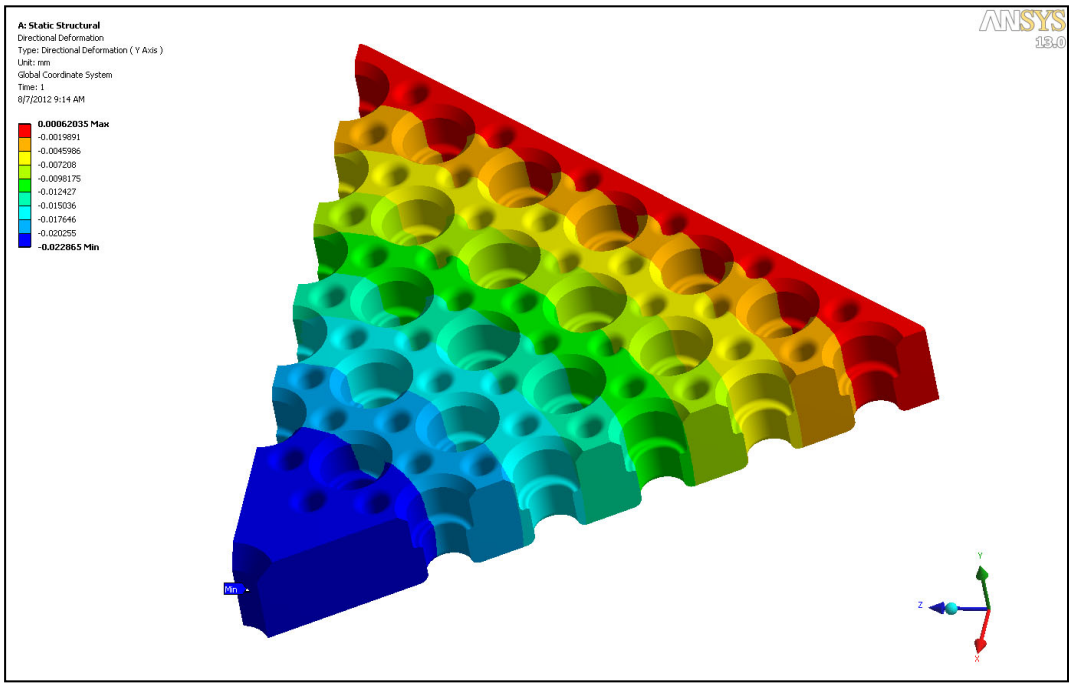

Figure III.6.2.9.3. Vertical deflection (mm)

III.6.2.10 Discussion

Accepted engineering principles were used to evaluate the feasibility of the grid plate. Yielding was evaluated by comparing the von Mises stress as defined by the maximum distortion energy failure theory directly to the yield strength of the material.

The assumptions listed above are reasonable and prudent for the analysis. Von Mises stresses are low, so the use of a linear elastic isotropic homogeneous material model is justified. Deflections are small, so small deflection theory is appropriate. The other assumptions generally fit within the context of the analysis. Within these assumptions, it is believed that this analysis accurately represents the performance of this design for the intended use.

The stresses are very low, and result in high safety factors, indicating that this design will perform properly in its intended use.

III.6.2.11 Conclusions

Based on the results of this analysis, and subject to the listed assumptions, it is concluded that the subcritical assembly grid plate is a structurally feasible design.

References

III.6.1. ANSYS Mechanical, Version 13.0, Build date 11/2/2009, Ansys Inc, Pittsburg, PA.
III.6.2. Metallic Materials Properties Development and Standardization, DOT/FAA/AR-MMPDS-01, Office of Aviation Research, Washington DC, 2003.
III.6.3 Aluminum 6061-O, www.matweb.com.
III.6.4. Shigley, J. E. and Mitchell, L. D. *Mechanical Engineering Design, Fourth Edition*, McGraw Hill, New York, 1983, Chapter 7.
III.6.5. Pilkey, W. D., *Peterson's Stress Concentration Factors*, John Wiley and Sons, New York, 1997, Table 4.83.
III.6.6. ASME Boiler and Pressure Vessel Code, Section VIII, Division 2, Part 5, American Society of Mechanical Engineers, New York, NY 2010.

III.7 SCA Mechanical Design

The KIPT subcritical assembly (SCA) is contained within a water-filled aluminum tank. The water moderates the neutrons within the SCA and carries heat away from the fuel and the target assemblies. As shown in Fig. III.7.1, the SCA tank is within the biological shielding, which provides radiological shielding for personnel working within the subcritical assembly hall.

The SCA tank contains the graphite reflector ring, the grid plate assembly, the fuel racks for storage within the SCA tank, the fuel assemblies, the target assembly, the neutron beamline channel cans, the neutron flux detectors, and the water temperature detectors. Figure III.7.2 shows a cutaway view of the target, the fuel assemblies and the beryllium reflector assemblies seated on the grid plate, the graphite reflector ring, and the cold

neutron source well. The various sections of the tank interior can be seen in the photo in Fig. III.7.3.

The SCA tank is formed by joining aluminum plates by tungsten inert gas welding. There are no penetrations in the SCA tank wall below the normal operation water level. Side and top views of the tank are presented in Figs. III.7.4 and III.7.5. The SCA tank contains the fuel transfer station, a fuel assembly location that provides the interface between the fuel handling machine and the fuel transfer cask system. It also contains the fuel orientation device, it provides a means of determining the angular orientation of a particular fuel assembly so that it can be properly oriented for placement in the grid plate.

The cold neutron source well is a re-entrant pocket in the side of the SCA tank that provides a location for the cold neutron source moderator. The inner face of the cold neutron source well is close to the graphite reflector ring, minimizing the amount of water between the graphite reflector and the cold neutron source moderator. The location of the cold neutron source well can be seen in Figs. III.7.4, through III.7.6.

The SCA tank is fastened to the building foundation by eight nuts. The tank is dielectrically isolated from the foundation structure by a non-metallic isolation plate. Nonmetallic washers and sleeves provide isolation at the eight nuts. This configuration is diagrammed in Fig. III.7.7, which shows also how the tank is mounted within the biological shielding. The SCA tank does not contact, and is not supported by, the biological shielding.

The aluminum walls of the SCA tank allow the passage of neutrons to the neutron experiments and the cold neutron source moderator. The neutron beamline channel cans are aluminum cans, filled with helium, which provide a streaming pathway for neutrons to reach the neutron experiments. Figs. III.7.8 through III.7.10 show the locations of the cans within the tank.

The cooling water is drawn out of the SCA tank below the subcritical assembly, which draws water through the fuel assemblies downward through the subcritical assembly. The cooled water is returned from the intermediate heat exchanger to the tank below the grid plate (see Figs. III.7.11 and III.7.12) and diffused to reduce its flow velocity in a way that promotes consistent temperature throughout the tank and minimizes stagnation points within the tank. The water drawn out of the tank flows upward through a pipe in the annular space between the SCA tank wall and the outside of the graphite reflector ring (see Fig. III.7.11). An overflow port is provided on the side of the tank above normal operating water level. Two liquid level measuring devices are provided within the tank to monitor the tank water level. A series of gravitational reservoirs provide supplemental water to fill the tank in the case of a significant and sustained loss of coolant.

The two pipes that remove and return water have provisions to prevent gravitational siphoning of the coolant water from the SCA tank (see Fig. III.7.13). The suction pipe is protected from siphoning by a short snorkel tube which will be uncovered if the water level drops. The return pipe is protected against siphoning by a series of small holes below the normal water level of the tank. If a pipe break were to cause gravitational siphoning of

water from the tank, the resulting reduction of the water level would uncover the anti-siphon ports, allowing air to be drawn into the pipe, breaking the siphon.

There are four inspection channels under the dome of the SCA tank which provide a means for video inspection of the lower surface of the tank dome and supporting structure. Two of these channels are shown in Fig. III.7.14. The dome forms the bottom of the tank. Air is circulated through the inspection channels to prevent condensation on the bottom surface of the tank.

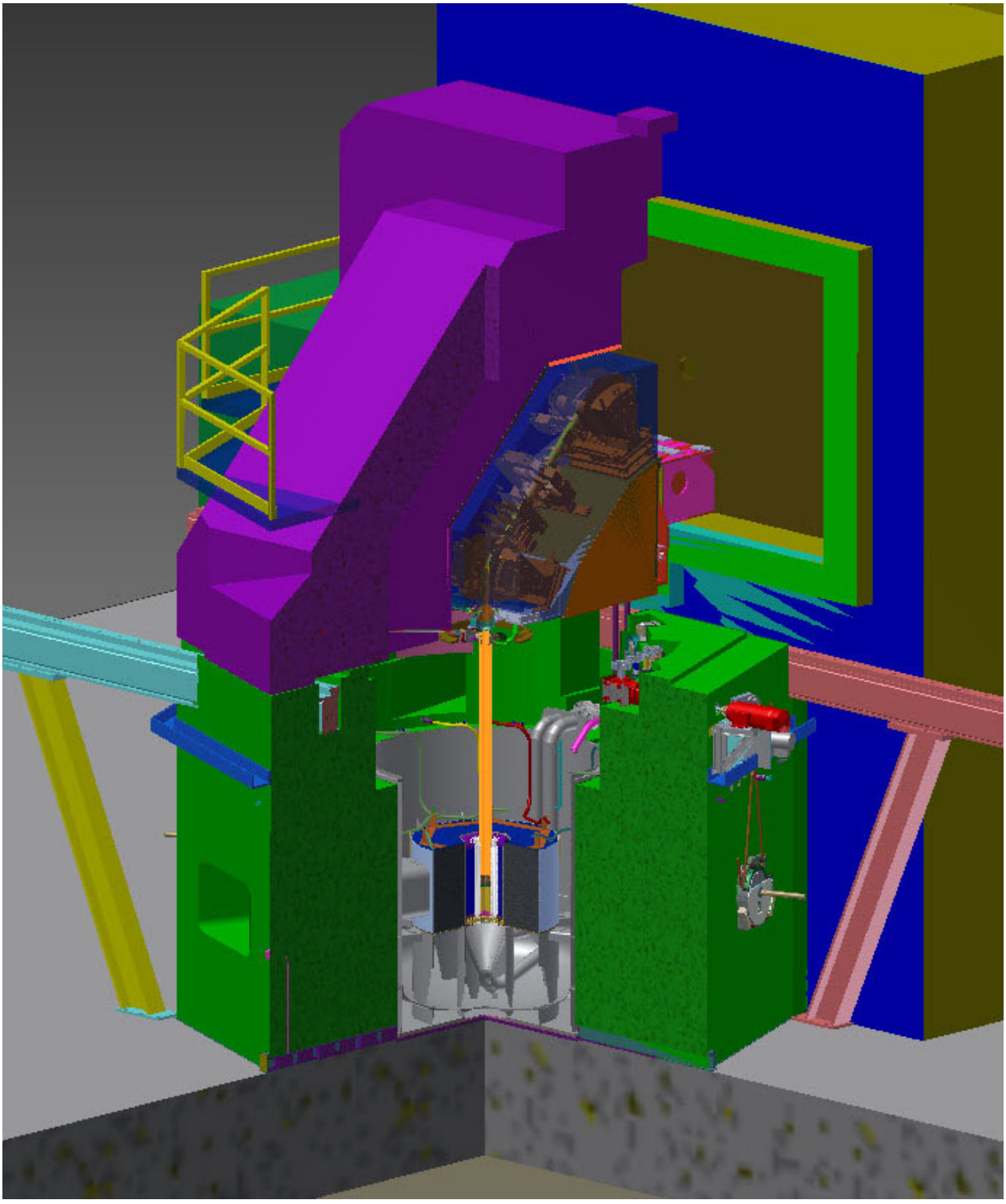

Figure III.7.1. Section view through the SCA tank showing the general configuration. The SCA tank is contained within the biological shielding, shown with green color.

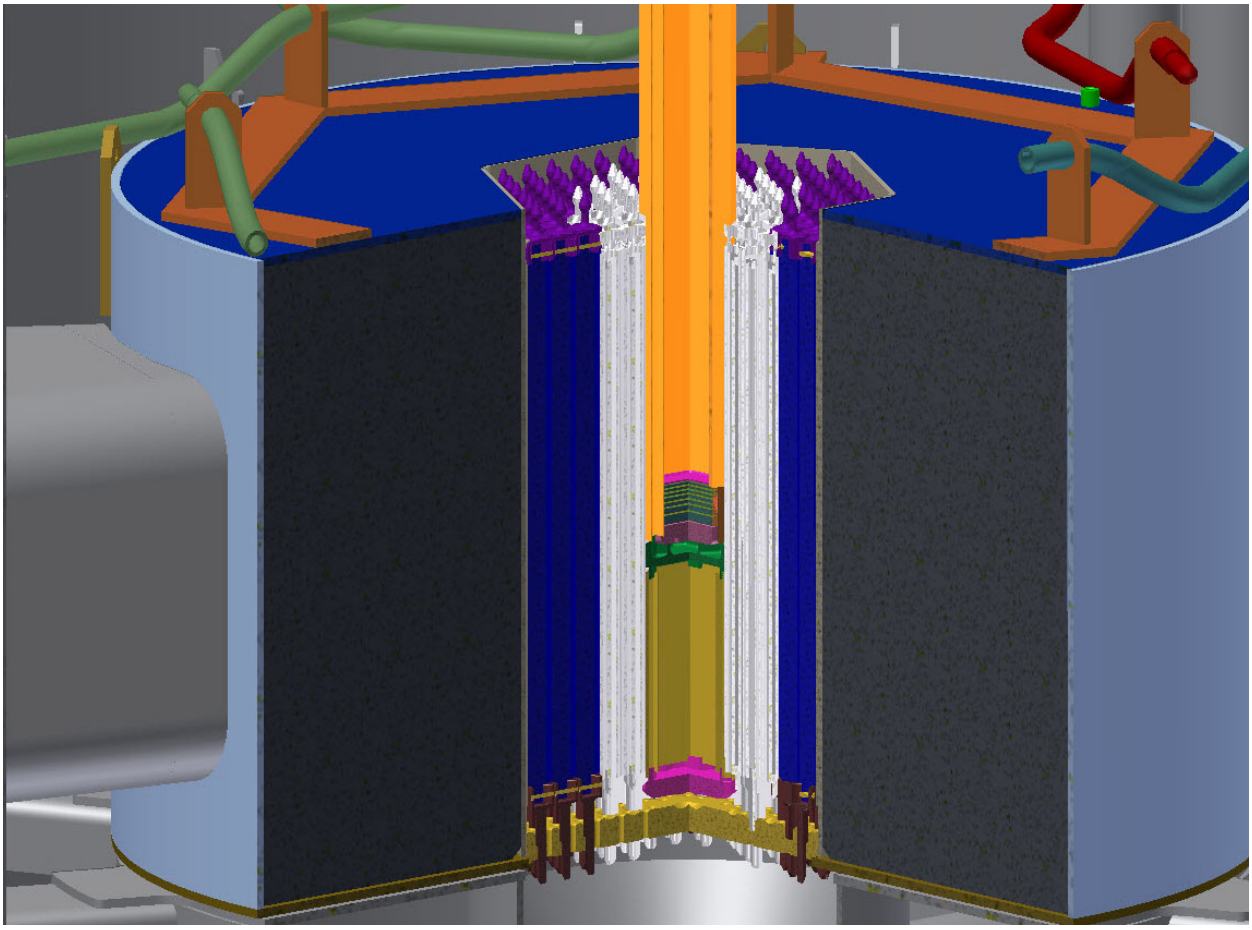

Figure III.7.2. Section through graphite reflector ring (black), the hexagonal arrangement of the fuel assemblies (silver), and the beryllium reflector elements (purple) on the grid plate are shown. The cold neutron source well is the gray object on the left, outside the graphite reflector ring.

Figure III.7.3. Interior of the SCA tank is shown being filled with water during manufacturing testing. Two fuel racks (upper left and center), one neutron beamline channel can (center right), the fuel orientation device, and the fuel transfer station are visible in this photo. The graphite reflector ring fits in the space being filled with water, between the hexagonal part if the SCA and the circular aluminum wall; about half of the space is shown in this photo.

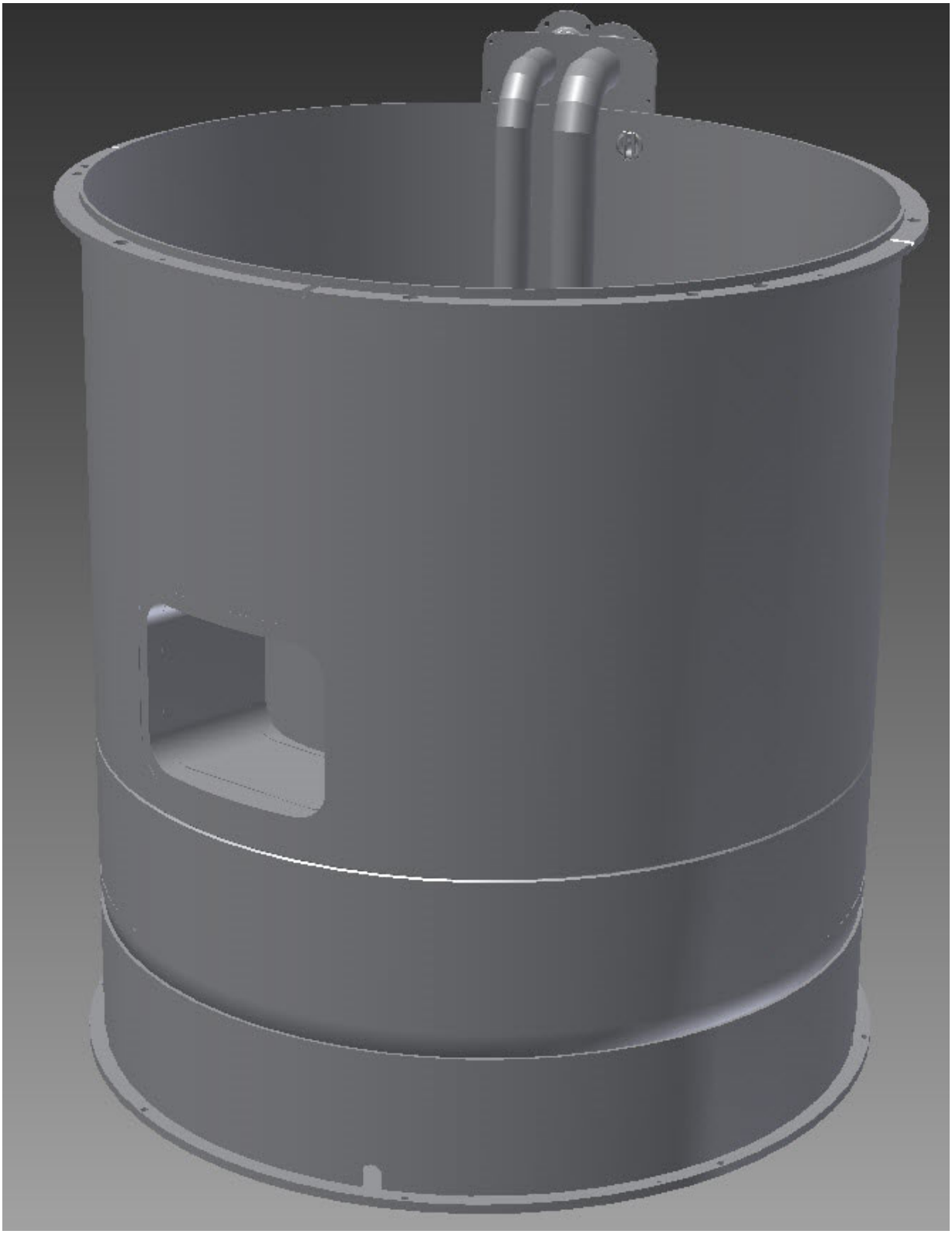

Figure III.7.4. View of the outside of the SCA tank weldment, showing the coolant pipes, the overflow port, one inspection hole at the bottom, and the cold neutron source well (left).

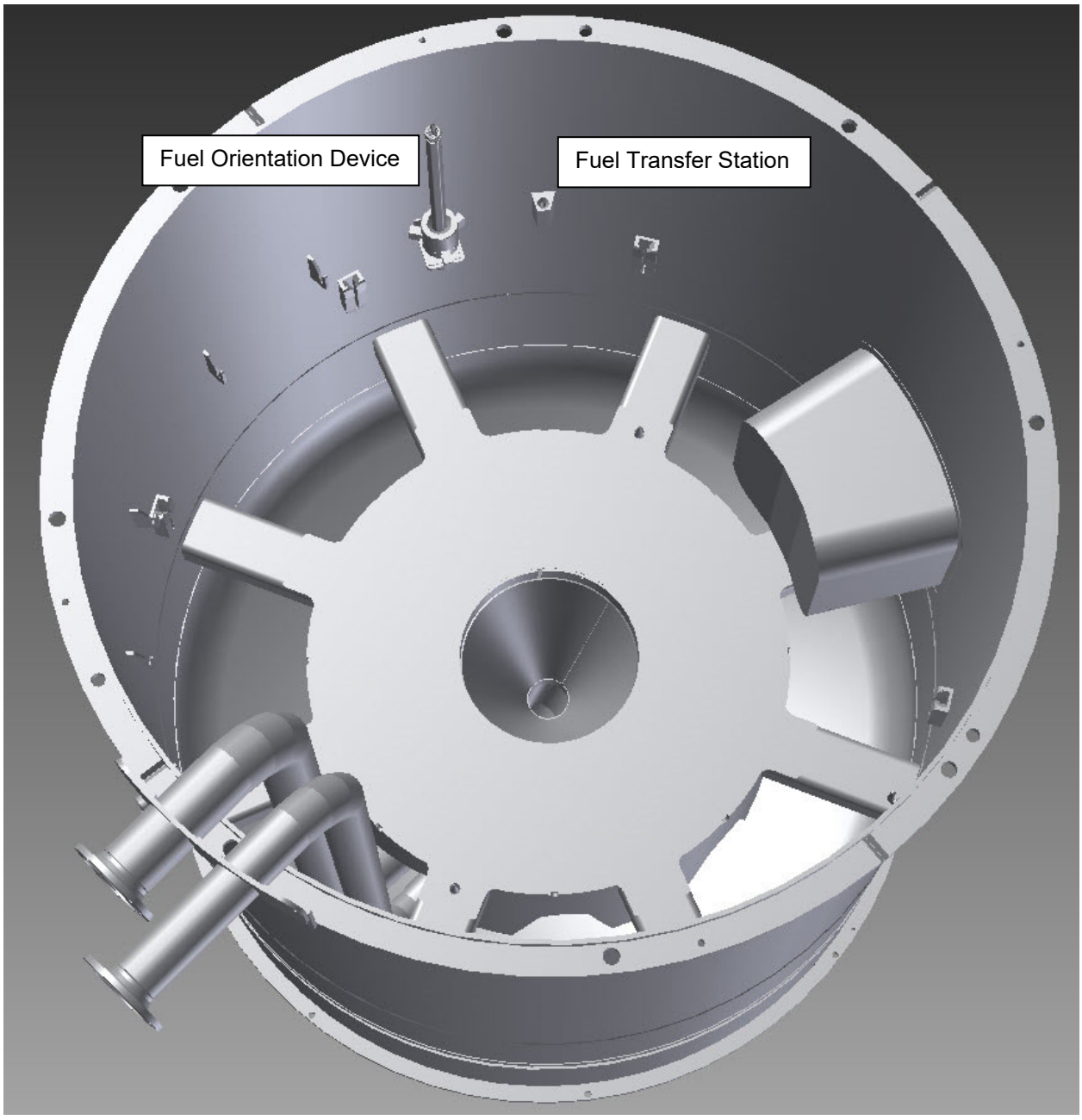

Figure III.7.5. View of the inside of the SCA tank weldment, showing the fuel transfer station, the fuel orientation device, the coolant pipes (left) and the suction funnel (center), and the cold neutron source well (right).

Figure III.7.6. SCA tank shown during the manufacturing process, the bottom of the cold neutron source well (left side of the tank) is being machined in this photo.

Figure III.7.7. Section view of the SCA tank flange shows one of the tank attachment nuts, the dielectric spacer plate under the gray tank, and the foundation plate. The biological shielding is the green region to the right of the nut and accompanying sleeve.

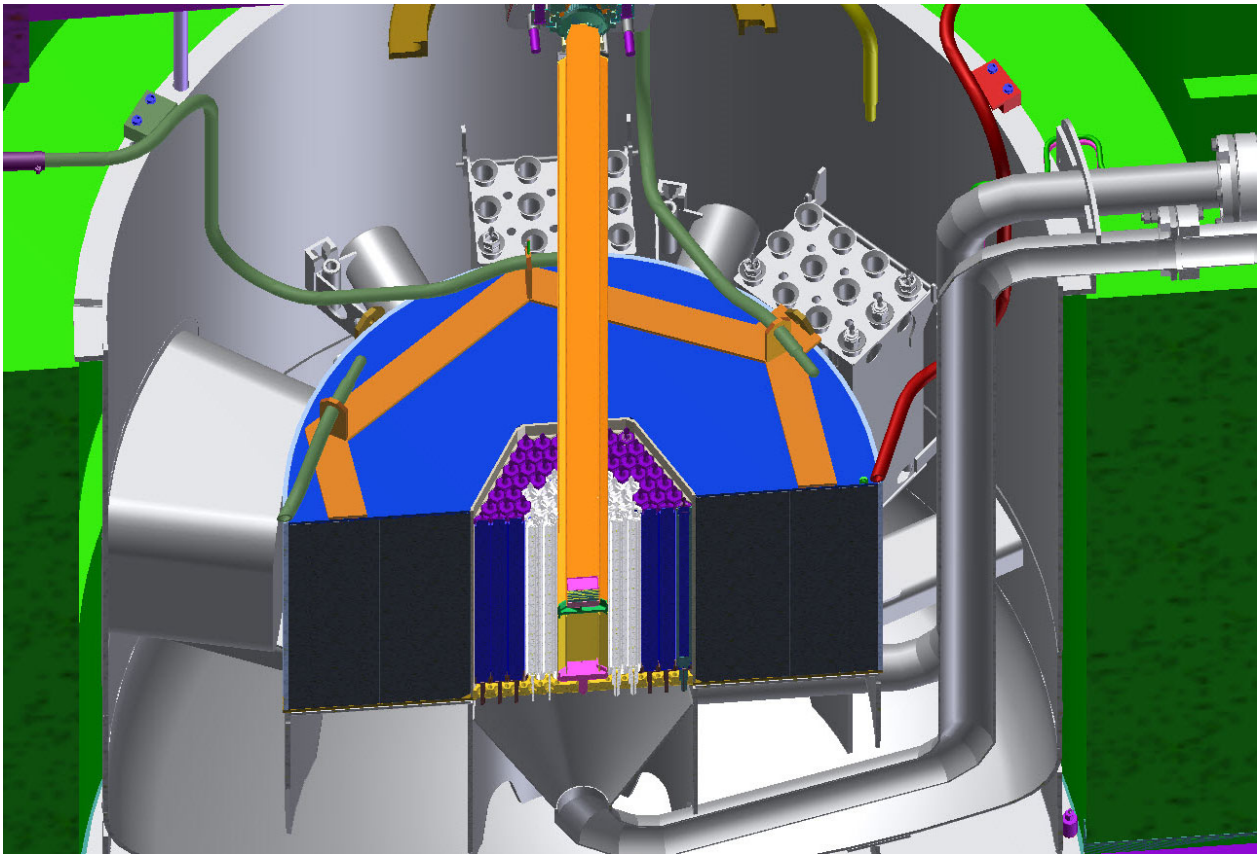

Figure III.7.8. Section view showing the subcritical assembly, the graphite reflector ring, the target, the fuel storage racks (top and top right in the figure), the cold neutron source well (left, between the graphite reflector ring and the tank wall), and the neutron beamline channel cans (to either side of the fuel storage rack at the top of the figure).

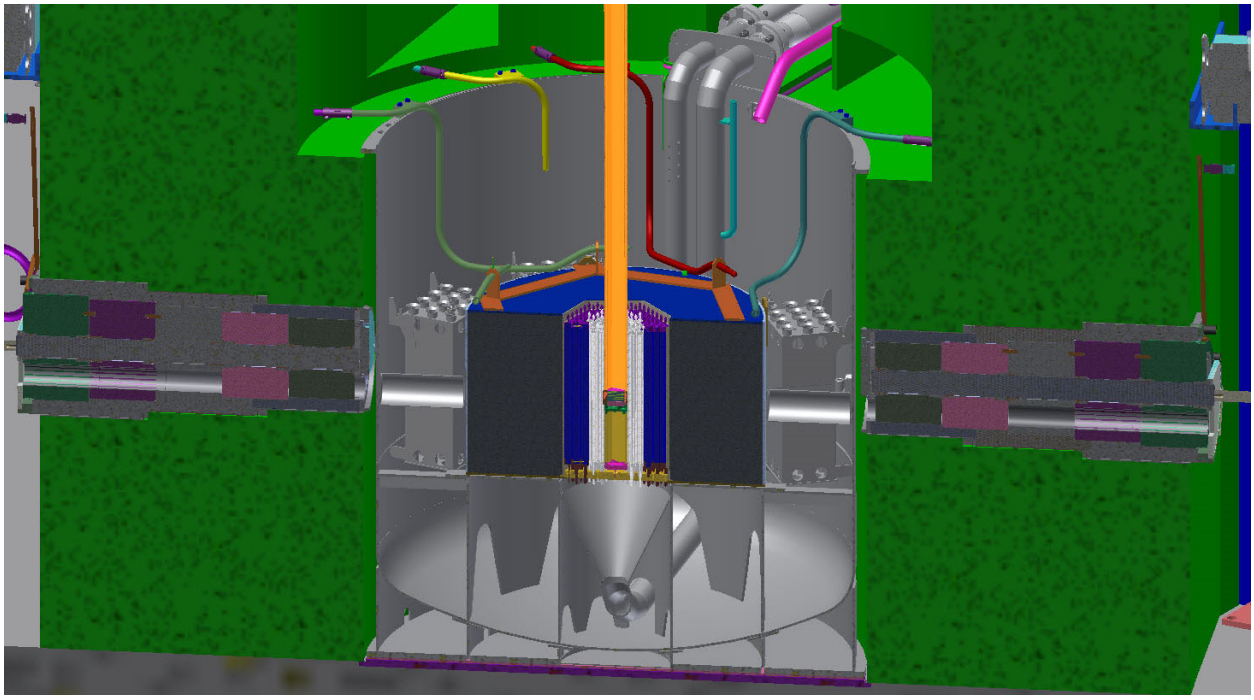

Figure III.7.9. Section through the neutron channels number 5 (left) and the number 1 (right). The neutron channels pass through the biological shield (mottled green).

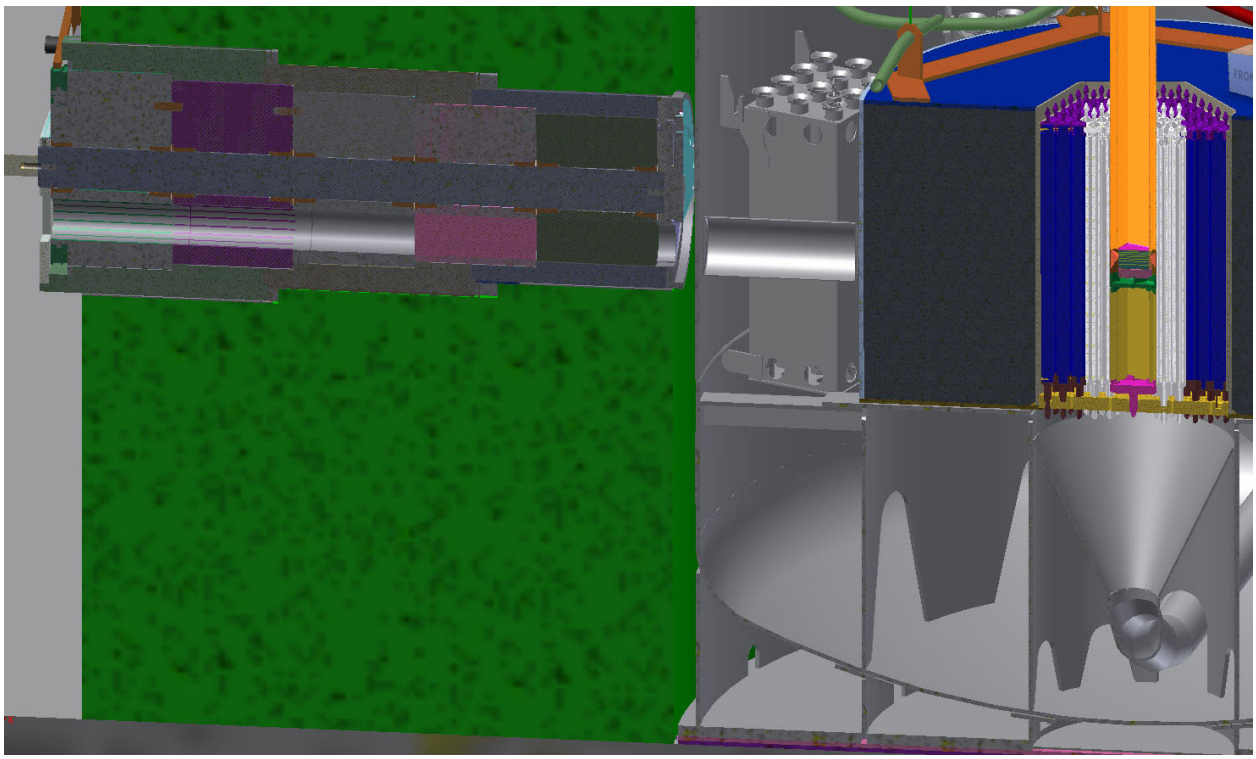

Figure III.7.10. Section through the neutron channel number 5, showing (from right to left) the subcritical assembly, the graphite reflector ring, the neutron channel can, and the neutron channel shutter.

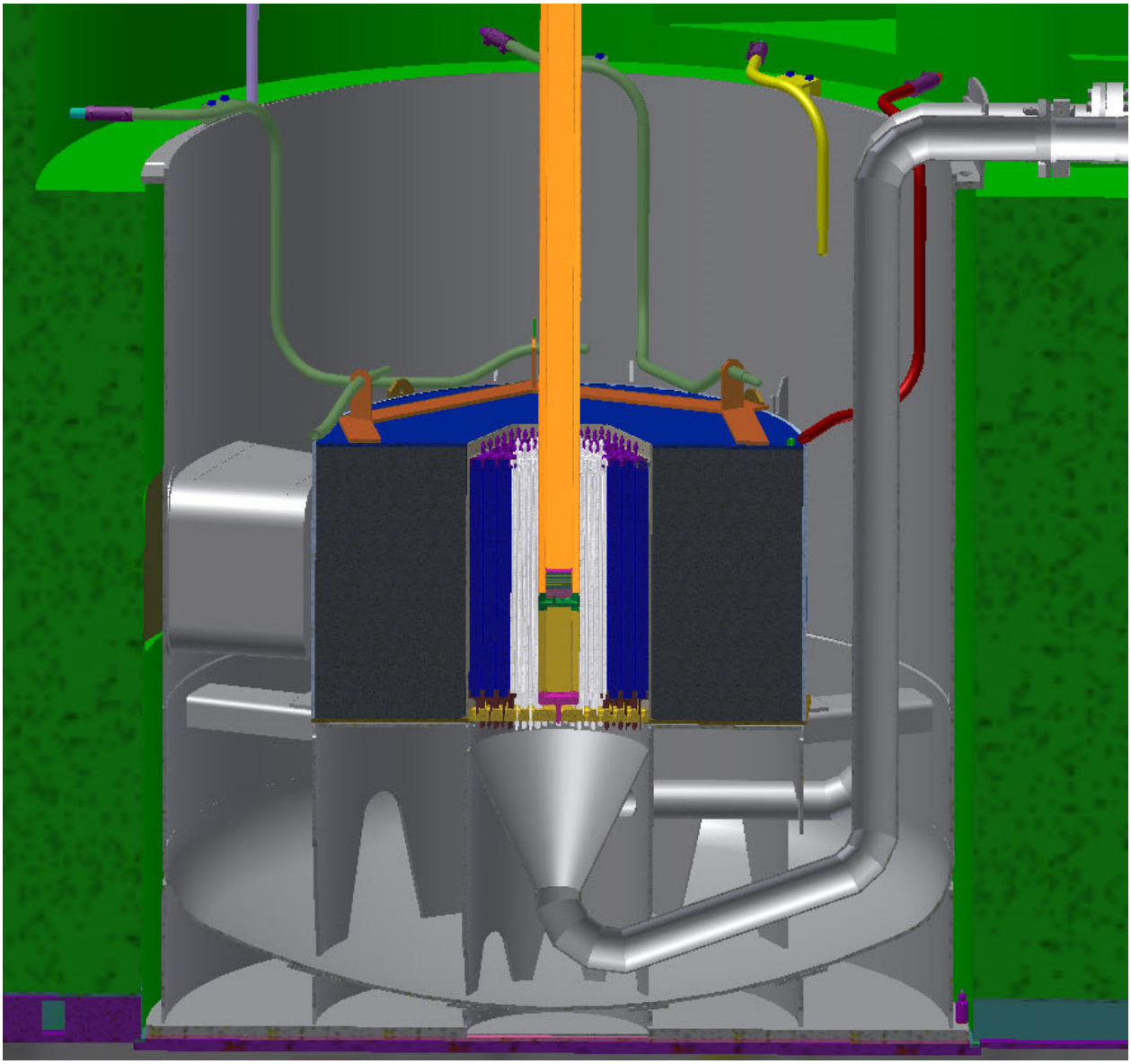

Figure III.7.11. Section view through the subcritical assembly tank, showing the target assembly, the fuel assemblies, the graphite reflector ring, and the neutron flux detector tubes (green and red color tubes).

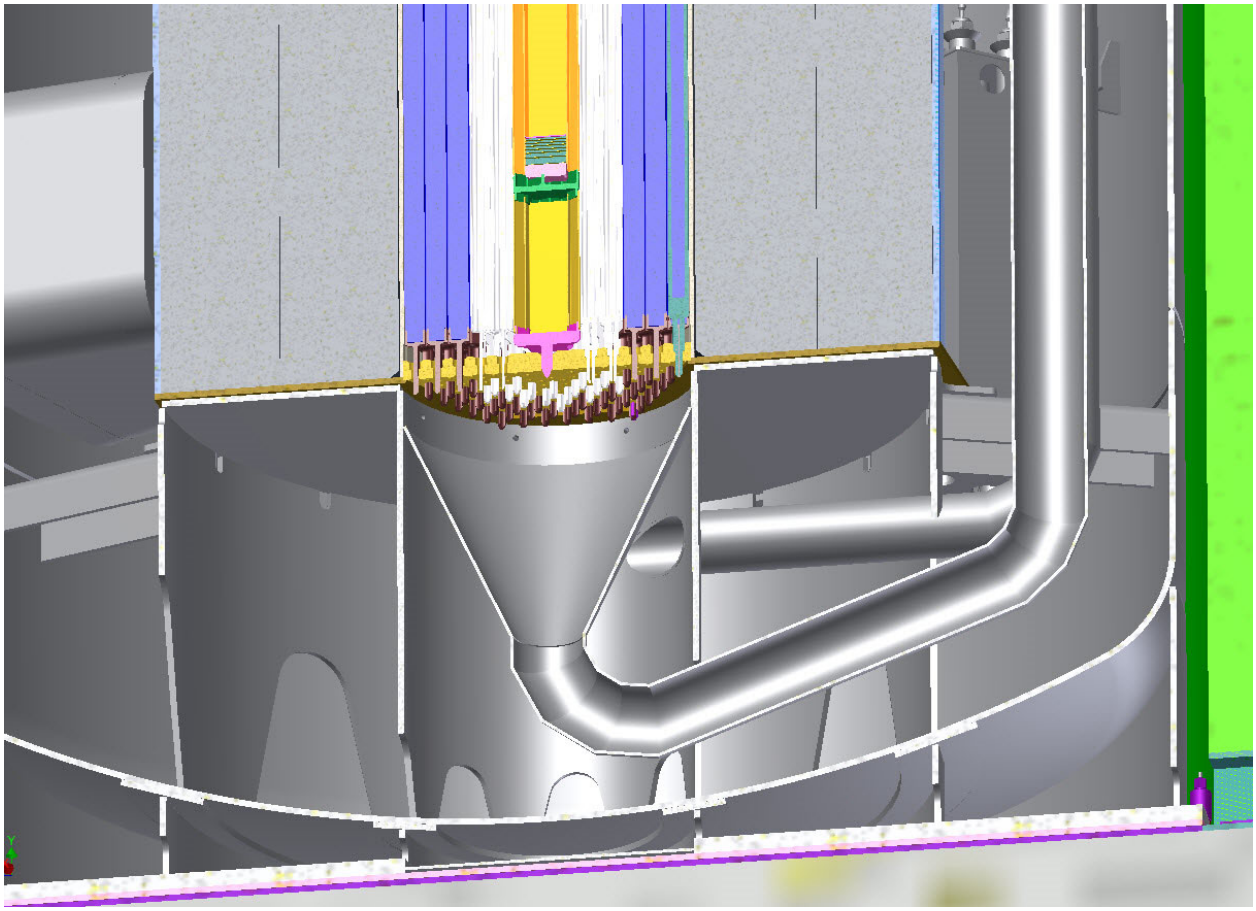

Figure III.7.12. Section view of the lower part of the subcritical assembly tank showing the grid plate, the suction funnel, the water coolant pipe, and the return pipe. Return flow is diffused through eight cutouts in the inner support cylinder and eight cutouts in the outer support cylinder. Three cutouts are visible in the inner support cylinder and two are visible in the outer support cylinder in the figure. Swirling motion and the location of the cutouts at the bottom of the support cylinders prevent stagnation areas within the subcritical assembly tank.

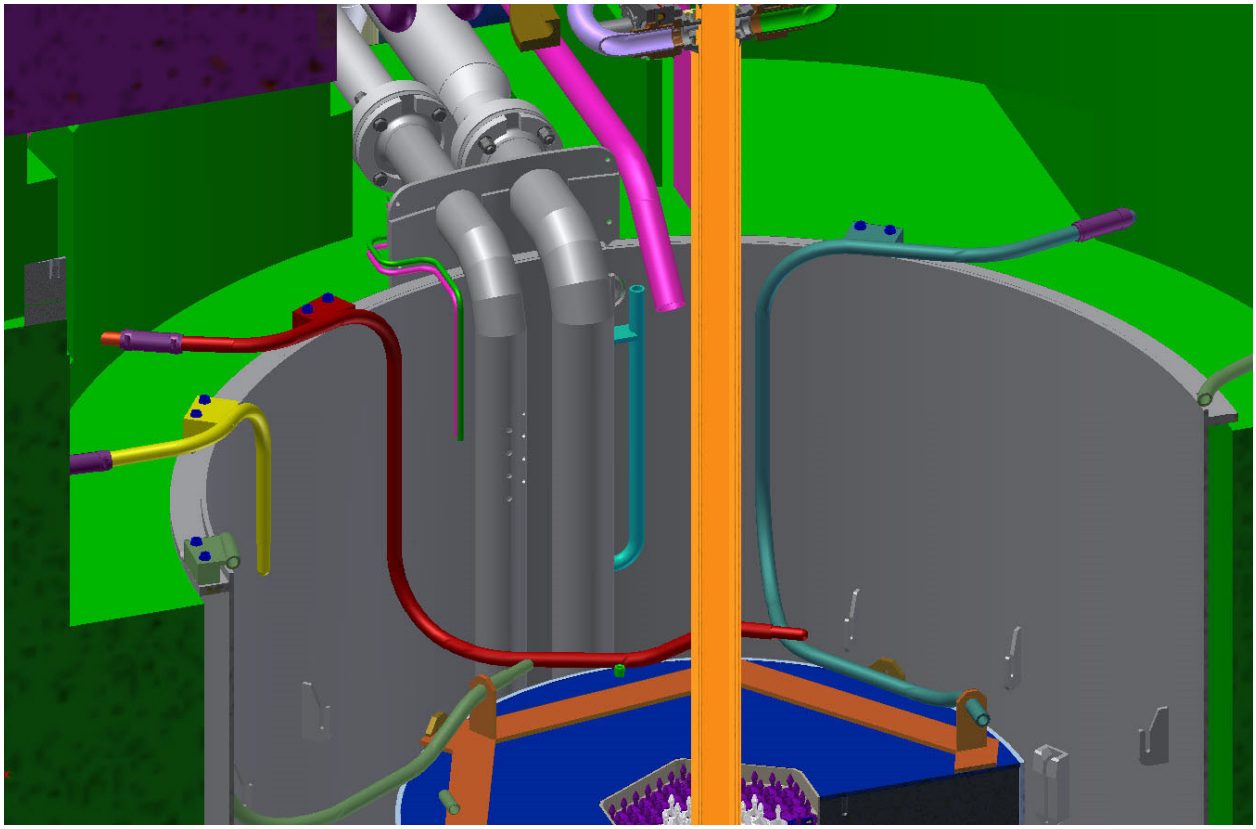

Figure III.7.13. Section view through the subcritical assembly tank showing the coolant suction and the return pipes, the anti-siphon features, the supplemental fill tube, and the liquid level measurement tubes (the two small tubes next to the main coolant tubes).

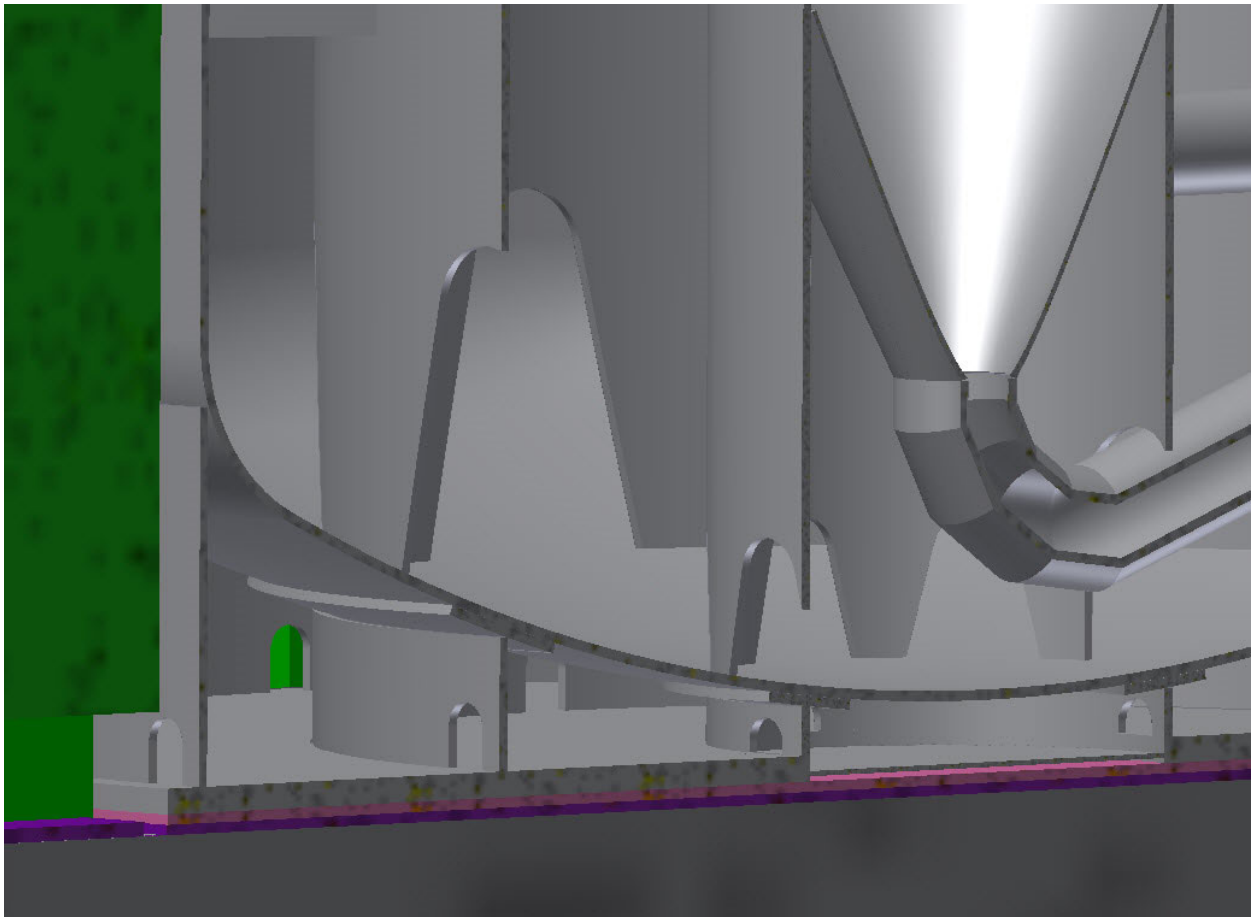

Figure III.7.14. Section view shows the video inspection holes under the dome of the subcritical assembly tank. The biological shield is the green area on the left side, beyond the tank.

III.8 Subcritical Assembly Primary Cooling Loop

III.8.1 Introduction

The subcritical assembly (SCA) has the uranium fuel assemblies, the beryllium reflector assembles, and the graphite ring reflector. During operation, nuclear heat is generated within the SCA. The generated heat is carried away by the forced water flow. The SCA cooling system provides coolant flow, the heat removal, the filtration, and the chemistry control functions. The SCA cooling system is separate from, and shares no components with the target cooling system, which removes the heat from the target assembly. The target cooling system is discussed in section II.6. Up to 250 kW of heat can be removed from the SCA during operation.

III.8.2 Cooling System Overview

The SCA cooling system uses forced circulation of a demineralized water coolant to remove the heat. While the SCA cooling system is isolated from the target cooling system, the two systems do both interface with three facility systems: 1) both systems use the same chilled water facility as a secondary heat sink, 2) both systems use an inert gas system for coolant purge and leak testing, and 3) both systems use the same special ventilation system facility. The two cooling systems do use separate water quality monitoring stations, to prevent cross-contamination between the systems. Figure III.8.2.1 is a simplified schematic diagram of the SCA cooling system.

III.8.3 SCA Cooling System Design

The SCA cooling system is comprised of two overlapping loops. The heat removal loop provides coolant flow through the subcritical assembly and heat exchanger. The heat removal loop flow paths are shown in Fig. III.8.3.1, and more details on the heat removal loop design are given in Sec. III.7. The filtration loop removes contamination from the coolant and provides a means for monitoring the quality of the water coolant. The two-loop cooling system permits more precise control of the operation of the SCA and allows the filtration loop to operate without the cooling loop running.

III.8.3.1 SCA Cooling System Heat Removal Loop.

Centrifugal pumps provide coolant flow through the SCA subcritical assembly. Since the coolant is forced downward through the subcritical assembly, a relatively high flow rate (22.6 liter/sec or 359 gal/min) is used. This requires relatively large components and pipes for the heat removal loop. After the coolant leaves the SCA it passes through a heat exchanger to remove heat from the coolant. The facility cooling water is used as the secondary fluid in the heat exchanger. The coolant then returns to the SCA tank.

III.8.3.2 SCA Cooling System Filtration Loop

The filtration loop pump draws coolant from the SCA tank and circulates it through a filter and a demineralizer before returning the coolant to the SCA tank. The filter removes

particulates from the water coolant. The demineralizer removes dissolved minerals from the water coolant. The demineralizer will accumulate activated particles during operation and is therefore enclosed in a radiological shield. The water coolant quality sampling station is attached to the filtration loop and measures the pH value, particle content, conductivity (resistivity), activation level, and cesium content.

III.8.3.3 SCA Cooling System Reservoir

The SCA tank acts as a reservoir for the SCA cooling system. The SCA tank allows the fluid velocity to be reduced so that entrained gas can be separated. The SCA tank is equipped with liquid level sensors to monitor coolant level and detect and monitor coolant loss. Atmospheric air over the SCA tank is directly removed via the special ventilation system facility to prevent the accumulation of gas byproducts.

III.8.3.4 SCA Cooling System Drain Tank

A drain tank provides short-term storage of coolant that has been drained from part of the system for component service. The inert gas system is used to pressurize the drain tank to prime the secondary pump, which pumps the coolant through the filter and demineralizer and back to the SCA tank.

III.8.3.5 SCA Cooling System Inert Gas System

An inert gas system provides pressurized gas from a multi-bottle manifold to remove coolant from the target pipes, pumps, heat exchanger, filter, and demineralizer prior to component exchange, to minimize the amount of coolant lost. The inert gas system also provides a means of checking the system for leaks after component service or replacement without losing coolant. As the SCA tank is open to the atmosphere, no gas cover atmosphere is provided.

III.8.4 Normal Operating Parameters for the SCA Cooling System

III.8.4.1 SCA Tank Level

During the SCA cooling system operation, the level of the coolant in the SCA tank is monitored via a level sensor. A decrease in the coolant level may indicate a loss of coolant. Loss of coolant creating a fluid level deviation exceeding 20mm during operation will trigger an accelerator shutdown. Smaller changes will trigger operator alerts to determine root cause. An increase in the level of the coolant within the SCA tank may indicate a vapor void within the system. An increase in coolant level exceeding 20 mm during operation will also trigger an accelerator shutdown. Distilled water can be added to the system to make up for lost coolant, but it is critical to monitor the amount of make-up water added over time to identify trends and spot possible leak conditions. Fluid levels will change as parts of the system are drained for service. Following service, it will be necessary to run the cooling systems to purge air from components and then add fluid and recalibrate the fluid level.

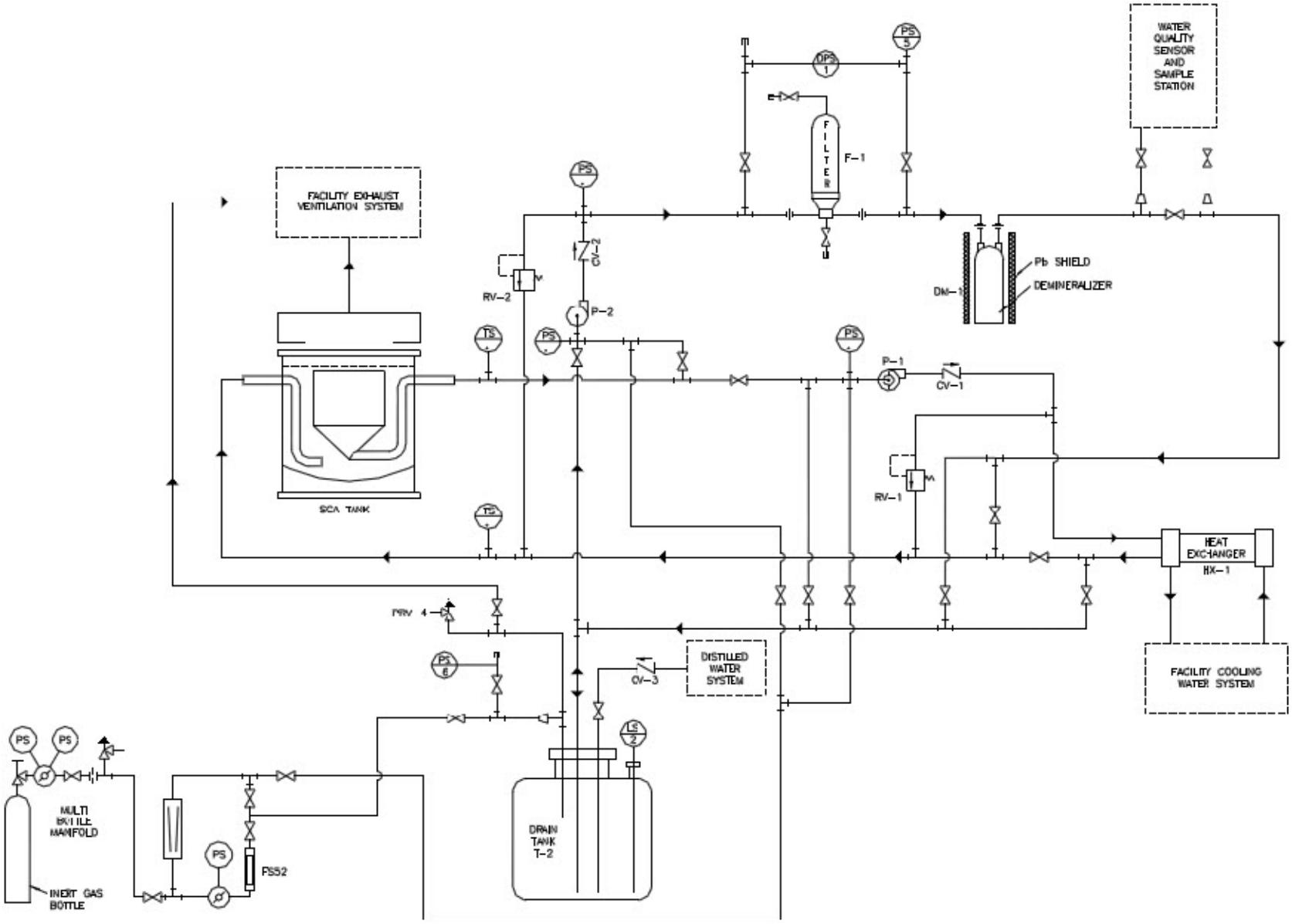

Figure III.8.2.1. Simplified schematic of the SCA cooling system

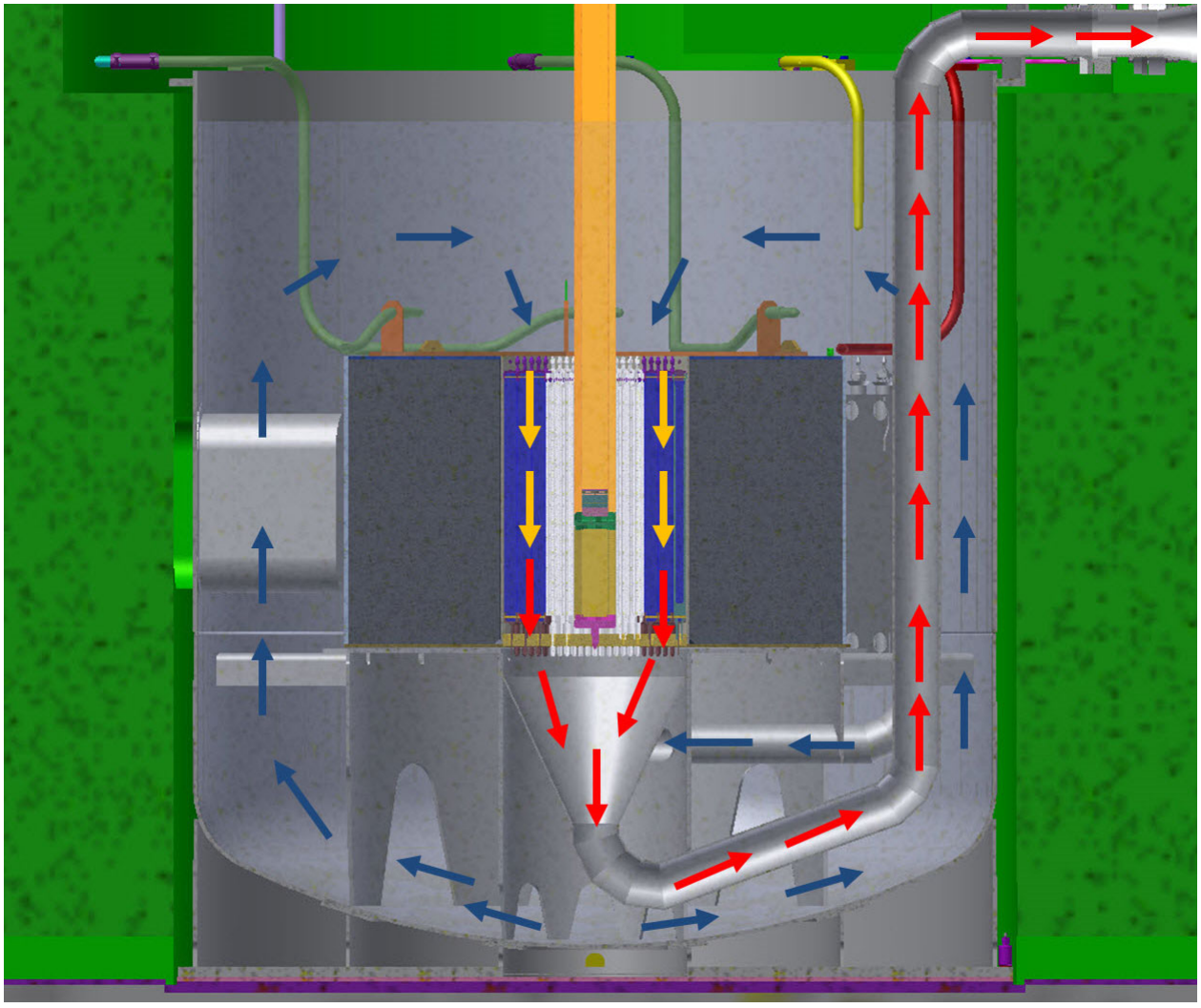

Figure III.8.3.1. Section view through the SCA tank is showing the coolant flow path. Heating of the coolant occurs primarily within the SCA components. Heated fluid is indicated by red arrows. The blue arrows show the cooled water flow returning from the IHX and entering below the SCA grid plate, then flowing up and back into the top of the SCA. Yellow arrows indicate water being heated as it flows down through the SCA.

III.8.4.2 Operating Pressures

Pressures are measured at several key points of the SCA cooling system. These data are used to calculate flow rates and make inferences about the operational condition of various components during operation. Pressure sensors are calibrated at each start-up when system pressures are assumed to be static head pressures. The SCA tank is open to the atmosphere. Pressure drops through lengths of piping are used to calculate flow rates. Operational pressure limits are in some cases based on derived differential pressures. The pressures across the filter and demineralizer are monitored as a predictive tool for management of service of these components.

III.8.4.3 Operating Temperatures

The SCA cooling system operates at nearly room temperature. In general, the temperature information available in the SCA cooling system is used as a secondary tool to monitor the performance of various components and make operating adjustments.

III.8.4.4 Synthesized Data

Knowing both the differential pressure and the differential temperature across the subcritical assembly system provide insight into the conditions within the SCA. Knowing pressure differentials allows calculation of mass flow rates and knowing the temperature differential plus the mass flow rate allows calculation of the power output of the SCA.

III.9 Subcritical Assembly Main Parameters

Table III.9.1. Inner and outer radius for each ring of the WWR-M2 fuel assembly

	Inner Clad		Fuel meat		Outer Clad	
	Inner radius, mm	Outer Radius, mm	Inner Radius, mm	Outer Radius, mm	Inner radius, mm	Outer Radius, mm
Ring 1 (inner)	3.0	3.75	3.75	4.75	4.75	5.5
Ring 2 (middle)	8.5	9.25	9.25	10.25	10.25	11.0
Ring 3* (outer)	13.5	14.25	14.25	15.25	15.25	16.0

* Hexagonal shape - outer flat-to-flat is 32 mm

Table III.9.2. WWR-M2 fuel assembly parameters

U-235 enrichment (wt %)	19.7 %
Active height of fuel	50 cm
Total height of fuel assembly	75 cm
Averaged U-235 mass/fuel assembly	41.7 g
Averaged uranium density in fuel meat	2.226 g/cm^3
averaged fuel meat (UO2 + Al) density	4.603 g/cm^3

Table III.9.3. Density and impurities of reflector materials

Reflector material	Density	Impurities
Beryllium	1.855 g/cm^3	1.77%
Graphite	1.85 g/cm^3	0.0026%

Table III.9.4. Thermal-hydraulic parameters for the subcritical assembly

Mass flow rate	22.6 kg/s
Pressure drop (fuel assembly only)	13.7 kPa
Inlet temperature	25 ºC
Average outlet temperature	27.2 ºC - uranium target
Total power (reflector & assembly)	208.5 kW - uranium target
Total power, hottest unit cell	6.84 kW - uranium target
Peak fuel temperature	39 ºC - uranium target

IV Biological Shield

IV.1 Introduction

The subcritical assembly (SCA) is contained within a heavy concrete structure. The heavy concrete provides radiological shielding around the SCA. The biological shield also provides atmosphere containment and liquid leak containment and collection.

A shielding study was performed to define the biological dose equivalent outside the biological shield of the facility in the radial and vertical directions during operation as a function of the shield geometry and thickness. The main objective is to define a shielding configuration which minimizes the radiation dose as much as possible, to permit personnel to work around the subcritical assembly during operation. The shield design is configured to maintain the biological dose during operation less than 0.5 mrem/hr, which is required by Ukraine regulations, and this value is five times less than the allowable dose (2.5 mrem/hr) set by the USNRC (Ref. IV.1.1) for adults to work 40 hours per week for 50 weeks per year. In the shielding design process, both cost and engineering considerations were addressed. The physics analysis is described in Sec. IV.2, and an evaluation of the energy deposition is presented in Sec. IV.3. Mechanical design features of the biological shield are covered in Sec. IV.4.

Reference

IV.1.1. United States Nuclear Regulatory Commission Regulations, 10CFR20, Subpart C, 20.1201, “Occupational dose limits for adults”.

IV.2 Physics Analysis and Design

IV.2.1 Radial shield analysis

The shielding study was aimed at defining the biological dose outside the biological shield of the facility in the radial and vertical directions during operation as a function of shield geometry and thickness. Such shielding analyses require accurate characterization of the neutron and gamma fluxes through the shield. The Monte Carlo computer code MCNPX [IV.2.1] was used with ENDF/B-VII nuclear data libraries for performing the analyses. Based on previous studies [IV.2.2, IV.2.3], the neutron dose is orders of magnitude higher than the photon dose when the subcritical assembly is driven by high-energy electrons ($E \geq 100$ MeV). Therefore, the neutron dose profile calculation plays a significant factor in the shield design. The studies documented in Refs. IV.2.2 and IV.2.3 also concluded that neutrons with energies greater than 10 MeV generated in the target assembly are the major contributors to the dose outside the shield, even though their yield is a very low fraction of the total neutron yield, < 0.7 % for the tungsten target and < 0.4 % for the uranium target. These neutrons have a large mean free path and consequently a high probability of reaching the outer shield boundary. Considering that the total neutron yields per electron are ~0.029 and ~0.048 for the tungsten and the uranium targets, respectively,

the corresponding high-energy neutron yield per electron is ~0.00020 and ~0.00019. These low yield values present a challenge to the MCNPX calculation for obtaining an accurate estimate of the neutron dose outside the shield boundary, the use of conventional Monte Carlo calculations for the shielding analyses is problematic.

The weight windows variance reduction technique [IV.2.4] of MCNPX is a useful tool for performing shielding analyses. However, it cannot be used by itself for the current problem because of the low yield per electron of high-energy neutrons. Therefore, a new procedure has been developed for performing the shielding calculation with MCNPX for the ADS facility [IV.2.3]. The basic idea is to generate a volumetric neutron source during the MCNPX calculation, starting from electron source particles and recording all the new-born neutrons generated inside the target cells from photonuclear reactions initiated by the electrons. This neutron source file records the position, energy, weight, and direction of the new-born neutrons. This volumetric neutron source can be utilized to drive the subcritical assembly in an independent MCNPX calculation, which preserves the generated neutron yield and the parameters of each generated neutron. The volumetric neutron source can be used for weight window generation and, in the final run, for calculating the biological dose equivalent, because the neutron yield from the electrons is preserved.

The TALLYX user subroutine of MCNPX, which allows users to modify any tally, is utilized to generate the neutron source file for driving the subcritical assembly. First, the neutron source is generated by performing a MCNPX calculation while the neutron fission reactions are turned off. The TALLYX subroutine is initiated through the input deck by using the F4:n neutron flux tally card for the target cells associated with the FU4 card [IV.2.1]. Once a neutron is born inside a target cell, its weight, energy, direction, and position are recorded in the external source file. Then the neutron history is terminated to avoid generating secondary neutrons through (n,xn) and fission reactions. This elimination of the fission events during the calculation ensures that all the recorded neutrons are produced by electrons, without incorrectly recording any neutrons resulting from fission. Removal of the source neutrons after the recording process avoids duplication of the same source neutrons in other target cells.

In subsequent MCNPX calculations, the SOURCE user subroutine is invoked by ensuring the SDEF, SSR, and KCODE cards are absent from the input file. The SOURCE subroutine reads the external neutron source file to start the neutron transport process. In MCNPX calculations, the SOURCE subroutine receives one neutron record for each starting source neutron. The selected number of neutrons to be run is the NPS value specified in the input file. If the NPS value is greater than the number of records in the source file, the SOURCE subroutine repeats the process of reading the source file to satisfy the requested number of neutrons. In this way, each record can be used multiple times; the repetition factor is determined by the NPS value, and the number of records stored in the file.

Furthermore, the neutron source file can be used to record only high-energy neutrons (E>10 MeV) for the initial shield analyses, since, as stated above, these neutrons dominate the biological dose outside the biological shield. This allows the MCNPX run to

focus on the high-energy source neutrons that determine the shielding thickness. This reduces the computational requirements, i.e., computation time is significantly reduced. This approach is very useful for the complex top shield design, which requires several iterations to define the shield geometry.

Although the proposed method calculates the neutron dose outside the shield with much smaller statistical error than the traditional Monte Carlo calculation, method verification is required because the statistical error of the neutron source calculation is not included in the results. Therefore, sampling adequacy of the neutron source must be examined, including the impact on shield results. These issues can be evaluated by calculating the neutron dose outside the shield as a function of the number of electron particles that were sampled for generating the neutron source file. Seven neutron source files were generated for each target configuration and used for calculating the dose outside the shield boundary as a function of the number of electrons sampled during source generation. In the first two files for each target, 60 million electrons were sampled for generating the neutron source files. In the first file, all neutrons that were generated were recorded, and the neutron source files that were produced included 1.7 million neutrons for the tungsten target and 2.9 million for the uranium target. The second file recorded only neutrons with energy >10 MeV. In this case, the numbers of neutrons were 11,600 and 11,000 for the tungsten and the uranium targets, respectively. In the other five files, only neutrons with energy >10 MeV were recorded, and the numbers of electrons were 180, 360, 720, 1,440, and 2,000 million for each target assembly. The corresponding numbers of recorded neutrons were about 35.5, 70.5, 141.0, 281.5, and 392.0 thousand for the tungsten target, while those for the uranium target were 32.5, 65.0, 130.0, 260.7, and 360.0 thousand.

These seven neutron source files are utilized for the radial shield analysis of the KIPT neutron source facility. The radial shield configuration with heavy concrete (density 4.8 g/cm^3) is shown in Fig. IV.2.1.1. An annular tally is located next to the shield boundary with axial height 50 cm, which is aligned with the active fuel length. A shield design study performed with MCNPX is reported in References IV.2.2, IV.2.3; this study used 200 MeV electrons and concluded that 180 cm of heavy concrete would be needed for the radial shield to reduce the neutron dose at the shield surface below 0.5 mrem/hr. However, the final facility accelerator design has 100 MeV electrons so a new series of MCNPX scoping simulations were performed using different thicknesses for the radial shield. This analysis concluded that, to keep the neutron dose below 0.5 mrem/hr, the thickness of the heavy concrete shield must be 140 cm thick in the radial direction. Fission reactions were simulated when using source file number one, while they were turned off in the calculations using source files two through seven. When the neutron fission reactions were turned off, computation time was significantly reduced, as shown in Table IV.2.1.1.

The calculated neutron dose outside the radial shield, as well as the computation time for the source generation and the neutron dose calculation, are given in Table IV.2.1.1 for the seven source files of both target configurations. The statistical error of the neutron dose

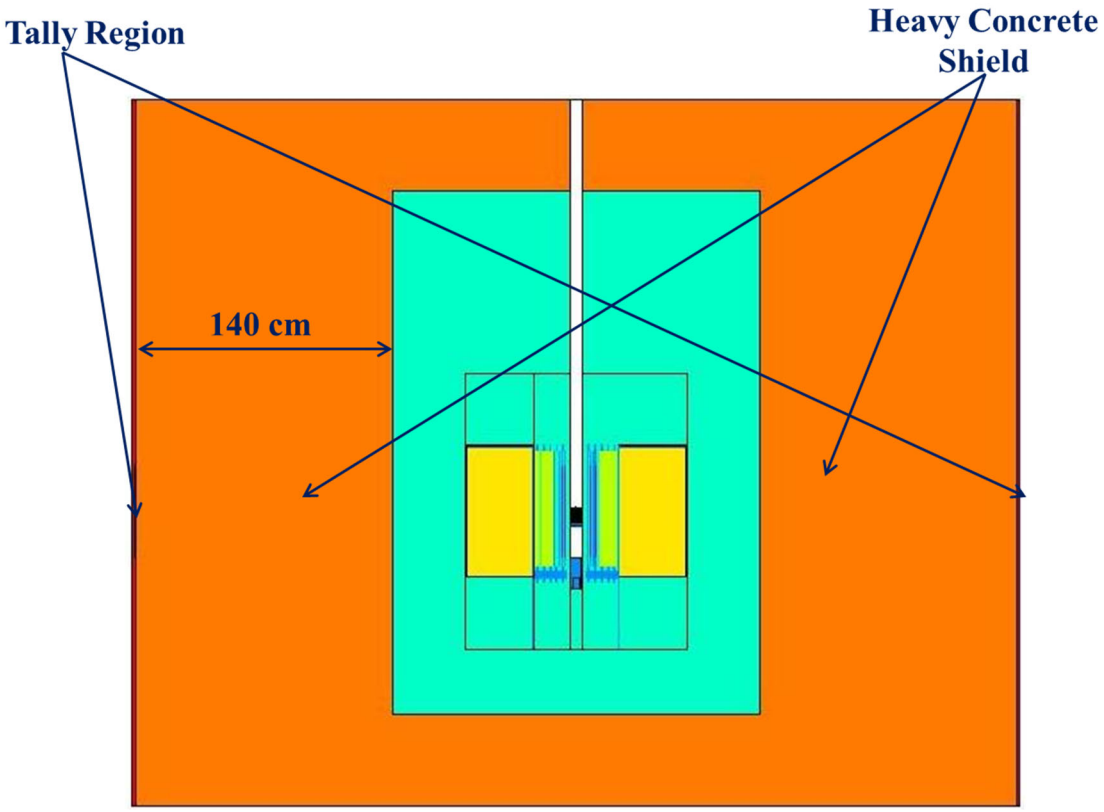

Figure IV.2.1.1. Vertical cross section of MCNPX geometrical model of radial shield configuration

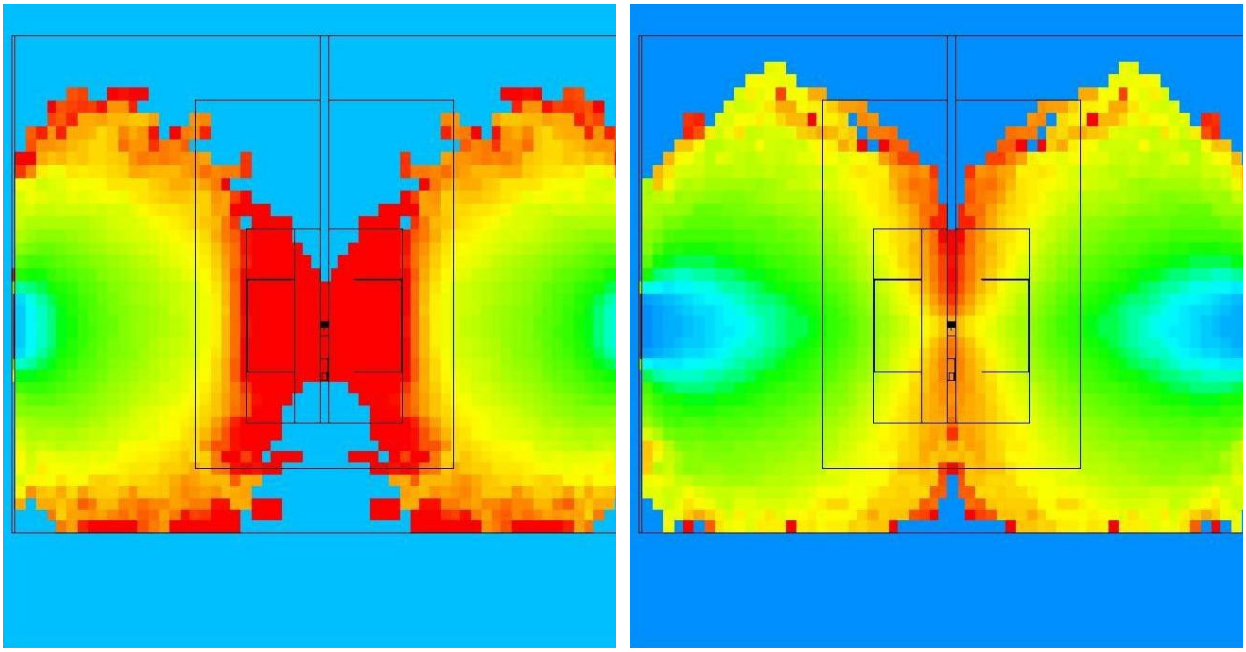

***E* < 10.0 MeV** ***E* > 10.0 MeV**

Figure IV.2.1.2. Two-group neutron weight windows for the radial shield with tungsten target

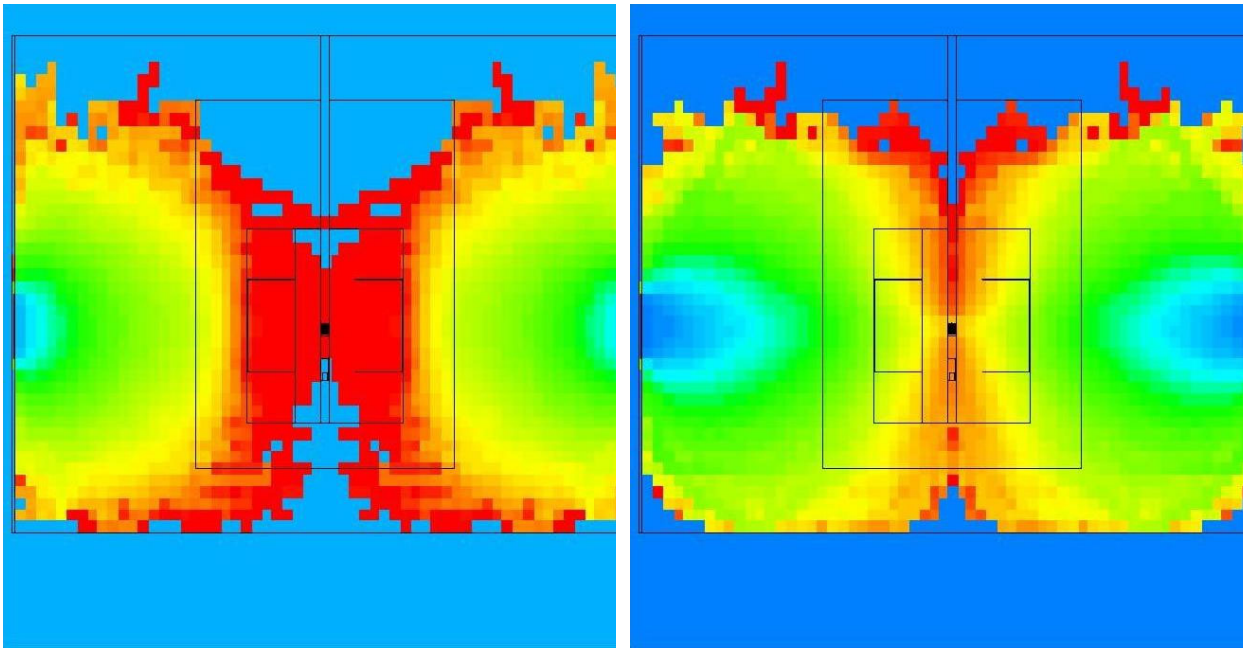

***E* < 10.0 MeV** ***E* > 10.0 MeV**

Figure IV.2.1.3. Two-group neutron weight windows for the radial shield with uranium target

calculation is also presented in Table IV.2.1.1 for each analysis. The weight windows variance reduction technique was used for these calculations. The two-energy-group weight windows were generated by using the neutron source files with 2 billion electrons sampled and are plotted in Fig. IV.2.1.2 for the tungsten target option and in Fig. IV.2.1.3 for the uranium target option.

The biological dose results at the shield boundary obtained from the first two source files show small differences within the statistical errors. This confirms that the contribution from low-energy neutrons (E<10 MeV), including fission neutrons, to the dose value at the shield boundary is negligible compared to that from the high-energy neutrons generated in the target. Moreover, the required computer time for the dose calculation without fission events was reduced by a factor of more than 25. The differences in the calculated dose using files 2 and 5 are ~30% and 33% for the tungsten and uranium target configurations, respectively, although the statistical error in the dose calculation is <1%. This indicates that the source file sampling for source file 2 is insufficient. When the dose values obtained with files 5 through 7 are compared, the differences are very small, thus confirming the sampling adequacy of these source files for the dose calculations.

The calculated dose values for both targets are presented in Fig. IV.2.1.4 as a function of the number of electrons sampled for generating the source file. The dose values reach saturation as the number of sampled electrons exceeds 720 million, so increasing the number of electrons above that level does not benefit the dose calculation. Source generation time is relatively high, but it is done only once. However, the shield calculations

need several iterations to generate the weight windows and determine the shield parameters to reach the required dose value. Changing the outer shield boundary does not require repeating the source generation process. Therefore, this approach provides an efficient procedure for designing the biological shield within a reasonable time without excessive computer resources.

The photon doses have also been calculated, with the calculations starting from the electron source. Weight windows were again generated and used in the calculation. The two-energy-group photon weight windows are plotted in Figs. IV.2.1.5 and IV.2.1.6. The calculated photon, neutron, and total doses outside the radial shield are shown in Table IV.2.1.2, the neutron doses of this table were calculated using neutron source files with 2 billion electron particles sampled. The total dose outside the radial heavy concrete shield, with shield thickness 140 cm, is below the 0.5 mrem/hr guideline for both target cases. It can be also seen that the neutron dose outside the shield boundary is larger when the tungsten target is used than it is when the uranium target is used, even though the neutron flux in the subcritical assembly region is much lower for the tungsten target case (see section III.3). This is due to the larger yield of high-energy neutrons from the tungsten target.

Table IV.2.1 1. Neutron biological dose values outside the radial shield calculated with different neutron source files

Subcritical Assembly Configuration	Source File Number	Number of Source Particles		Computation Time (hr)		Biological dose (mrem/hr)
		Electrons	Neutrons	Source File Generation	Neutron Dose Calculation	
Tungsten with 38 fuel assemblies	1	60 million	200 million	45.83	102.15	0.379 ±4.19%
	2	60 million	40 million	45.83	3.79	0.372 ±0.83%
	3	180 million	80 million	135.86	8.25	0.336 ±0.62%
	4	360 million	80 million	284.66	7.94	0.299 ±0.67%
	5	720 million	160 million	554.82	15.91	0.286 ±0.48%
	6	1.44 billion	160 million	1106.35	15.57	0.285 ±0.50%
	7	2 billion	160 million	1535.33	15.93	0.285 ±0.48%
Uranium with 37 fuel assemblies	1	60 million	200 million	56.90	165.32	0.175 ±6.83 %
	2	60 million	40 million	57.68	4.72	0.181 ±0.97 %
	3	180 million	80 million	159.16	8.80	0.162 ±0.70 %
	4	360 million	80 million	334.91	8.42	0.141 ±0.76 %
	5	720 million	160 million	680.96	16.75	0.136 ±0.57 %
	6	1.44 billion	160 million	1355.85	16.54	0.133 ±0.56 %
	7	2 billion	160 million	1886.66	16.72	0.134 ±0.56 %

Table IV.2.1 2. Neutron, photon, and total biological dose outside the radial shield

particles	Biological dose (mrem/hr)	
	Tungsten target with 38 fuel assemblies	Uranium target with 37 fuel assemblies
neutron	0.285 ± 0.48%	0.134 ± 0.56%
photon	0.042 ± 1.25%	0.065 ± 2.28%
total	0.327 ± 0.45%	0.199 ± 0.83%

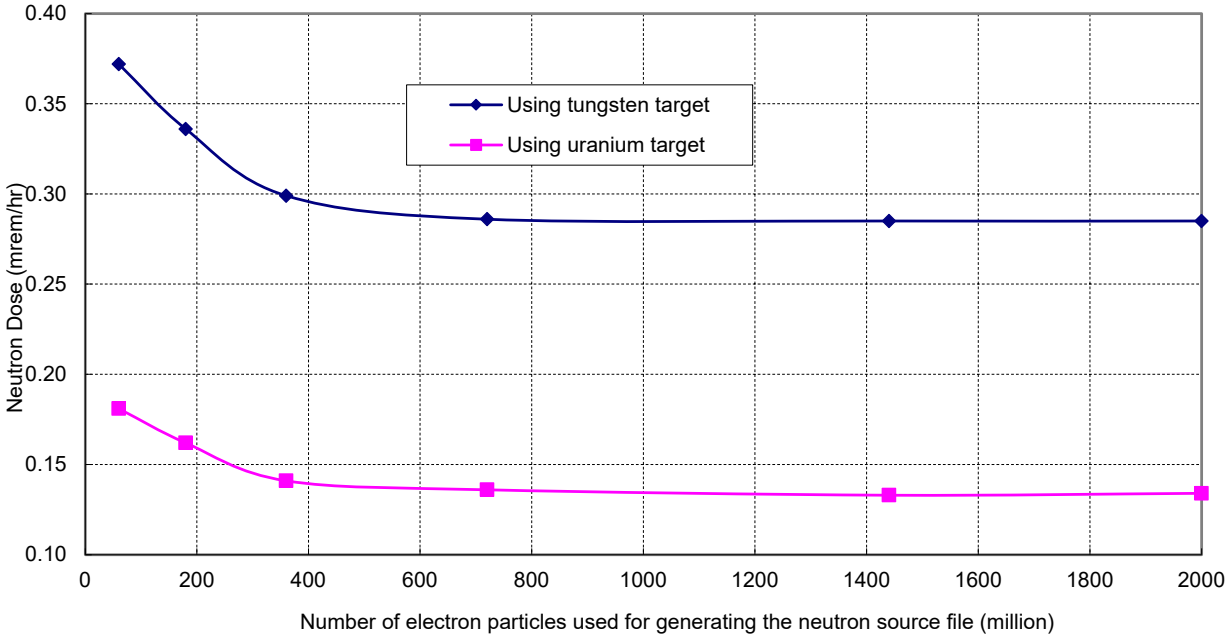

Figure IV.2.1.4. Neutron biological dose outside the radial shield with various numbers of electron particles used for generating the neutron source file

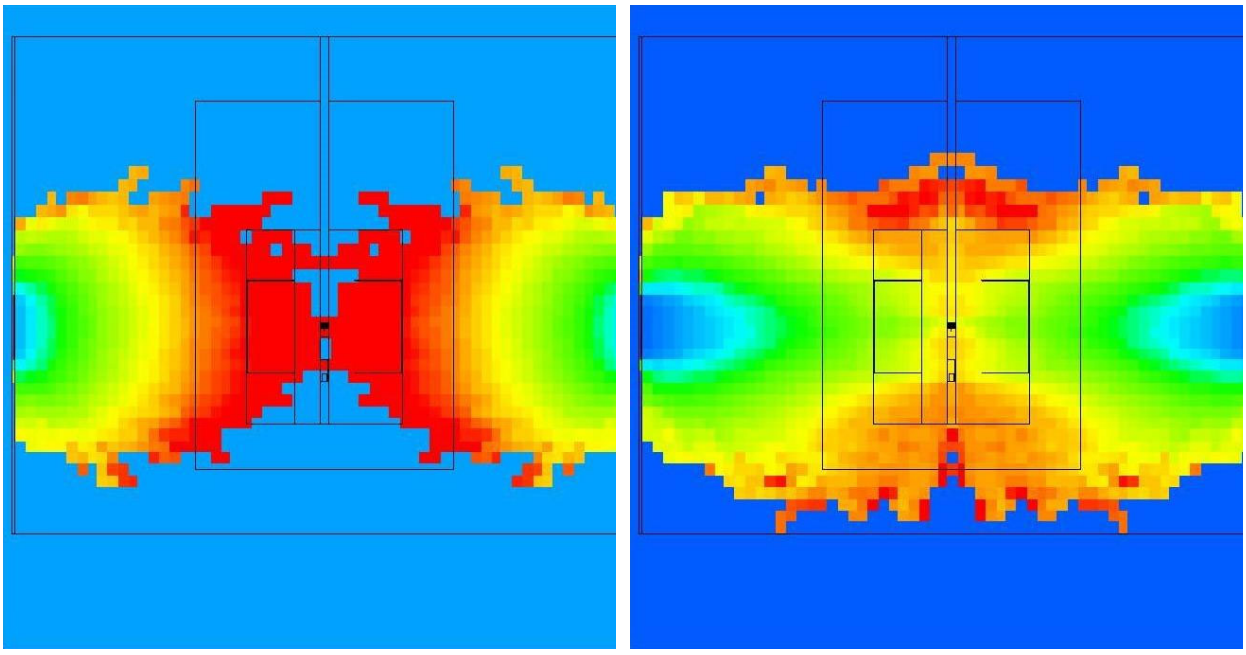

E < 1.0 MeV *E* > 1.0 MeV

Figure IV.2.1.5. Two-group photon weight windows for the radial shield with tungsten target

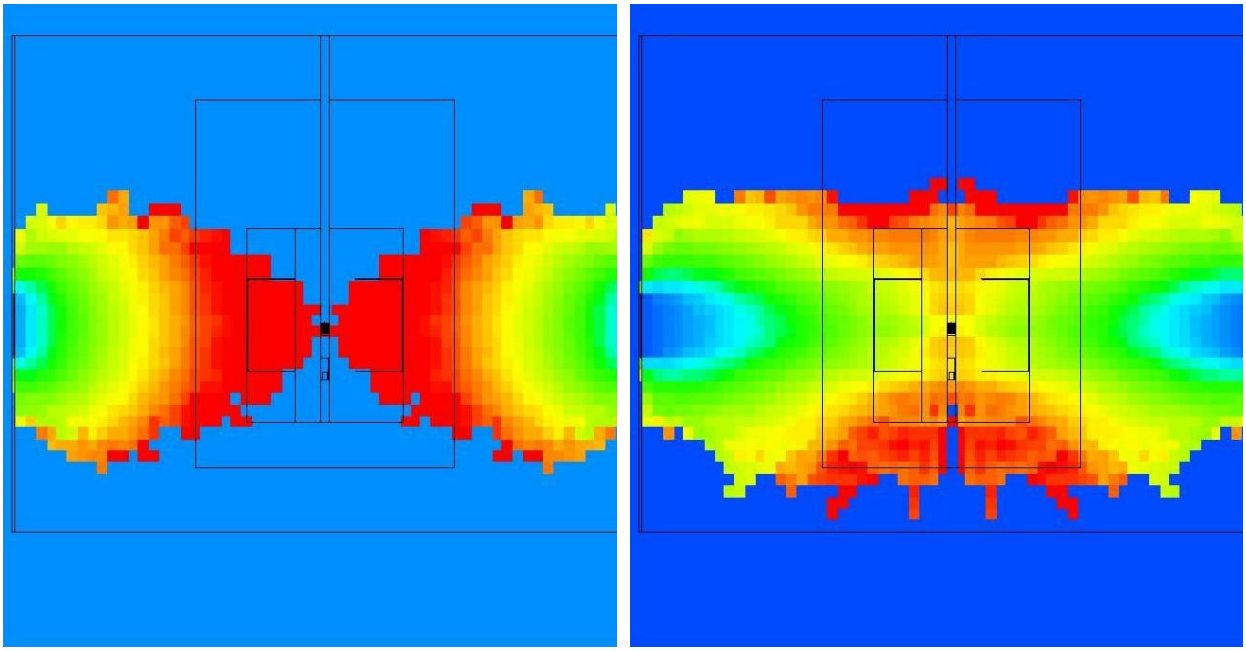

E < 1.0 MeV *E* > 1.0 MeV

Figure IV.2.1.6. Two-group photon weight windows for the radial shield with uranium target

IV.2.2 Top Shield Analyses

The neutron source file was also utilized for the top shield design and analyses, which is more complicated due to the lack of geometrical symmetry. In addition to the radiation from the target and the subcritical assembly, the biological dose due to electron beam losses at the bending magnets must also be considered. Most of the electron losses occur at the B1 bending magnet for the electrons with energy more or less than 100 MeV. In this analysis, the electron beam loss at the B1 bending magnet is ~700 W, which is estimated by the accelerator manufacturer as the maximum possible beam losses during operation. In addition, these electrons have a uniform distribution between -5º and 30º relative to the electron beam axis as shown in Fig. IV.2.2.1.

The top biological shield is composed of two pieces that can be separated along the electron beam line for installing the target. During normal operation of the facility, these two sections of the shield are closed to form a continuous shield envelop. However, it is difficult to fabricate large shield parts with zero gap thickness between the two large moving parts, a conservative gap thickness of 10 mm is assumed for the analyses. Heavy concrete is selected as the shield material. After a series of MCNPX calculations and analyses, the geometry and parameters of the top shield were determined; these are shown in Figs. IV.2.2.2 and IV.2.2.3. The contacting gap has a staggered shape to reduce the leakage of neutrons and photons as shown in Fig. IV.2.2.3. The geometry and parameters of the gap are shown in Figs. IV.2.2.4 and IV.2.2.5.

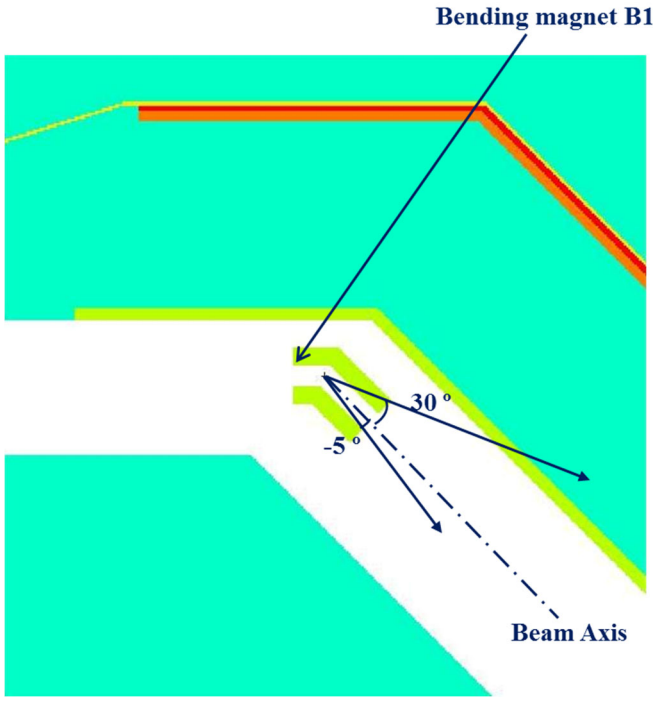

Figure IV.2.2.1. Electron beam losses at the B1 bending magnet

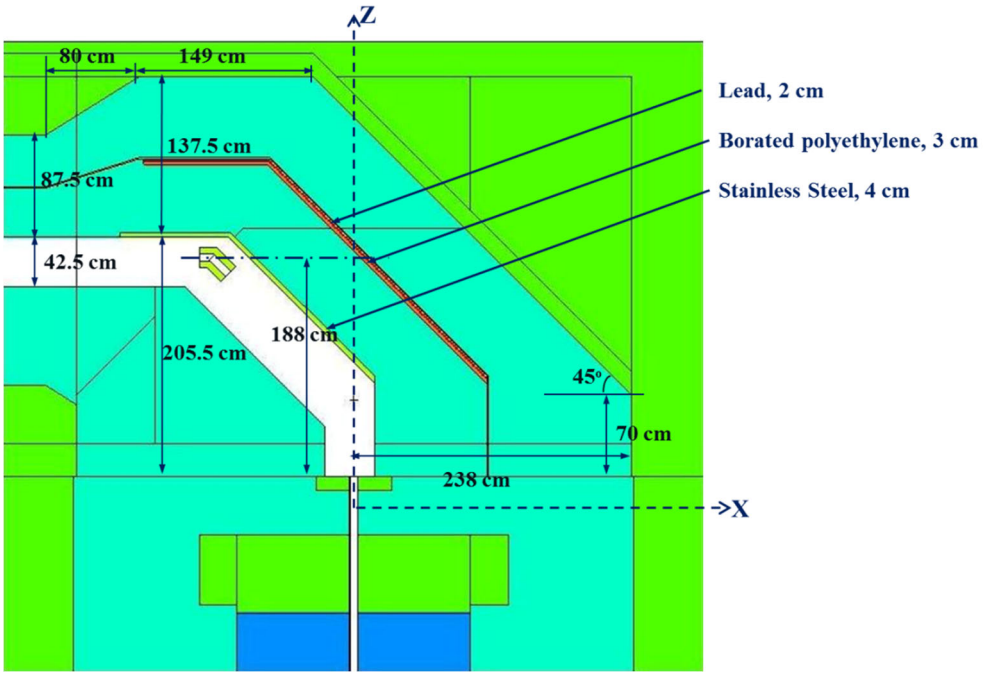

Figure IV.2.2.2. X-Z cross section of the top shield geometry at Y=0

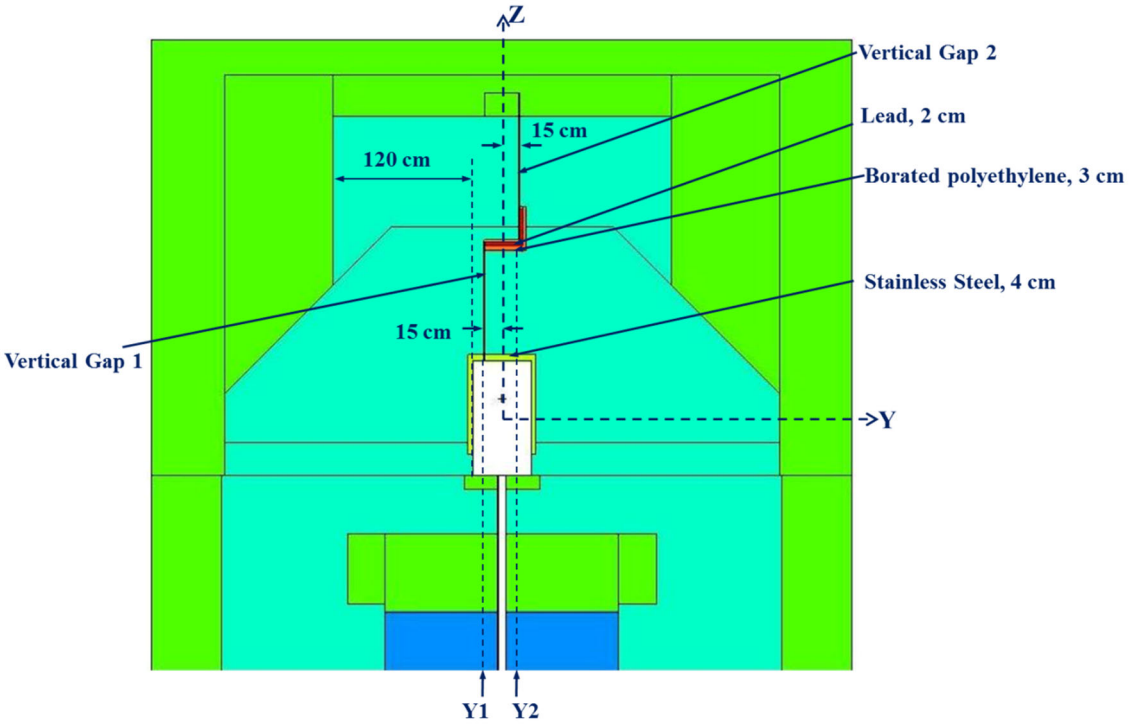

Figure IV.2.2.3. Y-Z cross section of the top shield geometry at X=0

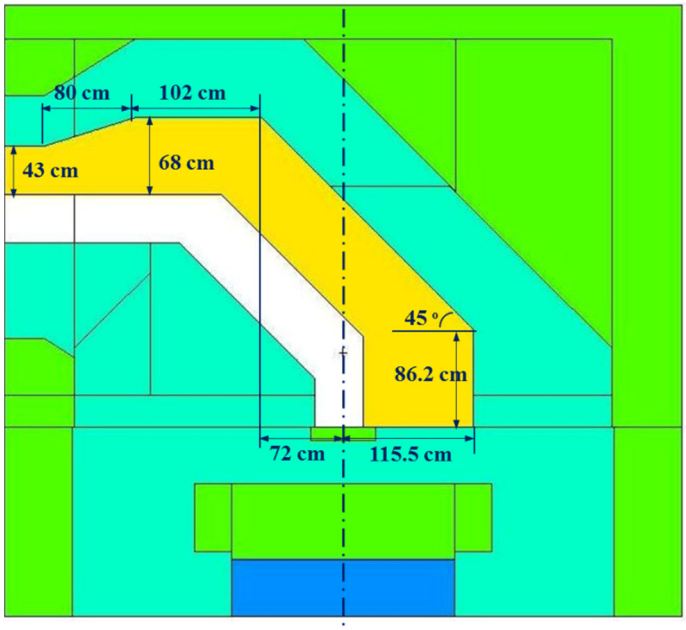

Figure IV.2.2.4. X-Z cross section of the top shield geometry at Y=-15 cm

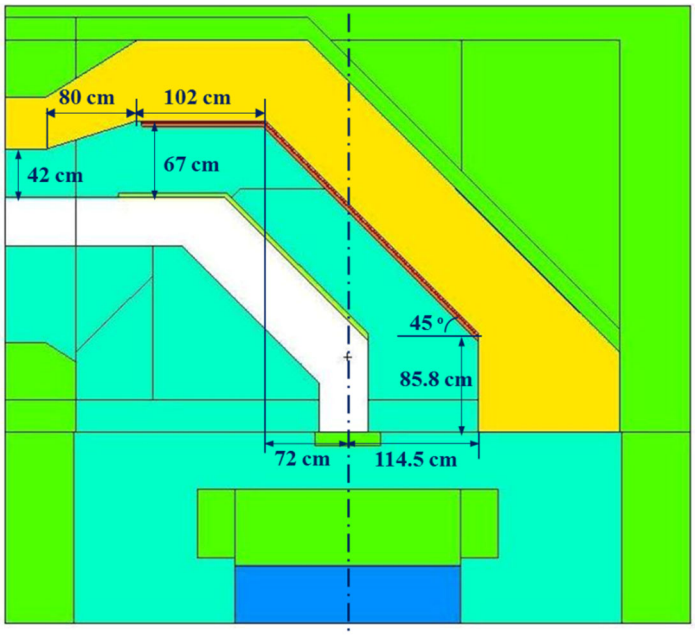

Figure IV.2.2.5. X-Z cross section of the top shield geometry at Y=+15 cm

To reduce the neutron and the gamma leakage from the 10 mm gap, a layer of borated polyethylene (thickness 3 cm thick) and a layer of lead (2 cm thick) are added along the boundary of the gap. A stainless-steel layer with a thickness of 4 cm is also added at the border between the shield and the electron beam, to reduce the nuclear heating in the heavy concrete from the electron losses, see Sec. IV.3 for the analysis. The positioning of these layers is shown in Figs. IV.2.2.6 and IV.2.2.7, as well as in Figs. IV.2.2.2 and IV.2.2.3.

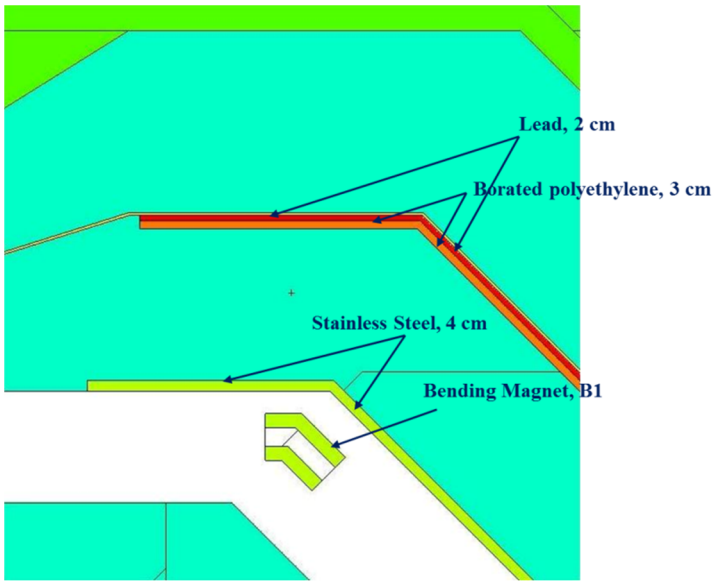

Figure IV.2.2.6. Borated polyethylene, lead, and stainless steel to account for the electron losses in the X-Z plane

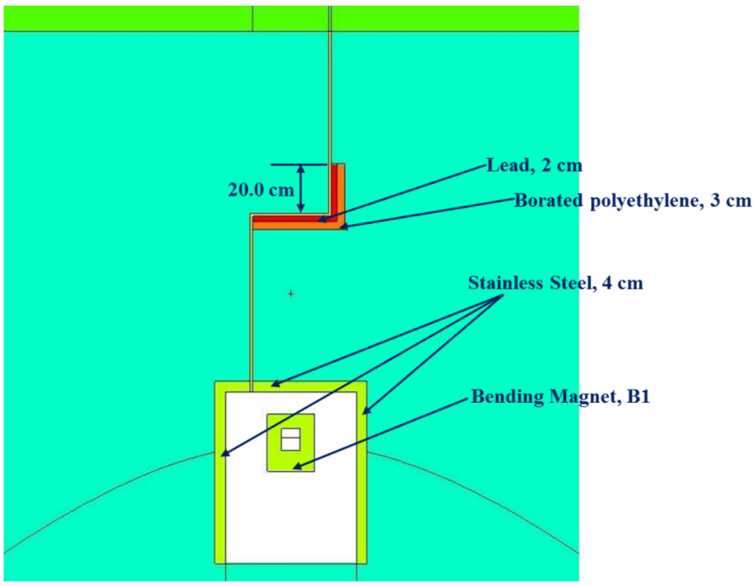

Figure IV.2.2.7. Borated polyethylene, lead, and stainless steel to account for the electron losses in the Y-Z plane

The neutron and photon dose profiles through the top shield due to the electron beam losses at the B1 bending magnet have been calculated by MCNPX. The neutron dose is calculated by generating and using a neutron source file, as discussed previously. The neutron source file records neutrons in the whole energy range, because low-energy neutrons could leak through the contacting gap and cause additional biological dose outside the shield. The photon dose is calculated by using an electron source. The weight windows variance reduction technique is also utilized in the calculation, optimizing the tally along the shield boundary in the X-Z plane. The neutron and photon dose profiles through the top shield have been calculated using the mesh tally capability of MCNPX.

The calculated dose profiles in the X-Z plane are plotted in Figs. IV.2.2.8 through IV.2.2.13. The dose profiles are tallied at different Y positions. One set of dose profiles is tallied at Y=15 cm and averaged over the 1.0 cm gap thickness, to show the maximum dose value caused by neutron and photon leakage from the gap. Another set of dose profiles is tallied at the centerline and averaged over in the Y direction from Y=-15 cm to Y=15 cm. The dose values averaged over the gap thickness are larger than those averaged in the Y direction around the centerline. The photon dose averaged over the gap thickness is larger than the neutron dose. Therefore, the contribution of both neutron and photon doses must be included.

As shown in Fig. IV.2.2.12, the 0.5 mrem/hr contour line is beyond the shield boundary. However, these results assume a 10 mm uniform gap. The actual manufacturing tolerance of the two pieces of top shield would be expected to produce a contacting gap with an average thickness of less than 5 mm. Another set of calculations has been performed with the same shield geometry but reducing the gap thickness to 5 mm. The dose profiles averaged over the 5 mm gap thickness are shown in Figs. IV.2.2.14 to IV.2.2.16 compared with the cases with the 10 mm gap thickness, the plots in Figs.

IV.2.2.14 through IV.2.2.16 indicate that the dose values averaged over the 5 mm gap thickness are much smaller. Fig. IV.2.2.16 shows the 0.5 mrem/hr contour line is slightly beyond the shield boundary near the B1 bending magnet. In reality, the dose will be much less because of a) the gap thickness will vary from 0 to 5 mm, b) the beam losses of 700 W from 100 MeV electrons is an upper estimate, and c) the shield model does not include the magnet materials and the support steel structure. All these factors will significantly reduce the dose values.

The dose profiles in the Y-Z plane were also calculated for X=0 at the center of the B1 bending magnet to determine the required thickness of shielding needed in the Y direction. The configuration of the top shield in the Y-Z plane for X=0 at the B1 bending magnet is shown in Fig. IV.2.2.17. The weight windows have been generated to optimize the tally outside the shield boundary along the X direction, and the tally positions are also shown in Fig. IV.2.2.17. The calculated dose profiles are shown in Figs. IV.2.2.18 through IV.2.2.20. Based on the analysis results, the 120-cm of heavy concrete along the Y direction is sufficient to keep the total dose below 0.5 mrem/hr and that the photon dose outside the shield is much smaller than the neutron dose. The required shield thickness in the Y direction is much smaller than that in the Z and X directions, primarily because there is no contacting gap along the Y direction.

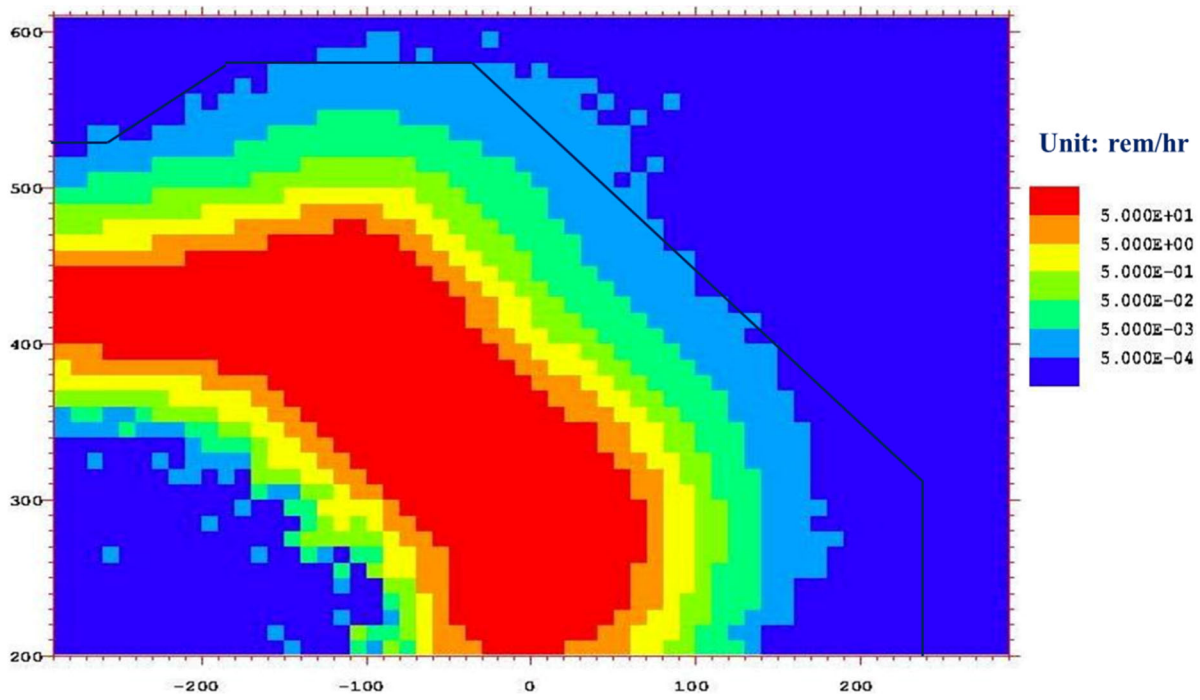

Figure IV.2.2.8. Neutron biological dose profile due to the electron beam losses in the X-Z plane at Y=15 cm averaged over the 1 cm gap thickness

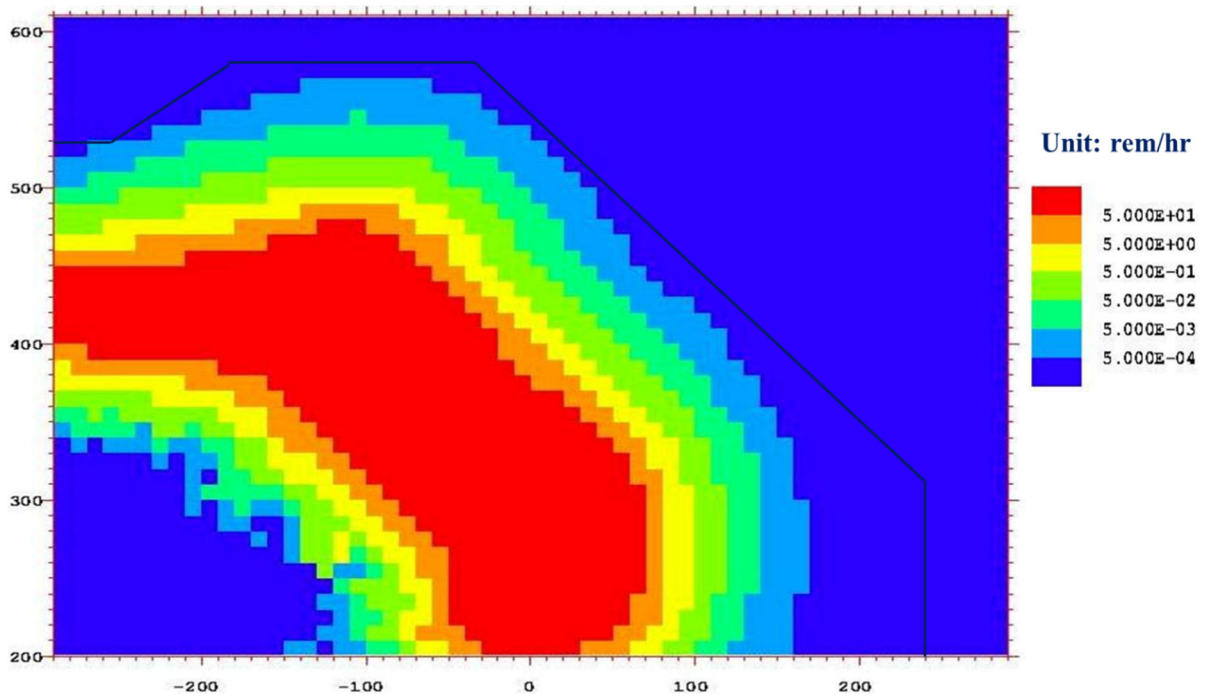

Figure IV.2.2.9. Neutron biological dose profile due to the electron beam losses in the X-Z plane averaged in the Y direction from Y=-15 to +15 cm

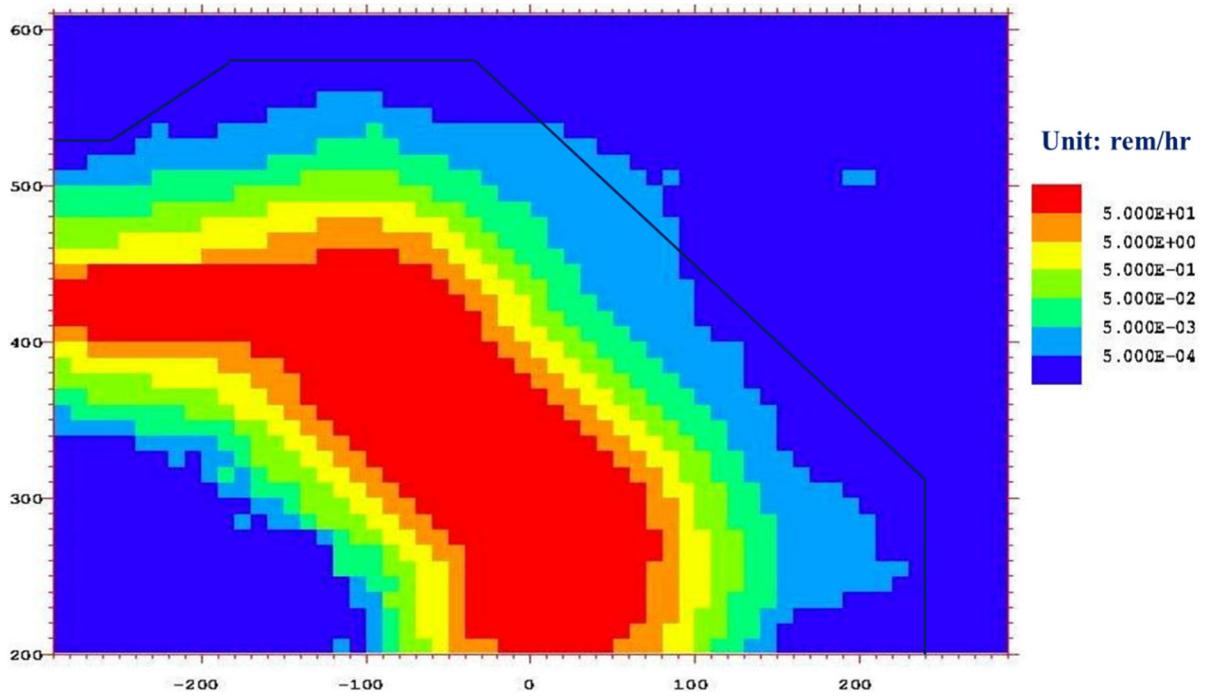

Figure IV.2.2.10. Photon biological dose profile due to the electron beam losses in the X-Z plane at Y=15 cm averaged over the 1 cm gap thickness

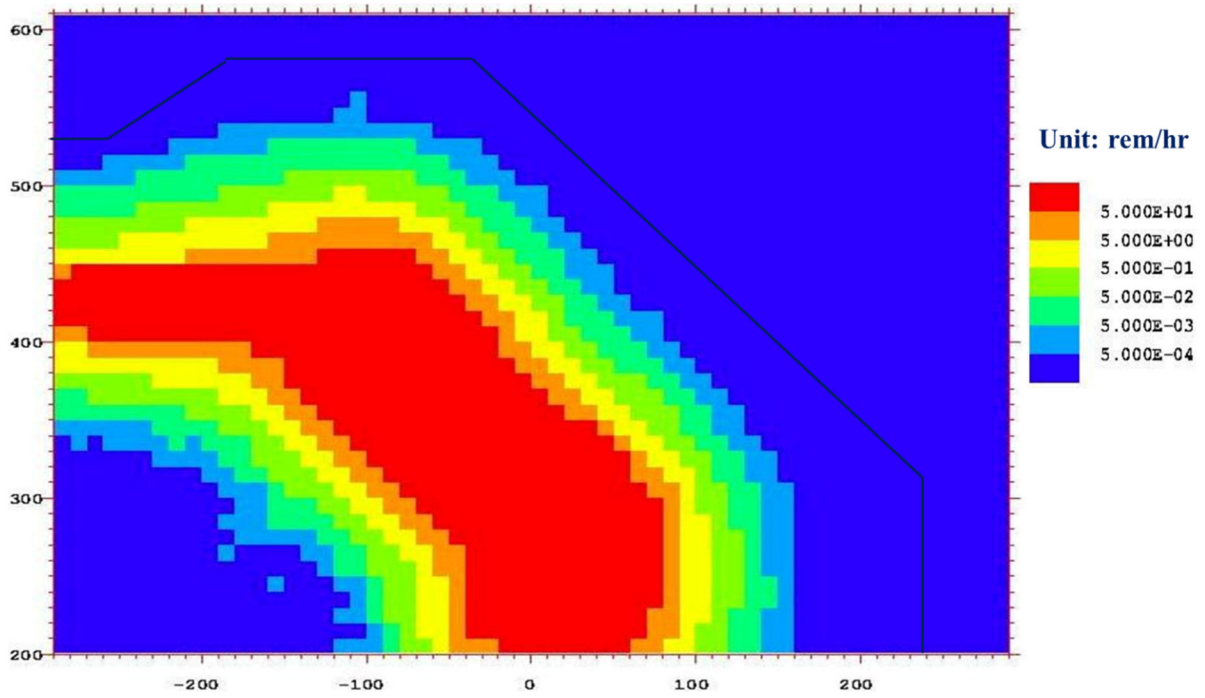

Figure IV.2.2.11. Photon biological dose profile due to the electron beam losses in the X-Z plane averaged in the Y direction from Y1=-15 to +15 cm

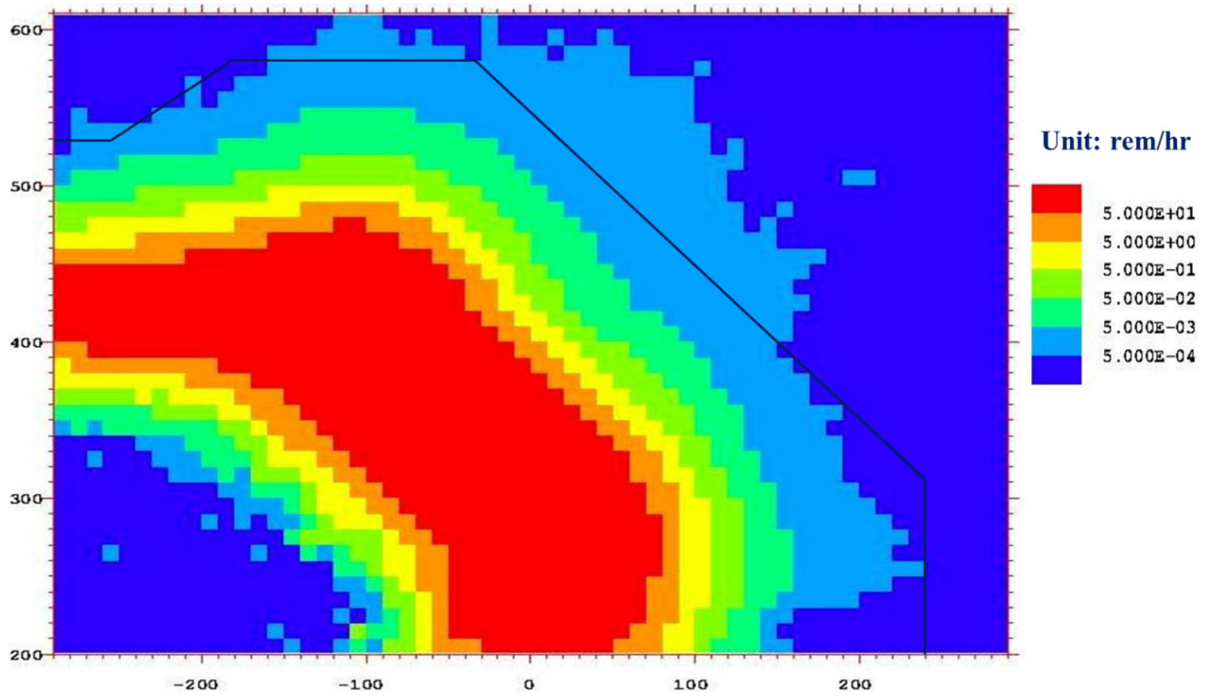

Figure IV.2.2.12. Total biological dose profile due to the electron beam losses in the X-Z plane at Y=15 cm averaged over the 1 cm gap thickness

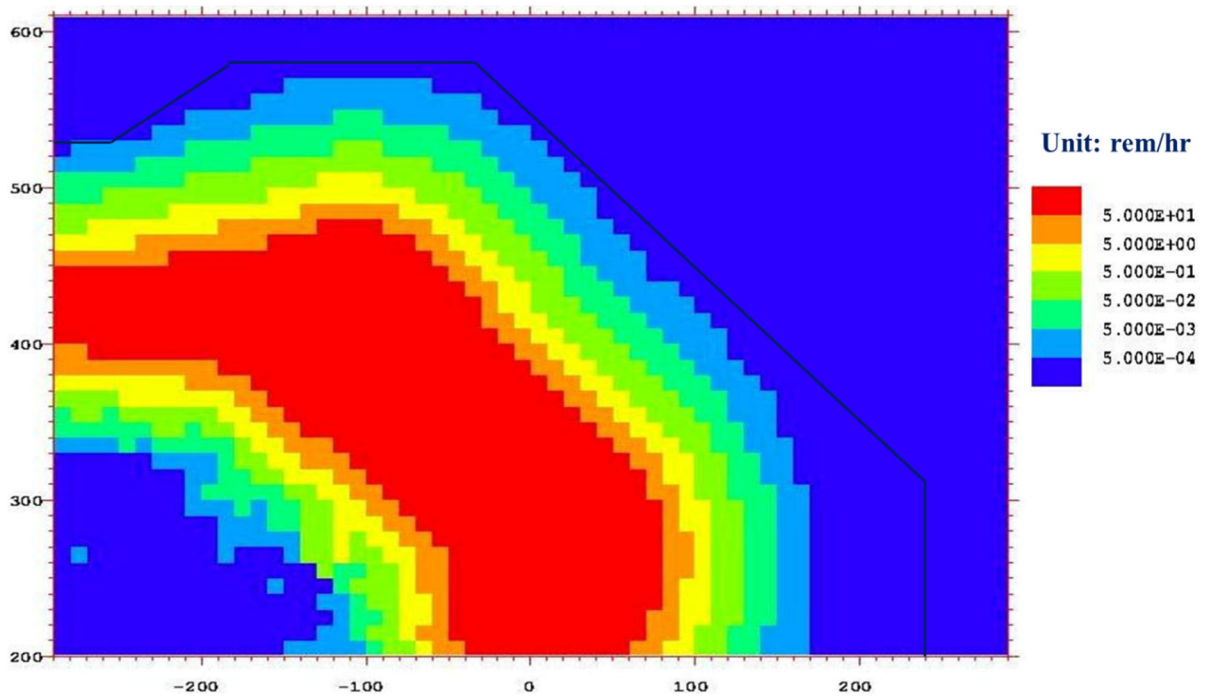

Figure IV.2.2.13. Total biological dose profile due to the electron beam losses in the X-Z plane averaged in the Y direction from Y1=-15 to +15 cm

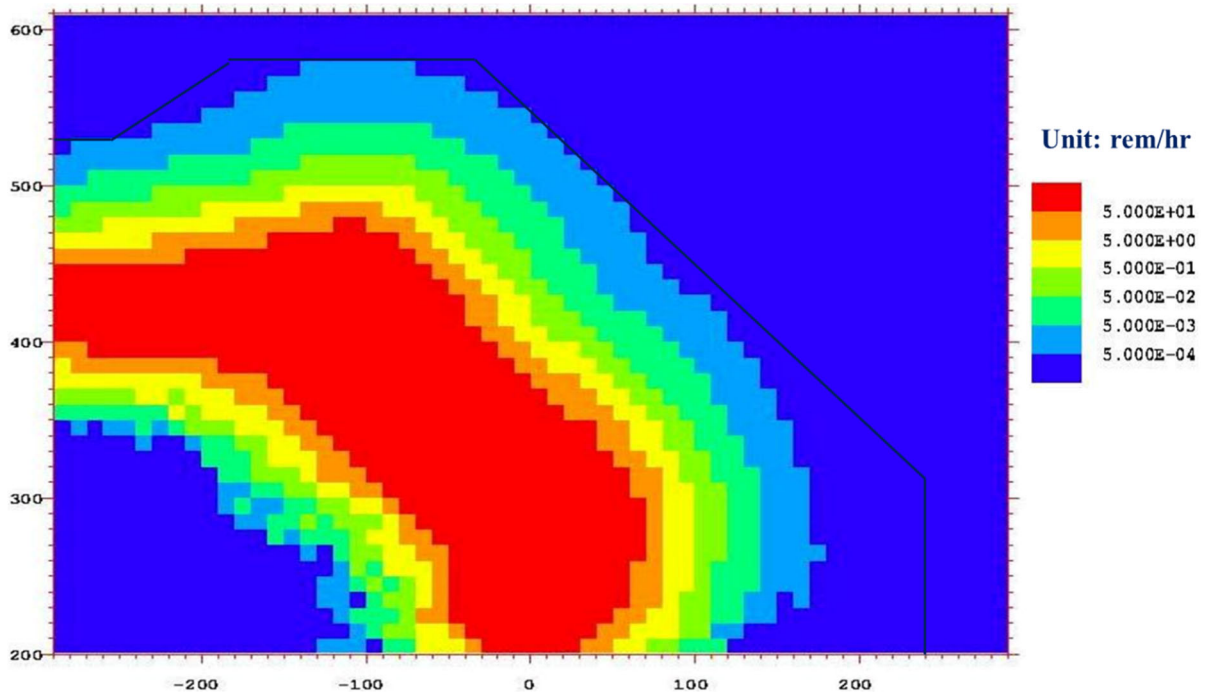

Figure IV.2.2.14. Neutron biological dose profile due to the electron beam losses in the X-Z plane at Y=15 cm averaged over the 0.5 cm gap thickness

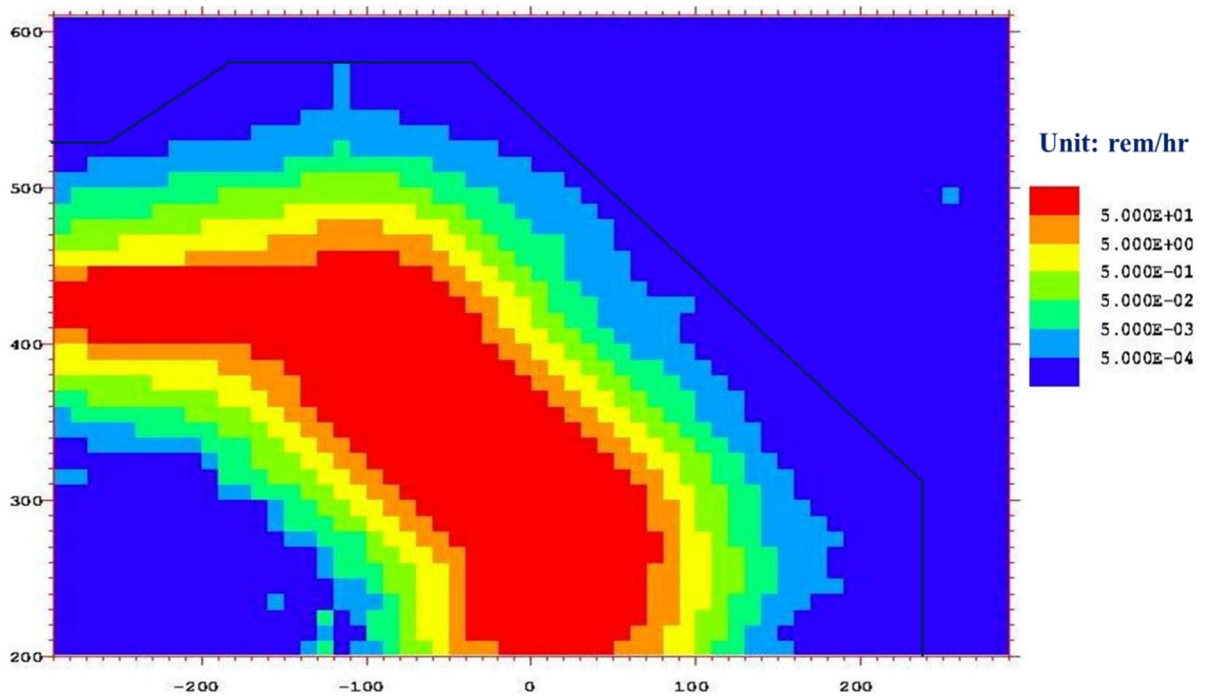

Figure IV.2.2.15. Photon biological dose profile due to the electron beam losses in the X-Z plane at Y=15 cm averaged over the 0.5 cm gap thickness

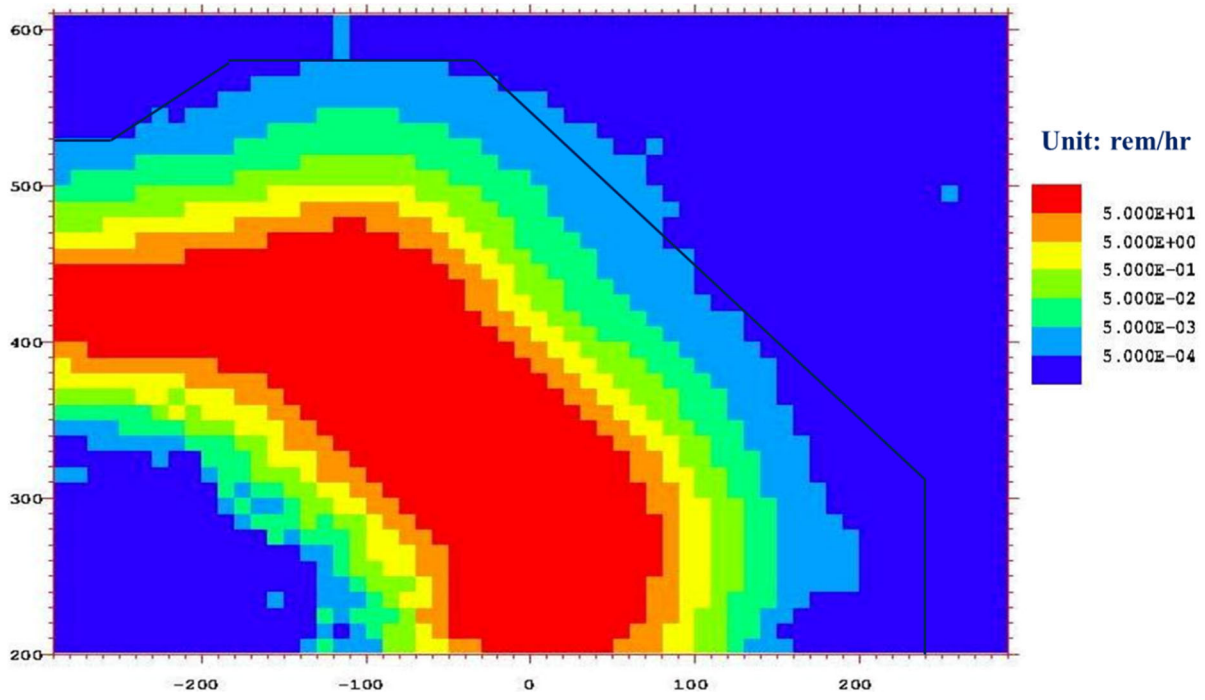

Figure IV.2.2.16. Total biological dose profile due to the electron beam losses in the X-Z plane at Y=15 cm averaged over the 0.5 cm gap thickness

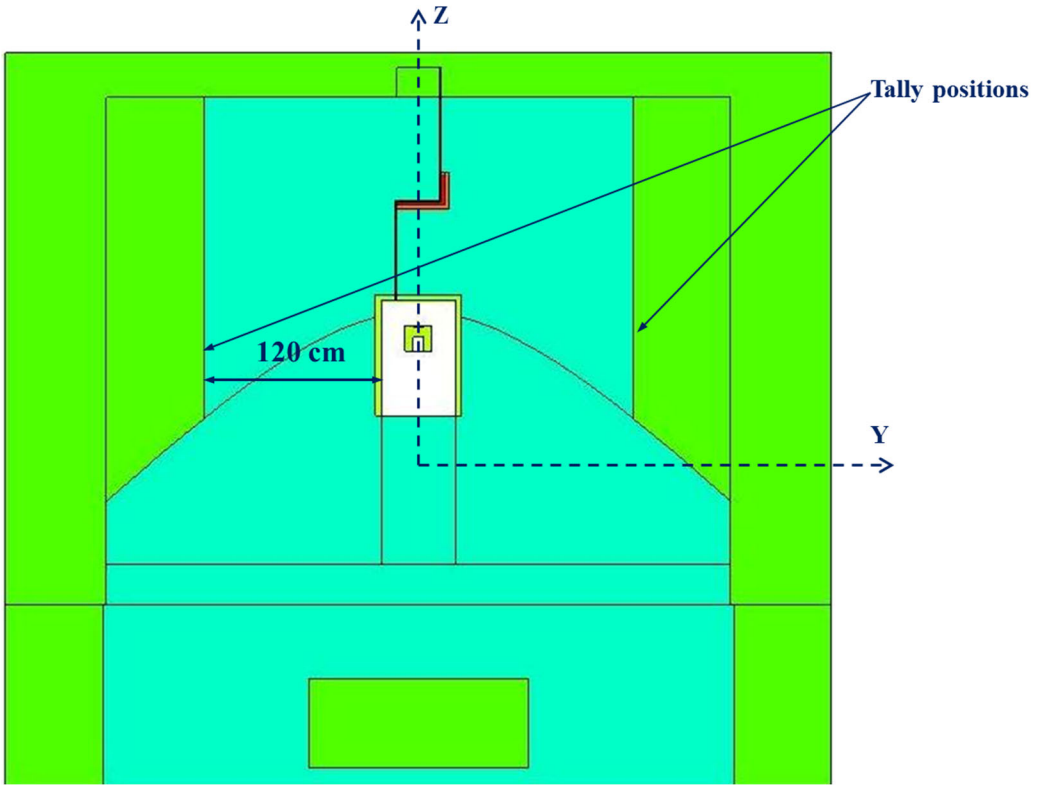

Figure IV.2.2.17. Configuration of top shield, in the Y-Z plane at the B1 bending magnet

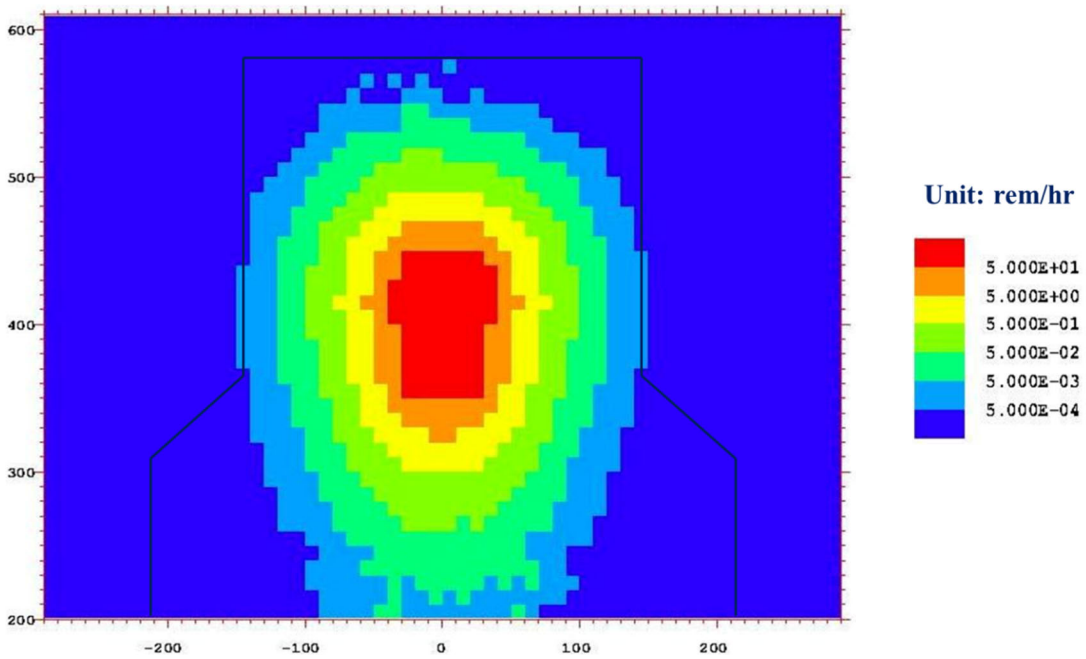

Figure IV.2.2.18. Neutron biological dose profile due to the electron beam losses in the Y-Z plane at the B1 bending magnet averaged over 10 cm in the X direction

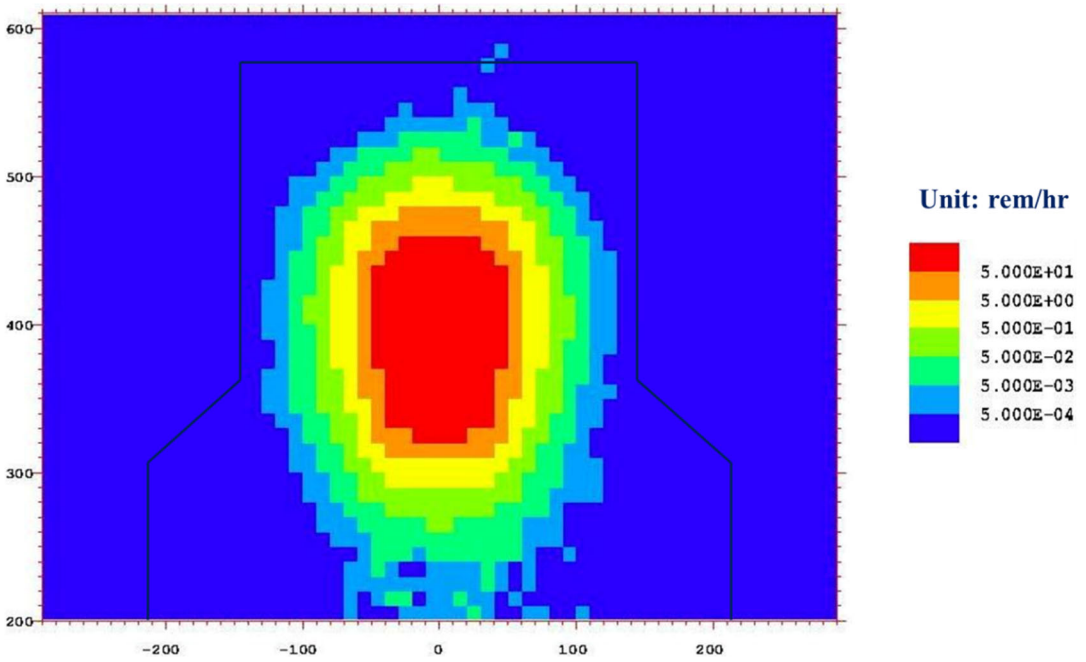

Figure IV.2.2.19. Photon biological dose profile due to the electron beam losses in the Y-Z plane at the B1 bending magnet averaged over 10 cm in the X direction

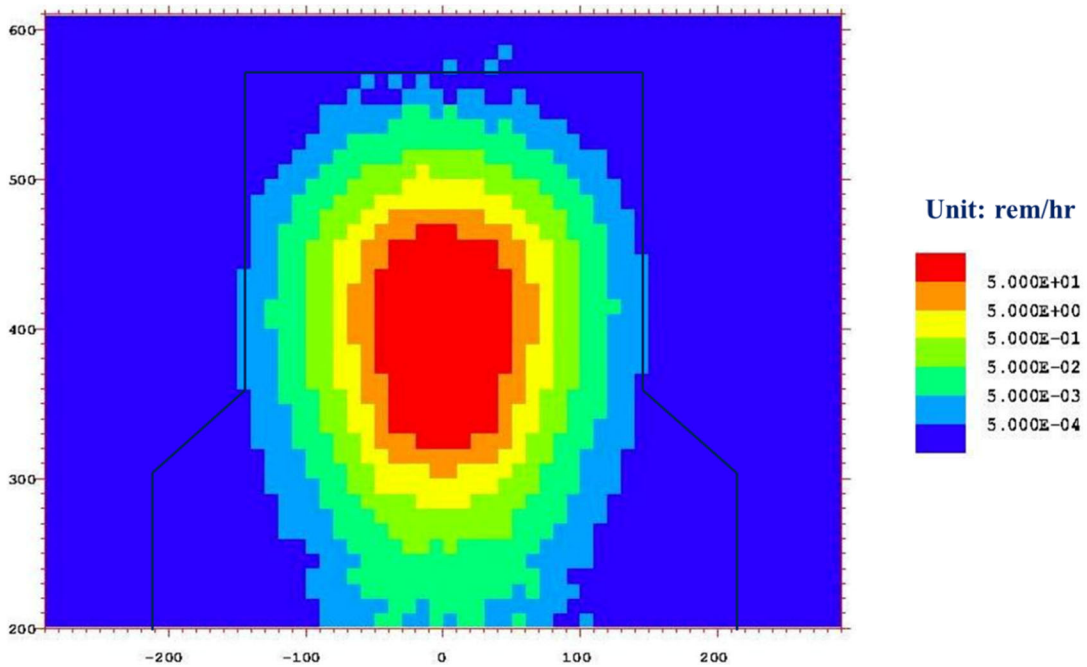

Figure IV.2.2.20. Total biological dose profile due to the electron beam losses in the Y-Z plane at the B1 bending magnet averaged over 10 cm in the X direction

Also, a horizontal contacting gap exists between the top shield and the water tank cover. The horizontal gap also has a staggered shape to reduce the neutron and photon leakage. Unlike the vertical gap, the biological dose along the horizontal gap is primarily due to the neutrons and photons coming from the target and the subcritical assembly. An MCNPX model with azimuthally symmetric geometry has been introduced, as shown in Fig. IV.2.2.21. The gap thickness is conservatively assumed to be 1.0 cm.

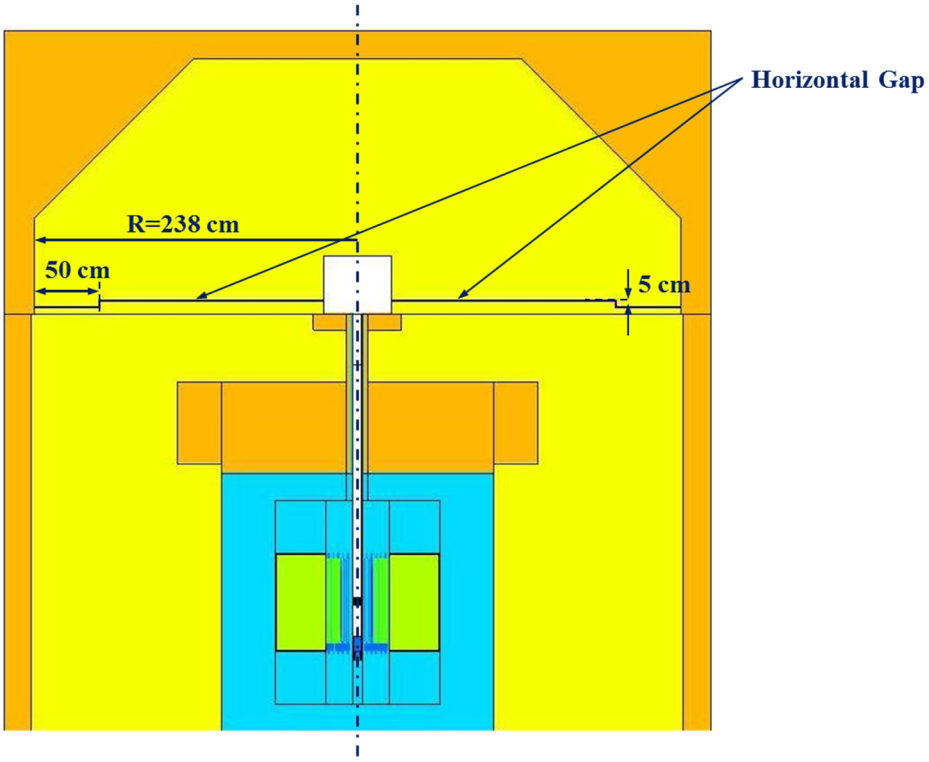

Figure IV.2.2.21. MCNPX model with a horizontal gap between the top shield and the water tank cover

The biological dose calculated by MCNPX radially outside the shield, along the horizontal gap, is presented in Table IV.2.2.1 for both the tungsten target with 38 fuel assemblies and the uranium target with 37 fuel assemblies loaded. The total biological dose from both cases is less than the 0.5 mrem/hr requirement.

The biological dose caused by the tungsten and the uranium target configurations were analyzed for the top shield design. For the tungsten target case with 38 fuel assemblies, the neutron, photon, and total biological dose profiles through the top shield have been calculated by MCNPX and shown in Figs. IV.2.2.22 to IV.2.2.24. The 0.5 mrem/hr contour line is inside the shield boundary. Similar analyses were performed for the uranium target case with 37 fuel assemblies and the results are shown in Figs. IV.2.2.25 to IV.2.2.27. Again, the 0.5 mrem/hr contour line is also inside the shield boundary. Therefore, the biological dose through the top shield from the target and subcritical assembly is negligible in comparison with biological dose from the electron losses.

Table IV.2.2.1. Neutron, photon, and total biological dose outside the shield along the horizontal gap between top shield and water tank cover to the radiation leakage from the subcritical assembly

Particles	Biological dose (mrem/hr)	
	Tungsten target with 38 fuel assemblies	Uranium target with 37 fuel assemblies
neutron	0.299 (± 3.96 %)	0.166 (± 6.39 %)
photon	0.061 (± 6.30 %)	0.129 (± 10.14 %)
total	0.360 (± 3.46 %)	0.295 (± 5.71 %)

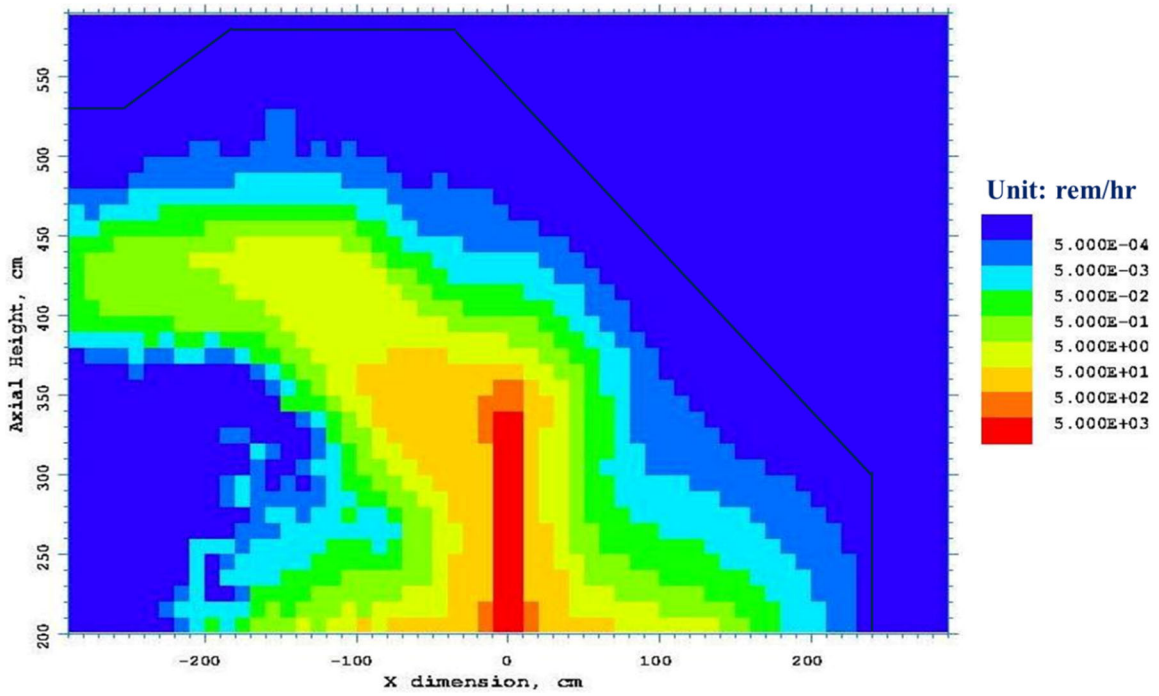

Figure IV.2.2.22. Neutron biological dose profile due to the neutron leakage from the subcritical assembly with tungsten target in top shield in the X-Z plane

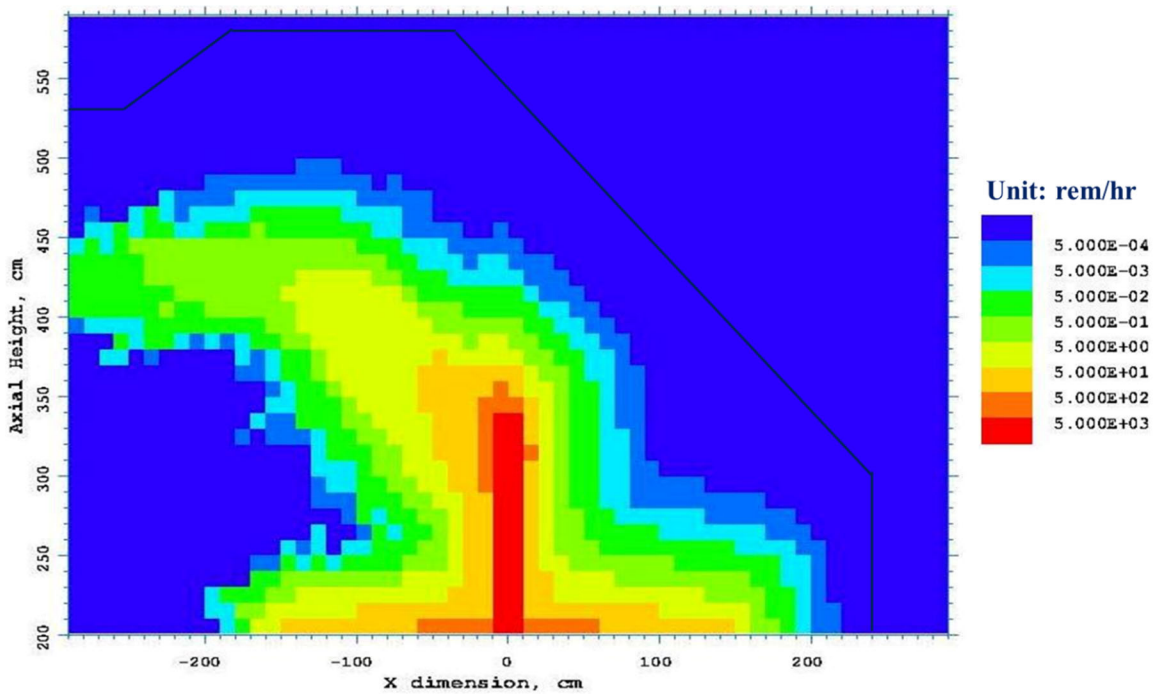

Figure IV.2.2.23. Photon biological dose profile due to the photon leakage from the subcritical assembly with tungsten target in top shield in the X-Z plane

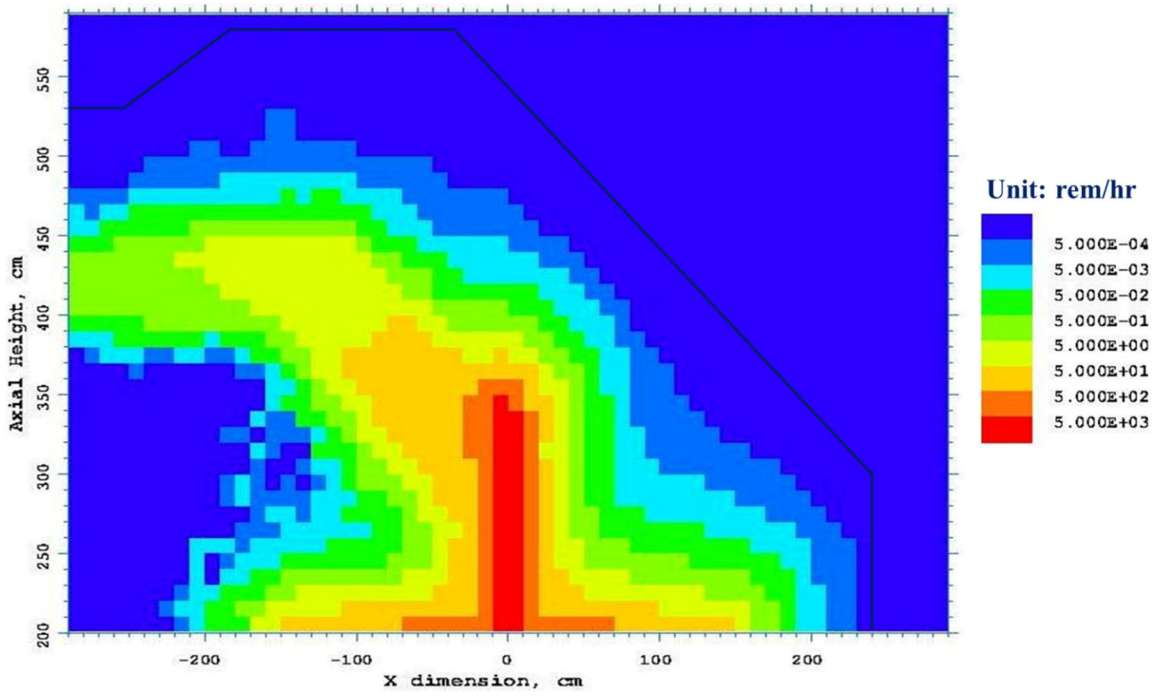

Figure IV.2.2.24. Total biological dose profile due to the neutron and the photon leakage from the subcritical assembly with tungsten target in top shield in the X-Z plane

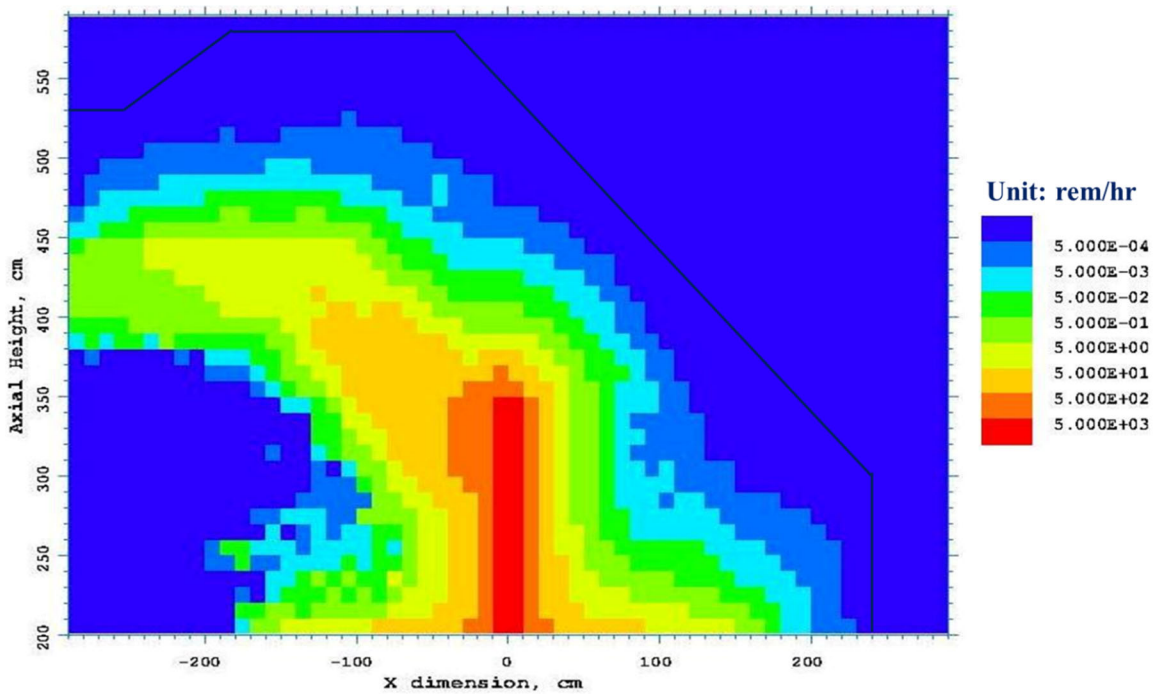

Figure IV.2.2.25. Neutron biological dose profile due to the neutron leakage from the subcritical assembly with uranium target in top shield in the X-Z plane

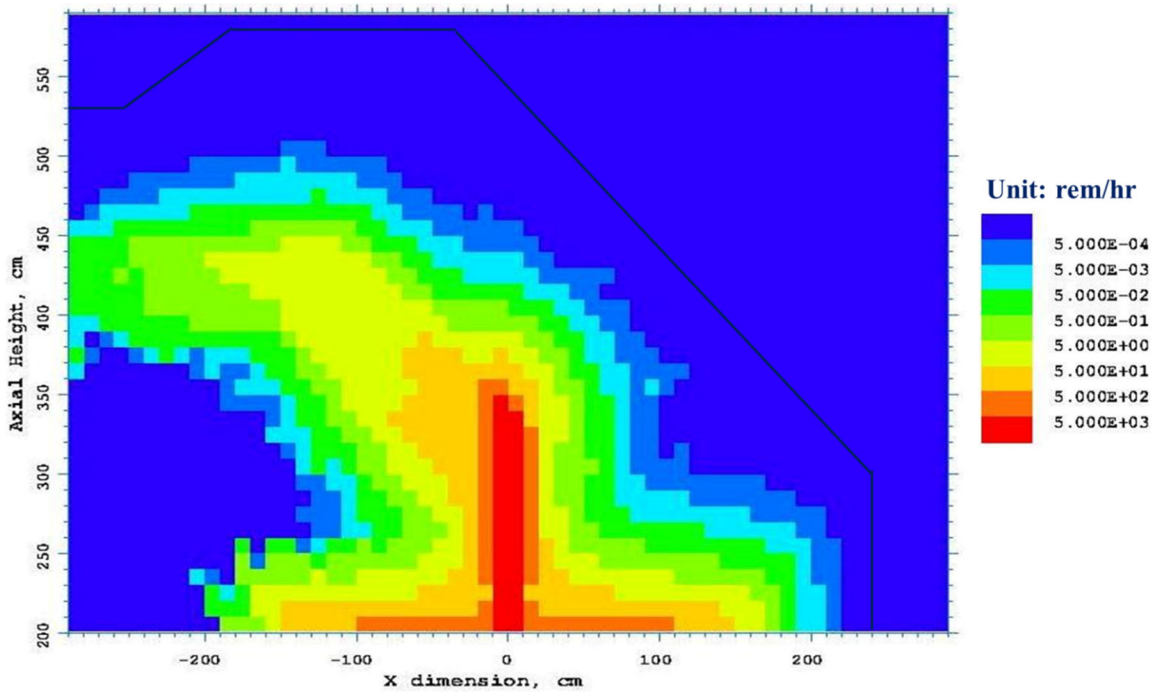

Figure IV.2.2.26. Photon biological dose profile due to the photon leakage from the subcritical assembly with uranium target in top shield in the X-Z plane

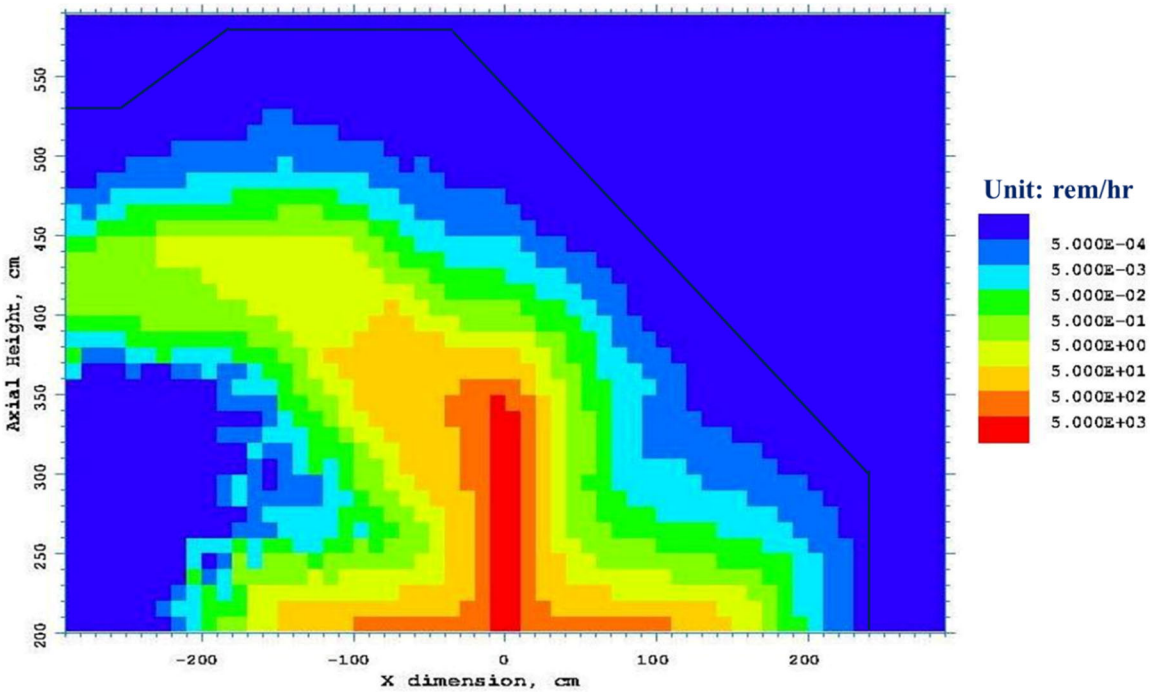

Figure IV.2.2.27. Total biological dose profile due to the neutron and the photon leakage from the subcritical assembly with uranium target in top shield in the X-Z plane

IV.2.3 Accelerator Tunnel Shield Analysis

A shield analysis was performed for the electron accelerator tunnel to define the tunnel shield thickness. The total length of the electron accelerator tunnel is ~30 m, and the tunnel can be divided into two parts. The first part contains the electron gun and the first accelerator section. This section has high electron losses, but the electron energy is relatively low. The second part includes the rest of the accelerator sections and has much lower electron loss. The leaked electrons generate photons and neutrons from their interactions with the surrounding component materials and shielding materials. Therefore, a biological shield must surround the accelerator components.

Electron beam losses were obtained from accelerator design analyses. Most occur at the first accelerator section where the electrons are accelerated to less than 15 MeV. Losses in the rest of the accelerator sections are relatively low. Electron energy changes along the accelerator tunnel are shown in Figure IV.2.3.1, and the corresponding electron losses are shown in Figure IV.2.3.2. The total power of the lost electrons shown in Fig. IV.2.3.2 is ~2.84 kW and it is distributed unevenly along the beam axis, Z. Peak electron beam loss occurs at Z = ~500 cm where the electron energy is ~12.4 MeV, as shown in Figs. IV.2.3.1 and IV.2.3.2. The peak area accounts for ~1.27 kW (45%) of the total losses. After the electron energy reaches 100 MeV, the beam losses have a uniform distribution of ~50 W/m, not shown in Figure IV.2.3.2. Although the beam losses beyond the first section are relatively much lower than those of the first section, they produce significant

photon and neutron biological doses because of the higher electron energy. The shield analyses considered all the losses along the length of the accelerator tunnel.

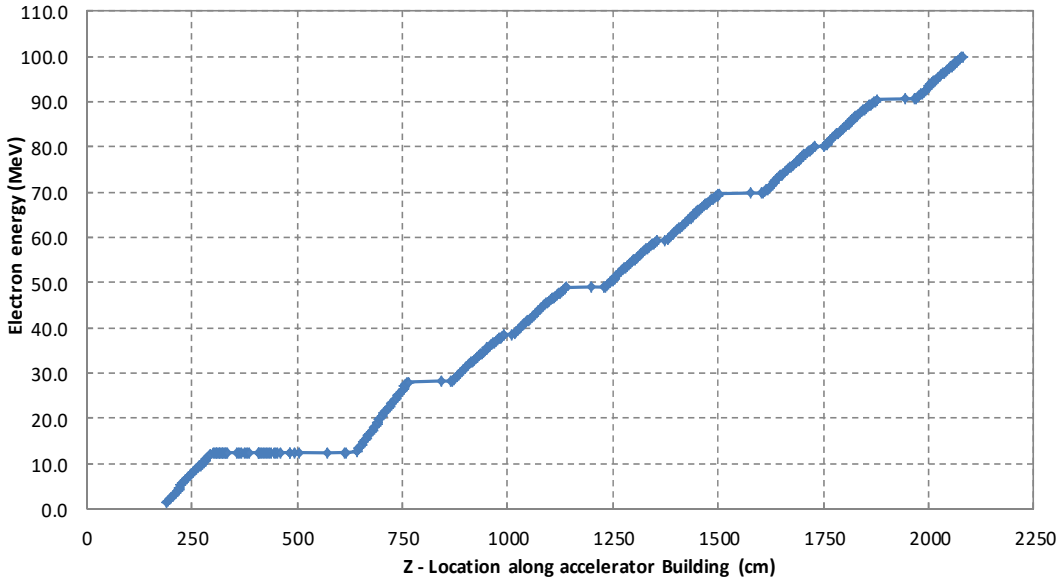

Figure IV.2.3.1. Electron energy along the accelerator tunnel

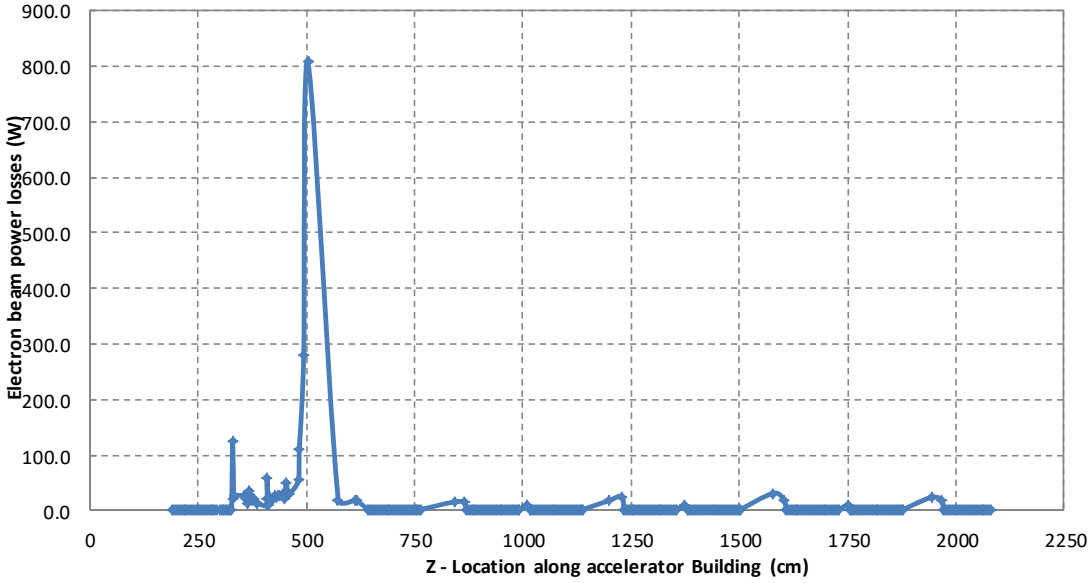

Figure IV.2.3.2. Electron beam power losses along the accelerator tunnel

The electron beam tube is made of 2-mm-thick stainless steel. The accelerator tunnel has a rectangular cross-section. Dimensions in meters from the beam center to the left, right, top, and bottom wall are 1.5, 1.5, 1.3, and 1.2 m, respectively, as shown in Figure IV.2.3.3. To improve computational efficiency, a cylindrical geometry was used for the

MCNPX model as shown in Figure IV.2.3.4. The inner radius of the shielding wall is set at 1.2 m, using the minimum distance between the beam tube center and the wall surface from Figure IV.2.3.3. In any plane perpendicular to the electron beam tube, electron losses have a uniform azimuthal distribution. Electrons are emitted at 10° relative to the beam direction. Therefore, an annular tally was utilized for the MCNPX calculation to reduce statistical errors in the tallied results.

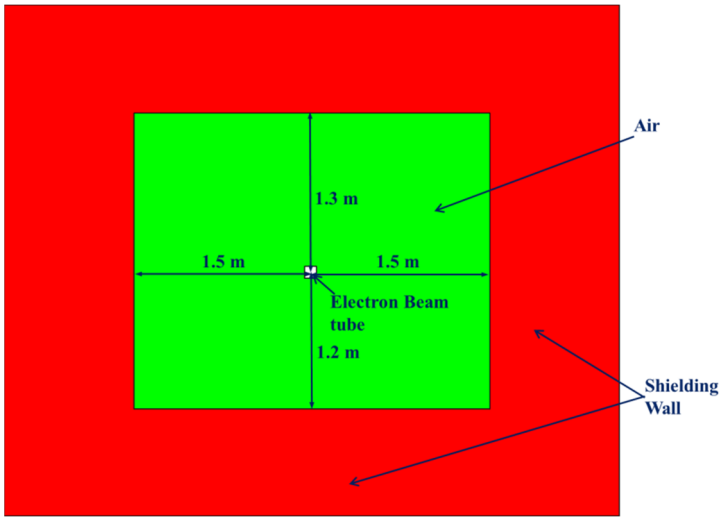

Figure IV.2.3.3. Cross section of the accelerator tunnel perpendicular to the electron beam tube

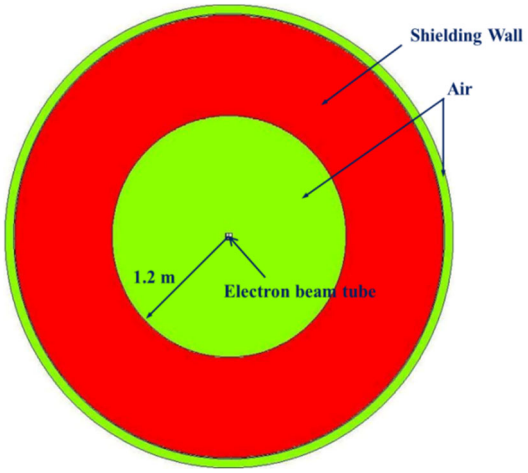

Figure IV.2.3.4. Cross section of MCNPX geometrical model of accelerator tunnel perpendicular to the electron beam tube

Heavy concrete is selected as the shielding material for the accelerator tunnel. A series of iterative MCNPX calculations was used to determine the shield design. The electron source in the MCNPX calculation is located along the beam axis, with a 10° angle relative to the beam axis and uniform distribution azimuthally. The spatial and energy distribution of the electrons is based on the data of Figs. IV.2.3.1 and IV.2.3.2 for the portion of the accelerator tunnel where the electron energy is less than 100 MeV. For the portion of the accelerator tunnel in which the electron energy is 100 MeV, the electron source has a uniform spatial distribution along the beam axis, with an intensity of 50 W/m as mentioned before.

As explained earlier, the neutron and photon biological dose profiles through the shield were obtained from separate MCNPX calculations. The photon dose was obtained from an MCNPX calculation starting with the electron source, while the neutron dose was calculated by a separate MCNPX calculation starting from the volumetric neutron source generated from the electron interactions with the surrounding materials by recording all neutrons generated by the photonuclear reactions from the previous MCNPX calculation. A mesh-based weight windows variance reduction technique was also utilized in both photon and neutron dose calculations to reduce the statistical error.

A series of MCNPX calculations determined that 1.0 m of heavy concrete is sufficient to keep the maximum biological dose less than 0.5 mrem/hr outside the shield. The calculated neutron and photon dose profiles by the mesh tally capability of MCNPX are shown in Fig. IV.2.3.5. The x-axis corresponds to the radius from the tunnel center, while the y-axis corresponds to the length along the electron beam axis. The dashed white line corresponds to the inner shield surface, and the solid white line corresponds to the outer shield surface. The outer radius of the shield boundary is 2.2 m in this MCNPX geometrical model.

From the results shown in Fig. IV.2.3.5., the neutron dose through the shield for $y < 900$ cm is very low, due to the low electron energy and the corresponding very small neutron yield. The neutron dose increases along the y-axis and peaks at $y > 2500$ cm, the 0.5 mrem/hr neutron dose contour line at this peak point coincides with the outer shield boundary. The neutron biological dose increases along the y-axis because the neutron yield increases, as the electron energy increases. The photon biological dose peaks at y=~500 cm, which is very close to the peak electron losses location. The total biological dose (neutron and photon) profile through the accelerator tunnel is also plotted in Fig. IV.2.3.6. The 0.5 mrem/hr contour line is consistently within the outer shield boundary. This means the 1-m heavy concrete shield thickness satisfies the shield design requirement. For most of the accelerator tunnel, the 0.5 mrem/hr total dose contour line is 10 cm away from the outer shield boundary. It should be noted that the MCNPX geometrical model does not have the accelerator equipment modeled, which will reduce the biological dose further.

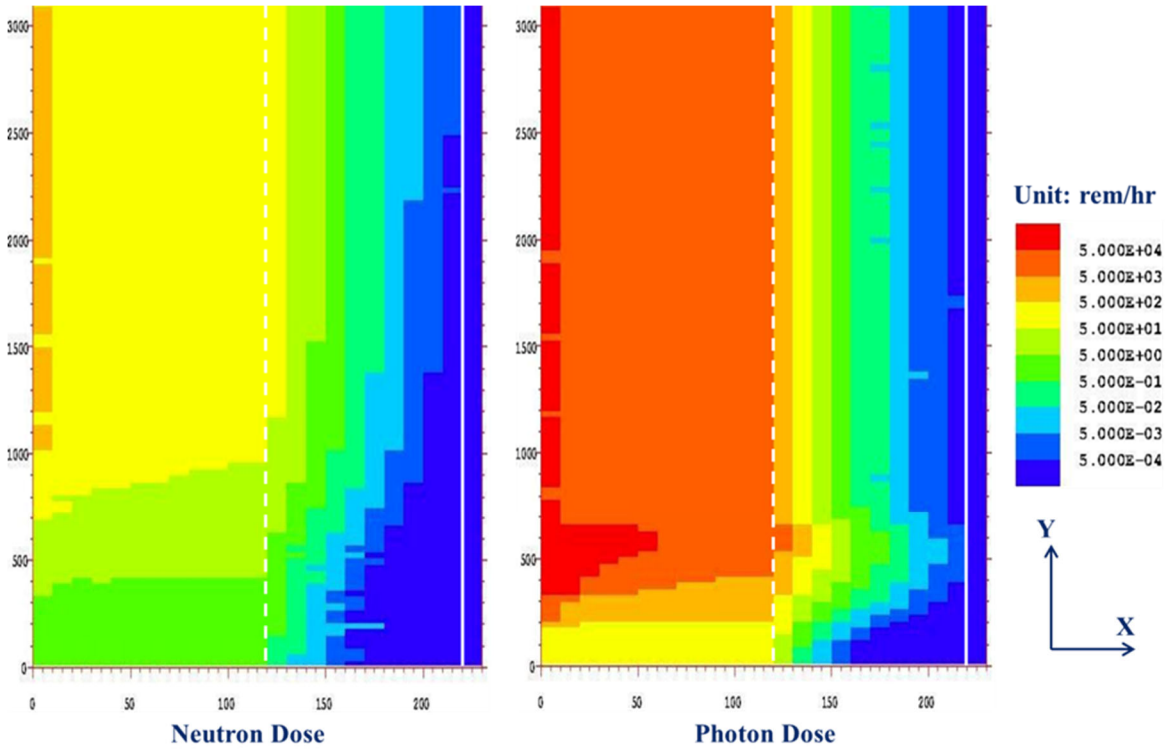

Figure IV.2.3.5. Neutron and photon biological dose profile in the accelerator tunnel

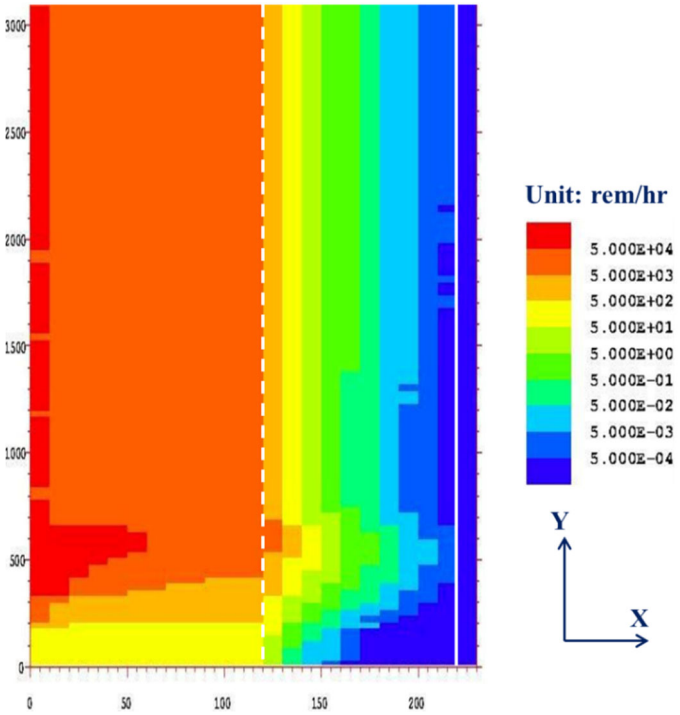

Figure IV.2.3.6. Total biological dose profile in the accelerator tunnel

References

IV.2.1 Denise B. Pelowitz, editor, "MCNPX™ USER'S MANUAL", Los Alamos National Laboratory Report, LA-CP-05-0369, April 2005.
IV.2.2 Z. Zhong and Y. Gohar, "Biological Shield Design and Analysis of KIPT Accelerator Driven Subcritical Facility," *Nuclear Technology*, *168* (2009), 871-876.
IV.2.3 Z. Zhong and Y. Gohar, "Shielding Design and Analysis of KIPT Neutron Source Facility," *Progress in Nuclear Energy*, *53* (2011), 92-99.
IV.2.4 C. N. Culbertson and J. S. Hendricks, "An Assessment of the MCNP4C Weight Window," Los Alamos National Laboratory report, LA-13668, 1998.

IV.3 Energy Deposition in the Concrete Shield

In the design of the KIPT neutron source facility, heavy concrete constitutes most of the shield materials. The energy deposition in the concrete must be evaluated to ensure that the maximum deposition rate is ≤ 1 mW/cm^3 [IV.3.1, IV.3.2] during operation. The energy deposition rate on the various heavy concrete surfaces was calculated using MCNPX at the locations with the highest neutron and photon flux values. Only the uranium target configuration with 37 fuel assemblies is analyzed in this study because the values of the neutron and the photon fluxes are higher than the corresponding values from the tungsten target configuration.

First, the energy deposition on the inner surface of the radial heavy concrete shield next to the water tank was evaluated for the concrete section facing the active fuel region. The model developed for this calculation is shown in Fig. IV.3.1. The figure shows the location of the annular tally cell, this cell has a thickness of 1 cm and an axial height of 50 cm. It is aligned with the active fuel region. The energy deposition value is ~0.55 mW/cm^3. The energy deposition rate from photons is orders of magnitude higher than that from neutrons.

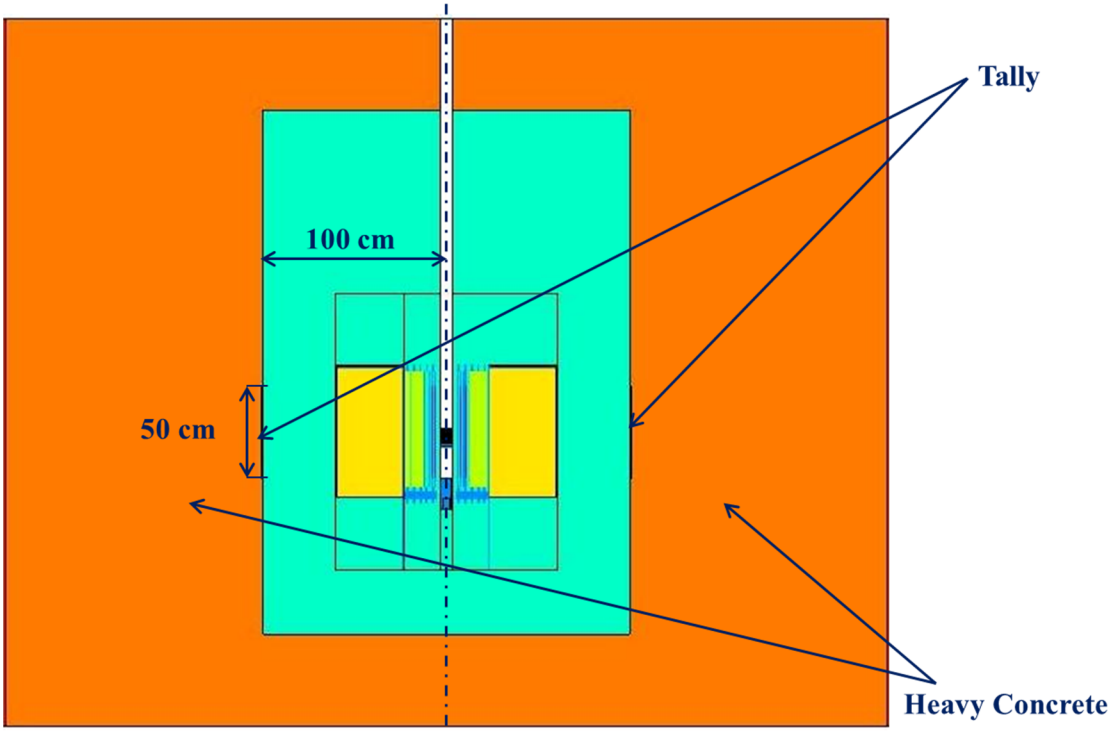

Figure IV.3.1. MCNPX geometrical model for calculating the energy deposition on the inner surface of the radial heavy concrete shield

Neutron channels are included in the KIPT neutron source facility for performing experiments outside radial shield. Therefore, energy deposition rate in the heavy concrete shield along the neutron channels was calculated to ensure that the energy deposition rate does not exceed 1 mW/cm^3. The calculational model is shown in Fig. IV.3.2. The neutron channels are located at the same radius from the active fuel region, and all have the same geometry. A single channel is considered for the analysis using an annular tally cell along the neutron channel axis. The tally cell thickness 1 cm and its length is 50 cm. The tally is divided into five equally sections, each is 10 cm long as shown in Fig. IV.3.2. The calculated energy deposition is shown in Table IV.3.1. Section 1 has the highest energy deposition rate because it is the closest to the fuel region. Still, the average energy deposition is less than 0.75 mW/cm^3.

Table IV.3.1. Energy deposition on the heavy concrete shield surface along the neutron channel

Tally Sections	Energy Deposition (mW/cm^3)
1	0.743 ± 1.29%
2	0.396 ± 1.78%
3	0.236 ± 2.34%
4	0.149 ± 2.96%
5	0.102 ± 3.65%

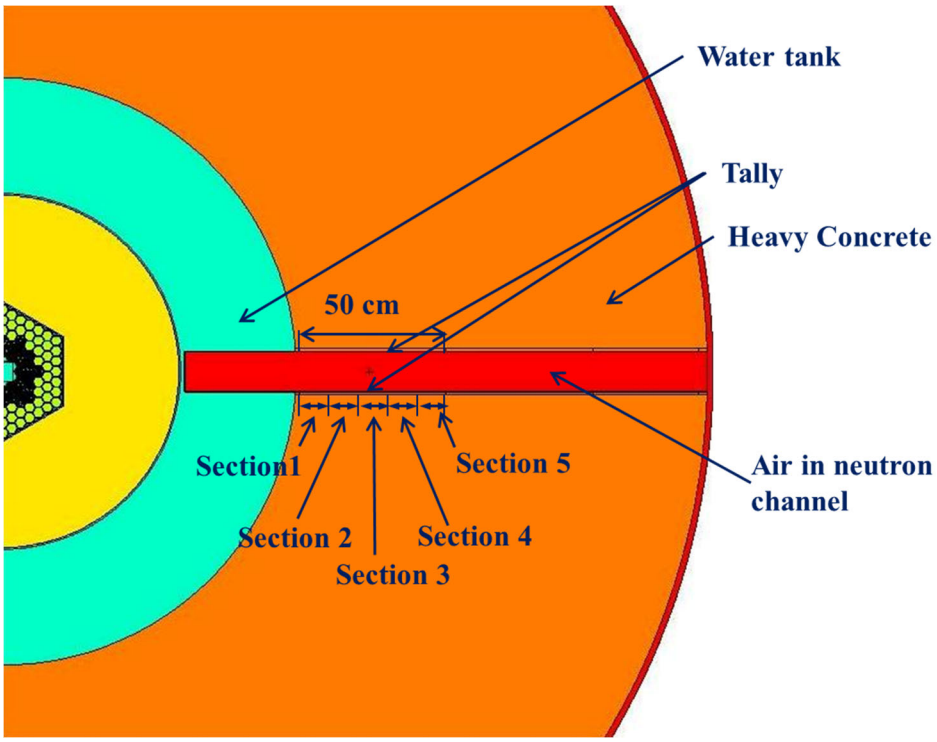

Figure IV.3.2. MCNPX model for calculating the energy deposition rate on the heavy concrete shield surface along a neutron channel

An MCNPX analysis was performed to determine the energy deposition rate on the heavy concrete surfaces facing B1 bending magnet due to the electron beam losses. As discussed in Sec. IV.2.2, the electron beam losses are ~700 W and these losses are evenly distributed between -5° and 30° relative to the beam axis. The energy deposition was tallied on the heavy concrete shield surface between B1 and B2 bending magnets, as shown in Fig. IV.3.3. The tally cell thickness is 1 cm, and it is divided into eleven subsections. Each subsection length is 20 cm to determine the energy deposition rate. The energy deposition results on the exposed heavy concrete surface along the beam axis are given in Table IV.3.2.

In principle, the electrons lost from the main beam can produce a large energy deposition at the concrete shield surface of up to nearly 70 mW/cm^3, which exceed exceeds the 1 mW/cm^3 requirement. Adding a stainless-steel layer, as shown in Fig. IV.3.3 can reduce the nuclear heating. Table IV.3.2 presents the nuclear heating results as a function of the stainless-steel clad thickness for the heavy concrete shield surface. A stainless-steel clad thickness of 4 cm is sufficient to reduce the maximum energy deposition to 1.0 mW/cm^3. In the actual design, the heavy concrete has 1.4 cm steel clad. In addition, the calculational model does not include the bending magnet materials, which has more than 4 cm of stainless steel. Therefore, the design satisfies the 1 mw/cm^3 design limit.

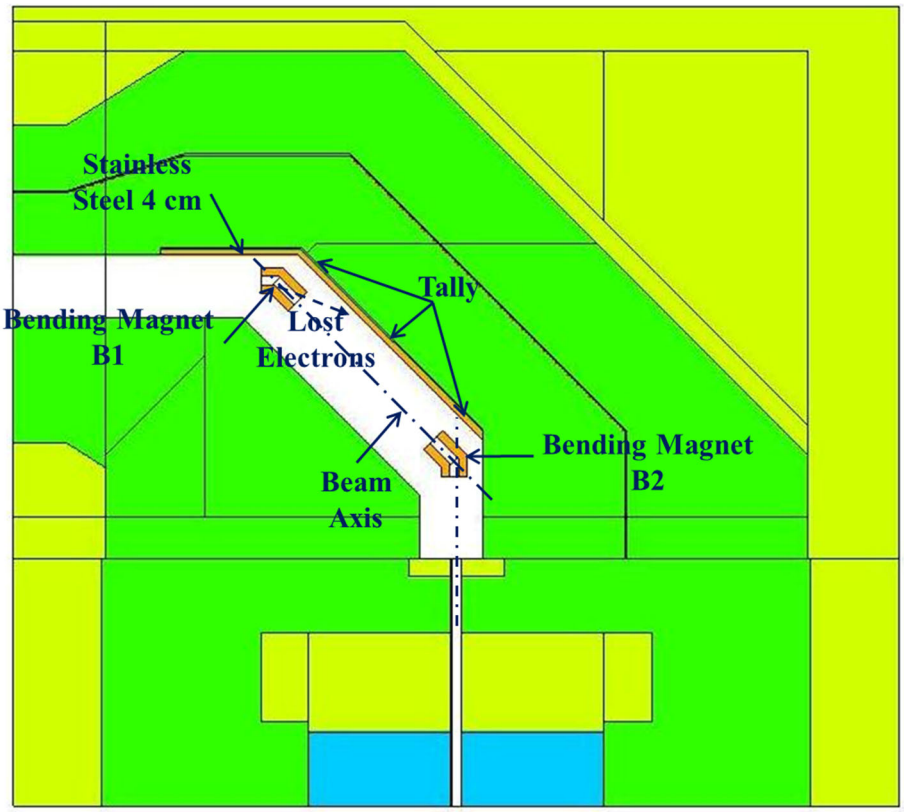

Figure IV.3.3. MCNPX model for calculating the energy deposition in the heavy concrete shield due to the electron losses from B1 bending magnet

Table IV.3.2. Maximum energy deposition on the heavy concrete surface

	Energy Deposition, mW/cm^3
No Cladding	70.0 ± 0.08%
2 cm Stainless Steel cladding	5.32 ± 0.13%
3 cm Stainless Steel cladding	2.17 ± 0.13%
4 cm Stainless Steel cladding	1.08 ± 0.13%

References:

IV.3.1 Y. Gohar, "Low Cost Shield for Tokamak Fusion Reactors," Nuclear Technology/Fusion 4, 1983.

IV.3.2 A. E. Profio, "Radiation Shielding and Dosimetry," A. Wiley – Interscience Publications, John Wiley & Sons, New York, 1979.

IV.4 Biological Shield Mechanical Design

The subcritical assembly (SCA) is contained within the biological shield. The biological shield provides radiological shielding function around the SCA. The biological shield also provides atmosphere containment, and liquid leak containment and collection.

IV.4.1 Biological Shield Structure

The biological shield is constructed as a reinforced stainless-steel box that is filled with high-density concrete. This method provides precision locations of critical features, durable surfaces that are easy to decontaminate. The biological shield is anchored to the building foundation to resist seismic loading. The biological shield configuration is shown in Fig. IV.4.1.1.

IV.4.2 Neutron Beamline Channels

The biological shield provides six channels for neutron experiments, three channels are visible in the side of the biological shield in Fig. IV.4.1.1. The neutron leakage from the graphite reflector provides the neutron current in the five channels. Two of these channels, 1 and 5, are shown in the cutaway view in Fig. IV.4.2.1. The sixth channel, channel 4, is provided for a cold neutron moderator. The cold neutron channel aligns with the cold neutron source well of the SCA tank. Each of the five channels is fitted with a shutter which can selectively block the passage of neutrons in the channel. The channels can be plugged when the shutter mechanism is removed; Fig. IV.4.2.2 shows channels 2 and 3 plugged.

IV.4.3 Movable Top Shield

Two movable top shield (MTS) pieces provide shielding above the SCA. The MTS are movable so that service access can be provided to the linear accelerator bending magnets, the fuel handling machine components, and the target assembly. Figure IV.4.1.1 shows the configuration of the MTS closed, while Figs. IV.4.2.1 and IV.4.3.1 show the two pieces opened. The rotating vessel cover can be removed when the MTS are open; this configuration is presented in Fig. IV.4.3.2. Staggered gaps are provided at the motion interfaces to minimize radiation streaming from the gaps. The MTS moves on rollers. The MTS is moved by electrical motors which operate through gear reducers, as diagrammed in Fig. IV.4.3.3. The MTS rollers roll on rails which are supported by a steel gantry frame structure, pictured in Fig. IV.4.3.4. The gantry structure is attached to and braced by the biological shield. The gantry structure is anchored to the building foundation and has sufficient strength to resist seismic loading.

The two MTS pieces are reinforced stainless steel structures that are filled with high-density concrete. The MTS has additional plates of lead and borated polyethylene near the bending magnets (see Fig. IV.4.3.5) to reduce the biological dose outside the shield boundary. Electrical switches are provided to detect the positions of the MTS and inhibit accelerator operation in unsafe configurations. Work platforms are provided on the MTS pieces for fuel transfer cask operations and for service of the MTS drive system components.

IV.4.4 Fuel Transfer Port

The south MTS has a port to accept the fuel transfer cask, as shown in Fig. IV.4.1.1. Fuel transfer operations are conducted with the MTS in the closed position. During operation of the SCA, a shield plug is placed in the fuel transfer port, as shown in Fig. IV.4.1.1. Figure IV.4.4.1 presents the south MTS with the shield plug removed for fuel transfer operation. Electrical switches detect the presence of the fuel transfer cask or the plug, and permit operation of the accelerator or the fuel handling machine under appropriate conditions.

IV.4.5 Rotating Vessel Cover

The rotating vessel cover (RVC) is above the SCA tank and under the movable top shield, as can be seen from Fig. IV.4.2.1. The RVC provides additional radiological shielding value. The RVC provides the rotational degree of freedom to the fuel handling machine. The RVC rotates on three support rollers and is guided by three centering rollers; some of these are visible in Fig. IV.4.3.2. The drive motor that controls the rotation of the RVC is external to the biological shield, placing it in a lower radiation environment and making it easier to service. Rotational position detectors that monitor the rotational position of the RVC are within the biological shield.

IV.4.6 Atmosphere and Air Flow

The biological shield provides the atmospheric containment around the SCA. The special ventilation system maintains the atmosphere within the biological shield at a pressure that is slightly lower than the air pressure within the SCA hall to capture any contamination that might migrate by airflow. The gaps between the MTS and the shield ring are covered by metal sealing to minimize the amount of air that flows in through the gaps and maximize the differential pressure. There are four air channels (mouse holes) at the floor level that provide a path for air to flow into the biological shield. This airflow provides a means of minimizing condensation on the lower surfaces of the SCA tank. These airflow channels can also be used for video inspection the SCA tank.

IV.4.7 Liquid Containment

The biological shield provides a liquid containment and collection system under and around the SCA tank, pictured in Fig. IV.4.7.1. The steel foundation plate under the SCA tank is welded to the steel shell of the biological shield, creating a hermetic boundary. A drain tube is connected to this collection volume, providing a means to drain and remove any spills or leakage to the special waste system. The airflow channels, mouse holes, have vertically raised sections at their outer ends to provide liquid containment up to the level of the shutter holes and to break radiation streaming through the mouse holes.

IV.4.8 Wire Channels

The biological shield has several staggered tube passageways that allow for the passage of wires for neutron flux detectors and thermocouples within the SCA. The locations of the passageways are shown in Fig. IV.4.8.1. These tubes allow the withdrawal and replacement of neutron flux detector and thermocouple elements from the exterior of the biological shield.

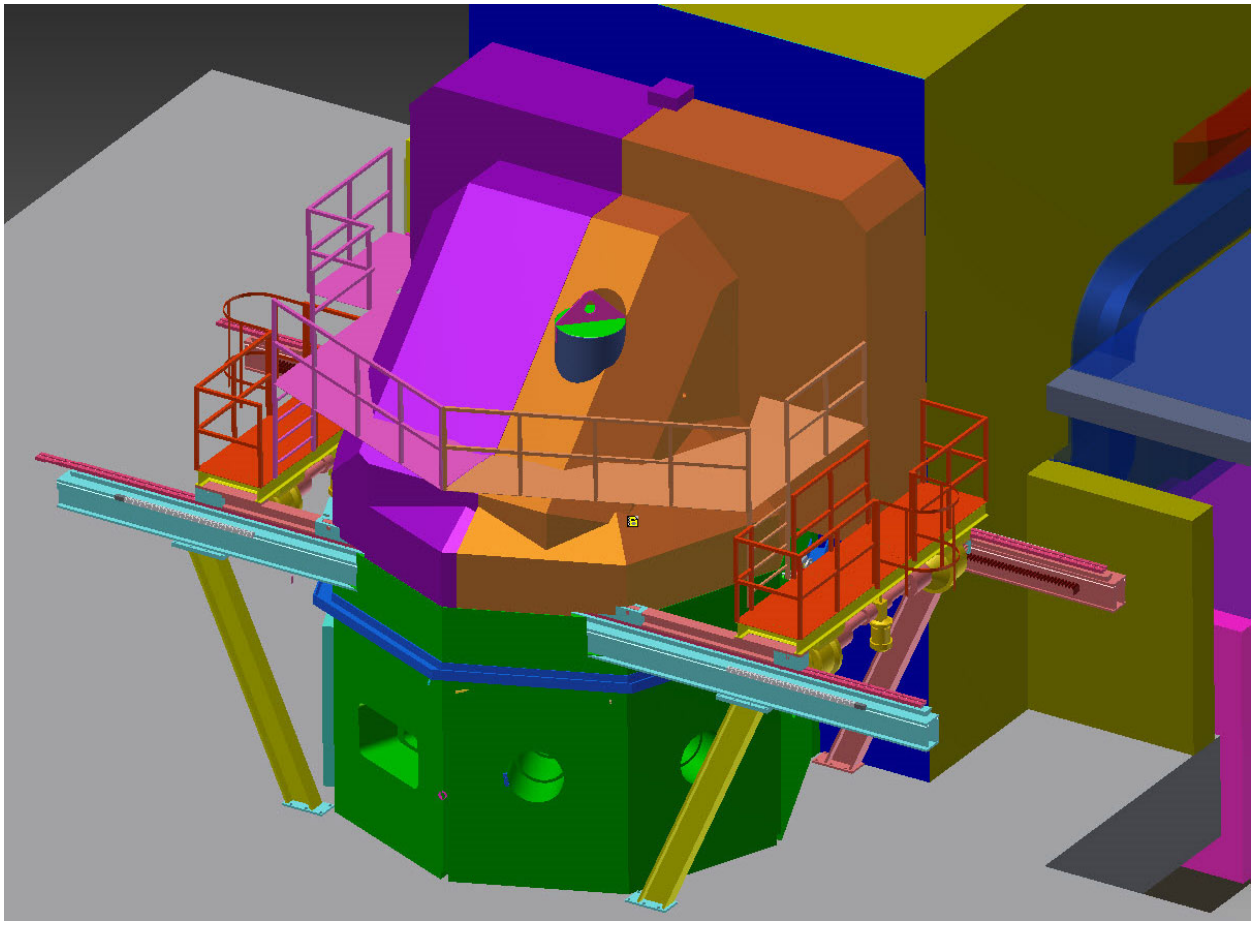

Figure IV.4.1.1. View of the biological shield (green), shown with the movable top shield, purple and orange sections above the biological shield), closed. This is the configuration that the biological shield would be in during operation.

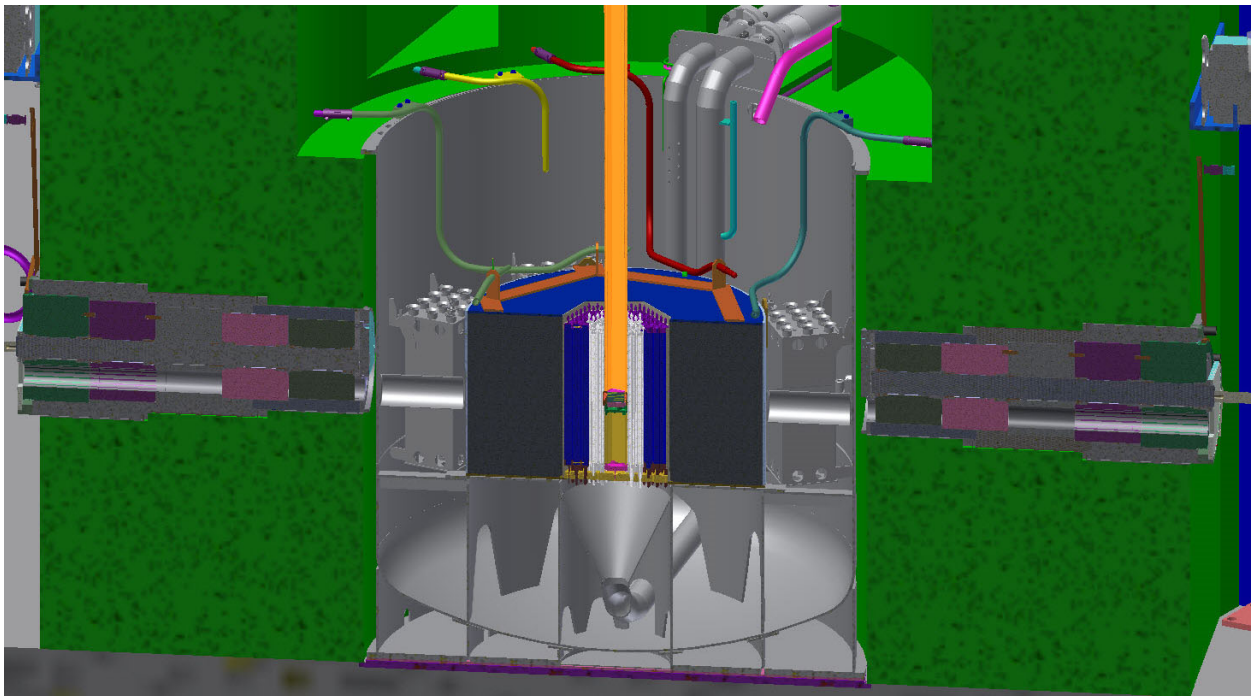

Figure IV.4.2.1. Section view through neutron channels 1 and 5.

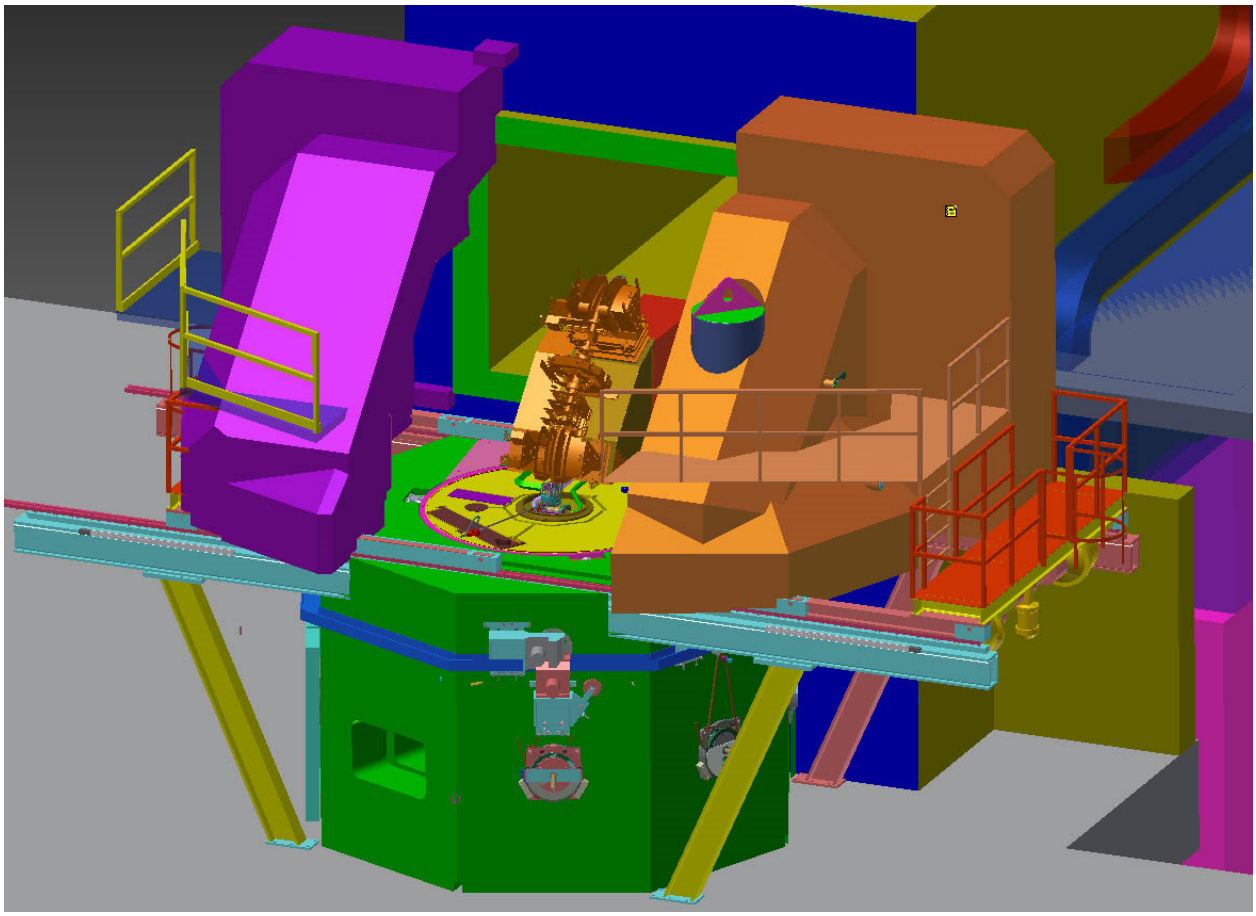

Figure IV.4.2.2. Biological shield view with movable top shield in the open position. Rotating vessel cover, light green, and electron beam bending magnets, above the rotating vessel cover, are visible.

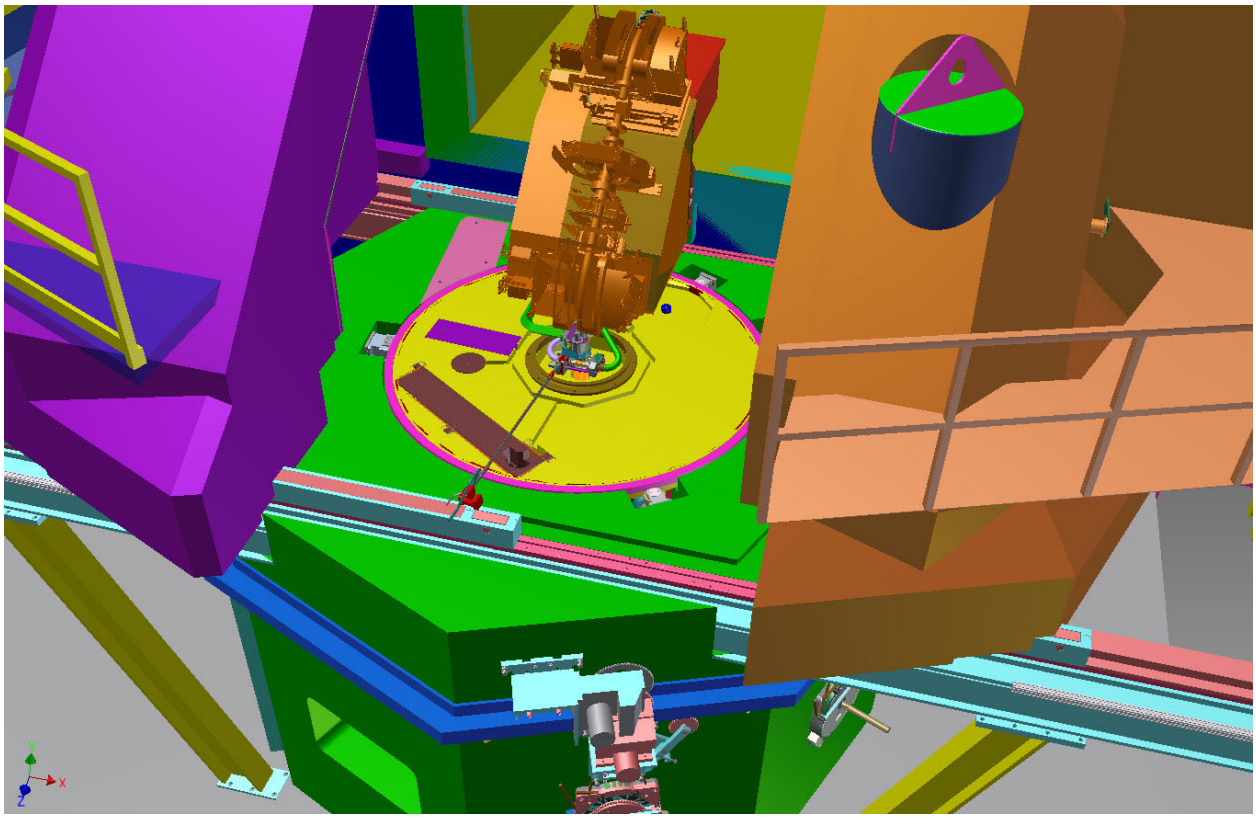

Figure IV.4.3.1. Biological shield view with movable top shield in the open position. Electron beam bending magnets and rotating vessel cover shown.

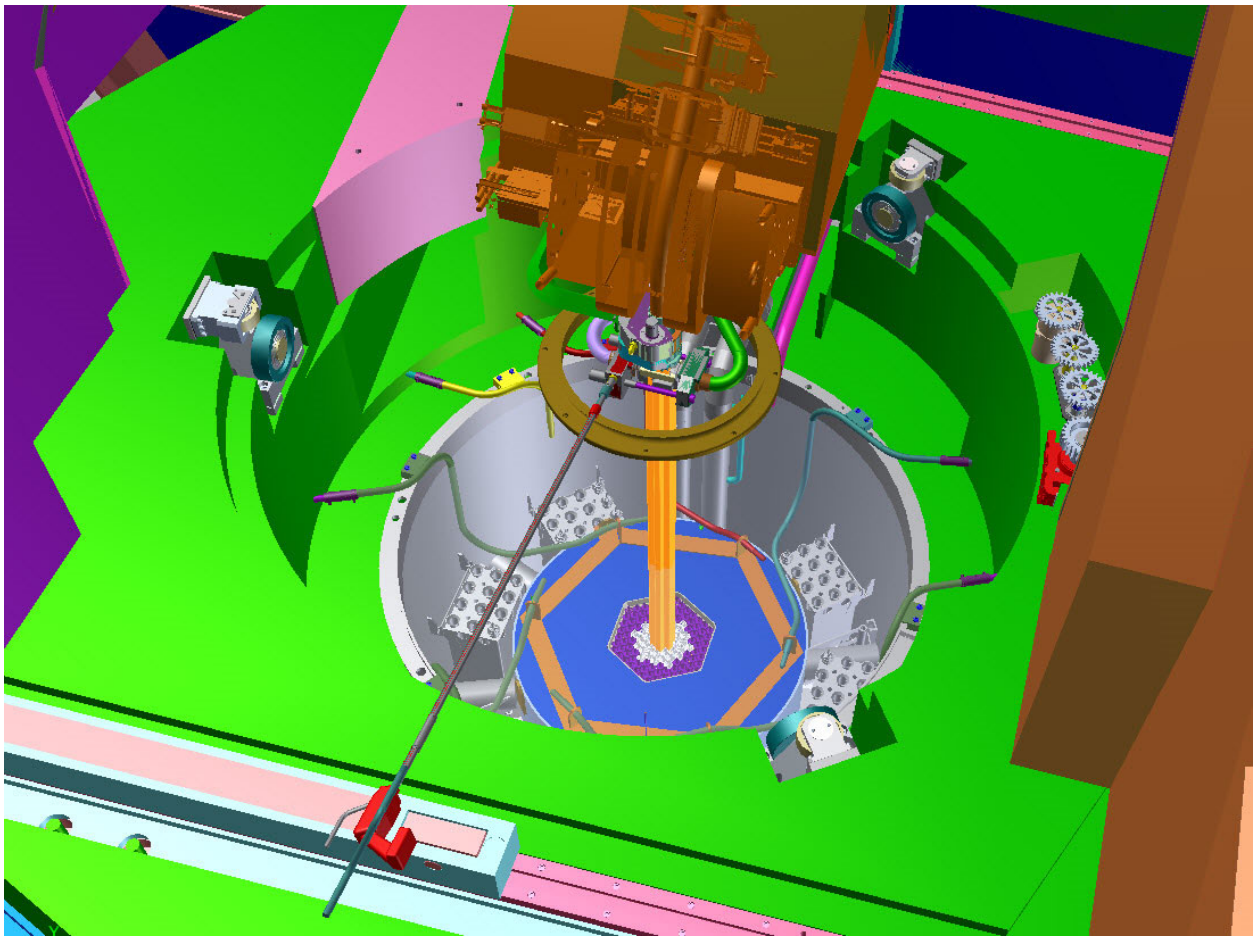

Figure IV.4.3.2. Biological shield view with the movable top shield open and the rotating vessel cover removed. Support and guide rollers for the Rotating Vessel Cover are visible around the outside of the graphite reflector ring, shown in blue.

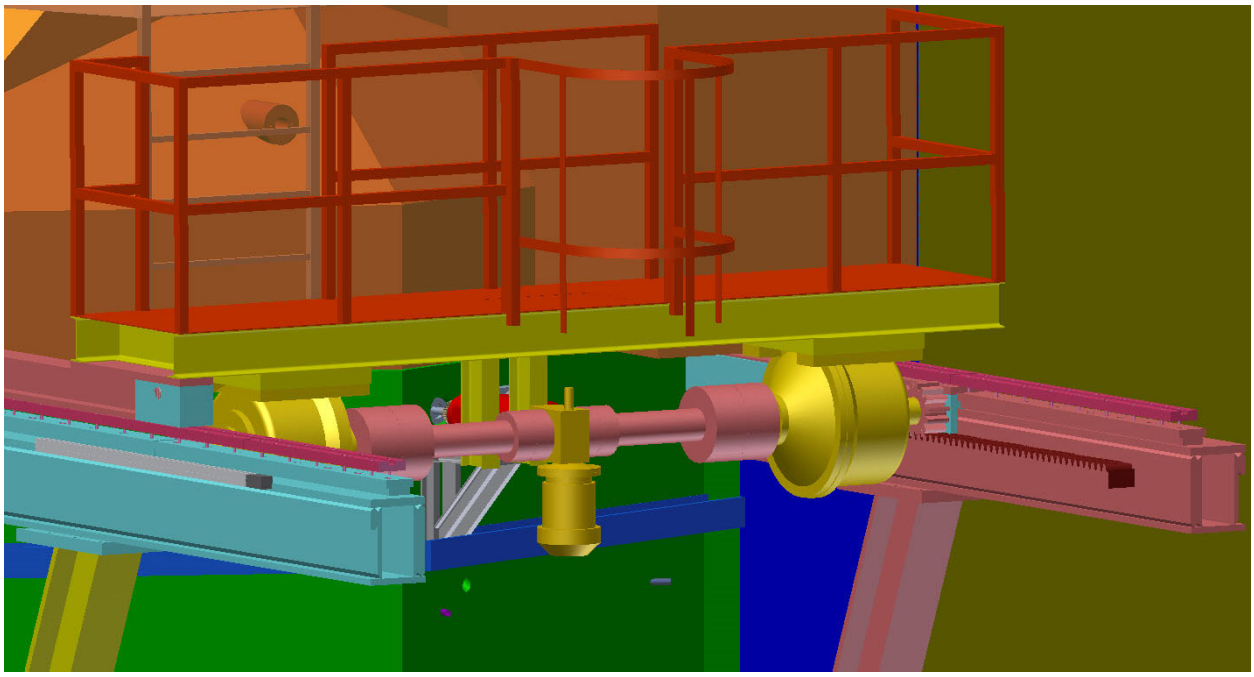

Figure IV.4.3.3. Drive mechanism of the movable top shield. A single motor drives two planetary gearboxes, turning gears that engage gear racks on the gantry structure, creating synchronized motion. South MTS drive mechanism is shown, north is similar.

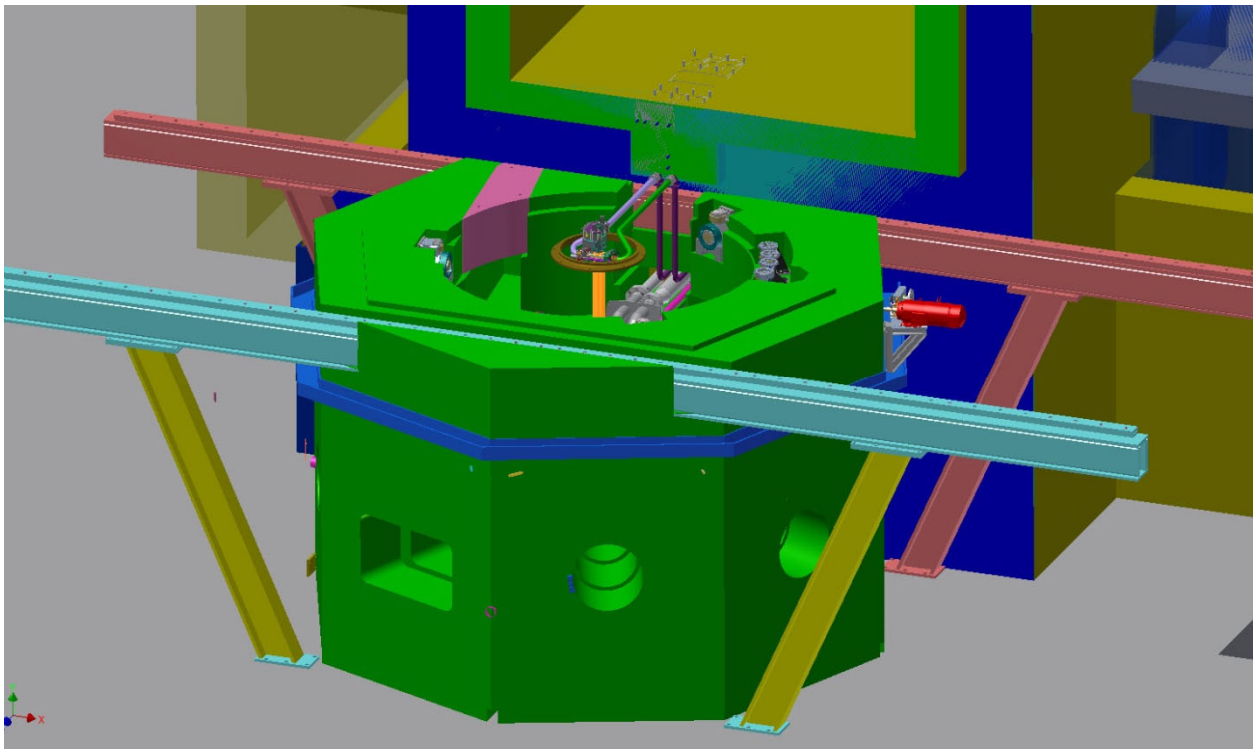

Figure IV.4.3.4. Biological shield ring shown with movable top shield pieces removed. Gantry structure, light blue and light red, is visible in this picture. Neutron channels 2, 3 and 4, right to left, are visible in this picture.

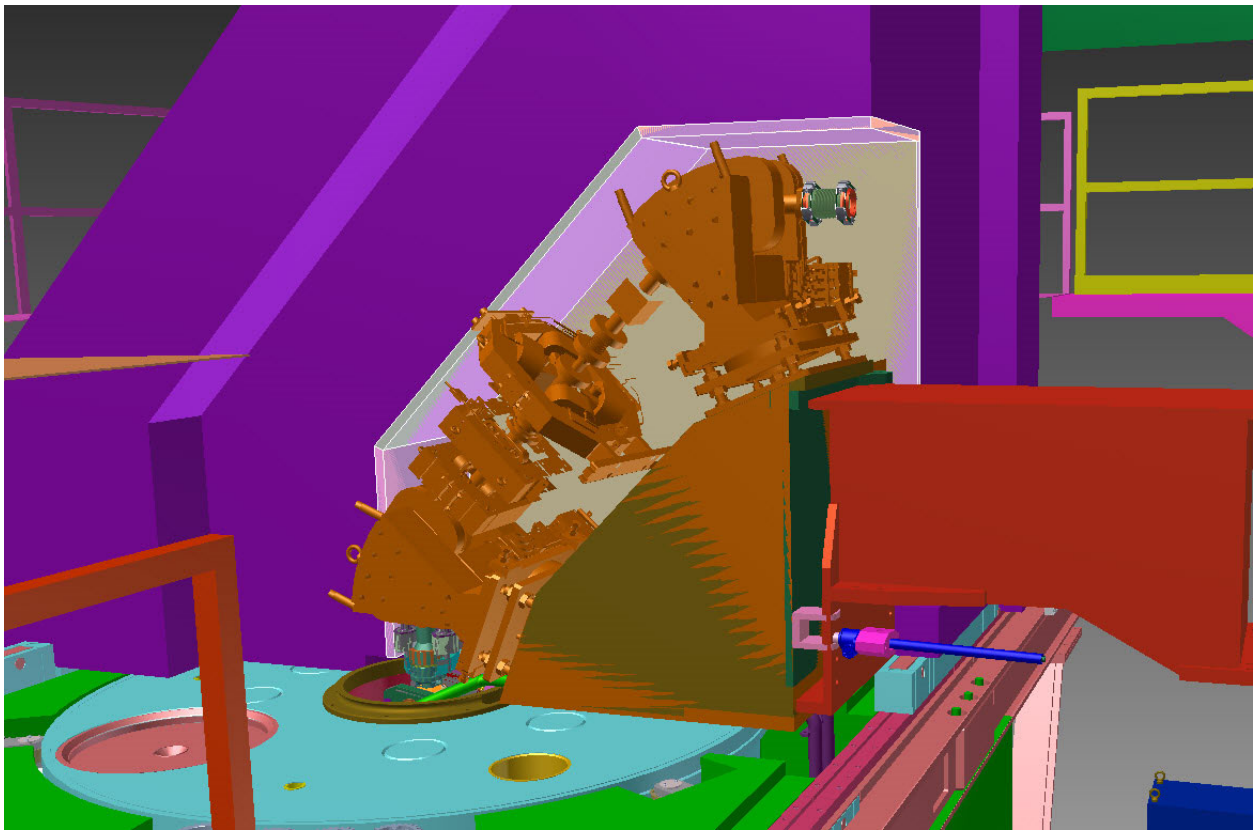

Figure IV.4.3.5. Interior view of north MTS piece, showing additional lead and polyethylene plates around bending magnets.

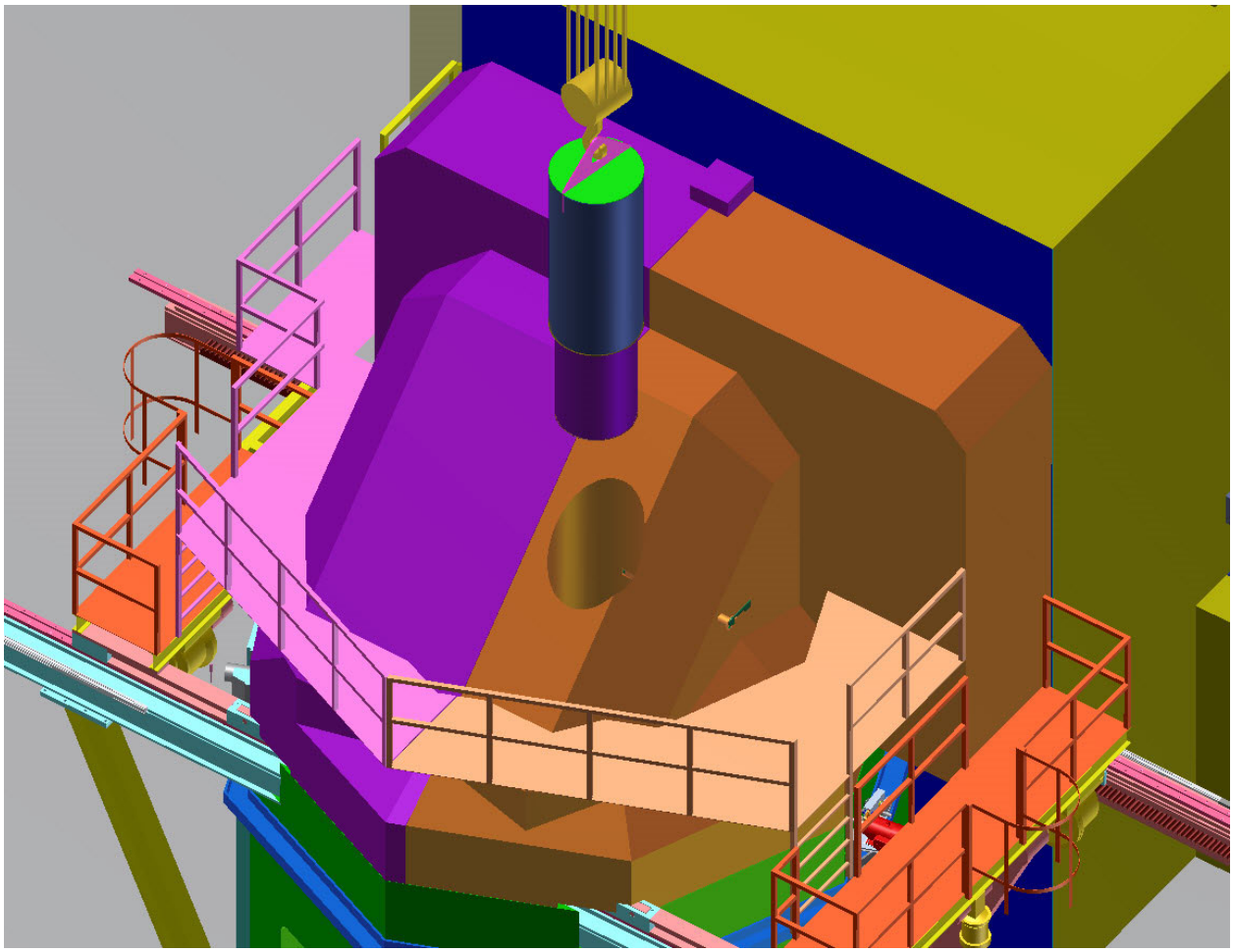

Figure IV.4.4.1. Movable top shield shown with plug removed for fuel transfer operation.

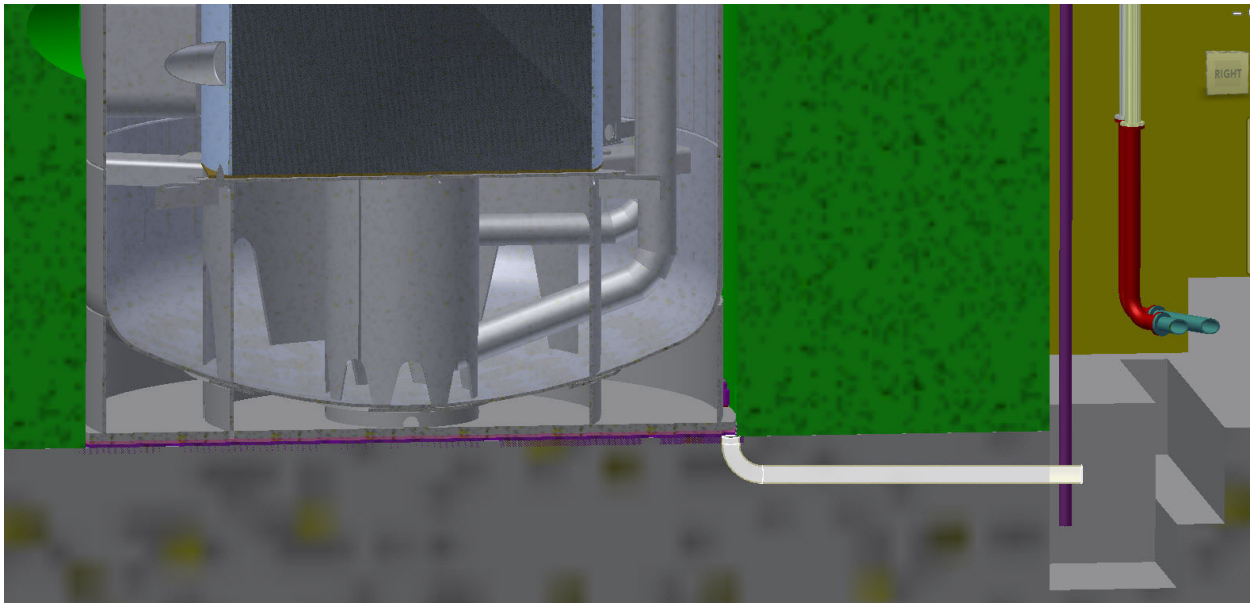

Figure IV.4.7.1. Section through biological shield showing liquid spill/leak collection and containment system. Liquids are removed to a special waste system.

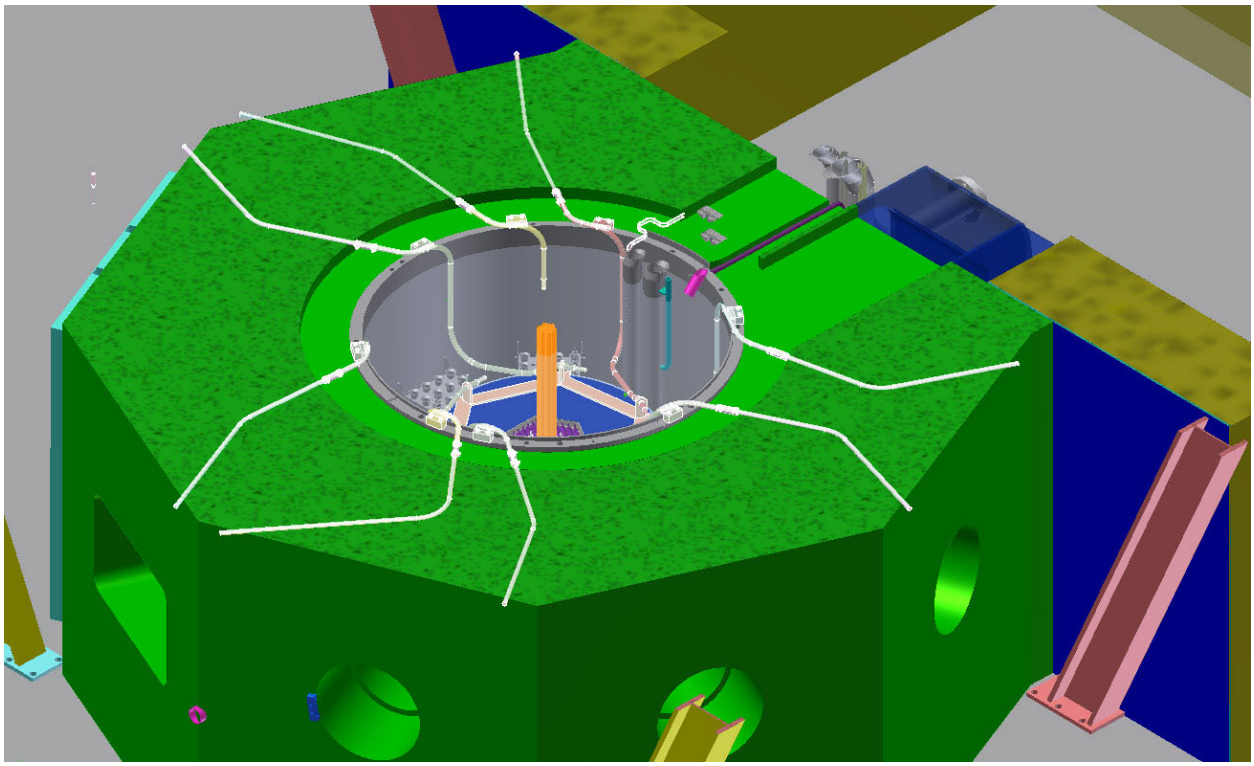

Figure IV.4.8.1. Horizontal section cut through biological shield, showing the staggered tubes for neutron flux detectors and thermocouples.

IV.5 Biological Shield Main Parameters

Table IV.5.1 Primary Parameters of the Radial Shield

Heavy concrete density	4.8 g/cm^3
Inner radius of radial shield	100 cm
Outer radius of radial shield	240 cm
Shield thickness	>145 cm
Neutron channel number	6
Tube passageways for wiring, neutron flux detectors and thermocouples.	12

Table IV.5.2 Primary Parameters of the Top Shield

Heavy concrete density	4.8 g/cm^3
Shield thickness in Z direction, above bending magnet B1	137.5 cm
Shield thickness in Y direction, along bending magnet B1	120 cm
Shield thickness in X direction, along bending magnet B1	210 cm
Total height of top shield	343 cm
Angle of the cone foundation of top shield	45 ^{o}
Bottom radius of the cone foundation of top shield	238 cm
Thickness of stainless steel surrounding the beam channel	4 cm
Thickness of borated polyethylene along the contacting gap	3 cm
Thickness of lead along the contacting gap	2 cm

Table IV.5.3. Primary Parameters of the Accelerator Tunnel Shield

Heavy concrete density	4.8 g/cm^3
Shield thickness	100 cm

V Fuel Storage Pools

V.1 Introduction

A spent fuel storage facility consisting of two identical independent pools has been designed to store spent fuel assemblies and used targets for the KIPT experimental neutron source facility. The pools are contained in separate rectangular pits below the floor level of the subcritical assembly hall floor, with the top surface of each pool flush with the hall floor. Only one pool will be used at a time; one pool is the normal storage pool, and the second pool stands by to receive spent fuel assemblies and used targets if the first pool develops a leak and requires repair. Each pool consists of an inner tank and an outer tank, with a removable cover over both tanks. Used targets and spent fuel assemblies are placed in the inner tank, surrounded by water that circulates through natural circulation inside the tank. The outer tank serves to catch any water that might leak from the inner tank.

Both pools have been designed to meet required physics, thermal hydraulics, and structural constraints. Physics analyses have been performed to ensure that either pool remains far subcritical ($k_{eff} < 0.5$) when fully loaded with spent fuel assemblies. Additional physics analyses have been used to determine the water level of the pool that will limit the photon dose, caused by decay of fission products and activation products in the spent fuel and used targets, to ≤ 0.5 mrem/hr. Sec. V.2 discusses these analyses.

Thermal-hydraulic evaluations were performed to ensure that the design meets the physics requirements. The water temperature in the pool remains well below boiling under all conditions. These analyses are described in Sec. V.3.

The pool tank design was subjected to a structural analysis by the finite element method. Finite element models were constructed and subjected to static loads, and results were compared to basic material properties. Commonly accepted engineering principles were applied to determine factors of safety. These analyses are presented in Sec. V.4.

Detailed descriptions of the components that make up the spent fuel storage facility are presented in Sec. V.5. This section also discusses the system for processing the water pool coolant and the forced air system that prevents water condensation between the two tanks. In addition, this system removes heat from the inner tank surface to the atmosphere through the special ventilation system. The processes for loading and unloading spent fuel elements and targets are also described.

V.2 Physics Design Analysis

A physics design analysis has been carried out to provide part of the information needed to design the storage pools that will be used to store the spent fuel and the used target assemblies. The thermal-hydraulic and the structural analyses that also contribute to the pool design are discussed in sections V.3 and V.4, respectively. Two identical storage pools will be available: one holds the spent fuel and the used target assemblies during normal operation and the second stays in a stand-by mode. The second pool is normally empty and is used only if the primary pool develops a leak and the spent fuel and the used target assemblies must be moved to the stand-by pool. So, the primary pool can be drained, and the leak fixed. Since the pools are identical, the analysis below applies to either pool.

The storage pool is filled with water and the spent fuel assemblies seated in the pool below the water surface. The space between fuel assemblies must be determined to keep the $k_\infty < 0.5$. This limit was set for the design analysis. A set of scoping calculations for the k_∞ of a single fuel assembly with water reflector axially and a reflective boundary radially has been conducted with MCNPX, using both square and hexagonal lattices with various lattice spacings. The obtained results are shown in Fig. V.2.1. So that the pool design will be valid for any fuel burnup level, fresh fuel is assumed in this analysis.

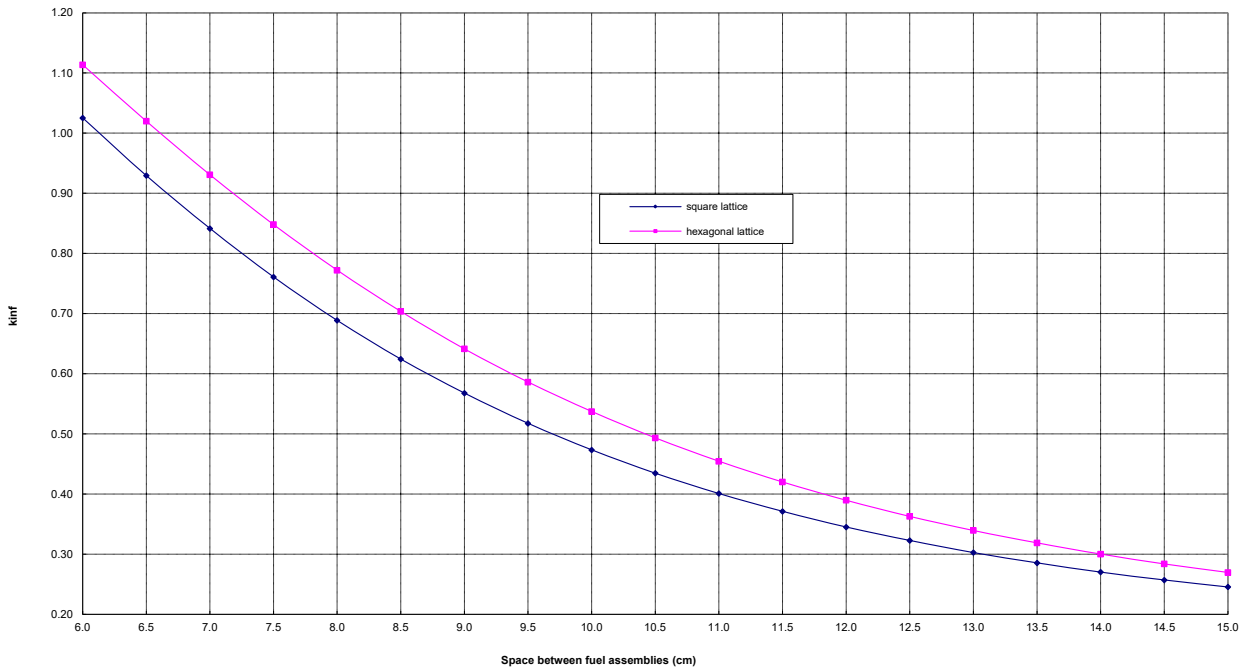

Figure V.2.1 Fuel assembly k_∞ for square and hexagonal lattices as a function of the lattice size

Based on the results shown in Fig. V.2.1, a square lattice with lattice spacing of 10 cm was selected for the fuel arrangement in the storage pool, allowing any number of

assemblies to be stored while keeping k_∞ below 0.5. Each fuel assembly will be seated in an aluminum holding tube with an outer radius of 2.1 cm and a thickness of 2 mm, as shown in Fig. V.2.2. The pool is designed to have the capability to store up to 64 fuel assemblies, plus six targets. The storage pool configuration with 64-fuel assemblies loaded is shown in Fig. V.2.3. The k_{eff} of the storage pool under normal conditions, water density 1.0 g/cm^3, with 64 (8×8) fresh fuel assemblies loaded, is 0.44568 ± 0.00008. When spent fuel assemblies are loaded instead, the k_{eff} value will be lower.

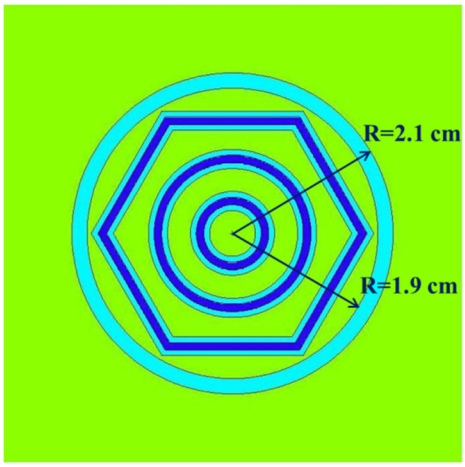

Figure V.2.2. Fuel assembly in storage pool, with aluminum holding tube

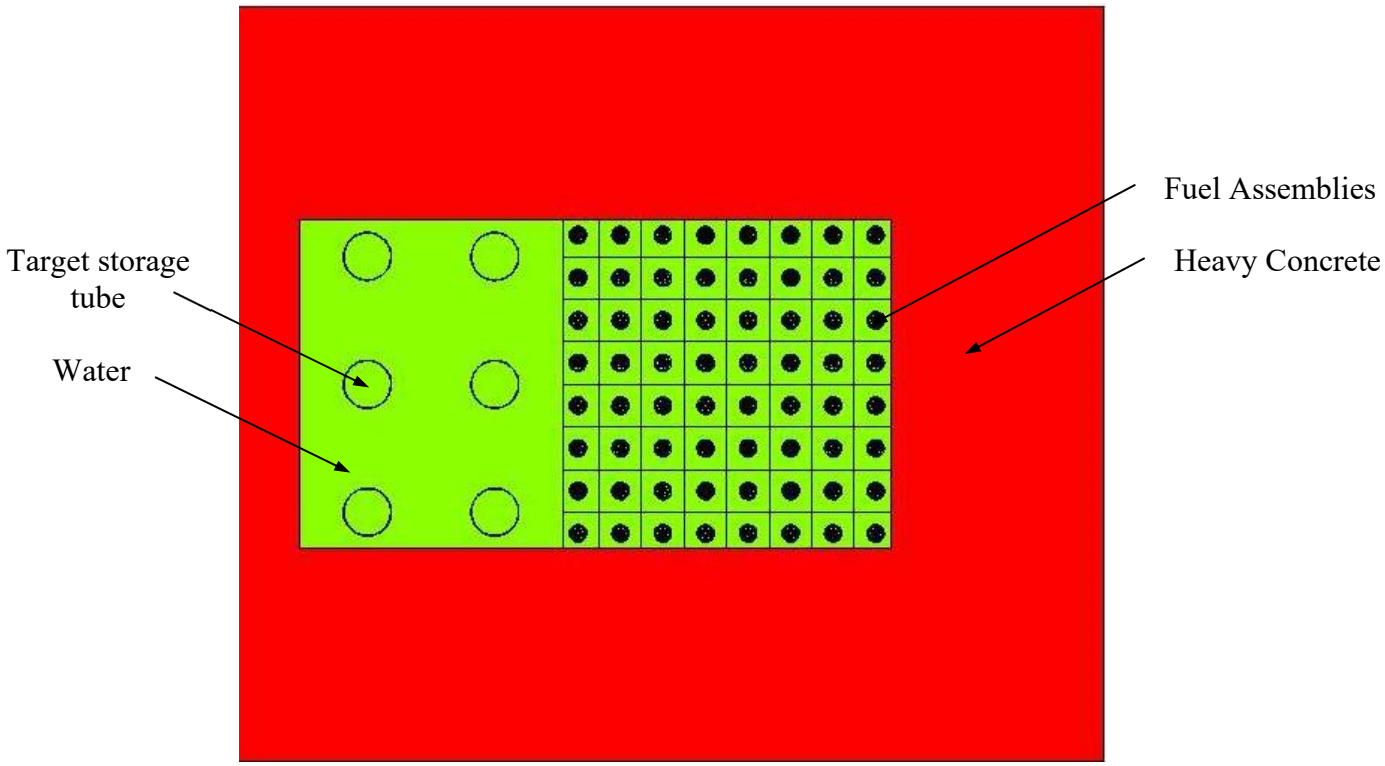

Figure V.2.3. Storage pool configuration

The k_{eff} of the storage pool with various water densities has been calculated and plotted in Fig. V.2.4. The fuel storage pool is an over moderated system under normal conditions with 1.0 g/cm^3 water density. When the water density is uniformly reduced, the k_{eff} increases, but the maximum value is still below 0.6. It should be noted that such condition of uniformly reduced density is not possible in an open water tank.

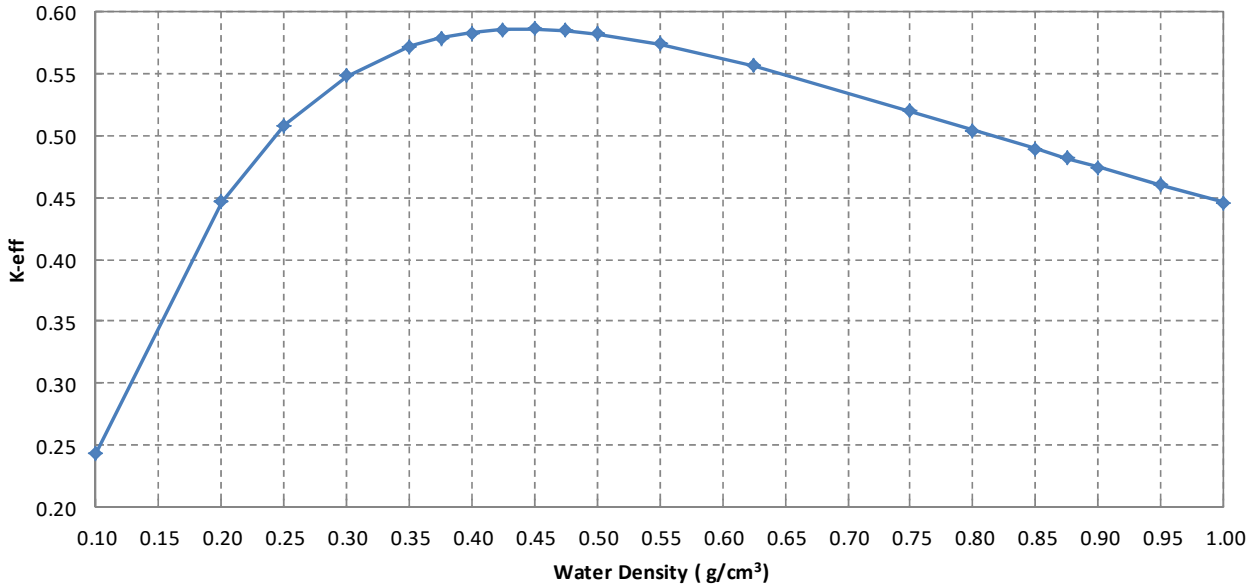

Figure V.2.4. Storage pool k_{eff} from 64 loaded fuel assemblies as a function of the water density

The axial cross-section of the storage pool is shown in Fig. V.2.5. The decay of fission and activation products of the spent fuel will release photons, as well as other particles. The biological dose at any location outside the storage pool must remain below 0.5 mrem/hr. The storage pool is placed underground, therefore only the radiation dose on top of the pool needs to be evaluated for normal operations. The water level above the spent fuel must be determined to keep the biological dose above the storage pool below 0.5 mrem/hr.

Coupled MCNPX/ORIGEN-2 simulations were used to determine the photon source from the spent fuel assemblies. These calculations were performed for the uranium target configuration. This configuration has higher neutron flux levels than the tungsten target configuration, therefore the amount of fission and activation products, and the biological dose are higher. The fission power of the hottest fuel assembly was calculated with MCNPX and then used into an ORIGEN-2 calculation for calculating the photon decay source. The fuel was assumed to have been burned in the subcritical assembly for one year. The spent fuel was cooled for thirty days prior the discharge from the subcritical assembly. The decay photon source from the spent fuel was calculated by ORIGEN-2 using 18-energy groups.

An MCNPX model was developed to calculate the photon dose above the storage pool, using the photon source generated by the MCNPX/ORIGEN-2 coupled calculation described above. In this model, the concrete wall and target storage tubes, which have very little impact on the biological dose above the storage pool surface are ignored. The pool geometry is assumed to be cylindrical, which reduces the statistical error of the MCNPX tally calculation by using symmetric mesh tallies. These assumptions result in conservative results. The configuration of this simplified model is shown in Fig. V.2.6.

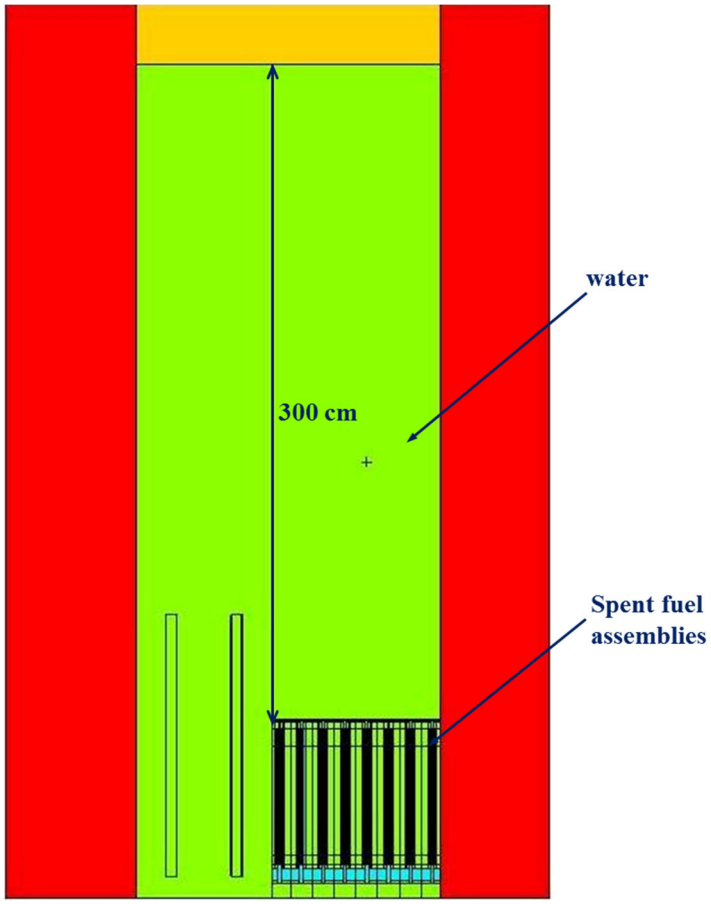

Figure V.2.5. Axial configuration of storage pool, with 300 cm of water above the spent fuel

The MCNPX calculation was performed for the limiting case of the 64-spent fuel assemblies stored in the pool, using a total photon source intensity of 3.695×10^{15} p/second, which is 64 times the photon source intensity calculated by ORIGEN-2 for the hottest spent fuel assembly. The photon dose profile in the storage pool was calculated using the mesh tally capability of MCNPX, and the resulting profile is shown in Fig. V.2.7. The MCNPX results indicate that when the water level above the top of the spent fuel is 300 cm, the biological dose satisfies the 0.5 mrem/hr dose requirement as shown in Fig. V.2.7.

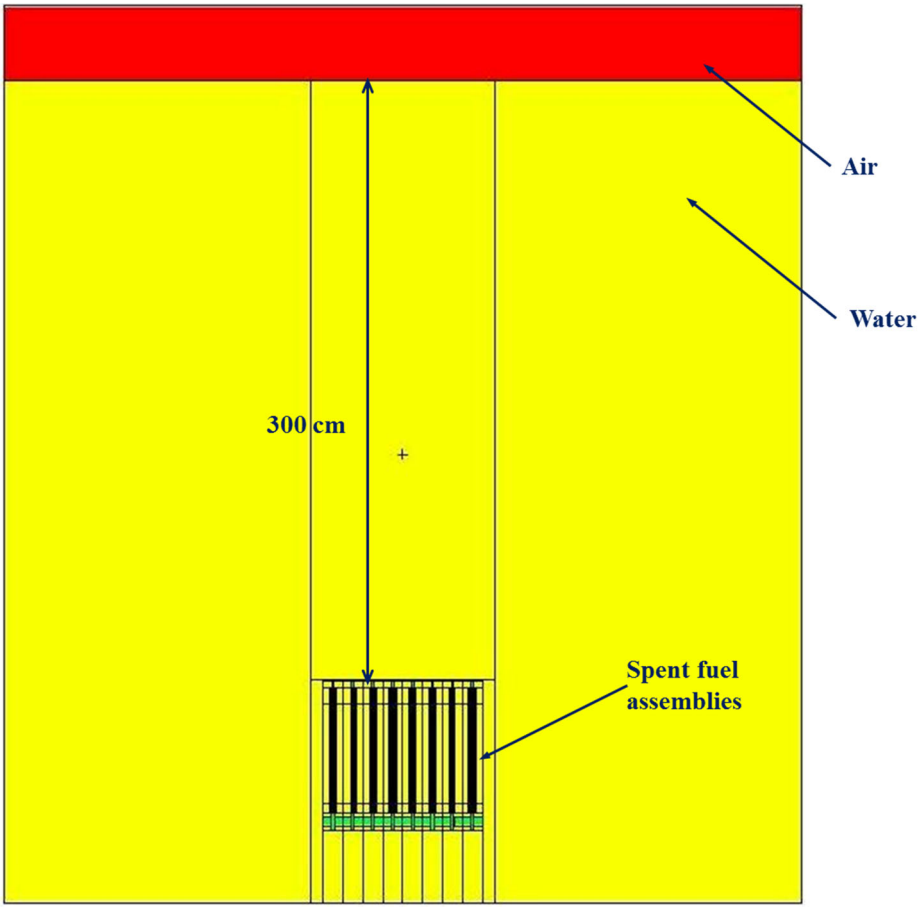

Figure V.2.6. MCNPX calculational model for storage pool biological dose analysis

In the case of the primary storage pool develops a water leak, the spent fuel and the used target assemblies will be moved to the backup pool. The backup pool is adjacent to the primary pool, and it has the same geometry. The primary pool will be drained, and photons may leak out from the backup pool to the primary loop through the shared wall between the two pools. This wall thickness is 70-cm of heavy concrete. An MCNPX model was developed, an X-Y cross section of the model is shown in Fig. V.2.8. The photon dose profile across the wall has been calculated using an MCNPX mesh tally, as shown in Fig. V.2. 9 using an X-Z view. The mesh size in the Y direction is 40 cm, and the tally cell position is shown in Fig. V.2.8.

In Fig. V.2.9, the X direction is perpendicular to the wall, the dotted line corresponds to the inner surface of the wall next to the stored fuel assemblies and the solid line corresponds to the outer surface of the wall. On the outer surface of the wall, the photon dose is < 0.5 mrem/hr when Z > 80 cm, the active fuel edge is at Z ≈ 60 cm. Therefore, the biological dose above the voided primary pool (Z > 300 cm) is less than the 0.5 mrem/hr. For the region with Z < 80 cm inside the empty pool, the biological dose is between 0.5 and 5.0 mrem/hr. However, this result is obtained based on a very conservative assumption that all the spent fuel assemblies have just been removed from

the subcritical assembly; in actual operation, most of the assemblies will have been out of the SCA for several years and the dose will be much lower than these values.

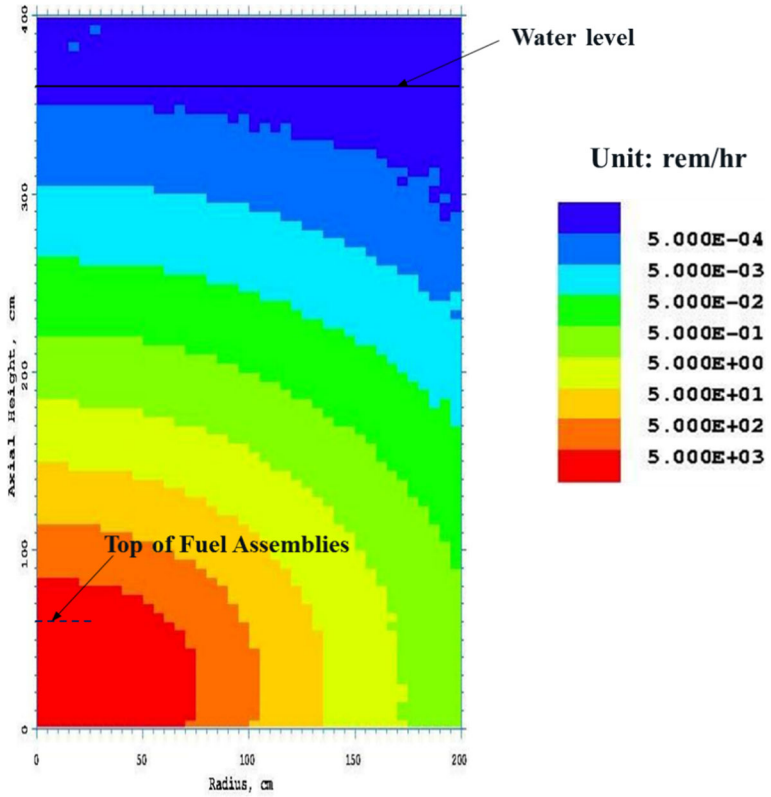

Figure V.2.7. Photon dose profile in the storage pool

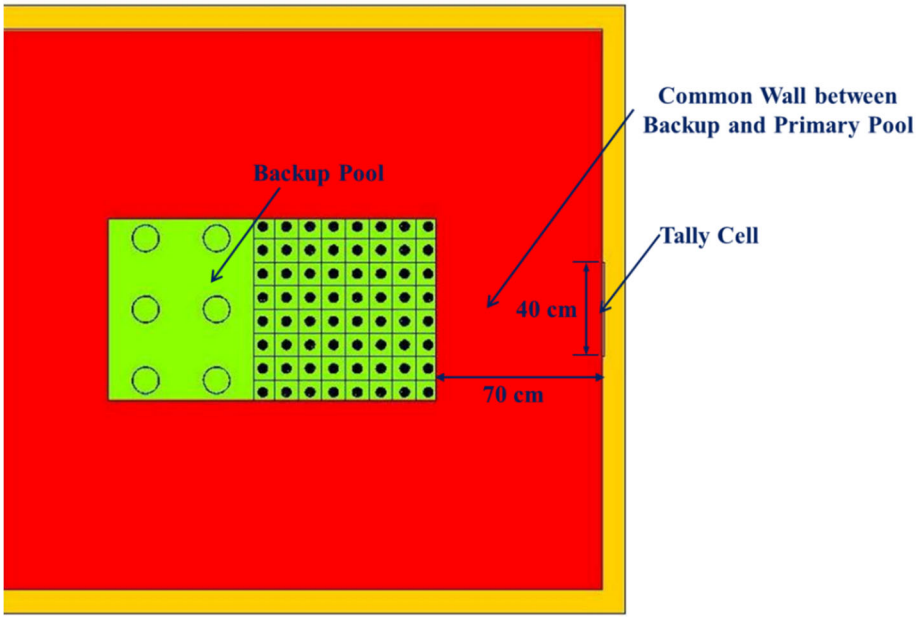

Figure V.2.8. X-Y cross section of the backup storage pool with 64 fuel assemblies stored, as well as the shared (common) concrete wall

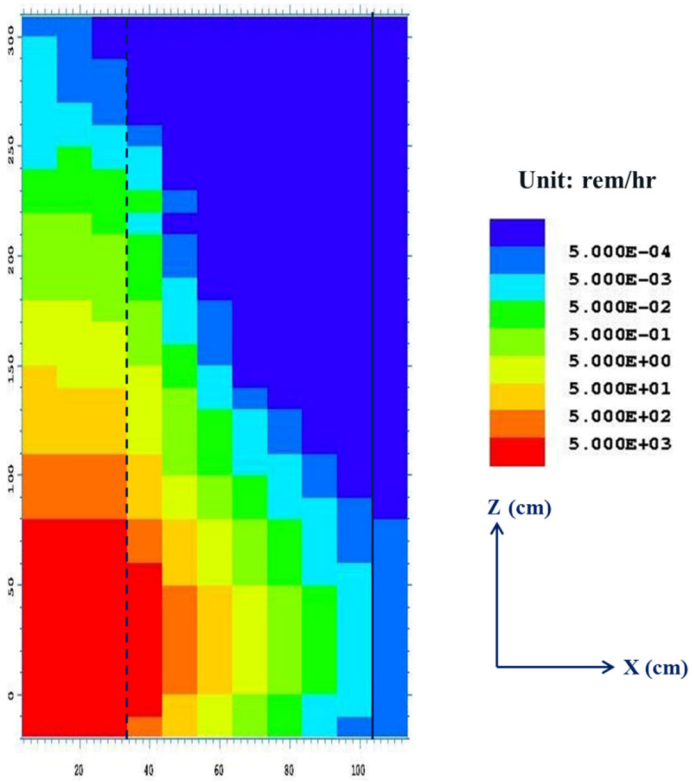

Figure V.2.9. Photon dose profile across the shared wall

V.3 Thermal-Hydraulic Analysis and Design

V.3.1 Introduction

In this section, the thermal-hydraulic analyses performed as part of the design of the spent fuel pools are summarized. Two identical independent storage pools for storing the spent fuel and target assemblies are in the subcritical assembly hall, isolated from the rest of the facility. Each pool consists of two concentric tanks separated by a gap filled with air and in open communication with the room environment. The analysis is focused on a single pool, since the two pools are identical, and the second pool is designed to be in stand-by mode to receive spent fuel and used target assemblies if the first one develops a water leak.

Originally the tanks were designed to be cooled by an air thermosiphon coupled to a water thermosiphon. The heat within the pool is removed by a water buoyancy-driven flow which transfers the heat from the fuel region to the tank surface, where the heat is transferred to the air thermosiphon. In Section V.3.2 this design is analyzed; it is relevant because it shows some of the early dimensioning of the pool and an extensive sensitivity study of the simulation conditions.

The final design relies on forced convection to remove heat. The heat within the pool is removed by a water buoyancy-driven flow which transfers the heat from the spent fuel and

used target to the tank surface, where the heat is transferred to the air. A fan provides a fixed amount of air flow to cool the surface of the tank. The details of this analysis are provided in section V.3.3.

V.3.2 Passive Design Analyses

A three-dimensional representation of the original passive design is shown in Fig. V.3.2.1. Four sets of simulations were performed, the full list is reported in Table V.3.2.1:

- Simulation sets A and B assumed a constant heat flux on the lateral walls in a simplified geometry representing the air thermosiphon alone. The value of the constant heat flux was determined by computing the maximum heat load corresponding to the decay heat 30 days after shutdown divided by the surface area of the pool. The power from the spent fuels after 30 days from shutdown was computed using ORIGEN-2, see Sec. V.2. for further details regarding the ORIGEN-2 analysis.
- Simulation set C presents a realistic geometry simulation of the air natural convection thermosiphon.
- Simulation set D is a fully coupled simulation in which the aluminum tank is simulated in detail. The heat sink was modeled in all cases by fixing the outer boundary temperature.

Modeling details of the four simulation sets are given below in Sec. V.3.2.1.

Initially a series of two-dimensional CFD calculations were performed to examine whether the gap alone would be sufficient for heat removal, through the establishment of a natural convection cellular structure of the type encountered in differentially heated cavities.

Table V.3.2.1. List of cases

Case	Loading %	Power[W]	Type, Comments
A1	48	234	2D, Air
A2	77	364	2D, Air
A3	100	494	2D, Air
B1	48	234	Simplified 3D, Air
B2	77	364	Simplified 3D, Air
B3	100	494	Simplified 3D, Air
C1	100	494	Full 3D, Air, see Table V.3.2.2.3
C2	100	494	Full 3D, Air, see Table V.3.2.2.3
C3	100	494	Full 3D, Air, see Table V.3.2.2.3
C4	100	494	Full 3D, Air, see Table V.3.2.2.3
D1	100	494	Full 3D, Air, Steel and Water, uniform heat
D2	100	494	Full 3D, Air, Steel and Water, porous medium

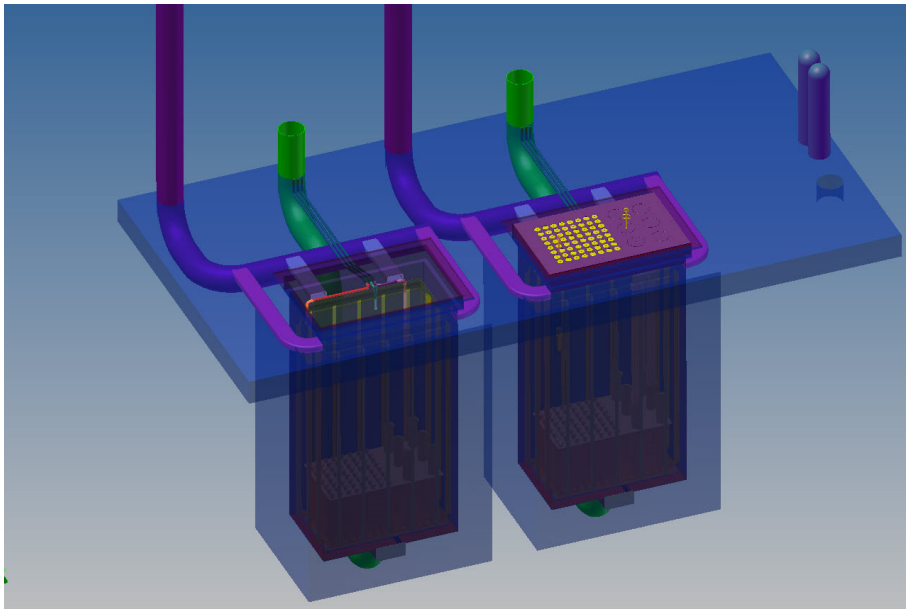

Figure V.3.2.1. CAD representation of the two independent spent fuel and used target assemblies storage pools, natural convection design.

Then another series of 2D CFD calculations were performed on an alternative design in which a duct was added at the bottom of the storage pool and directly connected to the external room; simulation set A. This duct helps create a natural circulation loop; the heat produced by the tank is dissipated in the room atmosphere by the air conditioning system. This series of calculations represents a scoping study to identify the key parameters in the system. The results will be discussed in Sec. V.3.2.2. The conclusion of this scoping study was that the natural circulation option using the duct is necessary for adequate heat removal from the pool, and a simplified 3D CFD simulation was performed for the actual design to verify that the design performance, Set B. The results of this simulation are also discussed in Sec. V.3.2.2.

The full geometry was investigated in sets C and D. Set C considered only the air thermosiphon, set D simulated the fully coupled system. A sensitivity study on the turbulence model was performed, and the results are reported in Sec. V.3.2.2. Results for the fully coupled simulation are reported in Sec. V.3.2.3.

V.3.2.1 Modeling practices

Both 2D and 3D simulations were performed using the STAR-CCM+5.06 (V.3.1) code. In all simulations performed within sets A, B, and C, the interior structure of the pool was not modeled. Each simulation was carried out assuming only air to be present inside the tank, to confirm whether a natural circulation pattern could be established. These simulations performed assumed, a constant heat flux on the lateral walls. The constant heat flux was determined by computing the total power 30 days from shutdown and dividing by the lateral flow area of the pool. The loadings for these cases are summarized in Table V.3.2.1.1

Table V.3.2.1.1. Power and heat flux for the loadings used in simulation sets A and B

Percent Loading	Power, W	Number of Spent Fuel Assemblies.
48%	234	18
77%	364	28
100%	494	38

The heat sink was modeled by fixing the temperature in the upper boundaries of the room. Several other options have been tested (such as a volumetric heat sink) without significant differences in the results. The heat sink role in the present case is to remove the heat in full, and due to the large size of the room above, this can be easily achieved without degrading the performance of the natural convection system. Thus, the form of the heat sink is not particularly relevant.

The boundary conditions for Case B are summarized in Fig. V.3.2.1.1. For case A, the boundary conditions were slightly different (See Fig. V.3.2.1.2) in that set A uses symmetry boundary conditions.

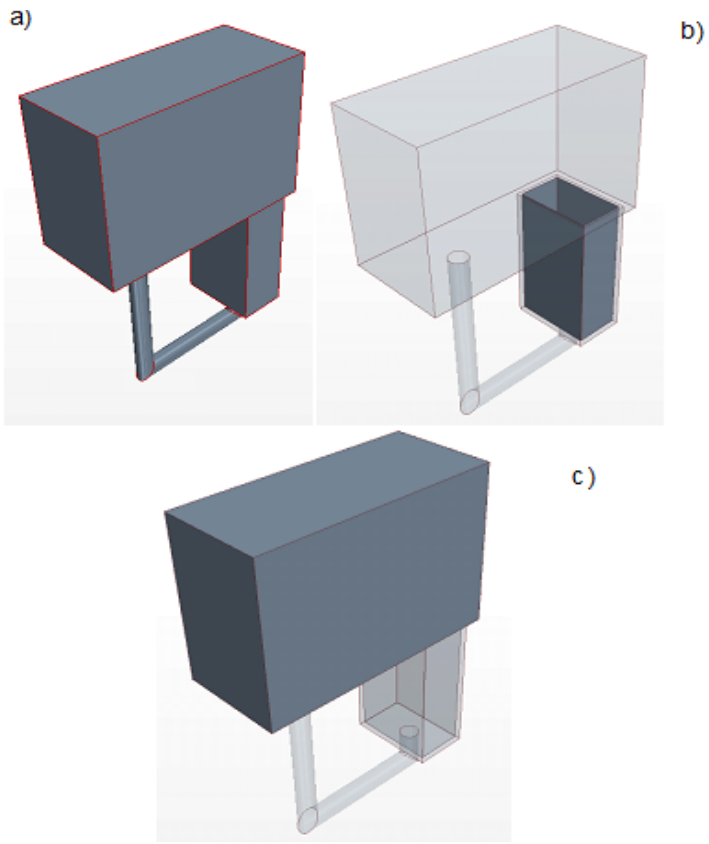

Figure V.3.2.1.1. Boundary conditions for case B. (a) 3D view, (b) heat source constant heat flux boundary on the lateral walls of the pool, (c) constant temperature at the room boundary.

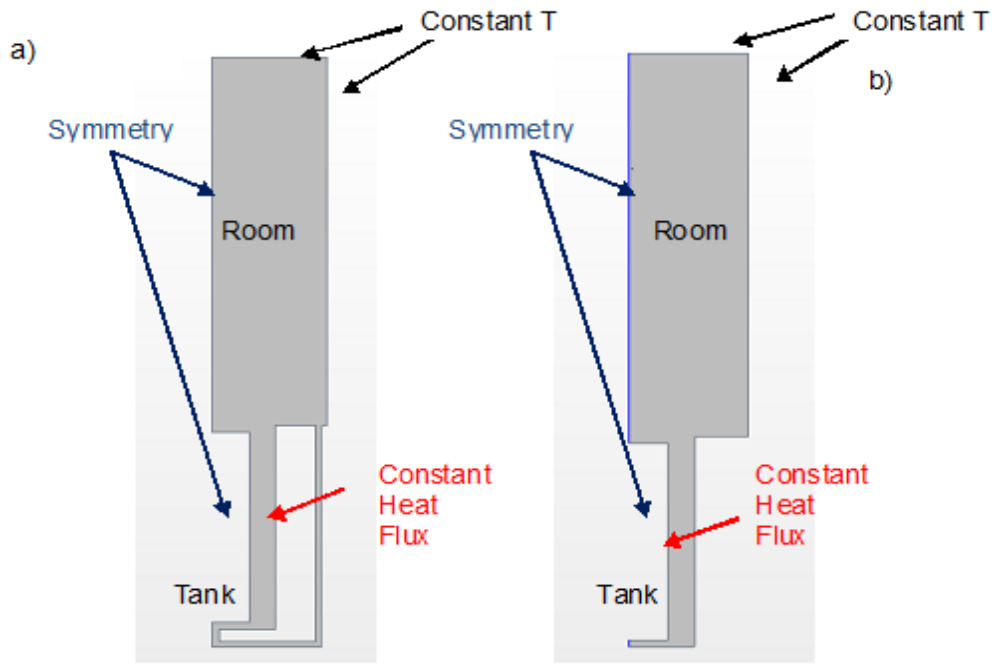

Figure V.3.2.1.2. Boundary conditions for the 2D cases of set A. (a) gap+ duct, (b) only gap.

In all cases the ambient temperature was set to 300 K, and the room above was assumed to be 2.5 m high (half the actual height of the room). In the 2D scoping cases (set A) the room was assumed to be half a meter taller. Moreover, a symmetry boundary condition was assumed in the middle of the tank, Fig. V.3.2.1.2.

Figure V.3.2.1.3 shows the boundary conditions for the full geometry cases C and D. Note that:

- in cases C1-C4, only the air thermosiphon is simulated.
- In case D1, the water tank is simulated as a homogenous medium.
- In case D2, the fuel region is separated from the water tank and simulated as a porous medium.
- In cases D1 and D2, the steel tank, 2 cm in thickness with a conductivity of 20 W/m^2K, is included in the simulation.

An advanced wall treatment (All-y+ wall treatment) was applied at the walls. The All-y+ treatment adapts the near wall strategy depending on the size of the first layer before the wall. If the first layer cell is sufficiently small, a wall-resolving strategy is adopted. If the first layer near wall cell is large, a wall-function approach is adopted. For intermediate values of the near wall cell a blend of the two approaches is adopted.

A realizable k-□ turbulence model was used. The Boussinesq approximation was used to consider the buoyancy effect. Most calculations were performed using the realizable

k- model with a buoyancy-driven two-layer all-y+ wall model, section V.3.2. Additional turbulence models were also tried, k- SST, realizable k-, with different models for the boundary layer, V.3.1, V.3.2, and the thermal stresses, section V.3.3. In fact, the way the wall boundary layer is modeled has a potential impact on the temperature distribution. The sensitivity of the peak pool surface temperature to the choice of turbulence model is discussed in Section V.3.2.2.

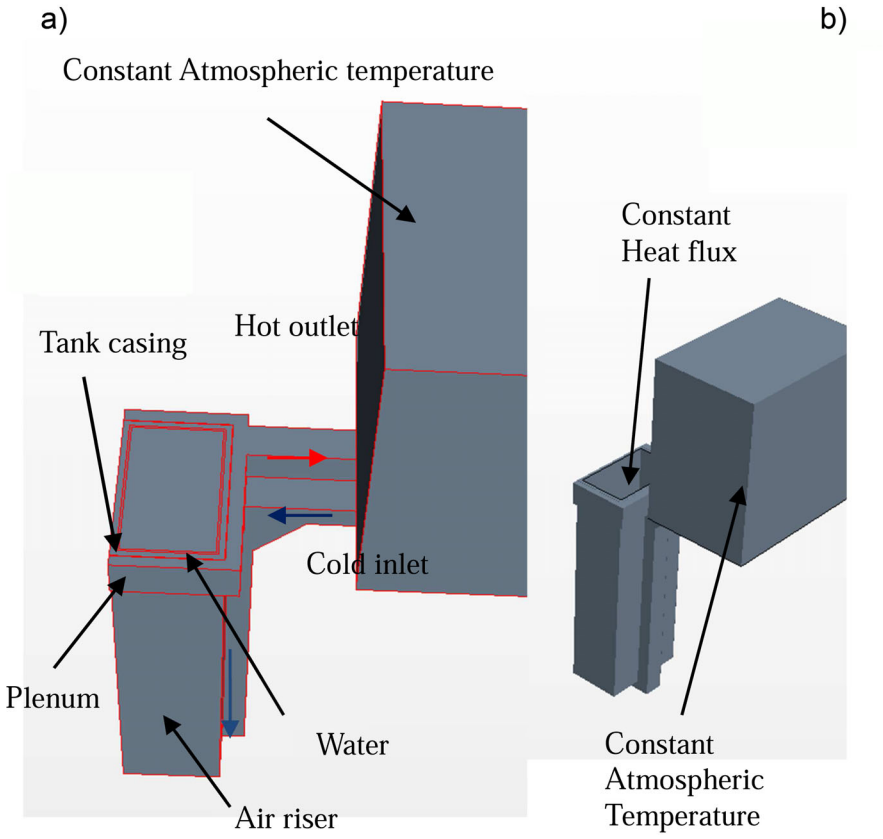

Figure V.3.2.1.3 Full domain for case D (a) and thermosiphon only (b).

For some cases, Case A3 with only the gap and case D1 and D2, the standard segregated solver did not produce a reliable steady state. In such cases the steady state results computed have high residuals and cannot be considered a true solution of the relevant equations. Therefore, in the 2D case A3, unsteady simulations were performed to establish whether the solution would change significantly, and it was demonstrated that the peak temperature oscillates within a few degrees Kelvin from the steady state solution in a quasi-ergodic state. In cases D1 and D2 the segregated solver failed to produce a reliable solution in both steady and unsteady mode. In fact, boundary heat transfer conservation was not satisfied. Therefore, as discussed later, a coupled solver, i.e., a solver that solves momentum, continuity, and energy equation at the same time, has been used with much better results.

The discretization scheme used was a blended second-order upwind scheme for the momentum equation and energy equations. The results tend to be sensitive to the mesh discretization near the wall. Enough points near the wall are necessary to simulate properly the heat transfer. This can be achieved either with trimmed meshes or polyhedral meshes with a prism layer. For case D the only possible option is polyhedral meshes due to the need for a conformal mesh at the boundary.

A mesh convergence study was conducted for each simulation. Mesh convergence was judged sufficient when successive mesh refinements resulted in less than a 1% change in the temperature and velocity of ten monitored points. Each refinement reduced the mesh size by a factor of two. This led to high mesh requirements of up to 15 million points for set B simulations, Figs. V.3.2.1.4c and V.3.2.1. 4d show the final mesh selected for the set B cases, 30 million points for set C, and over 40 million points for set D. Figure V.3.2.1.5 shows the mesh used for cases D1 and D2. Figure V.3.2.1.5 shows the mesh details in the fuel region of case D2, presented as a separated porous region of higher energy density.

V.3.2.2 Preliminary results (sets A-C)

A series of 2D scoping cases (set A) have been performed with a heat flux imposed as a boundary condition at the tank surface, since the tank is not simulated. A preliminary test case was run with four different gap sizes and four different duct sizes, with each combination of gap size and duct size using an imposed boundary heat flux of 55 W/m^2. The solution is remarkably different with the addition of a lower duct than it is without the lower duct. Without a lower duct, the flow in the gap has a cellular structure, the flow rises near the vertical heated boundary and falls in the adjacent vertical boundary, and the peak temperature on the pool surface becomes highly sensitive to the gap size, Table V.3.2.2.1.

Figure V.3.2.2.1 shows the temperature distribution along the gap and in the room above for two cases with different gap sizes and without duct. A small gap is unable to discharge heat to the room properly, causing a strong peak in the temperature within the gap, which means the temperature within the tank will also be high. However, increasing the size of the gap is not feasible, since the larger gap would weaken the current support structures design and require a design modification to enlarge the size of the overall system.

With the introduction of a duct, the flow structure becomes simpler, and a natural circulation pattern is established, Figs. V.3.2.2.2 and V.3.2.2.3. Moreover, scoping calculations with STAR-CCM+ indicate that the temperature distribution does not depend significantly on the size of the duct, provided that the latter is sufficiently large. Even for a gap size as small as 6 cm, the peak temperature on the pool surface predicted by the simulation results was acceptable, Fig. V.3.2.2.4.

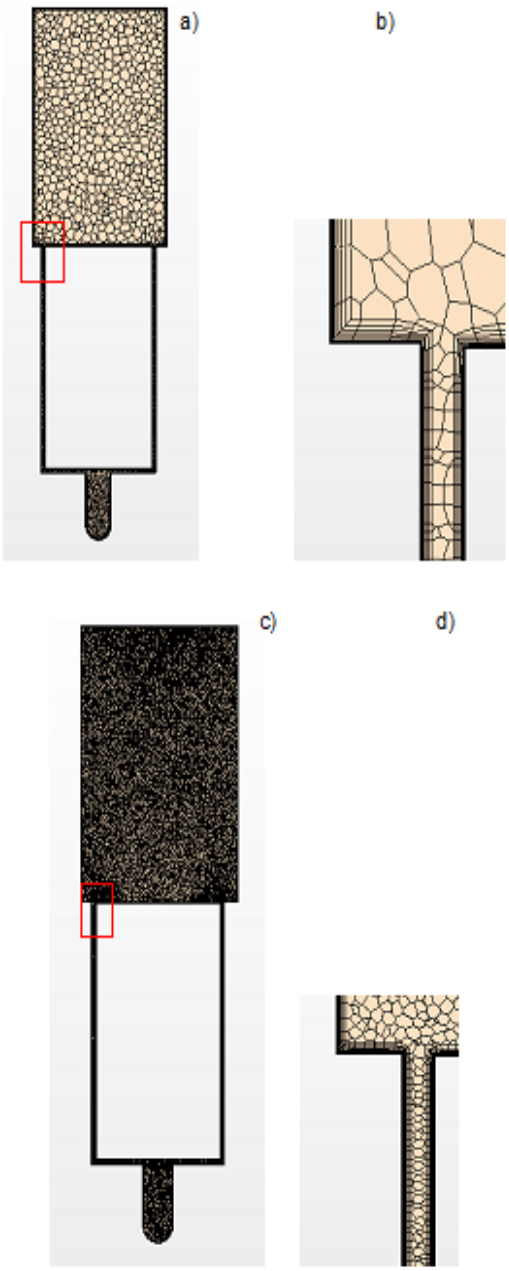

Figure V.3.2.1.4. Mesh (a) Set B, coarse mesh, (b) detail of the mesh (c) set B, fine mesh, (d) detail of the fine mesh

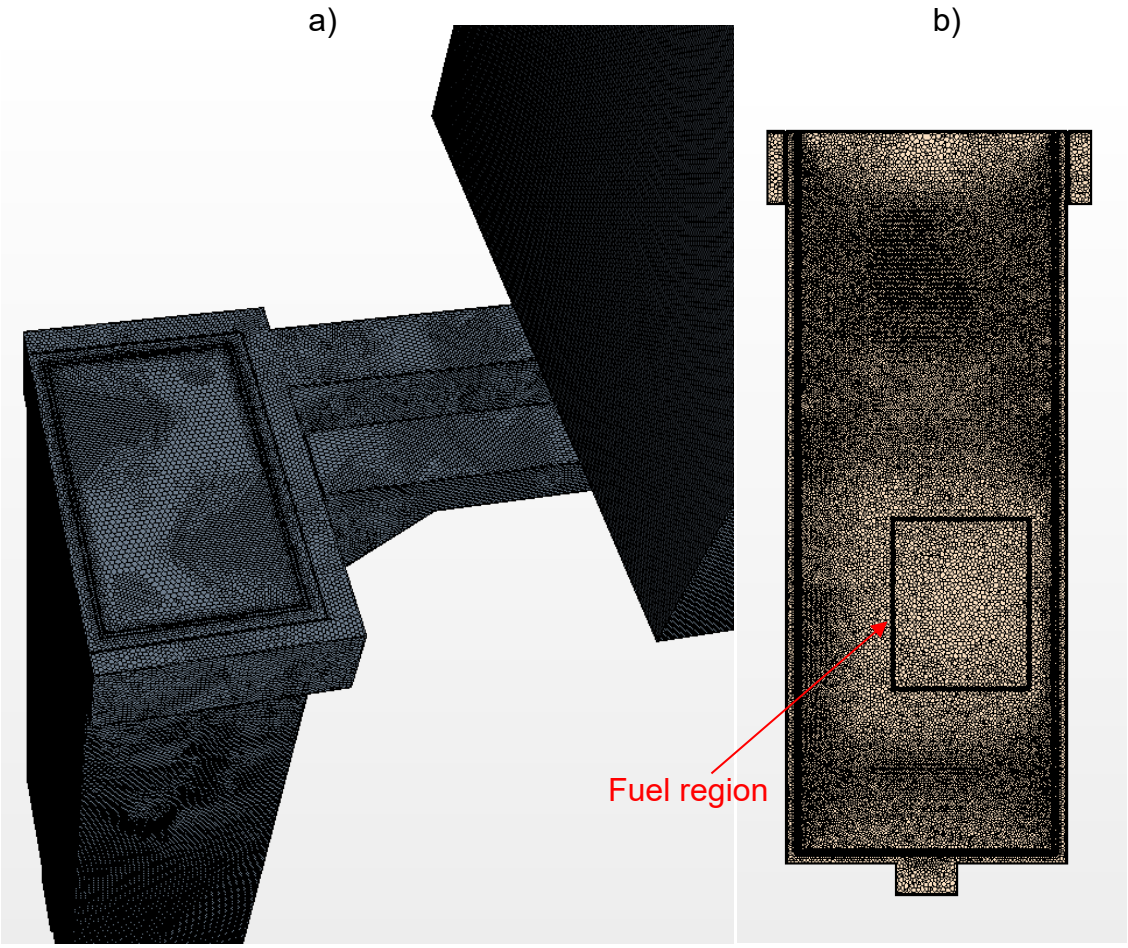

Figure V.3.2.1.5. Polyhedral Mesh, Cases D1 and D2 a) Full geometry b) Cross section in the fuel region and water tank

Table V.3.2.2.1. Peak temperature on the pool surface as a function of the gap size for a constant heat flux of 55 W/m^2

Gap [cm]	Peak [K]
10	374
20	336
30	321
40	318

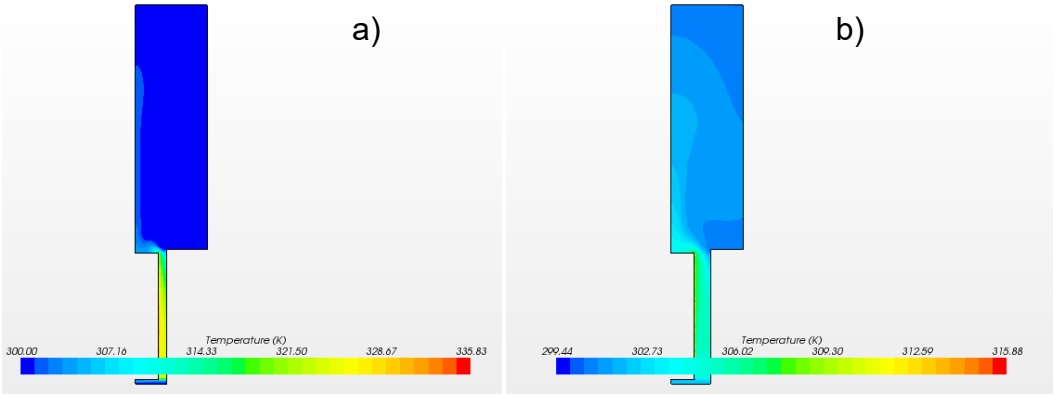

Figure V.3.2.2.1. Temperature for gap size 20 cm (a), for gap size 40 cm (b)

Based on this scoping study, the gap size was limited as much as possible, 6 cm, and a duct with a diameter of 20 cm was placed underneath the tank. The duct diameter was chosen based on equivalence of the hydraulic diameter between the 2D case shown in Figs. V.3.2.2.2, V.3.2.2.3, and V.3.2.2.4 and the 3D geometry.

The results obtained with the 3D simulations confirmed the soundness of the results previously obtained with set A just discussed. An example of the temperature distribution is shown in Fig. V.3.2.2.5 for Case B2. The peak of the temperature distribution as a function of the loading factor is shown in Table V.3.2.2.2.

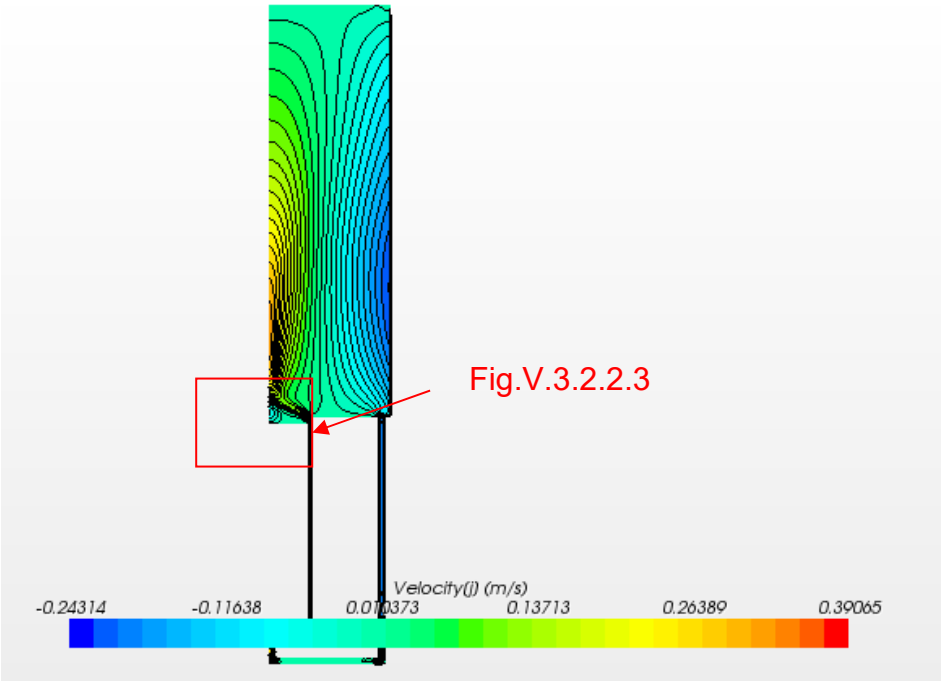

Figure V.3.2.2.2. Vertical velocity, gap size 6 cm, constant heat flux 28 W/m^2

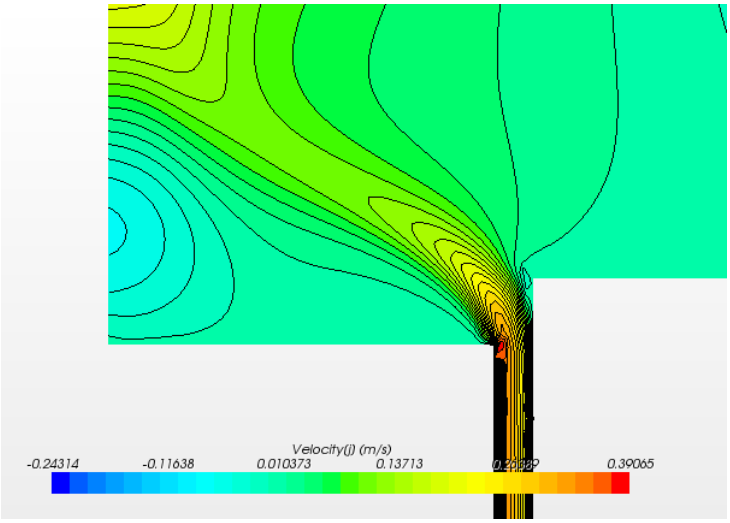

Figure V.3.2.2.3. Vertical velocity, gap size 6 cm, constant heat flux 28 W/m^2

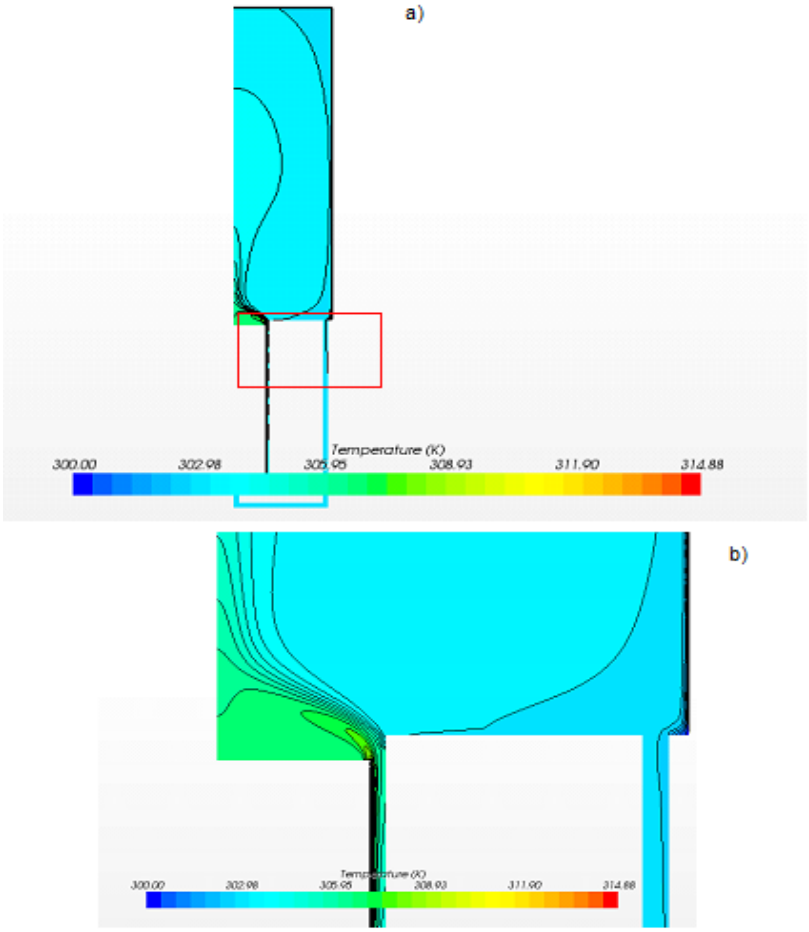

Figure V.3.2.2.4. Temperature, gap size 6 cm, duct size 10 cm, Constant heat flux 28 W/m^2. Full case (a), and Detail (b)

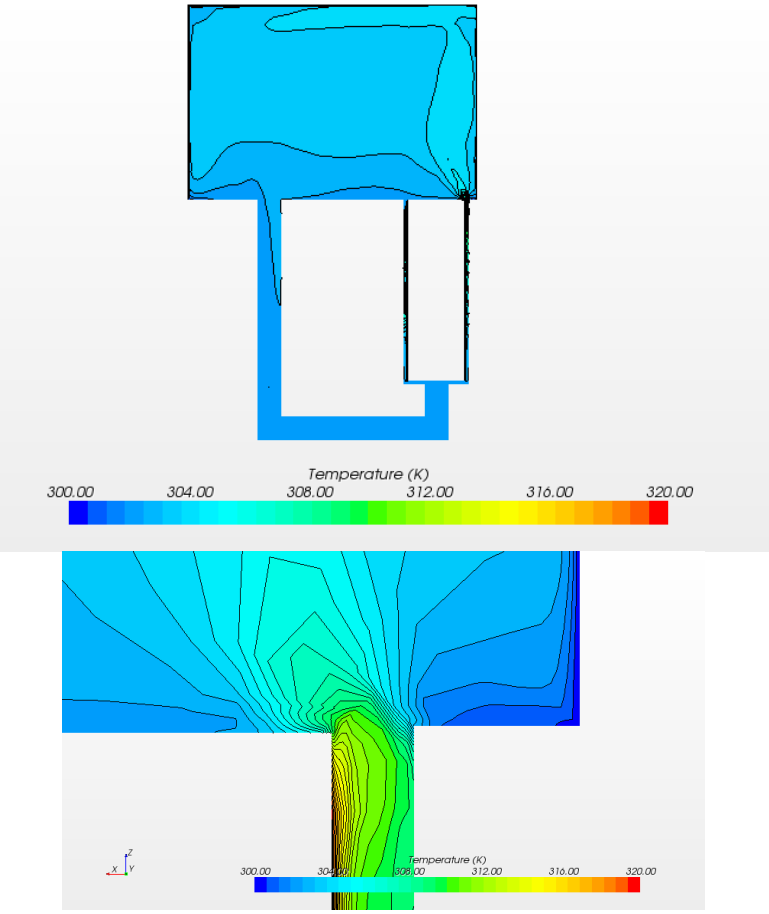

Figure V.3.2.2.5. Temperature distribution for Case B2, coarse mesh.

Table V.3.2.2.2 Peak temperature on the surface as a function of the loading factor.

Case	Loading factor	Peak, K
A	48%	316
B	77%	322
C	100%	328

The 3D simulations verify that the introduction of a duct below the spent fuel pool ensures the cooling of the spent fuel pool, with a peak surface temperature of about 316 K for a half loading of spent fuel and 328 K for a full loading.

Figure V.3.2.2.6 shows the plume that develops on top of the spent fuel pool. Note that the plume is slightly asymmetrical due to the asymmetrical layout of the room, which reflects the presence of a second pool.

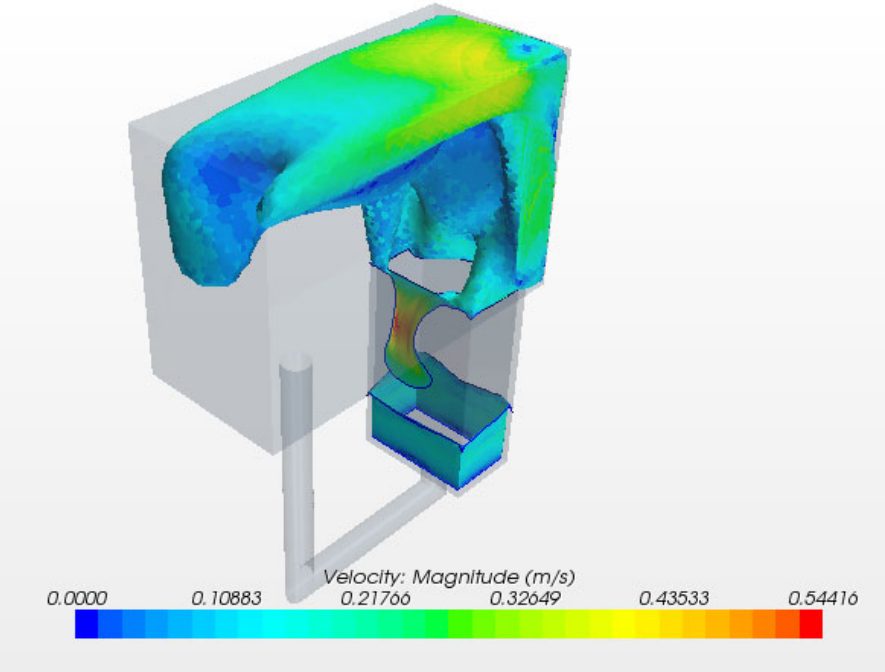

Figure V.3.2.2.6. Iso-surface of the temperature at 304 K, with velocity magnitude projected on it.

To verify the results of simulation set B, a set of simulations C has been performed reflecting the actual geometric layout. Set B evaluated a preliminary design used only to verify that conclusions drawn for a 2D design hold for a 3D design. Set C performed simulations on the final design. The results for the two simulations are shown in Fig. V.3.2.2.7 for case C1 showing the velocity and temperature distribution in the risers. They are clearly compatible with previous results and show a remarkable degree of independence from geometric details. Fig. V.3.2.2.7 confirms that the temperature at the water tank surface is below 328 K for an atmospheric temperature of 303 K.

The geometry of the pool design with the added duct features an upper plenum connected by four orifices to the gap between the tank and the outer structure. The flow is three-dimensional and complex, as Fig. V.3.2.2.7 shows. Peak velocities reach the 1 m/s range, and the flow is turbulent. Since there is no turbulence model specifically designed for the present application, a sensitivity analysis on the effect of the choice of turbulence model was considered.

To assess the effect of turbulence modeling upon the temperature distribution, four different turbulence model options were examined; these are summarized in Table V.3.2.2.3. As shown in the table, all models reported peak temperatures within 2 K. The highest impact of the turbulence model can be seen at the orifices between the air riser and the plenum, Figs. V.3.2.2.8 and V.3.2.2.9.

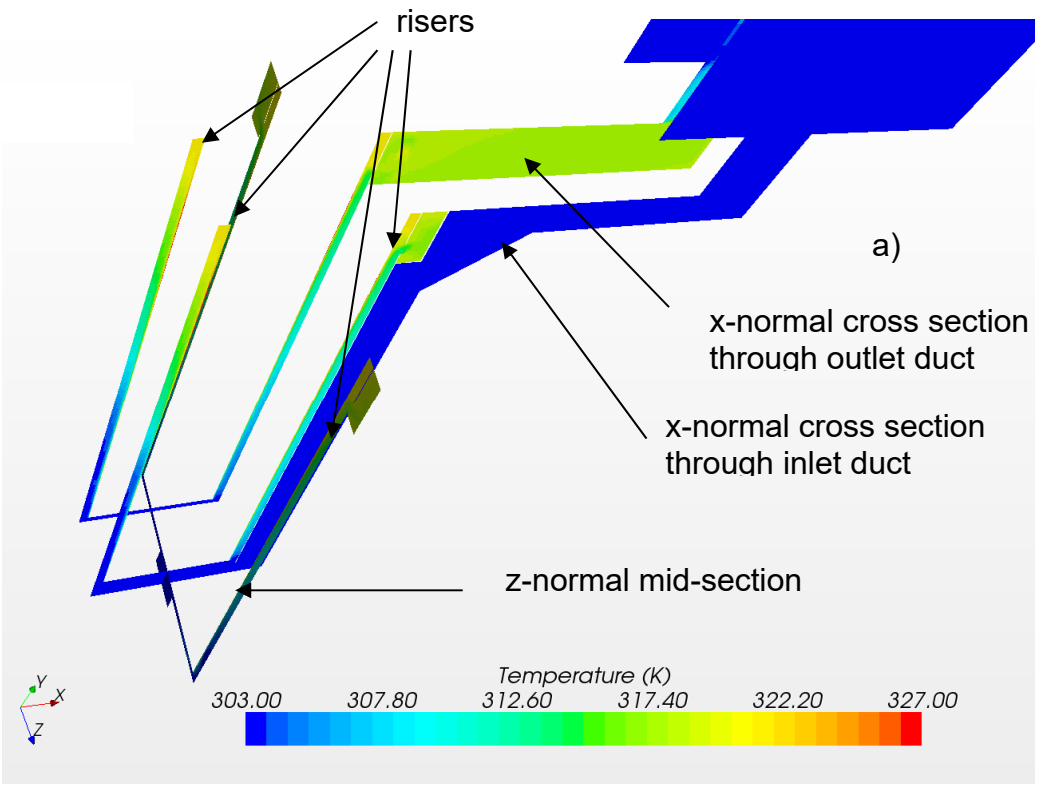

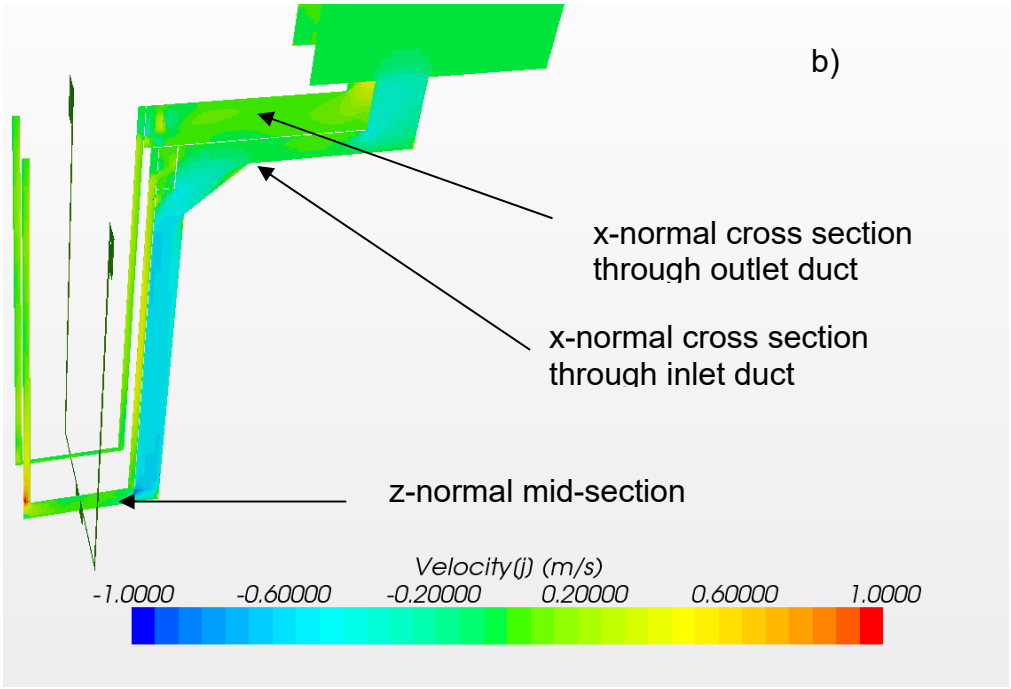

Figure V.3.2.2.7. Multiple cross sections for case C1. Temperature (a) and velocity (b).

Table V.3.2.2.3. Peak pool surface temperature as a function of the turbulence model

Case	Loading factor	Peak Temp., K	Turbulence model
C1	100%	327	Realizable k-ε, Buoyancy Driven wall model
C2	100%	328	Realizable k-ε, Shear Driven options
C3	100%	327	Realizable k-ε, Buoyancy Driven wall model, advanced thermal stresses option
C4	100%	329	k-ω SST

Figures V.3.2.2.8 and V.3.2.2.9 show a comparison between case C1 and case C4 for the temperature and the turbulent kinetic energy in the riser and the orifice regions. Within the riser, the temperature distribution tends to be more homogenous in case C1. In the plenum and in the orifice region the turbulent kinetic energy and the temperature are significantly perturbed. The turbulent kinetic energy maintains low levels throughout the whole domain.

The k-□ SST model, without ad-hoc models for buoyancy, used in case C4 shows an increased level of turbulent kinetic energy in the riser and therefore likely an overestimation of the friction. Cases C1 and C3 delivered nearly indistinguishable results. Case C2 delivered a result between C3 and C1, so results from these three cases are essentially the same. Overall, the choice of turbulence model seems to have little effect on the maximum pool surface temperature predicted by the simulation.

In conclusion, the sensitivity analysis performed showed that the peak temperature has little sensitivity to the turbulence model employed. Therefore, the turbulence model used in case C1 has been used for the coupled simulations, since it has ad-hoc models for turbulence in buoyancy-driven systems.

V.3.2.3 Full Simulation (set D)

A series of fully coupled simulations (set D) was performed to verify the results reported in the previous section. In these calculations, the water pool has been modeled as part of the domain. The heat generation within the pool has been modeled either with a constant localized power in the water (D1) or in a porous region representing the fuel (D2). In case D1 no additional flow resistance is added within the pool. In case D2 flow resistance in the porous region is determined by adding a term in the momentum equation proportional to the velocity

$$\vec{P} = -\overline{K}\vec{v} \quad (1)$$

Where $\overline{K}$ is a tensor and represents the viscous distributed forces. The components of $\overline{K}$ are determined using Darcy's Law in the streamwise direction (vertical direction), while in the remaining directions $\overline{K}$ is set to an arbitrary value three orders of magnitude higher than in the streamwise direction (orthotropic porous medium). In the direction of the flow, the resistance will be determined considering that:

$$K_{22} = \frac{\Delta p}{Lv} = 32\frac{\rho v}{D_h^2} \sim 888\ \frac{kg}{m^3 s} \quad (2)$$

The geometric parameters are taken from the fuel data described in Sec. III.2. The hydraulic diameter D_h is determined by using the standard definition $D_h = 4A/P$, with the cross-sectional area A being the entire cross-sectional area of coolant in the fuel region and the wetted perimeter P being the total wetted perimeter in the fuel region. The porosity used in case D2 is determined by considering the ratio between the coolant cross-sectional area and the total area (see area information given in Tables III.5.2.1.1 and III.5.2.1.2). The total value of porosity obtained is equal to 0.57.

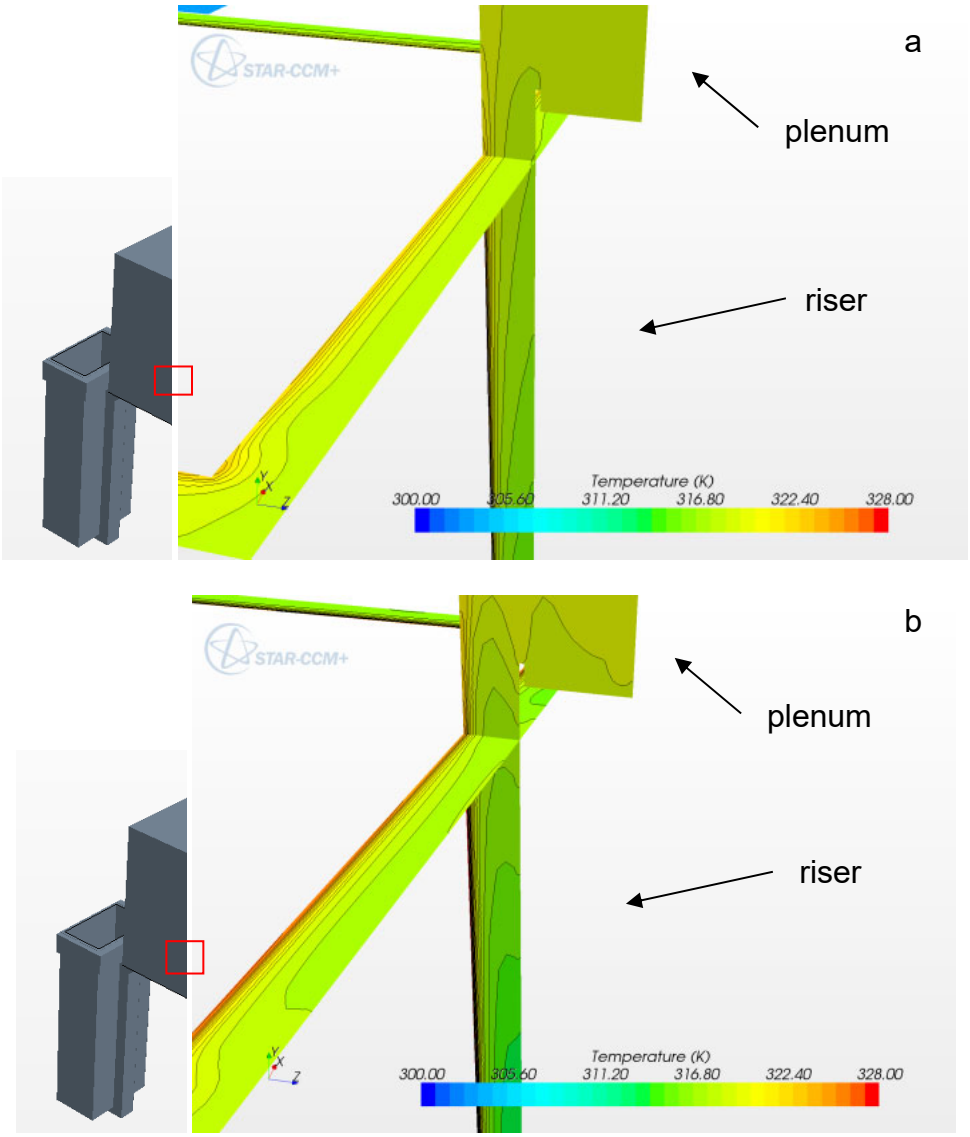

Figure V.3.2.2.8. Temperature distribution at one of the riser-plenum orifices (a) Case C1 (b) Case C4

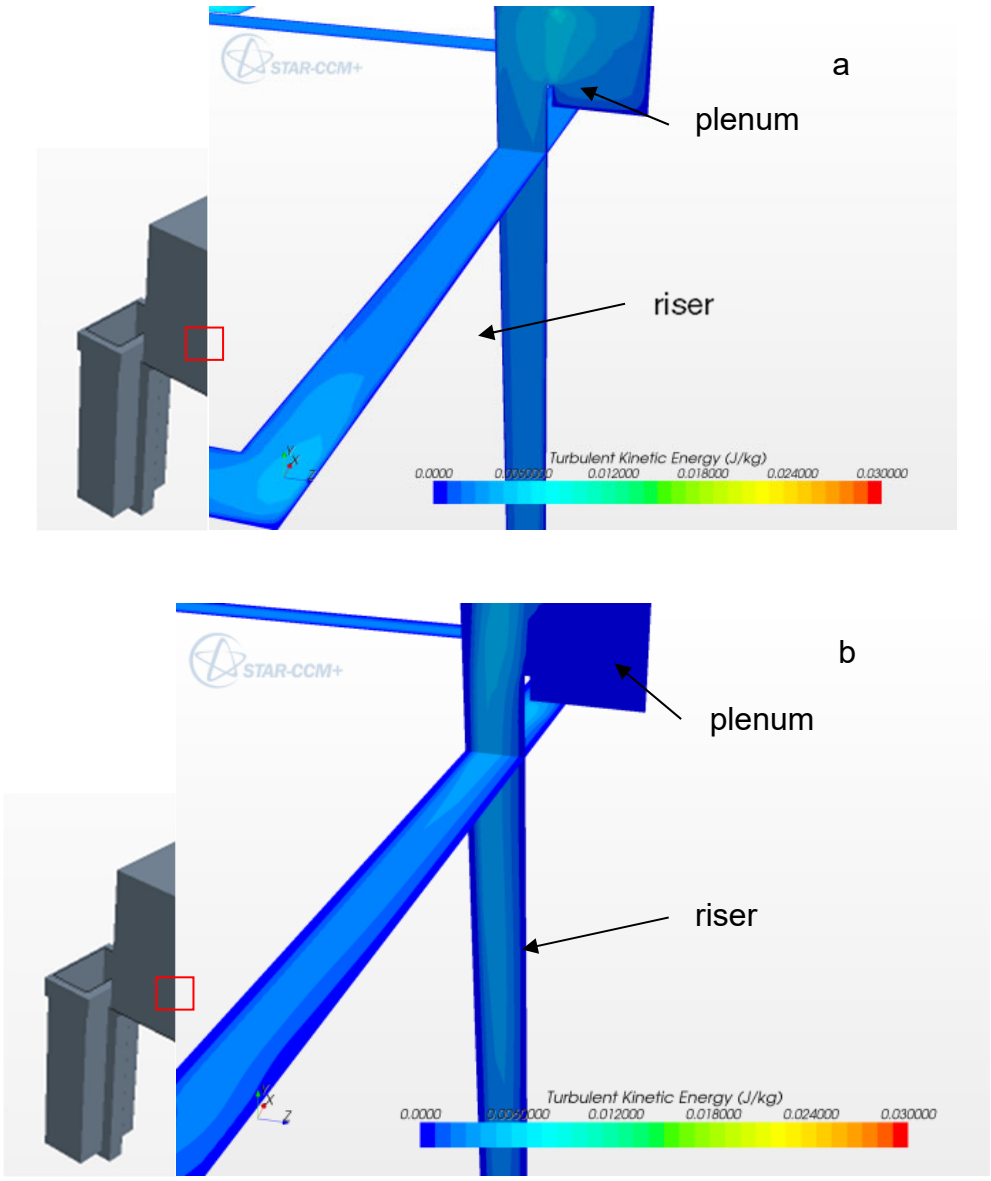

Figure V.3.2.2.9. Turbulent Kinetic Energy distribution at one of the riser-plenum orifices (a) Case C1 (b) Case C4

In case D1 the power is assumed to be distributed homogeneously throughout the first 2 m. from the bottom of the tank (Fig. V.3.2.3.1). The total heat corresponds to a 100% loading factor (494 W). The atmospheric temperature is assumed to be 303 K.

In case D2, the power is assumed to be constant and to be generated within a small limited porous region. Cases D1 and D2 are not necessarily representative of the physical conditions at any given time in the pool but instead represent two bounding cases: a localized power source and a distributed power source.

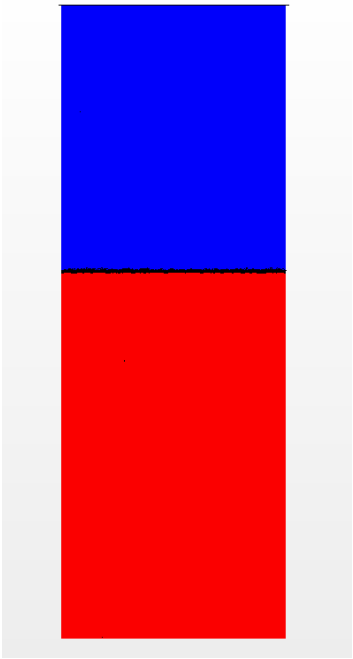

Figure V.3.2.3.1. Cross section of the tank (z=0). The red represents the power region (a height of 2 m. from the bottom of the tank) for case D1

The predicted temperature distribution within the tank is plotted in Fig. V.3.2.3.2 for simulation case D1 and in Figs. V.3.2.3.3 and V.3.2.3.4 for simulation case D2. Note the very small difference in peak temperatures between the two simulations, despite the different assumed power distributions. The actual power distribution within the pool will change over time and it depends on many factors including the fuel discharge scenario and the fuel cooling time before the discharge. However, since the peak temperature does not differ dramatically between these two bounding configurations, it is reasonable to assume that the bounding cases determine a realistic peak of the temperature distribution.

A brief sensitivity study on the parameters of the simulation (porosity, extension of heating length, and arrangement of the fuel region) did not lead to significant changes in temperature distribution – only a fraction of a Kelvin. This is due to the very low power of the system.

In case D2, a natural convection-driven plume develops on top of the spent fuel assembly storage region, as can be seen in plots of iso-contours of the velocity in the vertical direction in Figs. V.3.2.3.5 (flow = 7 mm/s) and V.3.2.3.6 (flow = 5 mm/s). Both plots also show the temperature profile of the fluid moving at the specified velocity. Figure V.3.2.3.7 shows both the iso-contour upwards at 5 mm/s above the spent fuel assemblies and the downward flow iso-contour at -5 mm/s in the corner regions that completes the natural circulation flow pattern and shows that the natural circulation flow is balanced in a near-symmetrical configuration, consistent with the storage pool geometry.

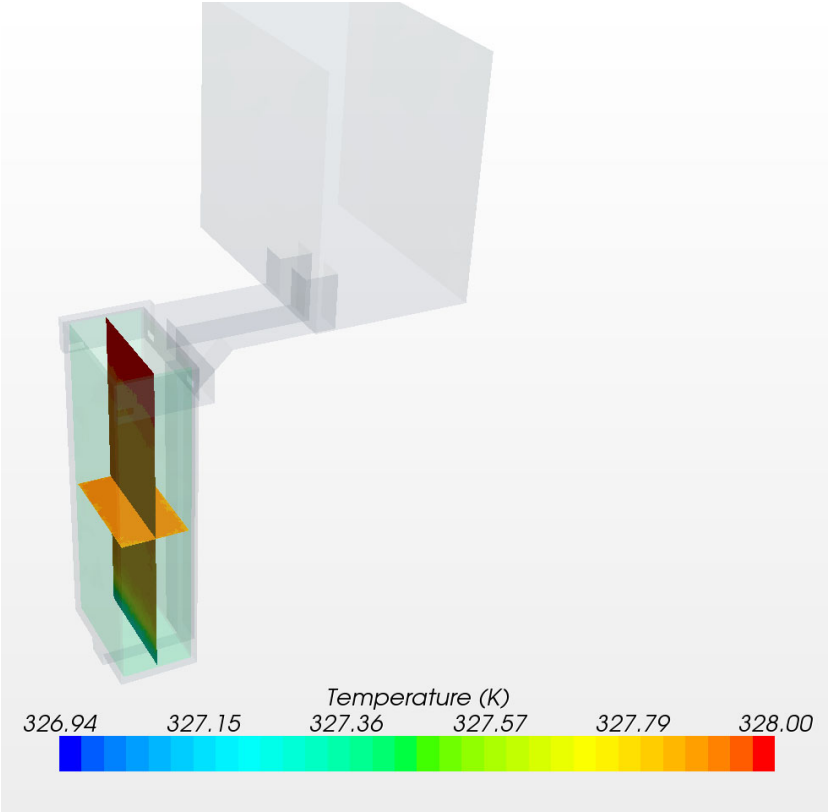

Figure V.3.2.3.2. Temperature in the water tank for case D1.

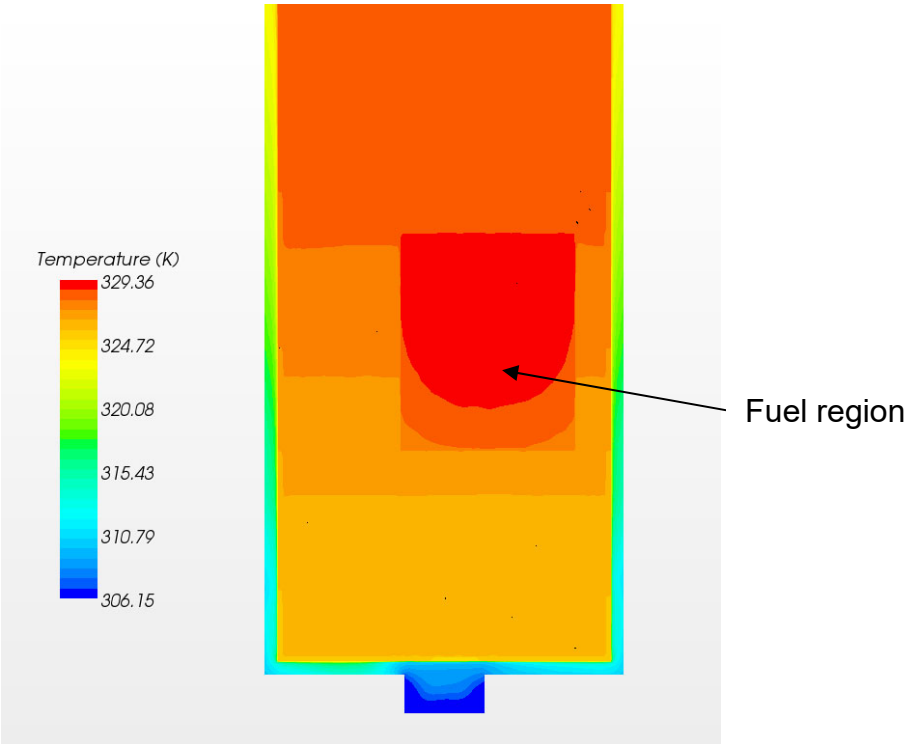

Figure V.3.2.3.3. Temperature in the water tank for case D2. Cross section in the fuel region.

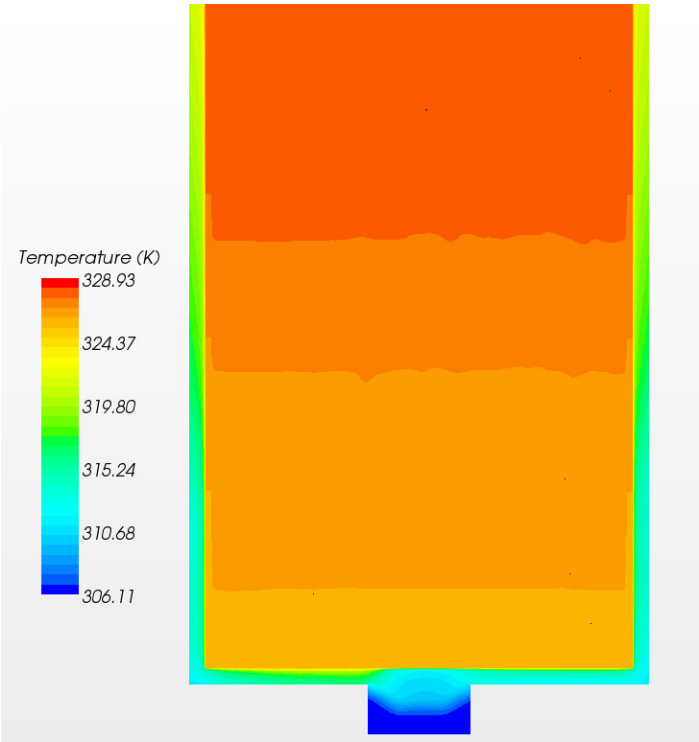

Figure V.3.2.3.4. Temperature in the water tank for case D2. Cross section outside the fuel region.

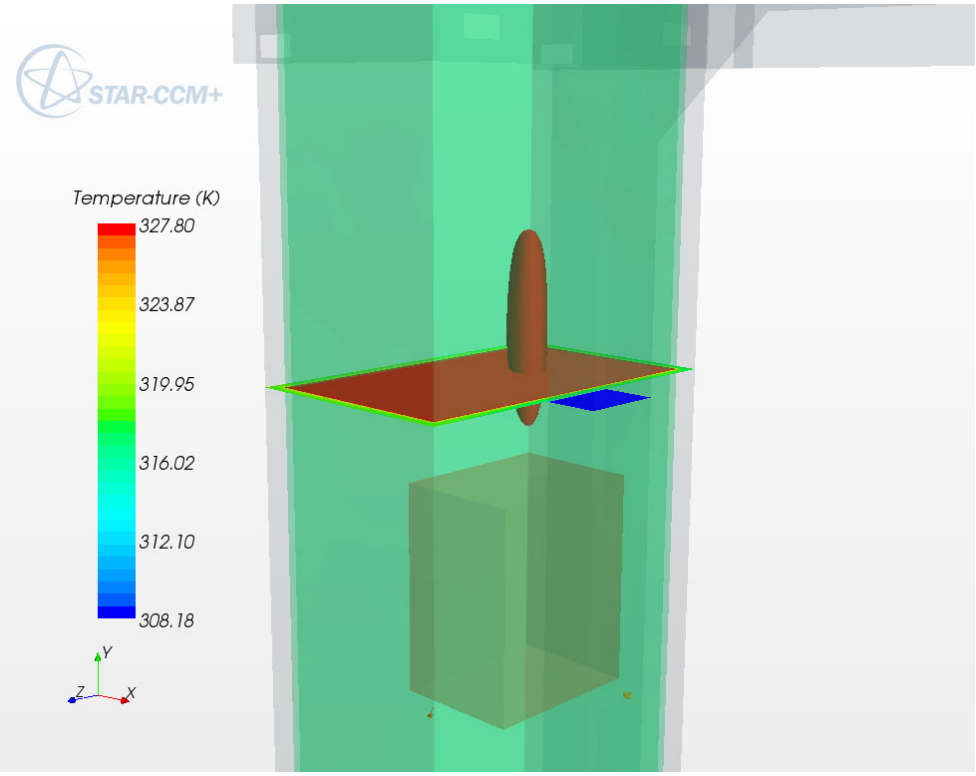

Figure V.3.2.3.5. Iso-contour of the velocity at 7 mm/s and corresponding temperature profile.

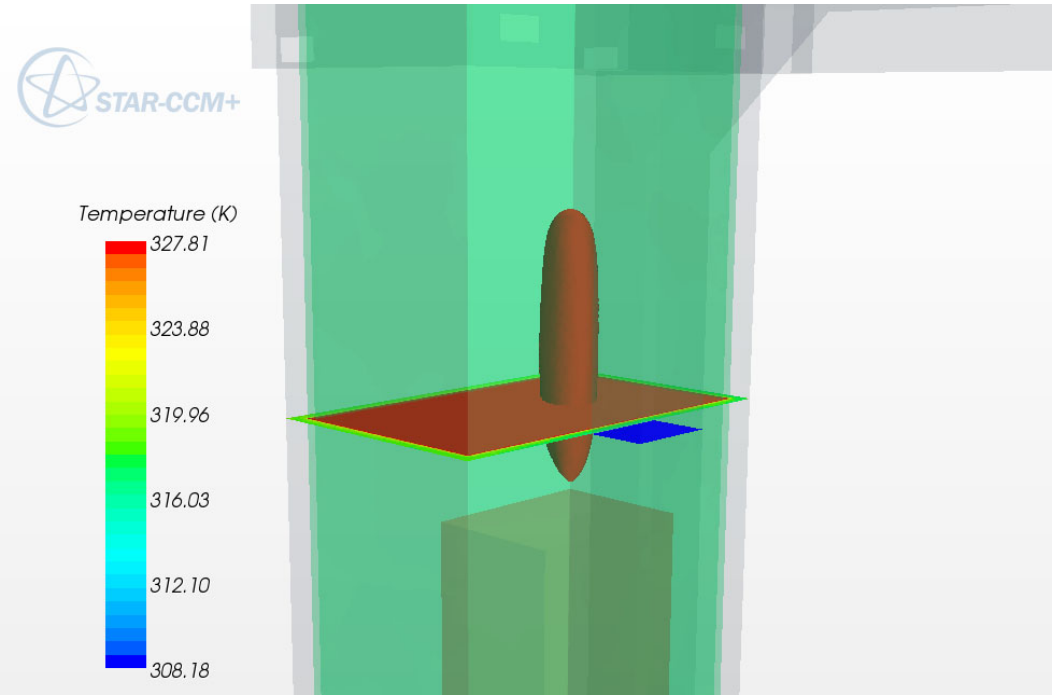

Figure V.3.2.3.6. Iso-contour of the velocity at 5 mm/s and corresponding temperature profile.

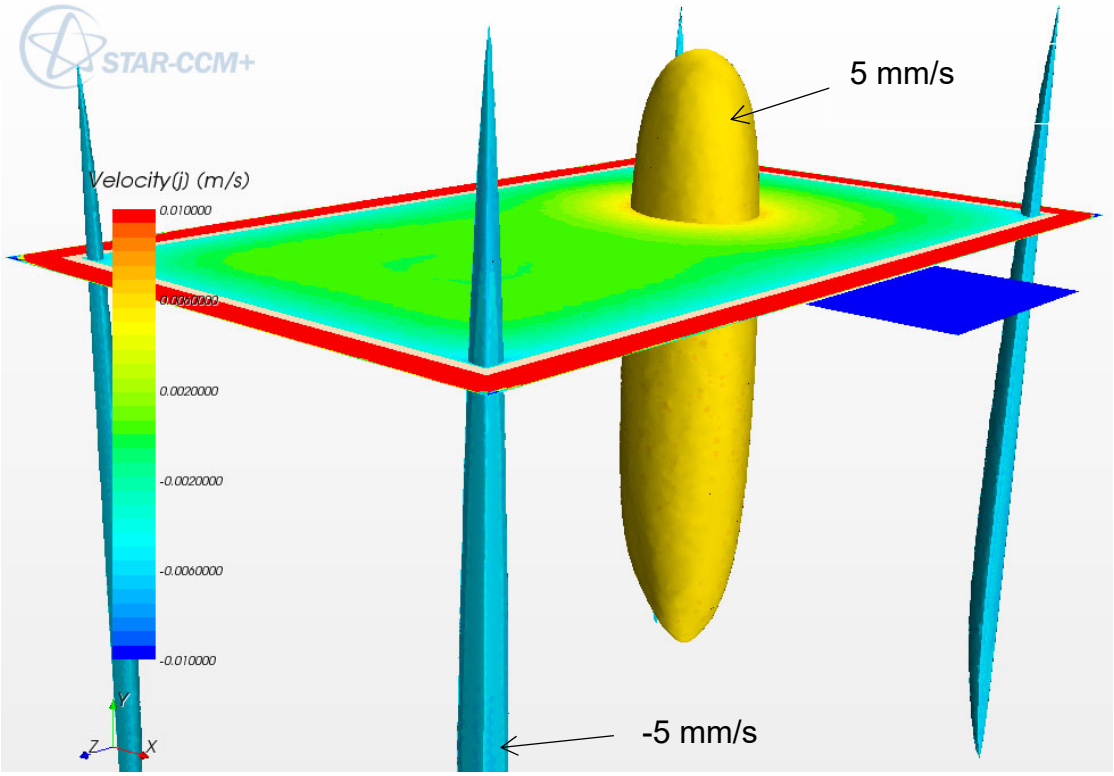

Figure V.3.2.3.7. Iso-contour of the velocity at 5 mm/s and -5 mm/s and cross section of the velocity in the tank showing upward and downward flow.

Due to the high conductivity of the fuel and cladding material and the very low power density, the fuel can be considered in equilibrium with the water and therefore to reach a surface temperature no higher than the peak temperatures of cases D1 and D2.

V.3.2.4 Conclusions

The fuel pool design was analyzed by means of 3D CFD, and it was found that the water pool peak temperature is well below the saturation point of water at atmospheric pressure. The highest water temperature calculated, based on a conservative assumption on the fuel power distribution, is 329.4 K.

V.3.3 Forced Convection Design

The geometry of the final design presents significant differences when compared to the passive design examined in the previous section:

1. The pool was changed to an L-shape (Fig. V.3.3.1d).
2. The external cooling mode of the pool was changed from natural convection to forced convection; a downward forced air flow cools the exterior of the pool.
3. Fins to support the outer structure of the pool have been added.
4. The size of the tubes has been reduced.

For this reason, a new set of calculations has been developed; these calculations are summarized in Table V.3.3.1.

The mass flow rate has been assumed to be equal to 250 m^3/h, a value provided as part of the design to ensure that no aerosols would deposit. The methodology used for all cases involves practices like what were described in section V.3.2.1, with the following differences:

1. The boundary conditions are straightforward in this case since the pool is cooled by an external air forced flow. An inlet-outlet set of boundary conditions has been applied at the extremities of the inlet and outlet channels, Fig. V.3.3.1a.
2. The Realizable k-□ turbulence model has been applied to both air-cooling system and pool. Only the shear-driven boundary layer option has been tried since the flow is shear driven.
3. The present problem is overall much more stable than the natural convection case: the segregated solver has proven to yield converged results; thus, the coupled solver has not been used.
4. Structures, pool, and air-cooling system are modeled explicitly. Since it was proven that the results are overall not sensitive to the assumptions within the pool, the most simplistic assumption is made: the power in the pool is assumed evenly distributed as discussed for case D1.

The pool, the structures and the air-cooling system meshes are shown in Figs. V.3.3.2 and V.3.3.3.

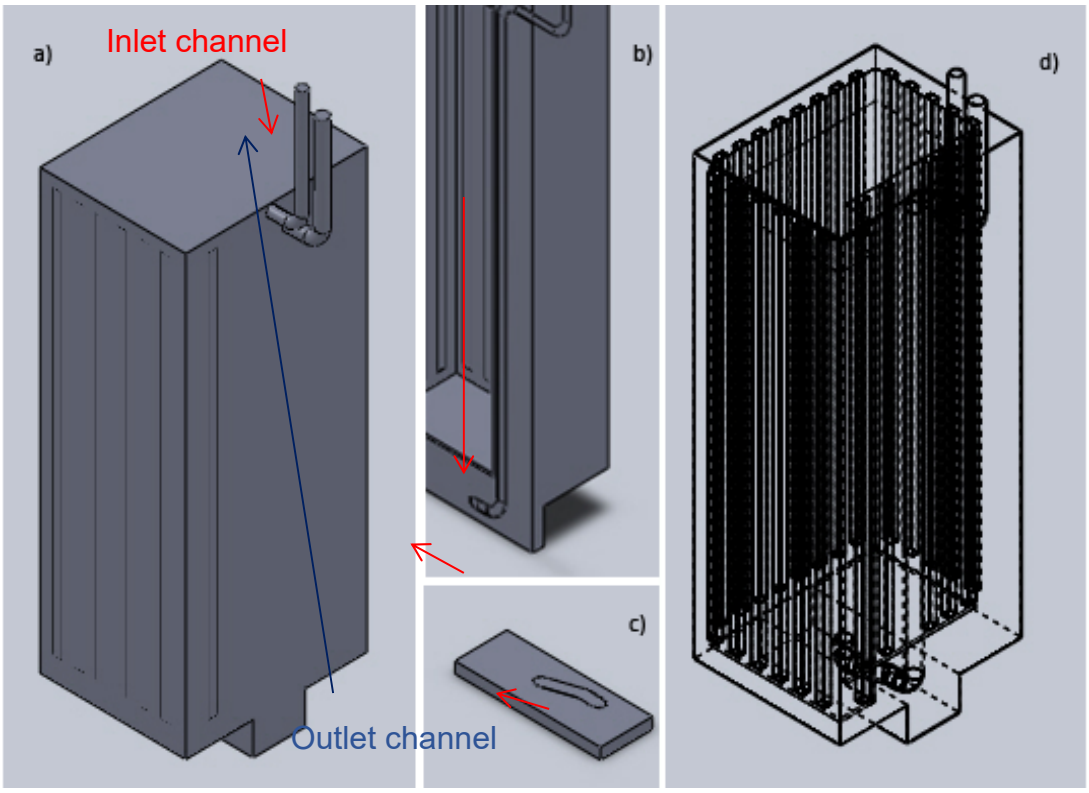

Figure V.3.3.1. a) 3D view of the pool with air cooling system, b-c) section highlighting the inlet channel path, d) 3D view highlighting internals.

Table V.3.3.1. Cases run for the forced convection pool

Case	Loading factor	Number of finite volumes	Turbulence model
E1	100%	~5,000,000	Realizable k-ε, Shear Driven boundary layer in both pool and air-cooling system
E2	100%	~10,000,000	Realizable k-ε, Shear Driven boundary layer in both pool and air-cooling system
E3	100%	~40,000,000	Realizable k-ε, Shear Driven boundary layer in both pool and air-cooling system

A natural convection flow very similar to what is discussed in Sec. V.3.2.3 develops within the pool. A large vertical ascending plume can be observed at the center of the pool (Fig. V.3.3.4 - left), characterized by a positive vertical velocity, while the vertical velocity is negative near the pool walls. Due to the asymmetry of the present design, the plume is slightly off-center and does not have a regular shape (Fig. V.3.3.4 - right). Since the air system cross section is not uniform, the air flow is unbalanced (average flow is higher where the cross section is larger, Fig. V.3.3.5), leading to a slight imbalance in heat transfer coefficient. The positive vertical velocity region is shifted toward the pool surface closer to the air system region with less flow, since such a region will have slightly higher temperatures.

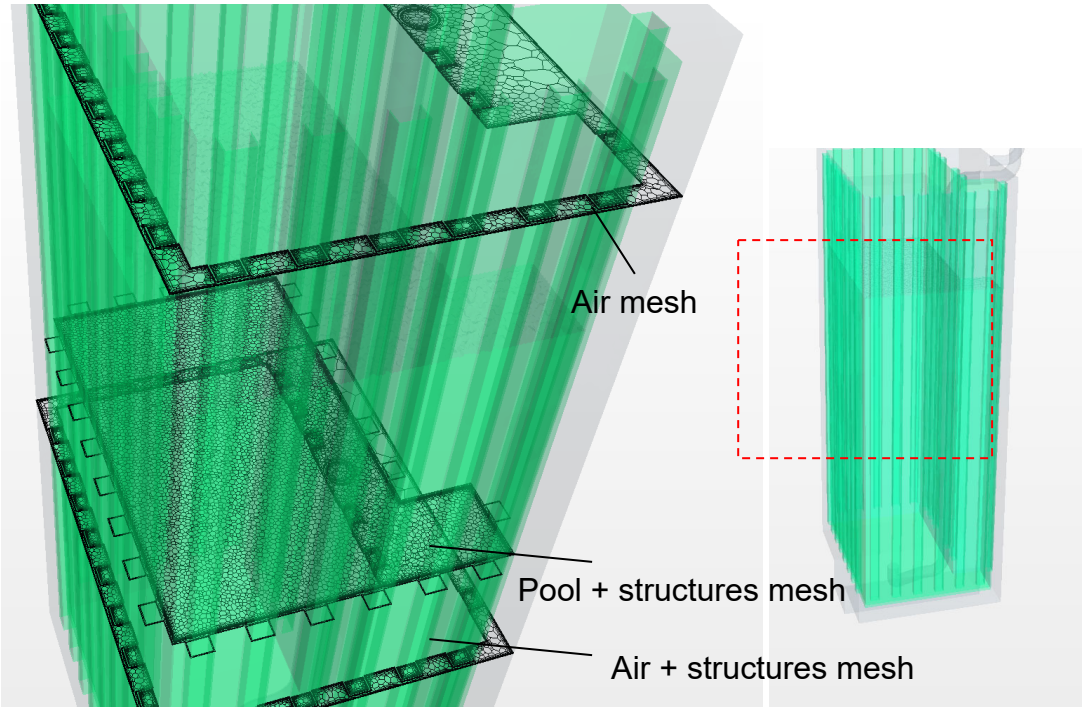

Figure V.3.3.2. 3D view of the pool with sections of the mesh. Calculation E2.

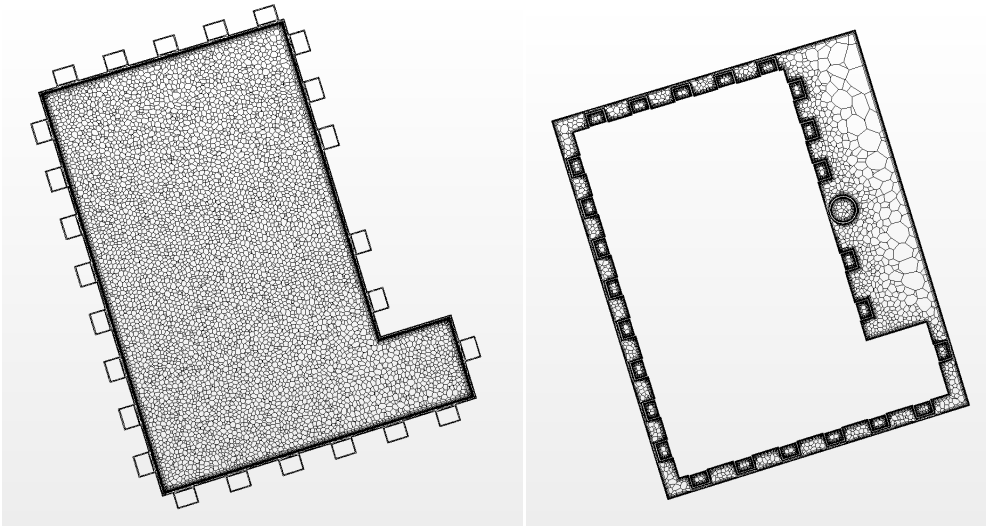

Figure V.3.3.3. Mesh of pool and structures (left) and mesh of the air system (right) at a cross section in the pool region. Calculation E2.

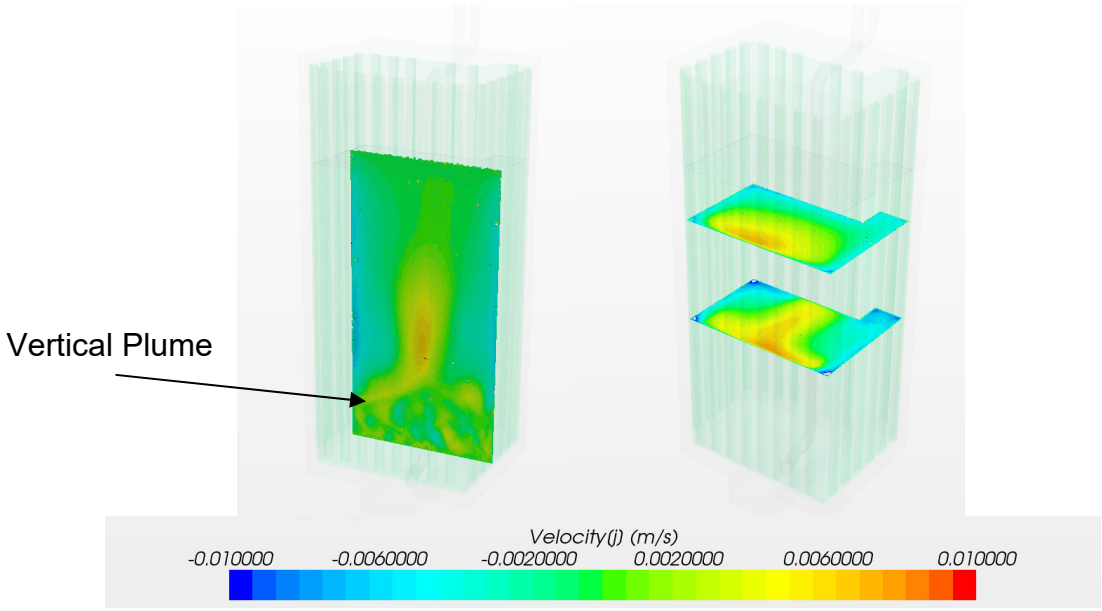

Figure V.3.3.4. Vertical velocity in the pool. (left) vertical cross section. (right) horizontal cross section. Calculation E2.

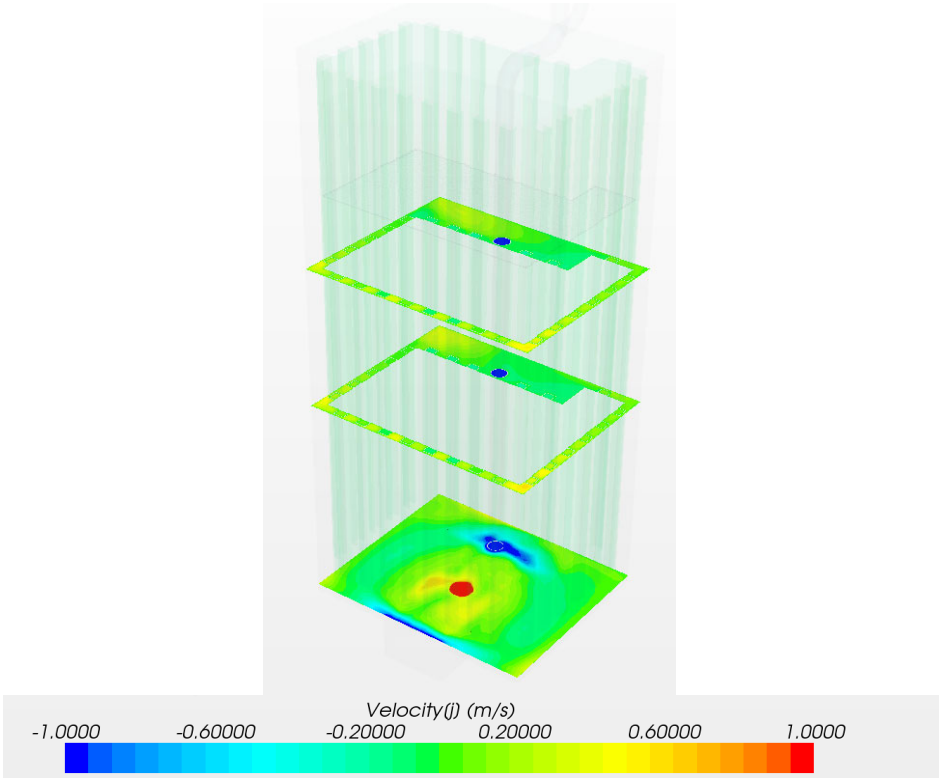

Figure V.3.3.5. Vertical velocity in the air system. Cross sections at different heights. Calculation E2.

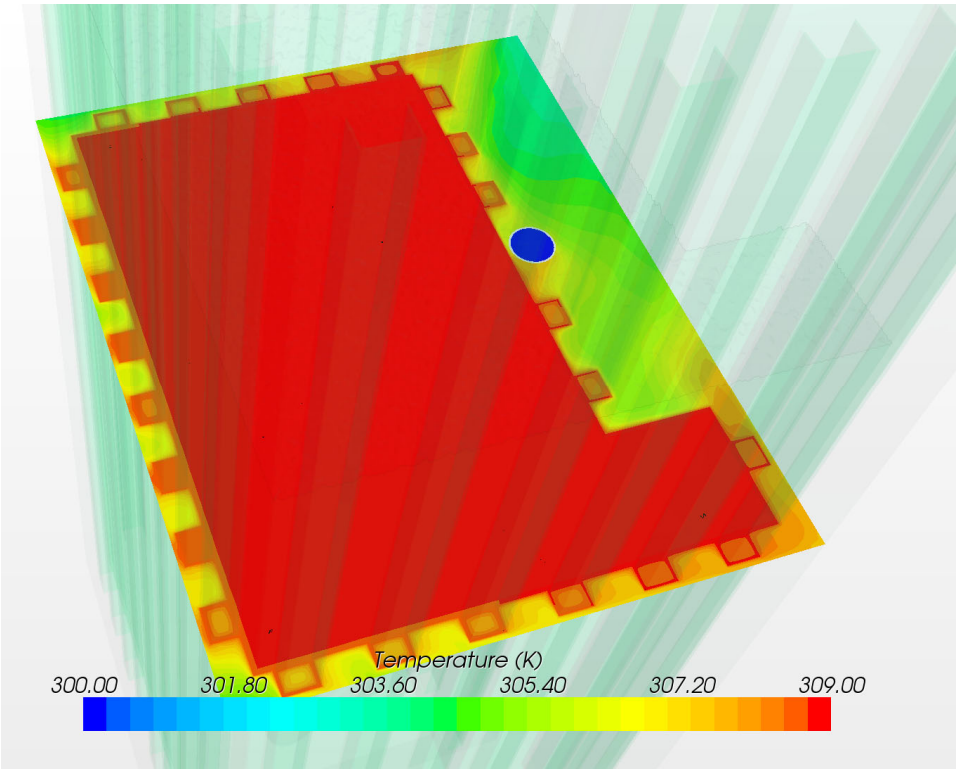

Figure V.3.3.6. Horizontal cross section of the temperature across the domain. Calculation E2.

The inlet temperature in the calculation is assumed to be 300 K. The outlet temperature in the calculation is 306 K, consistent with the results of a heat balance. The peak temperature within the pool is 309 K for all three calculations reported (E1, E2, E3). In fact, the differences among the three calculations are less than 0.1 K.

The temperature within the pool is nearly uniform, with variations of less than one Kelvin, Figs. V.3.3.6 and V.3.3.7. The temperature distribution within the air system is considerably more complex due to the presence of several recirculation regions driven by the high velocity, Fig. V.3.3.5 and V.3.3.8.

In conclusion, the forced convection design was found to present an inlet-outlet temperature difference of 6 K and a peak temperature 9 K higher than the inlet temperature. Assuming an air temperature of 300 K, this leads to a peak temperature of 309 K in the pool, thus assuring a margin of approximately 64 K to boiling.

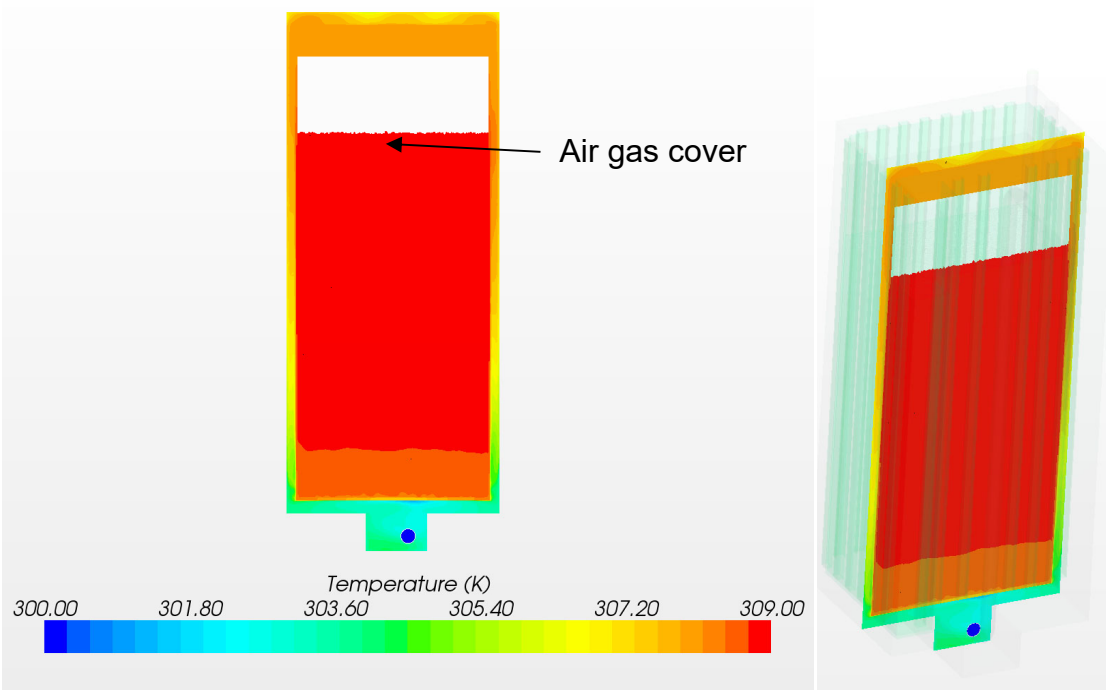

Figure V.3.3.7. Temperature plot with vertical cross section of the pool and air system. Calculation E2

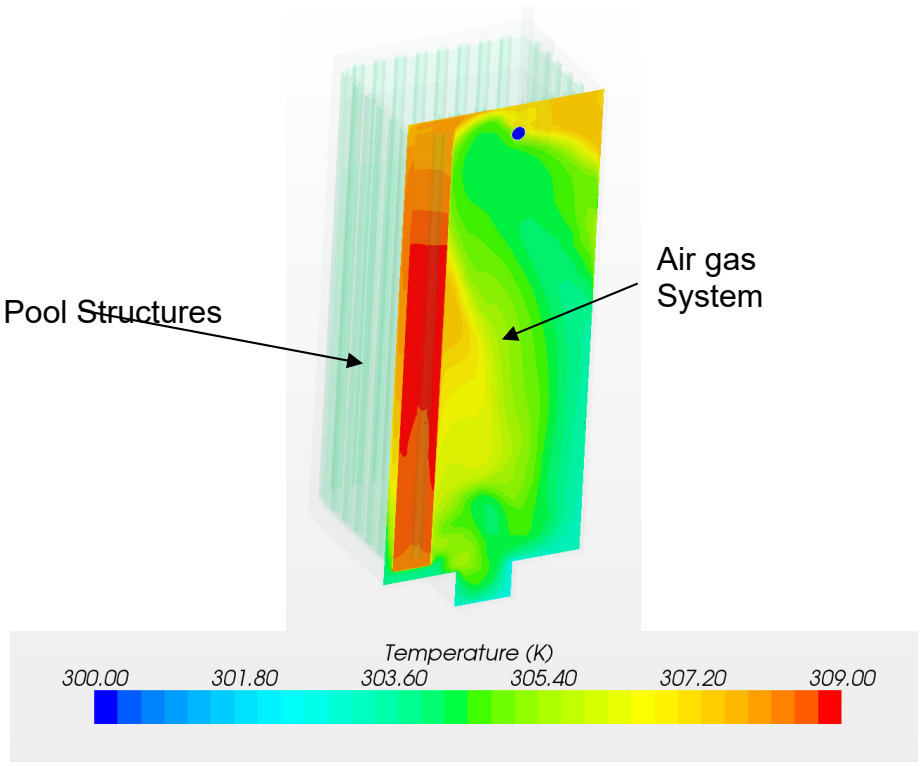

Figure V.3.3.8. Temperature plot with vertical cross sections of the pool and air system. (left) cross section through the structures in the short L branch of the pool.

References

V.3.1. STAR-CCM+ 5.06 Users Guide, CD-adapco, Mellville, NY, USA
V.3.2. Xu, W., Chen, Q., and Nieuwstadt,. “A new turbulence model for near-wall natural convection”, *Int. J. Heat Mass Transfer*, **41**, pp. 3161-3176 (1998).
V.3.3. E. Baglietto, “An Algebraic Heat Flux Model in STAR-CCM+ for Application to Innovative Reactors”, *Proceedings of the NURETH14 Conference*, Toronto, Ontario, Canada (2011)

V.4 Spent Fuel Storage Pool Structural Analysis and Design

V.4.1 Storage Pool Inner and Outer Tanks

V.4.1.1 Objective

The objective of this analysis was to perform a structural feasibility study for the design of the storage pool used to store used targets and spent fuel assemblies of the subcritical assembly at the KIPT ADS experimental neutron source facility.

V.4.1.2 Scope

The scope of this analysis is to simulate static and seismic loadings on the aluminum metal tanks of the storage pool. The concrete pit was not included in the analysis.

V.4.1.3 Methodology

This analysis was carried out with the finite element method, using the ANSYS R13.0 finite element program [Ref. V.4.1.1]. A finite element model was constructed and subjected to estimated loads developed during the design process. Results were compared to basic material properties and commonly accepted engineering principles were applied to determine a factor of safety.

V.4.1.4 Overview of Analysis

A total of five load cases were examined and are summarized in Table V.4.1.4.1.

V.4.1.5 Assumptions

This analysis is based on the following assumptions:

1. The material response is linear elastic.
2. The material response is constant with time (no effects of aging, creep, etc.).
3. The materials are isotropic and homogeneous.
4. The material responses are consistent with small strain and small displacement.
5. The effects of gamma rays on material properties are not included.
6. The residual stresses are not included.
7. The pool tanks operate at room temperature.

8. The effects of water flow are not included.
9. The loads are static. The dynamic effects were not included in the lifting analyses.
10. Butt welds are assumed to be continuous, full penetration and uninspected.
11. Fillet welds are assumed to be continuous, un-machined, and uninspected.
12. The material yielding was evaluated by comparing the von Mises stress, as defined by the maximum distortion energy failure theory, directly to the yield strength of the material. No knockdown factors for boundary condition uncertainty, material variability, surface finish, construction variations, etc. were applied.
13. The load cases did not include components like piping stresses, fluid swirling, and temperature loading.

Table V.4.1.4.1. Summary of load cases

Load Case	Description	Loads			
		Weight of Assemblies and Racks	Weight of Water	Weight of Tank	Seismic
1	In place, inner tank full, outer tank empty, static loading	yes	yes	yes	no
2	In place, inner tank full, outer tank empty, seismic loading	yes	yes	yes	yes
3	In place, inner tank full, outer tank full, static loading	yes	yes	yes	no
4	Lifting analysis, inner tank, empty static loading	no	no	yes	no
5	Lifting analysis, outer tank, empty static loading	no	no	yes	no

V.4.1.6 Geometry

The finite element model used in the structural analysis was based on solid modeling geometry. A file containing the specifications for this geometry was imported into ANSYS Design Modeler, where a midplane surface model, shown in Fig. V.4.1.6.1, was created. This model was taken into the Workbench module of ANSYS R13.0, where a quad dominant mesh with quadratic quad and tri shell elements were created. This model is shown in Fig. V.4.1.6.2.

V.4.1.7 Materials

Mechanical properties for SAV-1 used for this analysis are shown in Table V.4.1.7.1. Strength values for the bulk material are based on “tempered and naturally aged” heat treatment of rolled plate from Ref. V.4.1.2. Strength values in the heat affected zone (HAZ) are the “stabilized” (annealed) values from Table 5 of Ref. V.4.1.3. Other material properties for SAV-1 were not readily available, so common values for similar grades were used when necessary.

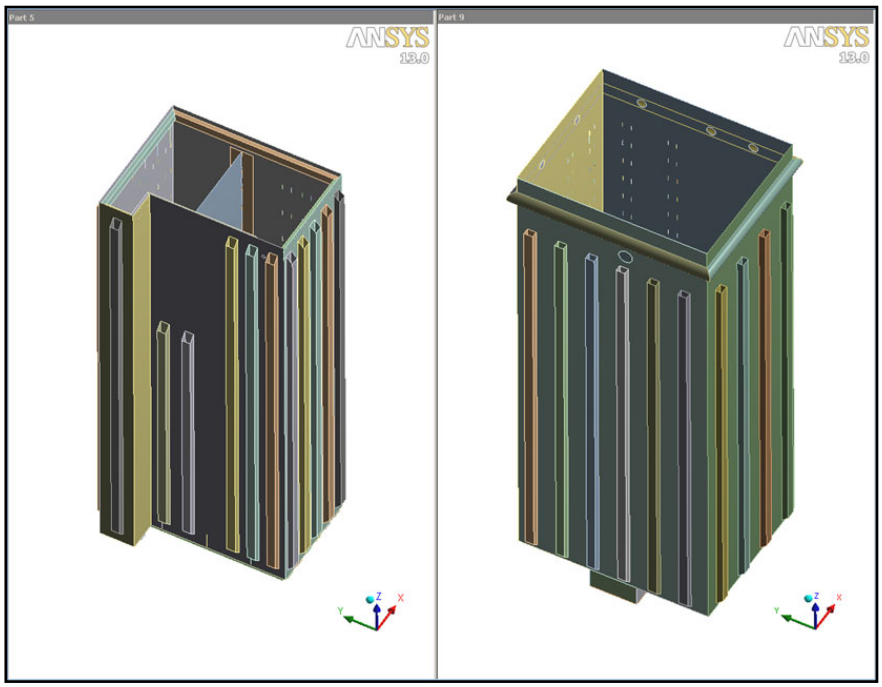

Figure V.4.1.6.1. Midplane surface model

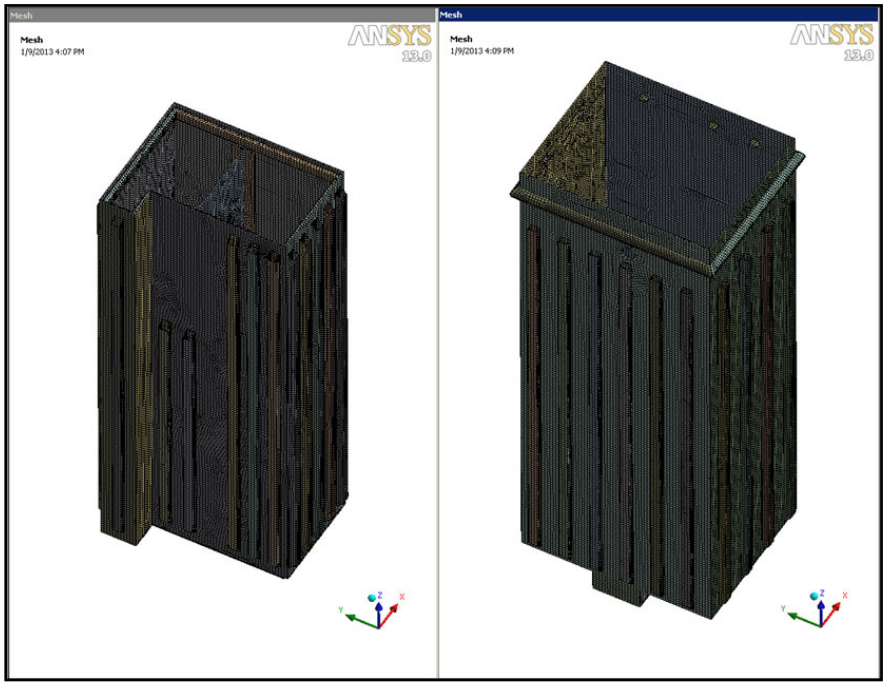

Figure V.4.1.6.2. Finite element model

Table V.4.1.7.1. Material properties for SAV-1

Property	Bulk Material	HAZ	Source
Density (kg/m^3)	2,770		Common value
Elastic Modulus (MPa)	71,000		Common value
Poisson's Ratio	0.33		Common value
Ultimate Tensile Strength (MPa)	216	150	Bulk material: Ref. V.4.1.1; HAZ, Ref. V.4.1.3, Table 5
Yield Strength (MPa)	118	90	

V.4.1.8 Loads and Boundary Conditions

The loads and boundary conditions used for Load Case 1 are shown in Figs. V.4.1.8.1 and V.4.1.8.2. The bottom surface of the outer tank is fixed on the dielectric mounting pads using six bolts. The inner tank is fixed with bonded contact between the bottom contacting surfaces of the two tanks. Static loads were applied to the bottom of the inside tank to simulate the weight of the fuel and target assemblies and their holding racks. A hydrostatic pressure was applied to the inside of the inner tank to simulate loads resulting from the cooling water. Finally, standard earth gravity was applied to all solid components.

The loads and boundary conditions used for Load Case 2 are shown in Figs. V.4.1.8.3 and V.4.1.8.4. This load case is essentially Load Case 1 with the addition of a static seismic load (AX = AZ = 0.1g, AY = 0.07g), following the International Atomic Energy Agency recommendation for design levels of horizontal acceleration for facilities associated with a radiation hazard (see Ref. V.4.1.4 for a more detailed explanation). This seismic load exceeds the requirements of the Ukrainian regulations.

The following changes were made to the Case 1 loads and boundary conditions to create Case 2 loads. First, a point mass equal to the mass of the cooling water was added at the approximate centroid of the volume of the inner tank. This mass was transferred to the walls and bottom of the inside tank. Next, the standard earth gravity load was replaced with a general acceleration with component values set to apply the seismic and gravity loads. Last, the hydrostatic load was removed from the bottom of the tank to avoid applying the weight of the water twice.

Case 3 loads are identical to the Case 1 loads except that the hydrostatic pressure is moved from the inner tank to the outer tank. This is shown in Fig. V.4.1.8.5. This load case represents an undetected leak in the inner tank that is allowed to continue until the outer tank is full. This represents a bounding condition for this type of failure. Water level sensors, a transfer pump, and an alarm are present to warn of any leakage and the removal of cooling water from the inner tank, so that remedial action would be expected to be taken before the outer tank became filled with water.

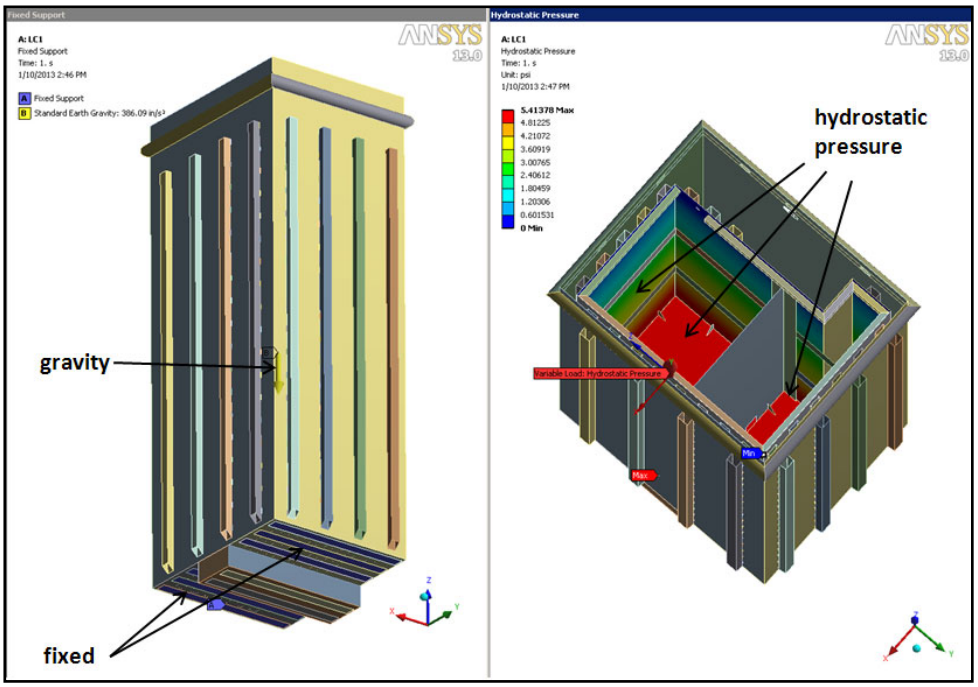

Figure V.4.1.8.1. Boundary conditions for Case 1

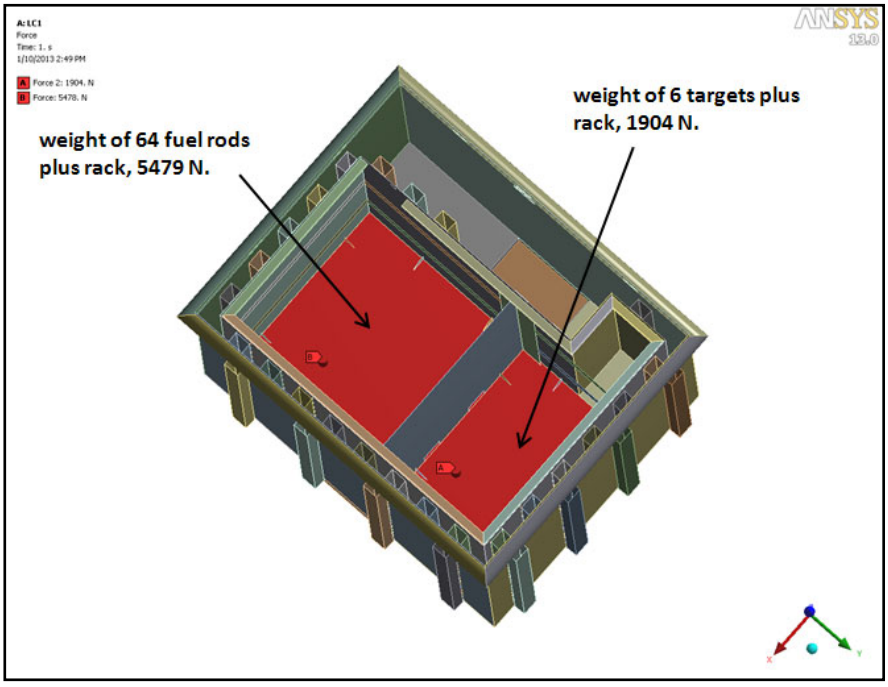

Figure V.4.1.8.2. Static loads on the inside tank bottom for Case 1

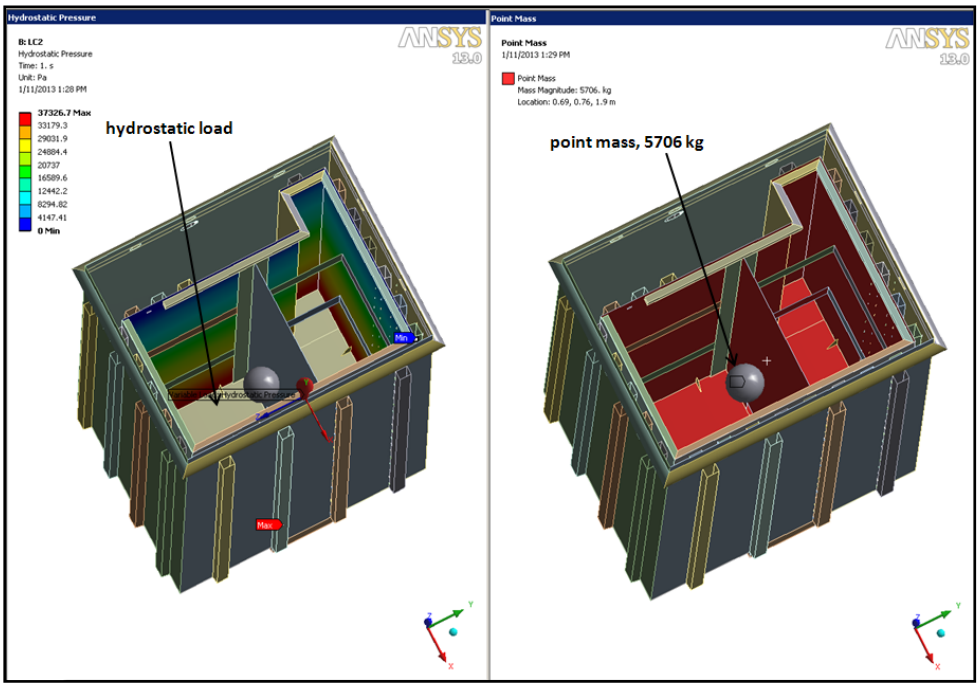

Figure V.4.1.8.3. Boundary conditions for Case 2

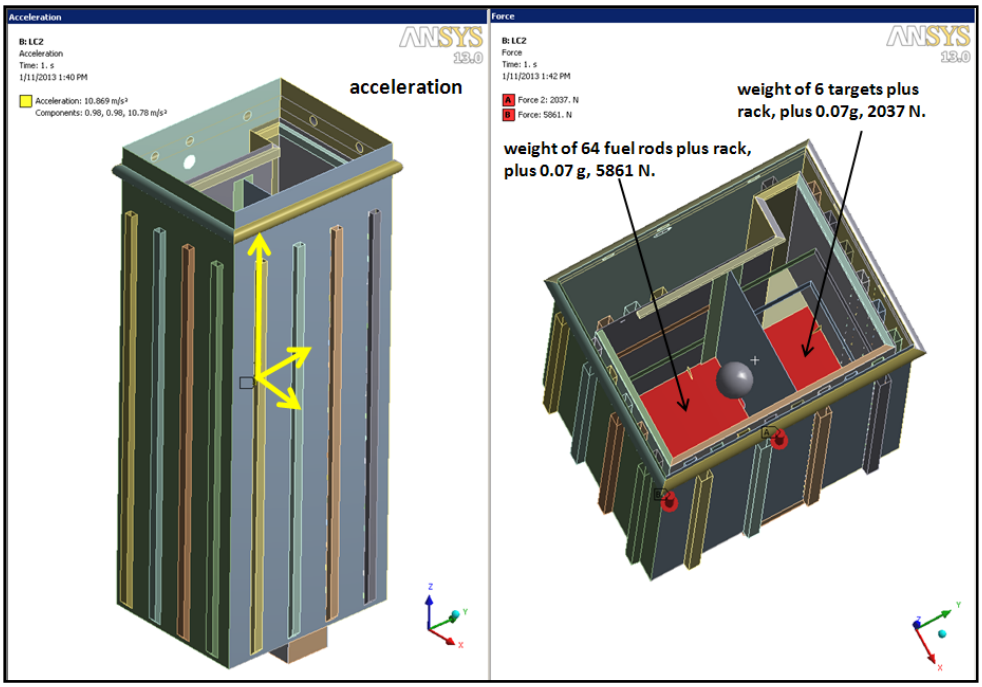

Figure V.4.1.8.4. Seismic and gravity loads plus static loads, for Case 2

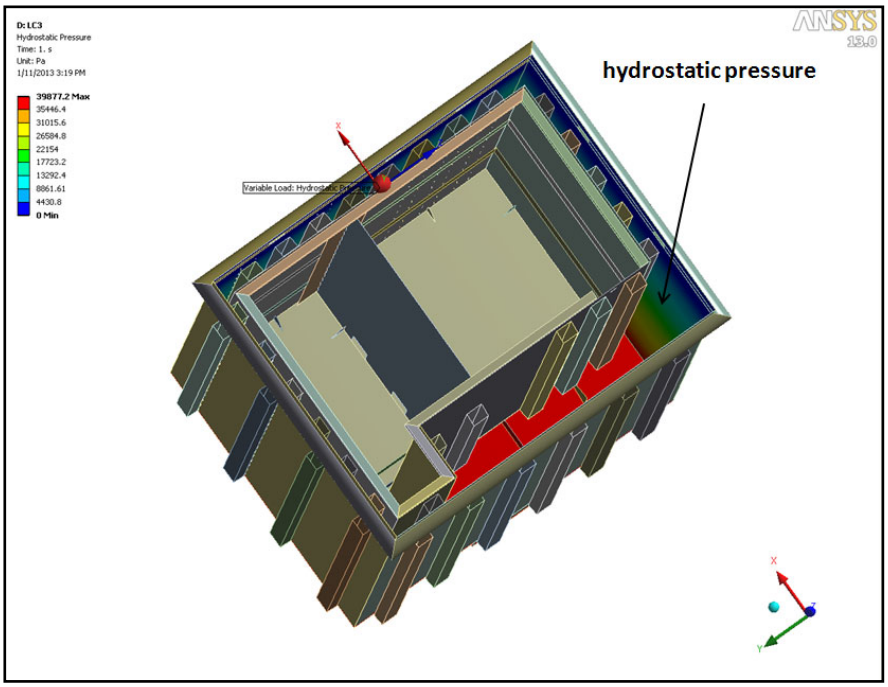

Figure V.4.1.8.5 Boundary conditions for Case 3

Case 4 loads are a lifting analysis of the inner tank. Four lifting lugs were added to the empty inner tank, with meshed line elements used to simulate lifting cables. The cables are configured to form a 10° angle from vertical. This is shown in Fig. V.4.1.8.6. The model was constrained with a fixed boundary condition at the top of the cables and loaded with gravity.

Case 5 loads are a lifting analysis of the outer tank. As before, four lifting lugs were added to the empty outer tank, with meshed line elements used to simulate lifting cables. This is shown in Fig. V.4.1.8.7. This model was also constrained with a fixed boundary condition at the top of the cables and loaded with gravity.

V.4.1.9 Results

a) Case 1 - Filled Inner Tank in Place, Static Loading

As described above, Case 1 evaluates a filled inner tank, inside the outer tank, both tanks in place within the spent fuel pool concrete pit, and static loads applied to the bottom of the inner tank. Results for this evaluation are given in Figs. V.4.1.9.1 through V.4.1.9.4. The maximum allowable stress is 118 MPa.

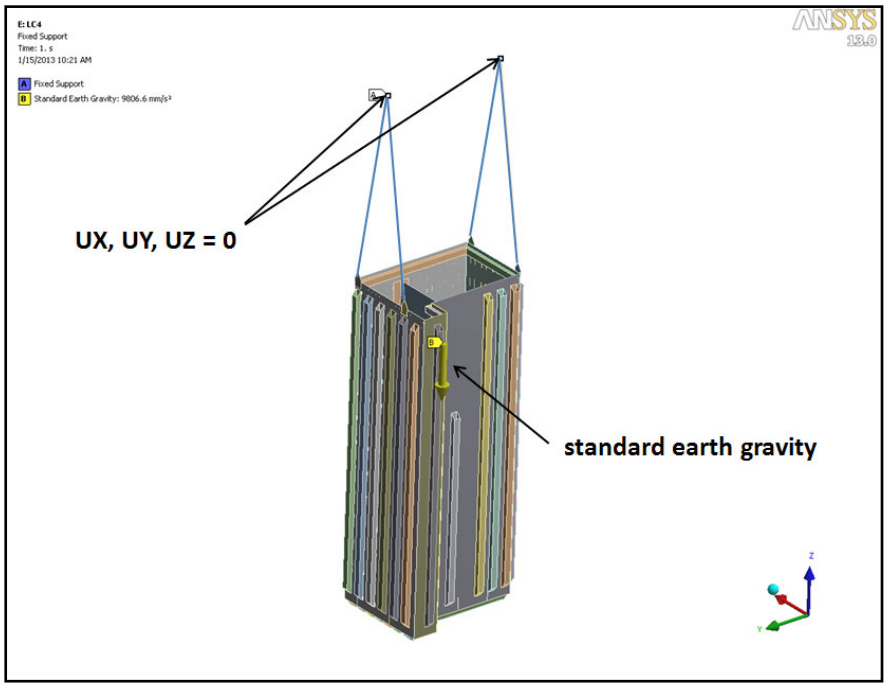

Figure V.4.1.8.6. Boundary conditions for Case 4

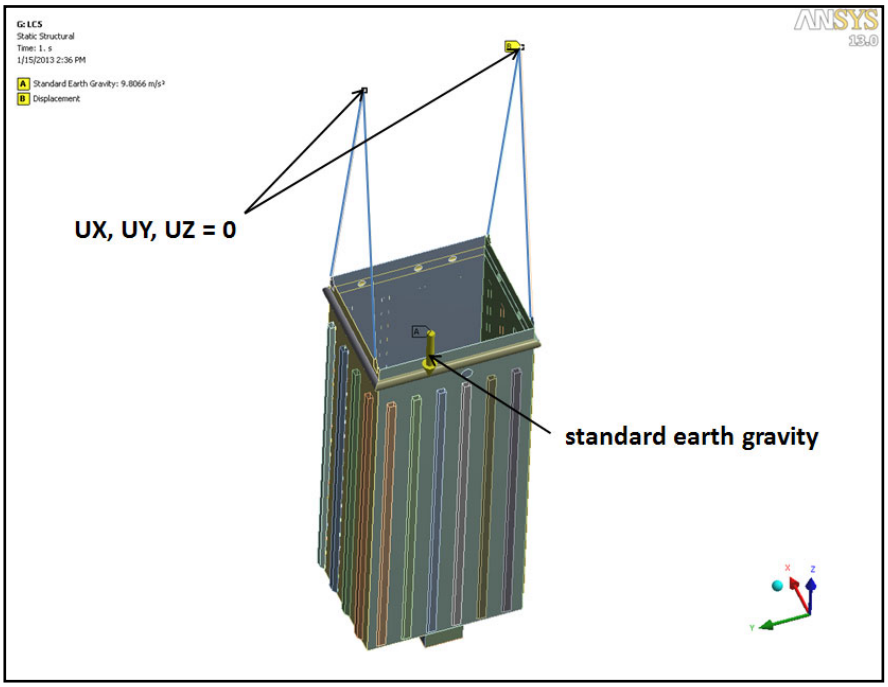

Figure V.4.1.8.7. Boundary conditions for Case 5

Figures V.4.1.9.1 (a) through (e) show the locations of the largest von Mises stresses predicted by the ANSYS calculation in the inner tank. The maximum stress predicted by the calculation in the inner tank is 130.5 MPa, indicated by the red marker in Fig. V.4.1.9.1 (a). This is along weld 6 (location shown in Fig. V.4.1.9.5 (b)) and does not represent an accurate value for the stress; it is an artifact of the calculation, caused by two shell elements in the finite element mesh meeting at a 90° angle. As such, this stress must be evaluated by an alternative approach that is applied to welds and it is discussed below.

The maximum real stress in the inner tank is about 100.5 MPa, near weld 19, Fig. V.4.1.9.1 (b), in one of the inner braces. The safety factor here is 1.17 for the parent material. The next two highest stresses are also near welds in the inner braces and are about 80.2 MPa (Fig. V.4.1.9.1 (d), SF=1.07) and 78.9 (Fig. V.4.1.9.1 (c), SF=1.14). The highest stresses in the tank body are near corner welds 13 and 14 and are about 58.4 MPa (Fig. V.4.1.9.1 (e), SF= 1.54).

Stresses in the outer tank are very low. The maximum calculated stress in the outer tank is 13.9 MPa and is in the bottom of the tank, Fig. V.4.1.9.2 (b). The stresses seen in the side of the tank in Fig. V.4.2.9.2 (a) are due to contact between the inner and outer tanks.

Deflections in the tanks are shown in Figs. V.4.1.9.3 and V.4.1.9.4. The maximum deflection in the inner tank is 5.36 mm, as shown in Fig. V.4.1.9.3 (a), and results in contact with the outer tank. The maximum deflection in the outer tank is 0.34 mm (Fig. V.4.1.9.4) and results from the contact with the inner tank. Fig. V.4.1.9.4 (b) shows contact status of the contact elements on the stiffening tubes on the inner tank.

Selected welds were evaluated by inspecting plots of von Mises stress, deflection, and selecting representative welds in high stress and high deflection locations. These welds are shown in Fig. V.4.1.9.5. Weld configurations and properties are found in Tables V.4.1.9.1 and V.4.1.9.3, and weld loads, stresses and safety factors are summarized in Tables V.4.1.9.2 and V.4.1.9.4. All welds were assumed to be fillet welds, with a basic size equal to the thinnest wall in the joint and with a throat width of 0.707 times the basic size. Weld details were taken from Ref. V.4.1.7. To evaluate these welds, the weld reactions were found by summing the nodal reactions of the nodes at the weld. These reactions were then used to calculate traction and shear stresses and finally a weld stress, per the analysis approach described in Ref. V.4.1.5. The weld stress was then compared to an allowable value determined per Table J.2.2.2 of Ref. V.4.1.7. This method required ultimate tensile and shear strength data in the HAZ for the base material and the ultimate shear strength of the weld filler. Ultimate tensile strength in the HAZ was taken as that for annealed SAV-1, and the ultimate shear strength was estimated at half the ultimate tensile strength. The weld filler to be used for the construction has not been finalized, so a value of 50 MPa was used as a lower bound for the ultimate shear strength. This value is the lowest value listed in Table J.2.1M of Ref. V.4.1.6.

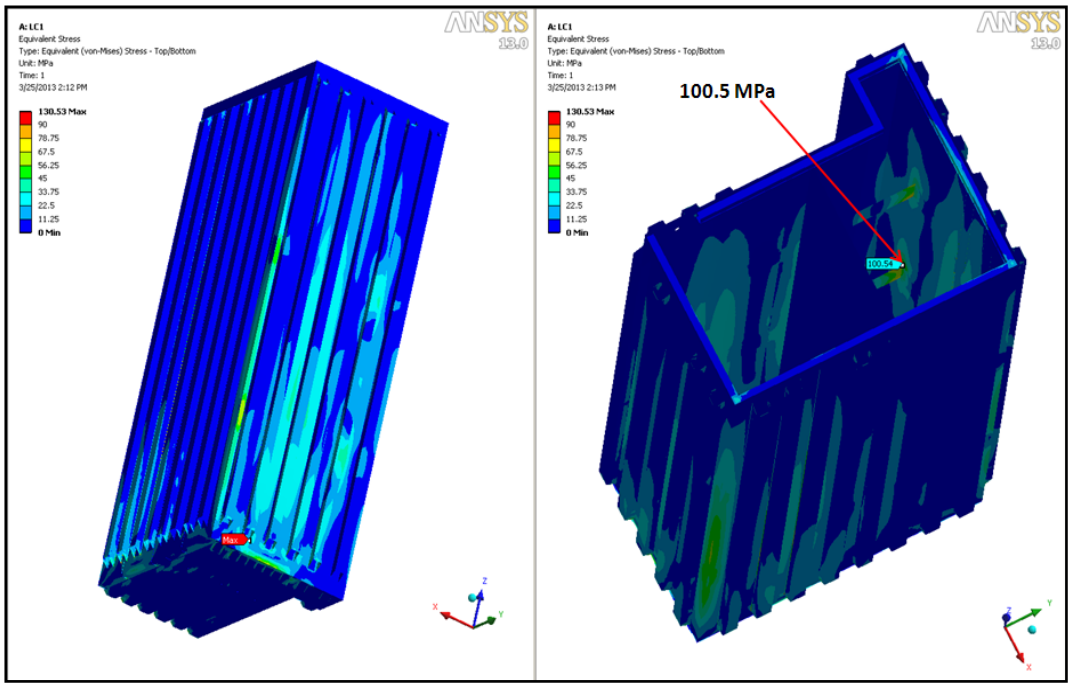
A: LC1
Equivalent Stress
Type: Equivalent (von-Mises) Stress - Top/Bottom
Unit: MPa
Time: 1
3/25/2013 2:12 PM
130.53 Max
90
78.75
67.5
56.25
45
33.75
22.5
11.25
0 Min
ANSYS
13.0
A: LC1
Equivalent Stress
Type: Equivalent (von-Mises) Stress - Top/Bottom
Unit: MPa
Time: 1
3/25/2013 2:13 PM
130.53 Max
90
78.75
67.5
56.25
45
33.75
22.5
11.25
0 Min
100.5 MPa
ANSYS
13.0

(a) (b)

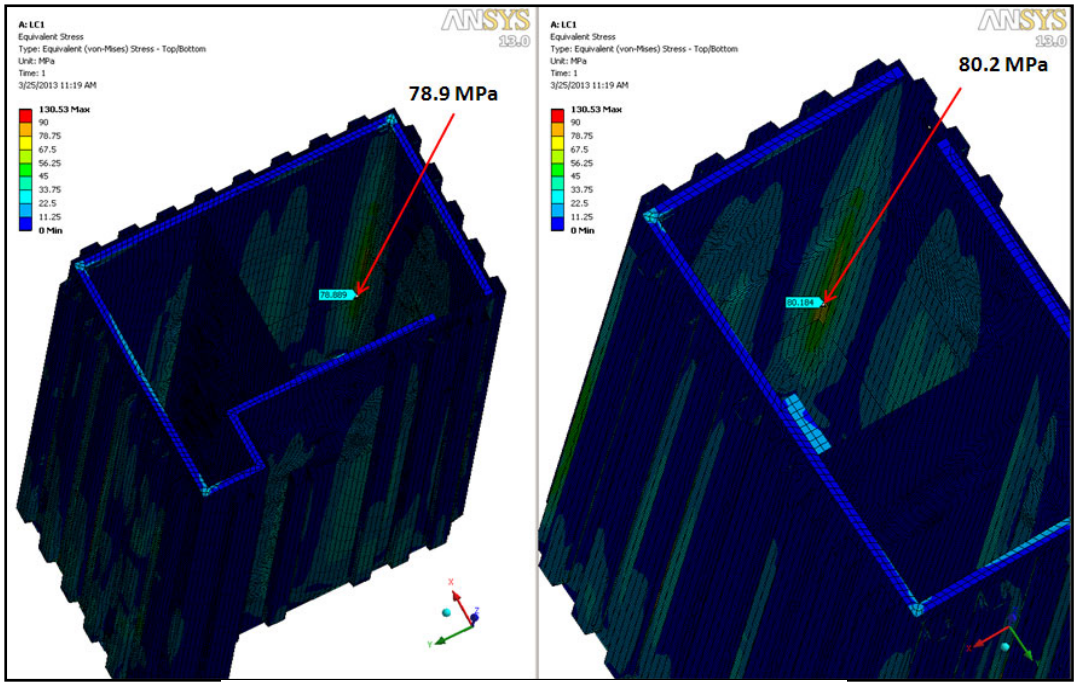
A: LC1
Equivalent Stress
Type: Equivalent (von-Mises) Stress - Top/Bottom
Unit: MPa
Time: 1
3/25/2013 11:19 AM
130.53 Max
90
78.75
67.5
56.25
45
33.75
22.5
11.25
0 Min
78.9 MPa
ANSYS
13.0
A: LC1
Equivalent Stress
Type: Equivalent (von-Mises) Stress - Top/Bottom
Unit: MPa
Time: 1
3/25/2013 11:19 AM
130.53 Max
90
78.75
67.5
56.25
45
33.75
22.5
11.25
0 Min
80.2 MPa
ANSYS
13.0

(c) (d)

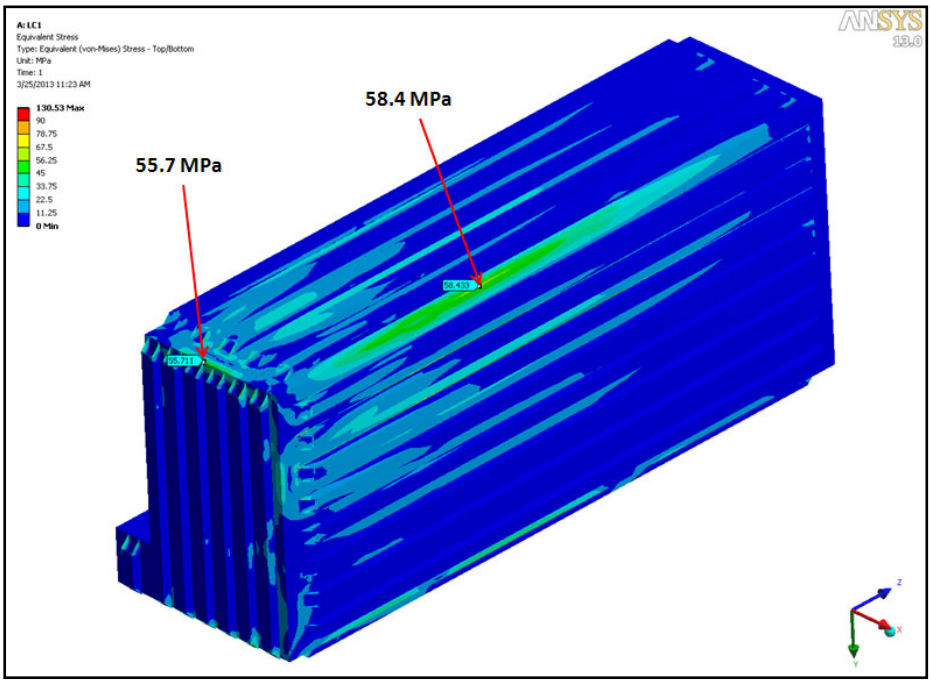

(e)

Figure V.4.1.9.1. Case 1, von Mises stress of the inner tank

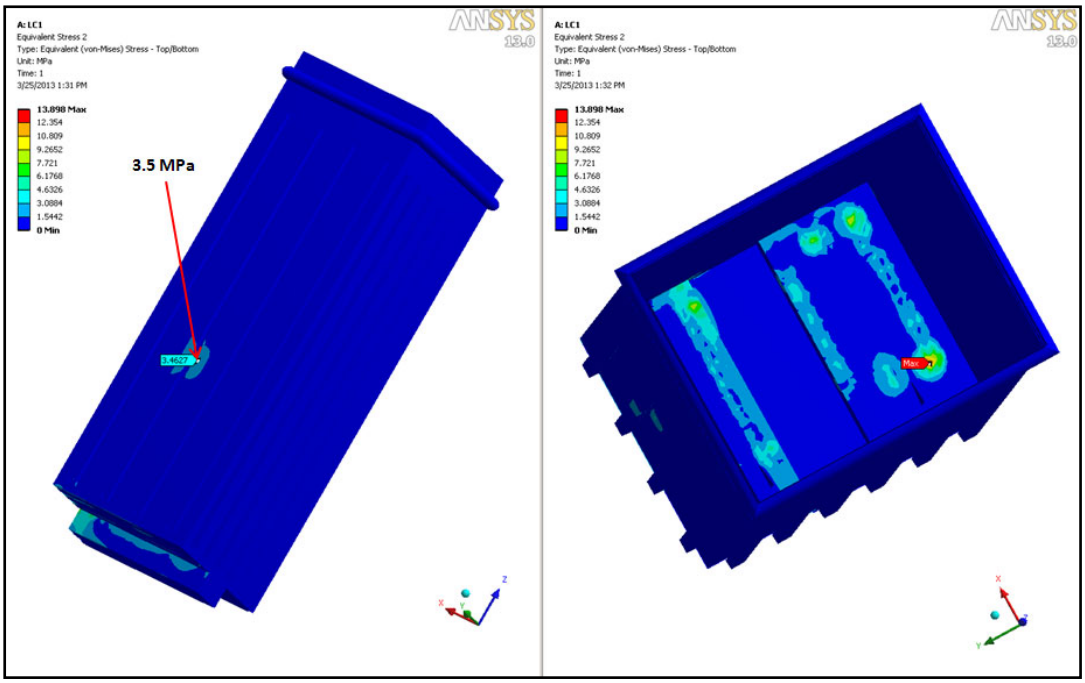

(a) (b)

Figure V.4.1.9.2. Case 1, von Mises Stress of the outer tank

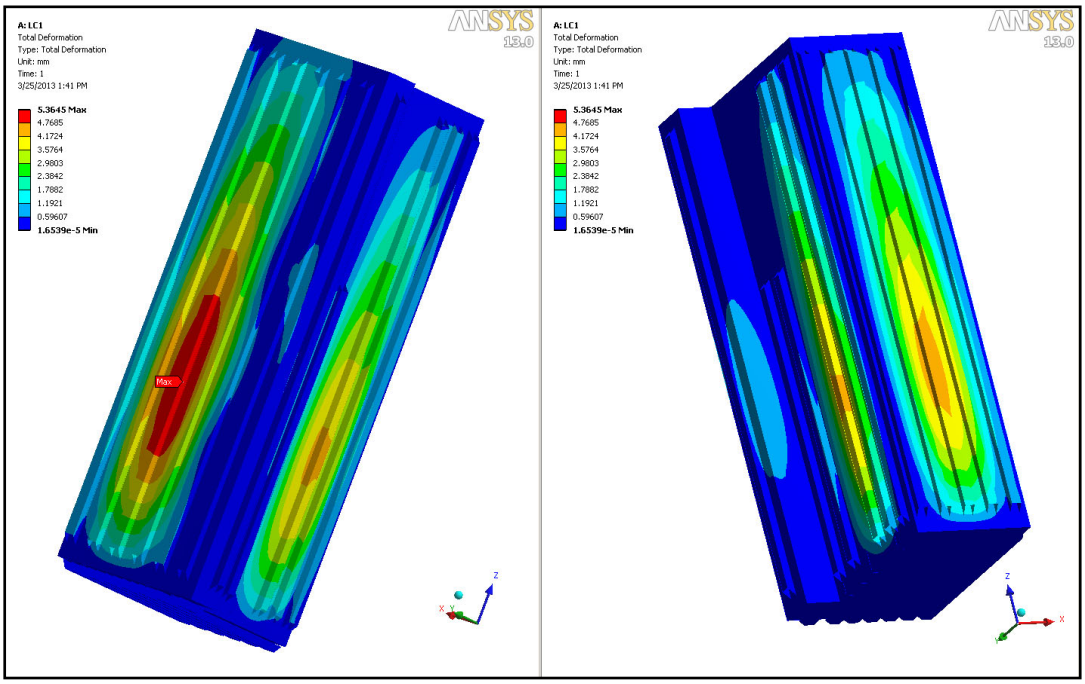

(a) (b)

Figure V.4.1.9.3. Case 1, Summed deflection of the inner tank

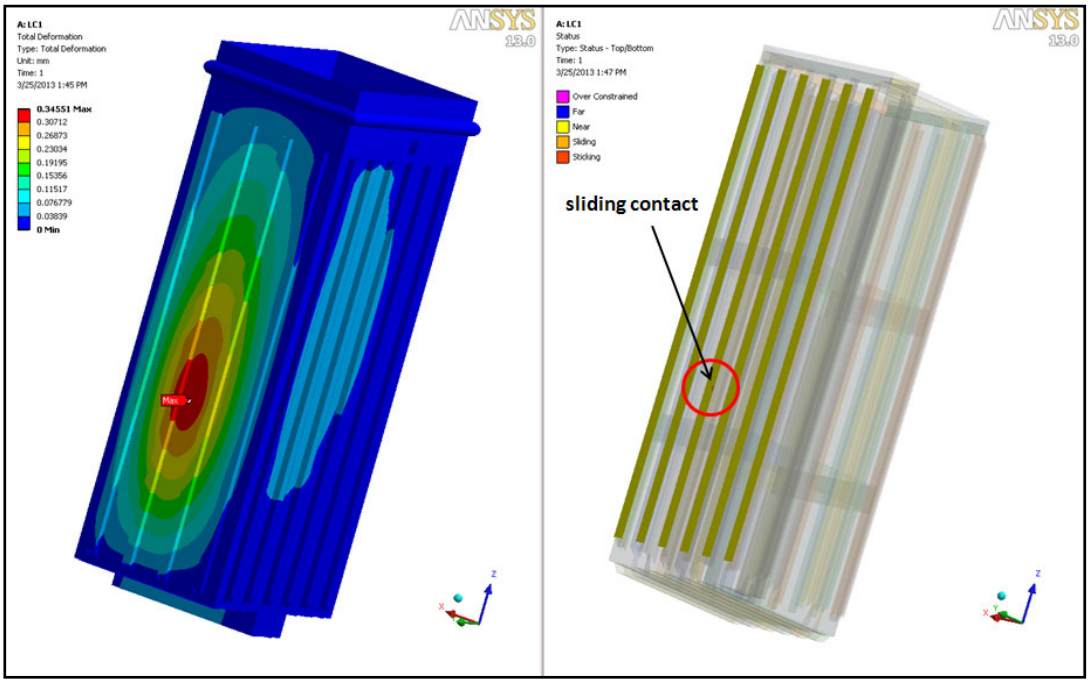

(a) (b)

Figure V.4.1.9.4. Case 1, (a) Summed deflection of the outer tank and (b) Contact status of the inner tank

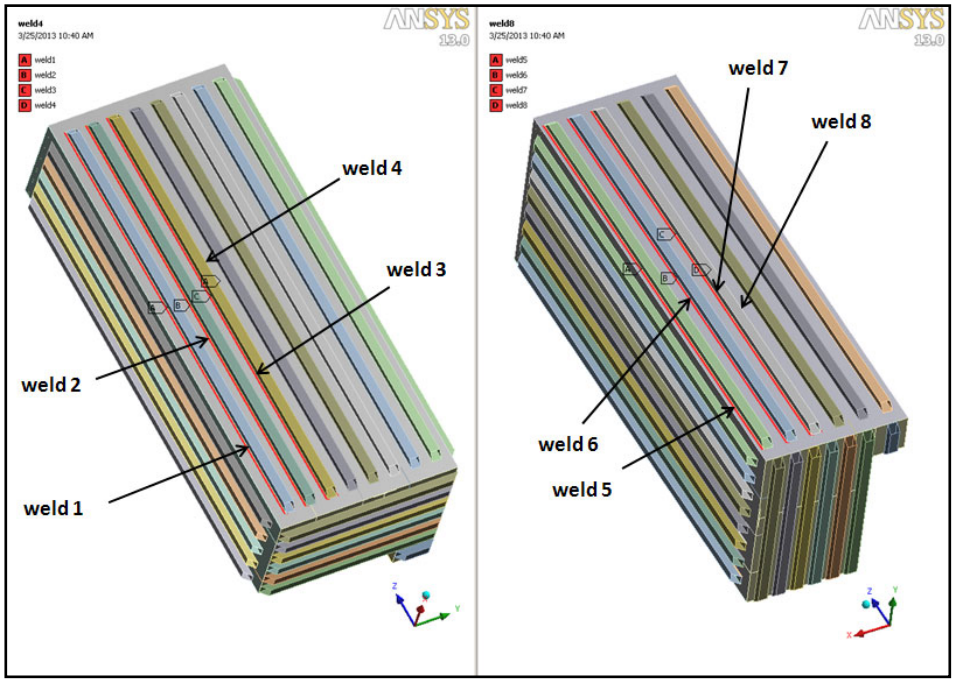
weld 4
weld 3
weld 2
weld 1
weld 7
weld 8
weld 6
weld 5

(a) (b)

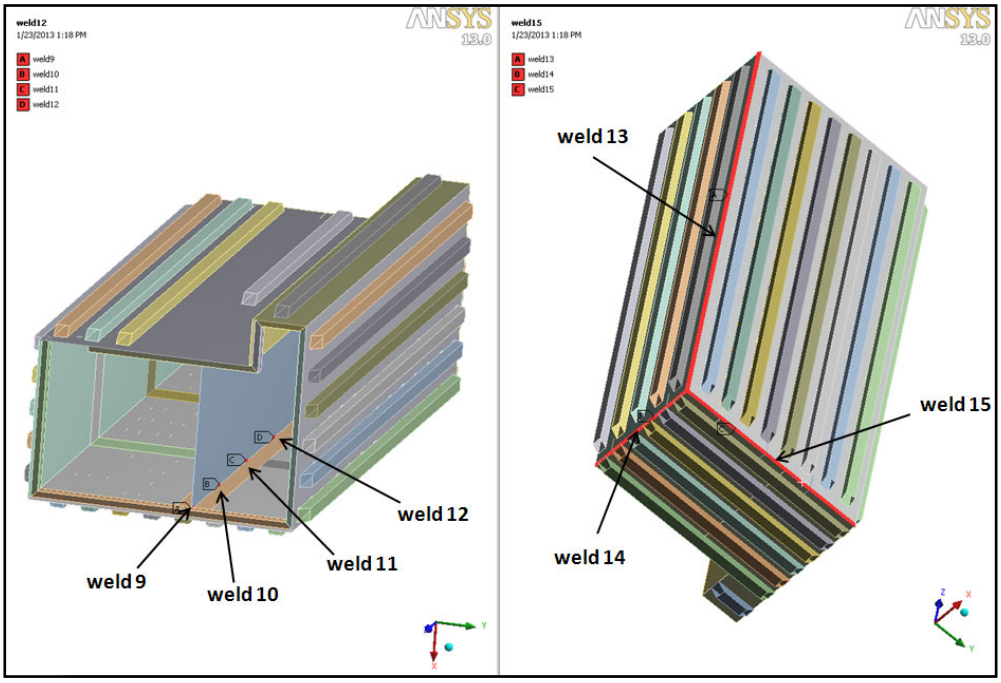
weld 12
weld 11
weld 9
weld 10
weld 13
weld 15
weld 14

(c) (d)

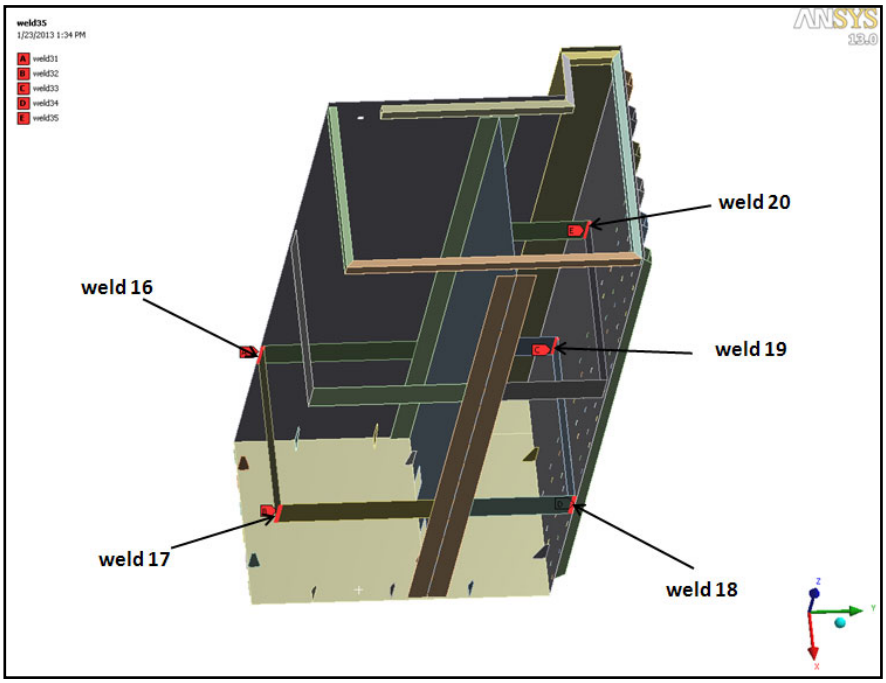

(e)

Figure V.4.1.9.5. Weld locations Case 1

Table V.4.1.9.1. Case 1 single-sided fillet weld configurations

Weld	Description	Leg Length (mm)	Weld Size (mm)	Throat Area (mm^2)	Y_{bar} (mm)	Unit MOI_x (mm^3)	MOI_x (mm^4)	Unit Polar MOI_z (mm^3)	Polar MOI_z (mm^4)	Sec. Mod. (x) (mm^3)	Sec. Mod. (z) (mm^3)
1	continuous	3596	4	10169.5	1798.0	3875054395	10958653828	3875054395	10958653828	6094913	6094913
2	continuous	3596	4	10169.5	1798.0	3875054395	10958653828	3875054395	10958653828	6094913	6094913
3	continuous	3596	4	10169.5	1798.0	3875054395	10958653828	3875054395	10958653828	6094913	6094913
4	continuous	3596	4	10169.5	1798.0	3875054395	10958653828	3875054395	10958653828	6094913	6094913
5	continuous	3596	4	10169.5	1798.0	3875054395	10958653828	3875054395	10958653828	6094913	6094913
6	continuous	3596	4	10169.5	1798.0	3875054395	10958653828	3875054395	10958653828	6094913	6094913
7	continuous	3596	4	10169.5	1798.0	3875054395	10958653828	3875054395	10958653828	6094913	6094913
8	continuous	3596	4	10169.5	1798.0	3875054395	10958653828	3875054395	10958653828	6094913	6094913
13	continuous	3805	10	26901.4	1902.5	4590740427	32456534819	4590740427	32456534819	17059939	17059939
14	continuous	920	10	6504.4	460.0	64890667	458777013	64890667	458777013	997341	997341
15	continuous	1520	10	10746.4	760.0	292650667	2069040213	292650667	2069040213	2722421	2722421
16	continuous	200	10	1414.0	100.0	666667	4713333	666667	4713333	47133	47133
17	continuous	200	10	1414.0	100.0	666667	4713333	666667	4713333	47133	47133
18	continuous	200	10	1414.0	100.0	666667	4713333	666667	4713333	47133	47133
19	continuous	200	10	1414.0	100.0	666667	4713333	666667	4713333	47133	47133
20	continuous	200	10	1414.0	100.0	666667	4713333	666667	4713333	47133	47133

Table V.4.1.9. 2. Case 1 summary of single-sided fillet weld analysis

Weld	Shear (FX) (N)	Shear (FY) (N)	Normal (FZ) (N)	Moment (X) (N-mm)	Torsion (Z) (N-mm)	F_{bend_mx} (MPa)	F_{normal_fz} (MPa)	F_{shear_fx} (MPa)	F_{shear_fy} (MPa)	F_{shear_xmz} (MPa)	$F_{traction}$ (MPa)	F_{shear} (MPa)	F_{weld} (MPa)	FoS
1	-31521.7	10335.4	646.6	-1661644.8	-2326005.6	0.27	0.06	3.10	1.02	0.38	0.34	3.63	4	13.73
2	73842.1	9089.5	362.2	-1091937.4	12919823.6	0.18	0.04	7.26	0.89	2.12	0.21	9.42	9	5.30
3	107080	-593.5	-79.9	265844.1	29614025.6	0.04	0.01	10.53	0.06	4.86	0.05	15.39	15	3.25
4	-107080	479	79.9	-262344.8	-29654783	0.04	0.01	10.53	0.05	4.87	0.05	15.40	15	3.25
5	75210.7	-2483	765.5	955717.5	-20922025	0.16	0.08	7.40	0.24	3.43	0.23	10.83	11	4.62
6	-70134.4	-10800.3	503.2	1533105.3	13961343.6	0.25	0.05	6.90	1.06	2.29	0.30	9.25	9	5.40
7	-126295.6	2765.1	-0.8	-152802.7	27846322	0.03	0.00	12.42	0.27	4.57	0.03	16.99	17	2.94
8	126295.6	-2650.6	-349	-44463.2	-28052130	0.01	0.03	12.42	0.26	4.60	0.04	17.02	17	2.94
13	-3425.6	-2157.6	8724.3	8909833.5	5763873.3	0.52	0.32	0.13	0.08	0.34	0.85	0.47	1	51.58
14	-5345.4	195.9	-17946.7	285534	128067.2	0.29	2.76	0.82	0.03	0.13	3.05	0.95	3	15.67
15	5999.7	-611.1	2175.1	164005.1	187852.2	0.06	0.20	0.56	0.06	0.07	0.26	0.63	1	73.27
16	-9318.2	96.6	9437.7	-6851	-5371.9	0.15	6.67	6.59	0.07	0.11	6.82	6.70	10	5.23
17	9122.9	107.4	11324	12831.7	-1156.5	0.27	8.01	6.45	0.08	0.02	8.28	6.48	11	4.76
18	-1336	-174.4	18485.9	171259.1	5002	3.63	13.07	0.94	0.12	0.11	16.71	1.06	17	2.99
19	7812.7	-158	19074.5	45449.1	-2053.3	0.96	13.49	5.53	0.11	0.04	14.45	5.57	15	3.23
20	-1189.5	947.6	13987.5	-231951.3	-5084.8	4.92	9.89	0.84	0.67	0.11	14.81	1.16	15	3.37

Table V.4.1.9.3. Case 1 double-sided fillet weld configurations

Weld	Type	Plate Thick (mm)	Leg Length (mm)	Weld Size (mm)	Throat Area (mm^2)	X_{bar} (mm)	Y_{bar} (mm)	Unit MOI_x (mm^3)	MOI_x (mm^4)	MOI_y (mm^4)	Polar MOI_z (mm^3)	MOI_z (mm^4)	Sec. Mod. (x) (mm^3)	Sec. Mod. (z) (mm^3)	Sec. Mod. (xz) (mm^3)	Sec. Mod. (yz) (mm^3)
9	50 x 300 skip	10	50	10.00	707.10	8.54	25.00	20833	147292	51502	28118	198794	5892	6034	7952	23292
10	50 x 300 skip	10	50	10.00	707.10	8.54	25.00	20833	147292	51502	28118	198794	5892	6034	7952	23292
11	50 x 300 skip	10	50	10.00	707.10	8.54	25.00	20833	147292	51502	28118	198794	5892	6034	7952	23292
12	50 x 300 skip	10	50	10.00	707.10	8.54	25.00	20833	147292	51502	28118	198794	5892	6034	7952	23292

Table V.4.1.9.4. Case 1 Summary of double-sided fillet weld analysis

Weld	Shear (FX) (N)	Shear (FY) (N)	Normal (FZ) (N)	Moment (X) (N-mm)	Moment (Y) (N-mm)	Torsion (Z) (N-mm)	F_{bend_mx} (MPa)	F_{bend_my} (MPa)	F_{normal_fz} (MPa)	F_{shear_fx} (MPa)	F_{shear_fy} (MPa)	F_{shear_xmz} (MPa)	F_{shear_ymz} (MPa)	$F_{traction}$ (MPa)	F_{shear} (MPa)	F_{weld} (MPa)	FoS
9	-13.3	-158.3	74.8	2253.9	-1076.9	495.8	0.38	-0.18	0.11	0.02	0.22	0.0624	0.0213	0.31	0.26	0.40	123.95
10	11.2	-438.2	1272.3	3202.6	9533.3	322.8	0.54	1.58	1.80	0.02	0.62	0.0406	0.0139	3.92	0.64	3.97	12.58
11	14.8	-635.2	2278.2	1379.8	14532	190.4	0.23	2.41	3.22	0.02	0.90	0.0239	0.0082	5.86	0.91	5.93	8.43
12	15.2	-984	3332	4121.7	17020.9	-24.6	0.70	2.82	4.71	0.02	1.39	0.0031	-0.0011	8.23	1.39	8.35	5.99

b) Case 2 - Filled Inner Tank in Place, Seismic Loading

Case 2 evaluates a filled inner tank located within an outer tank, with both tanks in place within the spent fuel pool, but in this case the inner tank is subjected to a seismic loading instead of a static load. The maximum allowable stress remains 118 MPa. Results for this evaluation are given in Figs. V.4.1.9.6 through V.4.1.9.9.

The stresses predicted by the Case 2 simulation do not differ much from those for Case 1. This is to be expected since the increase in load for Case 2 relative to Case 1 is minimal. The computational anomaly at weld 6 does not occur in the Case 2 simulation, and so the maximum calculated stress in the inner tank is 101 MPa and it is again near weld 19 (Fig. V.4.1.9.6 (b)) in one of the inner braces. The safety factor at this location is 1.17 for the parent material. The next two highest stresses are also near welds in the inner braces and their values are about 81.5 MPa (SF = 1.08) and 78.4MPa (SF = 1.14), Figs. V.4.1.9.6

(c) and (d). The highest stresses in the tank body are again near corner welds 13 and 14 and are about 58 MPa, SF = 1.97, Fig. V.4.1.9.6 (d).

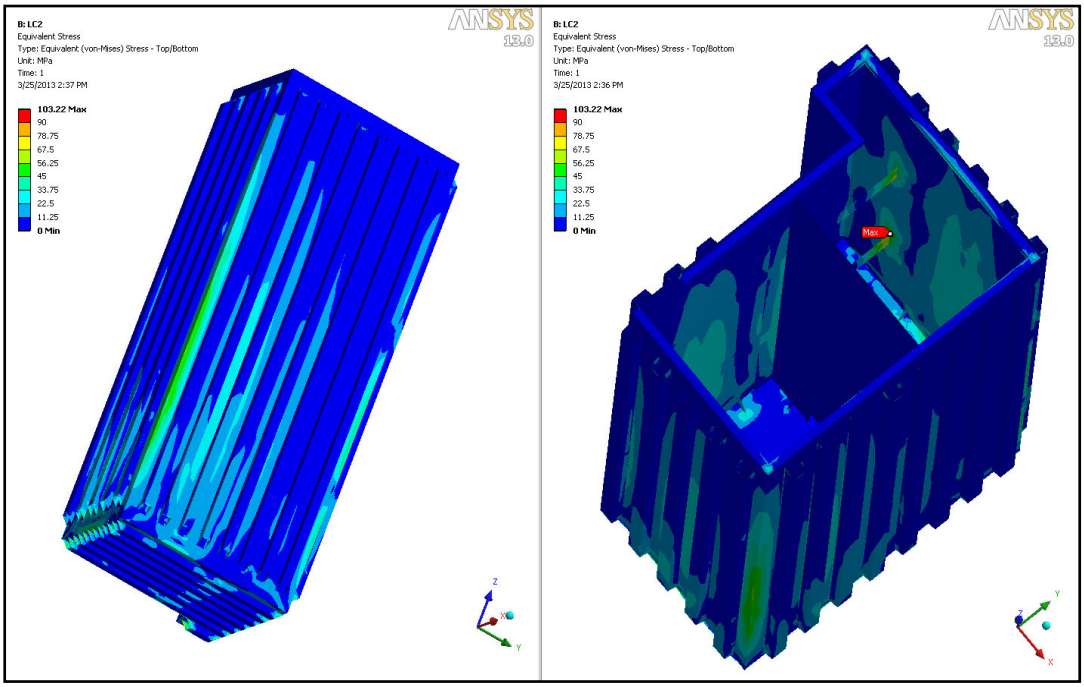

(a) (b)

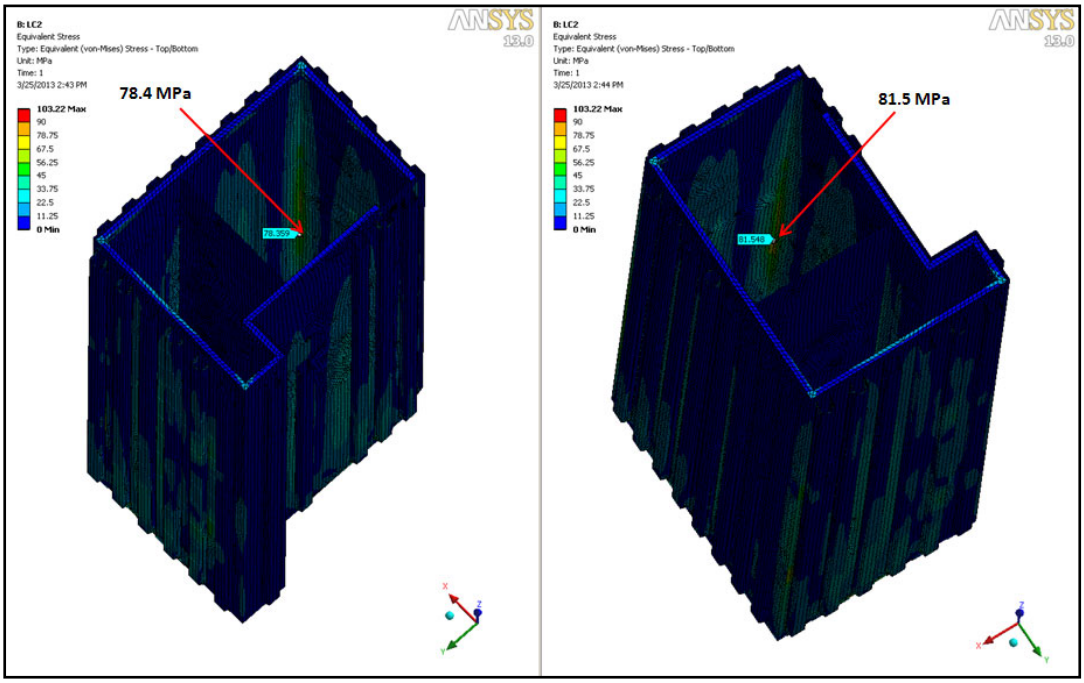

(c) (d)

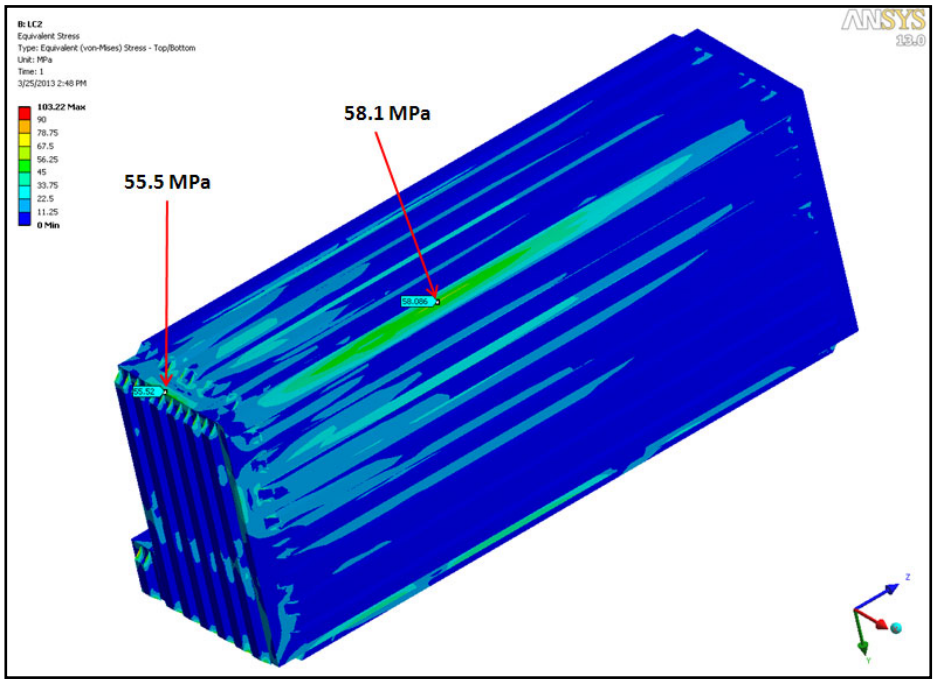

(e)

Figure V.4.1.9.6. Case von Mises stress of the inner tank

Stresses in the outer tank are very low. The maximum stress in the outer tank is 18.5 MPa and it is located in the bottom of the tank, Fig. V.4.1.9.6 (b). As before, the stresses seen in the side of the tank in Fig. V.4.1.9.6 (a) are due to contact between the inner and outer tanks.

The deflections in the tanks are shown in Figs.V.4.1.9.8 and V.4.1.9.9. The maximum deflection in the inner tank is 5.57 mm, as shown in Fig. V.4.1.9.8 and results in contact with the outer tank. The maximum deflection in the outer tank is 0.54 mm (Fig. V.4.1.9.9 (a)), and results from the contact with the inner tank. Fig. V.4.1.9.9 (b) shows contact status of the contact elements on the stiffening tubes on the inner tank.

The fillet welds evaluated for Case 1 were re-evaluated for seismic loading, using the configurations presented in Tables V.4.1.9.5 and V.4.1.9.7 and the analysis approach described in Ref. V.4.1.5. These results are shown in Tables V.4.1.9.6 and V.1.4.9.8. All safety factors are well above 1.0.

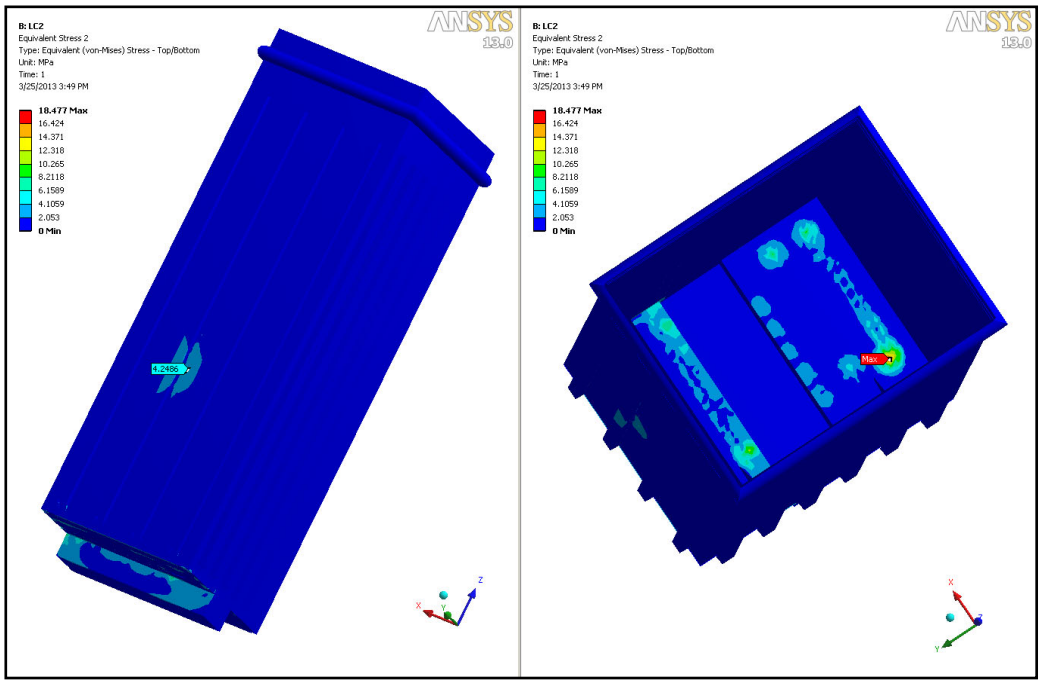

(a) (b)

Figure V.4.1.9.7. Case 2 von Mises stress of the outer tank

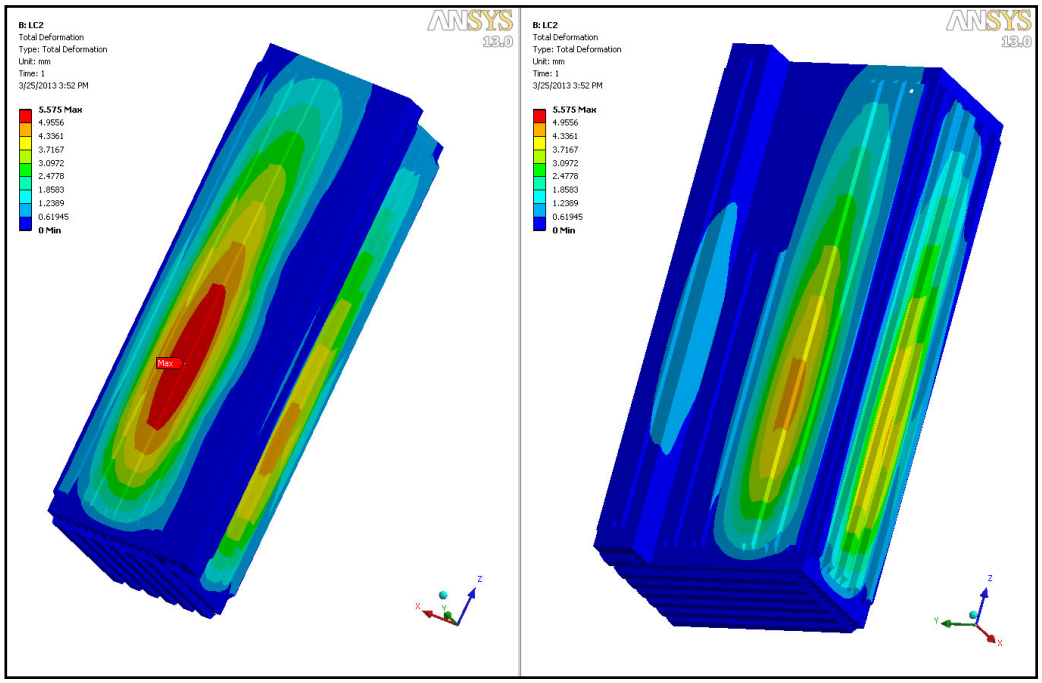

(a) (b)

Figure V.4.1.9.8. Case 2 summed deflection of the inner tank

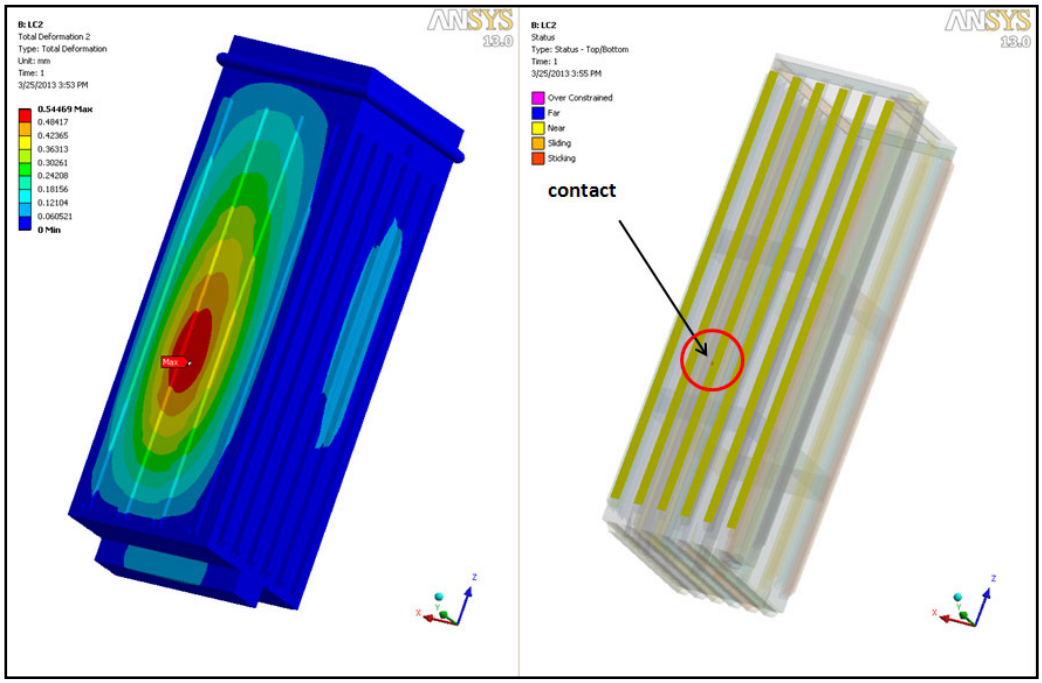

(a) (b)

Figure V.4.1.9.9. Case 2, (a) Summed deflection of the outer tank and (b) Contact status of the inner tank

Table V.4.1.9.5. Case 2 single-sided fillet weld configurations

Weld	Descripion	Leg Length (mm)	Weld Size (mm)	Throat Area (mm^2)	Y_{bar} (mm)	Unit MOI_x (mm^3)	MOI_x (mm^4)	Unit Polar MOI_z (mm^3)	Polar MOI_z (mm^4)	Sec. Mod. (x) (mm^3)	Sec. Mod. (z) (mm^3)
1	continuous	3596	4	10169.5	1798.0	3875054395	10958653828	3875054395	10958653828	6094913	6094913
2	continuous	3596	4	10169.5	1798.0	3875054395	10958653828	3875054395	10958653828	6094913	6094913
3	continuous	3596	4	10169.5	1798.0	3875054395	10958653828	3875054395	10958653828	6094913	6094913
4	continuous	3596	4	10169.5	1798.0	3875054395	10958653828	3875054395	10958653828	6094913	6094913
5	continuous	3596	4	10169.5	1798.0	3875054395	10958653828	3875054395	10958653828	6094913	6094913
6	continuous	3596	4	10169.5	1798.0	3875054395	10958653828	3875054395	10958653828	6094913	6094913
7	continuous	3596	4	10169.5	1798.0	3875054395	10958653828	3875054395	10958653828	6094913	6094913
8	continuous	3596	4	10169.5	1798.0	3875054395	10958653828	3875054395	10958653828	6094913	6094913
13	continuous	3805	10	26901.4	1902.5	4590740427	32456534819	4590740427	32456534819	17059939	17059939
14	continuous	920	10	6504.4	460.0	64890667	458777013	64890667	458777013	997341	997341
15	continuous	1520	10	10746.4	760.0	292650667	2069040213	292650667	2069040213	2722421	2722421
16	continuous	200	10	1414.0	100.0	666667	4713333	666667	4713333	47133	47133
17	continuous	200	10	1414.0	100.0	666667	4713333	666667	4713333	47133	47133
18	continuous	200	10	1414.0	100.0	666667	4713333	666667	4713333	47133	47133
19	continuous	200	10	1414.0	100.0	666667	4713333	666667	4713333	47133	47133
20	continuous	200	10	1414.0	100.0	666667	4713333	666667	4713333	47133	47133

Table V.4.1.9.6. Case 2 summary of the single-sided fillet weld analysis

Weld	Shear (FX) (N)	Shear (FY) (N)	Normal (FZ) (N)	Moment (X) (N-mm)	Torsion (Z) (N-mm)	F_{bend_mx} (MPa)	F_{normal_fz} (MPa)	F_{shear_fx} (MPa)	F_{shear_fy} (MPa)	F_{shear_xmz} (MPa)	$F_{traction}$ (MPa)	F_{shear} (MPa)	F_{weld} (MPa)	FoS
1	-32645.2	10465.2	632.2	-1672389.1	-2711122.8	0.27	0.06	3.21	1.03	0.44	0.34	3.80	4	13.12
2	53875.2	9138.5	268.4	-1174577.2	9252245.7	0.19	0.03	5.30	0.90	1.52	0.22	6.87	7	7.27
3	79218.4	506.7	-62.1	248132.1	22036404.1	0.04	0.01	7.79	0.05	3.62	0.05	11.41	11	4.38
4	-79207.9	-621.4	51.7	-244063.3	-21993275	0.04	0.01	7.79	0.06	3.61	0.05	11.40	11	4.39
5	77393.7	-4050.8	780.6	1055461.8	-21688628	0.17	0.08	7.61	0.40	3.56	0.25	11.18	11	4.47
6	-52727.5	-11746.9	392.6	1694042.2	10324696.7	0.28	0.04	5.18	1.16	1.69	0.32	6.98	7	7.16
7	-96131.6	1159.7	-93.5	-151143.8	20925940.2	0.02	0.01	9.45	0.11	3.43	0.03	12.89	13	3.88
8	96121.1	-1045	-396.7	-137453	-21009457	0.02	0.04	9.45	0.10	3.45	0.06	12.90	13	3.88
13	-3597.8	-4314.3	7979.7	8708159.8	5717754.3	0.51	0.30	0.13	0.16	0.34	0.81	0.50	1	52.79
14	-4781.9	2461.6	-22741.1	-648828.8	-45929.4	0.65	3.50	0.74	0.38	0.05	4.15	0.87	4	11.80
15	5789.8	1576.5	725.4	-277139.2	313329.5	0.10	0.07	0.54	0.15	0.12	0.17	0.67	1	72.34
16	-9325.7	381.5	8798.7	-9833.2	-19808.9	0.21	6.22	6.60	0.27	0.42	6.43	7.02	10	5.25
17	9030.7	-140.6	11094.5	16825.2	-1124.2	0.36	7.85	6.39	0.10	0.02	8.20	6.41	10	4.80
18	-1382.4	17.1	18953.7	139123.3	4997.2	2.95	13.40	0.98	0.01	0.11	16.36	1.08	16	3.05
19	7965.3	125.9	19756.6	42821.2	-2215.6	0.91	13.97	5.63	0.09	0.05	14.88	5.68	16	3.14
20	-1222.4	977.7	14250.8	-230636.3	-5249	4.89	10.08	0.86	0.69	0.11	14.97	1.20	15	3.33

Table V.4.1.9.7. Case 2 double-sided fillet weld configurations

Weld	Type	Plate Thick (mm)	Leg Length (mm)	Weld Size (mm)	Throat Area (mm^2)	X_{bar} (mm)	Y_{bar} (mm)	Unit MOI_x (mm^3)	MOI_x (mm^4)	MOI_y (mm^4)	Polar MOI_z (mm^3)	MOI_z (mm^4)	Sec. Mod. (x) (mm^3)	Sec. Mod. (z) (mm^3)	Sec. Mod. (xz) (mm^3)	Sec. Mod. (yz) (mm^3)
9	50 x 300 skip	10	50	10.00	707.10	8.54	25.00	20833	147292	51502	28118	198794	5892	6034	7952	23292
10	50 x 300 skip	10	50	10.00	707.10	8.54	25.00	20833	147292	51502	28118	198794	5892	6034	7952	23292
11	50 x 300 skip	10	50	10.00	707.10	8.54	25.00	20833	147292	51502	28118	198794	5892	6034	7952	23292
12	50 x 300 skip	10	50	10.00	707.10	8.54	25.00	20833	147292	51502	28118	198794	5892	6034	7952	23292

Table V.4.1.9.8. Case 2 summary of the double-sided fillet weld analysis

Weld	Shear (FX) (N)	Shear (FY) (N)	Normal (FZ) (N)	Moment (X) (N-mm)	Moment (Y) (N-mm)	Torsion (Z) (N-mm)	F_{bend_mx} (MPa)	F_{bend_my} (MPa)	F_{normal_fz} (MPa)	F_{shear_fx} (MPa)	F_{shear_fy} (MPa)	F_{shear_xmz} (MPa)	F_{shear_ymz} (MPa)	$F_{traction}$ (MPa)	F_{shear} (MPa)	F_{weld} (MPa)	FoS
9	-13.3	-158.3	74.8	2253.9	-1076.9	495.8	0.38	-0.18	0.11	0.02	0.22	0.0624	0.0213	0.31	0.26	0.40	123.95
10	11.2	-438.2	1272.3	3202.6	9533.3	322.8	0.54	1.58	1.80	0.02	0.62	0.0406	0.0139	3.92	0.64	3.97	12.58
11	14.8	-635.2	2278.2	1379.8	14532	190.4	0.23	2.41	3.22	0.02	0.90	0.0239	0.0082	5.86	0.91	5.93	8.43
12	15.2	-984	3332	4121.7	17020.9	-24.6	0.70	2.82	4.71	0.02	1.39	0.0031	-0.0011	8.23	1.39	8.35	5.99

c) Case 3 - Filled Inner and Outer Tanks in Place, Static Loading

Case 3 models a leak in the inner tank that is allowing water to enter the outer tank. The bounding case for this event is having both the inner and outer tanks filled with water, and this is the configuration that was evaluated for Case 3. This situation puts a severe load on the outer tank.

The initial simulation resulted in a prediction of deflections of the sides of the outer tank that were larger than the 10 mm gap between the outer tank and the concrete pool, so simple concrete walls were added to the basic model that had been used for Cases 1 and 2. Frictionless contact was then added between the tank and the inner surfaces of the wall. The walls are fixed in space at the bottom and fixed laterally normal to the outer wall surface, so that the wall is essentially rigid, as shown in Fig. V.4.1.9.10.

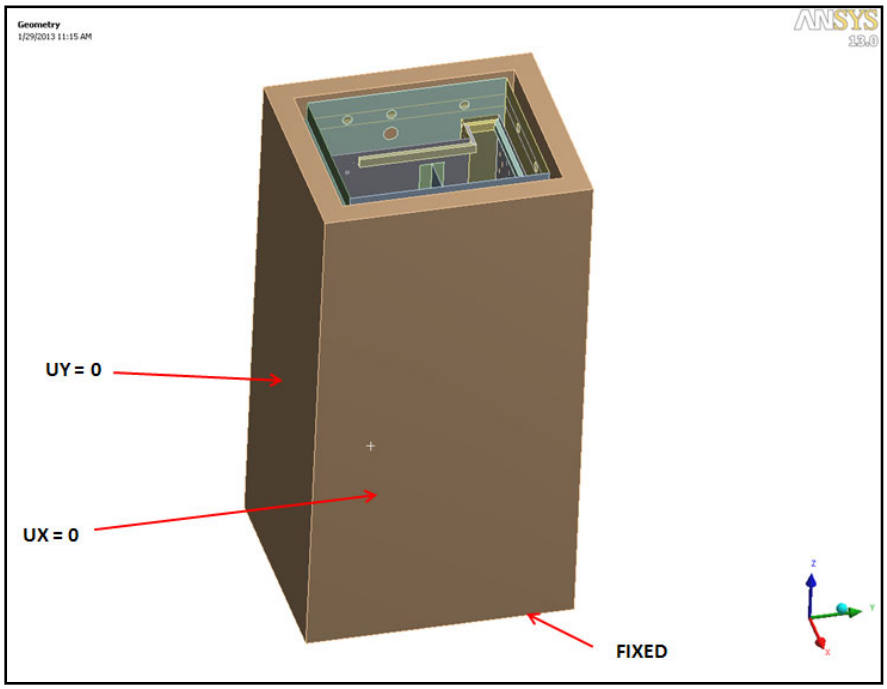

Figure V.4.1.9.10. Case 3 concrete pool walls

For this case, the largest stresses are in the outer tank, instead of the inner tank, since both sides of the inner tank walls are immersed in water and so pressures are the same on the inside and outside of the inner tank. As with Case 1, the maximum calculated stress is an anomaly of the modeling; in this case, the simulation produces a value of 500 MPa at a sharp corner at the bottom of the tank, as shown in Figs. V.4.1.9.11(a) and (b). The maximum real stress in the outer tank, taken one element away from this corner, is about 295 MPa, Fig. V.4.1.9.11(b). The safety factor here is 0.40 for the parent material, and 0.30 in the HAZ. The next two highest stresses are near corner welds (weld 31, see Fig. V.4.1.9.12(a) for location) and are about 140 MPa (SF = 0.64). The highest stress not at a weld is in the middle of the stiffening tubes on the wider side of the outer tank and is about 112 MPa (SF = 1.05). These locations are shown in Fig. V.4.1.9.11(c). Because the Case 3 analysis showed high stress at the bottom of the outer tank, as well as several welds with safety factors less than 1.0, numerous changes to the tank design were proposed and analyzed to obtain acceptable performance. These changes were reviewed, and the following changes to the initial outer tank design were adopted. First, the nominal clearance between the outer tank and the concrete pit was reduced from 10 mm to 5 mm. This will be accomplished by adding a dielectric epoxy fiberglass to the surfaces of each concrete pit. Second, both long sides of the outer tank will be fitted with six stiffening tubes. In the original design, one long side had six stiffening tubes, while the other had only four. This produces acceptable results, provided that the bottom ends of

all the stiffening tubes are continuously welded for the first 350 mm, and then skip welded along the remaining length. This configuration is shown in Fig. V.4.1.9.13.

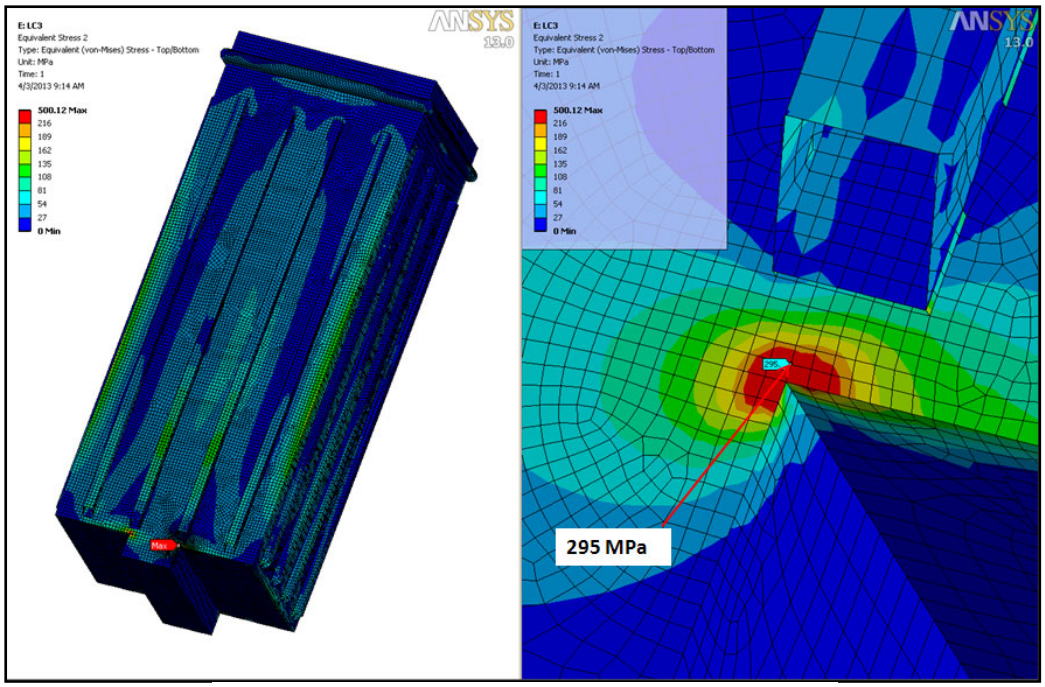

(a) (b)

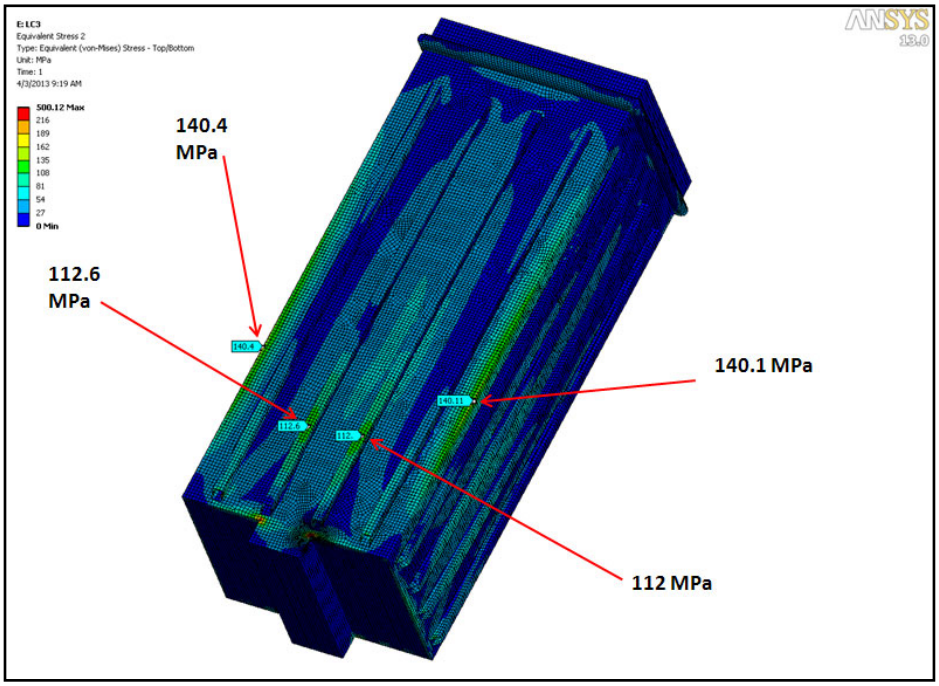

(c)

Figure V.4.1.9.11. Case 3 von Mises stress of the outer tank for the initial design

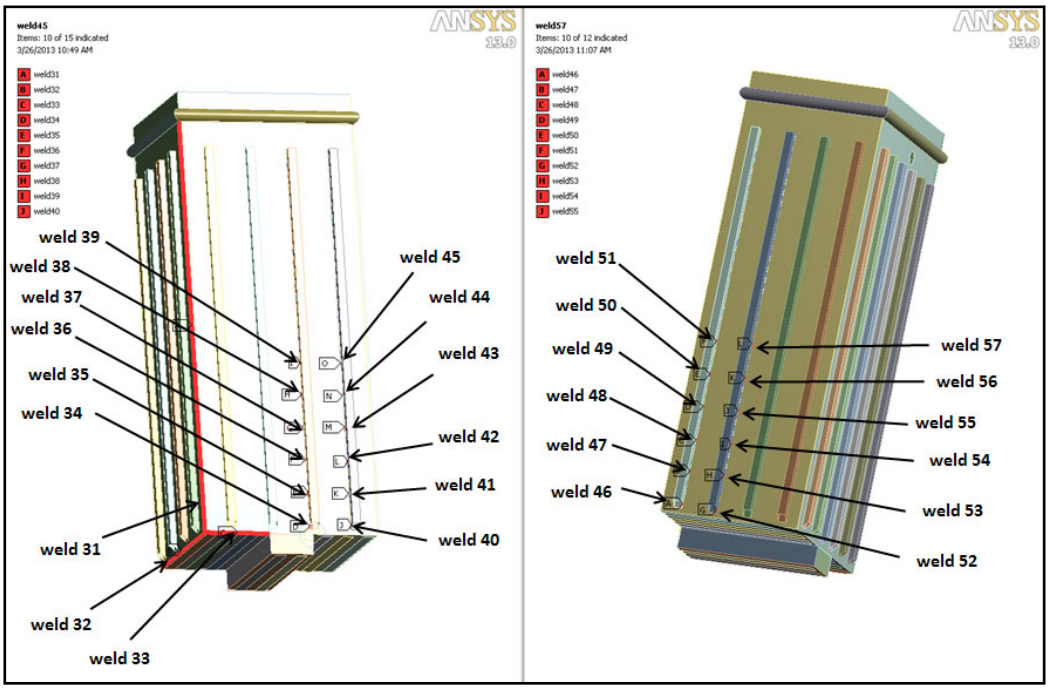

(a) (b)

Figure V.4.1.9.12. Case 3 Weld locations for the original outer tank design

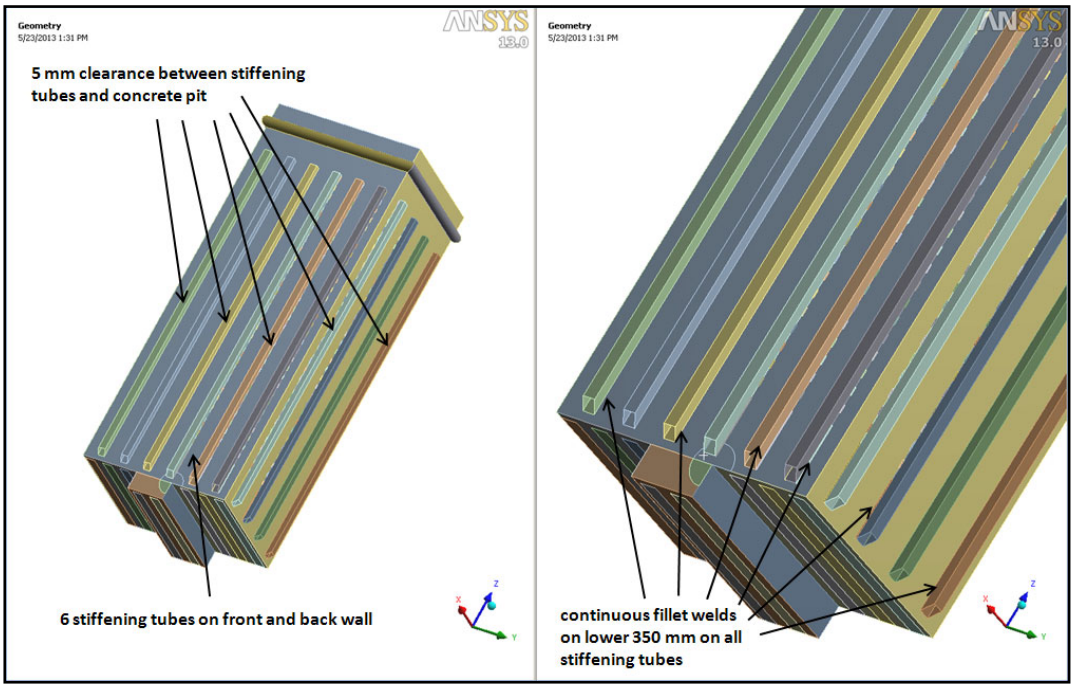

(a) (b)

Figure V.4.1.9.13. Modified outer tank design

Analysis of this modified tank design shows that the maximum stress in the outer tank is now 235.4 MPa (Fig. V.4.1.9.14). This is again at a sharp corner at the bottom of the tank and is a modeling artifact and can be ignored. The maximum stress one element away is 137.2 MPa. This is in the HAZ, where the yield strength is 90 MPa. If Glinka's correction [Ref. V.4.1.9] is applied, the corrected strain is less than the strain at the yield point (Fig. V.4.1.9.15), so the corrected stress is 90 MPa and the safety factor with respect to yield is 1.0. Stresses in the inner tank are low (Fig. V.4.1.9.16). The maximum stress is 7.63 MPa for a safety factor of 15.46.

Maximum deflection in the outer tank is limited to less than the 5 mm nominal clearance between the tank and the concrete wall. Deflections in the inner tank are plotted in Fig. V.4.1.9.17; the maximum deflection in the inner tank is only 0.037 mm.

As in Cases 1 and 2, selected welds were evaluated by inspecting plots of von Mises stress and deflection and selecting representative welds in high stress and high deflection locations. These welds are shown in Fig. V.4.1.9.18. Weld configurations and properties are presented in Table V.4.1.9.9, and weld loads, stresses and safety factors are summarized in Table V.4.1.9.10. Weld details were taken from Ref. V.4.1.8. As can be seen from Table V.4.1.9.10, the lowest safety factor among all welds was 2.13 at weld 54.

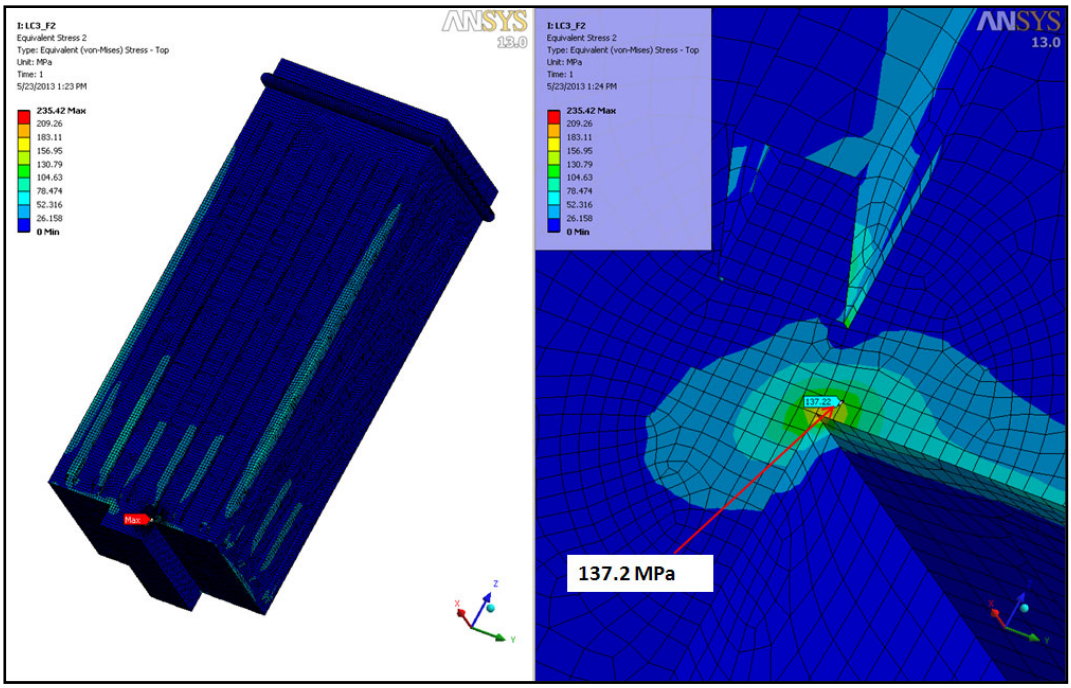

(a) (b)

Figure V.4.1.9.14. Von Mises stress in the full outer tank with dielectric spacers

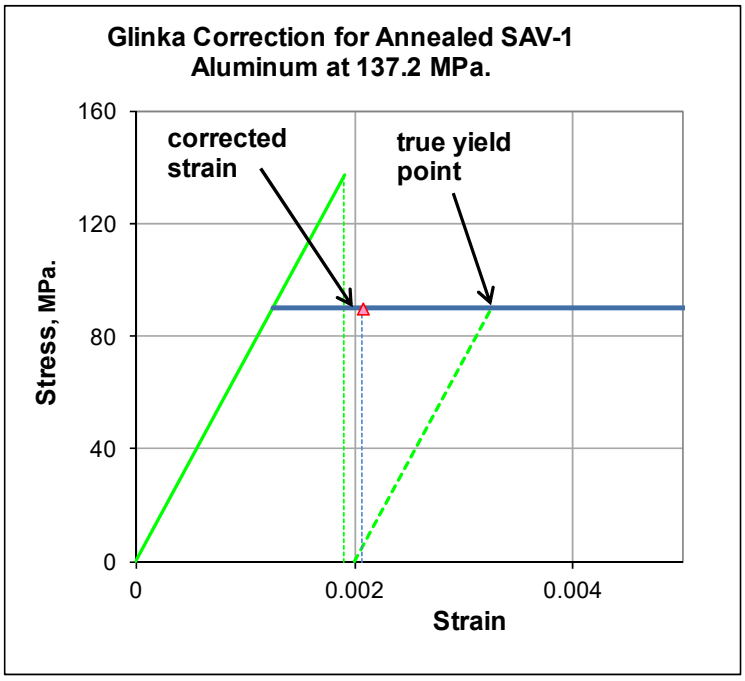

Figure V.4.1.9.15. Corrected strain at the peak stress location for the modified outer tank design

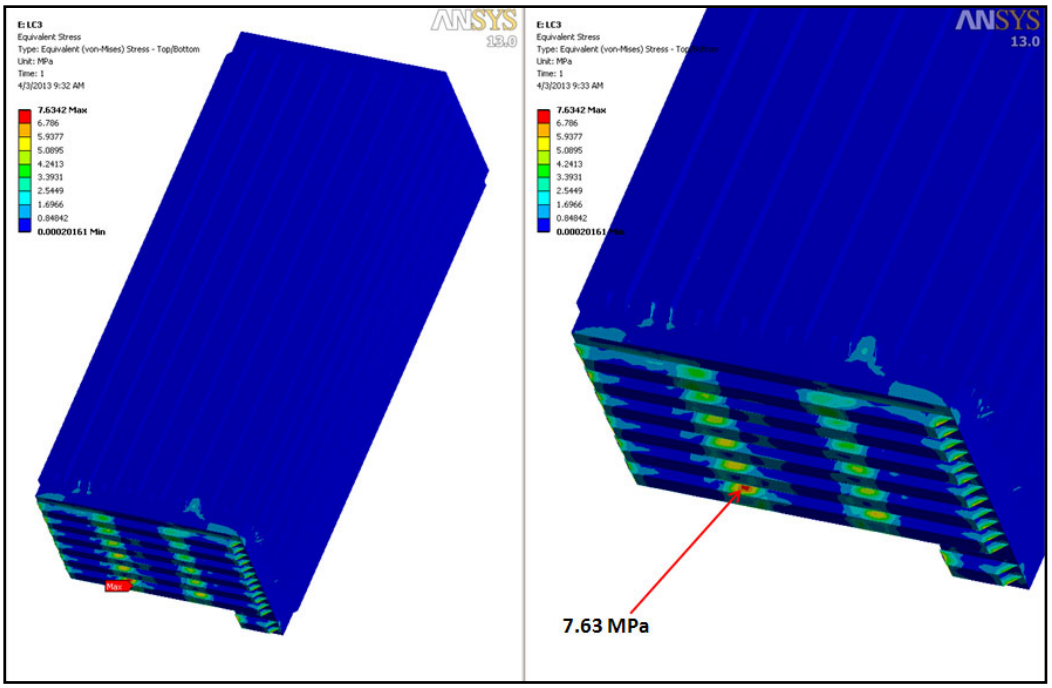

(a) (b)

Figure V.4.1.9.16. Case von Mises stress of the inner tank

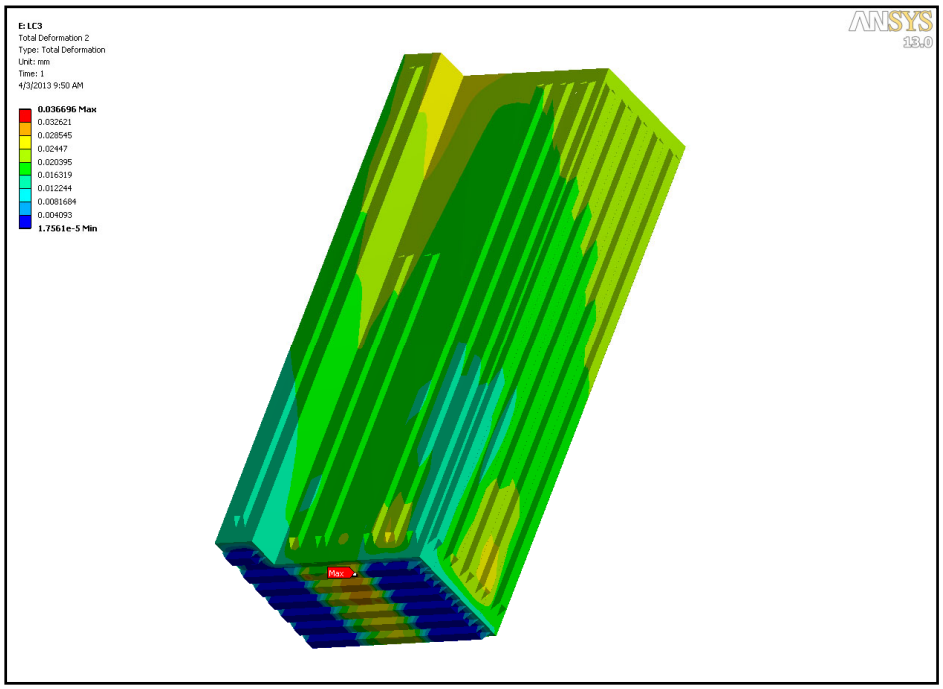

Figure V.4.1.9.17. Case 3 Summed deflection of the inner tank

d) Load Case 4 - Lifting Analysis of an Empty Inner Tank

Case 4 was used to determine stress levels when either inner tank is lifted for the placement. Results are shown in Figs. V.4.1.9.19 and V.4.1.9.20. Stresses and deflections in the inner tank are very low, since the tank has features welded near the upper edge that stiffen the structure and help prevent damage during lifting. The maximum stress in the tank, exclusive of the lifting lugs and chain, is only 2.9 MPa, for a safety factor of 40.7. The maximum deflection is in the bottom of the tank and is 0.102 mm.

e) Case 5 Lifting Analysis of an Empty Outer Tank

Case 5 was used to determine stress levels when the outer tank is lifted for the placement process. Results are shown in Figs. V.4.1.9.21 and V.4.1.9.22. Again, stresses and deflections in the tank are very low, due to the features welded near the upper edge that stiffen the tank. The maximum stress in the tank, exclusive of the lifting lugs and chain, is only 2.59MPa, for a safety factor of 45.5. The maximum summed deflection is in the bottom of the tank is 0.14 mm.

The outer tank design of the storage pool was modified to provide higher safety factors for the different loading cases. The modified fabricated design is shown in Fig. V.4.1.9.23. The main change is to use horizontal rips instead of the vertical rips with different spacing. The spacing is decreased near the top as shown in the fabricated picture of the outer tank.

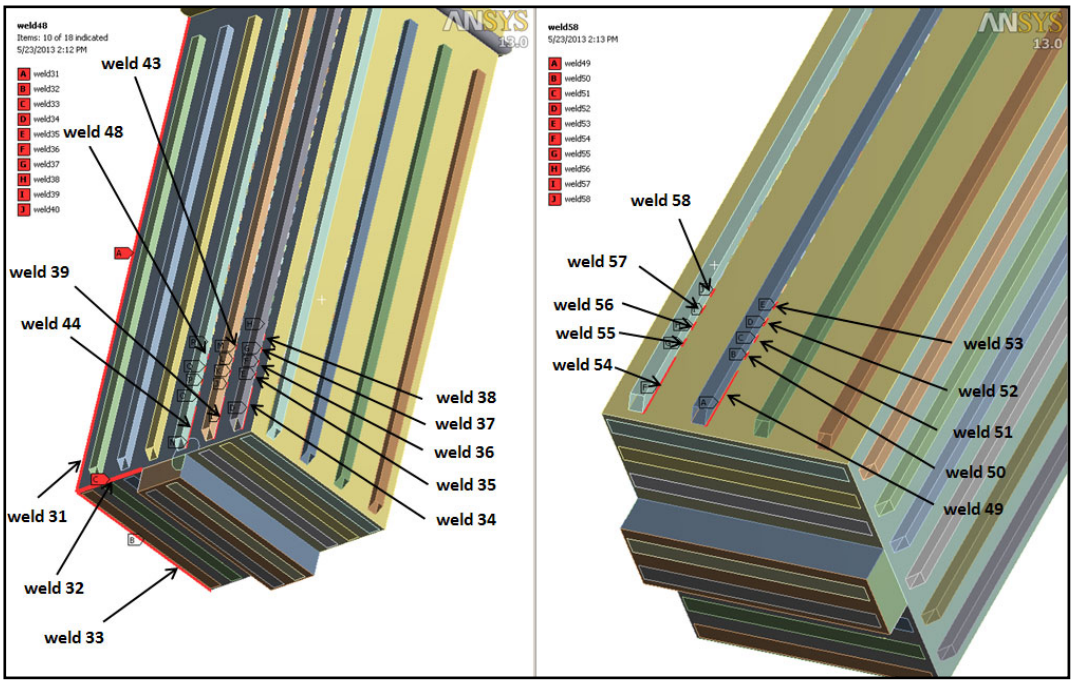

Figure V.4.1.9.18. Weld locations for the modified outer tank

Table V.4.1.9.9. Case 3 single-sided fillet weld configurations for the modified outer tank

Weld	Description	Leg Length (mm)	Weld Size (mm)	Throat Area (mm^2)	Y_{bar} (mm)	Unit MOI_x (mm^3)	MOI_x (mm^4)	Unit Polar MOI_z (mm^3)	Polar MOI_z (mm^4)	Section Modulus (x) (mm^3)	Section Modulus (z) (mm^3)
31	continuous	3898	10	27555.3	1948.8	4933749842	34881611386	4933749842	34881611386	17899480	17899480
32	continuous	1340	10	9473.8	670.0	200508667	1417596273	200508667	1417596273	2115815	2115815
33	continuous	630	10	4454.1	315.0	20837250	147319358	20837250	147319358	467681	467681
34	50 X 100 skip	350	4	989.8	175.0	3572917	10104208	3572917	10104208	57738	57738
35	50 X 100 skip	50	4	141.4	25.0	10417	29458	10417	29458	1178	1178
36	50 X 100 skip	50	4	141.4	25.0	10417	29458	10417	29458	1178	1178
37	50 X 100 skip	50	4	141.4	25.0	10417	29458	10417	29458	1178	1178
38	50 X 100 skip	50	4	141.4	25.0	10417	29458	10417	29458	1178	1178
39	50 X 100 skip	350	4	989.8	175.0	3572917	10104208	3572917	10104208	57738	57738
40	50 X 100 skip	50	4	141.4	25.0	10417	29458	10417	29458	1178	1178
41	50 X 100 skip	50	4	141.4	25.0	10417	29458	10417	29458	1178	1178
42	50 X 100 skip	50	4	141.4	25.0	10417	29458	10417	29458	1178	1178
43	50 X 100 skip	50	4	141.4	25.0	10417	29458	10417	29458	1178	1178
44	50 X 100 skip	350	4	989.8	175.0	3572917	10104208	3572917	10104208	57738	57738
45	50 X 100 skip	50	4	141.4	25.0	10417	29458	10417	29458	1178	1178
46	50 X 100 skip	50	4	141.4	25.0	10417	29458	10417	29458	1178	1178
47	50 X 100 skip	50	4	141.4	25.0	10417	29458	10417	29458	1178	1178
48	50 X 100 skip	50	4	141.4	25.0	10417	29458	10417	29458	1178	1178
49	50 X 100 skip	350	4	989.8	175.0	3572917	10104208	3572917	10104208	57738	57738
50	50 X 100 skip	50	4	141.4	25.0	10417	29458	10417	29458	1178	1178
51	50 X 100 skip	50	4	141.4	25.0	10417	29458	10417	29458	1178	1178
52	50 X 100 skip	50	4	141.4	25.0	10417	29458	10417	29458	1178	1178
53	50 X 100 skip	50	4	141.4	25.0	10417	29458	10417	29458	1178	1178
54	50 X 100 skip	350	4	989.8	175.0	3572917	10104208	3572917	10104208	57738	57738
55	50 X 100 skip	50	4	141.4	25.0	10417	29458	10417	29458	1178	1178
56	50 X 100 skip	50	4	141.4	25.0	10417	29458	10417	29458	1178	1178
57	50 X 100 skip	50	4	141.4	25.0	10417	29458	10417	29458	1178	1178
58	50 X 100 skip	50	4	141.4	25.0	10417	29458	10417	29458	1178	1178

Table V.4.1.9.10. Case 3 summary of weld analysis for the modified outer tank

Weld	Shear (FX) (N)	Shear (FY) (N)	Normal (FZ) (N)	Moment (X) (N-mm)	Torsion (Z) (N-mm)	F_{bend_mx} (MPa)	F_{normal_fz} (MPa)	F_{shear_fx} (MPa)	F_{shear_fy} (MPa)	F_{shear_xmz} (MPa)	$F_{traction}$ (MPa)	F_{shear} (MPa)	F_{weld} (MPa)	FoS
31	-30939.5	-1951.3	28315	9357271.9	1371824.9	0.52	1.03	1.12	0.07	0.08	1.55	1.20	2	25.49
32	-17102.3	136.7	-5862.6	228186.2	-73953.4	0.11	0.62	1.81	0.01	0.03	0.73	1.84	2	25.27
33	-9874.7	2814.7	1584.2	-3307091.3	-1739553.5	7.07	0.36	2.22	0.63	3.72	7.43	5.97	10	5.25
34	2444.8	-13761.8	-2974.1	167074.1	103519.1	2.89	3.00	2.47	13.90	1.79	5.90	14.54	16	3.19
35	330.9	-2851.6	53.3	11657.1	-16.2	9.89	0.38	2.34	20.17	0.01	10.27	20.30	23	2.20
36	466.6	-2679.7	287.3	10497.9	284.3	8.91	2.03	3.30	18.95	0.24	10.94	19.28	22	2.26
37	565.4	-2383.5	448.1	9255.8	298.9	7.85	3.17	4.00	16.86	0.25	11.02	17.38	21	2.43
38	653	-1997.8	518.3	8122.6	196.8	6.89	3.67	4.62	14.13	0.17	10.56	14.92	18	2.74
39	-769.1	835.3	-988	-240843.4	180087.7	4.17	1.00	0.78	0.84	3.12	5.17	3.99	7	7.66
40	-827	-923.5	-239.5	5099.8	1081.8	4.33	1.69	5.85	6.53	0.92	6.02	9.40	11	4.48
41	-1139.7	-1237.6	-46.1	5194	1247.6	4.41	0.33	8.06	8.75	1.06	4.73	12.64	13	3.70
42	-1414.9	-1428.1	68.6	5432.6	1115.9	4.61	0.49	10.01	10.10	0.95	5.10	14.90	16	3.18
43	-1642.1	-1485.1	129.7	5625.9	1028.1	4.77	0.92	11.61	10.50	0.87	5.69	16.32	17	2.89
44	352.1	17662.1	1521.6	-691031.8	-185387.5	11.97	1.54	0.36	17.84	3.21	13.51	18.20	23	2.21
45	140	1287.8	-506.1	-3529.1	-178.4	2.99	3.58	0.99	9.11	0.15	6.57	9.18	11	4.43
46	138.7	382.2	-515.6	-1706.2	-153.7	1.45	3.65	0.98	2.70	0.13	5.09	2.92	6	8.51
47	198.2	-540.9	-577.8	1331.6	-178.9	1.13	4.09	1.40	3.83	0.15	5.22	4.13	7	7.52
48	332.8	-1544.7	-654.8	4633.8	-118.9	3.93	4.63	2.35	10.92	0.10	8.56	11.20	14	3.55
49	757.4	-16706.4	1386	639102.5	-238406.3	11.07	1.40	0.77	16.88	4.13	12.47	17.57	22	2.32
50	100.5	-1269	-703.3	3310.9	345.5	2.81	4.97	0.71	8.97	0.29	7.78	9.03	12	4.19
51	268.8	-144.4	-695.1	676.2	410.4	0.57	4.92	1.90	1.02	0.35	5.49	2.47	6	8.31
52	411	1000.7	-702.2	-3379.9	599.1	2.87	4.97	2.91	7.08	0.51	7.83	7.86	11	4.51
53	545.9	2148.8	-697	-7217.2	783	6.12	4.93	3.86	15.20	0.66	11.05	15.86	19	2.59
54	486.3	-18274.8	2547.4	531103	-451928.7	9.20	2.57	0.49	18.46	7.83	11.77	20.25	23	2.13
55	-438	-2133.3	-308.8	7655.9	-165.5	6.50	2.18	3.10	15.09	0.14	8.68	15.43	18	2.82
56	-450.9	-1674.7	-416.6	6300.2	-292.7	5.35	2.95	3.19	11.84	0.25	8.29	12.33	15	3.36
57	-463.3	-1272	-462.1	4655	-286.5	3.95	3.27	3.28	9.00	0.24	7.22	9.66	12	4.15
58	-458.2	-900.1	-472.3	2961.3	-180.2	2.51	3.34	3.24	6.37	0.15	5.85	7.21	9	5.38

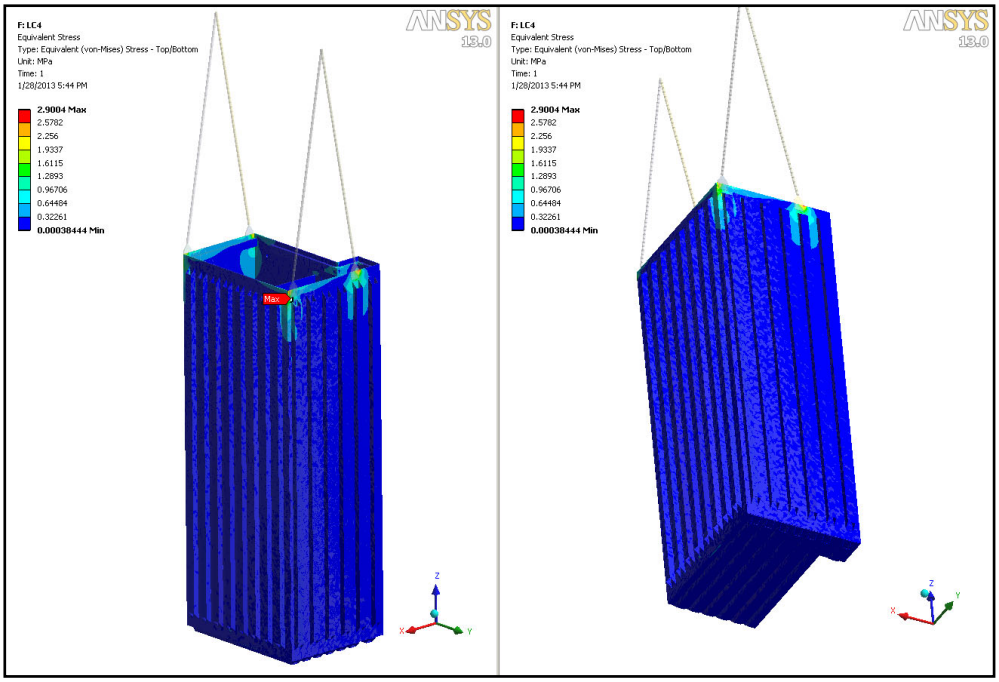

(a) (b)

Figure V.4.1.9.19. Case 4 von Mises stress of the inner tank

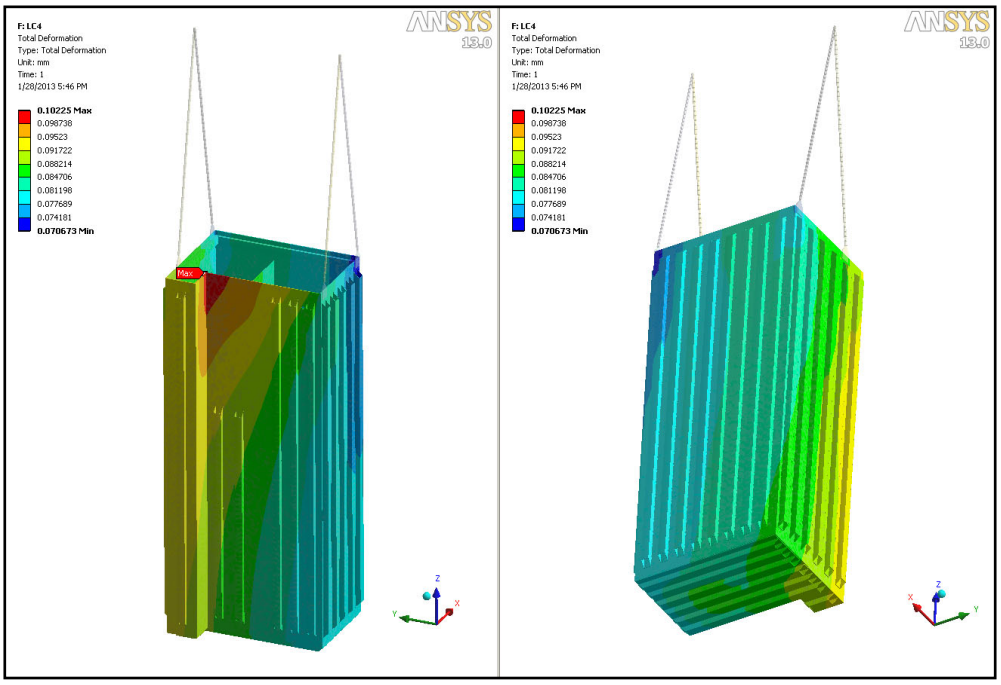

(a) (b)

Figure V.4.1.9.20. Case 4 Summed deflections of the inner tank

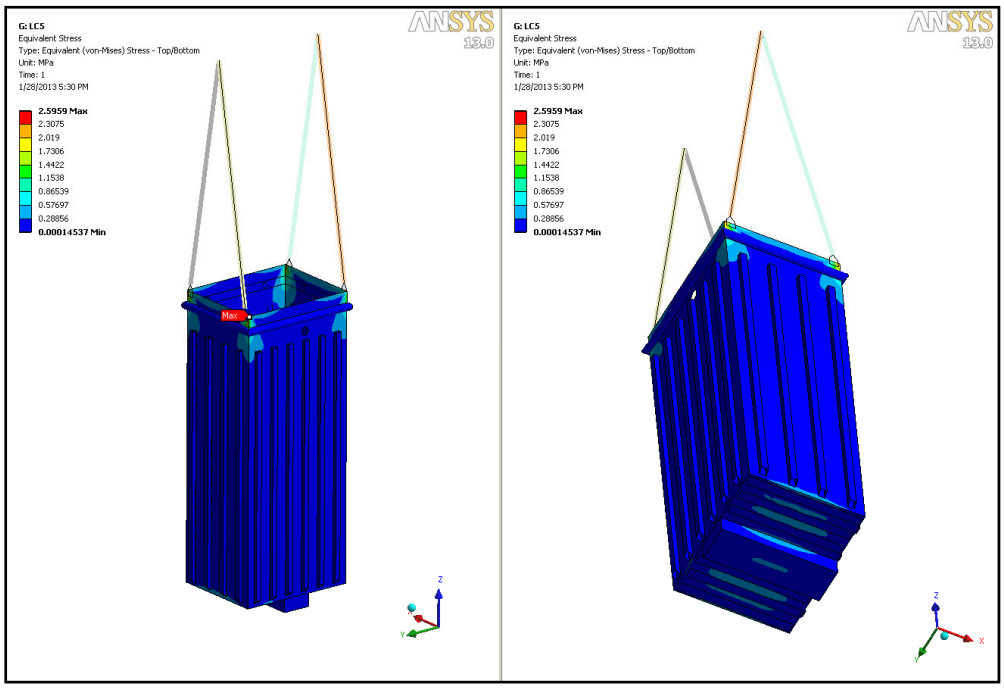

(a) (b)

Figure V.4.1.9.21. Case 5 von Mises stress of the outer tank

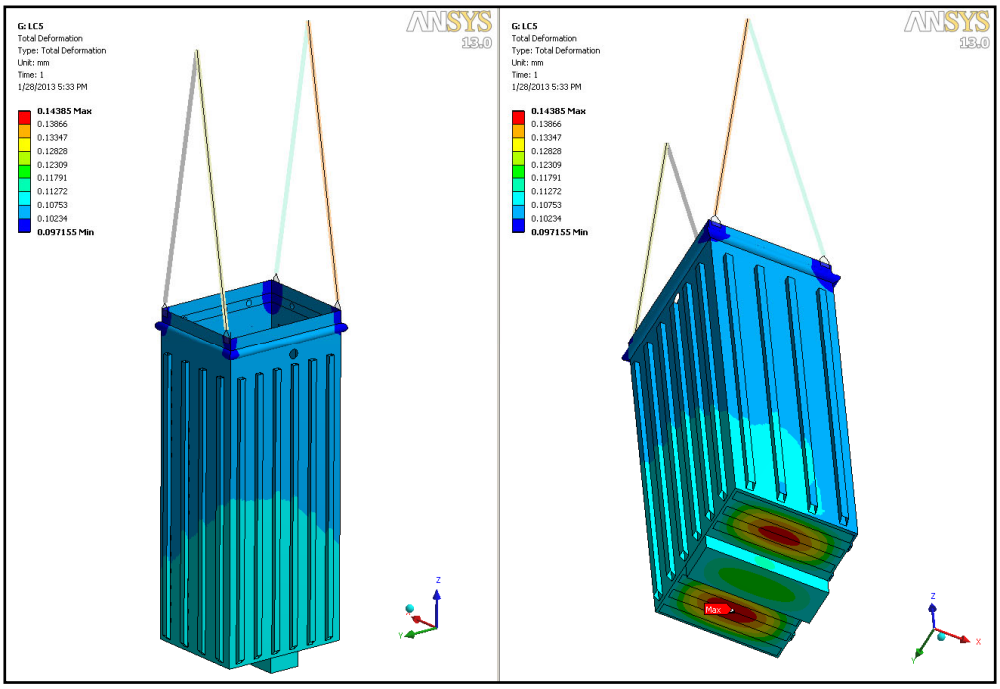

Figure V.4.1.9.22. Case 5 Summed deflections of the outer tank

V.4.1.10 Summary

Based on the results of this analysis, and subject to the listed assumptions, it is concluded that the subject storage pool, with the outer tank design modified as described above, is a structurally feasible design. In addition, horizontal rips are used instead of the vertical ribs, which provide higher safety factors for the different loading cases. This design modification was adapted for the outer tank.

References

V.4.1.1 *ANSYS Mechanical*, Version 13.0, Build date 11/2/2009, Ansys Inc, Pittsburgh, PA.
V.4.1.2 Sosny Corporation, private communication
V.4.1.3 Prokhorov, A, *Mechanical Properties of SAV-1*, KIPT, 2011.
V.4.1.4 “On seismicity of an industrial site for a neutron source, Contract 9J-31023-0004A”, Letter from V. V. Kvasil’chuk to I. Bolshinsky *et al*, May 20, 2011.
V.4.1.5 Shigley, J. E. and Mitchell, L. D. *Mechanical Engineering Design, Fourth Edition*, McGraw Hill, New York, 1983, Chapter 7.
V.4.1.6 *Aluminum Design Manual*, The Aluminum Association, Arlington, VA, 2010.
V.4.1.7 Storage Pool Body, Dwg. No. 101A.58.997.200.00СБ, Rev 2, dated 11.2012.
V.4.1.8 Cladding Assembly Drawing, Dwg. No. 101A.58.997.100.00СБ, Rev 2, dated 10.2012.
V.4.1.9 Glinka, G, “Energy Density Approach to Calculation on Inelastic Strain-Stress Near Notches and Cracks”, *Engineering Fracture Mechanics*, Vol,22, No. 3, 1985.

Figure V.4.1.9.23. The inner tank on the right and outer tank on the left of the fabricated spent fuel storage pool

V.5 Fuel Storage Pool Mechanical Design

The subcritical assembly uses low-enriched uranium fuel elements during its operation. Target assemblies have a finite life and are replaced periodically. The subcritical assembly hall contains two fuel storage pools for the storage of spent fuel and used target assemblies to allow safe radioactive decay until they can be shipped offsite.

V.5.1 Fuel Storage Pool Strategy

The subcritical assembly hall contains two identical fuel storage pools (FSP). The spent fuel pools are located below floor level. Only one fuel storage pool is used at a time; the second FSP is reserved as a stand-by unit in case the first FSP must be unloaded for repair work. The FSP's are filled with demineralized water, which distributes and conducts the decay heat and provides some radiation shielding function.

V.5.2 Fuel Storage Pool Structure

Each fuel storage pool is contained within a rectangular pit in the concrete hall floor. The location of the pools is shown in Fig. V.5.2.1. An outer tank is placed in the rectangular

concrete hole. An inner tank is placed within the outer tank. This configuration is diagrammed in Fig. V.5.2.2, with a closer view in Fig. V.5.2.3. The outer tank is intended to capture any liquid that might leak from the inner tank. The inner tank can be unloaded, drained, and removed for repair if required. There are liquid detectors between the inner and outer tanks that detect the presence of leakage. There is a system for pumping any leakage from the space between the inner and outer tanks.

The inner tank is divided into two chambers, as shown in Fig. V.5.2.2; one for the used target assemblies and the other for the spent fuel assemblies. A rack in each of the chambers provides storage locations for the target or the fuel assemblies. The storage location spacing is controlled to help distribute the decay heat and maintain $K_{eff} < 0.5$. The outer tanks, the inner tanks, and the storage racks are made of SAV-1 aluminum alloy.

V.5.3 Fuel Storage Pool Cover

Each fuel storage pool is covered by a steel cover that supports external loading and provides radiation shielding. The top surface of the cover is flush with the subcritical assembly hall floor, as indicated in Fig. V.5.1.1. The cover is made of carbon steel but is clad with a stainless-steel to resist wear and prevent corrosion. There are 64 fuel cell access holes in the cover and 6 target cell access holes. Each hole is co-axial with a cell in the rack below the cover. Each hole is filled with a plug which can be removed to access the cell in the storage rack below. The plug holes have a step in them to prevent radiation streaming, as do the corresponding plugs. Representations of the access holes and plugs are presented in Figs. V.5.3.1 and V.5.3.2.

V.5.4 Fuel Storage Pool Coolant Processing

Each fuel storage pool is served by a system that filters and demineralizes the coolant water. A schematic of the system is given in Fig. V.5.4.1. Decay heat and condensation are carried away from the FSPs by a system that exhausts air to the special ventilation system; the airflow channel location can be seen in Fig. V.5.2.3. A reservoir contains additional water that can be used to replace any water that has spilled, leaked, or evaporated.

V.5.5 Fuel Storage Pool Loading and Unloading

Spent fuel elements are transported from the subcritical assembly to the FSP in the fuel transfer cask. Figure V.5.5.1 shows a typical positioning of the fuel transfer cask for both pools. The cover plug that is directly over the intended storage rack cell is removed with a special tool that threads into the end of the plug. Two cask locators are inserted in adjacent plugs and serve to accurately place the cask over the cover hole, as shown in Fig. V.5.3.1. The cask is placed on the cover in registry with the hole with the aid of the cask locators.

As seen in Fig. V.5.5.2, a fuel dipstick is used to lower the fuel assembly from the fuel transfer cask to the rack in the FSP. The dipstick used to load and unload fuel assemblies

in the FSP is longer than the dipstick that interfaces with the fuel transfer station in the SCA tank, due to the greater depth of the FSP, but the two have similar configurations and functions. Target assemblies are loaded and unloaded by a similar method, using the target transfer cask and the target dipstick, also shown in Fig. V.5.5.2. The target dipstick used at the FSP is longer than the target dipstick used to remove target assemblies from the SCA, again due to the greater depth of the FSP.

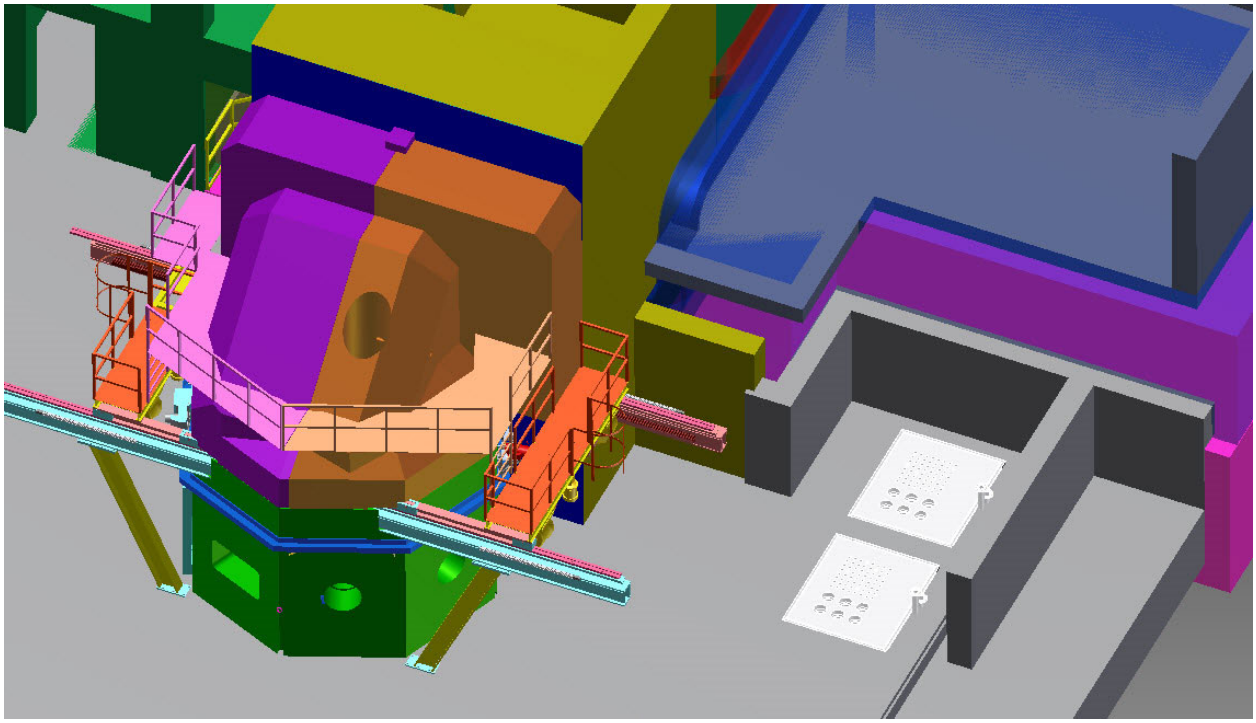

Figure V.5.2.1. Two fuel storage pool covers are visible at the right side of the SCA biological shield in this picture.

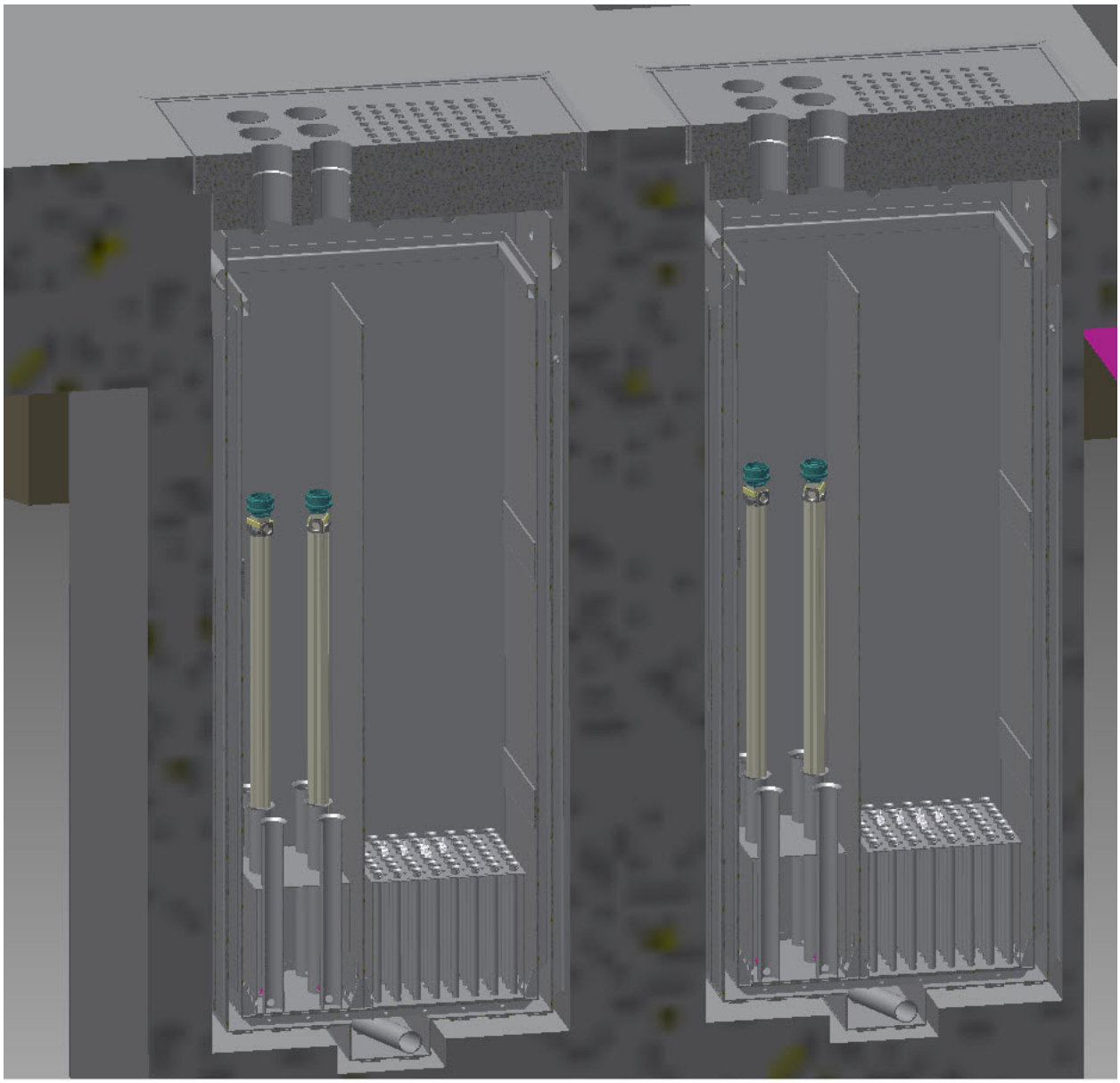

Figure V.5.2.2. Section view through the two fuel storage pools. Pool covers are visible at the top. The racks are visible at bottom.

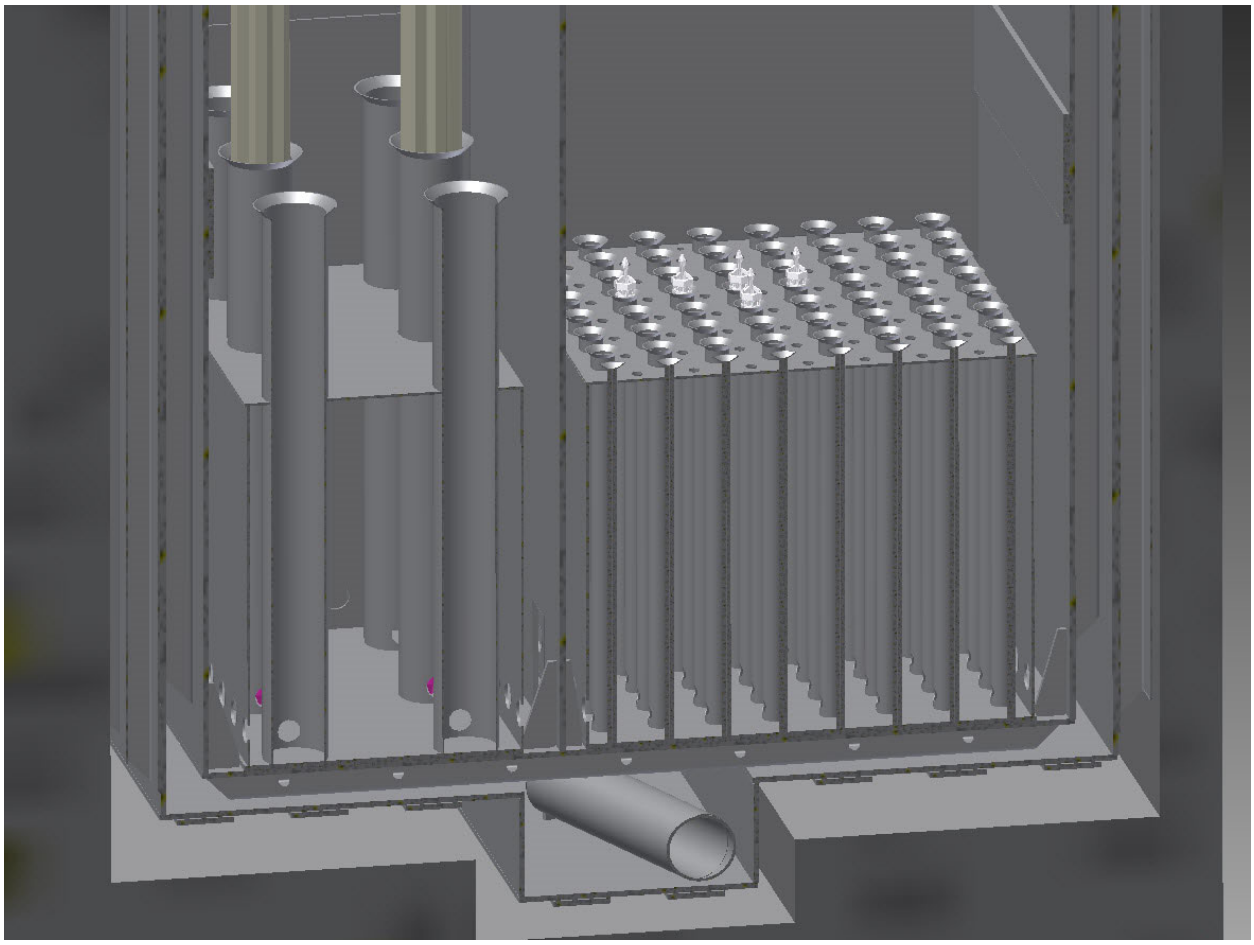

Figure V.5.2.3. The rack shown containing two target assemblies and five fuel assemblies. The inner and the outer tanks, and airflow channel are visible in this picture.

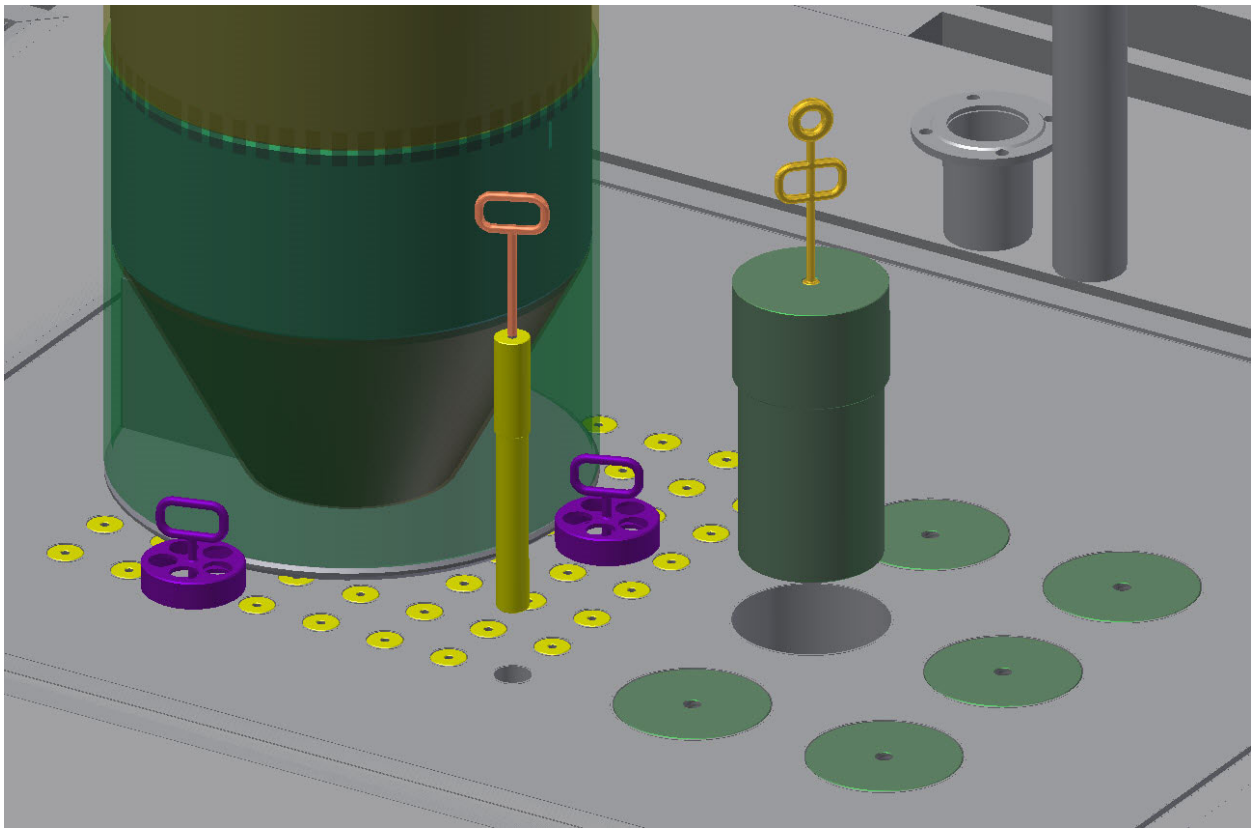

Figure V.5.3.1. The fuel storage pool cover, showing the plugs, the plug lifting devices, the fuel transfer cask, and the cask locators.

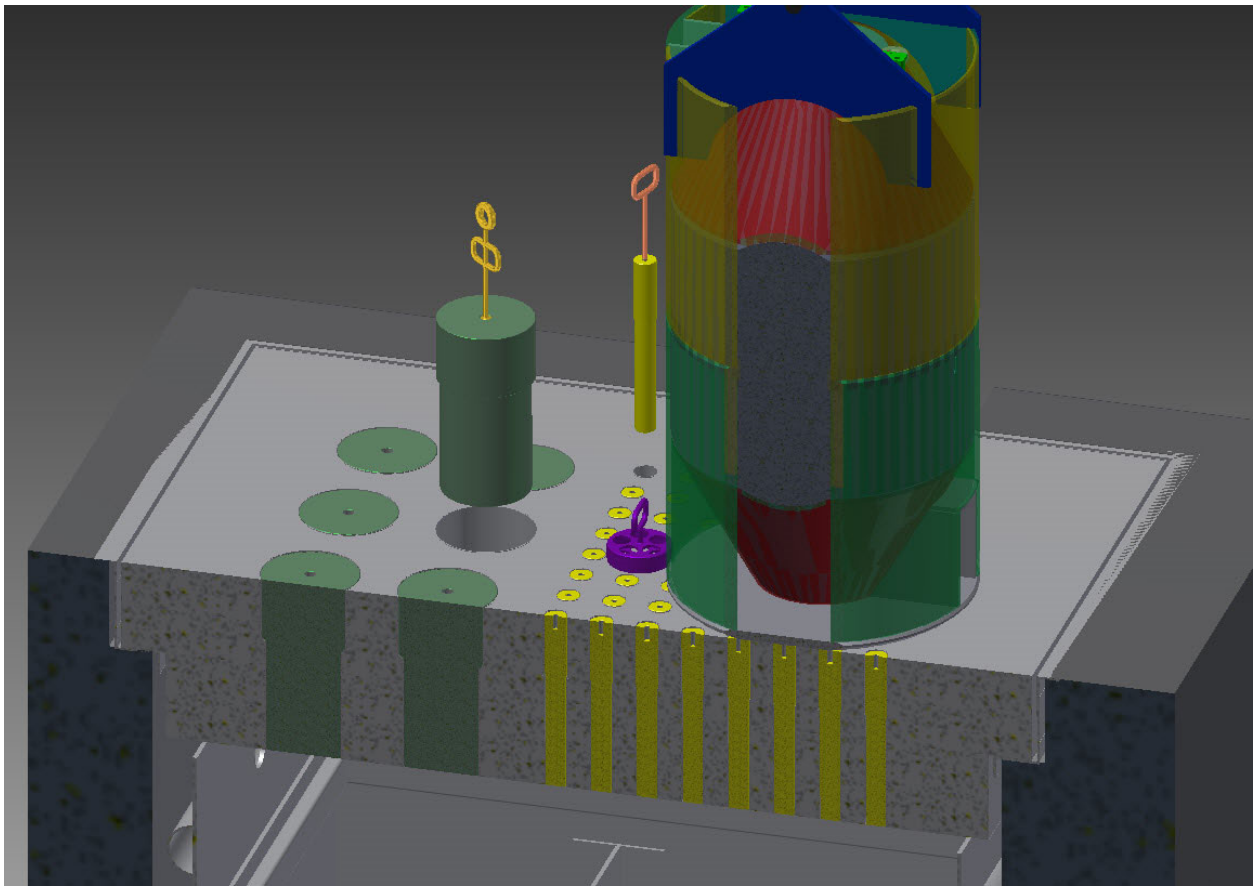

Figure V.5.3.2. Section view through FSP cover showing the target plugs and the fuel plugs.

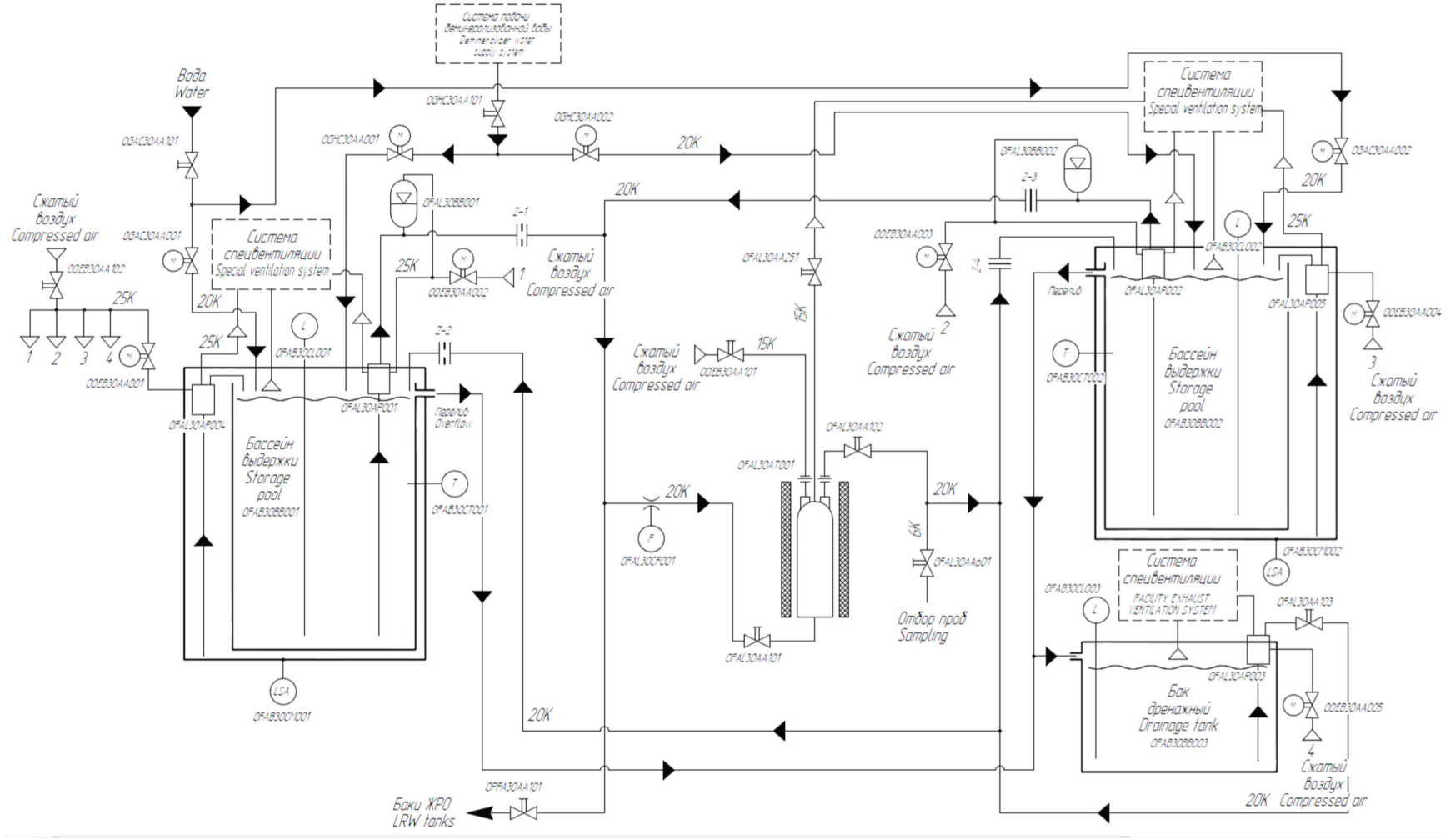

Figure V.5.4.1. Schematic of the FSP water conditioning system.

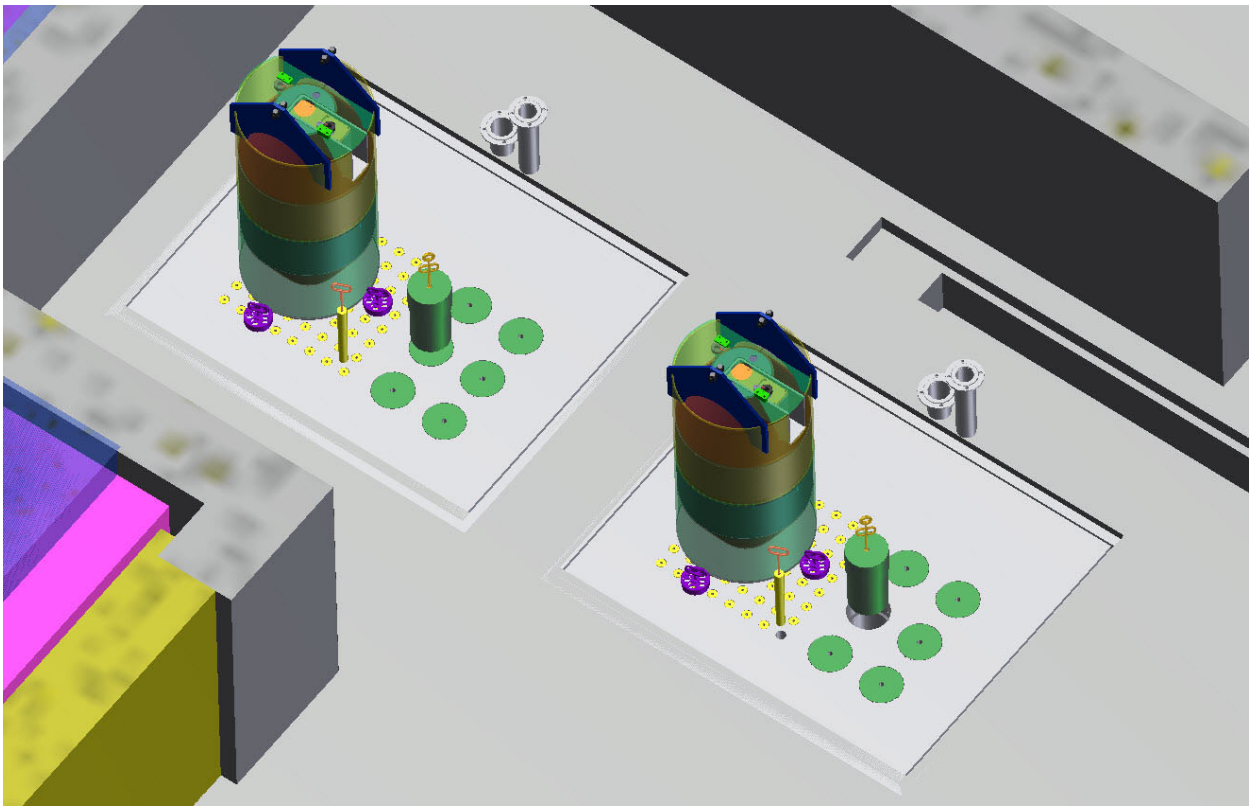

Figure V.5.5.1. View of the two fuel storage pools. The Fuel transfer cask is shown on each cover.

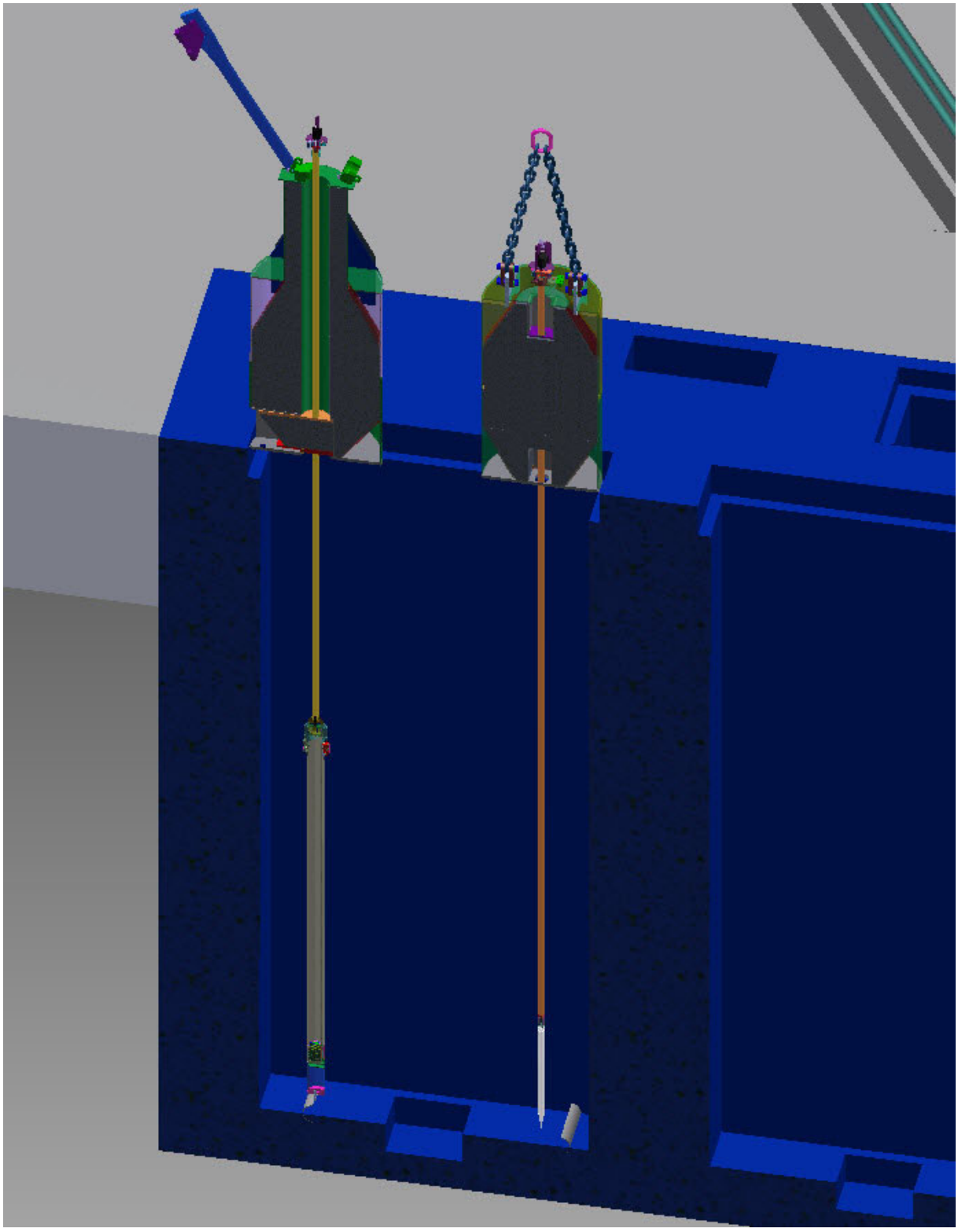

Figure V.5.5.2. Section view through the FSP, the fuel transfer cask, and the target transfer cask. Dipsticks are in place in both casks, reaching through the casks to grab a target assembly and a fuel assembly. Other components are not shown in this view.

V.6 Storage Pool Main Parameters

Table V.6.1. Geometric Parameters of the Storage Pool

Number of positions for spent fuel assemblies	64 (8×8)
Number of positions for discharged target assemblies	6
Space between stored fuel assemblies	10 cm
Inner/outer radius of fuel assembly holding tube	1.9 cm/ 2.1 cm
Height of water above the stored fuel assemblies	285 cm
Height of water above the top of the active target pack	321 cm
Inside depth of storage pool inner tank	380 cm
Outside height of storage pool inner tank	417 cm
Volume of each inner tank	5.58 m^3
Thickness of tank cover	40 cm
Number of pools	2

Table V.6.2. Thermal-Hydraulic Parameters for the Storage Pool

Inlet-outlet temperature difference	6 K
Peak temperature difference	9 K
Margin to boiling	64 K
Forced air mass flow rate	250 m^3/h

Table V.6.3. Structural Parameters for the Storage Pool

Number of stiffening tubes on each outer tank	20
Maximum stress during lifting of empty inner tank	2.9 MPa (Safety factor 40.7)
Maximum deflection during lifting of empty inner tank	0.102 mm
Maximum stress during lifting of empty outer tank	2.59 Mpa (Safety factor 45.5)
Maximum deflection during lifting of empty outer tank	0.14 mm

Table V.6.4. SAV-1 Material Properties

Property	Bulk Material	Heat Affected Zone
Density (kg/m^3)	2,770	2,770
Elastic Modulus (MPa)	71,000	71,000
Poisson's Ratio	0.33	0.33
Ultimate Tensile Strength (MPa)	216	150
Yield Strength (MPa)	118	90

VI Fuel and Target Transfer Casks

VI.1 Introduction

At the end of a burnup cycle, depleted fuel assemblies, and possibly a used target, are discharged from the subcritical assembly to the storage pool. The depleted fuel assemblies contain fission and activation products, and high photon radiation would be generated due to the decay of these products. The discharged target, especially the uranium target, is also highly radioactive. Transport casks have been designed for moving spent fuel assemblies and used target assemblies between the subcritical assembly and the spent fuel storage pool, with adequate shielding material in the spent fuel cask to maintain the dose level outside the cask below 0.5 mrem/hr and adequate shielding of the target cask to limit the dose level in the subcritical assembly hall to less than 0.5 mrem/hr up to 3 m. above floor level.

Sec. VI.2 presents the ORIGEN-2 and MCNPX analyses of the photon dose around each cask. In the case of the fuel transfer cask, the cask was assumed to contain the hottest fuel assembly. The assembly had been irradiated continuously for one full year and then cooled for thirty days prior to being moved in the cask from the subcritical assembly to the storage pool. In the case of the target transfer cask, the uranium target was evaluated, since it produces additional photon radiation from fission product decay, as compared to the tungsten target.

Structural analyses of both cask designs have been performed and are presented in Sec. VI.3, with the conclusion that both cask designs will perform their function with satisfactory structural safety margins.

The mechanical designs of both casks are described in Sec. VI.4. Key design parameters are summarized in Sec. VI.5.

VI.2 Physics Analysis and Design

Coupled MCNPX/ORIGEN-2 simulations were used to determine the photon source for the spent fuel assemblies. These calculations were performed for the used uranium target because it produces higher photon flux levels than the used tungsten target. The fission power of the hottest fuel assembly was calculated in MCNPX [VI.2.1] and used for ORIGEN-2 [VI.2.2] to calculate the photon source. The fuel was assumed to have been burned in the subcritical assembly for one full-power year. The fuel was then cooled for thirty days prior to being discharged. The photon source for this fuel assembly was calculated with ORIGEN-2 using 18 energy groups.

Following the used target discharge from the system, it will generate significant amount of photons from the decay of activation products. In the case of the uranium target, there will be additional photons from the decay of fission products that are not present in the tungsten target. Therefore, the uranium target is the limiting case for designing a target transport cask. The photon source for the uranium target was obtained using the same assumptions and analysis approach as for the hottest fuel assembly.

The ORIGEN-2 results found that the total photon source intensity of the hottest fuel assembly is 5.77 × 10^{13} photons/second, and the total photon source intensity of the uranium target is 6.35 × 10^{13} photons/second. These photon sources were used in the shield design of the discharged fuel and target casks. The objective of the cask shield design was to limit the photon dose at any point outside the cask to less than 0.5 mrem/hr, as required by Ukraine regulations.

For the shield design of the fuel transport cask, MCNPX was used to calculate the photon dose over nine surfaces around the cask, using the photon source provided by the MCNPX/ORIGEN-2 coupled calculation as stated above. The final geometry chosen for the cask is illustrated in Fig. VI.2.1, as well as the nine locations where the photon doses were calculated. Lead with stainless steel clad was selected as the shield material for the cask. The cask, which has a total weight of 3,654 kg, has a cylindrical configuration, with both the top and bottom cut to form a chopped cone to save weight. The stainless-steel cladding, shown in red in Fig. VI.2.1, it has a thickness of 1.0 cm. In Fig.VI.2.1 lead is shown in yellow, and air is shown in green. The cask is described in more detail in Sec. VI.4.1.

The calculated photon dose rates outside of the cask are given in Table VI.2.1 for the nine tally surface locations. The doses are given with their statistical uncertainties from the Monte Carlo simulations. The photon doses listed in Table VI.2.1 are well below the 0.5 mrem/hr limit for all the surfaces. The calculated dose was less than half of the allowable limit. Fig. VI.2.2 plots the calculated photon dose profile in the right half of the fuel cask shield.

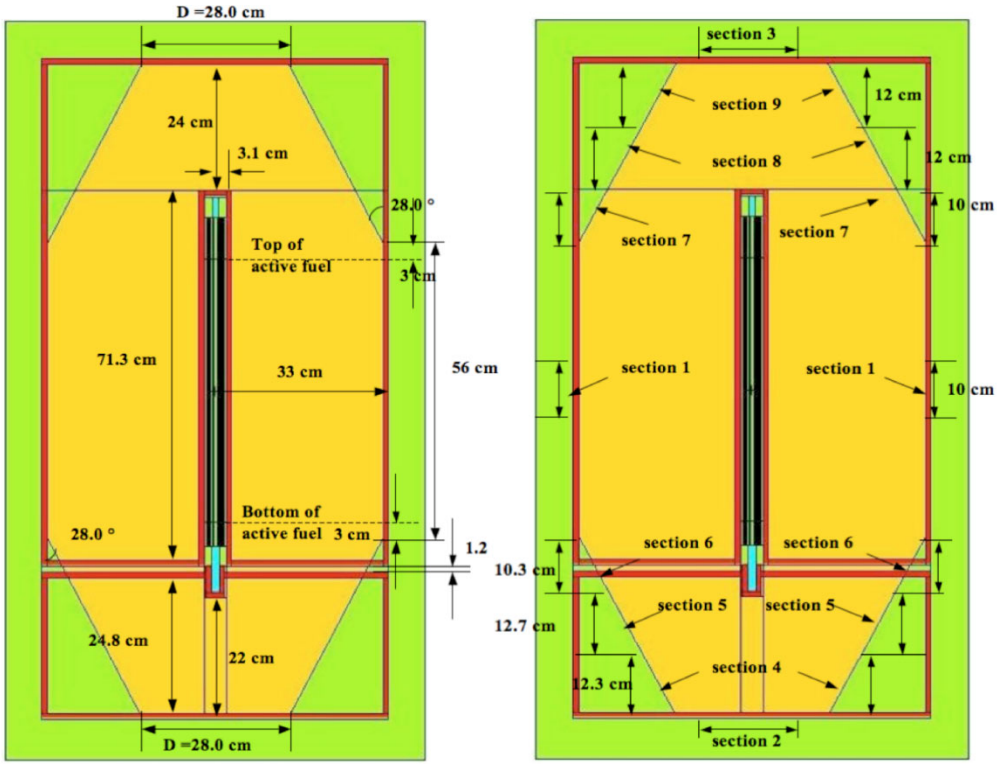

Figure VI.2.1. Geometry of the fuel discharge cask shield (left) and locations of the photon dose tally surfaces at the shield boundaries (right)

Table VI.2.1. Photon dose outside the cask shield from discharged fuel assembly

Tally location	Area (cm^2)	Photon dose (mrem/hr)
Section 1	2,104.87	0.219±5.46 %
Section 2	314.16	0.154±9.66 %
Section 3	314.16	0.144±0.63 %
Section 4	1,316.32	0.033±11.19 %
Section 5	1,721.16	0.210±8.05 %
Section 6	1,893.72	0.229±8.33 %
Section 7	1,843.58	0.141±0.38 %
Section 8	1,771.30	0.123±0.41 %
Section 9	1,290.22	0.025±1.17 %

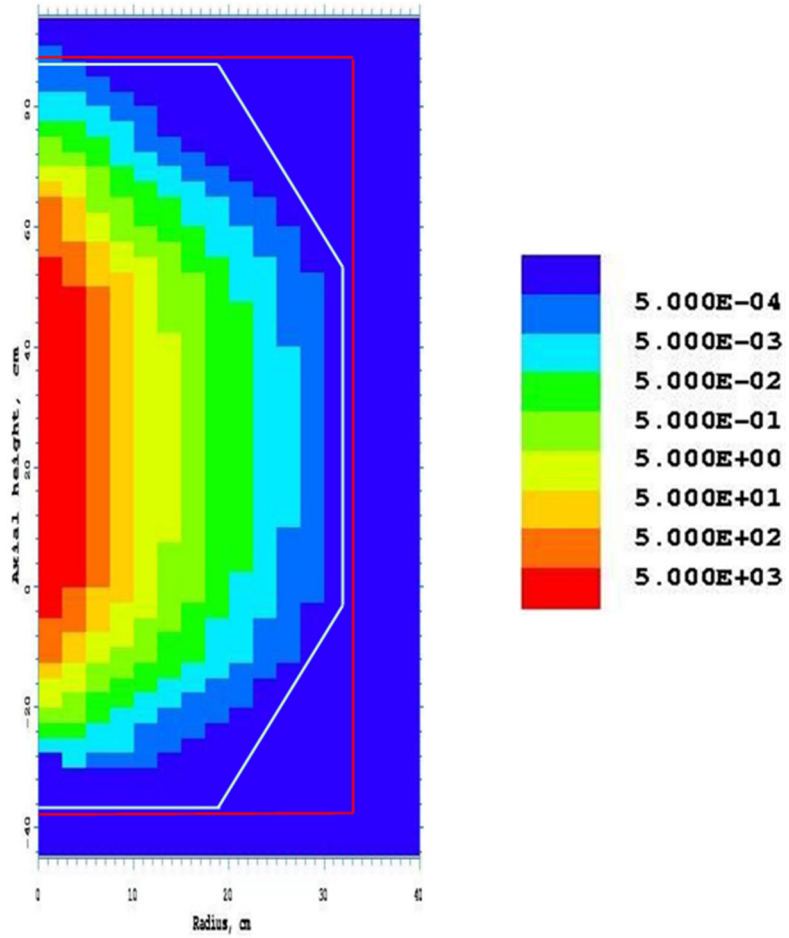

Figure VI.2.2. Photon dose (rem/hr) profile from discharged fuel assembly, which is loaded in the fuel discharge cask

A similar shielding analysis was performed for the target transport cask to size the required shield thickness during the used target transport from the subcritical assembly to the storage pool, based on the used uranium target. The photon dose was calculated at

eleven surfaces using MCNPX, and these results are given in Table VI.2.2. The geometry of the target cask and the location of the eleven tallying surfaces are presented in Fig. VI.2.3. Lead is indicated by red color, 1.0 cm thick stainless steel clad by blue color, and air by yellow color in the figure. The target cask shield has a shape like that of the fuel cask except for a 70 cm extension at the top to accommodate the electron beam tube. The total weight of the cask is 4,615 kg. The cask is described in more detail in Sec. VI.4.2. Photon doses have been tallied on the outer boundary of the shield, at eleven different locations, as shown in Fig. VI.2.3 and listed in Table VI.2.2. All tallying surfaces achieved photon doses less than the limit of 0.5 mrem/hr. Section 11, which is along the thin beam tube extension, experienced the largest dose of any surface, 0.191 mrem/hr, which is less than half of the limit. Many of the surfaces have photon doses approximately an order of magnitude lower than the limit.

Due to the long length of the beam tube (about 2.3 m) and the height limit of the facility building, the extension shield for the beam tube is only 70 cm. Part of the beam tube extends out of the cask, so the top of cask must be open. The photon leakage through this opening in the cask would cause the photon radiation dose to exceed 0.5 mrem/hr within the upper region of the subcritical assembly hall. To reduce the photon leakage from the top opening in the cask shield, a partial cover made of stainless steel with a thickness of 7.5 cm is used to fill the space between the beam tube and the cask shield, as shown in Fig. VI.2.3. The photon radiation above the cask could be further reduced by filling the beam tube (as well as the target coolant channels) with water if it is needed. The photon dose profile within the room has been calculated and it is shown in Fig. VI.2.4 for the cask design with a top partial cover and the beam tube filled with water, assuming the distance from the bottom of the cask to the roof is about 9.3 m and the roof thickness is 30 cm. To show the impact of the partial cover and having water in the tube, the photon dose profiles for the cases with and without the partial cover and with the beam tube voided have also been calculated and are plotted in Fig. VI.2.5. Comparing the photon dose profiles in Figs. VI.2.4 and VI.2.5, the top partial cover and having the beam tube filled with water can reduce the photon dose within the room significantly.

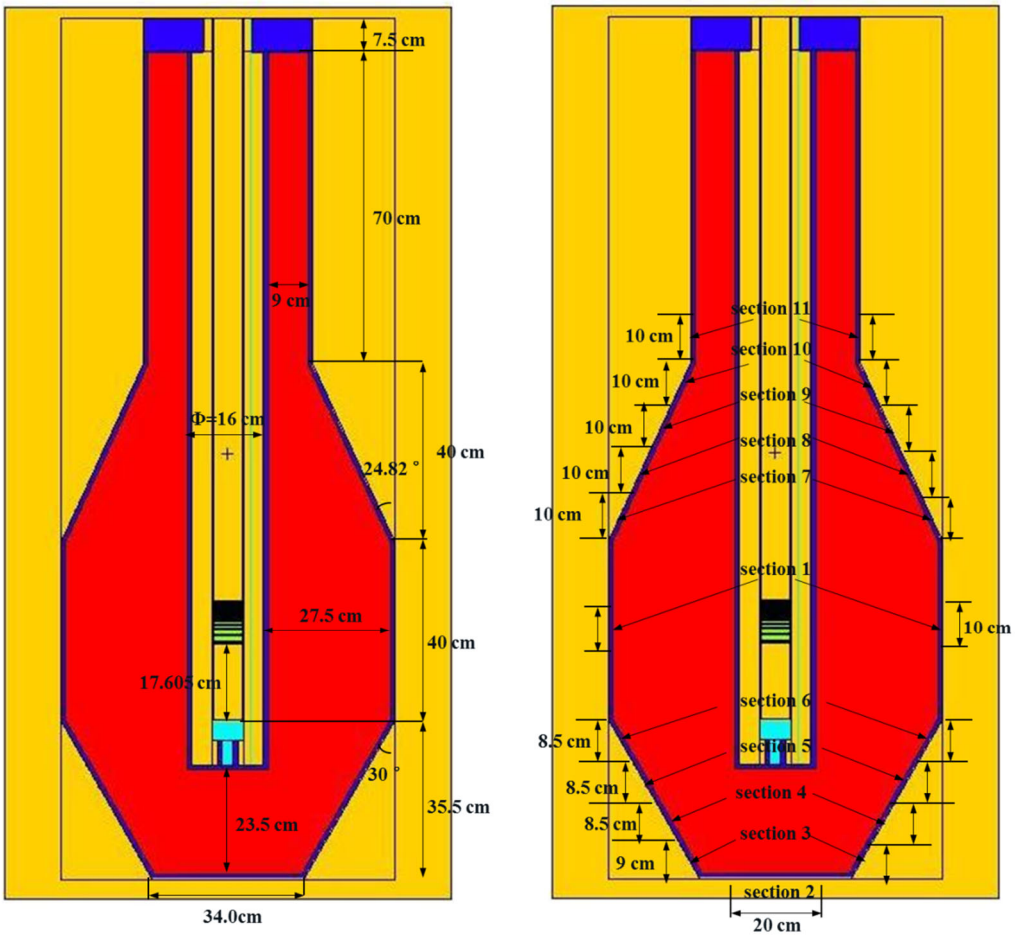

Figure VI.2.3. Geometry of the target cask shield (left) and the locations of the photon dose surfaces (right)

Table VI.2.2. Photon dose outside the cask shield for discharged uranium target

Tally location	Tally area (cm^2)	Photon dose (mrem/hr)
Section 1	2387.61	0.158 (± 4.45 %)
Section 2	314.16	0.152 (± 8.83 %)
Section 3	1108.48	0.069 (± 2.28 %)
Section 4	1488.83	0.042 (± 2.27 %)
Section 5	1609.62	0.028 (± 2.44 %)
Section 6	1871.72	0.022 (± 2.71 %)
Section 7	2210.90	0.071 (± 1.63 %)
Section 8	1920.30	0.067 (± 1.58 %)
Section 9	1629.70	0.055 (± 1.86 %)
Section 10	1339.10	0.126 (± 2.66 %)
Section 11	1193.80	0.191 (± 9.65 %)

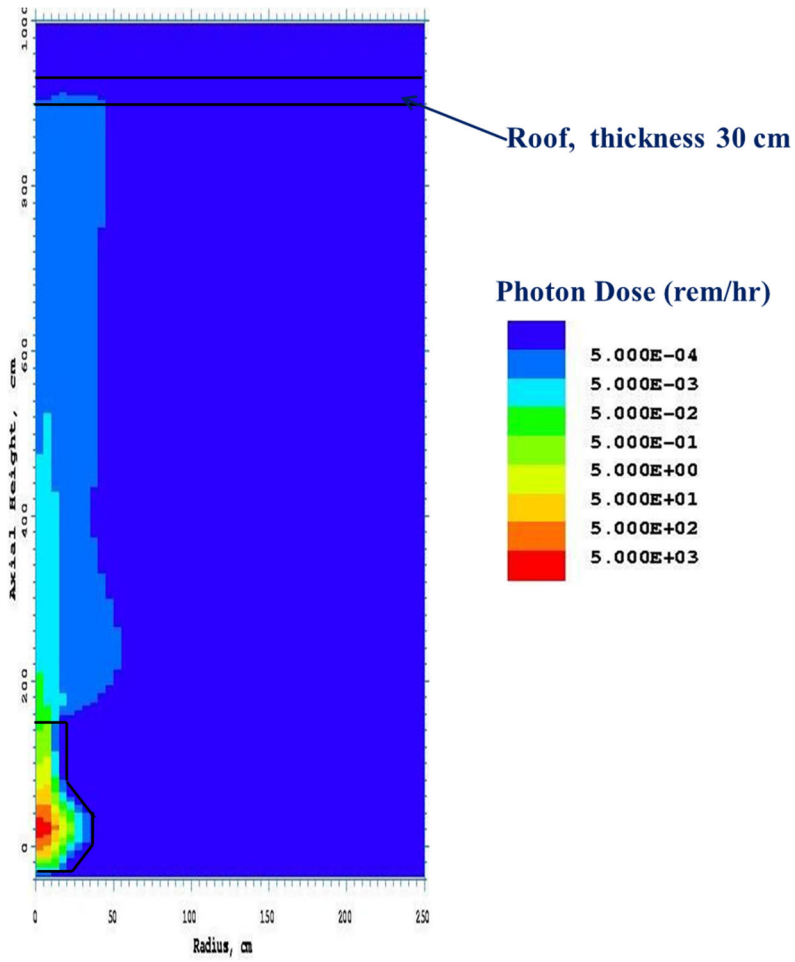

Figure VI.2.4. Photon dose profile (unit rem/hr) within the room, for the target cask shield with top partial cover and the beam tube filled with water

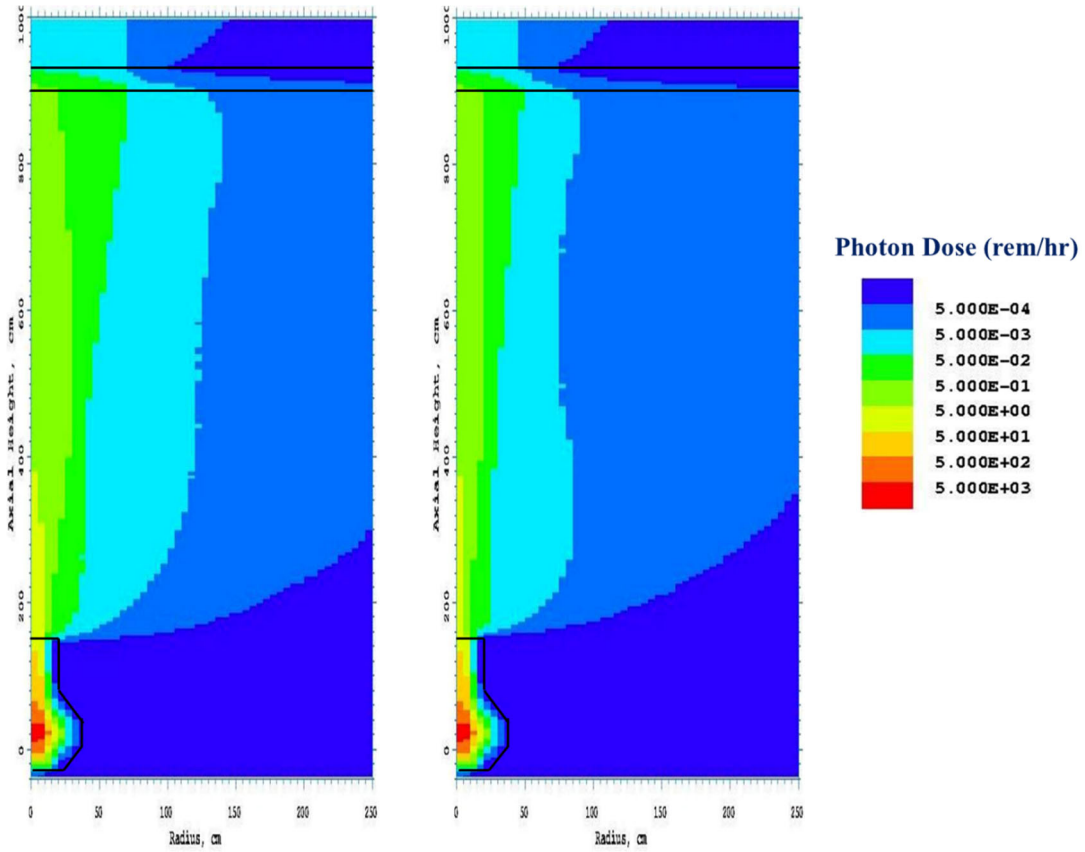

Figure VI.2.5. Photon dose profile (unit rem/hr) within the room, for the target cask shield without (left) and with (right) top partial cover, and voided beam tube

Based on the results shown in Fig.VI.2.5, the 0.5 mrem/hr contour line expands into a large volume within the subcritical assembly hall if the beam tube is not filled with water, even when a partial cover is not used on top of the cask. However, before the process of loading the target assembly into the shield cask begins, all personnel will be cleared from the upper region of the SCA hall and will remain on the floor level or outside the hall until the target has been secured within the spent fuel/target pool. The gamma dose in the hall is below 0.5 mrem/hr up to a height of over 3 m. above the floor, as shown in Fig.VI.2.5, so personnel at the floor level when the transfer is taking place will receive a dose level less than 0.5 mrem/hr. No personnel will be on the roof above the room when the transfer is taking place. Therefore, it was determined that a partial cover next to the beam tube at the top of the cask is more than sufficient to protect personnel and that the additional complexity of incorporating equipment to fill the beam tube with water before making the transfer is unnecessary.

References

VI.2.1. Pelowitz, Denise B. (Ed.), “MCNPX User’s Manual”, Los Alamos National Laboratory Report, LA-CP-05-0369, April 2005.

VI.2.2. Croff, A. G., “A User’s Manual for the ORIGEN-2 Computer Code”, ORNL /TM-7157, Oct. 1980.

VI.3 Structural Analysis and Design

VI.3.1 Objective

The objective of this analysis was to perform a structural analysis study on the design of the fuel and target transfer casks for the KIPT ADS experimental neutron source facility.

VI.3.2 Scope

The scope of this analysis is limited to simulation of static loading on fuel and target transfer casks which are used to facilitate changing of the target and the fuel assemblies. This analysis was conducted to examine the structural feasibility of these cask designs.

VI.3.3 Methodology

This analysis was carried out with the finite element method, using the Ansys R13.0 finite element program [Ref. VI.3.1]. A finite element model was constructed and subjected to estimated loads developed during the design process. There were no design standards specified for this analysis that could be used to define acceptance criteria except that a minimum safety factor of four was desired by the designers. Results were compared to the basic material properties and the commonly accepted engineering principles were applied to determine a safety factor.

VI.3.4 Analysis Overview

Two transfer cask assemblies were subjected to analysis. Each cask was subjected to finite element analysis where linear elastic models were statically loaded to determine stress levels. Stresses at the lifting points were beyond the elastic limit, so the lifting points were further evaluated with closed-form methods to determine suitability.

VI.3.5 Assumptions

This analysis is based on the following assumptions:

1. The material response is linear elastic.
2. The material response is constant with time (no effects of aging, creep, etc.).
3. The materials are isotropic and homogeneous.
4. The material response is consistent with small strain and small displacement.
5. The effects of irradiation on the material properties are not included.
6. The residual stresses are not included.
7. The grid plate operates at room temperature.
8. The loading is static, and it is assumed that the speed of the crane is low enough so that dynamic effects are negligible.
9.

VI.3.6 Geometry

The finite element model of the target cask was based on solid modeling geometry. The design file containing the specifications for this cask was imported into ANSYS Design Modeler, where a model was created as shown in Fig. VI.3.6.1. This model was then meshed with 109,783 6-node triangular and 10-node xixvelihvep$ipiq irxw. The finite element model is shown in Fig. VI.3.6.2. The model of the fuel cask was based on solid

modeling geometry. The design file containing the specifications for this geometry was imported into Ansys Design Modeler, where a model was created as shown in Fig. VI.3.6.3. This model was then taken into the Workbench module and meshed with 109,783 6-node triangular and 10-node tetrahedral elements. The finite element model is shown in Fig. VI.3.6.4.

VI.3.7 Materials

The Material was specified as stainless steel, with no exact grade specified. Fabrication of the casks is by welding of plate material, so type 304L was chosen for its weldability. Mechanical properties for 304L as used for this analysis are shown in Table VI.3.7.1.

Table VI.3.7.1. Material Properties for 304L Stainless Steel

Property	Value	Source
Elastic Modulus (MPa)	200,000	Ref. VI.3.3
Ultimate Tensile Strength (MPa)	485	Ref. VI.3.2
Yield Strength (MPa)	170	Ref. VI.3.2
Poisson's Ratio	0.27	Ref. VI.3.3
Density (kg/m^3)	7,930	Ref. VI.3.3

The fuel cask was loaded by hanging it from its lifting holes and applying gravity. To accomplish this, the holes in the lifting flanges were filled with shell elements, and beam elements were added to represent the lifting chain. The chain was connected to the cask with constraints to avoid transferring a bending moment to the cask. The top of the chain was fixed in space. This is shown in Fig. VI.3.8.2. Forces were added to account for the weight of the upper and lower sliding gates, as shown in Fig. VI.3.8.3.

VI.3.8 Loads and Boundary Conditions

The target cask was loaded by hanging it from the hole in the lifting bail and applying gravity. A narrow strip at the top of the hole was fixed in space, and forces were added to account for the weight of the upper pivoting gates and the lower sliding gate. These loads are shown in Fig. VI.3.8.1.

VI.3.9 Results

VI.3.9.1 Target Transfer Cask

Plots of von Mises stress are shown in Figs. VI.3.9.1.1 through VI.3.9.1.3. The maximum stress is at the lifting hole and is 997.6 MPa. This is well above the ultimate strength but is an artifact of the linear elastic material model. This material is very ductile, and localized yielding would reduce this value. The next highest stress is in the stiffening flange welded to the top of the handle and is 102.2 MPa, for a factor of safety with respect to yield of 1.67. The highest stress in the cask is 31.1 MPa, for a factor of safety of 5.47.

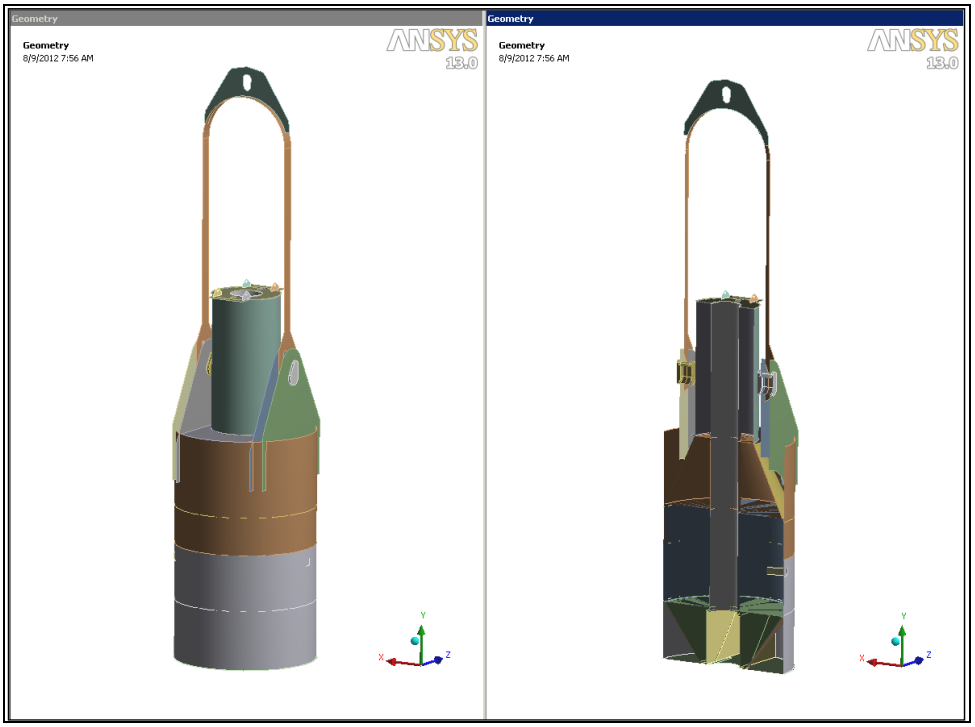

Figure VI.3.6.1. Solid model of the target cask

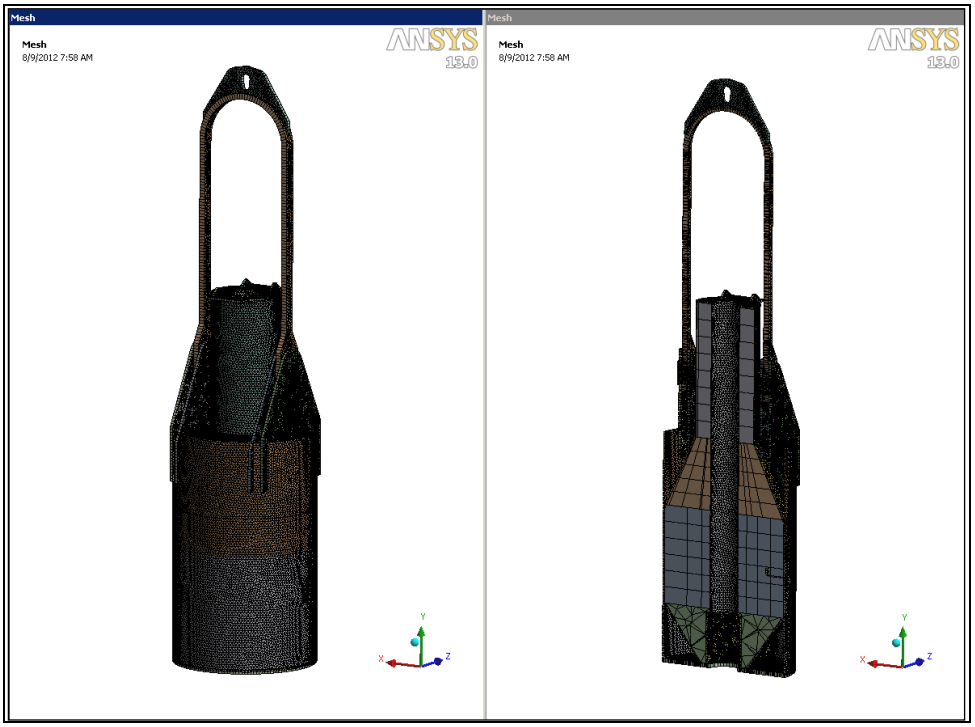

Figure VI.3.6.2. Finite element model of the target cask

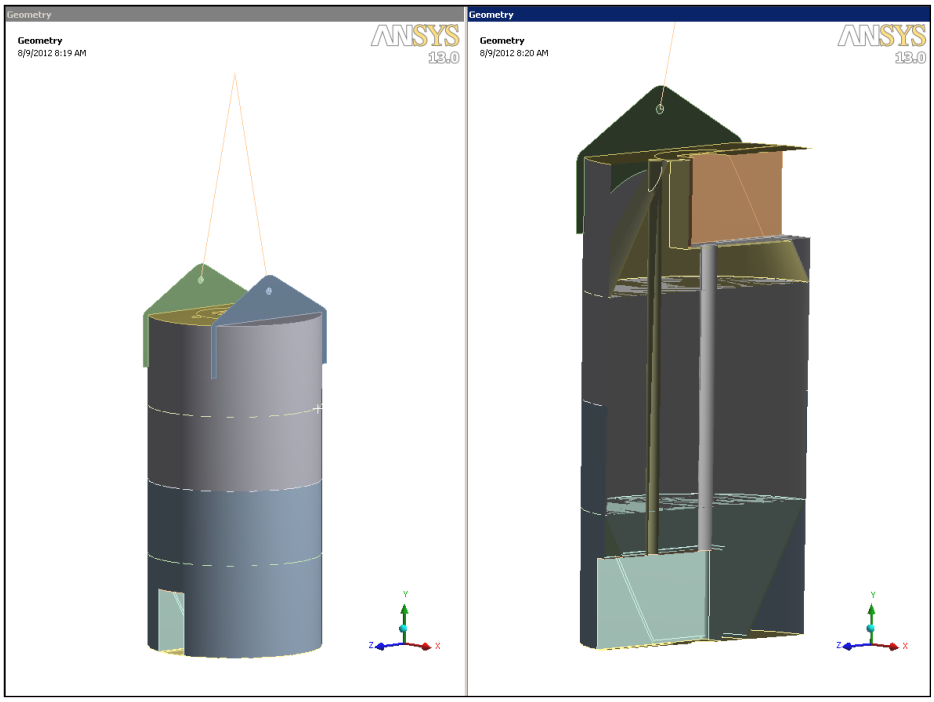

Figure VI.3.6.3. Solid model of the fuel transfer cask

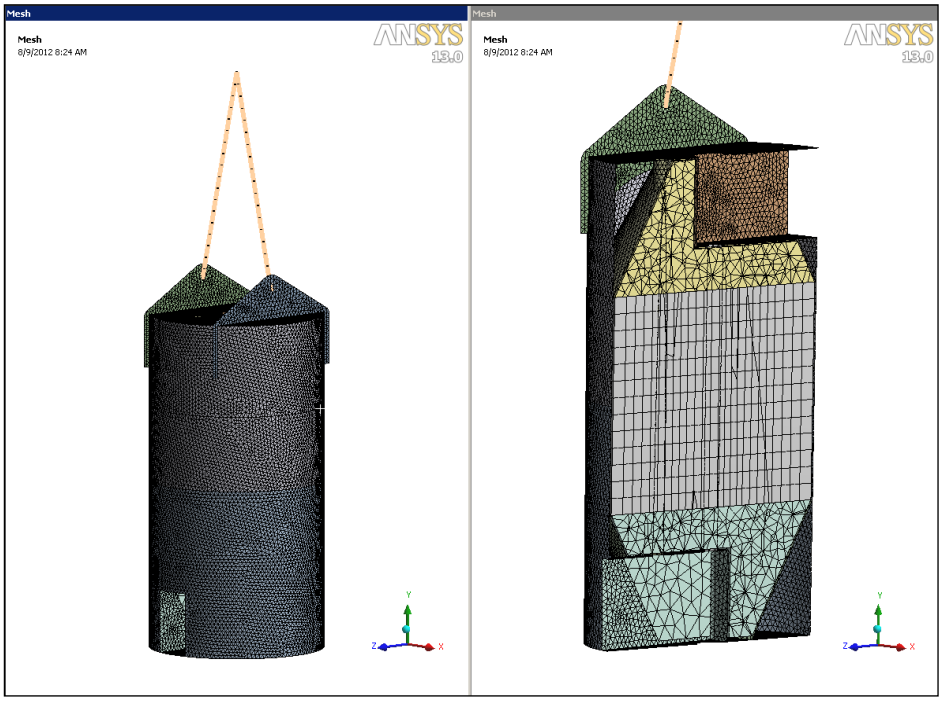

Figure VI.3.6.4. Finite element model of the fuel cask

At this point in the analysis, it was observed that the lifting handle would be difficult to fabricate due to the fitment of the stiffening flange to the curved top of the handle. An alternate design was proposed and is shown in Fig. VI.3.9.1.4. This design consists of a

horizontal yoke and a pair of vertical lifting straps. They are connected with welded mortise and tenon joints. The results for this configuration are shown in Figs. VI.3.9.1.5 and VI.3.9.1.6. The maximum stress is again at the lifting hole and is 321 MPa for a safety factor with respect to yield of only 0.53. This is down from the previous value, due to the thicker section (30 mm vs. 20 mm), and greater section depth (200 mm vs. 150 mm). The stress here is very localized, and it is again due to the linear elastic material model. The next highest stress is along the bottom of the yoke and is 30.74 MPa for a factor of safety of 5.55.

To determine if the high stress at the lifting hole is a problem, the hole was analyzed using the method described in section 3-3.3, “Pinned Connections”, of Ref. VI.3.4. Design Category A was assumed because the loads are predictable and environmental conditions are not severe. A spreadsheet was created using this method and the results are shown in Table VI.3.9.1.1. The factor of safety with respect to the allowable load is 2.0.

Figure VI.3.8.1. The target cask loads and the boundary conditions

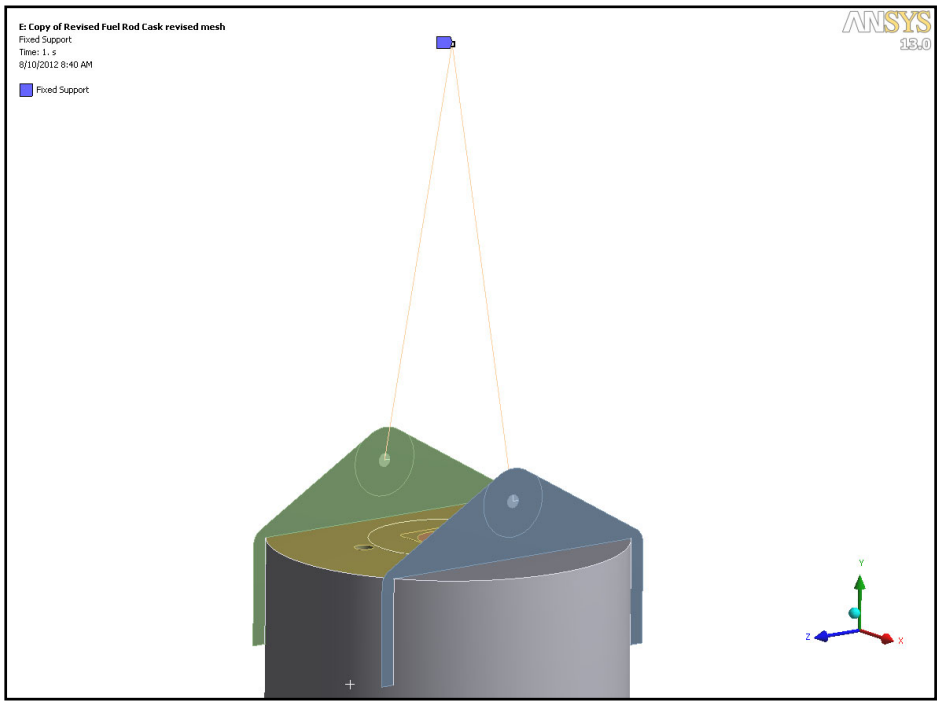

Figure VI.3.8.2. The boundary conditions for the fuel cask

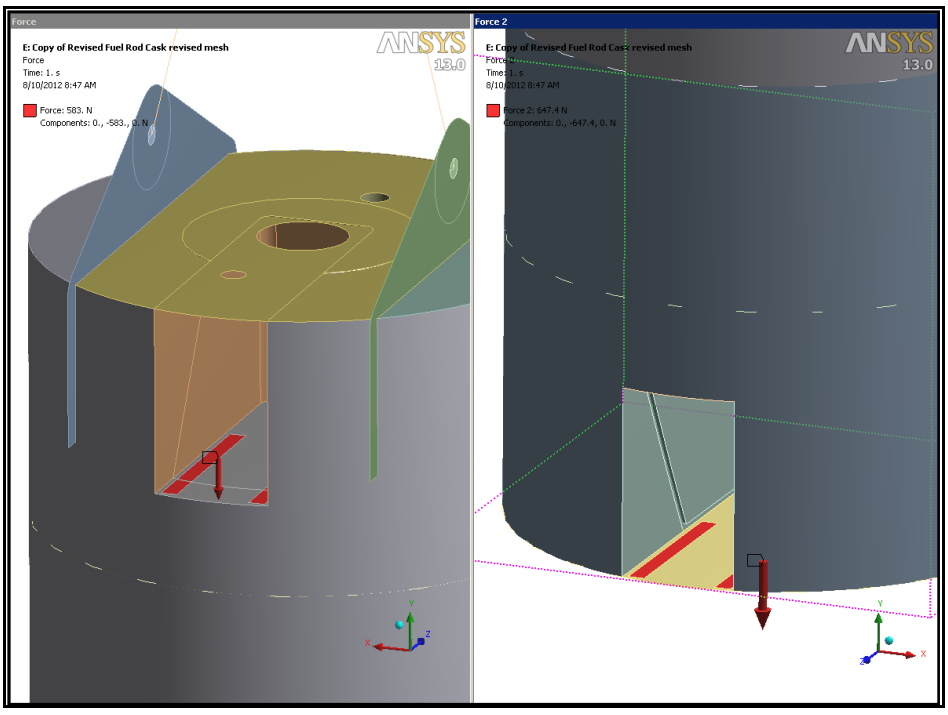

Figure VI.3.8.3. The gate loads on the fuel cask

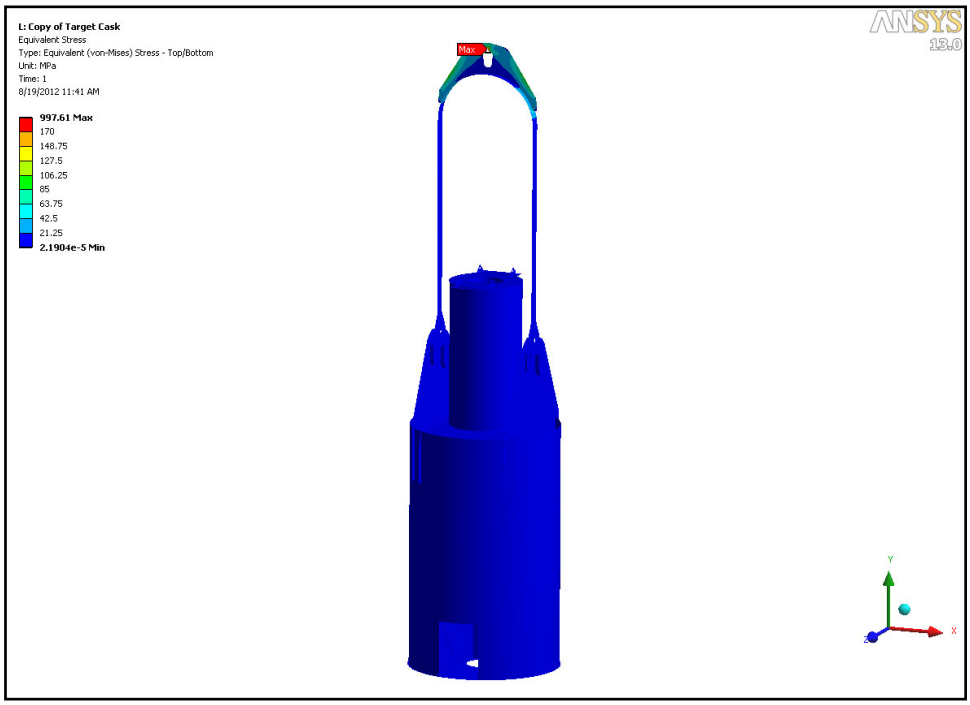

Figure VI.3.9.1.1. Von Mises stress in the target cask assembly

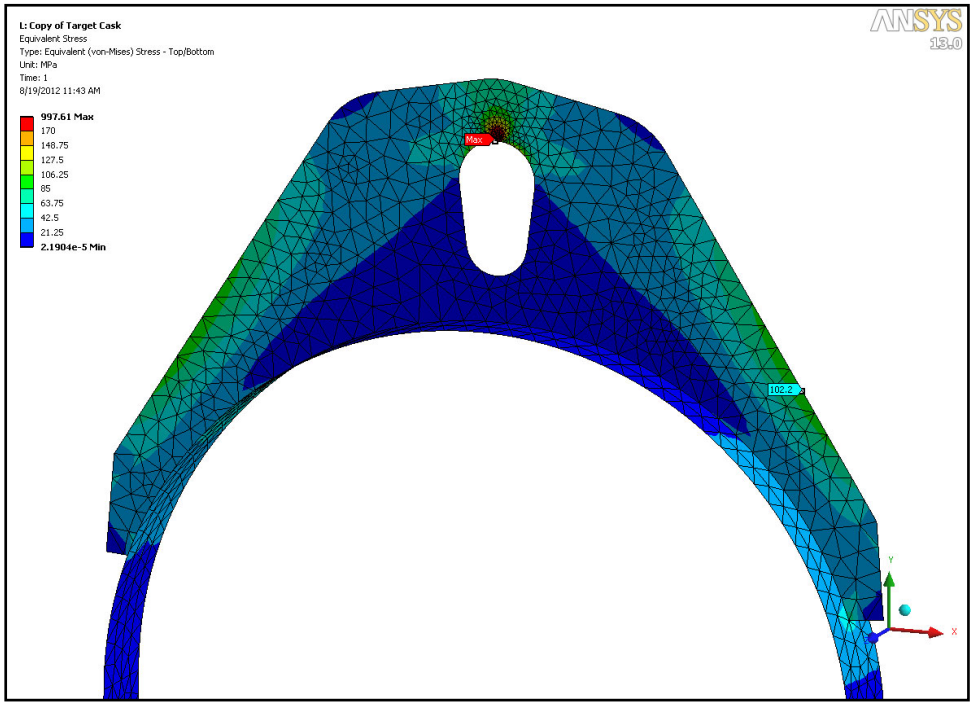

Figure VI.3.9.1.2. Von Mises stress in the target cask lifting handle

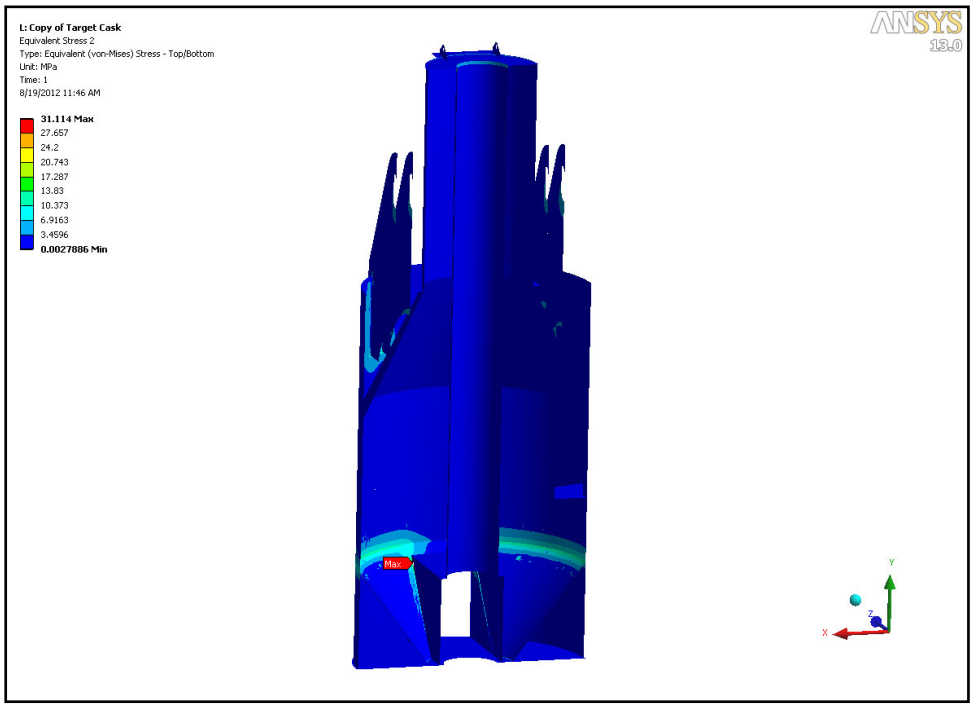

Figure VI.3.9.1.3. Von Mises stress in the target cask

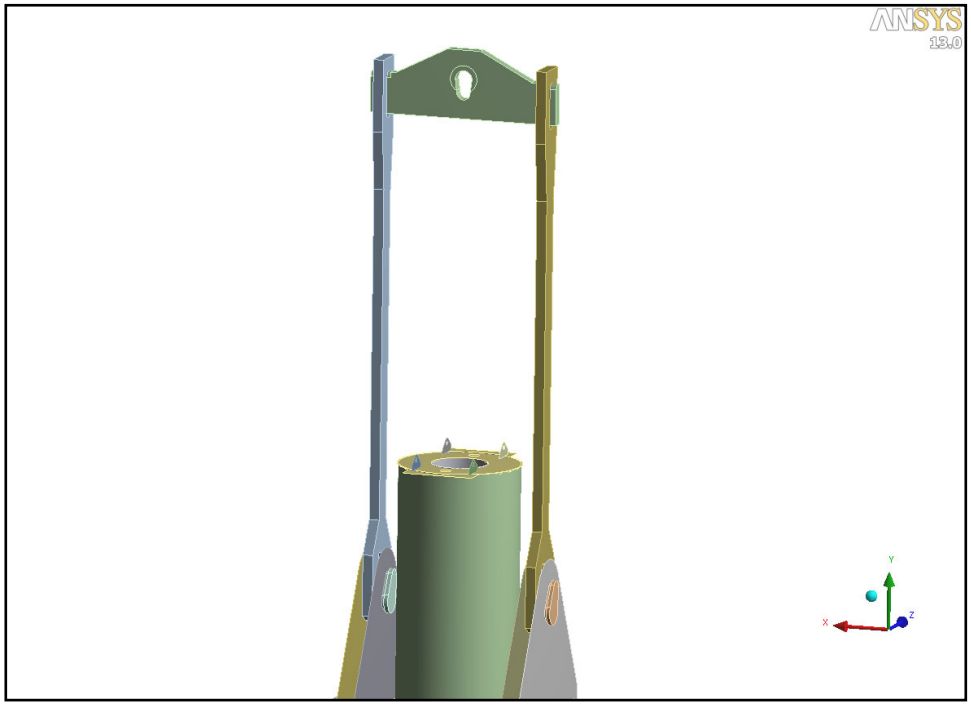

Figure VI.3.9.1.4. Alternate design for the lifting handle

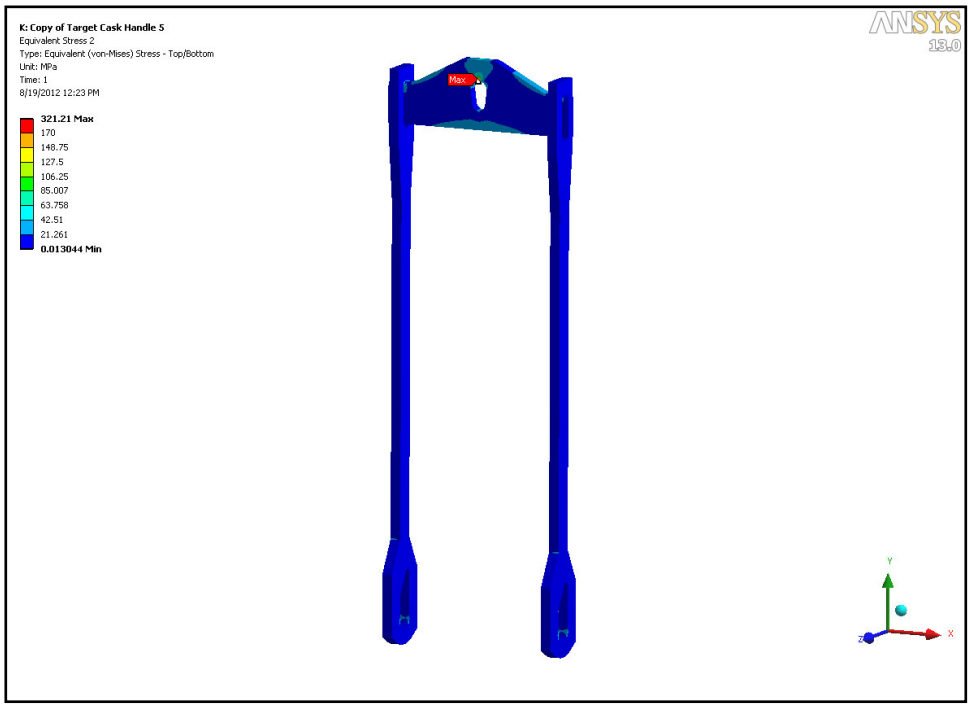

Figure VI.3.9.1.5. Von Mises stress in the revised lifting handle

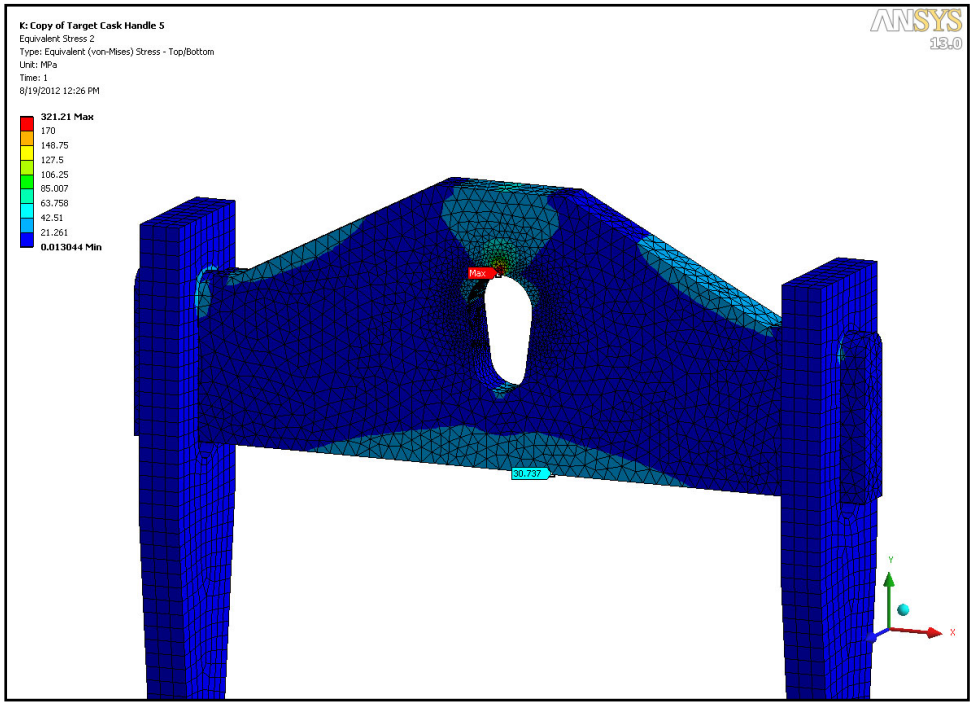

Figure VI.3.9.1.6. Von Mises stress in the yoke

Table VI.3.9.1.1. Pinned connection calculation for the yoke lifting hole

	pi	3.141593		
Ultimate Strength	Fu	485	MPa	
Yield Strength	FY	170	MPa	
Design Factor	Nd	2		3-1.3
Pin Dimeter	Dp	40	mm	
Hole Diameter	Dh	50	mm	
Overall Width	OW	410	mm	
Thickness	t	30	mm	
Distance to Top of Yoke	R	85	mm	
Net Width Adjacent to Pin	be	180	mm	
Net Thickness Above Pin	a	60	mm	Page 25
	be1	180	mm	
	be2	120	mm	3-47
	be3	162.3923	mm	3-48
Effective Width	beff	120	mm	Page 25
Strength Reduction Factor	Cr	0.835		3-46
Contact Angle	phi	0.44	radian	3-52
Double Shear Plane Area	Av	3600.035	mm^2	3-51
Tensile Strength Through the Pinhole	Pt	1214925	N	3-45
Single Plane Fracture Beyond Pinhole	Pb	525455.1	N	3-49
Double Plane Shear Strength	Pv	509255	N	3-50
Bearing Stress	Pp	127500	N	3-53
Allowable Load	Pa	127500	N	
Actual Load	p	63847	N	
Safety Factor	SFp	2.00		

VI.3.9.2 The Fuel Transfer Cask

Plots of von Mises stress for the fuel cask are shown in Figs. VI.3.9.2.1 through VI.3.9.2.3. The maximum stress occurs at the intersection of the top and the lifting flange, and it is 37.7 MPa, for a factor of safety with respect to yield of 4.51. The next highest stress is at a lifting hole, and it is 37.2 MPa. This is very low compared to the value seen with the target cask and is likely due to the elements added to connect the chain elements. These elements had the effect of filling the hole, and a more exact analysis is needed. A finite element model was created of the lifting flange and a typical lifting clevis, as shown in Fig. VI.3.9.2.4. A frictionless contact was used between the pin and the hole, and an elastic-linear plastic material was used in the area around the hole. A plot of von Mises Stress in the lifting flange is shown in Fig. VI.3.9.2.5, and the maximum stress is 179.6 MPa, which is above yield. As before, this is localized, and it is not a problem. As a check, the hole was analyzed using the method given in Ref. VI.3.4. The results are shown in Table VI.3.9.2.1. The factor of safety with respect to the total weight of 18,402 N is 2.77.

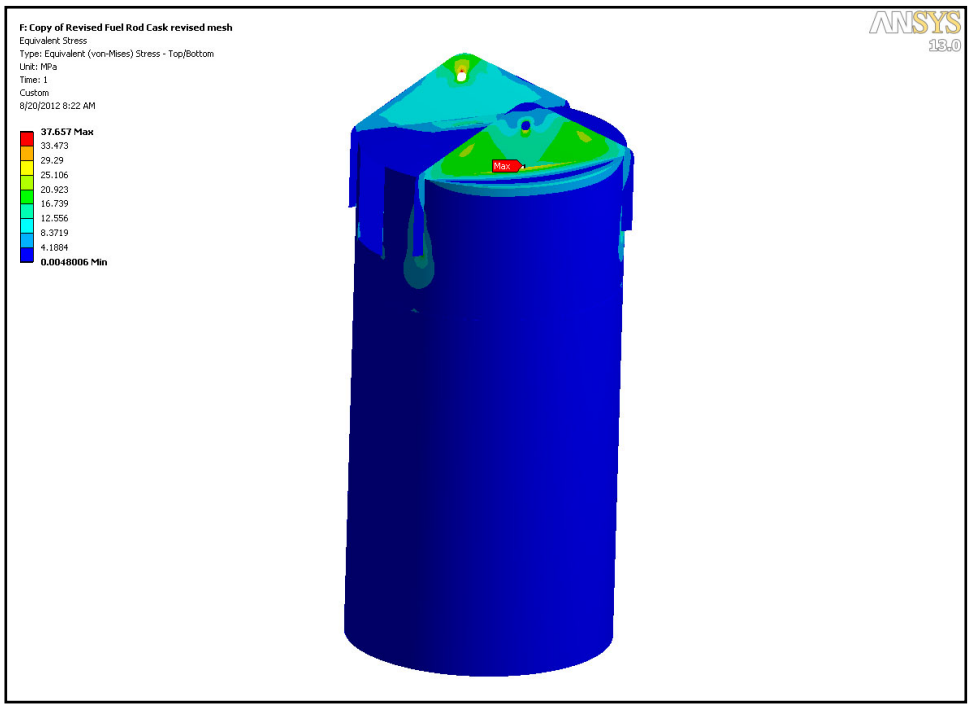

Figure VI.3.9.2.1. Von Mises stress in the fuel cask

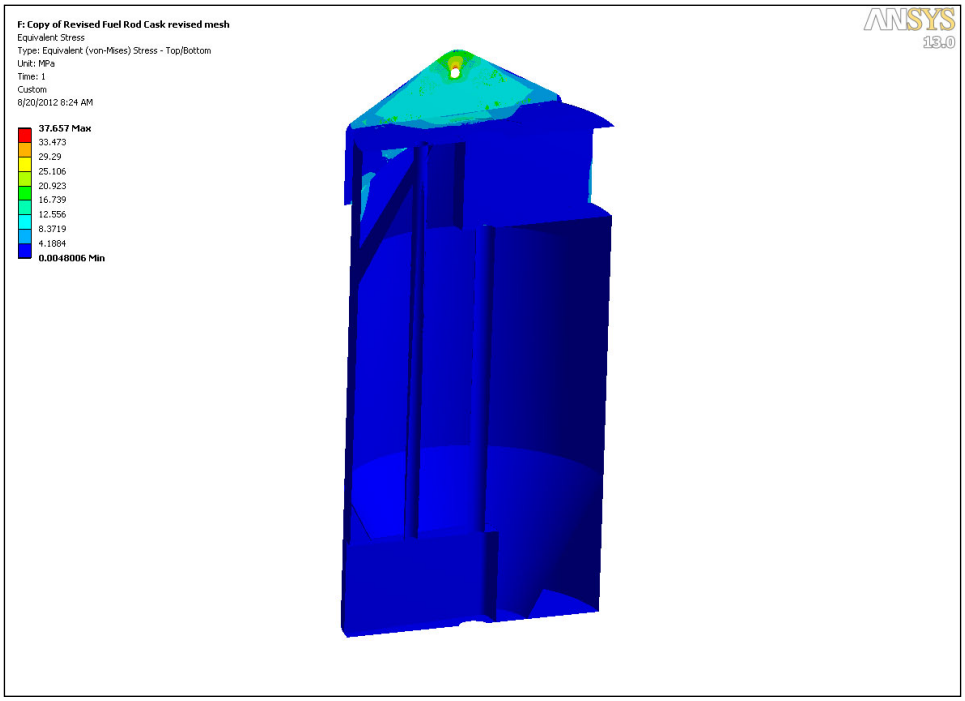

Figure VI.3.9.2.2. Von Mises stress in the fuel cask, an interior view

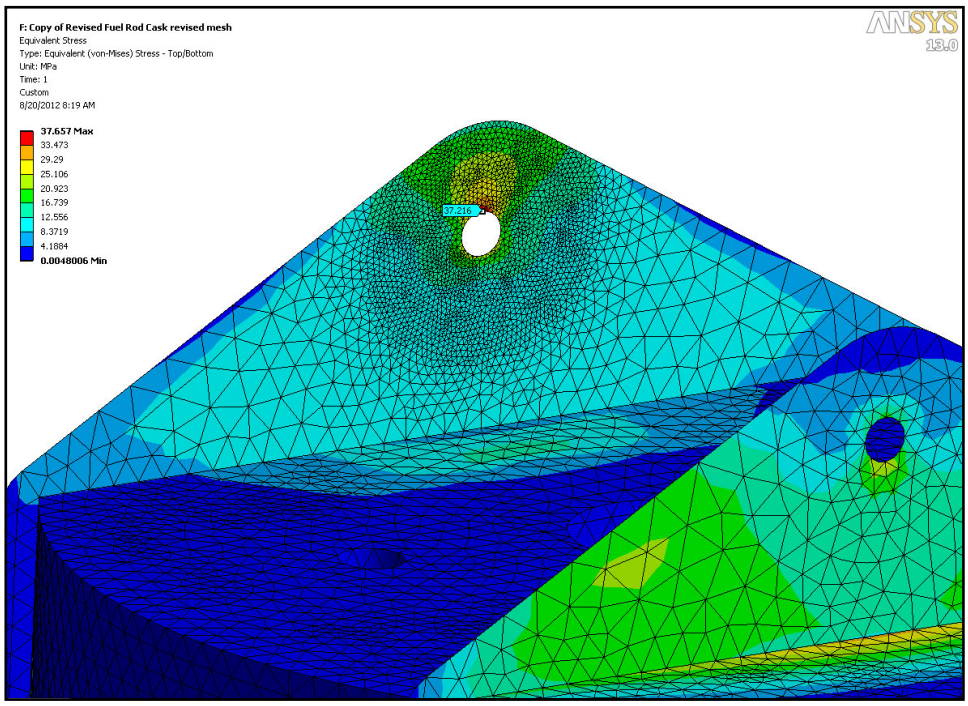

Figure VI.3.9.2.3. Von Mises stress at the lifting hole

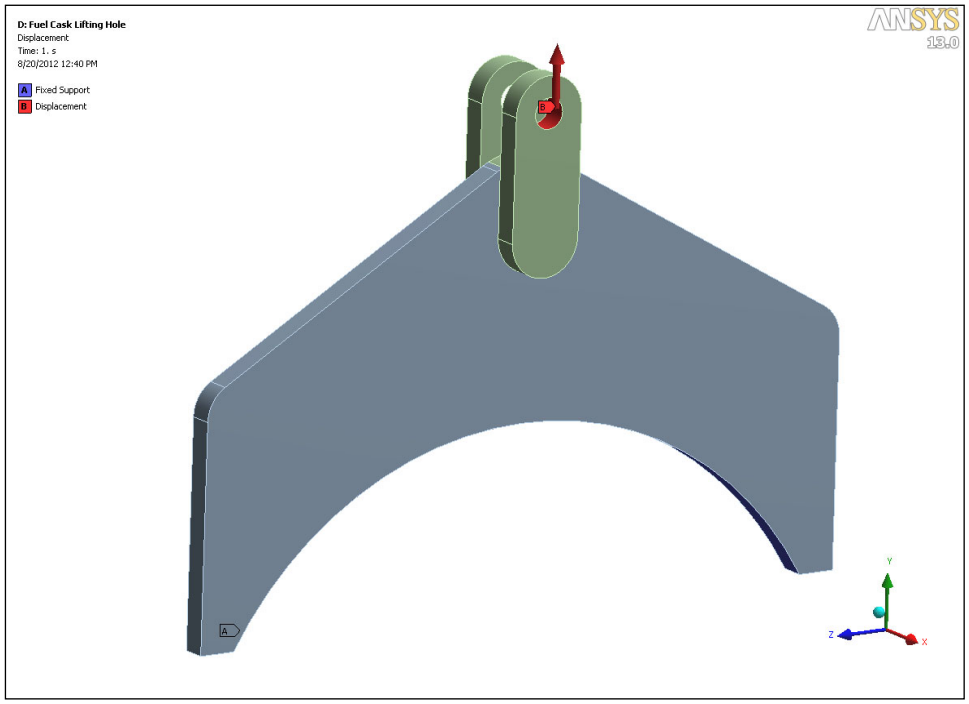

Figure VI.3.9.2.4. The lifting flange model

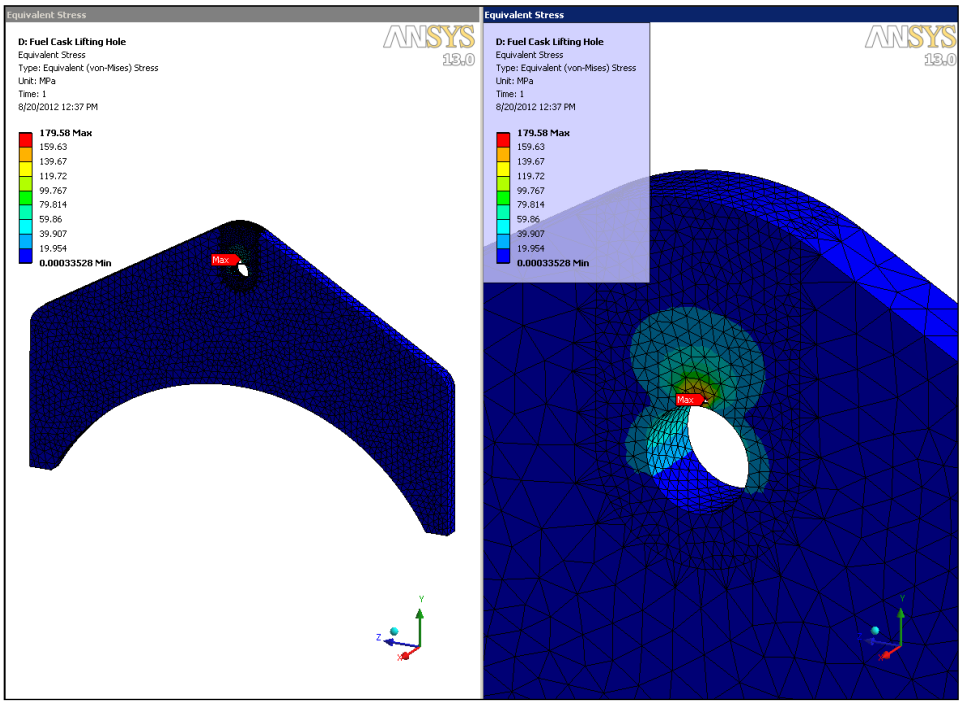

Figure VI.3.9.2.5. Von Mises stress at the lifting hole

VI.3.10 Discussion

This analysis was carried out on a conceptual design. Load cases were simplistic and did not include seismic loading, temperature loading, etc. No standards were specified for the design of the transfer casks, so none could be used for evaluation.

Generally accepted engineering principles were used to evaluate the feasibility of the grid plate. Yielding was evaluated by comparing the von Mises stress as defined by the maximum distortion energy failure theory directly to the yield strength of the material. No knockdown factors for boundary condition uncertainty, material variability, surface finish, construction variations, etc. were applied.

Material was not specified, so the analysis was based on 304L stainless steel. This material was chosen for its weldability. No weld schedule was available, so a weld analysis was not performed.

The desired safety factor of 4.0 can be applied when von Mises stresses are compared directly to the yield strength. This accounts for things like variability in material properties, idealized boundary conditions, manufacturing uncertainties, etc. In general, stresses are very low, and safety factors are generally over 4.0. The exception is at the lifting holes, where contact stresses resulted in localized high stress. At these locations, the method described in Ref. VI.3.4 was used to determine an acceptable load. This method accounts for these variabilities and uncertainties by choosing conservative calculation methods, and

with appropriate knock-down factors, so a factor of safety of 1.0 is considered sufficient. The reported safety factors at the lifting holes of 2.0 and 2.77 indicate a healthy safety margin.

The original design for the lifting handle on the target cask is not recommended. It appears difficult to make and its strength is dependent on a weld on a curved surface, where fitment of components is problematic. The revised design shown in Fig. VI.3.9.1.4 should be easier to fabricate, and its strength is not dependent on weld integrity. A STEP file of this geometry was forwarded to the designers for incorporation in the assembly at the fabrication time.

The assumptions listed above are reasonable and prudent for the analysis of the conceptual design. Von Mises stresses are generally low, so the use of a linear elastic isotropic homogeneous material model is justified. Where high stresses were reported at the lifting holes, an alternate method of analysis was used to determine feasibility. Deflections are small, so small deflection theory is appropriate. The other assumptions generally fit within the context of this analysis. Within the limits of these assumptions, and the assumption of 304L stainless steel, it is believed that this analysis accurately represents the performance of this design for the intended use.

VI.3.11 Conclusions

Based on the results of this analysis, and subject to the listed assumptions, it is concluded that the target transfer cask with the modified lifting handle, shown in Fig. VI.3.9.1.4, and the fuel transfer cask are structurally feasible designs.

References

VI.3.1. Ansys Mechanical, Version 13.0, Build date 11/2/2009, Ansys Inc, Pittsburg, PA.
VI.3.2. Technical Data Blue Sheet, Stainless Steels, Chromium-Nickel, Types 302, 304, 304L, 305, Allegheny Ludlum Corporation, Pittsburg, PA, 2009.
VI.3.3. Metallic Materials Properties Development and Standardization, DOT/FAA/AR-MMPDS-01, Office of Aviation Research, Washington DC, 2003.
VI.3.4. ASME BTH-1-2008, Design of Below the Hook Lifting Devices, American Society of Mechanical Engineers, New York, 2008.

Table VI.3.9.2.1 Pinned connection calculation for the lifting flange hole

	pi	3.141593		
Ultimate Strength	Fu	485	MPa	
Yield Strength	FY	170	MPa	
Design Factor	Nd	2		3-1.3
Pin Dimeter	Dp	24	mm	
Hole Diameter	Dh	25	mm	
Overall Width	OW	240	mm	
Thickness	t	20	mm	
Distance to Top of Yoke	R	60	mm	
Net Width Adjacent to Pin	be	107.5	mm	
Net Thickness Above Pin	a	47.5	mm	Page 25
	be1	107.5	mm	
	be2	80	mm	3-47
	be3	88.73977	mm	3-48
Effective Width	beff	80	mm	Page 25
Strength Reduction Factor	Cr	0.923		3-46
Contact Angle	phi	0.528	radian	3-52
Double Shear Plane Area	Av	1900.02	mm^2	3-51
Tensile Strength Through the Pinhole	Pt	596873.3	N	3-45
Single Plane Fracture Beyond Pinhole	Pb	269844.1	N	3-49
Double Plane Shear Strength	Pv	268773.7	N	3-50
Bearing Stress	Pp	51000	N	3-53
Allowable Load	Pa	51000	N	
Actual Load	p	18402	N	
Safety Factor	SFp	2.77		

VI.4 Mechanical Design

VI.4.1 Fuel Transfer Cask Mechanical Design

As part of the operation of the KIPT subcritical facility, spent fuel assemblies are moved from the subcritical assembly to the fuel storage pool. A fuel transfer cask is used for moving the spent fuel assemblies within the neutron source facility hall. The fuel transfer cask provides adequate radiological shielding to keep the external dose level below 0.5 mrem/hr, as discussed in Sec. VI.2. The fuel transfer cask is also used to transfer sample cassettes, beryllium reflector elements, and boron carbide absorber elements to/from the subcritical assembly.

The fuel transfer cask is fabricated of stainless-steel plates welded to form a strong, liquid-tight container, and then filled with molten lead. After the cask has been filled with lead, the lead access holes are welded to provide environmental containment of the lead. The fuel cask has a mass of 3,654 kg. A photograph of the fuel transfer cask is shown in Fig. VI.4.1.1.

The fuel transfer cask is lifted and moved by the overhead crane within the neutron source facility hall. A chain bridle is attached to the cask and interfaces with the lifting hook of the overhead crane. The chain bridle and attachment points have been physically tested to support 150% of the cask weight. The fuel transfer cask is not intended to leave the neutron source facility hall.

The fuel transfer cask is a bottom entry cask. Figure VI.4.1.2 diagrams how a fuel assembly is unloaded into the spent fuel pool through the cask bottom. Movable top and bottom gates allow access to the central cavity of the cask. Both gates are opened and closed by turning shafts that protrude through the top of the fuel cask. The shafts are turned with a handheld tool. The gates and actuation mechanisms are diagrammed in Figs. VI.4.1.3 through VI.4.1.5.

To load/unload the cask, a long slender dipstick with a gripper on the lower end is lowered through the cask to grip the fuel element and lift it into/lower it from the fuel transfer cask. The dipstick has four rotatable jaws that engage features in the fuel element to provide a robust and secure means of lifting the fuel element. The dipstick is composed of two concentric tubes. The outer tube provides structure and carries the load of the fuel assembly. The inner tube is free to rotate and translate axially relative to the outer tube. The rotation of the inner tube opens and closes the dog jaws to engage/release the fuel assembly. The inner tube translates axially when the dipstick interfaces with the fuel assembly, unlocking the dog jaws so that they are free to rotate, and tripping micro-switches at the top of the dipstick to indicate condition of fuel element engagement by lighting LEDs on the control pendant. Micro-switches also detect the rotation condition of the inner tube, thereby lighting LEDs on the control pendant to indicate dog jaw position. A step motor at the top of the dipstick rotates the inner tube to open and close the dog jaws, as commanded by a toggle switch on the control pendant. Two different length dipsticks are needed because of large differences between the depth of the SCA tank and the spent fuel pool. Several views of details of the fuel dipstick are presented in Figs. VI.4.1.6 through VI.4.1.8.

Figure VI.4.1.1. The fuel transfer cask shown during the manufacturing process.

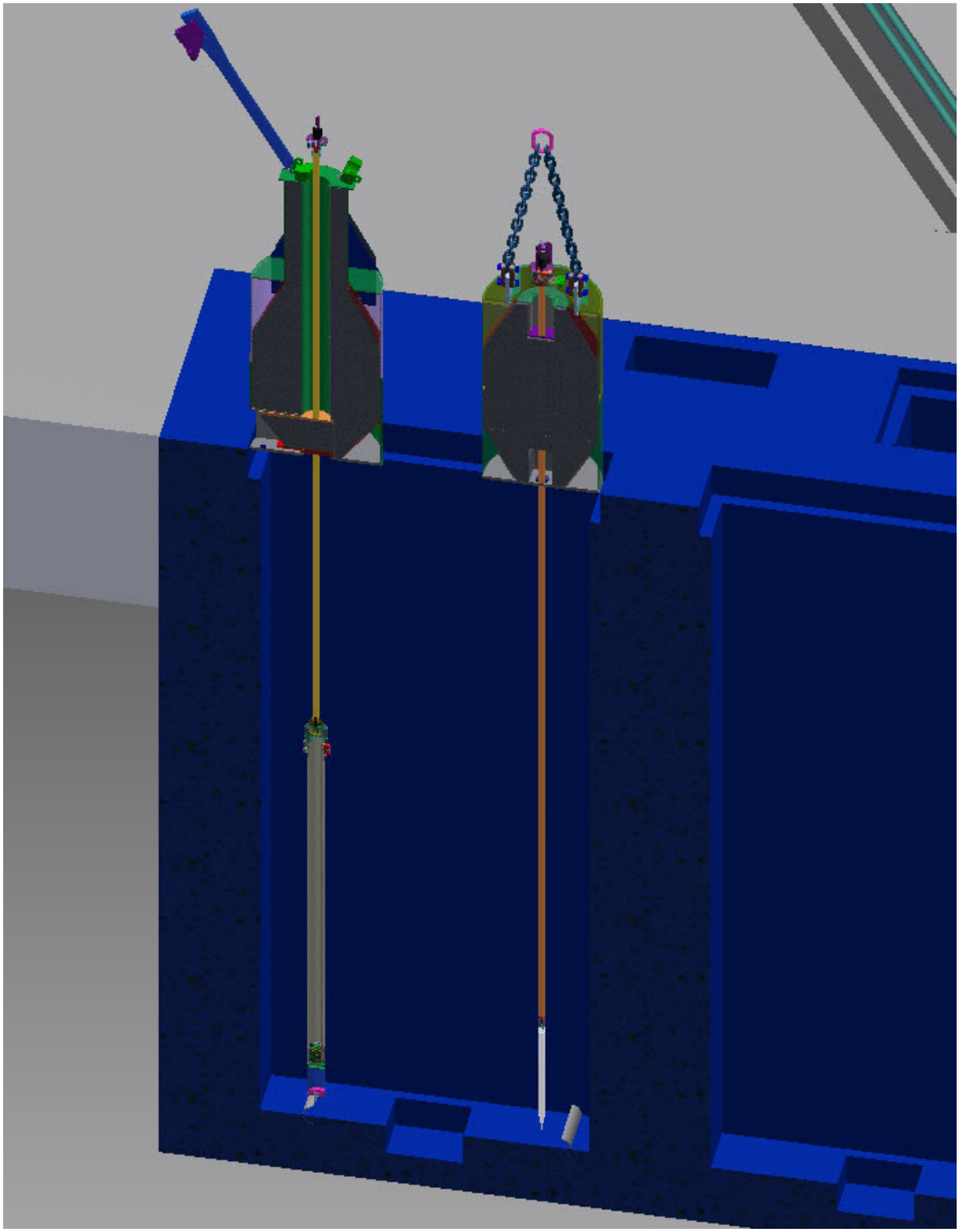

Figure VI.4.1.2. The fuel cask (right) and the target cask (left) shown over the spent fuel pool.

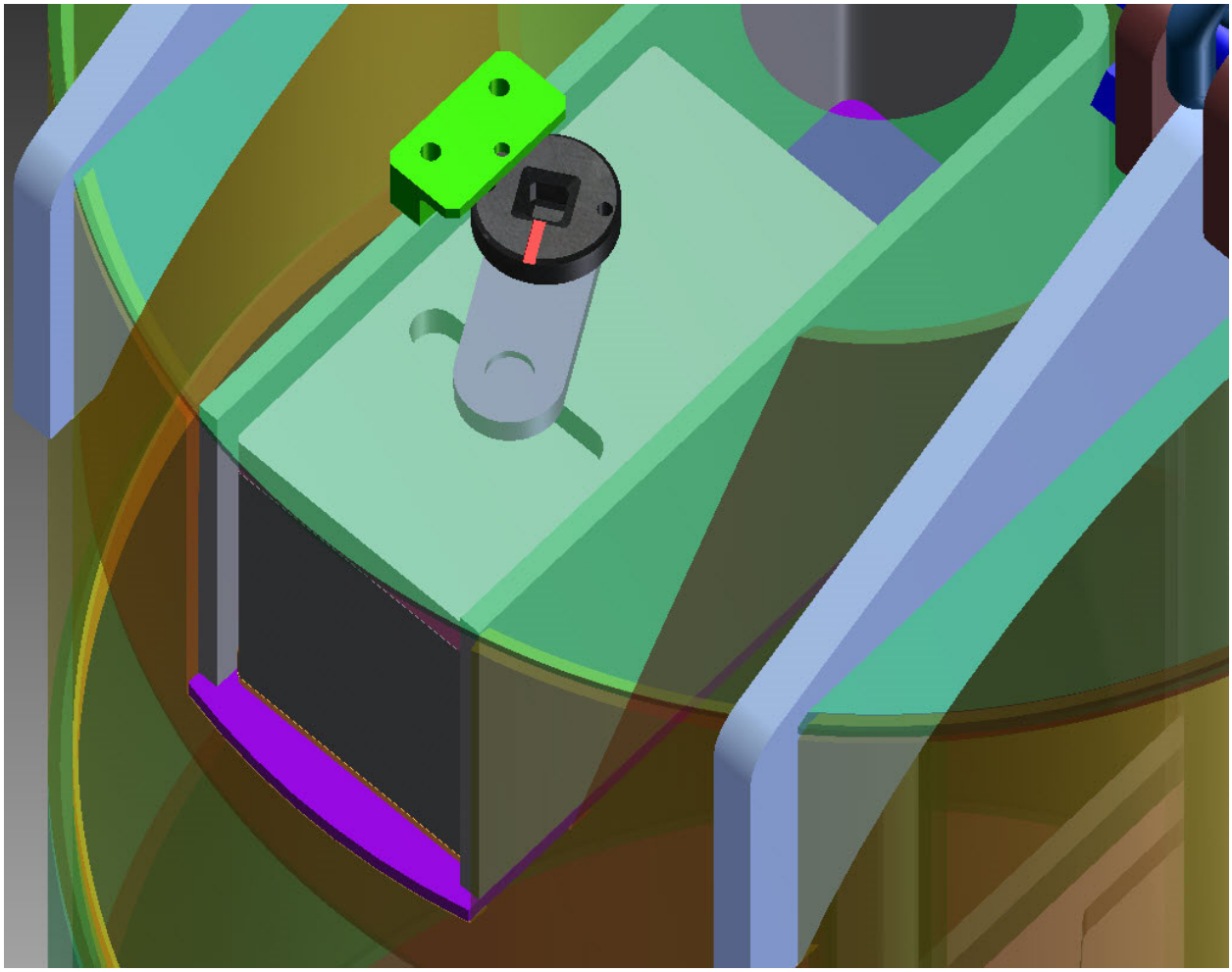

Figure VI.4.1.3. The fuel transfer cask top gate and the actuation shaft.

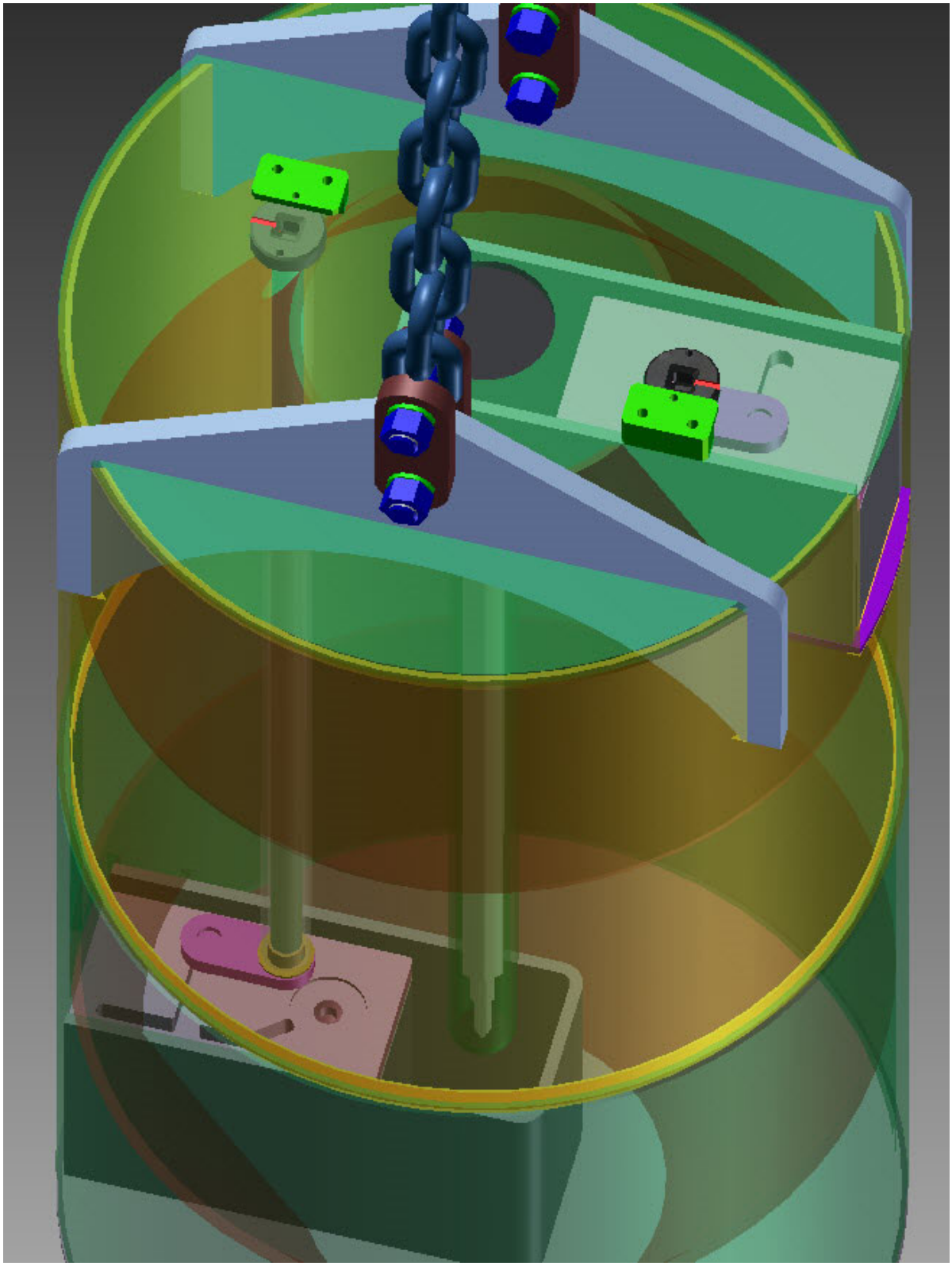

Figure VI.4.1.4. Translucent view of the fuel transfer cask showing the top and the bottom gates and the actuation mechanisms.

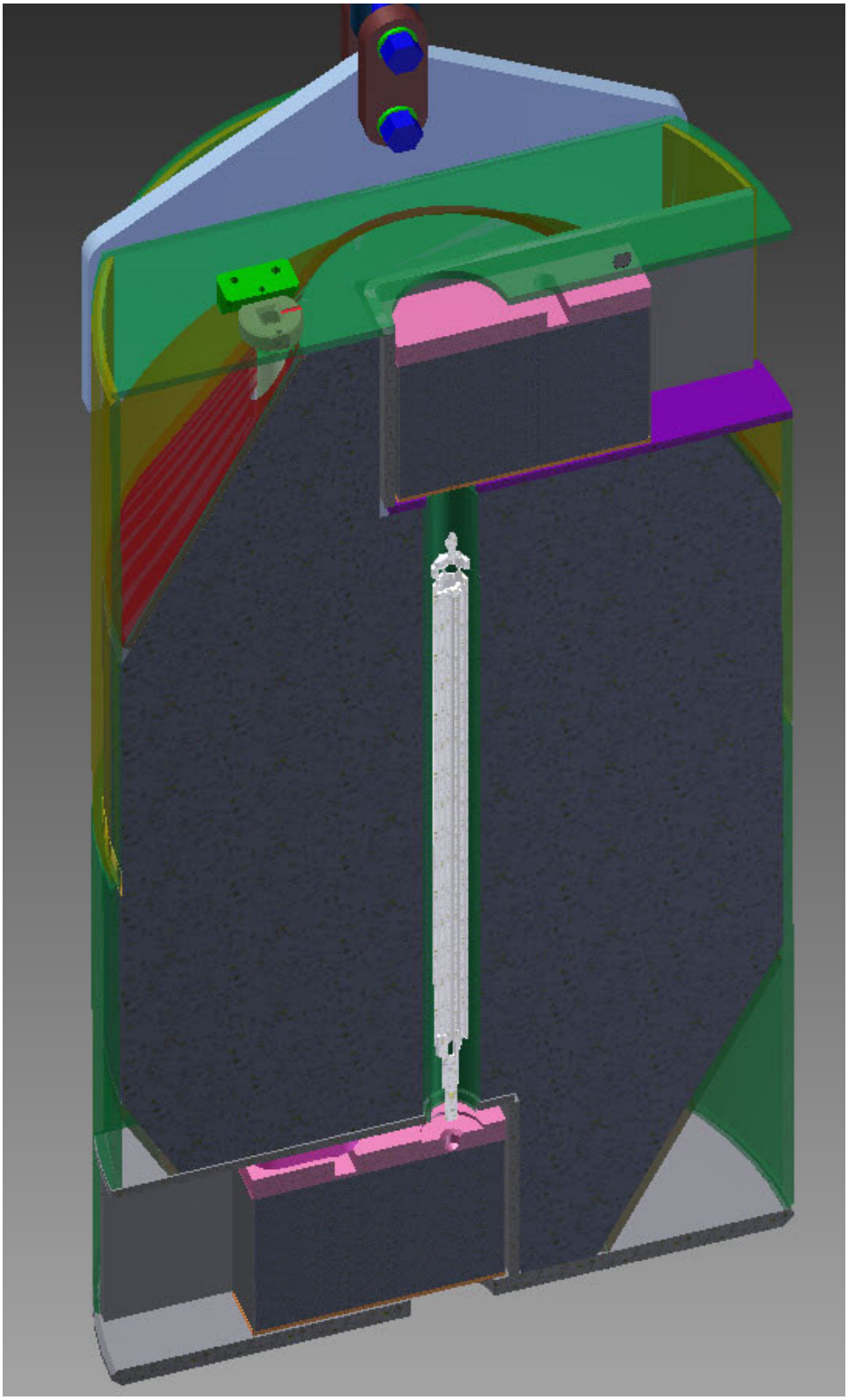

Figure VI.4.1.5. Section view through the fuel transfer cask, showing the upper and the lower gates closed with a fuel assembly.

Figure VI.4.1.6. Top of fuel dipstick showing the step motor and the micro-switches.

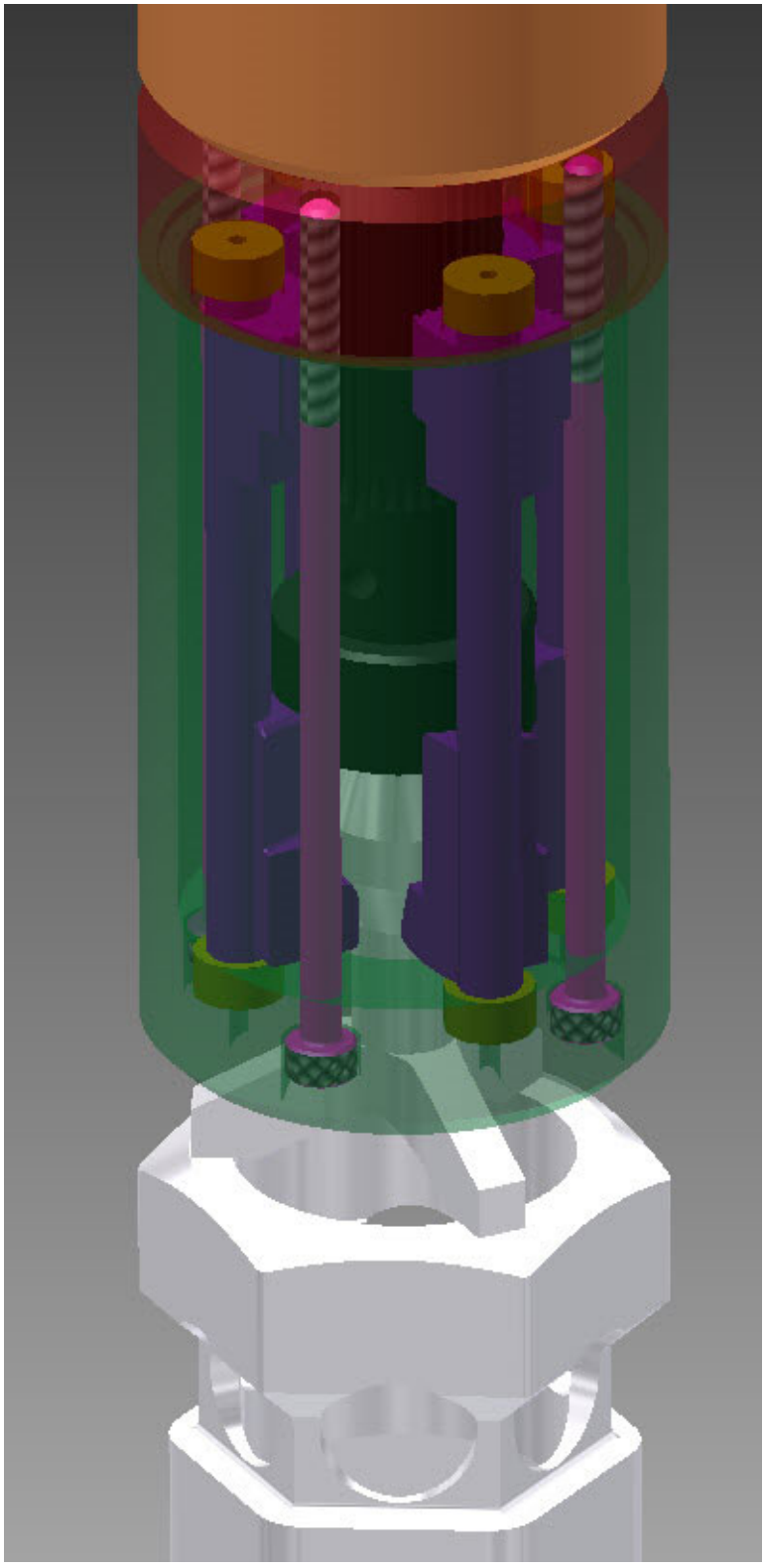

Figure VI.4.1.7. Bottom of the fuel dipstick shown engaged with a fuel assembly.

Figure VI.4.1.8. Section view of the fuel dipstick showing the rotating dog jaws and a fuel assembly.

VI.4.2 Target Transfer Cask Mechanical Design

The target assembly used in the operation of the KIPT NSC will have a finite life. When the end of the target productive life is reached, the used target assembly must be removed from the subcritical assembly (SCA) and replaced with a fresh target assembly. The target transfer cask is used for removing the used target assemblies from the SCA and moving it to the spent fuel pool. The target transfer cask provides adequate radiological shielding to maintain the external dose level below 0.5 mrem/hr over the bottom and side surfaces of the cask, but because the target beam tube is so long (about 2.3 m.), the beam tube protrudes past the end of the beam tube extension on the cask and so the cask is open at the top. As discussed in Sec. VI.2, this results in a photon dose level above 0.5 mrem/hr. in the upper regions of the subcritical assembly hall while the spent target is being loaded and transferred. However, since no personnel are in the upper regions of the subcritical assembly hall during the transfer and the dose where personnel are located on the room floor during the transfer is well below 0.5 mrem/hr, therefore the high photon dose in the upper regions of the SCA hall while the target is being transferred is not a concern.

The target transfer cask is fabricated of stainless-steel plates welded to form a strong liquid-tight container, and then filled with molten lead. After the cask has been filled with lead, the lead access holes are closed to provide environmental containment of the lead. The cask has a mass of 4,615 kg. A photograph of the target transfer cask is shown in Fig. VI.4.2.1; the corresponding CAD model is presented in Fig. VI.4.2.2.

The target transfer cask is lifted and moved by the overhead crane within the subcritical assembly hall. A steel lifting bail is attached to the cask and interfaces with the lifting hook of the overhead crane. The lifting bail automatically folds 30 degrees to one side when the target cask is set down, allowing access to the target assembly for loading and unloading the cask. The lifting bail and attachment points have been physically tested to support 150% of the weight of the cask. The target transfer cask is not intended to leave the subcritical assembly hall.

The target transfer cask is a bottom entry/exit cask. A movable bottom gate allows access to the central cavity of the cask, as shown in Figs. VI.4.2.3 through VI.4.2.5. Figures VI.4.2.6 and VI.4.2.7 indicate how a target is loaded into the cask from either the SCA or the spent fuel pool. The bottom gate is opened and closed by turning a threaded shaft with a handheld tool. To load/unload the cask, a long slender dipstick with a gripper on the lower end is lowered through the cask to grip the target and lift it into the target transfer cask. The dipstick has four rotatable jaws that engage features in the target assembly to provide a robust and secure means of lifting the target assembly. The dipstick is composed of two concentric tubes. The outer tube provides structure and carries the load of the target assembly. The inner tube is free to rotate and translate axially relative to the outer tube. Rotation of the inner tube opens and closes the dog jaws to engage/release the target assembly. The inner tube translates axially when the dipstick interfaces with the target assembly, unlocking the dog jaws so that they are free to rotate, and tripping micro-switches at the top of the dipstick to indicate condition of target engagement by lighting LEDs on the control pendant. Micro-switches also detect the rotation condition of the inner tube, thereby lighting LEDs on the control pendant to indicate dog jaw position.

A step motor at the top of the dipstick rotates the inner tube to open and close the dog jaws, as commanded by a toggle switch on the control pendant. Two different length dipsticks are needed because of large differences between the depth of the SCA tank and the spent fuel pool. Several views of details of the target dipstick are presented in Figs. VI.4.2.8 through VI.4.2.10.

Figure VI.4.2.1. The target transfer cask, shown during the manufacture.

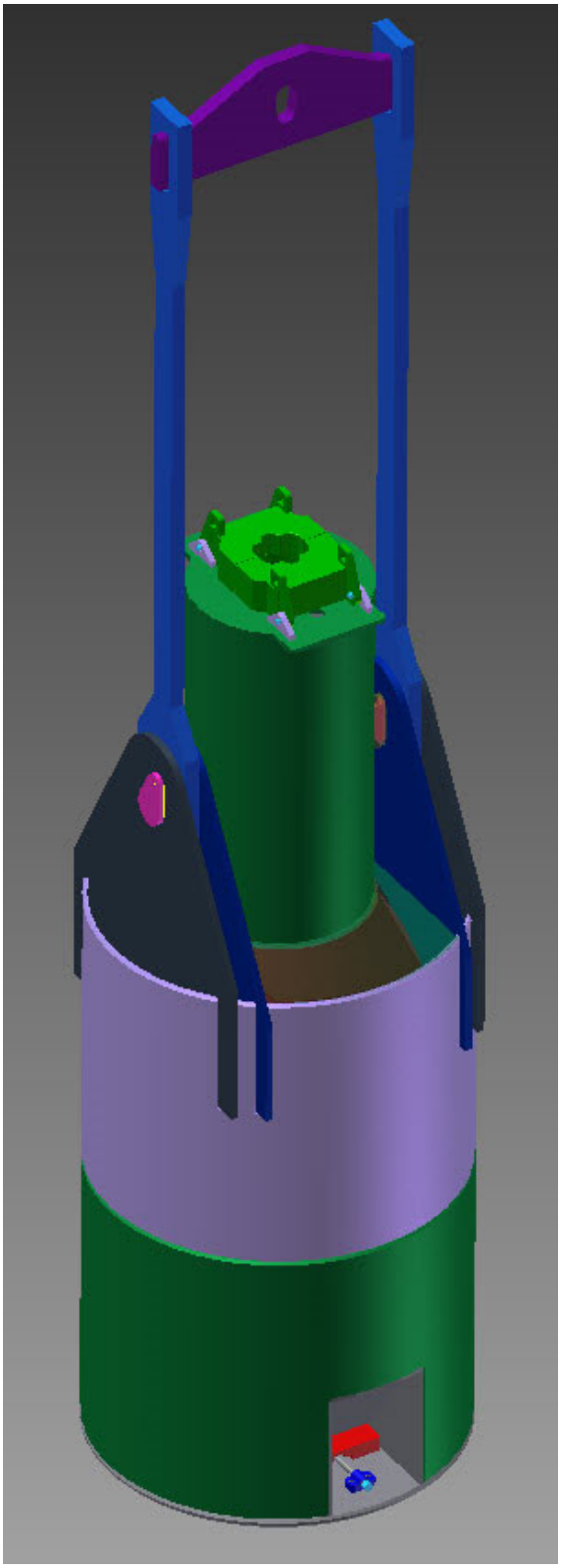

Figure VI.4.2.2. The target cask shown as a CAD model.

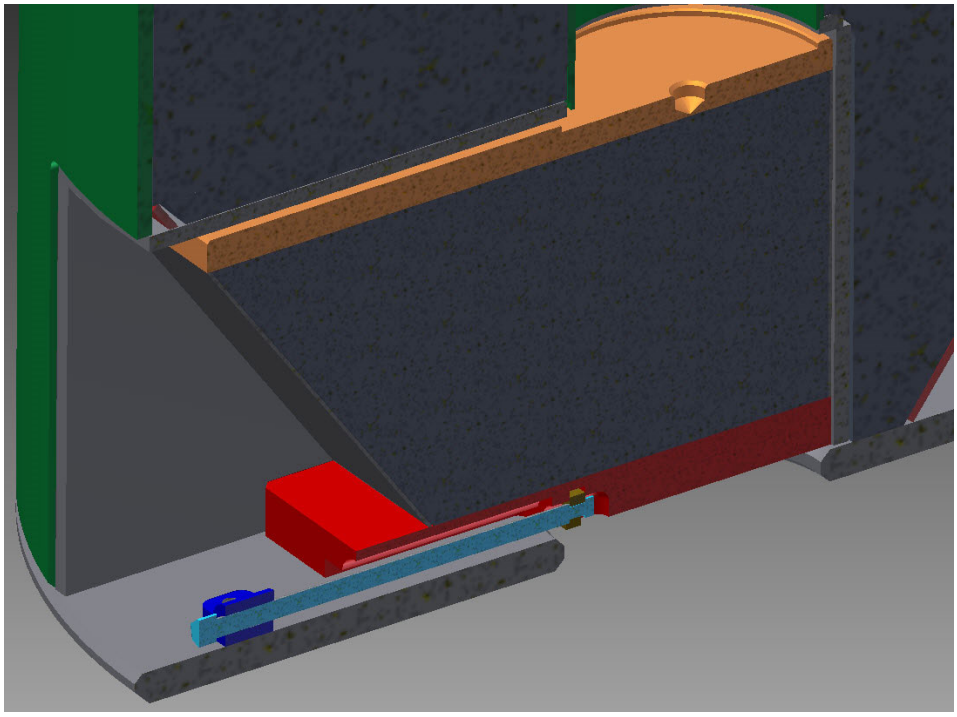

Figure VI.4.2.3. Section view of the target cask bottom gate, shown in closed position.

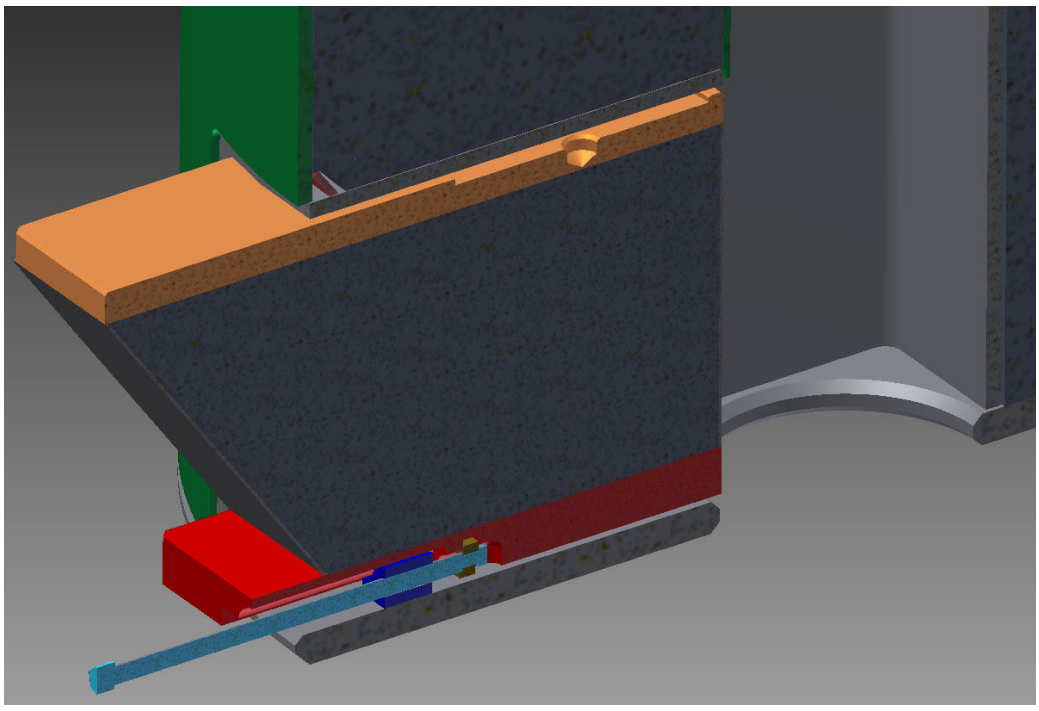

Figure VI.4.2.4. Section view of the target Cask bottom gate, shown in opened position.

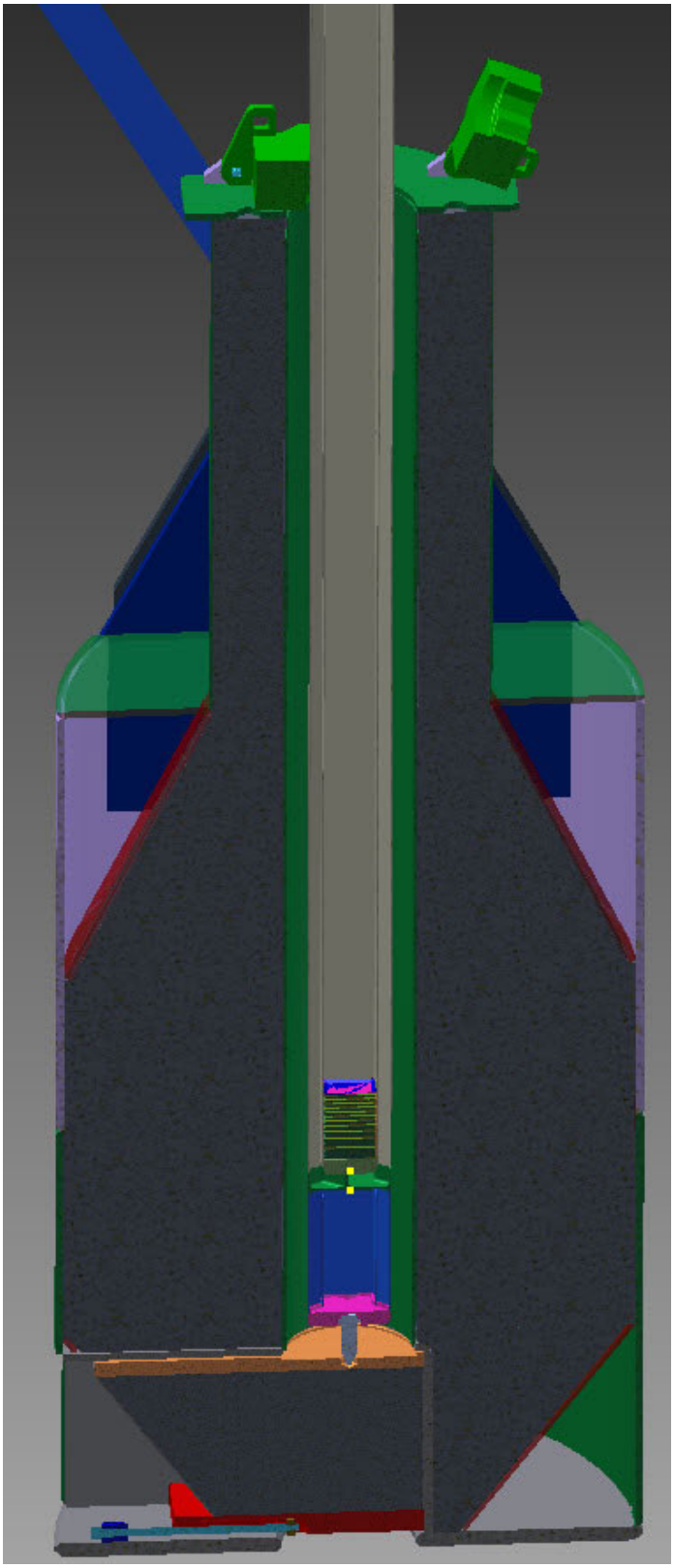

Figure VI.4.2.5. Section through the target cask and the target, showing the bottom gate, the top support, and the lead (Pb) shielding.

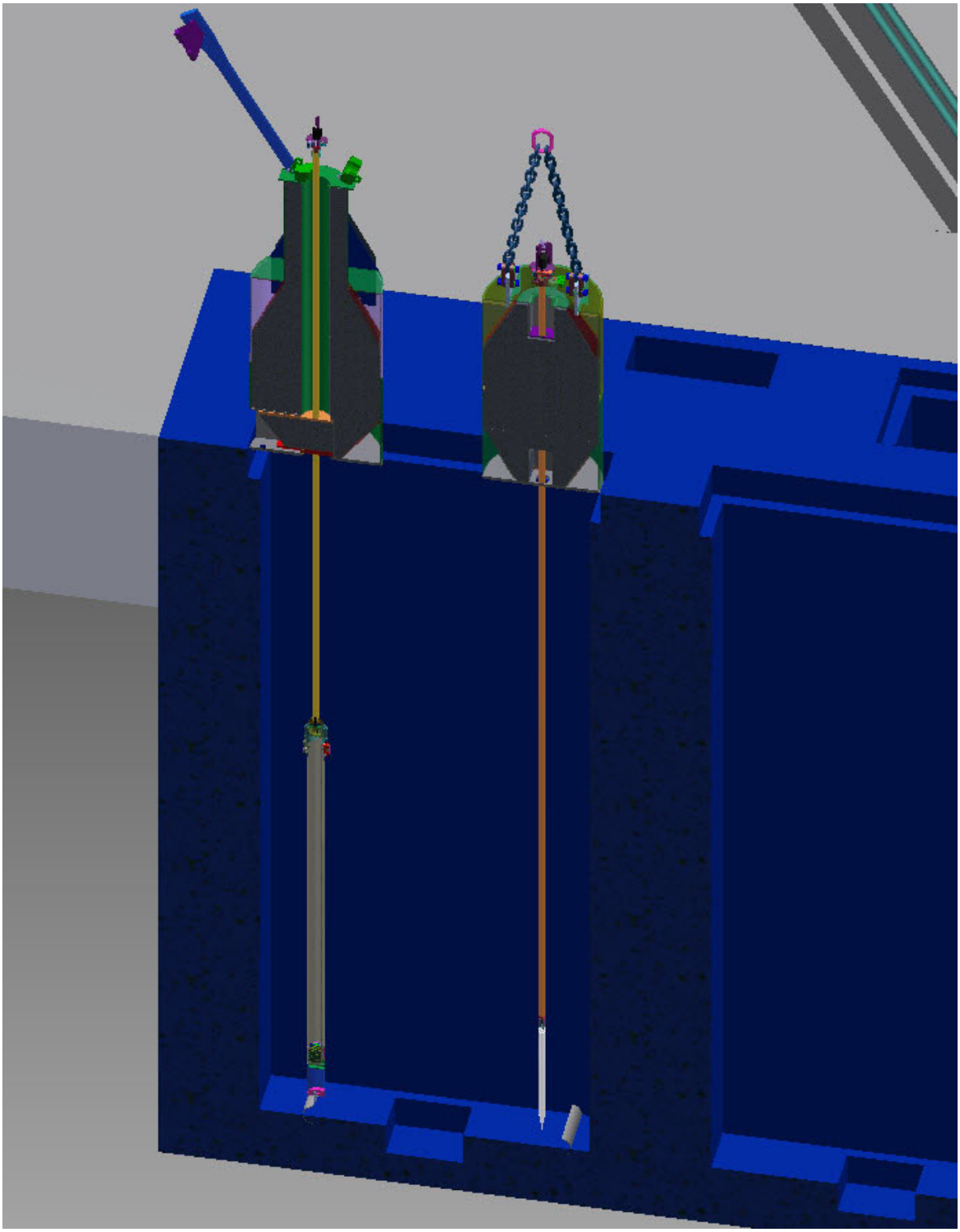

Figure VI.4.2.6. Cross section of the spent fuel pool showing both the target cask and the fuel cask in simulated loading condition. Long dipsticks are used to place/retrieve assemblies in the spent fuel pool.

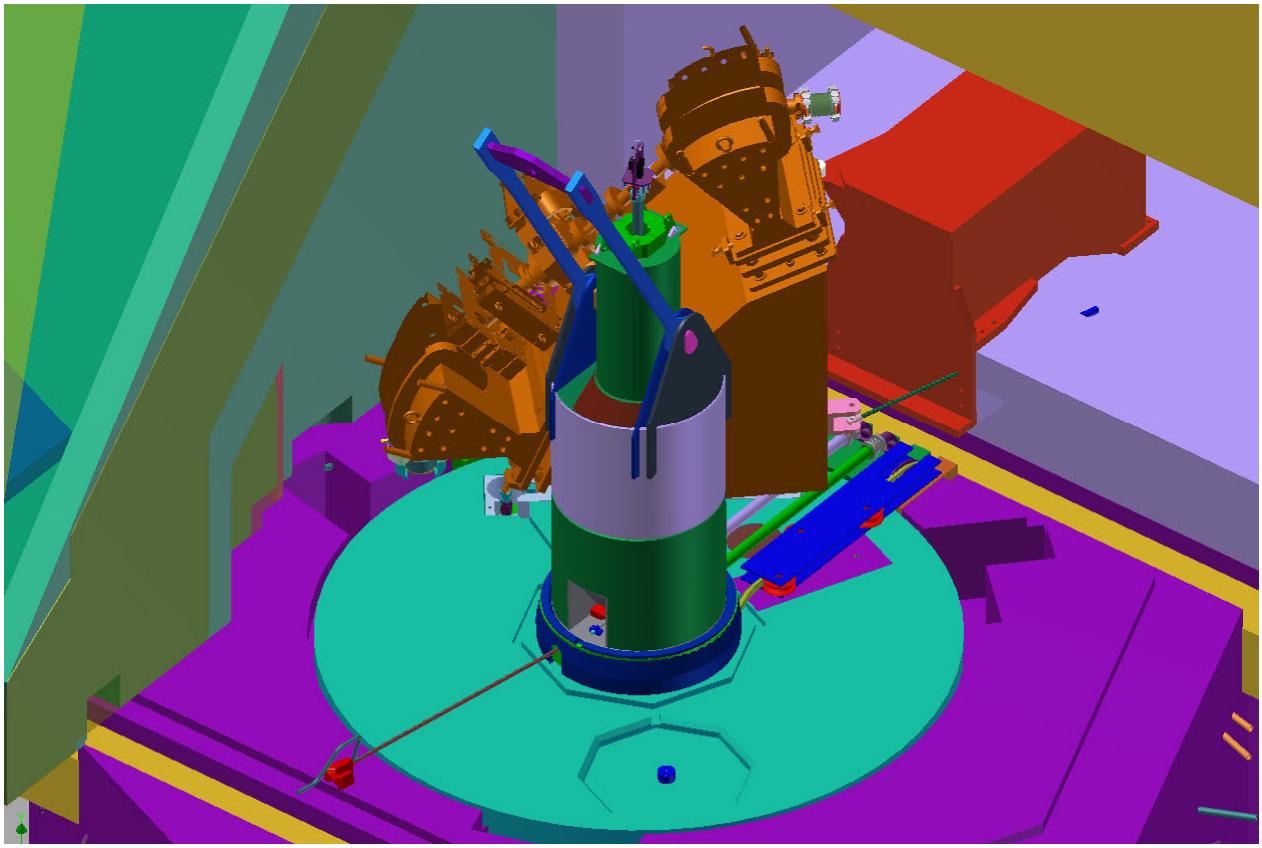

Figure VI.4.2.7. The target cask shown on the top of the subcritical Assembly during the loading of used target assembly.

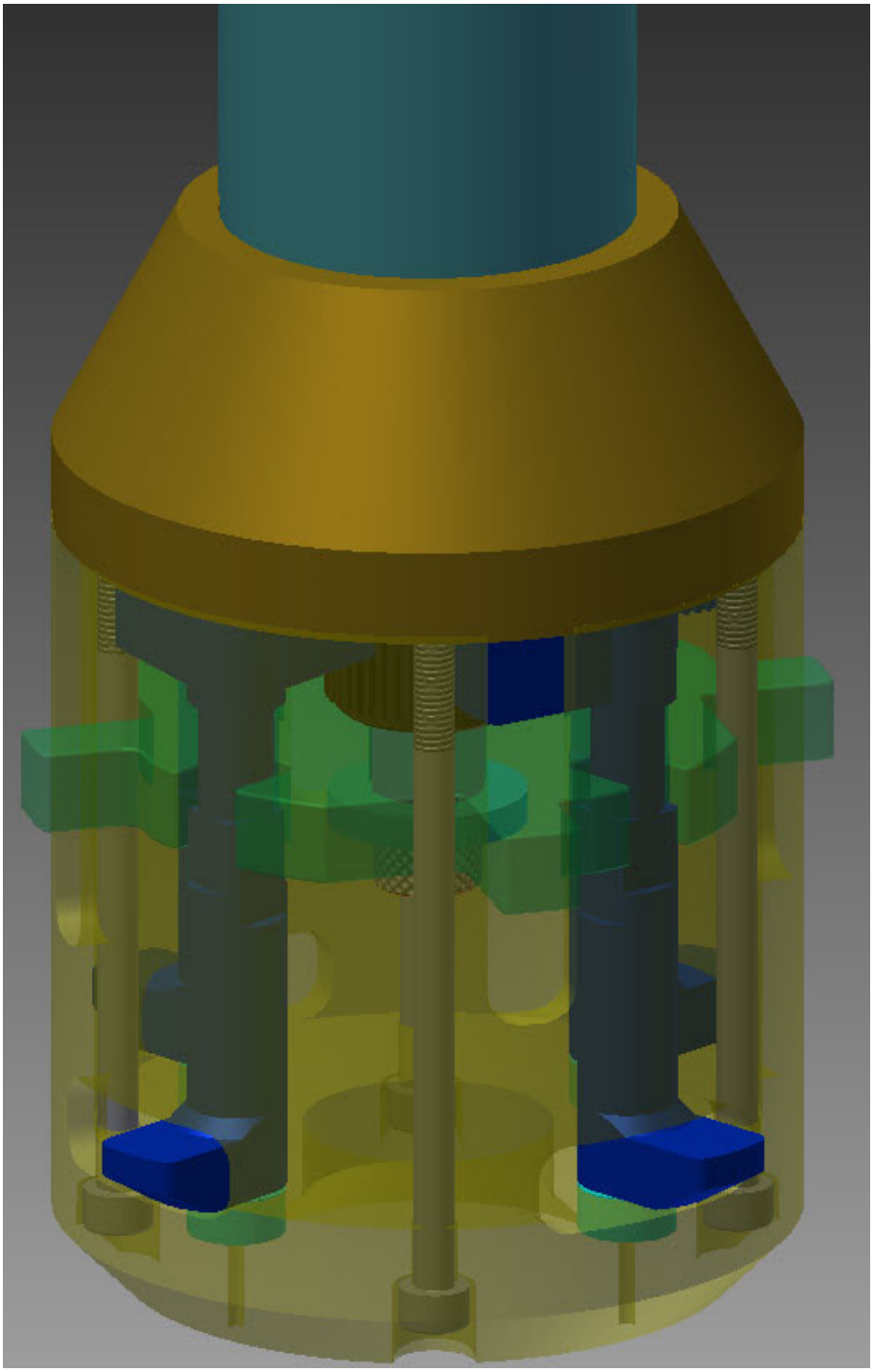

Figure VI.4.2.8. Detail of the target dipstick gripper. Dog jaws (blue) are rotated by the step motor to engage the target. Presence plate detects engagement with the target Asssembly and mechanically prevents dog jaws from rotating until the target assembly is adequately supported.

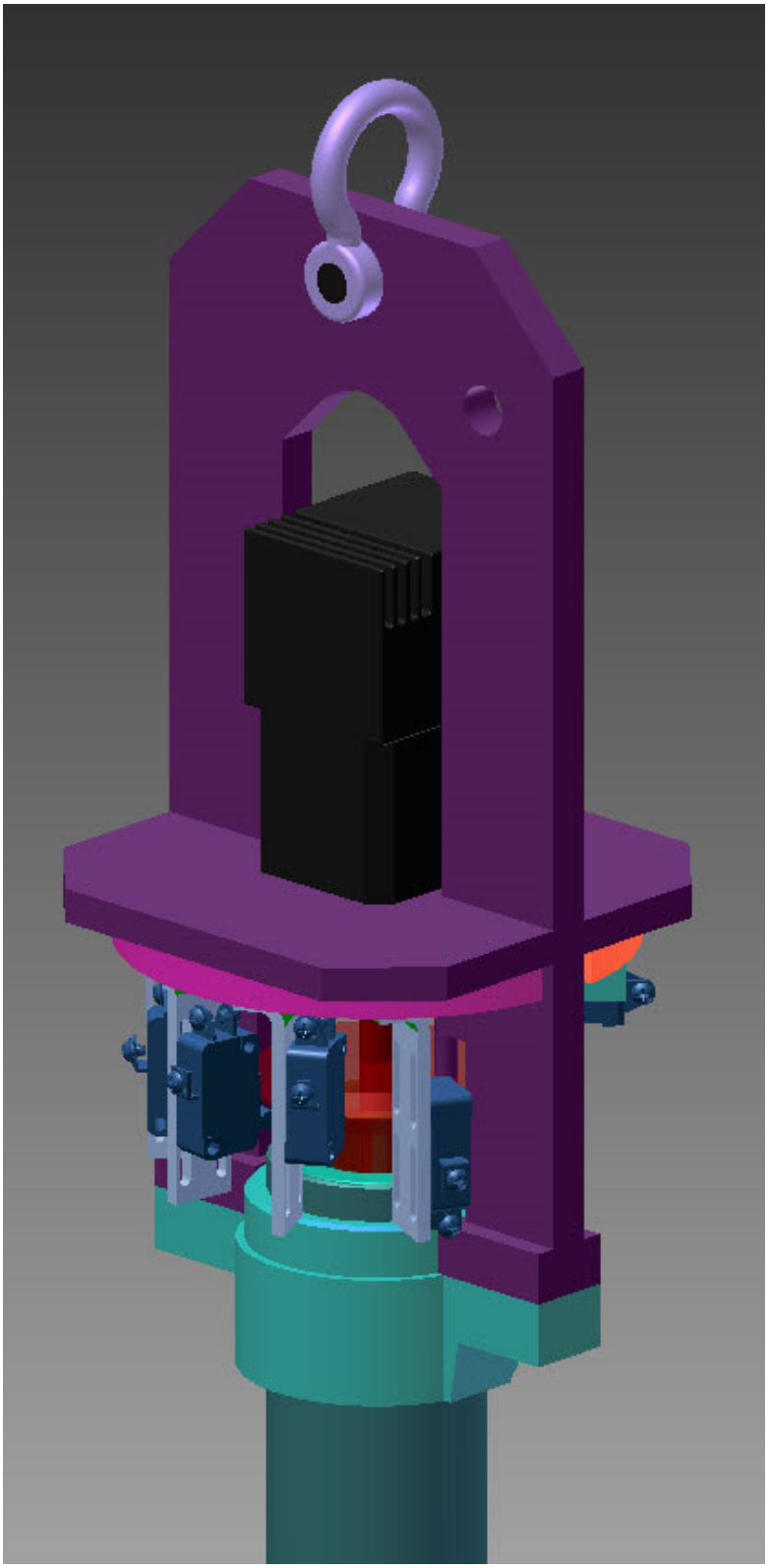

Figure VI.4.2.9. Upper end of the target dipstick, showing the step motor and the micro-switches.

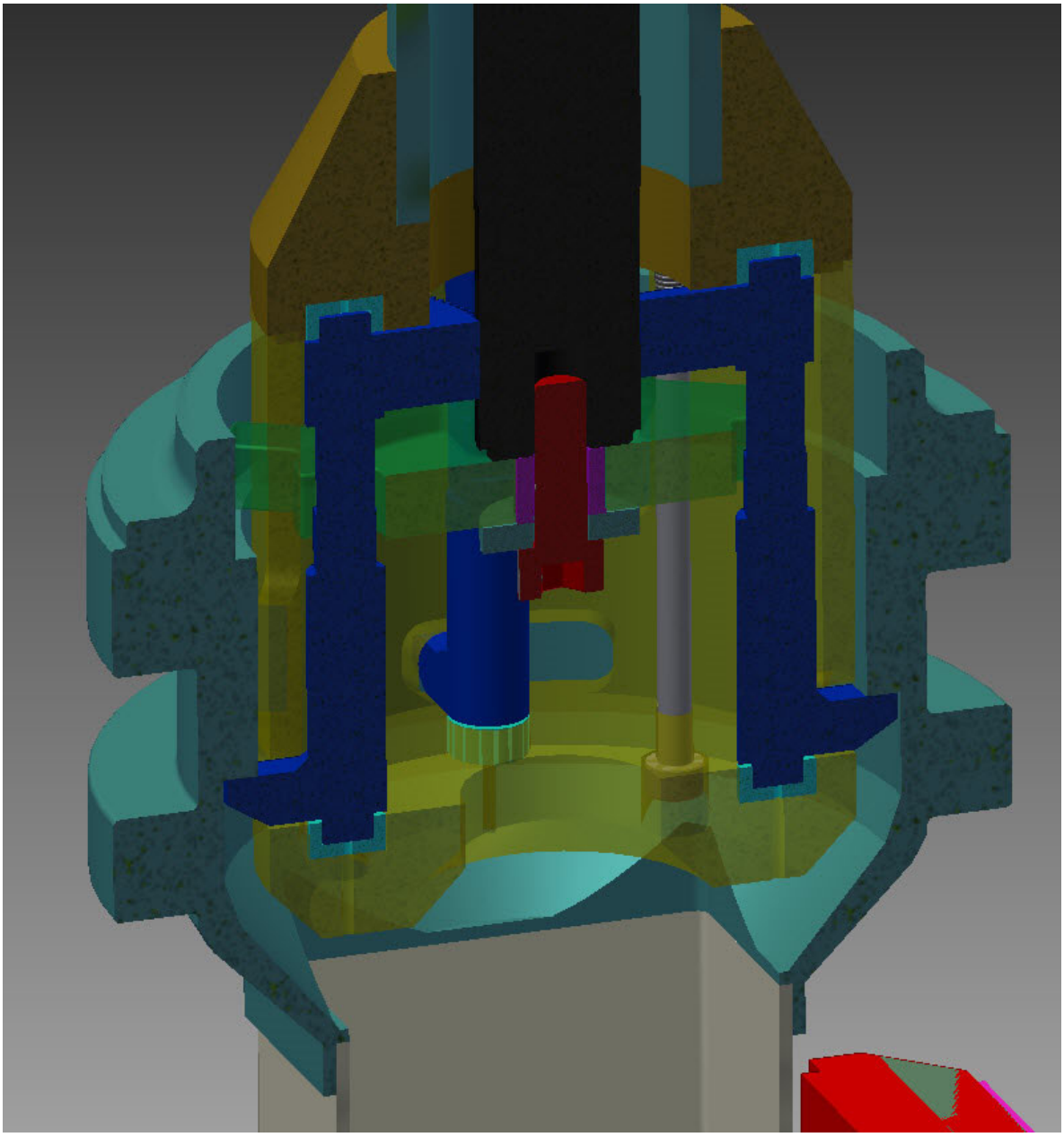

Figure VI.4.2.10. Section through the target dipstick and the flange of the Target assembly showing interaction of dog jaws and presence indicator.

VI.5 Main Parameters

Table VI.5.1. Design Parameters for the Fuel Transfer Cask Shield

Primary Shield material	Lead (cladded with stainless steel)
Thickness of the stainless steel clad	1.0 cm
Inner Radius of the radial shield (Including the stainless steel clad)	2.1 cm
Outer Radius of the radial shield (including the stainless steel clad)	33 cm
Lead thickness below the fuel assembly	22 cm
Lead thickness above the fuel assembly	24 cm
Angle of the bottom corner cut	28°
Height of bottom corner cut	35.3 cm
Angle of the top corner cut	28°
Height of the top corner cut	34 cm
Total height of the cask	125.3 cm

Table VI.5.2. Design Parameters for the Target Transfer Cask Shield

Primary Shield material	Lead (cladded with stainless steel)
Thickness of stainless steel clad	1.0 cm
Inner Radius of radial shield (Including the stainless steel clad)	8.0 cm
Outer Radius of radial shield (Including the stainless steel clad)	37.5 cm
Lead thickness below the fuel assembly	23.5 cm
Angle of the bottom corner cut	30º
Height of the bottom corner cut	34.5 cm
Angle of the top corner cut	24.82º
Height of the top corner cut	40 cm
Height of the top extension	70 cm
Height of the top partial cover	7.5 cm
Total height of the cask	193 cm
Total weight of the cask	~4.2 tons

Table VI.5.3. Material Properties for 304L Stainless Steel

Property	Value
Elastic Modulus (MPa)	200,000
Ultimate Tensile Strength (MPa)	485
Yield Strength (MPa)	170
Poisson's Ratio	0.27
Density (kg/m^3)	7,930

Table VI.5.4. Maximum Stresses and Safety Factors

Location	Maximum Stress (MPa)	Safety Factor at the Highest Stress
Target cask yoke lifting hole	85.1	2.00
Target cask body	31.1	5.47
Fuel cask lifting flange hole	61.4	2.77
Fuel cask top/lifting flange intersection	37.7	4.51

VII Fuel Handling Machine

VII.1 Introduction

The subcritical assembly of the KIPT Experimental Neutron Source Facility uses low-enriched uranium fuel elements within the subcritical assembly (SCA). During operation the fuel assemblies become depleted and need to be moved or replaced. The fuel handling machine moves fuel elements between the grid plate, the storage racks, and the fuel transfer station within the SCA tank. The fuel handling machine also moves sample cassettes, beryllium reflector elements, and boron carbide absorber elements within the SCA tank. The location of the FHM within the facility is indicated in Fig. VII.1.1.

VII.2 Mechanical Design

VII.2.1 Fuel Handling Machine Operation Strategy

The fuel handling machine (FHM) moves the fuel assemblies, the sample cassettes, the beryllium reflector elements, and the boron carbide absorber elements within the SCA tank. All motions are controlled by the FHM control computer. The FHM motions are driven by electric motors. Each motor has a position-indicating device to create position feedback for the control computer. A system of administrative controls limits operator authority to use the FHM and tracks inventory and configuration of the subcritical assembly.

All element movements are from a known location to another known location. The motions of the FHM are controlled by a computer that calculates an efficient path from the start location to the end location. During operation, the operator specifies an element movement start and end point, and the computer checks for authorization of the requested move, calculates the move path, moves the element, logs the move, and updates the inventory register to show the current SCA configuration.

The FHM only operates during times when the linear accelerator is turned off, resulting in a low neutron flux within the subcritical assembly. When the accelerator is on, the FHM is parked in a special parking garage (Figure VII.2.1.1) in the biological shield. This strategy minimizes radiation damage of susceptible components on the fuel handling arm and the fuel assembly gripper. The FHM parking garage is partially formed by a cover that can be removed to provide service or recovery operations.

VII.2.2 Fuel Handling Machine Structure

The fuel handling machine is constructed of radiation- and corrosion-resistant materials. The use of nickel is minimized to reduce activation of the FHM components.

VII.2.3 Fuel Handling Machine Motion

The FHM has five independent degrees of motion. The rotating vessel cover (RVC) rotates about its vertical axis, providing the first motion. The RVC is supported on three support rollers and centered by three guide rollers, Figs. VII.2.3.1 through VII.2.3.3. The rotation of the RVC is driven by an electric motor that is external to the biological shield through a drive shaft and a right-angle gearbox mounted with a pinion gear that meshes with the ring gear on the periphery of the RVC, as shown in Figs. VII.2.3.2 and VII.2.3.4. It is necessary to rotate the RVC 360 degrees to access the entire grid plate, since the FHM arm cannot swing past the target assembly at the central axis of the subcritical assembly. A cable take-up mechanism on the top of the RVC allows 360-degree rotation

of the RVC while maintaining electrical connectivity to the motors, resolvers, and other devices that are mounted to the RVC. The RVC rotates about the target assembly, which is on the axis of the subcritical assembly.

The fuel handling arm (FHA) assembly is mounted to, and rotates with, the rotating vessel cover as shown in Fig. VII.2.3.5. The FHA axis of rotation is parallel to, and eccentric from, the rotational axis of the RVC, therefore the combination of RVC rotation and FHA swing will cover all areas of the grid plate and SCA tank. The FHA is mounted to a FHM plug that penetrates and is removable from the RVC, as shown in Fig. VII.2.3.6. The motor that drives the FHA rotation is on the top surface of the FHM plug, providing a low radiation environment and simplifying service operations as shown in Fig. VII.2.3.7. The FHM arm never rotates past the central axis of the SCA.

Vertical motion of the FHM is provided by a four-bar linkage mechanism that provides a true vertical lift path, as shown in Fig. VII.2.3.8. Figure VII.2.3.9 shows the limits of travel for the mechanism. The motor that drives the vertical motion is above the FHM plug, providing a low-radiation environment for the motor and simplifying service operations. The vertical motion motor drives a shaft that drives a 90-degree gearbox, which drives a horizontal ball screw in the FHA, as shown in Fig. VII.2.3.10. The ball nut that is driven by the ball screw drives one point of the four-bar linkage, resulting in a vertical motion at the opposite end of the linkage. The fuel gripper is attached to the opposite end of the vertical lift linkage, as shown in Fig. VII.2.3.11. The fuel gripper and the part of the vertical lift mechanism operate below the surface of the water coolant in the SCA tank during parts of the movement cycle.

The fuel gripper is attached to the distal end of the vertical lift linkage. The axis of the fuel gripper is maintained parallel to a vertical axis by a parallelogram linkage that connects back to the fuel handling machine arm. The fuel gripper contains a device that grips the knob of the fuel element (or other element being moved) with four rotatable jaws, as shown in Fig. VII.2.3.11. The rotatable jaws interface with a central gear that is driven by an electric motor, so that all four jaws rotate simultaneously. The jaws are mechanically locked against rotation until the element presence shaft is pushed upward by the head of the fuel assembly. This interlock prevents the jaws from rotating and dropping a fuel assembly. The jaws are unlocked when the fuel element is safely supported by the grid plate, transfer station, or storage rack. The motor that controls the gripper jaws is in the fuel gripper, as shown in Fig. VII.2.3.11.

The fuel gripper is equipped with a rotation device that rotates the fuel element about its vertical axis. This motion is necessary to rotate the fuel element into registry with the hexagonal grid plate. When a fuel element is to be placed in the grid plate, it is initially carried to and placed in the hexagon orientation device. The hexagon orientation device orients the rotation of the fuel element to a known rotation relative to the hexagonal grid plate, and the FHM can maintain this angular orientation by adjusting the rotation device as the element is being carried to its location in the grid plate. The motor that controls the gripper rotation is in the fuel gripper.

VII.2.4 Fuel Handling Machine Service Operations

The fuel handling machine can be removed from the RVC by lifting the FHM plug and carrying it to a service area, see Fig. VII.2.4.1. This allows service of components that

are under the RVC. When the FHM plug is removed for service, a blank plug is placed in the RVC to provide containment and shielding. The FHM plug is precisely located to the RVC by kinematic mounts, ensuring that the FHM plug returns to the correct position when reinstalled in the RVC. The RVC can be removed to provide service to the support rollers and guide rollers after securing the SCA. The RVC drive motor can be serviced or replaced at its location on the outer surface of the biological shield without opening the movable top shield. The FHM arm swing motor and the vertical lift motor can be replaced by opening the MTS. The RVC resolvers and 90-degree gearbox can be serviced by opening the movable top shield.

VII.2.5 Fuel Handling Machine Recovery Operations

The FHM is robustly designed to maximize uptime. The design of the FHM allows the manual mechanical actuation of all FHM motions necessary to recover and remove the FHM arm from the SCA tank for service and repair. The rotation of the rotating vessel cover can be manually controlled at the drive motor on the south side of the biological shield. The swing of the FHM arm and the vertical lift of the fuel gripper can be manually controlled by turning the motor shafts on top of the RVC. The grip of the fuel gripper can be manually opened by inserting a long tool through a special access port in the RVC and turning the fuel gripper shaft to open the jaws and release the fuel element. There is no mechanical recovery mode for the fuel gripper rotation function, as no recovery strategy requires this motion.

VII.2.6 Fuel Handling Machine Video Camera

The FHM is equipped with a radiation-tolerant video camera mounted on the fuel gripper. This camera can aid in the placement of fuel elements in the grid plate and may be useful in understanding and diagnosing off-normal conditions.

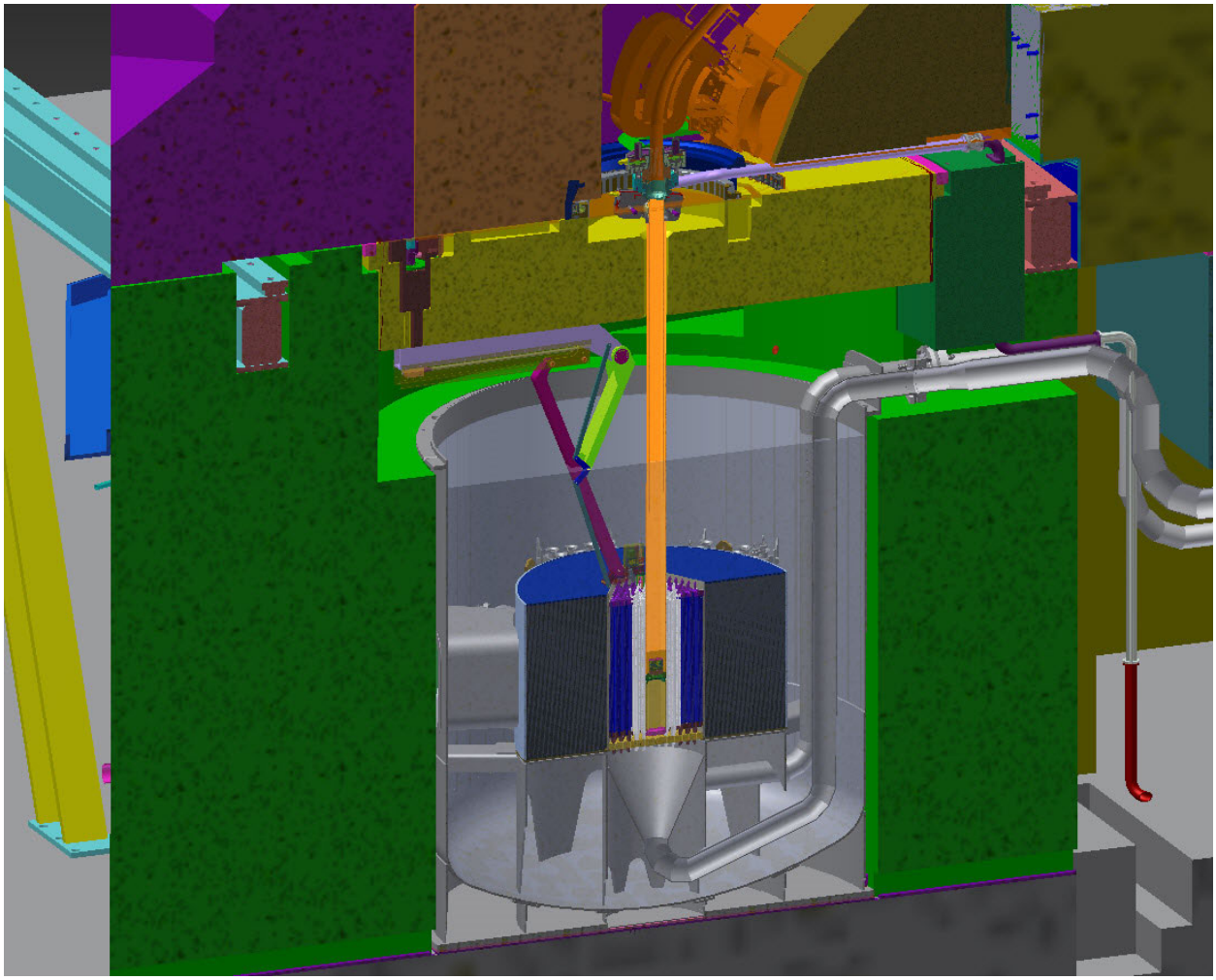

Figure VII.1.1. Section view through SCA, showing the biological shield (dark green), the SCA tank (silver), the rotating vessel cover (yellow), and the fuel handling machine (above the SCA and to the left of the accelerator beam tube (orange)).

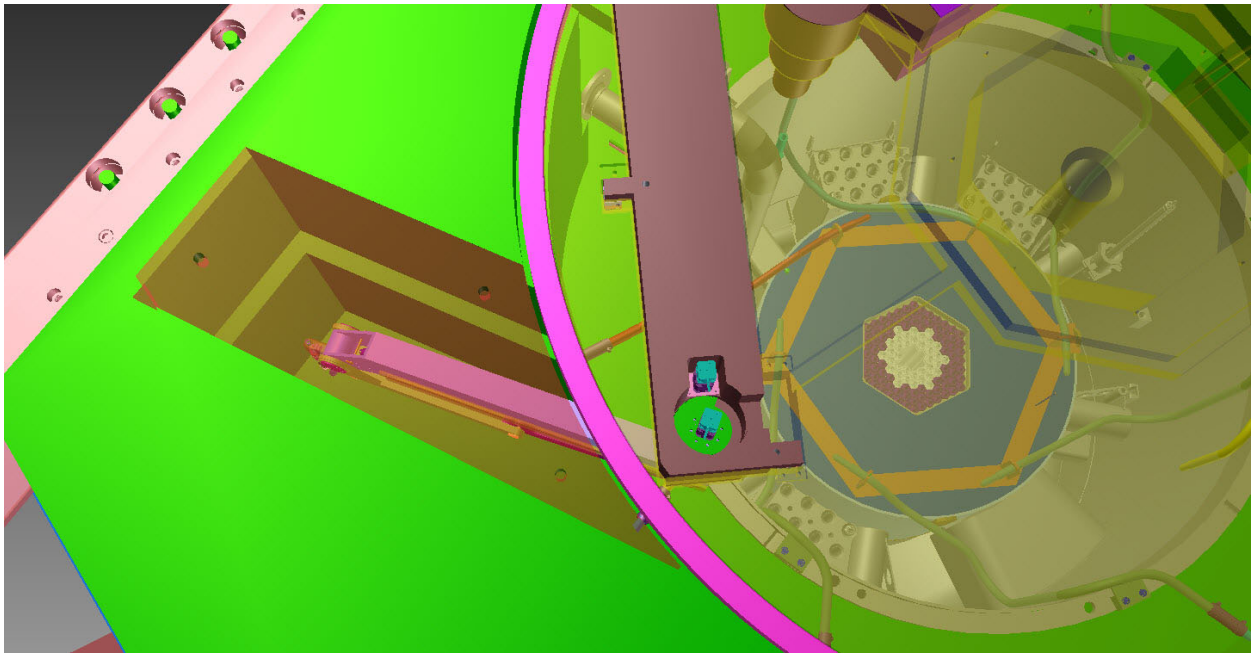

Figure VII.2.1.1. This image shows the FHM parking garage. The FHM parking garage cover is shown as transparent red.

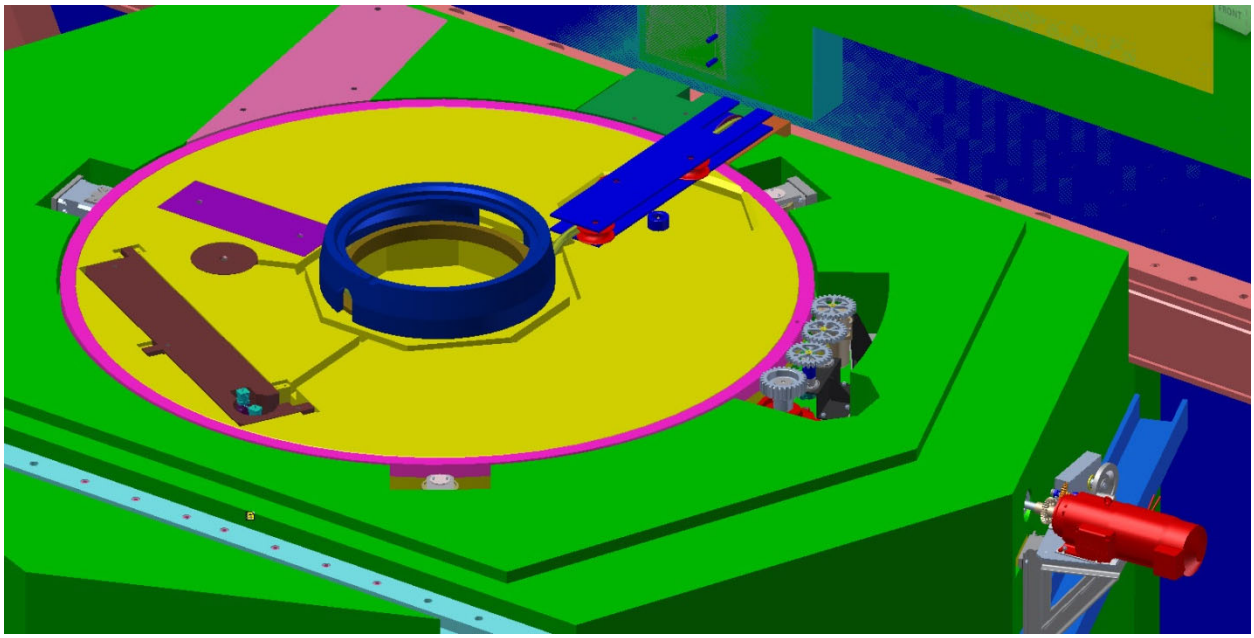

Figure VII.2.3.1. View of the top surface of the rotating vessel cover. The three guide rollers (at three points around the outside of the RVC), the RVC drive motor, the FHM parking garage (pink section at the top), and the FHM plug are visible.

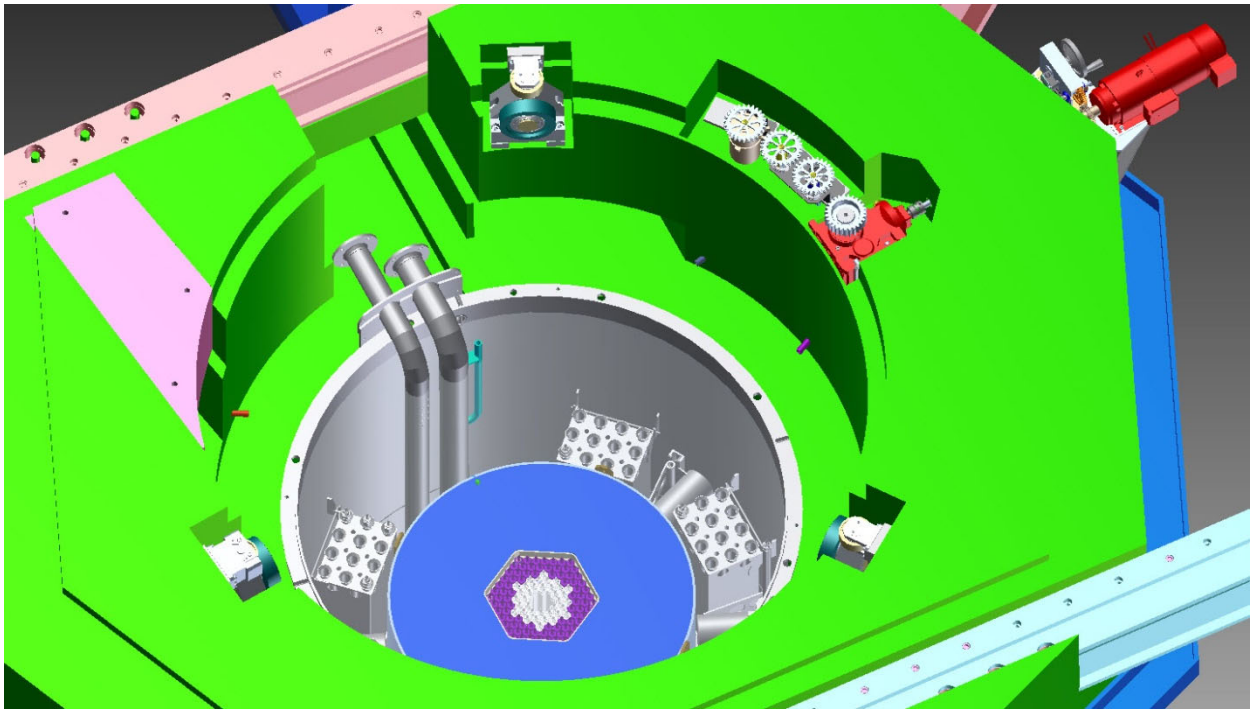

Figure VII.2.3.2. With the rotating vessel cover removed, the three RVC support rollers and the guide rollers are visible. Also visible are the RVC drive motor, the gearbox, and the resolvers.

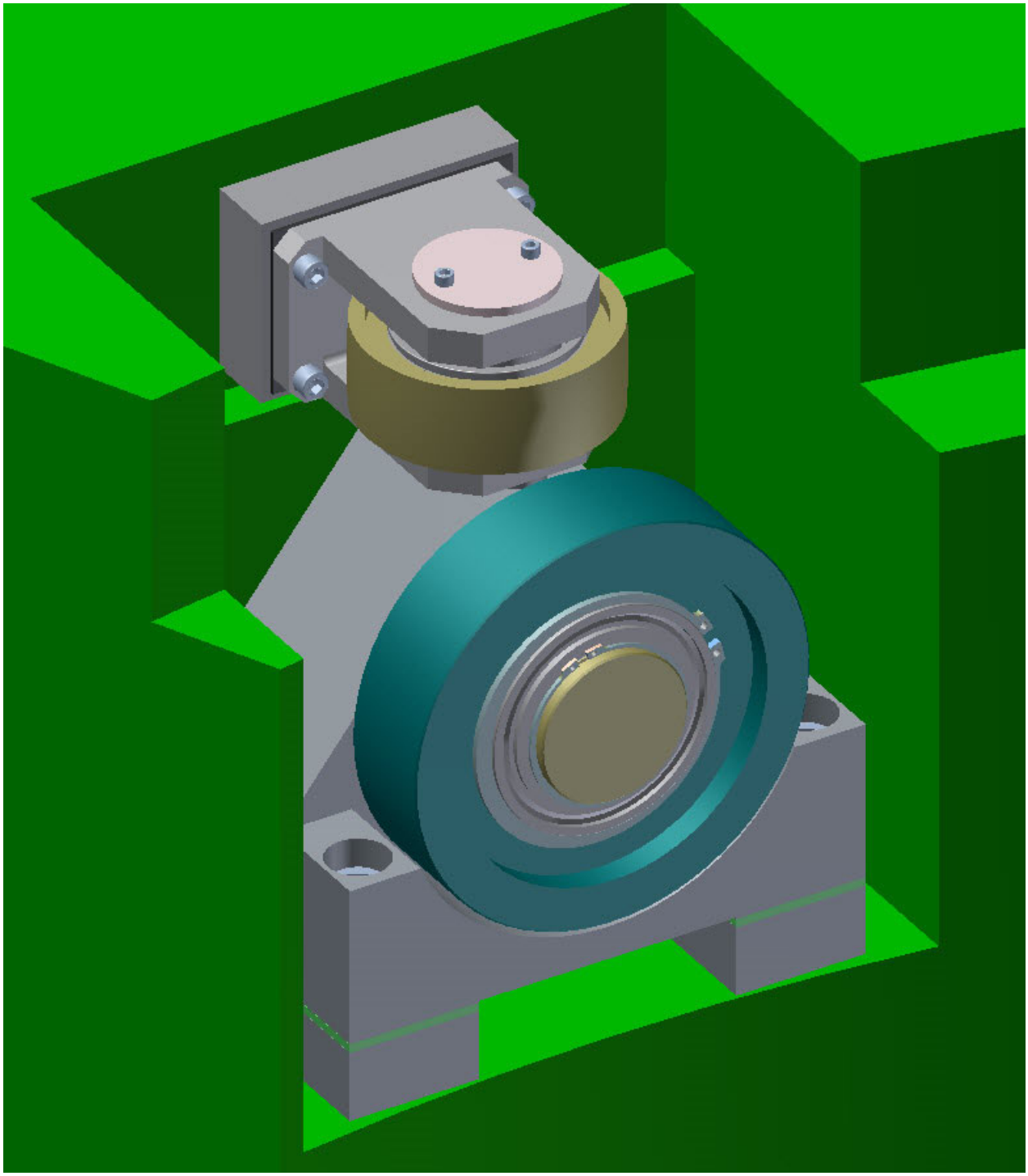

Figure VII.2.3.3. Detail of the RVC support roller (blue) and the guide roller (gold).

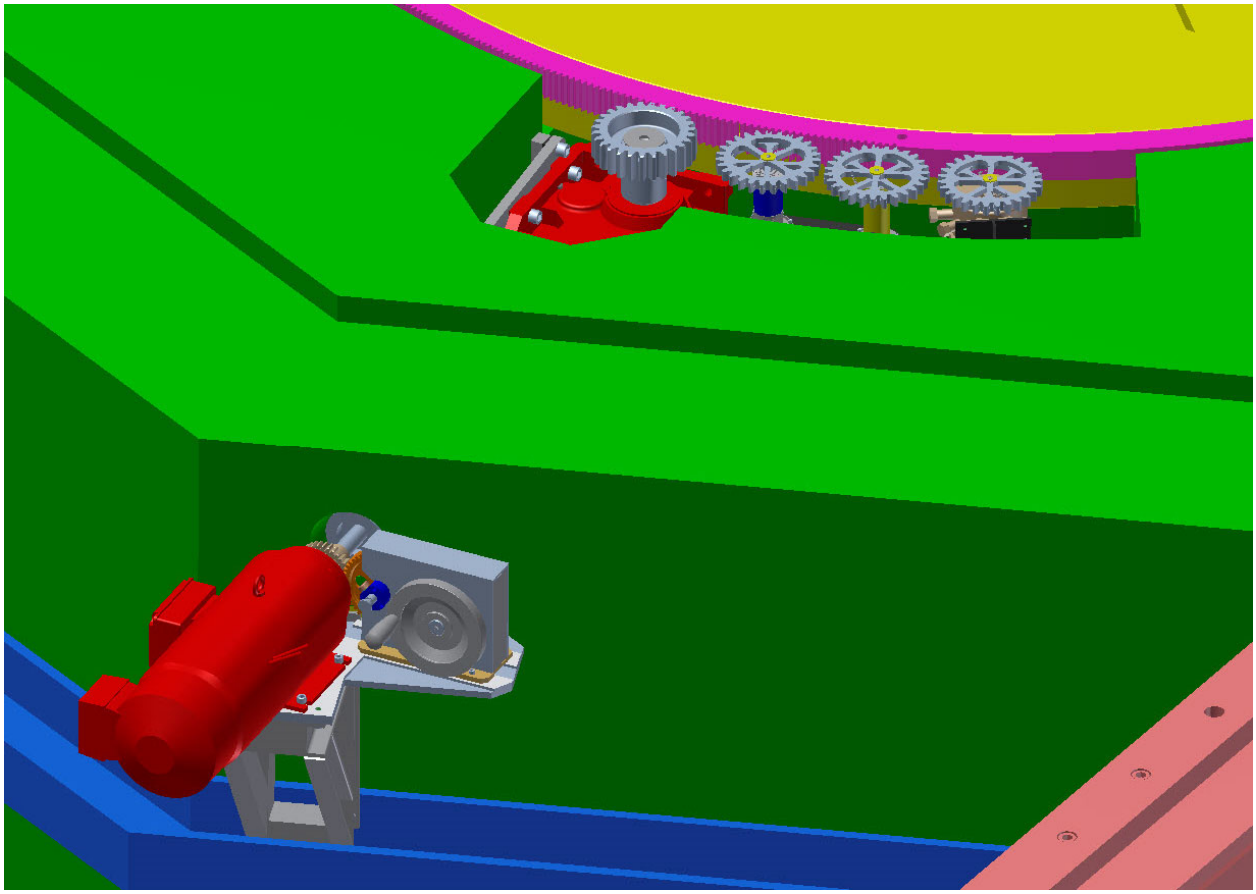

Figure VII.2.3.4. Detail view of rotating vessel cover drive motor, the gearbox, and the resolvers.

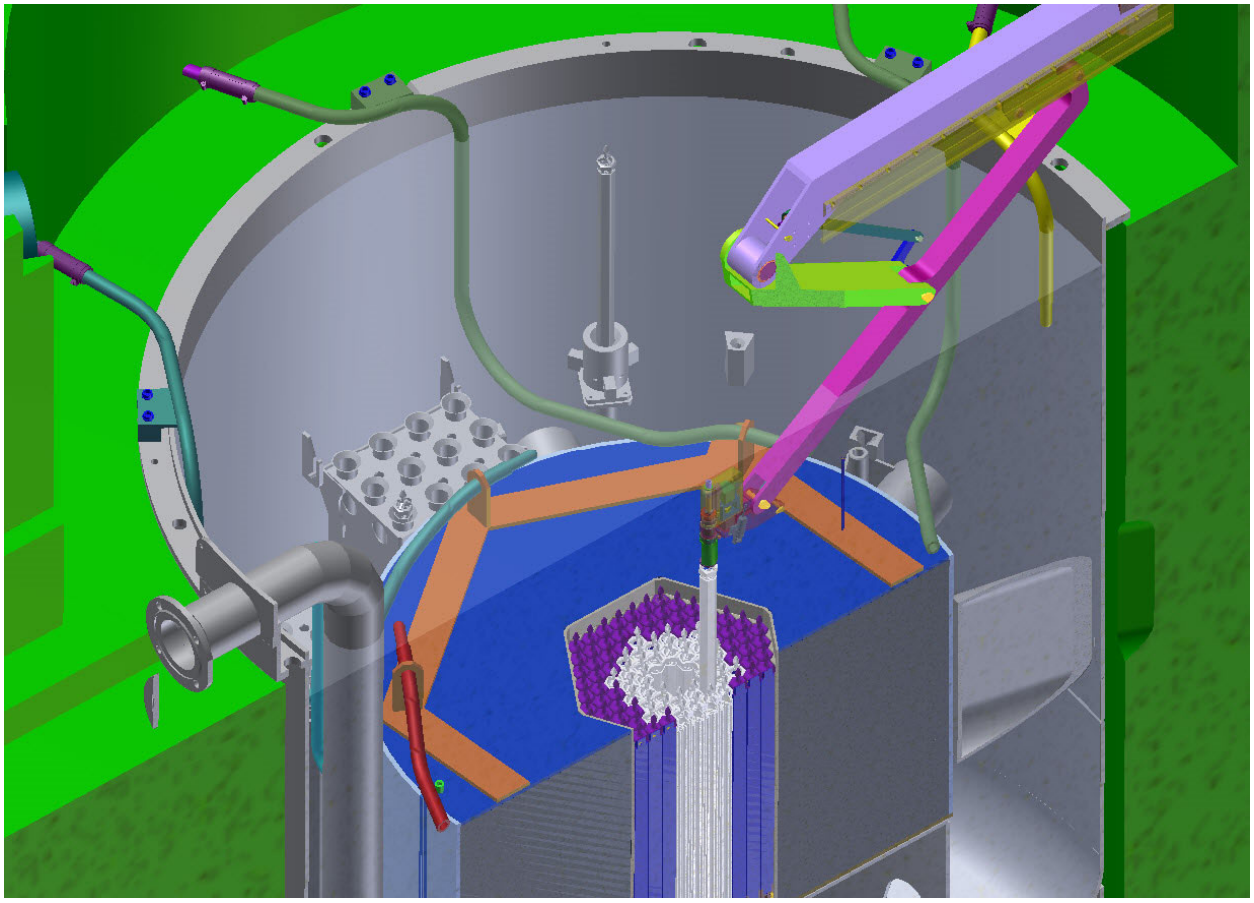

Figure VII.2.3.5. Section view through the SCA tank, showing the FHM arm, the subcritical assembly, the storage rack, the fuel transfer station, and the fuel orientation device.

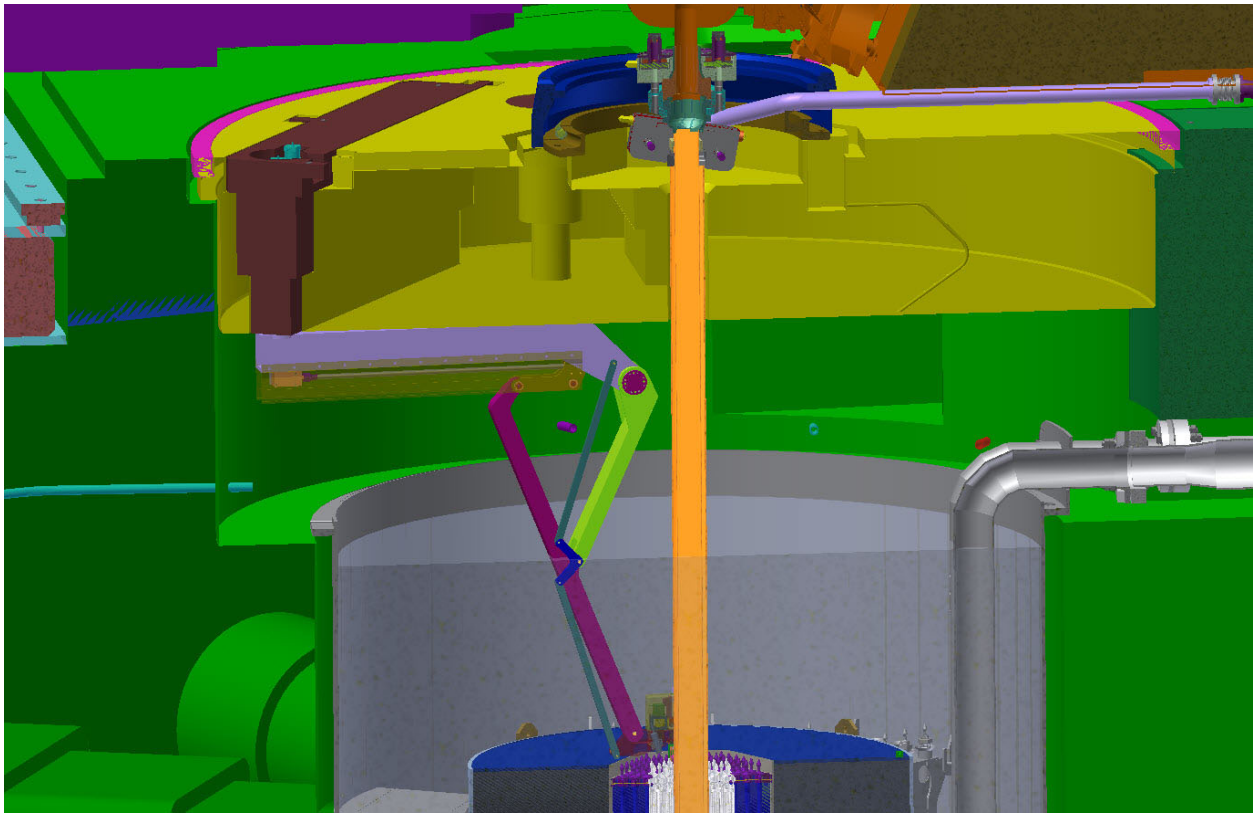

Figure VII.2.3.6. Section view through the rotating vessel cover (yellow) showing the FHM plug (dark red) and the FHM arm (light green and violet)

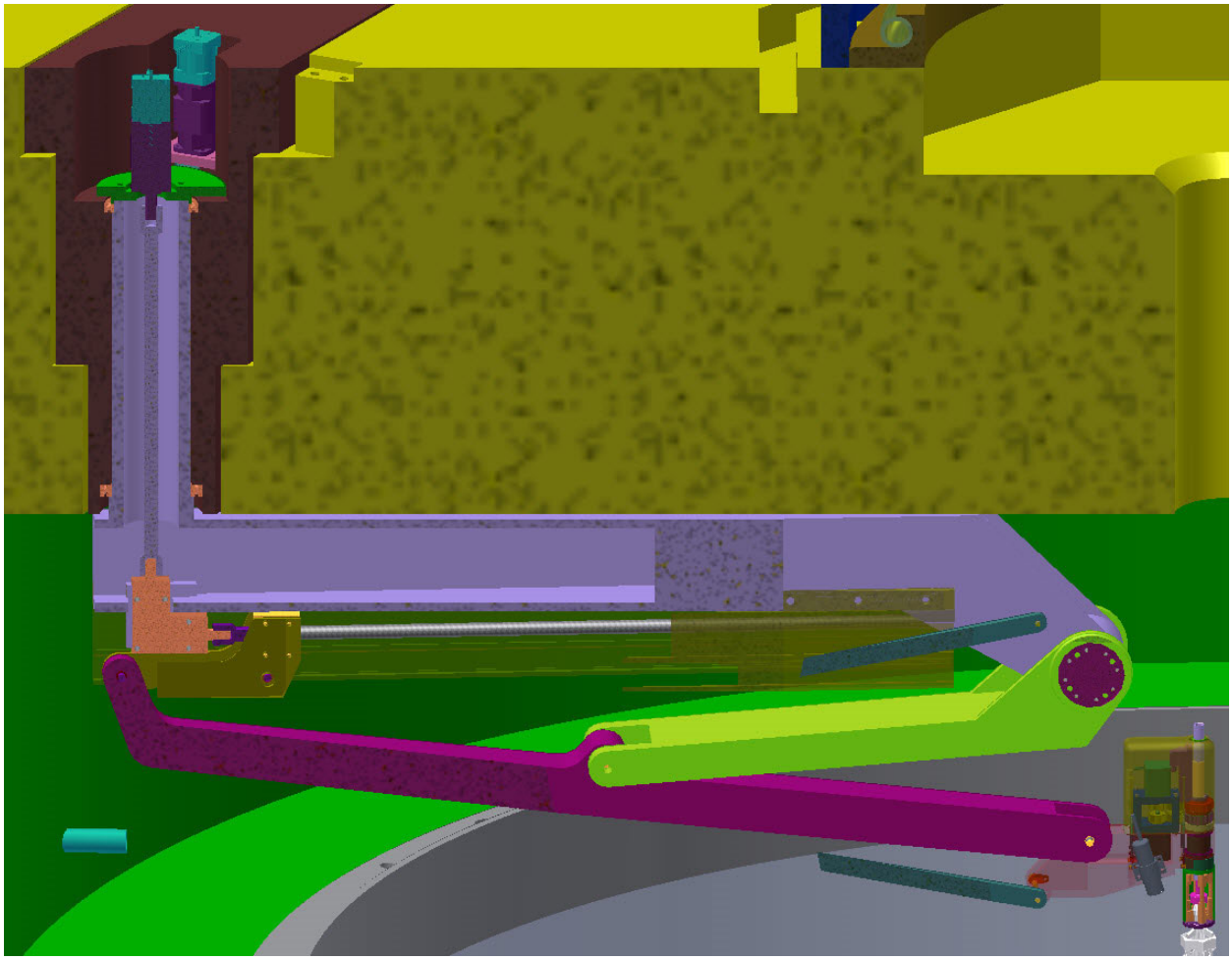

Figure VII.2.3.7. Oblique section view through FHM arm and FHM plug. The drive motors for swing and lift functions are visible in the FHM plug.

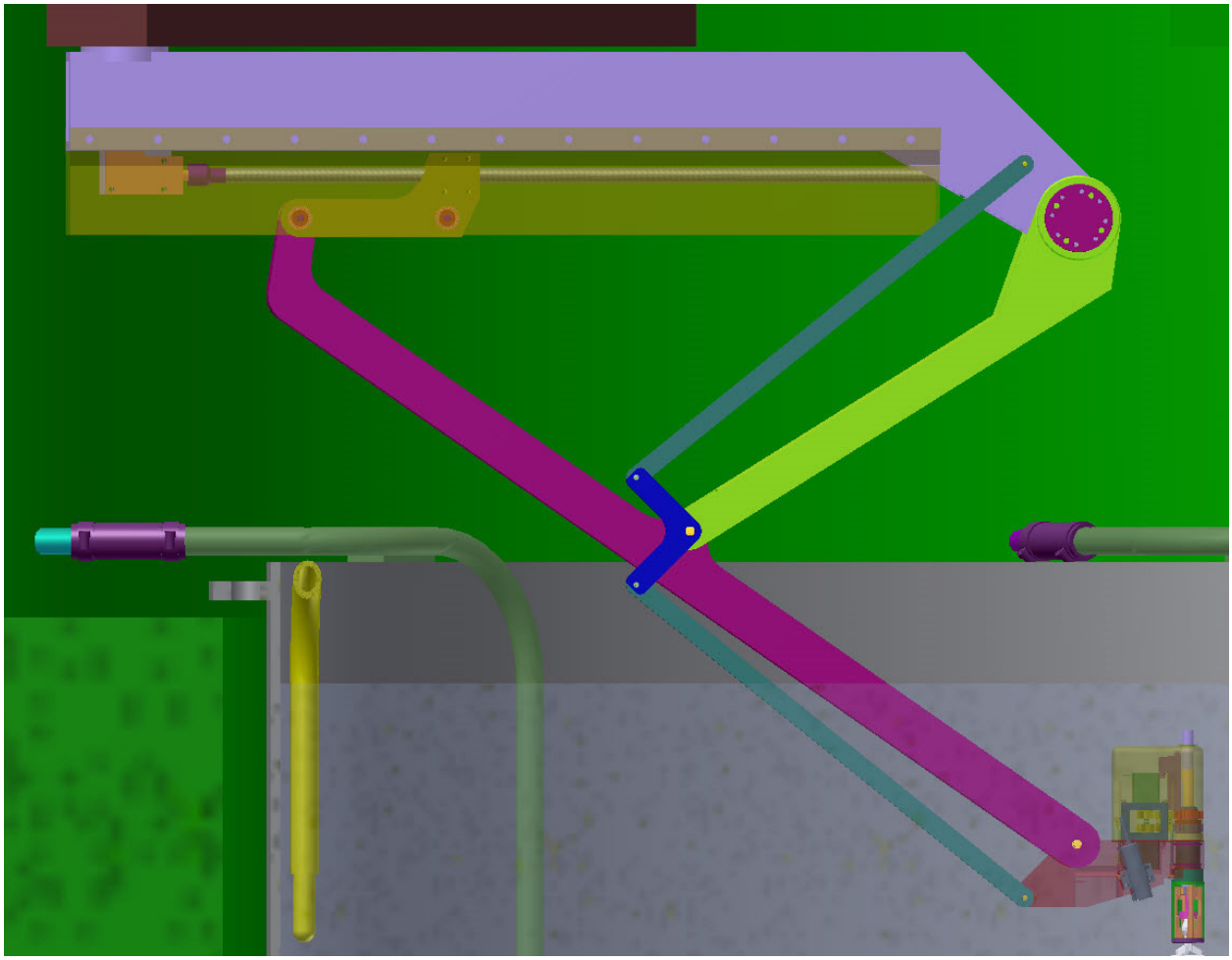

Figure VII.2.3.8. View of the FHM arm showing vertical lift mechanism and fuel gripper.

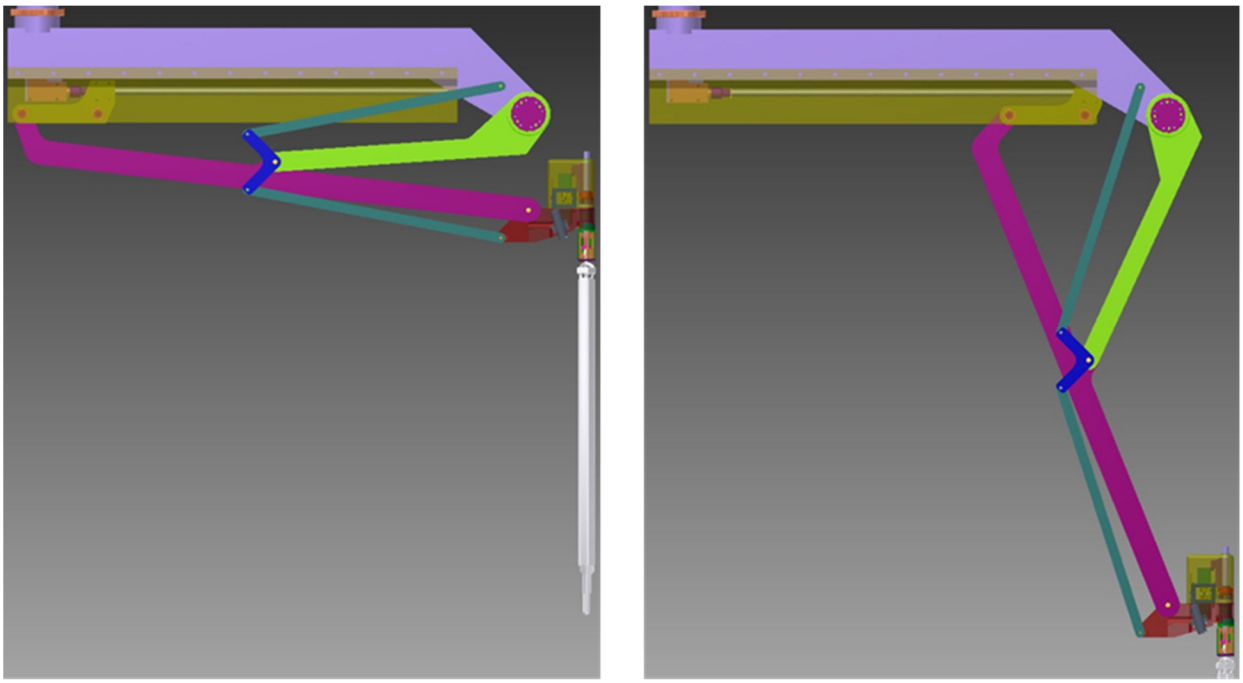

Figure VII.2.3.9. Vertical lift mechanism, shown the travel limits.

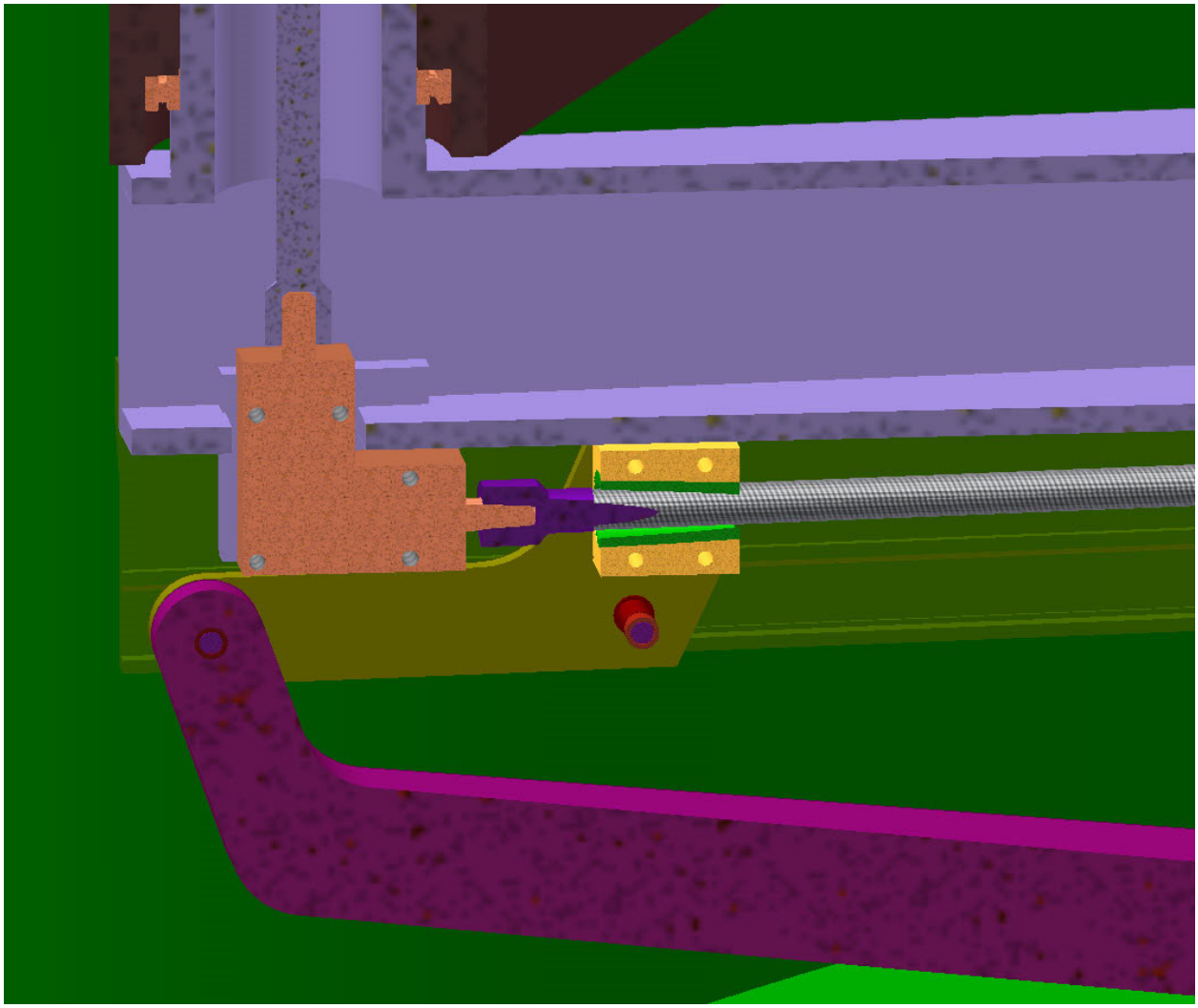

Figure VII.2.3.10. Section view of FHM arm showing the 90-degree gearbox, the ball screw, and the ball nut that provide vertical motion.

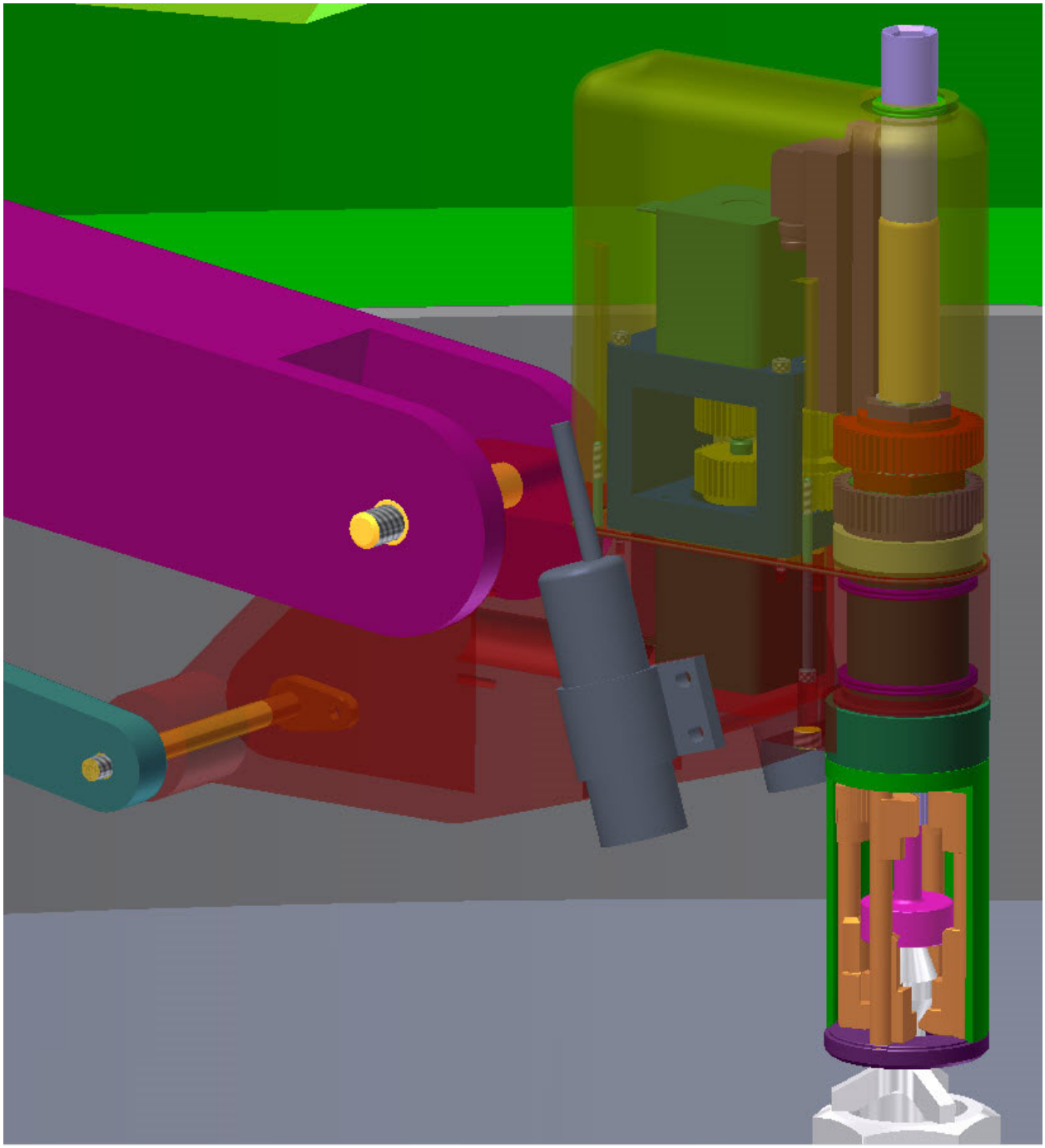

Figure VII.2.3.11. View of the fuel gripper showing the rotating jaws and the actuation motors.

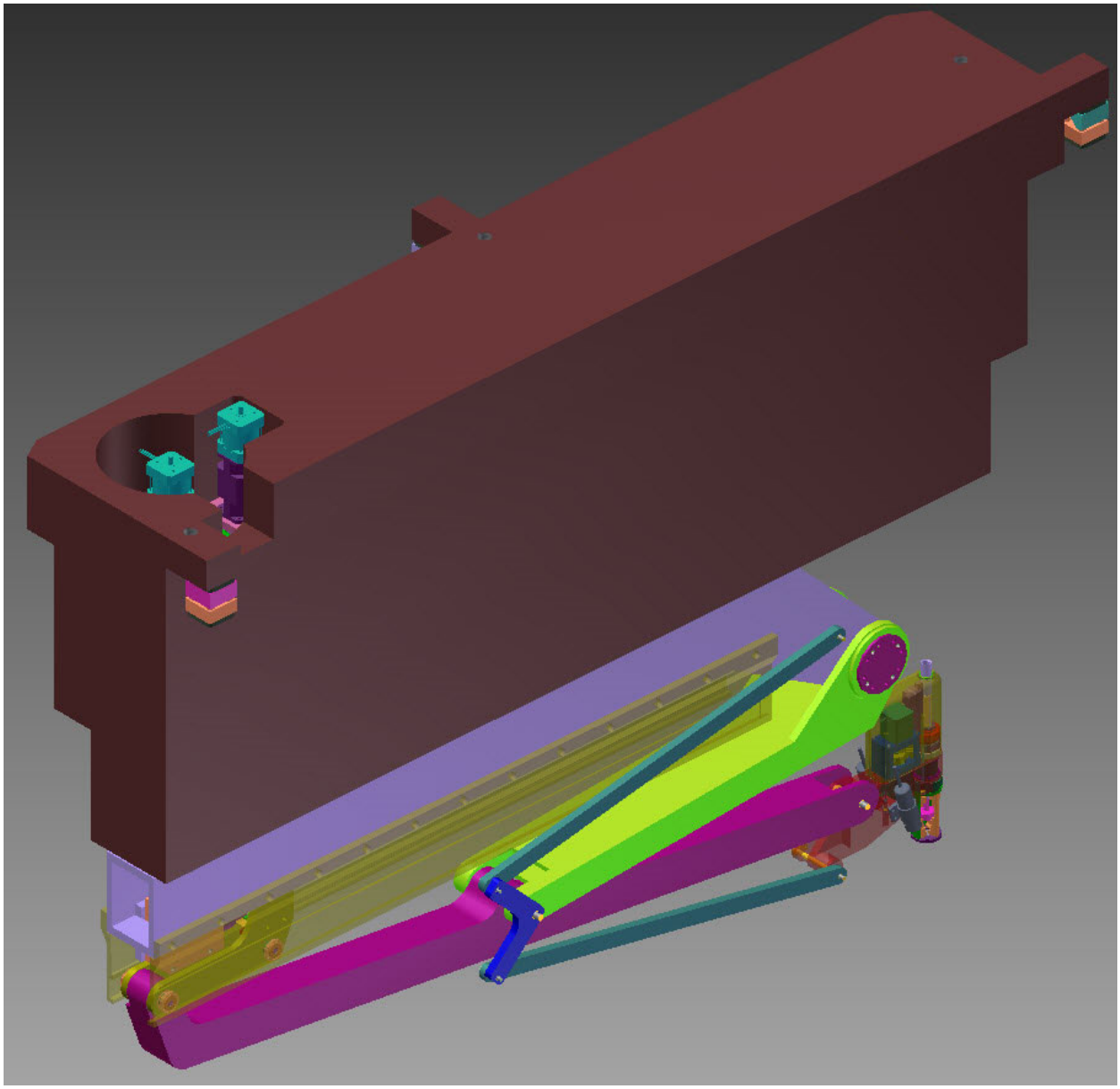

Figure VII.2.4.1. The FHM plug and the FHM arm, shown as it would be removed from the SCA for service work.

VIII Radioactive Isotope Production

VIII.1 Introduction

One of the design objectives of the neutron source facility (NSF) is to produce medical isotopes including Technetium-99. Therefore, the subcritical assembly design of the NSF permits loading different materials for irradiation at different locations to maximize their production rate. Medical isotopes are radioactive isotopes that are used for diagnostic and therapeutic applications in nuclear medicine [VIII.1-VIII.8]. The decay mode of radioactive isotopes may be α, β, ε (electron capture), or γ. The utilization of radioactive isotopes for medical purposes is classified into three categories: diagnosis, radiotherapy, and biochemical analyses. In diagnosis analyses, the short-lived isotopes are linked to chemical compounds that are administered to the patients by injection, inhalation, or ingestion. The radiation can be generated by either direct or indirect γ decay. The latter case occurs when a positron annihilates with an orbital electron, generating two gamma rays that propagate in opposite directions. The average dose for the patient is ~4.6 mSv while the natural background radiation level is ~2.4 mSv/y. In some areas of the world, background levels can reach as high as 150 mSv/y. A gamma or positron emission tomography (PET) camera using scintillation material interpolates the radiation source points and builds up an image of the patient organ to characterize its functionality. Software techniques construct three-dimensional images from two-dimensional images to provide diagnoses. ^{99m}Tc is used in ~80% of the nuclear medicine diagnosis procedures because of its ideal characteristics:

- Its half-life is six hours, which is long enough to examine metabolic processes and short enough to minimize radiation dose to the patient,
- The gamma ray energy is 140 keV,
- The emitted gamma rays escape the human body easily and reach the counting camera,
- It has versatile chemistry.

Another utilization of medical isotopes is the monitoring of the chemical compounds diffused in the body and absorbed by various organs. The radioactive isotopes are attached to the pharmaceutical substance and their activity is counted before the substance is administered to the patient. After administration, recounting the activity permits the examination of the blood flow in the brain or other organs such as: liver, lungs, heart, and kidneys. The functionality of different organs can be assessed after radioactive isotopes are expelled from the body by the normal biological processes.

In therapy applications, the gamma or beta emitter is located near or inserted inside the tumor mass with the aim of destroying the malignant cells. ^{60}Co was formerly used for external radiotherapy. Nowadays, brachytherapy (short-range) procedures have the benefit of giving a lower overall radiation dose to the body. The most common radioisotopes utilized for radiotherapy are ^{131}I for thyroid cancer; ^{192}Ir for head and breast

tumors; ^{89}Sr, ^{153}Sm and ^{186}Re for the relief of cancer-induced pain; ^{32}S for an excess of red blood cells produced by the bone marrow (Polycythemia vera); and ^{90}Y for non-Hodgkin's lymphoma. Iridium-192 is produced in a wire form that is introduced to the patient through a catheter that is removed after treatment. It is a gamma emitter and has a half-life of 74 days.

Table III of Ref. VIII.1 lists the major radioactive isotopes utilized in nuclear medicine with their decay mode and corresponding applications. The transmutation chains for producing the medical isotopes of Table III are summarized in Table IV of Ref. VIII.1, including the decay half-lives of the daughters and the abundance, the cross section, and the cumulative fission yield of the parents.

VIII.2 Computational Model for Activation Analysis

Reference VIII.1 discusses the medical isotopes production in the Kharkiv electron driven subcritical assembly. The calculations of this report update the analyses of Ref. VIII.1 using MCNPX [VIII.9] model of the facility and the more recent ENDF/B-VII.0 nuclear data library. Three irradiation positions in the subcritical assembly have been considered. The first position is next to the target, the third position is next to the beryllium reflector, and the second position lies in between the other two positions. Figures VIII.2.1-VIII.2.9 show different illustrations of the subcritical assembly (SCA) MCNPX model and the locations of the three irradiation positions. In Figures VIII.2.1-VIII.2.9, each color corresponds to a different material according to the following bullet list:

- orange fuel
- blue aluminum
- cyan water
- pink uranium target
- purple beryllium
- wheat graphite
- pale green concrete
- yellow/white air
- red molybdenum (irradiation sample)

The average flux in the three positions has been used to calculate more than forty different reaction rates by the tally multiplier option of MCNPX. This analysis aimed at selecting the isotopes that can be easily produced in the facility and the optimal position for their production.

In the calculations of Sections VIII.3.2-VIII.3.4, the neutron and the gamma fluxes have been averaged over a cylindrical volume with 0.75 cm radius and 10 cm height. Unless otherwise specified, the SCA has been loaded with 37 fuel assemblies and the (natural) material of the irradiation sample has not been modeled. In the calculations with self-shielding (Section VIII.3.4) the molybdenum material (Mo_2O_3 with 2 g/cm^3 density) has been modeled and the configurations with 37 and 38 fuel assemblies have been analyzed.

The configuration with 38 fuel assemblies uses a tungsten target instead of a uranium target. The aluminum holder of the irradiation sample has been modeled in all calculations.

The initial atomic density of the parent nuclide N_p^0 is given by equation 1, where d_{nat} is the natural mass density (g/cm^3) of the parent material, A is Avogadro's number, f is the natural abundance of the parent nuclide in the parent material, and W is the atomic weight of the parent material.

$$N_p^0 = \frac{d_{nat} \cdot A \cdot f}{W} \qquad 1)$$

The atomic density N of each of the daughter nuclides (medical isotopes) has been calculated by equation 2b below, which solves equation set 2a below. In these equations, λ is the decay constant of the daughter nuclide, N_p is the density of the parent nuclide, and $\sigma_p\Phi$ is the parent reaction rate. The latter parameter has been obtained by multiplying the reaction rate per source particle (electron), obtained from the MCNPX calculations, by the number of electrons per second, obtained by assuming 100 kW beam power and 100 MeV electron energy, in Ref. VIII.1 the electron energy is assumed to be 200 MeV. The standard deviation of the MCNPX reaction rates is generally lower than 1.4%; for (n,2n) reactions the standard deviation increases up to 4.5%. In all analyses, the daughter reaction rate $\sigma\Phi$ has been neglected due to its low value relative to the decay constant, medical isotopes have short half-life.

$$\begin{cases} \dfrac{dN}{dt} = -(\lambda + \sigma\Phi)N + \sigma_p N_p \Phi \\ \dfrac{dN_p}{dt} = -\sigma_p N_p \Phi \end{cases} \qquad 2a)$$

$$N(t) = \sigma_p \Phi N_p^0 \frac{e^{-\sigma_p \Phi t} - e^{-(\lambda+\sigma\Phi)t}}{\lambda + \sigma\Phi - \sigma_p \Phi} \qquad 2b)$$

When daughter nuclides are generated by a grandparent with density N_{gp}, and a parent with density N_p, the atomic densities have been calculated using equations 3b below, which solve equation set 3a below. The solution determined by solving equations 3b applies both to the case of a stable parent, by setting λ_p equal to zero, and to the case of a decaying parent, by setting N_p^0 equal to zero, as the case of ^{47}Sc and ^{188}W production.

$$\begin{cases} \dfrac{dN}{dt} = -(\lambda + \sigma\Phi)N + \sigma_p N_p \Phi \\ \dfrac{dN_p}{dt} = -(\lambda_p + \sigma_p \Phi)\cdot N_p + \sigma_{gp} N_{gp} \Phi \\ \dfrac{dN_{gp}}{dt} = -\sigma_{gp} N_{gp} \Phi \end{cases} \qquad 3a)$$

$$\begin{cases} N = \sigma_p \Phi N_p^0 \dfrac{e^{-(\lambda_p+\sigma_p\Phi)t} - e^{-(\lambda+\sigma\Phi)t}}{\lambda + \sigma\Phi - \lambda_p - \sigma_p\Phi} + \dfrac{\sigma_p \Phi N_{gp}^0 \sigma_{gp}\Phi}{\lambda_p + \sigma_p\Phi - \sigma_{gp}\Phi}\left[\dfrac{e^{-\sigma_{gp}\Phi t} - e^{-(\lambda+\sigma\Phi)t}}{\lambda + \sigma\Phi - \sigma_{gp}\Phi} - \dfrac{e^{-(\lambda_p+\sigma_p\Phi)t} - e^{-(\lambda+\sigma\Phi)t}}{\lambda + \sigma\Phi - \lambda_p - \sigma_p\Phi}\right] \\ N_p = N_p^0 e^{-(\lambda_p+\sigma_p\Phi)t} + \sigma_{gp}\Phi N_{gp}^0 \dfrac{e^{-\sigma_{gp}\Phi t} - e^{-(\lambda_p+\sigma_p\Phi)t}}{\lambda_p + \sigma_p\Phi - \sigma_{gp}\Phi} \\ N_{gp} = N_{gp}^0 e^{-\sigma_{gp}\Phi t} \end{cases} \qquad 3b)$$

Once the atomic densities are calculated by the previous formulas, the specific activity evaluation can be performed using Eq. 4,

$$\text{specific activity} = \frac{\lambda N}{d_{nat}} \qquad 4)$$

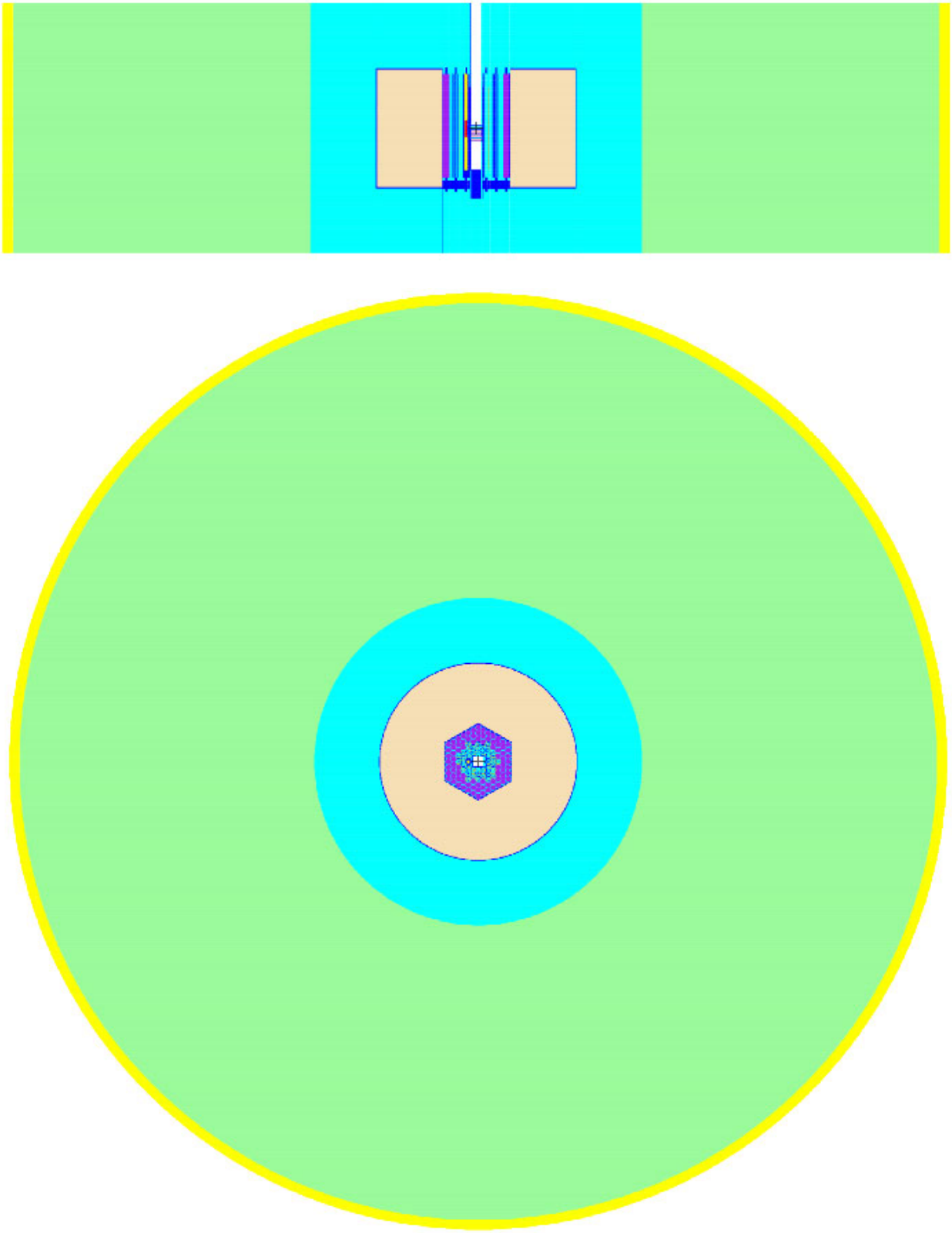

Figure 01. Vertical (top plot) and horizontal (bottom plot) section of SCA; configuration with 37 fuel assemblies; and irradiation sample cassette in position 1

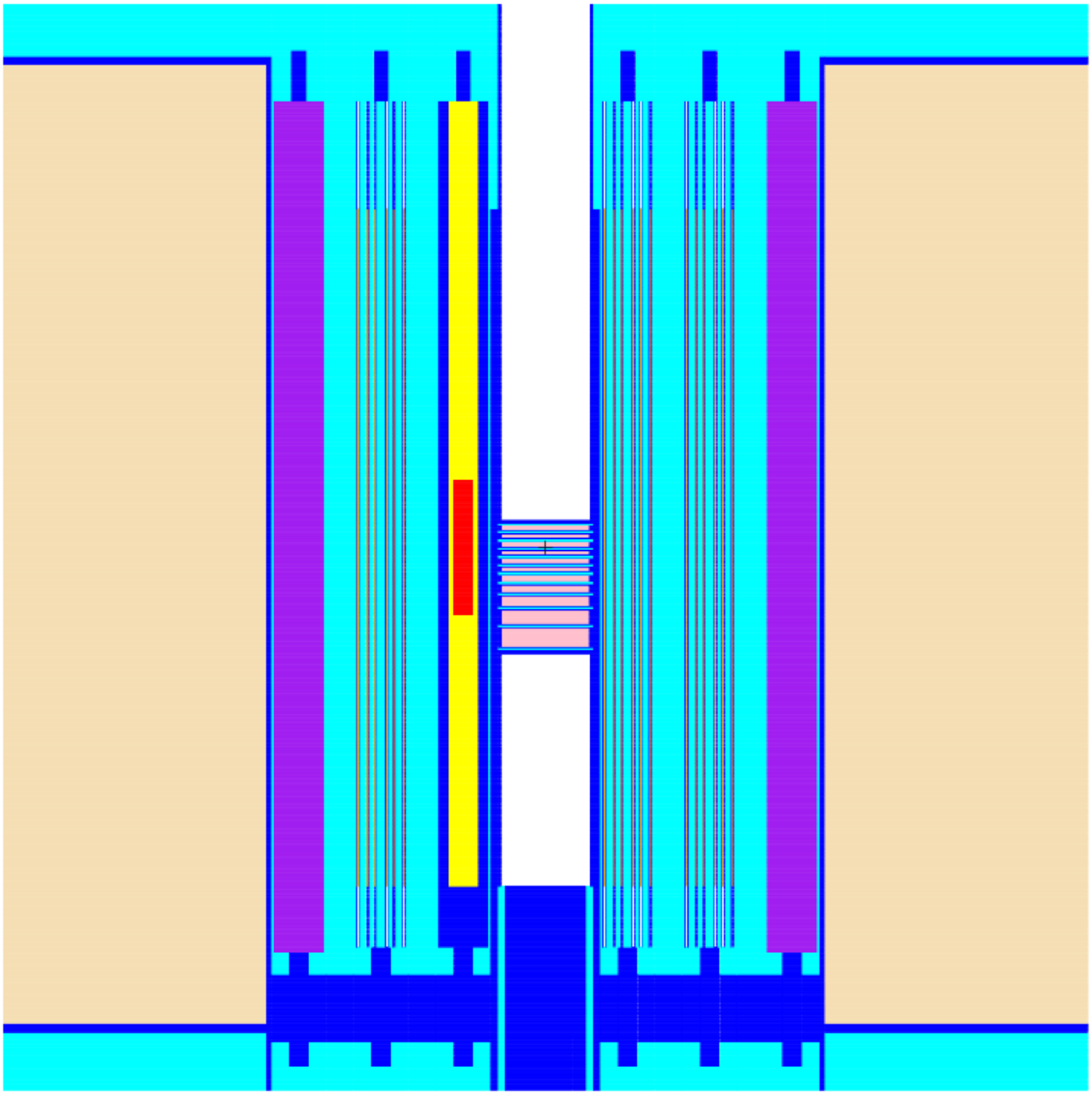

Figure 02. Vertical section of the fuel zone of the SCA; configuration with 37 fuel assemblies; irradiation sample cassette in position 1

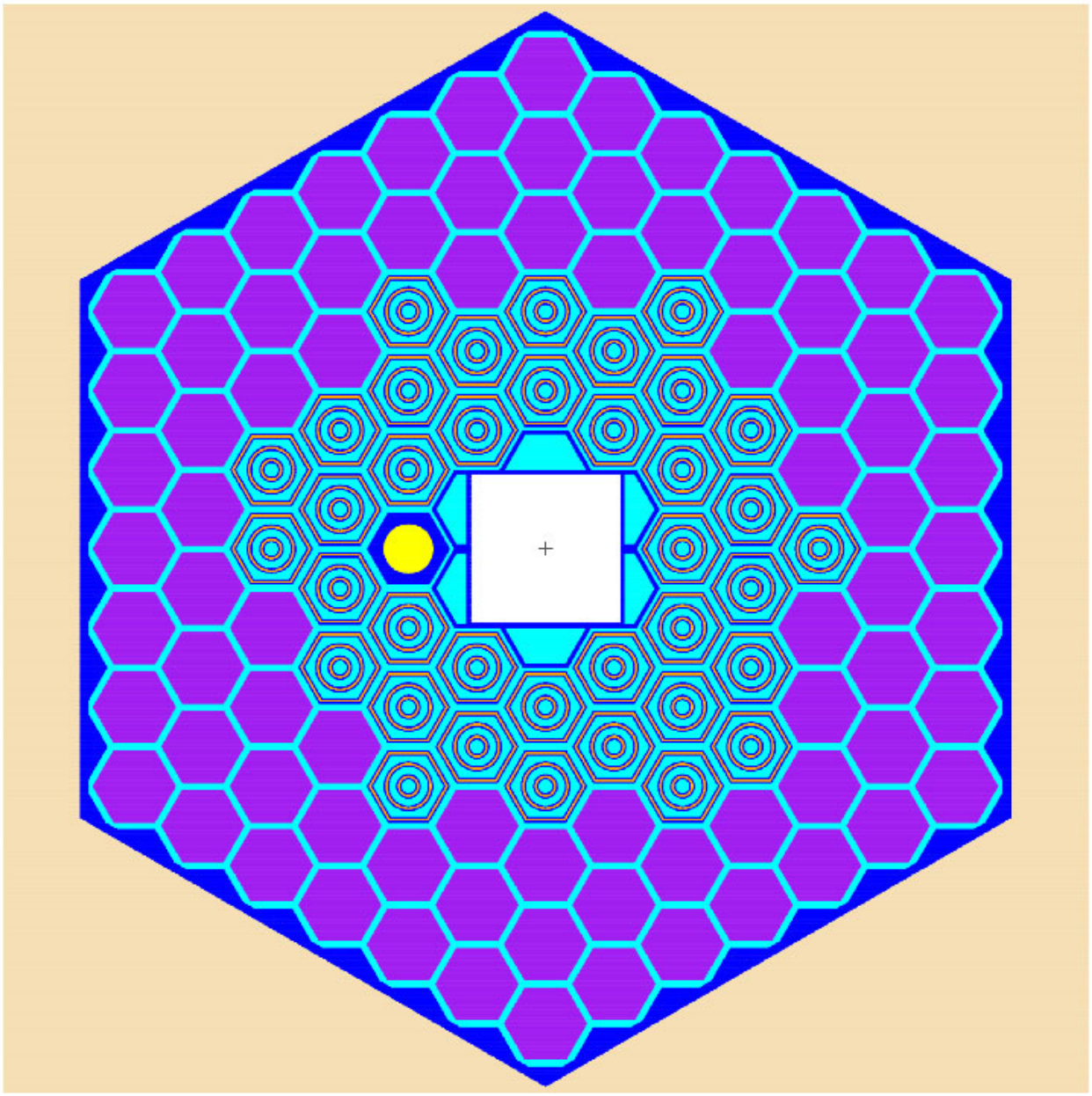

Figure 03. Horizontal section of the fuel zone of the SCA; configuration with 37 fuel assemblies; irradiation sample cassette in position 1

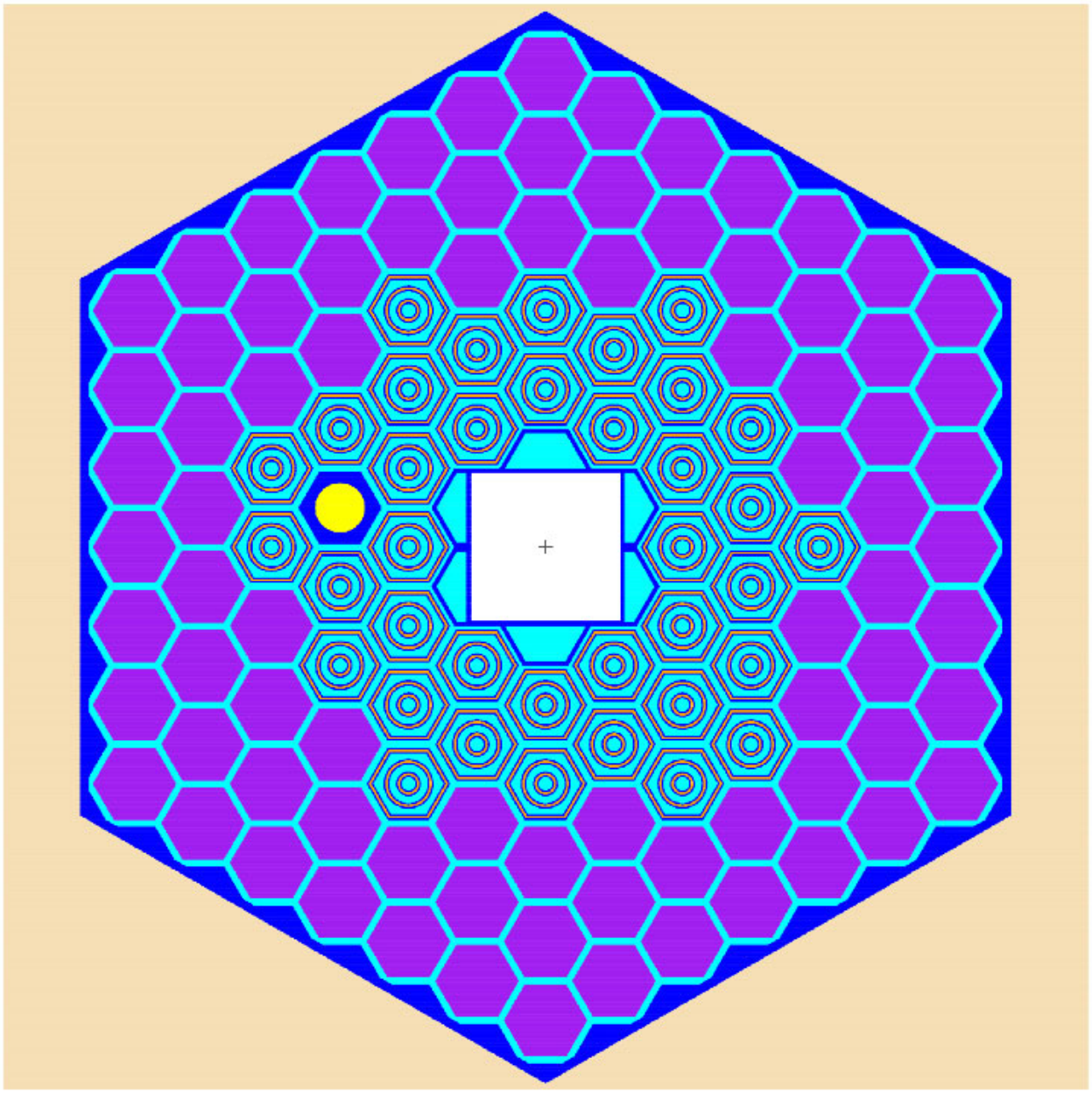

Figure 04. Horizontal section of the fuel zone of the SCA; configuration with 37 fuel assemblies; irradiation sample cassette in position 2

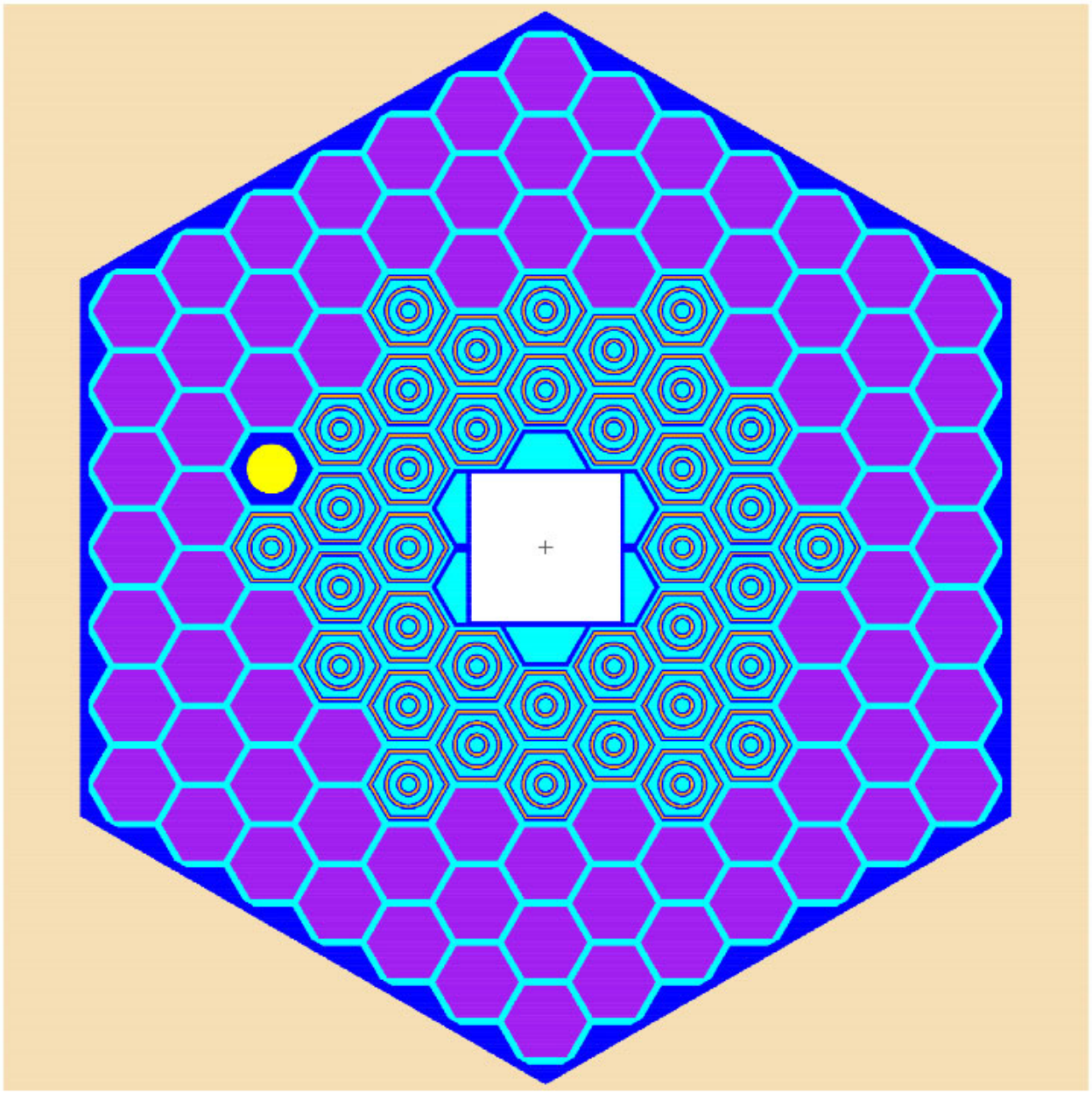

Figure 05. Horizontal section of the fuel zone of the SCA; configuration with 37 fuel assemblies; irradiation sample cassette in position 3

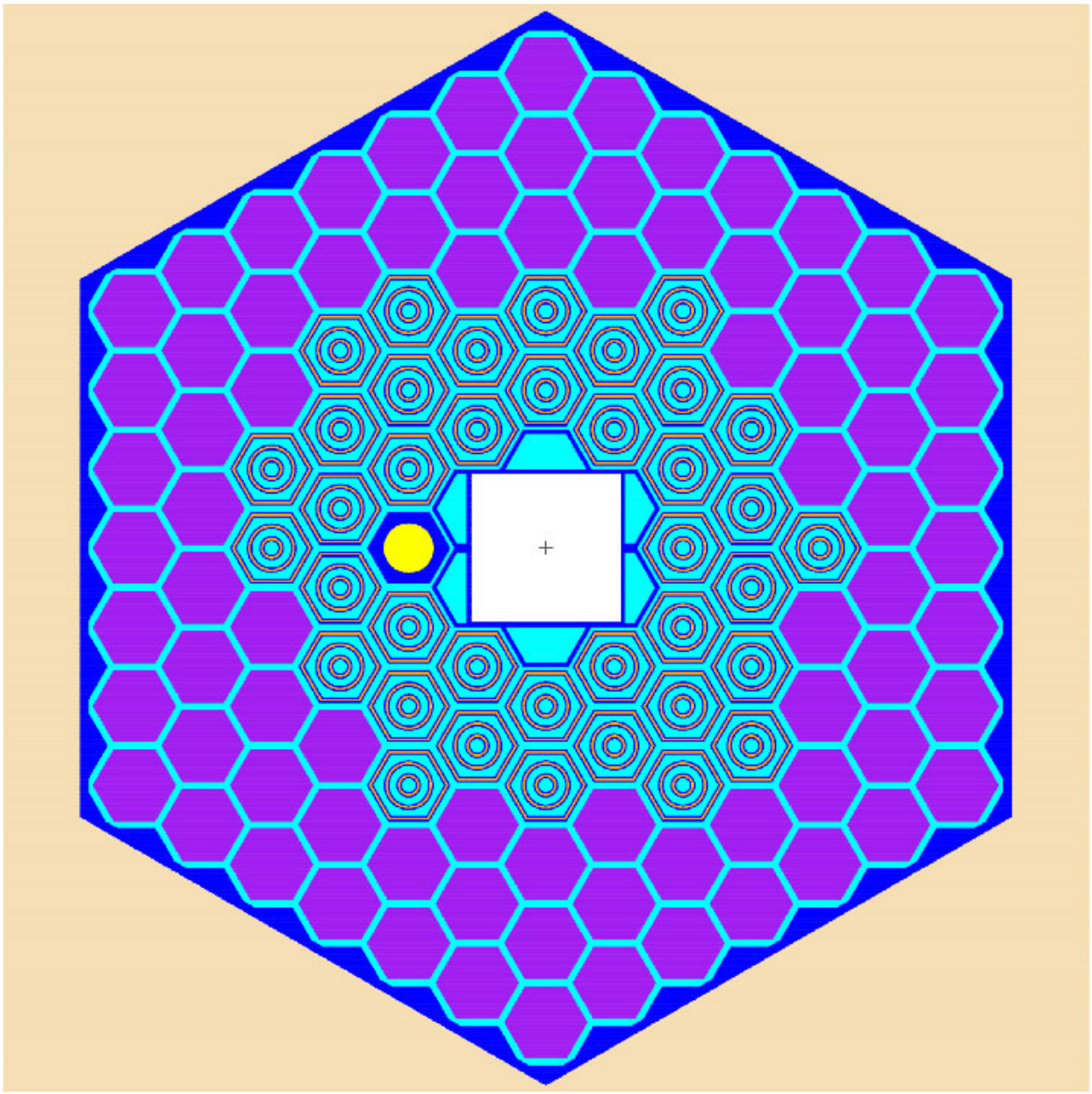

Figure 06. Horizontal section of the fuel zone of the SCA; configuration with 38 fuel assemblies; irradiation sample cassette in position 1

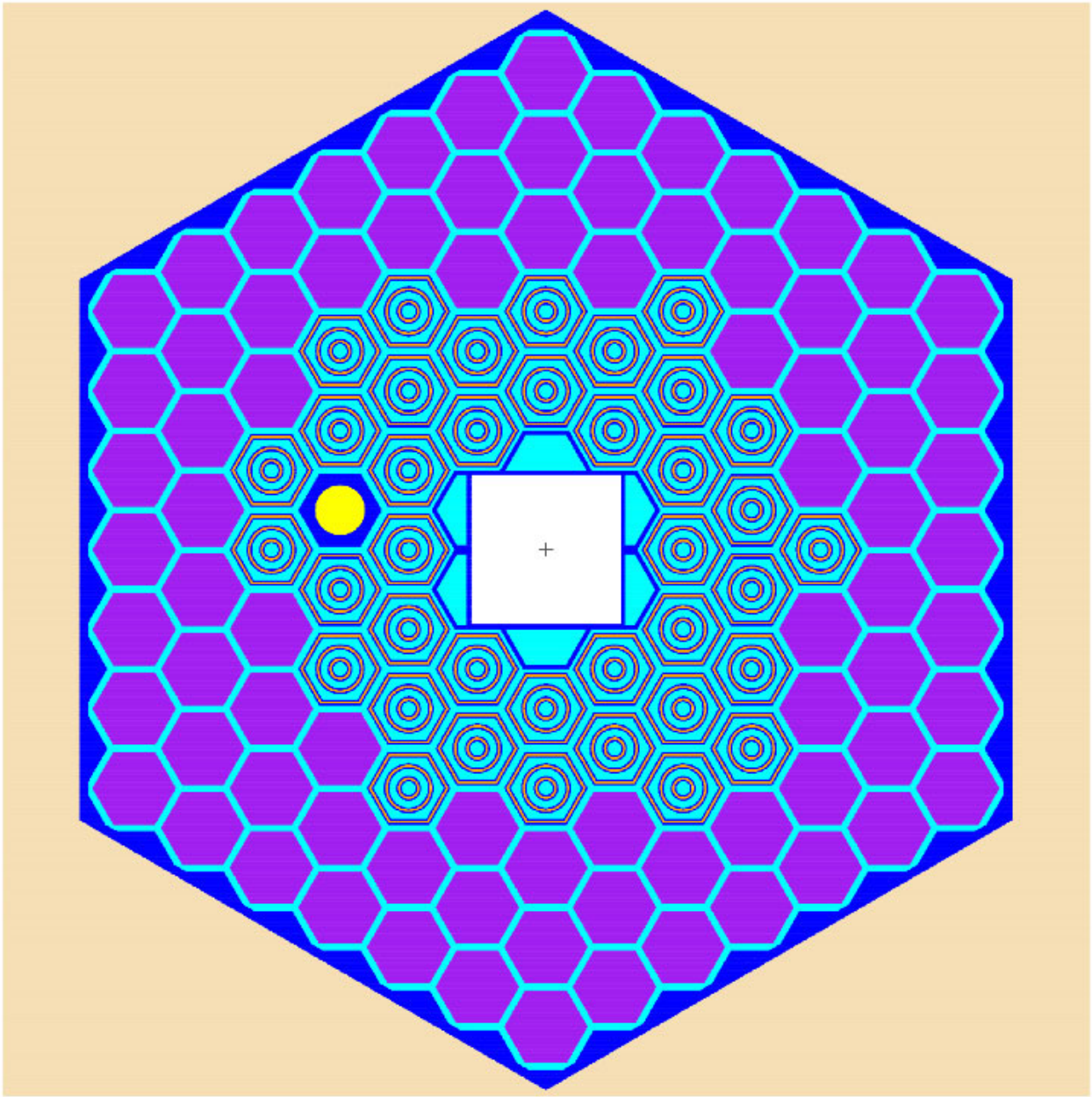

Figure 07. Horizontal section of the fuel zone of the SCA; configuration with 38 fuel assemblies; irradiation sample in position 2

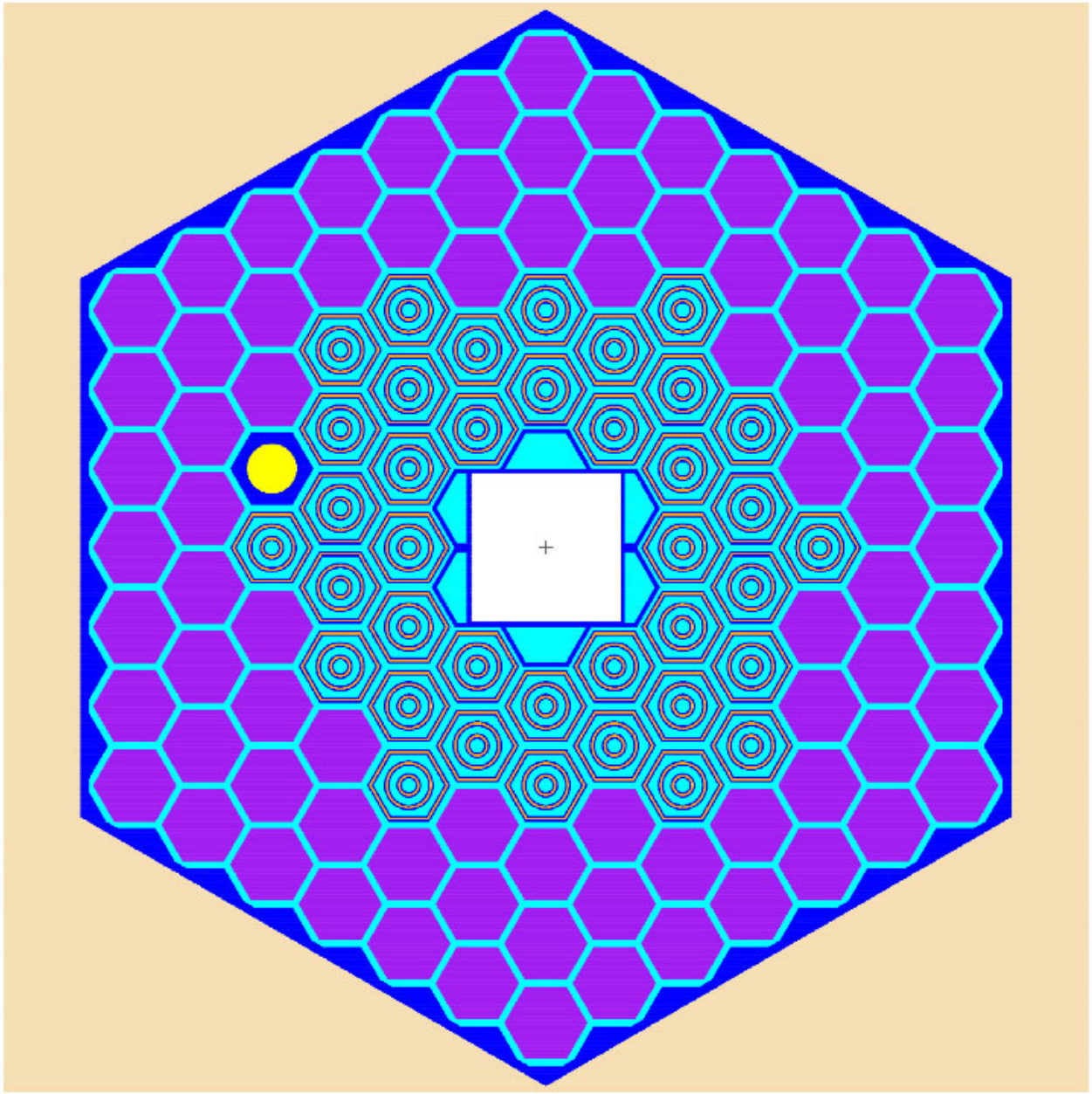

Figure 08. Horizontal section of the fuel zone of the SCA; configuration with 38 fuel assemblies; irradiation sample in position 3

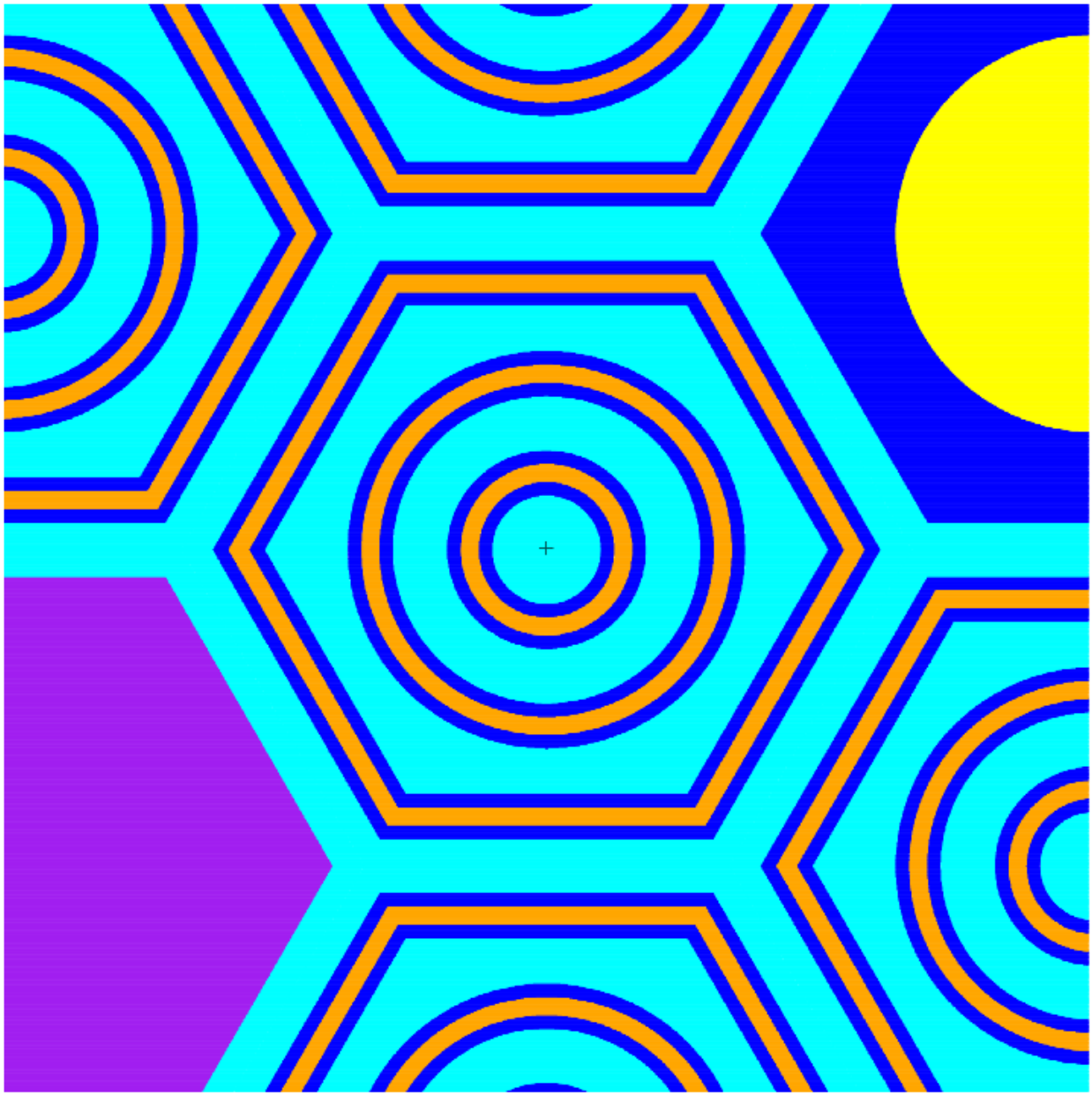

Figure 09. Close-up of the horizontal section of the fuel zone of the SCA, irradiation sample in position 2

VIII.3 Activation Analysis Results

VIII.3.1 Effective Multiplication Factor

Table VIII.3.1.1 summarizes the MCNPX effective multiplication factor, k_{eff}, obtained without modeling the external (electron) source for different fuel configurations and nuclear data libraries. The impact of these two parameters on the k_{eff} value is small, less than 110 pcm. The insertion of the molybdenum oxide irradiation sample, a cylinder with 0.75 cm radius and 10 cm height, has negligible effect on the neutron multiplication. The configuration using the tungsten target, loaded with 38 fuel assemblies, has a significantly lower multiplication factor than the configuration using the uranium target, loaded with 37 fuel assemblies.

VIII.3.2 Neutron and Photon Spectra

The neutron and photon spectra in the three irradiation positions are shown in Figs. VIII.3.2.1 and VIII.3.2.2, respectively. The fluxes have been normalized first to unity and then to lethargy. Irradiation position 3, next to the beryllium reflector, has the largest thermal neutron flux and the lowest fast neutron flux compared to the other two positions. However, at this position the total neutron flux is lower (1.7 neutrons/cm^{2}·s), than at the other two positions (where the neutron flux is 1.96 and 1.88 neutrons/cm^{2}·s).

The photon spectrum has a smooth profile, as expected from the Bremsstrahlung effect, with the exception of some isolated peaks caused by (n,γ) reactions. The 0.64, 2.2, and 7.7 MeV peaks are caused by the (n,γ) reaction with ^{235}U, water, and aluminum, respectively. The ^{238}U neutron capture reaction generates 0.01 MeV gamma rays [VIII.10].

VIII.3.3 Specific Activities of Radioactive Isotopes without Self-Shielding

Figures VIII.3.3.1-VIII.3.3.32 show the specific activities for the medical isotopes produced by incident neutron reactions. After 20 irradiation days: ^{82}Br, ^{64}Cu, ^{165}Dy, ^{166}Ho, ^{192}Ir, ^{194}Ir, ^{186}Re, ^{188}Re and ^{153}Sm have specific activities larger than 100 MBq/mg; ^{60}Co, ^{51}Cr, ^{159}Gd, ^{24}Na, ^{32}P (via (n,γ)), and ^{90}Y have specific activities between 10 and 100 MBq/mg; ^{111}Ag, ^{125}I, ^{42}K, ^{99}Mo, ^{32}P (via (n,p)), and ^{133}Xe (via (n,γ)) have specific activities between 1 and 10 MBq/mg; ^{58}Co, ^{59}Fe, ^{33}P, ^{103}Pd, ^{35}S, ^{47}Sc, ^{188}W and ^{133}Xe (via (n,2n) and (n,p)) have specific activities < 1 MBq/mg. Table VIII.3.3.1 reports the best positions for generating each isotope; these values may change if self-shielding is included [VIII.1 and VIII.2]; see Sec. VIII.3.5 below for more details. In general, the results show that isotopes generated through large thermal cross sections are better produced in the third position, next to the beryllium reflector, because this location has the highest thermal neutron fraction of the three locations where samples are irradiated. Isotopes generated through resonances or by threshold reactions are better produced in the first position, next to the target, because this location has the highest epithermal and fast neutron fractions.

Figures VIII.3.3.33-VIII.3.3.41 illustrate the specific activities of the medical isotopes that are produced by ^{235}U fission reactions. In this case, the parent material is 20% enriched metallic uranium. The third irradiation position, next to the beryllium reflector, maximizes the fission reaction rate because of the large thermal fission cross section of the ^{235}U

isotope. After 20 irradiation days: ^{131}I, ^{99}Mo, ^{89}Sr, and ^{133}Xe have specific activities higher than 10 MBq/mg; ^{111}Ag, ^{77}As, ^{137}Cs, ^{129}I and ^{90}Sr have specific activities lower than 1 MBq/mg. All these activities without the consideration of the self-shielding. These values are much lower if the self-shielding is taken into consideration as shown in the next section.

The specific activities of the medical isotopes generated through photonuclear reactions are small [VIII.1] and therefore they have not been investigated in the present study. All the specific activities obtained in the present study are lower than those obtained in Ref. VIII.1 because the electron energy has been reduced from 200 to 100 MeV in the final design configuration of the SCA.

VIII.3.4 Specific Activity of ^{99}Mo with Self-Shielding

The self-shielding effect can considerably affect the results obtained in Section VIII.3.3; this is clearly exemplified by the ^{99}Mo production. Figures VIII.3.4.1 and VIII.3.4.2 show the specific activity of ^{99}Mo obtained by (n,γ) and (γ,n) reactions after modeling the parent material (molybdenum oxide M_2O_3) in the irradiation sample. The values obtained by the (n,γ) reactions with self-shielding in Figure VIII.3.4.1 are much lower, about a factor 9, than those obtained without self-shielding in Figure VIII.3.3.16. The specific activities of ^{99}Mo obtained by the ^{100}Mo(γ,n) reaction in Figure VIII.3.4.2 are 40 times smaller than those obtained by the ^{98}Mo(n,γ) reaction in Figure VIII.3.4.1. The configuration using 37 fuel assemblies with a uranium target produces higher specific activities. The specific activities of ^{99}Mo is more than 0.7 MBq/mg after 12 days of irradiation time from ^{98}Mo(n,γ) reaction. The insertion of the molybdenum oxide irradiation sample, a cylinder with a 0.75 cm radius and 10 cm height, has a negligible effect on the effective multiplication factor, as shown in Table VIII.3.1.1.

If the 6-day Curie concept is used with Fig. VIII.3.4.1 assuming 10 days irradiation time; one day for processing, extracting, and shipping; and six days for the utilization. The generated ^{99}Mo activity is about 0.673 MBq/mg. Assuming 90% efficiency for the ^{99}Mo sample processing and extraction, the obtained activity is 0.53 Ci/sample. If the sample length is increased from 10 cm to 25 cm, half the active fuel length, the obtained activity is 1.33 Ci/sample. Assuming the total time for the processing, the extraction, and the shipping is one day, and the sample activity is utilized during the six days after shipping. Then, the number of the medical heart procedures is 14 per sample, assuming 87.5% utilization efficiency. The subcritical assembly has the capacity to load 6 samples in the first position or 8 samples in the second position, which can generate enough ^{99}Tc for 84 or 112 heart medical procedures every 10 days. About 12.5 mCi is required per medical heart procedure [VIII.11]. As shown in Table VIII.3.1.1, the impact of the Mo neutron absorption on the subcritical assembly reactivity is negligible, about 20 pcm per sample.

VIII.3.5 Specific Activity of ^{60}Co, ^{64}Cu, ^{159}Gd, ^{166}Ho, ^{192}Ir, ^{194}Ir, ^{186}Re, ^{188}Re, ^{153}Sm, and ^{188}W with Self-Shielding

This section discusses additional computer simulations for evaluating the self-shielding effect in the irradiation samples made of strong absorbers. In these simulations, four cylindrical irradiation samples have been simultaneously loaded into the assembly. Each irradiation sample has a 0.1 cm radius and 10 cm height. The holder of the irradiation samples has been placed in position 1, 2, or 3. Cobalt, copper, gadolinium, and holmium irradiation samples have been placed in locations A, B, C, and D, respectively, as illustrated in Figs. VIII.3.5.1 and VIII.3.5.2. In other simulations, the previously listed materials have been replaced by iridium, rhenium, samarium, and tungsten, respectively. Figures VIII.3.5.3 to VIII.3.5.12 show the specific activity of ^{60}Co, ^{64}Cu, ^{159}Gd, ^{166}Ho, ^{192}Ir, ^{194}Ir, ^{186}Re, ^{188}Re, ^{153}Sm, and ^{188}W, respectively, as a function of the irradiation time. For the previously listed isotopes, the self-shielding effect reduces the specific activity by a factor of 1.9, 1.4, 2.8, 2.3, 7.3, 8.0, 4.1, 2.6, 13.3, and 4.5, respectively. Obviously, the self-shielding effect is proportional to the magnitude of the absorption cross section of the irradiation sample. The highest specific activity occurs at position 3 for all isotopes, except for ^{159}Gd and ^{153}Sm; for these two nuclides, position 1 produces the highest specific activity because the irradiation samples are placed in location C. When the holder of the irradiation sample is placed at position 1, location C is next to the fuel assemblies (Fig. VIII.3.5.1); when the holder of the irradiation sample is placed at position 3, location C is next to the reflector blocks (Fig. VIII.3.5.2). The configuration using 37 fuel assemblies with a uranium target produces higher specific activities, relative to the configuration using 38 fuel assemblies, because it has a higher neutron multiplication as shown in Table VIII.3.1.1. The insertion of the irradiation samples may lower the effective multiplication factor by 200 pcm as shown in Table VIII.3.1.1.

Table VIII.3.1.1. Effective multiplication factor obtained by MCNPX criticality calculations. The standard deviation is less than 6 pcm.

Number of fuel assemblies – ENDF/B version	Irradiation Sample	Position of the Irradiation Sample		
		1	2	3
37 – VII.0	-	0.97094	0.97207	0.97138
37– VII.1	-	0.96948	0.97061	0.96991
38 – VII.0	Mo	0.95229	0.95339	0.95269
38 – VII.0	-	0.95254	-	-
38 – VII.1	Mo	0.95112	0.95214	0.95148
38 – VII.1	-	0.95133	-	-
37 – VII.0	Co Cu Gd Ho	0.96952	0.97078	0.97018
37 – VII.0	Ir Re Sm W	0.96868	0.97003	0.96949
38 – VII.0	Co Cu Gd Ho	0.95146	0.95230	0.95160
38 – VII.0	Ir Re Sm W	0.95059	0.95163	0.95078

Table VIII.3.3.1. Best position of the irradiation sample

Medical Isotope	Position Number	Medical Isotope	Position Number
^{111}Ag	1	^{24}Na	3
^{82}Br	1	^{32}P via (n,γ)	3
^{58}Co via (n,2n)	1	^{32}P via (n,p)	1
^{58}Co via (n,p)	1	^{33}P	1
^{60}Co	3	^{103}Pd via (n,γ)	3
^{51}Cr	3	^{103}Pd via (n,2n)	1
^{64}Cu	3	^{186}Re	3
^{165}Dy	3	^{188}Re	3
^{59}Fe	3	^{35}S	3
^{159}Gd	1	^{47}Sc	3
^{166}Ho	3	^{153}Sm	3
^{125}I	1	^{188}W	1
^{192}Ir	3	^{133}Xe via (n,γ)	1-2-3
^{194}Ir	3	^{133}Xe via (n,2n)	1
^{42}K	3	^{133}Xe via (n,p)	1
^{99}Mo	1	^{90}Y	3

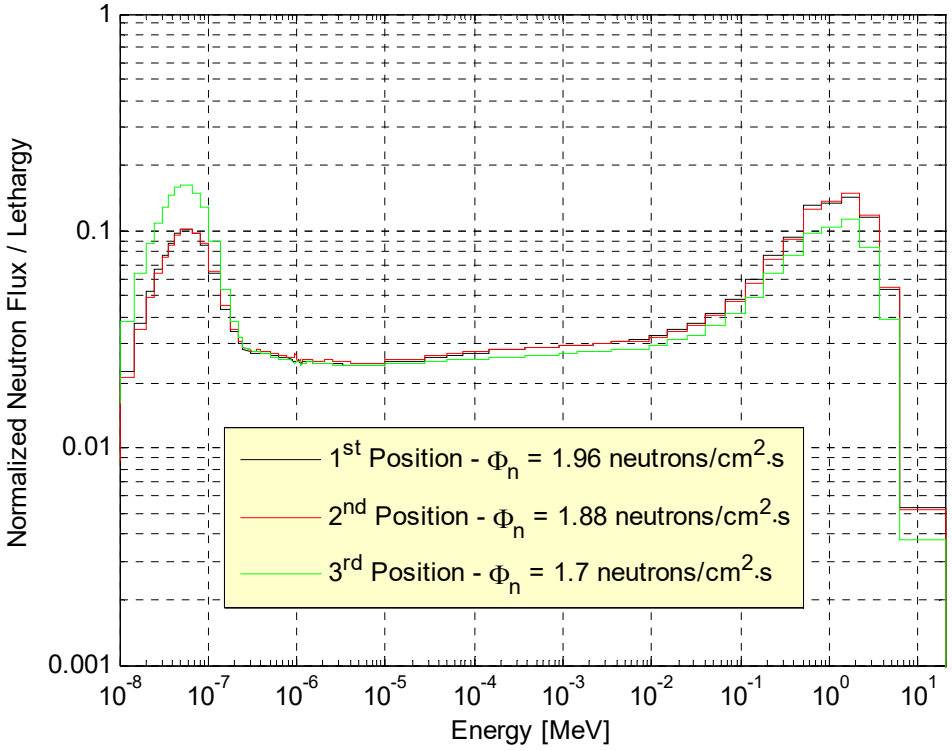

Figure VIII.3.2.1. Neutron spectrum in the different irradiation positions

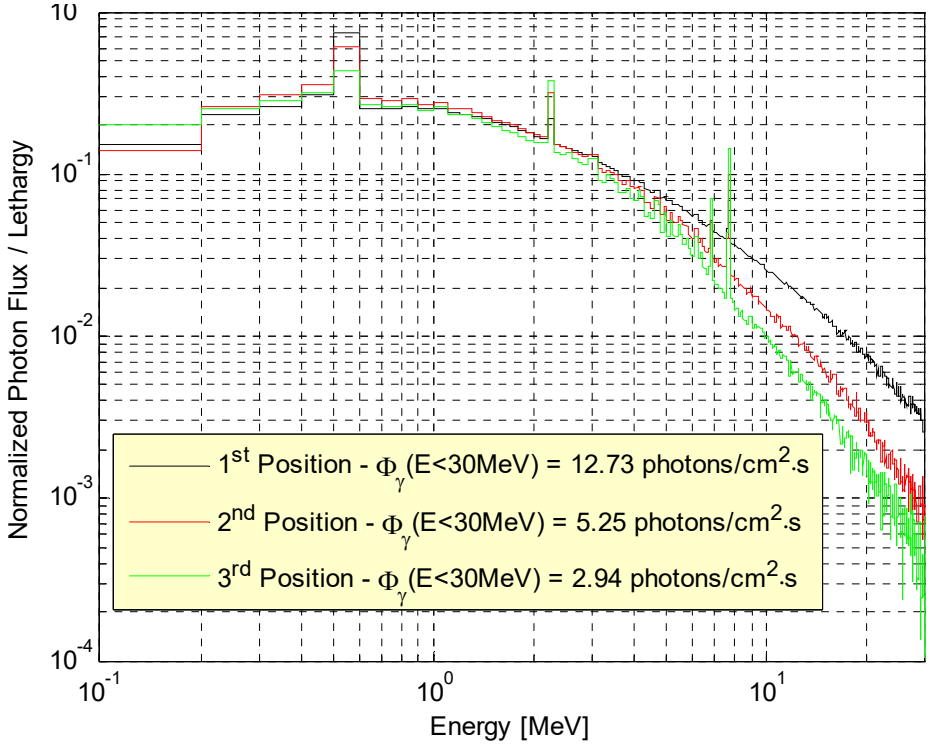

Figure VIII.3.2.2. Photon spectrum in the different irradiation positions

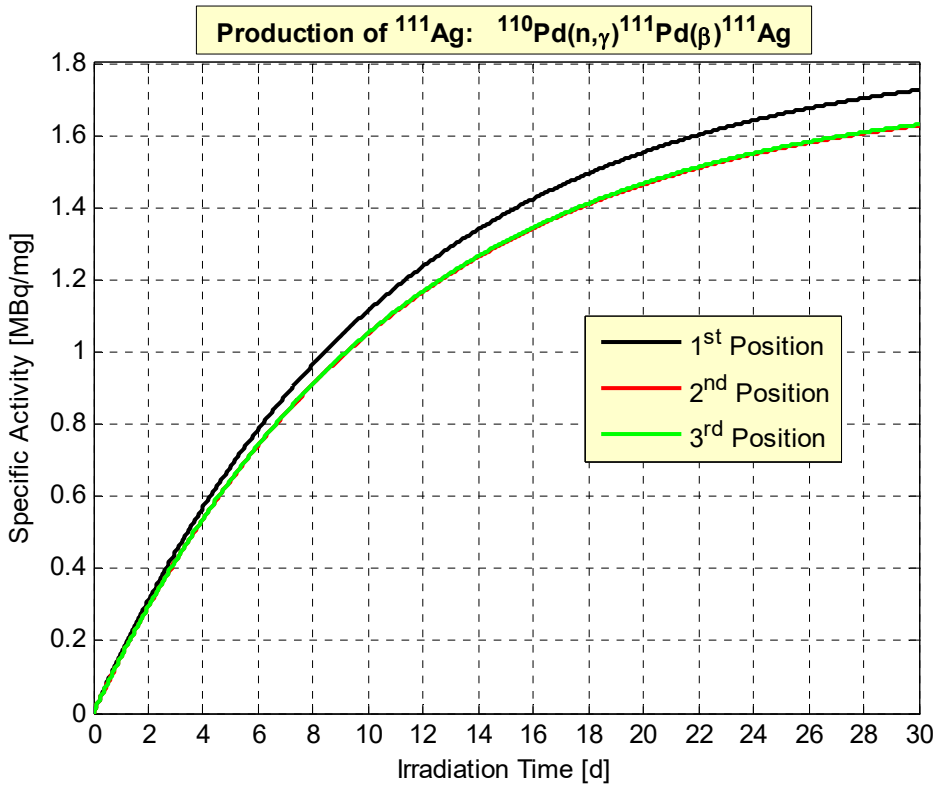

Figure VIII.3.3.1. ^{111}Ag activity as a function of the irradiation time

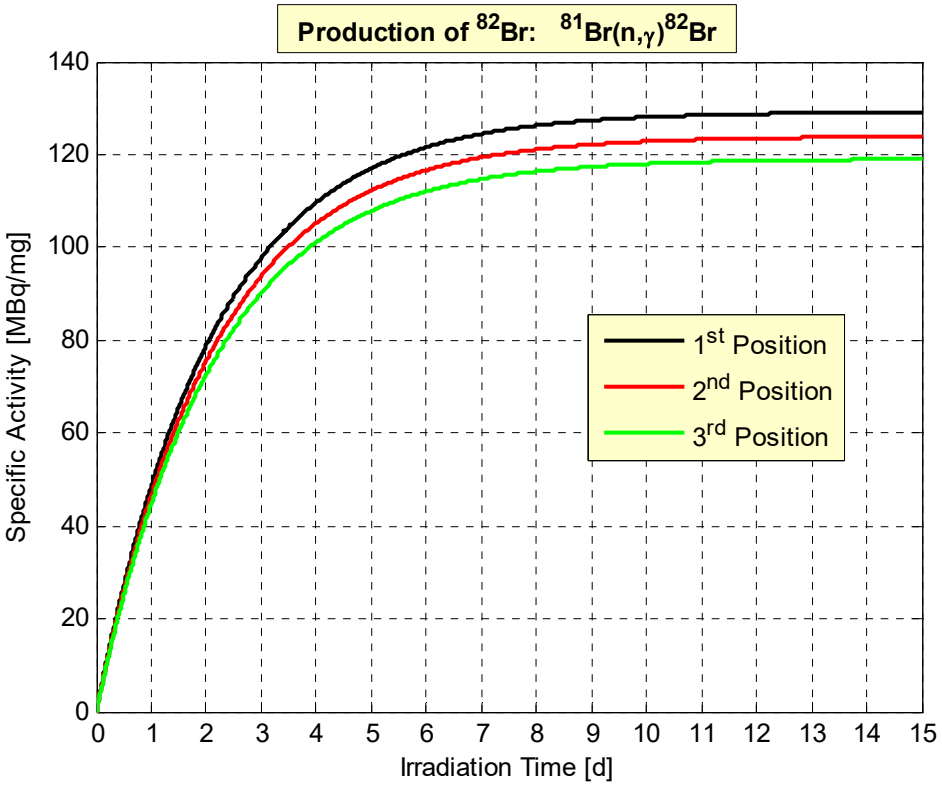

Figure VIII.3.3.2. ^{82}Br activity as a function of the irradiation time

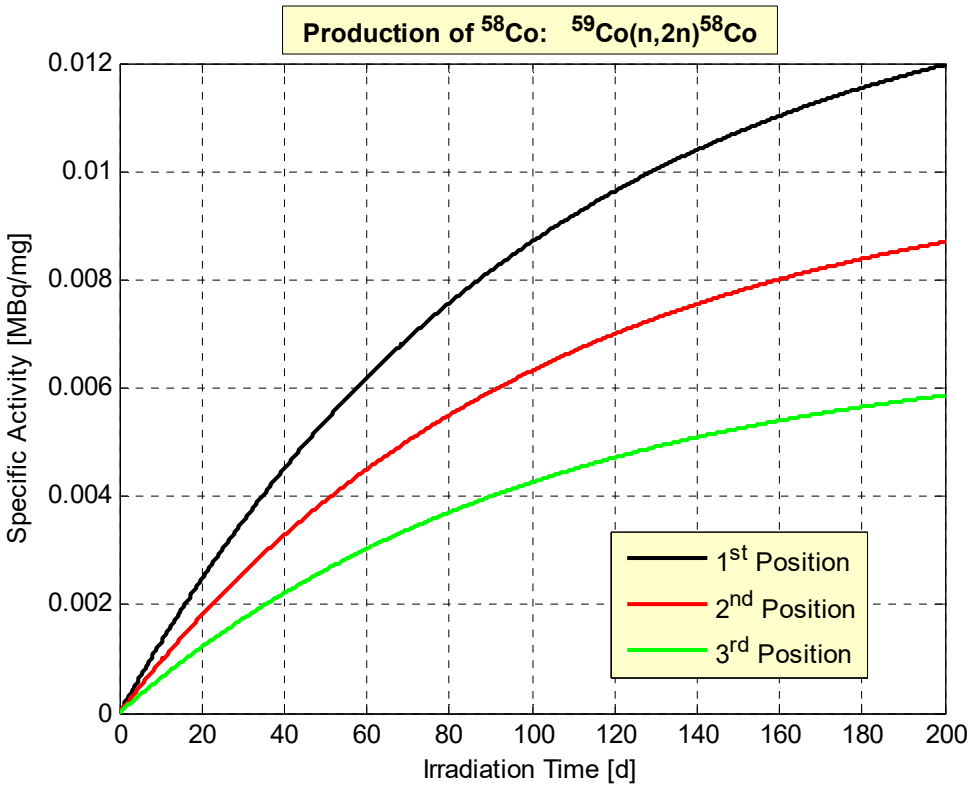

Figure VIII.3.3.3. ^{58}Co activity as a function of the irradiation time

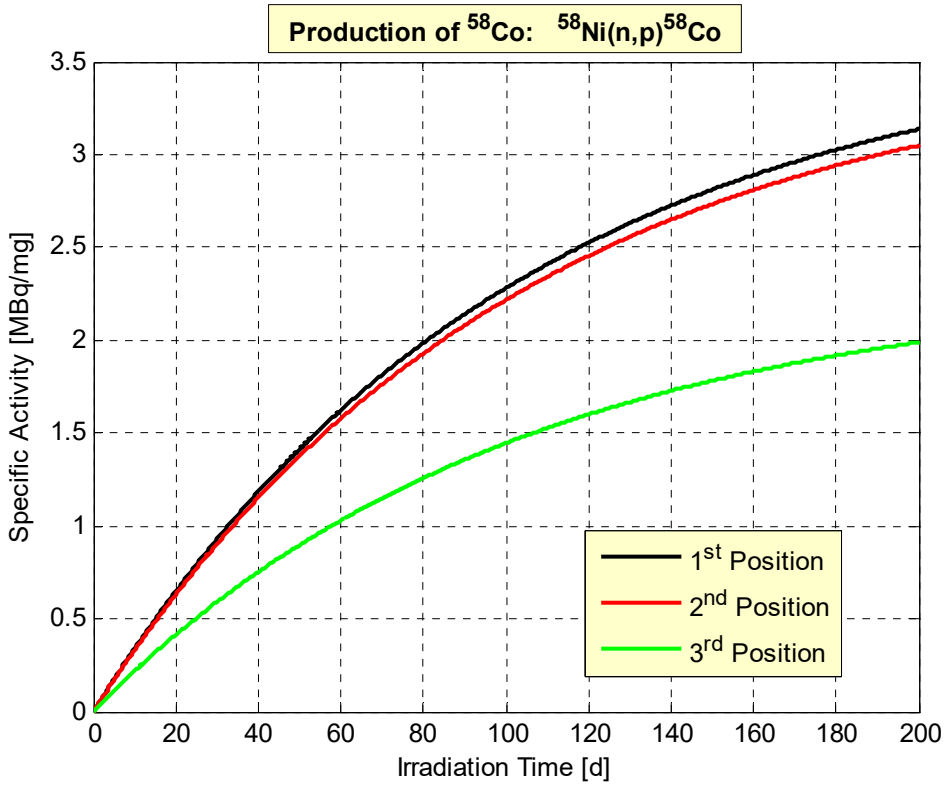

Figure VIII.3.3.4. ^{58}Co activity as a function of the irradiation time

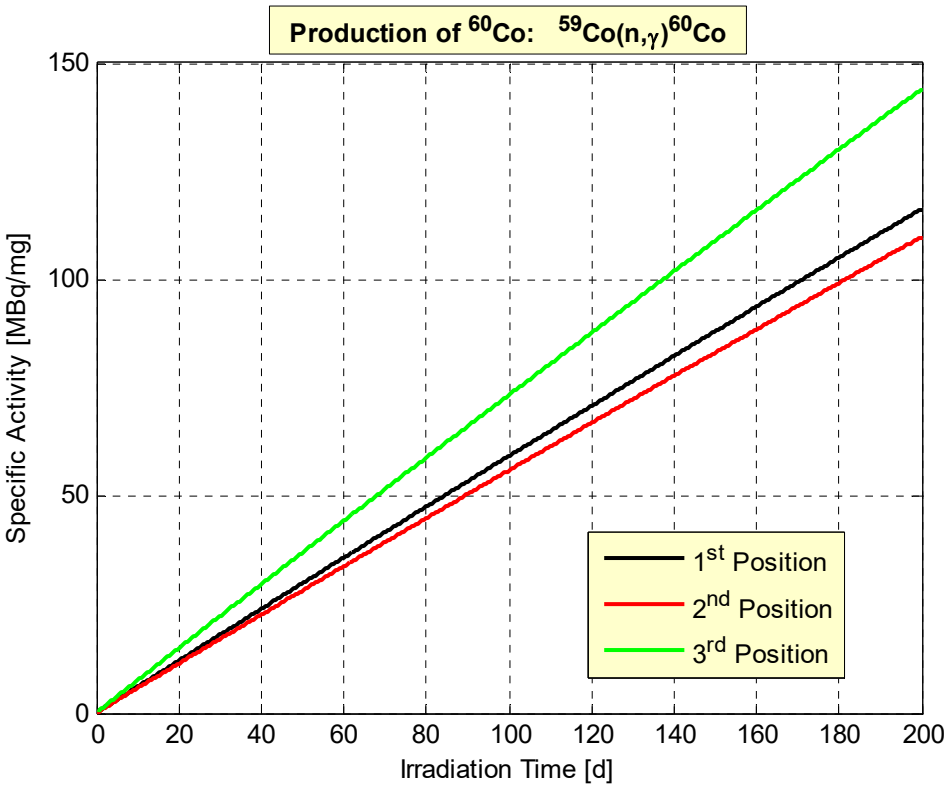

Figure VIII.3.3.5. ^{60}Co activity as a function of the irradiation time

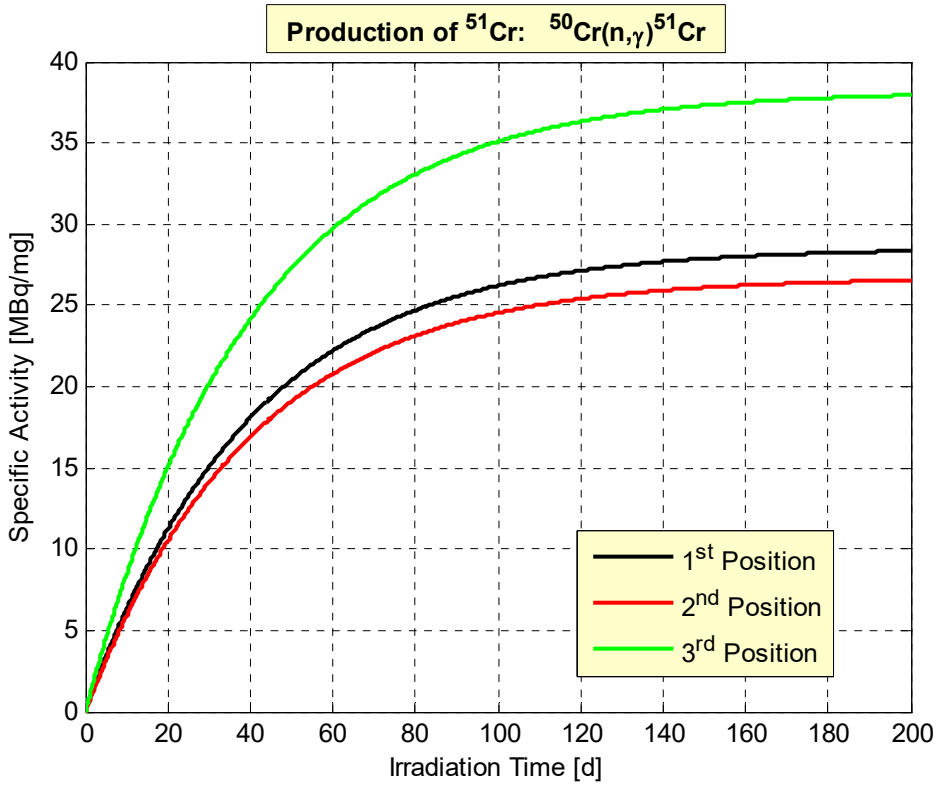

Figure VIII.3.3.6. ^{51}Cr activity as a function of the irradiation time

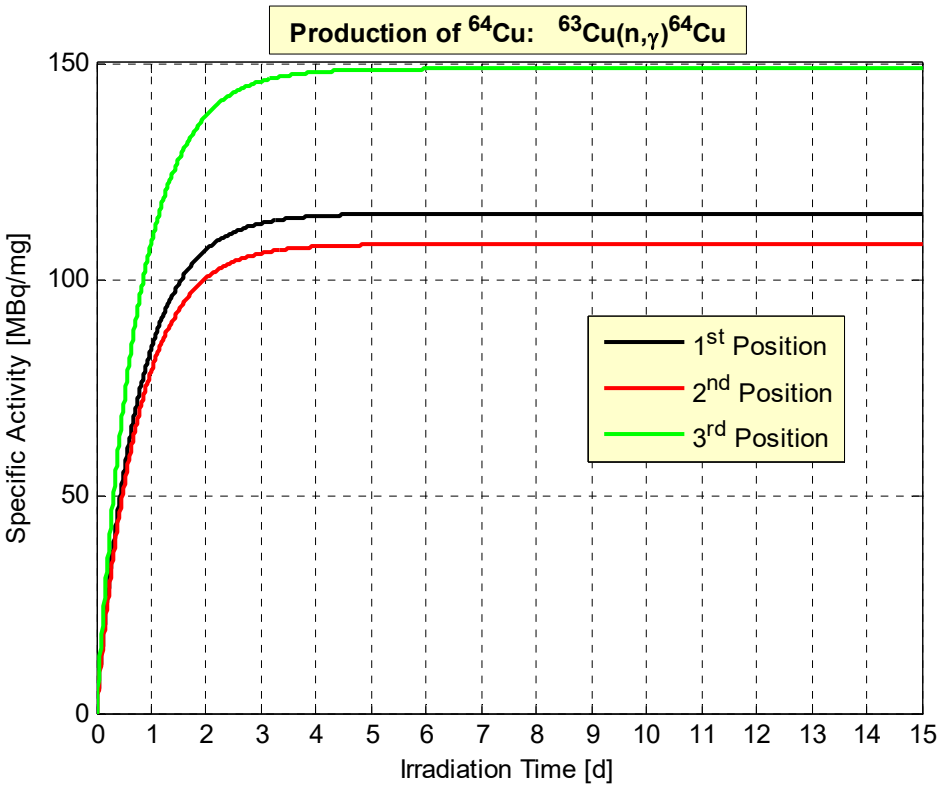

Figure VIII.3.3.7. ^{64}Cu activity as a function of the irradiation time

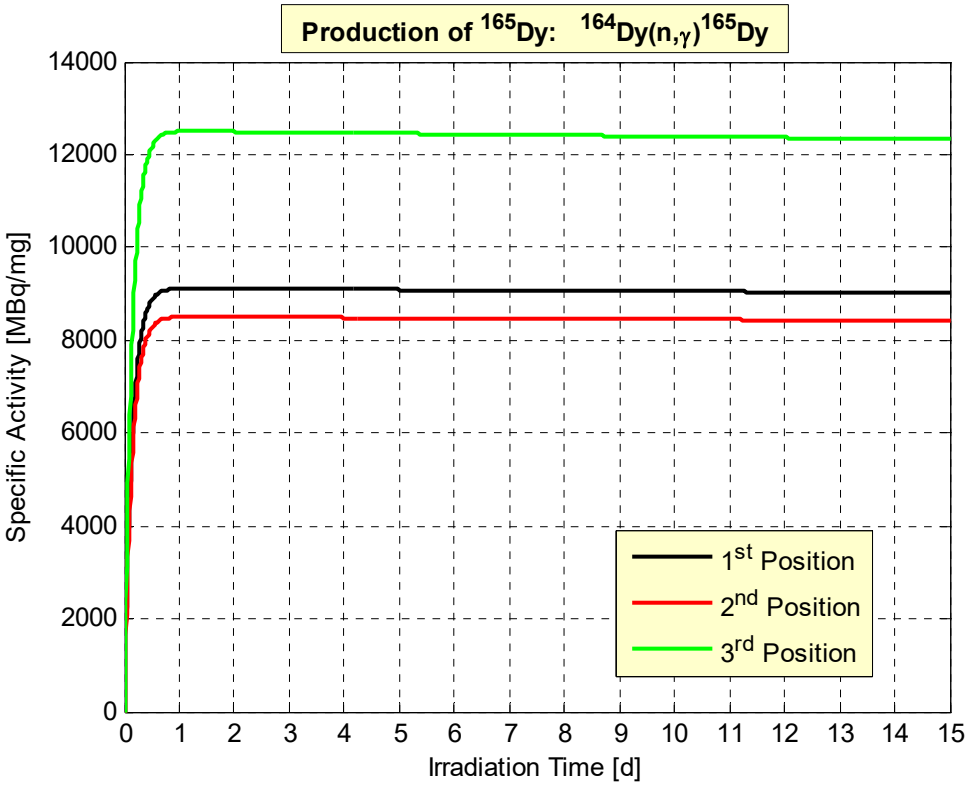

Figure VIII.3.3.8. ^{165}Dy activity as a function of the irradiation time

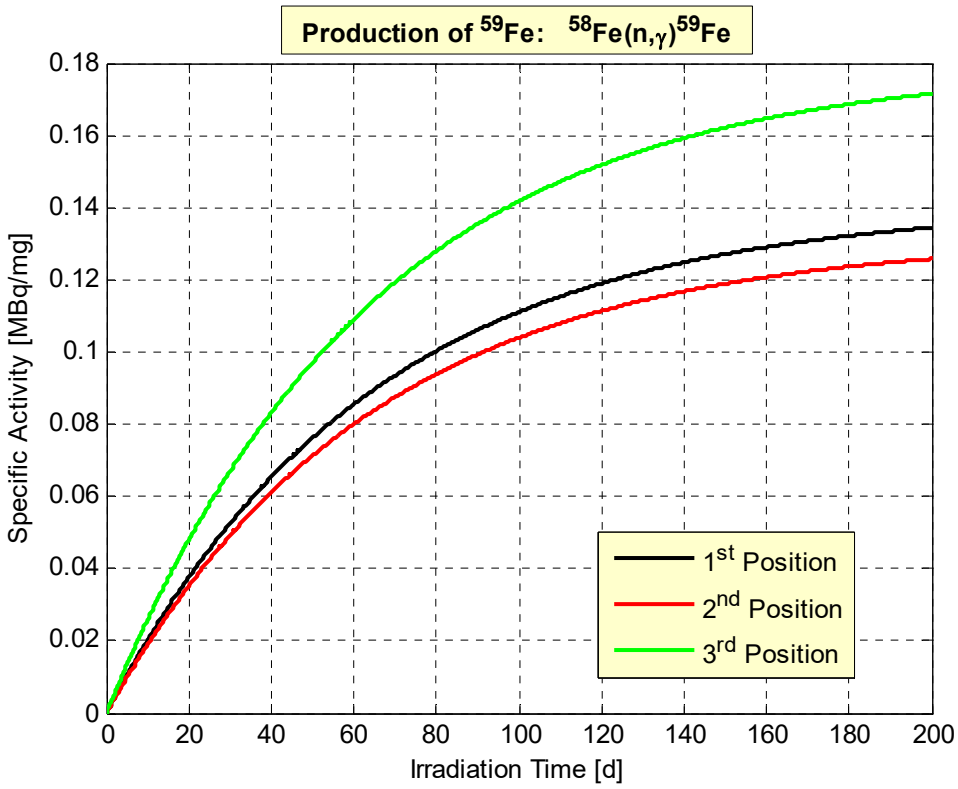

Figure VIII.3.3.9. ^{59}Fe activity as a function of the irradiation time

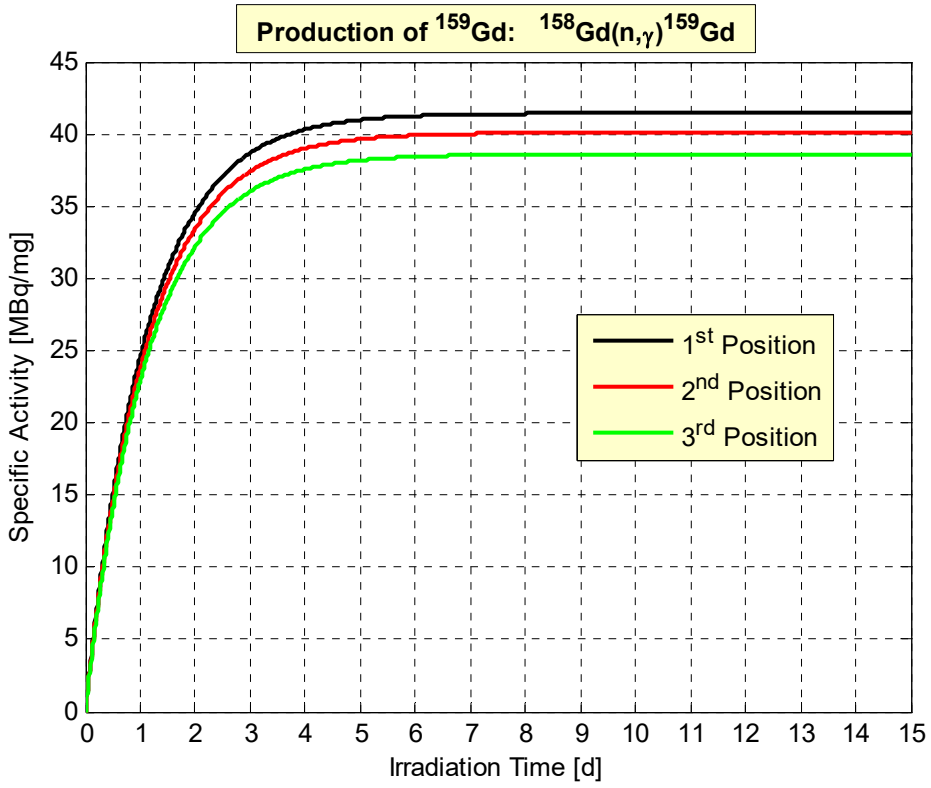

Figure VIII.3.3.10. ^{159}Gd activity as a function of the irradiation time

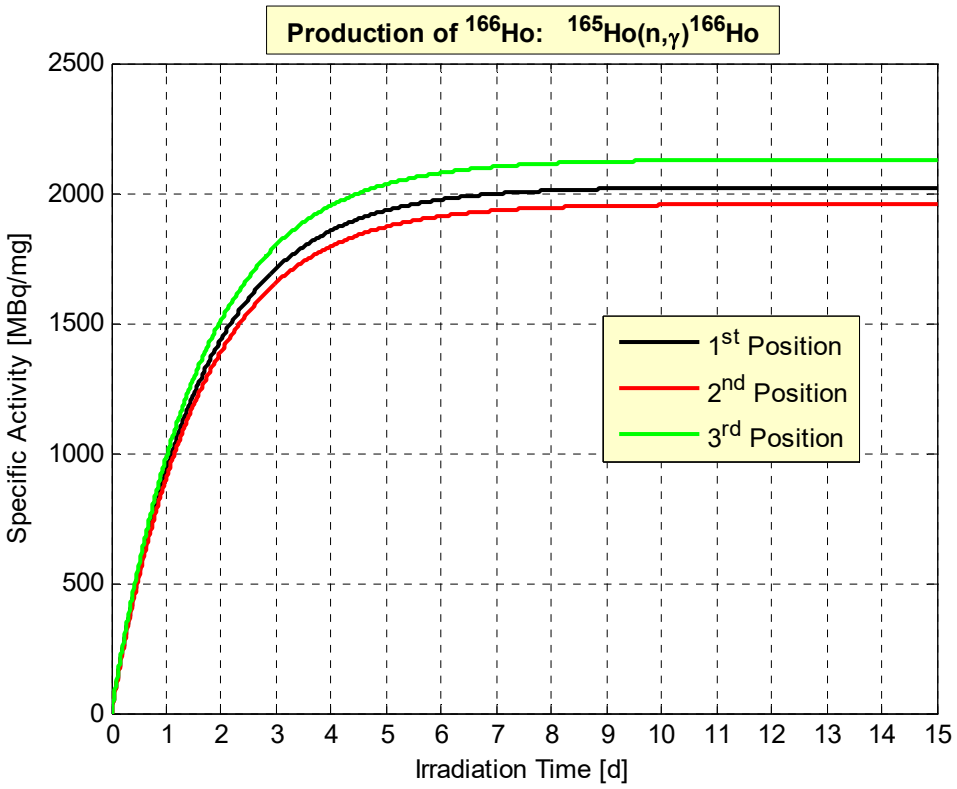

Figure VIII.3.3.11. ^{166}Ho activity as a function of the irradiation time

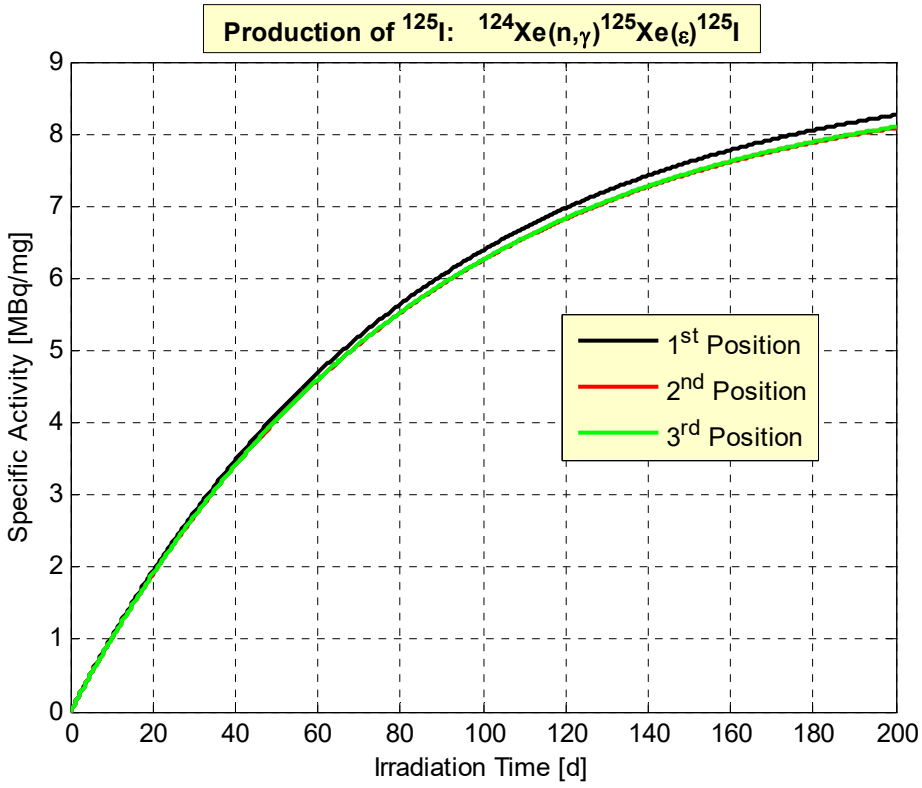

Figure VIII.3.3.12. ^{125}I activity a as function of the irradiation time

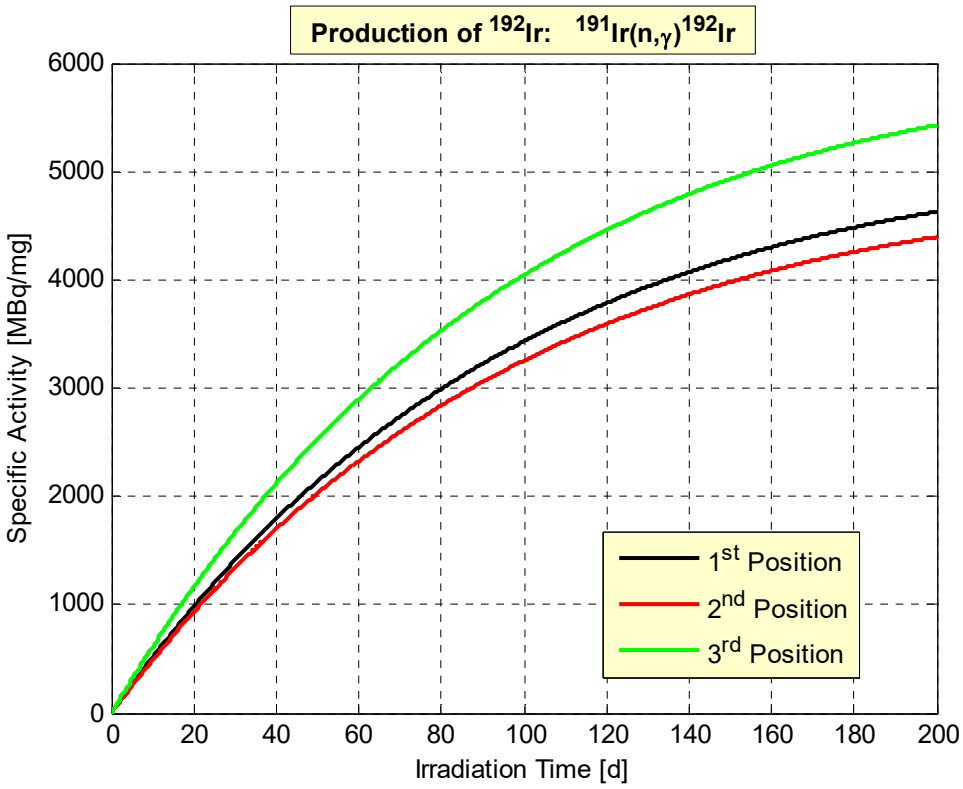

Figure VIII.3.3.13. ^{192}Ir activity as a function of the irradiation time

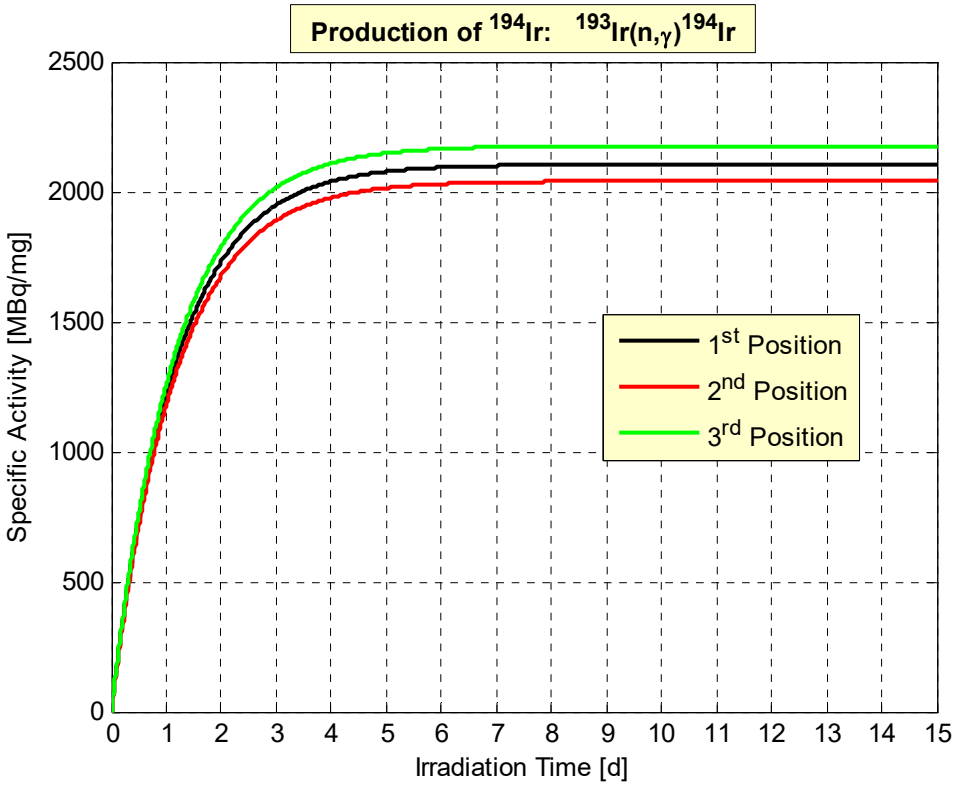

Figure VIII.3.3.14. ^{194}Ir activity as a function of the irradiation time

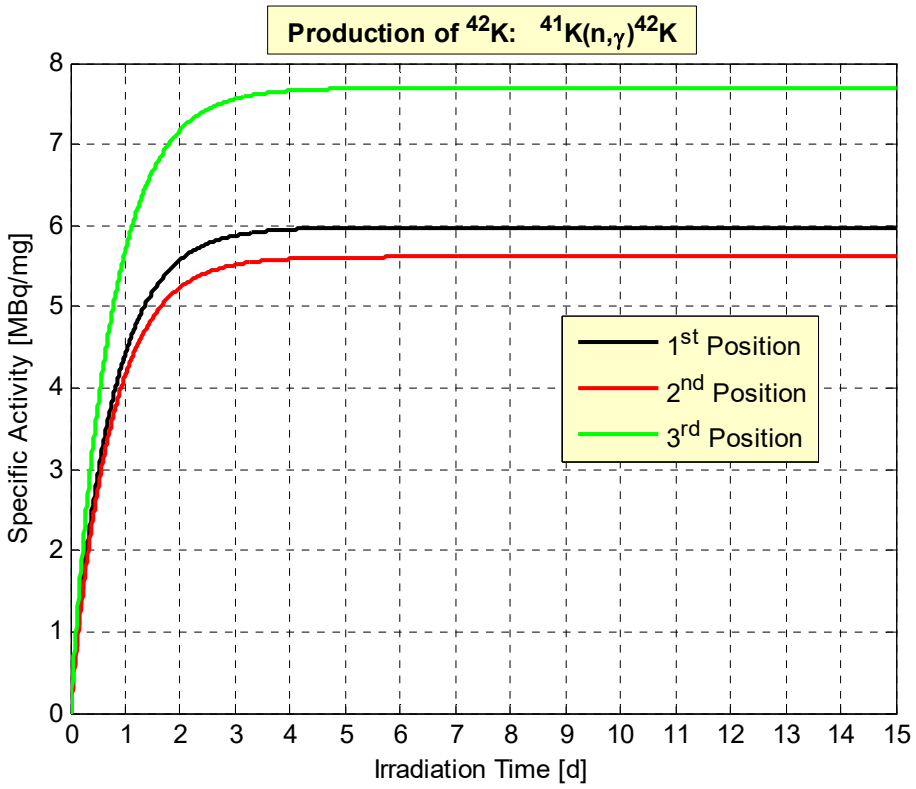

Figure VIII.3.3.15. ^{42}K activity as a function of the irradiation time

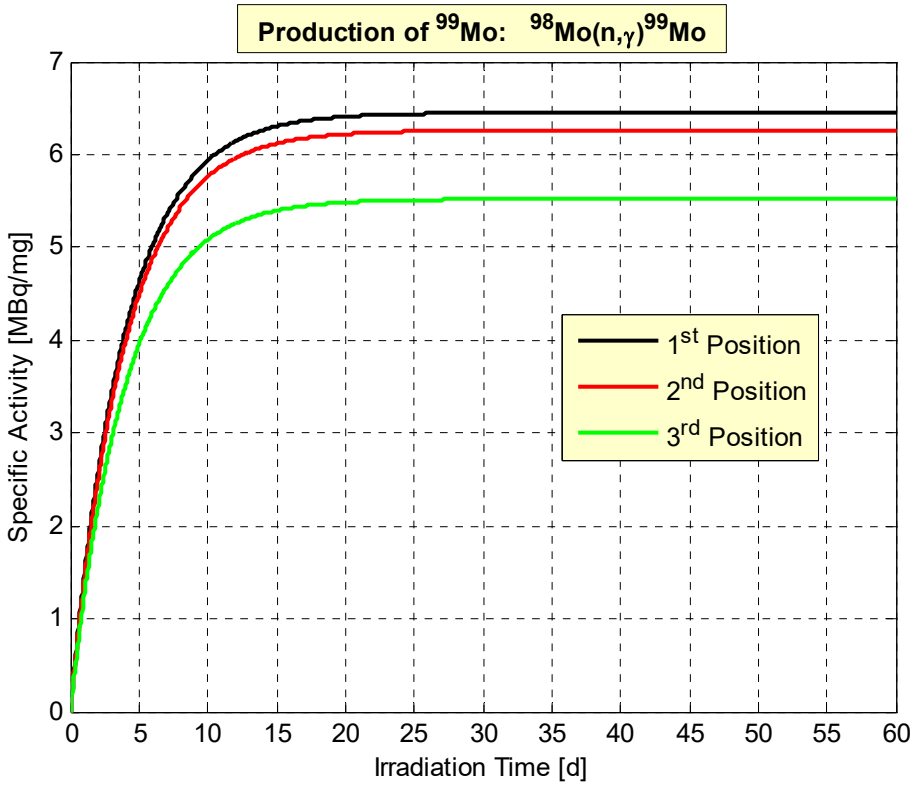

Figure VIII.3.3.16. ^{99}Mo activity as a function of the irradiation time

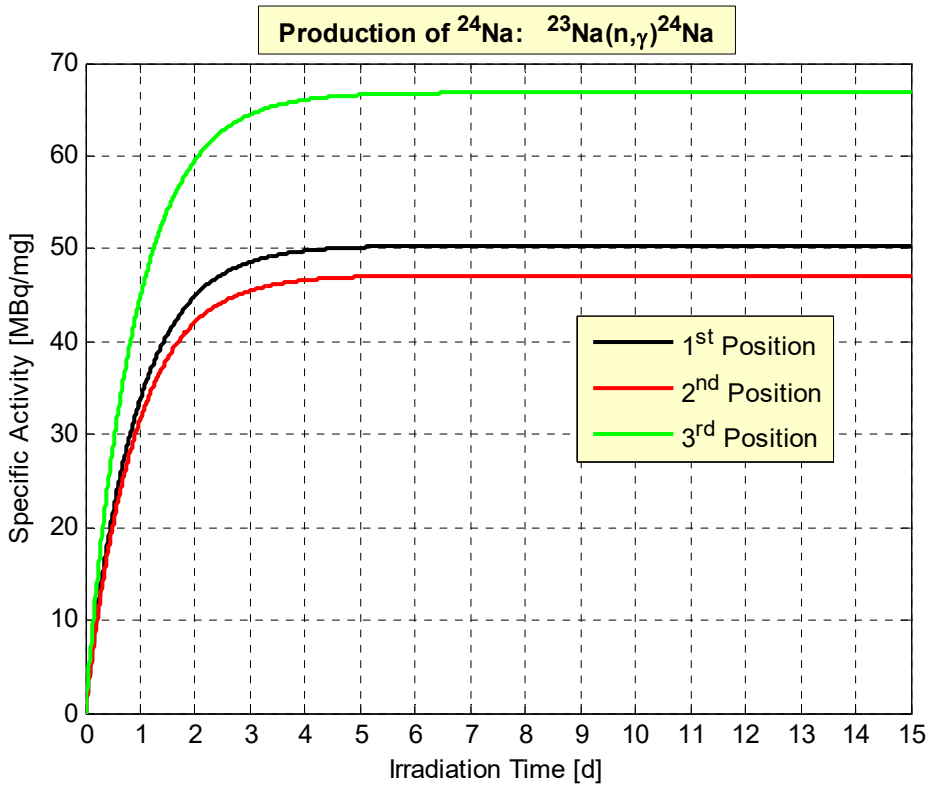

Figure VIII.3.3.17. ^{24}Na activity as a function of the irradiation time

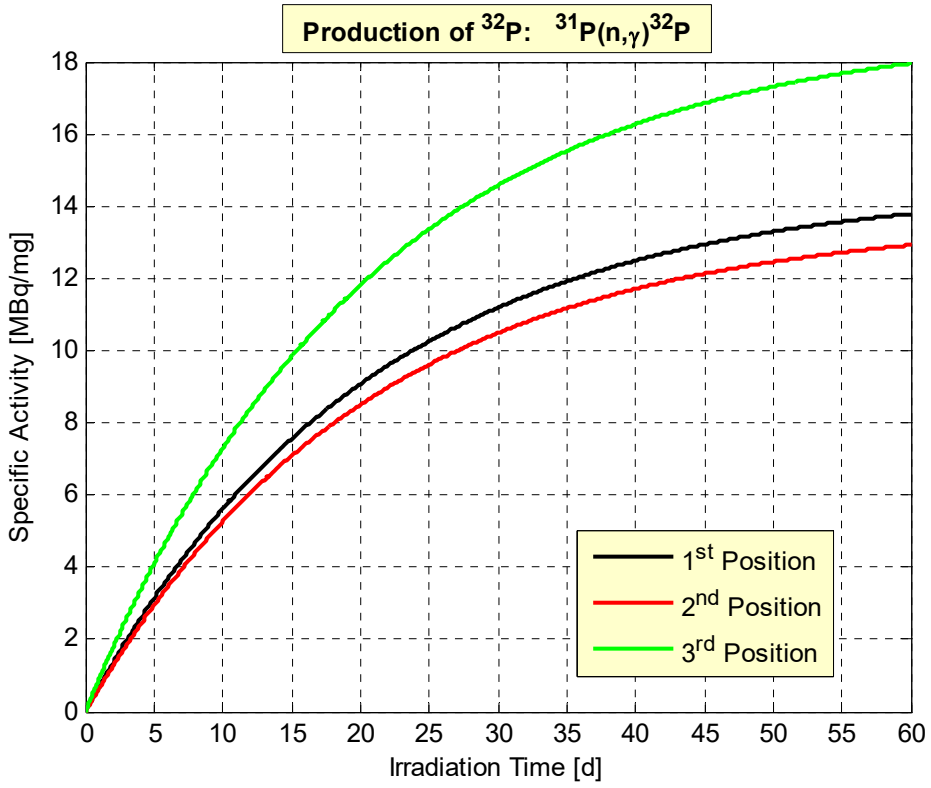

Figure VIII.3.3.18. ^{32}P activity as a function of the irradiation time

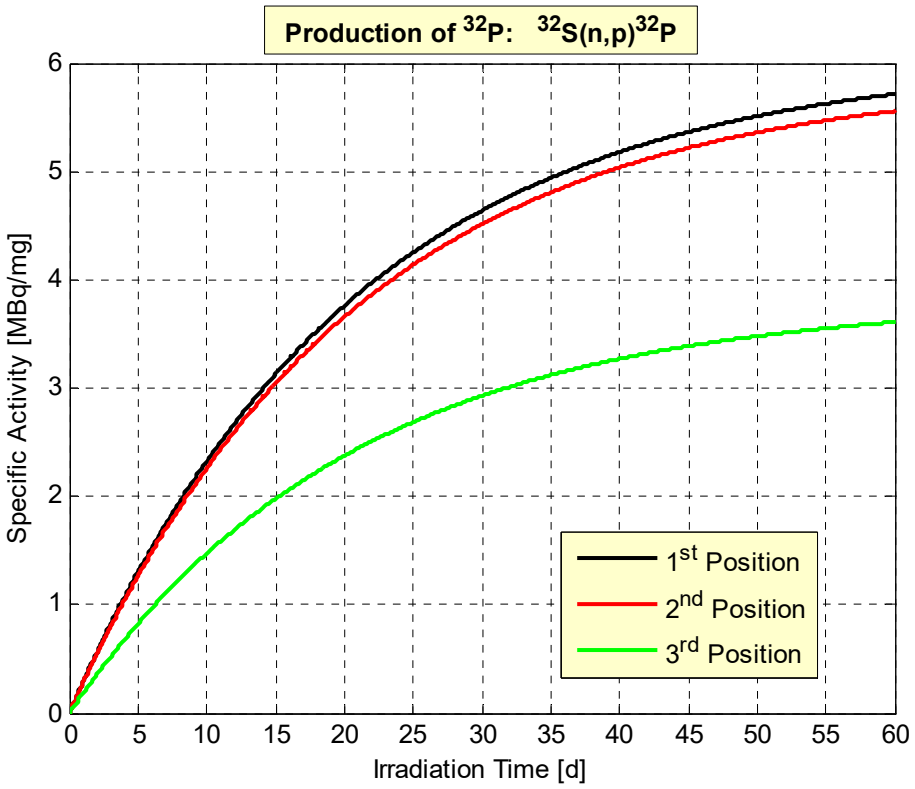

Figure VIII.3.3. 19. ^{32}P activity as a function of the irradiation time

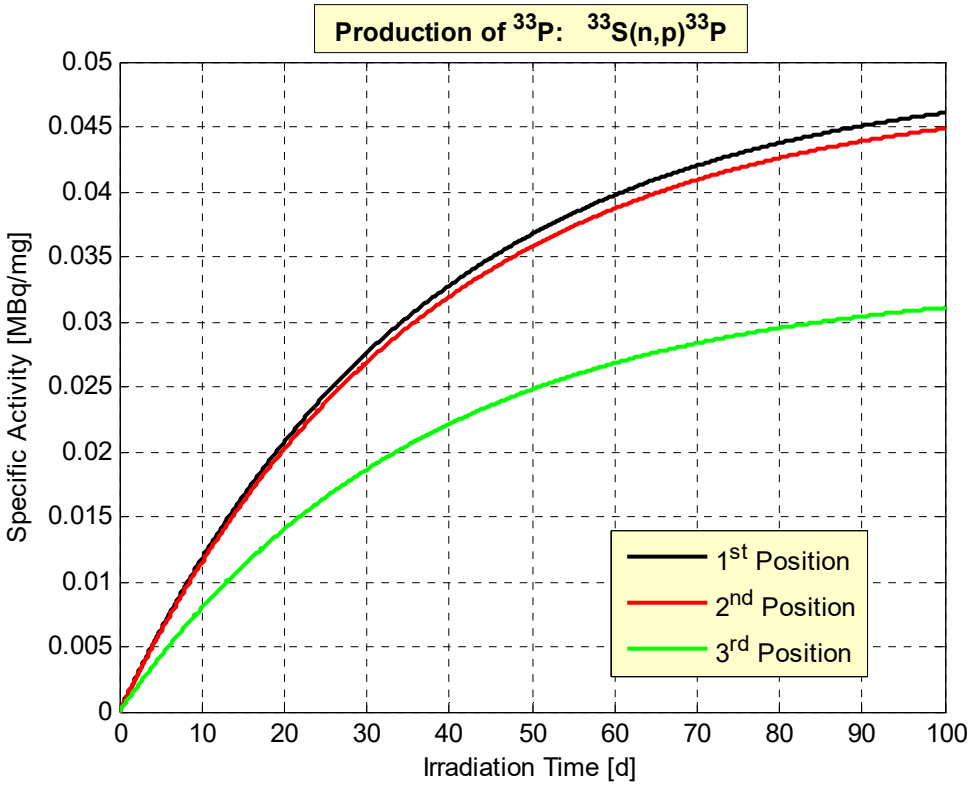

Figure VIII.3.3.20. ^{33}P activity as a function of the irradiation time

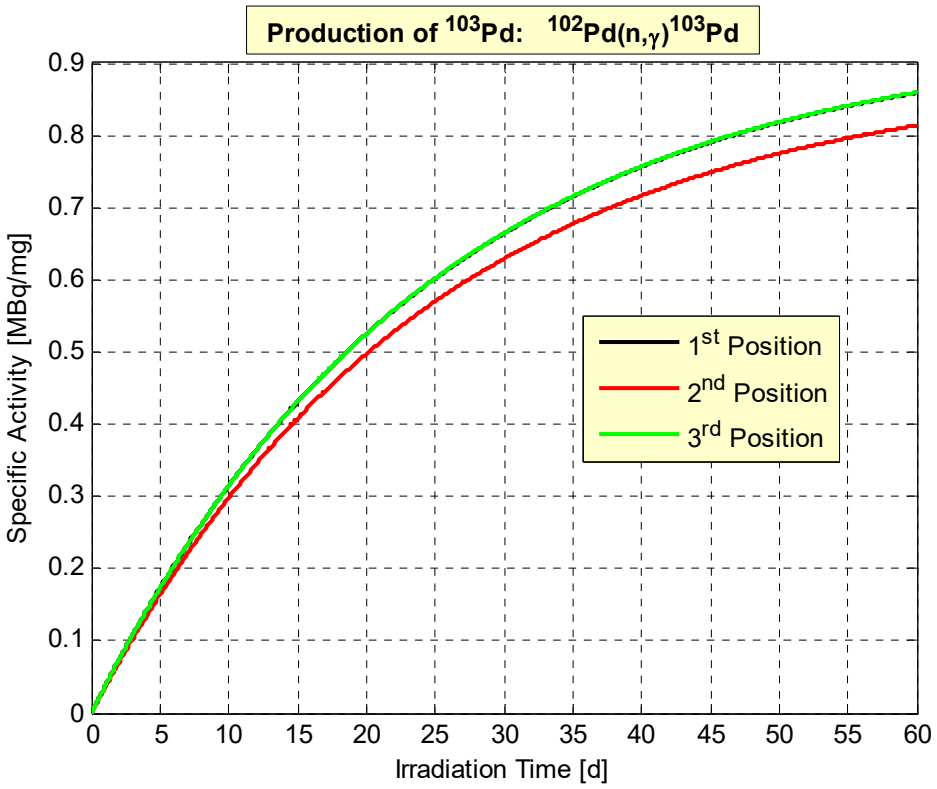

Figure VIII.3.3.21. ^{103}Pd activity as a function of the irradiation time

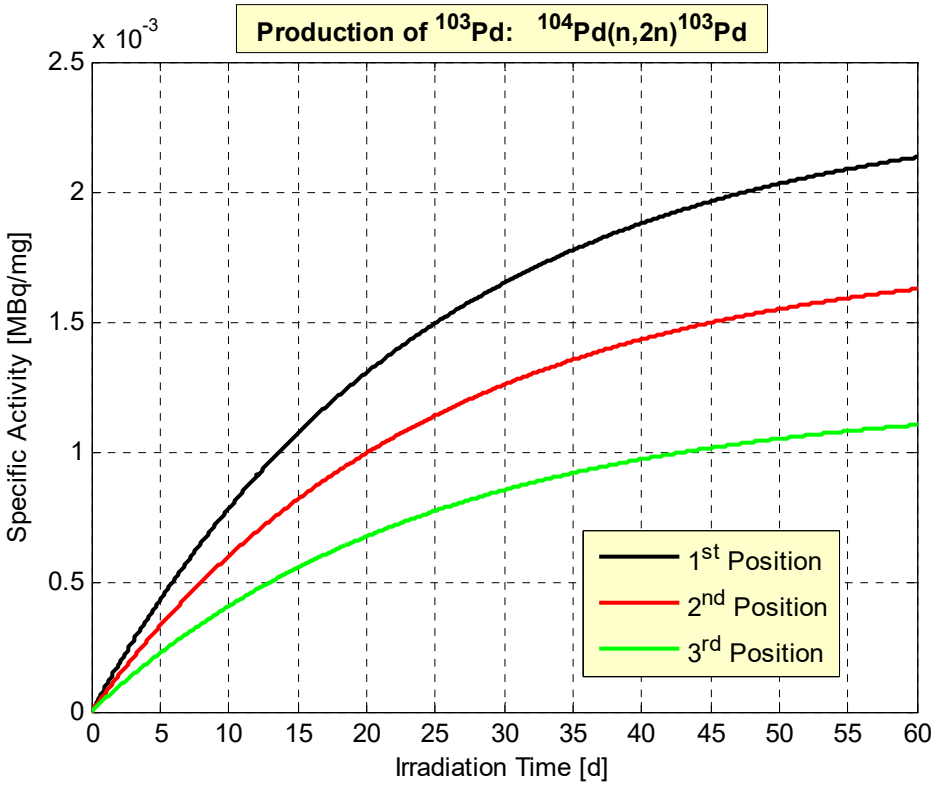

Figure VIII.3.3.22. ^{103}Pd activity as a function of the irradiation time

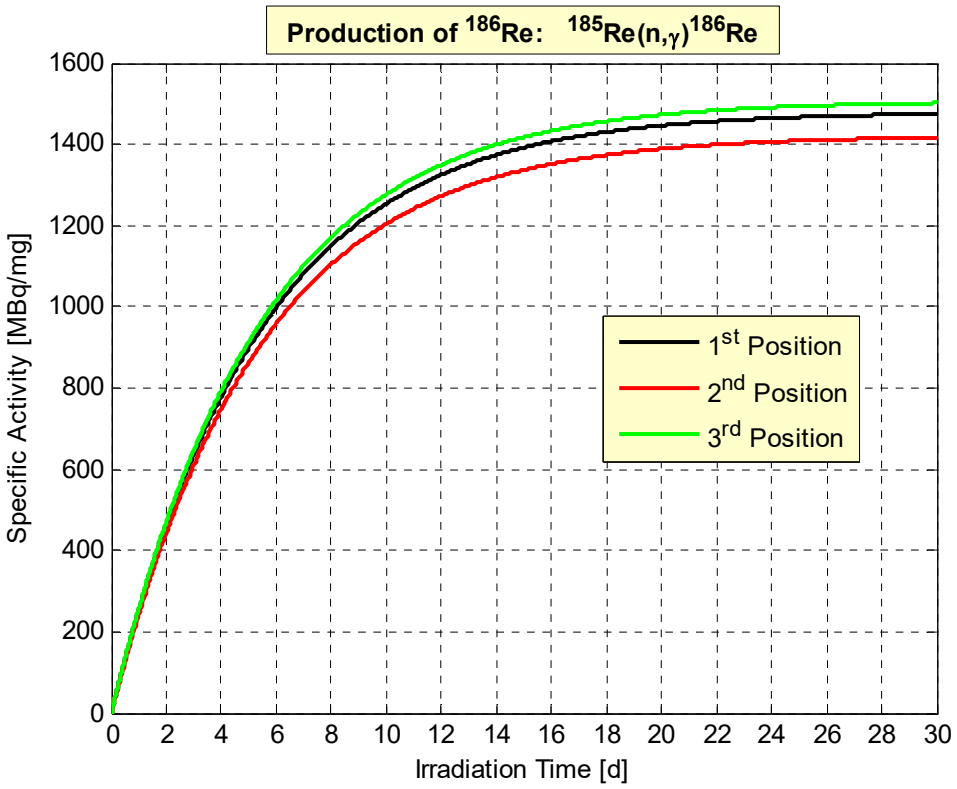

Figure VIII.3.3.23. ^{186}Re activity as a function of the irradiation time

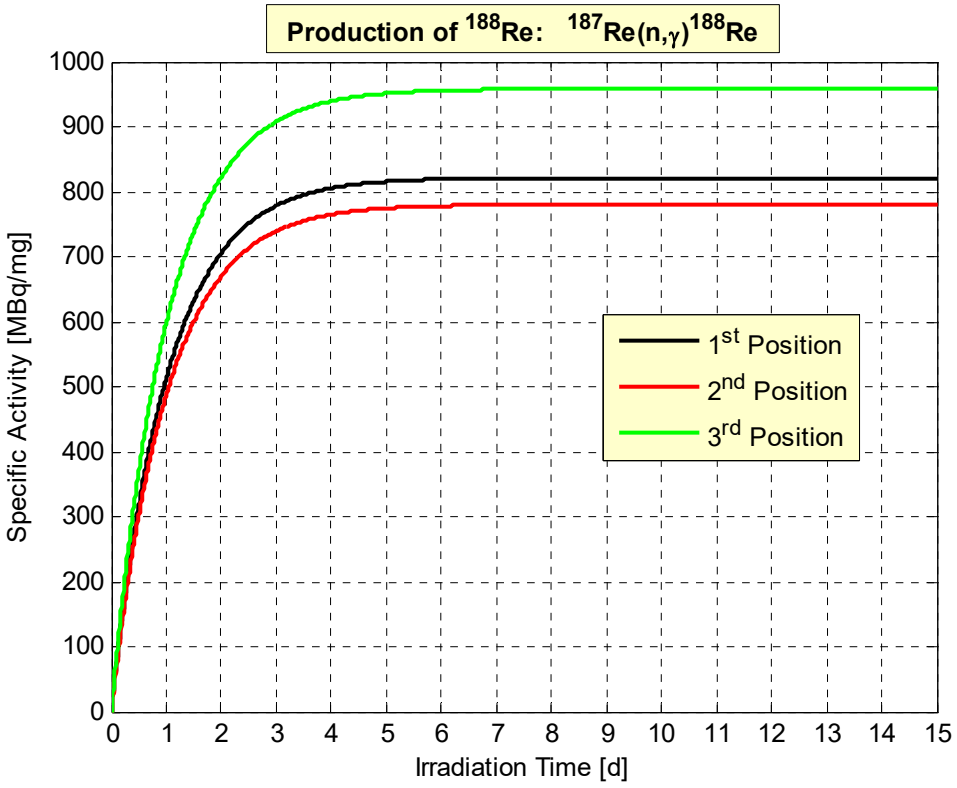

Figure VIII.3.3.24. ^{188}Re activity as a function of the irradiation time

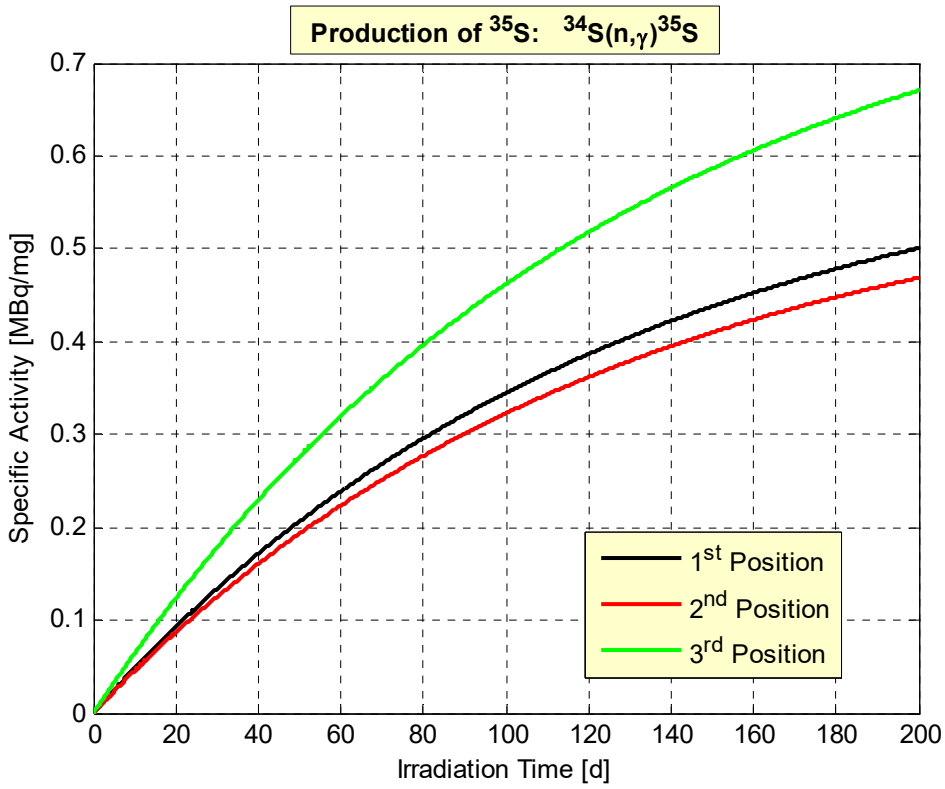

Figure VIII.3.3.25. ^{35}S activity as a function of the irradiation time

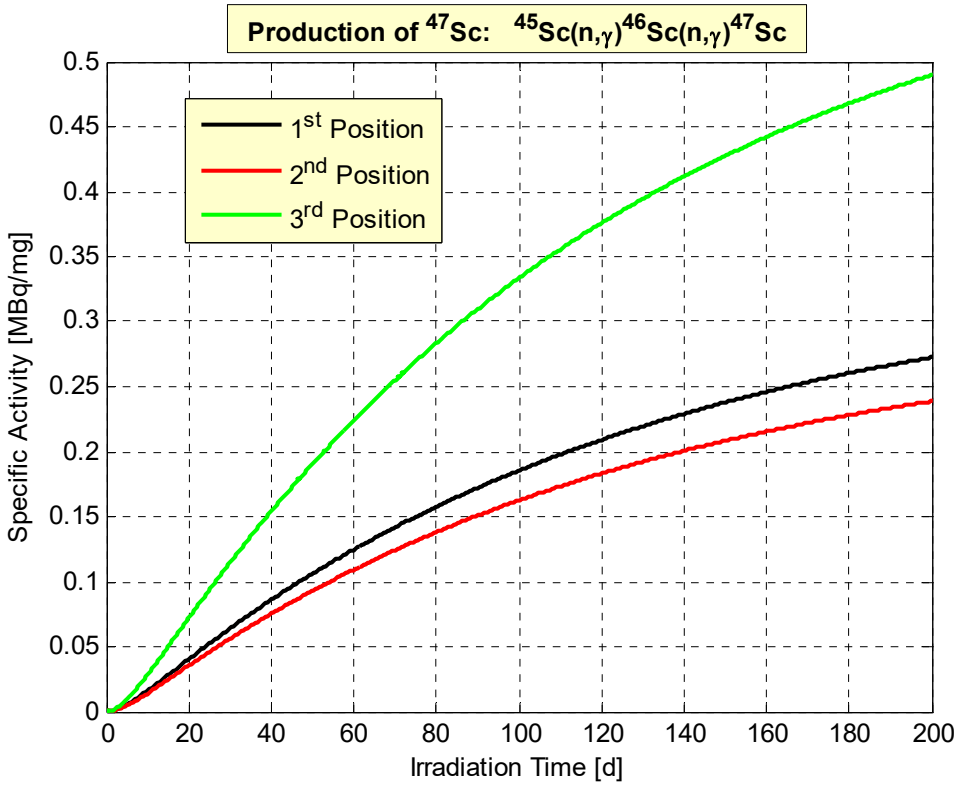

Figure VIII.3.3.26. ^{47}Sc activity as a function of the irradiation time

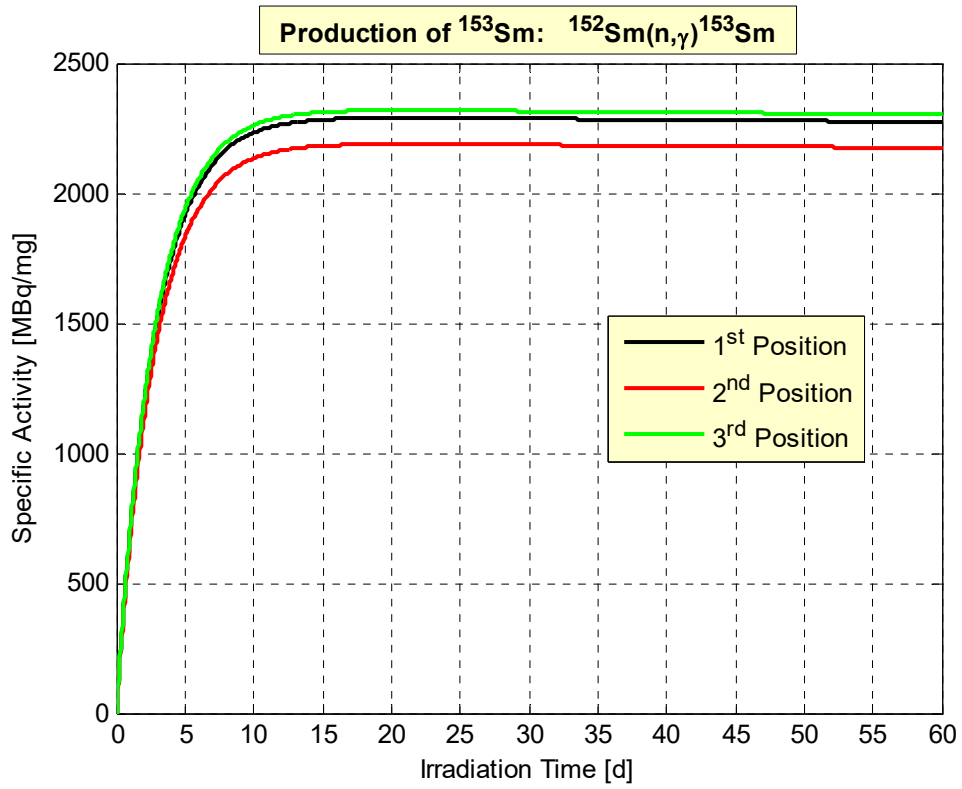

Figure VIII.3.3.27. ^{153}Sm activity as a function of the irradiation time

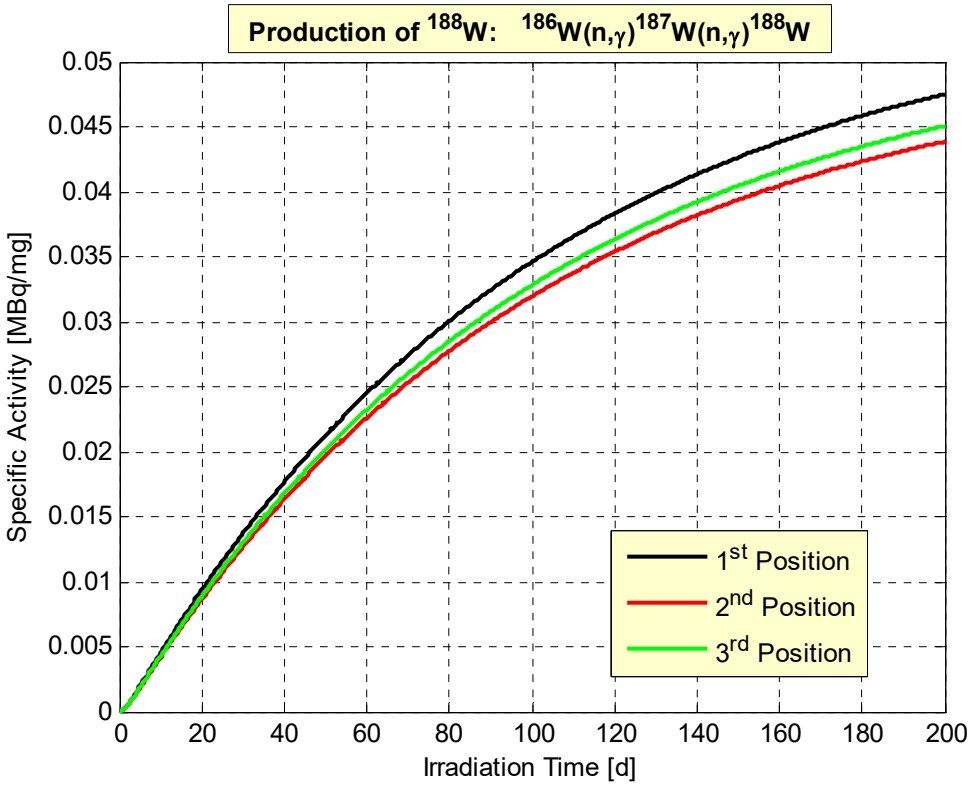

Figure VIII.3.3.28. ^{188}W activity as a function of the irradiation time

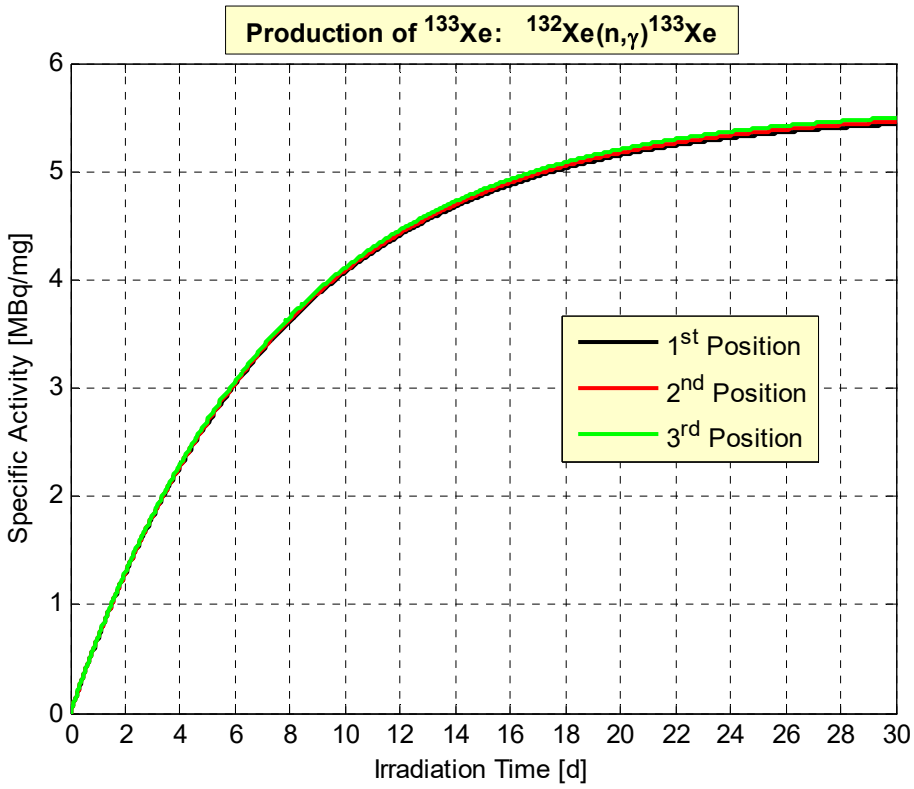

Figure VIII.3.3.29. ^{133}Xe activity as a function of the irradiation time from ^{132}Xe(n,γ)^{133}Xe

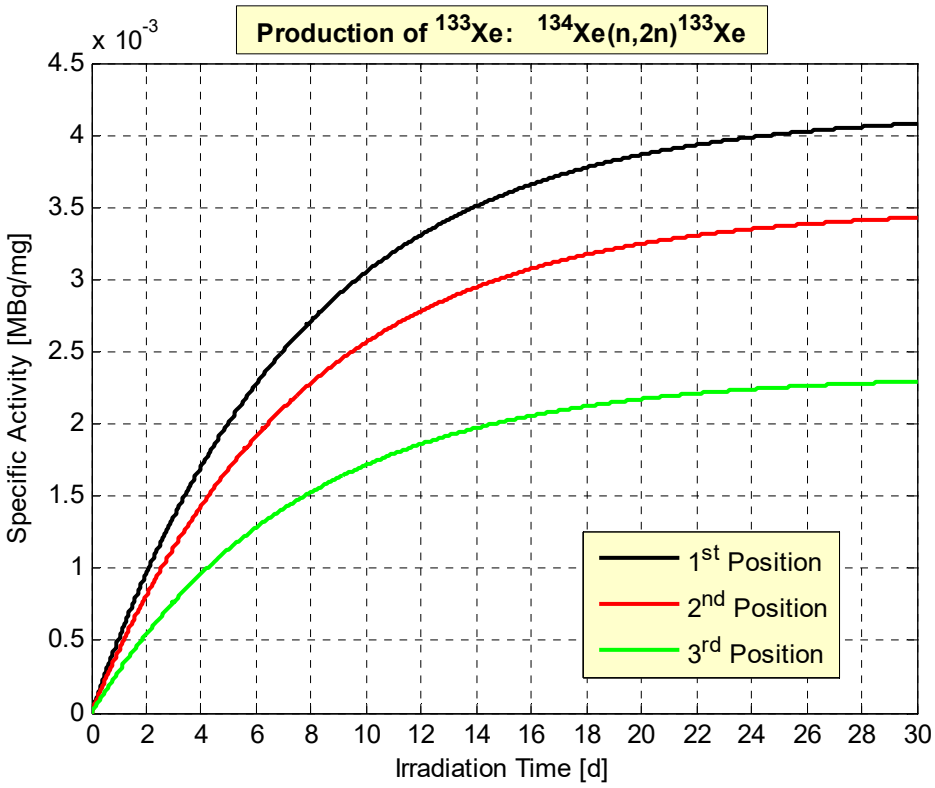

Figure VIII.3.3.30. ^{133}Xe activity as a function of the irradiation time from ^{134}Xe(n,2n)^{133}Xe

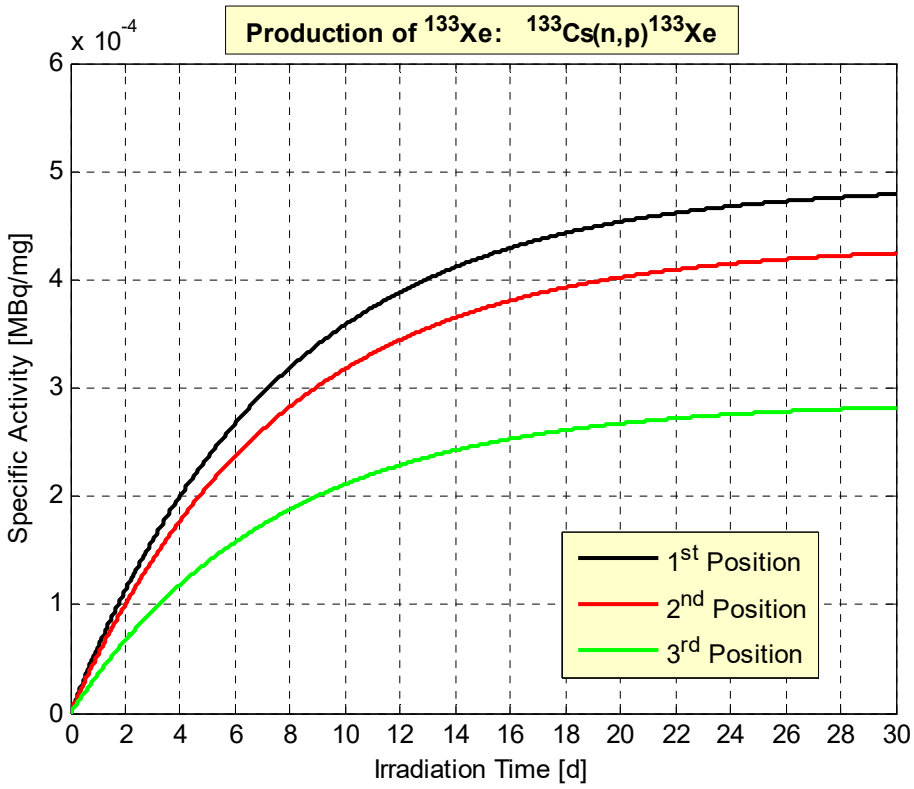

Figure VIII.3.3.31. ^{133}Xe activity as a function of the irradiation time from ^{133}Cs(n,p)^{133}Xe

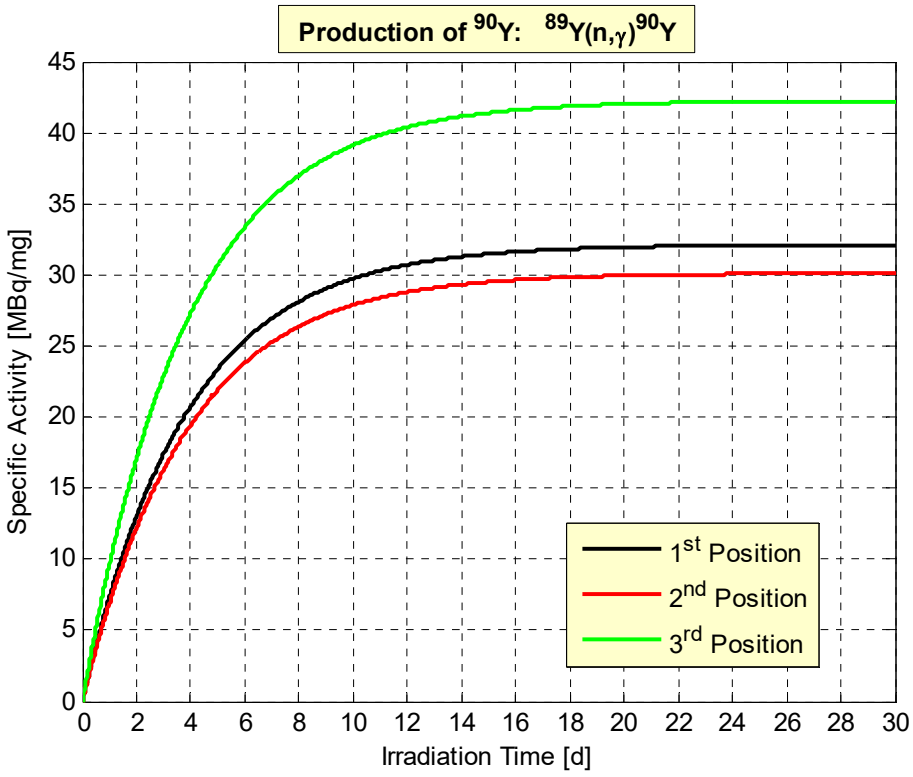

Figure VIII.3.3.32. ^{90}Y activity as a function of the irradiation time

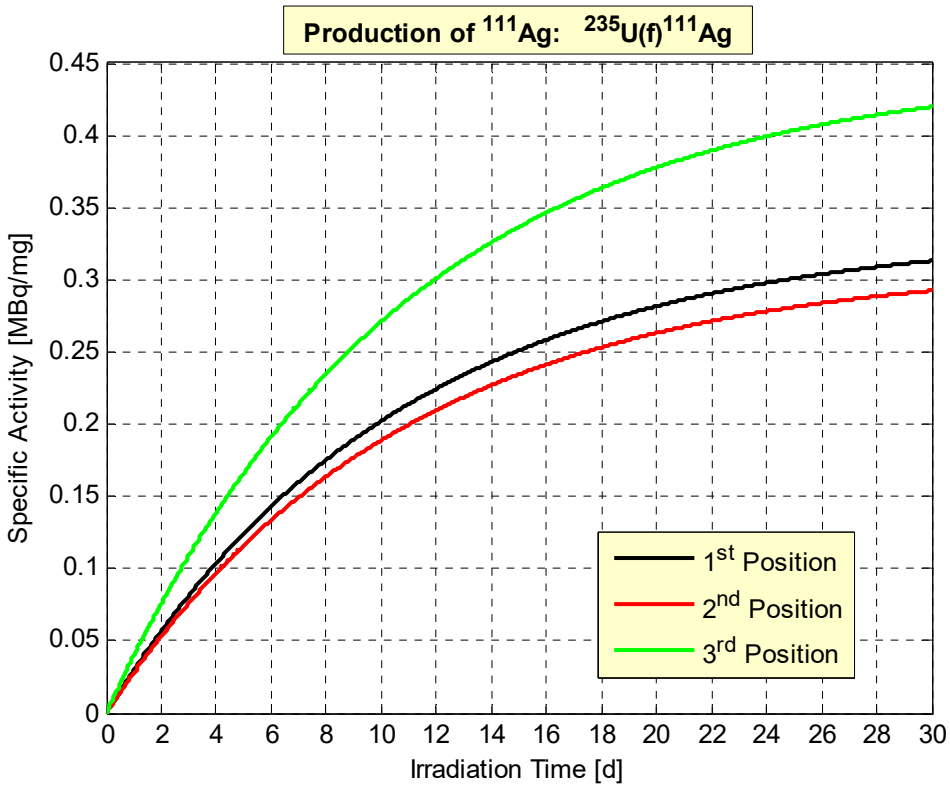

Figure VIII.3.3.33. ^{111}Ag activity as a function of the irradiation time

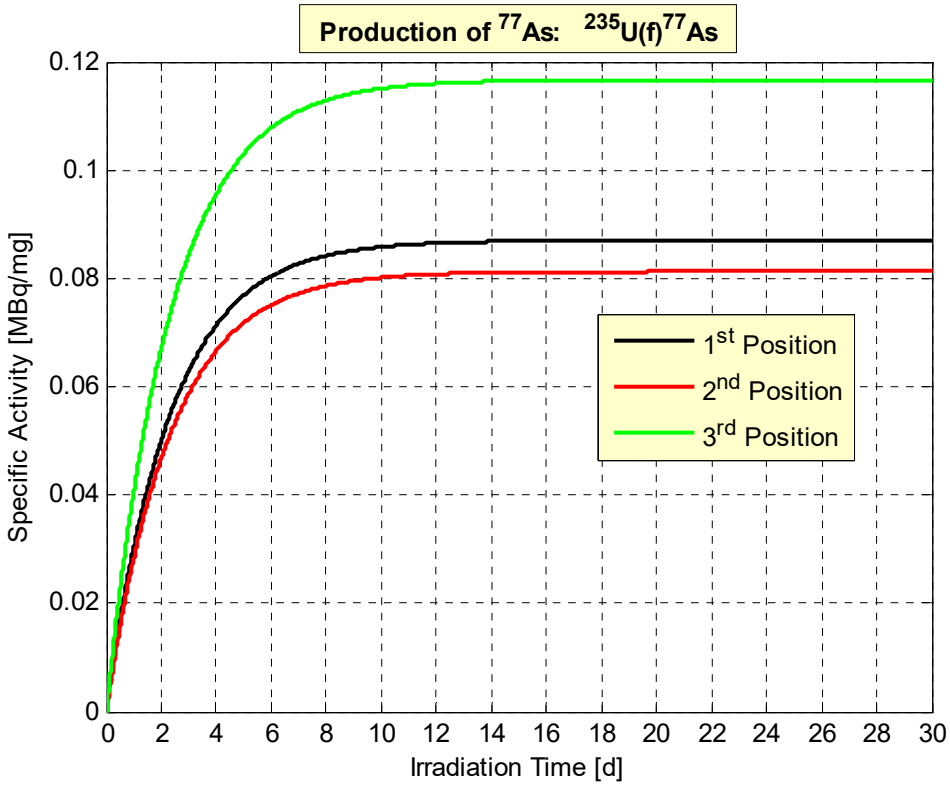

Figure VIII.3.3.34. ^{77}As activity as a function of the irradiation time

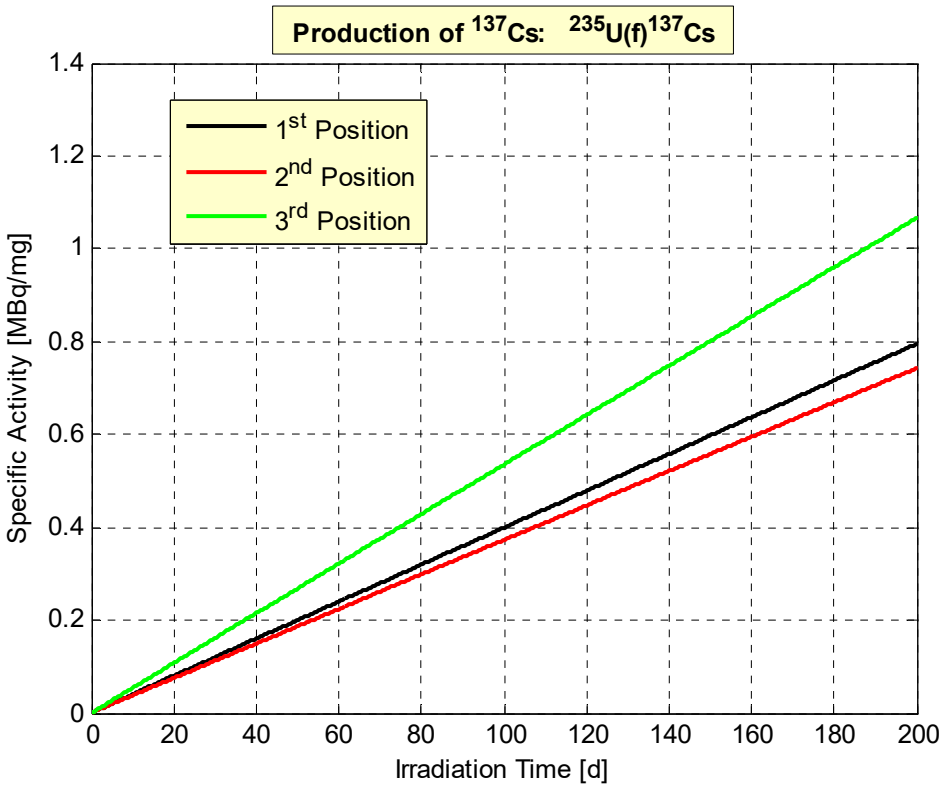

Figure VIII.3.3.35. ^{137}Cs activity as a function of the irradiation time

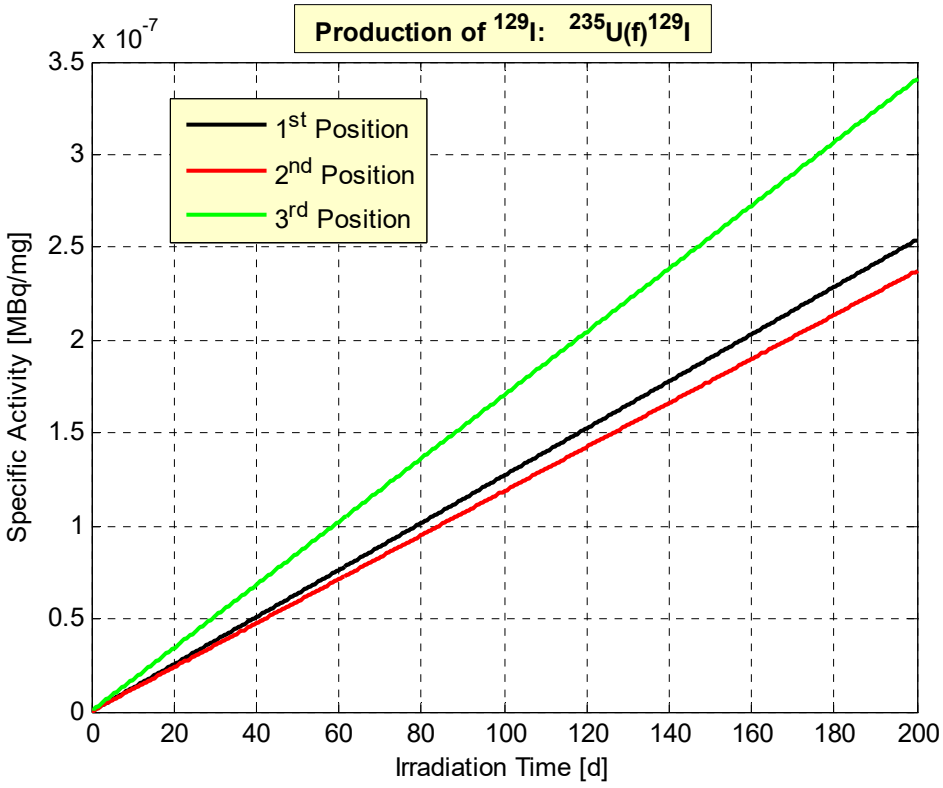

Figure VIII.3.3.36. ^{129}I activity as a function of the irradiation time

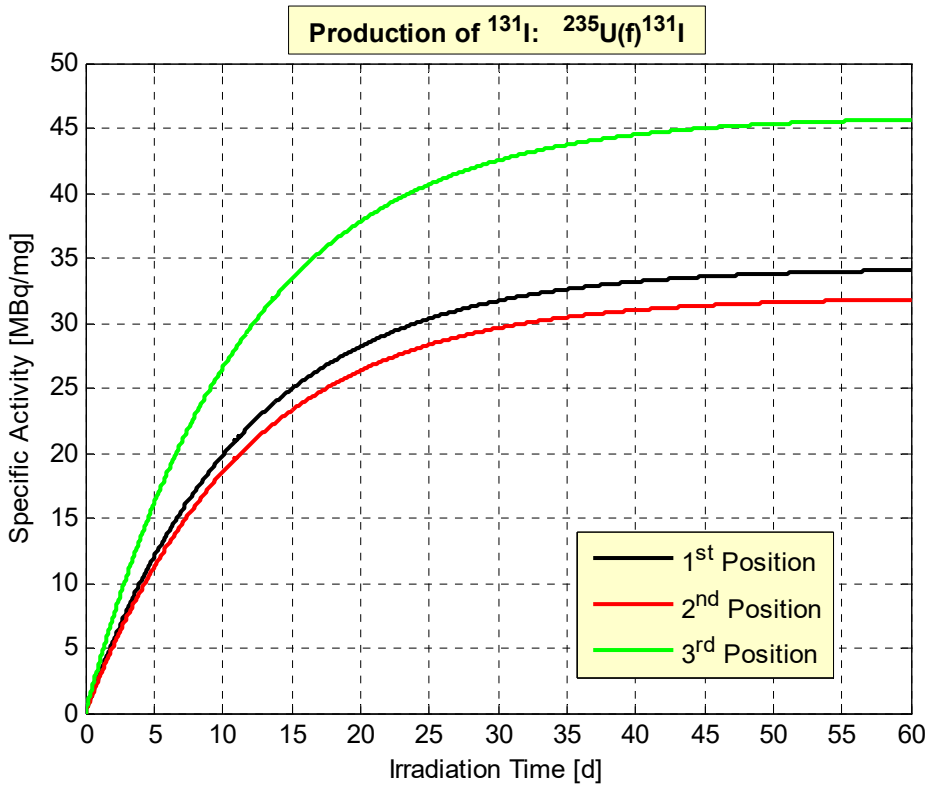

Figure VIII.3.3.37. ^{131}I activity as a function of the irradiation time

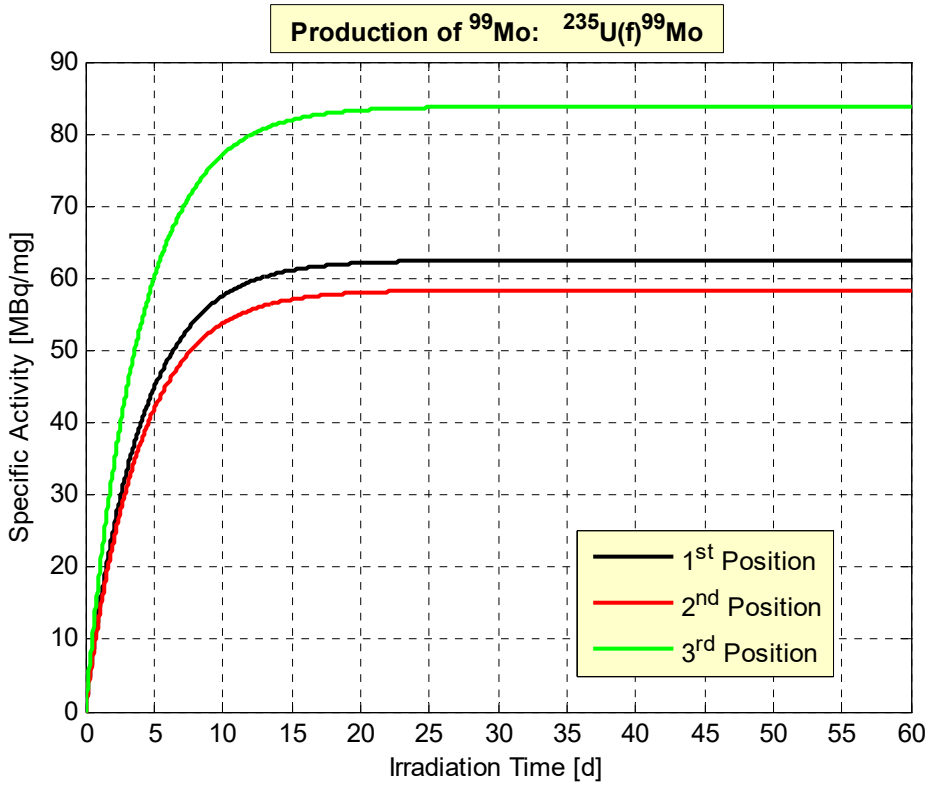

Figure VIII.3.3.38. ^{99}Mo activity as a function of the irradiation time

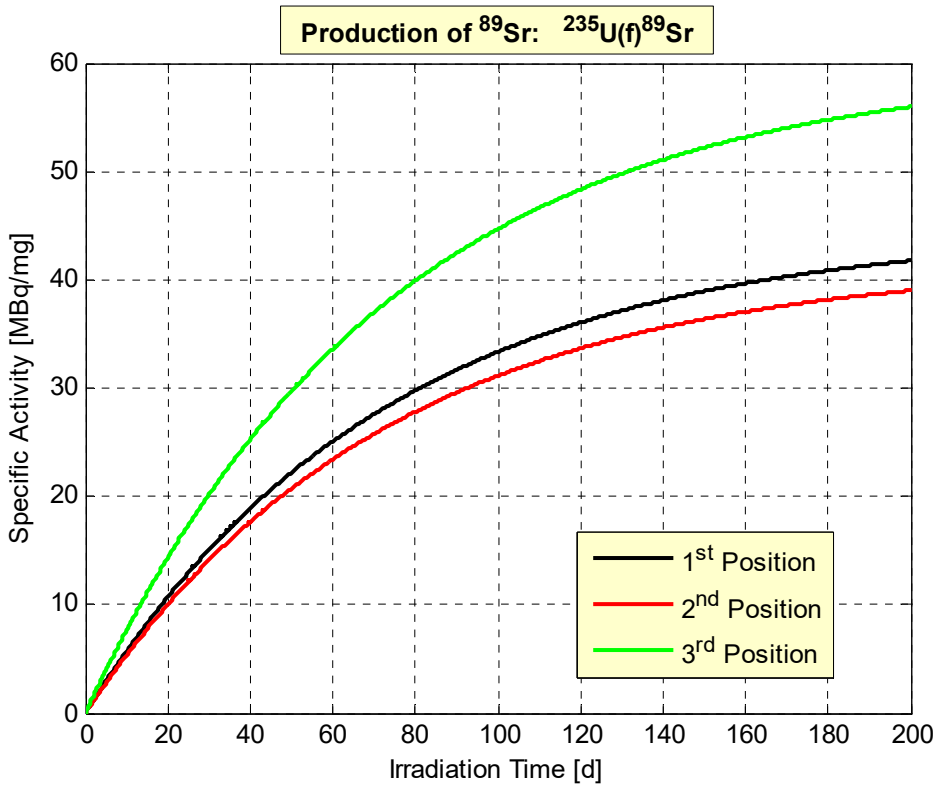

Figure VIII.3.3.39. ^{89}Sr activity as a function of the irradiation time

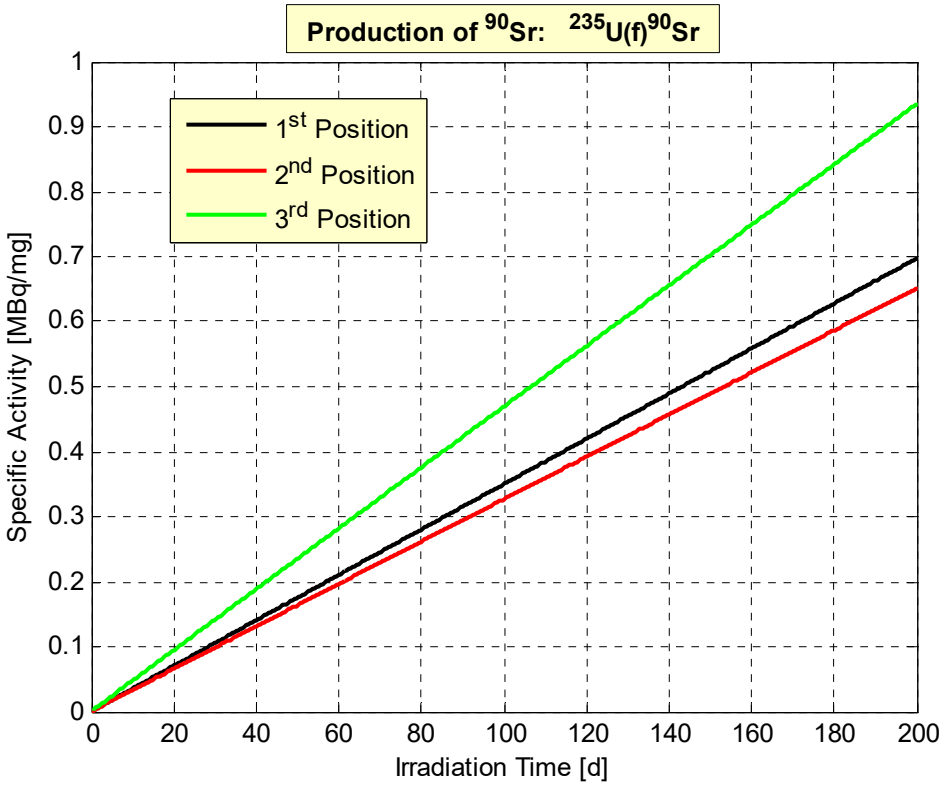

Figure VIII.3.3.40. ^{90}Sr activity as a function of the irradiation time

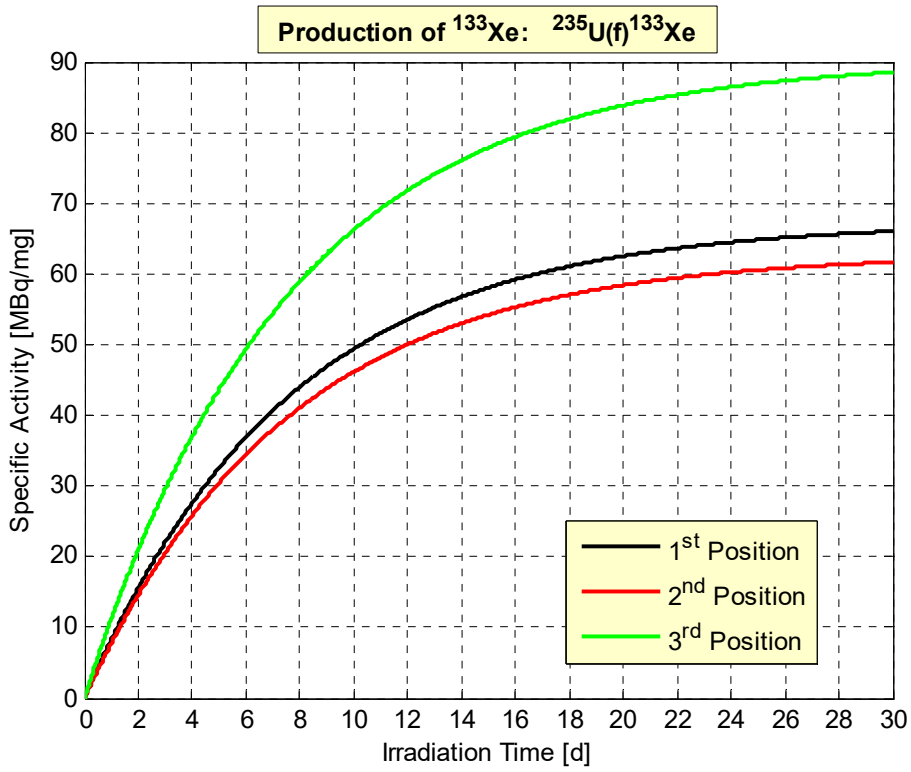

Figure VIII.3.3.41. ^{133}Xe activity as a function of the irradiation time

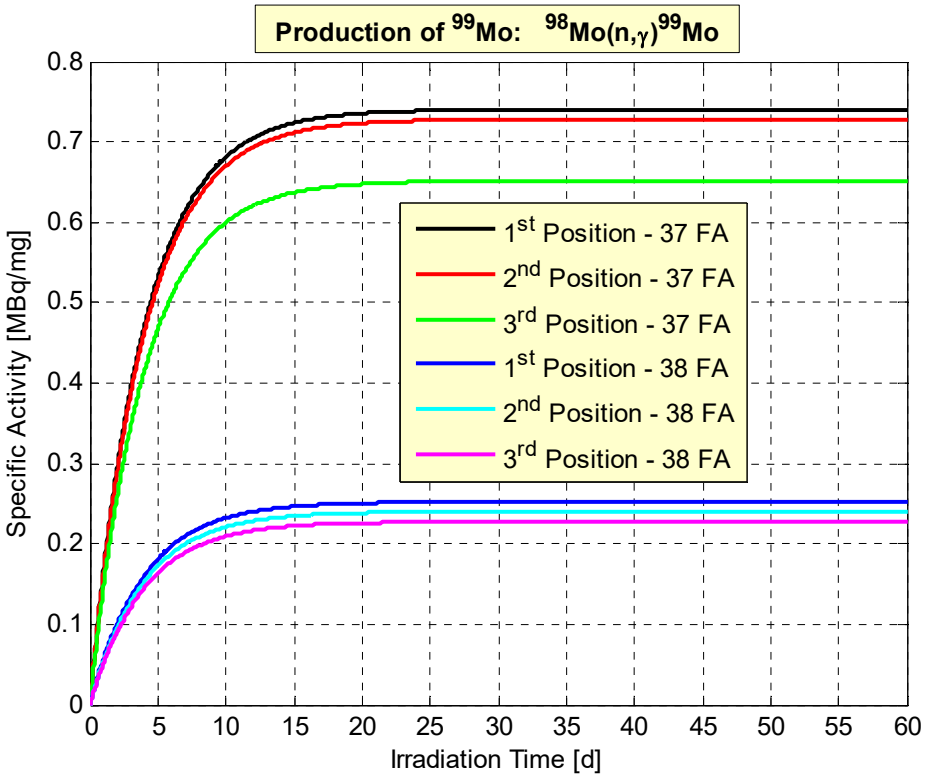

Figure VIII.3.4.1. ^{99}Mo activity as a function of the irradiation time, accounting for self-shielding

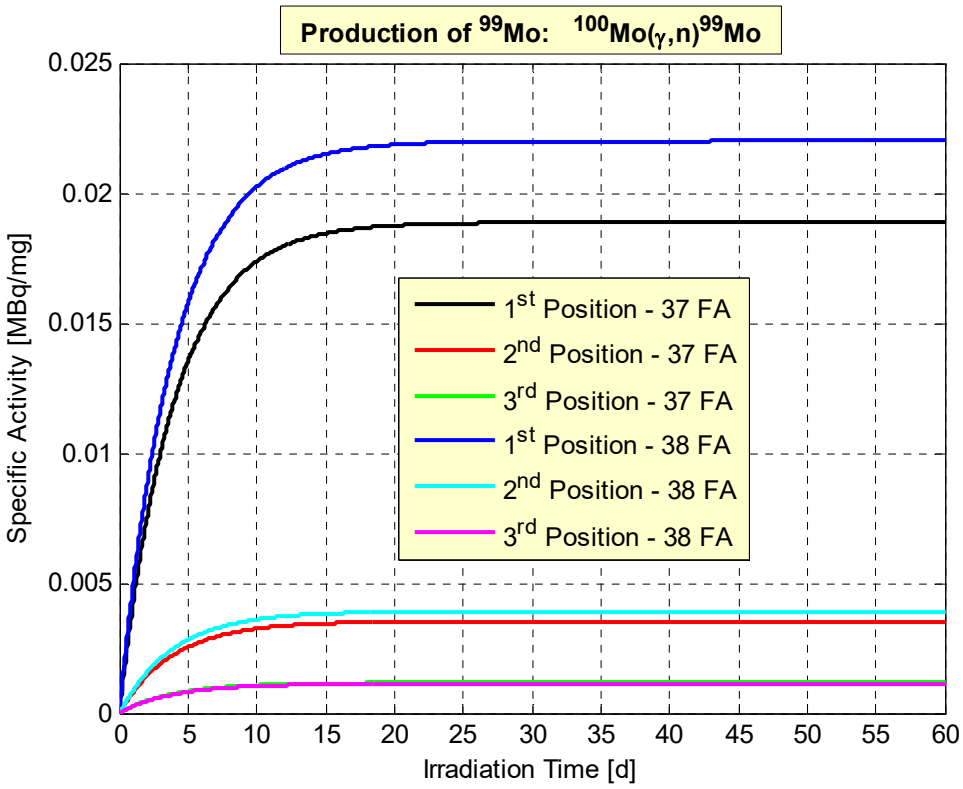

Figure VIII.3.4.2. ^{99}Mo activity as a function of the irradiation time

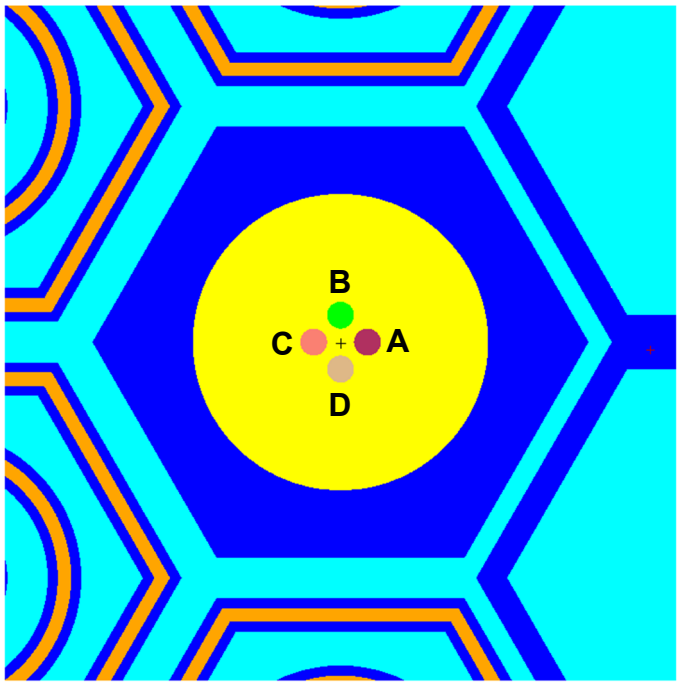

Figure VIII.3.5.1. Close-up of the horizontal section of the fuel zone of the SCA; configuration with 38 fuel assemblies; irradiation holder in position 1

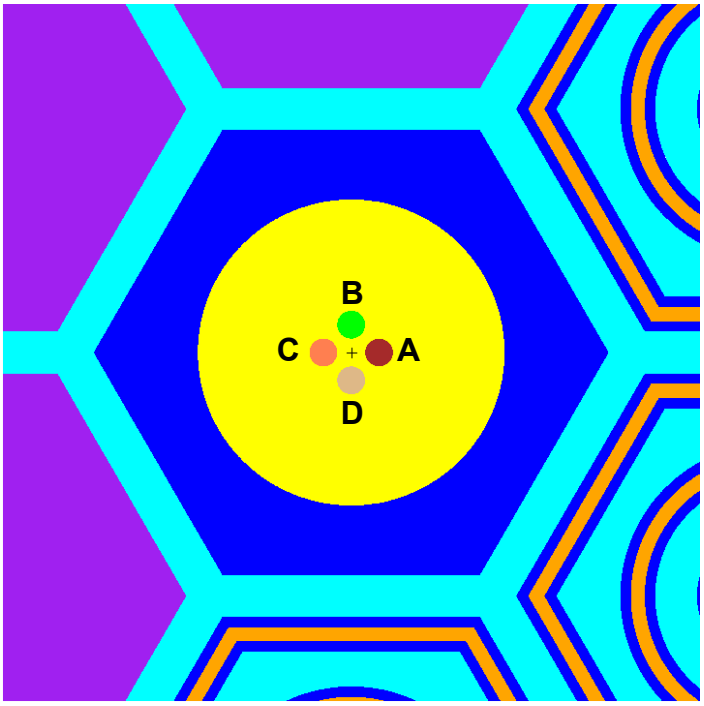

Figure VIII.3.5.2. Close-up of the horizontal section of the fuel zone of the SCA; configuration with 38 fuel assemblies; irradiation holder in position 3

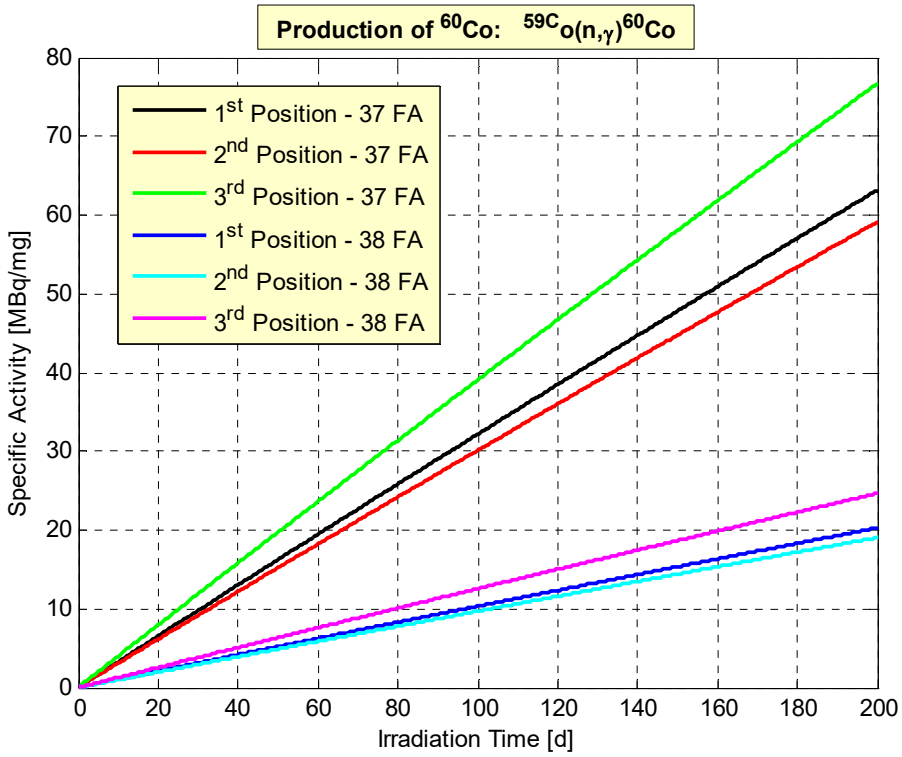

Figure VIII.3.5.3. ^{60}Co activity, with self-shielding effect, as a function of the irradiation time

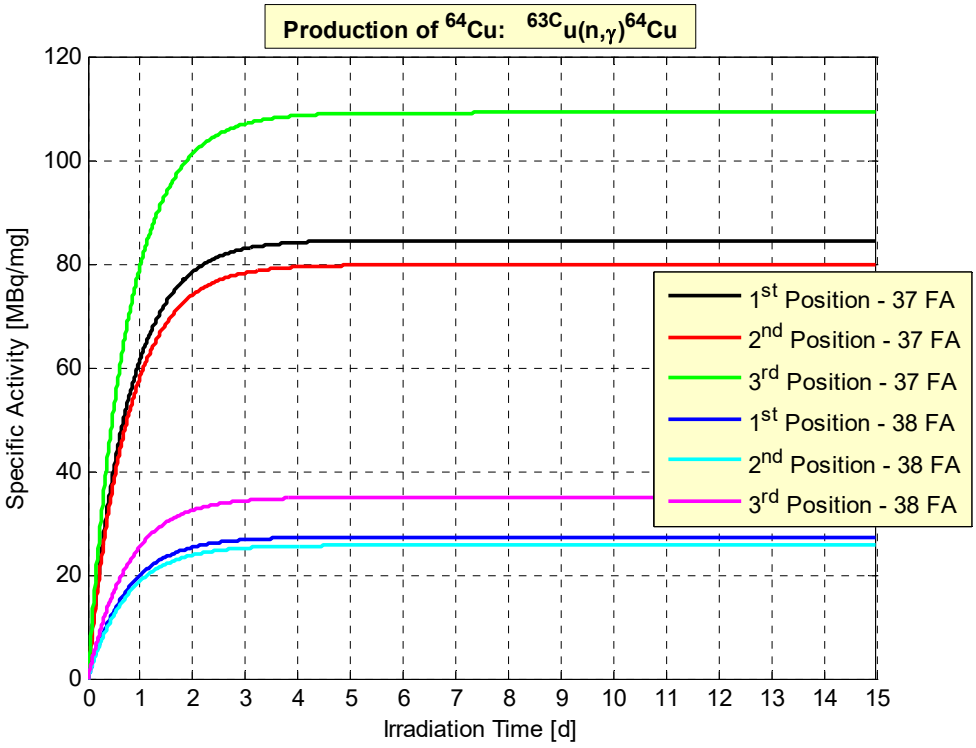

Figure VIII.3.5.4. ^{64}Cu activity, with self-shielding effect, as a function of the irradiation time

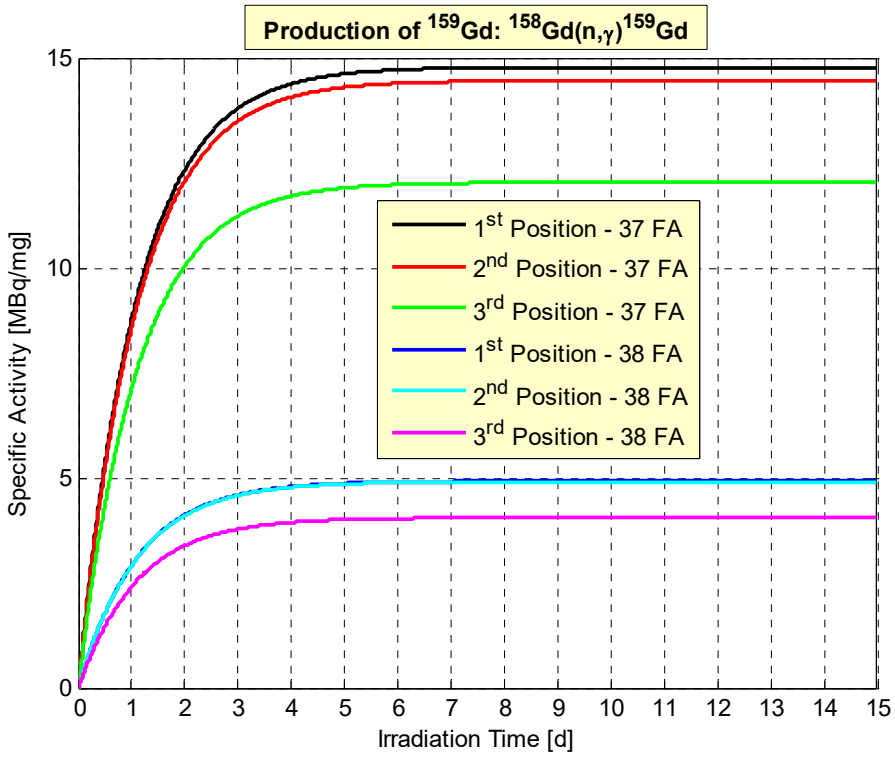

Figure VIII.3.5.5. ^{159}Gd activity, with self-shielding effect, as a function of the irradiation time

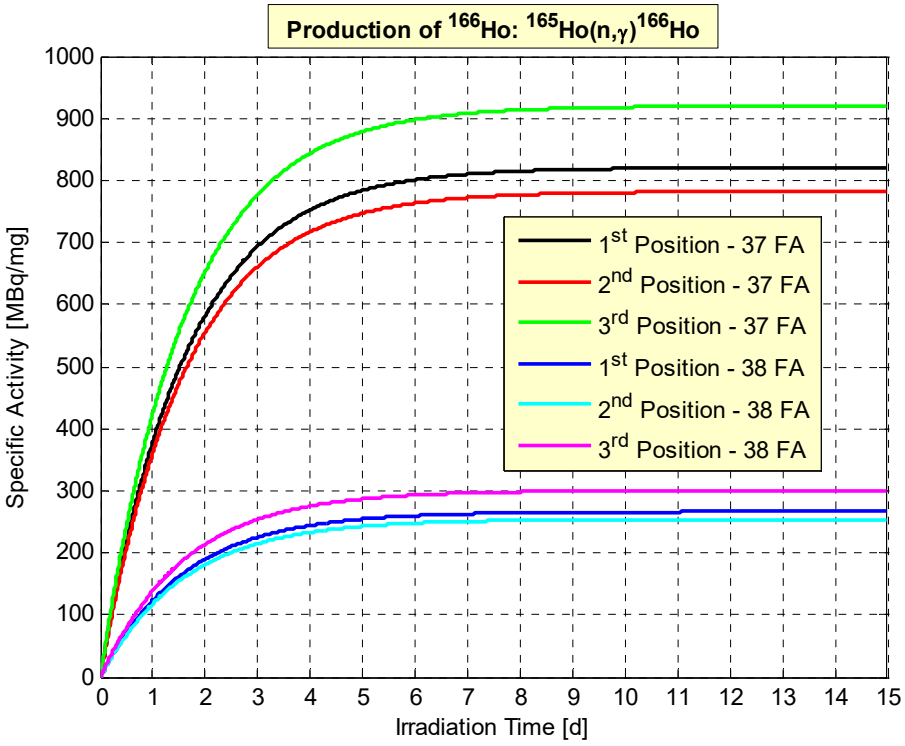

Figure VIII.3.5.6. ^{166}Ho activity, with self-shielding effect, as a function of the irradiation time

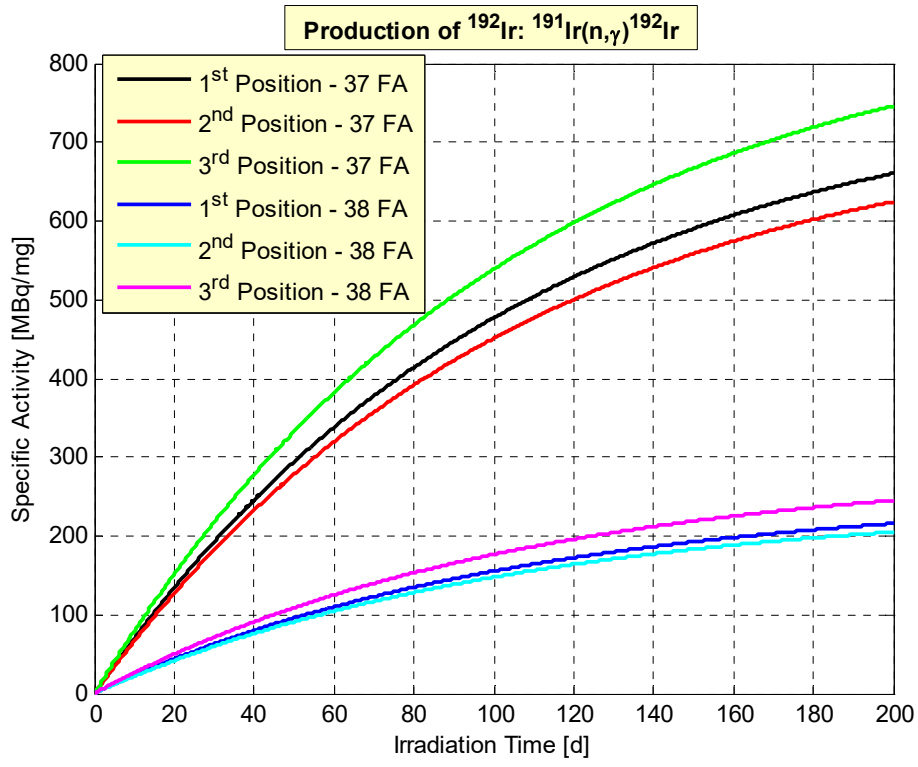

Figure VIII.3.5.7. ^{192}Ir activity, with self-shielding effect, as a function of the irradiation time

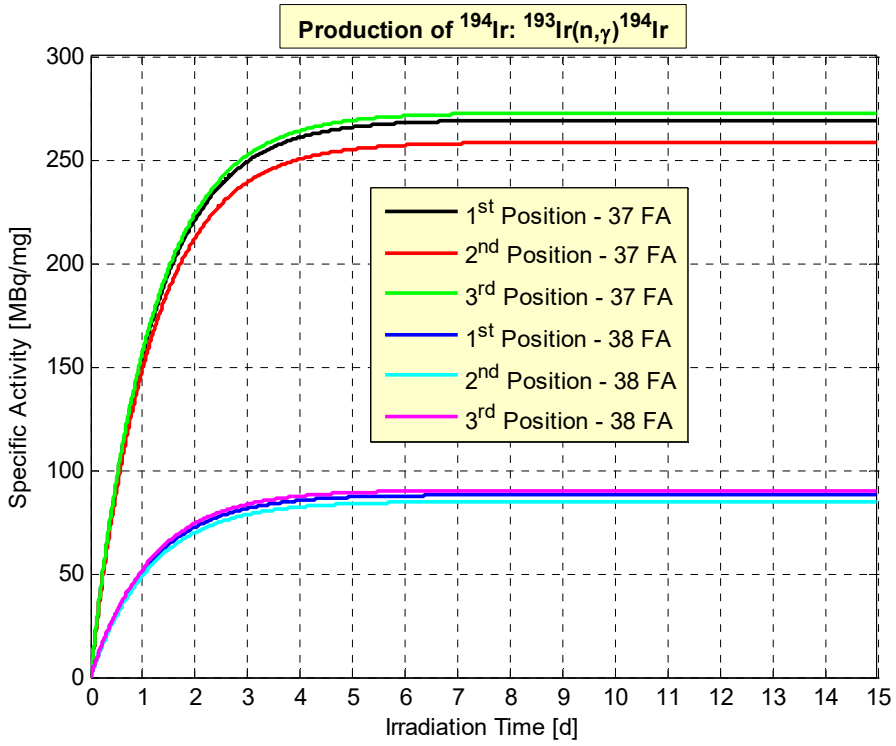

Figure VIII.3.5.8. ^{194}Ir activity, with self-shielding effect, as a function of the irradiation time

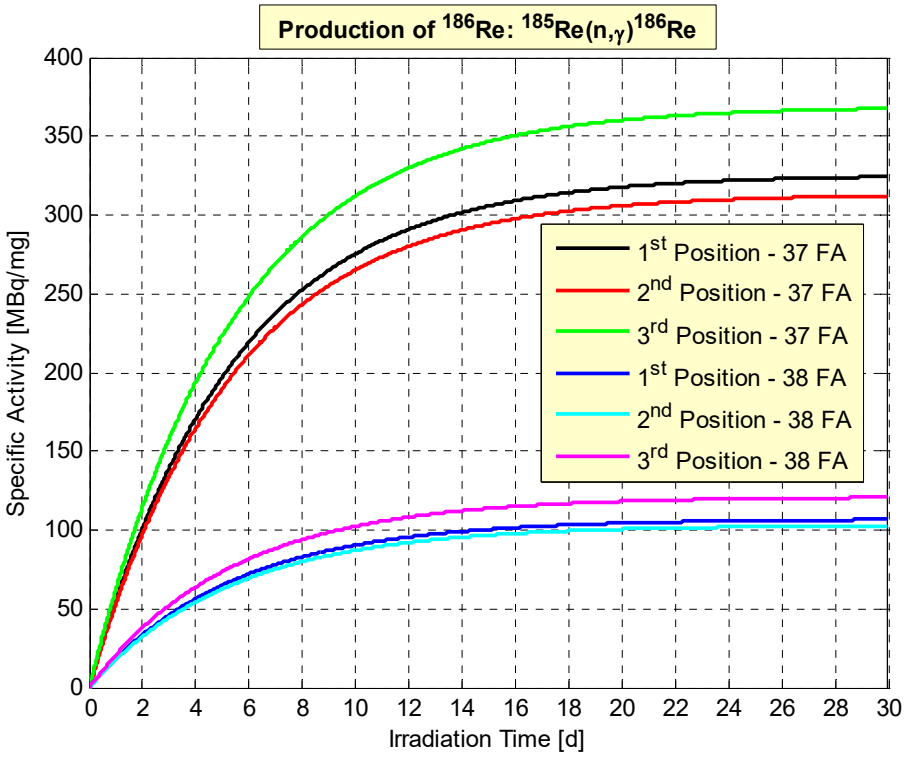

Figure VIII.3.5.9 ^{186}Re activity, with self-shielding effect, as a function of the irradiation time

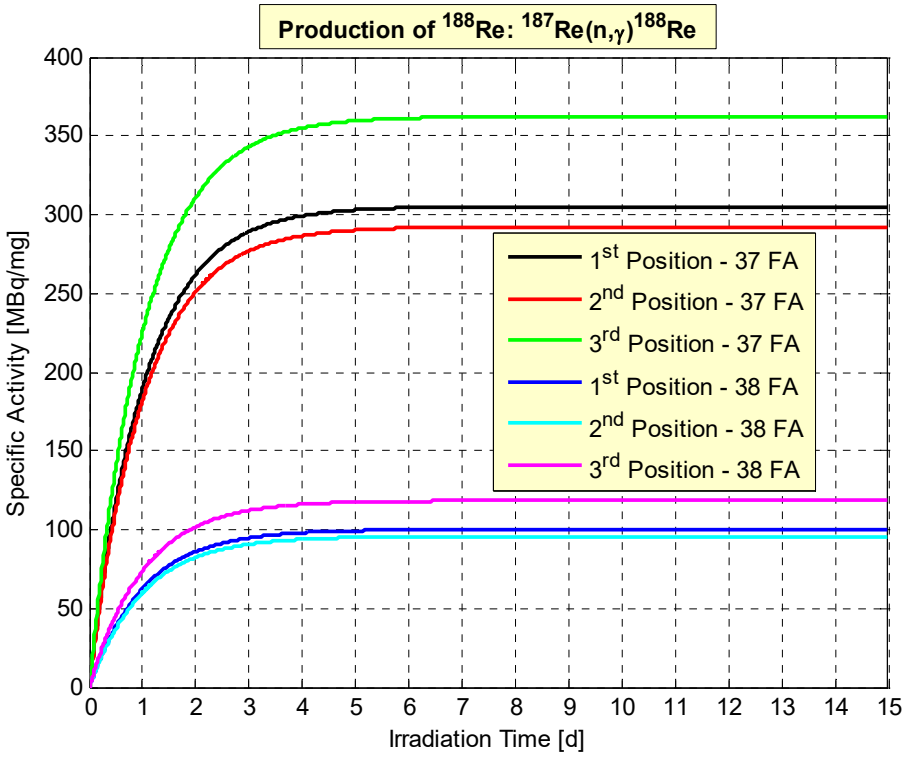

Figure VIII.3.5.10. ^{188}Re activity, with self-shielding effect, as a function of the irradiation time

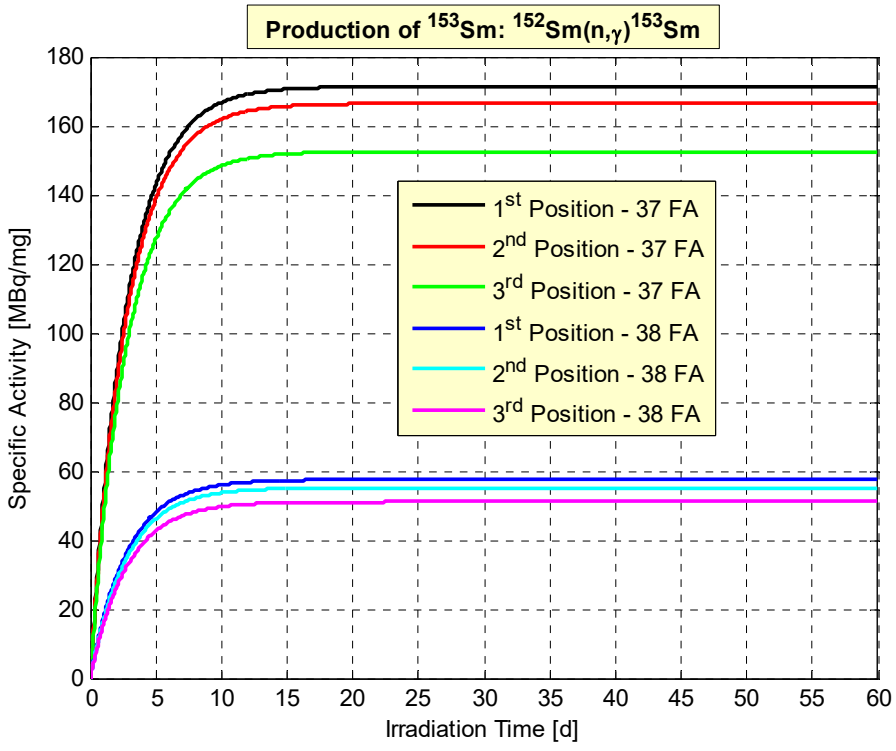

Figure VIII.3.5.11. ^{153}Sm activity, with self-shielding effect, as a function of the irradiation time

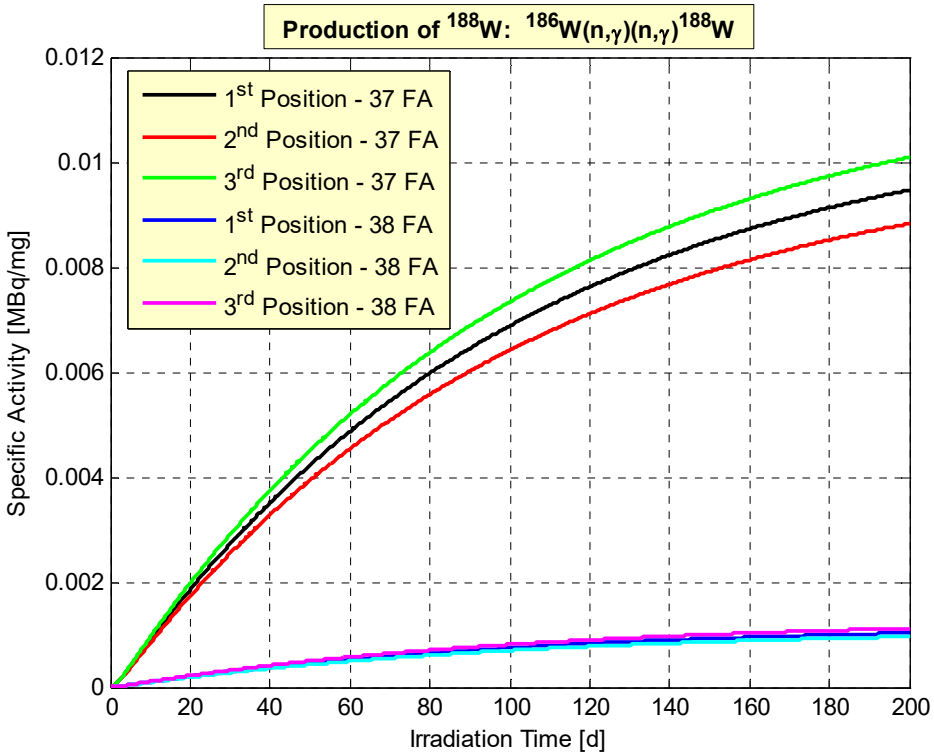

Figure VIII.3.5.12. ^{188}W activity, with self-shielding effect, as a function of the irradiation time

VIII.4 Sample Irradiation Cassette Design

The subcritical assembly provides an environment for irradiation of material samples. A sample cassette contains the sample and is used to move the sample in and out of the SCA.

VIII.4.1 Sample Cassette Strategy

The sample cassette is dimensionally like a fuel assembly and can be placed at any location in the grid plate or in the storage racks in the SCA. Figure VIII.4.1.1 shows a sample cassette placed in the subcritical assembly of the SCA. The sample cassette can also be placed in the fuel storage rack in the spent fuel storage pool. Figure VIII.4.1.2 shows the sample cassette side-by-side with a fuel assembly for comparison.

VIII.4.2 Sample Cassette Structure

The sample cassette is constructed of aluminum to allow minimal attenuation of the neutron flux. The cassette consists of a body and a cap. The cap of the cassette has a male thread which mates with a female thread in the cassette body. The cap has a knob which is used for moving the cassette with the dipsticks and the fuel handling machine, as shown in Fig. VIII.4.2.1. A metal C-ring seal prevents water from entering the sample cassette. Figure VIII.4.2.2 shows an exploded view of the sample cassette body, cap, and seal ring. The cassette can accommodate samples up to 20 mm in diameter and 500 mm long.

VIII.4.3 Sample Cassette Operation

The sample cassette is moved within the SCA by the fuel handling machine. The cassette has a hexagonal shape and must be oriented to the hexagonal pattern of the grid plate when being inserted into the grid plate.

The sample cassette is moved to and from the SCA in the fuel transfer cask to provide shielding of irradiated samples. The fuel transfer cask moves the cassette to the hot cell, where it is removed and opened for sample removal and processing. Figure VIII.4.3.1 shows the fuel transfer cask interfacing with the hot cell. The fuel transfer dipstick is used to lift/lower the sample cassette into/out of the fuel transfer cask, as shown in Fig. VIII.4.3.2. The overhead crane carries the fuel transfer cask from location to location within the subcritical hall.

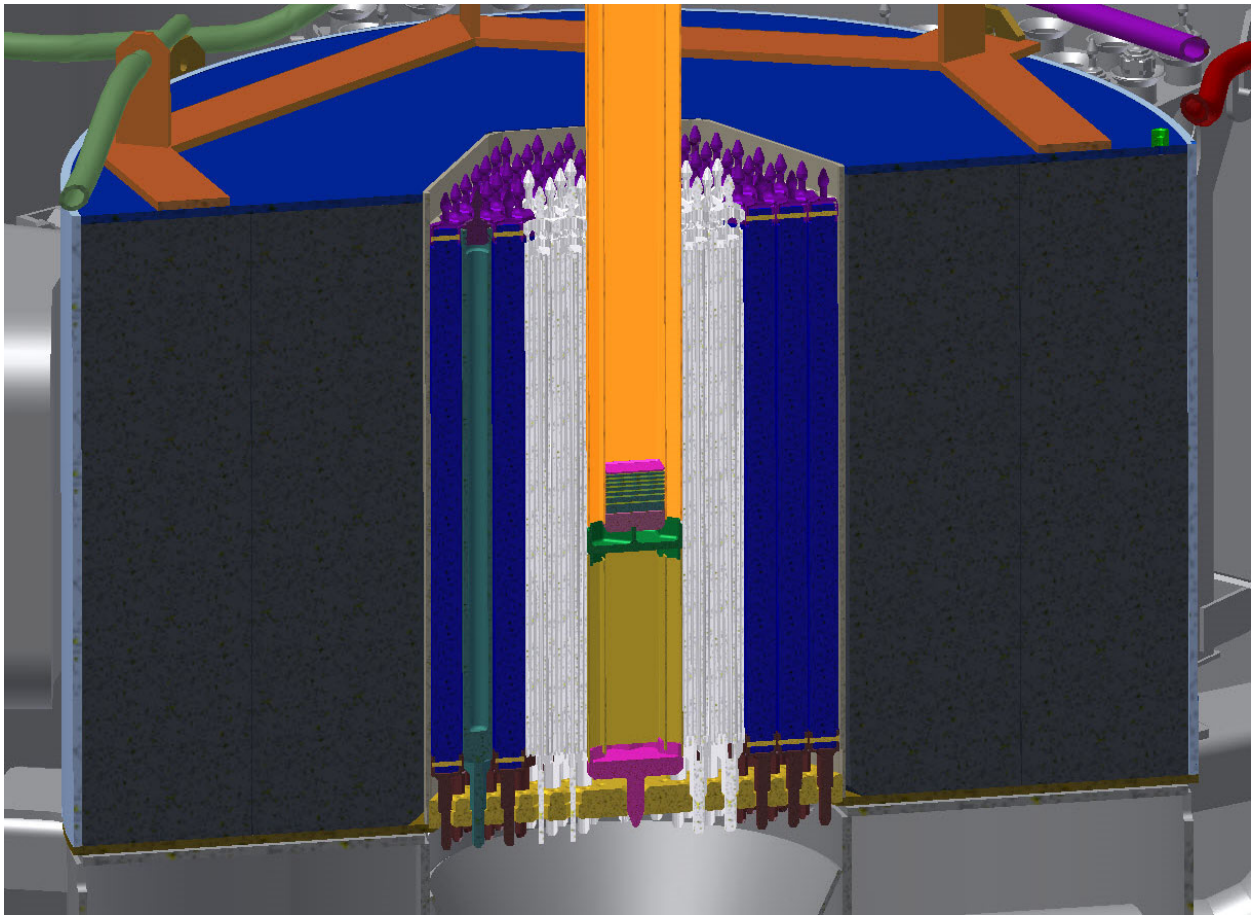

Figure VIII.4.1.1. Section view of the subcritical assembly, showing a sample cassette placed to the left of the target assembly. The sample cassette in this image contains no sample.

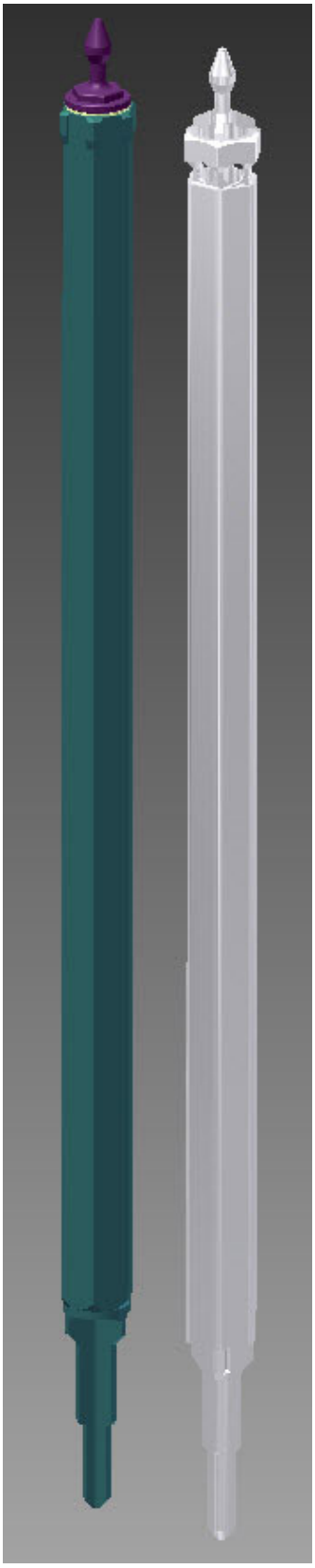

Figure VIII.4.1.2. View of the sample cassette next to a fuel assembly, right.

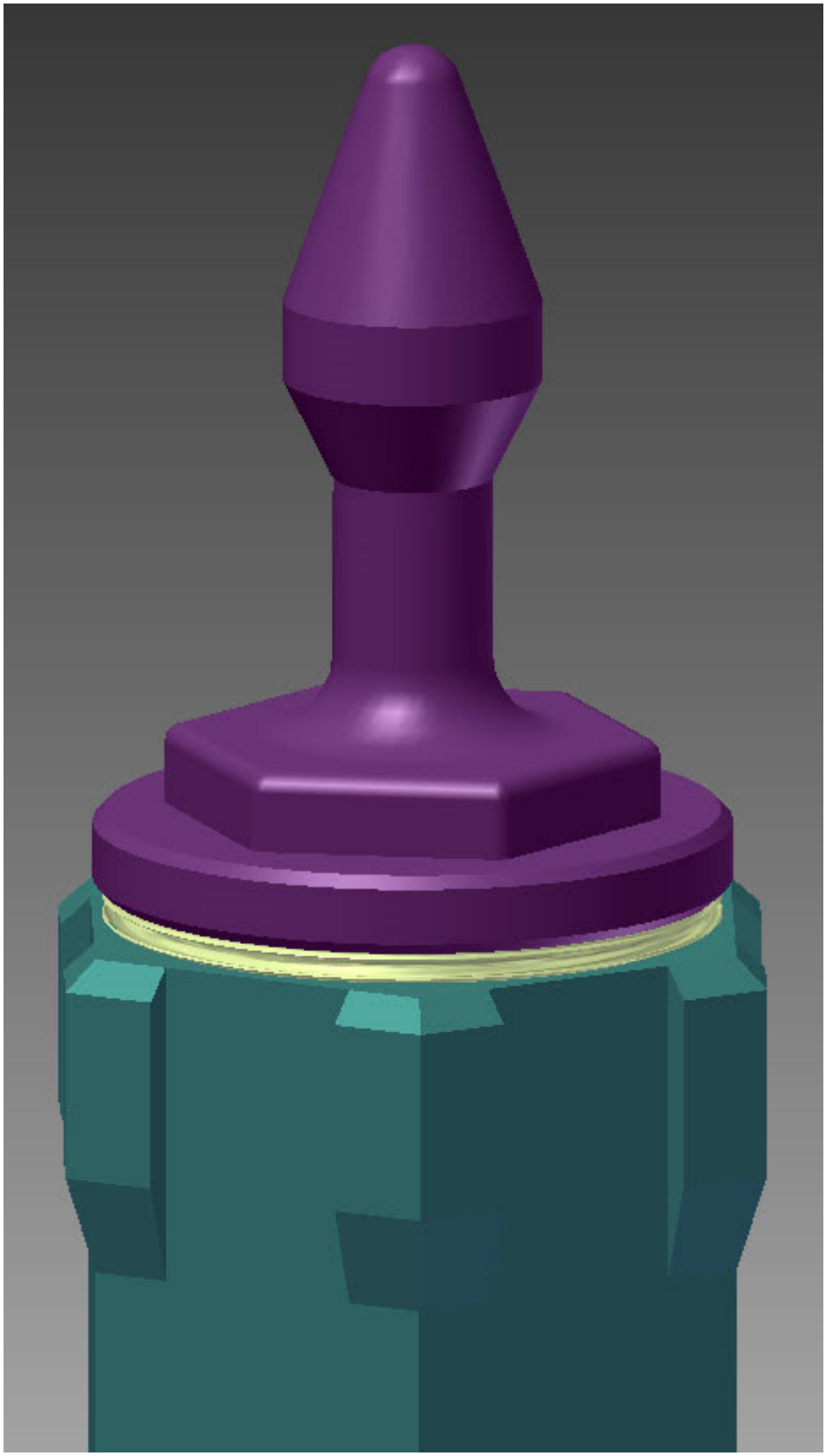

Figure VIII.4.2.1. Top of sample cassette, showing lifting knob and seal.

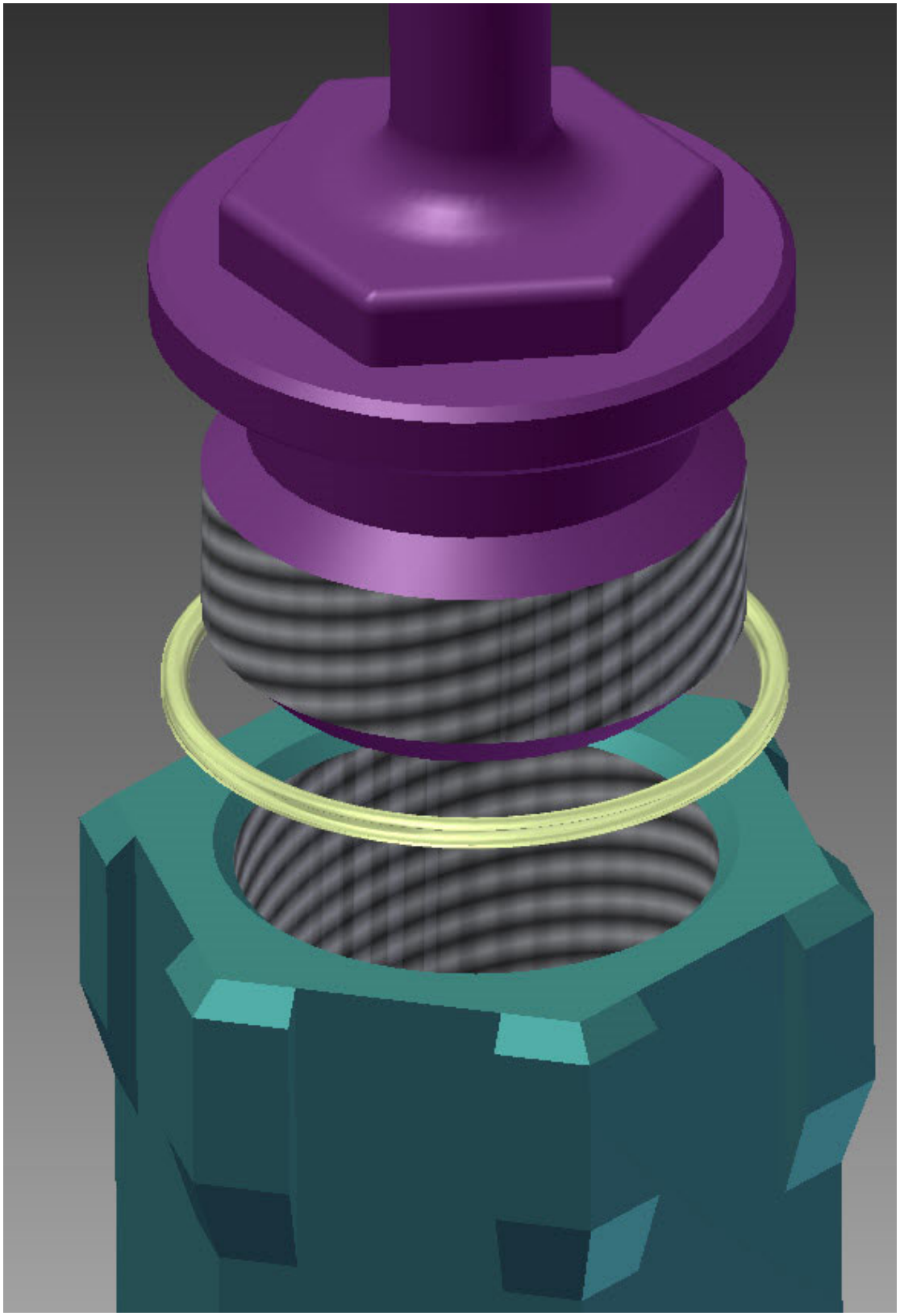

Figure VIII.4.2.2. Exploded view of the top of the sample cassette, showing threaded portions and metal C-ring seal.

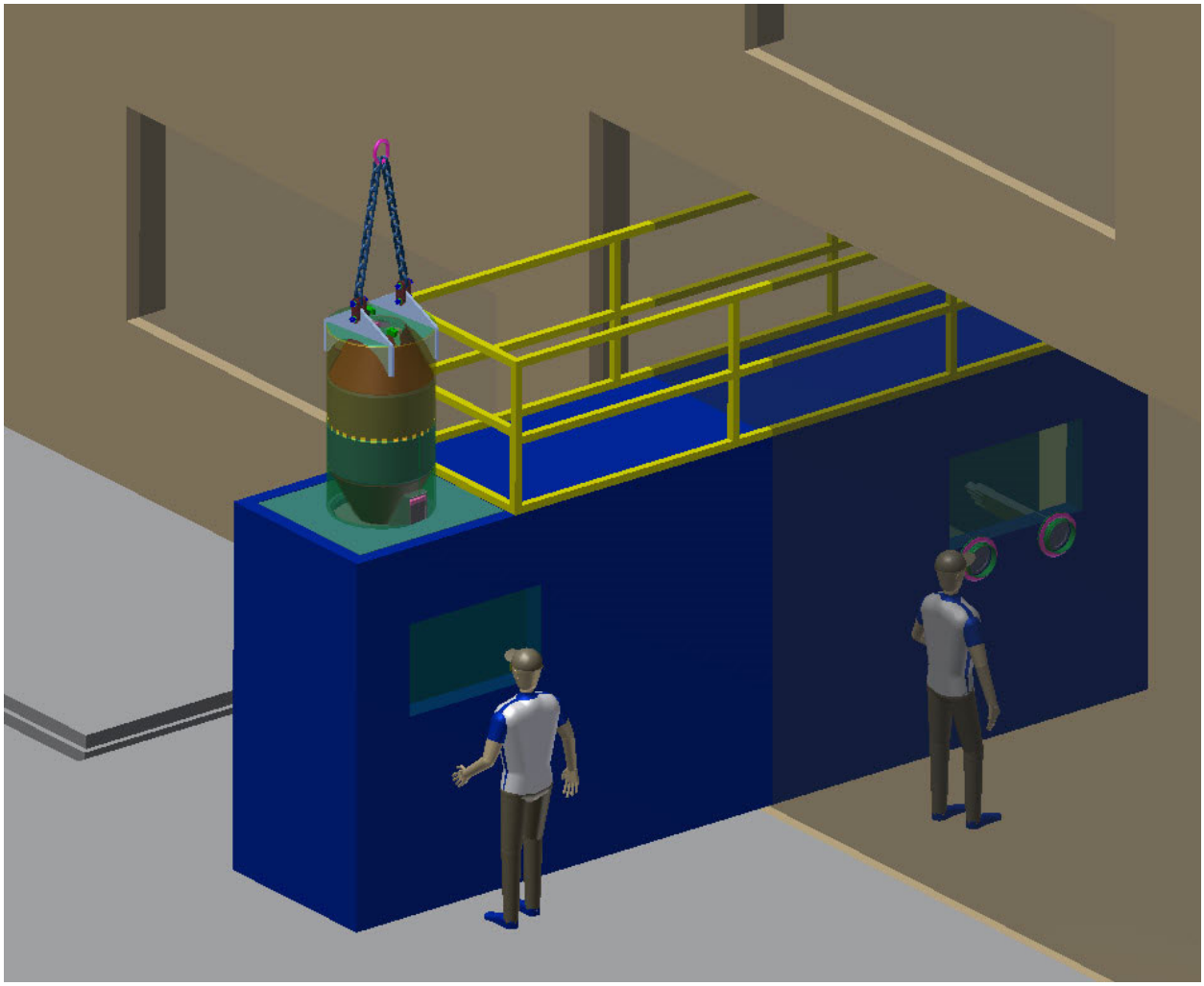

Figure VIII.4.3.1. Image of the hot cell, with fuel transfer cask transferring sample cassette to the hot cell.

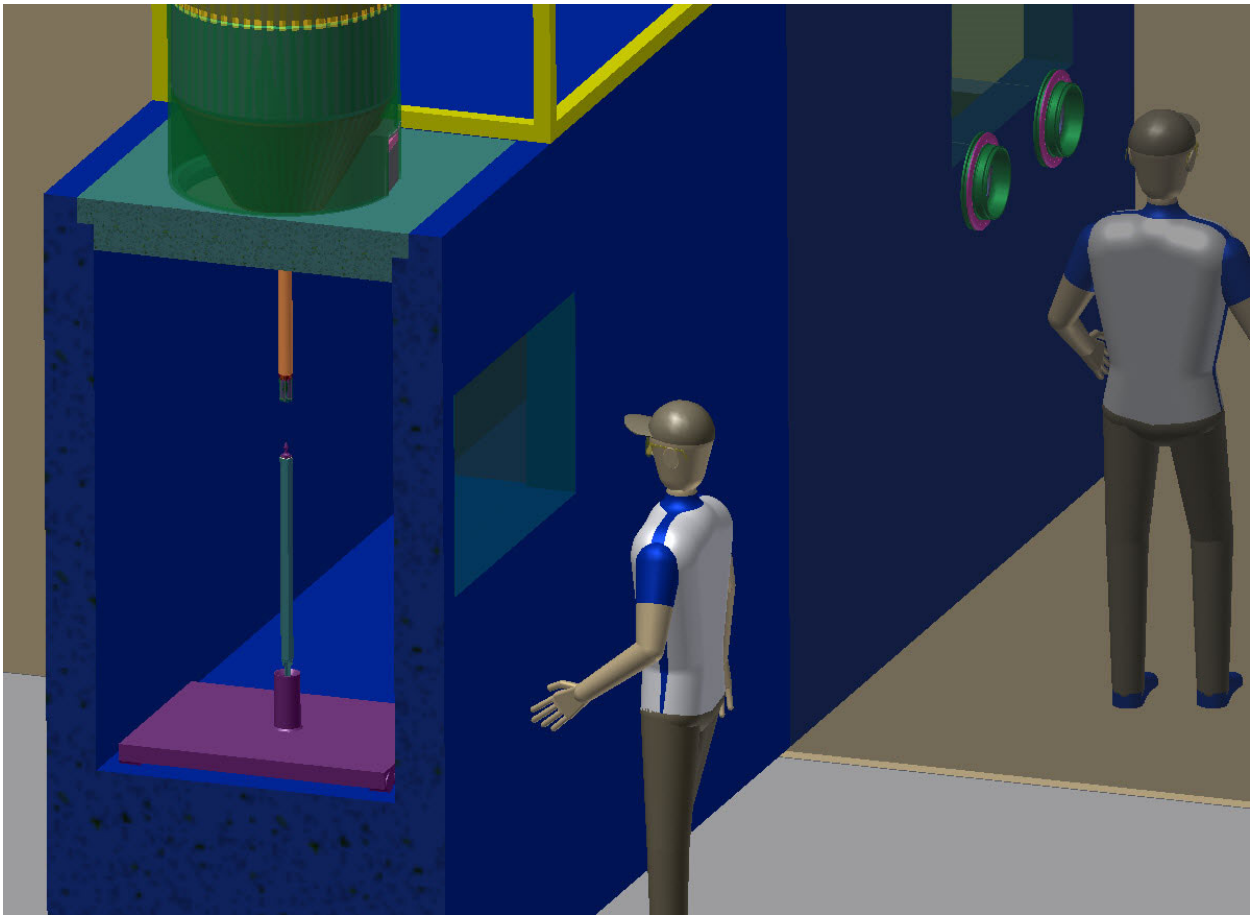

Figure VIII.4.3.2. Section view through the hot cell, showing fuel transfer cask, dipstick reaching through fuel transfer cask, and sample cassette in the hot cell.

VIII.5 Conclusions

This analysis has shown the capability of the Kharkiv facility to produce medical isotopes. After 20 irradiation days: ^{82}Br, ^{64}Cu, ^{165}Dy, ^{166}Ho, ^{192}Ir, ^{194}Ir, ^{186}Re, ^{188}Re and ^{153}Sm have specific activities, without the self-shielding effect, larger than 100 MBq/mg and therefore they can be produced in the SCA. The parent isotopes with large microscopic absorption cross sections require an accurate evaluation of the specific activity including the self-shielding effect. The latter phenomenon can reduce the specific activity by a large factor. Analyses of a molybdenum irradiation sample that account for self-shielding show that the self-shielding effect reduces the specific activity by a factor of 9. The specific activity of ^{99}Mo obtained from photon reaction is small. The specific activity of ^{99}Mo is more than 0.7 MBq/mg after 12 days of irradiation time from ^{98}Mo(n,γ) reaction. For ^{60}Co, ^{64}Cu, ^{159}Gd, ^{166}Ho, ^{192}Ir, ^{194}Ir, ^{186}Re, ^{188}Re, ^{153}Sm, and ^{188}W, analyses show that the self-shielding effect reduces the specific activity by a factor 1.9, 1.4, 2.8, 2.3, 7.3, 8.0, 4.1, 2.6, 13.3, and 4.5, respectively. The subcritical assembly has the capacity to generate enough ^{99}Tc for 112 heart medical procedures every 10 days.

References

VIII.1 A. Talamo and Y. Gohar, “Radioactive Isotope Production for Medical Applications Using Kharkiv Electron Driven Subcritical Assembly Facility,” Argonne National Laboratory, ANL-07/18, 2007.

VIII.2. A. Talamo and Y. Gohar, “Production of Medical Radioactive Isotopes Using KIPT Electron Driven Subcritical Facility,” Applied Radiation and Isotopes **66**, pp. 577-586, 2008.

VIII.3. IAEA, “Manual for Reactor Produced Radioisotopes”, International Atomic Energy Agency, IAEA-TECDOC-1340, 2003.

VIII.4. Committee on Medical Isotopes Production, “Medical Isotope Production without Highly Enriched Uranium”, The National Academies Press, ISBN 0-309-13040-9, 2009.

VIII.5. S. J. Adelstein, T.F. Budinger, R. E. Coleman, D. Danford, W.C. Eckelman, J.A. Nolen, L.L. Riedinger, T.J. Ruth, L. S. Schroeder, M.J. Welch, and S.W. Yates, “Isotopes for Medicine and Life Science,” The National Academies Press, ISBN 0-309-05190-8, 1995.

VIII.6. K. A. Van Riper, S. G. Mashnik and W.B. Wilson, “A Computer Study of Radionuclide Production in High Power Accelerators for medical and industrial applications,” Nuclear Instruments & Methods in Physics Research A **463**, pp. 576-585, 2001.

VIII.7. S. Mirzadeh, C.W. Alexander, T. Mc Manamy and F.F. Knapp, “Projected Medical Radioisotope Production Capabilities of the Advanced Neutron Source (ANS),” Oak Ridge National Laboratory, ORNL/TM-10210-S, 1994.

VIII.8. M. Neves, A. Kling and R. M. Lambrecht, “Radionuclide Production for Therapeutic Radiopharmaceuticals,” Applied Radiation and Isotopes **57**, pp. 657-664, 2002.

VIII.9. D. B. Pelowitz et al., “MCNPX 2.7A Extensions,” LA-UR-08-07182, 2008.

VIII.10. International Atomic Energy Agency, “Nuclear Data Section”, http://nucleus.iaea.org/sso/nucleus.html?exturl=http://www-nds.iaea.org/capgam/index.htmlx.

VIII.11. V. S. Le, “^{99m}Tc Generator Development: Up-to-date ^{99m}Tc recovery Technologies for increasing the effectiveness of ^{99}Mo Utilization,” Science and Technology of Nuclear Installations 345252, (2014).

IX Experimental neutron channels

IX.1 Introduction

The neutron channels of the KIPT neutron source facility were designed to provide neutron beams for experimental purposes. A beam shutter was designed to be able to close the neutron channel and reduce the radiation dose outside the shield below 0.5 mrem/hr. A five-piece shield design was selected for the shutter, with each piece being able to rotate at a different angle to close the beam. Two different shield materials, heavy concrete and stainless steel were used as filler for the shutter pieces.

Sec. IX.2 discusses the shutter design, the dose analysis with respect to the regulatory limit of 0.5 mrem/hr. Sec. IX.3 summarizes the mechanical design of the channel shutter and describes the shield plugs.

IX.2 Channel Shutter Shield Performance

A five-piece rotatable beam shutter has been designed to close each neutron channel. The mechanical design of the channel shutter is described in the next section. Each piece of the shutter has an empty cylinder with 10 cm diameter. During the operation of the facility, the empty cylinders of the five pieces can be aligned with the neutron channel to provide a neutron beam in an experimental channel. The beam can be closed by rotating the shutter pieces so that the holes are no longer aligned.

The objective of the shield design was to limit the biological dose to less than 0.5-mrem/hr when the neutron channel is closed. Stainless steel and heavy concrete are used as shield materials in the beam shutter. The best shield performance was obtained when the five pieces of the beam shutter are filled with stainless steel and heavy concrete in a sandwiched configuration, as shown in Fig. IX.2.1. Three pieces of the shutter are filled with stainless steel and the remaining two pieces are filled with heavy concrete.

The radial shield analysis of the KIPT neutron source facility shows that 140 cm of heavy concrete is needed radially to reduce the neutron dose outside the shield boundary to less than 0.5 mrem/hr as shown in see Sec. IV.2.1. The rotational positions of the five shutter pieces when the beam is closed are shown in Fig. IX.2.2, with the holes inside the shutters set 60° apart from each other.

If the five shutter pieces were filled with heavy concrete, the effective shield thickness would be less than 140 cm due to the holes inside the shutters. This increases the biological dose outside the neutron channel. Stainless steel is another option for shielding neutrons; it can slow down high energy neutrons (E > 10 MeV) more efficiently than the heavy concrete but is not as efficient as the heavy concrete for absorbing low energy neutrons (E < 10 MeV). An MCNPX calculation was performed with all five pieces of the beam shutter filled with stainless steel. The tungsten target case with 38 fuel assemblies was selected for this analysis because of its higher neutron dose outside the radial heavy concrete shield as shown in section IV.2. The calculated biological dose from neutrons outside the shutter is ~5.0 mrem/hr averaged over the whole shutter surface and ~16 mrem/hr averaged over the hole area of piece 5. Therefore, the beam shutter was

designed with a combination of stainless steel and heavy concrete regions to improve the shielding performance of the shutter.

MCNPX calculations were performed to tally the neutron biological dose on the outer surface of the beam shutter, when the neutron beam is closed by having the five shutter pieces rotated to the positions shown in Figure IX.2.2. The weight windows variance reduction technique was utilized in these calculations, and the neutron source files were utilized to save computation time, following the same process as used in the shield calculation of section IV.2. The neutron biological dose was tallied on the outer boundary of piece 5, as diagrammed in Fig. IX.2.3. The neutron biological dose was tallied across the hole cross section area, the stainless-steel axis cross section area, the outer stainless steel frame area, and the whole surface. The obtained results are summarized in Table IX.2.1.

Based on the results shown in Table IX.2.1, if the shutter hole is unplugged, there exists a large neutron dose across the hole for either target type. Therefore, a plug made of stainless steel was designed for the hole in piece 5. If the hole in piece 5 is plugged, the neutron dose across the hole is reduced considerably. The results also show that there exists a large neutron dose across the axis and outer frame, which are made of stainless steel, especially for the case using the uranium target, and that the doses in all locations are still unacceptably for both types of targets. To reduce the neutron dose below 0.5 mrem/hr, a layer of borated polyethylene with 3 cm thickness was added outside the beam shutter, as shown in Figure IX.2.1. With the addition of the borated polyethylene layer, the neutron dose outside the beam shutter can be kept below 0.5 mrem/hr for both targets when the beam is closed.

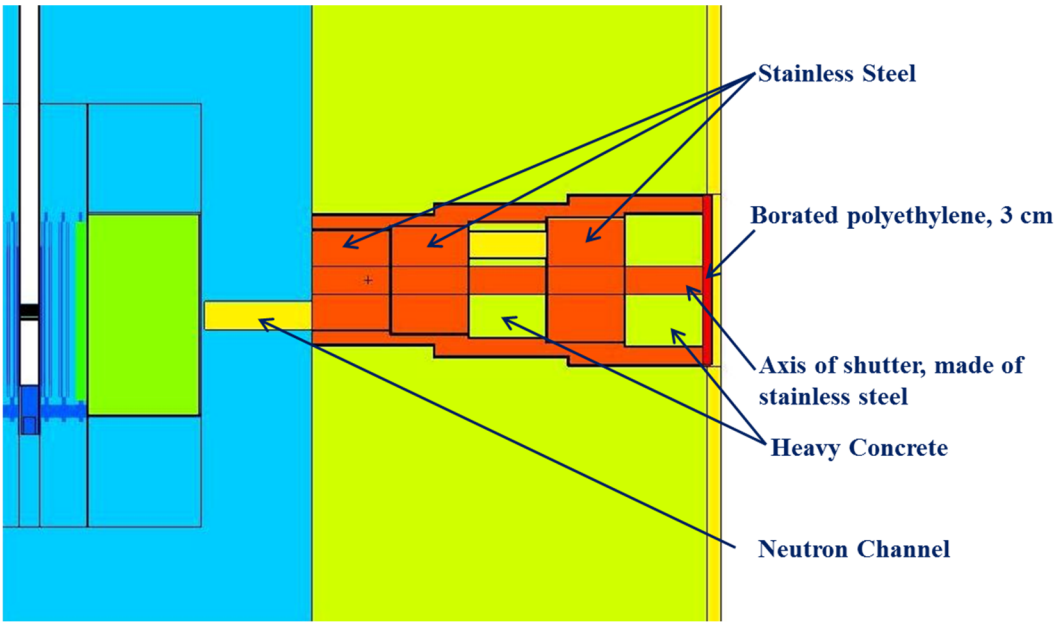

Figure IX.2.1. Configuration of the five-piece shutter of a neutron channel

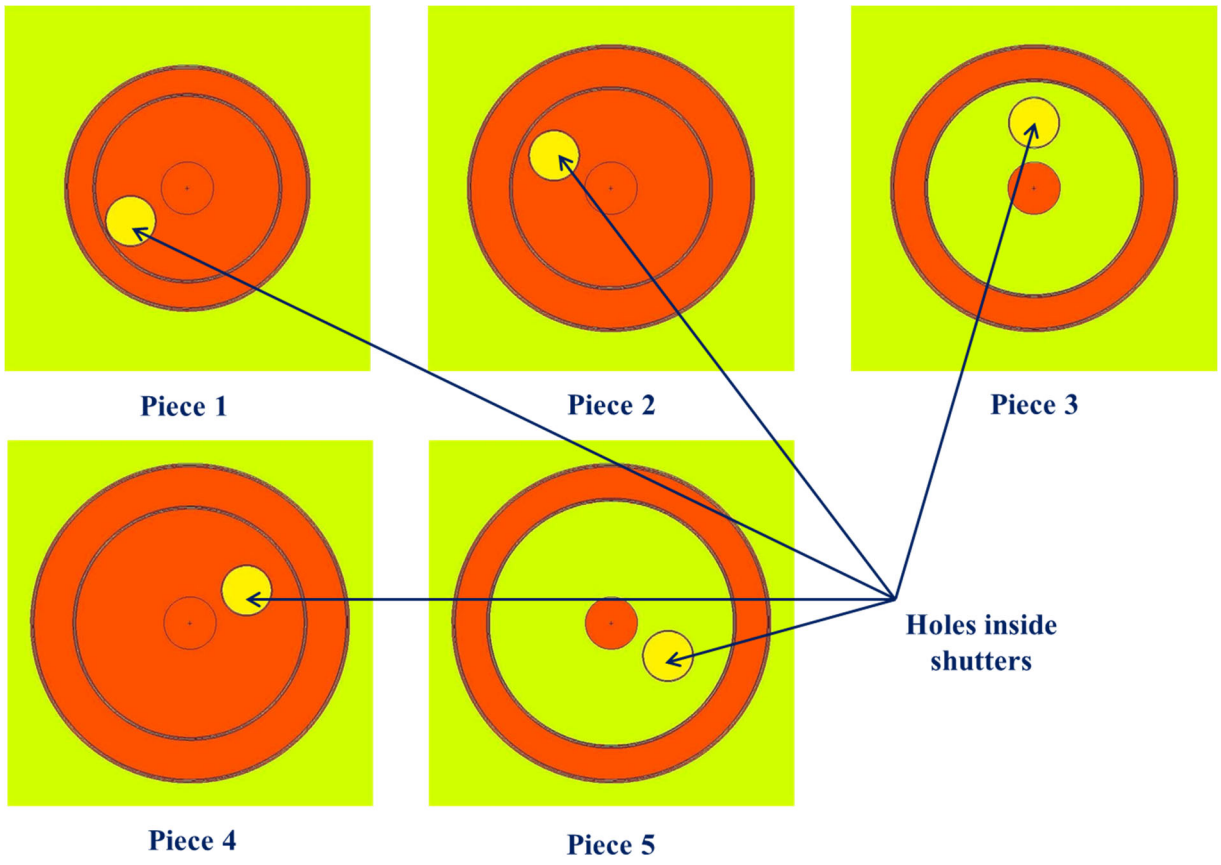

Figure IX.2.2. Positions of holes inside the shutters when the beam is closed

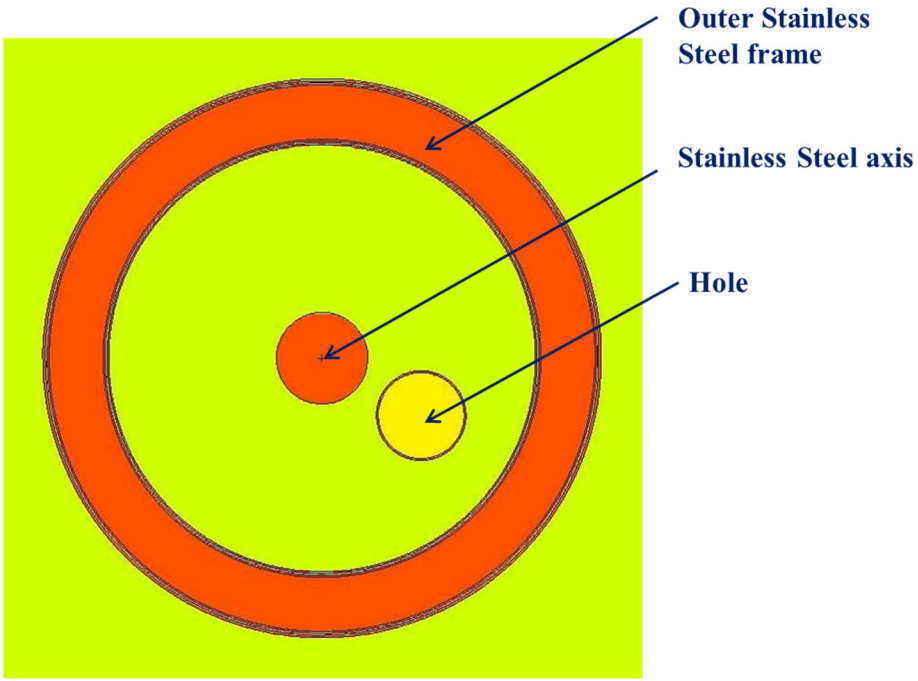

Figure IX.2.3. Axial view of neutron channel shutter showing the tally surfaces

Table IX.2.1. Neutron dose on the outer boundary of the beam shutter

Configuration	Shutter Status	Neutron Dose (mrem/hr) Surface			
		Hole	Stainless Steel Axis	Stainless Steel outer Frame	Whole Surface
Tungsten Target with 38 fuel Assemblies	Unplugged	1.397 ±08.56%	0.552 ±13.12%	0.664 ±5.99%	0.557 ±4.21%
	Plugged	0.528 ±12.20%	0.542 ±11.92%	0.661 ±6.92 %	0.535 ±5.41%
	Plugged*	0.214 ±12.02%	0.263 ±10.84%	0.283 ±7.93%	0.243 ±4.86%
Uranium Target with 37 fuel Assemblies	Unplugged	3.189 ±07.68%	1.263 ±13.87%	0.968 ±4.89%	0.841 ±3.69%
	Plugged	0.784 ±10.64%	1.207 ±13.27%	0.993 ±4.78%	0.730 ±4.55%
	Plugged*	0.167 ±13.53%	0.273 ±13.64%	0.229 ±6.20%	0.176 ±4.67%

* With 3 cm of borated polyethylene outside the beam shutter

IX.3 Neutron Channel Shutter Design

The subcritical assembly facility provides five neutron channels for neutron experiments. Each neutron channel is equipped with a shutter that can be closed to block the neutron streaming through that channel. The shutters are located within the biological shielding ring, outside of the SCA Tank. Figures IX.3.1 and IX.3.2 show the general arrangement of the neutron channel shutters.

IX.3.1 Neutron Channel Shutter Operation Strategy

The five neutron channel shutters control the neutron current to individual neutron experiments. The shutters are independently controlled to deliver neutron current or to or block the neutron current to the neutron experiments. During experimental operation, the signals to open or close each of the channel shutters are initiated by the experimentalist. The position of each shutter is reported to the main control system. The main control system issues permission for each neutron channel shutter to be opened, but the actual control of the neutron channel shutter is issued by a local control located in the subcritical assembly hall near the neutron channel. The global control system can close any or all shutters at any time.

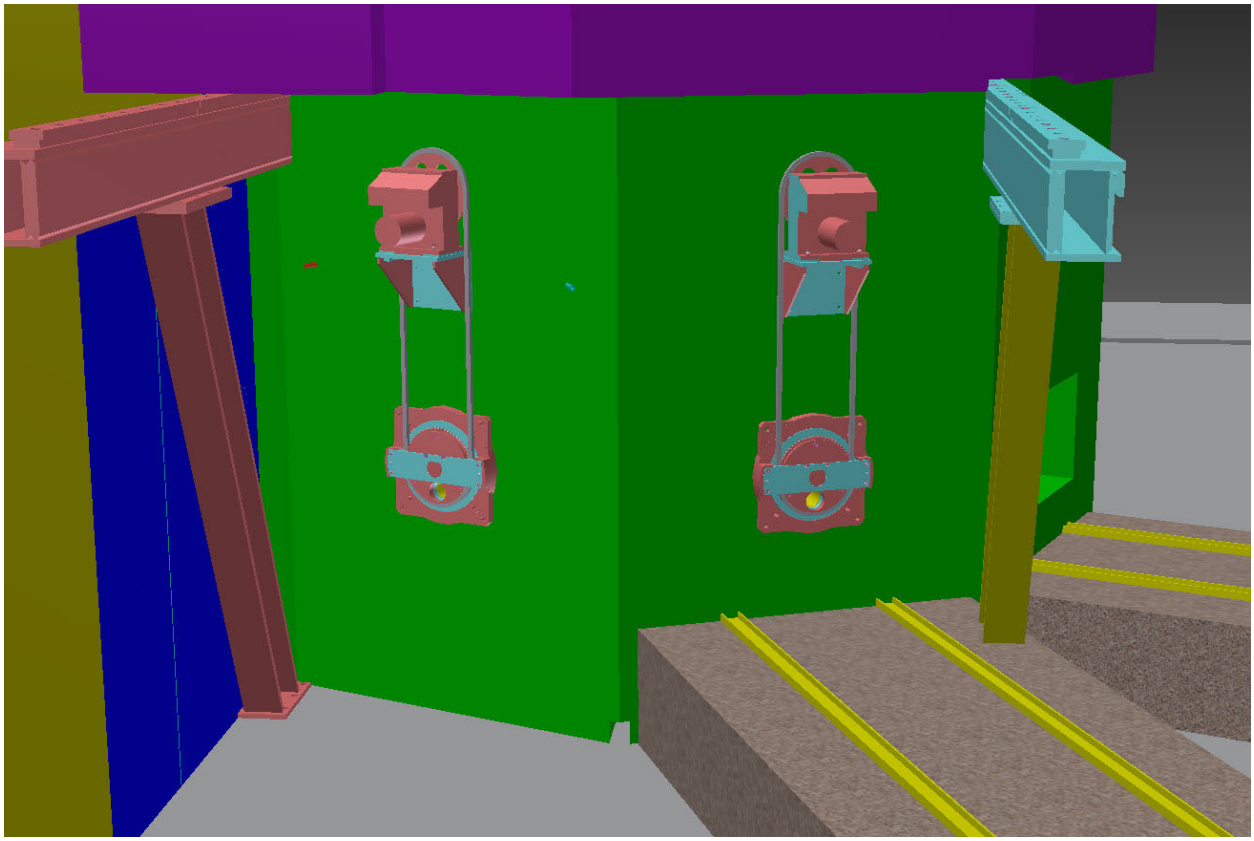

Figure IX.3.1. View of biological shielding ring showing two neutron channel shutters. Shutter drive motors are mounted. Channel shielding is not shown.

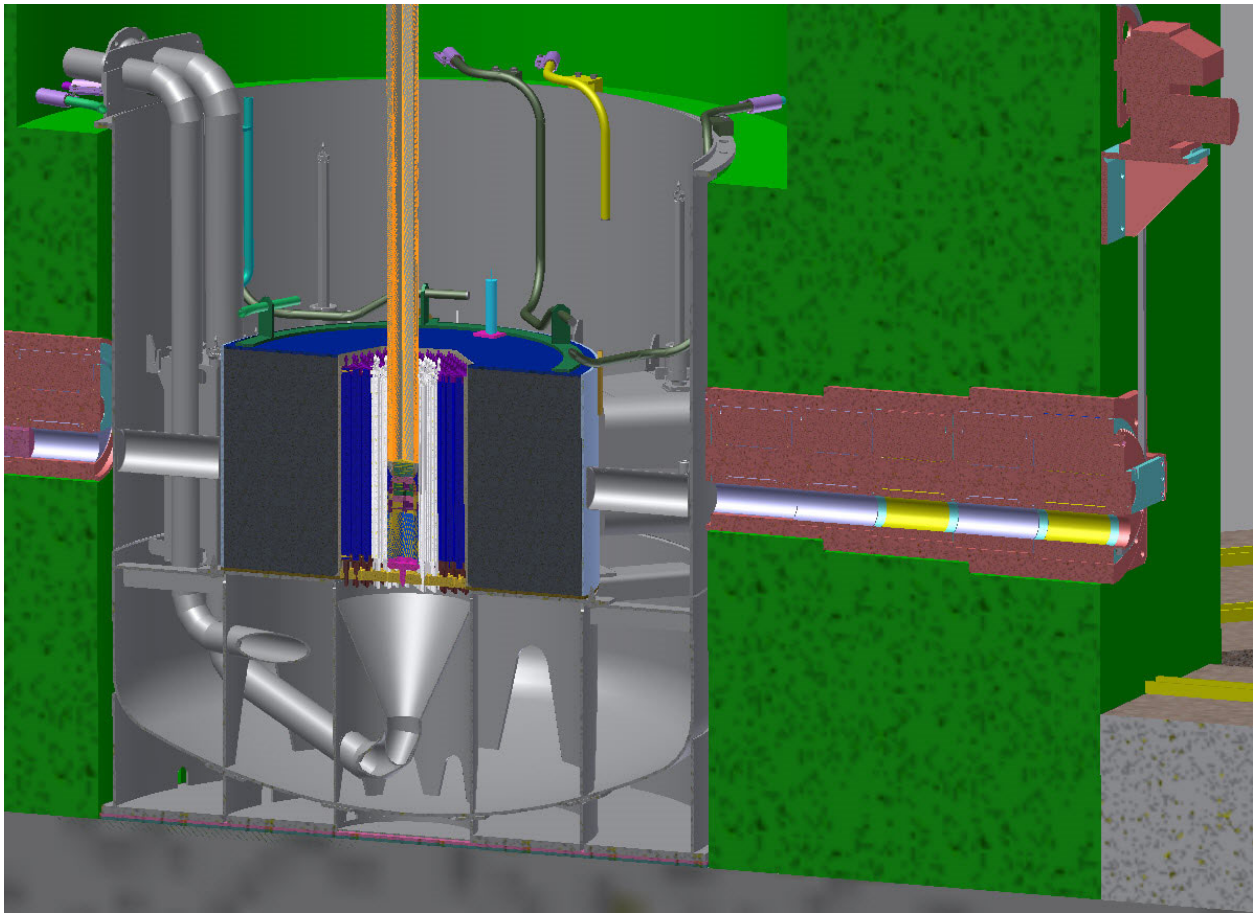

Figure IX.3.2. Vertical section view taken through Channel 5. The subcritical assembly tank, uranium fuel, beryllium and graphite reflectors, channel can, and channel shutter are shown. The shutter drive motor is visible on the outer wall of the biological shielding ring.

IX.3.2 Neutron Channel Shutter Structure

The five neutron channel shutters are structurally identical. Each shutter consists of five circular sections that are mounted on a common axis shaft. The five rotating sections are supported by brass bearings. Each section has a different outside diameter. Each section has an eccentric hole, which allows for the passage of the neutron current. When the holes in all five sections are aligned, neutrons current passes to the neutron experiment. When the five sections are rotated to different positions, the five holes do not align, and the shutter is closed. The axis shaft is supported at its ends by the shutter case. The shutter can be removed as a single unit for service operations. The exterior of the shutter case has three cylindrical sections of different diameters to prevent neutron streaming. The five rotating shutter sections are made of a variety of materials to provide the required shielding performance. The beamline shutters operate in air at atmospheric pressure. Figure IX.3.2.1 provides a cross section view of the neutron channel shutter

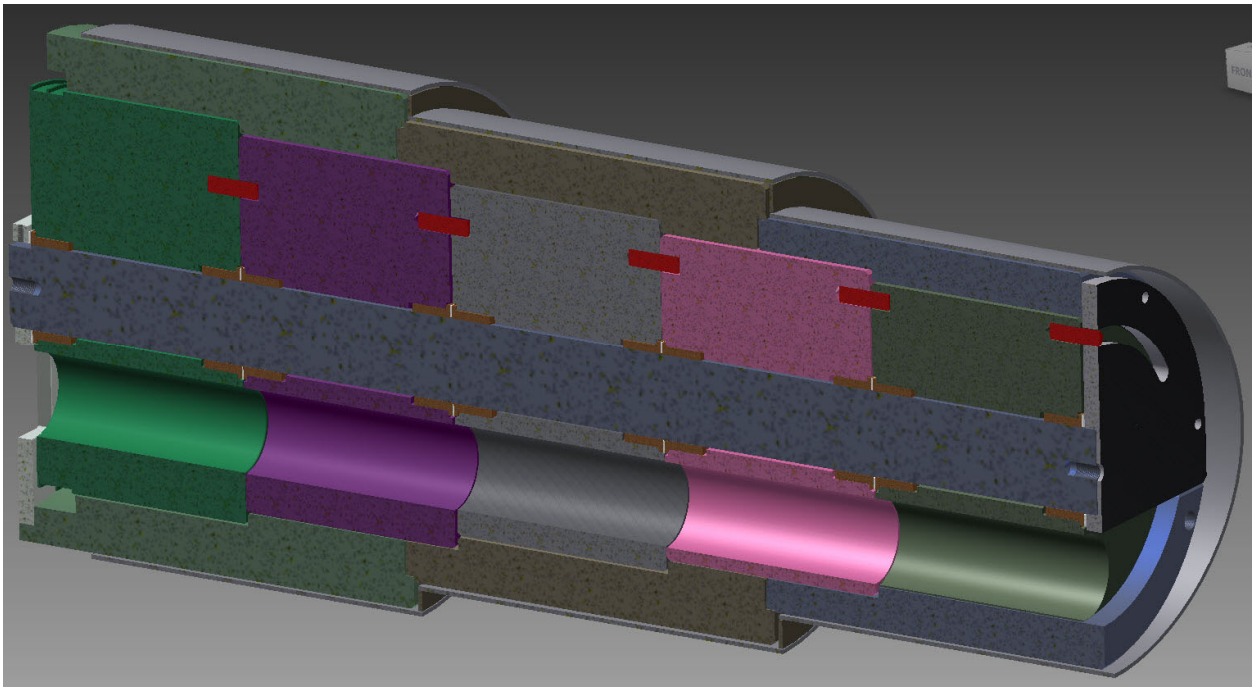

Figure IX.3.2.1. Vertical section view through an open shutter. The shutter case, central axis shaft, five rotating sections, bronze bushings, and index pins are visible.

IX.3.3 Neutron Beamline Shutter Motion

Each neutron channel shutter is driven by an electric motor mounted on the exterior surface of the biological shielding ring. The motor is connected to the outermost (fifth) shutter section by a roller chain. This arrangement positions the motor outside the biological shield, which is accessible for service. At each interface between adjacent shutter sections there is a provision to allow 60 degrees of relative rotation between sections. The inboard face of each section has a pin that fits in a curved slot in the outboard face of the adjacent section. The pin and slot interface are illustrated in Figure IX.3.3.1. The curved slot is concentric to the section and has an angular length of 60 degrees.

The relative rotation of adjacent shutter sections is limited by a pin on one section in a slot in the adjacent section. The slot curves through a 60-degree arc, allowing 60 degrees of relative rotation between sections. When the neutron channel shutter is open, all the eccentric beamline holes are aligned, and all of the pins are in the clockwise-most end of the slot. As the motor begins to close the shutter, section 5 (the outer-most section) rotates counterclockwise. After 60 degrees of rotation, the pin has reached the end of the slot in section 4 and begins to rotate section 4 counterclockwise. At 120 degrees of actuation, the pin in section 4 reaches the end of the slot in section 3 and begins to rotate section 3. At 180 degrees of actuation, the pin in section 3 reaches the end of the slot in section 2 and causes section 2 to begin to rotate. At 240 degrees of actuation, the pin in section 2 reaches the end of the slot in section 1 and causes section 1 to rotate. At 300 degrees of actuation, the pin in section 1 reaches the end of the slot

in the shutter frame end plate, limiting the rotation of all sections. This places the neutron channel shutter in the closed position, blocking the passage of the neutron current. Reversing the rotation of section 5 through 300 degrees opens the shutter.

End-of-motion switches are positioned to indicate when the shutter is fully closed and fully opened. These switches provide signals that stop the motor, inform the main control system of shutter position, and signal the neutron experiment.

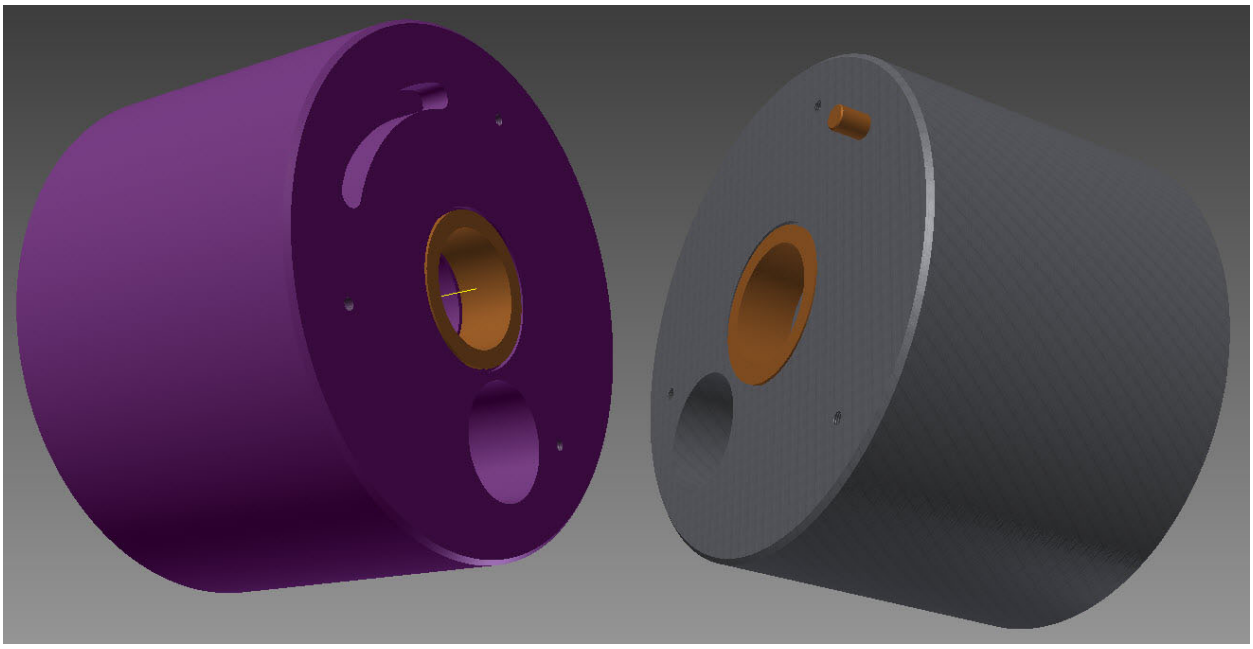

Figure IX.3.3.1. Image of mating faces of adjacent shutter sections. Note 60-degree slot in left section and index pin in the right section. Bronze bearings are in the center of the sections. Beam port is in the lower part of the sections

IX.3.3 Neutron Channel Shutter Service Operations

The channel shutter drive motors are located outside the biological shielding ring and above the channel shielding, where they are readily accessible for maintenance and repair. The motor, gearbox, and switches can be serviced from this position.

Each neutron channel shutter can be removed from the biological shielding ring as a unit for service operations. A shutter counterbalance tool is used to lift the beamline shutter out of the shutter port and carry it to the service area. The shutter counterbalance tool has a heavy mass at one end and a moveable lift point, such that it can be balanced by the overhead crane, either with or without the shutter attached. Some of the channel shutters do not have clear overhead crane access. To provide access to these beam ports, the counterbalance tool is equipped with rollers that will roll on temporary rails. The shutter counterbalance tool has adjustable wheels to provide minor adjustment for height and position of individual shutter cavities. This allows the beamline shutter to be moved from the biological shielding to the zone of overhead crane access.

Figure IX.3.4.1 illustrates the shutter counterbalance tool design and rollers as the tool is in the process of inserting a shutter into a shutter cavity.

The shutter counterbalance tool has an adjustable lift ring that provides for balanced carrying by the overhead crane, whether the shutter is attached or not. A shutter plug can be installed by the same shutter counterbalance tool to fill the shutter cavity when the shutter is removed for service. Removal of a channel shutter requires disassembly of the neutron experiment to provide the required access space.

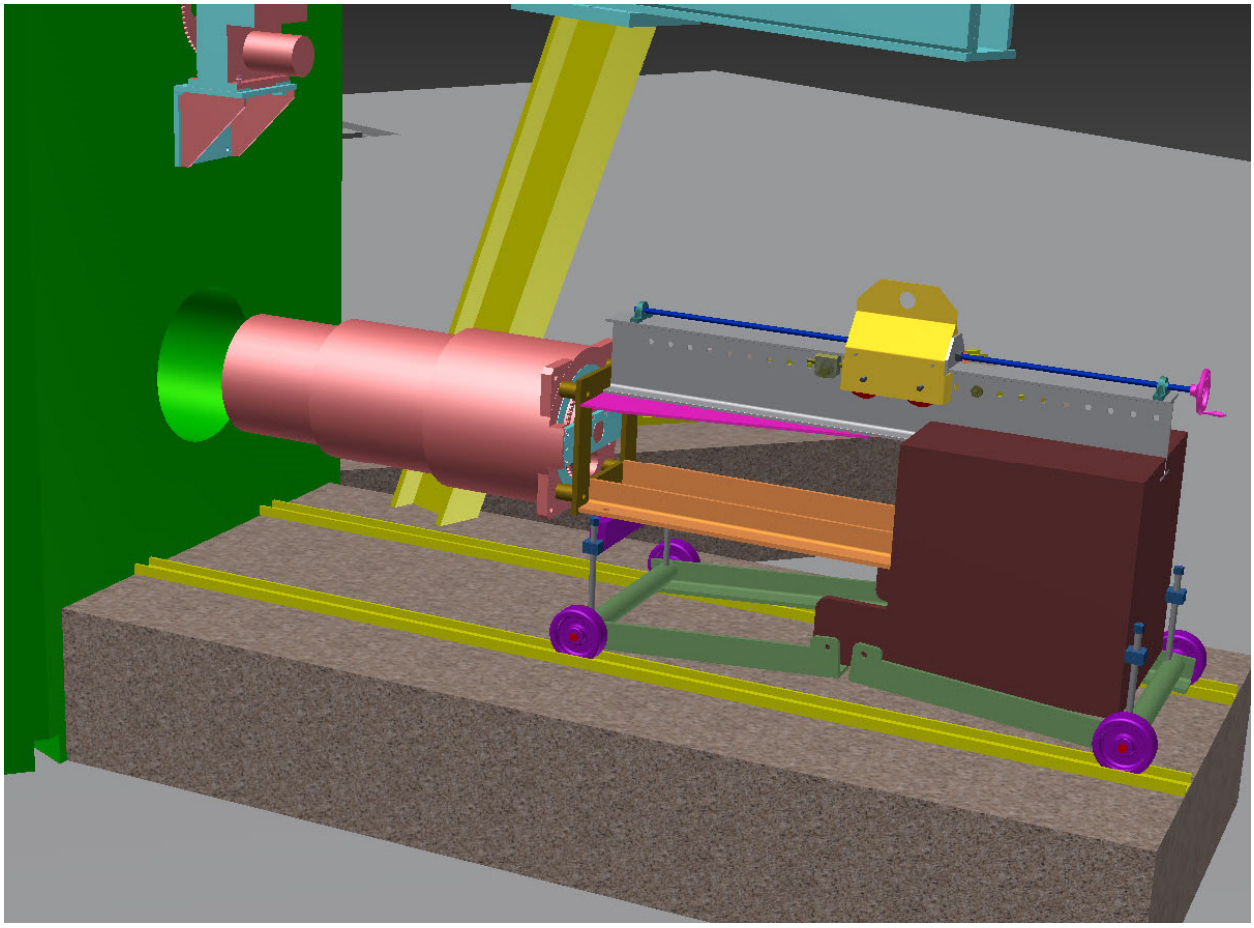

Figure IX.3.4.1. Shutter counterbalance tool shown inserting a shutter into a shutter cavity.

X Measuring and Monitoring the Reactivity of the Subcritical Assembly

X.1 Introduction

The neutron multiplication factor k_{eff} of the KIPT subcritical assembly must be less than 0.98 all the time to insure safe operation. The reactivity ρ, which is proportional to the inverse of k_{eff}, is monitored during the operation time. This section describes the procedure for measuring and monitoring the reactivity of the KIPT subcritical assembly. First, the reactivity of the KIPT subcritical assembly is measured while the KIPT subcritical assembly is loaded with fuel assemblies. At the beginning of the fuel loading process, the k_{eff} value is low, but the neutrons of the external neutron source are multiplied in the subcritical assembly, which register sufficient counts in the neutron counting systems. Pulsed-neutron experiments are performed, and the area-ratio method is applied to determine the reactivity of the subcritical assembly in units of dollars.

The reactivity of the KIPT subcritical assembly is measured consecutively while fuel assemblies are loaded into the subcritical assembly. The electron accelerator beam current is fixed or is monitored during each successive fuel loading step. The neutron fluxes are monitored by several U-235 fission chambers at the selected positions. The flux-to-current ratio method is applied to determine the relative reactivity of the subcritical assembly at each fuel loading step relative to the previous reactivity of the subcritical assembly measured by the area method.

Due to the presence of the external neutron source in the KIPT facility, the accuracy of the reactivities obtained from both the area-ratio method and the flux-to-current ratio method depends on the positions of the neutron detectors in the subcritical assembly. To determine the reactivity accurately, the detector positions have been carefully selected. Monte Carlo numerical simulations have been performed to obtain spatial correction factors for both methods at the selected detector positions. These correction factors are applied to the measured reactivities to correct for the spatial effects in the experiments at each fuel loading step.

The spatial correction factors are numerically calculated for each fuel loading step. In this section, the fuel loading patterns for two KIPT configurations are first described in the next section, followed by the detail descriptions of the experiments, and applying the spatial correction factors to determine the reactivity of the KIPT subcritical assembly for the selected fuel loading steps. A short summary is presented in the final section.

X.2 KIPT Fuel Assembly Loading Steps

The fuel loading steps for two KIPT configurations are shown if Fig. X.2.1. The maximum number of fuel assemblies loaded at the final step is 38 or 37 for the two configurations using the tungsten target or the natural uranium target, respectively. Monte Carlo eigenvalue calculations [X.1] show that the k_{eff} value is 0.952 for the configuration using the tungsten target, and 0.975 for the configuration using the natural uranium target, as listed in Table X.2.1 and X.2.2.

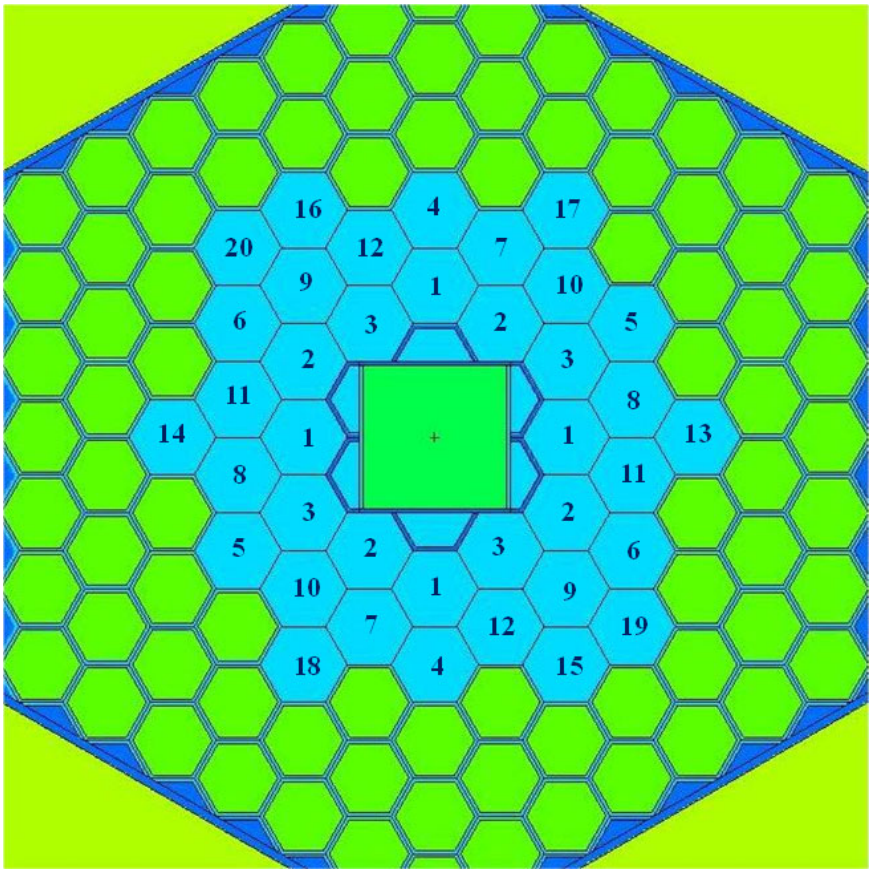

Figure X.2.1. The KIPT fuel assembly loading sequence has 20 steps with the tungsten target and 38 fuel assemblies. The same loading sequence is used for the uranium target with 37 fuel assemblies using only 19 steps. The last fuel assembly number 20 (upper left) is not loaded for the subcortical assembly with uranium target

Table X.2.1. Monte Carlo k-eigenvalue calculations of the reactivity from the numerical model of the KIPT neutron source facility with the tungsten target. ENDF/B-VII.1 library and the individual fuel assembly specifications were used for the MCNP Calculations

# FA	K_{eff}	K_{eff} - std	β	β - std	ρ^{mcnp}($)
4	0.27322	0.00001	0.00808	1.15	-329.21
8	0.43349	0.00001	0.00793	0.53	-164.80
12	0.54193	0.00001	0.00801	0.25	-105.53
14	0.59755	0.00001	0.00785	0.22	-85.80
16	0.64938	0.00001	0.00775	0.20	-69.67
18	0.69702	0.00001	0.00775	0.18	-56.09
20	0.73008	0.00001	0.00777	0.17	-47.58
22	0.76118	0.00001	0.00769	0.16	-40.80
24	0.79064	0.00001	0.00771	0.15	-34.34
26	0.81429	0.00001	0.00764	0.14	-29.85
28	0.83678	0.00001	0.00767	0.13	-25.43
30	0.85849	0.00002	0.00765	0.18	-21.55
31	0.87096	0.00001	0.00762	0.12	-19.44
32	0.88356	0.00001	0.00758	0.12	-17.39
33	0.89659	0.00001	0.00756	0.12	-15.26
34	0.90895	0.00001	0.00759	0.12	-13.20
35	0.92123	0.00001	0.00755	0.12	-11.33
36	0.93289	0.00001	0.00754	0.11	-9.54
37	0.9429	0.00001	0.00757	0.11	-8.00
38	0.95245	0.00001	0.00749	0.11	-6.67

Table X.2.2. Monte Carlo k-eigenvalue calculations of the reactivity of the numerical model of the KIPT neutron source facility with the nature uranium target. ENDF/B-VII.1 library and the average fuel assembly specifications were used for the MCNP Calculations

# Fuel Assemblies	k_{eff}	ρ	# Fuel Assemblies	k_{eff}	ρ
20	0.75114 ±0.00011	-0.33131	32	0.91645±0.00011	-0.09117
22	0.78212 ±0.00011	-0.27858	33	0.92917±0.00012	-0.07623
24	0.81309 ±0.00012	-0.22988	34	0.94137 ±0.00011	-0.06228
26	0.83918 ±0.00011	-0.19164	35	0.95413 ±0.00012	-0.04808
28	0.86451 ±0.00011	-0.15672	36	0.96589 ±0.00013	-0.03531
30	0.88957 ±0.00013	-0.12414	37	0.97547 ±0.00011	-0.02515
31	0.90293 ±0.00013	-0.10751			

X.3 The Pulsed-Neutron Experiment and the Area-Ratio Method

To determine the reactivity of the KIPT subcritical assembly at the different fuel loading steps, the area-ratio method is employed with the pulsed-neutron source. It is an effective method to determine the reactivity of the subcritical assembly. To start the experiment, an external neutron-pulse is repeatedly injected into the subcritical assembly for thousands of times till the neutron flux of subcritical assembly reaches an equilibrium status. The neutron fluxes are then measured by the U-235 fission chambers. Figure X.3.1 shows a typical output obtained in such an experiment. It has a peak which represents the prompt neutron population of the subcritical assembly, and it dies out very quickly. Subsequently, the detector responses decays slowly to an equilibrium presenting the delayed neutron population of the subcritical assembly.

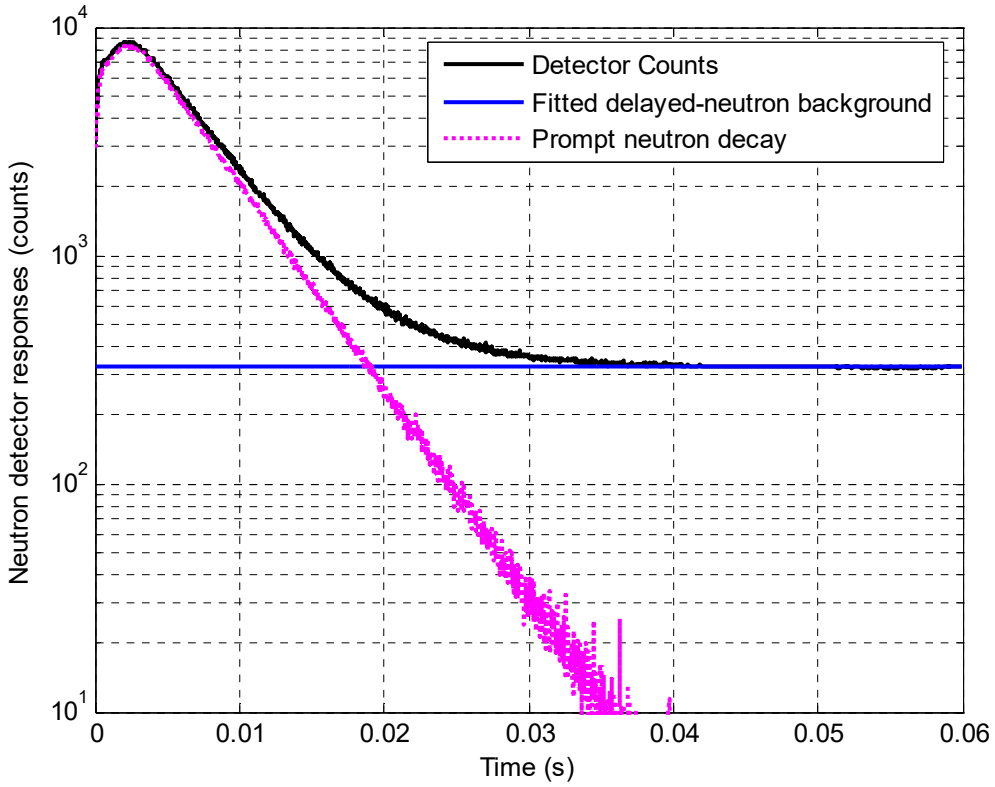

Figure X.3.1. A typical neutron detector response in the pulsed-neutron experiment and the diagram for calculating neutron areas for applying the area-ratio method

According to the area-ratio method, the reactivity ρ of a subcritical system in unit of dollars is the negative ratio of the prompt neutron area A_p to the delayed neutron area A_d [X.2]:

$$\rho(\$) = -\frac{A_p}{A_d}. \quad (1)$$

In a pulsed-neutron experiment, the neutron areas are measured based on the neutron detector responses as shown in Fig. X.3.1. Namely, the detector response after all the prompt neutron contributions die away is almost a constant, and its value can be obtained by averaging the detector counts within a fitting interval as shown in Fig. X.3.1. The

delayed neutron area A_d is simply the integration of this constant delayed neutron background over the pulse period. The prompt neutron area A_p is obtained as the result of the total neutron area under the detector response curve minus the delayed neutron area A_d.

In the KIPT neutron source facility, the neutron fluxes are monitored by two sets of neutron detectors. The first set of neutron detectors utilizes three U-235 fission chambers with neutron sensitivity of ~10^{-3} counts/neutron and it is placed at $(r, z) = (107.0, 25.0)$, which is inside the neutron channels in the biological shield, and it is about 107 cm away from the target centerline radially lined up at the fuel middle plane as shown in the left of fig. X.3.2. The second set of neutron detectors contains six U-235 fission chambers. Three high sensitivity detectors capable of 10^{-3} counts/neutron and three low sensitivity detectors capable of 10^{-6} counts/neutron. Those six detectors are all placed at the position $(r, z) = (54.0, 72.5)$, which is radially 54 cm away from the target centerline and axially 12.5 cm above the graphite reflector block with their sensitive sides directly facing one side of the hexagon fuel assembly as shown in the right figure of Figure X.3.2. In addition, the six detectors are arranged to alternate between the highly sensitive one and the low sensitive one in the azimuthal angle as shown in the right of Figure X.3.2.

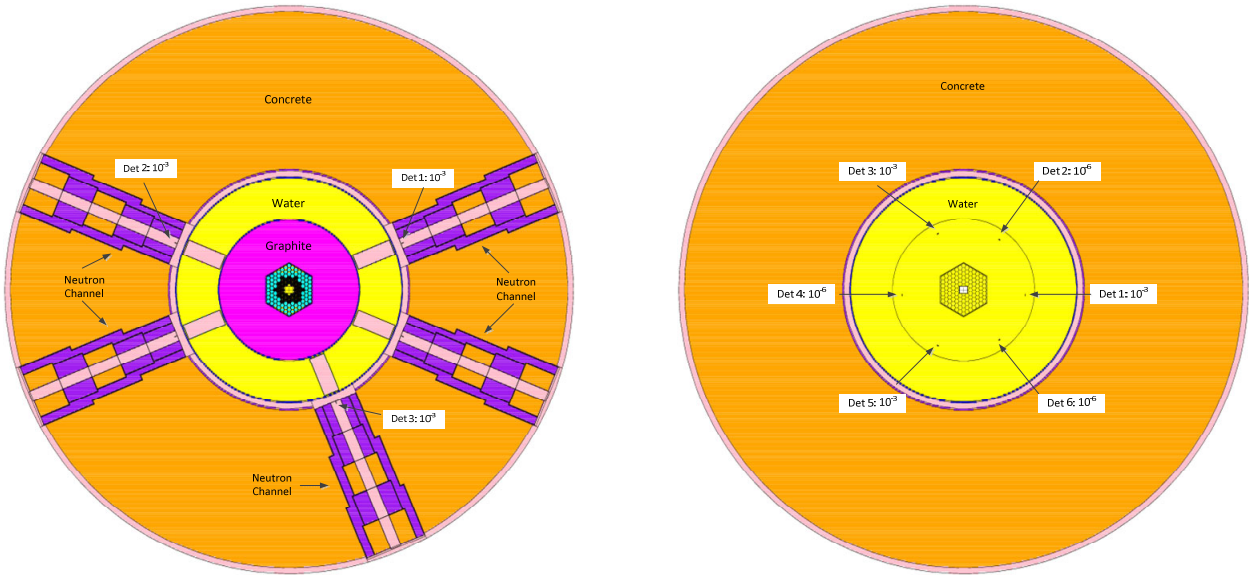

Figure X.3.2. Neutron detector locations in the neutron channel at the middle plane z=25.0 cm on the left (a). Neutron detector locations at z-plane z=72.5 cm on the right (b)

To perform the pulsed-neutron experiment, the external neutron source pulse period must be long enough such that the prompt neutron population dies out within each pulse period as shown in Fig. X.3.1. At the same time, the period cannot be too long such that during the pulse period, the delayed neutrons decay is negligible. To determine the proper length of the pulse period, Monte Carlo numerical simulations were first performed to simulate the neutron pulse decay in the KIPT neutron source facility.

The neutron detector responses have been first simulated numerically with one neutron pulse injected into the KIPT neutron source facility at t=0 as shown in Figure X.3.3 and

X.3.4. Four fuel loading steps starting from the initial reference step to the final full loading step for the two KIPT configurations are considered. The detector responses are calculated as the average fluxes from the six detector positions of the second detector set for simplicity and for obtaining low statistical errors. The prompt neutron fluxes with the delayed neutrons turned off in the simulations have been also calculated for the case with 37 fuel assemblies loaded with the uranium target as shown in Fig. X.3.4. The numerical results show that for the two KIPT configurations, the prompt neutron contributions to the neutron fluxes become negligible after about 40 ms for the fuel loading with high number of fuel assemblies. It takes about 20 ms for the prompt neutrons to die out in the low fuel loading cases. For all the cases shown in Figs. X.3.3 and X.3.4, the delayed neutron background does not vary significantly within the next 20 to 30 ms after the prompt neutrons die out.

In addition, in the pulsed-neutron experiment, the pulse period of the external pulse source should be shorter than the half-life of the fastest delayed neutron precursor group such that the delayed neutron contributions to the detector responses can be approximated as constants. Table X.3.1 listed the numerically calculated adjoint-weighted point kinetics parameters of the KIPT neutron source facility of the two KIPT configurations with the maximum number of fuel assemblies loaded. Among the six delayed neutron precursor groups, the fastest decay group has a half-life of about 80 ms. Thus, in the KIPT neutron source facility, the numerical simulations suggest that the adequate pulse period for a pulsed-neutron experiment is ~40 ms for the cases with the low number of the fuel assemblies, and around 60 ms for the cases with the high number of the fuel assemblies. The external source repeating frequencies are then calculated to be about 25 HZ and 16.7 HZ respectively. Monte Carlo simulations also show that 25 HZ is appropriate for all the fuel loading steps with less than 34 fuel assemblies. The frequency of 16.7 HZ is appropriate for all the other cases with a high number of the fuel assemblies loaded.

Table X.3.1. The calculated point kinetics parameters of the KIPT neutron source facility using the tungsten target with 38 fuel assemblies or using a natural uranium target and 37 fuel assemblies

# Delayed Neutron Group i	Tungsten Target		Uranium Target	
	β_i (pcm)	Half-life T_i (s)	β_i (pcm)	Half-life T_i (s)
1	27	55.5	24	55.5
2	116	21.8	127	21.8
3	120	6.3	125	6.3
4	354	2.2	335	2.2
5	102	0.51	100	0.51
6	31	0.08	37	0.08
Total β (pcm)	748±11		748±11	
Half-life $T\Lambda$(s)	141.9±0.5		135.1±0.5	

In the pulsed-neutron experiment, the area-ratio method can only be applied while the subcritical assembly reaches an equilibrium state. Monte Carlo simulations have been performed to seek the equilibrium state. Figure X.3.5 to X.3.8 show the different shapes of the neutron fluxes with more neutron pulses injected into the subcritical assembly for

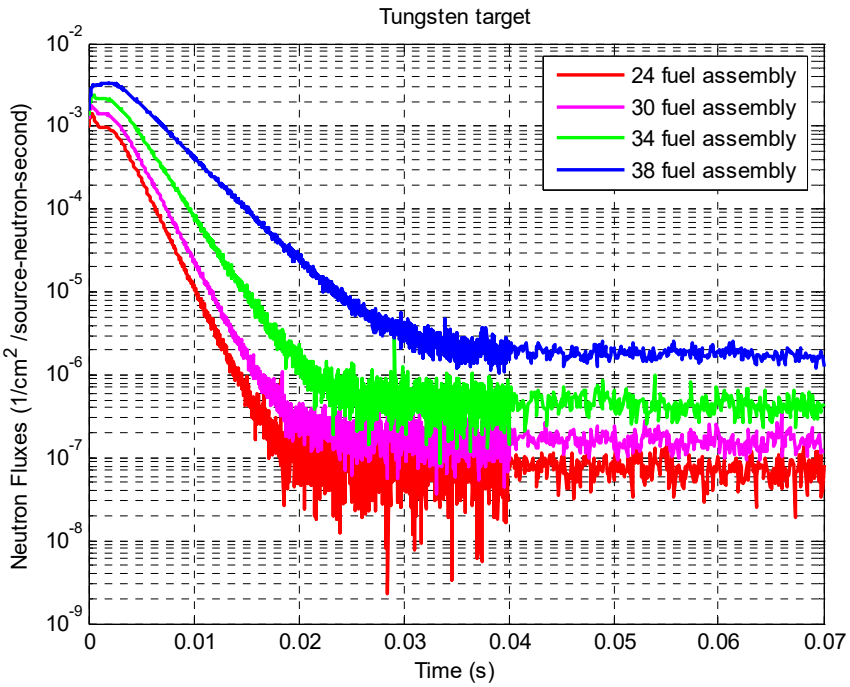

Figure X.3.3. Monte Carlo simulations of the neutron fluxes corresponding to one neutron pulse injected into the KIPT subcritical assembly with a tungsten target and 24 to 38 fuel assemblies loaded

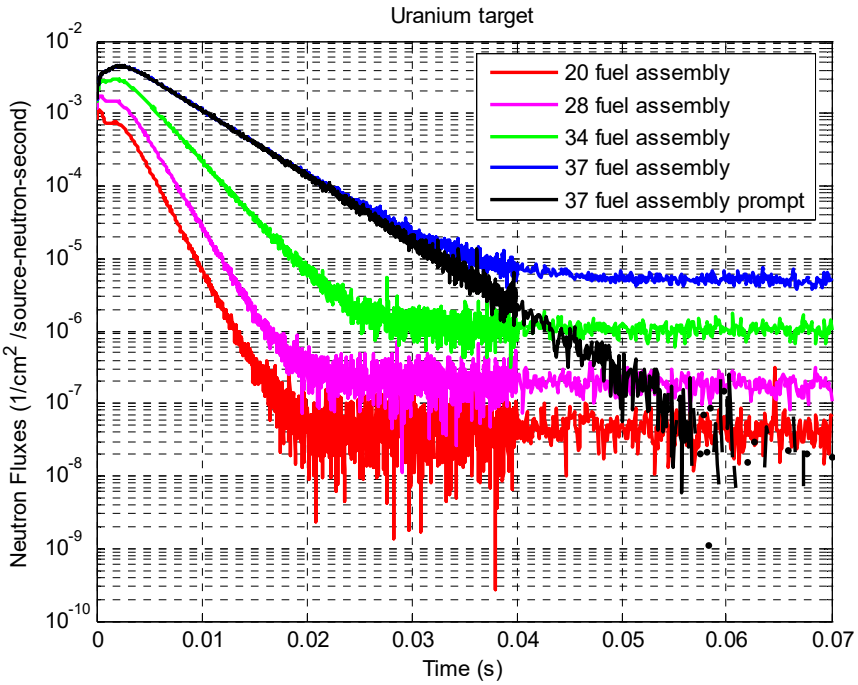

Figure X.3.4. Monte Carlo simulations of the neutron fluxes corresponding to one neutron pulse injected into the KIPT subcritical assembly with a natural uranium target and with 20 to 37 fuel assemblies loaded

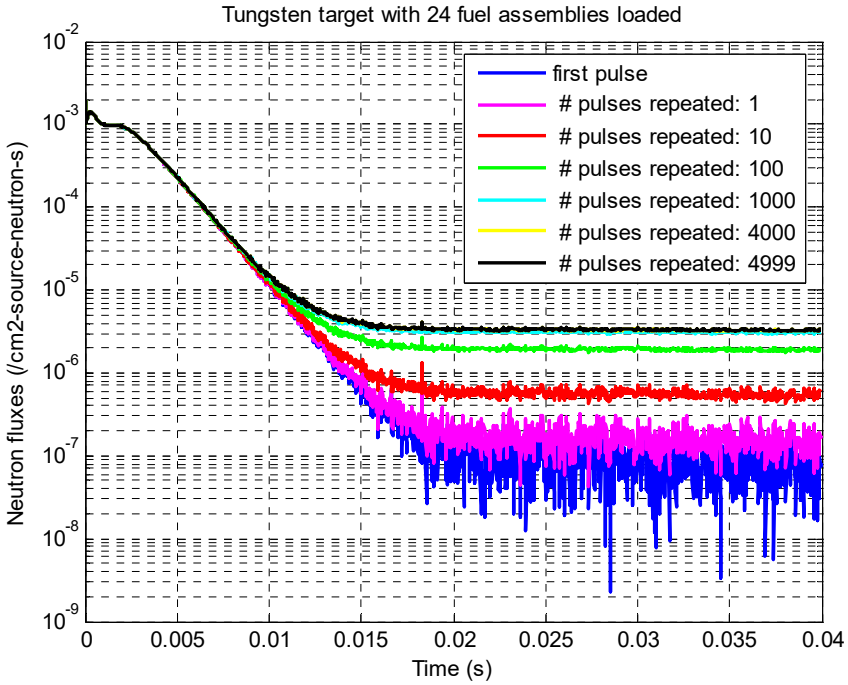

Figure X.3.5. Monte Carlo simulations of the neutron fluxes after 1 to 5000 neutron pulses injected into the KIPT subcritical assembly which utilizes a tungsten target with 24 fuel assemblies

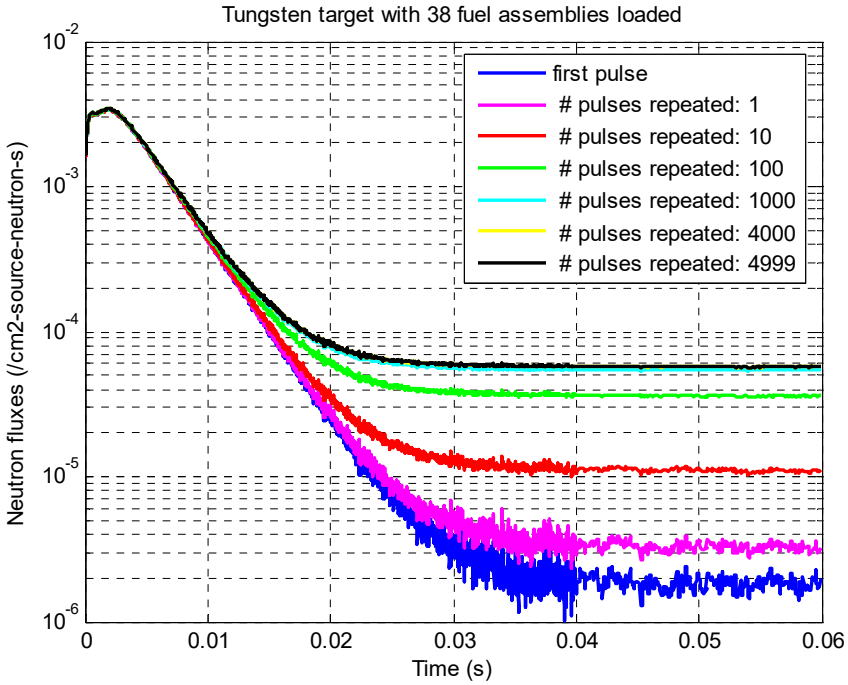

Figure X.3.6. Monte Carlo simulations of the neutron fluxes after 1 to 5000 neutron pulses injected into the KIPT subcritical assembly which utilizes a tungsten target with 38 fuel assemblies

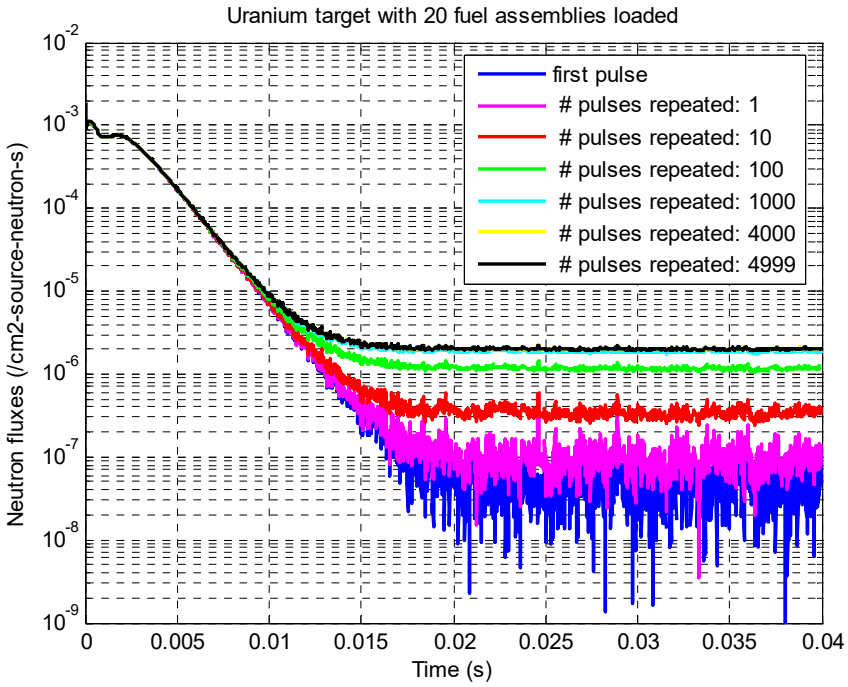

Figure X.3.7. Monte Carlo simulations of the neutron fluxes after 1 to 5000 neutron pulses injected into the KIPT subcritical assembly which utilizes a natural uranium target with 20 fuel assemblies

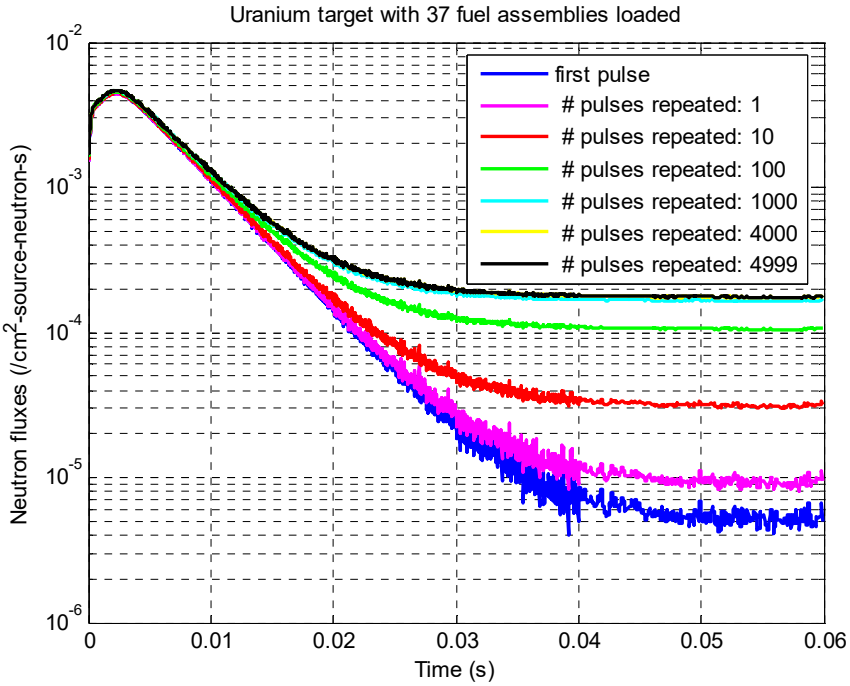

Figure X.3.8. Monte Carlo simulations of the neutron fluxes after 1 to 5000 neutron pulses injected into the KIPT subcritical assembly which utilizes a natural uranium with 37 fuel assemblies

the two KIPT configurations at the initial and the final fuel loading steps. For the full fuel loading steps of the two KIPT configurations, the neutron fluxes approach the asymptotic shape after about 4000 neutron pulses. It also takes more than a thousand neutron pulses to reach the equilibrium shapes at the low fuel loading cases.

Overall, the Monte Carlo numerical simulations suggest that in a pulsed neutron experiment, at least several thousand neutron pulses need to be injected into the subcritical assembly to reach equilibrium state. Neutron detector responses should be measured several minutes after the first neutron pulse injected into the subcritical assembly for the two KIPT configurations. Monte Carlo numerical simulations have calculated the asymptotic shape of the detector's responses (averaged over the six detectors) as shown in Figure X.3.9 and X.3.10 for the two KIPT configurations. The absolute values are normalized assuming that the 100 MeV electron beam power is 10 W and the detector sensitivity is 1.0×10^{-3} cps/n (counts/neutrons/cm^2-s) for all the configurations.

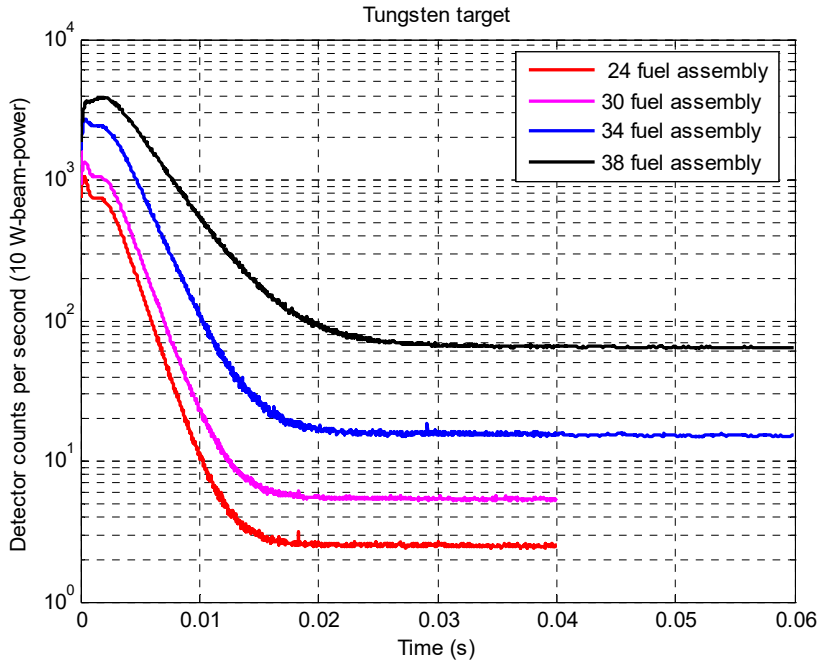

Figure X.3.9. Monte Carlo simulations of the detector counting rates after the delayed neutrons reached an equilibrium status from 10 W of neutron pulses injected into the KIPT subcritical assembly using the tungsten target with different number of fuel assemblies

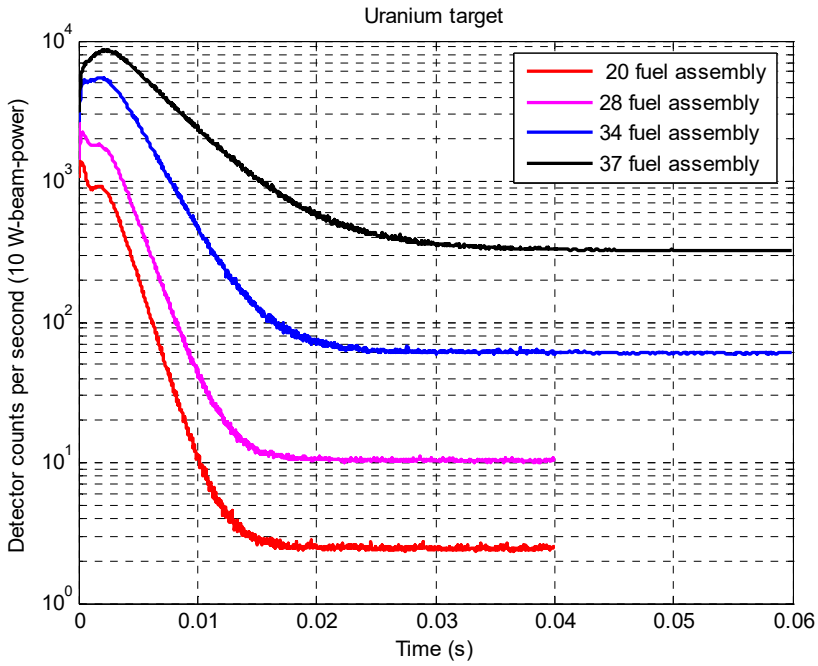

Figure X.3.10. Monte Carlo simulations of the detector counting rates after the delayed neutrons reached an equilibrium status from 10 W of neutron pulses injected into the KIPT subcritical assembly using the natural uranium target with different number of fuel assemblies

In the experiments, the area-ratio method is applied to each asymptotic detector response to obtain the reactivity of the subcritical assembly. For subcritical systems with k_{eff} less than one, due to the use of an external neutron source, the obtained reactivity from the area-ratio method is found to be sensitive to the neutron detector position and it is different from the actual reactivity of the subcritical assembly. Bell Glasstone spatial correction factor is calculated to correct for the spatial effects in the measured reactivities at each detector location [X.3]:

$$f^{cal}(r_d) = -\left[\frac{\rho^{cal}}{\beta^{cal}}\right] \times \left[\frac{A_d^{cal}(r_d)}{A_p^{cal}(r_d)}\right], \qquad (2)$$

Where f^{cal} is the spatial correction factor at the detector location r_d. The kinetics parameters ρ^{cal} and β^{cal}, the neutron areas $A_p^{cal}(r_d)$ and $A_d^{cal}(r_d)$ are calculated numerically. Table X.3.2 and X.3.3 list the calculated f^{cal} at all the selected U-235 fission chamber positions for the two KIPT configurations at the four fuel loading steps. In all the calculations, the Monte Carlo statistical errors are less than or around 1%.

The sensitive amount of U-235 material in a U-235 fission chamber is usually in the order of milligrams or smaller. The correction factors are obtained without simulating the detector geometry in the Monte Carlo model. The U-235 fission reaction rates are directly tallied using the FM tally of MCNP6. To verify that the spatial correction factors are not affected by the detector substances presence, Monte Carlo simulations are also performed simulating the tiny amount of U-235 detector sensitive material in the actual detector volume for the subcritical assembly at the initial reference states and at the final

full fuel loading states. The calculated correction factors for these two cases are then labeled as "-U235" as shown in Tables X.3.1 and X.3.2. The statistical error is around 2% and is significantly larger than in previous results, since the Monte Carlo tally zone is inside the U-235 coating layer which is a much smaller volume than the detector sensitive volume used in previous numerical calculations. The numerical simulations confirm that the tiny amount of U-235 material in the neutron fission chambers does not affect the calculated spatial corrections since the correction factors calculated for the cases with and without simulating the actual detector agree with each other within the statistical errors.

The correction factors obtained with the second set of six neutron detectors are calculated for all the fuel loading states and are plotted in Figure X.3.11 and X.3.12. The statistical errors of the correction factors are not plotted in those figures, but all of them are less than or at most 1%. Overall, as shown in Figs. X.3.11 and X.3.12, the variances between the detectors among the two sets are very small for all the fuel loading steps in the two KIPT configurations. The spatial corrections of the area-ratio method are around 7% or 15% for the KIPT subcritical assembly at the initial reference state using the tungsten target or the natural uranium target, respectively. The spatial corrections become smaller when more fuel assemblies are loaded into the subcritical assembly. At the full fuel loading states, the corrections are only about 2% or 3% for the two KIPT configurations respectively. This observation is consistent with the knowledge from past studies that the area-ratio method is more accurate near the critical condition [X.4]. In addition, the spatial corrections are larger in the KIPT configuration using the natural uranium target than using tungsten target, since more source neutrons are produced within the natural uranium target.

The reactivity $\rho^{correct}$ of the KIPT subcritical assembly obtained from the pulsed-neutron experiment at each detector location r_d after spatial corrections can be obtained as:

$$\rho^{correct}(r_d) = \rho^{exp}(r_d) \times f^{cal}(r_d), \tag{3}$$

Where $\rho^{exp}(r_d)$ is the reactivity obtained from the pulsed-neutron experiment, and $f^{cal}(r_d)$ is the calculated at the detector position r_d. The absolute reactivity of the KIPT subcritical assembly at the initial reference state is then the mean value averaged over all the detector locations:

$$\rho_{ref,i} = \frac{1}{n_{r_d}} \sum_{\mathrm{r_d}} \rho^{correct}(r_d). \tag{4}$$

In the pulsed-neutron experiment, the pulsed-neutron source is repeated many times. For each neutron pulse injected into the subcritical assembly, the neutron counting system is synchronized with the external source, such that the detector counts obtained each time of one pulse can integrated with the counting from the previous pulses to obtain better counting statistics.

Table X.3.2. Correction factors f^{cal} of the area-ratio method in the KIPT neutron source facility using the tungsten target ($\rho^{correct} = \rho^{exp} \times f^{cal}$)

# Fuel Assembly		24	24-U235	30	34	38	38-U235
$(r,z) = (54.0, 72.5)$	Det1	1.074±0.007	1.037±0.021	1.056±0.005	1.034±0.006	1.013±0.004	0.998±0.009
	Det2	1.072±0.007	1.079±0.022	1.059±0.005	1.039±0.006	1.012±0.004	1.020±0.010
	Det3	1.065±0.007	1.079±0.022	1.053±0.005	1.035±0.006	1.019±0.004	1.014±0.009
	Det4	1.079±0.007	1.130±0.022	1.056±0.005	1.040±0.006	1.017±0.004	1.024±0.010
	Det5	1.066±0.007	1.046±0.022	1.065±0.005	1.027±0.006	1.010±0.004	1.013±0.010
	Det6	1.082±0.007	1.074±0.022	1.053±0.005	1.036±0.006	1.013±0.004	1.024±0.009
	Avg135	1.068±0.005	1.069±0.024	1.058±0.006	1.032±0.005	1.014±0.004	1.014±0.005
	Avg246	1.078±0.005	1.074±0.033	1.056±0.003	1.038±0.002	1.014±0.003	1.015±0.010

Table X.3.3. Correction factors *f* of the area-ratio method in the KIPT neutron source facility using the natural uranium target ($\rho = \rho^{exp} \times f$)

# Fuel Assembly		20	20-U235	28	34	37	37-U235
$(r,z) = (107.0, 25.0)$	Det1	1.102±0.007		1.065±0.005	1.056±0.007	1.028±0.007	
	Det2	1.128±0.007		1.078±0.005	1.053±0.007	1.029±0.007	
	Det3	1.127±0.007		1.079±0.005	1.048±0.007	1.022±0.007	
	Avg	1.119±0.015		1.074±0.008	1.053±0.004	1.026±0.004	
$(r,z) = (54.0, 72.5)$	Det1	1.152±0.009	1.153±0.020	1.103±0.006	1.051±0.005	1.031±0.004	1.040±0.007
	Det2	1.139±0.009	1.109±0.019	1.101±0.006	1.056±0.005	1.024±0.004	1.035±0.007
	Det3	1.138±0.009	1.138±0.019	1.093±0.006	1.053±0.005	1.031±0.004	1.028±0.007
	Det4	1.159±0.009	1.195±0.020	1.103±0.006	1.059±0.005	1.026±0.004	1.024±0.007
	Det5	1.135±0.009	1.150±0.020	1.095±0.006	1.055±0.005	1.028±0.004	1.026±0.007
	Det6	1.153±0.009	1.181±0.020	1.104±0.006	1.055±0.005	1.029±0.004	1.034±0.006
	Avg135	1.142±0.009	1.147±0.006	1.097±0.006	1.053±0.002	1.030±0.002	1.031±0.005
	Avg246	1.151±0.011	1.161±0.046	1.103±0.001	1.057±0.002	1.026±0.003	1.031±0.006

Usually the pulsed-neutron experiment takes a relatively long time to accumulate sufficient counts from the delayed neutrons. As already shown in Figure X.3.9 to X.3.8 the counting rates from the subcritical assembly with low number of fuel assemblies are much lower than the counting rates from the subcritical assembly with high number of fuel assemblies. For the low fuel loading cases, a larger number of neutron-pulses is required. Monte Carlo simulations estimated the neutron counting time to be a few minutes when the subcritical assembly is fully loaded, or hours when the subcritical assembly is at the initial loading step to obtain an estimation of the delayed neutron background with statistical error of ≤ 1% assuming the neutron detector sensitivity of 10^{-3} count/neutron and the beam power of the external electron beam of 10 W. Of course, increasing the beam power reduces the required time for delayed neutrons to reach the asymptotic value.

Therefore, the pulsed-neutron experiment is time-consuming, especially when the subcritical assembly is in deep subcritical states. The area-ratio method utilizing the pulsed-neutron experiment is not suited to quickly track the change of the reactivity during one fuel assembly loading. The flux-to-current ratio method which utilizes only the steady state neutron fluxes or the average neutron fluxes are considered.

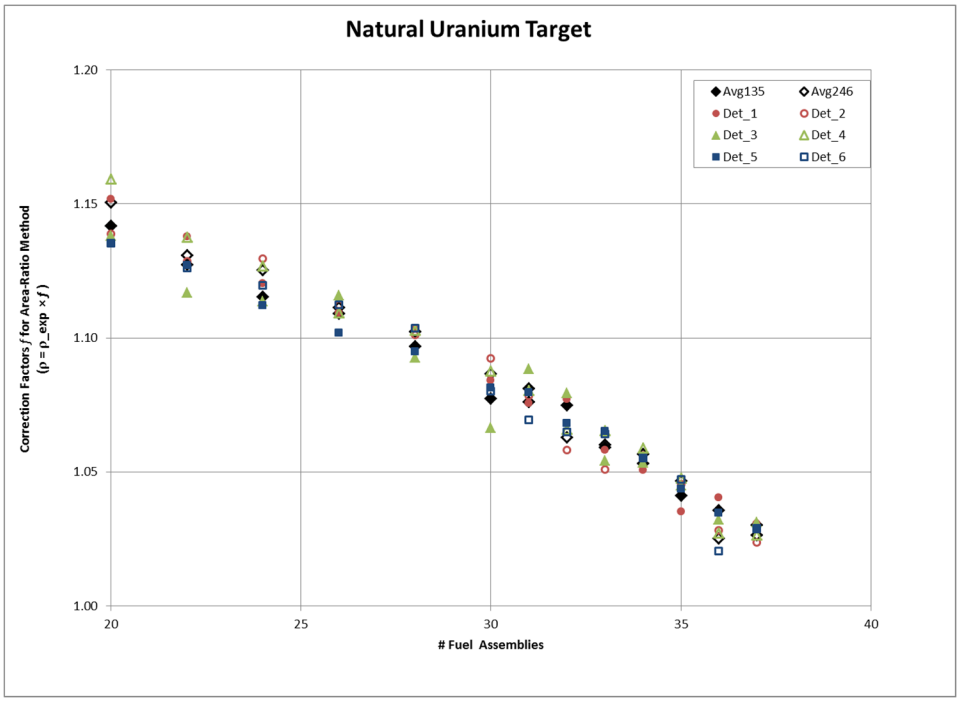

Figure X.3.11. Monte Carlo calculated correction factors of the area-ratio method with pulsed neutron experiment performed in the KIPT neutron source facility with a natural uranium target with 20 to 37 fuel assemblies

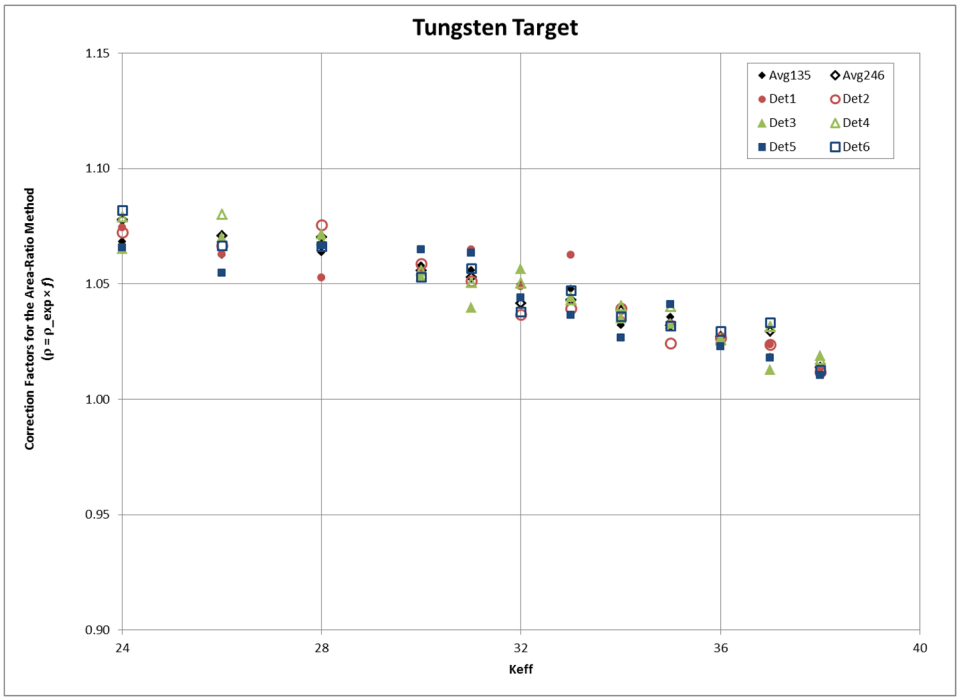

Figure X.3.12. Monte Carlo calculated correction factors of the area-ratio method with pulsed neutron experiment performed in the KIPT neutron source facility with a tungsten target and loaded with 24 up to 38 fuel assemblies

X.4 The Flux-to-Current Ratio Method

The flux-to-current ratio method is one of the simplest methods for monitoring the reactivity of subcritical assemblies. To determine the reactivity of a subcritical assembly, a reference state is required with its reactivity ρ_{ref} determined by the area-ratio method. When the subcritical assembly deviates from the reference state due to the extra fuel loading, or other reasons, the reactivity of the subcritical assembly at the new state ρ_n is obtained by the flux and current ratios between these two states [X.5]:

$$\rho_n = \rho_{ref}\left[\frac{I_n}{I_{ref}}\right]\left[\frac{<\epsilon, \phi_{ref}(r_d)>_E}{<\epsilon, \phi_n(r_d)>_E}\right], \tag{5}$$

where the subscript "n" represents the subcritical assembly at the new state, ϵ is the detector response function, I is the external accelerator beam current, and ϕ is the neutron flux measured at the detector location r_d when the subcritical assembly is at the new or reference state and is steadily driven by an external neutron source with external beam current I_n or I_{ref} respectively.

In the KIPT neutron source facility, the subcritical assembly is designed to be driven by an external electron accelerator coupled with a neutron generating target. At the startup, the fuel assemblies are loaded into the subcritical assembly, and the accelerator operates at a low power and a frequency of few tens Hz. After loading the fuel assemblies, the electron accelerator is operated at a high power "continuous" mode with a frequency of

625 Hz. At any of the two operation modes, since the external neutron source is a pulsed-neutron source, the neutron fluxes in the subcritical assembly are always in transient and are monitored instantly by the U-235 fission chambers.

Numerical analyses were performed for the KIPT subcritical assembly to compare the averaged neutron fluxes from a pulsed-neutron source and the neutron fluxes from steady state neutron source. Numerical simulations have been carried out for two transient cases: (1) a pulsed neutron source with the electron beam turning on at t=0 and (2) a pulsed neutron source transient with a reactivity transient obtained from the insertion of a fuel assembly into the subcritical assembly within 30 seconds. For the sake of simplicity, the point kinetics approximations have been adopted with the kinetics parameters obtained from the Monte Carlo simulations results listed in Table X.3.1. For the first transient, the pulsed neutron source was applied to the KIPT subcritical assembly configuration with the natural uranium target and 37 fuel assemblies fully loaded. The second transient case used the same target but simulating the insertion of the 37th fuel assembly in the subcritical assembly.

For the first transient, the transient neutron fluxes corresponding to a constant neutron source of the same source intensity of the pulsed-neutron source is turned on at t=0, and it is calculated as shown in Fig X.4.1. It is almost identical to the averaged neutron flux over all the transient periods. Both neutron fluxes are asymptotically approaching to the steady state neutron fluxes while the subcritical assembly is nearing the equilibrium status.

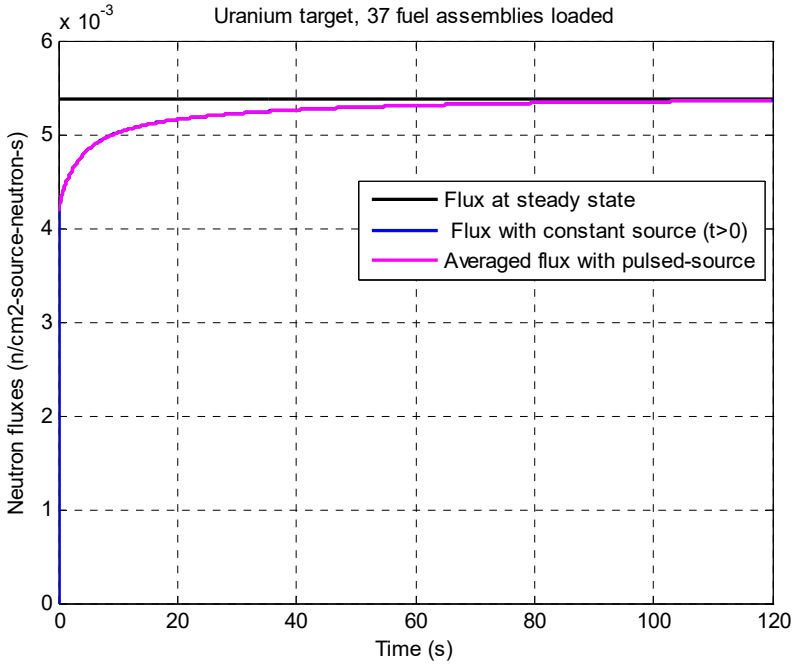

Figure X.4.1. Comparisons of the point kinetics calculated averaged neutron flux within the pulse period, the steady state neutron flux, and the neutron flux obtained with a constant source turned on at t=0 for the same KIPT configuration

Figure X.4.2 shows the neutron fluxes calculated for the second transient case. According to the previous Monte Carlo k-eigenvalue calculations, the total reactivity worth of the 37th fuel assembly is about 1.4$. The external neutron source is assumed to be turned on at t=0. At the same time, the fuel assembly starts to move into the subcritical assembly. Like the comparison shown in Fig. X.4.1, the average neutron fluxes obtained with a pulsed-neutron source are also almost identical to the transient neutron fluxes obtained with a constant source turned on at t=0. Overall, Figs X.4.1 and X.4.2 have shown that the average neutron fluxes within the pulse period are almost the same as the neutron fluxes obtained with an external neutron source which is a constant within the pulse period during the reactor transient. In other words, the pulse structure can be ignored during the transients and the average neutron fluxes can be utilized.

The above analyses utilized the point kinetics approximations. The same conclusion can be seen if directly integrating the time-dependent neutron transport equation within each pulse period:

$$\begin{aligned}\frac{\partial}{\partial t}\psi(r,E,\Omega,t)+\Omega\cdot\nabla\psi(r,E,\Omega,t)+\sigma(r,E,t)\psi(r,\mathrm{E},\Omega,\mathrm{t})\\ =\iint\sum_{x\neq f}\sigma_x f_x(r,\Omega',E'\rightarrow\Omega,E,t)\psi(r,\Omega',E',t)d\Omega' dE'\\ +\int_{-\infty}^{t}\iint\sigma_f(r,E',t)\psi(r,\Omega',E',t)\,d\Omega' dE'\\ \times\left[\widetilde{\chi_p}(E)(1-\beta)\nu\delta(t-t')\right.\\ \left.+\sum_j\widetilde{\chi_{dJ}}(E)\beta_j\lambda_j\nu e^{-\lambda_j(t-t')}\right]dt'+S(r,E)Q(t).\end{aligned} \tag{6}$$

For the neutron source transient case, the pulse period is very small compared with the time of the fission energy removed from the system. The amount of energy accumulated in the system at any time will be very similar as soon as the total number of external neutron source injected into the subcritical assembly $\int_{(n-1)T}^{nT}Q(t)dt$ is the same for the two cases with a pulsed source or a constant source. Thus, the reactivity variations represented as the time-dependent cross sections in the transport equation will be the same. Similarly, the external reactivity perturbations such as insertion of the fuel assembly are very slow, and the reactivity variations are very small within each pulse period, the cross sections in the transport equations can be approximated as constant while integrating the equation within the pulse period. Therefore, due to the pulse-period is very small, the integrated transport equations within the pulse period are identical for cases with the pulsed-neutron source or with the constant neutron source.

The neutron fluxes utilized in the flux-to-current ratio method are steady-state neutron fluxes at the reference and at the new state respectively. They are not measurable while the subcritical assembly is in the reactivity transient state. In the numerical simulations,

it can be obtained by assuming that an adiabatic steady state exists in the subcritical assembly, and the neutron fluxes are plotted as the steady state neutron flux curve in Figure X.4.2. Because the external neutron source is turned on at t=0 in this transient, the subcritical assembly needs to build-up the delayed neutron populations in the subcritical assembly. The calculated transient fluxes are consistently smaller than the steady state flux as shown in fig. X.4.2. In addition, in this numerical transient case, as the fuel assembly inserted into the assembly, more prompt neutrons in the subcritical assembly will instantly multiplied. However, the delayed neutron precursor densities in the subcritical assembly take time to adjust to the new levels.

To understand how the delayed neutrons affect the reactivities obtained from the flux-to-current ratio method using the transient fluxes averaged within the pulse period, another numerical simulation which only considers the reactivity transient is performed as shown in Fig. X.4.3. Namely, an equilibrium state is assumed in the KIPT assembly before the reactivity transient starts at t=0. Only the transient neutron flux with a constant source is calculated in this simulation since it is identical to the average neutron flux of a pulsed-neutron source. As shown in the figure, the transient neutron fluxes are smaller than the steady state neutron fluxes during the reactivity transient and then gradually approach to the steady state neutron fluxes at the new level after the fuel assembly completely inserted. Due to the lag of delayed neutrons, the maximum difference is between 2%-3% when the fuel assembly is completely inserted.

As shown in Figs. X.4.4 and X.4.5, the maximum differences between the transient fluxes and the steady state fluxes are reduced significantly at lower fuel loading states because the delayed neutrons become much less important in the deeper subcritical system. In the KIPT subcritical assembly, the general time to load a fuel assembly into the subcritical assembly is about half an hour and is much longer than the 30 s assumed in this analysis. Figure X.4.6 showed the corresponding calculations of the neutron fluxes with the insertion time of 20 minutes. The reactivity variation is so slow that it allows the delayed neutrons in the subcritical assembly to catch up during the transient. The transient neutron fluxes agree with the steady state flux with an error around 0.1%.

These numerical analyses have shown that in the KIPT subcritical assembly, with the fuel assembly insertion time of around few ten minutes, the flux-to-current ratio method can use the instantly averaged transient neutron fluxes to track the reactivity variations while loading the fuel assemblies into the subcritical assembly.

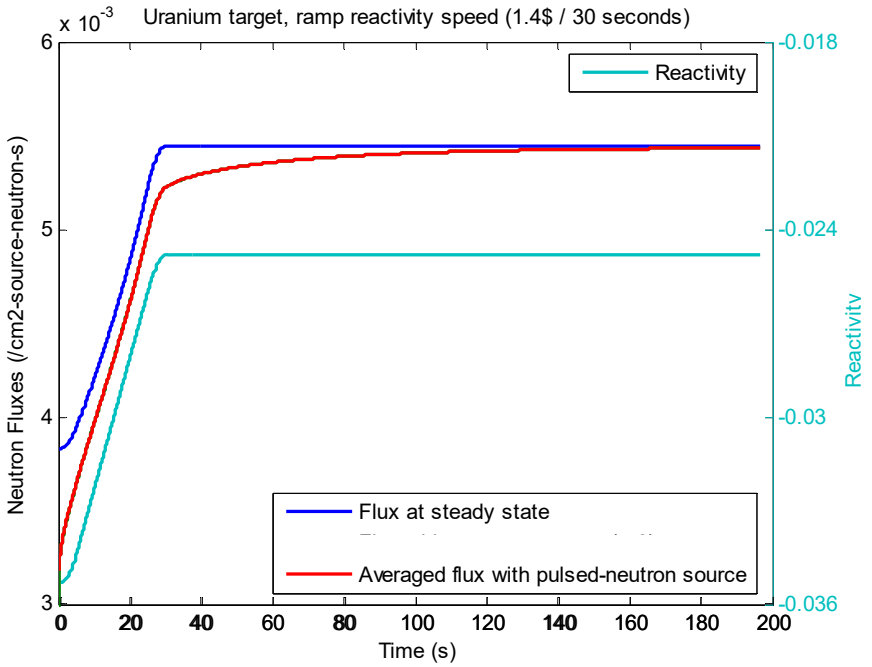

Figure X.4.2. Point kinetics calculations of the averaged neutron fluxes over the pulse period, the neutron fluxes with a constant source (t>0), and the steady state neutron fluxes for the reactivity insertion in the KIPT subcritical assembly with the natural uranium target and 36 fuel assemblies

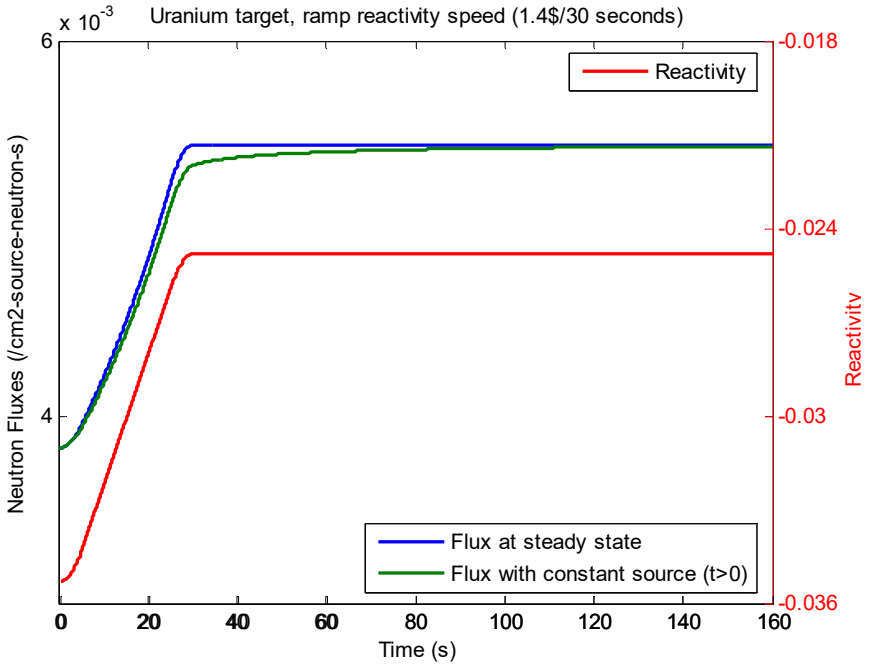

Figure X.4.3. Point kinetics calculations of the neutron fluxes with a constant neutron source and the steady state neutron fluxes for the reactivity insertion within 30s in the KIPT subcritical assembly with the natural uranium target and 36 fuel assemblies loaded

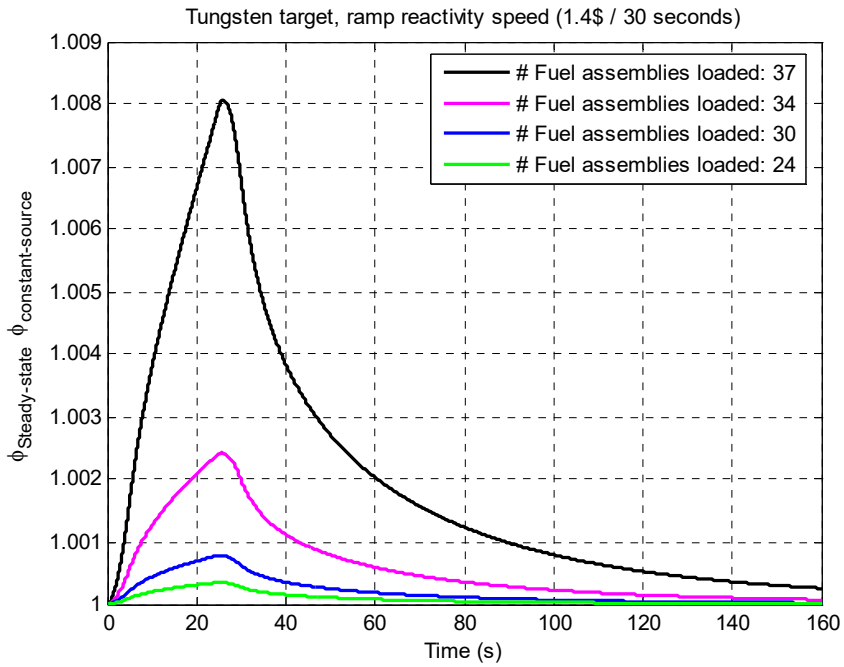

Figure X.4.4. Comparisons of the point kinetics calculations of the transient and steady state neutron flux with one extra fuel assembly inserted into the KIPT subcritical assembly with the tungsten target and 24 to 37 fuel assemblies

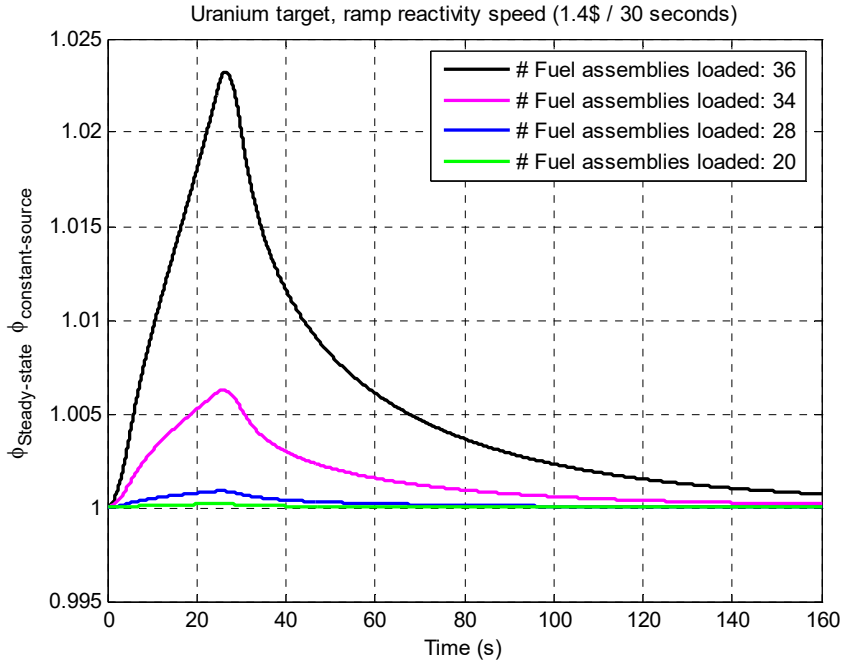

Figure X.4.5. Comparisons of the point kinetics calculations of the transient and steady state neutron flux while one extra fuel assembly inserted into the KIPT subcritical assembly with the natural uranium target and 20 to 36 fuel assemblies

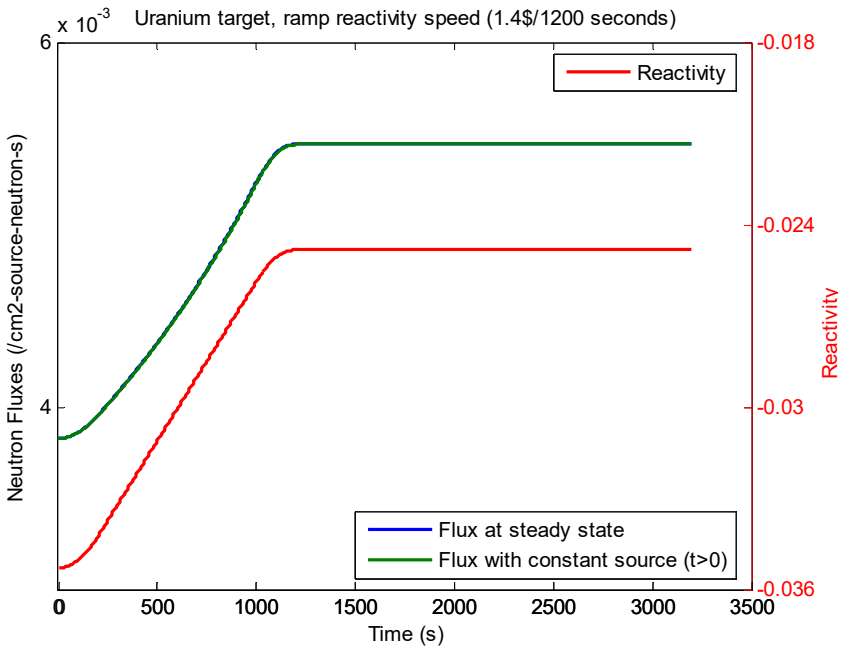

Figure X.4.6. Point kinetics calculations of the neutron fluxes with a constant neutron source and the steady state neutron fluxes for reactivity insertion within 1200s in the KIPT subcritical assembly with the natural uranium target and 36 fuel assemblies

The averaged neutron fluxes can be measured very accurately and very quickly. For instance, for the KIPT configuration with 20 fuel assemblies loaded, the average counting rate in the selected U-235 fission chambers within a pulse period is estimated to be about 103 counts/second. It only takes about 2 minutes to measure the average neutron fluxes with statistical error ≤ 1%, compared to hours required for the area-ratio method.

The flux-to-current ratio method is based on the point kinetics approximations together with a further extension of the approximation by replacing the total power of the subcritical assembly with the detector responses at certain locations. For a subcritical system away from critical, it is expected that the results obtained from this method are also dependent on the detector locations and the detector types.

The spatial dependence of the flux-to-current ratio method can be studied using the KIPT Monte Carlo model. In particular, the flux-to-current ratios between the reference state and the new states can be simulated with a Monte Carlo model to give the numerically calculated reactivity $\rho^{Flux-to-current}(r_d)$ at the detector location r_d. Meanwhile, for the subcritical assembly with different number of fuel assemblies loaded, its "true" reactivity ρ^{MCNP} can also be obtained by the direct Monte Carlo k-eigenvalue calculations. Therefore, the spatial dependence of the flux-to-current ratio method can be characterized by the spatial correction factor $f(r_d)$:

$$f^{cal}(r_d) = \frac{\rho^{MCNP}}{\rho^{Flux-to-current}(r_d)}. \quad (7)$$

The calculated spatial correction factor $f(r_d)$ is utilized to mitigate the spatial effects in the reactivities obtained from the experiment at the detector position r_d and for each subcritical assembly configuration:

$$\rho^{correct}(r_d) = \rho^{exp}(r_d) \times f^{cal}(r_d) \quad (8)$$

Where $\rho^{exp}$is the experimental value obtained at detector location r_d using Equation (5). For the KIPT neutron source facility, Monte Carlo simulations were performed to calculate the correction factor *f* at many detector positions. It is found that the flux-to-current ratio method has a strong spatial dependence. The spatial corrections are larger when the detectors are closer to the external source region and are much smaller at those detector positions away from the external neutron source. In addition, studies have found that optimal detector positions where the spatial corrections can be kept small for all the fuel loading cases exist in the KIPT neutron source facility. Therefore, the second set of six fission chambers are placed at the optimal position $(r, z) = (54.0, 72.5)$ cm. For the KIPT subcritical assembly using the natural uranium target with 37 fuel assemblies loaded, the neutron flux level at this position is calculated to be the highest among all the fuel loading states and is about 1.4x10^{10} n/cm^{2}s when the electron beam operated at full power of 100 kW. The corresponding background photon flux level is 2.9 x 10^{11} p/cm^{2}s. For the first set of neutron detectors, the calculated neutron flux level is lower, and it is ~6.2 x10^9 n/cm^{2}s.

The correction factors at the optimal detector positions are shown in Figs. X.4.7 and X.4.8. Almost all the spatial corrections are within or around 5%. The spatial correction factors have been averaged among the three detectors which have the same neutron sensitivities, i.e., detectors 1, 3, and 5; and detectors 2, 4 and 6. The average values are labeled as “avg135” or “avg246” and all the values are very close to 1.0 as shown in both figures. In other words, for the KIPT fuel loading steps with k_{eff} of the subcritical assembly estimated to in the range of 0.75 to 0.975 with the uranium target, and from 0.8 to 0.95 with the tungsten target, the averaged reactivities obtained from the flux-to-current ratio method at the optimal detector locations agree with the Monte Carlo k-eigenvalue calculated reactivities very well with a very small difference of less than 2%.

The correction factors shown in Figs. X.4.7 and X.4.8 are calculated by selecting the subcritical assembly initial state as the reference state. At this reference state, the reactivity obtained by the area-ratio method has already been found to have large spatial effects. It is also known that at this initial reference state, it is difficult to accurately measure the reactivity using the area method. Therefore, during the successive fuel loading process, the pulsed-neutron experiments are performed not only at the initial reference state but also at several intermediate fuel loading steps and at the final fuel loading step to provide updated reference points to the flux-to-current ratio method. The absolute reactivities at these reference states are determined by the same procedure described previously for the initial reference state. The selected reference states are listed in Table X.4.1 for the two KIPT configurations, respectively.

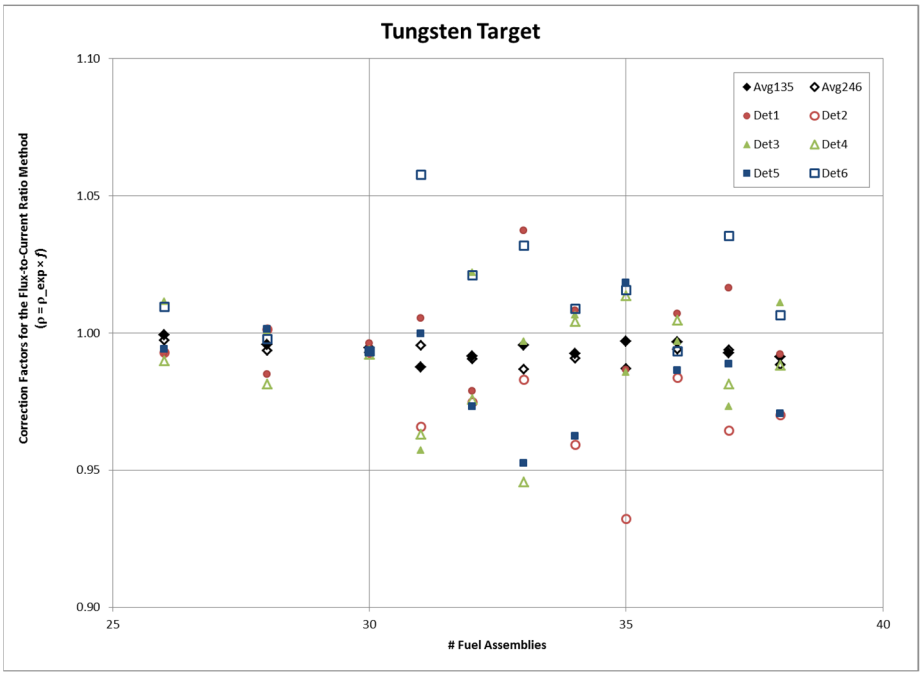

Figure X.4.7. Monte Carlo calculated correction factors for the flux-to-current ratio method with pulsed-neutron experiment performed in the KIPT neutron source facility which has a tungsten target at the center and loaded from 24 to 38 fuel assemblies respectively.

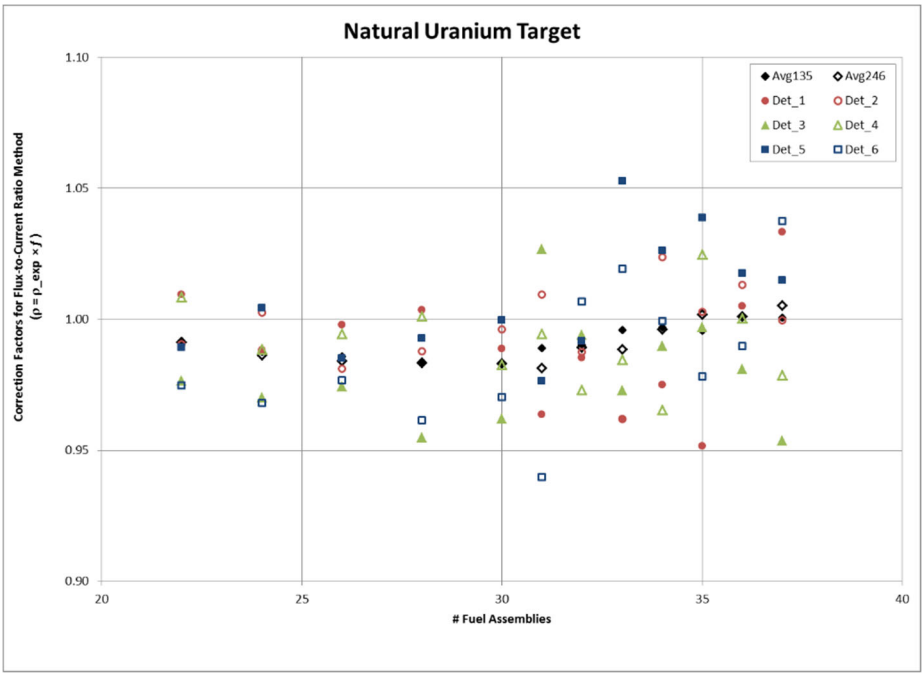

Figure X.4.8. Monte Carlo calculated correction factors for the flux-to-current ratio method with pulsed-neutron experiment performed in the KIPT neutron source facility which has a natural uranium target at the center and loaded from 20 to 37 fuel assemblies respectively.

Table X.4.1. Selected reference states for the flux-to-current ratio method in KIPT neutron source facility.

Reference States	Tungsten Target				Uranium Target			
	I	1	2	F	I	1	2	F
# Fuel Assembly	24	30	34	38	20	28	34	37

The correction factors based on the multi-reference points are listed in Table X.4.2 and X.4.3, which are calculated based on the most recent reference state. Most of these correction factors are calculated without directly simulating the detector sensitive material U-235 in the detector sensitive zone. Except at the final fuel loading states for both configurations, the correction factors are then labeled as "-U235" and they are consistent with the correction factors obtained without simulating the detector sensitive material U-235 and using the same initial reference state.

To reduce the spatial effects in the flux-to-current ratio method, an example is shown to determine the reactivity $\rho_{30}^{i}(r_d)$ of the subcritical assembly using the calculated correction factor at r_d:

$$\rho_{30}^{i}(r_d) = \rho_{28}^{ref}\left[\frac{I_{30}}{I_{28}}\right]\left[\frac{<\epsilon,\phi_{28}(r_d)>_E}{<\epsilon,\phi_{30}(r_d)>_E}\right] \times f_{30}^{i}(r_d), \quad (9)$$

Where, the reactivity ρ_{28}^{ref} is the closest reference reactivity obtained from the area-ratio method after the spatial corrections. The $f_{30}^{i}(r_d)$ is the one listed in Table X.4.3 with 30 fuel assemblies loaded. The initial estimation of the reactivities of this KIPT subcritical assembly with 30 fuel assemblies with the natural uranium target is calculated as the mean value of the reactivities among all the detector positions:

$$\rho_{30}^{i} = \frac{1}{n_{r_d}}\sum_{\mathrm{r_d}} \rho_{30}^{i}(r_d). \quad (10)$$

Similarly, the pulsed-neutron experiment is performed at the final reference state. A new estimation of the reactivities for each fuel loading step were obtained with the correction factors listed Tables X.4.4 and X.4.5. For instance, the new estimation of the reactivity for the KIPT subcritical assembly using the natural uranium target and 30 fuel assemblies loaded can be calculated as:

$$\rho_{30}^{n}(r_d) = \rho_{37}^{ref}\left[\frac{I_{30}}{I_{37}}\right]\left[\frac{<\epsilon,\phi_{37}(r_d)>_E}{<\epsilon,\phi_{30}(r_d)>_E}\right] \times f_{30}^{n}(r_d), \quad (11)$$

where, $f_{30}^{n}$is the correction factor listed in Table X.4.5, and the new estimation is the average among the values of all detector positions:

$$\rho_{30}^{n} = \frac{1}{n_{r_d}}\sum_{\mathrm{r_d}} \rho_{30}^{n}(r_d). \quad (12)$$

Tables X.4.6 and X.4.7 have the calculated average neutron counts of the six U-235 fission chambers above the graphite reflector for each fuel loading step with the tungsten target and the natural uranium target, respectively. The neutron detector sensitivity is assumed to be 10^{-3} counts/neutron. The electron accelerator beam power is assumed to be 10 W for the two KIPT targets.

The KIPT neutron source facility utilizes the 19.7% U235 UO_2-Al fuel. Due to the spontaneous fission reactions of the U238 fuel atoms, a background fission neutron source always exists and might register counts in the neutron detectors. The neutron flux at the detector position due to one background spontaneous fission source neutron in the subcritical assembly has been calculated to be around 2.7×10^{-6} n/cm^2-source if 20 fuel assemblies are loaded, or 2.55×10^{-5} n/cm^2-source if 37 fuel assemblies are loaded with uranium target. In addition, the total number of fission source neutrons emitted per each fuel assembly is estimated to be about 2.32 source neutrons per second. Thus, the neutron fluxes at the detector positions due to the presence of the background spontaneous fission source are ~1.266×10^{-4} n/cm^2-s at the initial fuel loading state and ~2.2×10^{-2} n/cm^2-s at the full fuel loading state for the configuration with the natural uranium target. Both values are negligible comparing the number of counts registered from using the 10 W electron beam power.

The selected detector position $(r, z) = (54.0, 72.5)$ is an optimal for the flux-to-current ratio method. At these positions, as demonstrated in Figs. X.4.9 and X.4.10, the inversed-neutron-flux curve can be utilized to extrapolate the reactivity of the subcritical system. In those figures, the neutron fluxes are the average values of neutron fluxes of the six detectors from the Monte Carlo fixed-source calculations at each fuel loading case and they are normalized to the values obtained with the maximum fuel loading case for the KIPT configurations. Similarly, the inversed-neutron-flux curve is also obtained at those detectors in the neutron channels. Clearly, at the optimal detector position, from the initial reference state to the final full loading state, the calculated 1/n flux curve and the reactivity curve matches each other very well. The number of fuel assemblies to reach critical derived from both curves agree with each other and they are 3 fuel assemblies more than the maximum fuel assemblies designed in the subcritical assembly for the two KIPT configurations. The inversed-neutron-flux curves at the first detector positions $(r, z) = (107.0, 25.0)$ in the neutron channels are also plotted in the same figures for the two KIPT configurations. Those curves are deviated from the reactivity curve, and thus less optimal to the flux-to-current ratio method.

Table X.4.2. Correction factors f^i for the flux-to-current ratio method referred to the initial and intermediate reference states in the KIPT neutron source facility with the tungsten target ($\rho^i = \rho^{exp} \times f^i$).

# Fuel Assembly		24	26	28	30	31	32	33
Detector Position (r,z) = (54.0,72.5)	DET1		0.993±0.002	0.985±0.002	0.996±0.002	1.009±0.002	0.982±0.002	1.041±0.001
	DET2		0.993±0.002	1.001±0.002	0.993±0.002	0.973±0.002	0.982±0.002	0.990±0.001
	DET3		1.011±0.002	1.001±0.002	0.994±0.002	0.963±0.002	1.028±0.002	1.003±0.001
	DET4		0.990±0.002	0.981±0.002	0.992±0.002	0.971±0.002	0.983±0.002	0.953±0.002
	DET5		0.994±0.002	1.002±0.002	0.993±0.002	1.006±0.002	0.980±0.002	0.959±0.002
	DET6		1.010±0.002	0.998±0.002	0.993±0.002	1.065±0.002	1.028±0.002	1.039±0.001
	AVG135		0.999±0.010	0.996±0.009	0.995±0.002	0.993±0.026	0.997±0.027	1.001±0.041
	AVG246		0.998±0.011	0.994±0.011	0.993±0.001	1.003±0.054	0.998±0.026	0.994±0.043
# Fuel Assembly		34	35	36	37	38	38-Initial-Reference	38-U235
Detector Position (r,z) = (54.0,72.5)	DET1	1.012±0.002	0.979±0.002	0.999±0.002	1.008±0.002	0.984±0.002	0.992±0.002	1.002±0.004
	DET2	0.966±0.002	0.972±0.002	1.026±0.002	1.006±0.002	1.011±0.002	0.970±0.002	0.978±0.004
	DET3	1.012±0.002	0.979±0.002	0.990±0.002	0.967±0.002	1.004±0.002	1.011±0.002	1.005±0.004
	DET4	1.012±0.002	1.009±0.002	1.000±0.002	0.977±0.002	0.984±0.002	0.988±0.002	0.985±0.004
	DET5	0.969±0.002	1.058±0.002	1.025±0.002	1.027±0.002	1.009±0.002	0.971±0.002	0.980±0.004
	DET6	1.015±0.002	1.007±0.002	0.985±0.002	1.026±0.002	0.998±0.002	1.007±0.002	1.007±0.004
	AVG135	0.998±0.025	1.005±0.046	1.005±0.018	1.001±0.022	0.999±0.013	0.991±0.002	0.996±0.014
	AVG246	0.998±0.028	0.996±0.021	1.004±0.021	1.003±0.037	0.998±0.014	0.988±0.002	0.990±0.015

Table X.4.3. Correction factors f^i for the flux-to-current ratio method referred to the initial and intermediate reference states in the KIPT neutron source facility with the natural uranium target. ($\rho^i = \rho^{exp} \times f^i$)

# Fuel Assemblies		22	24	26	28	30	31	32
Detector Position (r,z) = (107.0, 25.0)	Det1	1.000±0.002	0.984±0.001	0.969±0.001	0.971±0.001	0.977±0.003	0.966±0.004	0.960±0.005
	Det2	0.974±0.002	0.962±0.001	0.959±0.001	0.939±0.001	1.000±0.003	0.969±0.004	1.022±0.004
	Det3	0.990±0.002	0.964±0.001	0.965±0.001	0.954±0.001	0.984±0.003	1.007±0.004	0.987±0.004
	Avg	0.988±0.013	0.970±0.012	0.965±0.005	0.955±0.016	0.987±0.012	0.981±0.023	0.990±0.031
Detector Position (r,z) = (54.0,72.5)	Det1	1.010±0.002	0.988±0.002	0.998±0.002	1.004±0.002	0.985±0.002	0.960±0.002	0.982±0.002
	Det2	0.990±0.002	1.003±0.002	0.981±0.002	0.988±0.002	1.008±0.002	1.022±0.002	1.000±0.002
	Det3	0.976±0.002	0.970±0.002	0.974±0.002	0.955±0.002	1.007±0.002	1.075±0.002	1.041±0.002
	Det4	1.008±0.002	0.988±0.002	0.994±0.002	1.001±0.002	0.981±0.002	0.993±0.002	0.972±0.002
	Det5	0.989±0.002	1.004±0.002	0.985±0.002	0.993±0.002	1.007±0.002	0.984±0.002	0.999±0.002
	Det6	0.975±0.002	0.968±0.002	0.977±0.002	0.961±0.002	1.009±0.002	0.977±0.002	1.047±0.002
	Avg135	0.992±0.017	0.988±0.017	0.986±0.012	0.984±0.026	1.000±0.013	1.006±0.061	1.007±0.031
	Avg246	0.991±0.017	0.986±0.017	0.984±0.009	0.983±0.020	1.000±0.016	0.998±0.023	1.006±0.038
# Fuel Assemblies		33	34	35	36	37	37-Initial-Reference	37-U235
Detector Position (r,z) = (107.0, 25.0)	Det1	0.942±0.005	0.970±0.004	0.960±0.005	1.007±0.006	1.008±0.005	0.951±0.003	
	Det2	1.029±0.005	0.963±0.004	0.967±0.005	0.973±0.006	1.008±0.005	0.962±0.003	
	Det3	0.966±0.005	1.013±0.004	1.042±0.005	1.015±0.006	0.979±0.005	0.896±0.003	
	Avg	0.979±0.045	0.982±0.030	0.990±0.045	0.999±0.022	0.998±0.017	0.936±0.035	
Detector Position (r,z) = (54.0,72.5)	Det1	0.958±0.002	0.971±0.002	0.976±0.002	1.031±0.003	1.060±0.002	1.033±0.002	1.027±0.004
	Det2	0.974±0.002	1.036±0.002	0.980±0.001	0.990±0.002	0.976±0.002	1.000±0.002	0.999±0.004
	Det3	1.019±0.002	1.037±0.002	1.007±0.002	0.991±0.003	0.963±0.002	0.954±0.002	0.952±0.004
	Det4	0.983±0.002	0.964±0.002	1.062±0.002	1.036±0.003	1.014±0.002	0.979±0.002	0.984±0.004
	Det5	1.060±0.002	1.033±0.002	1.012±0.002	0.992±0.003	0.989±0.002	1.015±0.002	1.011±0.004
	Det6	1.060±0.002	1.039±0.002	0.979±0.002	0.991±0.003	1.038±0.002	1.038±0.002	1.031±0.004
	Avg135	1.012±0.051	1.014±0.037	0.998±0.020	1.004±0.023	1.004±0.050	1.001±0.042	0.997±0.039
	Avg246	1.006±0.047	1.013±0.043	1.007±0.048	1.006±0.027	1.009±0.031	1.005±0.030	1.005±0.024

Table X.4.4. Correction factors *f* for the flux-to-current ratio method referred to the final reference state in the KIPT neutron source facility with the tungsten target. ($\rho = \rho^{exp} \times f$)

# Fuel Assemblies		24	26	28	30	31	32
Detector Position (r,z) = (54.0,72.5)	Det1	1.008±0.002	1.000±0.002	0.993±0.002	1.004±0.002	1.013±0.002	0.986±0.002
	Det2	1.031±0.002	1.023±0.002	1.032±0.002	1.023±0.002	0.996±0.002	1.005±0.002
	Det3	0.989±0.002	1.000±0.002	0.990±0.002	0.983±0.002	0.947±0.002	1.011±0.002
	Det4	1.012±0.002	1.002±0.002	0.993±0.002	1.004±0.002	0.975±0.002	0.987±0.002
	Det5	1.030±0.002	1.024±0.002	1.032±0.002	1.023±0.002	1.030±0.002	1.003±0.002
	Det6	0.993±0.002	1.003±0.002	0.991±0.002	0.987±0.002	1.051±0.002	1.014±0.002
	Avg135	1.009±0.021	1.008±0.014	1.005±0.023	1.004±0.020	0.997±0.044	1.000±0.012
	Avg246	1.012±0.019	1.009±012	1.006±0.023	1.005±0.18	1.007±0.039	1.002±0.014
# Fuel Assemblies		33	34	35	36	37	
Detector Position (r,z) = (54.0,72.5)	Det1	1.045±0.002	1.016±0.002	0.994±0.002	1.015±0.002	1.024±0.002	
	Det2	1.013±0.002	0.989±0.002	0.961±0.002	1.014±0.002	0.994±0.002	
	Det3	0.986±0.002	0.996±0.002	0.975±0.002	0.986±0.002	0.963±0.002	
	Det4	0.957±0.002	1.016±0.002	1.026±0.002	1.017±0.002	0.993±0.002	
	Det5	0.981±0.002	0.991±0.002	1.049±0.002	1.016±0.002	1.019±0.002	
	Det6	1.025±0.002	1.002±0.002	1.009±0.002	0.987±0.002	1.029±0.002	
	Avg135	1.004±0.036	1.001±0.013	1.006±0.039	1.006±0.017	1.002±0.034	
	Avg246	0.998±0.036	1.002±0.014	0.998±0.034	1.006±0.016	1.005±0.020	

Table X.4.5. Correction factors *f* for the flux-to-current ratio method referred to the final reference state in the KIPT neutron source facility with the natural uranium target. ($\rho = \rho^{exp} \times f$)

# Fuel Assemblies		20	22	24	26	28	30
Detector Position (r,z) = (107.0, 25.0)	Det1	1.052±0.003	1.052±0.003	1.035±0.003	1.019±0.003	1.022±0.003	0.998±0.005
	Det2	1.040±0.003	1.013±0.003	1.001±0.003	0.998±0.003	0.977±0.003	0.976±0.004
	Det3	1.116±0.003	1.104±0.003	1.075±0.003	1.077±0.003	1.064±0.003	1.047±0.004
	Avg	1.069±0.041	1.056±0.046	1.037±0.037	1.031±0.041	1.021±0.044	1.007±0.036
Detector Position (r,z) = (54.0,72.5)	Det1	0.968±0.002	0.977±0.002	0.956±0.002	0.966±0.002	0.971±0.002	0.957±0.002
	Det2	1.000±0.002	0.991±0.002	1.003±0.002	0.982±0.002	0.988±0.002	0.997±0.002
	Det3	1.049±0.002	1.024±0.002	1.017±0.002	1.022±0.002	1.001±0.002	1.009±0.002
	Det4	1.022±0.002	1.030±0.002	1.010±0.002	1.016±0.002	1.023±0.002	1.004±0.002
	Det5	0.985±0.002	0.975±0.002	0.989±0.002	0.971±0.002	0.978±0.002	0.985±0.002
	Det6	0.964±0.002	0.939±0.002	0.933±0.002	0.941±0.002	0.927±0.002	0.935±0.002
	Avg135	1.001±0.043	0.992±0.028	0.988±0.030	0.986±0.031	0.984±0.016	0.983±0.026
	Avg246	0.995±0.029	0.987±0.046	0.982±0.043	0.980±0.037	0.979±0.049	0.979±0.038
# Fuel Assemblies		31	32	33	34	35	36
Detector Position (r,z) = (107.0, 25.0)	Det1	0.987±0.005	0.982±0.005	0.9620.006	0.992±0.005	0.952±0.005	0.999±0.005
	Det2	0.947±0.005	0.998±0.005	1.005±0.005	0.992±0.005	0.960±0.004	0.966±0.005
	Det3	1.072±0.005	1.050±0.005	1.028±0.005	1.022±0.005	1.065±0.004	1.038±0.005
	Avg	1.002±0.064	1.010±0.036	0.998±0.033	1.002±0.017	0.992±0.063	1.001±0.036
Detector Position (r,z)=(54.0,72.5)	Det1	0.933±0.002	0.954±0.002	0.931±0.002	0.944±0.002	0.921±0.002	0.973±0.003
	Det2	1.010±0.002	0.988±0.002	0.962±0.002	1.024±0.002	1.003±0.002	1.014±0.003
	Det3	1.077±0.002	1.042±0.002	1.020±0.002	1.038±0.002	1.045±0.002	1.029±0.003
	Det4	1.016±0.002	0.994±0.002	1.006±0.002	0.986±0.002	1.047±0.002	1.022±0.003
	Det5	0.962±0.002	0.977±0.002	1.037±0.002	1.011±0.002	1.023±0.002	1.003±0.003
	Det6	0.906±0.002	0.970±0.002	0.983±0.002	0.963±0.002	0.943±0.002	0.954±0.003
	Avg135	0.990±0.076	0.991±0.046	0.996±0.057	0.998±0.049	0.997±0.066	1.001±0.028
	Avg246	0.977±0.062	0.984±0.012	0.984±0.022	0.991±0.031	0.998±0.052	0.997±0.037

Table X.4.6. Monte Carlo calculated detector counting rates (counts/s) from 10 W electron beam power using the tungsten target at different fuel loading steps

# of Fuel Assemblies	Detector Position (r,z)=(54,72.5)	# of Fuel Assemblies	Detector Position (r,z)=(54,72.5)
24	83	33	182
26	93	34	210
28	106	35	249
30	122	36	305
31	138	37	365
32	158	38	450

Table X.4.7. Monte Carlo calculated detector counting rates (counts/s) from 10 W electron beam power using the uranium target at different fuel loading steps

# of Fuel Assemblies	Detector Position (r,z) (107,25)	Detector Position (r,z) (54,72.5)	# of Fuel Assemblies	Detector Position (r,z) (107,25)	Detector Position (r,z) (54,72.5)
20	60	103	32	206	371
22	70	121	33	245	445
24	94	146	34	298	546
26	100	175	35	385	707
28	122	214	36	529	969
30	151	271	37	755	1377
31	172	313			

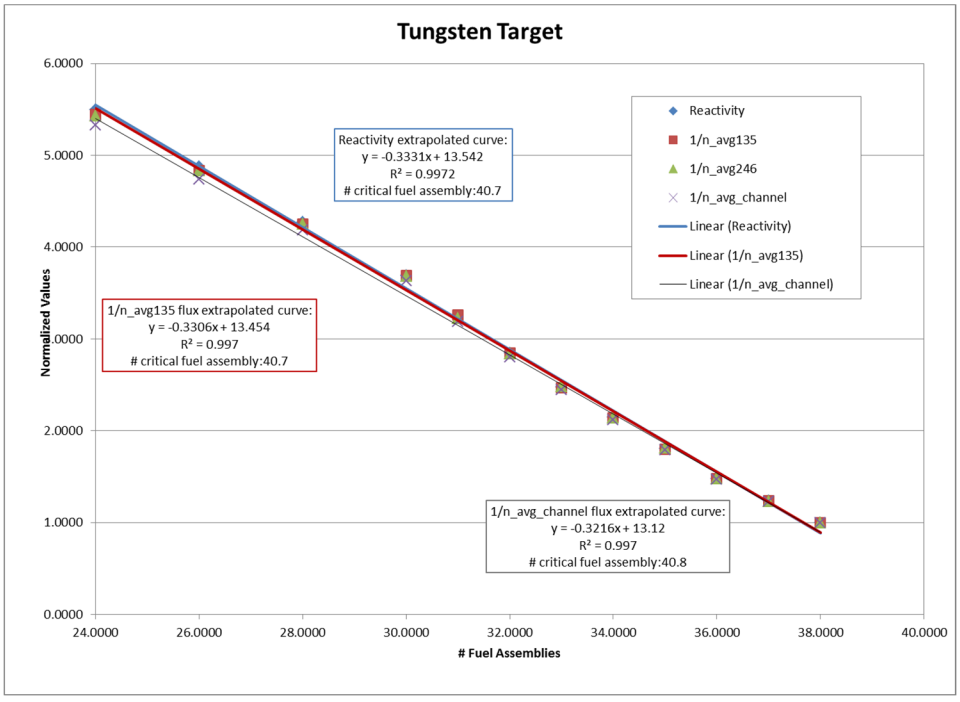

Figure X.4.9. The comparison of the calculated 1/n inversed-neutron-flux curve and the calculated reactivity curve of the KIPT neutron source facility using the tungsten target.

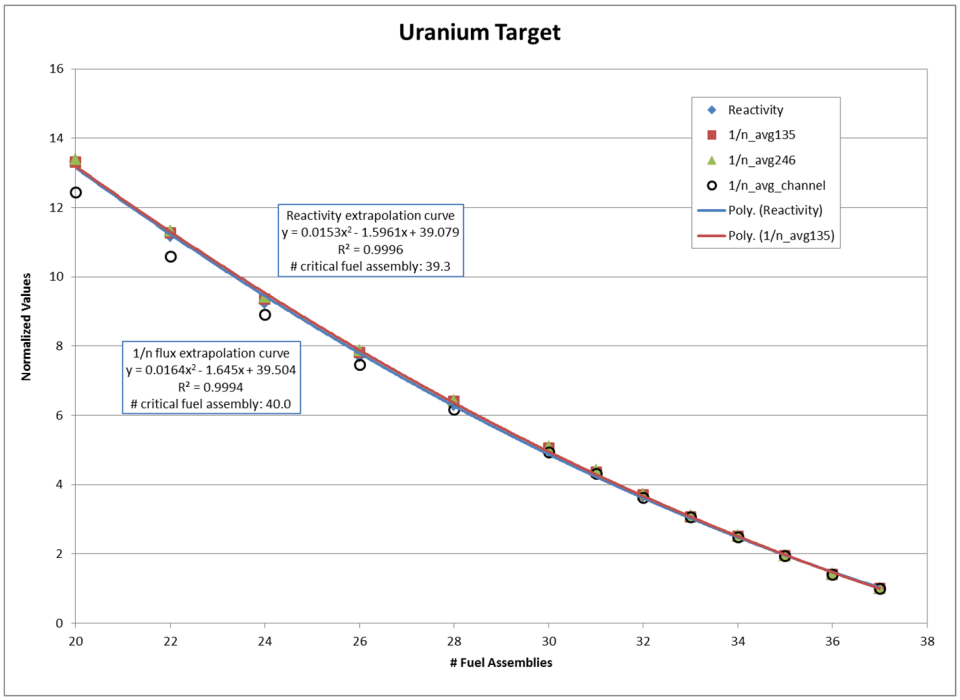

Figure X.4.10. The comparison of the calculated 1/n inverse-neutron-flux curve and the calculated reactivity curve of the KIPT neutron source facility using the natural uranium target.

The flux-to-current ratio method is considered to monitor the reactivity of the subcritical assembly not only while loading fuel assembly into the subcritical assembly, but also when the subcritical assembly is operated at the high or full power. At this state, the linear accelerator is operated with high frequency around 625 Hz. Due to the very short period of each neutron pulses, the prompt neutrons in the KIPT subcritical assembly will not die out completely within the pulse period and will be accumulated as well as the delayed neutrons. Monte Carlo simulations have been performed to calculate the neutron fluxes with the very high frequency neutron pulses at the detector positions. Like in the low frequency case, the subcritical assembly will also reach an equilibrium state after thousands of pulses. The time-dependent structure of the neutron fluxes at the selected detector positions has an asymptotic shape as numerically calculated in Figs. X.4.11 and X.4.12. The detector counting rates are normalized by assuming that the electron accelerator beam power is 100 KW, and the U235 fission chamber sensitivity is about 10^{-6} cps/neutron. Within each pulse period, the neutron fluxes are not a constant but slowly vary as a function of time.

Monte Carlo simulations have also been performed to calculate the neutron detector responses corresponding to the source transient with the accelerator beam turned on at t=0. The subcritical assembly has the natural uranium target and 37 fuel assemblies. The Monte Carlo simulation results shown in Fig. X.4.13 confirm that the neutron fluxes still have an oscillated component which has the same frequency of the external source, but with much smaller amplitudes compared with the amplitudes from the low frequency

operation. The averaged neutron fluxes within the pulse period are about the same as the fluxes calculated at the low frequency mode, and asymptotically approach the steady state neutron fluxes after the subcritical assembly reaching an equilibrium state. In other words, the time dependent behavior of the average neutron flux within a pulse period (the detector responses) is independent of the choices of the external neutron source frequency, as shown in Fig. X.4.14. Therefore, the average of the transient neutron fluxes within the pulse period can be utilized in the flux-to-current ratio method to monitor the reactivity variations of the KIPT subcritical assembly operated with the low and the high pulse frequencies.

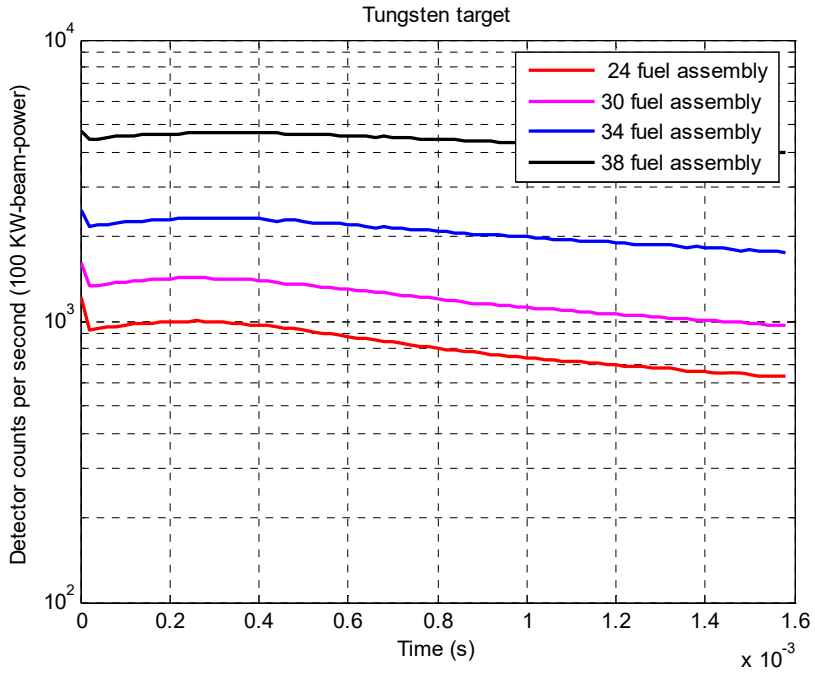

Figure X.4.11. Monte Carlo simulations of the asymptotic detector counting rates in the KIPT subcritical assembly which is driven by a pulsed neutron source with repeating frequency of 625 HZ with the tungsten target and 24-38 fuel assemblies.

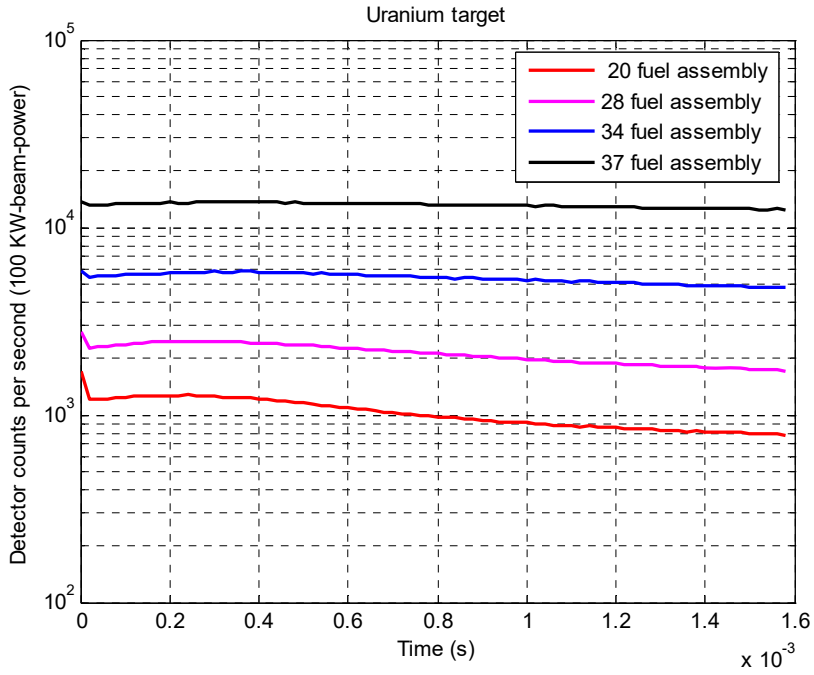

Figure X.4.12. Monte Carlo simulations of the asymptotic detector counting rates in the KIPT subcritical assembly which is driven by a pulsed neutron source with repeating frequency of 625 HZ with the natural uranium target and 20-37 fuel assemblies.

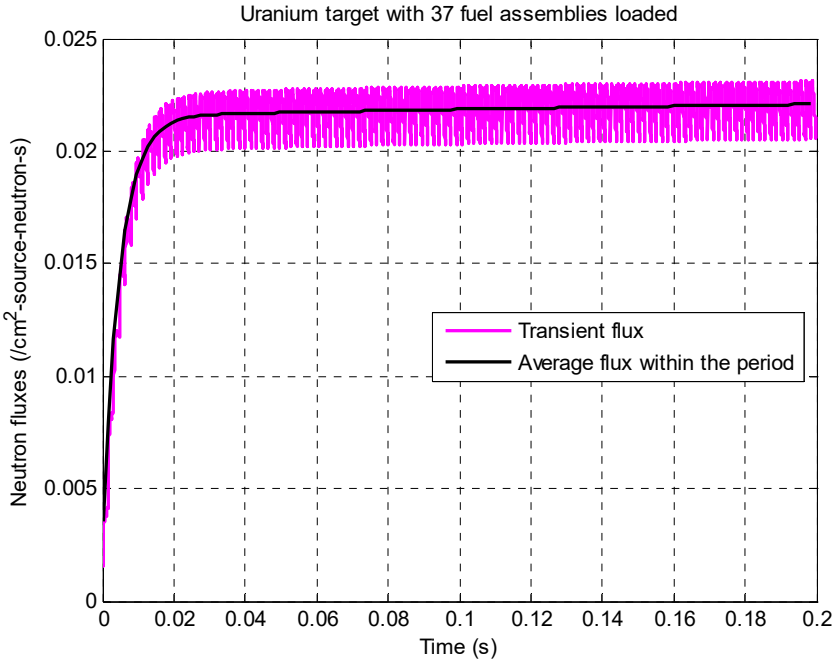

Figure X.4.13. Monte Carlo simulations of the transient neutron fluxes in the KIPT subcritical assembly which is driven by a pulsed neutron source turned on at t=0 with a repeating frequency of 625 HZ with the natural uranium target and 37 fuel assemblies.

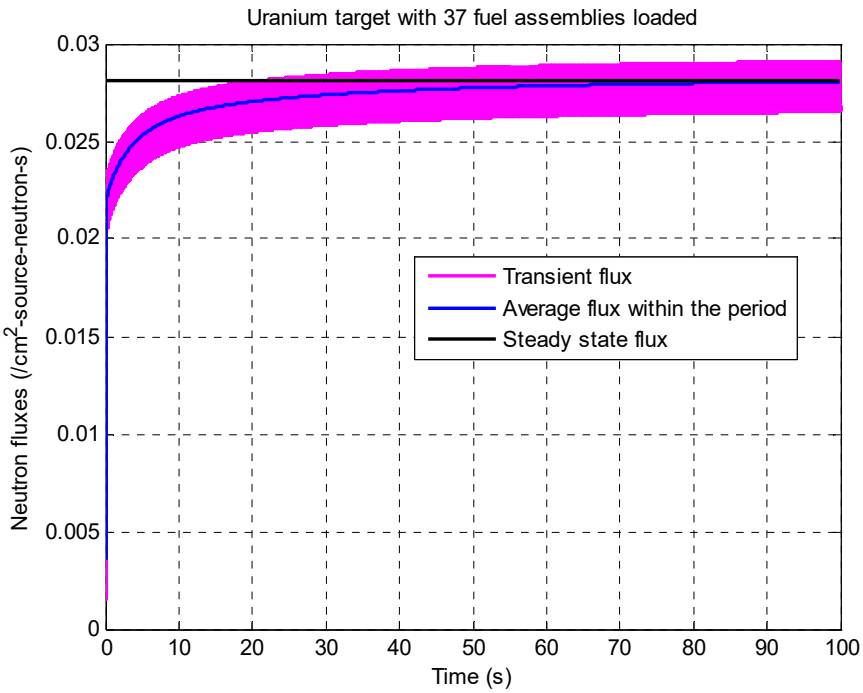

Figure X.4.14. Comparison of Monte Carlo simulated transient neutron flux, its averaged neutron flux, and the steady state neutron flux of the KIPT Subcritical assembly of Figure 26.

X.5 KIPT Subcritical Assembly Analyses Using the Individual Passport Fuel Specifications for Each Assembly Loaded in the Facility with the Tungsten Target and Different Nuclear Data Libraires

New MCNP simulations were performed for the subcritical assembly of the KIPT neutron source facility using the passport data of each loaded fuel assembly with the tungsten target. The individual passport data of each fuel assembly includes the exact active fuel length, the amount of fuel material, the U-235 fuel enrichment, and the main dimensions of the fuel assembly. Such data requires a separate model for each fuel assembly to include such details. In addition, the U-234 concentration was included in the fuel material. The analyses were performed for each fuel loading steps; 4, 8, 12, 16, 18, 20, 22, 24, 26, 28, 30, 31, 32, 33, 34, 35, 36, 37, and 38 fuel assemblies. In addition, the MCNP model was updated to include the neutron channels in closed position to account for the any impact on the neutron detector measurements.

The analyses used nuclear data libraries based on ENDF/B-VII.1 and ENDF/B-VIII.0 to study the impact of the different nuclear data base on the obtained results for the preparation to compare with the obtained experimental results. Figure X.4.1 plots the obtained K_{eff} results obtained with the two different nuclear data libraries. The obtained K_{eff} values are almost identical as shown in Fig. X.5.1, and Tables X.5.1. X.5.2. In addition, the adjoint-weighted kinetics parameters β_{eff} and Λ were also calculated for each fuel loading step to examine its change, which results from the geometrical change of the subcritical assembly. As shown in the two tables, the neutron mean generation time

(Λ) decreases significantly with more fuel assemblies loaded into the subcritical assembly. With more fuel assemblies replacing the dummy water assemblies, the neutron thermalization is reduced and the spectrum is harder. This neutron energy spectrum shift also leads to less importance of the delayed neutrons. Therefore β_{eff} also decreases by ~7%.

Previous correction factors obtained from the numerical simulations ignored the differences of β_{eff} at different fuel loadings. With the updated β_{eff}, the correction factors corresponding to each fuel loading case were recalculated. These data were used in the later analysis with the experimental data. Figure X.5.2. plots the correction factors for each fuel step and each detector including the statistical error, one standard deviation. The correction factors values are getting closer to unity compared with previous calculated correction factors for all the fuel loading cases which further confirms the detector locations selected are optimal. In addition, the values are getting close to unity as the K_{eff} of the subcritical assembly increase, as expected for the improved accuracy close to the critical state. Tables X.5.3 and X.5.4 lists the correction factors values for each detector at each fuel loading step.

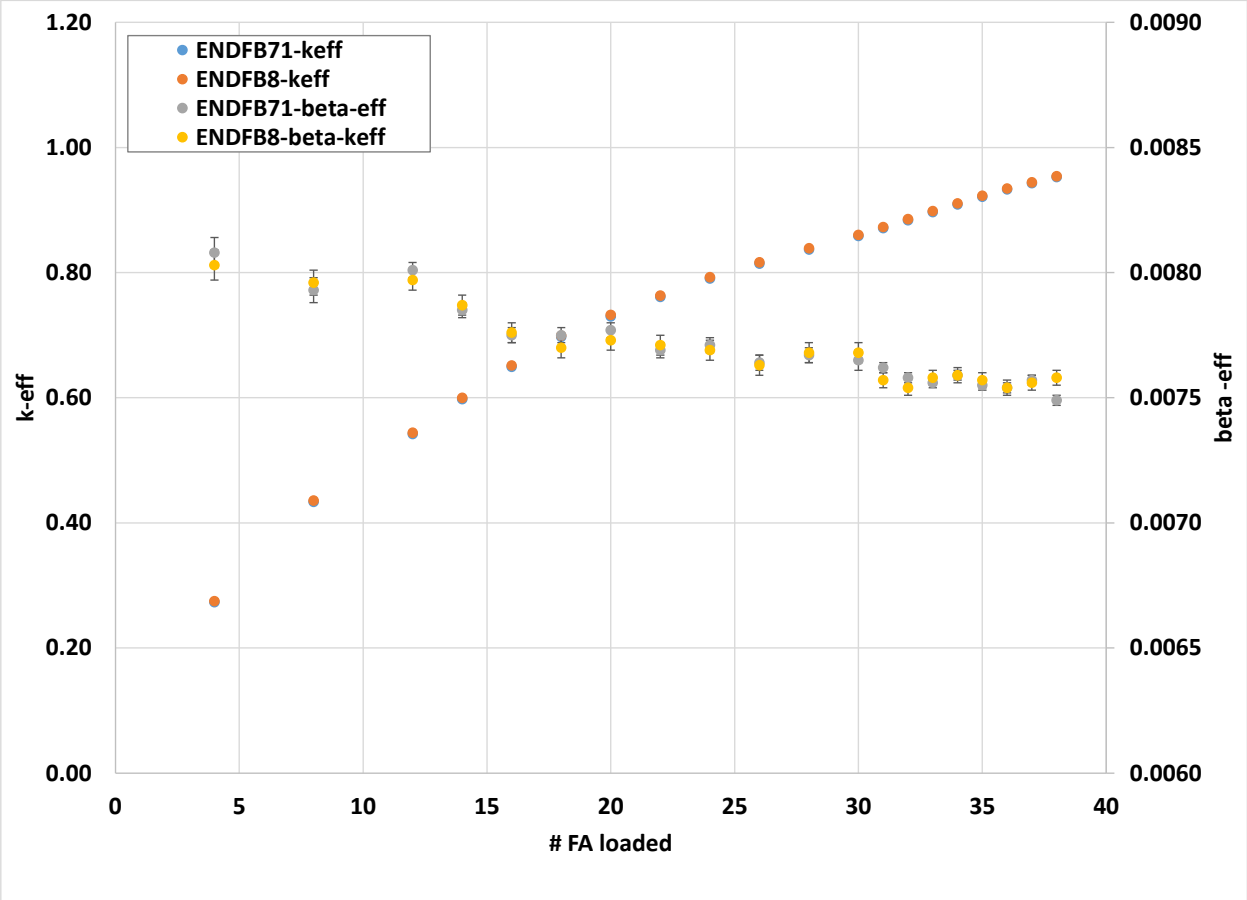

Figure X.5.1. K_{eff} and β_{eff} values for each fuel loading step of the subcritical assembly with the tungsten target based on ENDF/B-VII.1 and ENDF/B-VIII

Table X.5.1. K_{eff}, β_{eff}, and Λ (neutron generation time) values for each fuel loading step of the subcritical assembly with the tungsten target based on ENDF/B-VII.1

# FA	K_{eff}	std	β	std	Λ(ms)	std	ρ^{mcnp}($)
4	0.27322	0.00001	0.00808	0.00006	864.33	1.15	-329.21
8	0.43349	0.00001	0.00793	0.00005	451.75	0.53	-164.80
12	0.54193	0.00001	0.00801	0.00003	314.26	0.25	-105.53
14	0.59755	0.00001	0.00785	0.00003	284.91	0.22	-85.80
16	0.64938	0.00001	0.00775	0.00003	260.78	0.20	-69.67
18	0.69702	0.00001	0.00775	0.00003	240.34	0.18	-56.09
20	0.73008	0.00001	0.00777	0.00003	221.40	0.17	-47.58
22	0.76118	0.00001	0.00769	0.00003	205.04	0.16	-40.80
24	0.79064	0.00001	0.00771	0.00003	191.40	0.15	-34.34
26	0.81429	0.00001	0.00764	0.00003	180.03	0.14	-29.85
28	0.83678	0.00001	0.00767	0.00003	170.23	0.13	-25.43
30	0.85849	0.00002	0.00765	0.00004	161.26	0.18	-21.55
31	0.87096	0.00001	0.00762	0.00002	158.42	0.12	-19.44
32	0.88356	0.00001	0.00758	0.00002	155.88	0.12	-17.39
33	0.89659	0.00001	0.00756	0.00002	153.05	0.12	-15.26
34	0.90895	0.00001	0.00759	0.00002	150.39	0.12	-13.20
35	0.92123	0.00001	0.00755	0.00002	147.90	0.12	-11.33
36	0.93289	0.00001	0.00754	0.00002	145.27	0.11	-9.54
37	0.9429	0.00001	0.00757	0.00002	143.06	0.11	-8.00
38	0.95245	0.00001	0.00749	0.00002	140.86	0.11	-6.67

Table X.5.2. K_{eff}, β_{eff}, and Λ (neutron generation time) values for each fuel loading step of the subcritical assembly with the tungsten target based on ENDF/B-VIII

# FA	K_{eff}	std	β	std	Λ(ms)	std	ρ^{mcnp}($)
4	0.27485	0.00001	0.00803	0.00006	918.84	4.16	-328.56
8	0.43569	0.00001	0.00796	0.00005	474.61	1.85	-162.71
12	0.54430	0.00002	0.00797	0.00004	327.72	1.26	-105.05
14	0.59989	0.00002	0.00787	0.00004	295.68	1.09	-84.75
16	0.65169	0.00002	0.00776	0.00004	267.97	0.96	-68.88
18	0.69929	0.00002	0.00770	0.00004	245.92	0.89	-55.85
20	0.73231	0.00002	0.00773	0.00004	225.24	0.79	-47.29
22	0.76331	0.00002	0.00771	0.00004	210.13	0.77	-40.22
24	0.79274	0.00002	0.00769	0.00004	194.63	0.69	-34.00
26	0.81627	0.00002	0.00763	0.00004	181.48	0.65	-29.50
28	0.83867	0.00002	0.00768	0.00004	171.65	0.64	-25.05
30	0.86023	0.00002	0.00768	0.00004	161.71	0.59	-21.16
31	0.87273	0.00002	0.00757	0.00003	158.42	0.59	-19.26
32	0.88525	0.00002	0.00754	0.00003	157.10	0.59	-17.19
33	0.89822	0.00002	0.00758	0.00003	153.69	0.57	-14.95
34	0.91053	0.00002	0.00759	0.00003	151.24	0.57	-12.95
35	0.92274	0.00002	0.00757	0.00003	147.96	0.55	-11.06
36	0.93438	0.00002	0.00754	0.00003	144.58	0.53	-9.31
37	0.94433	0.00002	0.00756	0.00003	143.11	0.53	-7.80
38	0.95385	0.00002	0.00758	0.00003	140.09	0.52	-6.38

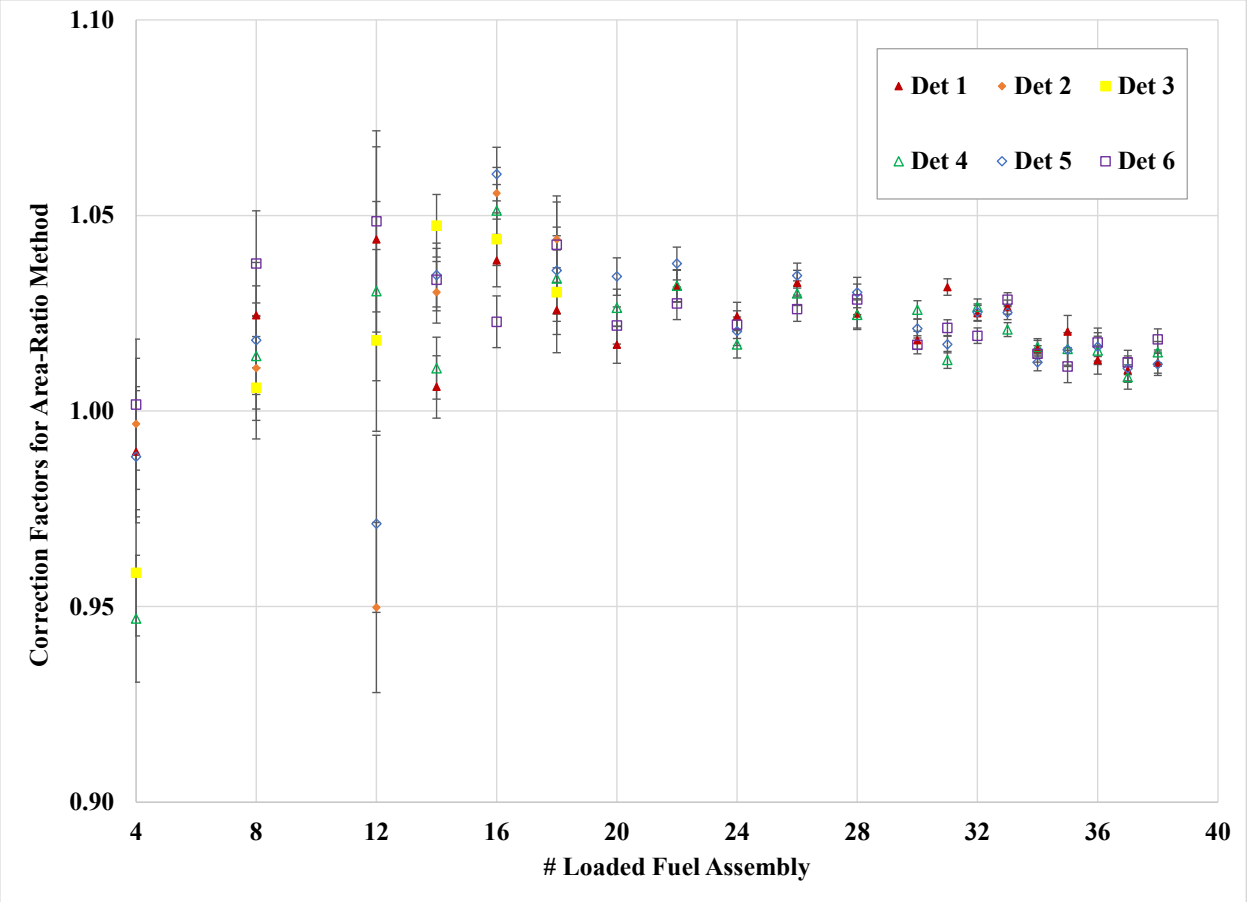

Figure X.5.2. Area method correction factor for each fuel loading step and each detector on the top of the graphite reflector

Table X.5.3. Area method correction factors for each fuel loading step and detector 1, 3, and 5 on the top of the graphite reflector

# FA	Det 1		Det 3		Det 5	
	f	std	f	std	f	Std
4	0.990	0.017	0.959	0.017	0.988	0.017
8	1.025	0.013	1.006	0.013	1.018	0.014
12	1.044	0.023	1.018	0.023	0.971	0.023
14	1.006	0.008	1.047	0.008	1.035	0.008
16	1.038	0.006	1.044	0.006	1.061	0.006
18	1.026	0.011	1.030	0.010	1.036	0.011
20	1.017	0.005	1.023	0.005	1.034	0.005
22	1.032	0.004	1.023	0.004	1.038	0.004
24	1.024	0.003	1.028	0.003	1.020	0.004
26	1.033	0.003	1.034	0.003	1.035	0.003
28	1.025	0.004	1.028	0.004	1.030	0.004
30	1.018	0.002	1.018	0.002	1.021	0.002
31	1.032	0.002	1.014	0.002	1.017	0.002
32	1.025	0.002	1.024	0.002	1.025	0.002
33	1.027	0.002	1.013	0.002	1.025	0.002
34	1.016	0.002	1.015	0.002	1.012	0.002
35	1.020	0.004	1.026	0.004	1.016	0.004
36	1.013	0.004	1.008	0.004	1.016	0.004
37	1.010	0.003	1.004	0.003	1.011	0.003
38	1.012	0.003	1.015	0.003	1.012	0.003

Table X.5.4. Area method correction factors for each fuel loading step and detector 2, 4, and 6 on the top of the graphite reflector

# FA	Det 2		Det 4		Det 6	
	f	std	f	std	f	Std
4	0.997	0.017	0.947	0.017	1.002	0.017
8	1.011	0.013	1.014	0.013	1.038	0.013
12	0.950	0.023	1.031	0.022	1.048	0.022
14	1.030	0.008	1.011	0.008	1.034	0.008
16	1.056	0.006	1.051	0.006	1.023	0.006
18	1.044	0.011	1.034	0.011	1.043	0.010
20	1.027	0.005	1.026	0.005	1.022	0.005
22	1.041	0.004	1.032	0.004	1.028	0.004
24	1.028	0.003	1.017	0.003	1.022	0.003
26	1.033	0.003	1.030	0.003	1.026	0.003
28	1.025	0.004	1.025	0.004	1.029	0.004
30	1.025	0.002	1.026	0.002	1.017	0.002
31	1.020	0.002	1.013	0.002	1.021	0.002
32	1.023	0.002	1.027	0.002	1.019	0.002
33	1.016	0.002	1.021	0.002	1.028	0.002
34	1.015	0.002	1.016	0.002	1.015	0.002
35	1.022	0.004	1.016	0.004	1.011	0.004
36	1.013	0.004	1.016	0.004	1.018	0.004
37	1.005	0.003	1.009	0.003	1.012	0.003
38	1.013	0.003	1.015	0.003	1.018	0.003

X.6 Summary

The procedures of measuring and monitoring the reactivity of the KIPT neutron source facility are presented. In particular, the reactivity of the KIPT subcritical assembly with 24 fuel assemblies loaded are used as the initial state for the configuration with the tungsten neutron target, or 20 fuel assemblies loaded as the initial state for the configuration with the natural uranium neutron target. The pulsed neutron experiments are analyzed in the initial subcritical assembly with two sets of U-235 fission chambers assumed to be utilized to monitor the neutron flux. The first set has three neutron detectors placed in the neutron channels at the midplane of the fuel assemblies, and the second set has six U-235 fission chambers placed at the selected positions which are about 54 cm away from the target center line radially and 12.5 cm above the graphite block. The area-ratio method is expected to be used to obtain the reactivity of the KIPT subcritical assembly at the initial state. This reactivity serves as the initial reference reactivity to the flux-to-current ratio method.

The pulse-neutron experiment was also assumed to be repeated at several intermediate fuel loading states and at the final fuel loading state. Numerical analysis showed that in those experiments, the external pulsed-neutron source can be operated with a low 25-Hz frequency if the number of fuel assemblies loaded is less than 34. The frequency can be

reduced to about 16.7-HZ in the subcritical assemblies with the number of fuel assemblies loaded higher than that.

Numerical calculations showed that for all the pulsed-neutron experiments performed, the accelerator beam power of 10 W is enough to obtain adequate neutron counts within a reasonable time. At this power level, the neutron counting still must be repeated for many thousands of pulse periods to obtain low statistical errors in the measurement of delayed neutron background. Therefore, the area-ratio method is time consuming, and it is not suitable for on-line reactivity monitoring and tracking.

The reactivities of the KIPT subcritical assembly can be monitored and measured consecutively while more fuel assemblies are loaded into the subcritical assembly after the initial states. The flux-to-current ratio method can be utilized to obtain the relative reactivity of the subcritical assembly at each fuel loading state to the initial reference state. Because the area-ratio method is always more accurate when the subcritical assembly is closer to critical state, the pulsed-neutron experiments are expected to be repeated at the selected intermediate fuel loading states to provide updated reference reactivities for the flux-to-current ratio method. Then at each fuel loading state, the initial estimated reactivities of the KIPT subcritical assembly can be obtained using the most recent reference state.

While loading more fuels, the KIPT subcritical assembly is driven by an external electron beam accelerator which is operated at low frequency and low power. The transient neutron fluxes in the subcritical assembly are monitored by the U-235 fission chambers. Due to the pulsed structure of the external source, the transient neutron fluxes also have an oscillated component. However, due to the very short time period of the external neutron source compared with the time to insert the fuel assembly, i.e., 60 ms for the pulse period, and half an hour or more for loading the fuel assembly, the U-235 fission chamber instant readouts averaged with each pulse period can be utilized in the flux-to-current ratio method to obtain the relative reactivities of the subcritical assembly relative to the reference state with negligible errors.

When all the fuel assemblies have been fully loaded, the pulsed-neutron experiments are performed to provide a final updated reference point. The flux-to-current ratio method can be utilized to provide a new estimation of the reactivities of the subcritical assembly for all the previous fuel loading states based on this final reference point.

The measured reactivities obtained from both the area-ratio method and the flux-to-current ratio method are known to have dependence on the detector locations. The spatial correction factors have been numerically calculated at each detector position, at each fuel loading state and for both KIPT configurations using the KIPT Monte Carlo model. To mitigate the spatial effects in the measured reactivities, the spatial correction factors must be applied on the measured reactivities from the area-ratio method before it is taken as the reference value. The correction factors are dependent on the detector locations and have to be applied correspondingly for both the area-ratio method and the flux-to-current ratio method at each detector location.

After all the spatial corrections applied, to combine the reactivities obtained from the different methods and at different detector locations, the actual reactivity of the KIPT subcritical assembly at each fuel loading step is calculated as the mean value of the corrected reactivities among all the detector positions.

In the KIPT subcritical assembly, the second set of U-235 fission chambers are selected to be placed at a position which is optimal to the flux-to-current ratio method. At these detector positions, the spatial corrections are small for all the fuel loading steps, and the inversed-neutron-flux curve are demonstrated to be accurate to extrapolate the reactivities of the subcritical system to critical state.

Finally, the flux-to-current ratio method not only can be utilized in monitoring the reactivity of the subcritical system while it is operated at low power, but also can be utilized while the linear accelerator is operated at the very high frequency “continuous” mode during the normal operation of the facility. The instant detector readouts averaged within the pulse period can be utilized in the flux-to-current ratio method which will be used to monitor the reactivity of the subcritical assembly during other physical transients or due to fuel burnups.

Reference

[X.1] B. PELOWITZ, “MCNP6TM USER’S MANUAL,” LA-CP-11-01708 (2011).
[X.2] B. Glasstone, *Nuclear Reactor Theory*, Van Nostrand Reinhold Co., (1970).
[X.3] Y. Cao and Y. Gohar, “YALINA-booster subcritical assembly pulsed-neutron experiments: data processing and spatial corrections,” ANL-10/22 (2010).
[X.4] R. Soule et al., “Neutronic Studies in Support of Accelerator-Driven Systems: The MUSE Experiments in the MASURCA Facility,” Nucl. Sci. Eng., **148**, 124-152 (2004).
[X.5] Y. Cao, Y. Gohar, and Z. Zhong, “Measuring and monitoring KIPT neutron source facility reactivity,” ANL-15/15 (2015).

Nuclear Science and Engineering Division
Argonne National Laboratory
9700 South Cass Avenue
Lemont, IL 60439

www.anl.gov

Argonne National Laboratory is a U.S. Department of Energy
laboratory managed by UChicago Argonne, LLC